

DRAFT SF 298

1. Report Date (dd-mm-yy)		2. Report Type		3. Dates covered (from... to)	
4. Title & subtitle Tri-Service Conference on Corrosion Proceedings				5a. Contract or Grant #	
				5b. Program Element #	
6. Author(s) Mr Thomas Naguy				5c. Project #	
				5d. Task #	
				5e. Work Unit #	
7. Performing Organization Name & Address				8. Performing Organization Report #	
9. Sponsoring/Monitoring Agency Name & Address Tri-Service Committee on Corrosion USAF WRIGHT-PATTERSON Air Force Base, Ohio 45433 ATTN: Mr. Thomas Naguy				10. Monitor Acronym	
				11. Monitor Report #	
12. Distribution/Availability Statement Approved for Public Release Distribution Unlimited					
13. Supplementary Notes					
14. Abstract					
15. Subject Terms Tri-Service Conference on Corrosion					
Security Classification of			19. Limitation of Abstract	20. # of Pages	21. Responsible Person (Name and Telephone #)
16. Report	17. Abstract	18. This Page			

000955

TRI-SERVICE CONFERENCE ON CORROSION



21-23 JUNE 1994

SHERATON PLAZA HOTEL
ORLANDO, FLORIDA

PROCEEDINGS

PROPERTY OF:

AMPTIAC LIBRARY

19971028 101

REPRODUCTION QUALITY NOTICE

This document is the best quality available. The copy furnished to DTIC contained pages that may have the following quality problems:

- **Pages smaller or larger than normal.**
- **Pages with background color or light colored printing.**
- **Pages with small type or poor printing; and or**
- **Pages with continuous tone material or color photographs.**

Due to various output media available these conditions may or may not cause poor legibility in the microfiche or hardcopy output you receive.

☐

If this block is checked, the copy furnished to DTIC contained pages with color printing, that when reproduced in Black and White, may change detail of the original copy.

Content of the papers presented in this document is the sole responsibility of the author. The Army Materials Technology Laboratory, United States Army accepts no responsibility for any consequences that might result from use of the information presented in this document.

Mention of any trade names or manufacturers in this report shall not be construed as advertising nor as an official endorsement or approval of such products or companies by the United States Government.

This document was prepared under the sponsorship of Tri-Service Committee on Corrosion, The Department of Defense. Neither the United States Government nor any person acting on behalf of the United States Government assumes any liability resulting from the use or publication of the information contained in this document or warrants that such use or publication will be free from privately owned rights.

Approved for public release; distribution unlimited.

CONTENTS

Tri-Service Conference on Corrosion Committee	1
Air Force Corrosion Program Overview - <i>Mr. Richard C. Kinzie</i>	3
USMC Corrosion Prevention and Control (CPAC) Program Overview - <i>Julie A. Jacks</i>	27
Session I: Corrosion Characterization	
Corrosion Consequences of Molten Salt Deposits in Combustion Turbines	
Burning Vanadium Contaminated Liquid Fuel - <i>D.V. Rathnamma and R. Nagarajan</i>	35
Detection and Thickness Characterization by X-Ray Backscatter of Second-Layer	
Corrosion in Aircraft Structures - <i>L.R. Lawson, N. Kim and J.D. Achenback</i>	57
Rapid Inspection of Tubing and Piping Due to Corrosion-Related Problems -	
<i>S.W. Borenstein, R. McCullough and J. Doyle</i>	69
Studies on Corrosion of Aluminum Alloys by JP-10 Fuel Using Electrochemical	
Impedance Spectroscopy - <i>R. Bhardwaj, M. Gunaji and H.D. Beeson</i>	79
Evaluation of the Corrosion Behavior of Storage Container Alloys in Halon	
1301 Replacement Candidate Agents - <i>J.F. Dante, M.R. Stoudt, J.L. Fink,</i>	
<i>C.R. Beauchamp, T.P. Moffat and R.E. Ricker</i>	91
Army Research Office Programs in Beam Technology and Surface	
Engineering - <i>R.R. Reeber</i>	103
Chemistry, Structure and Morphology of Native and Passive Oxide Films on	
Aluminum Rich Amorphous Al-Fe-Ce Alloys - <i>A.N. Mansour and C.A. Melendres</i>	129
Surface Analysis of Anodized Aluminum Panels that have been Painted, Bead Blasted,	
Cleaned, and Treated with a Chemical Conversion Coating - <i>J.J. Jusko</i>	145
Session II: Microbiological Corrosion	
Mechanisms of Reproducible Microbial Pitting of 304 Stainless Steel by a	
Mixed Consortium Containing Sulphate-Reducing Bacteria - <i>P. Angell, J-S Luo and</i>	
<i>D.C. White</i>	157
High-Resolution Microbial Pitting Corrosion Studies Utilizing a Two Dimension	
Scanning Vibrating Electrode Microscope (SVEM) System - <i>P. Angell, J-S Luo and</i>	
<i>D.C. White</i>	169
Microbiologically Influenced Corrosion of Corrosion Resistant Materials -	
<i>B. Little, R. Ray, P. Wagner and E.D. Thomas</i>	183
Evaluation of Nonpolluting Biofouling Control Methods for Titanium Seawater Piping -	
<i>M. Walch, J. Jones-Meehan, S. Hoover, M. Grothaus, M. Mazzola and B. Little</i>	193
Microbiologically Influenced Corrosion (MIC) of Steels: Weight Loss Measurements,	
ESEM/EDS and XRD Analyses - <i>J. Jones-Meehan, J.W. Cofield, B. Little, R. Ray,</i>	
<i>P. Wagner, M. McNeil and J. McKay</i>	205
An Innovative Method for Rapid Detection of Microbiologically Influenced	
Corrosion - <i>G.J. Licina and G. Nekoksa</i>	217
The Use of Electrochemical Impedance Spectroscopy (EIS) and Electrochemical	
Noise Analysis (ENA) for Monitoring of Biocorrosion - <i>F. Mansfield, H. Xiao</i>	
<i>and Y. Wang</i>	229
Identification of Sulfate-Reducing Bacteria in Saline Oil Field and Navy Platform	
Samples by Reverse Sample Genome Probing - <i>G. Voordouw and J. Jones-Meehan</i>	251
Session III: Corrosion Composites and Ceramics	
Nonequilibrium Alloying of Aluminum for Improving the Corrosion Resistance	
of Graphite-Reinforced Metal Matrix Composites - <i>B.A. Shaw, T.R. Schrecengost,</i>	
<i>P.L. Miller, R.G. Wendt and W.C. Moshier</i>	265
A Mechanism for Blistering of Carbon Fiber Composites - <i>S.K. Miriyala, T.J. Rockett,</i>	
<i>W.C. Tucker and R. Brown</i>	279

Microbial Degradation of Polymeric Materials - J-D Gu, T.E. Ford, K.E.G. Thorp and R. Mitchell	291
Biodegradation of Composites Materials - K.E.G. Thorp, A.S. Crasto, J-D Gu and R. Mitchell	303
The Effect of Carbon Fiber Type on the Electrochemical Degradation of Carbon Fiber Polymer Composites - J. Qin, R. Brown, S. Ghiorse and R. Shuford	315
Session IV: Detection and Monitoring of Corrosion NDI & E	
The Use of Superconducting Magnetometry to Detect Corrosion in Aircraft Alloys - D. Li, Y. Ma, W.F. Flanagan, B.D. Lichter and J.P. Wikswo, Jr.	335
OC-ALC Aging Aircraft Disassembly and Hidden Corrosion Detection Program - D.E. Nieser and D. Kraxberger.....	347
Topographic Radioscopic Metrology for Corrosion Mapping - J.C. Brausch.....	351
A Determination of V_2O_5 Activity in Corrosive Molten Vanadate-Sulfate Phases - R.L. Jones and R.F. Reidy	363
Session V: Environmental Cracking	
Yield Strength and Solution Composition Effects on Aqueous Environmental Cracking of Ti-8V-6Cr-4Zr-4Mo-3Al (β phase) - B.P. Somerday, J.A. G. and R.P. Gangloff.....	375
Fracture Toughness and Stress Corrosion Resistance of U-0.75 wt% Ti - C.V. Zabielski and M. Levy	393
The Resistance of High-Strength Alloys to Hydrogen Embrittlement - B.G. Pound	409
Hydrogen Effects on Some Titanium Aluminides at Ambient Temperature - J.A. Smith	421
A Fracture Mechanics Based Approach for Quantifying Corrosion Damage - M.T. Doerfler, A.F. Grandt, Jr., R.J. Bucci and M. Kulak.....	433
Shipboard Exposure Testing of Aircraft Materials - E.S. Tankins, J. Kozol and E. Lee	445
Session VI: Corrosion Mechanisms	
Evaluation of the Stress Corrosion Cracking Susceptibility of Fire Suppressant Storage Container Alloys in Replacement Candidates for Halon 1301 - M.R. Stoudt, J.L. Fink and R.E. Ricker	467
Materials Degradation and Fatigue Under Extreme Condition - L. Ballard, J. Jonas, D. Socie, S. Granick, A. Gellman, K.J. Hsia and J. Shang	479
Growth and Breakdown of Surface Films and Localized Corrosion of Aluminum in Concentrated Chloride Media - J. Lee, A.K. Mal and K. Nobe	487
Mechanism of Ennoblement by Biofilms on Active/Passive Alloys Immersed in Seawater - S.C. Dexter.....	499
Session VII: Coatings	
Nonchromate, Low Density, Waterborne Epoxy Primer - R. Chiang and C. Athanassioulas.....	513
Interfaces of High-Protection Performance Polyaryls-Coated Zinc Phosphated Steels - T. Sugama	523
An Innovative DC Polarization Method for Evaluating Coatings - A.S. Fabiszewski and V.S. Agarwala	535
Assessment of Some Advanced Protective Schemes, Including Chromate and Non-Chromate Conversion Coatings for Mg Alloy ZE41A-T5 Using Electrochemical Impedance Spectroscopy - F. Chang, R. Huie and B. Placzankis	549
Effectiveness of Thin Film Fluoropolymers as Protective Coatings in Marine Environments - J.F. McIntyre, R.K. Conrad and A. Sheetz	565
Warm Weather Surface Tolerant Coatings - S.C. Hobaica.....	583
Non Chromated Epoxy Primer for Aerospace Applications - D. Vorse and J. Gausman	591

Session VIII: Corrosion Control and Prevention

Effects of Alloy Chemistry Changes on Sacrificial Aluminum Anode Performance - <i>J.N. Murray, R.A. Hays and D.W. Smith</i>	601
USMC Corrosion Reduction Program: Vehicle Corrosion Surveys at Camp Lejeune, Camp Pendleton, and Twentynine Palms Marine Corps Bases - <i>E.B. Bieberich,</i> <i>T.J. Jackovic and R.M. Janeczko</i>	615
High Strength Alloys for Seawater Fastener Applications - <i>D.M. Aylor</i>	629
Cost-effective and Environmentally Safe Corrosion Prevention for 2nd Marine Air Wing Support Equipment Using Desiccant Wheel Dehumidification (DEW) - <i>D.J. McCarthy, A. Sandoval and H. Miller</i>	641
Ion Beam Enhanced Deposition as Alternative Pretreatment for Adhesive Bonding of Aircraft Alloys - <i>G.H. Koch and A.H. Deutchman</i>	655
Verification of the Boundary Element Modeling Technique for Cathodic Protection of Large Ship Structures - <i>H.P. Hack and R.M. Janeczko</i>	673
A Comparison of Alternatives to Chromic Acid Anodizing - <i>S.J. Spadafora</i> <i>and F.R. Pepe</i>	687
Suitability of Prepainted (Coil Coated) Metal and Adhesive Assembly for Military Application - <i>I.C. Handsy and M.T. Wolff</i>	699
Electroplating and Epoxy Repair Methods for Corroded 70/30 CuNi and Alloy 400 Seawater System Components - <i>T.J. Jackovic and E.B. Bieberich</i>	707

Session IX: Environmental Technology

Revision of Navy Paint Specifications - <i>D. Pulley</i>	725
Optimization and Prototyping of Medium Pressure Water (MPW) Depaint Process - <i>J. Stropki and R.L. Stearns</i>	731
Evaluation of Environmentally Acceptable Protection Schemes for High Strength Steel Fasteners - <i>B. Placzankis, M. Levy, J. Beatty, S. Isserow and M. Kane</i>	743
Elimination of Chromate Conversion Coatings from Army Tactical Vehicle Manufacturing Processes - <i>M. Ingle</i>	771
Evaluation of Environmentally Acceptable Multi-Layer Coating Systems as Direct Substitutes for Cadmium Plating on Threaded Fasteners - <i>M.W. Ingle</i> <i>and I.C. Handsy</i>	785
Adhesion Promotion and Corrosion Prevention from Coatings Based on Sol-Gel Technology - <i>L.C. Yanyo</i>	805

Attendance List	817
-----------------------	-----

Tri-Service Conference on Corrosion

Conference Chairman

Mr. Thomas Naguy
USAF Wright-Patterson Air Force Base

Conference Coordinator

Ms. Lori Mantia
Universal Technology Corporation

Program Committee

Dr. Vinod Agarwala
Naval Air Warfare Center

Ms. Denise Aylor
Naval Surface Warfare Center

Dr. John Beatty
US Army Research Laboratory

Mr. Paul Buckley
US Army Research Laboratory

Dr. Walter Cox
Naval Surface Warfare Center

Dr. Kumar Jata
USAF Wright-Patterson Air Force Base

Mr. Richard Kinzie
USAF Warner Robins Air Force Base

Dr. Robert Reeber
US Army Research Office

PLEASE CHECK THE APPROPRIATE BLOCK BELOW:

AO# M98-01-0200

☒ 1 copies are being forwarded. Indicate whether Statement A, B, C, D, E, F, or X applies.

☒ DISTRIBUTION STATEMENT A:
APPROVED FOR PUBLIC RELEASE: DISTRIBUTION IS UNLIMITED

☐ DISTRIBUTION STATEMENT B:
DISTRIBUTION AUTHORIZED TO U.S. GOVERNMENT AGENCIES ONLY; (Indicate Reason and Date). OTHER REQUESTS FOR THIS DOCUMENT SHALL BE REFERRED TO (Indicate Controlling DoD Office).

☐ DISTRIBUTION STATEMENT C:
DISTRIBUTION AUTHORIZED TO U.S. GOVERNMENT AGENCIES AND THEIR CONTRACTORS; (Indicate Reason and Date). OTHER REQUESTS FOR THIS DOCUMENT SHALL BE REFERRED TO (Indicate Controlling DoD Office).

☒ DISTRIBUTION STATEMENT D:
DISTRIBUTION AUTHORIZED TO DoD AND U.S. DoD CONTRACTORS ONLY; (Indicate Reason and Date). OTHER REQUESTS SHALL BE REFERRED TO (Indicate Controlling DoD Office).

☐ DISTRIBUTION STATEMENT E:
DISTRIBUTION AUTHORIZED TO DoD COMPONENTS ONLY; (Indicate Reason and Date). OTHER REQUESTS SHALL BE REFERRED TO (Indicate Controlling DoD Office).

☐ DISTRIBUTION STATEMENT F:
FURTHER DISSEMINATION ONLY AS DIRECTED BY (Indicate Controlling DoD Office and Date) or HIGHER DoD AUTHORITY.

☐ DISTRIBUTION STATEMENT X:
DISTRIBUTION AUTHORIZED TO U.S. GOVERNMENT AGENCIES AND PRIVATE INDIVIDUALS OR ENTERPRISES ELIGIBLE TO OBTAIN EXPORT-CONTROLLED TECHNICAL DATA IN ACCORDANCE WITH DoD DIRECTIVE 5230.25, WITHHOLDING OF UNCLASSIFIED TECHNICAL DATA FROM PUBLIC DISCLOSURE, 6 Nov 1984 (Indicate date of determination). CONTROLLING DoD OFFICE IS (Indicate Controlling DoD Office).

☐ This document was previously forwarded to DTIC on _____ (date) and the AD number is _____.

☐ In accordance with provisions of DoD instructions, the document requested is not supplied because:

☐ It will be published at a later date. (Enter approximate date, if known).

☐ Other. (Give Reason)

DoD Directive 5230.24, "Distribution Statements on Technical Documents," 18 Mar 87, contains seven distribution statements, as described briefly above. Technical Documents must be assigned distribution statements.

Print or Type Name

Authorized Signature/Date

Telephone Number

000955

1994-01-000

611

TRI-SERVICE CONFERENCE ON CORROSION



21-23 JUNE 1994

SHERATON PLAZA HOTEL
ORLANDO, FLORIDA

PROCEEDINGS

PROPERTY OF:

AMPTIAC LIBRARY

AIR FORCE CORROSION PROGRAM

OVERVIEW

Briefer:

Mr. Richard C. Kinzie

**Air Force Corrosion
Program Office**

AIR FORCE CORROSION PROGRAM

- Introduction
- Formalized Corrosion Program
- AF Corrosion Program Responsibilities
- AF Corrosion Program Elements
- Current Corrosion Requirements/Constraints
- Conclusions

AF CORROSION PROGRAM INTRODUCTION

- Corrosion Costs the AF \$1+ Billion Annually
- 90% of Toxic & Hazardous Materials Result From Corrosion Prevention & Control Efforts
- Corrosion Is a Major Factor In Aging Aircraft Concerns

FORMALIZED AIR FORCE CORROSION PROGRAM

- Unique in DOD
- Assures Common M & P Technology Across All Systems
- Applies Expertise of Government, Industry, & Academia
- Good News / Bad News

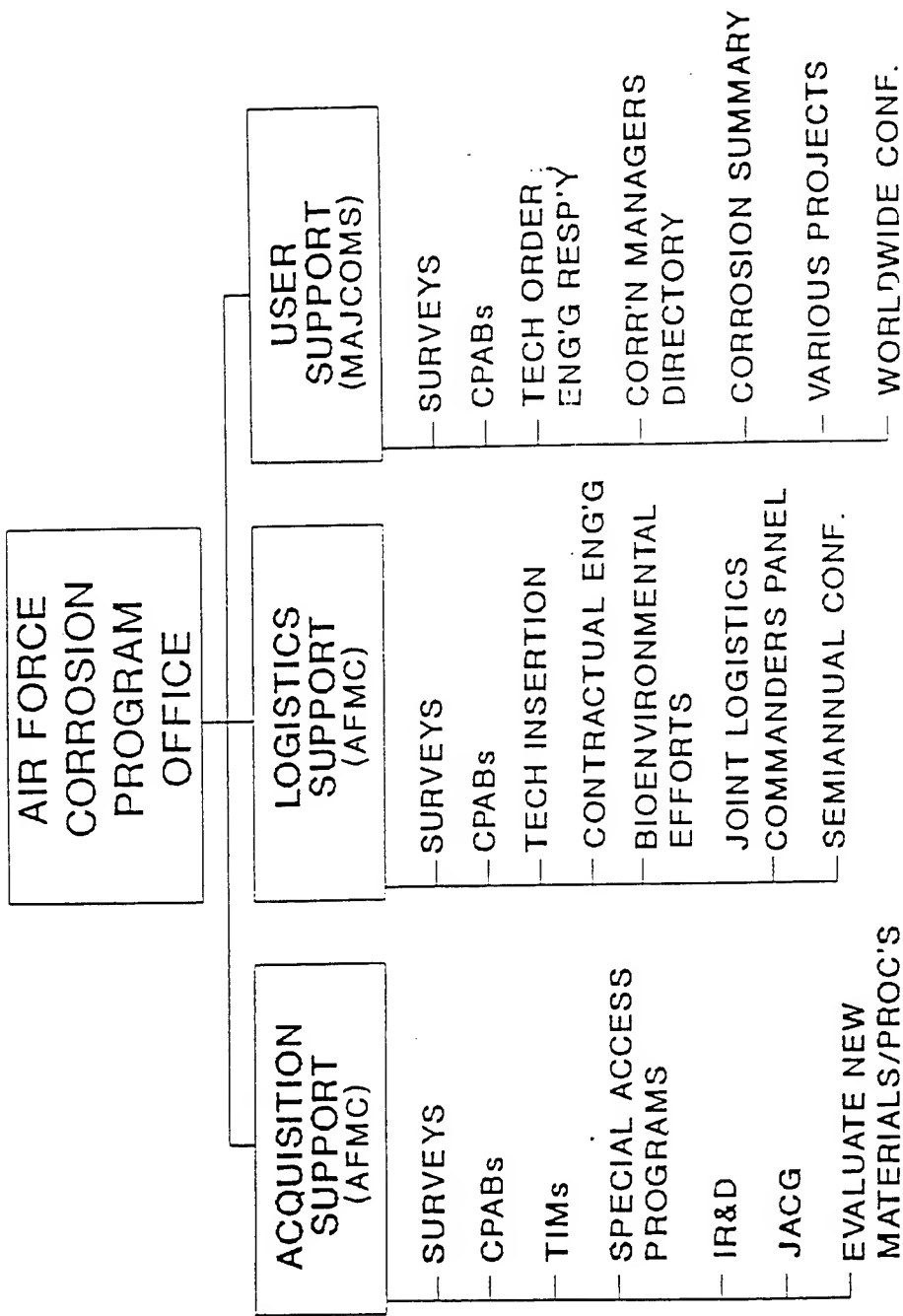
AIR FORCE CORROSION PROGRAM OFFICE

Who We Are

- Air Force Level (AF/LGMM) Program Office
- Organizationally Under WR-ALC/TIEA
- Staff
 - Lt Col - Chief, Program Office
 - 4 Senior NCOs - Corrosion Specialists
 - 6 Civilians - Materials/Corrosion Engineers
 - 1 Civilian - Editorial Assistant

AIR FORCE CORROSION PROGRAM OFFICE Responsibilities

- **Primary Objective:** Ensure that the Air Force has a Viable Program to Prevent, Detect, and Control Corrosion and Minimize the Impact of Corrosion on Air Force Systems
- **Extend the Service Life of Air Force Systems**
- **Impact the Acquisition Process for New Air Force Systems**
- **AFR 400-44 / AFI 21-105**



AIR FORCE CORROSION PROGRAM OFFICE RESPONSIBILITIES

TECHNICAL ORDERS

- T.O. 1-1-4 Exterior Finishes & Markings
- T.O. 1-1-8 Organic Coatings
- T.O. 1-1-686 Desert Storage & Preservation
- T.O. 1-1-689 Avionic Equipment
- T.O. 1-1-691 Cleaning and Corrosion

AIR FORCE CORROSION PROGRAM OFFICE RESPONSIBILITIES

TECHNICAL ISSUES FOCAL POINT

- Corrosion TAPM (Technology Application Program Manager)
- Advise MAJCOMs / ALCs
- Evaluate New Materials & Processes
- Corrosion Engineering Projects
- Technology Insertion Efforts
- Aging Aircraft Corrosion Focal Point
- Joint Service Focal Point for Corrosion
- Others

AIR FORCE CORROSION PROGRAM ELEMENTS

- Corrosion Prevention Advisory Boards
(CPAB)
 - Provide Engineering Assistance in Resolving Corrosion-Related Problems in Materials, Procedures, and Processes
 - Meet Once or Twice a Year (Active From Pre-Production thru Retirement)
- Over 25 Currently Active CPABs

AIR FORCE CORROSION PROGRAM ELEMENTS

MAJCOM SURVEYS

- Every Four years
- TDY Lasts Two to Five Weeks
- Team of Five or More
- Areas Checked

AIRCRAFT	MUNITIONS	MATERIALS
AGE	MANPOWER	PROCEDURES
MISSILES	FACILITIES	EQUIPMENT
VEHICLES	TRAINING	COM/ELECT.EQUIP

AIR FORCE CORROSION PROGRAM ELEMENTS

- **Annual Corrosion Program Manager's Conference**
 - Resolve Corrosion Related Issues
 - Crossflow of Information / New Technology
- **Corrosion Summary**
 - Distributed Semiannually to AF, Army, Navy and Other DOD Agencies
- **Corrosion Program Directory**
 - AF Points-of-Contact for Corrosion

AIR FORCE CORROSION PROGRAM ELEMENTS

- DOD - Industry Coating Removal Conference
- Tri-Service Corrosion Conference
- Joint Aeronautical Commanders Group
- Joint Depot Maintenance Advisory Group
- Joint Technology Exchange Group

AIR FORCE CORROSION PROGRAM ELEMENTS

MILITARY STANDARD 1568

- Defines Corrosion Program Requirements
- Defines General Technical Requirements
- Requires Corrosion Prevention & Control Plan
- Requires a Finish Specification
- Requires a Corrosion Prevention Advisory Board (CPAB)

AIR FORCE CORROSION PROGRAM ELEMENTS

MIL STD 1568 - CORROSION PREVENTION & CONTROL PLAN

- Establishes Contractor Corrosion Control Team
- Assures M & P is Responsible for Materials Related Issues
- Governs Flowdown of Reqmts to Subs
- Assures Contractor Support / Funding of Efforts
- Defines Involvement of All Contractor / Functions

AIR FORCE CORROSION PROGRAM ELEMENTS

MIL STD 1568 - FINISH SPECIFICATION

- Defines Processes
- Defines Materials and Finishes
- Identifies Nonstandard Materials & Processes
- Identifies variation From Mil Specs & Standards
- Gives Government Specific Opportunity for Approval

AIR FORCE CORROSION PROGRAM ELEMENTS

MIL STD 1568 - CORROSION PREVENTION ADVISORY BOARD

- **Membership**
- **Reviews & Makes Recommendations on All
Materials Related Issues**
- **Areas of Concern Include:**
 - MATERIALS COMPATIBILITY
 - TECHNICAL ORDERS
 - ENVIRONMENTAL COMPLIANCE
 - MAINTENANCE CONCEPTS
 - ENVIRONMENTAL TESTING
 - INTERFACE WITH R & M / OTHER DISCIPLINES
 - OTHER

AIR FORCE CORROSION PROGRAM

LESSONS LEARNED - TECHNICAL

- Dissimilar Materials
- Embrittlement of High Strength Parts
- Improper Coatings
- Sealing
- Nonstandard Parts
- Fastener Installation
- Avionics
- Incorrect Alloys
- Other

Cumulative Corrosion-Related Repair Cost
(Same Age and Corrosion Severity Exposure)
(Per Aircraft)

<u>Aircraft</u>	<u>Base Level</u>	<u>Base and Depot Level</u>	<u>% Improvement</u>
C-5A	\$299,810	\$2,326,175	
C-5B	\$244,762	\$1,007,417	56.69%
C-130E	\$83,023	\$3,947,503	
C-130H	\$38,771	\$1,270,379	67.82%
F-111*	\$100,624	\$553,936	
F-16	\$20,389	\$79,448	85.66%

* Corrosion work associated with wing sweep carry through structure and crew station ejection module removed from consideration. Aircraft size normalized to F-16 size.

AIR FORCE CORROSION PROGRAM

NEW SYSTEMS REQUIREMENTS

- Corrosion Characterization of New Materials
- Implementation of Existing Technology
 - MATERIALS AND PROCESSES
 - DESIGN
 - OTHER
- Insertion of New Technology

AIR FORCE CORROSION PROGRAM

AGING FLEET REQUIREMENTS

- Detection of Hidden / Inaccessible Corrosion
- Corrosion Monitoring System
- Corrosion Predictive Modeling

CURRENT THREATS TO AIR FORCE CORROSION EFFORTS

- Environmental Restrictions
- Reduced Resources
 - PROGRAMMATIC IMPACTS
 - IMPLEMENTATION IMPACTS

CONCLUSIONS

- Air Force Corrosion Program Office Has a Broad Spectrum of Responsibilities
- We Exist to Serve the Customer
- Severe Manpower & Funding constraints Limit Program Office Effectiveness
- Clear Lines of Authority Are Needed

USMC
CORROSION PREVENTION AND CONTROL
(CPAC) PROGRAM OVERVIEW



PRESENTED TO
TRI-SERVICE CONFERENCE ON CORROSION

21 JUNE 1994

Julie A. Jacks
MARCORSYSCOM PSE
(703)640- 551 DSN 278



USMC CPAC PROGRAM



POLICY

Draft Marine Corps Order Establishes Program, Responsibilities
and Objectives

Program Elements

Preventive and Corrective Action Program

Identify Major Problems

Field Evaluation Program

Training

Acquisition Management Support

Environmental Compliance



USMC CPAC PROGRAM



POLICY (con't)

CPAC Working Group
Oversee and Manage CPAC Program
Membership

MARCORSYSCOM

HQMC

MCCDC

MARFORLANT

MARFORPAC

MCLBA

MARRESFOR

TRI SVC-2
6/21/94



USMC CPAC PROGRAM



CORROSION INITIATIVES

Primers

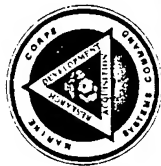
Investigating Alternate Primers

MEFDEP

Dehumidified Equipment Storage Program for
organizational equipment (based on similar effort with
aircraft)



USMC CPAC PROGRAM



CORROSION INITIATIVES

Identify most serious corrosion problems and recommend products to control corrosion (NSWC Carderock) to facilitate organizational maintenance.

TRI SVC-4
6/21/94



JT12V

TRI SVC-5
6/21/94

SESSION I
CORROSION CHARACTERIZATION

Chairman: *R. Reeber*

CORROSION CONSEQUENCES OF MOLTEN SALT DEPOSITS IN COMBUSTION TURBINES BURNING VANADIUM CONTAMINATED LIQUID FUEL

*Dasara V. Rathnamma

Naval Surface Warfare Center, Carderock Division
code 642, 3A Leggett Circle
Annapolis, MD 21402-5067

R. Nagarajan

IBM Corporation, 5600 Cottle Road, San Jose, CA 95193-0001

ABSTRACT

Molten salts condensing on marine turbine blades can dissolve the protective oxide coating and catastrophically attack the exposed alloy surface beneath-- a process known as hot corrosion. We present here the implications of a theoretical model of hot corrosion rate that is limited by diffusional dissolution of oxide species into the melt for the design of burner-rigs to test the corrosion-resistance of superalloy materials. Parameters expected to govern the dissolution rate of a given oxide are the rate of deposition of the multicomponent(sulfate-vanadate-oxide)'solvent'-liquid, liquid-layer thickness, and composition-dependent physical properties of the deposit, such as density and viscosity. The solid portion of deposit mass, being relatively inert with respect to hot corrosion, will not correlate well with experimental corrosion rates. These hypotheses are tested by comparing our model-predictions with one set of burner-rig corrosion rate measurements made during the combustion of vanadium-containing liquid fuel seeded with the same concentration of various metallic additives. Our findings indicate that the total weight (solids + liquid) of the deposit has no direct correspondence with its corrosive potential. However, additives that are effective in suppressing liquid phase formation will, in general, reduce the corrosion rate equally effectively. Liquid mass arrival rate and oxide

solubility in the liquid are quantities of relevance to the problem, but the best correlation of experimental data with theory is obtained for the oxide dissolution rate (which is approximately inversely proportional to the liquid layer thickness). Thus, burner-rigs designed to simulate either of these two parameters will reproduce the hot-corrosion characteristics of the engine with reasonable accuracy.

1. INTRODUCTION

1.1 Molten Salt Deposition and Its Corrosion Consequences:

Nickel-base superalloys, used extensively for gas turbine (GT) engine components because of their superior high temperature mechanical properties, are susceptible to a form of environmental attack known as hot corrosion. Hot corrosion is encountered when molten salts, e.g., sodium sulfates and vanadates, are deposited (as pure liquids or in solution) from the product gases of combustion onto turbine blades and guide-vanes. The adverse effects of molten alkali salt condensation have paralleled the growth of high-temperature energy technologies. Among such technologies are: coal gasification, direct coal-fired turbines, magneto hydrodynamic(MHD), molten salt fuel cells and of primary interest here, marine engines operating on vanadium-contaminated liquid fuels.

Blade surfaces are usually coated with metal alloys that form an adherent, refractory and corrosion-resistant oxide-layer on the gas-side of the coating. The following mechanism has been proposed[1] for the initiation and propagation of hot corrosion: At locations where the protective oxide scale is partially leached or completely dissolved by the condensed molten salt-'solvent', the metal substrate is more accessible, hence vulnerable to catastrophic corrosion. Local saturation of the liquid layer is prevented by dynamic fluxing due to aerodynamic- and centrifugal-shear forces which convey dissolved oxide from the site of dissolution to the tip and trailing-edge regions of the blade. The oxide dissolution rate is taken to be limited by high-Schmidt number Brownian diffusion of the oxide species in the melt (as well as by salt/oxide interfacial detachment kinetics). Thus (composition-dependent) deposit physicochemical properties such as density, viscosity, oxide diffusivity and solubility, and thickness will influence the oxide dissolution rate. Other parameters that will play a role include aerodynamic variables such as the convective flux of the gas phase alkali contaminants,

and material integrity characteristics of the blade alloy surface.

1.2 Burner-Rig Testing: An Assessment of Hot Corrosion Simulation Criteria

At present no standard testing procedure exists for determining the hot corrosion resistance for alloys of construction. Time and economy considerations have led to the development of two general types of laboratory hot salt corrosion test procedures, one involving burner rigs, the other involving furnaces. Comparison of the morphology of the corrosion product with that found on GT blades and other hot-section components indicates that burner-rig testing gives the most realistic simulation of service behavior[2]. However, even if dynamic testing under tightly-controlled conditions were to be performed in burner rigs, the success of the simulation effort would necessarily be judged on the basis of acquired ability to interpret and properly extrapolate test results to the real engine. This classical 'scale-up' problem demands an understanding of the mechanism of hot corrosion. We need to know what initiates it, what sustains it, at what rate it proceeds, and how the rate is related to the rate of deposition of the corrosive liquid.

Given the abundance of key variables in this hot-corrosive environment, (cf. Section 1.1) it is not surprising that a review of simulation criteria reported in literature reveals a wide spectrum of views regarding the crucial parameter on which to base the design of the test-rig. It has been reported[3,4,5] that hot corrosion (sulfidation) in gas turbines occurred only in places where alkali sulfates formed a molten deposit. Therefore, they suggest that the melting-point temperature, T_{mp} -- the 'threshold' temperature for initiation of the sulfidation attack-- and the dewpoint temperature, T_{dp} -- the 'terminal' temperature above which no sulfidation can occur-- be reproduced in the rig[6]. It has been studied that the chemical behavior of deposit forming components (sodium, vanadium, chlorine, sulfur) of GT flue gases, and concluded that the multicomponent salt physical chemistry needs to be reproduced in the low-pressure burner rig by appropriate elemental additions to the fuel. Studies[7] suggest on the basis of laboratory results that rig and engine tests should be compared in terms of the amount of contaminant passing through unit area in unit time. Studies advocate[8] that the partial pressure of the alkali vapor precursor be kept equal in the low- and high-pressure combustors. It has been identified[9] that deposition rate of alkali salt from the vapor phase as the single most important factor in determining corrosion rates. The amount of total deposit which collects on the blade surface dictates the rate of corrosive attack[10]. It has been

pointed out[11] that the thickness of the salt deposit is a key variable, often overlooked in mechanistic studies, in determining the transport of oxidant from the gas phase to the corrosion site. Some researchers[12] have proposed salt-'fluxing' of the underlying oxide layer as the rate-limiting step in the corrosion process. Computed relative oxide dissolution rate profiles would then be closely linked to corrosion 'maps' obtained experimentally[4]. The implication here is that these dissolution rate characteristics would have to be reproduced in a well-designed test-rig.

Comparison of these different simulation strategies for the same burner-rig (Figure 1) shows that each would result in a unique set of operating conditions chosen for the burner-rig. For instance, in order to reproduce the contaminant flux-rate characteristics of a 10 atmosphere turbine in an atmospheric pressure burner-rig, the Mach number (Ma) of combustion gas flow would have to be increased by a factor of about 8 over its engine value, and by a factor of more than 10 to simulate the engine deposition/oxide dissolution rates; whereas, in order to obtain an equivalent thickness of condensed salt, the rig Mach number would actually have to be lower than the engine Mach number. Thus, the choice of operating conditions for the burner-rig depends on the sensitivity of the parameter to be simulated. However, no firm conclusions were drawn, which of these simulation-strategies would give the best results. In this paper, we carry the analysis further, and demonstrate that a rig designed on the basis of equivalent oxide-dissolution rate will best simulate the corrosion characteristics of an operational turbine engine. This is done by means of comparisons of predicted deposition-related quantities, such as the deposition rate, the liquid layer thickness and oxide dissolution rate, with experimental hot corrosion (metal weight loss) data obtained on a burner rig. The effect of introducing the same level of various fuel-additives on observed hot corrosion rates is found to correlate best with the corresponding effect on computed oxide dissolution rate.

2. EXPERIMENTAL PROCEDURE

Corrosion rate-data used here for illustrative purposes were obtained from tests conducted in a battery of small atmospheric pressure combustion test rigs at David Taylor Naval Ship Research and Development Center (NSRDC). The fuel used in this investigation conforms to Specification MIL-F-859A, Burner Fuel Oil, Navy Special Grade. A listing of the properties of

this fuel may be found in the report[13]. AISI 310 alloy was chosen as the test material due to its widespread use; it is composed of 0.25% C, 24-26% Cr, 19-22% Ni, 1.5% Si and the balance Fe. Metallic additives tested with respect to their corrosion-inhibition capability were mostly metal-organic compounds in the form of oil-soluble naphthenates. Tests were conducted for a duration of 100 hours, mostly at a metal temperature of 1600 F. Upon completion of the tests, the specimens were photographed, weighed, and prepared for further analysis by removing the deposits in a molten salt bath. Specimen corrosion was measured as the difference in weight before test and after cleaning. Deposit weight was the weight difference between the untested specimen and the specimen after test exposure.

Data on weight change rate of the specimens from tests using an atomic ratio of six atoms of metal additive to one atom of vanadium in the fuel are plotted in bar diagram form in Figure 2. The amount indicated below the base line represents the weight loss, before and after descaling. The amount above the line indicates deposition of material from the gas stream plus the weight gain attributable to oxidation of the base material. The calculated weight gain due to the oxides is represented by the shaded portions of the total deposit bars. Figure 2 shows that lanthanum, iron and antimony are the most beneficial additives from the standpoint of both deposition and corrosion. Other metals seemingly worthy of consideration include magnesium, calcium, silicon, sodium, and rare earths such as cerium and neodymium. These favorable test data were, however, not exploited fully owing to a lack of fundamental understanding of the interdependency between the deposition and corrosion processes. Since additives influence corrosion primarily by modifying the deposition characteristics of the system, this proved to be a major obstacle. We have recently[14] analyzed the use of fuel additives to minimize corrosion of GT blade material in the following series of steps: first, a free-energy minimization computer program was employed for an equilibrium-thermodynamic prediction of condensed (ideal) solution composition; relevant physico-chemical properties of the molten solution were then estimated based on predicted equilibrium composition; oxide solubility and dissolution rate were then calculated for this solution in contact with various solid oxides. In this work, we will attempt to verify the model for the rate-determining process-- i.e., oxide dissolution-- in hot corrosion by comparison with appropriate hot corrosion test data, and by a process of elimination of other feasible parameters.

3. THEORETICAL MODEL TO PREDICT OXIDE DISSOLUTION RATE

The present model of hot-corrosion controlled by diffusion-limited dissolution of oxide species into the molten salt layer has been described fully[15,12], and also discussed[14,16]. The Brownian high-Schmidt number diffusional flux of oxide into the liquid may be represented as a product of a mass transfer coefficient and a concentration gradient:

$$j'_{o,w} = K_m \cdot (\omega_{o,w} - \omega_{o,b}) \quad (1)$$

where ω_o is the oxide mass fraction at the melt/oxide interface (w) or in bulk liquid solution (b), and k_m , the convective diffusion mass transfer coefficient is estimated[17]. It incorporates liquid density and viscosity, oxide diffusivity in liquid, local liquid layer thickness, upstream and local vapor deposition rates, and the total shear force exerted on the flowing liquid layer by the adjacent gas layer and the turbomachinery. For the sake of simplicity, the dissolution rate is estimated here for a stagnation line configuration, which is representative of the leading edge (LE) of a turbine blade and of the burner-rig geometry. In this limit of negligible liquid streamline flow, the local liquid layer thickness is calculated to be its 'stator-value':

$$\delta_l = [2\mu / (\frac{\partial \tau_{w,g}}{\partial x})_{x=0} \cdot (\frac{-\dot{m}_w + j'_{o,w}}{\rho_l})]^{1/2} \quad (2)$$

with the inclusion of the dissolved oxide contribution to the total liquid mass. Here, μ_l is the liquid viscosity, $(\partial \tau_{w,g} / \partial x)_{x=0}$ the shear stress gradient at the LE, $-\dot{m}''$ the local deposition rate of total liquid, and ρ_l the liquid density.

Individual liquid constituent properties, e.g., viscosity, freezing point, etc., and their temperature and/or composition dependencies are extracted from available literature and phase diagrams[18,19], and used as the basis for approximating the properties of multicomponent ideal solutions of these as arithmetic (weighted) means. The effect of nonideality, neglected here, can be incorporated as correction factor that is related closely to the heat of mixing[20]

In the present theory, single species diffusional fluxes to the surface are taken to be by single vapor precursor (e.g., $\text{Na}_2\text{SO}_4(\text{g})$) concentration

diffusion through a chemically frozen boundary layer. In the multicomponent case, individual constituents still deposit by single vapor species diffusion, but their molar fluxes are constrained to be in the same ratio as their steady-state mole fractions in the condensed phase. A more detailed discussion of these aspects, and other capabilities and limitations of the present theory is available elsewhere[21,22,1].

4. RESULTS AND DISCUSSION

The Complex Chemical Equilibrium Calculation (CEC) computer program, originally developed at NASA Lewis Research Center[23] and recently modified to include multiple ideal solutions in the condensed phase, predicts that for the vanadium-contaminated fuel under consideration, the likely condensed species are: $\text{Na}_2\text{SO}_4(1)$, $\text{NaVO}_3(1)$ and $\text{V}_2\text{O}_5(1)$, in varying fractions depending on the relative levels of sea-salt and vanadium ingested, and the local pressure and temperature. Thermodynamic calculations indicate that most metallic additives tend to enrich Na_2SO_4 in the liquid phase by preferentially forming gaseous and solid compounds with the vanadium present. All additives (except sodium) also tend to decrease the total fraction of condensed liquid in the product mixture, implying a corresponding reduction in the extent of liquid-'catalyzed' corrosion. This system was investigated (with no additives)[24] thermodynamically to determine the effects of varying turbine operating conditions on the limiting fuel impurity levels that will lead to condensation, and to compute the compositions and amounts of deposits for varying levels of sodium and vanadium. They also report that the species listed above comprise most of the condensate, with minimal amounts of higher order vanadates ($\text{Na}_4\text{V}_2\text{O}_7$, Na_3VO_4). They have treated NaVO_3 as $\text{Na}_2\text{V}_2\text{O}_6$ and assumed that the Na_2SO_4 - $\text{Na}_2\text{V}_2\text{O}_6$ mixture can be treated as an ideal solution. While their thermochemical analysis, which is extended over a wide composition range, necessarily deals with ternary Na_2SO_4 - $\text{Na}_2\text{V}_2\text{O}_6$ - V_2O_5 solutions, at the vanadium concentrations we are interested in, a simplified binary analysis (Na_2SO_4 - $\text{Na}_2\text{V}_2\text{O}_6$) is generally adequate. The treatment in literature[24] contains no vapor-phase transport calculations of deposition rates, and no references to the subsequent corrosion process. These are the issues we will specifically address in the remainder of this paper.

The oxide dissolution rate responds to liquid phase composition and total changes acting in concert. According to the present model, magnesium,

cadmium, cobalt, manganese, and nickel are the most effective suppressors of dissolution-limited hot corrosion, whereas cerium and aluminum are among the less effective. Added sodium and potassium enhance the corrosion rate. These trends are in excellent agreement with the experimental findings[13]; A more detailed comparison of theory and practice in this regard is in literature[18]. Our concern here rests more with the effect of additives on several deposition-related quantities, and on whether the predicted effect on the oxide dissolution rate systematically parallels the effect on observed corrosion rate.

Toward this end, we have attempted to correlate corrosion data collected[13] with measured total weight (solids + liquid) of the deposit, as well as with calculated quantities such as the weight of the liquid portion of the deposit, the 'ideal' solubility of the oxide species in the liquid, the phase fraction of condensed material in the combustion product gases, the total deposition rate of the liquid, the liquid layer thickness and the oxide dissolution rate. Figures 3 through 7 represent our efforts at correlating these potentially important parameters with the corrosion rate. In these figures, we plot the logarithm of the nondimensionalized corrosion rate with no additives as a function of various nondimensional parameters that were determined for no additives. The rate and weight data used here were obtained under the conditions reported in Figure 2 (metal-to-vanadium atomic ratio of 6, surface temperature of 1600 F). The metallic additives whose effects were considered here are titanium, tin, barium, strontium, zinc, sodium, indium, calcium, nickel, iron, manganese, cadmium, cerium, neodymium and lanthanum (at an atomic ratio of 3 to vanadium). CEC-predicted solution compositions and condensed phase fractions corresponding to these additives and a surface temperature of 1600 F are presented in Table 1. Deposition-related calculations that went into the construction of Figures 5 through 7 are based on these computed compositions. At this atomic level of added metal, the dominant species in solution for all additives except titanium and cerium are found to be $\text{Na}_2\text{SO}_4(1)$ and $\text{Na}_2\text{V}_2\text{O}_6(1)$; for those two metals, the primary solution components are $\text{Na}_2\text{V}_2\text{O}_6(1)$ and $\text{V}_2\text{O}_5(1)$. In the case of zinc, all liquid-phase component mole fractions are negligibly small, suggesting that the addition of zinc results in the enrichment of the condensed phase in the relatively benign (with respect to hot corrosion) solids.

From Figure 3, it is clear that there is no systematic relationship between corrosion rates and total deposit weights, possibly due to the fact that the

solid part of the deposit is inert with respect to corrosion. Indeed, any additive (e.g., zinc) that tends to increase the solids fraction in the deposit will prove to be an effective suppressant of hot corrosion, whereas trace impurities that result in the formation of low-melting eutectics (e.g., sodium, potassium, iron) invariably exacerbate the corrosion problem. Figure 4 is a log-log plot of the corrosion rate (nondimensionalized) versus condensed liquid mole fraction in the combustion gases (nondimensionalized against its no-additive value). Again, no direct correspondence is detected between these quantities, although one qualitative trend may be detected: in general, smaller condensed liquid inventories correspond to reduced corrosion rates. Thus, additives that suppress liquid phase formation via, e.g., homogeneous vapor phase chemical reactions that 'trap' condensable elements in gaseous compounds can prove beneficial in mitigating hot corrosion. This possibility was explored in our previous work on the use of fuel additives[14] to combat corrosion.

From Figure 5, it may be inferred that the oxide 'solubility' (here taken to be the saturation mass fraction of the oxide in the melt estimated at the temperature of the melt/oxide interface) does not directly correlate with measured corrosion rates either, although it does play a significant role in determining the oxide dissolution flux into the bulk liquid. Equilibrium-thermodynamic phase diagram analyses often employed to characterize the hot corrosion process on the basis of equilibrium-solubility of oxide species into molten-salt solvents are thus not complete representations of the corrosion situation. Corrosion rates are expected to be limited by mass-transport rates of the interfacial oxide from the solid phase into the liquid, and perhaps also by the kinetics of this interfacial-detachment process. The calculations shown in Figures 6 and 7, based on Fickian- and Brownian-rates of diffusion (of vapor to the wall, and of oxide into liquid, respectively), are thus likely to be more relevant to the liquid-induced corrosion problem than the previous analyses.

Figure 6 indicates that the deposition rate is a useful quantity to keep track of, since it obviously has an influence on the observed rate of hot corrosion. However, the coupling between the two may not be as close as previously suspected. As with the condensed liquid phase fraction, while the extremes match-- i.e., the additive that results in minimum deposition also brings about a minimum in corrosion rate, and the maxima coincide as well-- no systematic, physically-meaningful relationship between these two quantities emerges from our investigation (given the limitations of presently

available data). In Figure 7, we present results of correlating the corrosion rate data with other calculable deposition-related parameters-- viz., the liquid deposit weight, the liquid layer thickness and the rate of oxide dissolution into the liquid. An examination of this semi-logarithmic plot leads to the following important observations:

- o The corrosion rate is inversely proportional to the liquid layer thickness.
- o The corrosion rate is (approximately) inversely proportional to the weight of the liquid portion of the deposit.
- o The corrosion rate varies approximately linearly with predicted oxide dissolution rate.

The first two observations are understandable in light of the third. If the corrosion rate is limited by oxide diffusion across the liquid layer, the dissolution velocity, hence corrosion rate, of the oxide into the liquid may be approximated to be (at steady-state):

$$j'_{o,w}/\rho_l \approx D_{o,l} / \delta_l \quad (3)$$

(Where $D_{o,l}$ represents the oxide diffusivity in liquid.)

Thus, a direct linear dependence of the corrosion rate on oxide dissolution rate implies an inverse dependence on the liquid layer thickness. Both these trends are clearly visible from a comparison of our predictions with measured laboratory burner-rig corrosion rates, lending credence to our proposed fundamental mechanism of hot corrosion initiation. While we are constantly on the lookout for other data with which to verify our claim that the diffusional process of oxide dissolving into the condensed salt-solvent limits the rate at which the subsequent corrosion process proceeds, we are necessarily restricted at present to using Schab's data[13] as 'testing-ground' for our hypothesis. Readers with knowledge or data that will reinforce (or contradict) our basic theoretical concepts are urged to communicate these to the authors, so that progress may be sustained toward developing an 'international-standard' rig-testing procedure.

5. CONCLUSIONS

Our approach to the prediction of corrosion rates based on oxide dissolution into the condensed liquid has been found to be reasonably successful in explaining the effect of varying levels of any fuel additive, as well as the relative effect of the same level of various additives, on observed hot corrosion rates due to fuel impurities. We thus have a predictive tool that may be used to assist in the process of designing low-pressure corrosion simulation rigs, and in devising additive/fuel cleaning techniques to minimize corrosion of hot section components in marine gas turbines.

A critical re-examination of several elements of preliminary mechanistic theory presented in this paper indicates the following points:

1. While the 'chemically frozen' model of gas-phase chemistry is one tractable kinetic 'asymptote', the other would be one in which the gas-phase is in local thermochemical equilibrium (LTCE) everywhere. Deposition rates (and accompanying dissolution rates) computed in these two extremes of homogeneous kinetics are likely to be quite different in the high-temperature, dissociative environment of a combustor. Efforts were underway[1] to obtain the two limits within which observed deposition rates and dewpoints may be expected to lie for a given system.
2. Our model of non-reactive dissolution of oxide species into the molten salt liquid is of limited validity. The role of solvent/oxide interfacial kinetics and solvent/gas interfacial processes (e.g., gas-phase supersaturations, effect of vapor pressures on condensed phase electrochemistry, etc.) must be accounted for in a progressively more realistic model.

By the application of approximately the same principles, a model for molten salt corrosion of ceramics was developed[25] for GT model fuels.

A more advanced theoretical hot corrosion predictive model was developed[26].

Acknowledgement:

This work was supported by the Office of Naval Research, Code 33, Dr Alan Roberts.

6. REFERENCES

1. ROSNER, D. E. and NAGARAJAN, R., 'Vapor Deposition and Condensate Flow on Combustion Turbine Blades: Theoretical Model to Predict/Understand Some Corrosion Rate Consequences of Molten Alkali Sulfate Deposition in the Field or Laboratory', Int. J. Turbo Jet Engines (in press, 1987)
2. SANTORO, G. J., 'Hot Corrosion of Four Superalloys: HA-188, S-57, IN-617, and TD-NiCrAl', Oxid. Metals, 13, 405 (1979)
3. DeCRESCENTE, M. A. and BORNSTEIN, N. S., 'Formation and Reactivity Thermodynamics of Sodium Sulfate with Gas Turbine Alloys', Corrosion, 24, 127-133 (1968)
4. FRYXELL, R. E. and BESSEN, I. I., 'Coating Life Assessment in Gas Turbines Operated for Ship Propulsion', in Proceedings of 1974 Gas Turbine Materials in the Marine Environment Conference (J. W. Fairbanks, I. Maschlin, eds.), 24-26 July 1974, Marine Maritime Academy, Castine, Maine; p 259-276
5. RENTZ, W. A., WALTERS, J. J. and FREEMAN, JR., W. R., 'A Dynamic Hot-Corrosion Rig Testing Procedure', J. Materials, 4, 520-539 (1969)
6. HALSTEAD, V. D., 'Calculations on the Effects of Pressure and Temperature on Gas Turbine Deposition', in Deposition and Corrosion in Gas Turbines (A. B. Hart and A. J. B. Cutler, eds.), J. Wiley, 1973; p 22-23
7. HANCOCK, P., 'Rig Testing to Study Environmental Effects on Hot Corrosion Mechanisms', in Proceedings of 4th Conference on Gas Turbine Materials in the Marine Environment, 26-28 June 1979, U. S. Naval Academy, Annapolis, MD; p 465-473
8. TSCHINKEL, J. G., 'Formation of Sodium Sulfate in Gas Turbine Combustors', Corrosion, 28, 161-169 (1972)
9. SAUNDERS, S. R. J. and NICHOLLS, J. R., 'Hot Salt Corrosion Test Procedures and Coating Evaluation', Thin Solid Films, 119, 247-269 (1984)

10. LEE, S. Y., DeCORSO, S. M. and YOUNG, W. E., 'Laboratory Procedures for Evaluating High-Temperature Corrosion Resistance of Gas Turbine Alloys', ASME Trans., Ser. A. J. Engrg. Power, 93, 313-320 (1971)
11. SHORES, D. A., 'New Perspectives on Hot Corrosion Mechanisms', in High Temperature Corrosion (R. A. Rapp, ed.), NACE-6, pp 493-501 (1983)
12. ROSNER, D. E., NAGARAJAN, R., GOKOGLU, S. A. and KORI, M., 'Maximum Effect of Vapor Phase Chemical Reactions on CVD-Rates and Deposition Onset Conditions in the Absence of Interfacial Kinetic Barriers', to be presented at the 10th Intl. Conf. on Chemical Vapor Deposition (CVD-X), 172nd Meeting of the Electrochemical Society, October 18-23, 1987, Honolulu, Hawaii
13. SCHAB, H. W. and GESSNER, F. R., 'Reduction of Oil-Ash corrosion by Use of Additives in Residual Fuels', Research and Development Report 070034C, NS-072-504 (April 1957), U.S. Naval Engineering Experiment Station
14. Rathnamma, D.V. and D.W. Bonnell, "Contaminated Fuel Combustion And Material Degradation Life Prediction Model", Proceedings Vol II, "High Temperature Alloys for Gas Turbines and Other Applications 1986" Reidel Publishing Co, Editors W. Betz, R. Brunetaud, D. Coutouradis etc, pp 1105-1122.
15. NAGARAJAN, R., Theory of Multicomponent Chemical Vapor Deposition (CVD) Boundary Layers and Their Coupled Deposits, Ph.D. Thesis, Dept. of Chemical Engineering, Yale University, May 1986
16. RATHNAMMA, D. V. and R. NAGARAJAN, 'High Temperature Hot Corrosion Control by Fuel Additives (Contaminated Fuels)', in: Proc. 10th International Congress on Metallic Corrosion, 7-11 Nov 1987, Madras, India, Oxford and IBH Publishing, Vol. IV, pp. 3651-3664.
17. STEWART, W. E., 'Convective Heat and Mass Transport in Three-Dimensional Systems with Small Diffusivities', Physicochemical Hydrodynamics, 1, 23-63 (1977)

18. CUTLER, A. J. B., 'Molten Sulfates', in Molten Salt Techniques, Plenum Press, NY (1983)
19. JANZ, G. J., ALLEN, C. B., BANSAL, N. P., MURPHY, R. M. and TOMKINS, R. P. T., 'Physical Properties Data Compilation Relevant to Energy Storage. II. Molten Salts: Data on Single- and Multi-Component Salt Systems', NSRDS-NBS, 61, Part II (1979)
20. MOELWYN-HUGHES, E. A., Physical Chemistry, II Revised ed., Pergamon Press, NY (1964)
21. ROSNER, D. E. and NAGARAJAN, R., 'Transport-Induced Shifts in Condensate Dewpoint and Composition in Multicomponent Systems with Chemical Reaction', Chem. Eng. Sci., 40, 177-186 (1985)
22. ROSNER, D. E., Transport Processes in Chemically Reacting Flow Systems, Butterworth Publishers, Stoneham, MA (1986)
23. GORDON, S. and McBRIDE, B. J., "Computer Program for Calculation of Complex Chemical Equilibrium Compositions, Rocket Performance, Incident and Reflected Shocks, and Chapman-Jouguet Detonations", NASA SP-273, Interim Revision, March 1976
24. LUTHRA, K. L. and SPACIL, H. S., 'Impurity Deposits in Gas Turbines from Fuels Containing Sodium and Vanadium', J. Electrochem. Soc.: Solid State Sci. Technol., p 649, March 1982
25. Cook, L.P, D.W.Brennell, and D. Rathnamma, 'Corrosion and Corrosive Degradation of Ceramics', Ceramic Transactions, Vol 10, Editors: Richard E. Tressler. Michael McNallan. 1990, pp 251-276
26. RATHNAMMA,D.V. AND R. NAGARAJAN," Hot Corrosion Life Prediction Model for Marine Gas Turbine Blades and Guide Vanes" Proceedings of the TRI-SERVICE CONFERENCE ON CORROSION" Editor: Milton Levy, Army Research Laboratory, Water Town, Massachusetts May 12-14,1992, pp271-285.

TABLE 1.
MOLTEN SALT DEPOSITS IN COMBUSTION TURBINES
BURNING VANADIUM CONTAMINATED LIQUID FUEL
EFFECT OF METALLIC ADDITIVES ON CONDENSED PHASE
COMPOSITION

(ATOMIC RATIO OF ADDITIVE-TO-VANADIUM = 6:1)
SURFACE TEMPERATURE = 1600 F)

ADDITIVE	RELEVANT SOLUTION	SPECIES MOLE FRACTION		CONDENSATE FR.
		$\text{Na}_2\text{SO}_4(l)$	$\text{Na}_2\text{V}_2\text{O}_6(l)$ $\text{V}_2\text{O}_5(l)$	
NONE	$\text{Na}_2\text{V}_2\text{O}_6\text{-V}_2\text{O}_5$		0.265	0.293
TITANIUM	$\text{Na}_2\text{V}_2\text{O}_6\text{-V}_2\text{O}_5$		0.28	0.73
BARIUM	$\text{Na}_2\text{SO}_4\text{-Na}_2\text{V}_2\text{O}_6$	0.87	0.10	3.50X10 ⁻⁰⁷
STRONTIUM	$\text{Na}_2\text{SO}_4\text{-Na}_2\text{V}_2\text{O}_6$	0.91	0.054	3.50X10 ⁻⁰⁷
ZINC	$\text{Na}_2\text{SO}_4\text{-Na}_2\text{V}_2\text{O}_6$	0.028	0.0079	1.20X10 ⁻⁰⁷
SODIUM	$\text{Na}_2\text{SO}_4\text{-Na}_2\text{V}_2\text{O}_6$	0.83	0.16	8.10X10 ⁻⁰⁶
INDIUM	$\text{Na}_2\text{SO}_4\text{-Na}_2\text{V}_2\text{O}_6$	0.97		3.80X10 ⁻⁰⁷
NICKEL	$\text{Na}_2\text{SO}_4\text{-Na}_2\text{V}_2\text{O}_6$	0.49	0.46	3.65X10 ⁻⁰⁷
IRON	$\text{Na}_2\text{SO}_4\text{-Na}_2\text{V}_2\text{O}_6$	0.96	0.0049	3.40X10 ⁻⁰⁷
MANGANESE	$\text{Na}_2\text{SO}_4\text{-Na}_2\text{V}_2\text{O}_6$	0.67	0.30	3.55X10 ⁻⁰⁷
CADMIUM	$\text{Na}_2\text{SO}_4\text{-Na}_2\text{V}_2\text{O}_6$	0.97	0.0016	3.40X10 ⁻⁰⁷
CERIUM	$\text{Na}_2\text{V}_2\text{O}_6\text{-V}_2\text{O}_5$		0.35	0.64
NEODYMIUM	$\text{Na}_2\text{SO}_4\text{-Na}_2\text{V}_2\text{O}_6$	0.78	0.18	1.00X10 ⁻⁰⁷
LANTHANUM	$\text{Na}_2\text{SO}_4\text{-Na}_2\text{V}_2\text{O}_6$	0.38	0.58	3.50X10 ⁻⁰⁷
				3.70X10 ⁻⁰⁷

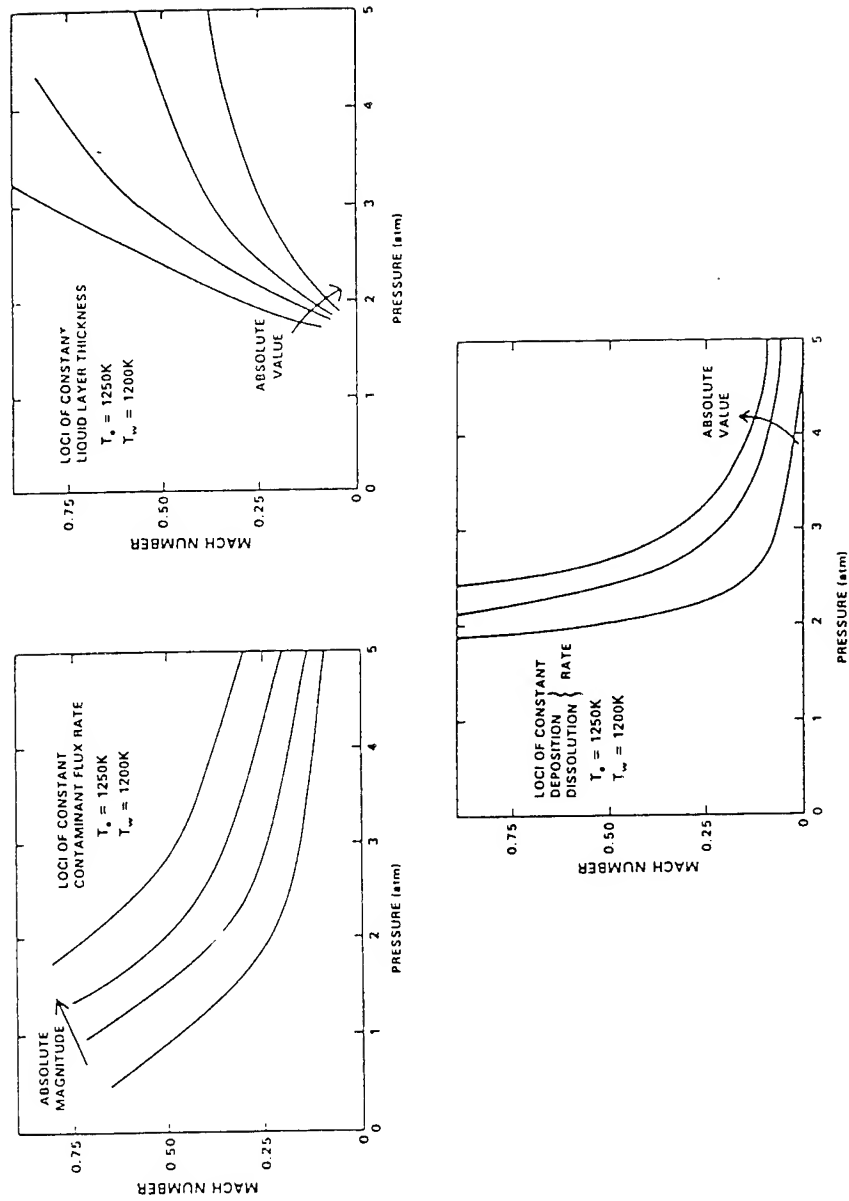


FIG 1. simulation- charts for rig-design to reproduce desired characteristics of the high-pressure turbine

CORROSION AND DEPOSITION EFFECTS OF OIL SOLUBLE ADDITIVES ON A HIGH TEMPERATURE ALLOY (AFTER SCHAB, 1957)

ATOMIC RATIO - 6:1
TEMPERATURE - 1600°F
FUEL - NAVY SPECIAL GRA
MATERIALS: 170-190 ppm VANADIUM
TIME - 100 HOURS

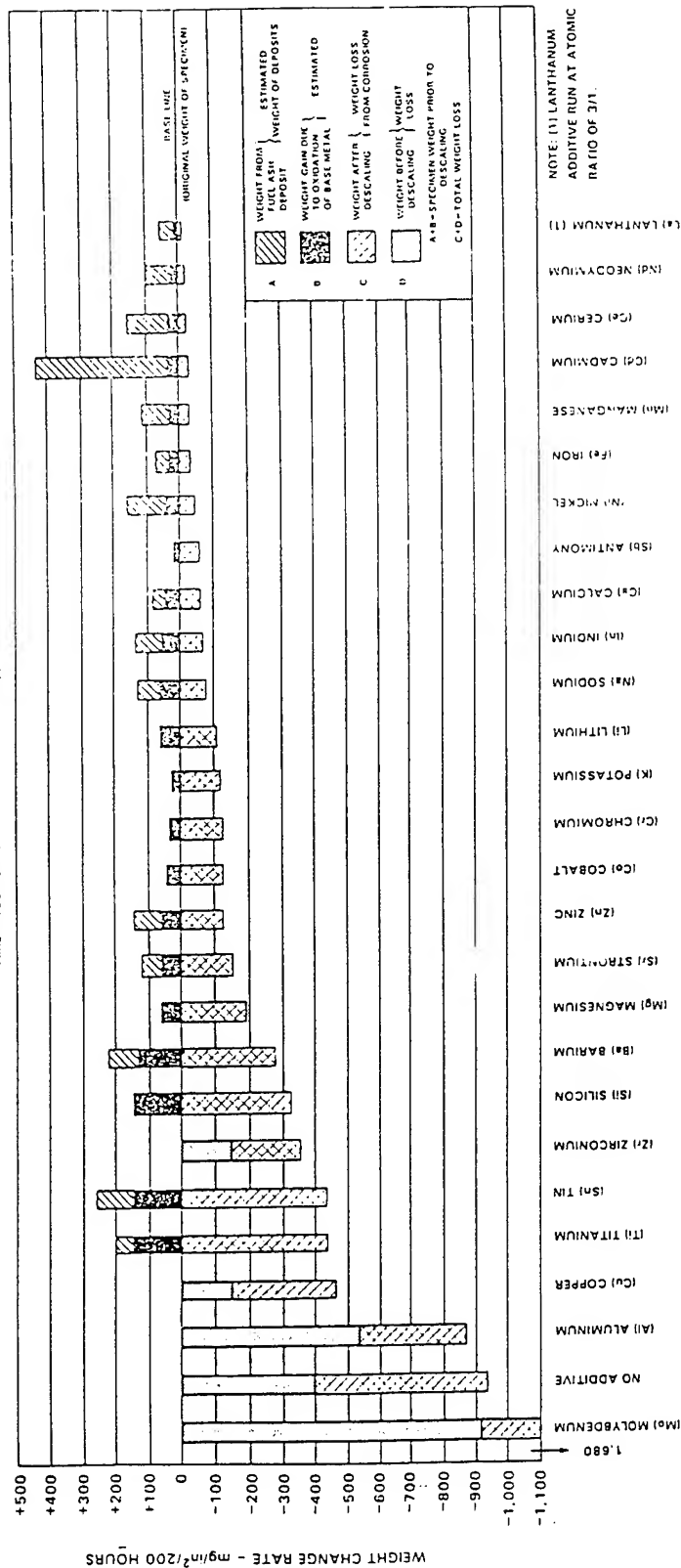


FIG 2.

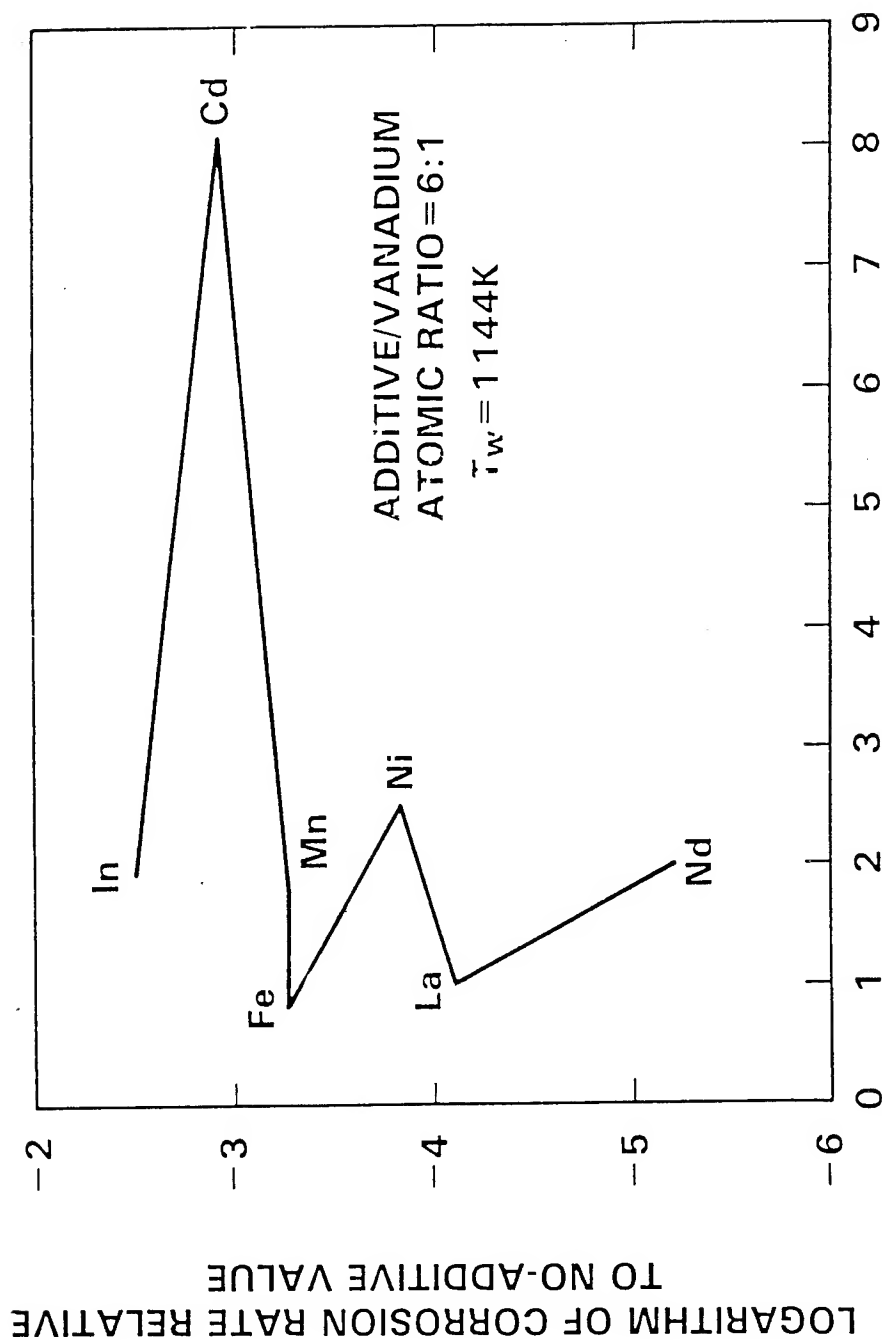


FIG 3. Total weight (Solids + Liquid) of Deposit
(relative to no-additive value)
(data from the bar graph)

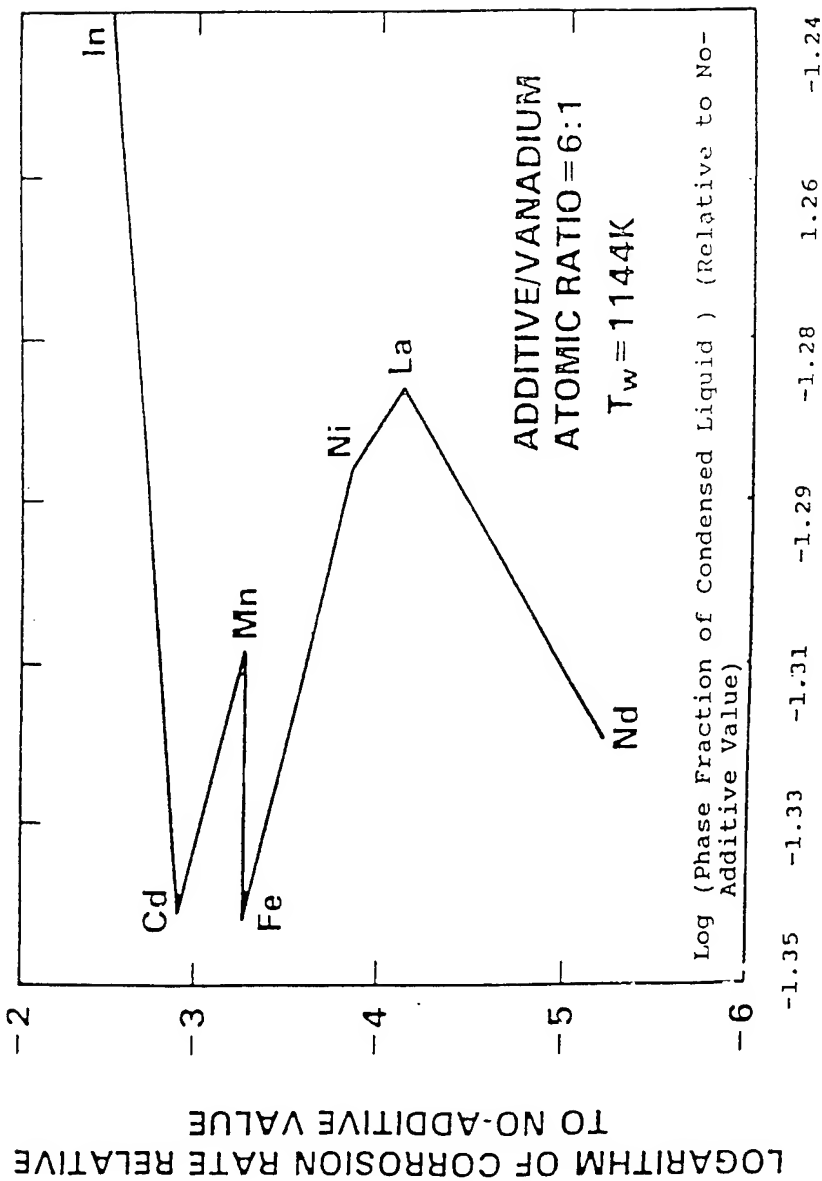


FIG 4. CORRELATION OF MEASURED CORROSION RATE DATA WITH CEC
PREDICTED LIQUID CONDENSATE MOLE FRACTIONS IN COMBUSTION
PRODUCT GASES

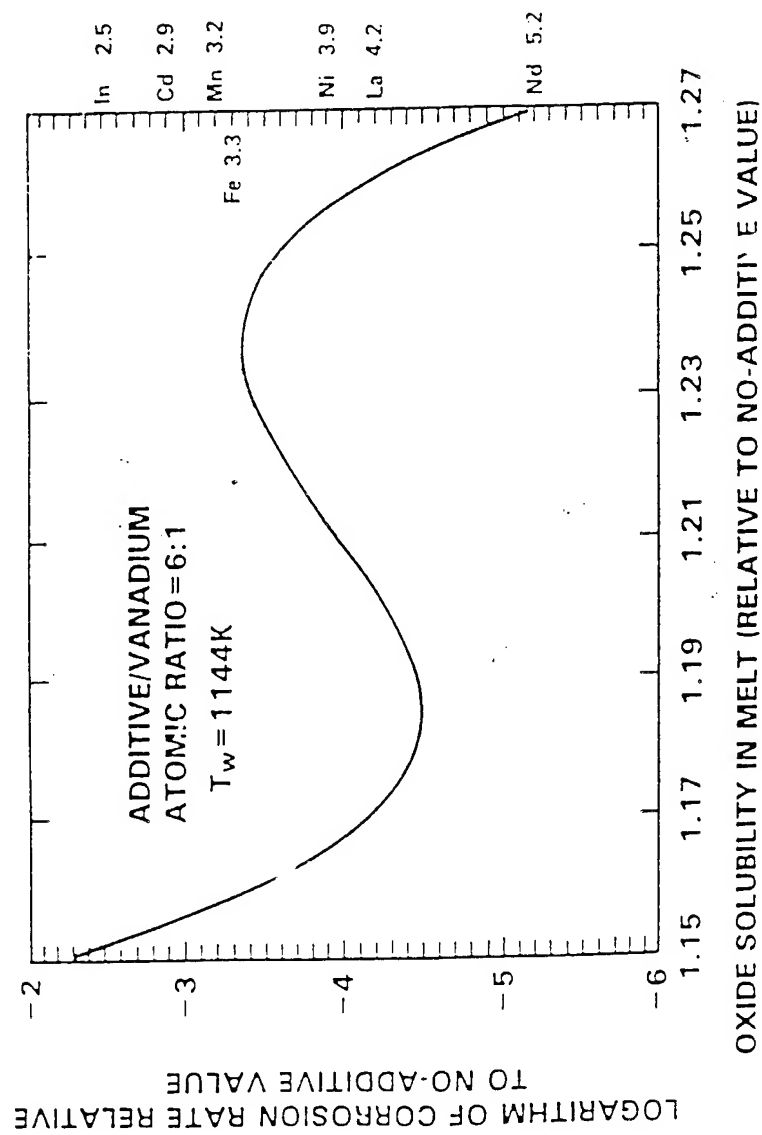
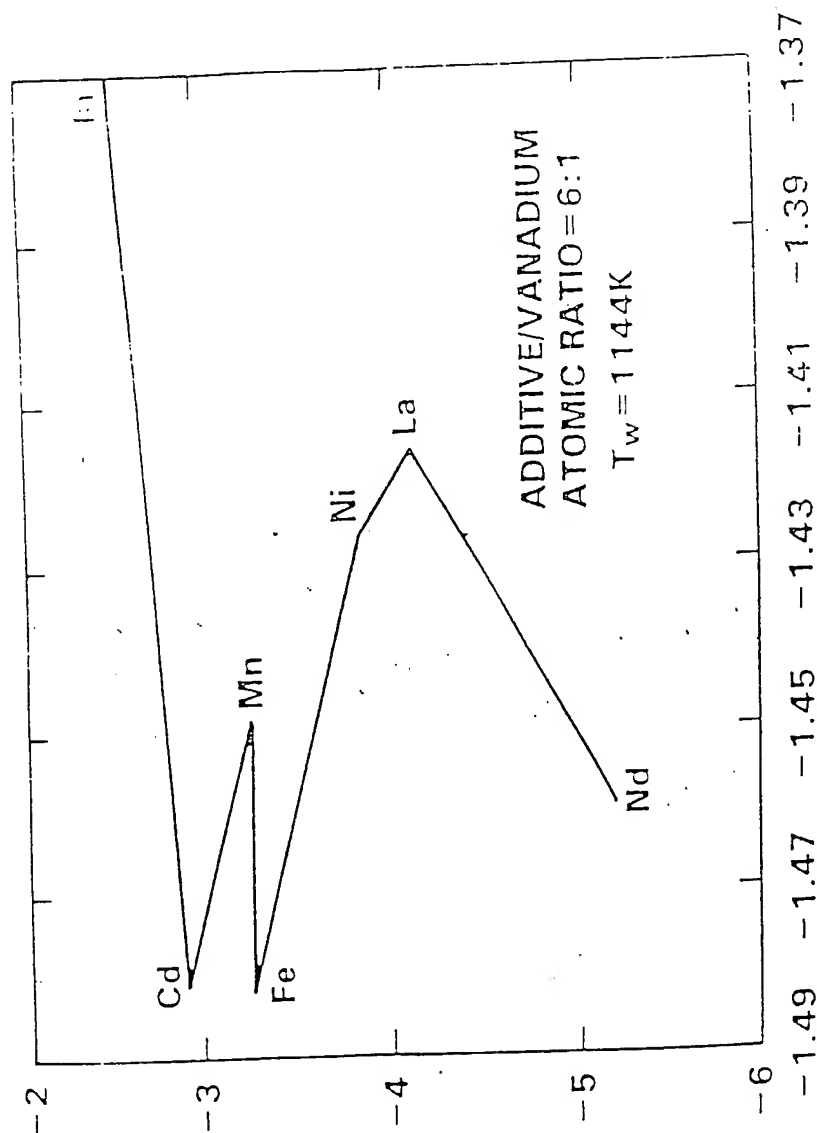


FIG 5. CORRELATION OF MEASURED CORROSION RATE DATA WITH COMPUTED 'IDEAL' SOLUBILITY OF OXIDE IN THE CONDENSED LIQUID

LOGARITHM OF CORROSION RATE RELATIVE
TO NO-ADDITIVE VALUE



LOG (CONDENSED SOLUTION DEPOSITION RATE)
(RELATIVE TO NO-ADDITIVE VALUE)

FIG 6 CORRELATION OF MEASURED CORROSION RATE DATA WITH COMPUTED
TOTAL DEPOSITION RATE OF LIQUID 'SOLVENT'-SOLUTION
(SAME FIG AS 5 WITH X-AXIS NUMBERS CHANGED)

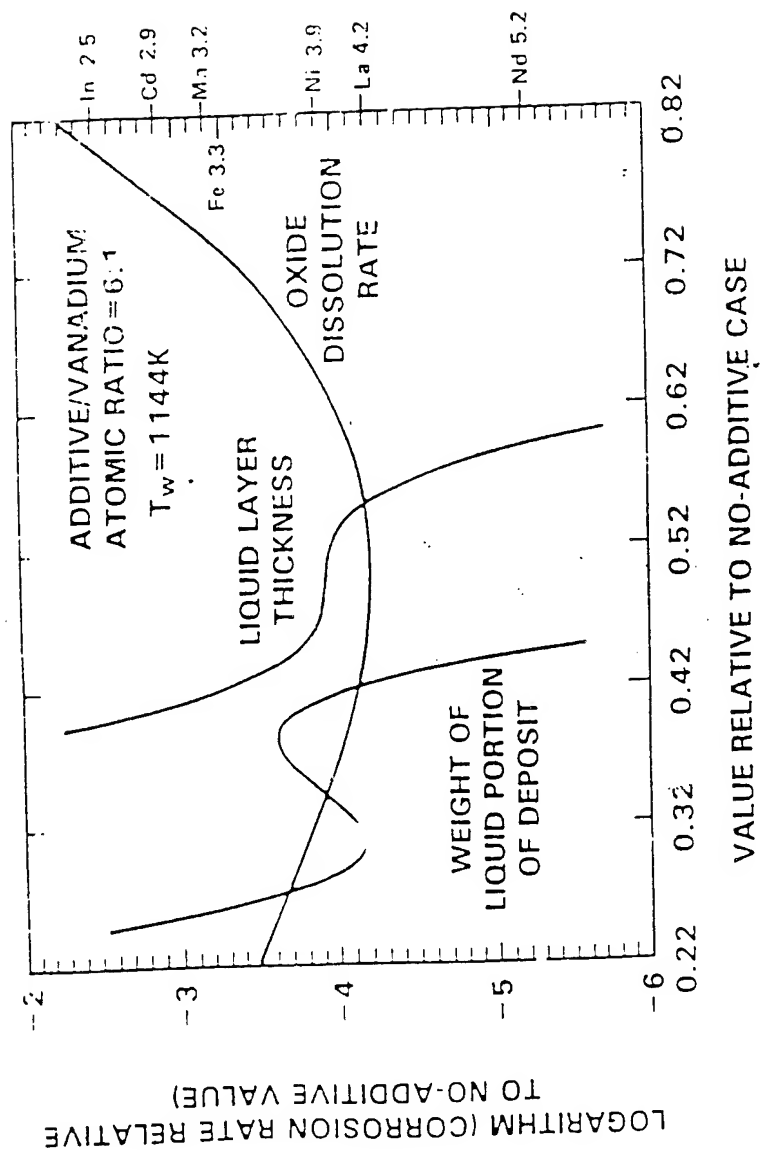


FIG 7. CORRELATION OF MEASURED CORROSION RATE DATA WITH COMPUTED LIQUID LAYER WEIGHT AND THICKNESS AND OXIDE DISSOLUTION RATE

Detection and Thickness Characterization by X-Ray Backscatter of Second-Layer Corrosion in Aircraft Structures

Dr. L.R. Lawson, Mr. N.Kim and Prof. J.D. Achenbach*

Center for Quality Engineering and Failure Prevention
Northwestern University
Evanston, IL 60208-3020

SUMMARY

This paper briefly describes the Concept, the Equipment and the Preliminary Validation of an X-Ray Backscattering Technique to obtain quantitative thickness profiles of layered aircraft structures for the purpose of detecting and characterizing second-layer corrosion.

The features of the system may be summarized as follows

- Gives a cross-sectional view of aircraft sheet metal joints.
- Allows dimensional measurement and material identification of sub-surface layers.
- Only one-sided access needed. Not a transmission (shadow casting) technique.
- 1/1000 inch measurement accuracy.
- No evacuations. Does not interfere with hangar activity.
- Self-propelled. Scaffolding and stands are not needed.
- Data are digital files. Easily stored and transmitted via Internet.

INTRODUCTION

Until now, Compton backscatter imaging has had little commercial application to the detection of aircraft corrosion, even though its ability to image structures without requiring access to both sides is a valuable asset and in spite of the presence of commercially available equipment [1]. Until recently, the highest reported resolution in a Compton backscatter imaging system was only about 1.5 lp/mm [2]. This is not sufficient to resolve metal loss sufficiently for aircraft applications. The flux and noise considerations of Compton backscatter imaging have been reviewed elsewhere with reference to nondestructive testing [3]. Several designs for Compton backscatter imaging devices have been reported [1,2,4,5].

Extensive technical details have been given elsewhere [6].

WHAT IS X-RAY BACKSCATTER DEPTH PROFILOMETRY?

Compton x-ray backscatter depth profilometry, abbreviated X-Ray BDP, is a digital imaging technique for examining cross-sections of layered structures. It is based on the backscattering of x-ray photons toward a detector. The technique was developed specifically for the inspection of aircraft structures for corrosion as seen in the cover illustration. Unlike conventional radiographic techniques and CAT scanning, it is not a shadow-casting technique. The important difference is that X-Ray BDP gives a true *cross-sectional* view of the object being examined while in conventional (transmission) radiography, all information on structural features within the beam is superimposed in a single recording. The other major difference is that, unlike conventional radiography, X-Ray BDP does not require access to both sides of the object being examined. It can perform inspections of aircraft structures from the outside of the plane.

X-Ray BDP is designed to provide a highly accurate depth profile in locations of interest. It eliminates the costly down time needed for rivet removal required for direct measurement with calipers. It also eliminates the potential for fatigue crack initiation caused by bending the sheet metal in order to get the calipers in place or make a visual inspection. A point measurement technique such as X-Ray BDP is needed when there is an indication of corrosion by pillowing or some other broad-area inspection method such as eddy current scanning, ultrasonic scanning or possibly thermal wave imaging. These methods give a 2-D map of the near sub-surface region quickly, but they have not been able to generate cross-sectional views of much accuracy nor depth profiles. X-Ray BDP gives that additional information about thickness which is needed to make the decision of whether or not repairs are needed -- and how soon.

To collect backscatter data, the special depth-profiling camera shown in figure 1 was developed. The camera, which includes the x-ray tube, consists of a radiation detector and a precision anisotropic collimation system for both the source and the detector. Four apertures define collimation, as shown in figure 1. The first two form the beam into a pencil with a narrow rectangular cross-section. The second two apertures select a limited-thickness region from which backscattered photons reach the detector. The selected backscattered beam falls upon a thallium-doped sodium iodide scintillation detector placed outside aperture 4. The intersection of the incident and backscattered beam paths forms a scattering zone. Sweeping this scattering zone through the structure to be examined allows visualization along the path of the electron density of the material, which for aluminum and lighter elements is proportional to their mass density. The camera is mounted on a positioner which scans it in a direction perpendicular to the surface of the structure.

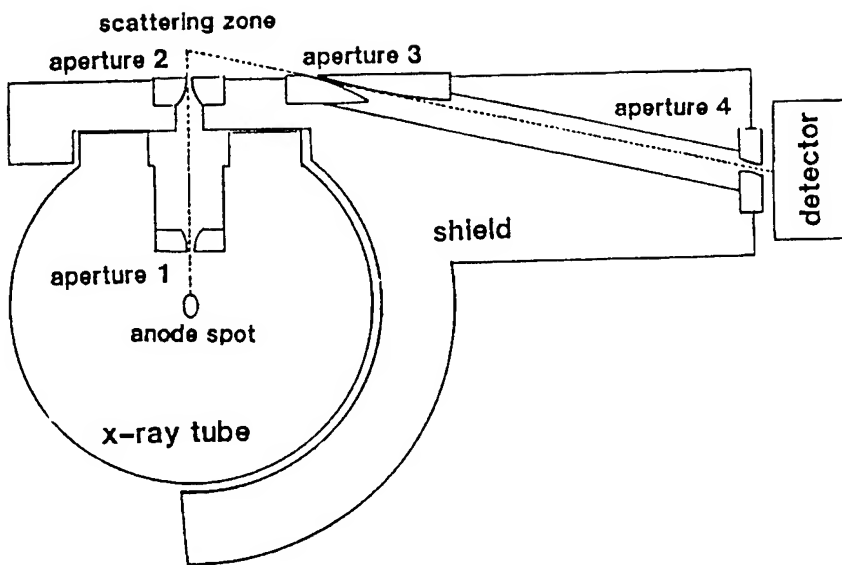


Fig. 1 Schematic representation of the backscatter camera

Like in other backscattering methods, the X-Ray BDP equipment could be used to generate 3-D images of entire volumes of material. Such an approach would, however, be very slow. In order to maximize the utility of backscatter data for aircraft inspection, X-Ray BDP reduces the image to one dimension. This makes the acquisition time on the order of 10 minutes per image--a practicable amount of time. The resulting image may be thought of as that of a core-drilled sample taken through the structure. The term "virtual core drill" has been coined to describe the X-Ray BDP machine for this reason. The design of the X-Ray BDP apparatus takes advantage of this limited dimensionality to obtain higher flux for a given resolution than could be obtained with a conventionally-designed backscatter imaging system. The shape of the scattering zone is made anisotropic and the beam angles are correspondingly chosen to maximize the flux.

The resolution of the X-Ray BDP system has been chosen to measure the thickness of the layers of aircraft skin with an accuracy of $\pm 0.001''$ which is about that of a common grade of dial caliper. This is near to the best accuracy obtainable when measuring metal which has not been polished smooth. Manufacturing tolerances, and of course corrosion, both limit the smoothness of real surfaces. Furthermore, measurement errors typically add quadratically on the average. Thus if a micrometer having a ± 0.001 inch accuracy were used to measure a surface having $0.001''$ roughness, than the average measurement error would be $\pm 0.0014''$. This is not the best accuracy possible with the X-Ray BDP technique but is close to the best meaningful accuracy possible since surface roughness less than $\pm 0.001''$ is not typical for most surfaces on aging aircraft structures.

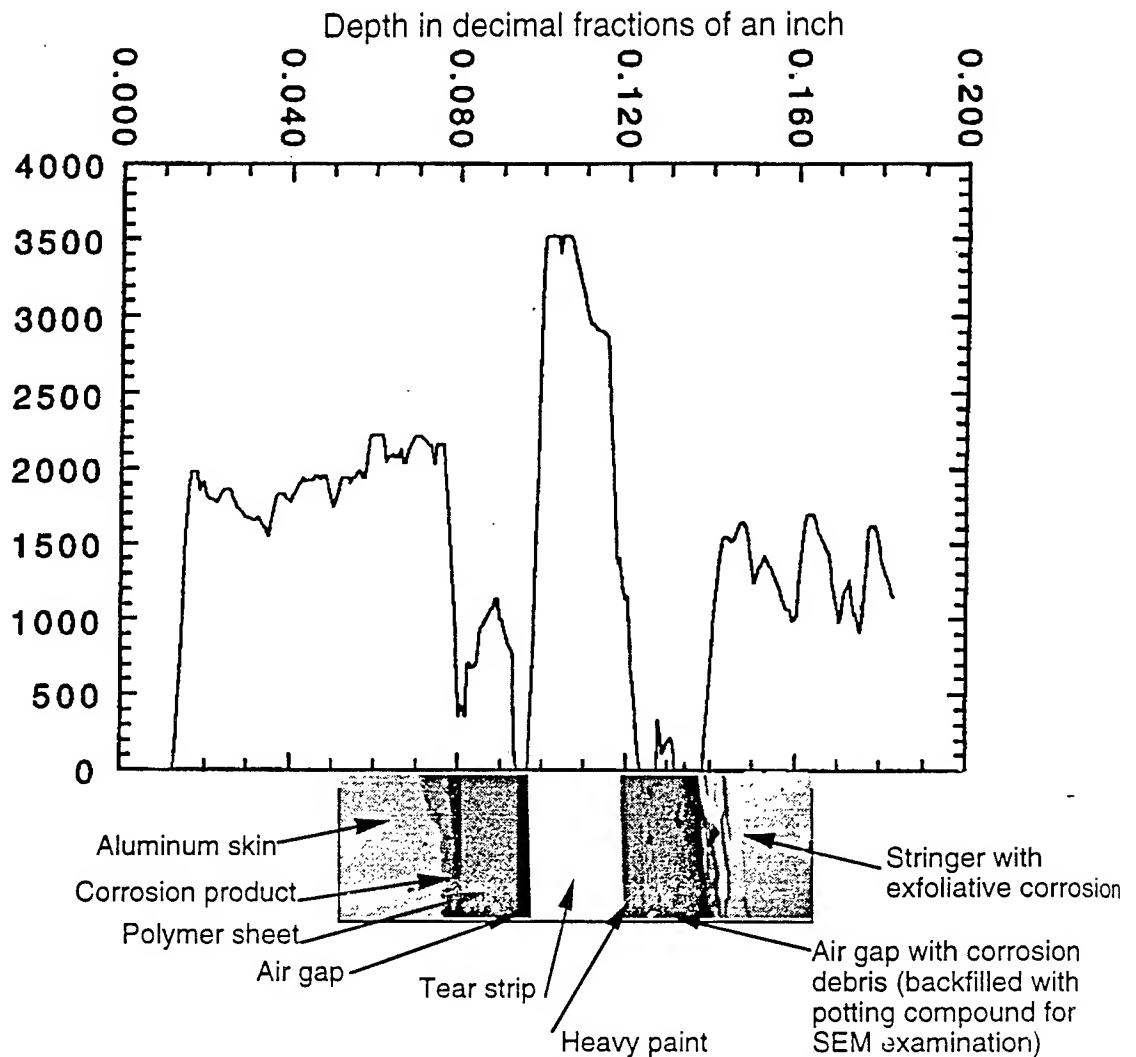


Fig. 2 Comparison of an X-Ray BDP scan, above, with an electron micrograph, below, of a cross section of an aircraft sheet metal joint.

X-Ray BDP reveals the details of layered aircraft structures. Figure 2 shows a comparison of an X-Ray BDP scan with an electron micrograph of a core sample drilled from the same location on a fuselage. The vertical axis on the scan represents the relative density of the material. The horizontal axis represents the depth into the fuselage measured from a point slightly above the surface at which the scan began. The electron micrograph displays the region between the outer skin and a stringer. In the scan, the outer layer, of aluminum, appears as a boxcar starting near 0.01". There follows a low-density region a couple thousandths of an inch in thick followed by a piece of plastic sheet, a faying strip, nearly 0.012" thick. Following that strip, there is an air gap. Beyond that gap, is a

stainless steel tear strip. The tear strip has a higher density than the aluminum. The back side of the tear strip is painted. Beyond the tear strip is a large air gap containing corrosion debris. Then follows the stringer. The paint on the back side of the tear strip is discernible. The stringer appears to be less dense than the skin, which is the result of iron in the tear strip exerting a shielding effect on layers beneath it. The presence of the heavy element, iron, in the tear strip can be deduced from the tilting down to the right of the top of the tear strip's boxcar while those of aluminum are flat.

Indications in a scan of unexpected low-density material, air gaps and thinning of metal are the hallmarks of corrosion in an aircraft structure. The presence of loose low density material signals active or untreated corrosion. Air gaps alone, unless greater than a few mils in width, do not by themselves indicate corrosion. Within the present field experience with X-Ray BDP, air gaps seem to be present in all joints in older aircraft. On one hand this is a benefit since it makes possible accurate determination of metal thicknesses while using larger data collection step sizes than would be otherwise allowable. But, it is the presence of these gaps which give rise to water trapping and corrosion in the first place. Corrosion products, when compacted, often appear as material having about half the density of their parent aluminum. Loose corrosion products often have still lower densities.

The corrosion process itself appears to determine the relatively low density of corrosion products as seen in X-Ray BDP. Water typically collects in small gaps between metal layers. Salts or other ionizable species from waste products, air pollution, ocean spray etc. find their way into the water. Chlorides appear to be especially detrimental. Sometimes ions of more noble metals such as copper also get into the joint. These can set up local electric currents which dissolve the aluminum much as the anode of a battery. More often the water and the thinness of the gap prevent air from entering uniformly. The parts of the gap that are deep inside become anodic due to the relative lack of oxygen and this sets off electric currents which dissolve the aluminum in these recesses. This process is called crevice corrosion. In all cases, ions must move through the corrosion product layer to support the electric current. This means that all corrosion products must be porous in order to grow. Their pores are the primary reason that corrosion products are less dense than aluminum itself. Figure 3 shows an electron micrograph of undisturbed corrosion product on the surface of a second-layer of skin. The relative volume of pores is 40%. The pores are the channels for the corrosion current to flow. Without pores, the corrosion product would be protective films since oxides and hydroxides are, by nature, insulators and ions cannot diffuse through them directly at temperatures below about 1000°C.

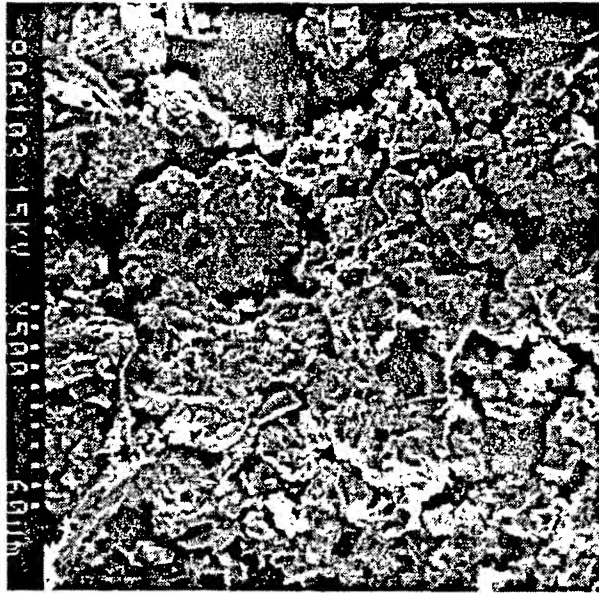


Fig. 3 Corrosion product on the surface of a second-layer of fuselage skin

HOW DO YOU USE X-RAY BDP?

The cover illustration shows X-Ray BDP being used to inspect a station along a lap splice on the Boeing 737 located at the FAA/AANC facility in Albuquerque, NM. The X-Ray BDP unit moves around under its own battery power. The unit is positioned at the point where the scan is to take place, and the scan head is guided to the exact location by an operator (typically on a ladder). The operator controls the boom and can pivot the scan head. When the scan head is in place, four feet rest against the planes surface. Then by operating the boom, the scan head is pressed against the plane. Friction of the feet against the surface holds the scan head in place. The boom itself is a giant spring which is constructed so as to have compliance in the axial as well as lateral directions. The boom supports the scan head and simultaneously applies pressure normal to the bottom surface of the scan head's feet in whatever position the head may be placed. The cover shows the scan head being pressed against the side of the plane. Figure 4 shows the scan head lifted into position for inspection of the belly section of an aircraft. The scan head when in use is thus aligned with the surface of the plane but is sufficiently independent of the motorized carriage, which transports it.

Once in place, the scan head is precisely re-aligned by computer-controlled stepper motors using position sensors which contact the plane; and, then the scan begins. Figure 5 shows the scan head. One of the motors is visible in the lower foreground; two of the four feet are seen at the

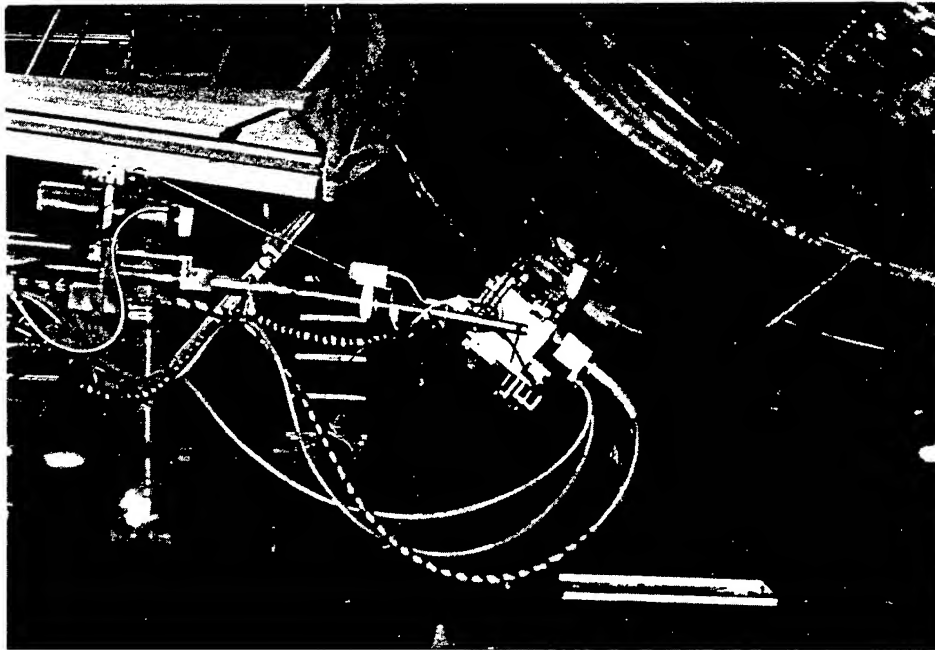


Fig. 4 X-Ray BDP Scan in place underneath an aircraft for scanning the belly section.

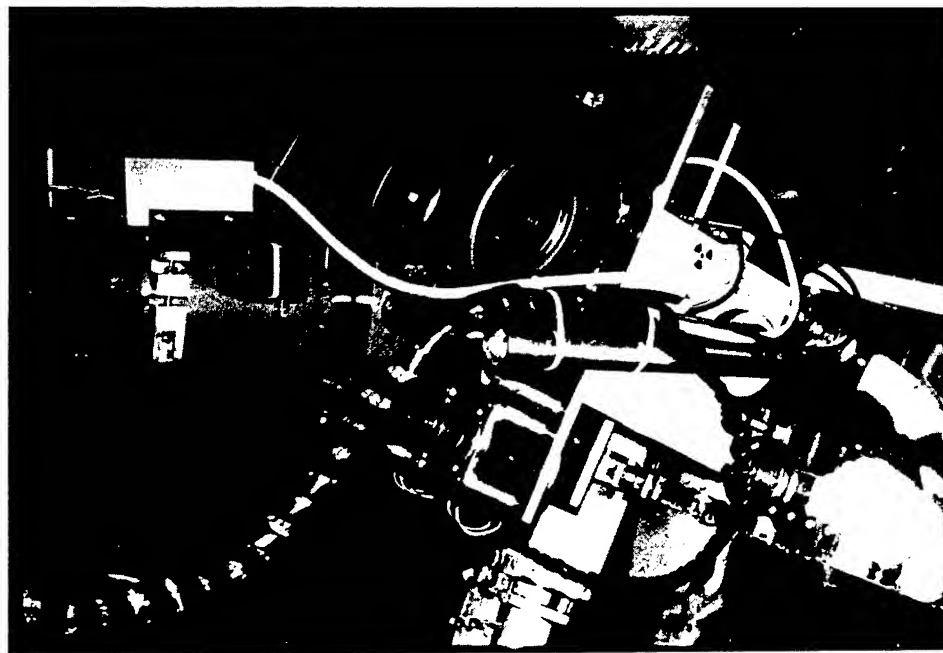
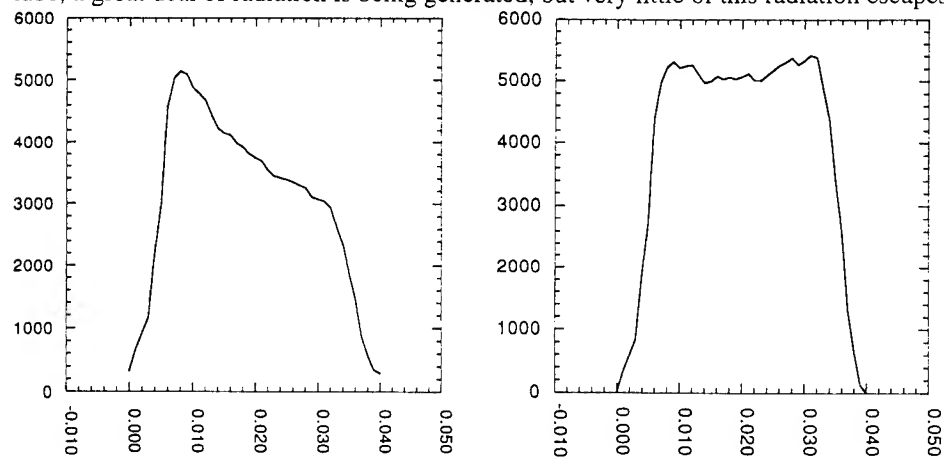
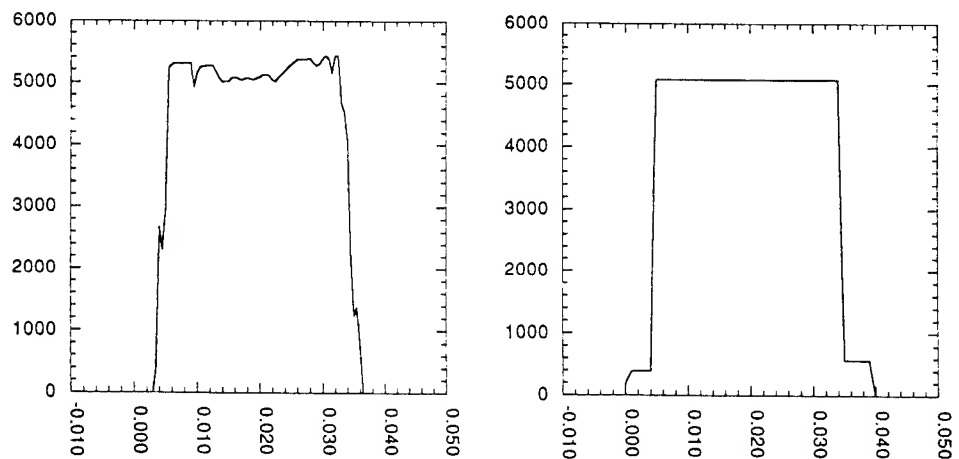


Fig. 5 Scan head. One of the stepper motors and two of the feet are visible.

right. The computer performs the scan, advancing the motors and stopping at intervals to collect data. These intervals are steps of usually 0.001" or 0.002". Because an edge appears as a slope in the unprocessed data, the edge can be precisely located so long as two data points are taken along the slope. Thus, for example, in principle, a 0.002" step will precisely locate an edge (within say 0.0001") provided that there is a gap of 0.004 or more inches between that edge and the next one. Of course, noise degrades this precision and the main source of noise is the statistical nature of photon counting. As a rule of thumb, 1000 counts are needed to locate the edge in the example to within 0.001". Increasing the number of counts increases the precision. While the scan is being made, the x-ray tube is operated typically at 150 KV and 15 mA. This means that, within the tube, a great deal of radiation is being generated, but very little of this radiation escapes. Only a



Figs. 6a,b Raw(a) and reconstructed(b) data for a scan through a single layer
The x-axis is depth in decimal inches, the y-axis is relative density.



Figs. 6c,d Deconvolved(c) and blocked(d) data.

very tiny beam is actually used. Heavy shielding near the x-ray tube is needed to confine the beam. Consequently, very little radiation escapes into the environment. During scanning, the radiation level is low enough that, by the standards of most States, workers who are not designated radiation workers may safely approach within as little as three feet from the operating x-ray tube. Greater than ten feet from the operating tube, the radiation level is extremely low. Mechanics may thus work on the outside of the plane in the vicinity of X-Ray BDP scanning. Because some of the beam becomes trapped inside, working inside the plane during scanning might be inadvisable. But the worst dose of radiation measured on the inside of a plane, directly on the other side of a fuselage skin at the point of irradiation, still amounted to only the equivalent of one chest x-ray per hour. During the scanning, the computer rechecks alignment and realigns the scan head as needed. If the count rate drops to too low a value, the computer interrupts the scan and queries the operator for instructions.

When the scan is completed, the computer displays the result as a graph similar to that in figure 2. Several processing steps are involved. These are illustrated in figures 6a-d. Figure 6a shows the raw data for a scan through a single piece of metal. The effect of reconstruction is shown in figure 6b. Reconstruction mathematically removes the shadows of upper layers on lower ones. In the case of a single layer it converts a boxcar with an exponential top, figure 6a, into one with a flat top, figure 6b. The next step removes the blurring effect of the aperture upon edges. This blurring effect gives sloping sides to the boxcars in figures 6a and 6b. Figure 6c shows the sides squared through deconvolution. A still more idealized form is obtained by further processing called "boxing" or "blocking". Blocking applies a slope threshold method of edge finding to the deconvolved data. A table of layer thicknesses is an important byproduct of the process. Unfortunately, this type of processing slightly degrades the accuracy of the measurement. A less-speedy approach based on using the deconvolved or blocked image as a guide to finding the actual edges in the raw data gives superior results.

EXAMPLES OF X-RAY BDP

The two examples which follow were taken from scans made at the FAA/AANC Validation Center, as part of the preliminary validation process of X-Ray BDP.

Figure 7 shows a scan of the Boeing 737 at the FAA/AANC facility. The scan is taken through a lap joint along the middle row of rivets. The scan has been processed through the deconvolution step shown in figure 6c. Large air gaps and loose material suggest the presence of corrosion. The front layer of skin measured 0.0375" using the deconvolved plot. The expected

accuracy under these circumstances is an average absolute error of 0.0015". Better accuracy could have been obtained by fitting the raw data, as mentioned above, but this is not yet routine.

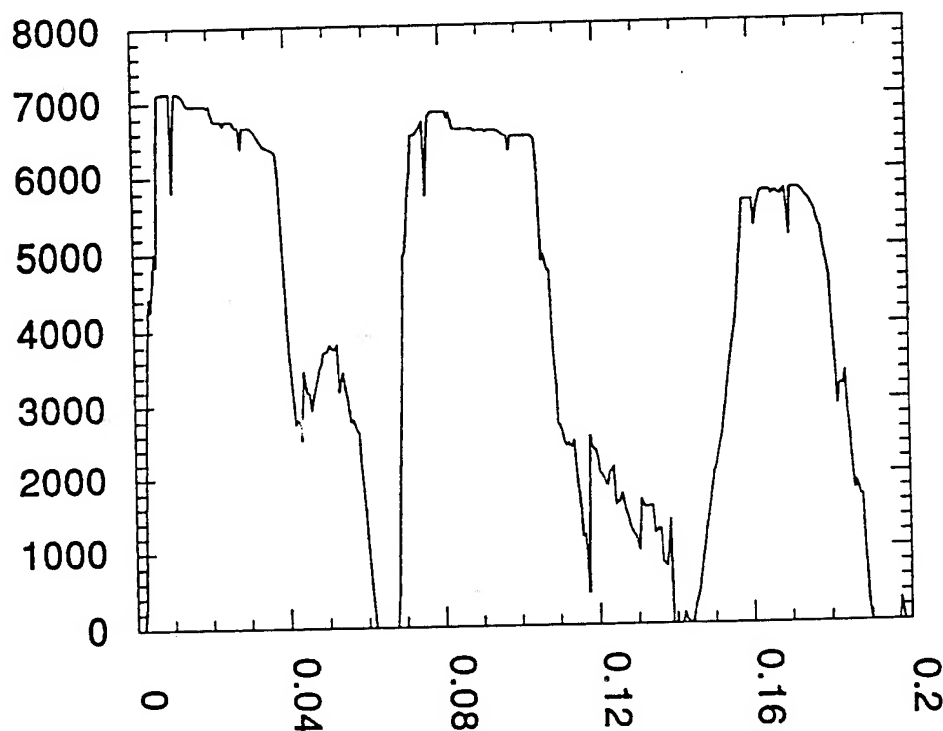


Fig. 7 Scan through a lap joint. Three metal layers are shown.

In what follows, the thicknesses will be quoted to the apparent accuracy on the scan, three or four decimal places, in order to avoid inviting cumulative rounding errors, since the accuracy of two layer thicknesses added together is still the same as that for each layer. Beneath the front layer was a faying strip of possibly scrim cloth and sealant. It resembles the layer of polymer seen in figure 2. The scan suggests that this layer has become detached from the front layer leaving a 0.001" gap. The low-density faying layer measured 0.0175". Below the faying layer was another air gap, 0.0097" wide. The second layer of skin, which begins below this gap, measured 0.0403". Its rear surface looks rough as indicated by the sloping of its front surface being asymmetrical to that of its back surface. It may also have been painted with primer. A small-step long-count-time scan of just the interface could be used to resolve this issue were it important. Beneath this layer of skin are the remains of another faying strip, probably reduced to an aggregate of sealant and corrosion product. It measured 0.0212". Its unusually-low density and looseness are strong indicators of corrosion. Beneath this is yet another air gap 0.0138" wide. The last layer is the

stringer itself. It measures only 0.0355". Micrometer examination within the plane showed that the stringer was indeed about this thickness.

Figure 8 shows a scan of a boron epoxy patch applied to a cold-bonded skin on the same plane. Although boron has a low atomic number, the density appears as if it were higher than that of aluminum. This is partially the result of the very low x-ray absorption coefficient of this material. The patch measured 0.0245" thick and appears to be composed of two layers of boron fiber separated by a layer of epoxy. The outer layer measured 0.013" while the second layer of patch measured 0.0105". Between the two layers was a layer of epoxy, about one mil thick. Beneath the patch at the point where the scan was made there appears to be a disbond with a gap 0.0035" wide. There also appears to be some warpage since the planes of the aluminum and the patch are not parallel at the interface. Underneath the patch is a bonded skin composed of two layers of aluminum. The first layer measured 0.038" thick while the second measured 0.0343" thick. The resin bond between the two layers measured about 0.003".

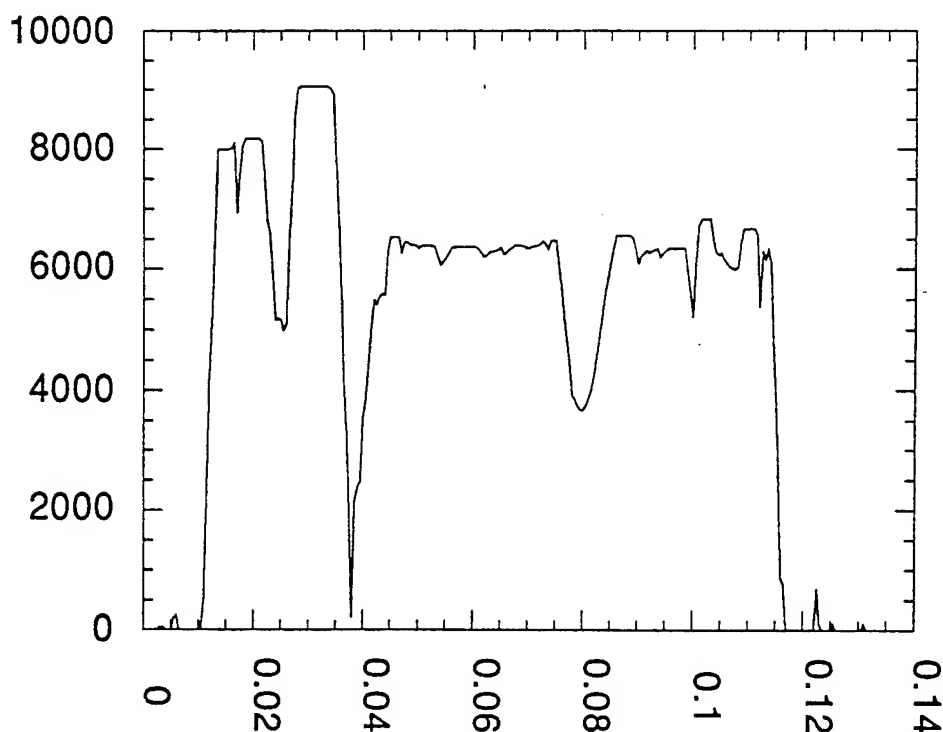


Fig. 8 Scan through a boron-epoxy patch applied to a cold-bonded skin.



Mobile X-Ray BDP unit in place for a scan of a lap joint of a B737

ACKNOWLEDGMENT

The development of the X-Ray BDP unit was funded by the Federal Aviation Administration as part of Northwestern University's participation in the Center for Aviation Systems Reliability Consortium.

REFERENCES

1. J. Kosanetzky et al., "Compton Back-Scatter Tomography of Low Atomic Number Materials with the Com-Scan System," Phillips Forschungslaboratorium, Hamburg (no date).
2. J. Smith, "Backscatter Imaging Tomography BIT (T.M.), presented "Advanced Development Computed Tomography Programs Industry Demonstrations and CT Workshop," Wright Laboratory/Hill Air Logistic Center, Salt Lake City, UT, May 5-7, 1992.
3. L. Lawson, in Review of Progress in Quantitative Nondestructive Evaluation (D.O. Thompson and D.E. Chimenti, Eds.), Vol. 11A, pp. 315-322, Plenum, New York, 1992.
4. J.A. Stokes, K.R. Alvar, R.L. Corey, D.G. Costello, J. John, S. Kocinski, N.A. Lurie, D.D. Thayer, A.P. Trippe, and J.C. Young, Nucl. Instrum. Methods 193, 261-267 (1982).
5. H. Strecker, Mater. Eval. 40, 1050-1056 (1982).
6. L. Lawson, Journal of X-Ray Science and Technology 4, pp. 18-36, 1993.

Rapid Inspection of Tubing and Piping Due to Corrosion-Related Problems

Mrs. Susan W. Borenstein, P.E.*
Structural Integrity Associates
3150 Almaden Expressway, Suite 145
San Jose, CA 95118-1217

Mr. Robert McCullough &
Mr. James Doyle
Quest Integrated, Inc.
21414 68th Avenue South
Kent, WA 98032

ABSTRACT

Military and commercial power-generating facilities often have failures to tubing and piping systems. In addition, marine tubing and piping systems are subject to increasing demands for better performance and longer service life. Primarily, the systems are degraded by fouling and corrosion. These can affect flow, heat transfer rates or structural integrity. This paper will discuss the failure modes, such as fouling and corrosion, particularly microbiologically influenced corrosion (MIC). MIC is the term for deterioration of metal by corrosion processes that occur either directly or indirectly as a result of the activity of organisms or their metabolites. Inspection methods for these degradation mechanisms are discussed. In addition, an advanced inspection system which integrates laser profilometry and fluorescence spectroscopy in a single probe is discussed. The probe scans the internal length of tube or pipe and generates a topographic map of the surface and characterizes the corrosion deposits to assess the severity of wall loss or pitting and the presence of deposits.

INTRODUCTION

Microorganisms have the capability to adhere to surfaces, grow and produce biofilms. Often biofilms create difficulties when they form, such as when slimes are produced on heat exchanger tubes and heat transfer capabilities are reduced. Sometimes corrosion occurs beneath the biofilm. Microbiologically influenced corrosion (MIC) is the term for the initiation or acceleration of corrosion by microorganisms or their metabolites, usually on metal surfaces.¹

Biofilms are usually made up of extracellular polymers (exopolymers) and a consortium of sessile organisms, debris and organic matter.^{1,2} The extracellular polymers are secretions that form a matrix of fibers and often envelop the organisms and contribute to collecting other material. Biofouling is the biological growth on surfaces in contact with natural water.² Biofouling often leads to corrosion underneath the deposits formed on metal surfaces.

The study of MIC and the need for better monitoring and inspection methods are relatively recent events. MIC monitoring and inspection is more complex than "normal" corrosion.³⁻⁵ First, more than one corrosion mechanism may be involved. Second, MIC is associated with extremely diverse microbiological environments. Inspection methods need to be able to detect diverse corrosion mechanisms on a wide variety of materials and components.^{6,7}

BACKGROUND

Several types of corrosion mechanisms are associated with military and commercial power-generating facilities. These include general corrosion, pitting, underdeposit or crevice corrosion, and MIC. Less commonly occurring problems include corrosion-assisted cracking and velocity-assisted corrosion.

Classifying corrosion can often be difficult. General corrosion is a general uniform loss of metal: usually a small amount over a large area. This is the form of corrosion (in almost every case) for which corrosion rates are tabulated. In contrast, localized corrosion is selective attack, such as pitting. For example, a large portion of the surface area of a pipe may be unaffected, and rapid corrosion occur at the weldments. Failures of this type may result in costly problems and may be difficult to monitor and

inspect. Lack of understanding the distinction between corrosion rate measurements, resulting from general corrosion, and localized corrosion may also lead to expensive problems and possible failures.

Crevice corrosion is another localized form of pitting corrosion. Crevice corrosion typically occurs under deposits or in crevices between mating surfaces, such as gasketed flanged connections. Often it occurs on film-protected (passive) metal surfaces, such as austenitic stainless steels. Some instances of MIC may be considered a form of crevice corrosion when the exopolymer film formed by the microorganisms creates a "living crevice", as shown in Figure 1. The role of organisms relates to the influence of differential aeration cells forming under a biological deposit where a pit initiates and tubercle forms.¹

DISCUSSION

Difficulties arise with characterizing MIC and biofouling on metal surfaces. To what extent are organisms involved and is the **microbiological** species important? Is the microbial ecology important or relevant? How much are the organisms involved and how do they **influence** the surfaces? What **corrosion** mechanisms are involved and are there any differences than in underdeposit corrosion without microorganisms involved? The following discussion highlights these three aspects of MIC as they relate to monitoring and inspection of biofouled surfaces.

Monitoring and Inspection Techniques

Microbiological analysis has frequently been done in conjunction with monitoring MIC of metals, particularly in problems of corrosion associated with the oil and gas industries. Sulfate reducing bacteria (SRB) and their action upon metals was the basis of a theory by von Wolzogen Kuhr and van der Vulgt.⁸ They theorized that the corrosion of iron buried in an aerobic soil was the result of activity by SRB. Since then Little and Wagner⁹ note, in addition to the SRB, the iron-oxidizing, sulfur-oxidizing bacteria and many other organisms have been shown to influence corrosion of metals. Borenstein and Licina⁵ discuss microbiological analysis methods.

It must be clarified that the presence of microorganisms in a fluid or in a deposit does not indicate how or how much those organisms may have influenced corrosion if they influenced it at all. Surfaces exposed to environments with biological activity would **always** be expected to have organisms present on the surfaces, often in very high numbers. The

organisms **may or may not** have been involved in or even a primary factor in corrosion. Examination of surfaces for chemical species produced by the microorganisms which interact with the metal surface to produce corrosion, or mineralogical "fingerprints" can be useful in determining the microbiological influence.¹⁰ McNeil and Little have found that certain types of corrosion products can be formed only in environments by biological processes. A fingerprint indicator occurs when minerals form that are not consistent with those able to form in normal environmental conditions. The direct cause-and-effect relationship between microbiology or microorganisms adhering to surfaces and corrosion occurring underneath is often difficult to establish.

The importance of inspection and the ability to decrease operation and maintenance costs by inspection prompted changes in inspection routines in the 1980's. A variety of established techniques were used and improved upon and innovative techniques are being developed that apply to inspections for MIC and other forms of corrosion. These include:

- performance monitoring
- nondestructive testing
- advanced techniques

Performance Monitoring

The performance of a system often gives an indication that problems are developing. Changes in temperature, pressure, and flow rates may indicate early signs of fouling in a heat exchanger, for example. Unfortunately, performance monitoring is not specific. The root cause of the problem is often not apparent from indirect records, so attempts to resolve a problem are often limited. Performance monitoring is not a corrosion monitoring technique, but is sometimes perceived to be.

Nondestructive Testing

Inspections normally begin with nondestructive examination to evaluate the condition of a system or component. Some combination or coordination of techniques is also common. Common inspection methods include:

- Visual Testing (VT)
- Ultrasonics Testing (UT)
- Magnetic Particle Testing (MT)
- Liquid Penetrant Testing (PT)

- Eddy Current Testing (ET)
- Radiographic Testing (RT)

Visual examination is used extensively. Based on what can be seen with the naked eye or with low powered optical lenses it is often the least expensive inspection method. Conditions of MIC, as well as biofouling, and various corrosion problems may be documented using a 35mm camera and closeup lenses. Pipe crawlers, et al., can perform remote visual inspections of interior surfaces.

Ultrasonic inspections use high frequency sound waves to detect both surface and subsurface flaws. The sound waves travel through the material and are reflected from interfaces. Flaws are detected by analyzing the reflected beam. Ultrasonic testing is sometimes unsuitable for MIC and corrosion problems because the rough or irregular surface gives difficult to interpret signals.

Liquid penetrant inspection reveals discontinuities that are open to the surface such as pits or cracks. After liquid penetrant is applied to the surface, the penetrant dye seeps into the discontinuity. Excess penetrant is cleaned away and a development powder is applied to the surface to draw out the dye from the discontinuity. It is sometimes suitable for corrosion and biofouling related problems. Not suited to field inspection of tubes or pipes.

Magnetic particle inspection is useful for inspecting ferromagnetic materials with surface or near surface discontinuities or flaws. The principle of operation relies on the nature of the material and the fact that when a metal is magnetized, the magnetic field formed is very sensitive to flux leakage at cracks or discontinuities. Although it is usually useful for surface flaws, it is sometimes suitable for MIC, corrosion, and biofouling-related problems.

Eddy current inspection is based on the principles of electromagnetic induction and may be used for ferrous and nonferrous alloys - although eddy current examination of ferrous alloys is much more limited. For example, plants often use eddy current testing for examining tubing for internal corrosion or damage. The induction coils are inserted into the tubing and indications can be determined by the change in flux of the induced current through the coil. From these effects, an estimate of defect thickness can be made. The accuracy and reliability is sometimes poor.

Radiographic testing uses either x-ray or gamma rays. When an object is exposed to radiation, the radiation will, in various measures, be absorbed, scattered or transmitted. The transmitted image is recorded on photographic film. Differences in film density are related to the thickness, including the flaws. For example, a pit would appear as an indication on the film. Radiography can be very useful for MIC or corrosion related problems. It is particularly useful for determining the extent of pitting of weldments.

Advanced Techniques

Advanced inspection techniques vary in complexity, maturity and capability. Selection of a method for inspection of flaws depends on a number of variables including:

- Nature of the flaw
- Accessibility of the flaw (such as at a weldment)
- Type of material
- Part geometry
- Number of items to be inspected
- Capabilities of the inspection method
- Level of inspection quality desired
- Economic considerations

Laser profilometry, such as the LOTIS™ technique developed by Quest Integrated, Inc., of Kent, Washington, uses a laser source, optic, and a photodetector in the front section of the probe for internal inspection of tubing.¹¹ Doyle discusses how this is useful for inspection systems that can rapidly scan the full length of a marine boiler tube, generate a quantitative topographic map of the tube surface, and tabulate a summary of the results (Figure 2). Internal corrosion and pitting are the primary mechanisms of degradation the system was designed to examine. It provides a high degree of precision and accuracy and distinguishes between cracks, pits and other defects. LOTIS is now being used to inspect heat exchanger and condenser tubes in both military and civilian applications.

An advanced inspection system is currently under development to identify and characterize MIC-affected tubing and piping through the use of advanced, cost-effective NDE methods. The system employs a noncontacting, laser-based sensor assembly that is capable of "fusing" laser-based profilometry and fluorescence spectroscopy data obtained using a single probe. The resulting inspection system will be capable of

rapidly and accurately scanning the length of a tube or pipe and generating a detailed topographic map of the internal surface. Superimposed on this image will be a false-color map that identifies the presence of MIC. The results will be displayed in a number of computer-graphic formats that will allow operators to quantitatively assess the level and severity of wall loss due to pitting and determine the presence and extent of MIC-affected surfaces.

FATS (Focused Array Transducer System) developed by Infometrics of Silver Spring, MD, is a UT system that improves the performance of ultrasonic examinations. Conventional UT techniques can be improved by using a focused transducer, made up of phased arrays of transducers and sophisticated electronics (Figure 3). In addition, the technique can be partnered with TestPro, also developed by Infometrics. TestPro is a data acquisition system with enhancement features.

CONCLUSIONS

Selection of inspection tools must focus on:

- resolution capabilities
- speed of inspection
- compatibility with operations and maintenance activities

New techniques, such as laser profilometry and the focused array transducer system, may provide greater resolution and specificity for unique problems.

ACKNOWLEDGEMENTS

We thank Mr. George Licina of Structural Integrity Associates, Inc., San Jose, CA and Mr. George Nekoksa of Corrosion Failure Analysis and Control, San Ramon, CA for their review of the manuscript.

REFERENCES

1. Borenstein, S.W., 1994, *Microbiologically Influenced Corrosion Handbook*, Woodhead Publishing, Ltd., Cambridge, U.K.
2. Little, B.J., 1985, "Succession in Microfouling", in *Proceedings of the Office of Naval Research Symposium on Marine Biodeterioration*, U.S. Naval Inst. Press, Bethesda, MD.

3. Licina, G.J. and Nekoksa, G, 1993, "An Electrochemical Method for On-line Monitoring of Biofilm Activity" CORROSION/93, paper No. 108, NACE, Houston, TX.
4. Licina, G.J. and Nekoksa, G, 1994, "Experience with On-line Monitoring of Biofilms in Power Plant Environments" CORROSION/94, paper No. 257, NACE, Houston, TX.
5. Borenstein, S.W. and Licina, G.J., 1994, "An Overview of Monitoring Techniques for the Study of Microbiologically Influenced Corrosion" CORROSION/94, paper No. 611, NACE, Houston, TX.
6. Borenstein, S.W. and Licina, G.J., 1994, "Monitoring and Inspecting Biofouled Surfaces" presented at the *Third European Federation of Corrosion Workshop on Microbial Corrosion*, March 13-16, Estoril, Portugal.
7. Borenstein, S.W. and Licina, G.J., 1994, "Inspecting Biofouled Surfaces" *1994 International Joint Power Generation Conference*, American Society of Mechanical Engineers, New York, NY.
8. von Wolzogen Kuhr, C. and van der Vlugt, 1934, "The Graphitization of Cast Iron as an Electrochemical Process in Anaerobic Soils", Water, 18, The Hague.
9. Little, B.J., and Wagner, P., 1992, "Quantifying Sulfate Reducing Bacteria in Microbiologically Influenced Corrosion", NSF-CONICET Workshop on Biocorrosion and Biofouling, Mar del Plata, Argentina, Oct. 1992.
10. McNeil, M. and Little, B.J., 1990, "Mackinawite Formation During Microbial Corrosion", *Corrosion*, Vol. 46, p. 599, NACE, Houston, TX.
11. Doyle, J, 1991, "Laser-Based Surface Profilometry: An Emerging Technology for Nondestructive Evaluation", *Materials Evaluation*, 49 (7).

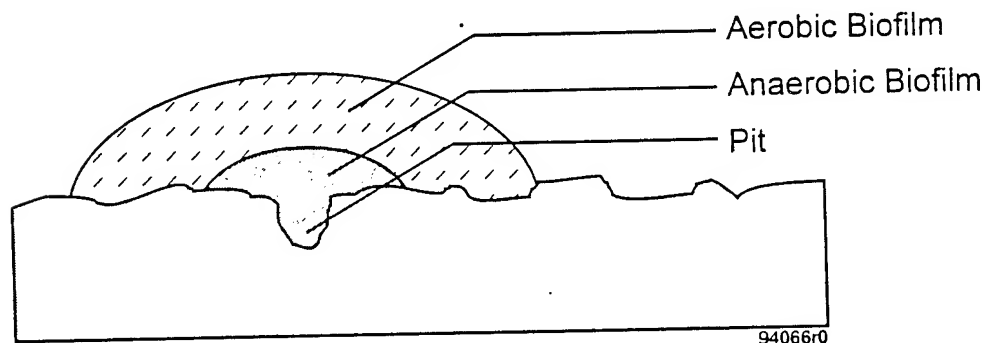


Figure 1. Biofilm Over Pitting Corrosion

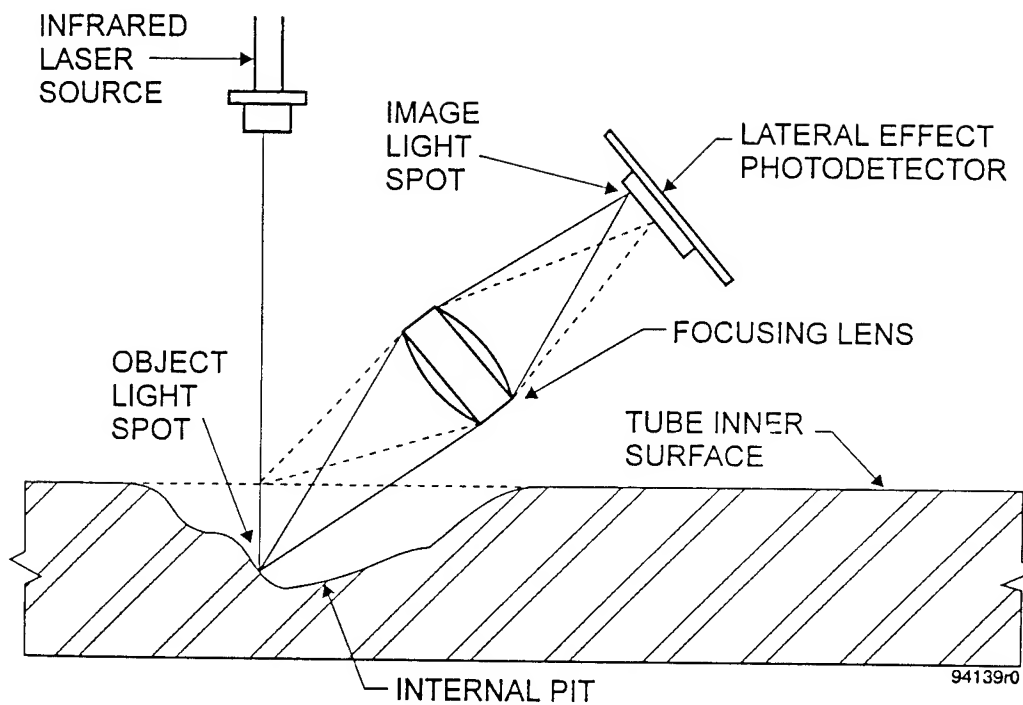


Figure 2a. Operation of Laser Scanner

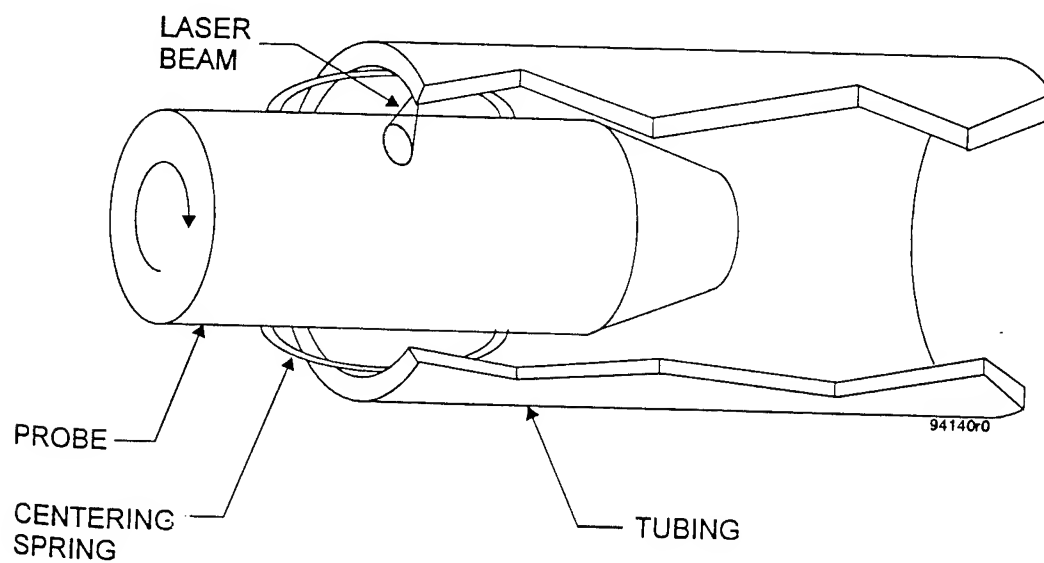


Figure 2b. Optics Housing of LOTIS™ Generates a Helical Map of Tube 1D

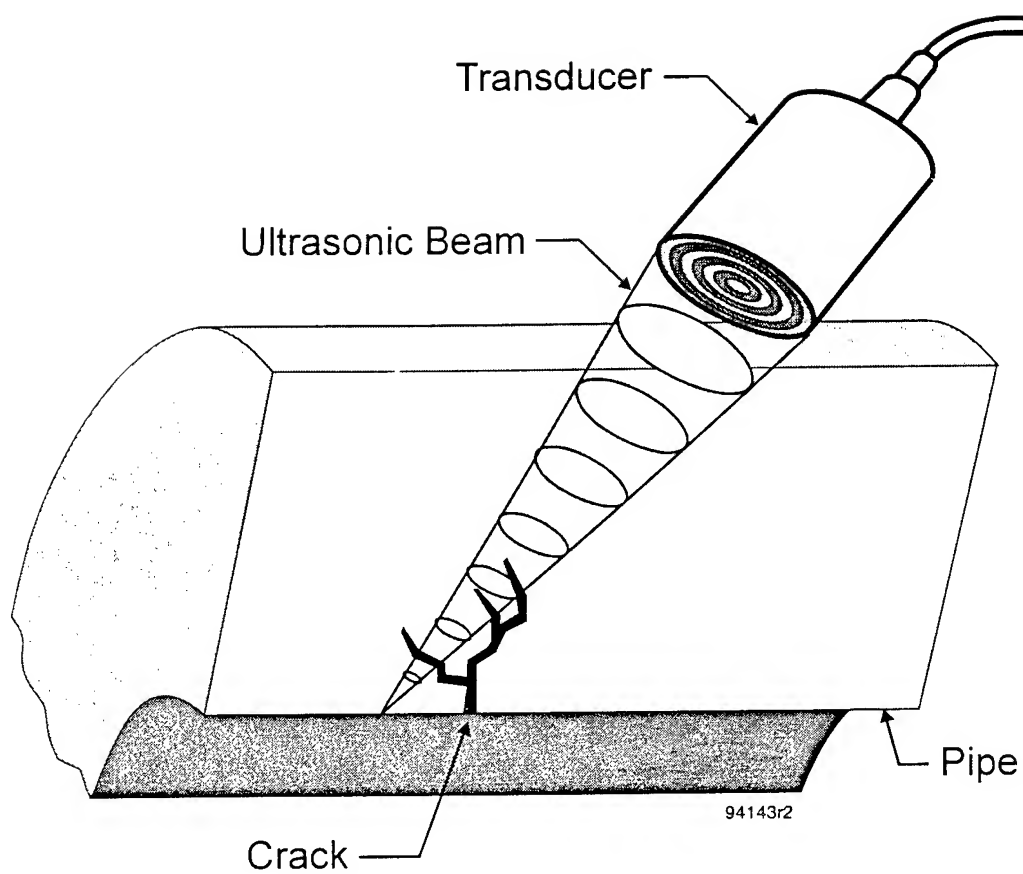


Figure 3 Focused Ultrasonic Beam Using Multiple Transducers

Studies on Corrosion of Aluminum Alloys by JP-10 Fuel Using Electrochemical Impedance Spectroscopy

Dr. Ramesh Bhardwaj^{*}
Rockwell Space Operations Company

Dr. Mohan Gunaji
AlliedSignal Technical Services Company

and

Dr. Harold D. Beeson
National Aeronautics and Space Administration

NASA, Johnson Space Center, White Sands Test Facility
P.O. Drawer M.M.
Las Cruces, NM 88004

ABSTRACT

A Government Industry Data Exchange Program alert has been issued that states that the fuel system icing inhibitor (FSII) in JP-10 fuel is corroding aluminum components in missile fuel systems during long-term storage under an anhydrous nitrogen atmosphere. Previous investigations into fuel-system corrosion have used extreme conditions such as high FSII concentration or temperature to accelerate corrosion. To better understand the effects of fuel additives on corrosion of aluminum alloy components, electrochemical impedance spectroscopy (EIS) was used to determine the corrosion rate as a function of additive type and concentration under conditions similar to those found in actual use. This paper presents the EIS results of corrosion studies conducted on Al 2024, Al 6061, Al A357, and Al 7075. The effects of concentration of the FSII, presence and absence of butylated hydroxytoluene, effect of water concentration, effect of temperature, and effects of coating on corrosion rates of these alloys will be presented and discussed in detail.

INTRODUCTION

Corrosion of the aluminum alloy fuel system components has been discovered in missiles fueled with JP-10. Missiles in which corrosion was discovered have been stored for long periods of time in temperature environments ranging from approximately -8 °C to 30 °C. An anhydrous nitrogen pad was placed in the fuel tank and exposed surfaces were coated to inhibit corrosion. The corrosion of the fuel system components was found to be localized pitting corrosion.

The Military Specification JP-10 is a synthetic hi-density fuel, the base component of which is Exo-Tetrahydrodi (cyclopentadiene), also known as C-10. The primary additives are an antioxidant, approximately 100 ppm of butylated hydroxytoluene (BHT), and a fuel system icing inhibitor (FSII). Typically the fuel will contain small traces of water (20-50 ppm). The FSII, as specified, is approximately 0.1 percent of either ethylene glycol monomethyl ether (EGME) or diethylene glycol monomethyl ether (DiEGME). It has been proposed that the FSII additives are responsible for the corrosion of the Al alloys.

Corrosion studies using immersion test methods similar to ASTM [1] have been shown to provide decisive results; however, conventional immersion testing is a lengthy process and is inconvenient for studies involving many variables the interaction of which is unknown. Because of these drawbacks, both DC and AC electrochemical methods have been developed to provide accelerated corrosion results which can be compared with long-term immersion experiments. Of the two electrochemical test methods, AC electrochemical impedance spectroscopy (EIS) is finding increased usage in the investigation of corrosion of bare metals [2-4] and also of coated systems [5-9]. In particular, EIS has been found to be very sensitive in the determination of pitting corrosion of aluminum [10]. One of the difficulties encountered in the application of electrochemical techniques is in the study of low conductivity media such as JP-10 fuel.

EIS has been used to investigate corrosion in nonaqueous low-conductivity media. Lawton et. al. [11], used EIS to study the corrosion of stainless steels AM 350 and AM 355 in nonaqueous media where very small differences in corrosion rates of these alloys in hydrazine were determined. Ontiveros et. al. [12], used EIS to study the corrosion behavior of mild steel coated with low conductivity inorganic zinc-rich primers in aqueous and nonaqueous solutions. Based on this previous research it was felt that EIS could be successfully applied to the investigation of corrosion of aluminum alloys in JP-10.

This paper describes the method used and the results of testing to determine the effect on corrosion current of concentration of FSII, presence and absence of BHT, temperature, and coating for several aluminum alloys.

EXPERIMENTAL

A Schlumberger potentiostat 1286 in conjunction with a 1260 impedance gain phase analyzer were used for the impedance measurements. The data were recorded between 1000 KHz and 1 Hz. An AC amplitude of 100 mV was used to collect data in the frequency range.

The electrochemical glass cell (Figure 1) was 7.04-cm-diameter and 2.05-cm long. The cell had an inlet and outlet for nitrogen purge which was also used for filling the cell with the fuel mixture. An aluminum

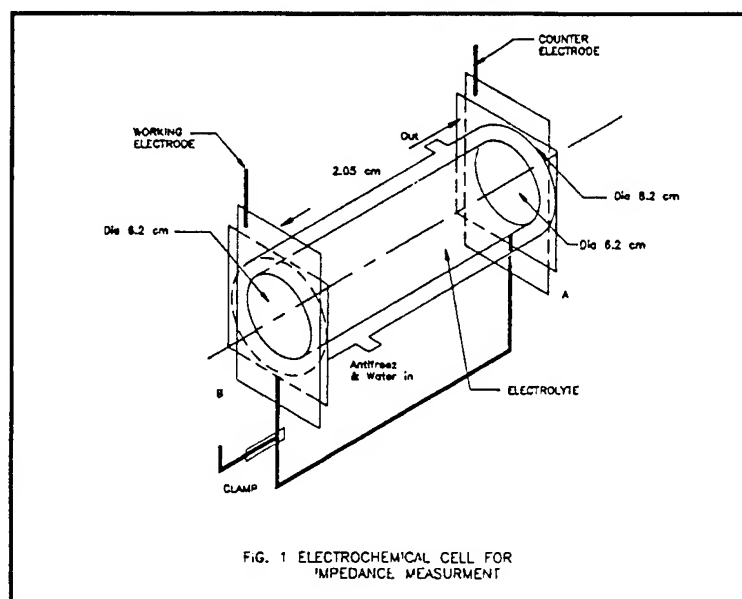


Figure 1
Schematic of Electrochemical Cell

test specimen and a viton gasket were placed on each end of the glass cell. The viton gasket had a 6.4-cm-diameter hole exposing the Al plates to the electrolyte (fuel mixture). The electrochemical cell for lower temperature studies was a double jacketed cylindrical cell. Temperature was maintained by circulating a water/antifreeze mixture from a controlled temperature bath through the outer jacket. The temperature of the electrolyte was monitored by a thermocouple.

The experiments reported here were conducted after purging nitrogen through the electrolyte and a nitrogen atmosphere was maintained in the cell. The aluminum plates served as the working electrode and the counter electrode. The working electrode was attached to the reference lead of the instrument making it the reference electrode.

Alloys tested were Al 2024, Al A357, Al 7075 and Al 6061. The EGME and DiEGME concentration was varied between 0.1 and 100 percent. The concentration of BHT was either 0 or 100 ppm. Water concentration was maintained at 22 ppm for the results reported here. Experiments were conducted at ambient temperature (23 ± 3 °C) except in controlled temperature experiments. The controlled temperature experiments were conducted at 0, 8 and 25 °C. For experiments with uncoated alloys the samples were polished with 600 grit Al_2O_3 powder to a consistent surface finish. Three coating systems were investigated, chromic acid anodization, Scotchweld EC 1290® which is an epoxy polyamide coating, and a chemical conversion coating. The coating systems were tested both individually and in combination (if applicable to the missile system).

RESULTS AND DISCUSSION

Effect Of Fuel Additives

Figure 2 is a plot of the corrosion current for uncoated Al 2024 measured after 22 days of exposure to C-10 with varying concentrations of EGME with and without BHT. The corrosion current is shown to increase over six orders of magnitude as the concentration of EGME increases in the C-10 fuel; however, the magnitude of the increase is less for C-10 solutions with BHT added. The corrosion current in 0.1 percent EGME in the absence of BHT was observed to be $1.955 \times 10^{-2} \mu\text{A}$ which increased to 4814 μA in 100 percent EGME. The change in EGME concentration from 0.1 percent to 100 percent in the presence of BHT

changed the corrosion rate from $1.648 \times 10^{-2} \mu\text{A}$ to $883 \mu\text{A}$. Similar trends were observed for solutions with DiEGME added. These results indicate that the corrosion of Al 2024 increases as a function of FSII concentration and that BHT has an inhibiting effect on corrosion.

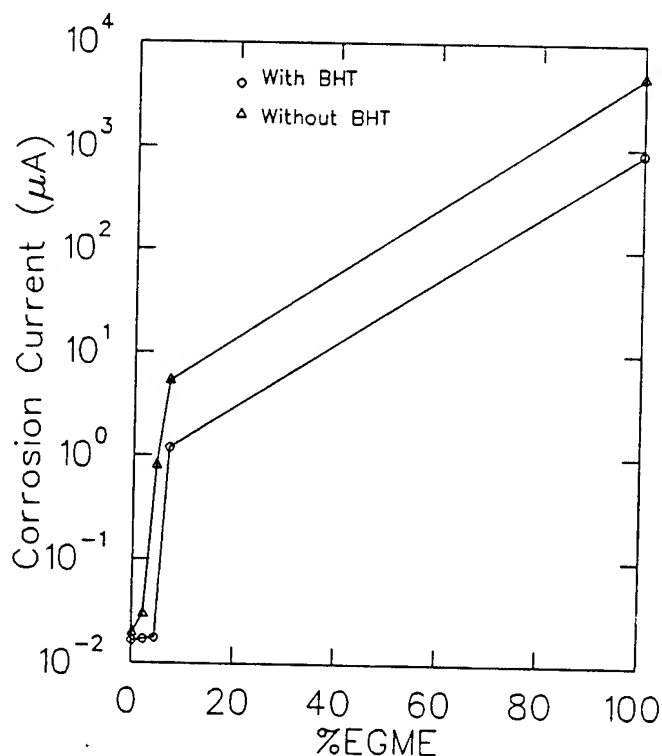
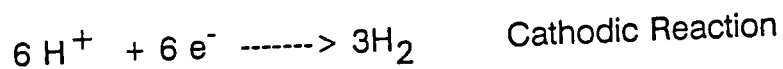
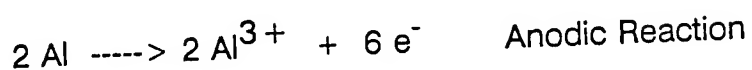


Figure 2
Variation of Corrosion Current Versus Percent EGME
in C-10 for AL 2024 (Room Temperature After 22
Days)

The corrosion reactions of Al with EGME/DiEGME could be attributed to the fact that EGME and DiEGME have weak acidic alcoholic hydrogens similar to methanol which react with aluminum forming Al-EGME complex liberating hydrogen ions in the solution. This is consistent with the reaction of methanol with polycrystalline Al in temperatures ranging from 198 K to 500 K reported by Rogers et. al. [13], which indicate the formation of methoxide species on the Al surface

with the formation of hydrogen ions. The reactions suggested are as follows:



hydrogen ions can also react with Al ions making aluminum hydride:

As the concentration of EGME increases the acidic group increases which reacts more vigorously with the Al surface which in turn increases the corrosion current as observed experimentally.

The inhibiting effect of BHT is probably due to a competitive inhibition mechanism. BHT, being a large sterically hindered phenolic compound, adsorbs on the surface of the aluminum forming a film several monolayers thick. The adsorbed BHT molecule competes with EGME for the aluminum surface which eventually decreases the corrosion rate. Phenolic compounds have been shown to inhibit corrosion in dilute salt solutions [14]. This mechanism is evidenced not only in the decreased overall corrosion current, but also by the fact that the corrosion current remains fairly constant until at higher concentrations of FSII the monolayer is broken down.

Visual and microscopic examination of the electrode after 22 days shows that the type of corrosion for EGME was localized pitting corrosion. The number and sizes of pits were found to increase as the concentration of EGME was increased. This type of corrosion is consistent to that found in missiles. The corrosion behavior observed with DiEGME was very similar to that observed with EGME; however, the pit was more diffuse and microscopic examination revealed the presence of intergranular corrosion for an electrode exposed to 4.0 percent DiEGME. No intergranular pitting was found for electrodes exposed to 4.5 percent EGME. Investigations are continuing into this result.

Effect of Temperature on Corrosion Current

The corrosion current as a function of time for Al 2024 in C-10 + 0.1 percent EGME at 0, 8 and 25 °C is shown in Figure 3. For a given temperature, the corrosion current increases as a function of time; however, the corrosion current decreases as a function of temperature.

This decrease as a function of temperature is shown in Figure 4 and is unexpected. Figure 4 indicates that the corrosion rate increases as the temperature is decreased from 25 to 0 °C but starts decreasing as the temperature drops below zero. The results can be explained by the fact that the FSII precipitates out of solution at approximately 0 °C and covers the surface of the Al electrode. Further decrease in temperature does not substantially increase the FSII concentration on the electrode but slows the corrosion rate as normally expected. A separate solubility experiment of EGME in C-10 fuel as a function of temperature was conducted. It was observed that EGME does come out of the solution and adheres as small drops on the walls of the measuring flask. The precipitation of EGME on the electrode in the form of drops increases the concentration at those locations resulting in pit formation.

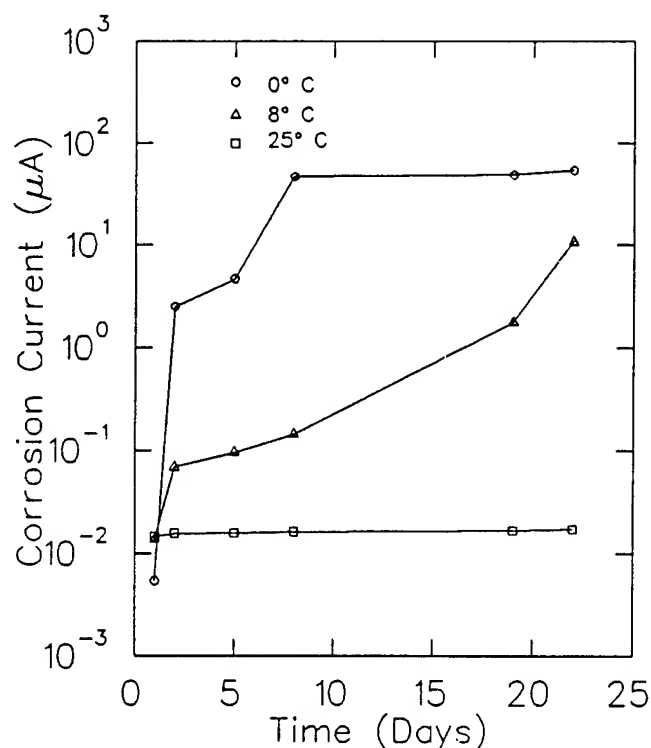


Figure 3
Variation of Corrosion Current With Time at 0, 8, and 25 °C for Al 2024 Exposed to C-10 Plus 0.1 Percent EGME

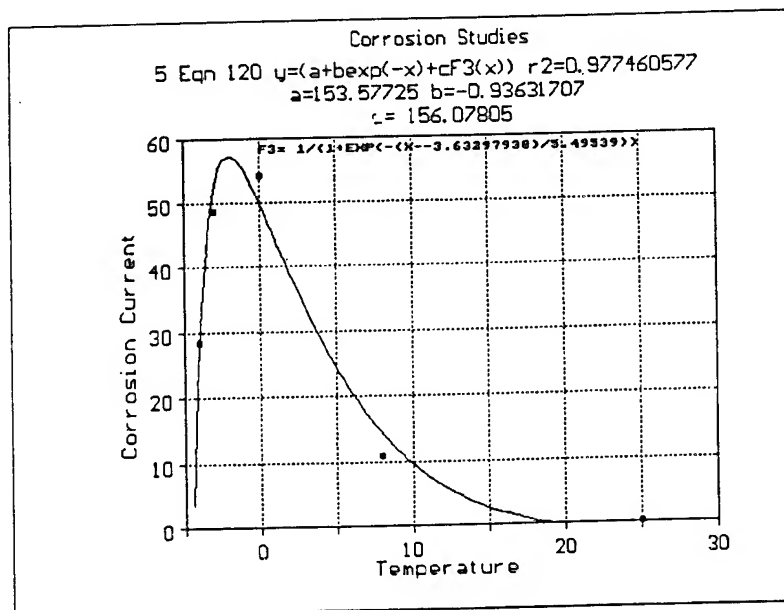


Figure 4
 Variation of Corrosion Current with Temperature for
 Al 2024 Exposed to C-10 Plus 0.1 Percent EGME

Effect of Metals on Corrosion Current

Corrosion current of different alloys in the presence of 0.1 percent and 7.0 percent EGME was determined as a function of time. Figure 5 shows the corrosion current as a function of time in 7 percent EGME for the alloys at 25 °C. The order of corrosion resistance in 7 percent EGME is Al A357 > Al 6061 > Al 2024 > Al 7075. In 0.1 percent EGME the corrosion resistance was reversed for Al 2024 and Al 7075. In all cases the corrosion current was lowest (greatest corrosion resistance) for Al A357.

The results can be explained by taking into account the alloying chemistry. The presence of chromium and silicon as alloying elements has been shown to increase the resistance of Al alloys to corrosion [15]. Al A357 has 7 percent Si and Al 6061 has 0.4 to 0.8 percent Si. These alloys have shown higher corrosion resistance than Al 2024 and Al 7075. The higher corrosion resistance of Al 7075 relative to Al 2024 at lower

FSII concentration is probably due to the presence of 0.18 to 0.28 percent Cr in Al 7075.

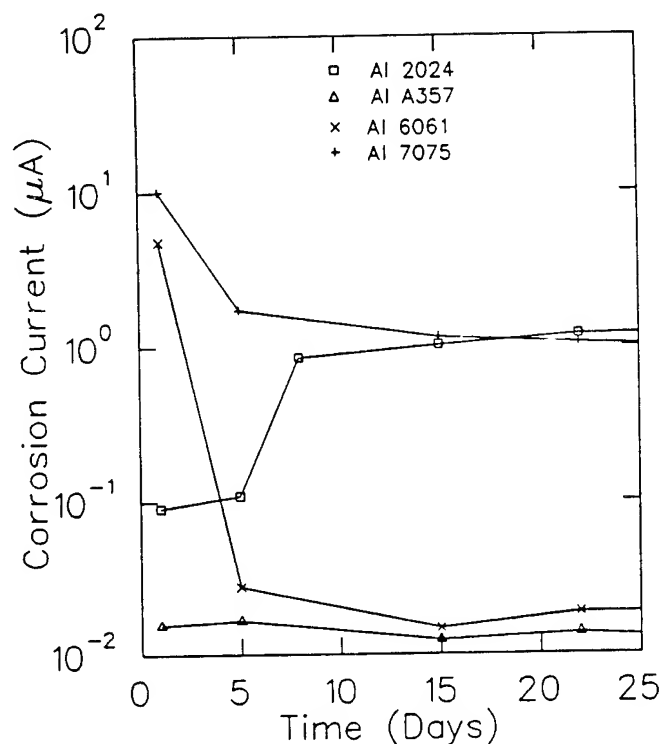


Figure 5
Variation of Corrosion Current with Time for
Aluminum Alloys Exposed to C-10 Plus 7 Percent
EGME

Effect of Coatings

The corrosion current for Al alloys with different coatings was measured in 0.1 percent and 7 percent EGME to evaluate the coatings' resistance to corrosion. Figure 6 shows the plot of corrosion current as a function time for Al 2024 exposed to C-10 with 7 percent EGME for three coating systems chromic acid anodized, Scotchweld EC 1290® primer coat, and a combination coating of chromic acid anodized and Scotchweld EC 1290® primer coat (topcoat). Initially on day 1, the corrosion current for all coated Al 2024 in 7 percent EGME was higher compared to that of uncoated Al 2024. The corrosion current decreased substantially in 5 days and remained stable for the 50 days of exposure

shown in Figure 6 (these tests are continuing to determine when and if the coating breaks down). Similar results were observed at other concentrations of EGME. These results clearly indicate that anodization and EC 1290 coating protects the Al alloys against corrosion. Additional tests of chemical conversion coating for Al 6061 have also shown similar corrosion resistance in 0.1 percent and 7 percent EGME solutions. Other testing is being conducted, on the coating systems, at lower temperatures to examine the effect of temperature on corrosion resistance.

That the corrosion current for coated samples are orders of magnitude higher initially but drop down considerably in 5 days is not fully understood at this time. However, it is known that the surface contamination by trace metals such as Cr, Zn, etc., (which is normally used during anodization and in primers) could contribute to higher corrosion current. It is postulated that contaminants are leached from the surface initially and reacted. This process cleans the surface and further corrosion reactions are inhibited by the coating system.

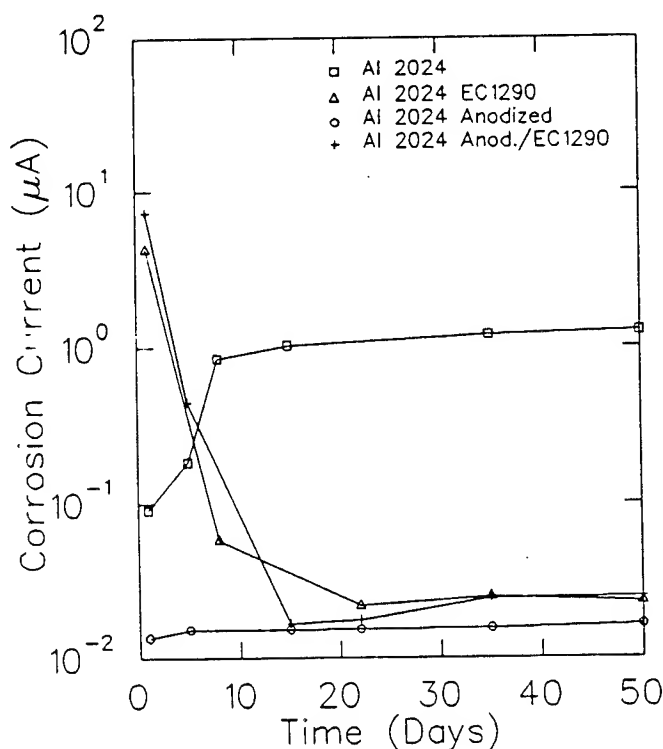


Figure 6
Variation of Corrosion Current with Time for Coated and Uncoated AL 2024 in C-10 Plus 7 Percent EGME

SUMMARY

An accelerated test method using AC Electrochemical Impedance Spectroscopy has been developed and used to measure the corrosion current in JP-10 missile fuel, a low conductivity, nonpolar solution. There is a general agreement in the trend between the experimentally observed values of corrosion current and corrosion resistance behavior of alloys. The corrosion current increases as a function of FSII concentration confirming the hypothesis that it is this additive that is responsible for the corrosion of aluminum fuel system components. Addition of BHT in a mixture of C-10 and EGME inhibits the corrosion of Al alloys. A decrease in temperature results in an increase in the corrosion current, due to the precipitation of FSII onto the aluminum surface, until a maximum corrosion current is reached between 0 and -3 °C. Of the four alloys tested Al A357 shows the highest corrosion resistance due to the presence of Si as an alloying element. Lower corrosion resistance was observed for Al 2024 and Al 7075 due to the absence of Si or Cr. Results to date of experiments involving anodization, Scotchweld EC 1290® epoxy primer, and chem film coating systems indicate that these coatings protect the aluminum surface against corrosion. It is clear from these results that EIS can be used as a technique to detect very small amounts of corrosion in low conductivity media and be used to evaluate solution chemistry, alloy corrosion resistance, and protective coatings.

REFERENCES

1. ASTM G31, Standard Practice for Laboratory Immersion Corrosion Testing of Metals, Annual Book of ASTM Standards, Vol. 03.02.
2. L. G. MacDonald, "Evaluation of Protective Coating Systems for Carbon Steel Exposed to Simulated SRB Effluent of Seacoast Exposure," Document No. MTB-268-86B, NASA, Kennedy Space Center, Material Testing Branch, 1988.
3. L. G. MacDonald, "Evaluation of High Performance Metal Alloys in the STS Launch Environment " Document No. MTB-610-89, NASA KSC, Material Testing Branch, 1990.
4. A.P. Rowe, L. M. Calle, "Accelerated Corrosion Test Method for Zinc-Rich Coatings," NASA/ASEE Summer Faculty Research Fellowship

Program, KSC, Aug., 1986.

5. S. Feliu, et. al., J. of Coatings Technology, Vol. 61, 775 (1989), p. 63.
6. S. Feliu, et. al., J of Coatings Technology, Vol. 61, 775 (1989), p. 71.
7. O. Forsen, et. al., " Evaluating the Possibilities for the Development of Testing Zinc-Rich Paints by Electrochemical Methods," International Congress on Metal Corrosion, Vol. 1, 1984, p. 477.
8. M. J. Mendrek, et. al., " An electrochemical Study of Corrosion Protection by Primer-Topcoat Systems on 4130 Steel With AC Impedance and DC Methods," NASA Technical Paper 2820, STID, 1988.
9. J. R. Scully, "Electrochemical Impedance of Organic Coated Steel," Report No. DTRC/SME-86/108, David Taylor Research Center, Ship Material Engineering Department, 1988.
10. F. Mansfield, S. Lin and H. Shih, "Detection and Monitoring of Localized Corrosion of Aluminum Alloys With Electrochemical Impedance Spectroscopy." ASTM Publication STP 1134, New Methods for Corrosion Testing of Aluminum Alloys, V.S. Agarwala and G. M. Ugiansky, Ed., American Society for Testing and Materials, Philadelphia, 1992.
11. E. A. Lawton, C. M. Moran and S. Distefano, "Corrosion of Metals by Hydrazine," Report on NASA Contract No. NAS7-91B, 1989.
12. C. Ontiveros and L. G. MacDowell, "Electrochemical Test Methods to Predict Performance of Zinc-Rich Primers," Corrosion 92, Paper No. 332.
13. J. W. Rogers, R. L. Hance and J. M. White "Investigation of the Interaction of Methanol With Polycrystalline Aluminum," Department of Defence, Technical Report No. AD-A087309 TR-14, (1980).
14. C. C. Nathan, "Corrosion Inhibition" National Association of Corrosion Engineers, Houston, 1973.
15. Material Engineering, Materials Selector Catalog, 1993.

Evaluation of the Corrosion Behavior of Storage Container Alloys in Halon 1301 Replacement Candidate Agents

*Mr. J. F. Dante
Mr. M. R. Stoudt
Mr. J. L. Fink
Mr. C. R. Beauchamp
Dr. T. P. Moffat
Dr. R. E. Ricker

Materials Science and Engineering Laboratory
National Institute of Standards and Technology
Gaithersburg, Md. 20899

Introduction

The Montreal Protocol of 1987 identified a number of halogenated chemicals which possess sufficient stratospheric ozone depletion potentials to warrant limitations on their production and use. Included on this list was Halon 1301 (CF_3Br), the fire suppression agent of choice for aircraft engine nacelles and dry bays (1). As a result, the relative performance of different chemical compounds with low ozone depletion potentials were evaluated as a CF_3Br fire suppressant replacement. Since corrosion of fire suppressant containers by the agent could affect the reliability of these vessels, the corrosion behavior of typical alloys used in these containers needed to be evaluated. Mass change tests were performed for 1 month in different agents at 150 °C. Electrochemical tests were desired to supplement and possibly replace the current mass change experiments. A major advantage of electrochemical testing is the significant reduction in time required to estimate corrosion rates and the effect that pollutants (HF , HCl , and H_2O) in various agents, compositional changes, and the temperature have on the corrosion rate.

The goal of this study is to 1) determine which alternative fire suppressants are most compatible with the metals used in storage vessels and 2) to determine which storage container metals have the highest corrosion resistance when exposed to alternative fire suppressants. Since no test methodology existed at the start of this phase of the work, mass change tests were used to evaluate the field of possible fire suppressant agents and container alloys in terms of corrosivity and corrosion resistance, respectively. Simultaneously, an electrochemical test was developed in order to perform accelerated testing of the corrosion resistance of storage container alloys in halon fire suppression alternatives.

* presenting author

Experimental Details

Mass change exposures

Experiments were designed and conducted to evaluate the corrosivity of the different potential fire suppressants during normal service in aircraft storage containers. These experiments had to consist of exposures that emulate the conditions under which corrosion is expected to occur followed by careful examination and evaluation of the resulting corrosion damage. Smooth coupon exposure tests, were conducted to evaluate changes in mass during exposure thereby yielding a measurement of the rate of formation of corrosion scales or removal of metallic species. The coupons were examined visually and by optical microscopy to assess the occurrence of pitting, intergranular corrosion and dealloying. From the mass change and the exposure time, the average mass change rate can be estimated allowing comparison between the agents and alloys. Tests to study localized corrosion and environmentally induced fracture were also conducted and the results are described elsewhere (2).

The materials chosen for this study were: 304 stainless steel, 13-8 Mo stainless steel, AM 355 stainless steel, stainless steel alloy 21-6-9 (Nitronic 40), 4130 alloy steel, Inconel alloy 625, CDA-172 copper/beryllium alloy and 6061-T6 aluminum alloy. The compositions of these alloys are given in Table 1. These alloys were selected for these experiments based on discussions with the Air Force on the materials typically used for aircraft storage container components.

The samples used for the mass change experiments were flat smooth surface coupons; width = 25.4 mm, length = 50.8 mm, and thickness = 1.6 mm. A 6.7 mm diameter hole was drilled in the center of the coupons. After machining, the surfaces were glass bead blasted to remove any remaining surface oxides or scale and to provide a consistent smooth surface finish (120 grit nominal). Each sample was then ultrasonically cleaned, first in acetone and then in alcohol, dried with warm air and immediately weighed. Three separate weighings were taken at approximately 30 second intervals and averaged. This average value was then referred to as the initial weight of the coupon. The balance used for these weight measurements was self calibrating on start-up to maintain an accuracy to within $\pm 10 \times 10^{-6}$ g with a reproducibility of no less than $\pm 1.51 \times 10^{-8}$ g. Representative photographs of the surface of each alloy were also taken prior to the start of testing.

At the start of each exposure test, three coupons of each of the eight alloys were mounted on a polytetrafluoroethylene (PTFE) rod with PTFE spacers between the samples as shown in Figure 1a. This was done to separate and electrically isolate the samples thereby eliminating the possibility of galvanic coupling. Three samples of each type of alloy were used and PTFE shields were placed between the different types of alloys to protect the samples from contact with any corrosion products that may form. The samples were next placed in a PTFE lined, two liter pressure vessel for testing. The vessel was then attached to a mechanical vacuum pump and evacuated for a minimum of 30 minutes.

Table 1
The Composition of the alloys listed in weight percent.

Element	Nit 40	Al 6061-T6	In 625	304 SS	CDA 172	13-8 Steel	SS Am355	AISI 4130
Ni	7.1	--	61.39	8.26	0.06	8.4	423	0.08
Cr	19.75	0.04	21.71	18.11	0.01	12.65	15.28	0.98
Mn	9.4	0.15	0.08	1.41	--	0.02	0.8	0.51
Mg	--	1	--	--	--	--	--	--
Si	0.5	0.4	0.09	0.49	0.08	0.04	0.16	0.23
Mo	--	--	8.82	0.17	--	2.18	2.6	0.16
Nb	--	--	3.41	--	--	--	--	--
N	0.29	--	--	0.03	--	0	0.12	--
C	0.02	--	0.02	0.06	--	0.03	0.12	0.32
Be	--	--	--	--	1.9	--	--	--
Co	--	--	--	0.11	0.2	--	--	--
Zn	--	0.25	--	--	--	--	--	--
Cu	--	0.15	--	--	97.9	--	--	--
Fe	bal	0.7	3.97	bal	0.06	bal	bal	bal
Al	--	bal	0.23	--	0.04	1.11	--	0.04
G/cm ³ *	7.83	2.7	8.44	7.94	8.23	7.76	7.91	7.85

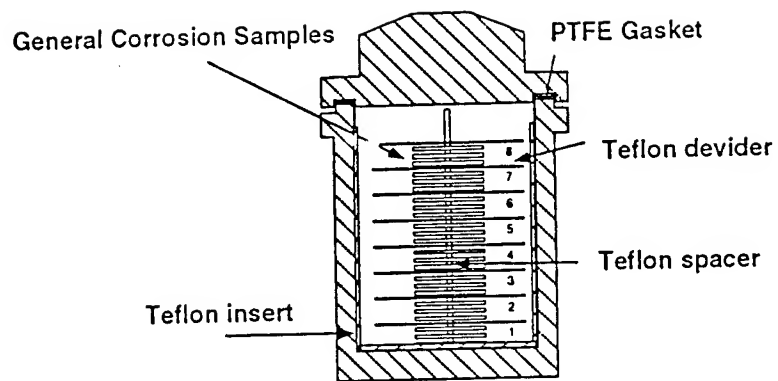
* Nominal Density

The mass of agent required to produce a pressure of approximately 5.86 MPa at 150 °C was determined from a computer program based on the available thermodynamic data, and the gas laws. To facilitate charging of the agents, the test vessels were chilled in a bath of either ice and water, or dry ice and alcohol, depending on the temperature necessary to maintain the liquid phase. The vessels were then placed on a balance that allowed weighing of the entire vessel and determination of the mass of the agent added continuously during filling. Upon completion of the charging step, the vessels were placed in proportionally controlled, calrod-type heaters that kept the temperature constant at 150 ± 1 °C for the 25 day exposure period.

At the conclusion of the testing period, the heaters were turned off and the vessels were allowed to cool naturally to ambient temperature. After the agent was released, the coupons were extracted and immediately reweighed using the same procedure that was used for the initial weight measurements. The average of those three measurements was then referred to as the final weight of the coupon. Representative photographs of the surfaces were again taken and compared to those of the initial condition.

Electrochemical Measurements

Electrochemical testing offers the possibility of more rapid evaluation of the corrosion rate and the effect of contaminants, material composition and temperature. Furthermore, numerous analytical electrochemical methods may be used to investigate the mechanisms of corrosion (3). However, the high resistivity of the aliphatic hydrocarbon solvents makes the implementation of such measurements extremely difficult, e.g. Halon 124, CF₃CHClF has a



- | | |
|-------------------------|-------------------------|
| 1 = Al Alloy AA 6061-T6 | 5 = In 625 |
| 2 = Cu Alloy CDA-172 | 6 = 304 Stainless Steel |
| 3 = AM 355 | 7 = AISI 4130 Steel |
| 4 = 13-8 Mo Steel | 8 = Nitronic 40 |

Fig. 1a: Immersion testing chamber for smooth coupon weight loss measurements.

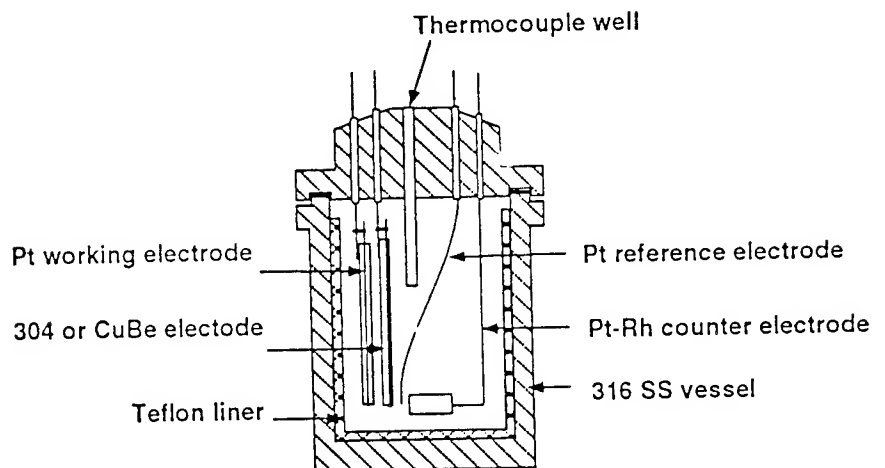


Fig. 1b: Electrochemical cell.

resistivity of $\sim 1.5 \times 10^9$ ohm \cdot cm. This value is similar to that observed for other non-aqueous solvents, i.e. acetonitrile, CH_3CN (4). In order to perform electrochemical measurements in such media a supporting electrolyte is required (4). Unfortunately, simple inorganic salts like NaCl or Na_2SO_4 are essentially insoluble in aliphatic solvents due to the low dielectric constant of the solvent, i.e. CF_3CHClF , $\epsilon \sim 6.73$. However, quaternary ammonium salts are known to be soluble in low dielectric constant media such as dichloromethane and chloroform, $\epsilon = 8.93$ and 4.81 respectively (5). Thus, we have investigated tetrabutylammonium hexafluorophosphate (Bu_4NPF_6) as a potential supporting electrolyte. In order to demonstrate the ability to perform well defined electrochemical measurements in the halon alternatives, the electrochemistry of a simple outer-sphere redox couple, ferrocene/ferrocenium ($\text{Cp}_2\text{Fe}^{0/+}$) was investigated by cyclic voltammetry (CV) at a platinum electrode. Because of its nonpolar character, ferrocene readily dissolves in aliphatic hydrocarbons like CF_3CHClF . This redox couple was also used to establish a reference potential (5).

A multipurpose high-pressure cell was designed for making electrochemical measurements in the halon alternative environments (manufactured by PARR Moline, Ill.). The vessel is made of 0.635 cm thick 316 stainless steel and is rated to ~ 6.9 MPa of pressure. The head of the cell was outfitted with four electrical feed throughs for performing two, three or four electrode electrochemical experiments. The vapor pressure in the cell was monitored by a pressure gauge mounted on the head of the cell. At higher temperatures, most of the alternative fire suppressants reach very high vapor pressures so a pressure release valve is incorporated in case of accidental over pressurization. Temperature was monitored with a thermocouple mounted in a well in the cell top. A teflon insert was used to prevent accidental electrical contact between the electrodes and the stainless steel cell. The insert also helped to minimize interactions between the electrolyte and the 316 cell wall. A schematic of the three electrode cell configuration is shown in Fig 1b. Measurements were made using an EG&G PAR 273 potentiostat / galvanostat in potentiostatic mode and M270 software.

All of the electrochemical tests were conducted in HCFC 124, CF_3CHClF , which has a vapor pressure of 3.393×10^5 Pa at 20°C . The conductivity was increased by adding 5×10^{-2} moles/ liter Bu_4NPF_6 (Aldrich). The cell top was left slightly opened and argon was flowed into the cell in order to remove water vapor. The head of the cell was then bolted down and the entire cell was chilled in dry ice. Chilling helped expedite filling of the cell with agent. After chilling, approximately 352 grams of CF_3CHClF were transferred into the cell. This resulted in about 3 cm, or 250 ml, of CF_3CHClF in the liquid phase in the bottom of the cell at room temperature. A large platinum rhodium electrode was used as a counter electrode and a separate platinum wire was used as a quasi-reference electrode. The quasi-reference electrode was placed between the counter and the working electrode. Heat shrinkable teflon tape was used to connect the electrodes to the electrical feed throughs and clips were used to make electrical contact.

In the first experiments $0, 5 \times 10^{-4}$, or 1×10^{-3} moles/ liter ferrocene (98% Aldrich) was added to the electrolyte. The tests were run at room temperature, 20°C . A platinum disk working electrode (area = 0.00317 cm^2) was prepared by encapsulating a platinum wire in glass followed by polishing to a $1\mu\text{m}$ finish. The potential scale of each experiment was referenced to a platinum quasi-reference electrode and then normalized afterwards to the half-wave potential of $\text{Cp}_2\text{Fe}^{0/+}$.

In subsequent experiments the slow sweep rate voltammetric or potentiodynamic characteristics of 304 stainless steel (area = 0.00785 cm^2)(Goodfellow) and Cu-1.9 wt%Be (area = 0.00196 cm^2)(Goodfellow) were investigated in 5×10^{-2} moles/ liter Bu_4NPF_6 in CF_3CHClF . These electrodes were encapsulated in glass and polished to a $1\mu\text{m}$ finish. Voltammetry of a platinum electrode in the same electrolyte helped establish the potential scale as revealed by the potential at which reduction of the electrolyte occurs. The potential axis of the voltammograms was then referenced to the half-wave potential of $\text{Cp}_2\text{Fe}^{0/+}$.

Results and Discussion

Mass change exposures

The mean mass changes observed from three samples of each of the alloys on exposure to each of the agents for 25 days at 150°C are given in Table 2 and the standard deviations determined for these measurements are given in Table 3. All of the mass changes are relatively small and most represent an increase in mass (positive values in Table 2). The mass change rate was estimated from these measurements by the relationship

$$R = \Delta M / (At) \quad (1)$$

where ΔM is the mass change, A is the total exposed area of the sample and t is the exposure time in days. This relationship estimates the average mass change rate over the exposure period and assumes that the mass change rate was essentially constant over the entire exposure period.

Table 4a gives a numerical value to an absolute mass change rate range as well as the equivalent penetration rate for each alloy for mass loss at the maximum rate for the range. The absolute value of the mass change rate, from Equation 1 and Table 2, for each alloy was compared with Table 4a and assigned a numerical rating, Table 4b. It was assumed that a mass increase was due to the formation of a surface film which formed as a result of exposure to residual gases, decomposition gases, or the agents themselves. In any case, the film composition will contain either a fraction of or no metal. Also, the corrosion rate for a metal with a surface film tends to decrease with time. Thus, the calculated rate of mass increase, and hence the numerical rating, will be an overestimate of the corrosion damage.

Taking into account propagation errors in both area and time measurements (6), it can be shown, in some instances, that the maximum and minimum confidence levels of the mass change rate, at 90% confidence,

Table 2
Mean Mass Change for Each Alloy in Each Agent
After 25 Day Immersion at 150°C [mg]

Positive Values = Scaling
 Negative Values = Mass Loss

Environment	Ni 40	Al 6061	In 625	304 SS	CDA 172	13-8 Steel	AM 355	AISI 4130	Agent Avg.	Std. Dev.
HCFC-22	0.176	0.458	-0.329	0.168	3.064	-0.033	-0.087	2.647	0.783	1.362
HCFC-124	0.092	0.219	-0.267	-0.037	1.474	-0.086	-0.206	0.319	0.189	0.557
FC-31-10	0.247	0.533	-0.037	0.583	2.663	0.357	0.219	1.102	0.708	0.858
HFC-227	0.009	0.128	-0.056	0.141	1.973	0.069	0.007	0.297	0.321	0.676
HFC-125	-0.011	0.199	0.031	0.136	0.89	0.151	0.029	0.673	0.262	0.333
FC-116	0.006	0.24	0.026	0.147	1.509	0.21	0.139	0.403	0.335	0.491
HFC-134a	0.013	0.131	-0.103	0.069	0.229	0.088	-0.014	0.262	0.084	0.122
HFC-236	0.024	2.479	-0.063	0.078	0.866	0.107	0.007	0.343	0.48	0.861
FC-C318	0.008	1.183	0.018	0.199	0.431	0.169	0.006	0.31	0.29	0.392
FC-218	0.153	0.373	0.051	0.09	0.768	0.279	0.15	0.381	0.281	0.232
HFC-32/125	0.3	0.587	0.146	0.241	2.263	0.492	0.311	0.227	1.96	3.851
NaHCO3	0.396	1.038	0.079	0.262	2.182	0.8	0.259	0.89	0.738	0.677
Alloy Avg.	0.118	0.631	-0.042	0.173	1.526	0.217	0.068	1.597		
Std. Dev.	0.137	0.675	0.138	0.152	0.911	0.243	0.15	3.152		

Table 3
Standard Deviation of mass change measurements
for each alloy in each environment (mg).

Environment	Ni 40	Al 6061	In 625	304 SS	CDA 172	13-8 Steel	AM 355	AISI 4130	Agent Avg.
HCFC-22	0.079	0.113	0.088	0.057	0.331	0.043	0.05	1.28	0.255
HCFC-124	0.045	0.091	0.048	0.04	0.294	0.072	0.103	0.099	0.099
FC-31-10	0.04	0.079	0.028	0.035	0.107	0.07	0.046	0.173	0.072
HFC-227	0.034	0.043	0.018	0.025	0.159	0.063	0.02	0.047	0.051
HFC-125	0.121	0.117	0.044	0.013	0.018	0.014	0.007	0.091	0.053
FC-116	0.124	0.087	0.025	0.033	0.157	0.012	0.063	0.013	0.064
HFC-134a	0.021	0.025	0.024	0.002	0.039	0.061	0.048	0.091	0.039
HFC-236	0.024	1.895	0.03	0.03	0.028	0.015	0.09	0.043	0.269
FC-C318	0.04	0.602	0.065	0.054	0.072	0.014	0.109	0.035	0.124
FC-218	0.083	0.048	0.011	0.05	0.032	0.021	0.044	0.08	0.046
HFC-32/125	0.033	0.324	0.022	0.037	0.217	0.14	0.035	0.122	0.116
NaHCO3	0.297	0.501	0.022	0.047	0.235	0.263	0.042	0.168	0.197
Alloy Avg.	0.078	0.327	0.035	0.035	0.141	0.066	0.055	0.187	

Table 4a
Mass Change Rate Values used in rating alloy/agent behavior
and equivalent penetration rate based on alloy nominal density

based on absolute value of mass change rate
penetration valid only for mass loss

Score	Mass Chg Rate		Equivalent Penetration Rate for Upper Boundary							
	mg/(m ² ·24h)		μm/year							
	Lower Bound	Upper Bound	Nit 40	Al 6061	In 625	304 SS	CDA 172	13-8 Steel	AM 355	AlSi 4130
1	0	0.1487	0.0069	0.0201	0.0064	0.0068	0.0066	0.007	0.0069	0.0069
2	0.1487	0.923	0.0431	0.1249	0.0399	0.0425	0.041	0.0434	0.0426	0.0429
3	0.923	5	0.2332	0.6764	0.2164	0.23	0.2219	0.2353	0.2309	0.2326
4	5	25	1.166	3.382	1.082	1.15	1.109	1.177	1.154	1.163
5	25	125	5.831	16.909	5.409	5.75	5.547	5.883	5.772	5.816
6	125	600	27.99	81.16	25.96	27.6	26.63	28.24	27.7	27.92
7	600	3,000	139.9	405.8	129.8	138	133.1	141.2	138.5	139.6
8	3,000	15,000	699.7	2029.1	649.1	690	665.7	706	692.6	697.9
9	15,000	75,000	3498	10146	3246	3450	3328	3530	3463	3490
10	75,000	—	—	—	—	—	—	—	—	—

Table 4b
Mass Loss Rate Evaluation of Agents and Alloys
based on 25 day immersion at 150 C

Environ-ment	Nit 40	Al 6061	In 625	304 SS	CDA 172	13-8 Steel	AM 355	AlSi 4130	Agent Avg.	Std. Dev.	Agent Rank
HCFC-22	3	4	3	3	5	2	3	5	3.5	1.07	9
HCFC-124	3	3	3	2	4	3	3	3	3	0.53	7
FC-31-10	3	4	2	4	5	4	3	4	3.63	0.92	11
HFC-227	1	3	2	3	5	3	1	3	2.63	1.3	1
HFC-125	2	3	2	3	4	3	2	4	2.88	0.83	4
FC-116	1	3	2	3	4	3	3	4	2.88	0.99	4
HFC-134a	2	3	3	3	4	3	2	3	2.75	0.46	3
HFC-236	2	5	2	3	4	3	1	3	2.88	1.25	4
FC-C318	1	4	2	3	4	3	1	3	2.63	1.19	1
FC-218	3	4	2	3	4	3	3	4	3.25	1.1	8
HFC-32/125	3	4	3	3	5	4	3	3	3.5	0.76	9
NaHCO ₃	4	—	3	3	5	4	3	4	3.75	0.71	12
Alloy Avg.	2.33	3.67	2.42	3	4.33	3.17	2.33	3.58			
Std. Dev.	0.98	0.65	0.51	0.43	0.65	0.58	0.89	0.67			
Alloy Rank	1	7	3	4	8	5	1	6			

Score Freq.

- 1 6 No evidence of attack ($t < 0.741$, 50% CI).
- 2 14 Some inconclusive evidence of attack ($0.741(50\% \text{ CI}) < t < 4.6(99\% \text{ CI})$).
- 3 47 Conclusive evidence of attack ($t > 4.6$, 99% CI).
- 4 22 Corrosion of little concern, (less than $\approx 1 \mu\text{m}/\text{year}$, $3\mu\text{m}$ for Al alloy).
- 5 7 Corrosion may be a concern
- 6 0 Corrosion rate should be considered in design
- 7 0 Corrosion about 1 to 5 mils per year
- 8 0 Rapid Corrosion
- 9 0 Very rapid corrosion
- 10 0 Extremely rapid corrosion

spans zero. This would indicate that we can not conclude that the corrosion rate is a value other than zero. However, a film appeared on the surfaces of many of these samples and there was evidence of spalling. These films were very thin and could be detected by a color change in the samples. Thus, it is believed that the confidence interval spans zero as a result of scaling of the metal surface followed by the spalling of this scale which increased the measurement scatter.

Mass increases are not uncommon during immersion testing and usually descaling techniques are employed to remove these scales for the determination of the remaining metal. Considerable research has been conducted in the area of descaling. Despite this concerted effort, however, some metal is removed in the descaling process. For long exposures or thick films, the metal is only a small fraction of the material removed and errors are small. In this study, the films are very thin and removal of any metal by descaling would result in significant errors. Additionally, techniques for descaling metals that were exposed to organic environments are not well developed. For these reasons, descaling was not attempted in this investigation.

Evaluation of the relative performance of the alloy/ agent combinations was hampered by the comparison of mass loss and mass gain measurements. Typically, mass loss measurements are evaluated by assuming that all of the lost mass was the result of corrosion and that no corrosion products were left on the surface to create errors in this determination. Then, the quantity of metal reacting and rate of the reactions can be calculated directly from the mass loss. Similarly, mass gain measurements can be evaluated if the reaction and the reaction products are known and it is assumed that none of the scale spalls off and is lost to the environment. However, when these are not known, evaluation contains greater uncertainties, but it is clear that the relative magnitude of mass change is still related to the reaction rate between the metallic species and the environment.

According to Table 4b, the most suitable materials for use in storage containers are Nit 40, SS AM355, In 625, and 304 SS. The most suitable agents for use as alternative fire suppressants from a corrosion viewpoint are HFC-227, FC-C318, HFC-134a, HFC-125, FC-166, and HFC-236. This ranking of materials and agents is based solely on smooth coupon exposure tests, however, and may change when other corrosion tests are taken into consideration (1).

Electrochemistry

Cyclic voltammetry of $Cp_2Fe^{0/+}$

A cyclic voltammogram for a Pt electrode in a solution containing 5×10^{-2} moles/ liter Bu_4NPF_6 reveals the onset of oxidation of the system at 1.2 V (vs PtQRE) and the reduction of electrolyte begins at -0.96 V (vs. PtQRE). The magnitude of the wave at -0.96 V varies each time the cell is reassembled and is thought to be the result of water contamination. This is

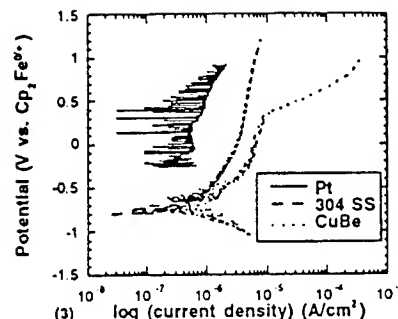
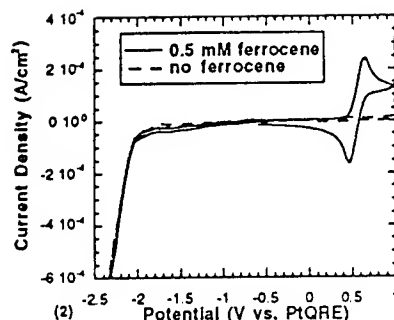


Fig. 2: 0.1 V/ s CV scan of ferrocene on a Pt electrode in CF_3CHClF with 5×10^{-2} moles/ liter Bu_4NPF_6 .

Fig. 3: 1 mV/ s anodic polarization scan of Pt, 304 SS, and CuBe in CF_3CHClF with 5×10^{-2} moles/ liter Bu_4NPF_6 .

supported by other experiments which demonstrated that the magnitude of the reduction wave scaled with the level of controlled H_2O doping of the electrolyte. Nonetheless, another reduction process becomes apparent at ~ -1.79 V (vs. PtQRE) and increases rapidly below ~ -2.02 V (vs. PtQRE). This latter value is similar to that observed for reduction of Bu_4N^+ in CH_3CN although reduction of the solvent may also occur in this potential regime (4). The position of the background reduction process remained unchanged throughout each series of tests, indicating there was no potential drift during the tests. Thus, the electrolyte exhibits at least a 2.16 V window where no reactions occur on platinum.

Performing the same experiment with 5×10^{-4} moles/ liter ferrocene added to electrolyte reveals a well defined quasi-reversible redox wave due to ferrocene oxidation and ferrocenium reduction as shown in Fig. 2. For a sweep rate of 0.1 V/s the peak potential splitting is 0.18 V. A reversible process should exhibit a value of 0.06 V. This deviation from reversibility may be due to slow electron transfer kinetics, or alternatively, may be an artifact of uncompensated solution resistance. For example, at sweep rates above 2 V/s the shape of the voltammogram is severely distorted due to iR effects. Nonetheless the peak current at slower sweep rates may be used to estimate the diffusion coefficient of ferrocene (3, 5) by assuming that the wave is reversible. The Randles-Sevcik equation (3) yields a diffusion coefficient of $3.26 \times 10^{-5} \text{ cm}^2/\text{s}$. The anodic and cathodic peaks of $\text{Cp}_2\text{Fe}^{0/+}$ are centered at 0.56 V (vs PtQRE). In another experiment, a doubling of the ferrocene concentration to 1×10^{-3} moles/ liter resulted in a doubling of the peak oxidation current. These experiments demonstrate the ability to

perform quantifiable electrochemical experiments in halon alternative solvents.

Cp₂Fe^{0/+} Reference Electrode

The well defined nature of the Cp₂Fe^{0/+} reaction may be used to firmly establish the potential scale. The platinum quasi reference scale while useful as a working reference, does not have a clear meaning in terms of a chemical potential. However, by noting the difference, -2.58 V between the onset of electrolyte reduction on a platinum working electrode at -2.02 V (vs PtQRE) and the half wave potential for Cp₂Fe^{0/+} 0.56 V (vs PtQRE) in the same solution, we can calibrate the potential scale of similar experiments performed in a ferrocene-free electrolyte by measuring the potential at which the onset of electrolyte breakdown occurs on platinum (vs a quasi reference electrode) and set the numerical value to -2.58 V vs Cp₂Fe^{0/+}. Thus, in the remaining portion of this manuscript the potential scale is referenced to E_{1/2}(Cp₂Fe^{0/+}) = 0.0 V.

Potentiodynamic curves for Cu-1.9wt%Be and 304 SS

The i-E characteristics of Pt, Cu-1.9wt%Be and 304 SS are shown in Figure 3. A small anodic background current was observed on Pt probably associated with the oxidation of impurities in the electrolyte. The 304 SS exhibits polarization characteristics of a spontaneously passive alloy with a near potential independent passive current in the range of 1-10 μ A/cm². In contrast Cu-1.9wt%Be exhibits a rapid increase in the dissolution rate at 0.4 V. Analysis of the electrode after removal from the cell revealed substantial metal loss. It is important to recall that the long term high temperature mass change experiments revealed a measurable mass change from the Cu-1.9wt%Be alloy while negligible attack was found for 304 SS. The favorable qualitative agreement between the mass change and electrochemical measurements clearly indicates that we can differentiate the susceptibility of various alloys to corrosion in fire suppressant media via rapid electrochemical experimentation. Future work will attempt to determine the affect of temperature, pollutant gasses, and water contamination on the corrosivity of metals in halon alternative media.

Conclusions

A program is underway to find an alternative fire suppressant to halon 1301. The selection of a replacement agent is, at least in part, dependant upon the corrosivity of the replacement agents towards storage container materials. Mass change data for flat smooth coupons of several such materials in replacement candidates has been presented. A ranking of the agents and container materials was evaluated based on this data. It was found that Nit 40, AM355, In 625, and 304 SS suffered the least amount corrosion damage. Agents that caused, on average, the least amount of corrosion damage were HFC-227, FC-C318, HFC-134a, HFC-125, FC-116, and HFC-236. It should be noticed, however, that a complete evaluation of the corrosion performance of the agent / alloy system would

include tests for localized corrosion and environmentally induced fracture.

An electrochemical test is being developed as a supplement or possible alternative to the mass change tests. It has been shown that electrochemical measurements can be made in low conductivity halon alternative environments and that it is possible to rank materials based on their corrosion current densities.

*Commercial products and companies mentioned in this paper are not endorsed by NIST.

Acknowledgements

The support of Wright Patterson AFB is gratefully acknowledged.

References

1. R. G. Gann, et al., "Agent/System Compatibility for Halon 1301 Aviation Replacement - Comprehensive Test Plan", NIST TN 1278, NIST, (1992).
2. R. E. Ricker, M. R. Stoldt, J. F. Dante, J. L. Fink, C. R. Beauchamp, and T. P. Moffat in "Evaluation of Alternative In-Flight Fire Suppressants for Full-Scale Testing in Simulated Aircraft Engine Nacelles and Dry Bays", W. L. Grosshandler, R. G. Gann, and W. M. Pitts eds., NIST SP 861, U. S. Government Printing Office, Washington D. C., (1994).
3. A.J. Bard and L.R. Faulkner, "Electrochemical Methods, Fundamentals and Applications", John Wiley & Sons, Inc, N.Y., (1980).
4. D.T. Sawyer and J.L. Roberts, "Experimental Electrochemistry for Chemists", John Wiley & Sons, N.Y., (1974); P.T. Kissinger and W.R. Heineman, Laboratory Techniques in Electroanalytical Chemistry, Marcel Dekker, Inc, N.Y., (1984).
5. M.H. Pournaghi-Azar and R. Ojani, *Electrochimica Acta*, 39, 53 (1994).
6. P. R. Bevington, "Data Reduction and Error Analysis for the Physical Sciences". McGraw-Hill, New York, (1969).

Army Research Office Programs In Beam Technology and Surface Engineering

Robert R. Reeber
Materials Engineer
Army Research Office
Research Triangle Park, NC 27709

The objective here is to provide some idea of needs and opportunities for future research with potential for providing new capabilities for Army systems. The technical objectives of the program are 1. to discover the atomic, molecular and macroscopic processes governing deterioration and adhesion of materials, 2. to provide improved materials stability and longer term performance capability for Army systems, and 3. to educate the next generation of skilled scientists in areas of Army research opportunities and needs.

Two principal thrust areas, (1) Beam Technology and Surface Modification and (2) Non-Destructive Characterization of Materials and Processes, are the templates for fulfilling the technical objectives of the program. New directions in nondestructive characterization, adhesion, non-equilibrium processing of refractory materials, ultrastrong laminates, green processing of corrosion resistant coatings and superhard coatings will be reviewed.

Research at the University of Wisconsin, Milwaukee (Carolyn Aita); has provided a characterization scheme (metastable phase maps) for refractory metal oxide sputter depositions. These results have depended on careful spectroscopic plasma characterization and determination of the crystallinity of films with x-ray, XPS and other methods. The University of Michigan (Bilello, Yalisove and Srolovitz) refractory metals laminates project where synchrotron topography and double crystal diffractometry techniques and theory are being applied to monitor and predict residual stresses and properties of nanolaminate materials.

A current program in chemical analysis with low and medium energy ion beams is underway at Vanderbilt University (Robert Weller). A new form of backscattering spectrometry using medium energy ions and time-of-flight detection has been developed that is particularly useful for characterizing surfaces and thin films. Currently some scaleup of the results is being accomplished with the cooperation of Semitech and Sandia National Laboratory.

A. Chemical/Biological Defense:

Previous work at the University of Connecticut, Koberstein, in the mid to late 1980's was cofunded by the National Science Foundation and related to surface tension measurements of polymer blends. At the same time at Cornell Kramer began seminal work to measure true diffusion coefficients of organics in polymer glasses with Rutherford Back-Scattering Spectrometry. After this work completed new efforts applying positron annihilation methods to polymers were started and are continuing. Their aim is to determine polymer free volume and its relationship to aging and transport in polymers (Case Western Reserve, McGervey, Simha and Jamieson).

B. Surface Modification/Beam Technology:

Although initially work was aimed at identifying unique properties of beam-treated materials, a growing awareness arose concerning environmental problems with plating wastes and the chemical solutions required for routine coating. This caused a

second look at what alternates were available. Some directions were identified that potentially could reduce the costs of the new technology. Lawrence Berkeley Laboratory's Ian Brown, an innovator in high current sources for implantation, was cofunded with the Office of Naval Research to further develop his technology. University of Wisconsin-Madison (John Conrad), has been evaluating the potential of Plasma Ion Implantation (PSII). The Madison group has had continuing transfers of technology to industry (Kearfoot-Singer) for space bearings, the auto industry and direct interactions with Army organizations ie. Corpus Christi Army Depot, Army Materials Technology Laboratory and Rock Island Arsenal. Their method permits non-line-of-sight implantation with relatively uniform doses.

C. Adhesion and Adhesives:

The previous sections as they relate to bonding and coating technology have already touched on some of the approaches to improved adhesion. A new STM effort addressing ceramic-metal bond integrity is ongoing with Arizona State (Ig Tsong). At Cornell, Ed Kramer is applying fracture mechanics and neutron reflectivity measurements to understand polymer/glass interface/interphase chemistry and improve bonding strengths in composites and other systems. Problems relating to effects of adhesive tackifiers are being addressed at the University of Akron and imaging of adhesive bonds is being attempted with electron holographic techniques at Stevens Institute of Technology.

D. Non-destructive Evaluation:

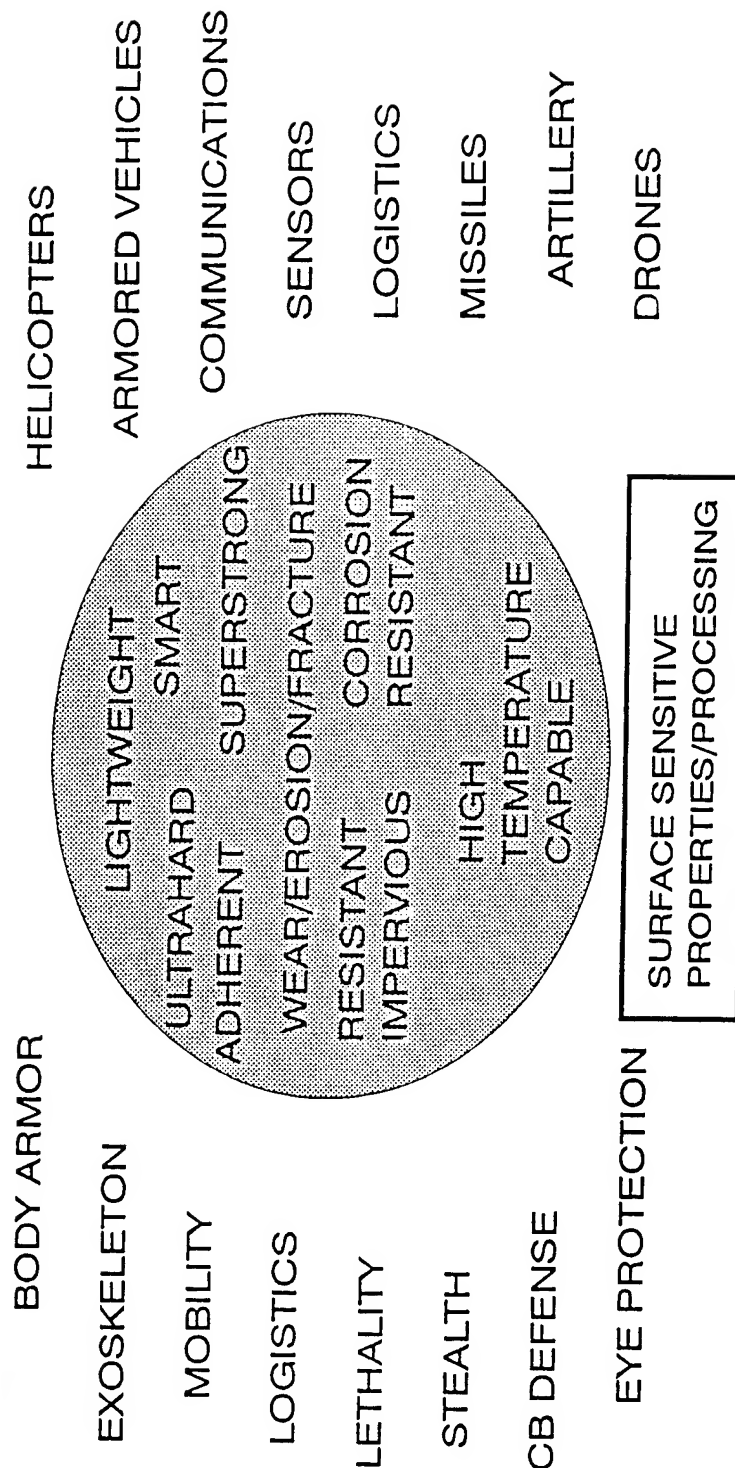
The strong subfield emphasis on materials characterization as reviewed above (hydrogen analysis, STM, laser diagnostics etc.) is included in the non-destructive characterization area. An ongoing program in the area is being carried out at the University of Houston (Salama) with the cooperation of the German Fraunhofer Institute for Non-Destructive Analysis in Saarbrücken. Here metal matrix composite third order elastic constants are being measured as a function of temperature. The results are useful in formulating mechanical equations of state for these materials. Additionally, several new small business programs have

been initiated addressing NDE needs in chemical biological materials.

I. New Needs and Directions:

The Army of the next century will require greater mobility, less reliance on logistics, and the ability to project a strong force quickly into a potential trouble spot. Such requirements can be translated into lighter weight systems and increased reliability. Higher temperature/pressure operations lead to increased efficiency but also increased stresses on equipment and munitions. New materials including lighter weight ceramic engines, a range of composite materials, graded coatings, and new polymers/elastomers will be required. Novel hard materials such as CVD diamond and cubic boron nitride are already being considered for unusual thermal and wear resistant applications. Smart coatings that provide stealth effects (neural control of color and emissivity), decontamination capabilities, self repair etc. are within the realm of possibility. New non-destructive techniques are required both to assess remaining system life and to provide in-situ monitoring of quality manufacturing. Additional research will be required to improve tribological properties of ceramics. Coatings and camouflage for polymers and polymer composites will have increasing importance. All new materials and systems processing will have to respond to increasing requirements for environmentally benign processing and recyclability. Since systems performance can often be significantly accelerated by technical breakthroughs, it is difficult to say what else to expect. Our ability to construct and characterize materials at the nanolevel will certainly reap future basic research dividends, many of which are now unforeseen.

ARMY APPLICATIONS



DEGRADATION, REACTIVITY & PROTECTION

I. BEAM TECHNOLOGY/SURFACE MODIFICATION

	FY 93 (CORE) (ALT)	FY94 (CORE) (ALT)
ION/LASER	117 351	89 0
NANOLAMINATES	145 600	114 500 e
ADHESION/SMART/GREEN	273 156	232 7.98 e
OTHER		50

II. NONDESTRUCTIVE CHARACTERIZATION

ADHESION/INTERFACES	263 0	292 0
INSERVICE	109 141	198 247
INSITU PROCESSING	86 434	59 250
TOTALS	993 1682	984 1845

BEAM PROCESSING OF MATERIALS

ATOMIC LEVEL SURFACE TREATMENT

METHODS:

- LASERS
- ION IMPLANTATION
- ION BEAM ENHANCED DEPOSITION
- PLASMA SPUTTERING
- CVD - MOCVD - MBE
- PLASMA SOURCE ION IMPLANTATION
- ELECTRON BEAM TREATMENTS

EFFECTS:

- SURFACE ZONE REFINEMENT
- MORPHOLOGY CHANGES
- AMORPHIZATION
- SURFACE MIXING
- PLANARIZE SURFACE
- ALLOYING FROM GAS & PREDEPOSITED LAYERS
- IMPROVED ADHESION
- IMPROVED CORROSION RESISTANCE

ARMY RESEARCH THRUST

01 MATERIALS SCIENCE SUBAREA: STRUCTURAL MATERIALS BEAM ENGINEERING/SURFACE MODIFICATION

MAJOR PERFORMERS

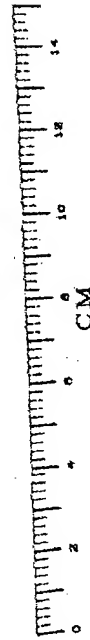
- UNIVERSITY OF CONNECTICUT
- UNIVERSITY OF WISCONSIN, MADISON
- CORNELL UNIVERSITY
- UNIVERSITY OF MICHIGAN
- BROOKHAVEN NATIONAL LAB
- IMPLANT SCIENCES, INC

ARMY RELEVANCE:

- FIRE SUPPORT, MOBILITY, AVIATION, SOLDIER

RECENT ACCOMPLISHMENTS:

- TWO IR100 AWARDS
- SUPERSTRONG NANOLAMINATES
- HIGH TEMPERATURE AI COATING
- WEAR RESISTANT CrN COATINGS
- CHROMATE-FREE CONVERSION COATINGS



MINIATURE PLASMA GUN

EXAMPLES OF RECENT TRANSITIONS TO ARMY, DoD, OR PRIVATE SECTOR PROGRAMS:

- AUTO FASTENER CONVERSION COATING TRANSFERRED TO TRW/CALUMET/ RDEC/TTCP
- LONG ISLAND LIGHTING CO IS TESTING HIGH TEMPERATURE AI COATING FOR HEAT EXCHANGERS
- GM/LAS/UNIVERSITY OF WISCONSIN, CRDA FORMED TO UTILIZE PLASMA SOURCE ION IMPLANTATION

NONDESTRUCTIVE CHARACTERIZATION OF COATINGS (WHITE, UNIV. MO. - COLUMBIA & MANSFELD, USC)

• ZINC PHOSPHATE CONVERSION COATINGS

	MORPHOLOGY	CHEMISTRY
MODIFIED*	5-10 MICRON GRAINS	ZnPHOSPHATEDIHYDRATE
UNMODIFIED	10-20 MICRON GRAINS	ZnPHOSPHATEDIHYDRATE
* ("WAVY" AND LESS ANGULAR THAN UNMODIFIED)		

• CERIUM-BASED ALUMINUM PROTECTIVE COATINGS

CHLORIDE-RESISTANT COATINGS

CERIUM CONCENTRATIONS - AT LOCAL CHEMICALLY ACTIVE REGIONS

RESULTS - MINIMAL PITTING OR LOCALIZED CORROSION

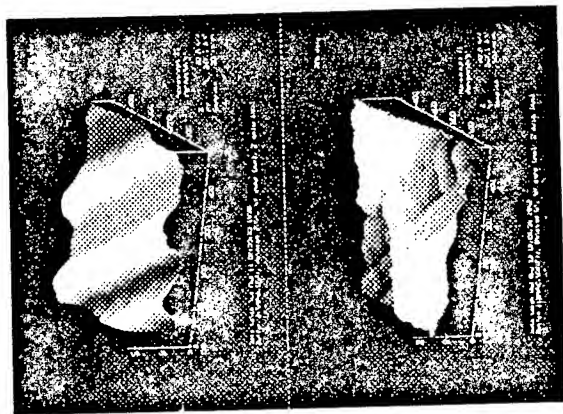
• ALUMINUM/SiC METAL MATRIX COMPOSITES

RAMAN & MICRORAMAN SPECTROSCOPY

MODIFIED INTERFACES - SILICON CONTAMINATION

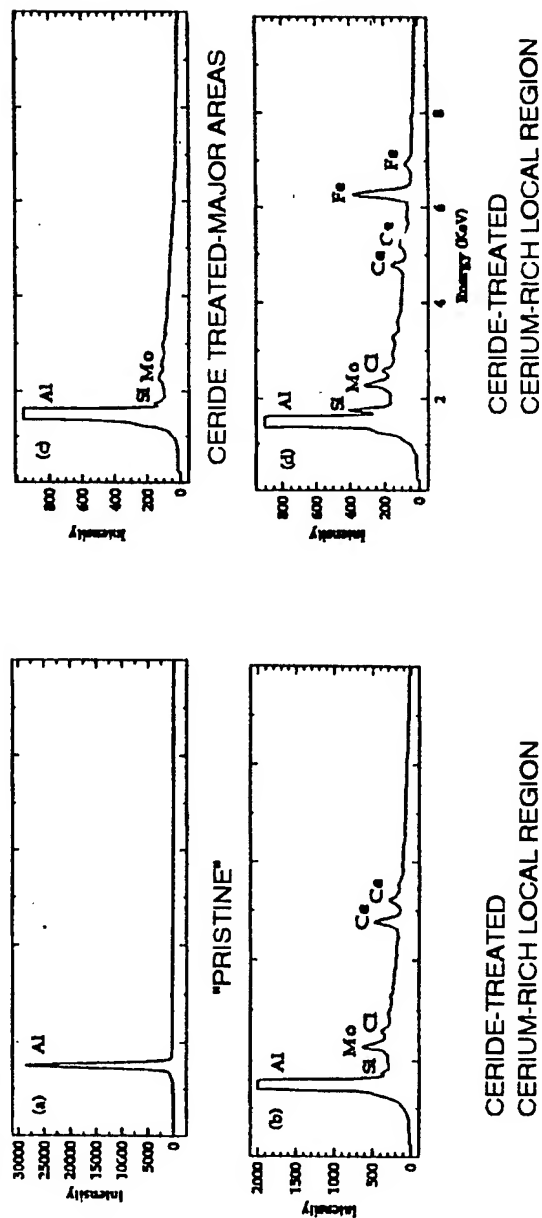
UNMODIFIED (PRISTINE) - SiC - ALUMINUM

ZINC PHOSPHATE COATING MORPHOLOGY



ENERGY DISPERSIVE X-RAY ANALYSIS

AL 6061-T6 SURFACES (WHITE-UNIV. MO, COLUMBIA)



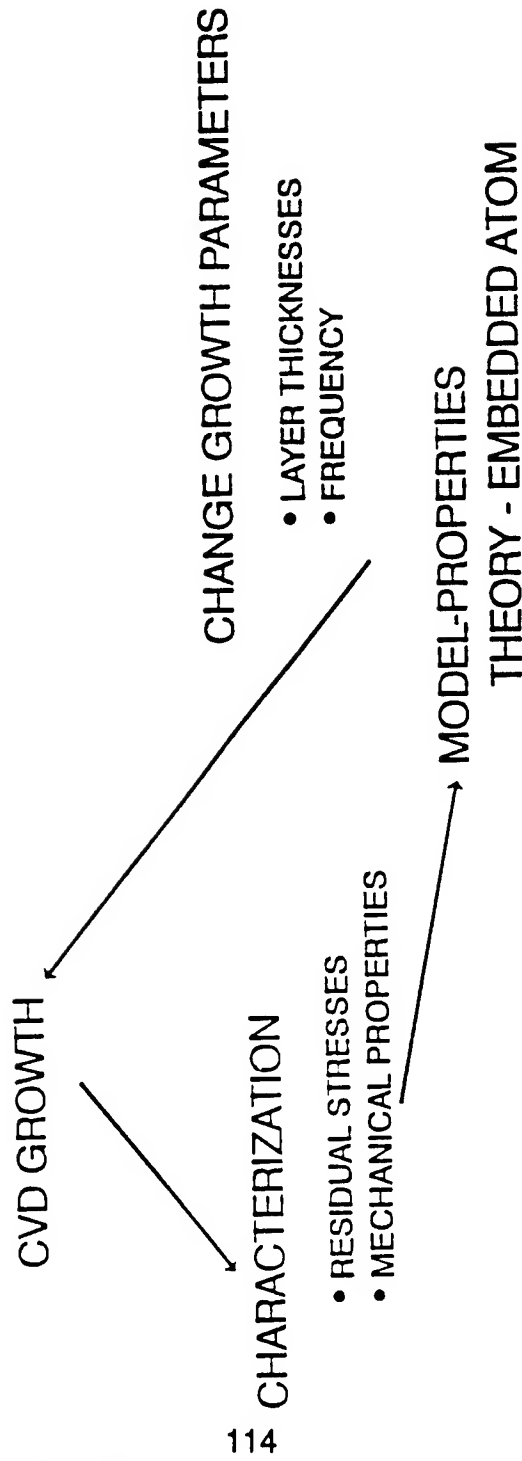
POTENTIAL: IMPROVED PITTING/LOCALIZED CORROSION RESISTANCE

TRANSFER: SAMPLES PROVIDED BY ONR PROJECT

REFRACTORY COATINGS

(BILELLO, YALISOVE, SROLOVITZ - UNIV. MICHIGAN)

METAL - METAL NANOLAMINATES



TUNGSTEN - MOLYBDENUM

APPLICATIONS

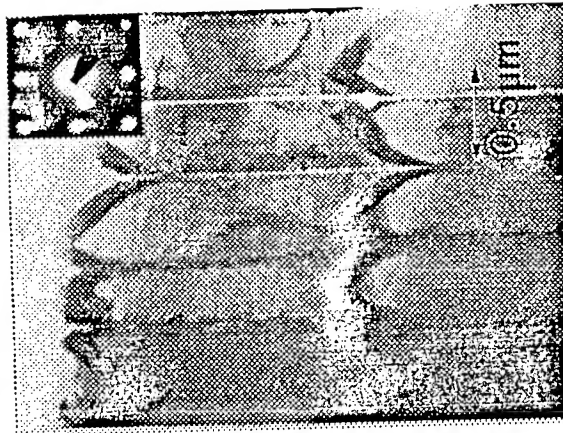
HIGH TEMPERATURE ENGINES
SUPERSTRONG MATERIALS

TUNGSTEN - MOLYBDENUM

APPLICATIONS

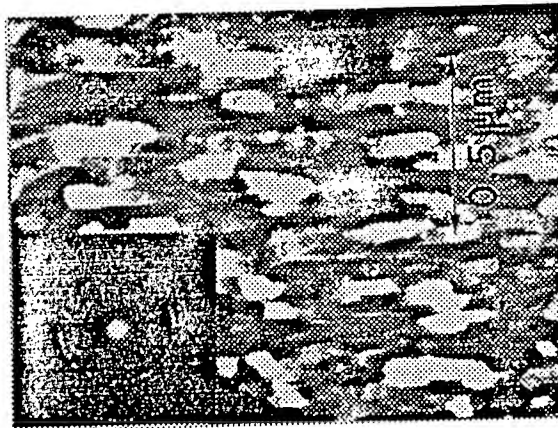
HIGH TEMPERATURE ENGINES
SUPERSTRONG MATERIALS

NANOLAMINATES (UNIVERSITY OF MICHIGAN)



BRIGHT FIELD

BRIGHT - MO TOUGHENING LAYERS
DARK - MO/W STRENGTHENING LAYERS



DARK FIELD

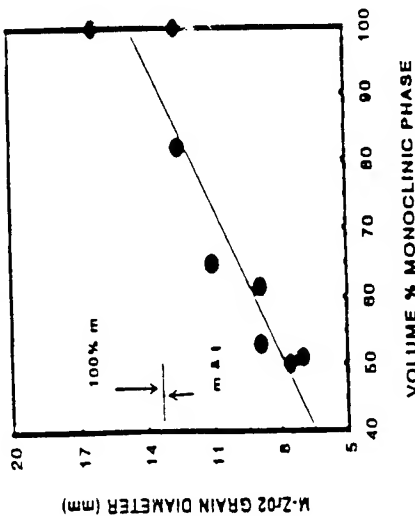
BRIGHT - INDIVIDUAL GRAINS OR GROUPS OF
GRAINS WITH SIMILAR ORIENT. 15° SECTOR OF MO
(110) RING.

TEM MICROGRAPHS

REFRACTORY COATINGS

C. AITA - UNIVERSITY OF WISCONSIN, MILWAUKEE

Zirconia Phase Distribution
(111) Monoclinic



APPROACH:

- MONITOR SPUTTER CHEMISTRY (TRANSITION METAL OXIDES, NITRIDES & OXYNITRIDES)
- MONITOR CATHODE VOLTAGE
- STRUCTURAL CHARACTERIZATION (ORDER-DISORDER)
- STRUCTURAL/MORPHOLOGY CONTROL

OBJECTIVE:

UNDERSTAND INTERRELATIONSHIPS

- PROCESS PARAMETERS
- GROWTH ENVIRONMENT
- FILM PROPERTIES

PAYOFFS:

SCIENCE

- IMPROVED COATING TECHNOLOGY
- 21 REFERRED PUBLICATIONS, 4 Ph.D, 3 MS
- 1 PATENT DISCLOSURE

ARMY

- TRANSFORMATION TOUGHENED COATINGS
- CORROSION RESISTANT HIGH TEMP. COATINGS
- NANOLAMINATE CERAMIC MATERIALS

REFRACTORY CERAMIC COATINGS

(BUNKER - IMPLANT SCIENCES INC)

APPLICATIONS:

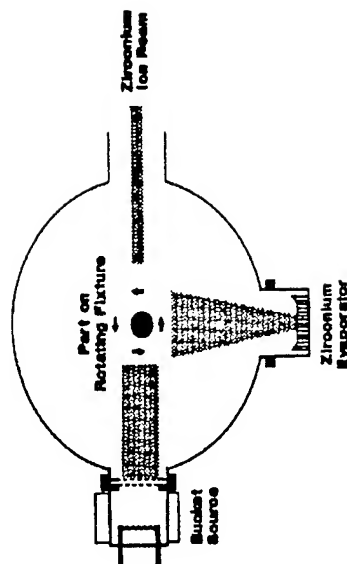
- DIESEL INJECTOR PROTECTION
- PROTHESIS (ORTHOPAEDIC DEVICES)
- CUTTING TOOLS

PROGRAM MANAGEMENT

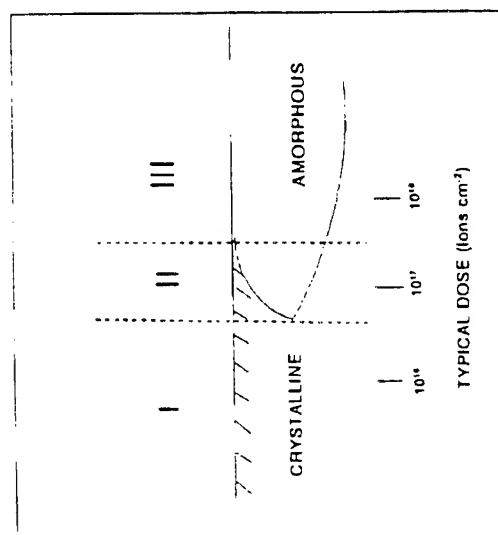
- Zr ION IMPLANTATION- OXYGEN AMBIENT
- OXYGEN IN-DIFFUSION
- C-RADED TRANSITION LAYERS
- IBAD-TO THICKEN COATING
- TEST ZrO₂ COATINGS IN SIMULATED ENGINE ENVIRONMENTS

RESULTS:

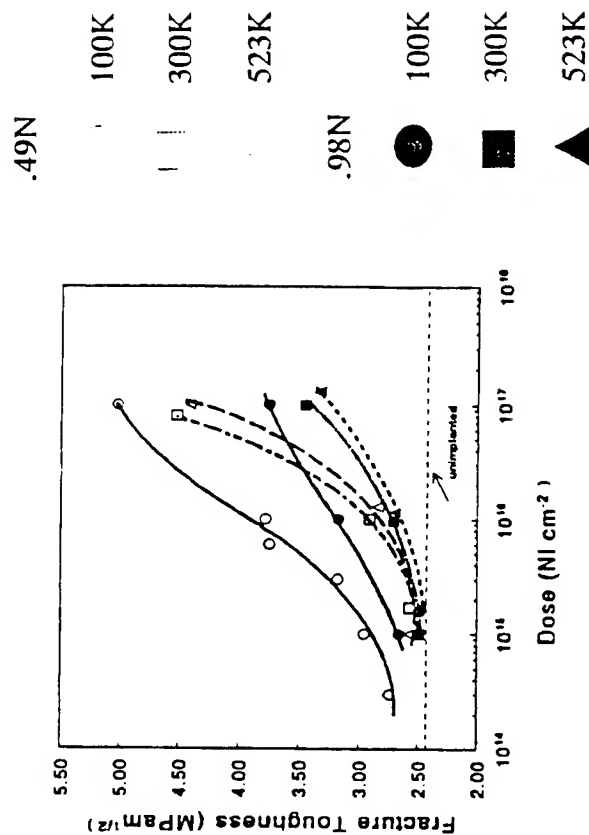
- TWO PATENT APPLICATIONS
- TECHNOLOGY INTERACTIONS
- AMBAC, INTERNATIONAL (INJECTOR), ARL-MD, BIOMEDICAL FIRMS



ION IMPLANTATION FRICTION AND WEAR



MICROSTRUCTURAL REGIMES AS
f (DOSE)
(AFTER BURNETT & PAGE)



SURFACE FRACTURE TOUGHNESS AS
f (DOSE) Ni IN ALUMINA
(HIOKI et al.)

SURFACE TREATMENTS

BORON CARBIDE

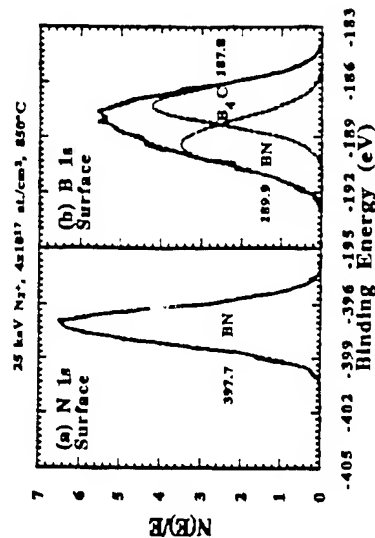
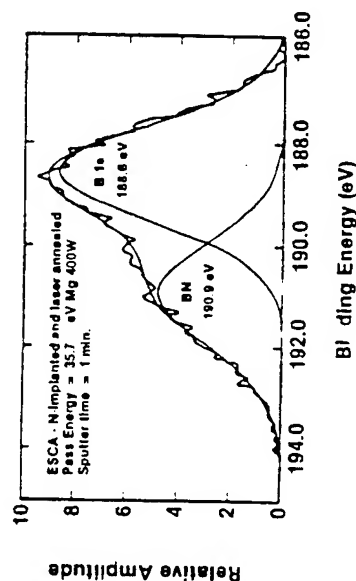
(REEBER & COWORKERS)
(YU & COWORKERS)

APPROACHES:

N^{+} - ION IMPLANTATION & LASER ANNEAL

N^{+} - ION IMPLANTATION AT $850^{\circ}C$

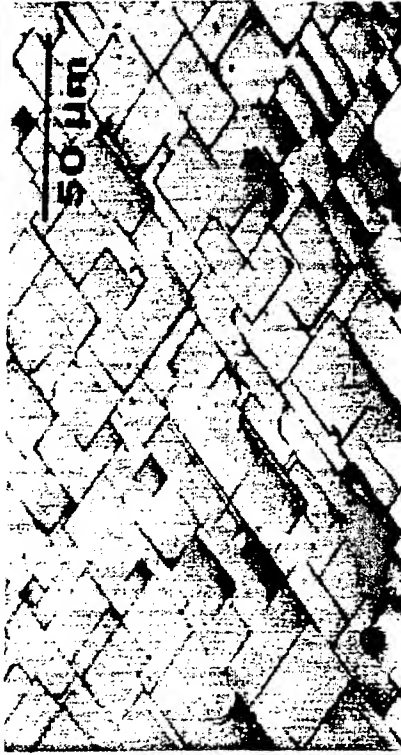
119



OBJECTIVES:

IMPROVE TRIBOLOGICAL PROPERTIES
BY INTRODUCING SOLID LUBRICANT
BN.

LASER MELTING TITANIUM ON ZIRCONIA (ZALESKI, JERVIS & MAYER)

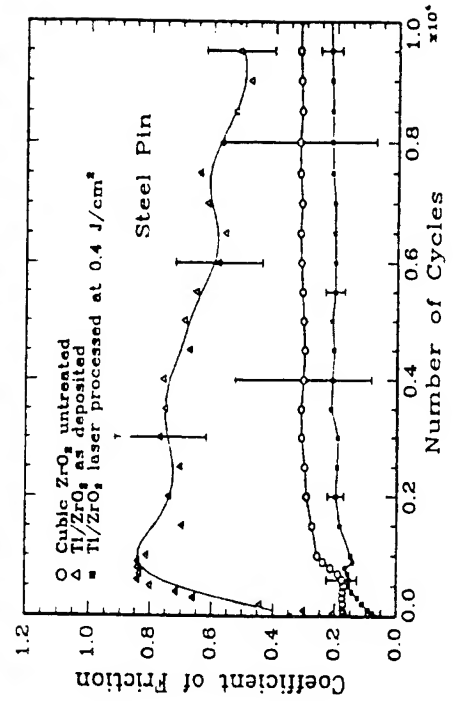


OBJECTIVE:

IMPROVED TRIBOLOGICAL
PROPERTIES

APPROACH:

- NOVEL MICROSTRUCTURE
CHANGES
- SLIGHTLY SOFTER MORE
PREDICTABLE
- LOWERED FRICTION
COEFFICIENT



NON-EQUILIBRIUM PROCESSING SUPERHARD MATERIALS COATINGS SMALL BUSINESS PROJECTS ---

- SI DIAMOND INC., BN, PHASE I
- IONWERKS, INC., BN, CN, PHASE II
- STRUCTURAL MATERIALS INDUSTRIES, INC., CN, PHASE I
- F.S. LAB, DIAMOND-CN, PHASE I, PHASE I
- SPACE POWER, INC, BN, PHASE I
- IMPLANT SCIENCES INC, DIAMOND, PHASE I

APPROACHES: ION/LASER/PLASMA
 LIQUID INTERMEDIARY

SUMMARY

METHODS FOR IN-SITU CONTROL

- HOLOGRAPHIC
- ION BEAM ANALYSIS
- X-RAY ANALYSIS - REAL TIME
- THERMAL WAVE IMAGING
- LASER - PULSED ELECTRON GUN
- COHERENT ANTI-STOKES RAMAN (CARS)
- OTHER SPECTROSCOPIC TECHNIQUES
- ELLIPSOMETRY
- GAMMA RAY/NEUTRONS

ARMY

RESEARCH THRUST

01 MATERIALS SCIENCE SUBAREA: STRUCTURAL MATERIALS NONDESTRUCTIVE CHARACTERIZATION



MAJOR PERFORMERS

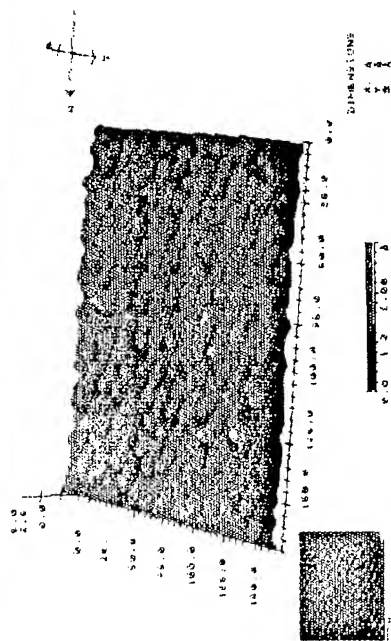
- MIT
- ARIZONA STATE UNIVERSITY
- VANDERBILT UNIVERSITY
- UNIVERSITY OF HOUSTON
- TEXAS RESEARCH INSTITUTE - AUSTIN
- IONWERKS INC.
- STEVENS INSTITUTE OF TECHNOLOGY
- CASE WESTERN RESERVE UNIVERSITY

ARMY RELEVANCE:

- COMBAT SUPPORT, CHEMICAL DEFENSE, MOBILITY, SOLDIER, CLOSE COMBAT HEAVY

RECENT ACCOMPLISHMENTS:

- REAL TIME ANALYSIS CVD DEPOSITION
- NEW NDE METHOD CBD SUIT INTEGRITY



BETA-SiC 3X3 (III) FACET

EXAMPLES OF RECENT TRANSITIONS TO ARMY, DoD, OR PRIVATE SECTOR PROGRAMS:

- SILICON WAFER CONTAMINANT CHARACTERIZATION TO SEMITECH/LASL
- ION SOURCE AND REAL TIME ANALYSIS OF CVD DEPOSITION (IBM YORKTOWN)
- ELECTRON HOLOGRAPHIC CHARACTERIZATION OF ADHESIVE BONDS (ARL)

NONDESTRUCTIVE TESTING BIOLOGICAL/CHEMICAL SUITS
(BRAY-TEXAS RESEARCH INST, AUSTIN)

APPROACH:

- FLUORESCENT PENETRANT DEVELOPMENT
- PROTOTYPE TEST KIT MANUFACTURING
- ACCELERATED WEAR TESTING OF MATERIALS
- FIELD TESTING

USERS:

BATTLE LAB, ERDEC, NRDC, FIRE DEPARTMENTS CHEMICAL COMPANIES

DEGRADATION, REACTIVITY & PROTECTION TECHNOLOGY TRANSFER

UNIVERSITIES

WISCONSIN, MADISON

WISCONSIN, MILWAUKEE

STEVENS INST. TECHNOLOGY

CORNELL

CONNECTICUT

MIT

MICHIGAN

VANDERBILT

MISSOURI, COLUMBIA

USERS

ROCK ISLAND ARSENAL, CORPUS CHRISTI,
ARL-MD, CRDA WITH LOS ALAMOS & G.M.

ARDEC-BENET

ARL-MD

DOW, DUPONT ELECTRONICS, MONSANTO

ARL-ED, ARL-MD

NRDC, ARL-MD, GENERAL ELECTRIC, FORD

ARPA, PRATT & WHITNEY, MARTIN MARIETTA

SANDIA, SEMITECH, SMALL BUSINESS

MCDONALD-DOUGLAS, ONR

DEGRADATION, REACTIVITY & PROTECTION TECHNOLOGY TRANSFER

NATIONAL LAB/SBIR

USERS

BROOKHAVEN

TARDEC, TRW-FASTENERS, CALUMET, TTCR,
LONG ISLAND LIGHTING, DOE, GAS
RESEARCH INSTITUTE

LAWRENCE BERKELEY

ARDEC, IR100, EPRI, DOE

IMPLANT SCIENCES

ARL-MD, CUMMINS DIESEL, AMBAC, INT.

ION WORKS, INC

IBM YORKTOWN, COMMONWEALTH

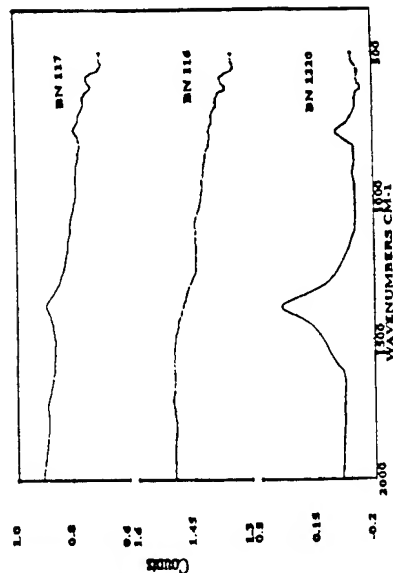
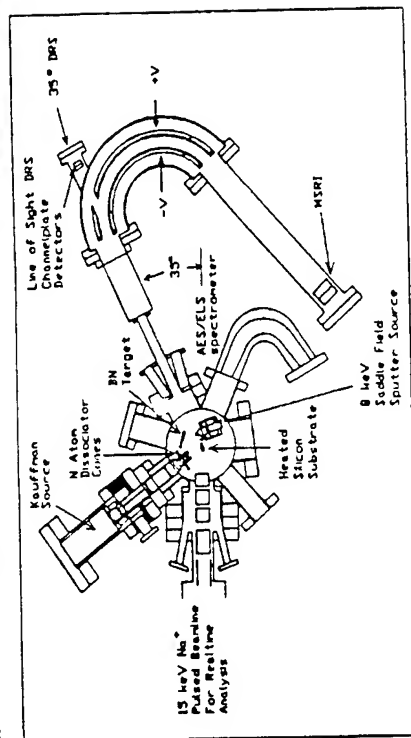
SI DIAMOND, INC

MCDONALD DOUGLAS AIRCRAFT CO.

CONTROLLED ATOMIC BEAM DEPOSITION CUBIC & HEXAGONAL BN (EIPERS-SMITH, WATERS & SCHULTZ)

APPROACH:

- BROAD BEAM - HIGH FLUX
ATOMIC NITROGEN SOURCE
- HIGH PRESSURE IN-SITU
SURFACE ANALYSIS



TRANSMISSION IR OF h-BN & C-BN FILMS

OBJECTIVES:

- CONTROLLED GROWTH OF
EPILAYER C-BN FILMS

Chemistry, Structure and Morphology of Native and Passive
Oxide Films on Aluminum Rich Amorphous Al-Fe-Ce Alloys

Dr. A. N. Mansour*
Naval Surface Warfare Center, Code R34
10901 New Hampshire Avenue
Silver Spring, MD 20903-5000

Dr. C. A. Melendres
Argonne National Laboratory
Materials Science and Chemical Technology Divisions
Argonne, IL 60439-8111

Abstract

Aluminum based metallic glasses are of technological importance due to their high strength, low density, and anticipated high resistance to corrosion. We report on the corrosion characteristics such as corrosion potentials, corrosion currents, and pitting potentials of melt-spun ribbons of $\text{Al}_{90}\text{Fe}_{10-x}\text{Ce}_x$ ($x = 3, 5, 7$). In addition, we have examined the chemistry, structure, and morphology of the native and passive oxide films using X-ray Absorption Fine Structure Spectroscopy, X-ray Photoelectron Spectroscopy, and Scanning Electron Microscopy. Passive oxide films were induced by anodizing below the pitting potential in an aqueous solution of 0.9 wt% NaCl for 30 and 60 minutes using potentiodynamic polarization techniques.

Introduction

Aluminum based metallic glasses with remarkably high Al content are relatively new materials that were discovered independently by He et al.¹ and Tsai et al.² Typical composition is Al-TM-RE where TM is a late transition element such as iron, cobalt, or nickel and RE is a rare earth element such as yttrium, gadolinium or cerium. These amorphous alloys can be prepared with high aluminum content by rapid solidification

from the liquid phase using the melt-spinning method^{1,2} or by vapor quenching using the dc magnetron sputtering method.³ The amorphous phase is formed with an Al content as high as 90 atomic percent and are truly non-crystalline alloys which combine the properties of a metal with the short range order of a glass. They are very homogenous and lack the defects such as grain boundaries and dislocations typical of a crystalline material. The homogeneity and the lack of grain boundaries have led to a number of remarkable mechanical^{4,5} and magnetic⁶ properties. Amorphous ribbons of melt spun materials have high strength, ductility, and low density. It is also expected that, due to lack of grain boundaries, this material will have high resistance to corrosion. Consequently, these materials are potentially important metallic materials for many critical engineering applications.

In this paper, we report on the corrosion characteristics as well as the chemistry, structure and morphology of the native and passive oxide films of melt-spun $\text{Al}_{90}\text{Fe}_{10-x}\text{Ce}_x$ ($x = 3, 5$ and 7) using Scanning Electron Microscopy (SEM), X-ray Photoelectron Spectroscopy (XPS), and X-ray Absorption Fine Structure Spectroscopy (XAFS).

Experimental

Sample Preparation:

Amorphous samples in the form of 25 micron thick ribbons with nominal composition, $\text{Al}_{90}\text{Fe}_x\text{Ce}_{10-x}$ ($x = 3, 5$ and 7), were prepared by rapid solidification from the liquid phase using the melt-spinning method. For comparison purposes, crystalline $\text{Al}_{90}\text{Fe}_3\text{Ce}_7$ was prepared from amorphous $\text{Al}_{90}\text{Fe}_3\text{Ce}_7$ by heating in an inert atmosphere.

Corrosion Measurements:

Corrosion characteristics such as corrosion potentials, corrosion currents and pitting potentials of these alloys were determined by means of potentiodynamic polarization measurements made on samples immersed in an aqueous solution of 0.9 wt% NaCl (0.15M). The measurements on the alloys were compared with those of pure aluminum and iron. Passive films were formed in the 0.9 wt% NaCl solution by anodizing below the pitting potential for 30 and 60 minutes. Passivation of $\text{Al}_{90}\text{Fe}_7\text{Ce}_3$ was also induced in 3.5 Wt% (0.6 M) NaCl by anodizing below the pitting potential for 30 minutes. The passivated samples were

then pulled from the solution and dried in a stream of nitrogen gas. The effect of sample rinsing with copious amounts of deionized H₂O on the chemistry and structure of passive films was also investigated.

SEM Measurements:

An Amray 1000A scanning electron microscope (SEM) was used to investigate the morphology of control (no passivation) and passivated alloys. An electron beam at a voltage of 20 KeV, current of 0.01 na, and a diameter of the order of 100 Å was employed. Compositional analyses were made by means of Energy Dispersive Analysis of X-Rays (EDAX). At the conditions of our experiment, the EDAX determined composition represents that of the bulk (roughly 2 μm deep). Experiments were performed at a system pressure less than 10⁻⁶ Torr.

XPS Measurements:

XPS spectra were collected using a Perkin-Elmer/Physical Electronics Division photoelectron spectrometer (model 5400) under computer control. All spectra were obtained with monochromatized Al x-rays (hν=1486.6 eV). The anode operated at 15 KV drawing a current of 40 mA. The composition and chemistry of the native oxide films were investigated using angle resolved XPS. During the XPS measurements, the analysis chamber pressure was kept in the range of (1-3)×10⁻⁸ Torr. The XPS data were collected from an analysis area of 1mm x 1mm. All binding energies were referenced to the C 1s photoelectron line for adventitious hydrocarbon set at 285.0 eV.

XAFS Measurements:

The X-ray absorption experiments were performed on beamline X-11A of the National Synchrotron Light Source (NSLS) at Brookhaven National Laboratory (BNL) with the electron storage ring operating at an electron energy of 2.5 GeV and a stored current in the range of 110 to 220 mA.⁷ Data were collected with a variable exit double-crystal monochromator using two flat Si(111) crystals. Spectra of the Ce L₃-edge and Fe K-edge data for the alloys were obtained using transmission, fluorescence⁸ and total electron yield⁹ detection modes. The fluorescence and total electron yield data were obtained using a specialized fluorescence ion chamber detector¹⁰ and total electron yield detector,¹¹ respectively. The X-ray intensities were monitored using

ionization chambers filled with nitrogen gas for the incident beam, an appropriate mixture of nitrogen and argon gases for the transmitted beam and krypton gas for fluorescence signal. The electron yield detector had helium gas. The background component due to elastic and Compton scattering of the incident X-rays was minimized by using an aluminum Soller slit assembly and V and Mn filters, each with an effective thickness of three absorption lengths, for the Ce L₃-edge and Fe K-edge, respectively. Due to surface sensitivity of the electron yield data and, hence, enhanced sensitivity to the passive film structure, only the electron yield spectra for the passivated alloys will be discussed in this paper. The energy calibration for Fe, and Ce was monitored using a Fe foil and a CeO₂ reference and employing a third ion chamber filled with the same gas as that of the transmitted beam ion chamber.

Reference samples of bulk Fe (5 μ m thick foil), Fe₂O₃, Ce(NO₃)₃, and CeO₂ were also investigated to serve as standards for comparison and subsequent data analysis. The XAFS measurements for the Fe foil, Fe₂O₃, Ce(NO₃)₃, and CeO₂ were made in the transmission mode. Research grade Fe₂O₃, Ce(NO₃)₃, and CeO₂ were prepared for the x-ray absorption measurements by grinding into a fine powder and selecting particles less than 20 μ m by sieving through a 20 μ m size nylon screen. The fine powder was then deposited on Kapton tape and several layers were then stacked to give a relatively uniform thickness appropriate for XAFS measurements. Two and four layers were used in separate runs for Fe₂O₃ giving a $\Delta\mu x$ of 0.53 and 1.00, respectively. Six layers were used for Ce(NO₃)₃ giving a $\Delta\mu x$ of 0.64. Six layers were used for CeO₂ giving a $\Delta\mu x$ of 0.61. All spectra were measured at room temperature (300 K).

Results

Potentiodynamic Polarization Studies:

Figure 1 shows typical anodic dissolution/passivation curves for amorphous and recrystallized Al₉₀Fe₃Ce₇. A summary of corrosion potentials, corrosion currents and pitting potentials for the alloys as a function of composition and for pure crystalline aluminum and iron foils is presented in Table I. The corrosion potentials are nearly the same for the alloys and pure aluminum while the corrosion currents (hence, corrosion rates) for the amorphous alloys are larger than that for pure aluminum. The corrosion current for amorphous Al₉₀Fe₃Ce₇ is significantly

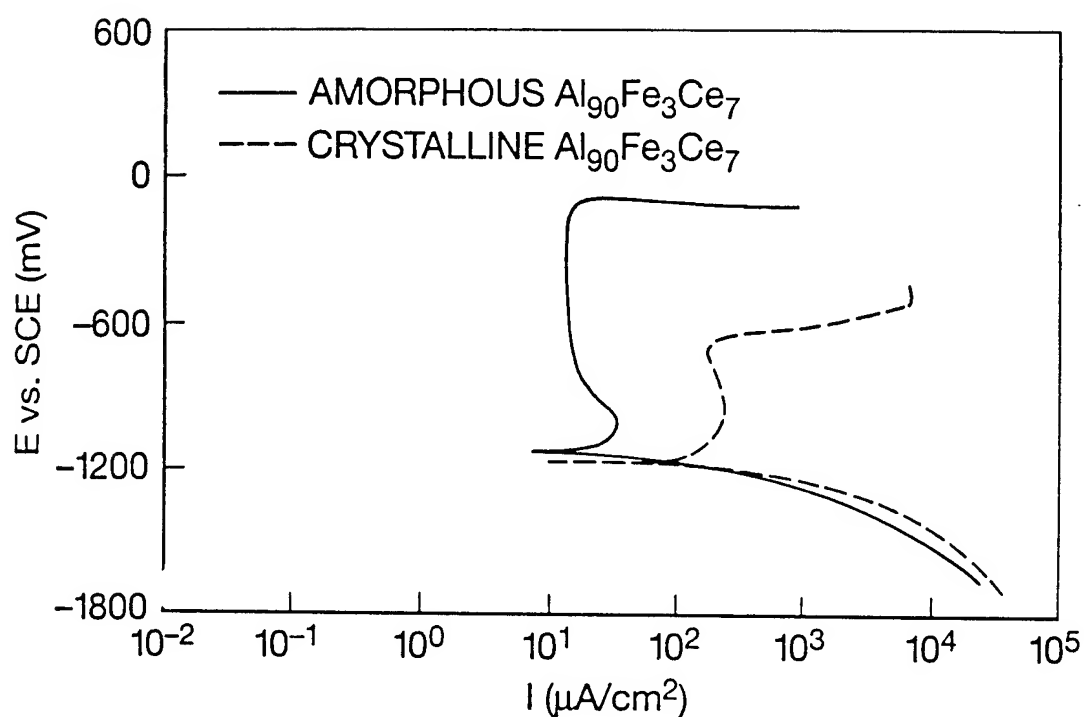


Figure 1. Typical anodic dissolution/passivation curves for amorphous and recrystallized $\text{Al}_{90}\text{Fe}_3\text{Ce}_7$.

Table I. Corrosion potentials, corrosion currents and pitting potentials for liquid-quenched alloys immersed in an aqueous solution of 0.9 wt% NaCl.

Composition	Structure	$E_{\text{corrosion}}$ (mV vs. SCE*)	$I_{\text{corrosion}}$ ($\mu\text{V}/\text{cm}^2$)	E_{pitting} (mV vs. SCE*)
$\text{Al}_{90}\text{Fe}_7\text{Ce}_3$	Amorphous	-1075	325	-150
$\text{Al}_{90}\text{Fe}_5\text{Ce}_5$	Amorphous	-1028	65	-100
$\text{Al}_{90}\text{Fe}_3\text{Ce}_7$	Amorphous	-1079	20	-90
	Crystallized	-1167	851	-675
Al metal	Crystalline	-1046	0.15	-700
Fe metal	Crystalline	-500	42	-225

* SCE \equiv Saturated Calomel Electrode.

smaller than that of crystalline $\text{Al}_{90}\text{Fe}_3\text{Ce}_7$ which is probably due to lack of grain boundaries in the amorphous state as will be shown later from SEM micrographs. The corrosion currents for the amorphous alloys also decrease with increase in cerium content. Pitting potentials for the amorphous alloys are more positive than that for pure aluminum or crystalline $\text{Al}_{90}\text{Fe}_3\text{Ce}_7$ alloy indicating that the physical and chemical nature of passive films for the amorphous alloys are more resistant to pitting than for pure aluminum and crystallized alloys.

SEM Studies:

Figure 2 shows a comparison of SEM micrographs for amorphous and recrystallized $\text{Al}_{90}\text{Fe}_3\text{Ce}_7$ indicating the lack of grain boundaries in the amorphous state in contrast to the crystalline state. Figure 3 shows SEM micrographs for the control (no passivation) and passivated amorphous $\text{Al}_{90}\text{Fe}_7\text{Ce}_3$. Again, these micrographs display no grain boundaries revealing the amorphous nature of the alloys. EDAX elemental analysis confirms that the few crystallites displayed by the SEM micrograph on the surface of passivated $\text{Al}_{90}\text{Fe}_7\text{Ce}_3$ (Figure 3) represent contamination by NaCl crystallites from the solution.

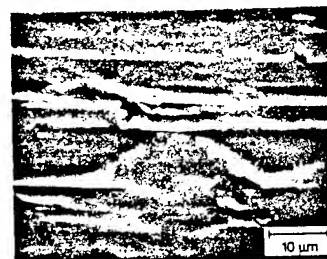


$\text{Al}_{90}\text{Fe}_3\text{Ce}_7$ (AMORPHOUS)

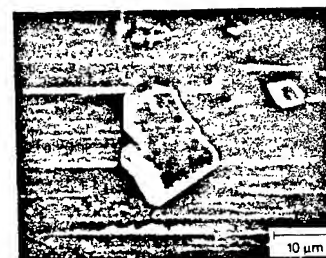


$\text{Al}_{90}\text{Fe}_3\text{Ce}_7$ (CRYSTALLINE)

Figure 2 SEM micrographs for amorphous and recrystallized $\text{Al}_{90}\text{Fe}_3\text{Ce}_7$.



$\text{Al}_{90}\text{Fe}_7\text{Ce}_3$ (CONTROL)



$\text{Al}_{90}\text{Fe}_7\text{Ce}_3$ (0.9WT% NaCl, 30 MIN PASSIVATION)

Figure 3 SEM micrographs for the control and passivated amorphous $\text{Al}_{90}\text{Fe}_7\text{Ce}_3$.

A summary of elemental concentrations, in atomic percent, as determined by EDAX is listed in Table II.

Table II. Elemental concentrations for amorphous (A) and recrystallized (C) alloys in the as received conditions (control) and after passivation by anodizing below the pitting potential: a) in 0.9 wt% NaCl for 30 minutes (PS #1) and 60 minutes (PS #2) and b) in 3.5 wt% NaCl for 30 minutes (PS #3). Concentrations in parentheses correspond to Al, Fe and Ce normalized to 100% to allow for comparison with those for the control samples.

Sample	Treat.	Concentration (atomic percent)					
		Al	Fe	Ce	Cu	Na	Cl
Al ₉₀ Fe ₇ Ce ₃ (A)	Control	88.5	7.4	3.7	0.4		
	PS #1	80.8 (86.4)	8.2 (8.8)	4.5 (4.8)	0.6	3.7	2.3
	PS #2	74.7 (84.0)	9.1 (10.2)	5.1 (5.7)	0.5	9.6	1.0
	PS #3	77.2 (86.8)	7.6 (8.5)	4.1 (4.6)	0.4	8.4	2.3
Al ₉₀ Fe ₅ Ce ₅ (A)	Control	88.3	5.1	6.1	0.5		
	PS #1	80.7 (84.9)	6.6 (6.9)	7.7 (8.1)	0.5	4.1	0.4
	PS #2	79.7 (86.6)	6.0 (6.5)	6.3 (6.8)	0.6	6.5	0.9
Al ₉₀ Fe ₃ Ce ₇ (A)	Control	88.8	3.2	7.9	0.1		
	PS #1	82.3 (85.8)	3.9 (4.1)	9.7 (10.1)	0.0	3.3	0.8
	PS #2	76.7 (85.9)	3.6 (4.0)	9.0 (10.1)	0.2	6.8	3.7
Al ₉₀ Fe ₃ Ce ₇ (C)	Control	88.9	3.0	7.9	0.1		

The copper impurity is an artifact of the sample preparation procedure which employs a copper wheel as part of the melt spinning apparatus; sodium and chlorine are observed in the analysis of passivated samples and are due to contamination from the aqueous NaCl solution. The concentrations for the control samples are in good agreement with nominal compositions aimed for during sample preparation. A slight decrease in the Al content and a significant increase in the Fe and Ce concentrations for the passivated alloys relative to the control alloys are observed suggesting segregation of both Fe and Ce from the bulk into the near surface region as a result of the passivation procedure.

XPS Studies:

Survey spectrum, high resolution multiplexes of the C 1s, O 1s, Al 2p, Al 2s, Fe 2p, and Ce 3d photoelectron lines and the valence band region, and Al 2p, Al 2s and O 1s angle resolved XPS spectra for the control $\text{Al}_{90}\text{Fe}_7\text{Ce}_3$ have been published elsewhere¹²; these will only be briefly discussed here. Figures 4 and 5 show angle resolved XPS spectra of Al 2p and O 1s photoelectron lines for control $\text{Al}_{90}\text{Fe}_7\text{Ce}_3$. Angle resolved spectra of the Al 2p and O 1s photoelectron lines were measured for θ (electron emission angle as measured relative to sample plane) = 80, 78, 75, 70, 65, 60, 55, 45, 35, 25, 15, 5. The Al 2p spectra display two components with strong dependence on electron emission angle. It is shown that the intensity of the high binding energy component increases with decrease in θ in contrast with the low binding energy component whose intensity decreases with decrease in θ . Thus, the high binding energy component at ≈ 74.5 eV corresponds to oxidized Al in the native oxide film. The low binding energy component at ≈ 71.6 eV, on the other hand, corresponds to Al in $\text{Al}_{90}\text{Fe}_7\text{Ce}_3$ underlying the native oxide film. Angle resolved spectra of the O 1s photoelectron line consists of an asymmetric peak due to the presence of two sub-peaks which are not quite resolved from each other but were resolved using standard curve fit analysis procedures. Based on curve fit analysis, two components with binding energies of ≈ 531.2 and 532.4 eV were resolved corresponding to hydroxyl groups and ionic oxygen indicating that the composition and chemistry of the native oxide can be depicted as $\text{AlO}_x(\text{OH})_y$. The O 1s spectra show that the intensity ratio of the peak corresponding to hydroxyl groups to that of ionic oxygen decreases with increase in θ . The observed angle dependencies for both the Al and O 1s lines are consistent with a layered structure in which the $\text{Al}_{90}\text{Fe}_7\text{Ce}_3$ alloy

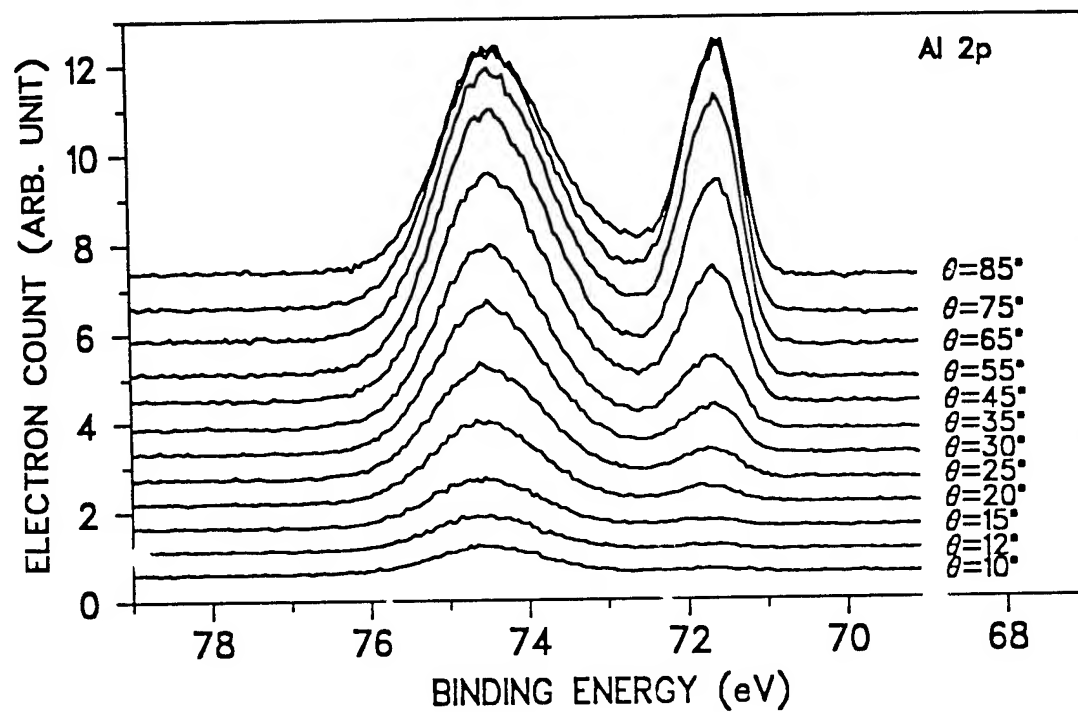


Figure 4. Angle resolved XPS spectra of Al 2p for control $\text{Al}_{90}\text{Fe}_7\text{Ce}_3$.

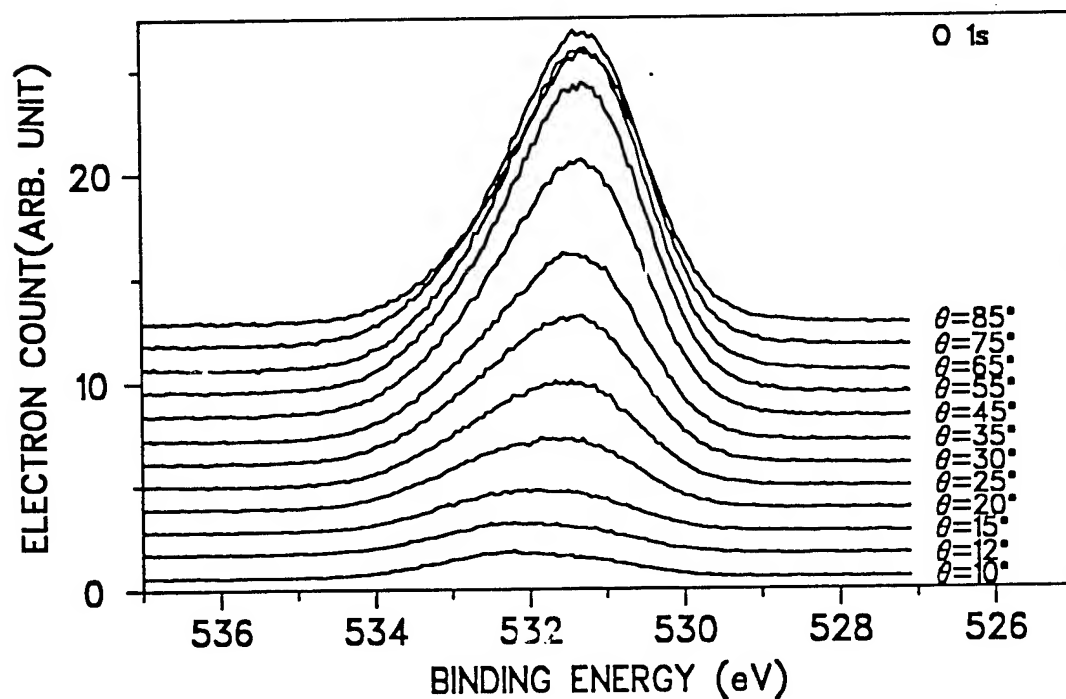


Figure 5. Angle resolved XPS spectra of O 1s for control $\text{Al}_{90}\text{Fe}_7\text{Ce}_3$.

is covered with native oxide of $\text{AlO}_x(\text{OH})_y$. The angle resolved XPS data can also be used to determine the film thickness of the native oxide.

XPS spectra of passivated alloys in 0.9 wt% NaCl solution for 60 minutes and then dried in a stream of dry nitrogen gas show that the Fe and Ce concentrations in the near surface region have significantly increased relative to their concentrations in the control alloys.¹³ Figures 6, 7, and 8 show comparisons spectra of Al 2p, Fe 2p and Ce 3d XPS spectra, respectively, taken at electron emission angle, $\theta = 45^\circ$, for control $\text{Al}_{90}\text{Fe}_7\text{Ce}_3$ and passivated $\text{Al}_{90}\text{Fe}_7\text{Ce}_3$ as well as passivated $\text{Al}_{90}\text{Fe}_3\text{Ce}_7$ in aqueous 0.9 wt% NaCl for 60 minutes. The Al 2p spectra for passivated alloys display a broad peak corresponding to oxidized Al in contrast to the control spectrum which display two components corresponding to oxidized and metallic Al. The Fe 2p spectrum of control $\text{Al}_{90}\text{Fe}_7\text{Ce}_3$ displays the spin orbit doublet ($2p_{1/2}$ and $2p_{3/2}$) with binding energies characteristic of metallic Fe. The Fe 2p spectra for passivated $\text{Al}_{90}\text{Fe}_7\text{Ce}_3$ and $\text{Al}_{90}\text{Fe}_3\text{Ce}_7$ show broad peaks which are shifted to higher binding energies relative to those of the control spectra. Based on comparison of the Fe 2p binding energies and their characteristic shake-up with reference spectra for Fe in various phases,^{14,15,16,17,18} we conclude that the Fe chemistry in the passive film

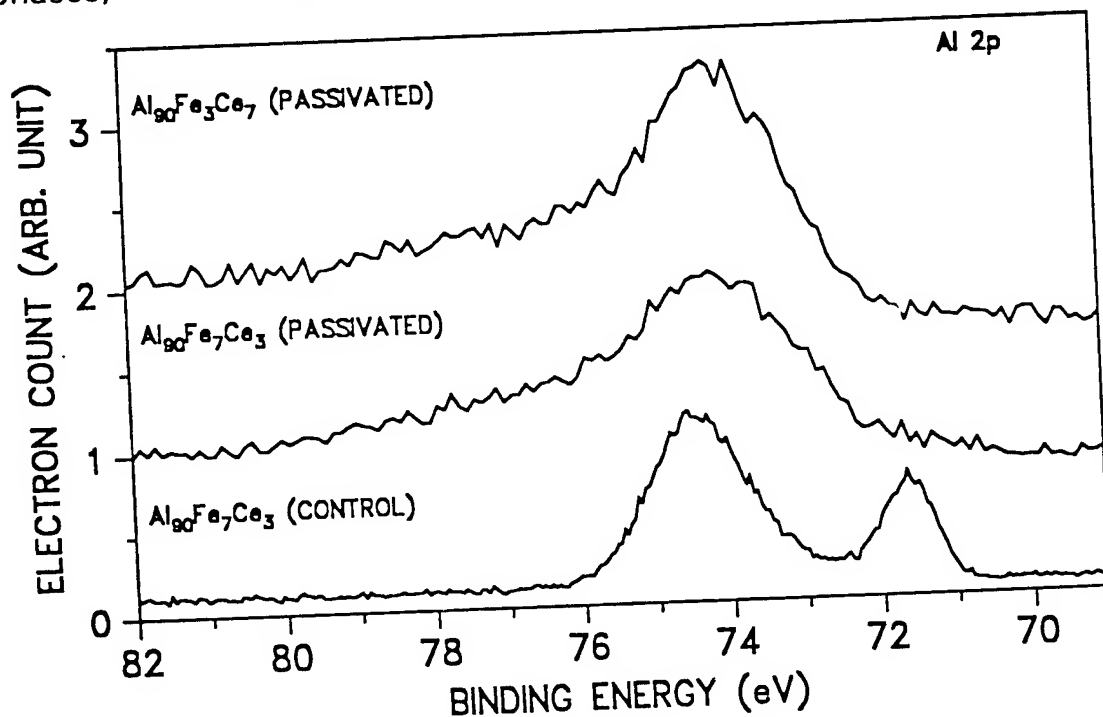


Figure 6. XPS spectra of Al 2p for control and passivated alloys.

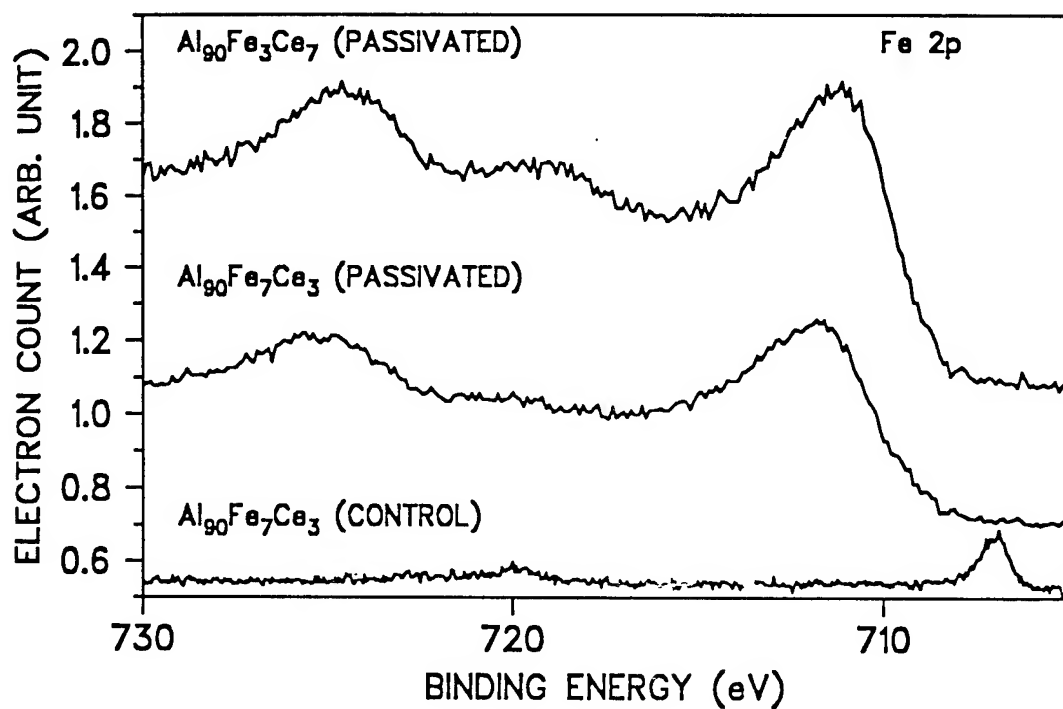


Figure 7. XPS spectra of Fe 2p for control and passivated alloys.

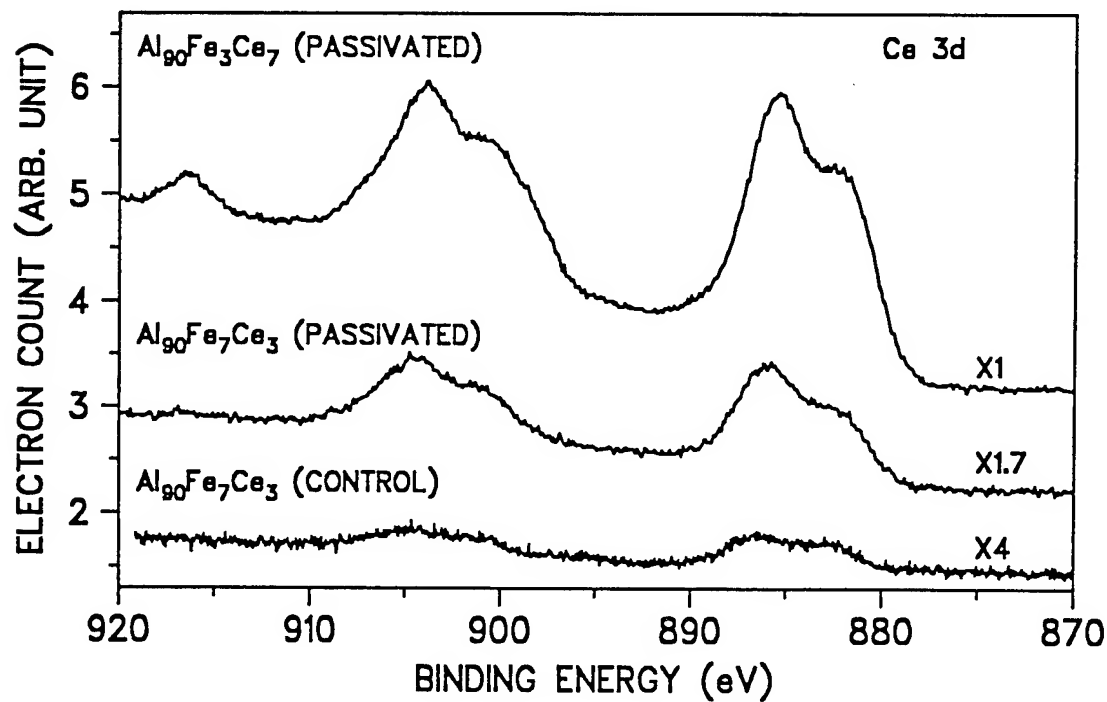


Figure 8. XPS spectra of Ce 3d for control and passivated alloys.

is similar to that of Fe in Fe_3O_4 for $\text{Al}_{90}\text{Fe}_7\text{Ce}_3$ and Fe in $\alpha\text{-Fe}_2\text{O}_3$ or FeOOH for $\text{Al}_{90}\text{Fe}_3\text{Ce}_7$.

The Ce 3d spectra of Figure 8 display broad lines for each of the $3d_{3/2}$ (high binding energy component) and $3d_{5/2}$ (low binding energy component) spin orbit doublet. The shoulders on the low binding energy side for each component corresponds to the well known shake-down structure.^{19,20,21,22,23} Based on the binding energy of the principal lines, the nature of the shake down structure, and the magnitude of the spin orbit splitting we conclude that the oxidation state of Ce in the passive film for $\text{Al}_{90}\text{Fe}_7\text{Ce}_3$ and $\text{Al}_{90}\text{Fe}_3\text{Ce}_7$ is mainly +3, i.e., similar to that of Ce in Ce_2O_3 or $\text{Ce}(\text{OH})_3$. A peak at roughly 916 eV in the Ce 3d spectrum for $\text{Al}_{90}\text{Fe}_3\text{Ce}_7$ is characteristic of Ce in the +4 oxidation state such as that of Ce in CeO_2 . Hence the chemistry of a fraction of Ce in the passive film of $\text{Al}_{90}\text{Fe}_3\text{Ce}_7$ is similar to that of Ce in CeO_2 .

XAFS Studies:

Figures 9 and 10 show the Fe K-edge and Ce L_3 -edge XANES spectra, respectively, for control alloys and alloys passivated in 0.9 wt% NaCl for 60 minutes and then dried in a stream of dry nitrogen gas. The Fe K-edge spectra were compared with the reference spectrum of structurally well defined $\alpha\text{-Fe}_2\text{O}_3$. The Fe K-edge spectra for the passivated alloys are clearly distinct from those of control alloys but resemble more closely the spectrum of $\alpha\text{-Fe}_2\text{O}_3$. Note that the XANES spectra of Fe_3O_4 , $\alpha\text{-Fe}_2\text{O}_3$, $\gamma\text{-Fe}_2\text{O}_3$, and $\gamma\text{-FeOOH}$ are very similar and can not be distinguished from each other. In all of these compounds the oxidation state of Fe +3 except for Fe_3O_4 where one-third of Fe is present in the +2 and two-thirds of Fe is present in the +3 oxidation states. Hence, the oxidation state of the majority of Fe in the passive film is +3. The Ce L_3 -edge spectra of Figure 10 were compared with reference spectra of structurally well defined $\text{Ce}(\text{NO}_3)_3$ and CeO_2 . It is shown that the spectra of passivated alloys are clearly distinct from those of the control alloys. The Ce L_3 -edge spectrum for passivated $\text{Al}_{90}\text{Fe}_7\text{Ce}_3$ resemble more closely that of $\text{Ce}(\text{NO}_3)_3$ while that of passivated $\text{Al}_{90}\text{Fe}_3\text{Ce}_7$ is identical to that of CeO_2 . The spectrum for passivated $\text{Al}_{90}\text{Fe}_5\text{Ce}_5$ is intermediate between those of $\text{Ce}(\text{NO}_3)_3$ and CeO_2 . Based on these results we conclude that the oxidation state of Ce in the passive film of $\text{Al}_{90}\text{Fe}_7\text{Ce}_3$ is mainly +3 with only a small amount of Ce in +4 state. The majority of Ce is present in the +3 oxidation state with the remainder being present in the +4 oxidation state in the

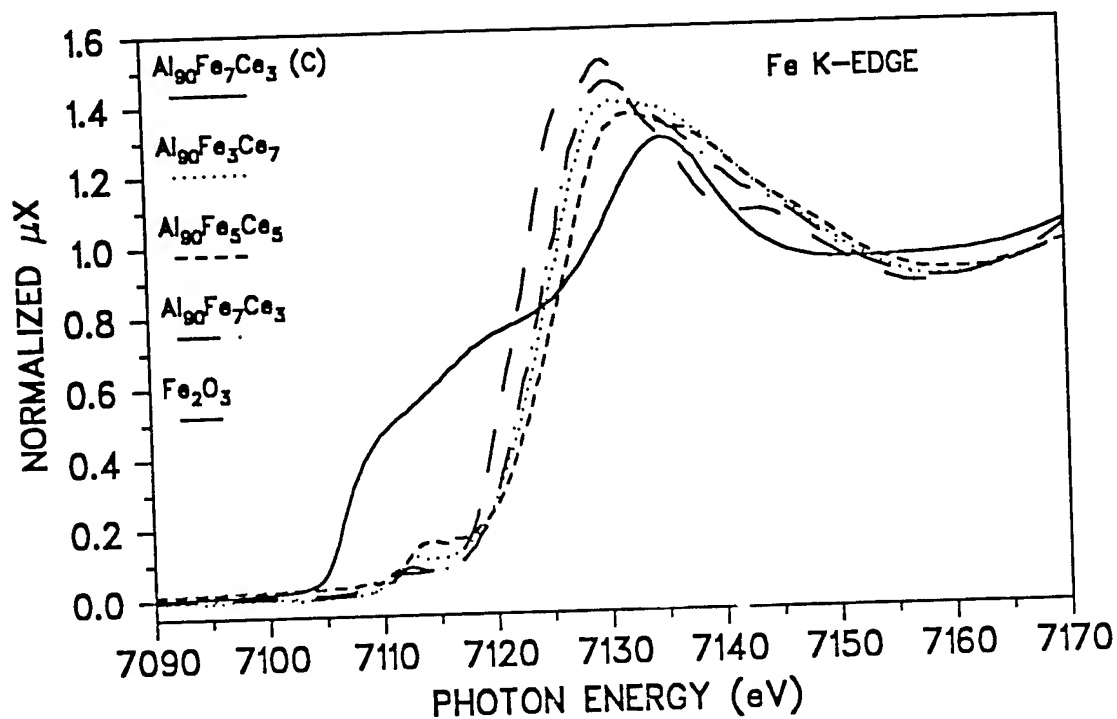


Figure 9. XANES spectra of Fe K-edge for control (C) and passivated alloys and $\alpha\text{-Fe}_2\text{O}_3$

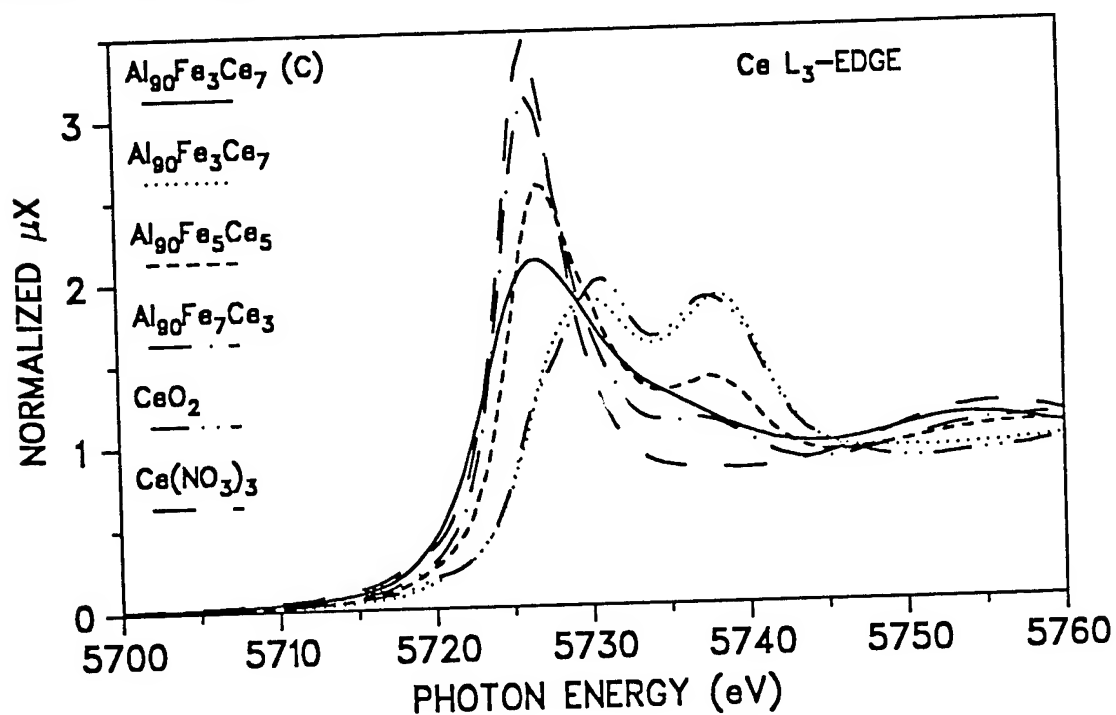


Figure 10. XANES spectra of Ce L_3 -edge for control (C) and passivated alloys, $\text{Ce}(\text{NO}_3)_3$ and CeO_2 .

passive film for $\text{Al}_{90}\text{Fe}_5\text{Ce}_5$. For $\text{Al}_{90}\text{Fe}_3\text{Ce}_7$, Ce in the passive film is present only in the +4 oxidation state. This indicates that the fraction of Ce in the +4 oxidation state increases with increase in the Ce content of the alloy. XANES spectra of passivated alloys rinsed with copious amounts of deionized H_2O (not shown here) show that the fraction of Ce in the +3 oxidation state decreased relative to those for samples dried in a stream of nitrogen gas. Thus, the effect of H_2O rinsing on the chemistry of Ce in the passive film region is to oxidize a fraction of Ce present in the +3 state to Ce in the +4 state. No change in the chemistry of Fe is observed in samples rinsed with copious amounts of deionized H_2O vis. samples dried in a stream of dry nitrogen gas.

Acknowledgement

This work was supported by the Independent Research Program of NSWCDD (ANM), and the U. S. Department of Energy, Materials Science Division, (CAM). We acknowledge the support of the U.S. Department of Energy, Division of Materials Sciences, under Contract Number DE-AS05-80-ER-10742 for its role in the development and operation of beam line X-11A at the National Synchrotron Light Source (NSLS). The NSLS is supported by the Department of Energy, Division of Materials Sciences and Division of Chemical Sciences, under Contract Number DE-AC02-76CH00016. We are also grateful to Professor S. J. Poon, Dr. Y. He, and Professor G. J. Shiflet of the University of Virginia, Charlottesville, VA 22903-2458 for providing the samples used in this investigation. The work at UV was supported by the U. S. Army Research Office under contract no. DAAH-94-G-0076. In addition, we are thankful to Dr. R. A. Brizzolara of NSWC for assistance during the XAFS data acquisition at BNL and to Dr. M. K. Norr also of NSWC for taking the SEM micrographs and EDAX analysis.

References

1. Y. He, S. J. Poon, and G. J. Shiflet, *Science* **241**, 1640 (1988).
2. A.-P. Tsai, A. Inoue, and T. Masumoto, *Metallurgical Transactions A* **19A**, 1369 (1988).
3. L. T. Kabacoff, C.-P. Wong, N. L. Guthrie, and S. Dallek, *Mat. Sc. Eng. A* **134**, 1288 (1991).

4. G. J. Shiflet, Y. He., and S. J. Poon, J. Appl. Phys. **64**(12), 6863 (1988).
5. A. Inoue, K. Ohtera, and A.-P. Tsai, Jap. J. Appl. Phys. **27**(4), 938, L479 (1988).
6. J. L. Wagner, K. M. Wong, F. S. Pierce, and S. J. Poon, Phys. Rev. B **39**(8), 5500 (1989).
7. D.E. Sayers, S.M. Heald, M.A. Pick, J.I. Budnick, E.A. Stern, and J. Wong, Nucl. Instr. and Meth., **208**, 631 (1983).
8. J. Jaklevic, J.A. Kirby, M.P. Klein, A.S. Robertson, G.S. Brown, and P. Eisenberger, Solid State Communications, **23**, 679 (1977).
9. M. E. Kordesh and R. W. Hoffman, Phys. Rev. **B31**, 191 (1984).
10. F.W. Lytle, R.B. Gregor, D.R. Sandstrom, E.C. Marques, J. Wong, C.L. Spiro, G.P. Huffman, and F.E. Huggins, Nucl. Instr. and Meth., **226**, 542 (1984).
11. F. W. Lytle, R. B. Gregor, G. H. Via, J. M. Brown, and G. Meitzner, J. De Physique, Colloque C8, **47**, C8-149 (1986).
12. A. N. Mansour, S. J. Poon, and Y. He, and G. J. Shiflet, Surface Science Spectra **2**, 31 (1993).
13. A. N. Mansour, C. A. Melendres, M. Pankuch, S. J. Poon, Y. He, and G. J. Shiflet, Surface Science Spectra, **2**, in press, (1994).
14. H. Konno and M. Nagayama, Passivity of Metals: Proceedings of the 4th International Symposium on Passivity, (Princeton, NJ: Electrochemical Society, 1978), editors: R. B. Frankental and J. Kruger, p. 585.
15. V. Stambouli, C. Palacio, H. J. Mathieu, and D. Landolt, Appl. Surf. Sce. **70/71**, 240 (1993).
16. K. Assami and K. Hashimoto, Corrosion Science **17**, 559 (1977).
17. G. C. Allen, M. T. Curtis, A. J. Hooper, and P. M. Tucher, J. C. S. Dalton, 1525 (1974).

18. T. L. Barr, J. Phys. Chem. 82, 1801 (1978).
19. P. Burroughs, A. Hamnett, A. F. Orchard,, and G. Thornton, J. Chem. Soc. Dalton 17, 1686 (1976).
20. T. L. Barr and C. G. Fries, J. Chem. Soc. Dalton Trans., 1825 (1983).
21. L. Schlapbach and J. Osterwalder, Solid State Communications 42, 271 (1982).
22. D. L. Perry and L. Tsao, J. Mat Sci Lett. 3, 1017 (1984).
23. D. D. Sarma and C. N. Rao, J. Electron Spectrosc. and Related Phenomena 20, 25 (1980).

Surface Analysis of Anodized Aluminum Panels that have
been Painted, Bead Blasted, Cleaned, and Treated
with a Chemical Conversion Coating.

Mr. John J. Jusko
Science and Engineering Laboratory
OO-ALC/TIELM 7278 4th St.
Hill AFB, UT 84056-5205

Abstract

Aluminum panels were prepared to simulate the process an aircraft undergoes for repainting. This process consisted of stripping the original paint down to the anodized aluminum by bead blasting with polymethyl methacrylate (PMMA), cleaning the surface, corrosion removal, followed by a chemical conversion coating. The chemical conversion coating was applied on panels from 0 to 15 minutes. The surface analysis was performed using a Surface Science Instrument Model 501 ESCA. The surface analysis has shown several interesting phenomena that occurred on the panels. The phenomena includes non uniformity of the surfaces, changes in the atomic concentrations, and changes in the organic layers. Changes in the chemical states of the elements vs the chemical conversion coating times were also detected. The non uniformities were present in both the elemental surveys and the high resolution scans. The elemental surveys showed that the atomic percent of the elements (especially Cr) changed with the chemical conversion coating time. The high resolution scan of carbon showed that a layer of PMMA was left on the surface after bead blasting. After cleaning and applying the chemical conversion coating compound, the organic layer consisted of mainly hydrocarbons and alcohols/ethers, however, areas with slight amounts of PMMA were also detected. The high resolution scans of the aluminum peaks showed that the chemical states of aluminum changed with the chemical conversion coating time. That is, the surface aluminum changed from an unoxidized aluminum to

a mixture of an oxide and a possible complex oxyfluoride surface at longer coating times.

Introduction

The surface preparations for repainting an aircraft have relied heavily on the use of volatile organic compounds such as Methyl Ethyl Ketone (MEK). The safety and environmental concerns of these compounds are rapidly limiting their use. The elimination of these compounds from the repainting process will effect the properties of the surface to be painted. These effects will be most notable in the removal of the organic contaminants, the quality of the chemical conversion coatings, and the adhesion of the environmentally compliant (low VOC) primers and topcoat paints. This surface study was undertaken to determine some of the possible changes that will occur.

Experimental Procedure

One square foot panels of 2024 T6 chromic acid anodized aluminum were used as the base alloy. The panels were primed and painted with a FMS 1058 and TTP-2760 primers and a MIL-C-85285 paint. The primers and paint were allowed to cure. The painting of the panels was preformed to simulate the aircraft skin prior to arrival at OO-ALC.

The painted test panels were subjected to the process that an aircraft currently undergoes for repainting at OO-ALC. The first step in the repainting process is to remove the old paint. This was accomplished by a plastic medium blast (PMB) in accordance with the T.O. 1-1-8. The plastic blast medium used was qualified to MIL-P-85891 type V. For the type V medium, MIL-P-85891 calls for a MEK or similar solvent wipe. The solvent used for the wipe was qualified to FMS-2004A. After the solvent wipe, the panels were scrubbed with a alkaline cleaner. A corrosion removal compound qualified to MIL-C-38334 was then applied to the surface in accordance to the T.O. The final step prior to repainting was the application of a chemical conversion coating qualified to MIL-C-81706. In this study the chemical conversion coating compound was applied to the panels from 0 to 15 minutes. A four inch square was cut from the center of the test panels for the surface analysis. There were three locations analyzed per sample.

The surface analysis technique used to analyze the panels was Electron Spectroscopy for Chemical Analysis (ESCA). The ESCA used

was a model 501 Surface Science Instrument. ESCA is also known as X-Ray Photoelectron Spectroscopy (XPS). The ESCA uses an Al $K\alpha$ X-ray source to knock out the photoelectrons. Each element has characteristic photoelectron energies which allows the elemental surface composition to be determined. The chemical state of the surface elements are determined by comparing subtle shifts in the photoelectron energies. These shifts are caused by the oxidation state of the element, and are evident in high resolution scans. The analyses were performed with the following parameters: The pressure in the analytical chamber was 1×10^{-9} Torr. The pass energy was set at 100 eV for the elemental surveys, and 50 eV for the high resolution scans. The 1000 μ spot was used for each analysis. The flood gun was turned on with an energy of 5 eV. The flood gun was required to reduce the effects of surface charging.

Chemical fingerprints of the anodized aluminum, PMB, cleaners, corrosion removal compound, and the chemical conversion coating compound were acquired. The ESCA fingerprints included elemental surveys and high resolution scans of key elements. The atomic percent of the elements were calculated from the elemental surveys using the instruments internal software program. The high resolution scans were performed on aluminum (Al 2p peak), chromium (Cr 2p₁ and Cr 2p₃ peaks), carbon (C 1s peak), and oxygen (O 1s peak). A curve fitting routine was used to determine the energy values of peaks in the high resolution scans. The hydrocarbon peak in the C 1s scan was adjusted to the reference value of 284.6 eV. The fingerprints were obtained for comparison to elemental surveys and high resolution scans that were taken during various steps in the repainting process.

Results and Discussion

The elemental and chemical fingerprints of the compounds used in the repainting process were obtained. These fingerprints provided information on the origin of the residues left on the panels' surface. The plastic blast medium was determined to be polymethyl methacrylate (PMMA). The blast medium was characterized with nuclear magnetic resonance (NMR), infrared spectroscopy (IR), and ESCA. The alkaline cleaner was found to leave a carbon film consisting of hydrocarbons and an alcohol/ether. The corrosion removal compound was found to contain an ether using Fourier Transform Infrared Spectroscopy (FTIR). The corrosion removal compound left a carbon surface residue that corresponds to an ether. The C 1s peak for the cleaning compounds, the

corrosion removal compound, and the PMMA contain a peak that corresponds to alcohols/ethers. This interference between these compounds did not allow for the exact determination of the origin of the alcohols/ethers on the final panels. However, the PMMA had a peak in the carbon high resolution scan that is not common with the other compounds. From this peak it was determined that there was PMMA on the chemical conversion coated panels.

The elemental surveys on the conversion coated panels detected the presence of the following elements: carbon, oxygen, nitrogen, silicon, sulfur, phosphorus, iron, calcium, fluorine, chromium, and aluminum. The elemental fingerprint for the solvent, alkaline cleaner, and corrosion removal compound account for P, and Si elements. The Cr, F, Fe, and N are from the chemical conversion coating compound. The Fe was only seen on the panels that had the chemical conversion coating compound applied for 10 and 15 minutes. The Al is from the base alloy. To determine the origin of the carbon on the surface the oxidation state had to be determined. This was done in the high resolution scans of the C1s peak.

The high resolution fingerprint for the C1s peak, of the bead blast medium, is shown in Figure #1. The peak locations [1] fit those of the functional groups in PMMA. The peak ratios of 3:1:1 also match that of PMMA. The high resolution scans for the O1s peak also matched the oxygen ratio for PMMA. To determine if bead blasting leaves a residue, a panel was analyzed after bead blasting, but prior to the solvent wipe. The C1s peak on the bead blasted surface showed an increase in the full width half maximum of the peaks, a surface charging phenomena, and an increase in the percentage of the hydrocarbon on the surface. The peak broadening may be due to a combination of the surface roughness, and the surface charge. Using the peak that corresponds to the ester in PMMA, the surface of the carbon film was calculated to contain 49% PMMA. The remainder of the carbon was a hydrocarbon. After the solvent wiping, alkaline scrub, and the application of the corrosion removal compound the percent of PMMA in the carbon peak was reduced. However, the cleaning process added a carbon film consisting of an alcohol/ether on the surface. Additional studies on the PMMA and the cleaning ability of solvents will be presented in future work. The chemical conversion coating compound was applied to the cleaned panels for 5, 10, and 15 minutes. After the application of the conversion coating compound, PMMA and alcohols/ethers were detected. The chemical conversion coated panels had three distinct characteristics: (1) there was a non uniformity of the coating, (2) the atomic percent of the

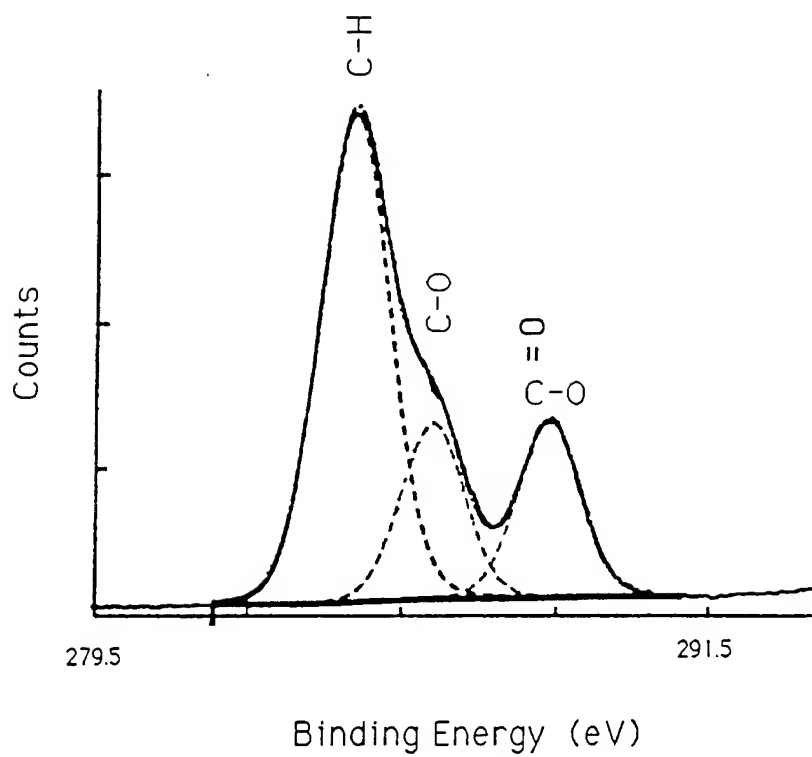


Figure #1 C1s high resolution scan of the bead blast medium.

elements changed with the coating time, and (3) the oxidation state of aluminum changed with the application time of the chemical conversion coating compound.

For a particular application time of the chemical conversion coating compound the oxidation state of chrome varied. High resolution scans of the Cr 2p₁ and Cr 2p₃ peaks were used to determine the oxidation state of the chrome. The chrome peak energies were found to correspond to literature [2,3] values for Cr⁺³ and Cr⁺⁶. There was no set ratio in the amount of Cr⁺³ to Cr⁺⁶ as found in a similar system analyzed by H. A. Katzman [4] et al. The ratio of the Cr⁺³ to Cr⁺⁶ was found to vary widely from location to location. Several articles [5,6] in the literature have found other non uniformities in chemical conversion coating films.

The atomic percent of Cr, F, Fe, and N on the surface changed with the application time of the chemical conversion coating compound. These elements were also detected in the fingerprint of the conversion coating compound. Figure #2 is a graphic representation of the average atomic percent of the elements vs the application time. The error bars represent the standard deviation. Iron was detected only on the panels with application times of 10 and 15 minutes.

The chemical state of the aluminum on the test panels changed with the application time of the chemical conversion coating compound. To determine the chemical state of the Al2p peaks their energy values were compared to literature [3, 7, 8, 9] values. The chemical state of the aluminum on the surface of the 5 minute panel consisted of mostly Al⁺⁰ (Figure 3a). Sunderland [10] found the surface aluminum in this state for a similar system. The 10 minute panel contained Al⁺⁰ and Al₂O₃ (Figure 3b). The aluminum oxidation state for the 10 minute sample differs from the 5 minute sample by an increase in the percent of Al₂O₃. The 15 minute panel contained Al⁺⁰, Al₂O₃, and a third peak at a higher energy (Figure 3c). This third peak was located between the Al₂O₃ peak location and that of AlF₃. No literature data was found that could give a chemical composition to this peak energy. However, this peak could correspond to an oxyfluoride that had been mentioned in other publications [5, 11, 12].

In the reaction chemistry for the chemical conversion coating presented in other publications [4, 13] one of the reactants is AlF₃. A panel that had not been painted and prepared for repainting was used for a comparison to the test panels. This panel had the chemical conversion coating compound applied for 5 minutes. The high resolution scan for the Al2p peak (Figure #3d) detected only Al₂O₃ and AlF₃. In the panels prepared for repainting, a peak located at the AlF₃ energy was not

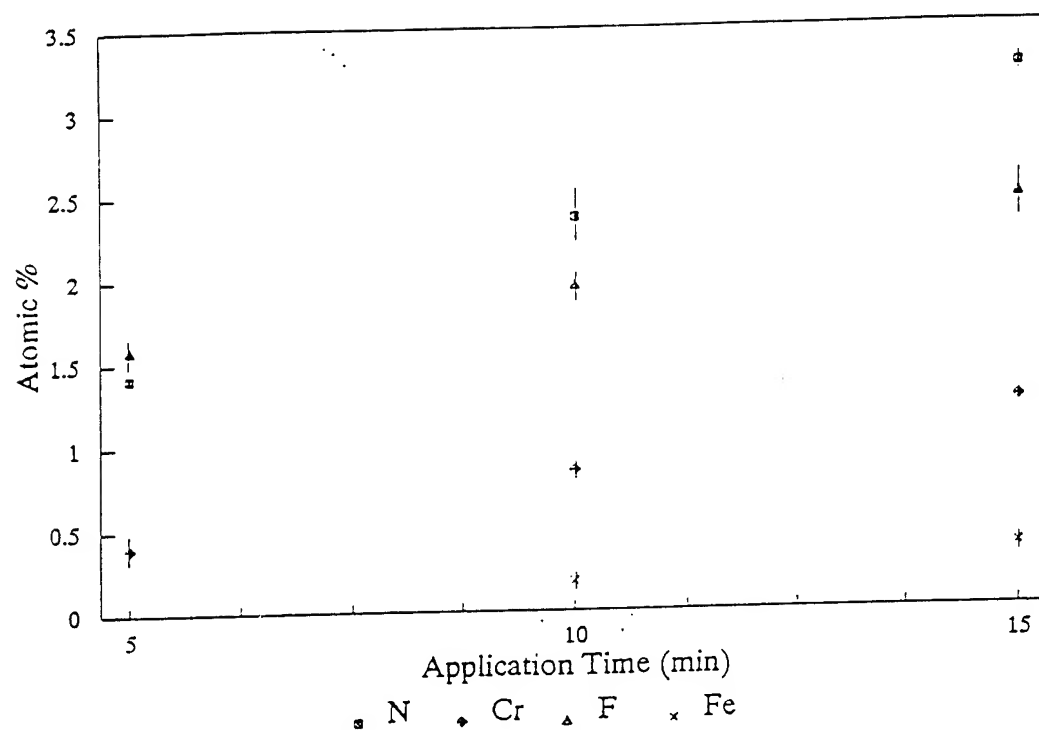


Figure #2 The surface atomic percent for chrome, fluorine, iron, and nitrogen vs the application time of the conversion coating compound. The error bars represent the standard deviation.

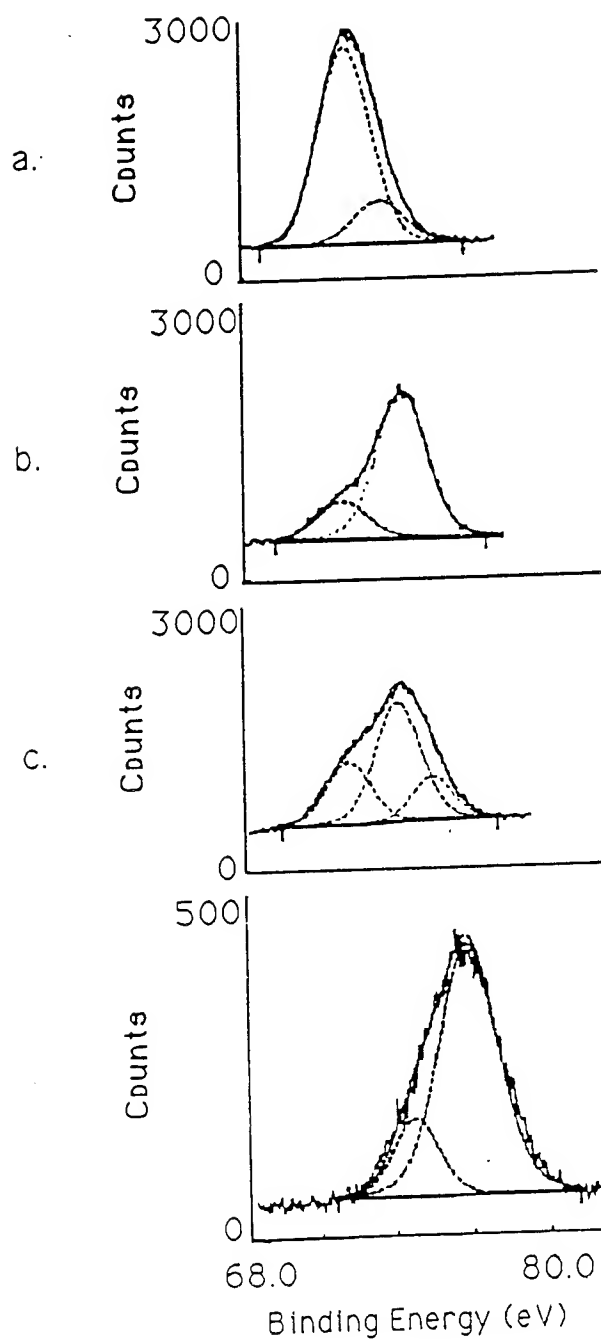


Figure #3 High resolution scans of the $\text{Al}2p$ peak vs application time of the conversion coating compound. a) 5 min. panel containing mostly Al^{+0} b) 10 min panel contains Al^{+0} and Al_2O_3 c) 15 min. panel contains Al^{+0} , Al_2O_3 , and a possible oxyfluoride d) 5 min. application of the chemical conversion coating compound on an anodized panel that did not undergo the repainting process. Contains Al_2O_3 and a peak near the energy of AlF_3 .

detected. This demonstrated that the preparation for repainting does have an effect on the chemical conversion coating.

Conclusions

This surface study of the repainting process has demonstrated four distinct results. First, the bead blast medium was not totally removed by the cleaning process. Second, the atomic percentage of chemical conversion coating elements on the surface was dependent on the application time. Third, the high resolution scans showed that the chrome was in the trivalent and hexavalent states. Fourth, the chemical state of the aluminum changed with the application time of the conversion coating.

References

1. D.T. Clark and H.R. Thomas, *J. of Polym. Sci. Polym Chem.* 16, 791 (1978)
2. J.C. Carver, G.K. Schweitzer and Thomas A. Carlson, *J. Chem. Phys.* 57, 980 (1972)
3. R. Holm and S. Storp, *Appl. Phys.* 9, 217 (1976)
4. H.A. Katzman, G.M. Malouf, R. Bauer, and G.W. Stupian, *Appl. Surface Sci.* 2, 416 (1979)
5. M.F. Abd Rabbo, J.A. Richardson, and G.C. Wood, *Corros. Sci.* 18, 117 (1978)
6. R.C. Furneaux, G.E. Thompson and G.C. Wood, *Corros. Sci.* 19, (1979)
7. G.E. McGuire, G.K. Schweitzer, and Thomas A. Carlson, *Inorg. Chem.* 12, 2450 (1973)
8. V.I. Nefedov, Ya. V. Salyn, G. Leonhardt, and R. Scheibe, *J. Elect. Spectros.* 10, 121 (1977)
9. V.I. Nefedov, V.S. Urusov, and M.M. Kaklana, *Geochemistry International*, p. 7 (1972)
10. Robert J. Sunderland, *Proc. 6th Internl. Vacuum Congr. 1974; Japan J. Appl. Phys. Suppl.* 2, Pt. 1, p. 347 (1974)
11. K. F. Lorking and J. E. O. Mayne, *Brit. Corros. J.* 1, 181 (1966)
12. J. A. Richardson and G. C. Wood, *J. Electrochem. Soc.* 120, 193 (1973)
13. G.W. Stupian and P.D. Fleischauer, *Appl. Surface Sci.* 9, 250 (1981)

SESSION II
MICROBIOLOGICAL CORROSION

Chairmen: *J. Jones-Meehan*
AND M. Walch

**Mechanisms of Reproducible Microbial Pitting of 304 Stainless Steel
by a Mixed Consortium Containing Sulphate-Reducing Bacteria.**

Dr. Peter Angell*

Dr. Jiunn-Shyong Luo

Dr. David C. White

Center for Environmental Biotechnology

10515 Research Drive, Suite 300

Knoxville, TN. 37932-2575

Abstract

Pitting corrosion is characterised by the formation of small anodes and corresponding large cathodes, which allow the formation of pits in the metal matrix. A number of mechanisms have been put forward to account for the involvement of SRB in this process including: cathodic depolarization of hydrogen, bacterial sulphide acting as the cathode, and changes in pH due to sulphate-reducing bacteria (SRB). To date there has been little success in reproducibly inducing SRB pitting of stainless steels in a laboratory system.

A concentric electrode has been designed in which a small anode is artificially produced within a large cathode by applying a galvanic current of $12 \mu\text{A cm}^{-2}$. During the application of this galvanic current, various consortia and axenic cultures of bacteria are allowed to colonise the surface of the stainless steel concentric electrode. After seventy-two hours the induced current is removed and the resultant current monitored. Electrochemical impedance spectroscopy (EIS) is carried out on both the anodes and cathodes in order to determine the charge transfer resistance (R_{ct} values) and changes in phase angles with time. At the termination of the experiment viable counts of both SRB & *Vibrio* sp. are recorded from the anodes and cathodes.

A coupling current of about $6 \mu \text{ A cm}^{-2}$ is maintained only in the presence of a mixed culture containing an SRB and a *Vibrio* sp.. In order for the current to be maintained, a low R_{ct} value is necessary at the anode $< 3 \text{ K}\Omega \text{ cm}^{-2}$. It appears that the mixed culture including SRB is necessary to maintain this low R_{ct} value. Also, the cathode must have a high R_{ct} value in excess of $100 \text{ K}\Omega \text{ cm}^{-2}$. This high value would appear to be dependant on the presence of the SRB on the cathode. It is also tentatively suggested that the magnitude of the resultant coupling current is a function of the number of bacteria on the anode.

These results indicate that microbial corrosion is not a simple process involving one bacteria and one mechanism. Rather, it is a complex phenomenon with mixed consortia working through a number of mechanisms.

Introduction

The microbial involvement in the corrosion (MIC) of steels has been recognized for many years, with a great deal of research having been carried out as reviewed by several authors [1,2]. The bulk of the literature to date deals with the effects of the sulphate-reducing bacteria (SRB) on mild steel. This has been due in part to two main factors. First, a vast quantity of mild steel is used in pipe lines, in marine and freshwater systems, where MIC has been seen to be a significant problem [3]. Second, mild steel is notably less resistant to microbial attack than stainless steels. The latter have proved to be notoriously difficult to obtain reproducible pitting in the laboratory. Most of the evidence that SRB are involved in MIC of stainless steel has come from their isolation from failures in field systems. The presence of sulphide in the regions of the pits has also served to further implicate the SRB in the process.

The heat treated zone of weldments are the areas in which most SRB failures of stainless steels have been reported to have occurred. The pits are characterized as being steep sided and often form a network of tunnels within the metals, reminiscent of Swiss cheeses. The resistance of stainless steel is thought to be due to the production of a passive film on the metal surface. The location of the pits, normally in the heat treated zone is also of significance as in this region the crystal lattice and surface chemistry have been altered by the elevated temperatures encountered during the welding process.

The vast majority, if not all, the literature on MIC of steels to date

has been concerned with either the reporting of field failures or test systems set up in natural flowing waters. To the knowledge of these authors no system has been reported to date in which reproducible pitting has been described in a laboratory system relating to the action of SRB on stainless steel. Field data has shown that stainless steels exposed to marine environments undergo ennoblement in which the open circuit potential (OCP) rises to the critical pitting range [4]. This ennoblement can be linked to the formation of a biofilm on the surface acting as an oxygen barrier decreasing the dissolved oxygen tension at the surface of the metal.

To date the primary mechanisms advanced for the MIC of steels by SRB have involved cathodic reactions as reviewed by Hamilton [5]. One mechanism involved the depolarization of the cathode by the reduction of cathodic hydrogen by the enzyme hydrogenase. The other involved bacterially produced iron sulphide acting as a cathode. Recently evidence has been suggested that a microbial biofilm is capable of creating corrosive metabolites such as hydrogen peroxide[6]. Also very low pHs, below 2, have been detected below naturally forming biofilms on stainless steel exposed to water in the Chesapeake Bay area[6],

In this paper a laboratory system will be described which could reproducibly sustain a corrosion current between an artificially generated anode and cathode in the presence of SRB. This system has facilitated the study of the mechanisms, and role of SRB in the MIC of stainless steel leading to some new insights into the action of these bacteria. The system is also suited to further studies concentrating on the mechanisms of pitting. These studies will allow for the determination of whether a link between bacterial metabolism and corrosion exists. Also, studies on the effect of the elevated temperatures encountered during welding are possible.

Materials and Methods

Bacteria used were a culture of *Desulfovibrio vulgaris* and an unidentified *Vibrio* sp.. The *Vibrio* was used due to its being a facultative anaerobe. Also, *Vibrio natrigens* has been shown by some reports to be involved in the MIC of metals[7]. The SRB was also found to tolerate low levels of oxygen. No quantification was carried out on the level of oxygen tolerance, but it was not killed by exposure to air during the plating procedure described below. It was also found to grow in previously degassed MPN tubes which had been opened and left open to the atmosphere in a laminar flow hood.

Concentric electrodes were machined from 304 stainless steel rod providing a small anode with a large surrounding cathode. The anode had a surface area of 0.031 cm^2 and the cathode had a surface area of 4.87 cm^2 . The anode was electrically isolated from the cathode by a Teflon spacer, care was taken in the machining of each component of the concentric electrode to ensure a snug fit. Electrical wire was soldered to the back of each electrode before the whole assembly was mounted in a cold cure epoxy. The electrical wire was passed through 1.5 cm length of 16 gauge silicone tubing. Half of the silicone tubing was sealed into the epoxy the other half was used to secure a piece of glass tubing to allowing positioning of the electrode within the reaction vessel. The electrical wires were passed through the center of the tubing to the outside of the vessel. The mounted concentric electrode was polished to a 600 grit finish using an abrasive paper. The polished electrode was then degreased by sonicating in acetone before being air dried.

The reaction vessel comprised a 600 ml glass vessel with a 316 stainless steel top. A number of ports were provided in the top sealed with compression fittings, allowing for: medium addition and removal, gas sparging and venting, a circulation loop to aid mixing in the vessel and ports for a titanium counter electrode and caramel reference electrode. The reference electrode was electrolytically connected to the vessel via a Lugin's bridge. The medium feed contained a drip tube to prevent bacterial grow back, of the bacteria, to the medium reservoir and cross contamination of the vessels.

For the initial part of the experiment during bacterial inoculation the system was run as a batch reactor to enhance bacterial attachment to the concentric electrode. The reactor vessel was sparged with a 95 % nitrogen 5 % hydrogen gas mixture to ensure anaerobic conditions. During this period mixing was carried out using a magnetic stirrer operating at approximately 100 rpm. Following the batch phase flow was initiated at 1 ml min^{-1} giving a dilution rate of 0.1 h^{-1} . The systems were operated at room temperature ($25 \text{ }^\circ\text{C} \pm 2 \text{ }^\circ\text{C}$). As electrochemical measurements were being made on the flowing system the magnetic stirrers were replaced by a circulation loop in which medium was pumped from the bottom of the vessel to the top.

In order to initiate the pitting for the first seventy-two hours while the bacteria were cultured under static conditions a galvanic current was applied to the concentric electrode. The current was applied via a

galvanostat such that an anodic current density of $12 \mu\text{A cm}^{-2}$ was maintained. At the end of this period of time the current was removed and the resultant current flowing between the anode and cathode was monitored. At various time points throughout the flowing cycle of the experiment electrochemical impedance measurements were made in order to determine the charge transfer resistance (R_{ct}) of each of the anodes and cathodes. The R_{ct} value is the inverse of the I_{cor} or the corrosion current, a measure of the rate of corrosion.

At the end of the experiment the concentric electrodes were removed from the vessels and the numbers of bacteria on each of the anodes and cathodes were enumerated. Enumeration was carried out by both the MPN method and plate counts on Iverson's Medium [8] using the technique of Miles and Misra [9]. Replicate plates were incubated both aerobically and anaerobically to provide counts on both SRB and the facultative *Vibrio* sp..

Results and discussion

Figure 1 shows a plot of the current density at the anode as measured over one hundred and twenty hours. It shows that in the presence of a mixed culture after the applied current is removed, after 72 hours, a current density of approximately $3 \mu\text{A cm}^{-2}$ was maintained for the remainder of the experiment. However, this was not the case with either the axenic SRB, axenic *Vibrio* or the sterile control. This current is the actual corrosion current flowing between the anode and cathode and is therefore an accurate measure of the rate of corrosion.

The R_{ct} values indicated that the lowest value is seen for the anode ($< 1 \text{ K}\Omega \cdot \text{cm}^2$) of the mixed culture in which corrosion was taking place. This system also showed the highest value for the cathode ($> 100 \text{ K}\Omega \cdot \text{cm}^2$). No other system showed such low anodic values, although similar high values were seen for the cathode in the SRB systems. All the other values fell between the two and were normally in the range of $10 \text{ K}\Omega \cdot \text{cm}^2$ to $80 \text{ K}\Omega \cdot \text{cm}^2$.

Table 1 shows the numbers of bacteria isolated from the various electrodes exposed to different conditions as well as the level of any current maintained. From this table it is seen that both SRB and the *Vibrio* were necessary on both the anode and cathode. In one experiment where a low number of SRB (10^4 cfu cm^{-2}) were present on the anode showed that the current was not maintained but slowly

dropped to zero over approximately twenty-four hours, as opposed to the sharp drop seen with the axenic cultures and the sterile control.

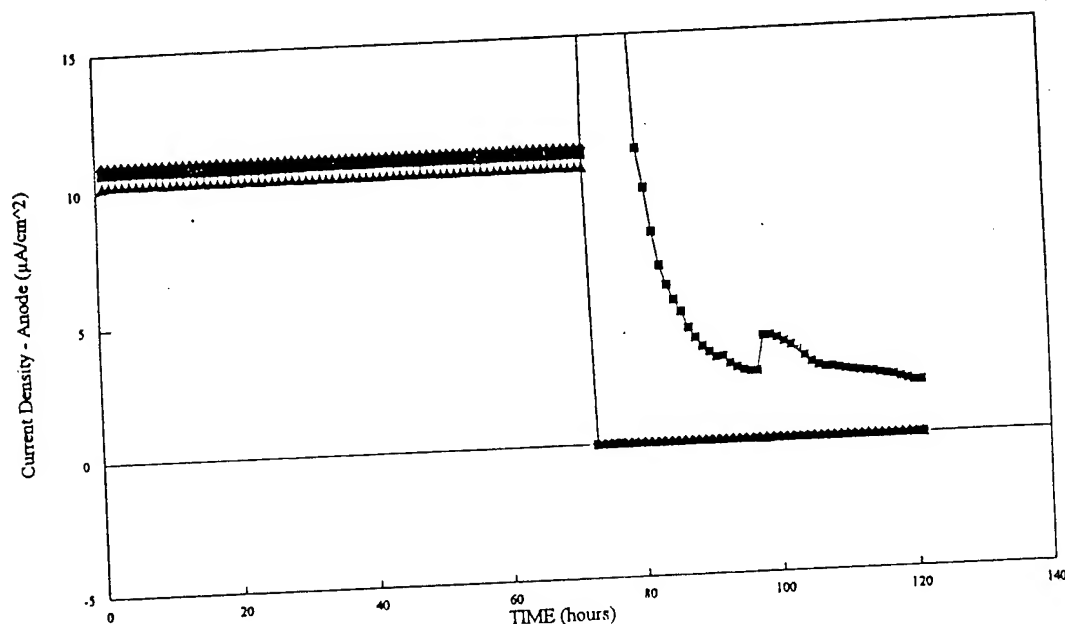


Figure 1 Time plot of measured current flowing between the anode and cathode; ■ mixed culture of *Desulfovibrio vulgaris* and *Vibrio* sp with a current maintained after applied current is removed, other plots are axenic SRB, axenic *Vibrio* and sterile showing no maintained current.

Table 1. Bacterial numbers and coupling current density for concentric stainless steel coupons with various treatments.

Coupon Treatment	SRB (cfu/ml)		<i>Vibrio</i> (cfu/ml)		Coupling Current
	Anode	Cathode	Anode	Cathode	
Sterile	-	-	-	-	-
Axenic SRB	3.2×10^4	2.0×10^1	-	-	-
Axenic <i>Vibrio</i>	-	-	1.0×10^8	1.0×10^7	-
Mixed	1.0×10^7	1.0×10^6	1.0×10^8	1.0×10^6	$3 \mu\text{A cm}^{-2}$
Mixed	3.2×10^4	2.0×10^5	1.6×10^7	2.8×10^5	*

* slow decline to zero

Figure 2. shows a run in which the corrosion current was maintained in the presence of a mixed culture for 30 hours at which point 10 mM sodium azide was added to the culture. Sodium azide is an inhibitor of aerobic respiration blocking the transfer of electrons from cytochrome a and a1 to O_2 . This system is not operative in the SRB although reports have suggested that sodium azide inhibited the growth of *Desulfovibrio* while actually stimulating the rate of sulphate reduction in H_2 [10]. On the addition of the sodium azide it can be seen that there was no effect of the level of the current density at the anode, there was no inhibition or enhancement.

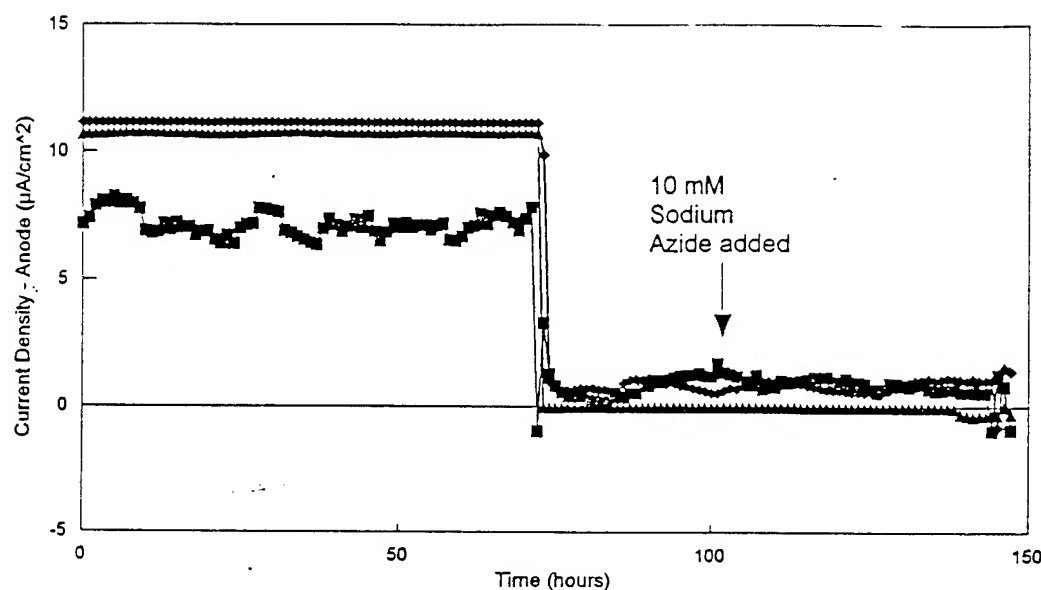


Figure 2 Time plots of measured current flowing between anode and cathode for: (■) & (♦) mixed culture of *Desulfovibrio vulgaris* and *Vibrio* sp, (▲) sterile control, with the addition of 10 mM sodium azide at 100 hours, note sodium azide is an inhibitor of aerobic respiration blocking the transfer of electrons from cytochrome a and a1 to O_2 and has no effect on the current being maintained by the mixed culture.

SRB use sulphate as their terminal electron acceptor instead of oxygen in which the sulphate is reduced to sulphide. One of the theories for the mechanism for SRB pitting is that this sulphide production acts as a cathode. If the sulphate is removed from the bacteria they are unable to produce the sulphide which if the theory is correct will stop the corrosion. In order to test this hypothesis various experiments were tried initially growing the bacteria in the absence of sulphate while the current

was being applied and then adding sulphate to the medium when the applied current was removed (Figure 2.). In this case there was no maintenance of the corrosion current even though both the *Vibrio* and the SRB were isolated from both the anode and cathode at the termination of the experiment. Similar results were seen when the experiment was reversed and the bacteria were grown in the presence of sulphate and then it was removed when the applied current was removed.

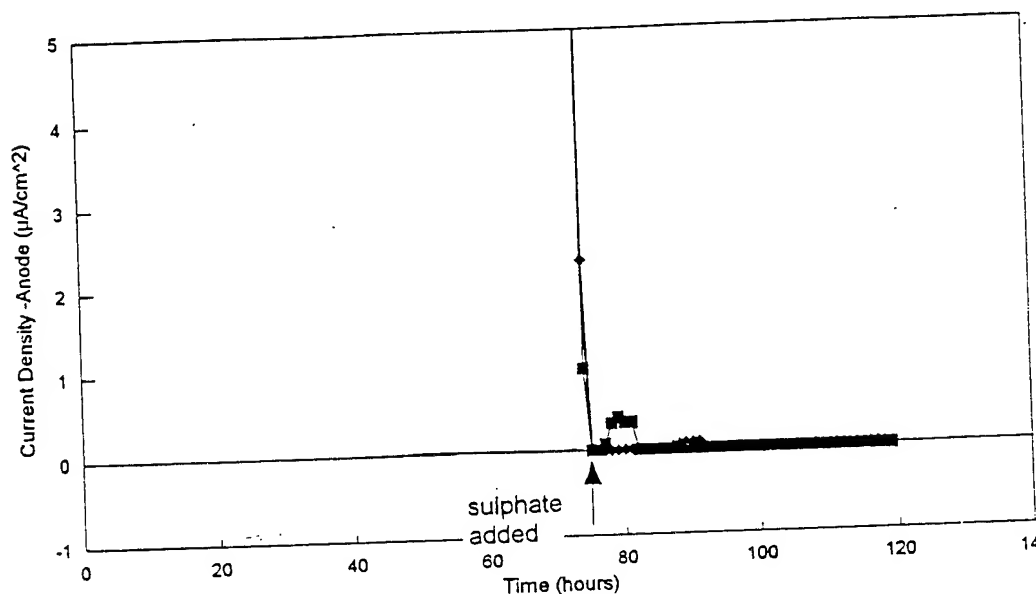


Figure 3 Time plot of measured current flowing between anode and cathode for mixed culture of *Desulfovibrio vulgaris* and *Vibrio* sp in the absence of sulphide while the current was applied and addition of sulphate to the medium when the applied current was removed, showing that no current was maintained.

Figure 4. shows a plot of current density with time for a run in which the electrodes were colonized with mixed bacteria in the presence of sulphate for 4 days. The medium was then drained and the vessels rinsed with sulphate free medium which was used through out the period that the current was applied and the system was static. When the applied current was removed sulphated medium was again added as an open system was operated. In this case the current was maintained. After it had been maintained for fifty hours the medium was again changed to one that contained no sulphate. This was fed to the vessel for a further 60 hours during which time 10 volumes had been replaced,

which should have been sufficient to remove any residual sulphate. However, this had no effect on the level of the coupling current. In fact the current was maintained for a further forty hours during which time no fresh medium was added.

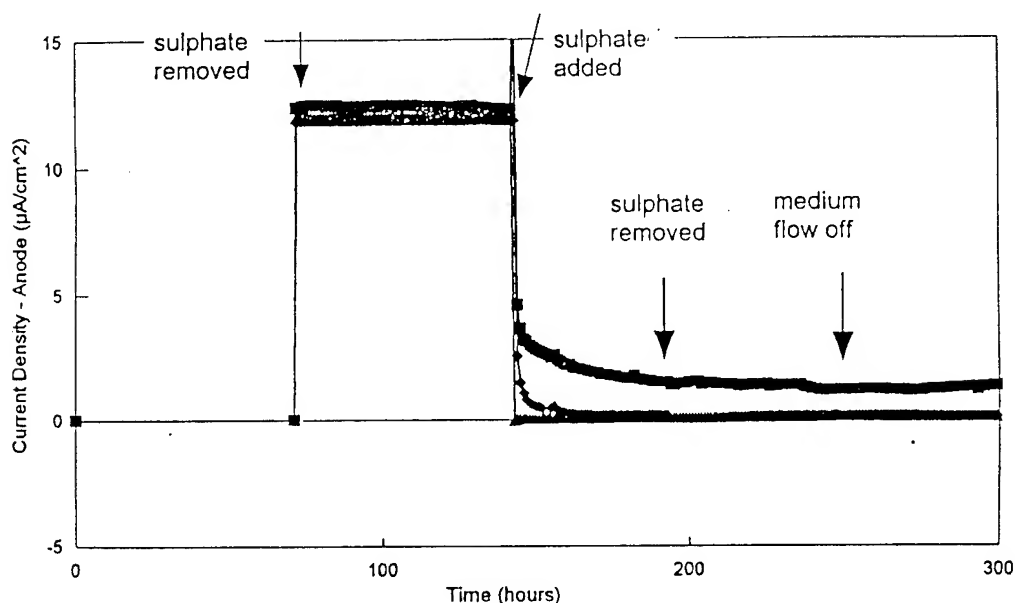


Figure 4 Time plot of measured current flowing between the anode and cathode for (■) and (♦) mixed culture of *Desulfovibrio vulgaris* and *Vibrio* sp. (▲) sterile control where sulphate was added for an initial colonisation period of 72 hours while no current was applied, sulphate was then removed while the current was applied and added again when the applied current was removed later sulphate was removed and experiment continued after medium flow was stopped. The current was maintained in one of the mixed cultures even after sulphate was removed and the medium flow was stopped.

Figure 5. shows a similar run in which sulphate was only added while the electrodes were being colonized. After this point for the rest of the experiment sulphate free medium was used. In this case only a very low level of current ($< 0.1 \mu\text{A cm}^{-2}$) was maintained. This level of current is higher than that seen in the sterile control but is far lower than those seen previously when sulphate was present.

It should be noted that the removal of the sulphate could be having one of two effects either it prevented the production of sulphide but allowed the cells to continue metabolism or it prevented metabolism and sulphide production. Certain *Desulfovibrio* sp. have been shown to be able to grow in the absence of sulphate using nitrate instead as the

terminal electron acceptor[11]. Preliminary studies using culture tubes suggest that the growth of the *Desulfovibrio vulgaris* strain used in this experiment was capable of very limited growth in the absence of sulphate at best. Further studies are planned utilizing the incorporation of radio-labelled acetate into the lipids of the bacteria as an indicator of growth in the absence of sulphate. Also stains will be examined and tested which have been reported to reduce nitrate in the absence of sulphate.

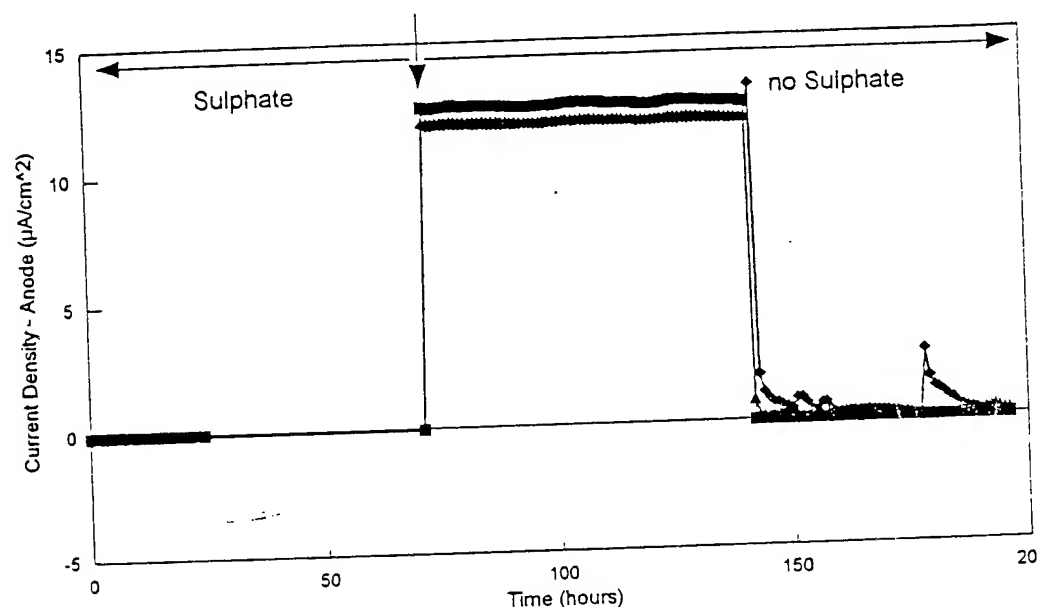


Figure 5 Time plot of current flowing between anode and cathode for (◆) and (▲) mixed culture of *Desulfovibrio vulgaris* and *Vibrio* sp., (■) sterile control where sulphate was added for the initial colonisation period but not for the remainder of the experiment showing that very little current was maintained in the mixed cultures.

From these results it would appear that sulphate is not necessary during the conditioning phase for the maintenance of the current. As noted above it is likely that the sulphate has a double effect of not only stopping the production of sulphide but also markedly reducing the metabolism of the cells. It is therefore not possible to determine to which effect the inability to maintain the current should be ascribed. However, it does appear that corrosion can be maintained when metabolism/sulphide production is only inhibited during the initiation phase and not subsequently. It would also appear that once the corrosion is initiated in the presence of sulphate metabolism/sulphide

production is no longer necessary. This could be attributed to the initiation of an electrochemical cell by the bacteria, that reaches a stage where it becomes self sustaining.

Further work is planned using a total metabolic inhibitor such as 2-heptyl-4-hydroxyquinoline N-oxide which blocks the electron transport chain between cytochrome b and cytochrome c which should be present in the SRB. It is also noted that few *Desulfovibrio* sp utilise nitrate in place of sulphate but the majority are able to use nitrite instead[12]. This will be tested in the SRB used in this study.

Acknowledgments

This work was supported by the Office of Naval Research under grant Nav' N00014-94-1-0441.

References

1. B. Little, P. Wagner, and F. Mansfeld. (1991). Microbiologically influenced corrosion of metals and alloys. *International Materials Reviews*, **36**, 253-272.
2. S.C. Dexter (1993). Role of microfouling organisms in marine corrosion. *Biofouling*, **7**, 97-128.
3. N.J.E. Dowling, M.W. Mittelman, and D.C. White (1991). The role of consortia in microbially influenced corrosion. In: *Mixed Cultures in Biotechnology*, eds G. Zeikus, and E.A. Johnson., McGraw-Hill, New York, 341-372.
4. S.C. Dexter, and S-H. Lin (1988). Mechanism of corrosion potential ennoblement by marine biofilms. Presented at 7th Intl Cong Marine Corrosion and fouling, Valencia, Spain.
5. W.A. Hamilton (1985). Sulphate-reducing bacteria and anaerobic corrosion. *Annual Review of Microbiology*, **39**, 195-217.
6. P. Chandrasekaran and S.C. Dexter (1993). Mechanisms of potential ennoblement on passive metals by seawater biofilms. Paper #493, *Corrosion 93*, NACE, Houston, Tx.
7. N.J.E. Dowling, J. Guezennec, M.L. Lemoine, A. Tunlid, and D.C. White. (1988). Analysis of carbon steel affected by bacteria using electrochemical impedance and direct current techniques. *Corrosion*, **44**, 869-874.
8. W. P. Iverson (1966). Growth of *Desulfovibrio* on the surface of

agar media. *Applied Microbiology*, **14**, 529-534.

9. A.A. Miles, and S.S. Misra (1938). The estimation of the bacteriocidal power of blood. *Journal of Hygiene, Cambridge*, **38**, 732.
10. J.R. Postgate (1975). The sulphate-reducing bacteria. Cambridge University Press, London, 81.
11. T. Dalsgaard, and F. Bak (1994). Nitrate reduction in a sulfate-reducing bacterium, *Desulfovibrio desulfuricans*, isolated from rice paddy soil; sulfide inhibition, kinetics, and rgulation. *Applied and Environmental Microbiology*, **60**, 291-297.
12. G.J. Mitchell, J. G. Jones, and J.A. Cole (1986). Distribution and regulation of nitrate and nitrite reduction in *Desulfovibrio* and *Desulfotomaculum* species. *Archives of Microbiology*, **144**, 35-40.

High-Resolution Microbial Pitting Corrosion Studies Utilizing a Two Dimension Scanning Vibrating Electrode Microscope (SVEM) System.

Dr. Peter Angell*

Dr. Jiunn-Shyong Luo

Dr. David C. White

Center for Environmental Biotechnology, Suite 300,
Knoxville, TN., 37932-2575.

Abstract

Traditionally, electrochemical techniques used in corrosion studies have been limited by their lack of spatial and temporal resolution. Microbial corrosion is often evidenced as pitting in which small anodes and correspondingly large cathodes are formed. Techniques such as electrochemical impedance spectroscopy, which are unable to differentiate the anode from the cathode, therefore underestimate the rate of corrosion due to the fact that it averages both anodic and cathodic processes. Vibrating micro-electrodes allow mapping of the current densities over a corroding metal surface where the resolution is determined by the height of the electrode above the surface (resolution = twice the height) and the number of measurements made. This theoretical value is approached by vibrating the electrode in the vertical plane as well as the horizontal plane helping to smooth out irregularities in the surface topography. By scanning such an electrode over the surface, a current density map can be generated showing the size and location of both the anodic and cathodic regions with time. Due to the rapid nature of the scans (<5 minutes), the temporal resolution is also enhanced.

A system giving a resolution of approximately 300 μm has been coupled with a microscope (resolution: better than 1 μm) and a photon counting imaging system capable of detecting the light produced by a single luminescent bacterium. This system allows the congruent mapping of bacterial locations and activity (bioluminescence) with the resultant current

densities. It has been shown that anodic regions are formed below colonies of bacteria. Manipulation of these colonies of bacteria have shown that 10^6 cfu cm^{-2} are necessary to form an anodic region. Further investigations, including the incorporation of genetically engineered "reporter bacteria" containing the luxB gene will allow the determination of the mechanisms whereby microbial corrosion takes place. The proximity between components of a microbial consortium necessary for inducing MIC can be determined as well.

Introduction

Microbial corrosion of metals normally entails the establishment of an area of low potential (anodic region) relative to a corresponding area of high potential (cathodic region) on the surface. As current flows from the area of high potential to low potential metal ions are lost from the surface, when the anodic region is maintained and localized in one region a pit is formed. Due to the localized nature of pitting the area of attack is normally quite small, less than 5 mm in diameter.

A number of methods of microbial attack on metal surfaces have been postulated [1]. Of these the most studied has involved the action of the sulphate reducing bacteria (SRB) on mild steel. However, it needs to be noted that microbially influenced corrosion is not limited to SRB and mild steel. MIC has been reported for numerous metals and metal alloy as reviewed by Little *et al.*, [2]. Even the relatively toxic copper compounds have been shown to be vulnerable to MIC in fresh water [3].

As pitting is an electrochemical process the magnitude of the current flowing can be measured by electrochemical techniques, including linear polarization and electrochemical impedance spectroscopy. However, due to the relative small size of the active regions in relation to the total area of the test coupon the magnitude of the rate of corrosion is often under estimated. These methods also are unable to provide any information on the spatial correlation between any microorganisms possibly involved in the process and the site of attack.

A system has been described in the literature which allows for the mapping of local current densities to be measured in a conductive solution above a metal surface [4],[5]. The system is based on the ability of a vibrating electrode to capacitively detect a potential drop between its two extremities of oscillation. This potential drop is determined by the local current density at that point in the solution. In order to achieve a high

resolution of the current densities a platinum black coated stainless steel or platinum microelectrode with a tip diameter of 20-30 μm is utilized. With such a microelectrode positioned close to a metal surface it is possible to achieve a resolution in the region of 100 - 300 μm . By running the system under the control of fast modern microcomputers it is possible to quickly scan relatively large areas, for example an area of 25 mm^2 can be scanned with a resolution of 15 x 15 data points in approximately five minutes. This allows for good temporal resolution to be achieved as well as the spatial resolution.

Franklin *et al.* [5] utilizing such a system, with the probe being vibrated in one plane parallel to a mild steel surface, showed that the presence of a culture of Pseudomonas sp. could prevent the repassivation of locally formed anodic regions seen in sterile controls. Although this system was able to show the localized nature and magnitude of the anodic regions associated with bacterial activity it was unable to provide information on the spatial relationship between the bacteria and the anodic region.

Davenport *et al.* [6] showed that the resolution of the vibrating electrode could be enhanced nearer it's theoretical maximum by vibrating the probe in the vertical plane at the same time as the vertical plane. Angell *et al.* [7] took the system a stage further by incorporating the microelectrode with a microscope fitted with a CCD camera system capable of detecting the light emitted by a single bacterium. They were able to demonstrate that the anodic region formed below a "pseudo" colony of bacteria placed on a mild steel coupon. This system was, however, static with no nutrient feed and the anodic region was maintained for less than twenty four hours.

The bacteria used by Angell *et al.* [7] had been isolated from a corrosion tubercule formed on a stainless steel pipe carrying fresh water in a power generation plant. These bacteria had been genetically manipulated to carry in a plasmid the luxB gene inserted into certain pathways of interest. It has been shown using such methods that the production of light can be correlated to the initiation of the pathway of interest [8].

This paper will show the way in which this powerful tool, the scanning vibrating electrode microscope (SVEM), has been used in order to further understand the mechanisms of pitting in mild steels by non sulphate reducing bacteria.

Materials and Methods

Bacteria:

A genetically engineered bacteria, containing the plasmid PUTK50, was primarily used in this study. PUTK50 is a plasmid containing the luxB gene which encodes for bioluminescence [9]. The bacteria was Pseudomonas aeruginosa FRD1 isolated from the lungs of a cystic fibrosis patient. This bacteria was chosen due to its ability to produce copious amounts of the exopolymer (EPS) alginate.

Medium:

The medium used was chosen for its ability to enhance polymer production in biofilm grown cells as determined by both light production and EPS assays. It should be noted that this requirement often resulted in a sub optimal medium from the corrosion point of view, with excess sodium chloride being present. For the FRD1 experiments the medium contained in (g L⁻¹): glutamic acid 0.015, glycerol 0.045, magnesium sulphate 0.009, sodium chloride 8.5, Kanomycin 0.05, Carbenicillin 0.05 and 1 ml of phosphate buffer containing (g L⁻¹): 20.8 sodium orthophosphate, 58.6 dipotassium phosphate.

SVEM:

A two-dimensional scanning vibrating electrode microscope (2D-SVEM) utilizing a 2 channel lock-in amplifier system was used. A four axis motion system allowed movement of the probe in the X, Y plane, and Z plane as well as focusing the Zeiss Axioplan microscope in the W plane. The microscope allowed visual images, both bright field and photon, to be collected via a Hamamatsu C2400-47 photon-detecting camera attached to the microscope. This system was found to work well with the long working distance objectives available allowing both low power images of a 5 x 5 mm area (2.5 x obj.) as well as high power images viewing individual bacterium (40 x obj.) All the images were processed by the Argus 10 image analyzer before being sent to the computer for use by the VP software (ScienceWares, Woods Hole, MA). The VP software controlled the location and movement of the probe relative to the visual image and logged the local current densities at each sampling site. This information could then either be plotted congruently with the visual image as a surface contour plot, or both could be exported to other software programs with more sophisticated plotting routines. Stainless steel probes electrolytically coated with platinum black were used through out this experiments. At the start of each experiment each electrode was calibrated using a glass pipette drawn to a

fine point filled with potassium chloride and coupled to a Ag/AgCl half cell. A known current was passed through this calibration electrode at a known distance from the probe, in both the x and y planes, allowing the computer to make calibrations of the probe for current densities. It should be noted that the probe actually measures the local current density in the solution at its operating height above the metal coupon. This is not the current density at the surface as there is a gradient away from the surface.

Electrochemical DC polarisation measurements were conducted by Softcorr corrosion measurement software associated with EG & G model 273 (option 92) potentiostat. For linear polarisation resistance, current densities were monitored within ± 30 mV versus open circuit potential with a scan rate of 0.17 mV/sec.

Specimens:

Test specimens used were 16 mm diameter disks of AISI C1020 carbon steel. These disks were mounted into epoxy resin casts and wet-polished in sequence with 240, 400, and 600 grit SiC paper, ultrasonically cleaned with distilled water, degreased with acetone and sterilized with 70 % propan-1-ol for 30 minutes and allowed to air dry in a laminar flow hood. All other tubing and containers were sterilized by autoclaving at 121 °C and 15 PSI for 20 minutes.

Results and Discussion

Two sets of data will be presented that are representative of two variations used for inoculating the system. First a twenty-four hour broth culture was added as the bulk phase, allowing random colonisation over the whole surface. Second 25 ml of a twenty-four hour broth was spun down and resuspended in 250 μ l of phosphate buffered saline (PBS) and a 1 μ l drop of this concentrated bacterial solution allowed to sit on the coupon for thirty minutes. This method promoted localised attachment over a small area approximately 1 mm in diameter. PBS was used as it allowed slight evaporation to take place without increasing the salt level too much for the bacteria.

Figure 1 shows a series of scans over a forty-two hour period of the current density measure perpendicular to the surface of the coupon, when the bacteria had been applied to the bulk phase. Initially when the bacteria were added (1a) there was one large anodic spike, it is likely that this is a noise artifact as it was only one point. It is also unlikely that the bacteria

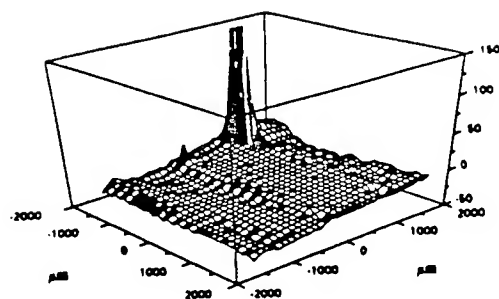


Figure 1a. (Time = 0 hr)

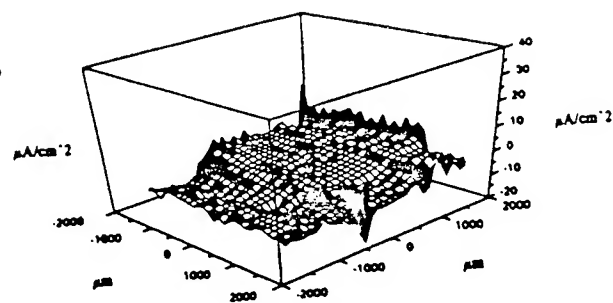


Figure 1b. (Time = 1 hr)

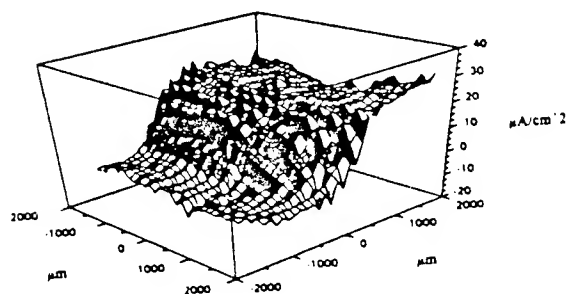


Figure 1c. (Time = 19 hr)

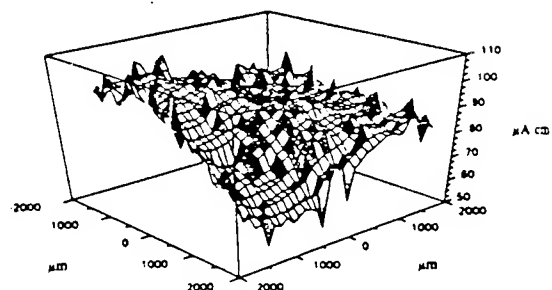


Figure 1d. (Time = 22 hr)

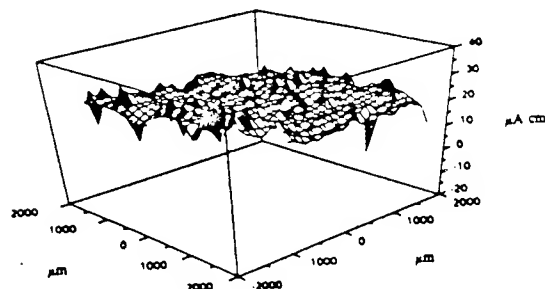


Figure 1e. (Time = 30 hr)

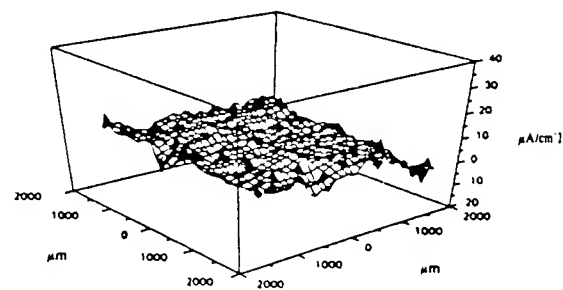


Figure 1f. (Time = 42 hr)

Figure 1. Current density (Z axis) scans resulting from the addition of a 24 hr broth culture of *Pseudomonas aeruginosa* FRD1 was added to the bulk phase over a mild steel coupon.

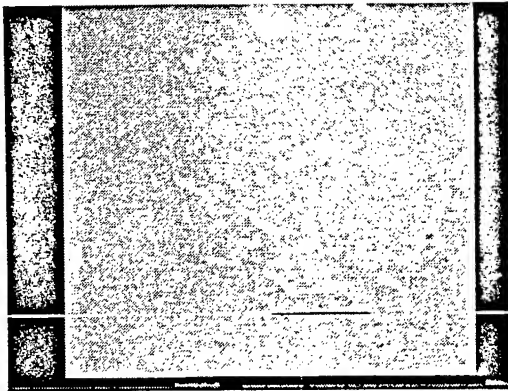


Figure 2a.

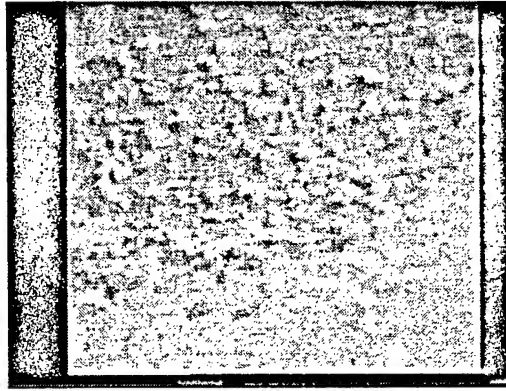


Figure 2b

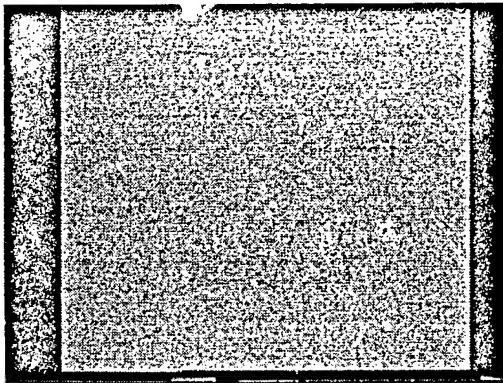


Figure 2c.

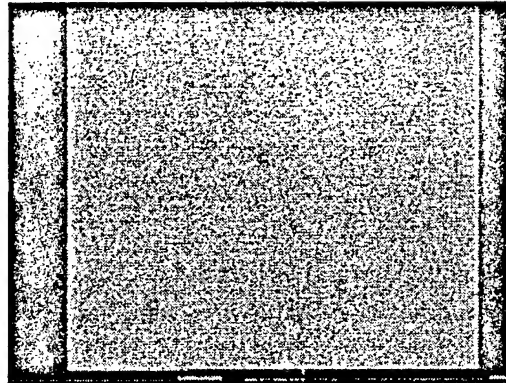


Figure 2d

Figure 2. Images of *Pseudomonas aeruginosa* FRD1 on mild steel coupon: a) visual image after 1 hour exposure, b) visual image after nineteen hours, c) photon image after 1 hour showing little light, b) photon image after nineteen hours showing more light.

would have had sufficient time to really start to attach to the surface and be exerting an effect. After one hour (1b) there appeared to be a slight increase in the anodic current over roughly two-thirds of the coupon. This anodic region had grown in magnitude until nineteen hours (1c). By twenty-two hours (1d) this anodic region had shifted slightly and covered most of the area being observed. However, after thirty hours (1e) the anodic region has disappeared with the plot showing general noise. This was similar to the resultant scan seen at forty-two hours (1f).

The corresponding images for the above scans are shown in Figure 2. These show both "brightfield" images where the image area is the same as the scans approximately 4.5 mm x 3.5 mm. These images were collected by the Hamamatsu C2400-47 camera with the gain turned down, the images appear hazy due to the image intensifier, that gives very high light sensitivity but poor spatial resolution. The other form of image is collected with the gain set on high allowing single photons to be collected. The image was acquired for five minutes. In order to remove the background noise counts were made with no bacteria present and the Argus 10 manipulated to drop out all the noise. This resulted in the loss of some dimmer bacterial light from the final image but at least allowed the brighter bacterial areas to be detected without any background insuring the light seen on the screen was from bacteria.

Figure 2a is the visual image taken after one hour, showing that some material settling on the surface of the coupon. The larger light coloured amorphous material is thought to be alginate. Figure 2b shows another brightfield image this time taken after nineteen hours. This time the surface has been covered by a "fluffy" type material thought to be an iron oxide, mixed with alginate. This picture corresponds to the point when the anodic region was covering most of the coupon (1c). Looking at the photon images it is evident that after 1 hour there is very little light being produced by the bacteria (2c). By nineteen hours (2d) there was a lot of light with a number of bright areas indicating the presence of bacteria with the alginate pathway activated. This level of light was maintained until the end of the experiment at forty-two hours indicating that the bacteria were still alive and active, even though the anodic region had been passivated.

When a drop of concentrated bacteria was added to a localised area the results were as shown in Figure 3. After 1 hour a localised anodic region was present (3a) and was seen to correlate with the visual image collected at the same time (4a) where the bacteria and their associated polymers are seen as the light central area on the metal. After three hours

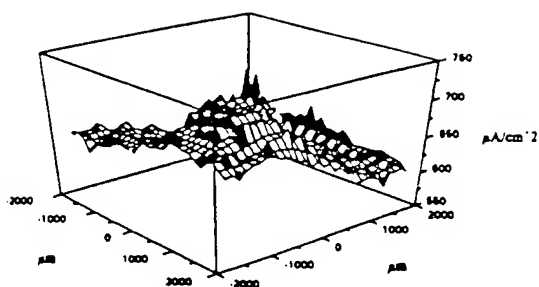


Figure 3a. (Time = 1 hr)

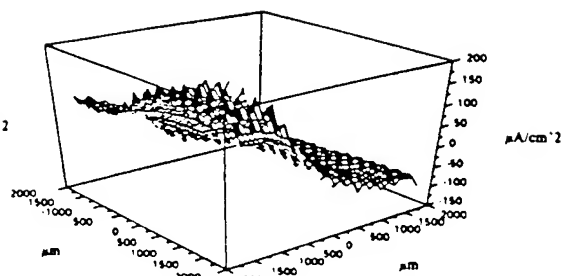


Figure 3b. (Time = 3 hr)

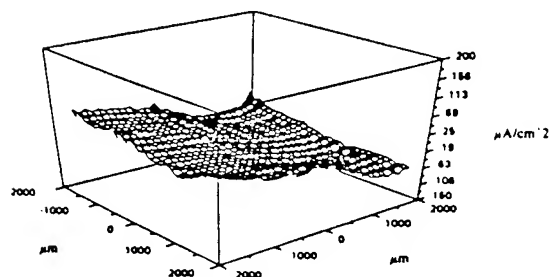


Figure 3c. (Time = 20 hr)

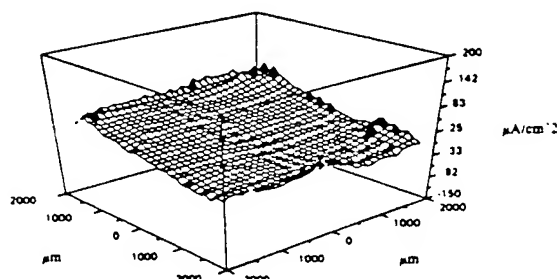


Figure 3d. (Time = 24 hr)

Figure 3. Current density (z axis) scans resulting from the addition of a concentrated drop (1 μ l) of a 24 hour culture of *Pseudomonas aeruginosa* FRD1 placed on a mild steel coupon.

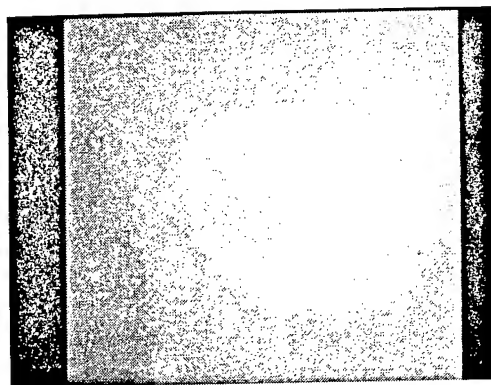


Figure 4a.

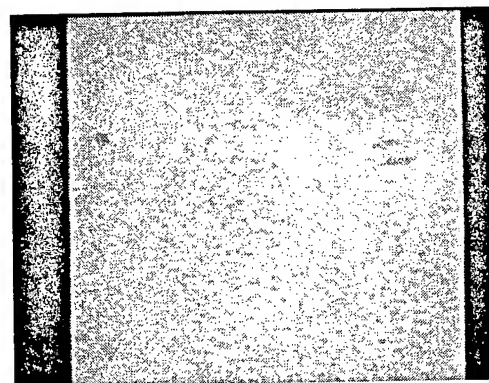


Figure 4b

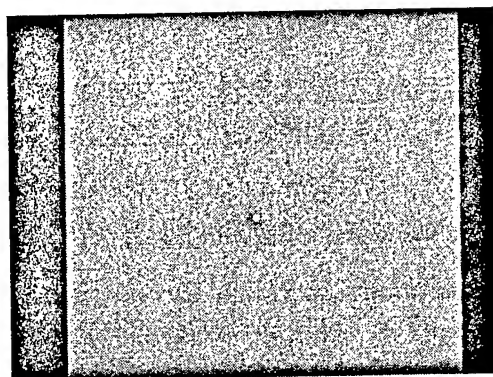


Figure 4c.



Figure 4d.

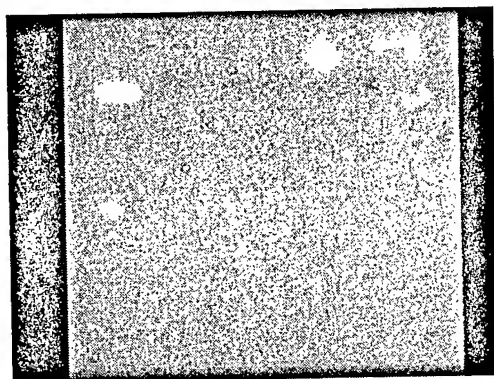


Figure 4e.

Figure 4 Images of *Pseudomonas aeruginosa* FRD1 on mild steel coupon: a) visual image after 1 hour exposure, b) visual image after 3 hours showing spread of bacteria, c) photon image taken after 1 hr showing little light, d) visual image taken after 24 hours, e) photon image taken after 24 hours showing the bacteria are still active.

the anodic region is seen to have grown and covered a larger area reaching the edge of the area examined (3b). Again this correlates well with the visual image (4b) that shows that the bacteria and polymer have also spread to cover a similar area. The direction of spread is parallel to the direction of flow and it is thought that the flow of the medium through the system has facilitated the spread of the bacteria. For the corresponding time periods figure 4c shows that after one hour there are a few bright areas where the bacteria are active. After three hours more light areas were visible which again showed good correlation with the visual image of where the majority of the bacteria were.

By twenty-hours this anodic region had disappeared (3c) the visual image (4d) shows that by this time the bacteria and the polymer have spread over the whole surface along with corrosion products. At twenty-four hours the results were principally the same with little anodic activity over the surface (3d) but the photon image (4e) shows that there was a lot of bacterial activity and that the alginate pathway was indeed active. This state persisted until the end of the experiment after forty-two hours.

Once again it was evident that initially there was some anodic activity which could be attributed to the location of the bacteria but was short lived as the bacteria colonised more of the surface of the coupon. The photon images indicate that the bacteria were still active after the anodic activity had halted. The link between the light and the production of alginate was demonstrated by this lab (unpublished data).

One of the major questions regarding the use of the scanning vibrating electrode technique is whether it can detect the current through a biofilm. It is arguable with these results that the anodic current was still present but could not be detected through the biofilm and corrosion products. In order to determine if this was the case a set of experiments were run using traditional dc polarisation techniques to determine the corrosion rates of mild steel electrochemically in the presence of the bacteria FRD1 and in a sterile control.

Figure 5. shows the inverse of the polarisation resistance plotted against time for both the sterile control and the FRD1 inoculated cells. Both of conditions follow similar trends with an initial increase in the rate of corrosion which then drops before a slight increase at the end of the eight day run. The initial rise in the sterile control would appear to be larger than the FRD1 cell, but proportionally to the starting value they are similar. These results correlate well to the findings in the SVEM, where initially corrosion (anodic current) was seen for the first couple of days which then decreased in magnitude.

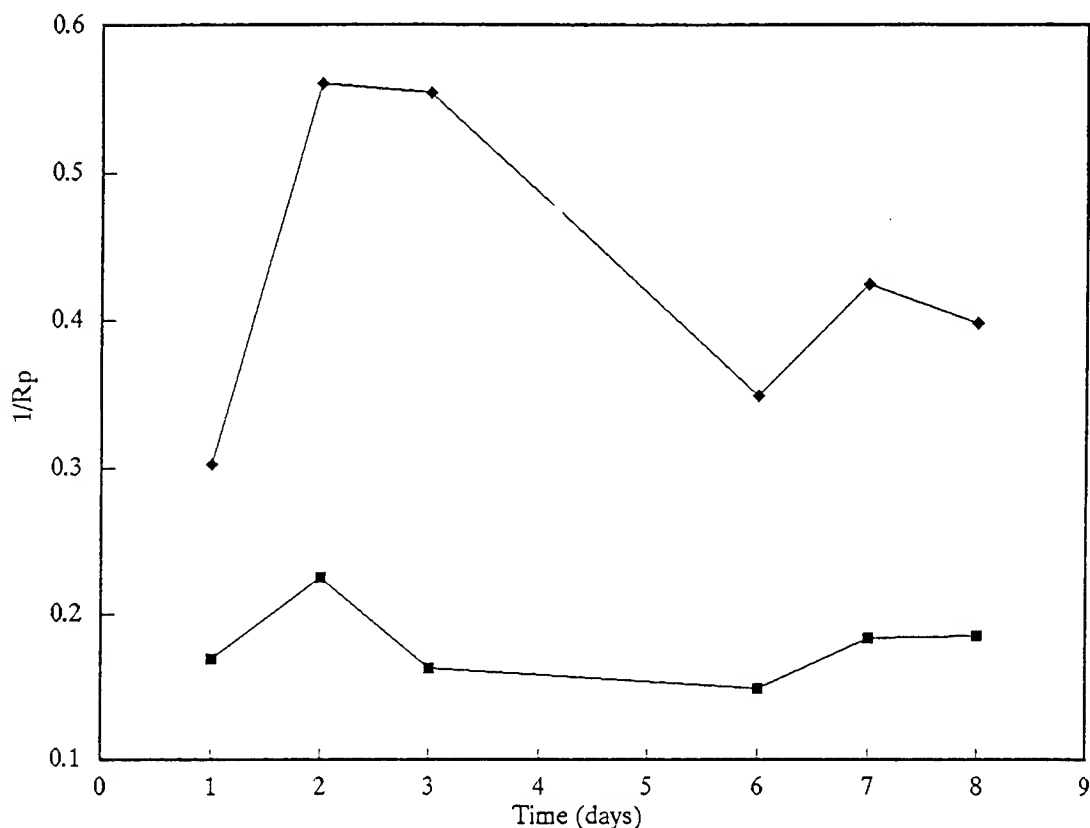


Figure 5. Time plot of the inverse of the polarisation resistance of mild steel coupons exposed to *Pseudomonas aeruginosa* FRD1 (■) and sterile control (♦).

Conclusion

It is suggested that the bacteria *Pseudomonas aeruginosa* FRD1 and in particular alginate are not of themselves capable of microbial induced corrosion. It is thought that the initial corrosion is due to the bacteria forming a heterogenous biofilm that allows differential oxygen cells to be set up. These electrochemical cells are not capable of fully establishing themselves into self sustaining pits and are rapidly passivated as the bacteria further grows to cover the surface.

The SVEM has also been demonstrated to be a very useful tool providing further insight into the mechanisms of microbially induced corrosion providing information on both the location and magnitude of anodic regions on a metal surface. The SVEM is able to provide this information at a resolution not previously possible with traditional electrochemical methods.

Acknowledgments

This work was supported by a grant from the U.S. Office of Naval Research. The authors would also like to thank Eric Karplus of Science Wares for all his help in the installation and fine tuning of the SVEM.

References

1. Menzies, I.A. (1991). Introductory Corrosion. In: Microbial Aspects of Metallurgy, Ed. J.D.A. Miller, MTP, Aylesbury, 37-60.
2. Little, B., Wagner, P. and Mansfeld, F. (1991). Microbiologically influenced corrosion of metals and alloys. International Materials Reviews. **36**, 253-272.
3. Chamberlain, A.H.L. and Angell, P. (1991). Influences of microorganisms on pitting of copper tube. In: Microbially Influenced corrosion and biodeterioration. Eds: N.J.E. Dowling, M.W. Mittleman and J.C. Danko, Knoxville, 3.65-3.72.
4. Isaacs, H.S. and Ishikawa (1985). Applications of the vibrating probe to localized current measurements. Proc. NACE Corrosion/85, Paper 55.
5. Franklin, M.J., White, D.C. and Isaacs, H.S. (1991). Pitting corrosion by bacteria on carbon steel, determined by the scanning vibrating electrode technique. Corrosion Science, **32**, 945-952.
6. Davenport, A. J., Aldykiewicz, A.J. & Isaacs, H.S. (1992). Application of 2d scanning vibrating probe measurements to the study of corrosion inhibitors. Paper 234, Corrosion '92, NACE, Houston, Texas.
7. Angell, P., Luo, J-S. and White, D.C. (1994). Use of 2d-vibrating electrode technique in MIC studies. Paper 266, Corrosion '94, NACE, Houston, Texas.
8. Mittleman, M.W., King, J.M.H., Sayler, G.S. and White, D.C. (1992). On-line detection of bacterial adhesion in a shear gradient with bioluminescence by a Pseudomonas fluorescens (lux) strain. Journal of Microbial Methods, **15**, 53-60.
9. Wallace, W.H., Flemming, J.T., White, D.C. & Sayler, G.S. (1994). An alg-D-bioluminescent reporter plasmid to monitor alginate production in biofilms. Microbial Ecology, in press.

Microbiologically Influenced Corrosion of Corrosion Resistant Materials

**Dr. Brenda Little,* Mr. Richard Ray, Mrs. Patricia Wagner
Naval Research Laboratory
Stennis Space Center, MS 39529-5004**

**Mr. E. Dail Thomas
Naval Research Laboratory
Washington, D.C. 20375-5000**

Abstract

The corrosion resistance of materials cannot be accurately determined in abiotic electrolytes. Field and laboratory studies document microbiologically influenced corrosion (MIC) of corrosion resistant materials including copper and nickel alloys, stainless steels containing 6% molybdenum and polymeric composites.

Discussion

Microbial biofilms develop on all surfaces in contact with aqueous environments. Chemical and electrochemical characteristics of the substratum influence formation rate and cell distribution of microfouling films during the first hours of exposure. Electrolyte concentration, pH, organic and inorganic ions also affect microbial settlement. Biofilms produce an environment at the biofilm/surface interface that is radically different from that of the bulk medium in terms of pH, dissolved oxygen, and inorganic and organic species. Reactions within biofilms can control corrosion rates and mechanisms. The term microbiologically influenced corrosion (MIC) is used to designate corrosion resulting from the presence and activities of microorganisms within biofilms. Reactions are usually localized and can include: 1) sulfide production, 2) acid production, 3) ammonia production, 4) metal deposition, 5) metal oxidation/reduction and (6) gas production.

Copper Alloys

Copper alloys are frequently used for seawater piping systems and heat exchangers due to their good corrosion resistance combined with mechanical workability, excellent electrical and thermal conductivity, ease of soldering and brazing, and resistance to macrofouling. In oxygenated seawater a film of cuprous oxide, cuprite (Cu_2O), forms on copper alloys. Copper ions and electrons pass through the film. Copper ions dissolve and precipitate as $\text{Cu}_2(\text{OH})_3\text{Cl}$, independent of alloy chemistry.

Copper alloys are vulnerable to biocorrosion. Differential aeration, selective leaching, underdeposit corrosion and cathodic depolarization have been reported as mechanisms for MIC of copper alloys. Pope et al.¹ proposed that the following microbial products accelerate localized attack: CO_2 ; H_2S ; NH_3 ; organic and inorganic acids; metabolites that act as depolarizers; and sulfur compounds such as mercaptans, sulfides and disulfides.

In the presence of sulfides, copper alloys form a porous layer of cuprous sulfide with the general stoichiometry Cu_{2-x}S , $0 < x < 1$. Copper ions migrate through the layer, react with more sulfide, and produce a thick black scale. McNeil and Odom² described a model that predicts sulfide-induced corrosion in the presence of sulfate-reducing bacteria (SRB). Corrosion is initiated by sulfide-rich reducing conditions in the biofilm where the oxide layer is destabilized and acts as a source of metal-containing ions. The authors concluded that if any reaction of metal oxide with sulfide has a high negative standard free energy of reaction, SRB-related MIC will occur. If the reaction has a high positive standard free energy of reaction, this form of corrosion will not occur. Negative standard free energies of reactions were used to predict SRB-MIC for copper alloys. Analysis of sulfide corrosion products recovered from corroding copper alloys confirmed the prediction.

Alloying nickel and small amounts of iron into copper increases resistance to turbulence induced corrosion. Little et al.³ demonstrated dealloying of nickel from 90/10 copper/nickel in association with SRB. SRB are not necessary for MIC-induced pitting of copper alloys. Wagner et al.⁴ described dealloying of nickel in 70/30 copper/nickel exposed to flowing natural seawater (Figure 1). While the role of the biofilm in copper pitting is not entirely clear, it appears that the presence of the biofilm contributes to corrosion by maintaining enhanced local chloride concentrations and differential aeration cells. Pope¹ documented MIC

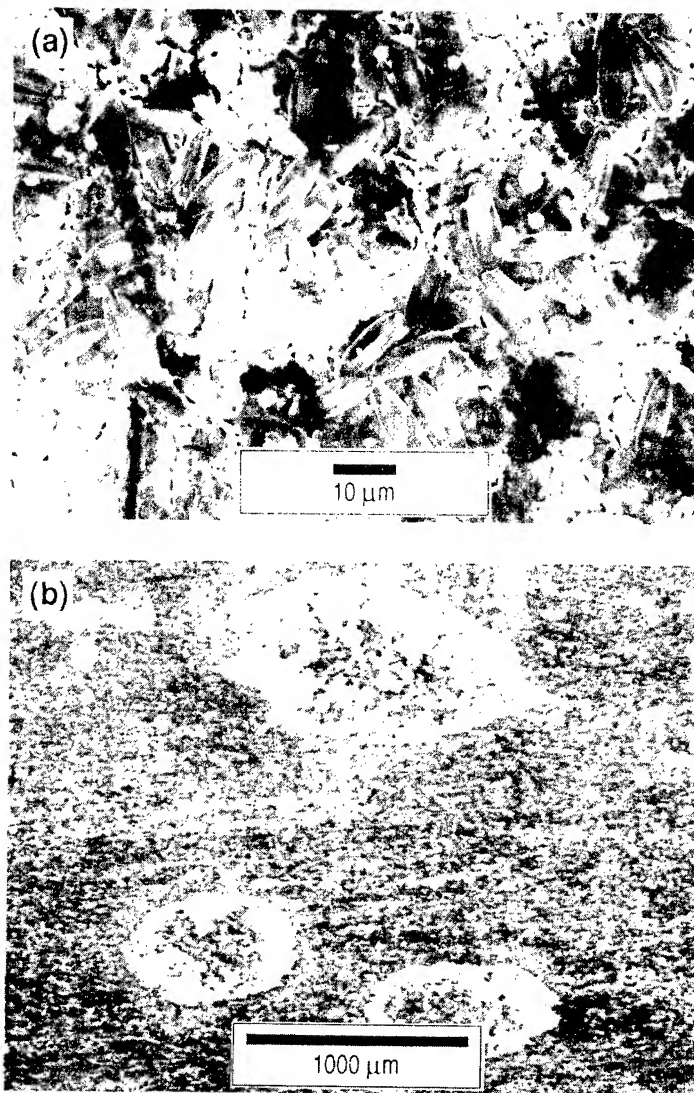


Figure 1. (a) Biofilm within pits on 70/30 Cu/Ni after 1 month exposure to natural seawater and (b) areas of localized corrosion after removal of biofilm.

of 90/10 copper/nickel, admiralty brass (UNS C44300), aluminum brass (C68700), and welded aluminum bronze at electric generating facilities using fresh or brackish cooling waters. Most of the copper/nickel tubes had underdeposit corrosion due to formation of deposits by slime-forming

organisms in association with iron- and manganese-depositing bacteria. Ammonia-producing bacteria were isolated from scale and organic material on the admiralty brass tubes suffering ammonia-induced stress corrosion cracking. Geesey et al.⁵ demonstrated the role of bacterial exopolymers in corrosion of copper exposed to drinking water.

Nickel Alloys

Nickel alloys are superior to predominantly copper alloys because the protective surface film remains intact under turbulent and erosive conditions. Nickel alloys are used extensively in highly aerated, high velocity seawater applications. Uhlig and coworkers⁶ calculated that a critical nickel concentration of 35% was required for passivity. Nickel alloys containing less than this amount behave like copper. The formation of the protective film on nickel is aided by the presence of iron, aluminum and silicon.

Monel 400 (UNS N04400) is susceptible to pitting and crevice corrosion attack where chlorides penetrate the passive film. Sulfides can cause either a modification or breakdown of the oxide layer. Schumacher⁷ reported that Monel 400 was susceptible to underdeposit corrosion and oxygen concentration cells formed by bacteria. Gouda et al.⁸ demonstrated localized corrosion of Monel 400 tubes exposed in Arabian Gulf seawater where pits developed under deposits of SRB and nickel was selectively dealloyed. Pope¹ reported a case study from nuclear power plants in which severe pitting corrosion associated with dealloying was observed under discrete deposits on Monel heat exchanger tubes. Deposits formed by iron- and manganese-depositing bacteria in association with SRB contained large amounts of iron and copper, significant amounts of manganese and silicon, and reduced amounts of nickel.

Stainless Steels

The corrosion resistance of stainless steels (SS) is due to the formation of a thin passive chromium-iron oxide film at additions of chromium in amounts of 12% or more. Metal-depositing organisms, important in MIC of SS, may catalyze the oxidation of metals, accumulate abiotically oxidized metal precipitates, or derive energy by oxidizing metals. Dense deposits of cells and metal ions create oxygen concentration cells that effectively exclude oxygen from the area

immediately under the deposit. Underdeposit corrosion is important because it initiates a series of events that are, individually or collectively, extremely corrosive. In an oxygenated environment, the area immediately under the deposit becomes a relatively small anode compared to the large surrounding cathode. Cathodic reduction of oxygen may result in an increase in pH of the solution in the vicinity of the metal. The metal will form metal cations at anodic sites. If the metal hydroxide is the thermodynamically stable phase in the solution, metal ions will be hydrolyzed by water with formation of H^+ ions. If cathodic and anodic sites are separated from one another, the pH at the anode will decrease and that at the cathode will increase. The pH within anodic pits depends on specific hydrolysis reactions. The lowest pH values are predicted for alloys containing chromium and molybdenum.

One of the most common forms of MIC attack in austenitic SS is pitting at or adjacent to welds at the heat affected zone, the fusion line, and in the base metal. Borenstein⁹ made the following observations for MIC in 304L (UNS S30403) and 316L (UNS S31603) weldments: both austenite and delta ferrite phases may be susceptible; and varying combinations of filler and base materials have failed, including matching, higher and lower alloyed filler combinations. Microsegregation of chromium and molybdenum with chemically depleted regions increases susceptibility to localized attack.¹⁰

Stainless steels containing 6% or more molybdenum, often called superaustenitic SS, were once thought to be immune to MIC because molybdenum increases resistance to chloride and acid solutions. However, Scott et al.¹¹ documented MIC in laboratory testing of SMO254 (UNS S31254) and AL6X (UNS NO8366) SS, both containing 6.5% molybdenum. Little et al.¹² observed deep etching of SMO254 SS after exposure to both an iron/sulfur-oxidizing mesophilic bacterium and a thermophilic mixed SRB culture (Figure 2).

Ennoblement of corrosion potential (E_{corr}) for SS exposed to natural seawater has been reported by several investigators. The practical importance of ennoblement is increased probability of localized corrosion as E_{corr} approaches the pitting potential (E_{pit}) for SS vulnerable to crevice corrosion, especially types 304 (UNS S30400) and 316 (UNS S31600). Sustained ennoblement does not indicate corrosion but persistence of passivity. At the onset of localized corrosion, E_{corr} moves from noble to active regions. Ennoblement has also been reported for SS containing 6% molybdenum and other corrosion-resistant materials.

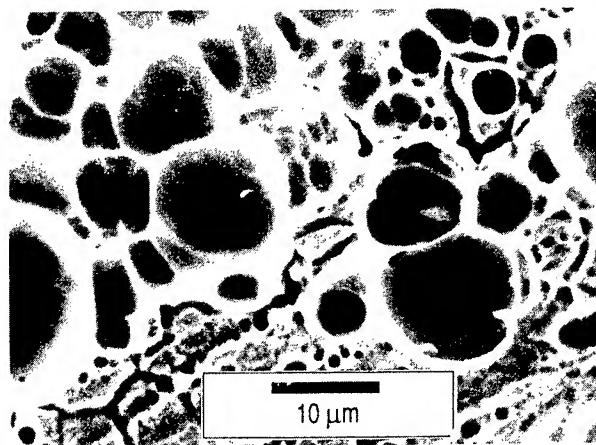


Figure 2. Pitted SMO254 SS after 75-day exposure to mesophilic iron/sulfur-oxidizing bacteria.

Johnsen and Bardal¹³ reported that E_{corr} approached -50 mV (vs. saturated calomel electrode (SCE)) after 28 days for SS that contained 1–3% molybdenum, and 50–150 mV (SCE) in the same time period for SS containing 6% molybdenum.

Aluminum and Aluminum Alloys

The corrosion resistance of aluminum and its alloys is due to an aluminum oxide passive film. Anodizing produces thicker insulating films and better corrosion resistance. The natural film on aluminum alloys can be attacked locally by halide ions. The susceptibility of aluminum and its alloys to localized corrosion makes it particularly vulnerable to MIC. Most reports of MIC are for aluminum (99%), 2024 (UNS A92024) and 7075 (UNS A97075) alloys used in aircraft or in underground fuel storage tanks. Localized corrosion attributed to MIC occurs in the water phase of fuel-water mixtures in the bottom of tanks and at the fuel-water interface.¹⁴ Contaminants in fuel include surfactants, water, and water soluble salts that encourage growth of bacteria. Two mechanisms for MIC of aluminum alloys have been documented: production of water soluble organic acids by bacteria and fungi, and formation of differential aeration cells.

Titanium and Titanium Alloys

There are no case histories of MIC for titanium and its alloys. Schutz¹⁵ reviewed mechanisms for MIC and titanium's corrosion behavior under a broad range of conditions. He concluded that at temperatures below 100°C titanium is not vulnerable to iron/sulfur-oxidizing bacteria, SRB, acid-producing bacteria, differential aeration cells, chloride concentration cells and hydrogen embrittlement. In laboratory studies, Little et al.¹² did not observe any corrosion of Grade 2 titanium (UNS R50400) in the presence of SRB or iron/sulfur-oxidizing bacteria at mesophilic (23°C) or thermophilic (70°C) temperatures. Using the model of McNeil and Odom² one would predict that titanium would be immune to SRB-induced corrosion. There are no standard free energy reaction data for the formation of a titanium sulfide. If one assumes a hypothetical sulfide product to be titanium sulfide, the standard enthalpy of reaction is +587 kJ. While standard free energies of reaction are not identical to standard enthalpies of reaction, it is still unlikely that titanium will be derivatized to the sulfide under standard conditions of temperature and pressure.

Polymeric Composites

Polymeric composites are subject to many kinds of environmental degradation. Tucker and Brown¹⁶ showed that carbon/polymer composites galvanically coupled to metals are degraded by cathodic reactions in seawater. Jones et al.¹⁷ demonstrated that epoxy and nylon coatings on steel were breached by mixed cultures of marine bacteria. Pendrys¹⁸ reported that p-55 graphite fibers were attacked by a mixed culture of *Pseudomonas aeruginosa* and *Acinetobacter calcoaceticus*, common soil isolates. Possible mechanisms for microbial degradation of polymeric composites include: direct attack of the resin by acids or enzymes, blistering due to gas evolution, enhanced cracking due to calcareous deposits and gas evolution, and polymer destabilization by concentrated chlorides and sulfides.

In laboratory experiments Wagner et al.¹⁹ demonstrated that epoxy resin and carbon fibers, either individually or in composite, were not degraded by sulfur/iron-oxidizing, hydrogen-producing, calcareous-depositing, or SRB. Bacteria colonized resins, fibers and composites, but did not cause damage. SRB preferentially colonized vinyl ester composites at the fiber-resin interfaces and hydrogen-producing bacteria

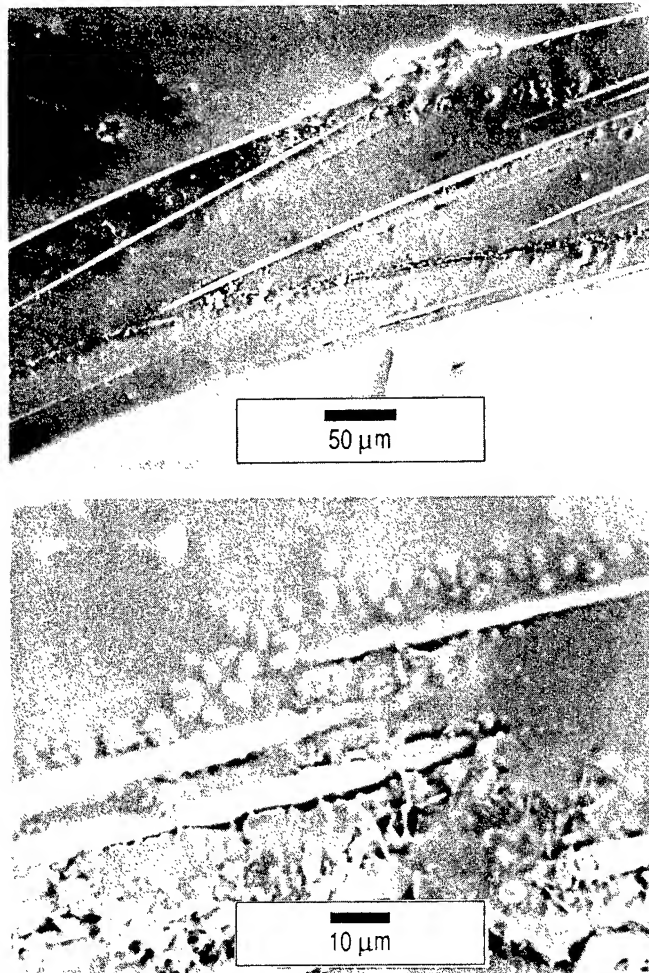


Figure 3. Hydrogen-producing bacteria at disrupted interfaces between fibers and vinyl ester resin.

appeared to disrupt the fiber-vinyl ester resin bonding with penetration of the vinyl ester resin.

Acknowledgments

This work was supported by the Office of Naval Research, Program Element 0601153N, through the NRL Defense Research Sciences

Program; the University of Rhode Island Seagrass Foundation, Kingston, RI, and the Offshore Technology Research Center, Texas A&M University, College Station, TX. Approved for public release; unlimited distribution. NRL Contribution Number NRL/PP/7333--93-0024.

References

1. D. H. Pope, Microbial Corrosion in Fossil-Fired Power Plants – A Study of Microbiologically Influenced Corrosion and a Practical Guide for Its Treatment and Prevention (Palo Alto, CA: Electric Power Research Institute, 1987).
2. M. D. McNeil, A. L. Odom, "Prediction of Sulfiding Corrosion of Alloys Induced by Consortia Containing Sulfate Reducing Bacteria (SRB)," International Symposium on Microbiologically Influenced Corrosion (MIC) Testing (Miami, FL: ASTM, 1992).
3. B. Little, P. Wagner, R. Ray, M. McNeil, Marine Technology Society J. 24(3) (1990): p. 10.
4. P. Wagner, B. Little, R. Ray, J. Jones-Meehan, "Investigations of Microbiologically Influenced Corrosion Using Environmental Scanning Electron Microscopy," Corrosion/92, paper no. 185 (Houston, TX: National Association of Corrosion Engineers, 1992).
5. G. G. Geesey, M. W. Mittleman, T. Iwaoka, P. R. Griffiths, Materials Performance 23(2) (1986): p. 37.
6. H. H. Uhlig, W. R. Revie, Corrosion and Corrosion Control: An Introduction to Corrosion Science and Engineering, Third Edition (NY, NY: Wiley-Interscience, 1985).
7. M. Schumacher, Seawater Corrosion Handbook (Park Ridge, NJ: Noyes Data Corporation, 1979).
8. V. Gouda, I. Banat, W. Riad, S. Mansour, Corrosion 49(1) (1993): p. 63.
9. S. W. Borenstein, Materials Performance 30(1) (1991): p. 52.
10. J. Kearns, S. Borenstein, "Microbially Influenced Corrosion Testing of Welded Stainless Alloys for Nuclear Power Plant Service Water Systems," Corrosion/91, paper no. 279 (Houston, TX: National Association of Corrosion Engineers, 1991).
11. P. J. B. Scott, J. Goldie, M. Davies, Materials Performance 30(1) (1991): p. 55.

12. B. Little, P. Wagner, R. Ray, "An Experimental Evaluation of Titanium's Resistance to Microbiologically Influenced Corrosion," Corrosion/92, paper no. 173 (Houston, TX: National Association of Corrosion Engineers, 1992).
13. R. Johnsen, E. Bardal, Corrosion 41 (1985): p. 296.
14. R. C. Salvarezza, H. A. Videla, Acta Cientifica Venezolana 35 (1984): p. 244.
15. R. W. Schutz, Materials Performance 30(1) (1991): p. 58.
16. W. C. Tucker, R. Brown, J. Composite Materials 23(4) (1989): pp. 389-395.
17. J. M. Jones, M. Walch, F. B. Mansfeld, "Microbial and Electrochemical Studies of Coated Steel Exposed to Mixed Microbial Communities," Corrosion/91, paper no. 108 (Houston, TX: National Association of Corrosion Engineers, 1991).
18. J. P. Pendrys, J. Electrochemical Society 136 (1989): p. 113C.
19. P. Wagner, R. Ray, B. Little, W. Tucker, "Microbiologically Influenced Degradation of Fiber Reinforced Polymeric Composites," Corrosion/94, paper no. 255 (Houston, TX: National Association of Corrosion Engineers, 1994).

Evaluation of Nonpolluting Biofouling Control Methods for Titanium Seawater Piping

Dr. Marianne Walch*, Dr. Joanne Jones-Meehan, Mr. Scott Hoover
Naval Surface Warfare Center, Dahlgren Division
10901 New Hampshire Ave.
Silver Spring, MD 20903-5640

Dr. Michael Grothaus
Southwest Research Institute
6220 Culebra Road
San Antonio, TX 78228-0510

Dr. Michael Mazzola
Electrical and Computer Engineering Department
Mississippi State University
Mississippi State, MS 39762

Dr. Brenda Little
Naval Research Laboratory - Code 7333
Stennis Space Center, MS 39529-5004

I. Introduction

Corrosion and biofouling of shipboard seawater piping and cooling systems reduce readiness, impact operations and are costly to prevent and to remediate (Jones and Little, 1990). The materials most widely used currently by the Navy in these systems are copper-nickel alloys, which are susceptible to erosion corrosion and microbiologically influenced corrosion (Little *et al.*, 1990; Little *et al.*, 1991). Titanium has been proposed for more extensive use by the Navy in seawater piping and heat exchanger applications because of its high corrosion resistance, high strength, and light weight. Titanium is susceptible to biofouling, however, and currently used chemical fouling control methods, such as

chlorination, may soon be phased out due to their adverse environmental impact.

Alternative biofouling control technologies are available, and new technologies currently are under development. Ultraviolet (UV) sterilization and ozone disinfection are two technologies that have been used successfully to maintain control of microbial populations in a wide variety of both freshwater and seawater applications. Ozone has the added advantage of removing dissolved and suspended organics, color and odor from the water. Both ozonation and ultraviolet irradiation are non-polluting and are economically competitive with chlorination for water treatment when the expense is considered of dechlorination chemicals and injection equipment that are necessary in order to meet strict government regulations for effluents.

We have been testing the effectiveness of several potential alternative methods to chlorination for environmentally safe control of biofouling in seawater piping. NSWC/Code R33 has a titanium test loop at Ft. Lauderdale, Florida. Through a Cooperative Research and Development Agreement (CRADA) with Ingalls Shipbuilders in Pascagoula, Mississippi (POC: Mr. Robert Erskine), an ozone generator and an ultraviolet sterilizer were incorporated into the loop in order to test their effectiveness in reducing microbial and larval populations in the seawater and in decreasing fouling of the piping. A summary of the results of these CRADA-supported studies are reported here.

In addition, we have conducted an independent, preliminary study of biofouling control using pulsed acoustic waves in seawater. A separate test loop, constructed of PVC plastic pipe, was built at the Ft. Lauderdale test site. Biofouling was shown to be significantly reduced in the portion of the loop that received pulsed power treatment, compared to an untreated control. Results of that test also are summarized in this report.

II. Evaluation of Ozonation and UV Sterilization

Study Design

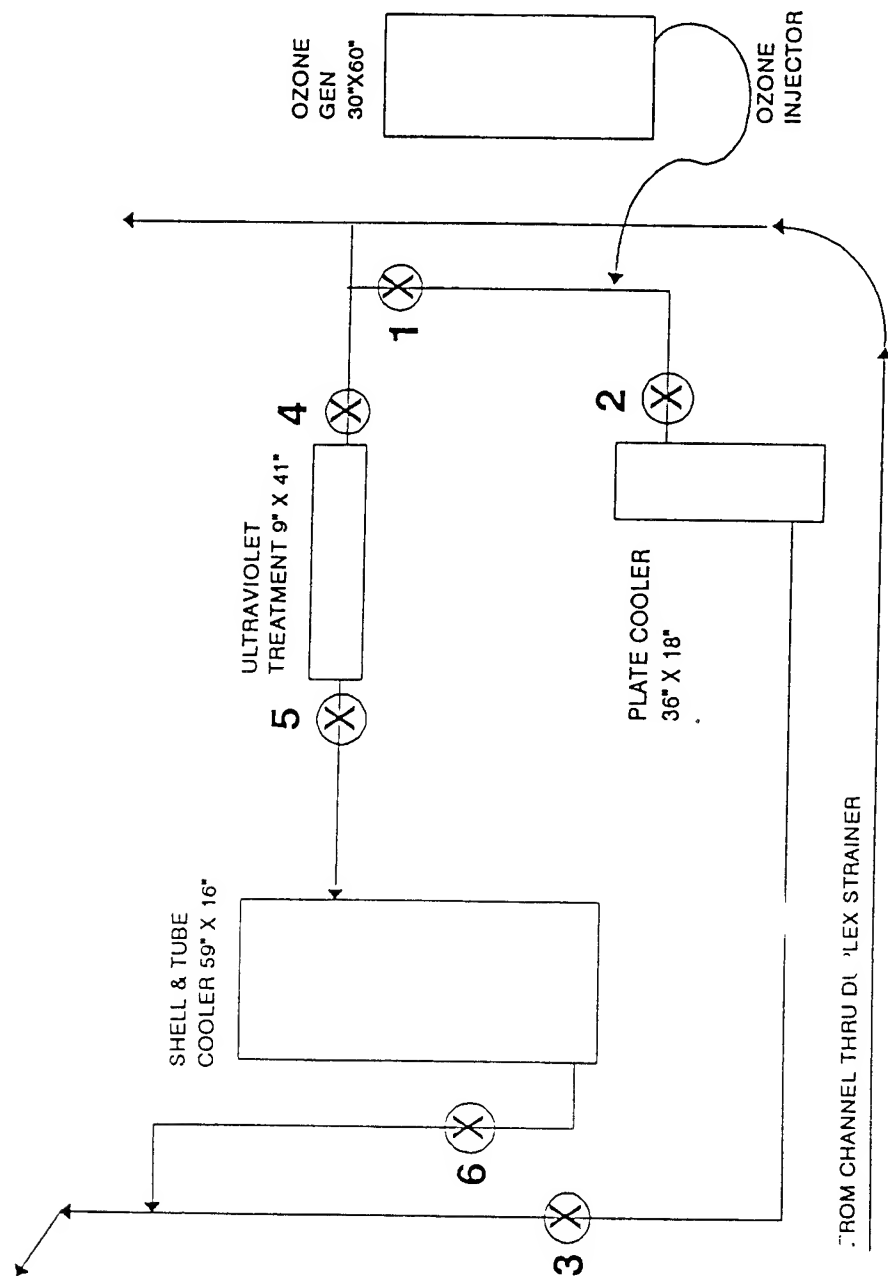
A test loop was constructed of Grade 2 Titanium at the NSW/C/Code R33 corrosion test facility located in Ft. Lauderdale, Florida. This test site is located at the mouth of the Port Everglades shipping channel. Seawater is pumped directly from the channel, passed through a coarse duplex strainer (3/16-inch pore diameter) to filter out large shells and, from there, is pumped through the test loop and back into the channel. The loop was designed originally to test, among other things, the effects of different flow rates on the extent of fouling in various areas of the piping. Legs of varying diameter piping were incorporated into the loop to achieve flow velocities of 3, 8, and $>10 \text{ ft}\cdot\text{sec}^{-1}$. A blank-off and stagnant leg were also included. More recently the test loop was modified to include an ozone generator (Trailsgraz Ozone Co.), an ultraviolet treatment unit (Aquafine Corp.), and two titanium heat exchangers: a plate heat exchanger obtained from Alfa-Laval, and a shell and tube heat exchanger provided by CDNSWC/Annapolis, MD. These were built into the test loop such that the plate heat exchanger was treated by ozonation, and the shell and tube heat exchanger was treated by UV irradiation. The two treatments were installed into separate parallel legs of the loop but used the same source water (Figure 1).

As part of the CRADA with Ingalls Shipbuilders, a detailed, three-week evaluation of ozone and UV treatments was performed during the summer of 1993. Flow rates through the legs of the loop that contained the heat exchangers were maintained at $5.7 \text{ ft}\cdot\text{sec}^{-1}$ for the ozonation and $3.1 \text{ ft}\cdot\text{sec}^{-1}$ for the UV. The test involved 10 days of continuous treatment (ozonation or UV irradiation)¹ in each of the two legs of the loop, followed by 10 days of no treatment as a control.

Both biological/organic and physical/chemical parameters were measured before and after treatment. Physical/chemical parameters measured included: dissolved oxygen, water temperature, air temperature, pH, salinity/conductivity, metals content (by atomic absorption spectrophotometry), flow rate, and ozone injection rate/UV

¹Ozone generated from dry air: 82 V, 6.5-7.0 amps, 300-340 watts, 15 lb air pressure, inject 0.04. Ultraviolet total 313 hours of operation, % irradiance ranging from 50-90%.

FIGURE 1. SCHEMATIC OF TITANIUM TEST LOOP BIOFOULING CONTROL TEST, SHOWING LOCATION OF TREATMENT UNITS, HEAT EXCHANGERS, AND SAMPLING SITES.



irradiation level (using monitoring devices on the equipment). Biological and organic parameters measured included: microbial counts of water samples (aerobic heterotrophic bacteria, general anaerobes, acid-producing bacteria, sulfate-reducing bacteria, marine fungi, and total direct counts)², total organic carbon, total dissolved carbon, total particulate carbon, total suspended solids and total dissolved solids. Samples were collected throughout the 20-day test period at each of the six sites marked in Figure 1.

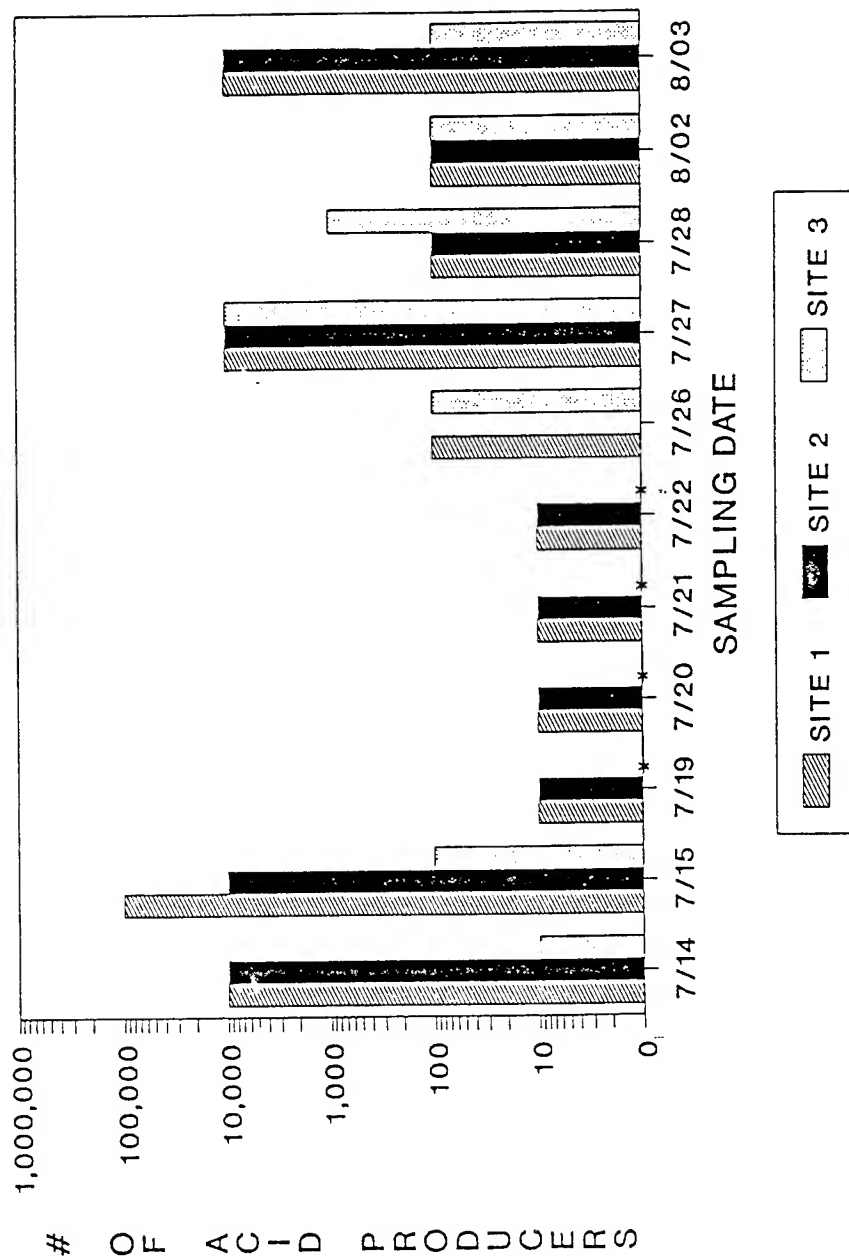
Results

Both micro- and macrofouling have been monitored throughout the test loop for nearly two years using counts of aerobic bacteria, sulfate-reducing bacteria (SRB) and marine fungi, examination of scrapings with environmental scanning electron microscopy (ESEM), and examination of the piping surfaces with fiber optics. Biofilm microorganisms have been present in numbers expected for flowing marine systems (10^5 - 10^8 cells·cm⁻²), with higher numbers detected in the stagnant leg and blank-off. SRB have been found intermittently at several sites. Biofilm and mineral stains on the insides of the pipes are readily removed by wiping. No significant macrofouling has been detected in sections of the test loop in which flow rates exceeded 8 ft·sec⁻¹. Relatively low levels of fouling, including tunicates and tubeworms, have been observed in lower flow areas.

During the three-week biofouling control test, ozone and UV treatments were applied to separate, parallel legs of the test loop for a period of 10 days. Then both treatments were removed, and the test was run for an additional 10 days. Results of the biological analyses indicated that both treatment methods were effective in reducing microbial numbers in flowing seawater by several orders of magnitude, leading to lower fouling rates compared to controls. Typical results of microbial counts are presented in Figures 2-4. Figure 2, for example, shows an approximately three log decrease in counts of acid-producing bacteria (APB) during the first ten days of ozone treatment. Once the treatment was stopped,

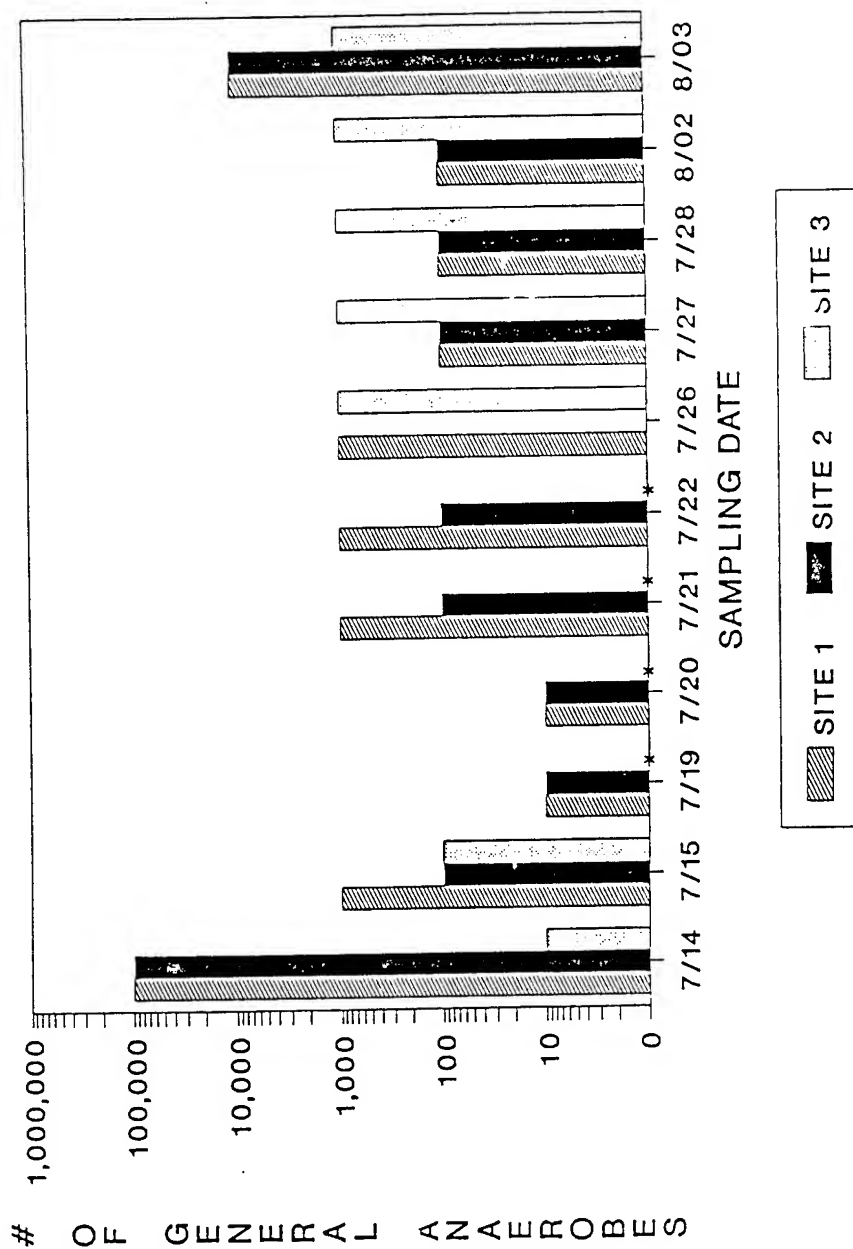
²Aerobic, heterotrophic bacteria counted by spread plate on Difco Marine Agar 2216. Marine fungi cultured on Difco Sabouraud Dextrose Agar amended with NaCl to seawater concentration. Sulfate-reducing bacteria, general anaerobes and acid-producing bacteria counted by serial dilution in media obtained from Bioindustrial Technologies, Inc., Georgetown, TX. Direct counts by acridine orange staining and epifluorescence microscopy.

FIGURE 2. COUNTS OF ACID-PRODUCING BACTERIA WITH (7/15-7/22) AND WITHOUT (7/26-8/03) OZONE TREATMENT. SAMPLING SITES ARE THOSE INDICATED IN FIGURE 1 OF THIS REPORT.



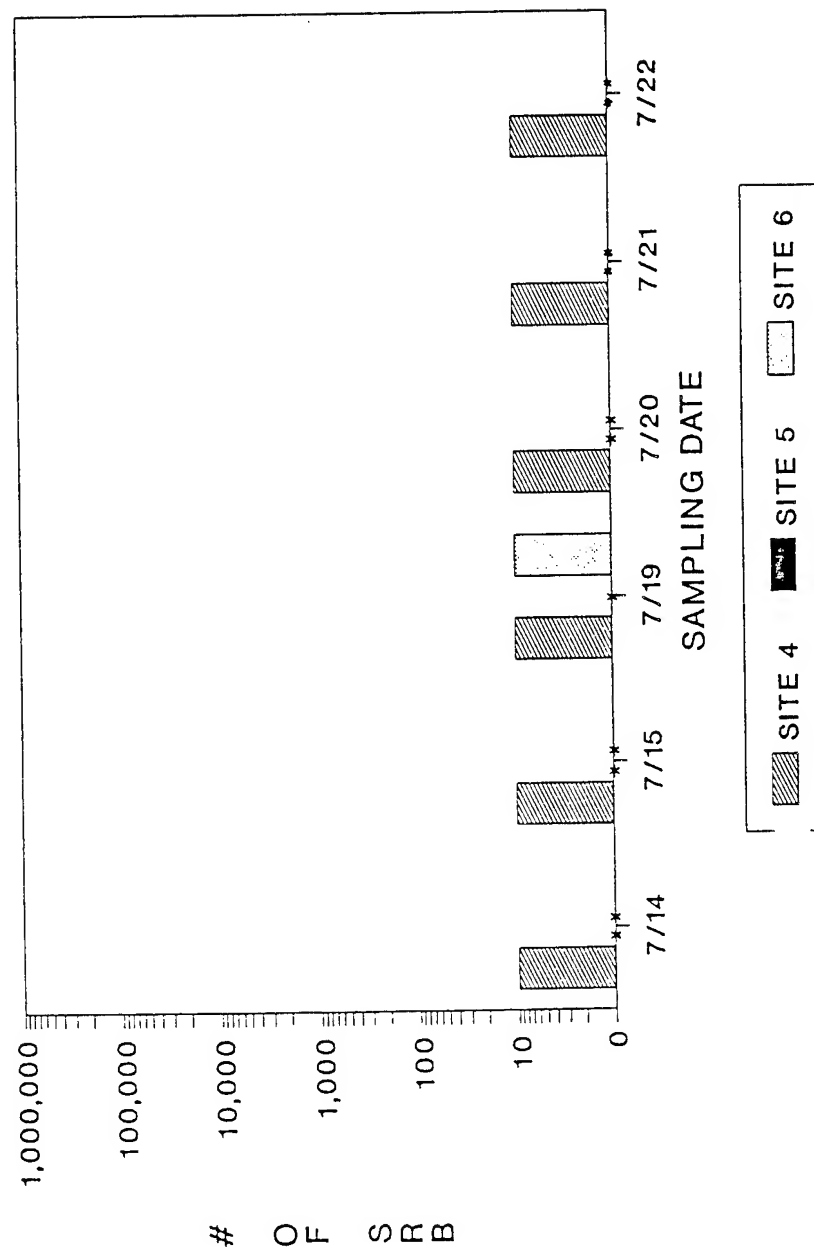
• - NO BACTERIA FOUND

FIGURE 3. COUNTS OF ANAEROBIC BACTERIA WITH (7/15-7/22) AND WITHOUT (7/26-8/03) OZONE TREATMENT. SAMPLING SITES ARE THOSE INDICATED IN FIGURE 1 OF THIS REPORT.



* - NO BACTERIA FOUND

FIGURE 4. COUNTS OF SULFATE-REDUCING BACTERIA DURING TREATMENT OF SEAWATER BY ULTRAVIOLET STERILIZATION. SAMPLING SITES ARE THOSE INDICATED IN FIGURE 1 OF THIS REPORT.



SRB - SULFATE-REDUCING BACTERIA
 * - NO BACTERIA FOUND

however, counts climbed to their previous levels within a couple of days. Similarly, numbers of general anaerobes were reduced by 2-4 orders of magnitude (Figure 3). SRB counts in the UV-treated water dropped to undetectable levels (Figure 4). Visual and microscopic inspections of the piping and heat exchanger plates and tubes showed noticeably lower levels of both micro- and macrofouling during the first ten days of treatment than during the last ten days of the test when no treatment of the water was used.

These results agree with those of a previous, preliminary test on the effectiveness of UV sterilization of seawater entering the titanium test loop. In that test, seawater prior to UV irradiation contained approximately 10^1 SRB per ml, 10^3 acid-producing bacteria per ml, and 10^4 general anaerobes per ml. After treatment all of these groups of microorganisms dropped to undetectable levels.

Chemical analyses of the seawater both before and after treatment by ozonation and UV sterilization demonstrated that total organic carbon (TOC) and total dissolved organic carbon (TDOC) increased after the treatments stopped. Total suspended solids (TSS), total dissolved solids (TDS) and total particulate organic carbon (TPOC) values were similar throughout the testing, both before and after treatments.

III. Evaluation of Pulsed Power Treatment

Acoustic methods for biofouling control have been studied for many years. Recently, conventional ultrasonic sources have been field tested for possible prevention of fouling by the freshwater zebra mussel (*Dreissena polymorpha*) (Levy, 1993). Another study, using pulsed acoustics, reported prevention of algae accumulation in freshwater piping over a range of over 15 ft. (Bryden, 1993). This study, however, lacked adequate controls, so interpretation of results was difficult.

Pulsed acoustic shock wave technology differs from conventional sonic/ultrasonic technologies in several important respects. First, the cavitation threshold is much higher for short-pulse, high-frequency acoustic waves than for low-frequency, continuous-wave ultrasonics (Urlick, 1983). For biofouling control, this offers two advantages: (1) more acoustic power can be delivered to the water at higher efficiency, thus

allowing larger areas to be treated at greater range; and (2) based on results of our own work, biofouling control does not appear to be related to cavitation as in conventional ultrasonics, and thus the potential for materials damage is greatly reduced. Secondly, in contrast to ultrasonics, the hardware required to produce pulsed acoustic shock waves uses underwater electrical discharges formed by simple, relatively inexpensive arc-discharge equipment.

In a previous study, we demonstrated the feasibility of using pulsed acoustic waves at intensities above the cavitation threshold to remove accumulated scale and/or biofouling from the inside walls of piping (Grothaus *et al.*, 1993). An alternative that we are currently studying is to use low energy acoustic shock waves to *prevent* biofouling.

Study Design

A seawater PVC test loop was constructed in February 1994 at the NSWC/Code R33 test site in Ft. Lauderdale. The loop was built from schedule 40, 2-inch diameter clear PVC plastic piping. As in the titanium test loop experiments described above, seawater from the Port Everglades shipping channel was pumped continuously through the loop at $0.5 \text{ ft} \cdot \text{sec}^{-1}$ for a period of ten days. The acoustic pulse source consisted of a high-voltage power supply that produced an underwater electrical arc discharge. The repetition rate of the acoustic pulse was 0.5 Hz (once every two seconds). Treatment was maintained for approximately 10-12 hours per day. Biological analyses included visual inspection of fouling, bacterial counts of scrapings from pipe walls, and ESEM analyses of nylon coupons inserted into the pipes.

Results

The experiment demonstrated effective non-chemical biofouling prevention both upstream and downstream of the acoustic source. Specifically, a significant reduction in the rate of both micro- and, particularly, macrofouling was observed in the treated loop compared to an untreated control. Based on biofilm counts of aerobic heterotrophic bacteria, SRB, acid-producing bacteria, and general anaerobes, at least an order-of-magnitude reduction in the rate of microbial accumulation was observed at ranges of at least 10 feet for acoustic pulse treatments of less than 25 W average power ($4 \text{ W} \cdot \text{ft}^{-2}$ treated). Direct observation of

treated and untreated surfaces with ESEM revealed significant prevention of bacterial and algal fouling compared to the control. No degradation to the plastic piping of the loop was observed.

IV. Conclusions

The studies described here demonstrated that both ozone injection and UV irradiation treatments were effective in reducing microbial numbers in flowing seawater by several orders of magnitude. Although kill is not complete, the levels of microbial reduction seen in this study are sufficient to lead to significantly lowered fouling rates compared to untreated controls. Slow build-up of a microbial slime layer should not be of significant concern from a corrosion standpoint, as no cases of microbiologically-influenced corrosion of titanium have been reported (Little *et al.*, 1991; Little *et al.*, 1992). Almost complete prevention of macrofouling was observed in our system under both treatment regimes. Both treatment technologies can be adapted to the high-volume seawater requirements of the Navy. The Diablo Canyon Power Plant in San Luis Obispo, California, for example, uses prefiltration followed by UV sterilization to treat 1,000 gpm of seawater before it is transferred to reverse osmosis (RO) membranes for desalination (S. Hoover and J. Jones-Meehan, personal communication). Ozonation and UV sterilization both appear to represent potentially effective and environmentally-compatible alternatives to chemical treatments for control of biofouling in shipboard titanium piping and cooling systems.

Preliminary tests of pulsed acoustic treatments for biofouling prevention show promise, but much more work is needed to optimize the effects and develop the technologies for practical use.

Acknowledgments

The authors wish to acknowledge support for these studies from the AEGIS Combat Systems Program Office N05 and the Venture/Seed Program of the Naval Surface Warfare Center, Dahlgren Division. We also gratefully acknowledge the assistance of Mr. Robert Erskine (Ingalls Shipbuilders), Mr. John Braker (Nova Univ.), Mr. Richard Ray (NRL-Detachment) and Ms. Mary Beard (NSWCDD/Code R31).

References

- A. Bryden. 1993. "New application of an acoustic device," Presented to 3rd Inter. Zebra Mussel Conf., Toronto, Ontario, Canada, Feb. 1993.
- M.G. Grothaus, M.S. Mazzola, M. Walch, and J. Jones-Meehan. 1993. "Pulsed power remediation and prevention of biofouling," Presented to 9th Inter. Pulsed Power Conf., Albuquerque, NM, June 1993.
- S. Levy. 1993. "Final report on Electrical Methods for the Control of Zebra Mussels," EPRI Power Electronics Applications Center, Knoxville, TN, May 1993.
- B. Little, P. Wagner, R. Ray, and M. McNeil. 1990. "Microbiologically influenced corrosion in copper and nickel seawater piping systems." *Mar. Technol. Soc. J.* 24: 10.
- B. Little, P. Wagner, and F. Mansfeld. 1991. "Microbiologically influenced corrosion of metals and alloys," *International Materials Review* 36: 253-272.
- B. Little, P.A. Wagner, and R.I. Ray. 1992. "An experimental evaluation of titanium's resistance to microbiologically influenced corrosion," Corrosion/92, Paper No. 173, National Association of Corrosion Engineers, Houston, TX.
- J.M. Jones and B.J. Little. 1990. "USS PRINCETON (CG 59): Microbiologically Influenced Corrosion (MIC) and Macrofouling Status of Sea Water Piping Systems," Naval Surface Warfare Center Technical Report 90-176, June 1990.
- R.J. Urick. 1983. *Principles of Underwater Sound*, pp. 78-79. McGraw-Hill, New York.

Microbiologically Influenced Corrosion (MIC) of Steels:
Weight Loss Measurements, ESEM/EDS and XRD Analyses

Dr. Joanne Jones-Meehan* and Mr. Jon W. Cofield
Naval Surface Warfare Center/Codes R301 and R33
Silver Spring, MD 20903-5640

Dr. Brenda Little, Mr. Richard Ray and Mrs. Patricia Wagner
Naval Research Laboratory/Code 7333
Stennis Space Center, MS 39529-5004

Dr. Michael McNeil
Nuclear Regulatory Commission
Washington, D.C. 20555

Ms. Jennifer McKay
University of Western Ontario/Dept. of Earth Sciences
London, Ontario N6A 5B7

ABSTRACT

Carbon (1018 and 4340), stainless (304SS) and HY80 steel coupons were exposed to three, mixed marine communities containing sulfate-reducing bacteria (SRB) for time periods up to eight months. Data on surface topography and chemistry (environmental scanning electron microscopy [ESEM] coupled with energy dispersive spectroscopy [EDS]), weight loss measurements and X-ray diffraction [XRD] patterns of minerals in the biofilm have been obtained from controls (no bacteria added) and from experimental samples exposed to the mixed bacterial communities. Microbes were distributed throughout the surface layers (i.e., sulfides, corrosion products, inorganic deposits, microbial exopolymers, etc.). The thickness and chemistry of the corrosion layers, as well as, the severity of corrosion varied among the steels. A patchy biofilm developed on 304SS, but no corrosion was detected during the eight month exposure period. The increased corrosion indicated by weight loss data for 1018, 4340 and HY80 exposed to SRB was statistically significant compared to the controls. For HY80, the increased amount of corrosion observed with CG-59 SRB community (originally isolated from corroding seawater piping on a Navy

ship) was statistically significant compared to the two other SRB communities tested. Dealloying of Cr was observed in the 4340 coupons exposed to the three SRB communities, while Cr was dealloyed only in HY80 coupons exposed to CG-59 SRB community (no Cr dealloying in HY80 coupons exposed to the other two SRB communities). Carbon and HY80 steels exposed to SRB showed the production of mackinawite $[\text{Fe}_9\text{S}_8]$ and vivianite $[\text{Fe}(\text{PO}_4)_2 \cdot 8\text{H}_2\text{O}]$ with minor amounts of other minerals. Vivianite was sometimes accompanied by siderite $[\text{FeCO}_3]$.

INTRODUCTION

Microbiologically influenced corrosion (MIC) resulting from the activities of sulfate-reducing bacteria (SRB) does not produce any unique form of localized corrosion. Pitting, crevice corrosion, under-deposit corrosion and dealloying have been attributed to SRB.^{1,11,14,15,17} Biofilms produce an environment at the biofilm/metal interface that is very different from that of the bulk medium in terms of pH, dissolved oxygen, and inorganic and organic species.¹⁷ SRB are ubiquitous, but they predominate in anaerobic marine biofilms because of the presence of 2.5gmL^{-1} sulfate in seawater. SRB in biofilms enhance corrosion of steel through both direct (hydrogen removal) and indirect (hydrogen sulfide and iron sulfide production) processes.

SRB-enhanced corrosion of 1018 steel under aerobic bulk liquid medium was reported by Lee et al. (1993).¹⁰ The number of marine SRB was higher in biofilms recovered from carbon steel piling sites which experienced high rates of corrosion.¹ Metabolic activity was different for three SRB communities (one from Portsmouth, UK; one from Alaska; and one from Indonesia) isolated from a severe case of marine corrosion of mild steel. SRB isolated from sheet piling in Portsmouth gave rise to very high corrosion rates compared to the Alaskan and Indonesian SRB strains (as measured by linear polarization method).¹ Bryant et al.² reported that a SRB biofilm with active hydrogenase activity (i.e., corrosion pipeline microbes) was associated with significantly higher corrosion rates (7.79 mm/year) on SAE 1020 steel relative to a hydrogenase-negative SRB biofilm (0.48 mm/year). No hydrogenase activity was detected on studs or from planktonic SRB until after 23 days incubation when some SRB biofilms on the steel studs showed strong hydrogenase activity. The induction of hydrogenase was probably caused by a shift from chemoorganic to chemolithotrophic metabolism by some of the SRB in the mixed biofilm because of the very low level of utilizable carbon (lactate and acetate) left

in the recycled medium. This induction of hydrogenase may be due to microbes capable of utilizing cathodically produced hydrogen as an alternate energy source.²

Pitting at or adjacent to welds at the heat-affected zone (HAZ), the fusion line and in the base metal was observed in MIC of type 300 series austenitic stainless steel.⁷ Tatnall observed that biodeposits containing SRB correlated directly with crack locations at tube-tubesheet junctions in vertical condensers constructed of 304SS.¹⁶ SRB corrosion was observed on carbon steel, stainless steel and galvanized steel in a wastewater system.⁹

MATERIALS AND METHOD

Laboratory Testing. The isolation, maintenance, and characterization of the SRB communities have been described elsewhere.^{6,13} For each material (1018, 4340, HY80 and 304SS), 100 coupons were weighed and exposed to sterile medium (25 coupons for each material) or to one of three mixed, marine communities containing SRB (25 coupons for 49Z bacteria, 25 coupons for P14 bacteria and 25 coupons for CG-59 bacteria). The coupons were incubated anaerobically at room temperature for 2, 4 and 6 months, as well as a 6 month anaerobic exposure followed by a 2 month aerobic exposure to determine if any alterations in corrosion product(s) would occur after exposure to an aerated solution. At the end of each time period, coupons were removed as indicated below:

Sample	<u># of Coupons Tested For Each Steel Substrate^a</u>			<u>Wt Loss</u>
	<u>XRD</u>	<u>ESEM/EDS</u>		
Control	1	1		3
49Z Bacteria	1	1		3
P14 Bacteria	1	1		3
CG-59 Bacteria	1	1		3

^aThe number of coupons analyzed for the 6 month anaerobic incubation followed by the 2 month aerobic incubation was doubled.

Using 2-tail t-test for comparison of means of independent groups, the weight loss for each steel substrate at each exposure time for each bacterial community was compared to the appropriate control. At the end of the exposure periods, surface topography and chemistry were documented using an Electroscan Model E-30 environmental scanning electron microscope (ESEM) and a NORAN SERIES II Model 5502 energy

dispersive x-ray spectrometer (EDS). Coupons were removed from the culture medium, carried through a series of salt water/distilled water washes and examined directly from distilled water. X-ray diffraction patterns were collected using cobalt K radiation in a Rigaku High Brilliance Rotating Anode Diffractometer with a 5°/min scan rate.

Coupons of 4340 were exposed to pure cultures of SRB isolated from three mixed communities in an anaerobic hood for 2 months at room temperature. Coupons were analyzed for weight loss, biofilm surface topography and chemistry as described above.

Steels. The elemental composition for (1) 4340 is 0.41% C, 0.82% Cr, 0.15% Cu, 0.76 Mn, 0.26 Mo, 1.89% Ni, 0.012% P, 0.004% S and 0.24% Si; (2) 1018 is 0.15-0.20% C, 0.060-0.90% Mn, 0.040 P (max) and 0.050 S (max); (3) HY80 is 0.1-0.2 C, 0.2-0.45 Mn, 0.12-0.38 Si, 0.02 P (max), 0.002-0.02 S, 2.1-2.5% Ni 0.25-0.4% Mo, 0.94-1.86 Cr, 0.03 V (max), 0.02 Ti (max) and 0.25 Cu (max); and (4) 304SS is an austenitic SS (18%Cr-8%Ni).

RESULTS AND DISCUSSION

Microbes were distributed throughout the surface layers (i.e., sulfides, corrosion products, inorganic deposits, exopolymers, etc.) on 4340, 1018 and HY80 steels (Figures 1 and 2). The increased corrosion as measured by weight loss for 1018, 4340 and HY80 exposed to SRB was statistically significant compared to the control (no SRB present; data not shown). For HY80, the increased amount of corrosion observed with CG-59 SRB community (originally isolated from corroding seawater piping) was statistically significant compared to the two other SRB communities tested (data not shown).

Dealloying of Cr was observed in the 4340 coupons exposed to the three SRB communities (Figure 3), while Cr was dealloyed only in HY80 coupons exposed to the CG-59 SRB community (no dealloying in HY80 coupons exposed to the two other SRB communities; Figure 4). Pure cultures of the SRB from the mixed communities have been isolated and characterized for hydrogenase activity. SRB from 49Z and P14 mixed communities are hydrogenase-positive, while SRB from CG-59 mixed community is hydrogenase-negative.⁶ After a two month exposure of 4340 coupons to pure SRB cultures from the three mixed communities (49Z, P14 and CG-59), dealloying of Cr was observed in 4340 coupons exposed to

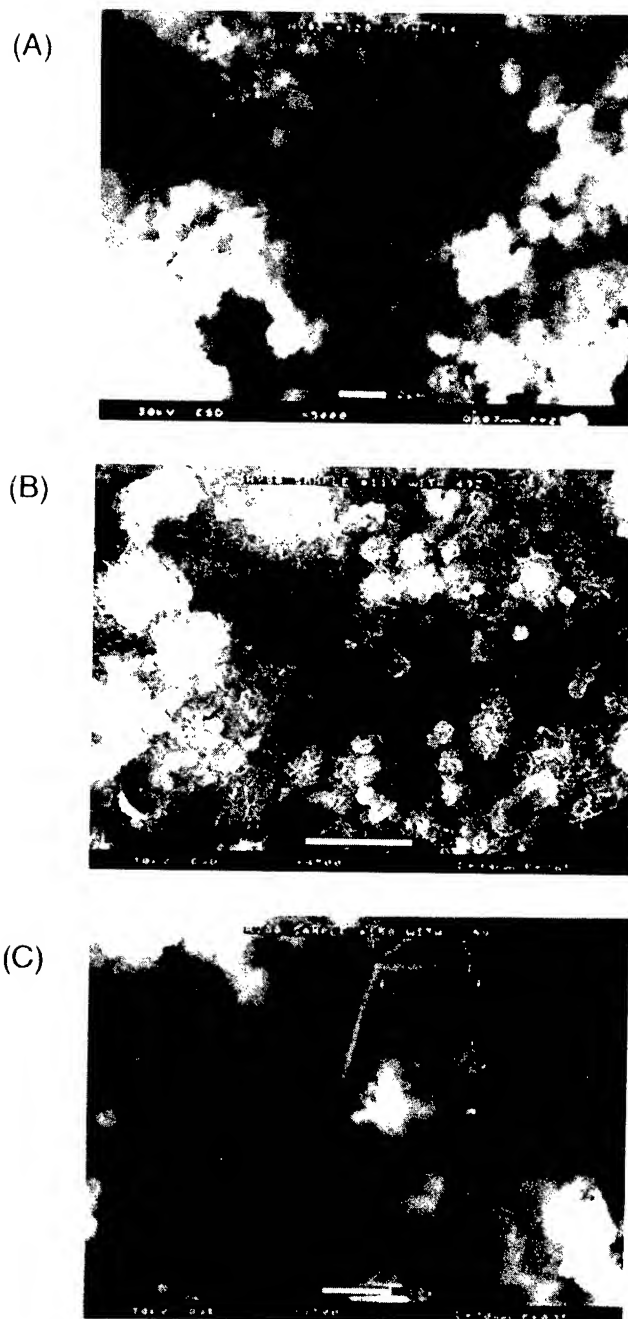
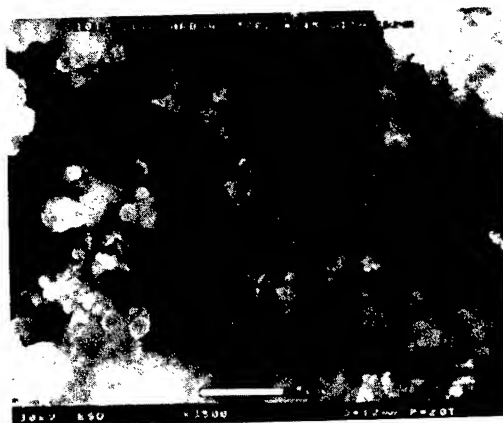
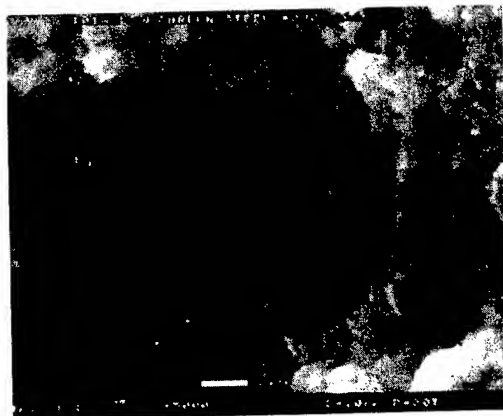


Figure 1. ESEM micrograph showing biofilms on HY80 steel coupons after a two month exposure to three mixed, marine communities containing SRB (A, P14 bacteria; B, 49Z bacteria; and C, CG-59 bacteria). Scale bar in the micrographs: A, 2 microns; B, 5 microns; and C, 10 microns.

(A)



(B)



(C)



Figure 2. ESEM micrograph showing biofilms on 1018 steel coupons after a two month exposure to three, mixed marine communities containing SRB (A, 49Z bacteria; B, CG-59 bacteria; and C, P14 bacteria). Scale bar in the micrographs: A, 5 microns; B, 2 microns; and C, 10 microns.

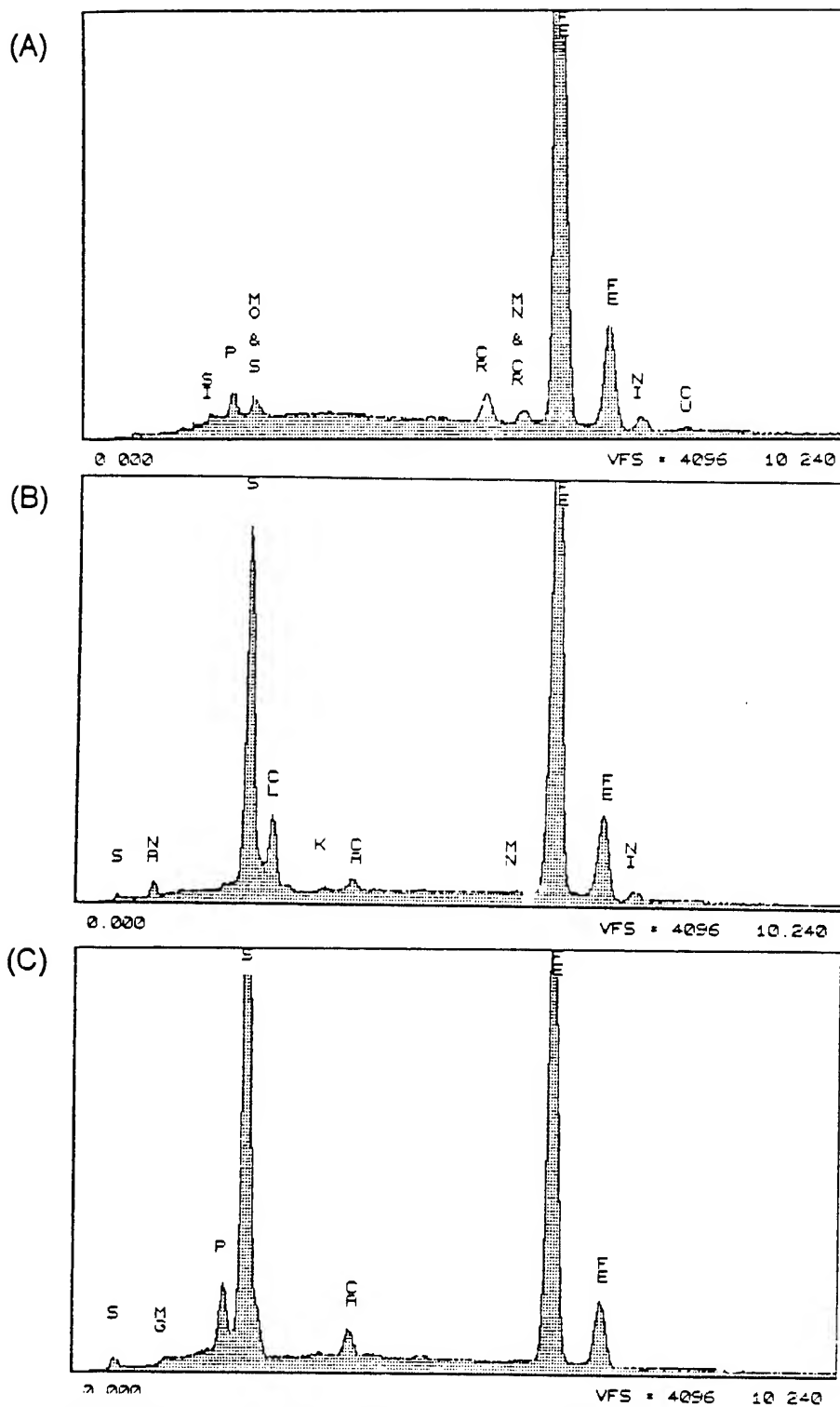


Figure 3. EDS spectra of 4340 after 2 months: (A) control, (B) exposed to 49Z mixed bacteria and (C) exposed to a pure culture of 49Z SRB.

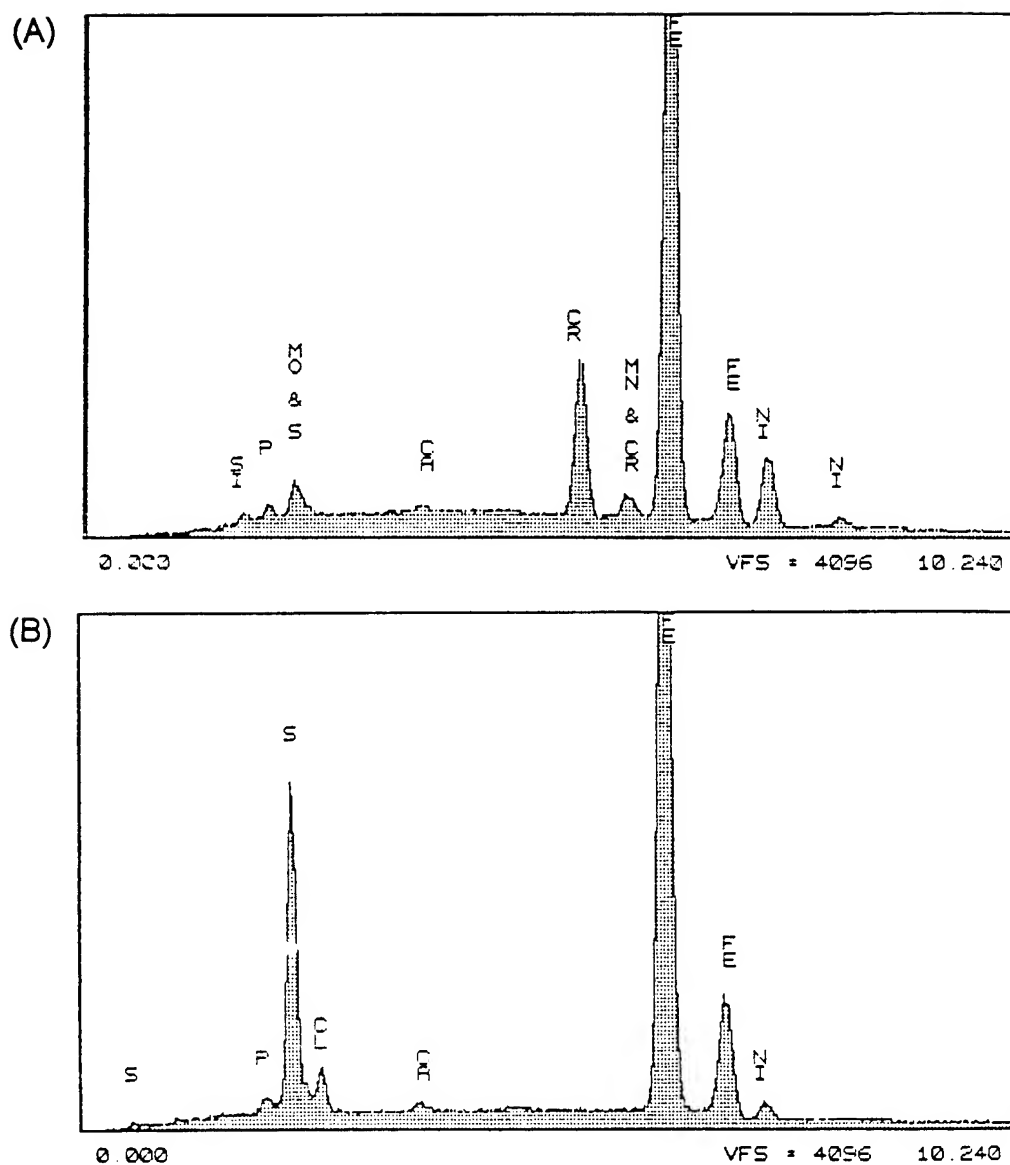


Figure 4. EDS spectra of HY80: (A) control (no SRB present); and (B) exposed to CG-59 mixed community with SRB for 6 months.

pure SRB cultures but no dealloying of Cr was observed for the control (no SRB present; Figure 3A,C).

A patchy biofilm developed on 304SS (data not shown), but no corrosion was detected during the six month exposure period. The corrosion resistance of stainless steels (SS) is due to the formation of a thin passive film. Mansfeld et al. (1992) reported no localized corrosion in three stainless steels (304SS, 316SS and A16XSS) and titanium grade 2 after a 4 month exposure to flowing Pacific Ocean seawater where 10-100 SRB cm^{-3} were present.¹² With longer exposure times to SRB, MIC of type 300 series austenitic stainless steels has been observed at or adjacent to welds in the HAZ, the fusion line and in the base metal.⁵ Gillis et al. (1994) reported that the facultative anaerobe, *Citrobacter freundii*, selectively colonized grain boundaries of 316L stainless steel which resulted in a significant depletion of Cr in near-surface regions at the grain boundaries while the sterile controls showed no depletion of Cr.³ Significant depletion of iron was reported in near-surface regions at grain boundaries colonized by a co-culture of *C. freundii* and *Desulfovibrio gigas* (a SRB), but not in sterile coupons or in coupons exposed to *C. freundii* alone.³ Gillis et al. suggested that the early stages of surface colonization leading to changes in alloy elemental composition near the surface may be critical steps that fix anodic and cathodic sites required for subsequent localized attack and pit formation and propagation.³

McNeil et al. (1991) identified unique copper sulfide minerals formed by SRB in biofilms on copper surfaces that did not form abiologically at standard conditions of temperature and pressure.¹³ Non-adherent chalcocite (Cu_2S) layers were indicators of SRB-influenced corrosion. It has been recognized that when iron alloys are corroded by SRB, specific sulfide minerals form.⁸ Exposure of low carbon and HY80 steels to SRB resulted in the production of mackinawite (Fe_9S_8), vivianite [$\text{Fe}(\text{PO}_4)_2 \cdot \text{H}_2\text{O}$], and minor amounts of other minerals (i.e., siderite [FeCO_3], green rust [either JCPDS 13-91 or JCPDS 13-90] and some distinct smythite [Fe_9S_{11}]; see Table 1). Most specimens, except stainless steel, show significant vivianite patterns. Consortia containing SRB have been reported to produce phosphorus-containing minerals on iron.⁴ Vivianite and mackinawite persist on exposure to air or oxygenated medium. Green rust is a significant alteration product found on some of the 1018, 4340 and HY80 coupons exposed to SRB, while green rust was not observed in controls (no SRB present; see Table 1). This observation differs from some other laboratory and field studies in the literature, but it is consistent with extensive

Table 1. XRD Data for 1018, 4340 and HY80 Steels^a

Steel/ Culture	(A) Pattern V	(B) Pattern V	(C) Pattern V	(D) Pattern V	(E) Pattern V
1018 Control					
1018/P14	V	V,MC,SI GR	V,MC,GR	V,SI,MC GR	V, MC GR,si
1018/49Z	V,MC,si	V,MC,SI	V,MC	V,SI,MC GR	V,MC GR,si
1018/CG59	V,MC,si	V,MC,GR si	V,GR,MC	V,MC,GR si	V,MC GR,si
4340 Control	V	V,o	V,si,o	V,o	V,si
4340/P14		V,MC	V,MC	V,MC,SI GR	V,MC SI,GR
4340/49Z		V,MC	V,MC,SI	V,SI,MC	V,MC,SI
4340/CG59			V,SI,mc	V,SI,mc	V,SI,MC
HY80 Control			V	V	V
HY80/P14	MC	MC	MC	MC, . y	V,MC,gr
HY80/49Z	MC	MC,V	MC,V	MC,V	MC,V,si
HY80/CG59	V,si	V,MC,si	V,MC,si,gr	V,MC,si	V,MC,si

^a Patterns : (A), 120 days anaerobic exposure; (B), 120 days anaerobic then 14 days aerobic exposure; (C), 171 days anaerobic exposure; (D), 192 day anaerobic exposure; (E) 180 day anaerobic exposure then 60 days aerobic exposure. Minerals: GR, green rust (either JCPDS 13-91 or JCPDS 13-90); MC, mackinawite; O, oxide; SI, siderite; SY, smythite; V, vivianite. Lower case indicates minor quantities of mineral observed.

field observations at Nova Husky (Tom Jack, personal communication).

CONCLUSIONS

The increased corrosion indicated by weight loss data for 1018, 4340 and HY80 exposed to SRB was statistically significant compared to controls. ESEM/EDS analyses of 4340 steel coupons before and after the addition of three mixed communities containing SRB or pure SRB cultures revealed dealloying of Cr. No dealloying of Cr was observed in controls. ESEM/EDS analyses of HY80 steel coupons revealed dealloying of Cr only for coupons exposed to CG-59 SRB community. Carbon and HY80 steels exposed to SRB showed the production of mackinawite and vivianite with minor amounts of other minerals such as siderite, green rust and/or smythite.

ACKNOWLEDGEMENTS

This work was supported by the Office of Naval Research by Dr. Michael Marron, ONR Code 341. NRL Contribution No. NRL/PP/7333-94-0036, Program Element 61153N. The authors acknowledge the technical assistance of Mary Beard (NSWC/Code R31) with the weight loss measurements.

REFERENCES

1. **Beech, I.B., A. Campbell and F.C. Walsh**, "Microbiological Aspects of the Low Water Corrosion of Carbon Steel", Preceedings of the 12th International Corrosion Congress, Vol. **5B**, pp.3735-3746 (Houston, TX: NACE, 1993).
2. **Bryant, R.D., W. Jansen, J. Boivin, E.J. Laishley and J.W. Costerton**, "Effect of Hydrogenase and Mixed Sulfate-Reducing Bacterial Populations on the Corrosion of Steel", Appl. Environ. Microbiol. **57** (1991): pp. 2804-2809.
3. **Gillis, R.J., R. Avci, and G.G. Geesey**, "Bacterial Colonization and Modification of Grain Boundaries on 316L Stainless Steel", Abstract Q-203, Proceedings of the Annual Meeting of the American Society of Microbiology (1994): p. 424.
4. **Iverson, W.P.**, "Mechanism of Anaerobic Corrosion of Steel by Sulfate-Reducing Bacteria", CORROSION/83 paper no. 243 (Houston, TX: NACE, 1983).
5. **Iverson, W.P.**, "Microbial Corrosion of Metals", Advances in Applied Microbiology **32** (1987): pp. 1-36.

6. **Jones-Meehan, J., K.L. Vasanth, R.K. Conrad, M. Fernandez, B.J. Little, and R.I. Ray**, "Corrosion Resistance of Several Conductive Caulks and Sealants From Marine Field Tests and Laboratory Studies with Marine, Mixed Communities Containing Sulfate-Reducing Bacteria (SRB)", ASTM STP 1232, J.R. Kearns and B.J. Little, Eds., American Society for Testing and Materials (Philadelphia, PA: 1994), pp. 217-233.
7. **Kearns, J. and S. Borenstein**, "Microbially Influenced Corrosion Testing of Welded Stainless Alloys for Nuclear Power Plant Service Water Systems", CORROSION/91 paper no. 279 (Houston, TX: NACE, 1991).
8. **King, R.A., J.D.A. Miller, and D.S. Wakerley**, "Corrosion of Mild Steel in Cultures of Sulphate-Reducing Bacteria: Effect of Changing the Soluble Iron Concentration During Growth," British Corrosion Journal 8 (1973): pp. 89-93.
9. **Kobrin, G.**, "Corrosion by Microbiological Organisms in Natural Waters", Materials Performance 15 (1976): pp. 38-43.
10. **Lee, W., Z. Lewandowski, S. Okabe, W.B. Characklis, and R. Avci**, "Corrosion of Mild Steel Underneath Aerobic Biofilms Containing Sulfate-Reducing Bacteria. Part I: At Low Concentrations of Dissolved Oxygen Concentration", Biofouling 7 (1993): pp.197-216.
11. **Little, B., P. Wagner and F. Mansfeld**, "Microbiologically Influenced Corrosion of Metals and Alloys", International Materials Review 36 (1991): pp. 253-272.
12. **Mansfeld, F., R. Tsai, H. Shih, B. Little, R. Ray and P. Wagner**, "An Electrochemical and Surface Analytical Study of Stainless Steels and Titanium Exposed to Natural Seawater", Corrosion Science 33 (1992): pp. 445-456.
13. **McNeil, M., J. M. Jones and B.J. Little**, "Production of Sulfide Minerals by Sulfate-Reducing Bacteria During Microbiologically Influenced Corrosion of Copper", Corrosion 47 (1991): pp. 674-677.
14. **Pope, D.H.**, "A Study of Microbiologically Influenced Corrosion in Nuclear Power Plants and a Practical Guide for Countermeasures", Electric Power Research Institute, Palo Alto, CA (1986).
15. **Pope, D.H., D. Duquette, P.C. Wayner, and A.H. Johannes**, "Microbiologically Influenced Corrosion: A State-of-the-Art Review", 2nd Edition, (St. Louis, MS: The Materials Technology Institute of the Chemical Process Industries, Inc.; MTI Publication no. 13, 1989).
16. **Tatnall, R.E.**, "Microbiologically Induced SSC?", Materials Performance 32 (1994): pp.68-69.
17. **Wagner, P. and B. Little**, "Impact of Alloying on Microbiologically Influenced Corrosion-A Review", Mat. Performance 32 (1993): pp. 65-68.

An Innovative Method For Rapid Detection of Microbiologically Influenced Corrosion

Mr. George J. Licina*
Structural Integrity Associates
3150 Almaden Expressway, Suite 145
San Jose, CA 95118-1217

Mr. George Nekoksa
Corrosion Failure Analysis and Control
209 Gaucho Court
San Ramon, CA 94583

INTRODUCTION

Microbiologically influenced corrosion (MIC), the interaction of biological activity with corrosion processes, is a significant cause of degradation of piping and heat transfer surfaces in cooling water systems. MIC can produce localized corrosion and through-wall penetration of piping and heat exchanger tubing at rates 10 to 1000 times more rapid than those normally encountered.

Monitoring of biofilm formation on line provides the system operator with the information needed to initiate mitigation activities, such as cleaning and water treatment, well before the structural integrity of piping or components is jeopardized. On-line monitoring of biofilms, and timely actions, taken before corrosion has initiated or thick biofilms are formed on piping or heat exchanger tube surfaces, can significantly improve the effectiveness of mitigation activities. Continuous monitoring of biofilm activity permits close control of biocide additions (to avoid over-treatment of the water) and scheduling of **preventive** maintenance activities so that unplanned downtime due to MIC is avoided.

The electrochemical aspects of MIC have been discussed by a number of authors [1-8]. Since MIC affects electrochemical reactions that influence corrosion, biofilm activity may be tracked by electrochemical monitoring methods that are specific to those electrochemical reactions by which biofilms can influence corrosion. An electrochemical device, the BIoGEORGE™ probe, has been developed¹ to provide a method for determining the onset of biofilm formation on metal surfaces and tracking biofilm activity on line in a power plant or industrial environment [9].

BACKGROUND

The BIoGEORGE probe (Figure 1) consists of two sets of identical metallic disks, separated from each other by an insulating epoxy. The cylindrical probe is inserted into the plant environment via a standard access fitting, such as a threaded tee. A simple control system cathodically polarizes one electrode (i.e., set of disks) relative to the other for a short period (30 minutes to one hour) each day. The electrodes are connected through a precision resistor (e.g., 1000 Ω) at all other times. By monitoring the current required to achieve the pre-set potential over a period of days or weeks, the influence of biofilms on operative half-reactions may be readily detected. The "gentle" cathodic polarization simulates electrochemical conditions similar to those resulting from local anodic sites (e.g., inclusions or weldments) and produces local environments that result in differences in the types and numbers of microorganisms present on each electrode [3, 10-11].

The **applied current**, the current which flows when the external power source is on, is tracked daily. When a biofilm becomes established on the probe surfaces, this applied current exhibits a distinct increase. Examination of the trend of applied current thus provides rapid, real time indication of biological activity on the probe surfaces. The **generated current**, the current that flows through the shunt resistor which connects the electrodes when the power source is off, is monitored at all other times. Initially, the generated current is zero or very near zero as would be expected for two nominally identical electrodes exposed to the same environment. Laboratory tests have shown that the generated current also

¹ Patent rights to the BIoGEORGE probe are owned by the Electric Power Research Institute. The patent application was filed in October, 1991. U.S. Patent Number 5,246,560 was issued on September 21, 1993.

increases when a biofilm forms. Biofilm formation is monitored by tracking both parameters.

APPROACH

Probes were tested in seawater environments typical of those encountered in piping and heat exchangers of Naval vessels. Probes were assembled using electrodes with materials with different film-forming characteristics. The influences of material type and the polarization schedule (i.e., length of time that electrodes are polarized and the pre-set potential) on the sensor's ability to indicate the formation of biofilm and the onset of MIC were evaluated. These probes were then installed into natural and synthetic seawater systems and tested over periods of six to eight weeks. The applied and generated currents were monitored.

Copper alloys and titanium are commonly used in seawater systems because of their superior resistance to pitting in chloride-containing environments. Standard design probes, with Type 304L stainless steel electrodes, and probes with 90-10 copper-nickel, and titanium (Grade 2) electrodes were exposed in both static laboratory tests and in a slowly flowing seawater flume at the Naval Surface Warfare Center's Corrosion Test Facility (Ft. Lauderdale, FL).

The on-line measurements were supplemented by post-exposure testing to characterize the microbiology, local chemistry (including corrosion deposits and areas away from the local corrosion site), and corrosion of surfaces.

Static Seawater Tests

Probes were exposed to a synthetic seawater environment (ASTM D-1141) in a 10 liter plexiglass vessel that was covered with aluminum foil to keep out light. Communication with room air was permitted. Deionized water was added as needed to keep the level well above the probe electrodes.

Data acquisition was accomplished using a single two-channel Allen recorder and a series of timers and switches that produced a trace for each probe two times a day. The results were input to QuattroPro, Version 5.0, for analysis and plotting.

The stainless steel electrodes were polarized to 100 mV, the 90-10 copper-nickel to 50 mV, and the titanium electrodes to 400 mV. These values were selected to provide readily measurable currents, hopefully, without corroding the electrodes excessively.

After permitting the cells to stabilize for three days, a mud was slowly added to the system (volume of mud = 4% of total electrolyte volume) to introduce organic activity. The mud was produced by mixing a soil taken from Pacific Gas & Electric's Pittsburg (California) Power Plant site and mixing it with artificial seawater in a 1:1 volume ratio. A number of components from the power plant had experienced MIC attack, generally the result of SRB, in this soil.

After approximately 50 days of exposure, a 5.25% sodium hypochlorite solution was added to the electrolyte to produce a concentration of approximately 8 ppm free chlorine. Probe response was then monitored for an additional eleven days. Nine days later, free chlorine concentration was measured at 1 ppm. At the end of the test, no free chlorine was detected.

Electrodes were monitored for microbiological activity 47 days after inoculation in the second test using MICKits (Bioindustrial Technologies, Incorporated, Georgetown, TX). Local pH on the probe electrodes was determined (Horiba Compact pH Meter, Model Cardy C-1) 47 days into the test and at the completion of the testing. The pH of the environment was tested at the beginning and the end of the test. Chlorine was measured using an Olin, HTH test kit.

Flowing Seawater Tests

Probes were also exposed to flowing natural marine environments at the Naval Surface Warfare Center at a continuous, slow flow to optimize microbiological colonization (transport of nutrients, etc.) without stripping biofilms from the metal surfaces. Like the static exposures, these tests were run such that the probe and test environment were always completely dark, as would be the case for shipboard heat exchange systems.

The BIOGEORGE™ probe electrodes at NSWC were initially polarized to 200 mV (relative to each other) for 30 minutes per day using the standard probe control system. Data were recorded using a Chessell Model 4200 recorder interfaced to an XT-class computer. Data trends were plotted in QuattroPro, Version 5.0.

After 79 days of exposure, the probes were removed from the flume, photographed, and the surfaces characterized. Field microbiological analysis was performed on samples from the positive and negative polarity electrodes from each probe using MICKits. The probes were then cleaned and returned to service.

For the second flowing test, the polarization potential was increased for the titanium probe (from 200 to 400 mV) and decreased for the stainless steel (from 200 to 60 mV) and 90-10 copper-nickel (200 to 25 mV). The polarization time for all probes was increased to one hour.

RESULTS

Static Seawater Tests

Figure 2 summarizes the results from the static tests. The applied and generated currents for the stainless steel probe remained stable following the inoculation of the cell, but both currents changed rapidly ten days later. Interestingly, the generated current shifted in the negative direction several days after the inoculation and was of a sufficient magnitude so that the applied current was also negative. The **difference** between the applied current and generated current provided the most useful parameter for plotting. The addition of sodium hypochlorite caused the current difference to return to near its original value.

The applied and generated currents from the titanium probe were much smaller, however, the response characteristic was very similar to that of the stainless steel probe. The applied current exhibited a distinct increase eleven days after inoculation. The generated current was essentially zero initially, but exhibited a very definite increase fourteen days after inoculation. The response of the probe to the destruction of the biofilm by hypochlorite is also readily apparent.

Both the stainless steel and titanium electrodes exhibited an increased concentration of general aerobic bacteria, general anaerobic bacteria, acid producers, and SRB when compared to the bulk fluid. Following biocide addition, the enrichment of SRB was no longer observed. The 90-10 copper-nickel electrodes exhibited low concentrations of all the detectable microbes, consistent with the lack of response from the probe.

Flowing Seawater Tests

In the first month of exposure, the applied and generated current traces from the stainless steel probe were very similar to those from the static tests. Applied currents stabilized after a few days, then both applied and generated currents increased steadily for the next three days. The applied current reached a maximum of $\sim 100 \mu\text{A}$ and the generated current increased from $-20 \mu\text{A}$ to nearly $33 \mu\text{A}$, both currents remained at those levels until a problem with the system pump caused an eighteen day interruption to system flow. During the time that the flow was interrupted, applied current decreased and became more unstable while the generated current decreased to near zero. When the pump was restarted, the applied current quickly returned to a value near $100 \mu\text{A}$. The generated current responded more slowly but reached a value of about $10 \mu\text{A}$ that persisted through the end of the test. The generated current appeared to provide the more sensitive indicator of biofilm activity (Figure 3).

The titanium probe exhibited very small applied currents (of the order of $1 \mu\text{A}$) and even smaller generated currents ($-0.4 \mu\text{A}$) as shown in Figure 4. The applied current remained very steady, until the eighteen day stagnant period. About ten days after the flow stopped, the applied current increased rapidly to a value in excess of $5 \mu\text{A}$, then gradually decreased to a steady value slightly higher than that which had been observed prior to the abrupt increase. Once the pump was restarted, the new, higher value persisted for 21 days. When the generated currents were plotted on an expanded scale, a very definite positive shift in generated current was observed five days after the start of the test, in exact agreement with changes in the generated current on stainless steel. While the pump was off, the generated current was much less stable. Once the pump was returned to service, the generated current again exhibited a positive shift.

As in the static tests, the 90-10 copper nickel probe gave no indication of biofilm formation. Post-test examination of the probes revealed minimal deposition on the 90-10 and titanium probes, and heavy, rust colored deposits on the stainless steel probe. The stainless steel probe exhibited some macrofouling and very heavy deposition of corrosion products on the probe body. Rusty deposits were observed on the electrodes, especially the disks near the bottom of the probe. All of the 90-10 copper-nickel electrodes were a fairly uniform, greenish-tan color. Small copper or rust colored spots were obvious on all of the 90-10 electrodes. The titanium electrodes were a uniform matte gray color with little or no evidence of deposits.

Microbiological and chemical samples were collected from the three disks of each polarity nearest the end of the probe (i.e., the most deeply submersed disks) on sterile cotton swabs. Serial dilutions were then performed in accordance with the kit instructions and detailed microbiological analysis (by microscopy) and chemical analysis for pH, chloride, iron, manganese, and calcium were performed by BTI. A summary of the results is given in Table 1.

The microbiological results confirmed the presence of biofilms on the stainless steel and titanium electrodes. Comparing the relative proportions of sulfate reducing bacteria, acid producing bacteria, and general aerobic and general anaerobic populations on the different electrodes and the bulk water revealed that the negative electrodes of the stainless steel and titanium probe supported a biofilm of the same approximate composition as that of the bulk water. Far fewer acid producers were detected on the positive electrodes of each of those probes. Iron depositing bacteria were only detected (microscopically) on the stainless steel electrodes and in the deposit from the probe body. Almost no viable microorganisms were detected on the 90-10 copper-nickel probe electrodes; consistent with the absence of any increases in applied current or generated currents from the probe.

The deposits were removed and the probes returned to service for Test #2. The cleaning process was very simple. The copper-nickel and titanium probes were cleaned completely by a fresh water rinse only. Considerable deposit remained on the stainless steel electrodes even after wiping the probe with a wet paper towel. The deposit was removed by popping it loose with a fingernail. Removal of the deposits revealed bright and shiny electrodes with no evidence of corrosion damage.

In the second test at the NSW Corrosion Test Site, the polarization parameters were modified to decrease corrosion damage on the stainless steel and 90-10 copper-nickel probes and to produce values of applied currents on the titanium probe that were more readily measured.

The stainless steel probe responded in a very similar fashion as in Test #1 except that the magnitude of the applied current was less than that for Test #1 where the applied potential was higher. Both applied and generated currents appeared to be sensitive to flow, as before. Once again, the applied current decreased and generated current became less stable when the flow was interrupted. Generated current again provided a

more sensitive indicator - currents increased from essentially zero to near 20 μA a week or so after the start of the exposure.

The applied and generated currents on the 90-10 copper-nickel probe were smaller than had been observed in the first test, however, the probe still did not appear to provide any useful information on biofilm activity on surfaces, probably because little or no biofilm was grown on the electrodes.

The larger applied potential between the titanium electrodes provided very stable outputs and readily measurable applied and generated currents. The applied current was stable at a value of about 2 μA for most of the exposure. As noted in the first test, the magnitude of the currents increased and became less stable when the flow was stopped. The generated current remained at essentially zero for the first week of exposure, then increased rapidly to about 0.25 μA .

CONCLUSIONS

- The BioGEORGE™ probe provides a practical method for the detection of biofilms, on-line, in a seawater system.
- Probes fabricated using either stainless steel or titanium electrodes provide positive indications of biofilm formation, and the destruction of the biofilm from the application of biocide.
- Probes using 90-10 copper-nickel were not as successful in static seawater, inoculated with a high SRB mud, or in a flowing, natural seawater environment.
- Indications of biofilm activity were confirmed by post-test examination.
- Additional refinements of the hardware and method are recommended.

ACKNOWLEDGMENTS

This work was sponsored by the Naval Surface Warfare Center, Dahlgren Division Detachment, under the Small Business Innovative Research Program (Project Number N60921-93-C-0100). The Project Manager was Dr. Marianne Walch.

Mr. Alex Johns of Structural Integrity Associates developed the computer software that permitted values of potential and current to be recorded on a chart and written to a file for construction of trend plots.

Mr. Scott Hoover and Mr. John Braker of the NSWC Corrosion Test provided valuable assistance with installation and data acquisition.

REFERENCES

1. R. E. Tatnall, "Experimental Methods in Biocorrosion", Biologically Induced Corrosion, NACE-8, National Association of Corrosion Engineers, Houston, TX, 1986.
2. G. J. Licina, "Electrochemical Aspects of Microbiologically Influenced Corrosion", 1988 Proceedings of EPRI Microbial Corrosion Workshop, ed. by G. J. Licina, EPRI ER-6345, Electric Power Research Institute, Palo Alto, CA, 1989.
3. V. Scotto, "Electrochemical Studies of Biocorrosion of Stainless Steel in Seawater", 1988 Proceedings of EPRI Microbial Corrosion Workshop, ed. by G. J. Licina, EPRI ER-6345, Electric Power Research Institute, Palo Alto, CA, 1989.
4. R. Johnsen and E. Bardal, "Cathodic Properties of Different Stainless Steels in Natural Seawater", *Corrosion*, Volume 41, No. 5, May, 1985, pp. 296-302.
5. S. C. Dexter and G. Y. Gao, "Effect of Seawater Biofilms on Corrosion Potential and Oxygen Reduction of Stainless Steel", *CORROSION/87*, Paper No. 377, NACE, Houston, TX, 1989.
6. F. Mansfeld and B. Little, "The Application of Electrochemical Techniques for the Study of MIC - A Critical Review", *CORROSION/90*, Paper 108, NACE, Houston, TX, 1990.
7. B. Little, et al., "Electrochemical Behavior of Stainless Steels in Natural Seawater", *CORROSION/90*, Paper 150, NACE, Houston, TX, 1990.
8. D. J. Duquette and R. E. Ricker, "Electrochemical Aspects of Microbiologically Influenced Corrosion", Biologically Induced Corrosion, NACE-8, National Association of Corrosion Engineers, Houston, TX, 1986, pp. 121-130.
9. G. J. Licina and G. Nekoksa, "An Electrochemical Method for On-Line Monitoring of Biofilm Activity", *CORROSION/93*, Paper No. 403, NACE, Houston, TX, 1993.
10. G. Nekoksa and B. Gutherman, "Cathodic Protection Criteria for Controlling Microbially Influenced Corrosion in Power Plants", EPRI NP-7312, Electric Power Research Institute, Palo Alto, CA.
11. J. Guezennec, et al., "Cathodic Protection in Marine Sediments and the Aerated Seawater Column", *Microbially Influenced Corrosion and Biodeterioration*, ed. by N. J. Dowling, M. W. Mittleman, and J. C. Danko, University of Tennessee, 1991.

Table 1

Chemical and Microbiological Characterization of Electrodes -
NSWC Test #1

(Microbial counts as cells/cm²)

Sample	SRB	APB	General Aerobic	General Anaerobic	Iron Depositing Bacteria ¹
SS+	≤1	~1	~10 ²	~10 ²	+
SS-	≤1	~10 ⁴	~10	~10	+
90-10+	ND	ND	≤1	ND	-
90-10-	ND	~1	ND	~1	-
Ti+	≤1	~10	~10	~10 ²	-
Ti-	≤1	~10 ³	~10	~10 ²	-
PLUG ²	ND	ND	ND	ND	+
Microbial Counts as cells/cc					
Bulk Water	1→10	10 ³ →10 ⁴	10→100	10 ² →10 ³	-

Sample	pH	Chemical Analysis, ppm (except for pH)								
		Fe	Mn	Cr	Ni	Mg	Ca	Cu	Ti	Cl
SS+	8.1	<1.5	0.75	<2.5	<2.0	NA	38	NA	NA	2100
SS-	8.0	<0.75	<0.25	<1.3	<1.0	NA	18	NA	NA	1400
90-10+	8.1	3.6	<0.25	NA	2.4	NA	9.1	9.7	NA	530
90-10-	6.3	<0.75	<0.25	NA	<1.0	NA	3.1	0.63	NA	960
Ti+	7.6	<0.75	<0.25	NA	NA	NA	5.6	NA	<10	2500
Ti-	8.0	<0.75	<0.25	NA	NA	NA	7.9	NA	<10	1900
Bulk water	8.0	NA	0.38	NA	NA	1300	440	NA	NA	19200

¹From direct microscopic examination by BTI

²Corrosion deposit from stainless steel body of titanium probe

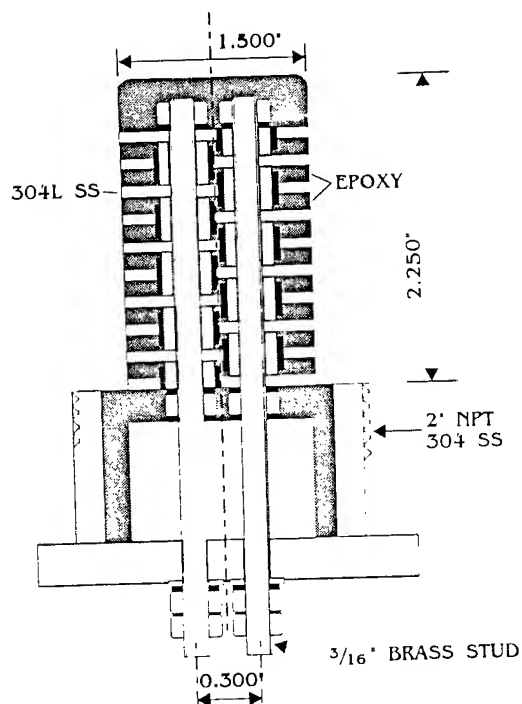


Figure 1. BIOGEORGE Electrochemical Biofilm Probe

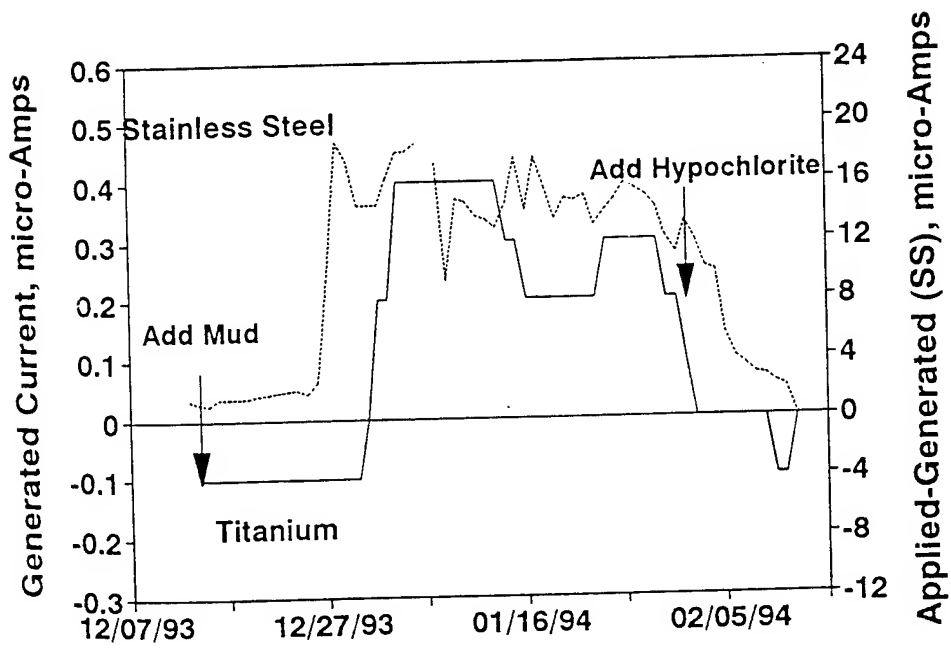


Figure 2. Results from Static Seawater Test
(Titanium at 400mV; Stainless Steel at 100mV)

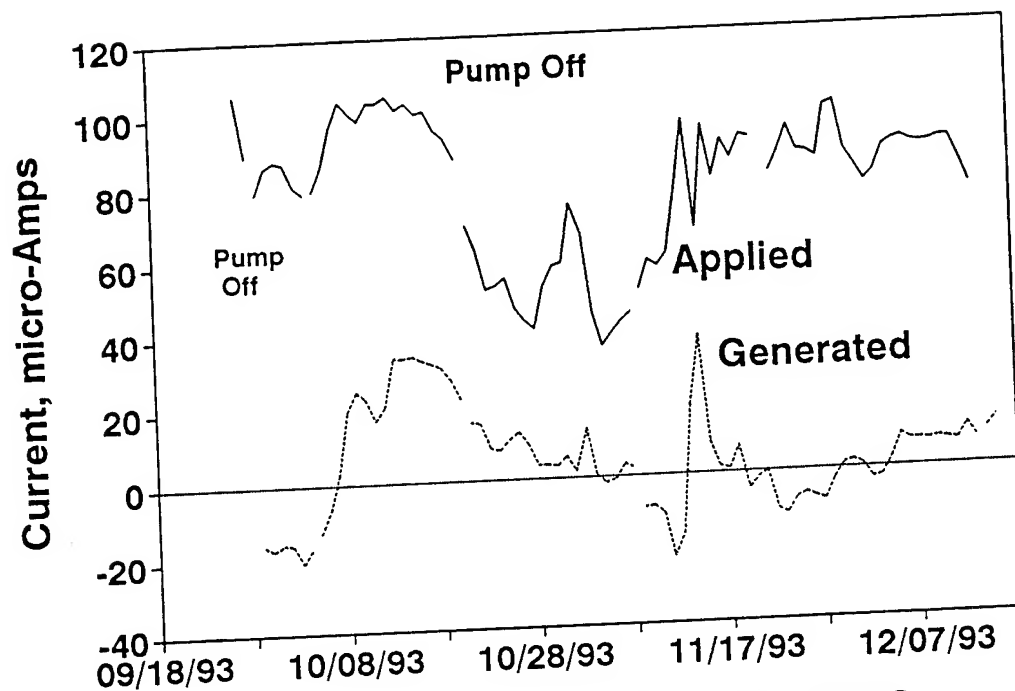


Figure 3. BloGEORGE Probe Results from NSW (Stainless Steel, 200 mV, Test #1)

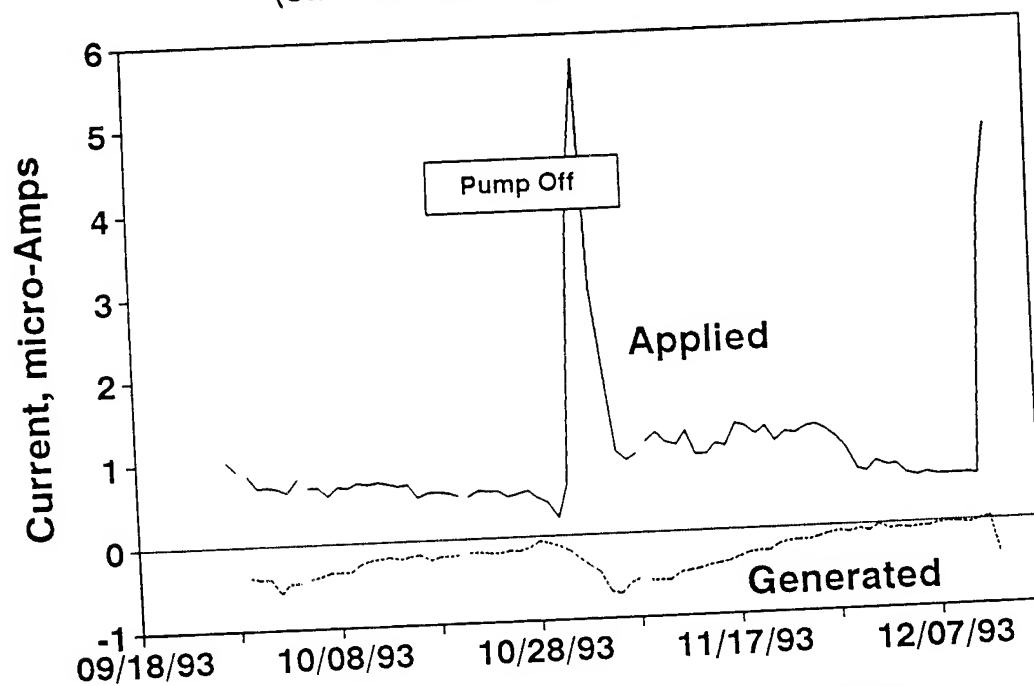


Figure 4. BloGEORGE Probes Results from NSW (Titanium, 200mV, Test #1)

THE USE OF ELECTROCHEMICAL IMPEDANCE SPECTROSCOPY (EIS) AND ELECTROCHEMICAL NOISE ANALYSIS (ENA) FOR MONITORING OF BIOCORROSION

Dr. F. Mansfeld*, Mr. H. Xiao and Mr. Y. Wang
Corrosion and Environmental Effects Laboratory (CEEL)
Department of Materials Science and Engineering
University of Southern California
Los Angeles, CA 90089-0241

Abstract

The use of electrochemical impedance spectroscopy (EIS) and electrochemical noise analysis (ENA) for non-destructive evaluation of corrosion processes is illustrated for three model systems. EIS can be used to detect and monitor localized corrosion of Al alloys and determine pit growth laws which can be used for lifetime prediction purposes. Electrochemical potential and current noise data can be analyzed in the time and the frequency domain. A comparison of noise data obtained for Pt and an Al 2009/SiC metal matrix composite (MMC) exposed to 0.5 N NaCl has shown that the use of potential noise data alone can lead to misleading results concerning corrosion kinetics and mechanisms. The electrochemical noise data have been evaluated using power spectral density (PSD) plots in an attempt to obtain mechanistic information. The system Fe/NaCl has been used to determine the relationship between the polarization resistance R_p obtained from EIS data and the noise resistance R_n determined by statistical analysis of potential and current noise data. Potential and current noise can be recorded simultaneously allowing construction of noise spectra from which the spectral noise resistance R_{sn}^0 can be obtained as the limit for zero frequency. Good agreement between R_p , R_n and R_{sn}^0 has been observed for iron exposed to NaCl solutions of different corrosivity. For polymer coated steel exposed to 0.5 NaCl for five months analysis of EIS data allows to draw conclusions concerning the degree of disbonding of the coating and the decrease of the coating resistivity with exposure time. R_n and R_{sn}^0 obtained from electrochemical noise data for an alkyd coating on cold rolled steel agree with each other and show the same time dependence as R_p and the pore resistance R_{po} determined from EIS data, but are significantly lower than R_p and R_{po} . The relationships of derived noise parameters such as R_n and R_{sn}^0 to coating properties and to the remaining lifetime of a polymer coating are not clear at present.

Introduction

In evaluating the use of electrochemical monitoring techniques for the detection and quantification of microbiologically influenced corrosion (MIC), a few limitations of such techniques have to be considered. A weakness of most electrochemical techniques is the failure to give quantitative results in cases of localized corrosion. These techniques give average readings for the surface of a test electrode and it is not clear whether a measured corrosion current corresponds to uniform corrosion of the entire surface or to localized corrosion of just a few sites on this surface. In the latter case corrosion rates will be severely underestimated if the measured corrosion loss is not normalized to the area at which localized corrosion occurs - a quantity which is usually unknown. This general disadvantage of electrochemical techniques is especially bothersome in the case of MIC, where most corrosion processes are of a localized nature. Recently, techniques such as electrochemical impedance spectroscopy (EIS) have been shown to contain information which is specifically related to localized corrosion processes [1-4]. EIS can be considered a well-established technique in corrosion research which has been applied successfully in studies of many corrosion systems [4,5]. Due to the practical importance of localized phenomena in areas such as MIC, it is desirable to apply EIS to studies of pitting and crevice corrosion with the aim of quantifying these corrosion processes through measurements of pit growth rates and other parameters uniquely related to localized corrosion.

Another new technique is electrochemical noise analysis (ENA), which is considered by some as the ideal tool for the study of localized corrosion phenomena. ENA has the advantage that it is a non-destructive technique which monitors naturally occurring phenomena. No external signal has to be applied to collect noise data. Unfortunately, very few studies have demonstrated that localized corrosion can be detected and analyzed quantitatively by ENA for a system for which no previous information concerning its corrosion mechanism is available. So far ENA has been used mainly to detect the onset of localized corrosion and to monitor its progress in a qualitative manner. On-going work at CEEL is devoted to comparisons of information concerning types and rates of localized corrosion processes which can be obtained with EIS and ENA and to evaluate the use of ENA as a corrosion monitoring tool in applications such as MIC. In the following, the application of EIS and ENA to three corrosion systems will be discussed in order to demonstrate this approach. While the results discussed below have been obtained in abiotic solutions, they still illustrate the experimental approach taken in applications of EIS and ENA and form the basis of

future projects to be carried out by the authors in which these techniques will be applied in evaluation of MIC phenomena.

Experimental Results and Discussion

Materials and Methods

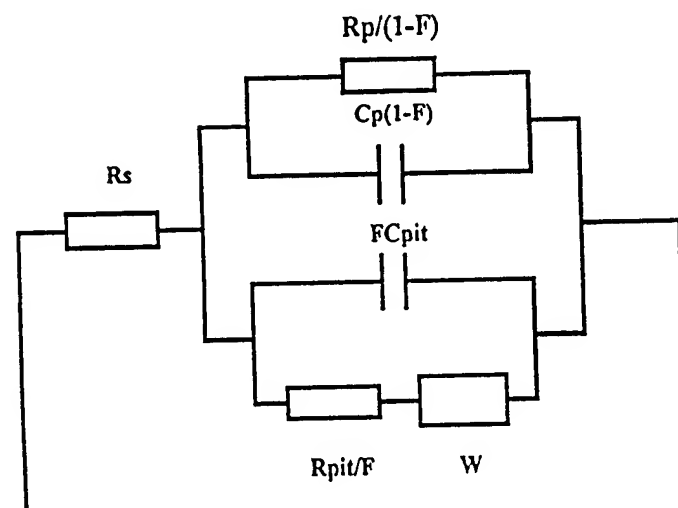
Materials and Test Solutions. In the study of pitting of Al-based materials impedance spectra were obtained for Al 6061 exposed to 0.5 N NaCl. Electrochemical noise data were determined for an Al 2009/SiC, T-8 metal matrix composite (MMC) containing 20% SiC particles and for pure Pt in the same solution. Comparison of EIS and ENA data for pure Fe (99.999 %) were carried out in three solutions of NaCl with different corrosivity. The study of polymer coated cold-rolled steel with EIS and ENA was carried out in 0.5 N NaCl for two different coating systems.

Methods. EIS data for Al 6061 were determined with a three-electrode system using Solartron model 1186 or 1286 potentiostats and a Solartron model 1250 frequency response analyzer (FRA). Impedance spectra were analyzed using the PITFIT software [6]. Potential and current noise data for Al 2009/SiC and pure Fe were determined sequentially for a two-electrode system using a Solartron model 1286 potentiostat as a ZRA and a HP model 3475A voltmeter. The noise data for Al 2009/SiC data were collected over a 4096 sec. time period with a sampling rate of 2 points/sec, while the data for pure Fe were collected during a 500 sec. time period. Noise data for pure Fe were also collected simultaneously using two digital voltmeters (HP 3457A and 3478A) and software developed at CEEL as described elsewhere [7,8]. The same technique was used for the evaluation of two polymer coatings on cold-rolled steel. EIS data were collected for the same two-electrode system after each noise measurement which was carried out for 1024 sec and a sampling rate of 2 points/sec.

1. Localized Corrosion of Al Alloys and Al-Based Metal Matrix Composites.

Mansfeld and co-workers have demonstrated that the pitting model shown in Fig. 1 can be used to determine pit growth rates from impedance spectra collected at the corrosion potential E_{corr} [6,9]. C_p and R_p refer to the passive surface, while C_{pit} , R_{pit} and W are properties of active pits. Fig. 2 shows experimental data for Al 6061 in the untreated condition (Fig. 2a and b) and after surface modification in the Ce-Mo Process which produces excellent resistance to localized corrosion (Fig. 2c) [10,11]. This is demonstrated by the capacitive nature of the Bode

plots in Fig. 2c, the very high values of R_p and the lack of change in the impedance data during exposure to 0.5 N NaCl for 30 days.



$$0 \leq F \leq 1, W = (K/F)(j\omega)^n, n < 0$$

Fig. 1. Pitting model for Al alloys

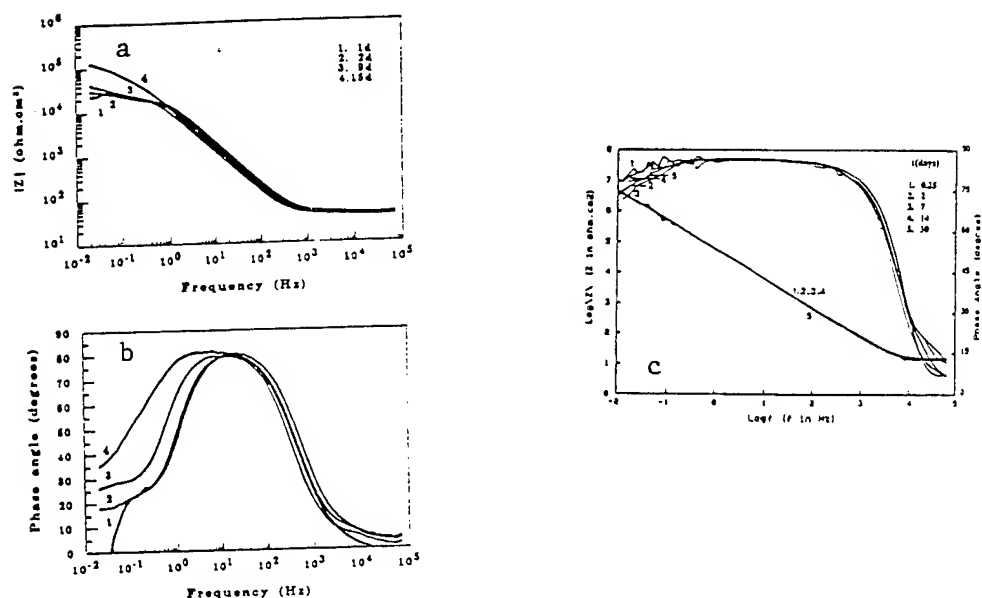


Fig. 2. Impedance spectra for untreated (Fig. 2a and b) and surface modified (Fig. 2c) Al 6061 with different exposure times in 0.5 N NaCl

Determination of pit growth rates for the untreated samples requires calculation of the specific pit polarization resistance $R_{pit}^0 = R_{pit} \times A_{pit}$ from the fit parameter R_{pit} and the pitted area A_{pit} as a function of exposure time. $A_{pit} = 2FA$ is calculated from the time dependence of the area fraction F at which pitting occurs (Fig. 1) and the total area A assuming hemispherical pits [12]. Fig. 3 shows the time dependence of R_{pit} (Fig. 3 a) and A_{pit} (Fig. 3 b) for two samples of Al 6061 with different surface preparation (as-received vs. polished). Pit growth rates v_{pit} have been expressed as [11]:

$$v_{pit} = a(t - t_0)^b \quad (1),$$

where t_0 is the time at which pits were first observed and a and b are parameters which have to be determined experimentally.

Since v_{pit} is proportional to $1/R_{pit}^0$, Eq. 1 can be written as:

$$\log (1/R_{pit}^0) = \log a' + b \log (t - t_0) \quad (2)$$

in order to apply the experimental impedance data, i.e. R_{pit}^0 .

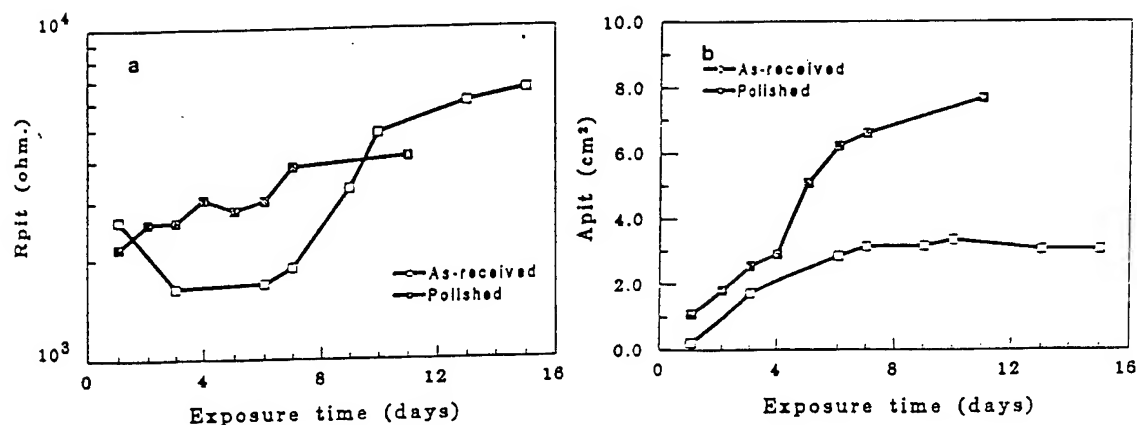


Fig. 3. Time dependence of R_{pit} (Fig. 3a) and A_{pit} (Fig. 3b) for untreated (as-received vs. polished) Al 6061 exposed to 0.5 N NaCl

Experimental results for Al 6061 based on the data in Fig. 3 are shown in Fig. 4, where pits originated during the first day of exposure ($t_0 < 1$ day). Straight lines with a slope close to -1 were obtained in log - log plots. Pit growth rates were higher for as-received sample (Fig. 4). For Al 2024, 6061 and 7075 exposed to 0.5 N NaCl it was found that b was close to -1 as shown in Table I which lists t_0 and the fit parameters $\log a'$ and b . According to Eq. 1 with $b = -1$, pit growth rates are inversely proportional to exposure time [12]. It has to be noted that these measurements were carried under natural conditions, i.e. at E_{corr} , rather than at an applied potential exceeding the pitting potential. The pit growth law in Eq. 1 can be used to make lifetime predictions based on short-time laboratory investigations.

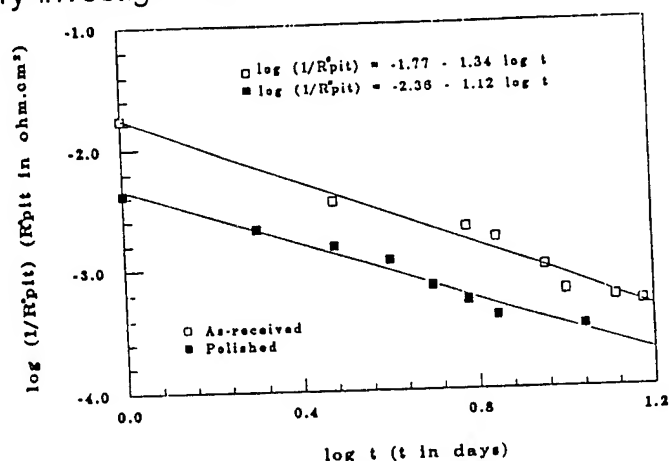
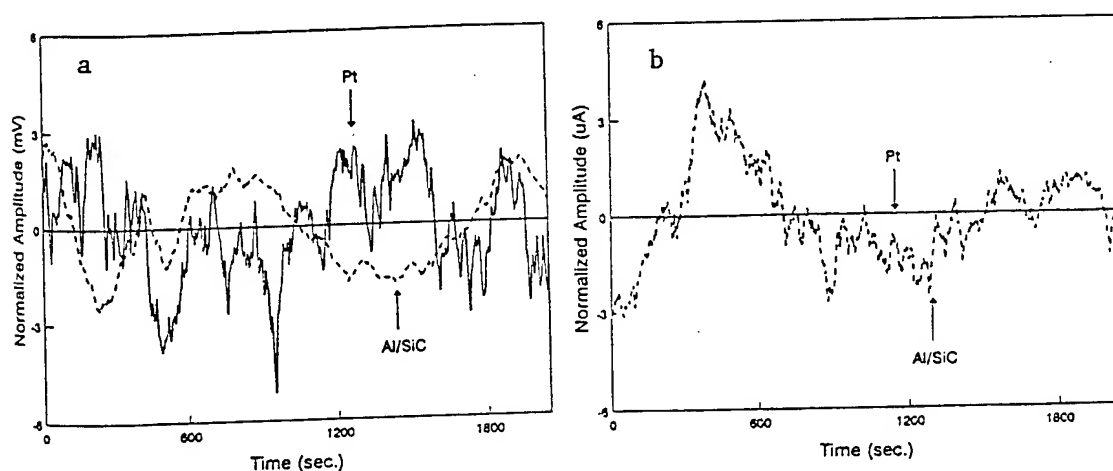


Fig. 4. Time dependence of $1/R^0_{\text{pit}}$ for untreated (as-received vs. polished) Al 6061 exposed to 0.5 N NaCl

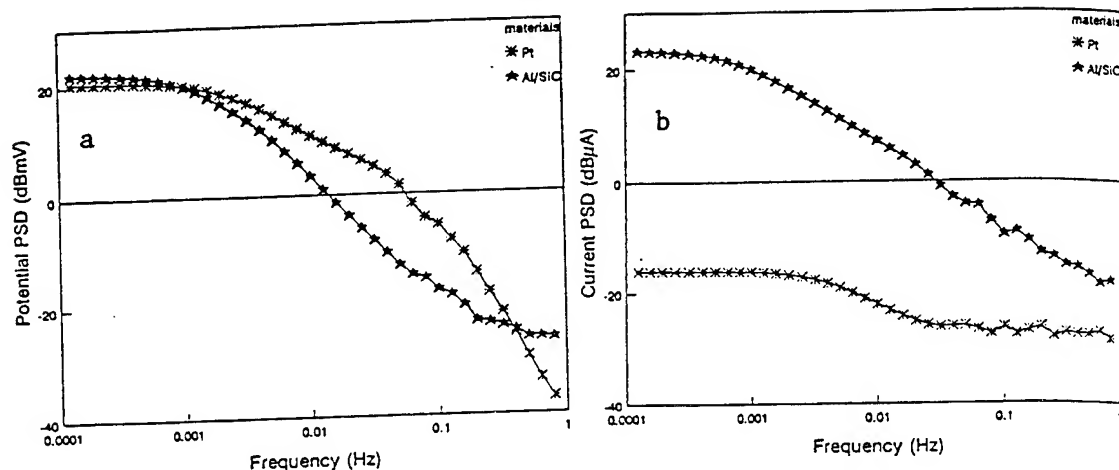
Table I Parameters $\log a'$, b and t_0 in pit growth law for Al alloys

Alloy	$\log a'$	b	t_0 (days)
Al 7075-T6/passivated in CeCl_3	-3.00	-0.99	>25
Al 7075-T6/polished	-1.50	-1.35	≤ 1
Al 7075-T73/as-received	-1.93	-1.07	≤ 1
Al 7075-T73/deoxidized	-1.84	-1.11	≤ 1
Al 6061-T6/as-received	-1.77	-1.34	≤ 1
Al 6061-T6/polished	-2.36	-1.35	≤ 1
Al 6013-T6/as-received	-1.89	-0.86	≤ 1
Al 6013-T6/modified by Ce-Mo	-2.28	-1.25	>30

Electrochemical noise data have been obtained in the time domain as potential and current noise for an Al 2009/SiC MMC during exposure to 0.5 N NaCl (open to air). For comparison, noise data have also been collected for Pt in the same solution. Fig. 5a shows the potential noise data obtained during the first day of immersion during which pits initiated on the MMC which is very susceptible to localized corrosion. The noise data in Fig. 5 were normalized to remove the drift of the mean value during the measurement time. The potential noise fluctuations were of similar magnitude for both materials (Fig. 5a). However, the current noise were very large for the MMC and very small for Pt (Fig. 5b). The potential noise fluctuations for Pt, which is inert and has a poorly biased open-circuit potential, are considered due to minor changes in the mass transport conditions during the measurement. Obviously, only the current noise fluctuations are uniquely related to corrosion phenomena. The experimental data in Fig. 5 have been analyzed using power spectral density (PSD) plots. For the potential noise data similar dc limits were observed in the PSD plots for both materials (Fig. 6a). The slope in the linear region of the PSD plot was about - 20 dB for the MMC, while a more complicated frequency dependence was observed for Pt. In the current PSD plot the dc limit was very low and close to the background noise of the potentiostat for Pt, while it was very high for the MMC. The slope in the linear region for the MMC was about - 15 dB. These results show that measurements of potential noise alone can be misleading in terms of evaluation of the (localized) corrosion behavior.



5. Normalized potential noise (Fig. 5a) and current noise (Fig. 5b) data for an Al 2029/SiC MMC and Pt exposed to 0.5 N NaCl.



6. Potential (Fig. 6a) and current (Fig. 6b) PSD plots for Al 2009/SiC MMC and Pt exposed to 0.5 N NaCl (data of Fig. 5)

Fig. 7 shows potential and current PSD plots for the Al 2009/SiC MMC exposed to 0.5 N NaCl for 14 days. The potential PSD plots did not change much with exposure time (Fig. 7a). A dc limit was observed at the lowest frequencies and a linear portion in the PSD plots at higher frequencies with a slope of about -20 dB was found for all exposure times. The current PSD plots displayed essentially the same features, however the dc limit, which is considered to be related to the intensity of localized attack, decreased sharply after one day and the slope was about -15 dB (Fig. 7b). The results from the current noise data agree with the observation based on EIS data that for this MMC pitting is severe in the earliest stages of exposure, but decreases in intensity with time. Attempts to correlate the characteristic parameters of the PSD plots such as dc limit, roll-off frequency and slope (Fig. 6 and 7) with the rate and type of the corrosion reaction have been made [13]. In addition, the noise resistance R_n defined as the ratio of the standard deviation of potential and current noise data has been used to follow the time dependence of localized corrosion processes for Al alloys and Al-based MMCs.

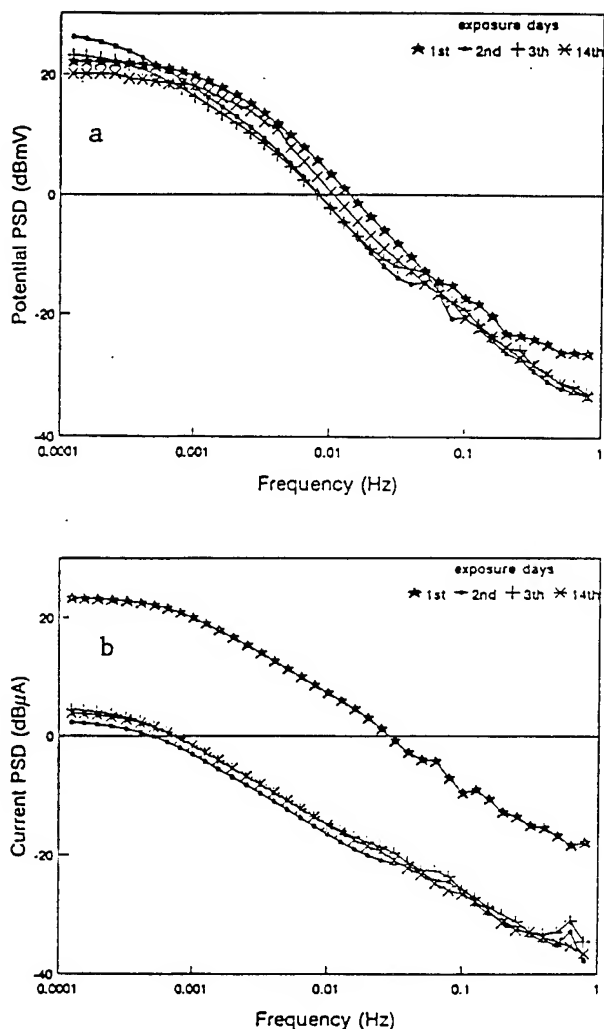


Fig. 7. Potential (Fig. 7a) and current (Fig. 7b) PSD plots for Al 2009/SiC MMC exposed to 0.5 N NaCl for 14 days.

2. Iron Exposed to NaCl Solutions of Different Corrosivity

This model system has been used to evaluate the relationship of R_p determined by EIS with the noise resistance R_n obtained from ENA [7,8]. The noise resistance R_n is defined as the ratio of the standard deviation of the potential fluctuations ($\sigma\{V(t)\}$) and the standard deviation of the current fluctuations ($\sigma\{I(t)\}$) determined from electrochemical noise data [13]:

$$R_n = \sigma\{V(t)\} / \sigma\{I(t)\} \quad (3)$$

Fig 8 shows the time dependence of the mean values of E_{corr} , while the mean values of the coupling current are plotted in Fig. 9 for pure iron exposed to 0.5 N NaCl which was saturated with air, deaerated or contained 10 mM NaNO_2 as inhibitor. E_{corr} was measured vs. a reference electrode (SCE) as the potential of two iron electrodes connected to a potentiostat which acted as a ZRA, while the coupling current between the two electrodes was measured at the potentiostat

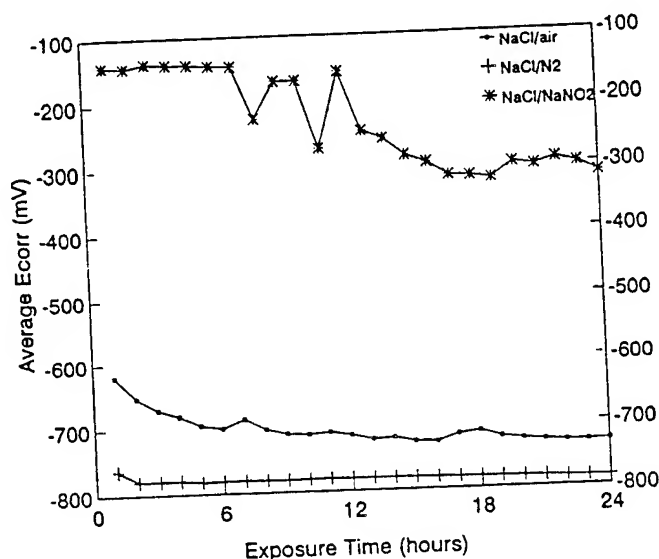


Fig. 8. Time dependence of the mean value of E_{corr} for iron exposed to solutions of different corrosivity.

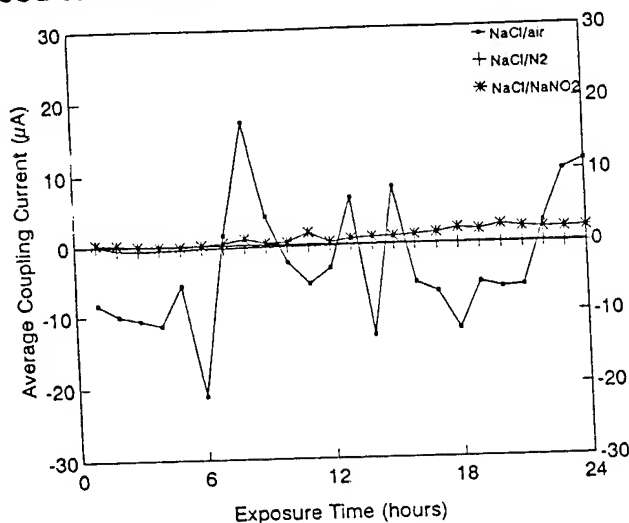


Fig. 9. Time dependence of the mean value of the coupling current for iron exposed to solutions of different corrosivity.

output [7,8]. The $\sigma\{V(t)\}$ and $\sigma\{I(t)\}$ data are plotted as a function of exposure time in Fig. 10 and 11, respectively. The time dependence of R_n determined according to Eq. 3 is shown in Fig. 12. R_n had the highest values for the inhibited solution and the lowest values with the most pronounced fluctuations for the NaCl solution open to air. It will be noted that the values of $\sigma\{V(t)\}$ (Fig. 10) are the highest for the solution with the lowest corrosivity (Fig. 12) for which very low values of $\sigma\{I(t)\}$ were recorded. This result shows again that potential noise data alone cannot be used to determine corrosion kinetics and mechanisms.

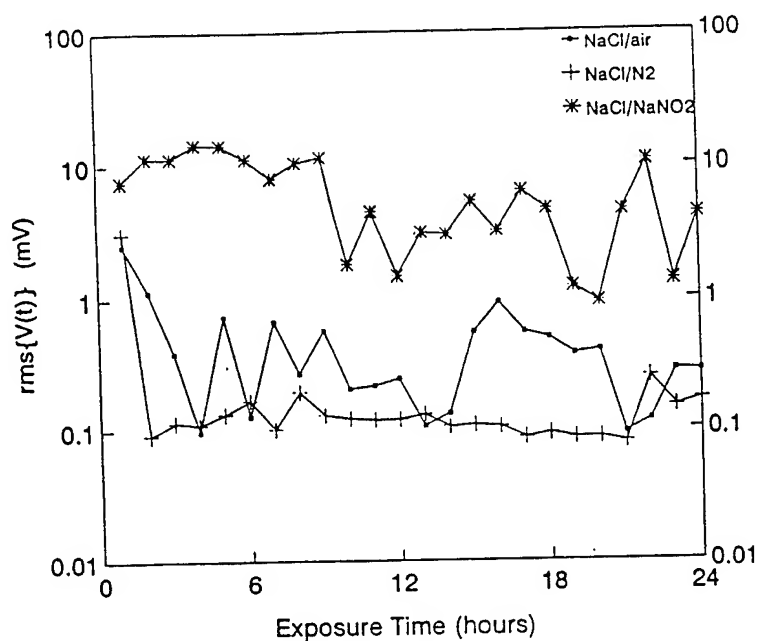


Fig. 10. Time dependence of $\sigma\{V(t)\}$ for iron exposed to solutions of different corrosivity.

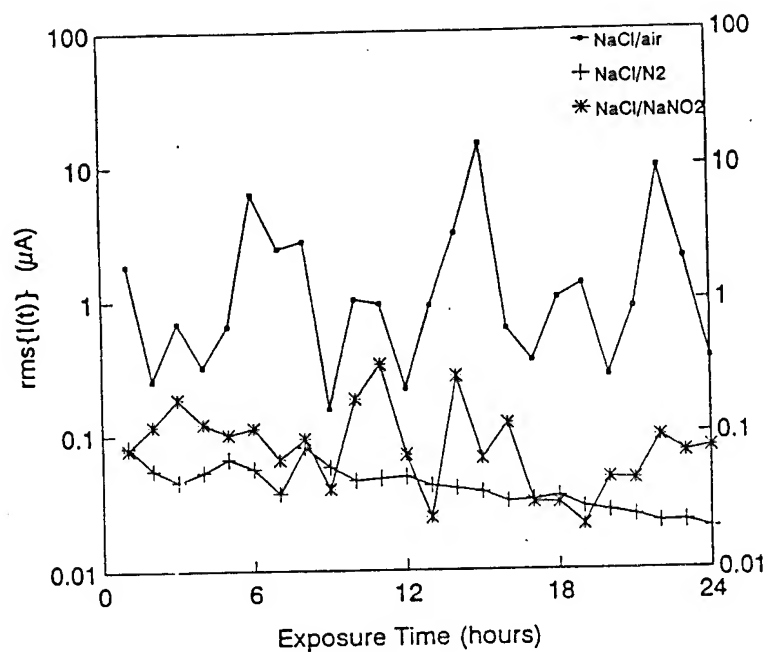


Fig. 11. Time dependence of $\sigma\{I(t)\}$ for iron exposed to solutions of different corrosivity.

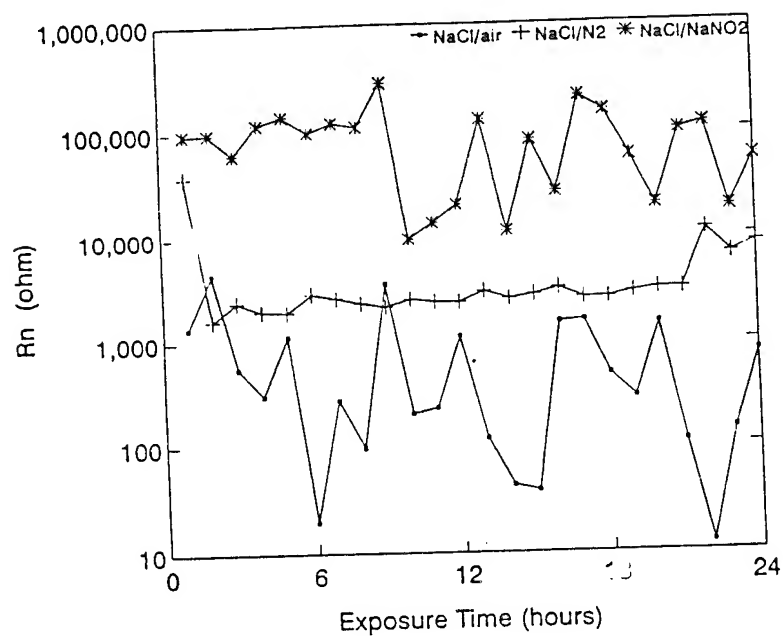


Fig. 12. Time dependence of noise resistance R_n for iron exposed to solutions of different corrosivity

At the end of the 24 hour exposure time EIS data were obtained for the three systems. From these data the polarization resistance R_p was obtained by fitting to a simple one-time-constant model. Satisfactory agreement between R_p and R_n was observed (Table II).

Table II. Comparison of R_n and R_p for three different test environments

	open to air	deaerated (N_2)	inhibited ($NaNO_2$)
$R_n(K\Omega)$	0.8	8.3	54.7
$R_p(K\Omega)$	1.6	15.9	22.1

Recently, a new experimental approach has been introduced which allows simultaneous collection of potential and current noise [7,8]. From these data R_n can be obtained, but it is also possible to construct noise spectra in which the spectral noise data are plotted as a function of frequency after transformation of the experimental data from the time domain into the frequency domain using FFT. The ratio $R_{sn} = V(f)/I(f)$ of the values for potential $V(f)$ and current noise $I(f)$ at each frequency is recorded from which the spectral noise resistance R_{sn}^0 can be determined as the limit of $R_{sn}(f)$ for zero frequency:

$$R_{sn}^0 = \lim_{f \rightarrow 0} \{R_{sn}\} \quad (4).$$

Fig. 13 shows noise spectra for iron exposed for 1 and 24 h to NaCl with and without $NaNO_2$. For the uninhibited solution R_{sn} is low and independent of frequency, while for the inhibited solution a slope close to -0.5 is observed. A comparison of R_p , R_n and R_{sn}^0 is given in Table III for the two solutions. Satisfactory agreement between R_p obtained from EIS and R_n and R_{sn}^0 obtained from ENA is observed. It has to be emphasized that a theoretical analysis of the relationship of R_n and R_{sn}^0 to R_p and (localized) corrosion rates does seem not exist at present.

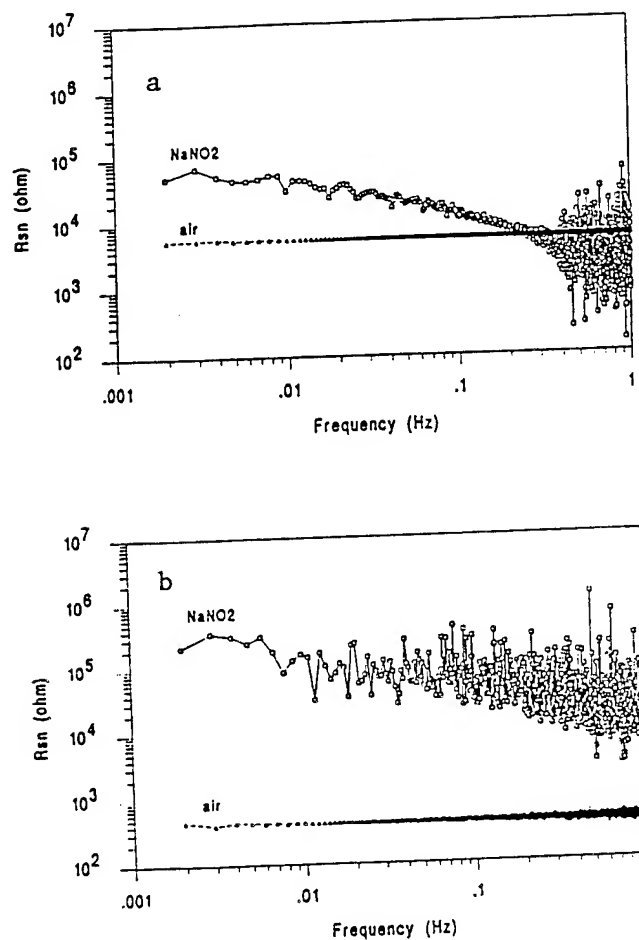


Fig. 13. Noise spectra for iron exposed to 0.5 N NaCl (open to air) with and without 10 mM NaNO₂ for 1 h (Fig. 13a) and 24 h (Fig. 13b).

Table III. Comparison of R_n , R_{sn}^0 and R_p for simultaneously recorded noise data

	open to air	inhibited (NaNO ₂)
$R_n(K\Omega)$	0.4	195.8
$R_{sn}^0(K\Omega)$	0.4	79.1
$R_p(K\Omega)$	1.4	220.0

3. Polymer Coatings on Steel

One of the most successful applications of EIS is the evaluation of the properties of polymer coatings on metals and their degradation with exposure time to corrosive environments which leads to corrosion at the metal/coating interface [4,5]. Mansfeld and Tsai [5,15,16] have shown that the fit parameters obtained for the coating model or certain parameters measured in the high-frequency region can be used to monitor coating degradation. For an alkyd system (CR 2) on cold-rolled steel exposed to 0.5 N NaCl, it was shown that initially the main degradation process was disbonding of the coating, while at longer exposure times the coating resistivity decreased as conducting paths developed [5,16,17]. Fig. 14 shows the time dependence of the delamination ratio $D = A_d/A$, where A_d is the delaminated area and A the total area, calculated as the average value from three parameters (C_{dl} , f_b/f_{min} and Φ_{min}) obtained from the analysis of the impedance spectra in Fig. 15 [5,17]. These parameters are identified in the model for polymer coatings and a theoretical impedance plot in Fig. 16. It was assumed that $D = 10^{-4}$ after 32 days. D increased by a factor of thirty during immersion for four months. In Fig. 17, the parameter $f_b/(f_{min})^2 = 2\pi d\rho C_{dl}^0 = k\rho$ is plotted which can be used to determine changes of the coating resistivity ρ assuming that the coating thickness d and the specific double layer capacitance C_{dl}^0 remain constant during exposure. For $d = 25 \mu\text{m}$ and $C_{dl}^0 = 30 \mu\text{F}/\text{cm}^2$ a decrease of ρ from about $2 \cdot 10^{10} \text{ ohm.cm}$ to $3 \cdot 10^7 \text{ ohm.cm}$ is estimated between one and five months exposure for CR 2 [5,17]. These results demonstrate that EIS is capable of detecting localized corrosion phenomena such as disbonding of the coating and initiation of corrosion at the metal coating/interface as well as deterioration of the polymer coating and loss of its protective properties.

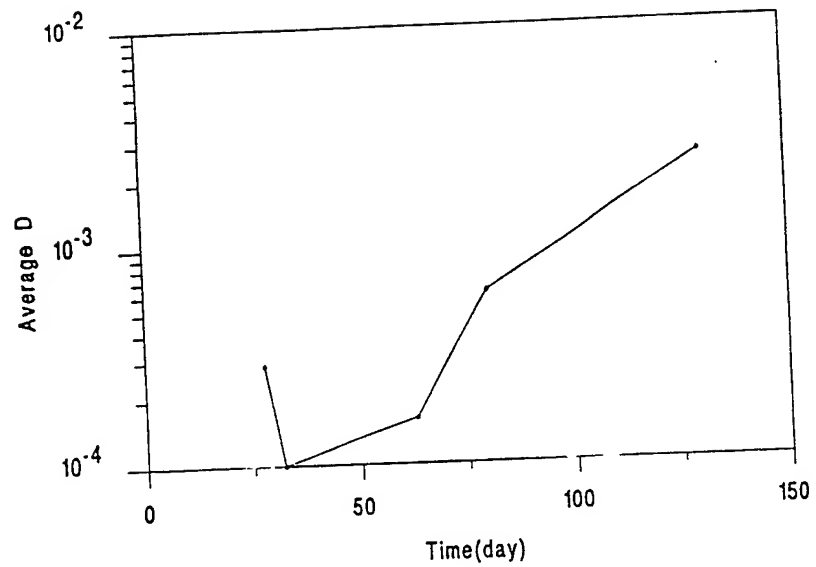


Fig. 14. Time dependence of the averaged delamination ratio D for coating system CR 2 exposed to 0.5 N NaCl (open to air)

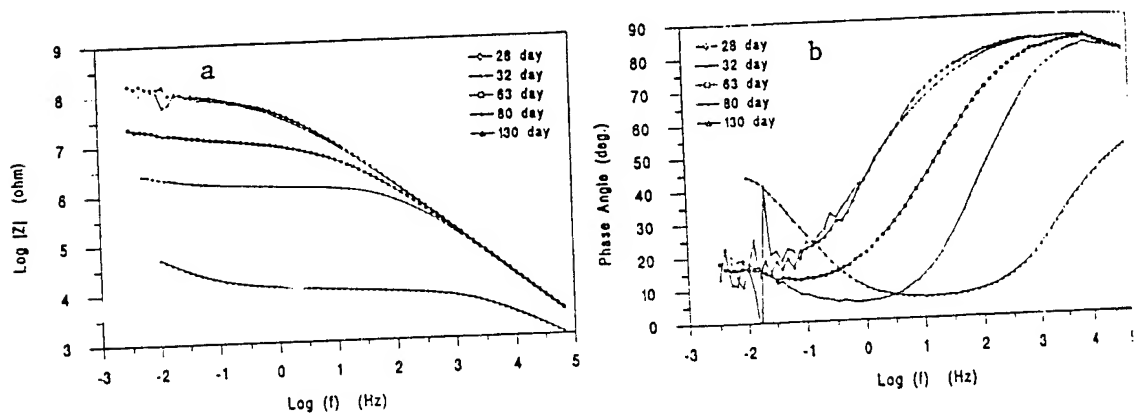


Fig. 15. Bode plots for CR 2 during exposure to 0.5 N NaCl

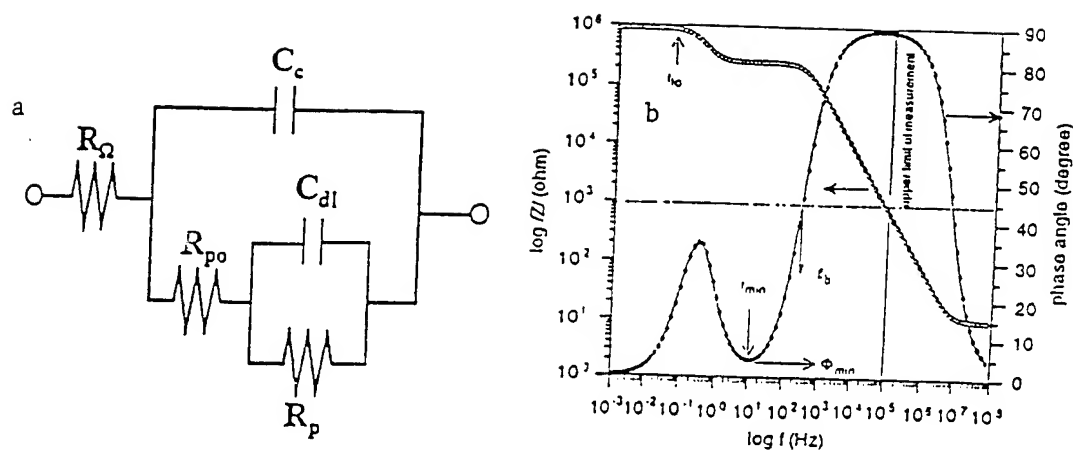


Fig. 16. Model for impedance of polymer coated steel (Fig. 16a) and theoretical impedance plot (Fig. 16b)

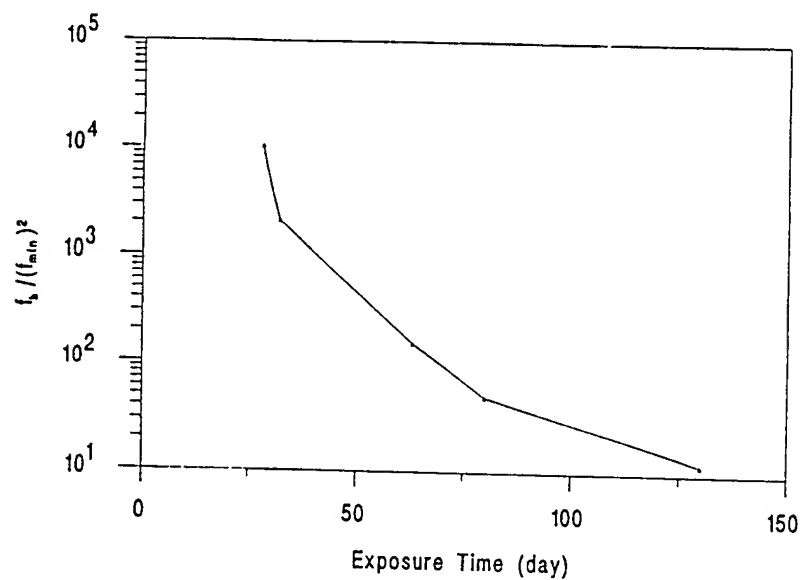


Fig. 17. Time dependence of $f_b/(f_{min})^2$ for coating system CR 2 exposed to 0.5 N NaCl.

The same coating system has been studied with ENA [17]. Fig. 18 shows a comparison of experimental potential (Fig. 18a) and current (Fig. 18b) noise data for CR 2 at exposure times of 28 and 130 days. It can be seen that the potential fluctuations for this less protective coating are much larger in the early stages of exposure than at longer times (Fig. 18a). On the other hand, the current fluctuations are much smaller on the 28th day than on the 130th day of exposure (Fig. 18b). This qualitative evaluation of noise data shows that potential noise levels decrease and current levels increase as the coating degrades. Similar observations were made by Skerry et al [14]. For the more protective epoxy polyamide coating (CR 9) no systematic changes of the noise levels with time were observed [17].

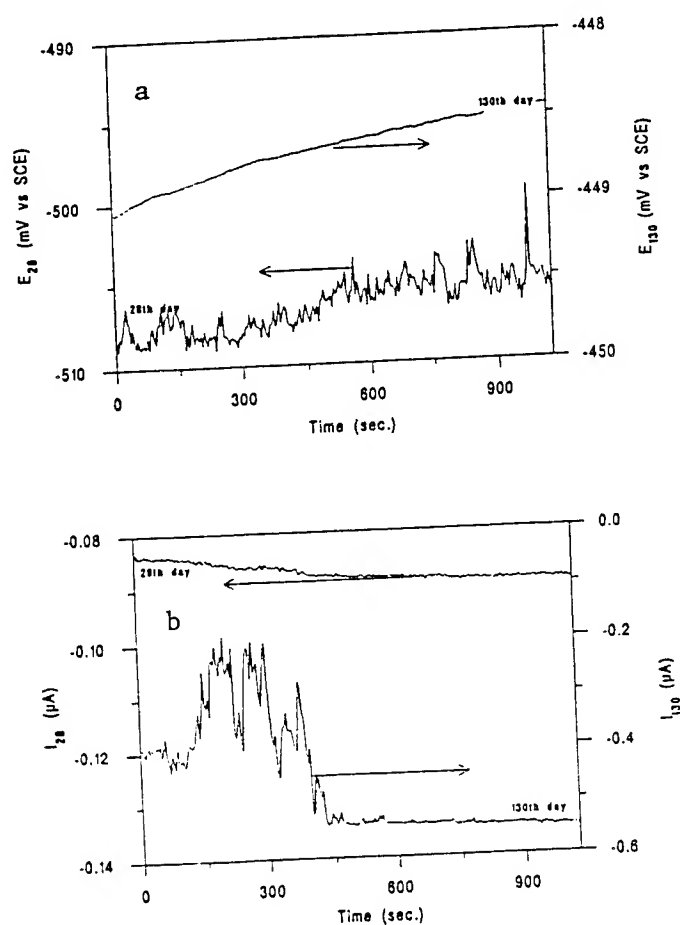


Fig. 18. Experimental potential (Fig. 18a) and current noise data (Fig. 18b) for coating system CR 2 after 28 and 130 days exposure to 0.5 N NaCl.

Noise spectra for the alkyd coating (CR 2) and the epoxy coating (CR 9) after exposure for 28 and 130 days are shown in Fig. 19. In all cases R_{sn} is independent of frequency with higher values for CR 9 for which no indication of deterioration and/or loss of corrosion protection was observed. The resistive parameters obtained from statistical and spectral noise analysis are plotted in Fig. 20. For CR 2 R_n and R_{sn}^0 decreased with time, while for CR 9, R_n and R_{sn}^0 remained at much higher values and did not change significantly with time indicating that degradation of the coating had not occurred in agreement with previous observations [5,16].

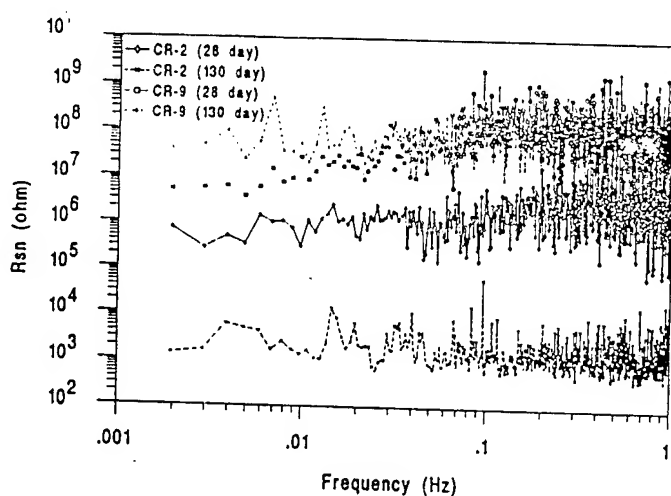


Fig. 19. Spectral noise plots for coating systems CR 2 and CR 9 after exposure to 0.5 N NaCl for 28 and 130 days.

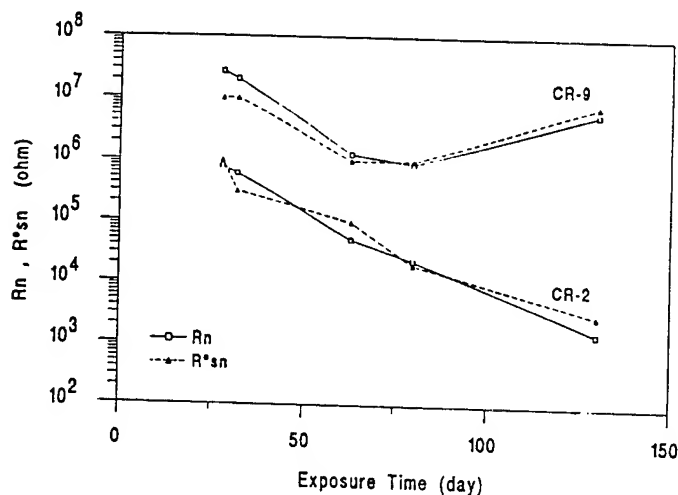


Fig. 20. Time dependence of R_n and R_{sn}^0 for CR 2 and CR 9.

In Fig. 21 the same time dependence of R_n and R_{sn}^o obtained from ENA and R_p and R_{po} obtained from EIS is observed. The numerical values of R_n and R_{sn}^o are very similar, but much lower than those of R_{po} and R_p . A comparison of the results obtained with EIS and ENA suggests that more detailed information concerning loss of corrosion protection with time can be obtained from EIS by analyzing the changes of individual fit parameters such as C_c , R_{po} , R_p and C_{dl} using known correlations of these parameters with water-uptake of the coating, decrease of coating resistivity and increase of the delaminated area, respectively [5,15,16].

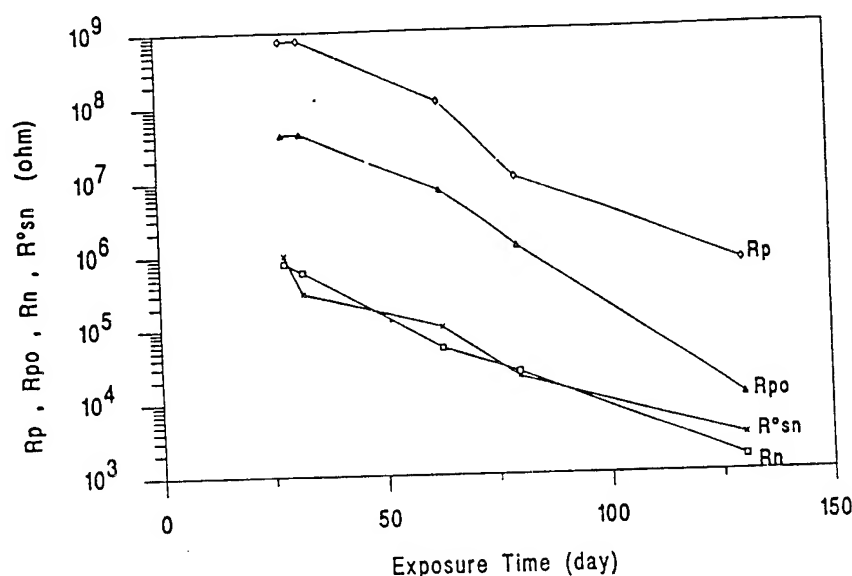


Fig. 21. Time dependence of R_p , R_{po} , R_n and R_{sn}^o for coating system CR 2 exposed to 0.5 N NaCl

The coatings CR 2 and 9 together with 10 other coating systems will be evaluated further in a joint project with J. Jones-Meehan and B. Little during exposure to natural seawater in Port Hueneme, California and Ft. Lauderdale, Florida and to artificial seawater. EIS and ENA data will be collected over six months periods using the techniques described above. After exposure samples will be evaluated with the environmental SEM (ESEM) by B. Little and co-workers to determine the structure of the biofilm, location of bacteria and damage to the polymer coating. Samples exposed by J. Jones-Meehan and co-workers to different

colonies of bacteria will be evaluated by EIS to determine changes of coating properties and the extent of corrosion at the metal/coating interface and by ESEM.

Summary and Conclusions

Both EIS and ENA can be used to obtain important kinetic information for different corrosion systems. At the present state of our understanding of ENA it seems that more detailed information can be derived from EIS data which are collected in a very wide frequency range. This conclusion has been reached from the analysis of EIS and ENA data for three different systems: Al/NaCl, Fe/NaCl and polymer coated steel/NaCl. Analysis of EIS data for polymer coated metals allows estimation of water uptake of the coating from the increase of C_c with time, decrease of coating resistivity, degree of disbonding of the coating and initiation of corrosion at the metal/coating interface based on the parameters shown in Fig. 16a and b. Electrochemical noise data are typically observed only for $f < 1$ Hz as shown for the three examples presented here. Analysis of noise data by statistical methods results in R_n , while from spectral analysis R_{sn}^0 can be obtained. While R_n and R_{sn}^0 have shown similar changes with time as R_p and R_{po} for a polymer coating with relatively poor performance, their numerical values are much lower than those of R_{po} and R_p . Both R_n and R_{sn}^0 remained at much higher values for the coating with excellent performance than for the coating with poorer performance.

The advantages of ENA are the low cost of equipment and the relatively simple methods for data collection which makes this method very attractive for corrosion monitoring. A disadvantage at present seems to be the difficulty of data interpretation. Further research concerning the correlation of potential and current noise with different phenomena occurring during localized corrosion is needed. Eventually, the main application of ENA might be found in corrosion monitoring using the simple statistical approach leading to R_n or more complicated analyses in the frequency domain in the form of PSD plots resulting in parameters related to corrosion phenomena or of spectral noise analysis leading to R_{sn}^0 .

More information concerning the application of EIS and ENA to MIC will become available in a project funded by the Office of Naval Research in which 12 different polymer coating systems will be exposed to natural seawater for six months periods at two locations and to

different colonies of bacteria. The experimental approach to be taken will be similar to that described above.

References

1. F. Mansfeld, S. Lin, S. Kim and H. Shih, J. Electrochem. Soc. 137, 78 (1990)
2. F. Mansfeld, S. Lin, S. Kim and H. Shih, Electrochim. Acta 34, 1123 (1989)
3. F. Mansfeld and B. Little, Corr. Sci. 32, 247 (1991)
4. F. Mansfeld and W. J. Lorenz, in "Techniques for Characterization of Electrodes and Electrochemical Processes", J. Wiley, 1991, p. 581 - 647
5. F. Mansfeld, "The Use of EIS for the Study of Corrosion Protection by Polymer Coatings - A Review", submitted to J. Appl. Electrochem.
6. F. Mansfeld, H. Shih, H. Greene and C. H. Tsai, ASTM STP 1188, 37 (1993)
7. F. Mansfeld and H. Xiao, J. Electrochem. Soc. 140, 2205 (1993)
8. F. Mansfeld and H. Xiao, Proc. 12th Int. Corrosion Congress, Houston, TX, Sept. 1993, p. 1388
9. F. Mansfeld, Y. Wang, S. H. Lin, H. Xiao and H. Shih, ASTM STP 1188, 297 (1993)
10. F. Mansfeld, H. Shih and Y. Wang, J. Electrochem. Soc. 138, L74 (1991)
11. F. Mansfeld, Y. Wang and H. Shih, Electrochim. Acta 37, 2277 (1992)
12. F. Mansfeld, Y. Wang, H. Xiao and H. Shih, in Proc. "Critical Factors in Localized Corrosion", The Electrochem. Soc., Proc. Vol. 92-9, p. 469 (1992)
13. F. Mansfeld and H. Xiao, in Proc. Symp. "Biofouling and biocorrosion in Industrial Water Systems", ACS, Washington, D.C., August 1992, Lewis Publ. (in press)
14. B. S. Skerry and D. A. Eden, Prog. Org. Coat. 15, 269 (1987); B. S. Skerry, A. Alavi and K. I. Lindgren, J. Coat. Techn. 60, 97 (1988); C. T. Chen and B. S. Skerry, Corrosion 47, 598 (1991)
15. F. Mansfeld and C. H. Tsai, Corrosion 47, 958 (1991)
16. C. H. Tsai and F. Mansfeld, Corrosion 49, 726 (1993)
17. H. Xiao and F. Mansfeld, "Evaluation of Coating Degradation with EIS and ENA", J. Electrochem. Soc. (in press)

Identification of Sulfate-Reducing Bacteria in Saline Oil Field and Navy Platform Samples by Reverse Sample Genome Probing

Dr. Gerrit Voordouw, Department of Biological Sciences, The University of Calgary, 2500 University Drive NW, Calgary (Alta), T2N 1N4, Canada

Dr. Joanne Jones-Meehan*, Naval Surface Warfare Center, 10901 New Hampshire Avenue, Silverspring, MD 20903-5000

Abstract

Reverse sample genome probing (RSGP) allows fingerprinting of environmental microbial communities in a single hybridization step. Application of this method to the analysis of microbial communities present on installed corrosion coupons in oil treaters in saline oil fields in Alberta indicated that of 20 different bacterial standards (defined as bacteria with little or no genomic crosshybridization), including 15 SRB only a few *Desulfovibrio* species were highly enhanced in the metal-associated biofilm, suggesting that these may be particularly active in promoting metal corrosion.

RSGP analysis of nine Navy platform isolates with master filters containing genomes of SRB from saline oil fields indicated the presence of significant amounts of two of these "corrosive" *Desulfovibrio* species in five of the nine platform isolates. The presence of these two *Desulfovibrio* species may correlate with the potential of the platform isolates to cause microbially influenced metal corrosion.

Introduction

Sulfate-reducing bacteria have been implicated as major causative agents of microbially influenced metal corrosion (MIC). MIC can develop whenever metal (e.g. iron) surfaces contact a non-sterile aqueous phase. Bacteria in the bulk liquid adhere to the metal to form a biofilm. Even when the bulk liquid phase is aerobic, anaerobic conditions may develop

in the underlying portions of the biofilm [1-3]. Under these conditions, SRB develop in the biofilm, especially when the bulk aqueous phase contains sulfate, the terminal electron acceptor for many of these bacteria. The precise mechanism of MIC and the function of SRB in this mechanism is not resolved. SRB are generally thought to accept low potential electrons from the metal surface (either through hydrogen as an intermediate, or via conduction through iron sulfide) [1, 4, 5, 6]. These electrons reduce sulfate to sulfide through a cytoplasmic sulfate reduction pathway. The excreted sulfide combines with the dissolving metal ions to form an FeS precipitate. SRB can thus catalyze an efficient anaerobic corrosion cycle. Because the resulting corrosion is highly localized (pitted [1]) substantial damage to metal walls of pipelines etc. can be done in rather short periods of time, which eventually leads to rupture or equipment failure. In assessing the ability of an environment to catalyze MIC, SRB are evaluated with a microbiological, gene or enzyme probe assay. In deciding on an appropriate SRB assay it must be recognized that SRB are a widely divergent bacterial group: in the eubacterial domain alone eight different genera are now recognized based on nutritional properties and 16S rRNA sequencing [7, 8]. An assay can either be generic (lumping together all eubacterial and possibly also archaeobacterial SRB by assaying a property that they all share) or specific (measuring the presence of a given species only). A survey of methods that can be used to evaluate SRB was presented recently [9]. The well known lactate-sulfate test in which the most probable number of SRB is evaluated in anaerobic media containing lactate as the carbon and energy source measures many (but not all) of the eubacterial SRB genera. The RSGP method is, on the other hand, species specific.

Reverse Sample Genome Probing

The RSGP method exploits the observation that chromosomal DNAs from different bacteria found in the environment often display little crosshybridization (<1%) in dot blots. A given chromosomal DNA can therefore be used as a specific probe for monitoring the presence of the bacterial species from which this DNA was isolated. This often holds true even for bacterial species within the same genus. As an example, many *Desulfovibrio* species have been isolated that display very little genomic crosshybridization [10, 11]. This is in agreement with the finding by 16S rRNA sequencing that this genus contains several deeply branching lineages [12]. Species with highly crosshybridizing genomes cannot be distinguished and these are operationally defined as being represented by the same standard. Although total DNA from an environmental sample can in principle be analyzed by sequentially hybridizing this DNA preparation with genomic probes for a diversity of standards, a more

PHASE I: Generation of targeted master filters.

- (i) Isolate a variety of bacteria from the target environment.
- (ii) Purify chromosomal DNA from cultures of these isolates.
- (iii) Define bacterial standards by evaluating crosshybridization of chromosomal DNAs in dot blots.
- (iv) Spot a defined amount of denatured chromosomal DNA for each standard, as well as for the internal standard λ , in defined positions of a filter membrane to create a master filter for analysis of the target environment.

PHASE II: Reverse sample genome probing.

- (i) Isolate total DNA from sample (S).
- (ii) To 100 ng of S add 100 pg of λ DNA. Label randomly. Hybridize master filter with the labeled, denatured reverse genome probe S*.
- (iii) Remove unbound probe by washing. Dry filter and autoradiograph.

RESULT:

In the example below the reverse genome probe is hybridized to a master filter containing 18 standard genomes as well as λ DNA.

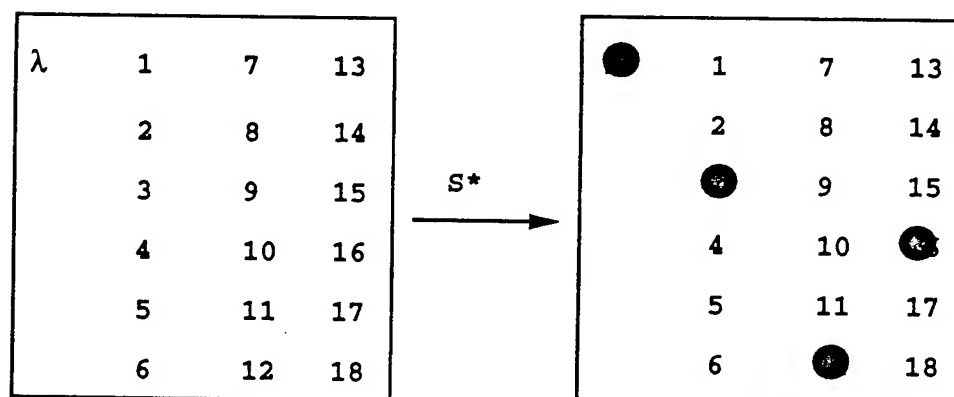


Fig. 1 Principle of RSGP

rapid way of analyzing a preparation of total environmental DNA is to first create a master filter, on which known amounts of denatured genomic DNA from a variety of standards isolated from the target environment (e.g. by colony purification on the appropriate plating media) are spotted (Fig. 1: PHASE I). Total community analysis is now achieved in a single step by hybridizing a randomly labeled reverse genome probe, spiked with a defined amount of an internal standard (λ DNA), with the master filter (Fig. 1: PHASE II). The result in Fig. 1 does not necessarily mean that the sample DNA preparation contains only genomes 3, 12 and 16, e.g. the community structure could be more complex if not all standards present in the community are represented on the filter. The use of adding the internal standard (λ) for RSGP analyses [13] is that it allows conclusions to be drawn in the following cases:

- (i) Lack of hybridization with the internal standard (λ) and any of the standards 1 to 18 indicates failed labeling of the spiked sample DNA preparation.
- (ii) Lack of hybridization to any of the standards 1 to 18 with good hybridization to λ indicates that the standard genomes on the filter do not represent those in the sample.

In earlier studies [10, 11] the denatured sample DNA preparation was spotted on the master filter as a positive control (Fig. 2 A to D: S). Although qualitatively this also allows evaluation of (i) and (ii), it prevents subsequent quantitation of the hybridization signals. The reason for this is that the signal strength of sample selfhybridization is not constant but dependent on complexity (the number of different genomes present in the sample and their fractions f_x). Addition of a fixed fraction f_λ of an internal standard genome (e.g. λ DNA) to the sample DNA, random labeling of the spiked DNA preparation and hybridization of the resulting spiked reverse genome probe to a master filter which contains spots with known amounts (c_λ) of the denatured internal standard genome gives hybridization intensities (I_λ) which are, in principle, constant and to which the other hybridization intensities (I_x) can be related for purposes of quantitation.

Qualitative RSGP

A variety of DNA preparations can be obtained from an environmental sample and used for RSGP analysis. Following collection of a sample (e.g. from soil, from oil field production waters, or a corrosion coupon) part can be transferred to a culture medium to enhance a specific bacterial fraction. As an example injection of part of the sample into liquid Pfennig's media [7], leads to selection of SRB. Depending on

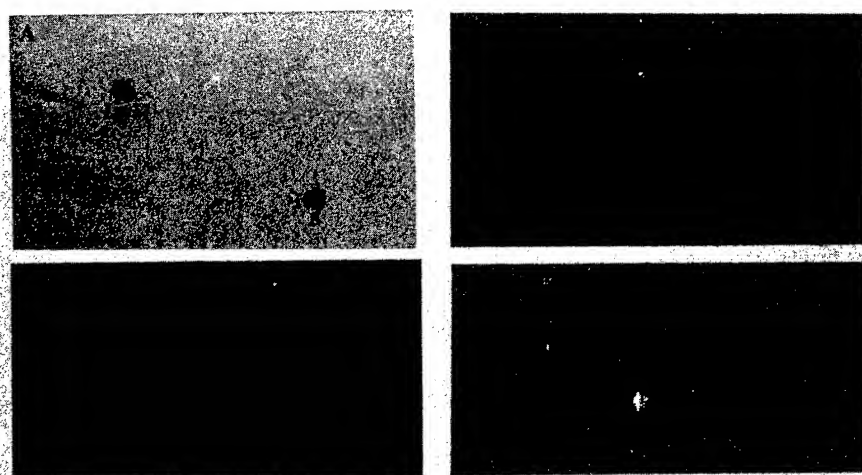


Fig. 2 Identification of SRB by qualitative RSGP. Chromosomal DNA was extracted either from cultures of colony purified isolates (A, B) or from liquid enrichment cultures (C, D). The DNAs were labeled and hybridized with a master filter containing 20 ng of denatured genomic DNA for 35 oil field SRB. The sample DNA analyzed was also spotted as a positive control (S). Reprinted with permission from Applied and Environmental Microbiology [11].

the carbon and energy source used (either lactate, ethanol, benzoate, decanoate, propionate or acetate) different SRB may be recovered. These are given three letter names indicating the carbon and energy source to which an identifying number is attached (e.g. *Lac15*, *Ben1* etc.). The liquid enrichment cultures may serve as a source for colony purified isolates. Hybridization of DNAs obtained from liquid enrichment cultures or cultures derived from colony purified isolates obviously does not give quantitative information on the microbial composition of the original environmental sample. These experiments only indicate some of the bacteria that were present. Because liquid enrichment and colony purification lead to a decrease of microbial diversity (relative to that in the original sample) one may expect the fractions f_x of several standard DNAs to be high (typically 10 to 100%). As a result, good results can be obtained by hybridization of DNAs extracted from liquid enrichment cultures to master filters on which relatively small amounts of chromosomal DNAs (20 to 40 ng) for each of the standards have been spotted. Examples of typical experimental results are shown in Fig. 2, in which the sample DNA itself was spotted on the filters to serve as a positive control. The colony purified isolates (Fig. 2: A, B) only show strong hybridization to one of the standards on the filter (*Lac17* and *Lac5*, respectively), indicating their identity to these standards, whereas the liquid enrichment cultures (Fig. 2: C, D) hybridize strongly with three standards (*Dec7*, *Pro10*, *Ben4* and *Ben3*, *Pro1*, *Ben4*, respectively). Most of the lactate grown standards are *Desulfovibrio* species, as verified by hybridization with a specific [NiFe] hydrogenase gene probe [10, 11, 14] and sequence analysis of their 16S rRNA genes [Armstrong et al., unpublished].

Quantitative RSGP

If total DNA, extracted directly from an environmental sample without prior growth, is hybridized with a master filter then the observed hybridization intensities I_x are a direct reflection of the fractions f_x of the standard genomes in the environmental DNA preparation. We assume that the empirical relationship: $I_x = k_x c_x f_x$, where c_x is the amount of standard x spotted on the master filter and k_x is a hybridization constant, holds throughout. Thus for the hybridization of the spiked reverse genome probe with the internal standard λ DNA we obtain: $I_\lambda = k_\lambda c_\lambda f_\lambda$. From these two relations f_x is obtained as:

$$f_x = (k_\lambda/k_x) * (I_x/c_x) * (c_\lambda/I_\lambda) * f_\lambda \quad (1)$$

By labeling defined mixtures of λ and chromosomal DNA for a selected standard and hybridizing these with filters containing known amounts of both it has been shown that $k_\lambda/k_x = (102 \pm 26)$ for SRB standards *Lac3*

and *Lac6* [13]. Possible variations in the ratio (k_{λ}/k_x), caused by different genome sizes of the bacterial standards on a filter cannot be taken into account and the determined value is therefore used in all calculations of f_x . Because lower fractions f_x may be expected in directly extracted environmental DNAs relative to DNAs obtained from enrichment cultures larger amounts of each standard (c_x) must be spotted on master filters used for analysis of these total DNAs.

Quantitative RSGP has been used extensively to fingerprint microbial communities in production waters of the Wainwright and Wildmere oil fields in eastern Alberta. In these fields oil is produced by water flooding. The produced oil-water mixture is separated in production units consisting of a free water knockout and a water plant. The produced oil is transferred to a pipeline system, whereas the produced water is reinjected into the reservoir. The reservoirs are shallow (600 m) with a resident temperature of ca. 25 °C. The production waters are saline and contained on average 6% (wt/vol) of NaCl.

Two different types of samples were obtained from this environment and analyzed by quantitative RSGP: production water and corrosion coupon samples. Production water samples, representing the planktonic microbial population yielded up to 50 µg of DNA per liter, whereas corrosion coupon samples yielded up to 400 ng of DNA per cm² [13]. Aliquots of these DNAs (100 ng) were spiked with the internal standard (λ DNA, 100 pg), labeled and hybridized with master filters containing 20 oil field standards. The general layout of the filter is indicated in Fig. 3. Standards 1 to 10 were *Desulfovibrio* species (*Lac1,2*, *Lac3*, *Lac4*, *Lac5*, *Lac6*, *Lac10*, *Lac24*, *Lac25*, *Lac26* and *Eth3*, respectively), standards 11 to 16 (*Ben1*, *Dec1*, *Pro12*, *Ace1*, *Ace3* and *Ace4*) were non-*Desulfovibrio* SRB and standards 17 to 20 (*Sty1*, *Sty2,3*, *Smg2* and *Sty4*) were non-SRB. In order to improve detection sensitivity, up to 70-fold more DNA was spotted on the master filters than on those used for analysis of liquid enrichment cultures. Because different amounts of DNA were available for master filter preparation, the standard DNAs were not spotted at a uniform concentration. The observed hybridization intensities (Fig. 3) are therefore not directly proportional to the fractions f_x of a given standard; f_x was calculated using equation (1) taking the differing c_x spotted into account. The results gave the bar diagrams in Fig. 3 A to D.

These indicate substantial differences between the planktonic population (Fig. 3A, B) and the metal attached biofilm. In the planktonic population all standards for which reliable data were obtained (standards 12 to 16 were excluded because c_x was too small) were present at $f_x = 0.2 - 2.5\%$. The non-SRB (the grey shaded bars in Fig. 3A, B) accounted for a substantial portion of the planktonic population. The sessile

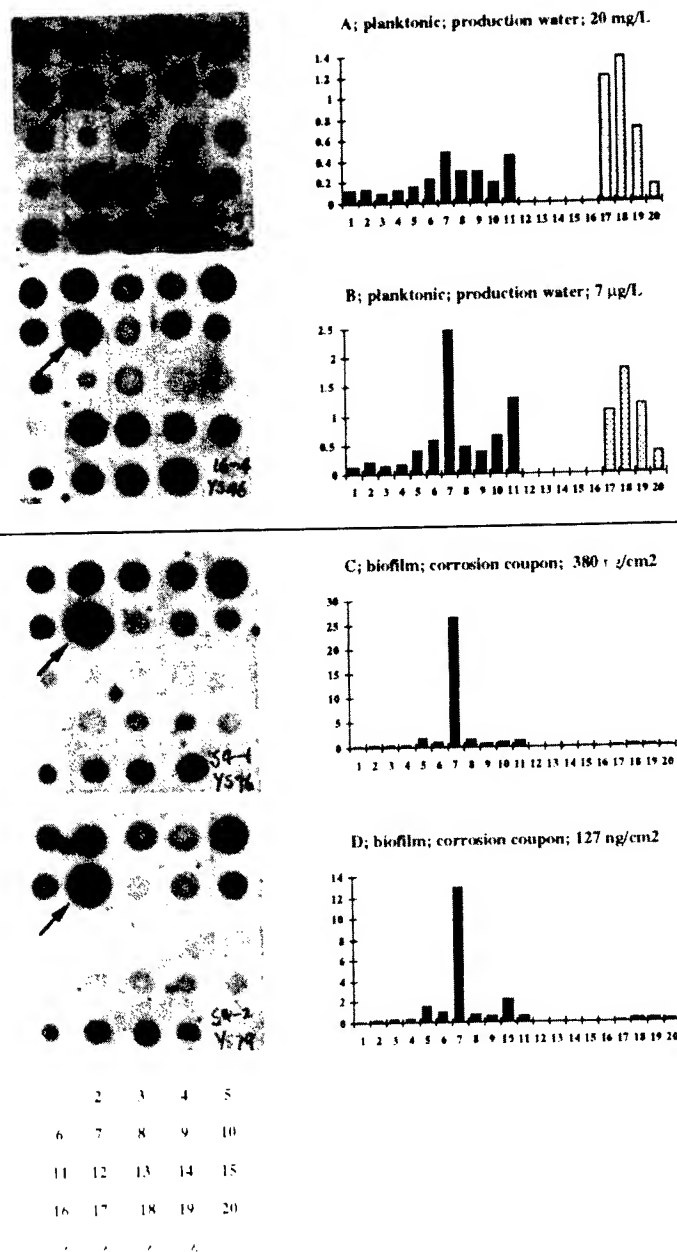


Fig. 3. Quantitative RSGP of DNAs extracted directly from oil field samples. (A, B) Production waters, (C, D) corrosion coupons. The abscissa (X-axis) represents the standard number (e.g. 1 to 10 are SRB, all of them *Desulfovibrio* species, 17 to 20 are non-SRB; see text). The ordinate (Y-axis) represents the percentage in the DNA preparation calculated for each standard using equation 1. Standard 7 (*Lac24*) is indicated by the arrows.

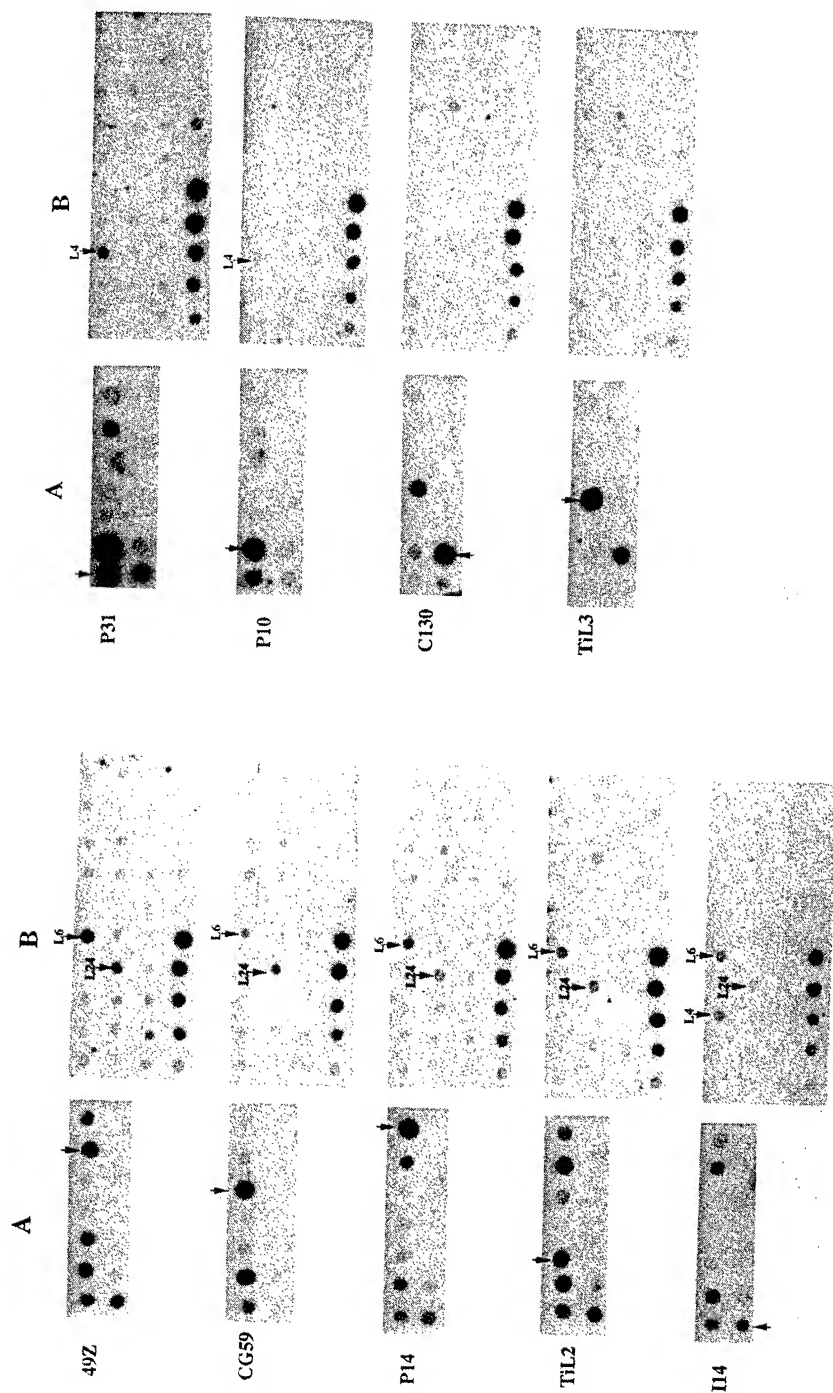


Fig. 4 Analysis of DNA from lactate-sulfate enriched Navy platform isolates with RSGP. (A) Selfhybridization of platform isolate DNAs. The DNA preparation used as the probe (by labeling 100 ng in the presence of 100 pg of λ DNA) is indicated. (B) Hybridization of the probe indicated in (A) with a master filter containing 35 oil field SRB genomes and a gradient of λ DNA concentrations (lower left). Hybridization of the probe with chromosomal DNA from *Desulfovibrio* species *Lac4*, *Lac6* and *Lac24* (*L4*, *L6* and *L24*, respectively) is indicated.

population (Fig. 3C, D) was dominated by selected SRB of the genus *Desulfovibrio*. Standard 7 (*Lac24*) was present at a calculated 15 to 25% of total population. Evaluation of a larger number of corrosion coupons indicated that a selected number of *Desulfovibrio* species (particularly standards 5, 7 and 10, *Lac6*, *Lac24* and *Eth3*, respectively) could be highly enhanced in the biofilm population. This observation agrees with the finding that *Desulfovibrio* can derive energy for growth from dissolving metal under anaerobic conditions [15].

Use of RSGP to characterize SRB in other environments

One of the limitations of the RSGP method is that, because of the specificity of chromosomal DNA, master filters containing chromosomal DNAs from standards isolated from a single environment are environment specific. On the positive side this means that "environmental homology" is indicated if two environments have similar RSGP patterns. Genomes from SRB isolated from fresh water environments do not usually hybridize to master filters representing the saline oil field population (Telang, A. et al., unpublished). However, since marine environments are also characterized by high salt concentrations, we decided to test whether SRB similar to those found in saline oil fields are present in these environments. Nine platform isolates obtained from US Navy systems were enriched for lactate-utilizing SRB. DNA was isolated from the enrichment cultures. Amounts of 40 ng of all nine platform DNAs were spotted on nine filters (Fig. 4A). One of these filters was, together with a master filter containing 35 DNAs from oil field SRB, hybridized with a labeled platform DNA, spiked with λ as described above. The results for all nine platform DNAs are shown in Fig. 4. DNAs from platform isolates 49Z, CG59, P14, TiL2 and I14 all crosshybridized (Fig. 4A). These DNAs hybridized with oil field standards *Lac6* and *Lac24* (Fig. 4B). The hybridization intensities are particularly strong in the case of DNA from platform isolate CG59, indicating that substantial amounts of similar *Desulfovibrio* species are present in this enrichment. The crosshybridization patterns for DNAs P31 and P10 indicate similarity of these enrichments (Fig. 4A). P31 displays fairly strong crosshybridization with *Lac4* (Fig. 4B). Finally, similarity of the C130 and TiL3 platform DNAs is indicated by crosshybridization (Fig. 4A). These did not hybridize significantly with any of the oil field SRB (Fig. 4B).

Discussion

Microbially influenced metal corrosion can be a serious problem in marine systems. The high concentration of sulfate in sea water (ca. 2 gram per liter) favors growth of SRB whenever anaerobic conditions are created (e.g. at water-metal interfaces). Metal coupons covered by protective coatings were readily attacked by marine microbial consortia

as soon as physical defects in the coatings were introduced [16]. SRB were found to be an important component of these consortia, as judged by measurement of hydrogenase activity, which ranked in the order 49Z=I14>P14>P10 for four of the consortia that were also studied here [16]. Although hydrogenase assays or other generic SRB tests may provide a broad indication of MIC potential these do not allow the level of differentiation that can be achieved with gene probe assays, like RSGP. Crosshybridization studies of DNA isolated from the 9 platform isolates (Fig. 4A) immediately indicated that these fall in three classes (49Z, CG59, P14, TiL2 and I14), (P31 and P10) and (C130, TiL3). The first of these frequently harbors *Desulfovibrio* species that are very similar to *Lac6* and *Lac24*, found in high concentrations on oil field corrosion coupons.

Although a quantitative link between MIC and the occurrence of *Lac6* and *Lac24* has not yet been established the occurrence of similar bacteria in corrosive consortia provides a strong incentive for further work on elucidating the role of these bacteria in the MIC process.

Acknowledgment

Work in GV's laboratory is supported by the Natural Science and Engineering Research Council of Canada.

References

- [1] Hamilton, W. A. 1985. Sulphate-reducing bacteria and anaerobic corrosion. *Annu. Rev. Microbiol.* 39:195-217.
- [2] Costerton, J. W. et al. 1987. Bacterial biofilms in relation to internal corrosion monitoring and biocide strategies. *Corrosion* 87. National Association of Corrosion Engineers, San Francisco, CA, Paper No 54.
- [3] Little, B., et al. 1990. Electrochemical behavior of stainless steels in natural seawater. *Corrosion* 90. National Association of Corrosion Engineers, Houston, TX, Paper No 150.
- [4] Pope, D. H., et al. 1990. Microbiologically influenced corrosion in the natural gas industry. Annual report to the Gas Research Institute, Chicago, IL.
- [5] Pope, D. H., et al. 1991. Microbiologically influenced corrosion in the natural gas industry. Annual report to the Gas Research Institute, Chicago, IL.
- [6] Ferris, F. G. et al. 1992. Corrosion products associated with attached bacteria at an oil field water injection plant. *Can. J. Microbiol.* 38:1320-1324.
- [7] Pfennig, N. et al. 1981. Dissimilatory sulphate-reducing bacteria. In Starr, M. P, Stolp, H., Trüper, H. G., Balows, A., Schlegel, H. G. (eds) *The Prokaryotes*, vol. 1. Springer-Verlag, Inc., New York, p. 926-940.

- [8] Devereux, R., et al. 1989. Natural relationships among sulfate-reducing eubacteria. *J. Bacteriol.* 171:6689-6695.
- [9] Little, B. J. and Wagner, P. A. 1994. Advances in MIC testing. In Kearns, J. R. and Little, B. J. (eds) *Microbiologically Influenced Corrosion Testing*, ASTM STP1232, American Society for Testing Materials, Philadelphia, p. 1-11.
- [10] Voordouw, G. et al. 1991. Reverse sample genome probing, a new technique for identification of bacteria in environmental samples by DNA hybridization, and its application to the identification of sulfate-reducing bacteria in oil field samples. *Appl. Envir. Microbiol.* 57: 3070-3078.
- [11] Voordouw, G. et al. 1992. Identification of distinct communities of sulfate-reducing bacteria in oil fields by reverse sample genome probing. *Appl. Envir. Microbiol.* 58: 3542-3552.
- [12] Devereux, R. et al. 1990. Diversity and origin of *Desulfovibrio* species: phylogenetic definition of a family. *J. Bacteriol.* 172:3609-3619.
- [13] Voordouw, G. et al. 1993. Quantitative reverse sample genome probing of microbial communities and its application to oil field production waters. *Appl. Environ. Microbiol.* 59: 4101-4114.
- [14] Voordouw, G. et al. 1990. The distribution of hydrogenase genes in *Desulfovibrio* and their use in identification of species from the oil field environment. *Appl. Environ. Microbiol.* 56: 3748-3754.
- [15] Cord-Ruwisch, R. and Widdel, F. 1986. Corroding iron as a hydrogen source for sulphate reduction in growing cultures of sulphate-reducing bacteria. *Appl. Microbiol. Biotechnol.* 25: 169-174.
- [16] Jones-Meehan, J. et. al. 1994. Corrosion resistance of several conductive caulks and sealants from marine field tests and laboratory studies with marine, mixed communities containing sulfate-reducing bacteria (SRB). In Kearns, J. R. and Little, B. J. (eds) *Microbiologically Influenced Corrosion Testing*, ASTM STP1232, American Society for Testing Materials, Philadelphia, p. 217-233.

SESSION III
CORROSION COMPOSITES
AND CERAMICS

Chairman: *D. Aylor*

BLANK

Nonequilibrium Alloying of Aluminum for Improving the Corrosion Resistance of Graphite- Reinforced Metal Matrix Composites

Dr. Barbara A. Shaw,* Ms. Tia R. Schrecengost, Mr. Paul L. Miller
The Pennsylvania State University, University Park, PA 16802

Mr. Robert G. Wendt and Dr. William C. Moshier
Martin Marietta Astronautics Group, Denver, CO 80201

INTRODUCTION

High modulus graphite (Gr) reinforced metal matrix composites (MMCs) offer a wide variety of attractive properties including: high specific modulus and strength (E/ρ and UTS/ρ), tailorable or zero coefficient of thermal expansion (CTE), and high thermal conductivity. Using Al as the matrix metal results in a reduction of the final density of the composite with high elastic modulus and excellent strength in the fiber direction. Unfortunately, MMCs, especially Gr reinforced composites, are extremely susceptible to corrosion with severe attack in chloride-containing environments occurring in as little time as several weeks for Gr/Al composites.¹⁻³

The overall objective of this research is to determine whether improving the inherent passivity of the matrix metal in a Gr/Al composite can alleviate, or at least minimize, galvanic corrosion between the graphite and the matrix metal. This galvanic corrosion is currently the limiting factor in utilization of these composites. Our research focuses on the unique properties of sputter deposited alloys. With sputter deposition it is possible to significantly increase the solubility of passivity enhancing species, thus dramatically improving their corrosion resistance.⁴⁻⁸ The approach being undertaken is to develop alloy systems capable of minimizing galvanic degradation of the composite. An essential step in this process is identification of alloy compositions which maintain enhanced passivity after processing into the bulk composite. Our earlier work^{4,5,8} indicated that Al-Mo alloys provide the best combination of thermal stability, corrosion resistance, and alloy density. This paper will address the thermal stability and corrosion resistance of selected

compositions of Al-Mo and Al-Mg-Mo alloys. Once the best candidate is identified from these alloys, sputter-coated graphite fibers can be consolidated into a component, such as the mirror support structure for a staring telescope schematically illustrated in Figure 1.

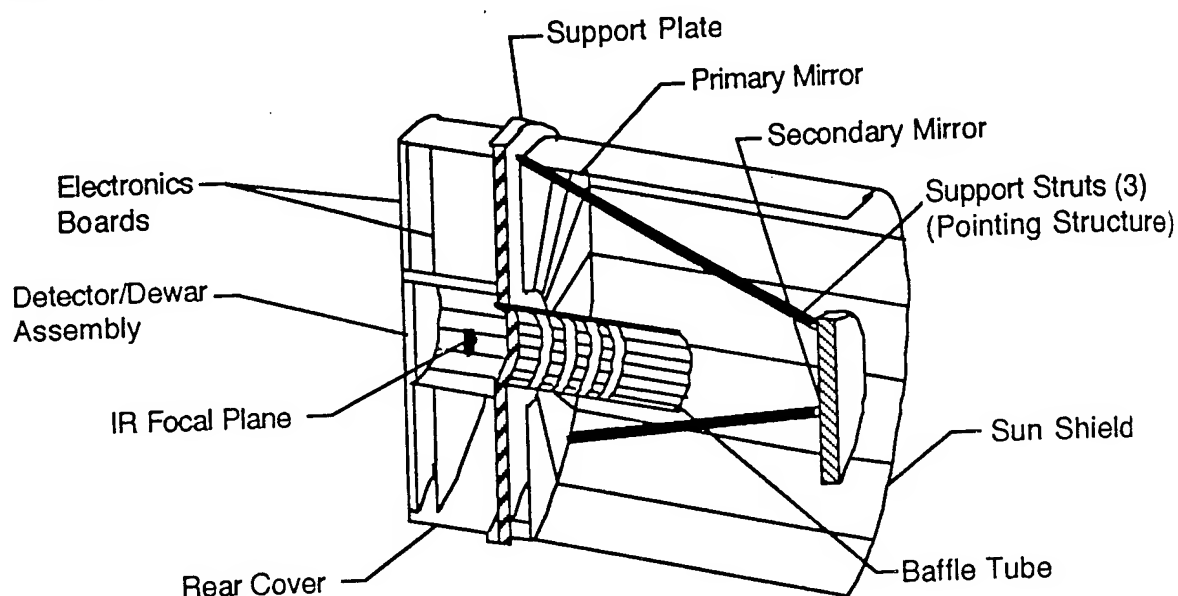


Figure 1. Schematic of a Staring Telescope.

EXPERIMENTAL

The alloys were fabricated by RF and DC magnetron sputter deposition using a 602RS Thin Film Deposition System. High purity targets were sputtered onto either sapphire or single crystal silicon wafers, yielding alloy films approximately 1 to 2 μm thick. Substrate temperature was not controlled during sputtering and reached a maximum temperature of approximately 100 $^{\circ}\text{C}$ during a 1 hour deposition. Pressure in the chamber was held constant at 7.0 mtorr during sputtering by introducing purified (< 10 ppb O_2) Ar gas at a flow rate of 200 standard cubic centimeters per minute (sccm) and adjusting the conductance of the system. Uniform alloy composition on each wafer was maintained by spacing the sputtering heads approximately 10 cm from the substrate, focused 60 $^{\circ}$ from the substrate normal and rotating the substrate at 30 rpm during deposition.

Prior to electrochemical testing, x-ray diffraction (XRD), selected area diffraction (SAD) and transmission electron microscopy (TEM) were used to characterize the structure of the alloys and determine if the solute was maintained in solid solution with the base metal.

Alloy surfaces were characterized using optical microscopy, scanning electron microscopy (SEM), and scanning laser microscopy (SLM). Optical microscopy and SLM were used prior to electrochemical testing to observe surface defects such as scratches and cracks incorporated during sputtering and handling (i.e., cleaving of the alloy-coated Si wafer) of the alloy. SEM was also used prior to polarization so that EDS could be employed for semi-quantitative compositional analysis. All three microscopy techniques were used following electrochemical testing so that the morphology of the breakdown regions could be evaluated.

Test specimens were prepared by cleaving the alloy-coated Si wafer into pieces with areas of approximately 4 to 5 cm². Individual pieces were then coupled to a potentiostat through a lead wire and all regions, except the test area, were coated with an adherent marine epoxy to ensure that environmental and electrical isolation were maintained. Anodic and cathodic polarization experiments were performed using a conventional three electrode technique, consisting of a saturated calomel reference electrode (SCE), graphite counter electrodes, and sample electrode. The polarization behavior was used to assess passivation behavior in the alloys and for the construction of galvanic diagrams. These diagrams are useful in predicting the coupled current in a galvanic cell. Unless specifically noted, all potentials reported in this paper are referenced to a SCE. Polarization scans were generated at a scan rate of 0.2 mV/sec in 0.1 M NaCl solution adjusted to a pH of 8 with 0.1 M NaOH solution. The corrosion potential (E_{oc}) was allowed to stabilize in the test solution for approximately 60 minutes prior to polarization. A minimum of two tests were conducted for each condition to confirm the validity of results.

Electrochemical response of the graphite fibers was measured by testing an AMOCO composite consisting of 62.5 vol. % P75 Gr fibers embedded in EPXL 1962. Prior to testing, the edges of the specimens (with an approximate graphite area of 0.74 cm²) were sanded to reveal the fibers and in order to make an electrical connection. The specimen was electrically isolated by embedding the AMOCO composite in an epoxide resin. The graphite was cathodically polarized at a scan rate equivalent to the anodic scans, and the area of the graphite was estimated by measuring the tested surface area and multiplying it by the fiber area fraction of the exposed surface (55 %) calculated with an image analyzer.

To confirm the galvanic diagram predictions, galvanic currents were measured by coupling either the as-sputtered or heat treated alloy specimens to P75 Gr fibers. The P75 Gr fibers were prepared for testing by embedding them into a non-conductive epoxy and electrically connecting them to a external lead. Area fractions of the exposed Gr

fibers were measured using a image analyzer. Nominal cathode-to-anode area ratios ranged from 0.2 to 1.1. The alloy specimen and the P75 Gr/epoxy composite were electrically coupled and immersed in a pH 8, 0.1 M NaCl solution. Galvanic current was monitored as a function of time using a potentiostat/zero resistance ammeter (operating in the ZRA mode).

RESULTS AND DISCUSSION

XRD revealed that all of the as-sputtered alloys were amorphous and contained no precipitates as shown in the representative pattern in Figure 2. Table 1 summarizes the XRD results of the alloys that were heat treated at 400°C, 500°C and 600°C for 1, 2, and 8 h to determine the effect of composite consolidation on the alloy structure. This table shows that as the concentration of Mo in the Al alloy increased, its propensity to form precipitates during heat treatment decreased. For example, Al-11Mo precipitated at the lowest time (1 h) and temperature (400°C); whereas, the Al-23Mo remained amorphous after being heat treated at 600°C for 2 h. This result was unexpected because as the Mo concentration increases, the thermodynamic driving force for precipitation increases. Lack of precipitation indicated the kinetics for precipitation in these alloys was very sluggish. The Al-Mg-Mo alloys were also amorphous in the as-sputtered condition, but were found to react at all heat treatment times and temperatures forming precipitates as well as oxides due to reaction of the Mg with the sapphire substrate.

TEM was conducted on the Al-18Mo in the as-sputtered condition and after heat treatment at 400°C for 2 and 8 h and 500°C for 2 and 8 hours. Figure 3 shows the representative structure of the as-sputtered alloy with the corresponding SAD pattern. Structure of the as-deposited Al-Mo alloy is featureless with the exception of the mottled appearance that resulted from the extensive ion milling used to thin the specimen. The SAD pattern shows two diffuse rings that correspond to the d-values calculated for the broad peaks found on the XRD patterns. Similar structures and SAD patterns were obtained for the Al-18Mo alloy heat treated at 400°C for 2 and 8 h which correlate with the XRD patterns that showed that the alloy remained amorphous after heat treatment. After heat treatment to 500°C for 2 and 8 h small precipitates began to appear (Figure 4). SAD of these precipitates indicate a structure of Al_{12}Mo , Al_5Mo , and Al. Not all the rings for each phase could be indexed and many of the rings could not be correlated with the expected Al-Mo intermetallic compounds. SAD of the Al-18Mo alloy heat treated at 500°C for 8 h shows an elongation of the diffraction spots which arises from fine precipitates that are preferentially oriented.

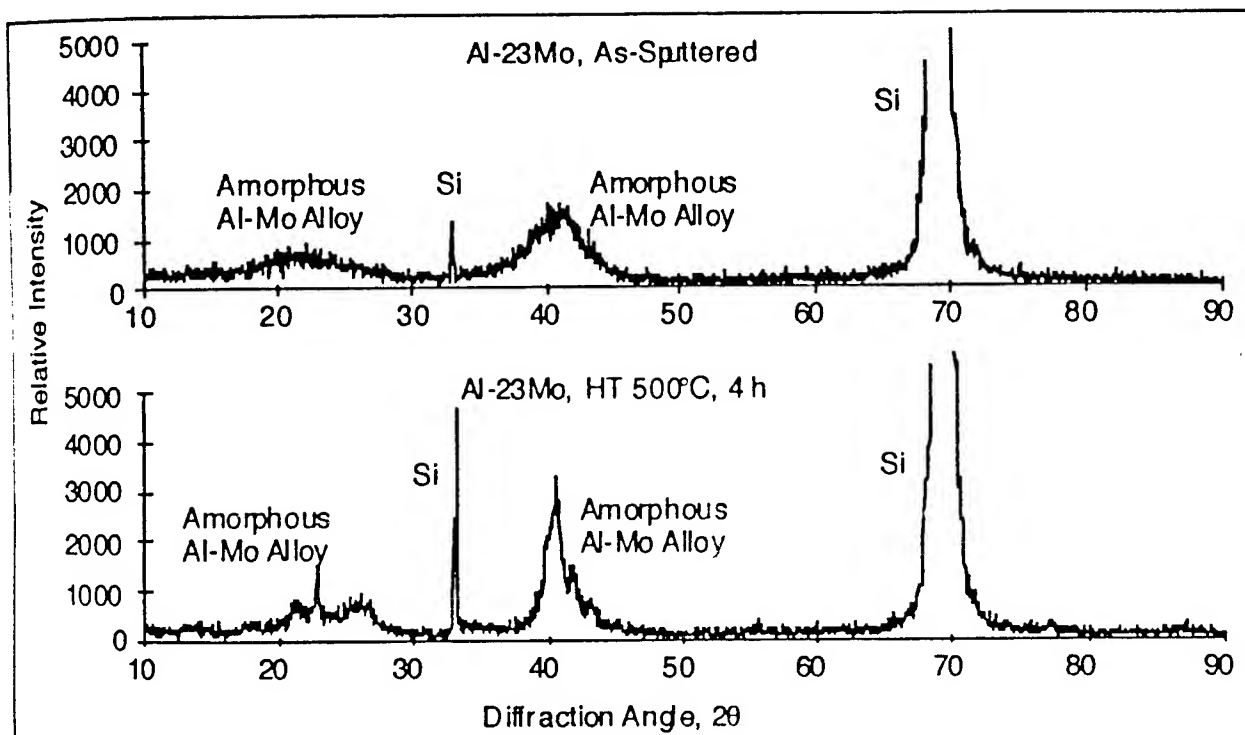


Figure 2. X-ray Diffraction of Al-23Mo in the As-Sputtered Condition and After Heat Treatment. As-Sputtered, the Alloy is Amorphous and it is Just Beginning to Precipitate after Heat Treatment at 500°C for 2 h.

Table 1. Summary of Al-Mo Alloy Structure as a Function of Heat Treatment Time and Temperature.

Heat Treatment Time (h)	Heat Treatment Temperature		
	400°C	500°C	600°C
1	Al-11Mo, ppt	Al-11Mo, ppt	Al-11Mo, ppt
	Al-18Mo, Amorphous	Al-18Mo, ppt	Al-18Mo, ppt
	Al-23Mo, Amorphous	Al-23Mo, Amorphous	Al-23Mo, Amorphous
2	Al-11Mo, ppt	Al-11Mo, ppt	Al-11Mo, ppt
	Al-18Mo, Amorphous	Al-18Mo, ppt	Al-18Mo, ppt
	Al-23Mo, Amorphous	Al-23Mo, Amorphous	Al-23Mo, Amorphous
8	Al-11Mo, ppt	Al-11Mo, ppt	Al-11Mo, ppt
	Al-18Mo, Amorphous	Al-18Mo, ppt	Al-18Mo, ppt
	Al-23Mo, Amorphous	Al-23Mo, Amorphous	Al-23Mo, ppt

ppt - fully precipitated

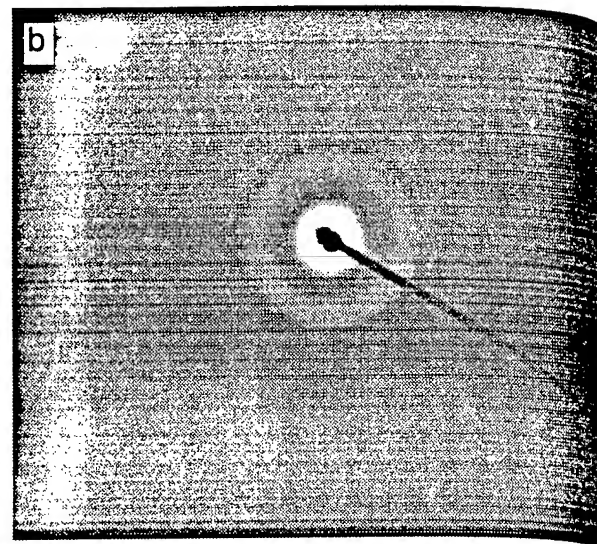
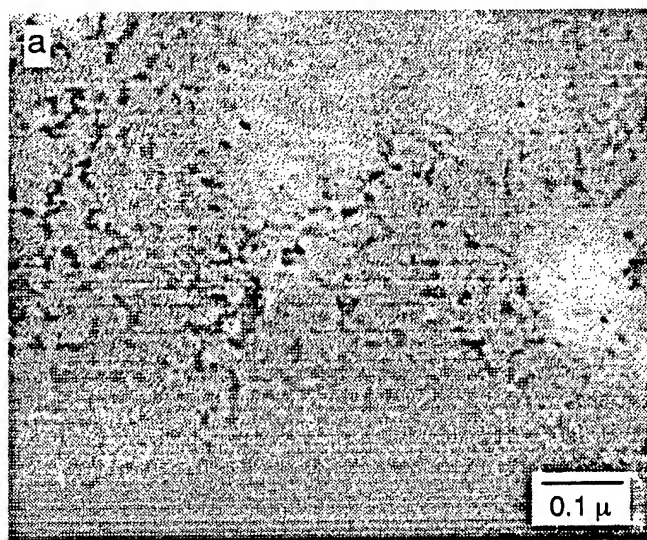


Figure 3. Structure and Associated SAD Pattern for the Amorphous Al-18Mo in the As-Deposited Condition and after Heat Treatment at 400°C for 2 and 8 h.

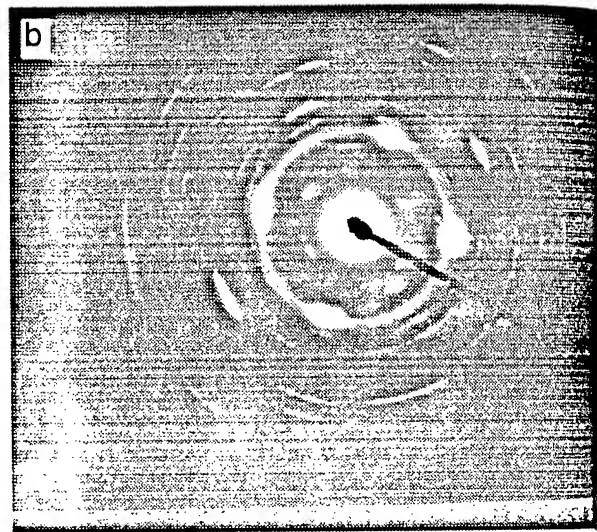
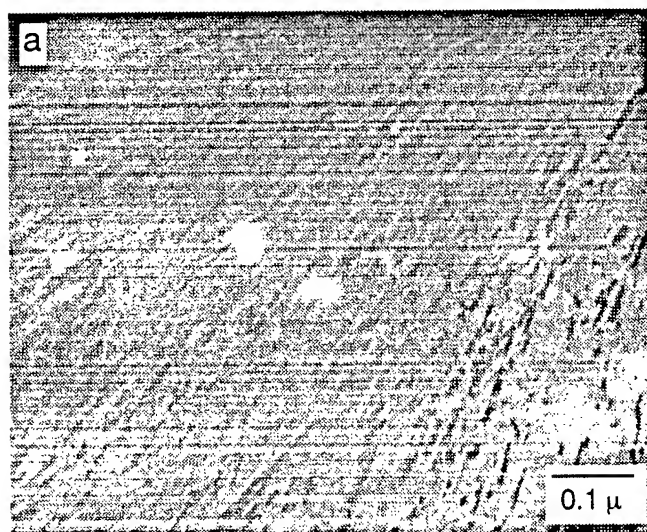


Figure 4. Structure (a) and SAD Pattern (b) for Al-18Mo, Heat-Treated at 500°C for 8 h. Fine Elongated Precipitates are Evident and the SAD Pattern Shows Elongated Spots that Correspond to the Fine Precipitate Structure.

Figure 5 summarizes the results of the anodic polarization experiments for the binary Al-Mo and ternary Al-Mg-Mo nonequilibrium alloys in the as-sputtered condition. All of the as-deposited Al-Mo alloys exhibited an extended passive region and an open circuit potential that was 500 to 600 mV more noble than pure Al. E_{oc} values for all of the alloys were measured to be between -600 to -450 mV_{SCE} with the majority of the measured E_{oc} values ranging from -520 mV_{SCE} to -580 mV_{SCE}. There was no apparent trend in E_{oc} as a function of solute concentration for the Al-Mo alloys tested, agreeing with the previous work on Al-Mo alloys.⁹⁻¹¹ Passive current densities (i_{pass}) for the as-deposited binary Al-Mo and ternary Al-Mg-Mo alloys ranged between 0.1 and 1.0 $\mu\text{A}/\text{cm}^2$, but as in the case of E_{oc} , no correlation between solute concentration and i_{pass} was evident. Variations in i_{pass} were attributed to general defects, i.e., scratches, pinholes, etc., in the alloy film. Breakdown potential (E_b) values for most of the as sputtered alloys were between 100 and 500 mV_{SCE} as compared to -690 mV_{SCE} for pure Al.

The polarization response of as-deposited and heat treated Al-11Mo alloys is shown in Figure 6. Although E_b for the heat treated Al-11Mo alloys decreased from ~420 mV_{SCE} (as-sputtered) to 50 mV_{SCE} (heat treated), E_{oc} remained relatively constant at approximately -550 mV_{SCE}. Reduction in E_b was likely the result of precipitates formed during heat treatment creating microgalvanic cells with the surrounding alloy. Conversely, i_{pass} decreased from ~1 $\mu\text{A}/\text{cm}^2$ for the as-deposited alloy to ~0.1 $\mu\text{A}/\text{cm}^2$ after heat treatment.

Both E_{oc} and E_b for the Al-18Mo alloy were not dramatically affected by heat treating up to 500°C for 2 h (Figure 7). Similar to the Al-11Mo alloys, i_{pass} for the heat treated Al-18Mo specimens was less than that for the as-sputtered alloy, with the exception of specimen heat treated at 400°C for 1 h. No cracks or defects which may contribute to lower E_b values were found during SEM examination of the heat treated alloys.

Heat treatment of the Al-12Mg-13Mo alloy resulted in a more active E_{oc} (approximately -800 mV_{SCE}) with no passive response during polarization with exception of heat treating at 400°C for 1 h where E_{oc} was maintained.

SEM examination and EDS analysis of a newly formed pit on the as-deposited Al-18Mo specimen immediately after polarization to the breakdown potential showed the Mo concentration had risen from 18 to 25 atomic percent in the pit. Increase in Mo in the forming pit indicates the pitting process involves the preferential dissolution of Al from the alloy, which is consistent with x-ray photoelectron spectroscopy work conducted during earlier studies.^{10,11}

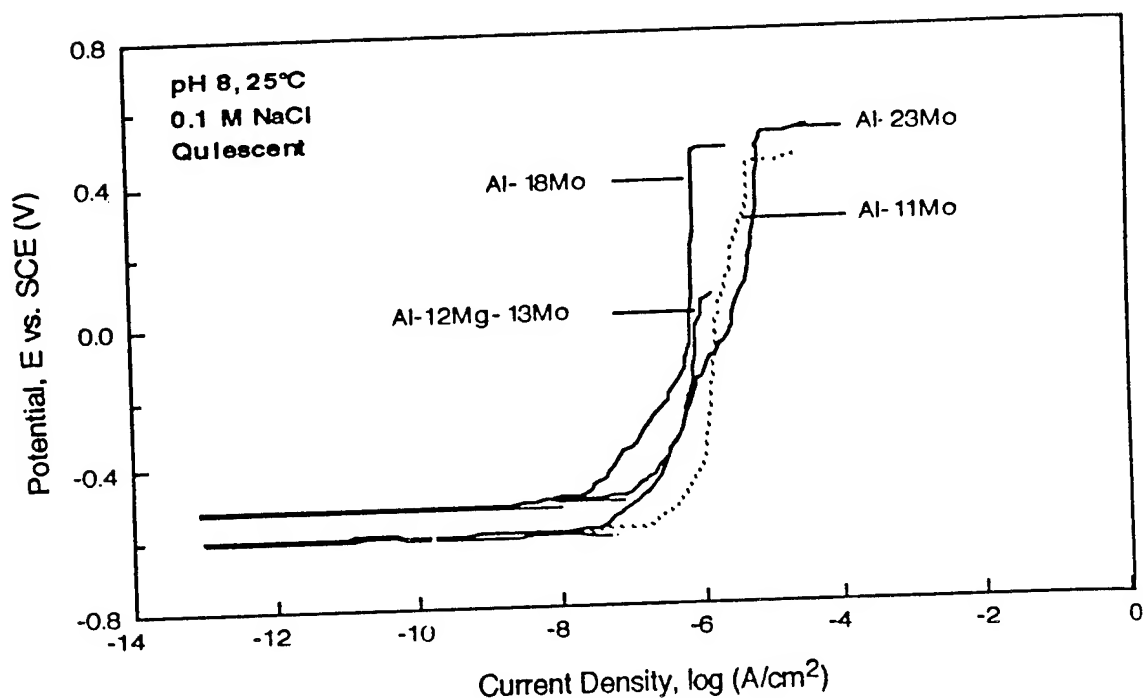


Figure 5. Anodic Polarization Response of Various Al-Mo Alloys, Polarized in 0.1M NaCl, pH 8, 25°C.

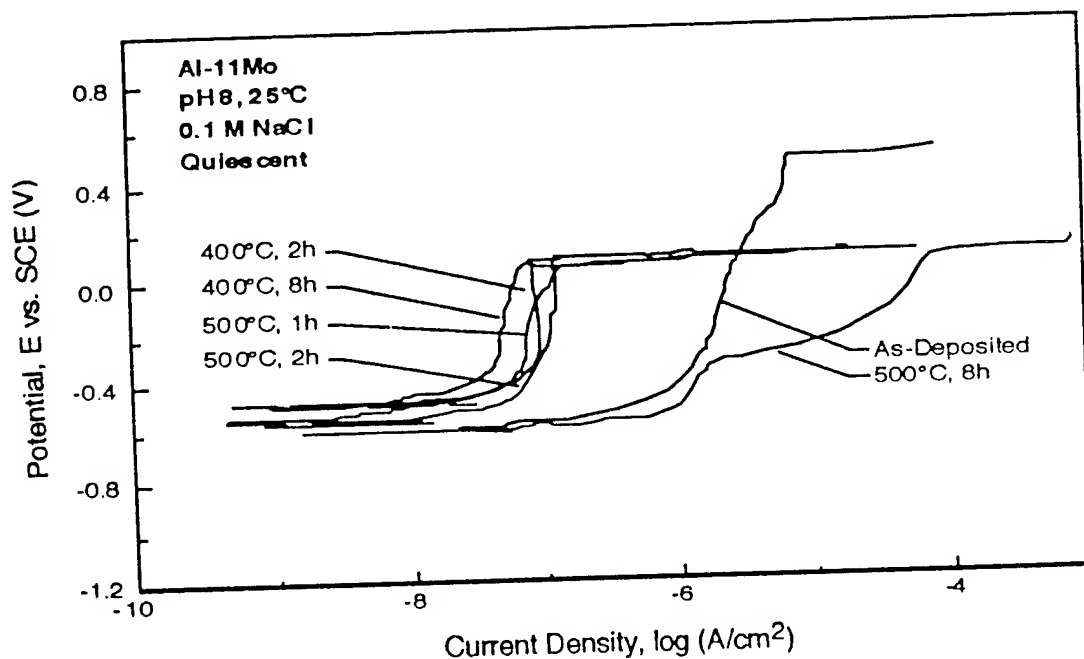


Figure 6. Anodic Polarization Response of Al-11Mo Before and After Heat Treatment at 400°C for 1 and 2 h and 500°C for 1, 2, and 8 h, Polarized in 0.1 M NaCl, pH 8, 25°C.

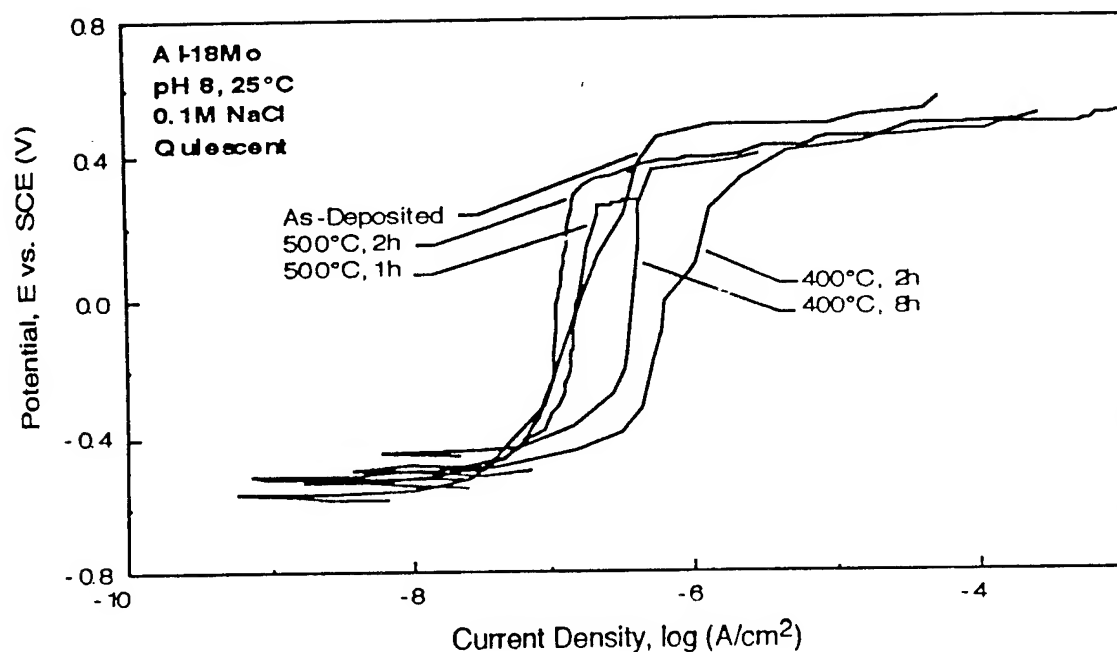


Figure 7. Anodic Polarization Response of Al-18Mo Before and After Heat Treatment at 400°C for 2 and 8 h and 500°C for 1 and 2 h, Polarized in 0.1 M NaCl, pH 8, 25°C.

The polarization data can be used to predict the current resulting in a galvanic couple. By superimposing the cathodic curve for graphite onto the anodic curves for the different sputtered alloys, the galvanic corrosion current can be estimated from the intersection of the two curves providing there is an insignificant IR drop, the contribution of other contributing reactions is small, and the current density is uniform.¹² Effects of the galvanic couple on the corrosion of the matrix metal can be easily estimated with such a diagram, and the diagrams can also be used to look at the effects of the cathode-to-anode area ratio and to determine if a reaction should be anodically or cathodically controlled. A galvanic diagram based on equal metal/Gr areas for pure Al, 6061 Al, and the Al-Mo alloys coupled to P75 Gr fibers is shown in Figure 8. This diagram estimates that the galvanic corrosion of pure sputtered and 6061 Al coupled to P75 Gr fibers are cathodically controlled with a relatively high current density value of $12.5 \mu\text{A}/\text{cm}^2$. For a cathodically controlled reaction, the cathodic curve shifts to a higher current density as the Gr-to-Al area ratio increases, which accelerates the corrosion rate of the Al matrix. Converse to pure Al, galvanic corrosion was anodically controlled for the Al-Mo alloys with an estimated galvanic current density of $1 \mu\text{A}/\text{cm}^2$ or less. For anodically controlled corrosion, changing the Gr-to-Al area ratio and subsequently shifting the cathodic curve to higher

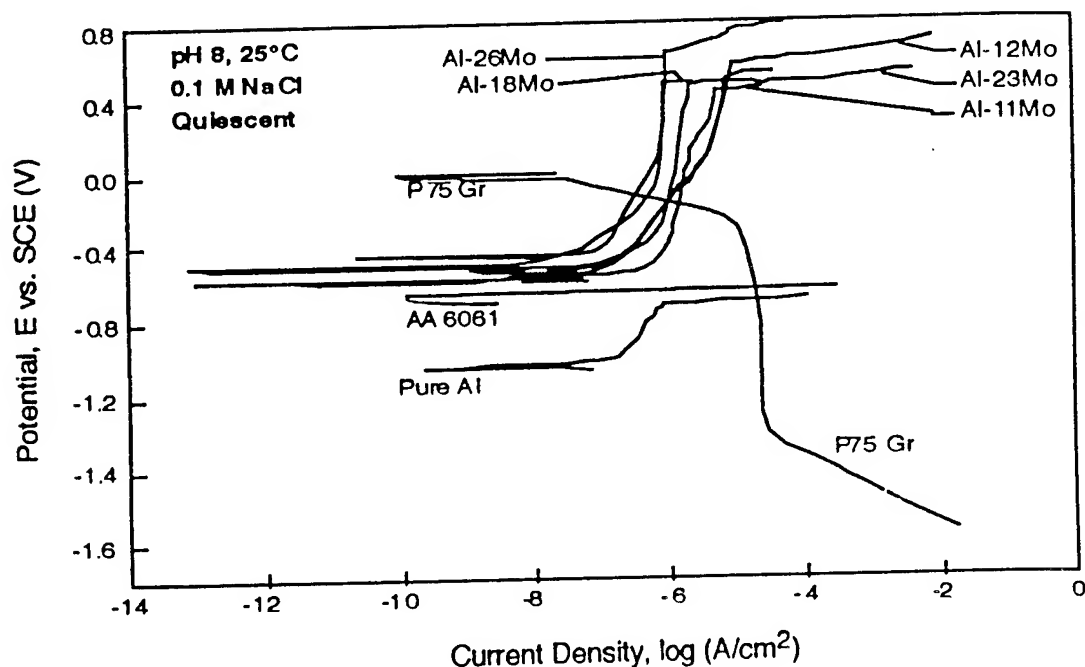


Figure 8. Galvanic Diagram with Anodic Curve of Pure Sputtered Aluminum, Wrought 6061 Al, and Various Sputtered Al-Mo Alloys Combined with the Cathodic Curve for an Equal Area of P75 Graphite Fibers, Tested in 0.1M NaCl, pH 8, 25°C.

current density values (or anodic curve to lower current density) would not significantly change the corrosion rate for the Al-Mo alloys. This result is important because modifying the Gr fiber volume, which is a key design feature of composites to achieve specific thermal or mechanical properties, will not result in dramatic changes in the corrosion response of the Gr/Al-Mo composite. The galvanic corrosion reaction remained anodically controlled for both the Al-11Mo and Al-18Mo alloys after heat treatment. Only after heat treating the Al-11Mo to 500°C for 8 h did control for the galvanic reaction change from anodic (Al passivation) to cathodic (oxygen reduction on Gr fibers).

To confirm the predictions made using the galvanic diagrams, long term galvanic current tests were conducted on sputtered Al, Al-11Mo, Al-18Mo, Al-23Mo, and ternary Al-12Mg-13Mo in the as-deposited condition by coupling the alloy to P75 Gr fibers (Figure 9). Galvanic current values are equivalent to current densities since the anode areas were 1 cm². For all the alloys, the galvanic current initially starts off at relatively high values between 3 and 30 $\mu\text{A}/\text{cm}^2$, but quickly drops to a low steady state value. The Al-18Mo and Al-23Mo reached low measured galvanic current densities of ~ 0.04 and ~ 0.08 $\mu\text{A}/\text{cm}^2$, respectively which were up to three orders of magnitude lower than the galvanic current density

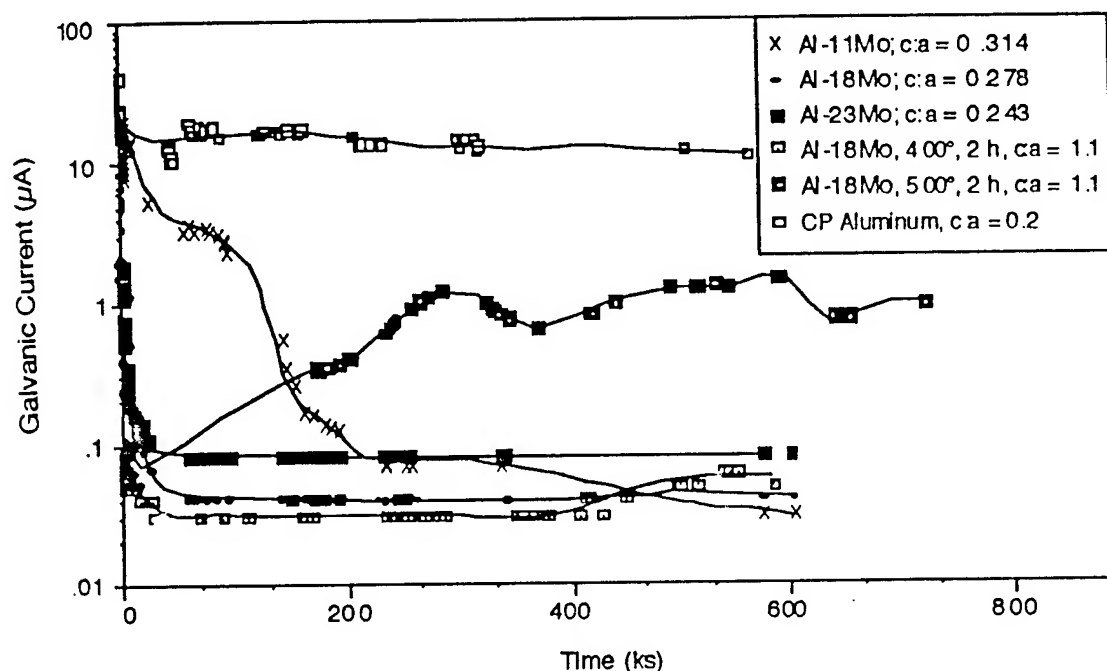


Figure 9. Galvanic Current for Commercially Pure Aluminum and Al-18Mo Alloys (As-Deposited and Heat Treated) Coupled to P75 Graphite Fibers in Quiescent 0.1M NaCl, pH 8, 25°C.

values of $30 \mu\text{A}/\text{cm}^2$ measured for pure sputtered Al. The current density of the Al-18Mo after heat treatment at 400°C for 2 h was comparable to the as-sputtered value of $0.08 \mu\text{A}/\text{cm}^2$. Even after heat treatment at 500°C for 2 h the galvanic current density was an order of magnitude lower than for pure sputtered Al. After galvanic testing for seven days (605 ks) the pure sputtered Al had completely dissolved from the Si wafer; whereas, the Al-Mo alloys remained intact and highly specular. The Al-12Mg-13Mo alloy exhibited a galvanic current value of $10 \mu\text{A}/\text{cm}^2$ which is greater than the binary Al-Mo alloys but still 3 times lower than that of pure Al. However, less than 12 h (40 ks) after immersion in the 0.1 M NaCl, pH 8, solution, the Al-Mg-Mo alloys coupled to P75 Gr fibers exfoliated and completely lifted away from the substrate. Due to the short time in solution for the Al-12Mg-13Mo alloy, data for this alloys is not included in Figure 9.

Conclusions

Nonequilibrium Al-Mo alloys fabricated by magnetron sputtering have clearly been shown to be promising matrix alloys for Gr/Al composites. Al with 18 to 23 atomic percent Mo exhibited excellent corrosion resistance in the as-sputtered condition and could be heat treated up to 400°C for 8 h without detectable precipitation or change in

corrosion behavior. In addition, the Al-23Mo could be heat treated to 600°C for 2 h without degrading the corrosion performance. Galvanic current densities measured for Al-18Mo and Al-23Mo of ~0.04 to ~0.08 $\mu\text{A}/\text{cm}^2$ were 3 orders of magnitude lower than the 30 $\mu\text{A}/\text{cm}^2$ measured for pure Al in the 0.1 M NaCl, pH 8 solution when coupled to P75 Gr fibers. Galvanic diagrams of the anodic response of the alloy superimposed with the cathodic curve for the P75 Gr fibers predicted the galvanic corrosion rate to be controlled by the rate of the anodic reaction and the Al-Mo alloys were found to be electrochemically stable when coupled to Gr fibers regardless of the area ratios (in a 0.1M NaCl electrolyte). Based upon these results, an Al-Mo alloy with a Mo concentration of approximately 18 atomic percent was chosen to be deposited onto graphite fibers.

The ternary Al-12Mg-13Mo alloy is attractive because of its lower density. Unfortunately, this alloy exhibited a much higher galvanic current density value (~10 $\mu\text{A}/\text{cm}^2$) and was found to precipitate during heat treatment at the shortest time of 1 h and the lowest temperature of 400°C which resulted in a loss of passivation.

Acknowledgments

The authors gratefully acknowledge the support of A.J. Sedriks. This work was funded by the Office of Naval Research under contract N00014-91-J-1196.

References

1. D.M. Aylor and R.M. Kain, ASTM STP864 - Recent Advances in Composites in the US and Japan, Vinson and Taya (editors), American Society for Testing and Materials, Philadelphia, 632 (1985).
2. W.H. Pfeifer, W.J. Renton (editor), American Institute of Aeronautics and Astronautics, New York 231 (1977).
3. M.G. Vassilaros, D.A. Davis, G.L. Steckel, and J.P. Gudas, Proceedings of the 1980 Tri-Service Corrosion Conference, Vol. 2, US Government Publication, 21 (1980).
4. T.R. Schrecengost, M.S. Thesis, The Pennsylvania State University (1992).
5. R.G. Wendt, M.S. Thesis, Colorado School of Mines (1993).
6. P.L. Miller, M.S. Thesis, The Pennsylvania State University (1994).
7. P.L. Miller, B.A. Shaw, R.G. Wendt, and W.C. Moshier, "Technical Note: Improving Corrosion Resistance of Magnesium by Nonequilibrium Alloying with Yttrium," *Corrosion*, **49**, 947 (1993).

8. T.R. Schrecengost, B.A. Shaw, R.G. Wendt, and W.C. Moshier, "Nonequilibrium Alloying of Graphite-Reinforced Aluminum Metal Matrix Composites," *Corrosion*, **49**, 842 (1993).
9. W.C. Moshier, G.D. Davis, J.S. Ahearn, and H.F. Hough, "Influence of Molybdenum on the Pitting Corrosion of Aluminum Films," *Journal of the Electrochemical Society*, 1986, vol. 133, pp. 1063-1064.
10. W.C. Moshier, G.D. Davis, J.S. Ahearn, and H.F. Hough, "Corrosion Behavior of Aluminum-Molybdenum Alloys in Chloride Solutions," *Journal of the Electrochemical Society*, 1987, vol. 134, pp. 2677-2684.
11. G.D. Davis, W.C. Moshier, T.L. Fritz, and G.O. Cote, "Evolution of the Chemistry of Passive Films of Sputter-Deposited, Supersaturated Al Alloys," *Journal of the Electrochemical Society*, 1990, vol. 137, pp. 427.
12. D.A. Jones, Principles and Prevention of Corrosion, Macmillan Publishing Co., New York, 167 (1992).

BLANK

A MECHANISM FOR BLISTERING OF CARBON FIBER COMPOSITES

S. K. Miriyala, T. J. Rockett, W. C. Tucker and R. Brown*
Department of Chemical Engineering
The University of Rhode Island, Kingston, RI 02881.

ABSTRACT

Blisters containing fluid with a high pH were induced in a carbon fiber vinyl ester polymer matrix composite by cathodic polarization in a sodium chloride solution. The oxygen content of the solution was varied in order to determine the effect of oxygen on the blister process. It was found that increasing the oxygen content in solution decreased the time for blister initiation, indicating that the reduction of oxygen to form hydroxyl ions was an important reaction. Calculations indicated that a similar cumulative charge density was required for blister initiation for the different oxygen contents, confirming the importance of oxygen to the blister process.

A mechanism for blister formation dependent upon oxygen reduction to hydroxyl ions and the subsequent formation of an osmotic cell is outlined from the results of this study.

INTRODUCTION

Blistering of carbon fiber polymer composites when the fibers are in contact with metals in the presence of sea water or salt water was termed 'galvanic blistering'. Galvanic blistering of carbon reinforced vinyl ester¹, polyester², epoxy³, and polyamide⁴ composites were reported. It follows that galvanic blistering is a characteristic degradation generic to several carbon fiber polymer composites. Carbon being electrically conductive and a noble cathodic material, carbon fibers in a carbon fiber polymer composite become cathodes in a galvanic couple formed with metals steel or aluminum. This composite/metal galvanic couple accelerates metal corrosion and therefore, poses a threat to metal structures that are in galvanic contact with carbon fiber composite structures. The galvanic blisters, formed on composite samples, were

filled with liquid with pH up to 14. The blister cavities formed along the fiber/matrix interface⁵. Therefore, growth of galvanic blisters would result in increased fiber/matrix debonding with time. The study of the electrochemical reactions involved and the underlying mechanisms that lead to galvanic blistering of carbon composites will be the focus of this paper.

In the current investigation, galvanic blistering of carbon fiber reinforced vinyl ester composite was studied. The composite samples showed blisters of sizes in the range 1 - 2 mm in diameter and small ones in the range of 10 - 100 μm . The large blisters form in the zones where the polymer thickness is maximum and the small blisters form on the fibers closest to the surface where the polymer thickness is minimum. Figures (1) and (2) show these blisters respectively.

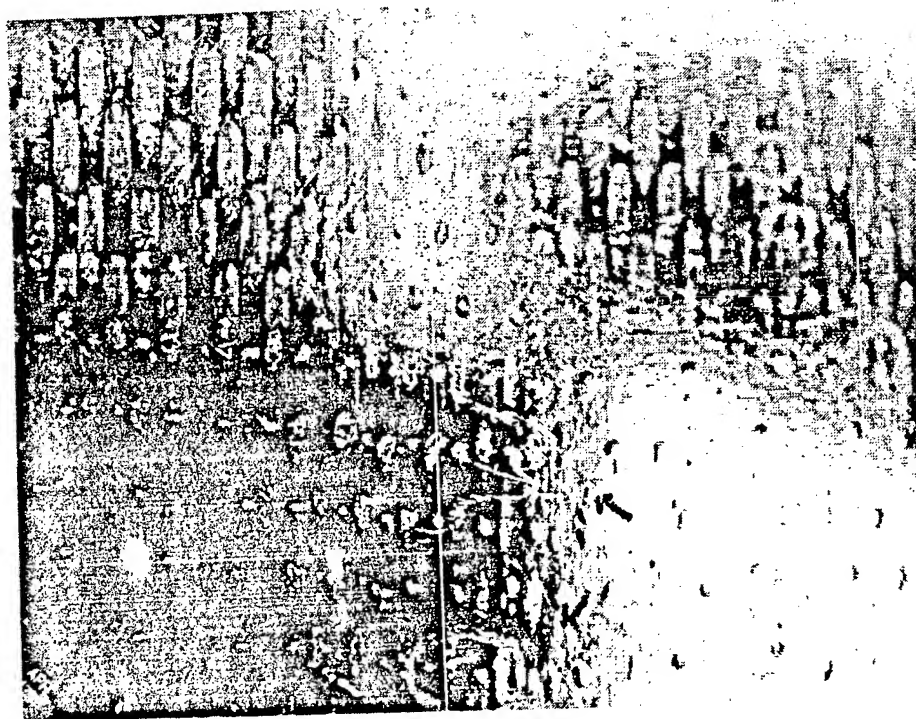
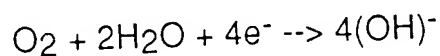


Figure 1. Large galvanic blisters on a carbon fiber vinyl ester composite.

The cathodic reaction on several carbon surfaces in neutral or alkaline environment is the electrocatalytic reduction of dissolved oxygen to hydroxyl ions⁶, that in equation form is:



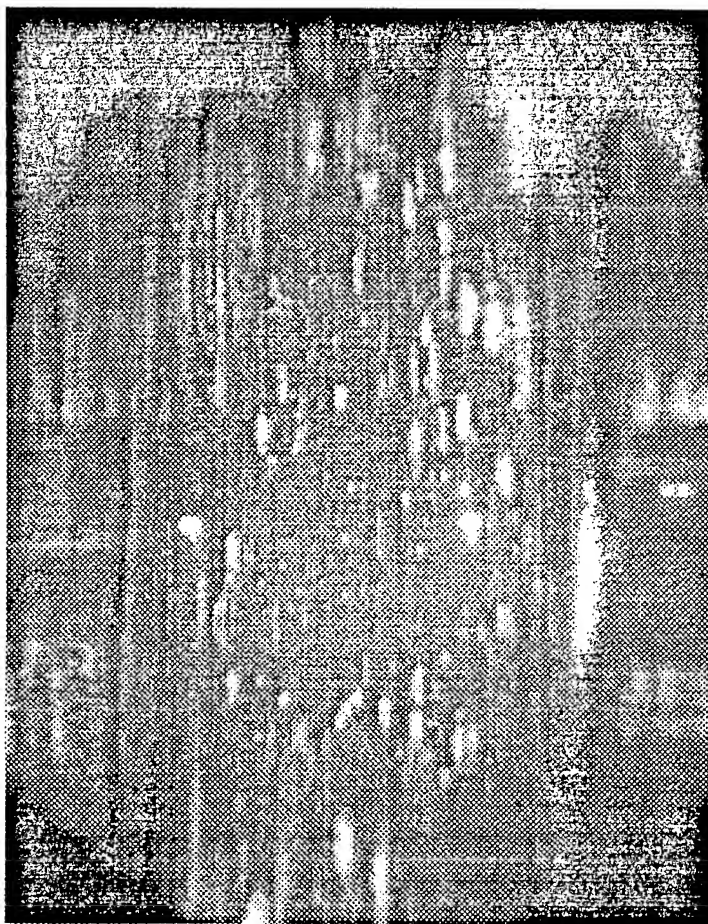


Figure 2. Small galvanic blisters on a carbon fiber vinyl ester composite.

The very high pH of the blister fluids suggests that this reaction is a possibility even on the carbon fibers embedded in a polymer matrix. Therefore, the effects of oxygen concentrations on corrosion currents, galvanic blister formation and electrochemical impedance response was investigated. A mechanism of galvanic blistering is proposed on the assumption that the cathodic reduction of oxygen occurs on carbon fibers in the composite. The results of the oxygen experiments will be discussed in light of the proposed mechanism.

EXPERIMENTAL PROCEDURES

Materials

An orthotropic laminate with unidirectional T300 carbon fiber tapes in a DERA KANE™ 470-36 vinyl ester matrix was studied. The laminate was characterized by a fiber volume fraction of 26%. Samples of dimensions 6 cm x 6 cm x 3 cm were cut from a 3 cm laminate. The resin-

rich faces of the samples were exposed to the electrolyte. The composite has several defects in the form of air bubbles which formed during processing. The exposed area is a 5 cm diameter circular area.

Electrolytes

The basic electrolyte used in the study was a 3.0 weight percent sodium chloride solution. The electrolyte was not changed during the period of experiments. The experiments were conducted at average ambient temperature of 70°F. Three different oxygen partial pressures in the electrolyte were chosen: (a) dissolved oxygen at 1 atmosphere by bubbling pure oxygen gas through the electrolyte; (b) dissolved oxygen at 0.2 atm. from dissolved air at one atmosphere in the electrolyte. (c) dissolved oxygen at 0.06 atm. attained by first preparing degassed sodium chloride solution from a freshly boiled, cooled, de-ionized and distilled water and the subsequent bubbling of nitrogen gas.

The oxygen concentrations were measured using a ORION Model 97-08-00 electrode. Since, the instrument can measure oxygen concentration up to 14 ppm only, the oxygen concentration at higher partial pressures i.e. oxygen concentration at 1 atmosphere was estimated by extrapolation. The activity coefficient was assumed constant in estimating the concentration of oxygen in the solution at a given gaseous partial pressure. Oxygen partial pressures used and the corresponding concentrations are given in the following table:

<i>Oxygen Partial Pressures in gas phase (atmospheres)</i>	<i>Concentrations of O₂ in solution (parts per million by weight)</i>
1.00 (high)	41.25 (estimated)
0.20 (medium)	8.25 (measured)
0.06 (low)	2.25 (measured)

Electrochemical Testing

The electrochemical apparatus for impedance testing is shown in figure (3). The cathodic potential applied to the samples was -0.9 volts versus a saturated calomel electrode (SCE). The potential of -.9 V was chosen because it is below the E_{corr} of carbon with several engineering metals and is the greatest cathodic potential reached above water stability limit. An EG&G PARC model 273 and model 363 potentiostats were employed to apply and maintain the potentials. Current values were recorded at different exposure times. The electrochemical impedance for these samples was also measured at various times during exposure. A Solartron model 1255 HF frequency response analyzer supplied the input signal and analyzed the response signal. The instruments were coordinated and the data acquired using an IBM personal computer. The

EG&G M388 user interactive software was used to execute the experimental procedures.

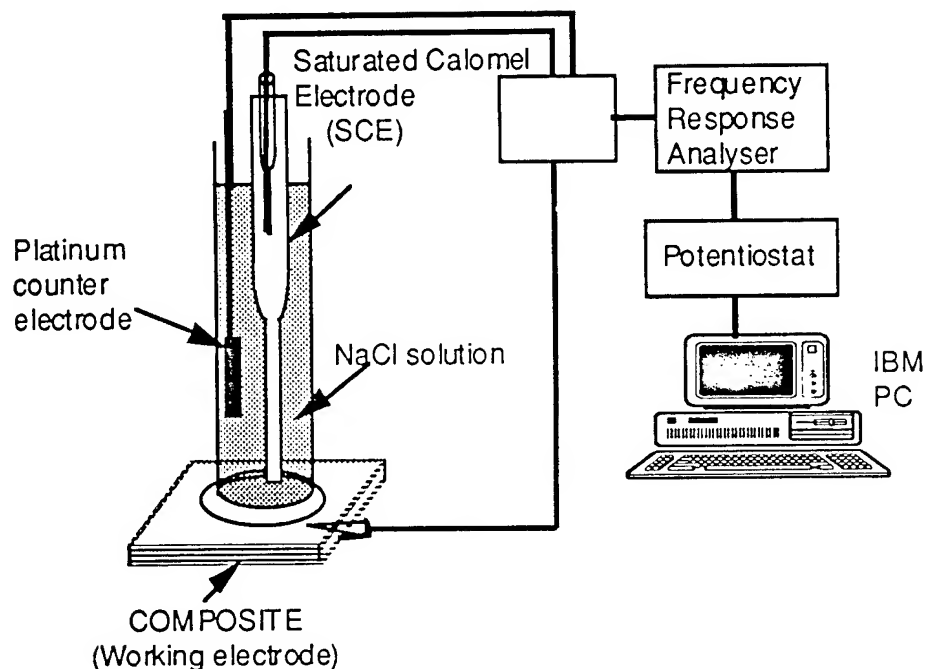


Figure 3. Experimental apparatus for electrochemical testing.

Surface Examination

Visual examination of samples was also conducted at different times during the period of exposure to examine for blisters. The time for blisters to grow to a diameter approximately 1 mm diameter was arbitrarily termed as the *blister detectability time* (BDT). Only the large blisters were detectable by this technique. The BDT was used as a criterion to compare the rate of blistering of the samples. Therefore, from definition it follows that the lower the BDT, the greater the rate of blister growth and vice-versa. The blister detectability times were recorded for the three samples.

RESULTS AND DISCUSSION

The proposed blistering mechanism

From the results of this study a mechanism can be proposed for blister formation. The first part of the process is the initiation of the blister at the carbon fiber/polymer interface. Two possible mechanisms are available to the initiation process. Both of the mechanisms involve the creation of a free volume. The first depends on decreasing the adsorption

of the polymer to the carbon fiber. The carbon fibers develop a negative surface charge when galvanically coupled. As a result, the electron dense parts of the adhering polymer chains do not absorb onto the carbon fibers as strongly. A local aqueous film nucleates in these debonded zones due to the initial zero partial pressure of water in these zones. The movement of water also brings sodium ions and oxygen into the region.

The second mechanism suggests that the carbon fiber to polymer interface is unlikely to be perfect. As a result local areas of no bonding between them will exist. The hydroxyl ion can be formed in these regions as water along with oxygen will tend to permeate to these defect regions preferentially. For both initiation mechanisms, oxygen reduction to hydroxyl ions takes place on the carbon surface. As a result sodium hydroxide solution is formed. Sodium hydroxide is highly hygroscopic and draws more water into this region. The coupled effects of (a) relatively greater diffusion rates of water through the polymer compared to sodium hydroxide solution and (b) the rate of production of hydroxyl ions being greater than the hydroxyl ion diffusion away from the cathodic sites, builds an osmotic pressure in the region.

Once the initiation stage is reached, the blister grows due to polymer layer deformation, creep and fiber/matrix interface failure or unzipping under this pressure. The growth is sustained by continuous production of hydroxyl ions which maintains high concentration of sodium hydroxide in the blister liquid. The blister growth therefore results in interface debonding with time.

Oxygen Experimental Results

The measured current densities (current divided by exposure area) as a function of exposure time for the three cases of oxygen concentrations: high, medium and low is shown in figure (4). The current increases to a high value rapidly within a few hours and drops off to a steady value for the cases of high and medium oxygen concentrations.

The steady state current density for the sample exposed to higher oxygen concentration is five times the current density for the case of medium oxygen concentration. At the same time, the high oxygen concentration is five times the medium oxygen concentration. It follows therefore, that the current density of the carbon fibers increases proportionally with increase in oxygen partial pressures in the electrolyte.

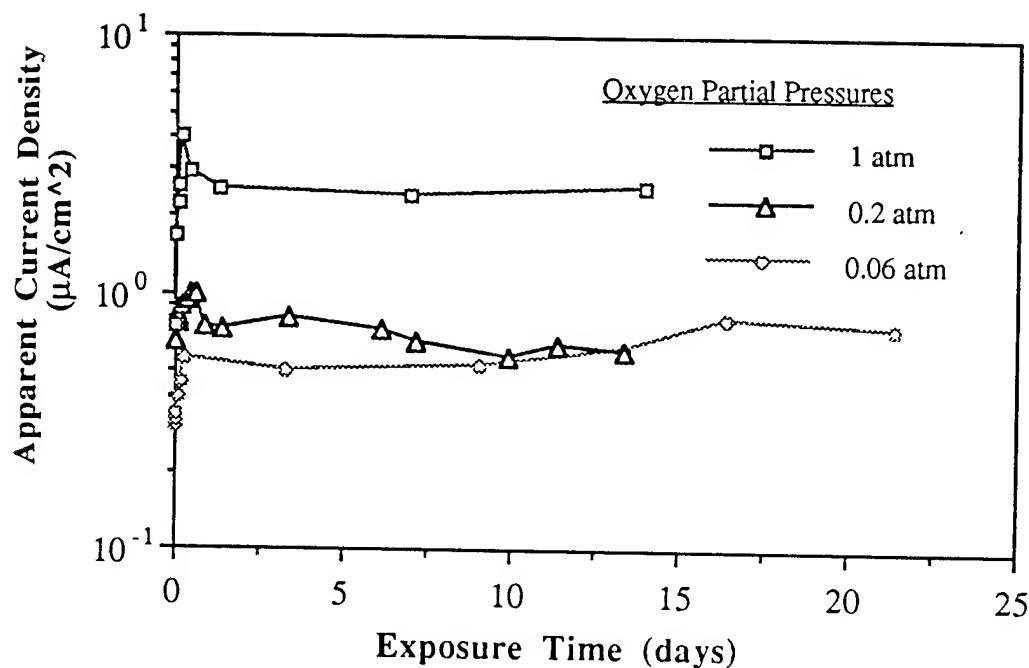


Figure 4. Current time profiles for three oxygen partial pressures at -900 mV(SCE) for a carbon fiber vinyl ester composite.

This indicates that the carbon fibers in the carbon fiber vinyl ester composite support oxygen reduction reaction producing hydroxyl ions under the applied potential conditions. Moreover, the variation of corrosion current with oxygen concentration is direct evidence that the current is diffusion limited by oxygen diffusion rates towards the cathode. The existence of diffusion limited current in carbon/vinyl ester composites was earlier reported² and is shown in figure (5).

The plot in figure (5) shows a comparison of potential-current density plots between a carbon fiber composite and free carbon fibers. It can be easily seen that the current is diffusion limited for both cases. The fact that increased debonded area results at higher oxygen concentrations coupled with the fact that the current density is proportional to oxygen concentration implies that the significant current is liberated only at these damaged areas of the composite and the current at the carbon/polymer interface is negligible. The steady state current value for the low oxygen case is same as that of the medium oxygen case. One possible reason for this behavior is as follows: The faces of the sample other than the exposed face to electrolyte were exposed to the ambient. Therefore, even though the electrolyte contains less oxygen for the low oxygen case, oxygen from the atmosphere (partial pressure = 0.2

atm) permeates through the sides of the sample, into the sample, resulting in a higher steady state current density.

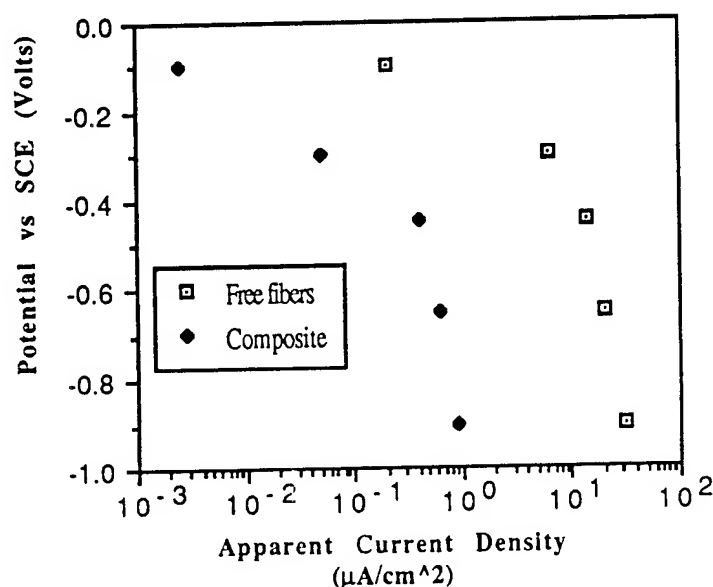


Figure 5. Potential current density data for free carbon fibers and for a carbon fiber vinyl ester composite.

The composite samples, before exposure, were all in equilibrium with atmosphere and therefore were saturated with air from the atmosphere. The higher current above the steady state values for the medium and high oxygen concentrations is due to the high oxygen concentration inside the composite at the initial condition. Once this happens, the near fiber region will be devoid of oxygen and the current drops to a steady value determined by the amount of oxygen in solution. However, the high initial current greater than the steady state value is absent for the low oxygen case because of the negligible contribution of oxygen from the electrolyte solution.

The blister detectability time as a function of oxygen partial pressures is shown in Figure (6). It can be seen that $1/\text{BDT}$, which is proportional to the blister growth rate, increases with increasing oxygen concentration. This indicates that indeed the blistering phenomenon is related to the oxygen reduction reaction and the data serves as a validation of the proposed blistering mechanism.

Since the amount of cathodic debonding is a function of charge liberated or the amount of hydroxyl ions produced at the cathode less the amount diffused away from cathodic sites, it is of interest to determine if the oxygen partial pressures affect the cumulative charge densities. The cumulative charge density (CCD) was calculated by numerically integrating the current densities with respect to time.

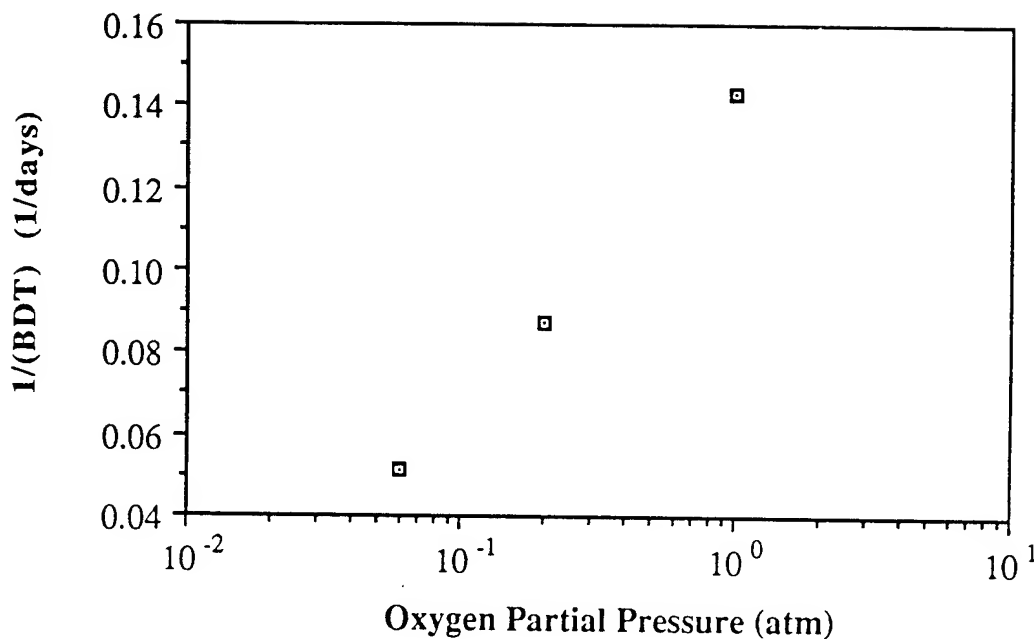


Figure 6. The effect of oxygen partial pressure on galvanic blister growth rate at an applied potential of -900mV(SCE).

The CCD as a function of time for the three cases of oxygen concentrations is shown in figure (7). It can be seen that the charge densities exponentially increase with time initially but at very slow rates at large exposure times.

The most interesting feature is that the cumulative charge densities increase by 4 orders of magnitude during the initial periods of exposure and at the blister detectability time, they all are within the order of magnitude of 1 coulombs per sq. cm. for this composite under the given experimental conditions. The rapid increase of CCD during the initial times was attributed to the combined effect of the increased area of exposure of carbon fibers to the diffusing electrolyte solution and to rupture of small blisters formed on the fibers closest to the surface that expose the fibers and to the change in polymer resistance as water and ions build up inside.

Because the blistering rates are greater for higher oxygen partial pressures, the electrochemical changes were rapid with increasing oxygen concentrations and therefore it would be interesting to compare the impedance behavior in all the three cases at the same normalized exposure time based on the blister detectability time. This comparison at 1% of the BDT for the three cases of oxygen concentration is shown in Figures (8a) and (8b). The Bode plots in these figures show somewhat similar profiles for all the samples.

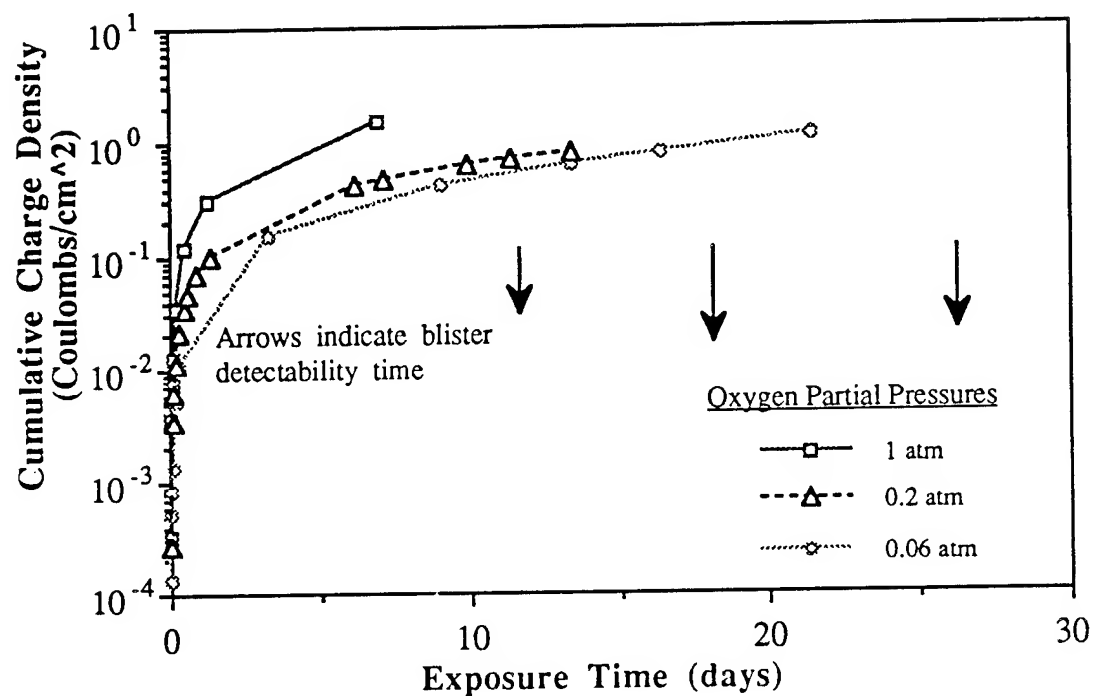


Figure 7. Temporal changes in cumulative charge density for blister detection.

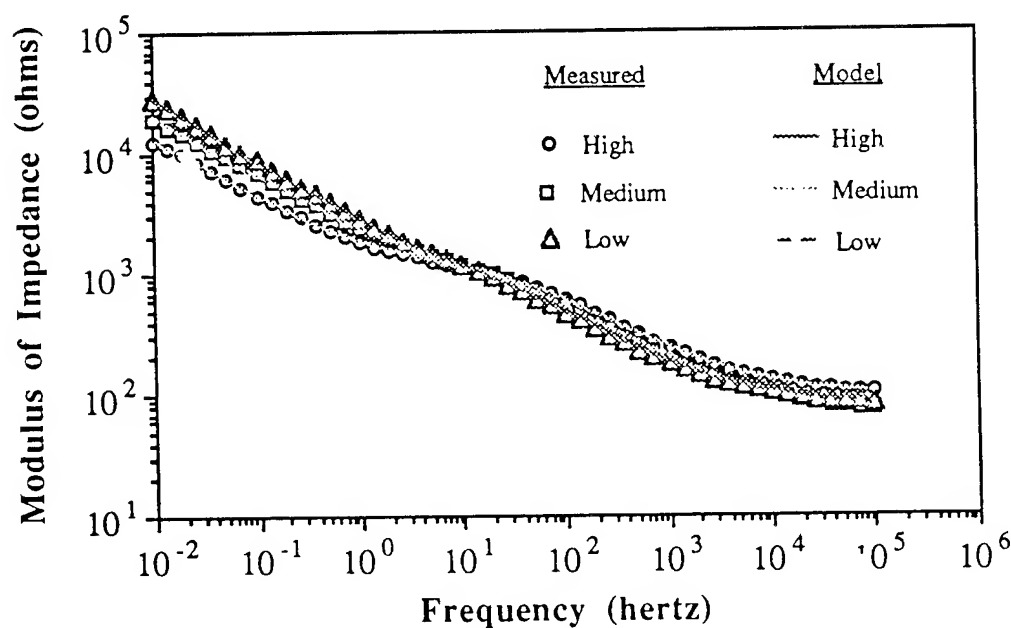


Figure 8a. Bode magnitude data and model fit for high (1 atm),

medium (0.2 atm) and low (0.06 atm) oxygen partial pressures at -900mV at 1% of blister detectability time.

The Bode phase angle plot shows that the phase angle maxima at lower frequencies shift to lower frequencies and the maxima at the higher frequencies shift to higher frequencies with increasing oxygen concentrations. This indicates that the two time constants differ more with increasing oxygen concentration because of greater reaction rates and increased debonded area for higher oxygen concentrations.

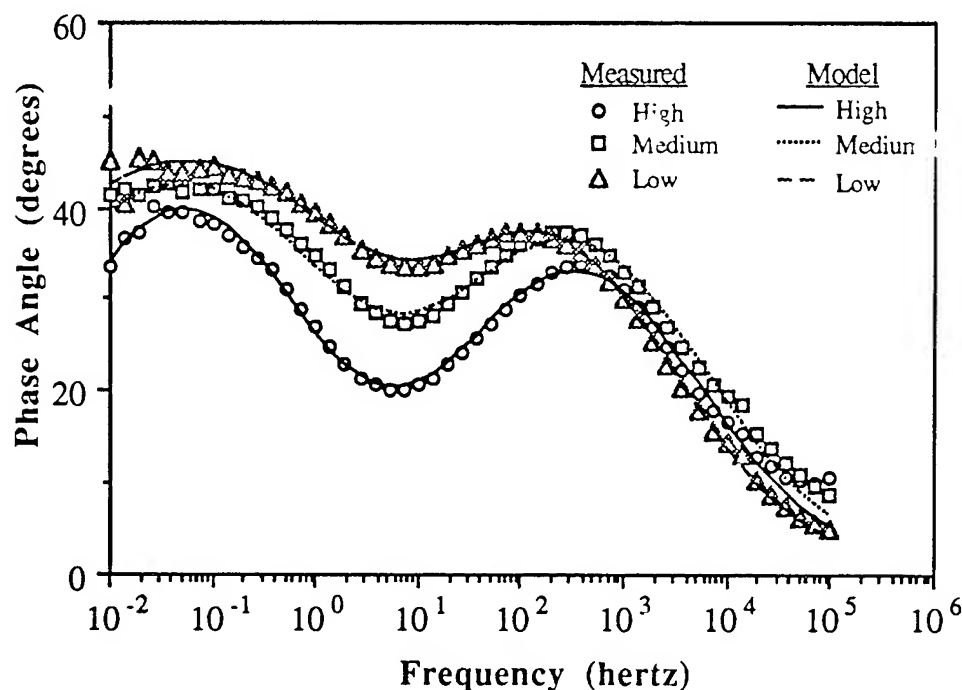


Figure 8b. Bode phase angle data and model fit for the same conditions as figure 8a.

Indeed, the existence of two time constants or two peaks in phase angle dispersion indicates defects in polymer layer where the fibers are directly exposed to the electrolyte. In an earlier investigation it was also proved that the shift of higher phase angle maxima to higher frequencies indicate greater area of exposed fibers to the electrolyte⁷. Therefore, it follows that higher oxygen concentrations in greater damage in the polymer layer due to greater number of blisters.

CONCLUSION

The effects of oxygen concentration on galvanic blistering in carbon fiber composites was investigated and a mechanism for blistering

CONCLUSIONS

1. The fiber type did not significantly influence the degradation mechanisms of the composites under galvanic exposure conditions. The polymer conditions, fiber surface treatment and interface behavior between fibers and polymer matrix are the more important control parameters.

2. The parameters from modeling provided an important degradation mechanisms of composites.

3. The decreasing in polymer resistance, R_p , with increasing time of exposure indicated that dynamic degradation processes were occurring due to the cathodic reaction at the fiber surface. The value of R_p also decreased with increasingly negative applied potentials.

4. The observed damage on exposed specimen provided an evidence of decreasing of impedance behavior of composites.

REFERENCES

1. W. C. Tucker and R. Brown, J. of Composites, Vol. 23, 1989, p.389.
2. Kaushik, D., M. N. Alias and R. Brown, Corrosion, Vol. 47, 1991, p.859.
3. M. N. Alias and R. Brown, Corrosion, Vol. 48, 1992, p.373.
4. S. Miriyala, W. C. Tucker, T. J. Rockett and R. Brown, "Proceedings of the Ninth International Conference on Composite Materials", Madrid, Spain, 1993, p. 586.
5. F. Mansfeld, M. W. Kendig and S. Tsai, Corrosion, Vol. 38, No. 9, 1982, p.498.
6. W. M. Kendig, F. Mansfeld and S. Tsai, Corrosion Sciences, 23 (1983), p.317
7. R. Delasi and J. B. Whiteside, Advanced Composite Materials - Environmental Effects, ASTM STP 658, J. R. Vinson, Ed., ASTM, 1978, p.2.
8. G. Lubin, Handbook of Composites, SPE. p. 513.
9. W. H. E. Reynolds, R. Brown and M. N. Alias, "Comparison of the Performance of a Carbon Fiber Composite Materials in Distilled Water and Chloride Solutions", NACE, 1994, Baltimore, MD.
10. I. Verpoest, "Interfacial Phenomena in Composite Materials '91", Proceeding of the second international conference held 17-19 September 1991 in Leuven, Belgium.
11. J. Qin and R. Brown, unpublished data.

Microbial Degradation of Polymeric Materials

Dr. Ji-Dong Gu^{1*}, Dr. T.E. Ford², Ms. K.E.G. Thorp³, and Dr. R. Mitchell¹

¹Laboratory of Microbial Ecology
Division of Applied Sciences
Harvard University
Cambridge, MA 02138-1903

²Department of Environmental Sciences
Harvard School of Public Health
677 Huntington Ave
Boston, MA 02115

³Nonmetallic Materials Division
University of Dayton Research Institute
300 College Park
Dayton, OH 45469

ABSTRACT

Microorganisms and their products may be responsible for changes in physical, chemical, and electrochemical properties of polymeric materials. We investigated microbial degradation of polyimides used as insulators in electronic packaging. Growth of microorganisms on these polymers was found to result in loss of their dielectric properties. Failure of polyimide films on stainless steel coupons caused by microbial degradation was evaluated with a fungal consortium partially identified as *Aspergillus versicolor*. We obtained distinctive electrochemical impedance spectroscopy (EIS) spectra showing failed polyimides in the presence of the fungal consortium. Decrease of film resistance by two orders of magnitude relative to uninoculated control systems was observed within one week of incubation. The relationship between changes of impedance spectra and microbial degradation of the coatings

was further established by scanning electron microscopic (SEM) observations of fungi on the surface of the polyimides.

We also studied the biodeterioration of fiber reinforced composites, graphite sheets, and graphite fibers used in composite materials. One set of samples was inoculated with the fungal consortium mentioned above, and another set was kept sterile. In all inoculated treatments the fungi adhered to and grew on the composites, graphite sheets, and fiber surfaces. SEM was used to determine adhesion of fungi and subsequent etching of the samples. Fungal penetration into composite resin and graphite sheets was observed. Our data indicate that fungi may cause substantial damage to composites under conditions favorable to fungal growth.

INTRODUCTION

Polyimides are an important class of electronic packaging materials used in fabrication of integrated circuits (Lai, 1989). They are also being utilized in the manufacture of new high-temperature resistant composites. Fiber reinforced composites (FRC) have wide applications in transportation, aviation, and aerospace (Delmonte, 1981). Recently, a new process of thermosetting composites using polyimides has been developed because of the high temperature resistance of this polymer. Further development of high strength, stiffness, and lower weight FRC's compared to alloys has been accelerated due to the corrosion resistance of this class of engineered materials.

Composites have a two-phase structure: a fiber which acts as the reinforcement, and a resin matrix which bonds and holds all the fibers. A maximum number of fibers is contained per unit volume as a means of increasing the strength of the composite material since the fiber dictates the strength, and each fiber takes its full share of the load. The structural integrity of the composite material is the key to its performance success.

A number of factors may influence the integrity of a FRC, including bonding between fiber and matrix, distribution and orientation of fibers in the matrix, and responses of each composite constituent to environmental conditions including moisture, temperature, and microbial contamination. Weakening of one composite constituent can cause progressive delamination, disbonding and separation of the fibers from reinforcing

resin matrices, resulting in reduced strength and stiffness. Failure initiation factors include imperfections, weakening of the interface bonding between the fibers and matrix, and further delamination and separation of the two components (Agarwal and Broutman, 1990). In a study of the corrosion of graphite fibers/magnesium alloy composites in a very dilute NaCl solution, Trzaskoma (1986) reported that severe degradation of graphite fibers was observed after a five-day exposure period.

It is suspected that biological damage to a composite material may significantly affect its physical integrity and fatigue performance. Since there are several chemically and physically distinguishable constituents in a composite, localized chemical changes resulting from growth and metabolism of microorganisms may accelerate damage to composite constituents. Specific surfaces or voids in the FRC may concentrate nutrients, providing a favorable microenvironment for microbial development. Fibers may serve as capillaries to improve the movement and distribution of moisture and chemical species within the composite, and may enhance the spread of microorganisms within the composite structure. Slight chemical changes in localized regions may drastically decrease the material's performance and weaken the composite's physical properties. Knowledge of the effect of microorganisms on the integrity of composite materials is needed for a comprehensive assessment of microbial damage and for the future development of resistant materials.

This report describes preliminary studies of microbial degradation of polyimides and composites by a fungal consortium under laboratory conditions. Electrochemical impedance spectroscopy (EIS) was used to measure polyimide coating deterioration in electrochemical cells.

MATERIALS AND METHODS

Electrochemical impedance spectroscopy (EIS): EIS cells were constructed by gluing a 50.0 mm long acrylic tube (30.0 mm diameter and 4.0 mm thickness of the wall) onto a steel coupon (50.0 X 50.0 mm) by epoxy (Devcon 5 minute Epoxy, Danver, MA 01923). The steel coupons were previously attached with a round piece of Kapton polyimide film as received from Du Pont Co. The adhering material for the film onto the coupon was silver epoxy (SPI Instrumental, West, PA). After drying, 15.0

mL of 0.2 M NaCl solution were added into the acrylic tube to serve as working electrode during determination. A diagram of the cell is shown below.

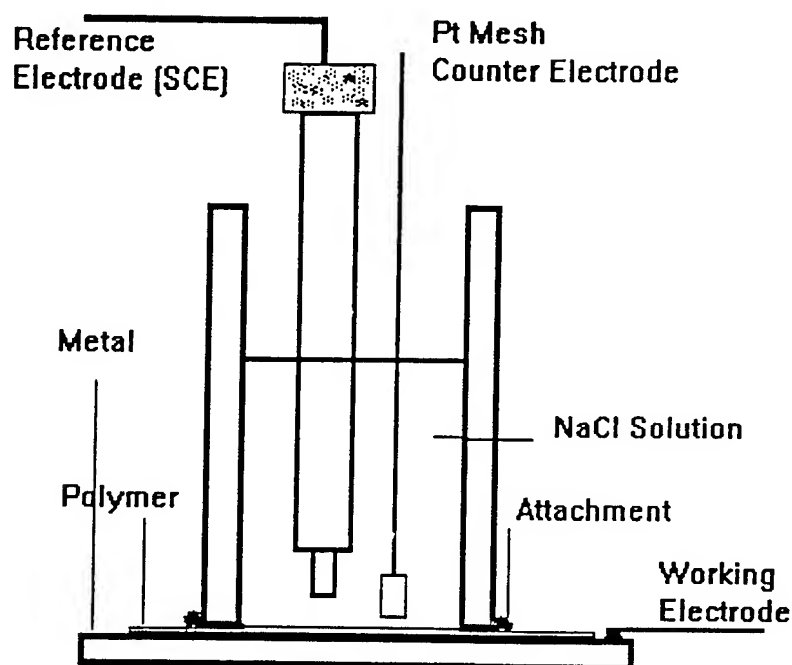


Figure 1. Schematic diagram of the electrochemical cell used

Our EIS consists of a Schlumberger 1250 frequency response analyzer with Schlumberger 1286 electrochemical interface. During data acquisition, samples were potentiostatically held at their open circuit potential (OCP) and a sinusoidal perturbation of 20-50 mV applied to the system. The impedance response was measured over a range of frequencies from 65 kHz to 1 mHz and spectra were recorded as a function of immersion time at ambient temperature. OCP were monitored versus a saturated calomel electrode. The electrode was polarized to its OCP and an AC signal of 20 mV superimposed. Frequency were swept from 65 KHz to 1 mHz and the gain and phase shift monitored. Both Bode plots were used to provide information on increases in porosity, local defects and delamination (Titz et al., 1990)

At weekly intervals, EIS celis of inoculated and sterile control coupons were determined on EIS for their impedance responses. When film failure was observed, film in the EIS cell was taken and prepared for examination by scanning electron microscopy (SEM).

SEM sample preparation: Samples of polyimide films, graphite sheets, fibers and composite material were prepared for SEM examination as follows: samples were treated with 3% glutaraldehyde buffered with 0.2 M sodium cacodylate in deionized water filtered through 0.2 μ m polycarbonate membrane filter (Gelman Science, Ann Arbor, MI), washed with 0.2 M Na cacodylate three times, fixed in 1% osmium tetroxide with 0.1 M Na cacodylate, and rinsed with Na cacodylate and deionized water. Dehydration of samples was accomplished in an ethanol-distilled water series of 40 to 80% ethanol with increments of 10%, and 85 to 100% ethanol with 5% increments. Samples were then critical point dried in liquid CO₂ (Samdri PVT-3B, Tousimis Research Co., Rockville, MD), coated with platinum and viewed under an AMR 1000 SEM.

Incubation studies: Composites (labeled from A to E), graphite sheets (Goodfellow Co., Malvern, PA), and graphite fibers (P-25, P-100, and Toray), were autoclaved before aseptic introduction into culture flasks containing 80 mL of Malt Broth medium (Difco Lab., Detroit, MI). One set of flasks was inoculated with the above mentioned fungal consortium and another set was kept sterile. At monthly intervals, samples from the inoculated and control flasks were taken for SEM examination.

RESULTS AND DISCUSSION

Biodegradation of Polyimides

Polyimide degradation was observed on the inoculated EIS cells within the first week of incubation (Fig. 2a). During the same period of time, there were no apparent changes in the sterile cells (Fig. 2b). EIS measures the resistive, capacitive, and inductive components of the overall interfacial impedance. Resistance of the polyimide films dropped from 10^8 to about 10^6 Ohms cm⁻² within the first week. A coating resistance of 10^7 Ohms cm⁻² is considered "good." Such a large decrease in resistance reflects significant microbially caused changes in the coating dielectric properties. These results suggest that EIS is a particularly useful analytical technique to carry out accelerated testing of microbial deterioration of coating materials.

Over the one week incubation, there was increased permeability of the polyimide coated metal indicating the failure of protective properties of the polyimide exposed to the fungi. Association of fungi with the

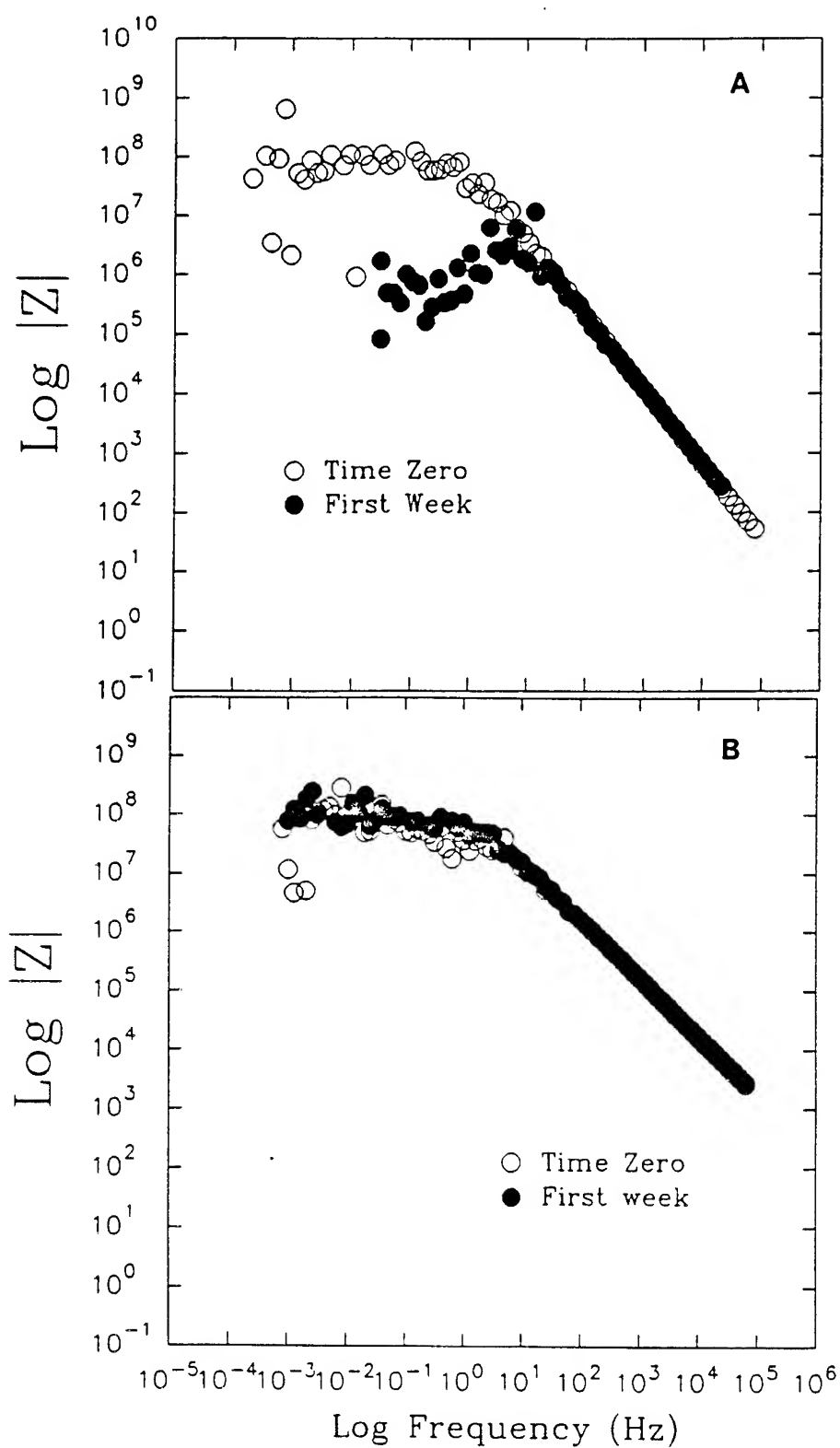


Figure 2. Bode plots of EIS cells inoculated with fungal consortium (A) compared to the sterile control (B)

polyimide failure was observed by SEM examination of the deteriorated film (Fig. 3). Fungi were found to be associated with the degradation of polyimide coating and the deterioration of coating dielectric properties. Though it is not conclusive at this stage if the fungi utilize polyimides as a source of carbon and energy, further studies will provide information on the mechanism by which polyimide coatings are degraded.

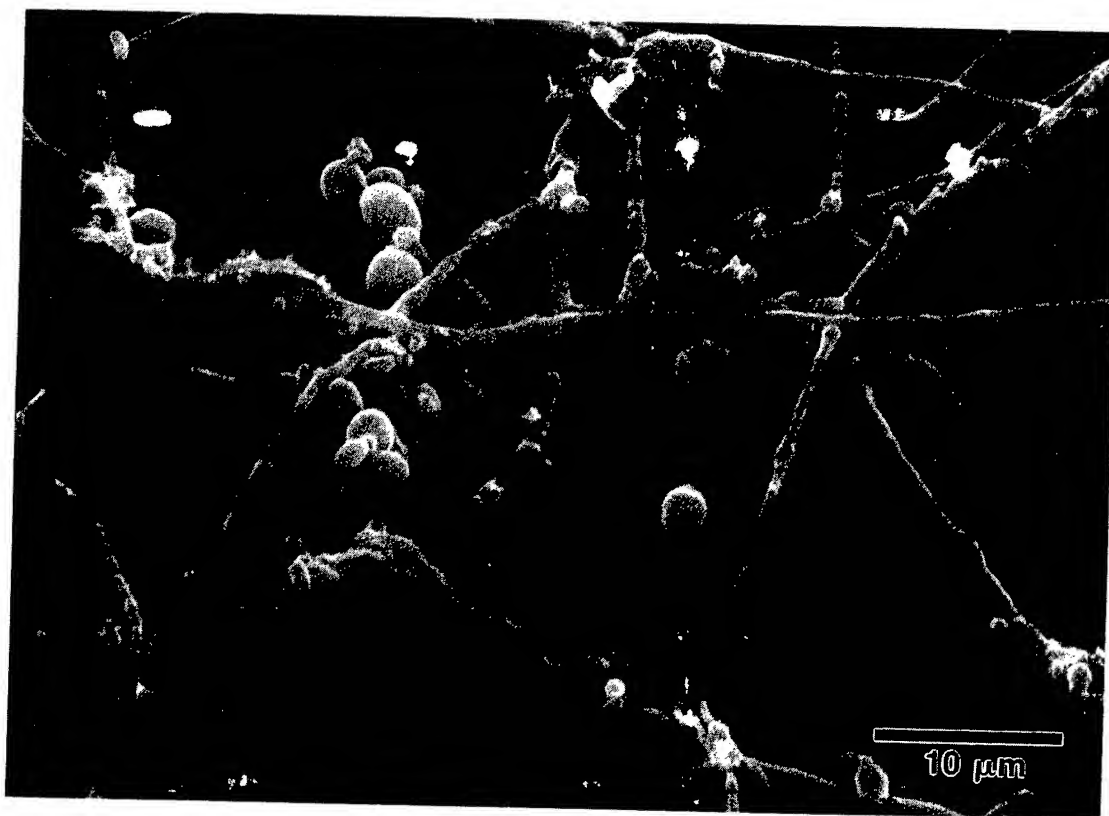


Figure 3. SEM micrograph of fungi on deteriorated polyimide films from an inoculated EIS cell after 7 days of inoculation

Susceptibility of fiber reinforced composites to fungi

We examined five composites for their susceptibility to degradation by our fungal consortium. Effects of fungal degradation on composite mechanical property are reported separately (Thorp et al., 1994). Results suggest that the composite (sample A) containing AFR-700 resin was the most susceptible to fungal attack. Localized penetration of composite resins by fungal hyphae was shown by SEM (Fig. 4). The stability of the resin is important to the performance of the complex composite materials.

Impurities can catalyze the breakdown and directly accelerate the degradation of the composite (Wilkins et al., 1982).

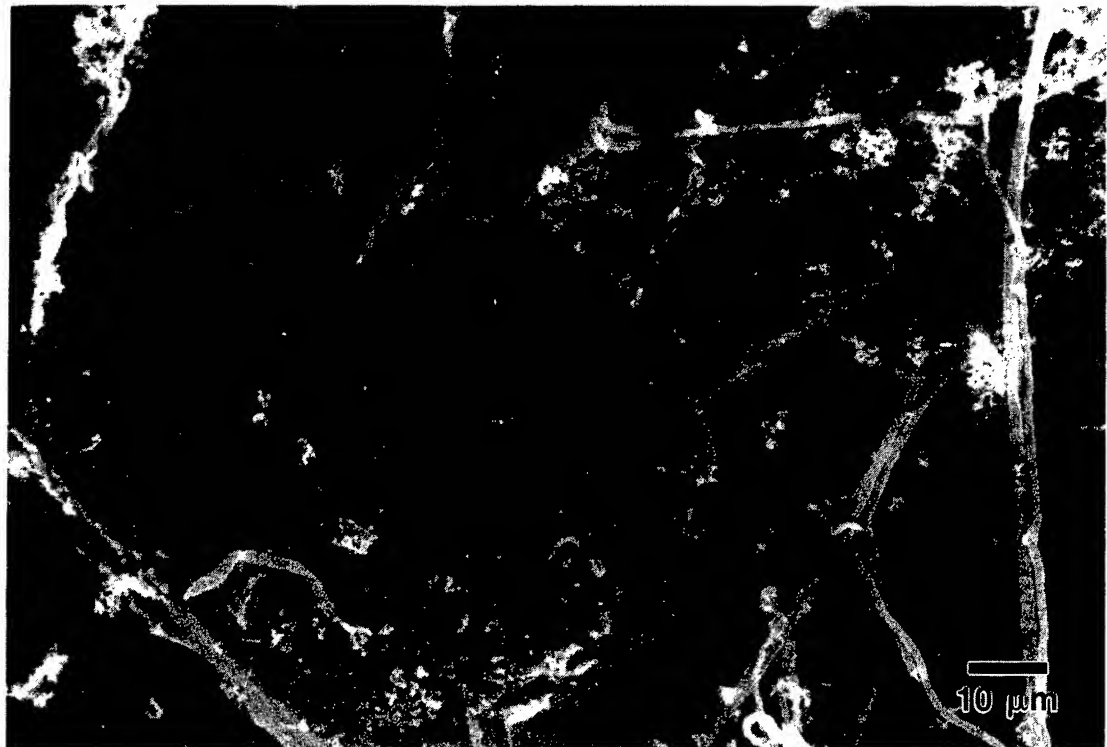


Figure 4. SEM micrograph of fungi on the composite containing AFR-700 resin after 30 days of incubation

These preliminary results prompted us to test the polymer constituents by incubating graphite sheets and graphite fibers (P-25, P-100, and Toray) with the same fungal consortium under the same conditions. Our results on these materials showed that fungi have the ability to colonize the surface of both graphite sheets and fibers extensively. Fungal penetration into graphite sheets was observed (Fig. 5). On day 84 P-100 fibers were found to be covered with fungal hyphae (Fig. 6). It appears that fibers in the composite promote fungal colonization by serving as capillaries for transporting chemicals from susceptible regions or external surfaces, stimulating extensive microbiological invasion and colonization of the composite materials.

Christner et al. (1987) suggested that material degradation advances by crack propagation. In acid environments, degradation occurs along crack lines. Microcracks in the composites are a result of

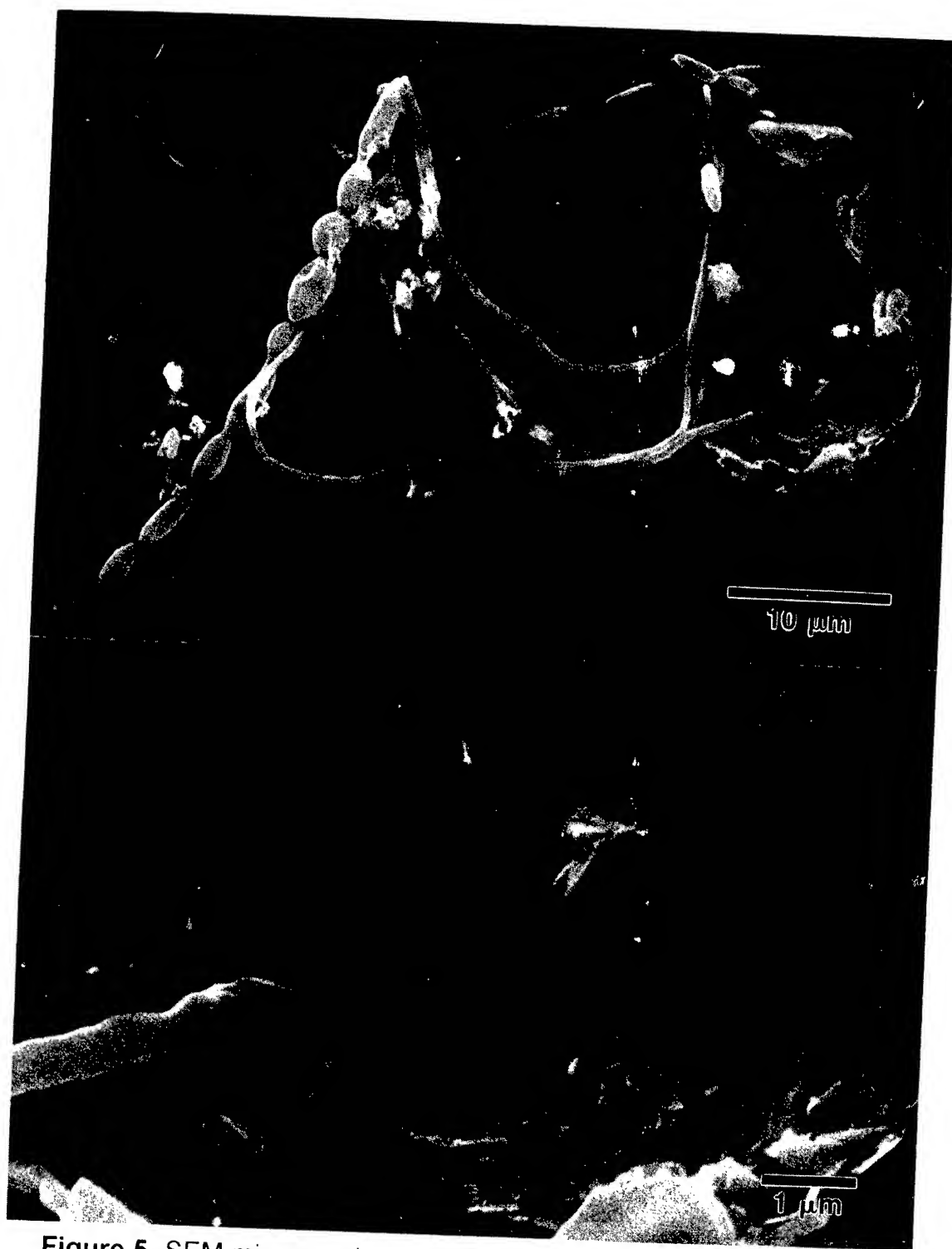


Figure 5. SEM micrographs of fungi penetrating a graphite sheet after 30 days of incubation

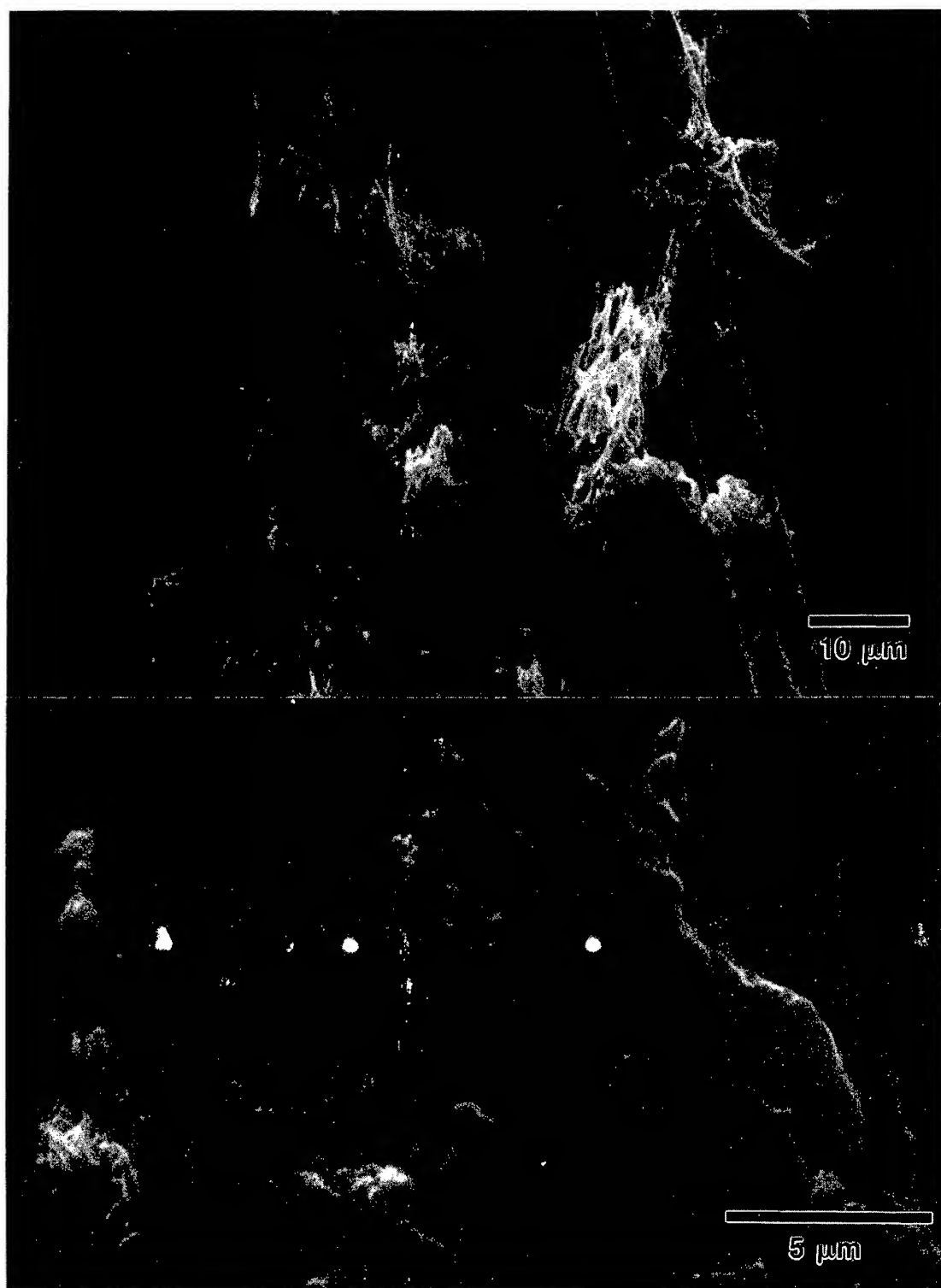


Figure 6. SEM micrographs of fungi growing on graphite fiber P-100 on day 84 of incubation

the curing process in which the resin becomes hard while forming a close association with the fibers embedded in it. Commonly used resins are polyesters, epoxies and phenolics which hold the fibers in position and serve as the matrix material. Epoxy or polyester resins can absorb up to 4-5% by weight of water when exposed to humid conditions (Agarwal and Broutman, 1990). However, the water is not evenly distributed in the resin matrix, but in micropores and microcracks that are sufficiently large for the colonization of microorganisms. The success or failure of FRCs is also governed by the degree of adhesion occurring between the fiber surface and the resin matrix.

It is standard practice to coat the surface of the filaments with a sizing chemical to provide a better bonding with the resin matrix and to prevent abrasion between individual fibers during shipping and handling. This treatment permits optimal stress transmission between filaments. The fiber sizing is often a starch-oil mixture used to minimize the degradation of strength resulting from abrasion between fibers, and as a coupling agent to the matrix. The sizing materials are highly susceptible to biodegradation and can be expected to decompose in the presence of contaminating microorganisms.

Biodeterioration of graphite sheets by our fungal consortium was also studied. However, it is not clear from this study to what degree graphite fibers may be degraded. The answer to this question requires more sophisticated studies using surface analytical techniques.

Further testing of resins and sizes will enable us to identify the susceptible constituents of composites and the extent of the damage to composite materials. In addition, application of surface characterization techniques should improve our understanding of the mechanism of microbial deterioration of the composites.

ACKNOWLEDGMENTS

This research was supported in part by the Air Force Office of Scientific Research Grant No. S49620-92-J-0108. We thank Mr. E. Seling for assistance with SEM preparation and observations.

REFERENCES

- Agarwal, B.D., and L.T. Broutman. 1990. Analysis and performance of fiber composites (2nd ed.). John Wiley & Sons, Inc., New York.
- Christner, L.G., H.P. Dhar, M. Farooque, and A.K. Kush. 1987. Corrosion of graphite composites in phosphoric acid fuel cells. *Corrosion*. 43:571-575.
- Delmonte, J. 1981. Technology of carbon and graphite fiber composites. van Nostrand Reinhold Company, New York.
- Lai, J. H. 1989. Polymers for electronic applications, CRC Press, Inc., Boca Raton, Florida.
- Thorp, T.E.G., A.S. Crasto, J.-D. Gu, and R. Mitchell. 1994. Biodegradation of composite materials (in this proceedings).
- Titz, J. G.H. Wagner, H. Spahn, M. Eber, K. Juttner, and W.J. Lorenz. 1990. Characterization of organic coatings on metal substrates by electrochemical impedance spectroscopy. *Corrosion* 46:221-229.
- Trzaskoma, P.P. 1986. Corrosion behavior of a graphite/magnesium metal matrix composite in aqueous chloride solution. *Corrosion*. 42:609-613.
- Wilkins, D.J., J.R. Eisenmann, R.A. Camin, W.S. Margolis, and R.A. Bensen. 1982. Characterizing delamination growth in graphite-epoxy. K.L. Reifsnider, Ed., Damage in composite materials. ASTM STP 775, p. 168-183. Philadelphia, PA.

Biodegradation of Composite Materials

Ms. Katie E. G. Thorp* and Dr. Allan S. Crasto
University of Dayton Research Institute
300 College Park
Dayton, OH 45469-0168

Dr. Ji-Dong Gu and Dr. Ralph Mitchell
Harvard University, Division of Applied Sciences
29 Oxford Street
Cambridge, MA 02138

ABSTRACT

The matrix- and interface-dominated properties of fiber-reinforced polymer composites are known to be sensitive to absorbed moisture. In addition there is a potential for electrochemical corrosion when a carbon fiber composite is mechanically coupled with a metal, such as aluminum, in an aqueous environment. When these composite materials are exposed to aqueous solutions of nutrients, a substantial amount of biological activity is noted on and around the composites. The biological species has been identified as a fungus which is believed to be present in the as-sectioned composite specimens. In light of these observations the question arises of whether composite degradation in humid environments may be assisted or enhanced by biological microorganisms. A study was conducted to investigate this premise wherein biologically-active and sterile composite specimens were immersed in distilled water and a solution of nutrients. The growth of microorganisms was investigated using scanning electron microscopy, and their influence on mechanical property degradation was determined from measurements of interfacial and interlaminar shear strengths on model glass/epoxy composites and unidirectional graphite/epoxy composites, respectively. Mechanical couples of aluminum and a graphite/BMI laminate were also subjected to similar treatments in

aqueous salt solutions, and corrosion of the laminates at the liquid/air interface was compared by SEM.

INTRODUCTION

It has long been known that polymeric materials are susceptible to biological degradation. Examples where such biodegradation is prevalent include pressure-sensitive tapes used for coating gas pipes, polyethylene lids on milk churns, coatings for buried pipes and cables, foams placed in the fuel tanks of military aircraft for explosion prevention, raincoats, liners of gasoline storage tanks, electronic component insulation, and plastic upholstery materials [1]. Most of the literature dealing with biodegradation of polymeric materials is associated with plasticized vinyl systems. The incorporation of plasticizers can enhance the biological attack of otherwise resistant polymers, and the study of microbial deterioration of polymeric formulations has centered mostly on the involvement of microbes with the plasticizer additives [1]. Polyvinyl chloride and other polymers containing suitable nutrients for fungal and bacterial growth require the addition of an antimicrobial agent to prevent growth of microorganisms. Many synthetic polymers are believed to be inert to biological degradation. The reason for this apparent microbial inertness is probably a combination of parameters including chemical bonding, molecular size, molecular configuration, and the ability to absorb water, as well as other undefined factors. Microbial attack can cause polymer property degradation and result in product embrittlement, cracking, and ultimate failure [2].

Microorganisms generally require C, H, O and N, among other elements, as nutrients for survival. Water is also usually required for the microorganisms to function properly. Many of these elements are present to some degree in fiber-reinforced composite materials. However, since synthetic composites to a large extent were thought to be biologically inert, limited work has been done on the biodegradation characteristics of these materials. A material which ordinarily is biologically inert may be susceptible to secondary degradation mechanisms caused or enhanced by biological activity. During their metabolic process microorganisms exude or deposit a variety of waste products which may interact with composite materials in a variety of ways. Possible mechanisms for microbial degradation of polymeric composites include direct attack of the resin by acids or enzymes produced by the microorganisms, blistering as a result of gas evolution within the polymeric phase, cracking due to by-product deposition, and/or

polymeric destabilization by concentrated chlorides or sulfides produced by the microorganisms [3]. Colonization of composite materials by microorganisms has been demonstrated; however, characterization of the degradation has been limited to examinations in optical and scanning electron microscopes, and analyses of mechanical property changes have been limited.

Thermosetting polymers were once considered immune to attack by microorganisms, and their need for protection against microbial attack is only now being realized. Microbial attack has been reported on thermosets such as styrene butadiene rubber (SBR) and urethane foams [4]. In these materials imperfections in the polymer surface can allow the harboring of foreign materials, including water, which then creates an ideal location for microbial growth. Likewise, the microscopically rough surface texture of fiber-reinforced composites may provide similar favorable bonding sites for microorganisms. Blistering and crystal growth on carbon fiber/polymer composites in marine environments has been documented [5]. The blistering is thought to arise from osmosis. Galvanic coupling of these composite specimens with steel and aluminum can result in blistering and the growth of aragonite (CaCO_3) crystals [6]. Specimens which were not galvanically coupled with the steel did not display either blistering or crystal formation. The crystal growth was apparently a result of the corrosion process which electrochemically caused a local change in pH near the polymer allowing nucleation and growth of aragonite crystals from the natural sea water. From a limited visual examination, blistering was not apparent on carbon fiber/epoxy composite materials. Further analysis of composite/metal joints and the investigation of possible degradation mechanisms is warranted.

Previous work has shown that inoculation of specimens with a consortia of fungi and bacteria is not necessary to initiate biological activity. A fungus was found to exist in the composite processing and sample preparation laboratory which colonized on the surface of a number of composite materials and their constituents [7]. This fungus may prove to be an ideal species for investigating the biodegradation of composite materials, since it is already present and has shown a proficiency for thriving in composite processing and fabrication environments.

EXPERIMENTAL PROCEDURE

Biodegradation of Composite Material Properties

A variety of materials and properties were tested in this study. Table 1 lists all the specimen sets tested and the different exposure and test conditions. Three to five specimens were tested in each set. All exposures were made in sterilized jars with solutions which had been sterilized prior to testing.

Table 1: Specimens Sets and Test Conditions

Specimen Set	Material	Condition	Sterilized	Days of Exposure
A	AS4/3501-6	Malt Broth	No	121
B	AS4/3501-6	Water	No	113
C	AS4/3501-6	Malt Broth	Yes	120
D	AS4/3501-6	Water	Yes	112
E	AS4/3501-6	Air	No	-
F	Glass Rod/epoxy	Malt Broth	No	91
G	Glass Rod/epoxy	Malt Broth	Yes	91
H	Glass Rod/epoxy	Air	No	-
I	Glass Rod/epoxy	Air	Yes	-
J	BMI/Al	Malt Broth	No	119
K	BMI/Al	Salt Water	No	119
L	BMI/Al	Salt Water	Yes	119

Interlaminar Shear Strength

A unidirectional 20-ply carbon fiber/epoxy composite panel (AS4/3501-6 from Hercules Inc.) was fabricated in an autoclave using the manufacturer's recommended cure procedure. Specimens were sectioned from this panel with a diamond-tipped wet saw blade to an appropriate size for mechanical testing (1.5 in x 0.5 in) and divided into five sets. Two sets, A and B, of as-sectioned specimens were conditioned in separate sterilized jars containing a malt broth solution of nutrients and deionized water, respectively. An additional two sets of specimens, C and D, were sterilized with an ethylene oxide gas

treatment to remove any microbial agents deposited on them as a result of the preparation and sectioning procedures, and similarly conditioned in malt broth and deionized water, respectively. Set E was retained in its as-sectioned condition as a control. After 16 weeks of conditioning, specimen sets B and D were removed and critical point-dried for observation in the scanning electron microscope. After 17 weeks of exposure, specimen sets A and C were also removed and critical point-dried. Following documentation of fungal activity in the SEM, the specimens were tested in three-point flexure with a span-to-depth ratio of 6:1 to promote interlaminar shear failure. Thin rubber pads were placed between the contact pins and specimen to prevent premature surface damage at these locations. Failure modes were noted and interlaminar shear properties were recorded.

Interfacial Shear Strength

Interfacial shear strength was determined from model glass/epoxy composite specimens. A glass rod, 3 mm in diameter, was aligned along the central axis of a rectangular silicone rubber mold, and an epoxy matrix (Epon 828 from Shell Chemical Co. cured with 35 phr Jeffamine D-230 from Texaco Chemical Co.) was cast around it and cured overnight at room temperature. Rectangular slices, approximately 0.25 in thick, were sectioned from this casting perpendicular to the axis of the embedded reinforcing rod and postcured at 80°C for two hours to complete the cure. One set of these specimens (F) and another set (G) - sterilized with ethylene oxide to remove any microbial agents - were placed in separate sterilized jars containing malt broth. A third set of specimens (H) was maintained as a control, while a fourth set (I) was sterilized with ethylene oxide to determine the influence of this treatment on the strength of the interfacial bond. After 13 weeks of exposure, sets F and G were removed from the conditioning environment, and one specimen from each set was critical point-dried for observation in the SEM. The other specimens were dried overnight in a vacuum oven and the interfacial shear strength determined by a "fiber" push-out test, wherein the axial force required to debond the glass rod from the surrounding epoxy was measured in an MTS test machine.

Biodegradation at Composite/Metal Joints

A carbon fiber/bismaleimide composite panel (IM7/5250-4 from Cytek, Inc.) was fabricated using a standard autoclave cure procedure. Rectangular specimens (approximately 3 in x 1 in) were sectioned with a

diamond-tipped wet saw blade and coupled with plastic tabs to aluminum sections of similar dimensions. Two sets of couples, J and K, were placed in sterilized jars containing a malt broth solution of nutrients and deionized salt water (3.5 weight percent NaCl), respectively. A third set, L, was sterilized with ethylene oxide and conditioned in sterile salt water to serve as a control. After 17 weeks of exposure the specimens were removed from their respective solutions and freeze-dried for observation in the SEM.

RESULTS AND DISCUSSION

Biodegradation of Composite Material Properties

Documentation of Fungal Growth

Biological activity was apparent on the as-sectioned composite specimens of set A after only five days of exposure in the malt broth. Observation of these specimens in the SEM revealed extensive fungal growth and interaction of the fungi with the matrix resin of the composite panels. Fungal mycelia were tenaciously attached to the surface of the panels, preferentially within crevices in the rough surface texture (Figure 1). In several locations the mycelia appeared to penetrate the surface of the resin (Figure 2).

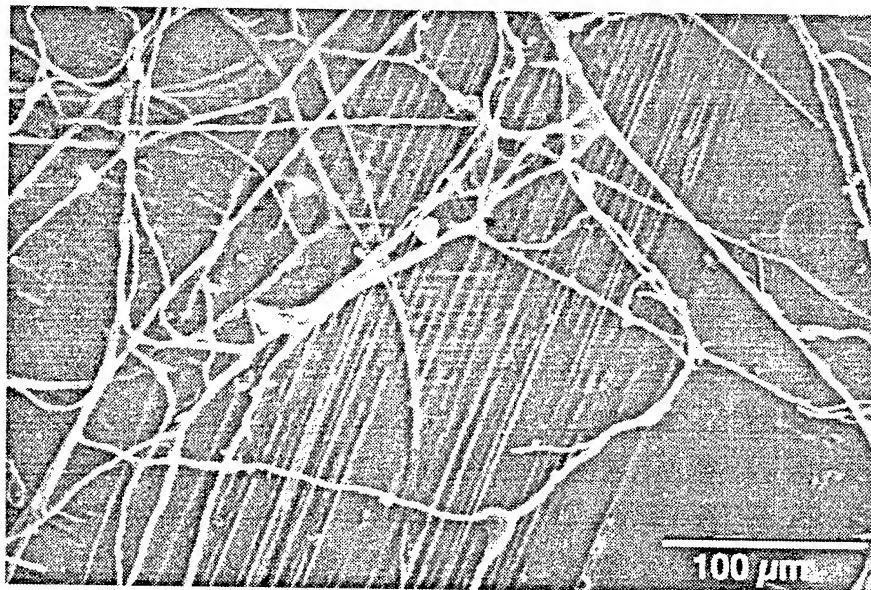


Figure 1: Fungal growth on composite panel which had been placed in a malt broth solution (Set A).

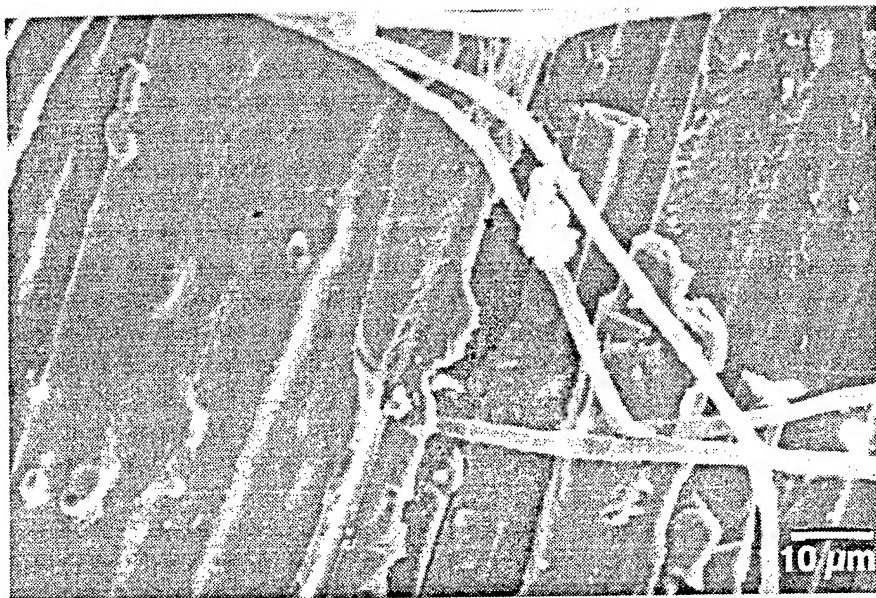


Figure 2: Interaction of fungal mycelia with composite panel (Set A).

Moderate biological activity was visible in the as-sectioned specimens conditioned in water (set B) after approximately 30 days, although SEM examinations of these specimens were required to confirm the existence of the fungi (Figure 3). The overall growth was much less than that observed in the specimens of set A, but was significantly greater than that observed in the sterilized control specimens of sets C and D. Similar interaction of fungal mycelia with the surface roughness characteristics was apparent. It would appear, therefore, that these fungi were able to colonize and grow in the sterile deionized water in the absence of externally-supplied nutrients (such as the malt broth). Consequently, it may be assumed that the composite itself provided the nutrients required for growth, implying that the epoxy matrix and/or carbon fiber is susceptible to microbial attack in the composite's normal working environment.

SEM examination of sterilized specimens conditioned in malt broth and water (sets C and D, respectively) revealed that the presence of fungi was almost nonexistent. The appearance of a few fungal mycelia on some of the specimens could be attributed to cross-contamination of specimens after treatment and prior to the SEM examinations; handling the specimens with tweezers during mounting and coating for SEM observation could have dislodged mycelia from the

as-sectioned specimens and transferred them to the control specimens. Alternatively, fungal activity may not have been completely terminated during the ethylene oxide sterilization process, and some fungal growth may have occurred on these specimens.

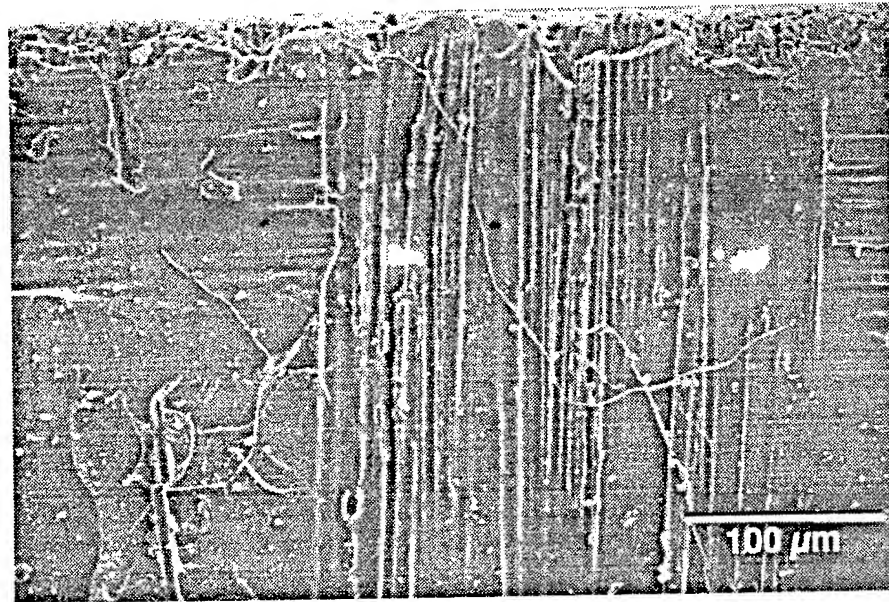


Figure 3: Fungal growth on composite specimen soaked in water (Set B).

Interlaminar Shear Strength

The average interlaminar shear strengths of specimens from sets A-E are listed in Table 2. Failure in all specimens initiated via interlaminar shear near the midplane as confirmed from optical microscopy of polished specimen edges. There was no significant difference in interlaminar shear strength between the panels with biological activity and those which had been sterilized, which suggests that the growth of the fungus on the composite panels did not significantly degrade the resin shear properties. However, other factors may account for the similar shear strengths. The exposure time of the composite sections to the fungus may not have been sufficient enough to degrade material properties. Alternatively, because the majority of the fungal growth occurred on the composite surface, interaction of the fungus may have been limited to the surface plies and edges of the panel. Since this three-point flex test initiates failure at the midplane, the

measured shear strength may not be sensitive to changes in shear properties which occur only at the surface of the panel. The effect of the ethylene oxide treatment on the shear properties is currently unknown as the set of control specimens which were subjected to an ethylene oxide treatment alone were not available for testing.

Table 2: Average Mechanical Properties

Specimen Set	ILSS (ksi)	Interfacial Strength (ksi)
A	15.0	
B	15.6	
C	15.3	
D	15.3	
E	16.3	
F		4.3
G		4.3
H		5.2
I		5.4

Interfacial Shear Strength

The relative shear strengths of the interfacial bond from push-out tests on the model glass/epoxy composites are given in Table 2. Failure was not "clean" as the glass rod fractured prior to being debonded, and the maximum load was used in calculation of the shear strength. The ethylene oxide treatment appears to have improved the shear strength relative to as-sectioned, untreated specimens, while immersion in the malt broth lowered the shear strength of the interfacial bond by approximately 17 percent, even though the specimens were dried prior to testing. In comparing the sterilized and unsterilized specimens conditioned in the malt broth, however, they appear to have equivalent shear strengths. The same reasoning employed to explain the equivalence of the interlaminar shear strengths of the unidirectional composite specimens holds in this case; an inability of the fungi to penetrate the interfacial region to any great length during the limited exposure period may account for the lack of sensitivity of the measured shear strengths to fungal growth.

Biodegradation at Composite/Metal Joints

Documentation of Fungal Growth

Fungal growth was apparent on the composite/Al couples conditioned in malt broth after approximately five days of exposure. The specimens in salt water did not show as significant an accumulation of fungal growth. However, upon observation of the composite halves of the couples in the optical and scanning electron microscopes, fungal growth was indicated on the nonsterilized specimens. In separating the components of the couple, crystals or particles were observed to adhere to the face of the composite which was in contact with the aluminum, and an example is shown in Figure 4. Further SEM analysis using energy dispersive spectroscopy showed that the crystals contained aluminum and oxygen and, in all likelihood, are alumina peeled off from the aluminum substrate. An interesting feature in this figure is the fungal mycelia traversing the face of the crystal, suggesting that they may have penetrated and weakened the interface between the aluminum and its oxide coating thereby dislodging the crystal.

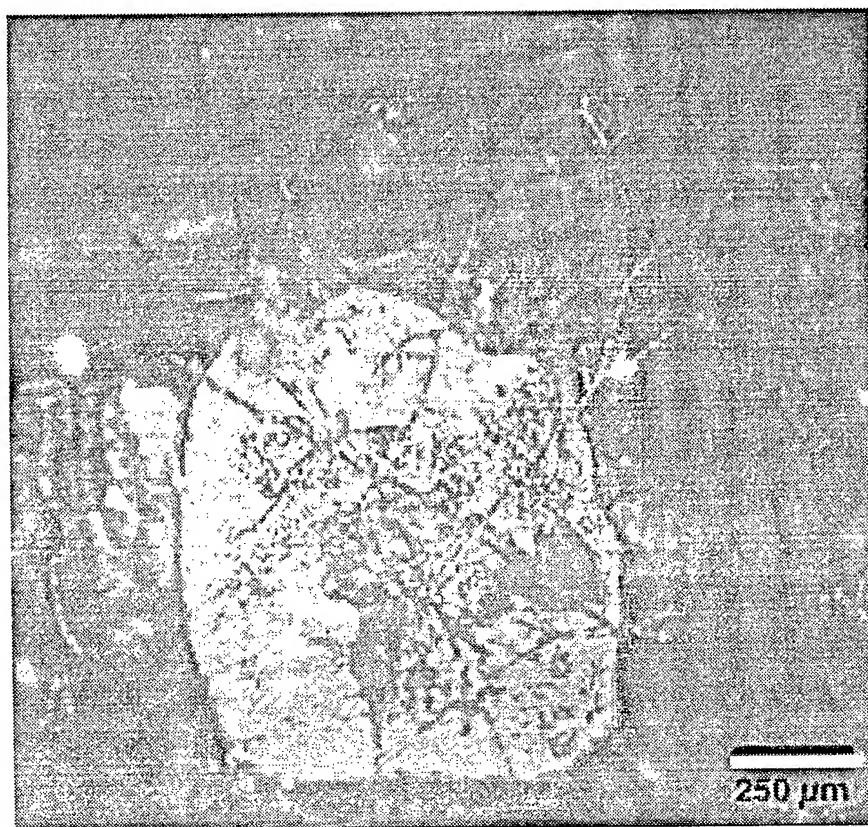


Figure 4: Fungi and crystal on BMI/Al sandwich specimen (Set J).

SUMMARY AND CONCLUSIONS

The ethylene oxide sterilization procedure appears to work fairly well at removing fungal spores from composite panels. The process did not appear to decrease the mechanical properties of the tested materials and may actually have increased the interfacial strength in some cases. Fungal growth is easily achieved on as-processed composite panels and appears within days in nutrient rich solutions. Fungal growth can also be achieved in sterilized water. Although the growth of the fungi in water is significantly less than that seen in malt broth solutions, it is apparent that nutrient rich solutions are not required for fungal development.

No significant decrease in interlaminar shear strength or interfacial strength was measured on these composites. The tests used may not have been ideal and additional testing is required to determine if the fungi are indeed degrading the mechanical integrity of either the resin, fiber, or fiber/resin interface.

The growth of fungi between composite/Al sandwiches was documented. The fungi appeared to have interacted with the surface of the aluminum and dislodged a portion of the natural Al_2O_3 coating. This could prove detrimental to the mechanical integrity of the aluminum and deserves further study.

ACKNOWLEDGEMENTS

The authors would like to thank the Air Force Office of Scientific Research (AFOSR) and Wright Laboratory (WL) for sponsoring this research under contract #F33615-91-C-5618. The authors would also like to acknowledge the gracious assistance of Mr. Bill Ragland, Mr. Ron Cornwell, Mr. Ron Esterline, Capt. Steven Chanell, and Major Gary Marit.

REFERENCES

1. Hardy, B., "A Review Paper on Microbial Biodegradation and Microbial Corrosion of Materials: A US Air Force Perspective," Private Communications, August, 1993.

2. Robitaille, T. E. and Robers K. P., "An Accelerated Microbial Challenge of Biologically Inert Polymers," ANTEC '93, pp 2977-2929.
3. Wagner, P. A., Ray, R. I., Little, B. J. and Tucker, W. C., "Microbiologically Influenced Degradation of Fiber Reinforced Polymeric Compsites," Corrosion 93, Paper # 255.
5. Tucker, W. C. and Brown, R., "Blister Formation on Graphite/Polymer Composites Galvanically Coupled with Steel in Seawater," J. Composite Materials, Vol 23, pp. 389-395.
6. Tucker W. C., "Crystal Formation on Graphite/Polymer Composite," J. Composite Materials, Vol 22, pp. 742-748.
7. Ji-Dong Gu, Timothy E. Ford, Ralph Mitchell and Katie E. G. Thorp, "Microbial Degradation of Polymeric Materials," this proceedings.

The Effect Of Carbon Fiber Type On The Electrochemical Degradation Of Carbon Fiber Polymer Composites

J. Qin¹, R. Brown^{1*}, S. Ghiorse² and R. Shuford²

1. Corrosion Laboratory, Dept. of Chemical Engineering, Crawford Hall, The University of Rhode Island, Kingston, RI 02881
2. Composites Development Branch, Materials Directorate, U.S. Army Research Laboratory, Watertown, MA 02172

ABSTRACT

The galvanic interaction between metals and carbon fiber/polymer matrix composite degrades not only the metals but the composite itself. The objective of this study was to investigate if the fiber type influenced either the mechanism or form of damage. Two different composites were examined. Both have same epoxy matrix, 3501-6 epoxy, but contain different carbon fibers, either AS4 or IM6. The surfaces of the composite materials were exposed to 0.5 N NaCl solution to simulate sea water at open circuit condition or cathodic potentials to simulate galvanic coupling of metals. Electrochemical impedance spectroscopy (EIS) was employed to monitor changes in the behavior of the composites. Modeling of experimental data indicated that the parameter, R_p , representing the polymer resistance decreased with increasing time of exposure for both open circuit conditions and applied cathodic potentials. The value of R_p also decreased with increasingly cathodic applied potentials. This suggested that a damage process for the polymer involving increased access of solution to the carbon fibers. SEM examination showed that cracks and polymer separations on the exposed but not on the unexposed surfaces. The fiber type did not appear to influence the damage mechanism in this study.

INTRODUCTION

Advanced carbon fiber reinforced polymer composites are currently being developed for numerous applications because of the important potential benefits of light weight, high specific modulus and good corrosion resistance. Various applications can be found in marine, aerospace, automotive and commercial structures. However, these materials are not used in isolation. They are connected to metallic materials such as fasteners and other components. As carbon is conductive and a very noble cathodic material, the coupling will result in accelerating corrosion of metal by anodic reactions and degrading the composite by cathodic reactions. Earlier studies indicated electrochemical degradation of carbon fiber composite materials. A time dependent phenomena of blistering was reported for several combinations of polymer on carbon fibers [1-4]. The blisters were filled with solution of high pH, greater than 10 [1]. Although a few degradation mechanisms were proposed and discussed, the effects of material parameters on the mechanisms of composite degradation are still poorly understood.

The objective of this study was to investigate if the fiber type influences either the mechanism or form of damage electrochemically induced in carbon fiber/polymer composites. Electrochemical impedance spectroscopy (EIS) was employed to monitor the behavior of the composites. This method, previously used to evaluate the protective coatings on metals [5,6], has recently been applied for the quantitative electrochemical studies of carbon/polymer composites [2-4]. Scanning electron microscopy was performed on both exposed and unexposed surfaces of the specimens to better understand the electrochemical degradation mechanism. The relationship between impedance data and surface features were examined. Solution chemistry resulting from degradation processes was monitored by pH measurement during the surface exposure.

EXPERIMENTAL PROCEDURES

Materials

The materials examined in this study were carbon/polymer composite materials. The composites were prepared using prepregs with the same polymer matrix, 3501-6 epoxy, but containing different carbon fibers, either AS4 or IM6. One other difference was that a sizing agent was used on IM6 fibers but not on AS4. The manufacturers standard processing cycle (350°F cure temperature) was used for both materials.

The materials were then post-cured in a convection oven for four hours at 350°F. The stacking sequence of both composite laminates (AS4/3501-6 and IM6/3501-6) were identical $(0^\circ/90^\circ)_4S$ as was the laminae thickness at 0.005 in nominal. The microstructure of composites is shown in fig. 1. The composites are 65% volume of fibers and 35% polymer for both materials.

Principle and technique of impedance measurements

Electrochemical impedance spectroscopy testing was conducted to investigate the electrochemically induced degradation mechanisms of the composites. The experimental setup for impedance measurement is schematically shown in fig. 2. With this arrangement, the solution must permeate through the polymer to contact carbon fiber. The surface area exposed to the electrolyte of 0.5 N NaCl for simulated sea water is 5.73 cm². A platinum sheet and a standard calomel electrode (SCE) serve as counter and reference electrodes respectively. EIS measurements in the frequency range between 1mHz and 100kHz were carried out using a frequency response analyzer (Solartron 1255) and a PAR 273 potentiostat interfaced to an IBM PC.

The experimental tests were performed on open circuit conditions or with negative potentials applied, $-0.65V_{SCE}$ and $-0.90V_{SCE}$, to simulate galvanic coupling of anodically active metals such as steel and aluminum alloys. The impedance data were displayed as Bode plots (impedance modulus $|Z|$ vs. frequency and phase angle vs. frequency).

pH Measurement

Solution pH was measured using a digital pH meter during exposure.

Scanning electron microscopy (SEM)

Scanning electron microscopy was conducted on both exposed and unexposed specimen surfaces for AS4 and IM6 composites. Evidence of surface changes was evaluated by comparison of these two surfaces.

EXPERIMENTAL RESULTS

Open Circuit Conditions

Long term exposure tests up to 360 days were conducted on both AS4 and IM6 composites under open circuit conditions. Bode plots of

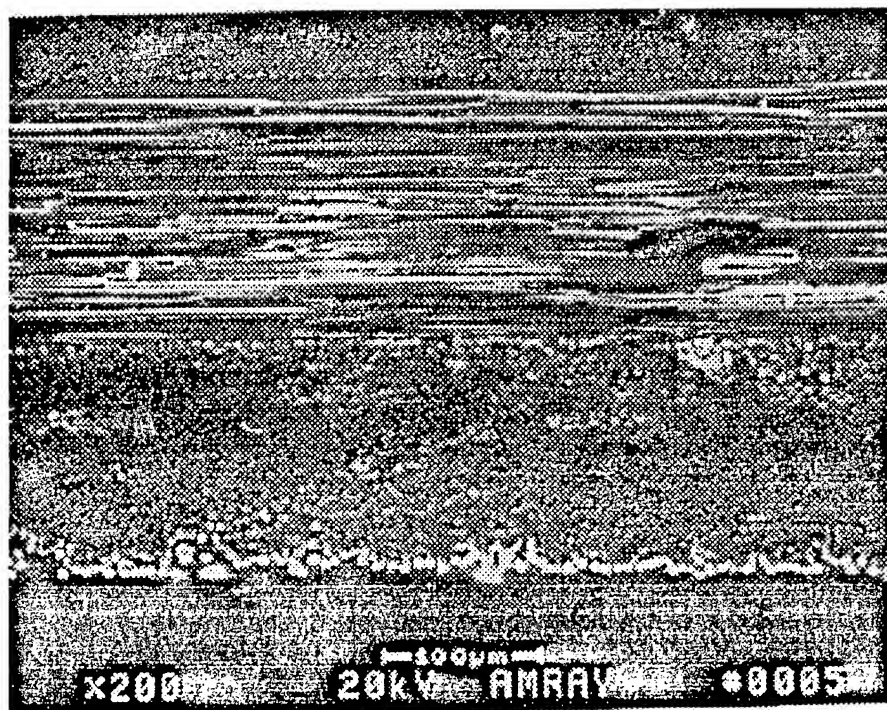


Figure 1. Microstructure of IM6/3501-6 Composite Material

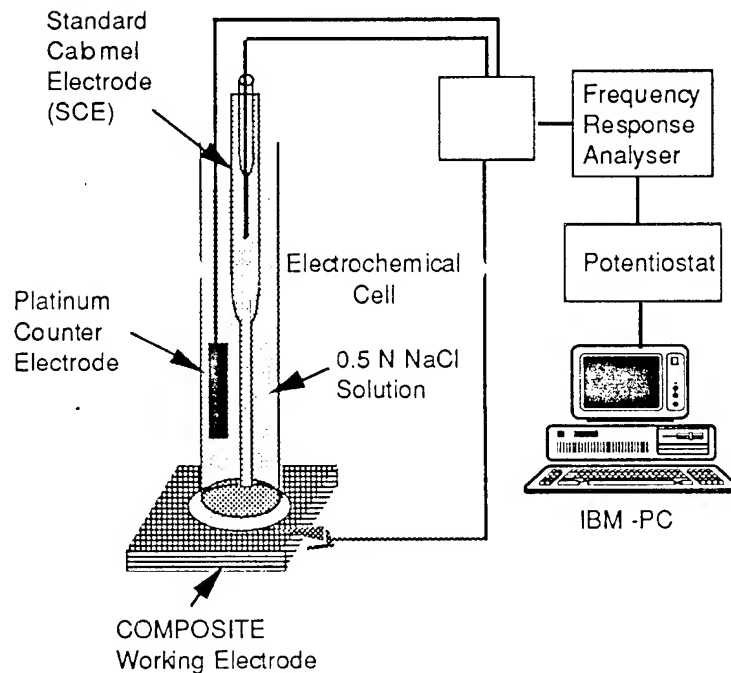


Figure 2. Experimental Setup for Impedance Spectroscopy

experimental data for the open circuit condition are shown in fig. 3 for AS4/3501-6 composite. The plots show the impedance responses from 5 hours up to 140 days of exposure. A decrease of impedance with increasing time of exposure was noticed. The most significant changes in impedance occurred in the first 100 days for both materials. The high frequency phase angle decreased in magnitude and shifted initially to the lower frequencies and then moved back to the higher values as the impedance response decreased. Identical behavior was also found for IM6/3501-6 material.

Applied Negative Potentials

Under polarized conditions, the exposure periods were up to 30 days at -650mV potential and 15 days at -900mV potential for both AS4/3501-6 and IM6/3501-6 materials. Bode plots of experimental data as the symbols at -650mV are shown in fig. 4 for AS4/3501-6 material and in fig. 5 for IM6/3501-6 material. The results reveal that the initial impedance response for cathodically polarized specimens was lower than open circuit conditions up to the high frequency arrest region. The phase angle maxima moved to the lower frequency and decreased in magnitude as the time of exposure increased. For IM6 composite, the impedance also decreased with the time of exposure. However, with AS4 composite, differences were found at applied -650mV potential. The solution resistance for AS4/3501-6 increased more than that of IM6/3501-6 material. In addition, the impedance at lower frequency increased with the time of exposure for AS4/3501-6 until 21 days then decreased.

The significant changes occurred in the first week at -900mV applied negative potential for both materials, as shown in fig. 6 for AS4/3501-6 composite. Similar features were also observed in the Bode plot for IM6/3501-6 material. It should also be noted that the indication of diffusion control was present for both -650mV and -900mV polarized materials. This was shown by a phase angle of 45° .

Modeling of Experiment Data

The impedance response was simulated using equivalent circuit modeling EQUIVCRT software. The two RC circuit model, first proposed by Mansfeld and Kendig [5] for most polymer-coated metals shown below was used to provide the best fit of impedance behavior of composites and extract the parameters which provide significant information of composite degradation due to electrochemical reactions.

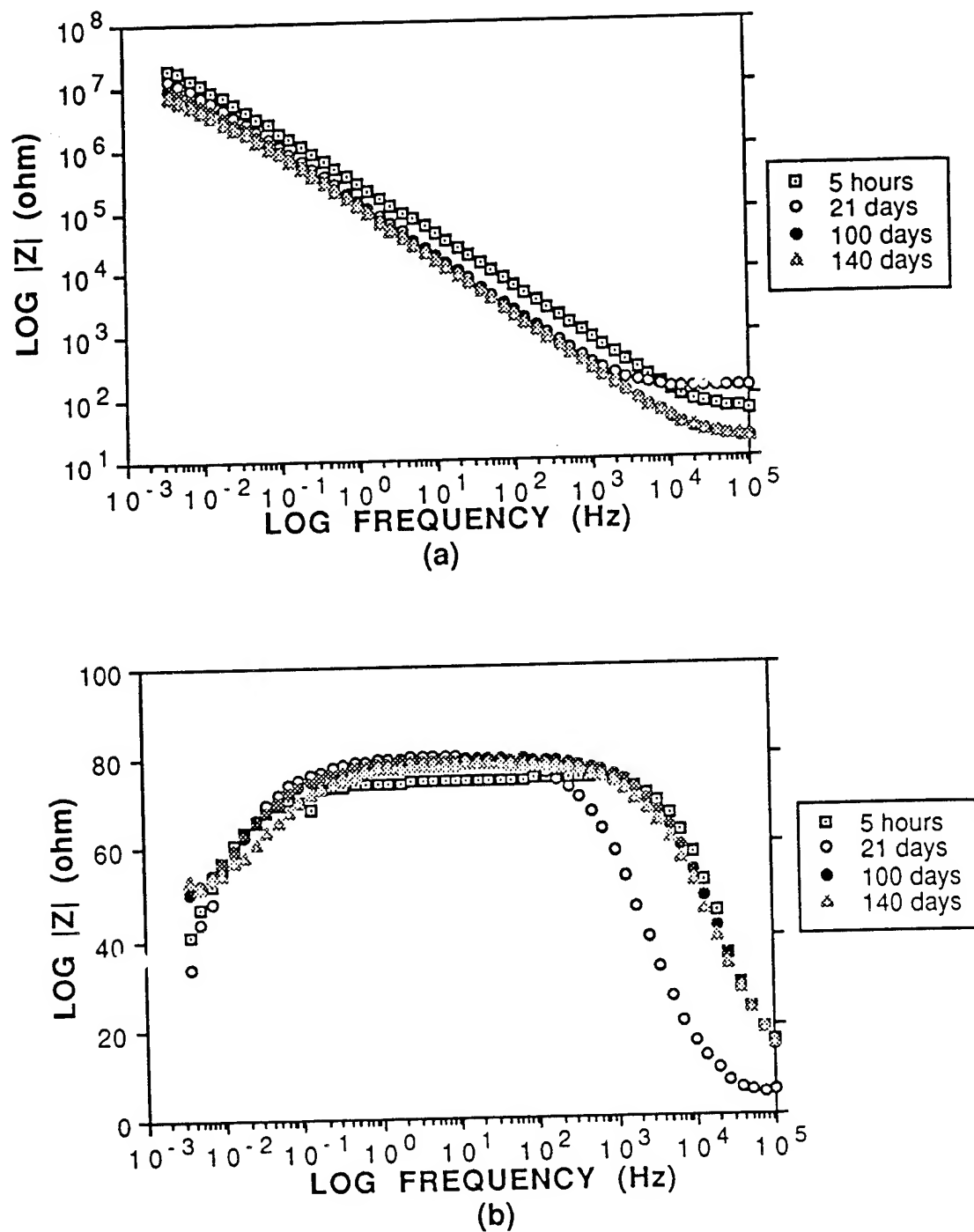


Figure 3. Bode Plot for AS4/3501-6 Composite at Open Circuit Condition

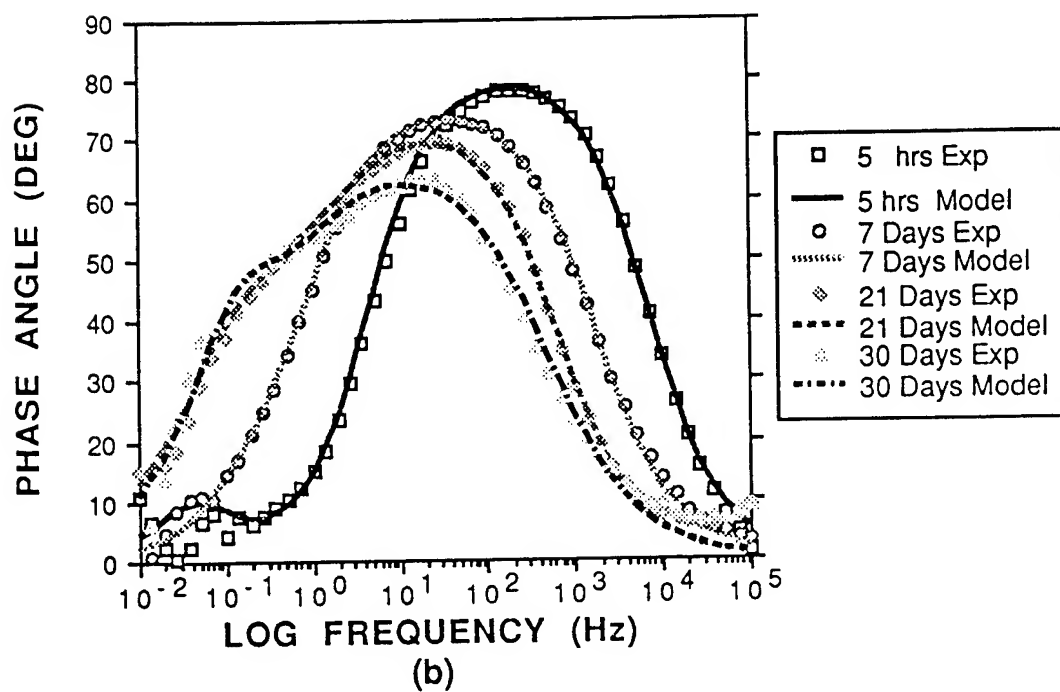
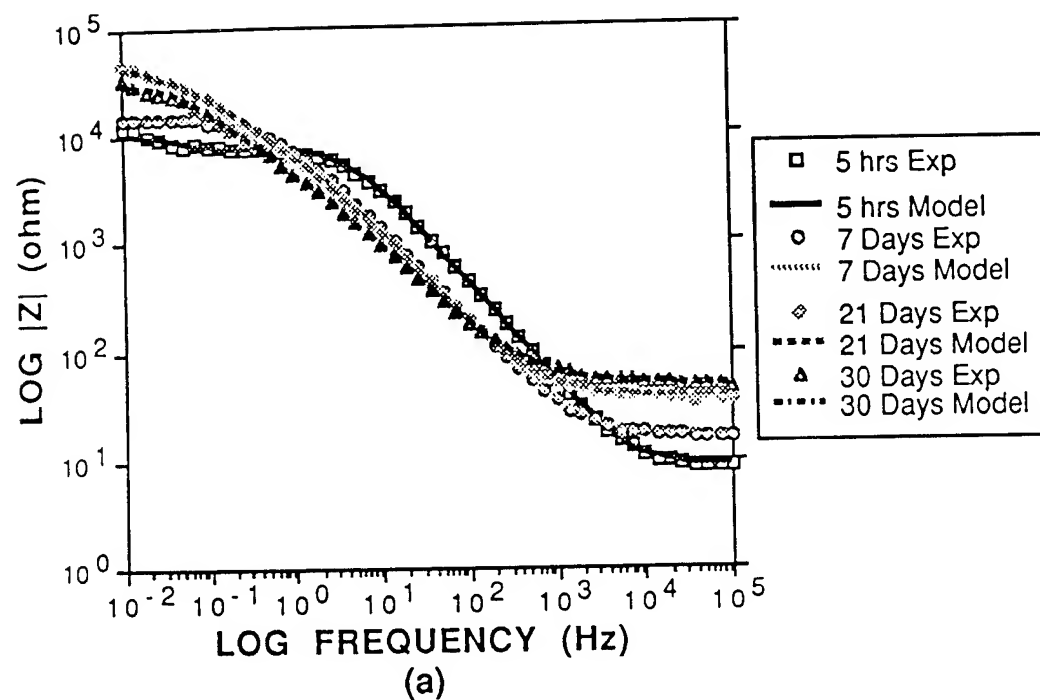


Figure 4. Bode Plot for AS4/3501-6 Composite at -650mV
Applied Potential

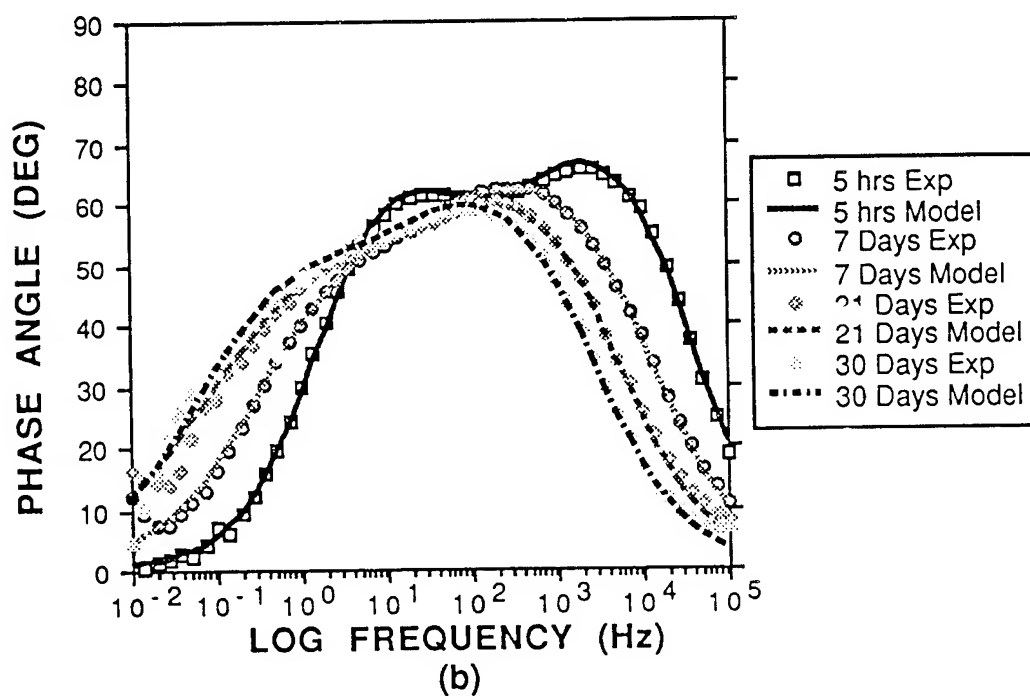
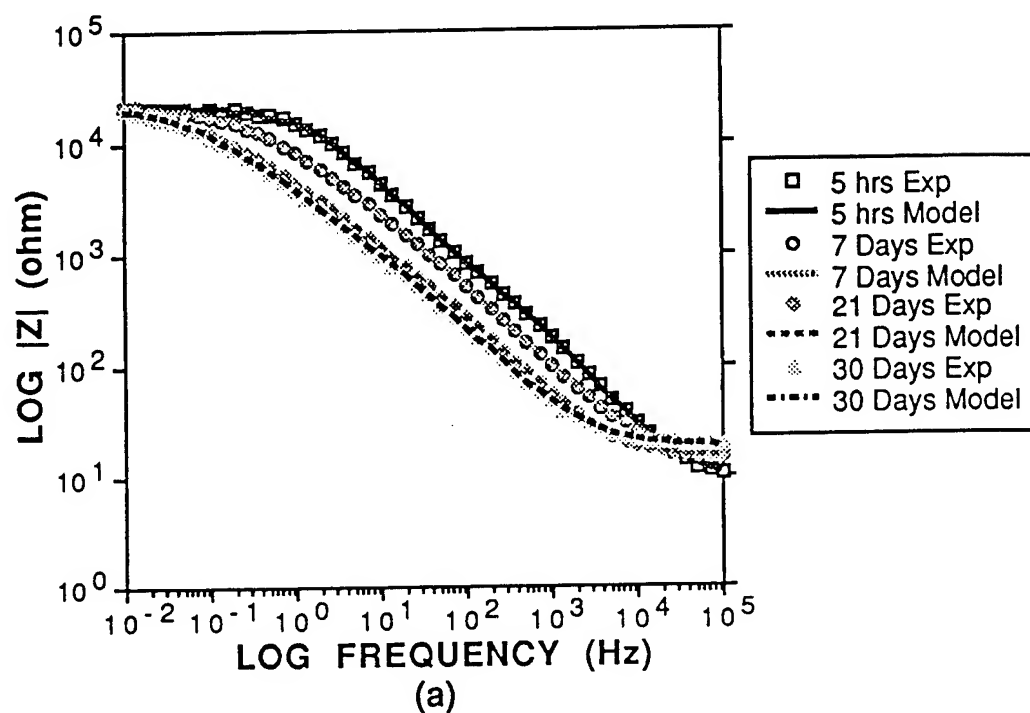


Figure 5. Bode Plot for IM6/3501-6 Composite at -650mV Applied Potential

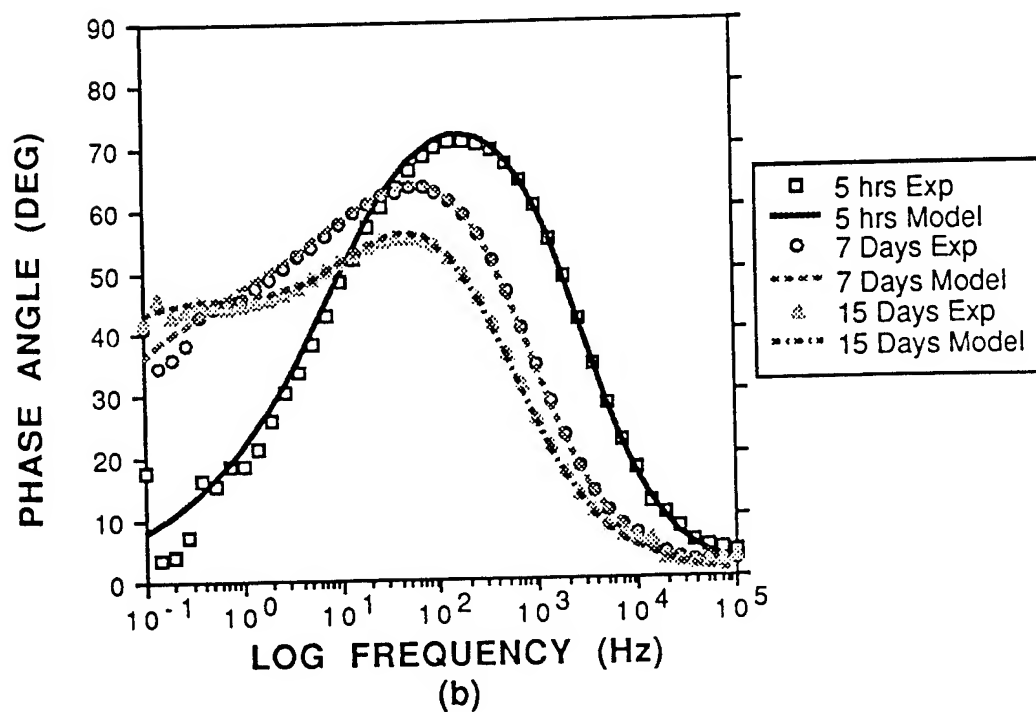
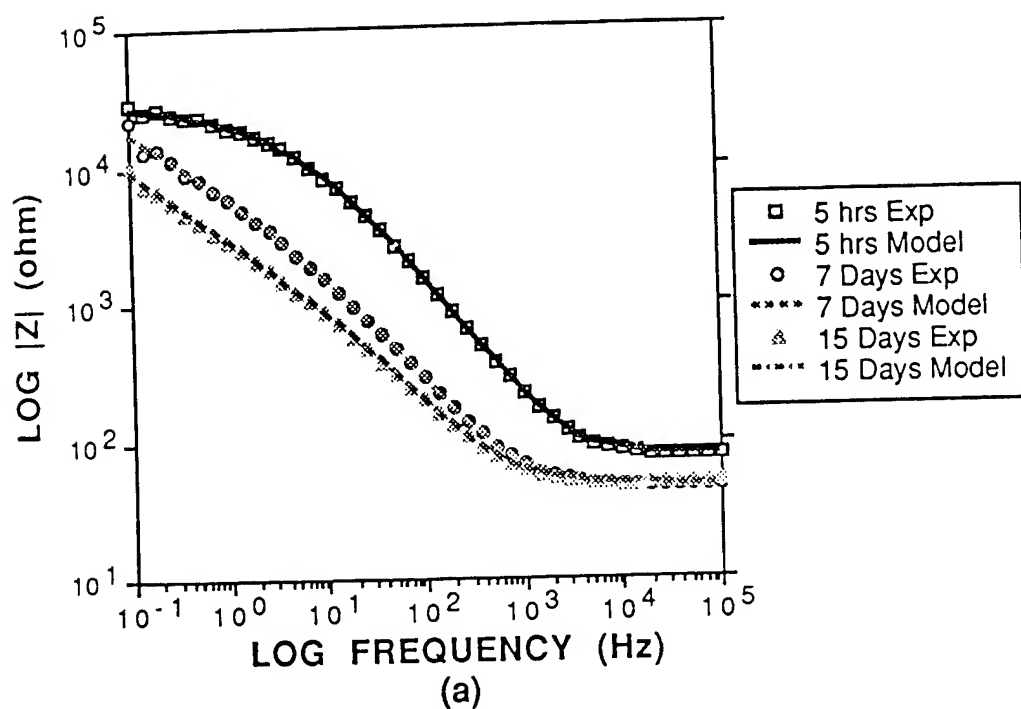
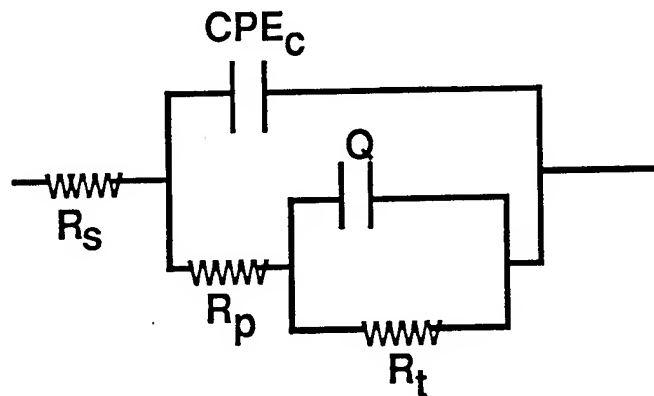


Figure 6. Bode Plot for AS4/3501-6 Composite at -900mV Applied Potential



where R_s is the solution resistance, CPE_c is the constant phase element of the polymer dielectric and R_p is the resistance of the polymer matrix due to the penetration of electrolyte through the defects and pores in the matrix. Q ($Q = Z_0(j\omega)^{-n}$) is a constant phase element which allows contribution of diffusion at the carbon fiber/moisture interface region. When $n=0$ and 1 , Q represents pure resistance and pure capacitance respectively. In the case of $n=-0.5$, Q behaves as a true diffusion impedance. R_t is the charge transfer resistance at the carbon fiber/polymer interface.

The simulated data from the equivalent circuit modeling are plotted as the lines together with the experimental data, as shown in fig. 3-6. The model provides a good fit to the data.

The parameters extracted through the equivalent circuit modeling varied significantly with different conditions. The parameter, R_p , representing the resistance of the polymer matrix separating fibers from electrolyte decreases rapidly with increasingly negative applied potentials, as shown in fig. 7 for AS4/3501-6 material and fig. 8 for IM6/3501-6 composite. The value of R_p also decreased with exposure time for both open circuit and applied cathodic potentials of -650mV and -900mV .

Solution pH variations

An increase in solution pH was found for both materials under cathodic polarized conditions. The pH variations for AS4/3501-6 material are shown in fig. 9. The value of pH was not significantly changed for open circuit condition. Similar results were also found on the second composite IM6/3501 system.

Microstructure Characterization

Detailed surface examinations were performed for both exposed and unexposed surfaces of composite specimens by SEM for better

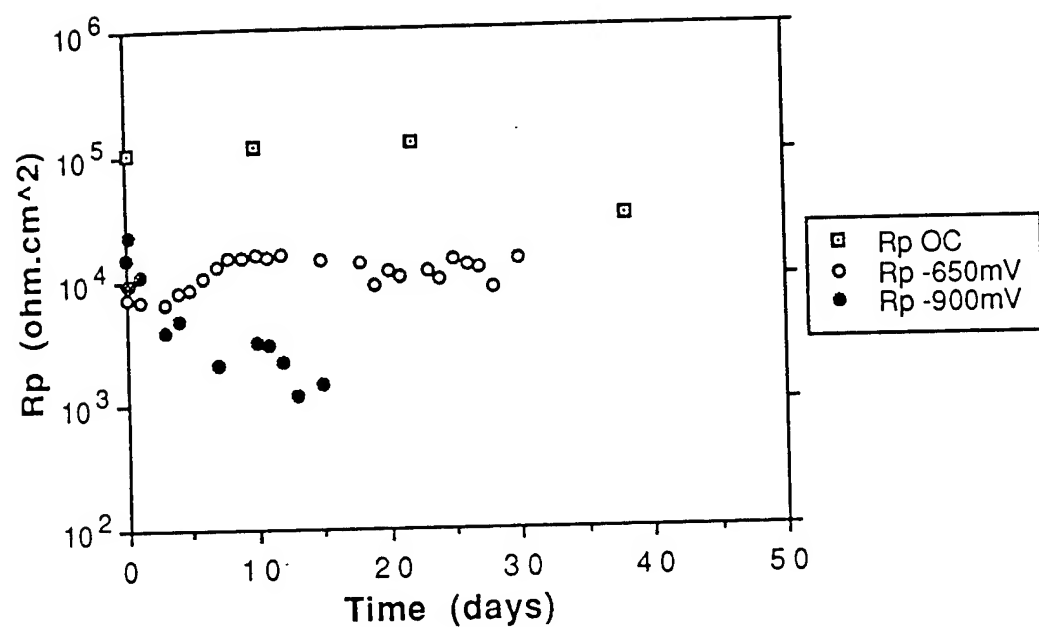


Figure 7. Polymer Resistance R_p vs. Time for AS4/3501-6 Composite

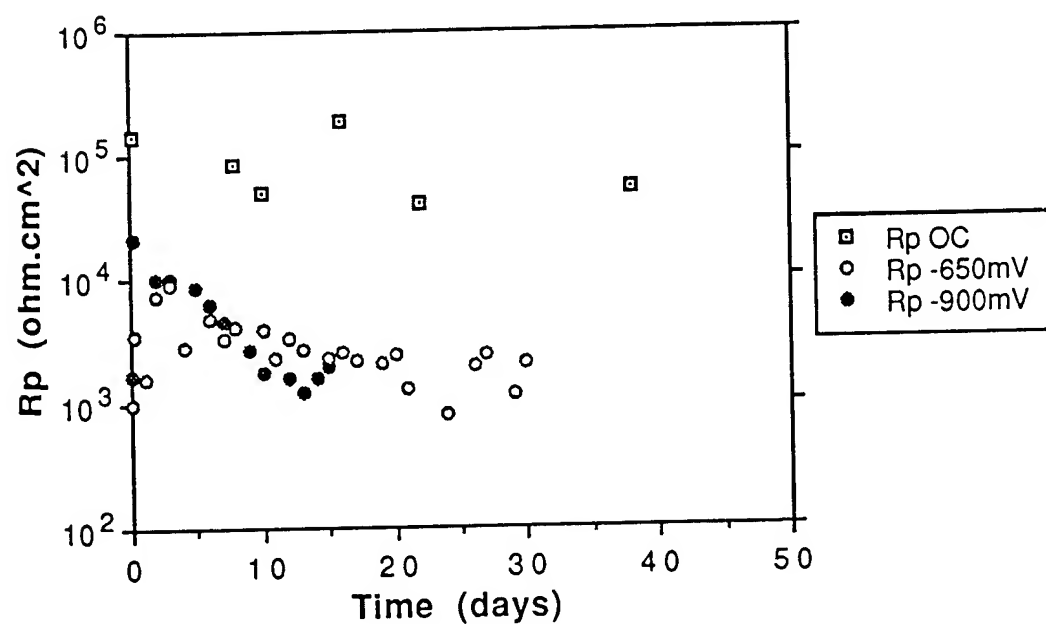


Figure 8. Polymer Resistance R_p vs. Time for IM6/3501-6 Composite

understanding of the degradation mechanisms. The results indicated that damage features were present on the exposed surfaces of different composites, but that features changed in size and density with exposure period and potential.

In general, the unexposed composite showed a very smooth surface, fig. 10. However, cracks and polymer separation were found running along the carbon fibers for all polarized samples, fig. 11 for IM6/3501-6 material and fig. 12 for AS4/3501-6 composite after exposed to the electrolyte at -650 mV applied potential for 30 days. For IM6/3501-6 composite, it appeared that large portion of polymer were removed exposing carbon fibers directly to electrolyte. The joining of several cracks can produce this effect.

DISCUSSION

Electrochemical impedance study

Open Circuit Conditions

With increasing exposure time, impedance decreased for both composite materials. One possible reason for time dependent decrease in impedance at open circuit conditions is moisture absorption and pre-existing defects in the polymer matrix.

The effects of moisture on composite materials have been studied in detail [7-8]. It was shown that moisture has a potentially degrading effect on epoxy matrix materials. Moisture is present in many forms such as contained in the polymer free volume after manufacture or the electrolyte solution and eventually penetrates by diffusion until the moisture equilibrium or saturation concentration is achieved. The absorbed water as well as ionic solutions may also be transported along fiber-matrix interfaces and cause delamination of the interface.

The electrolyte can also permeate through pre-existing defects to contact the cathodic site. Therefore the decrease in polymer resistance as a function of time represents damage to the composite from moisture induced processes. It was shown previously that impedance spectroscopy can monitor damage of composites under open circuit condition when osmotic blistering was noted after extended periods in both distilled water and sodium chloride solutions [9]. In this case, in addition to monitoring existing defects in the composite at initiation, the defects created during exposure were also identified.

Cathodically polarized conditions

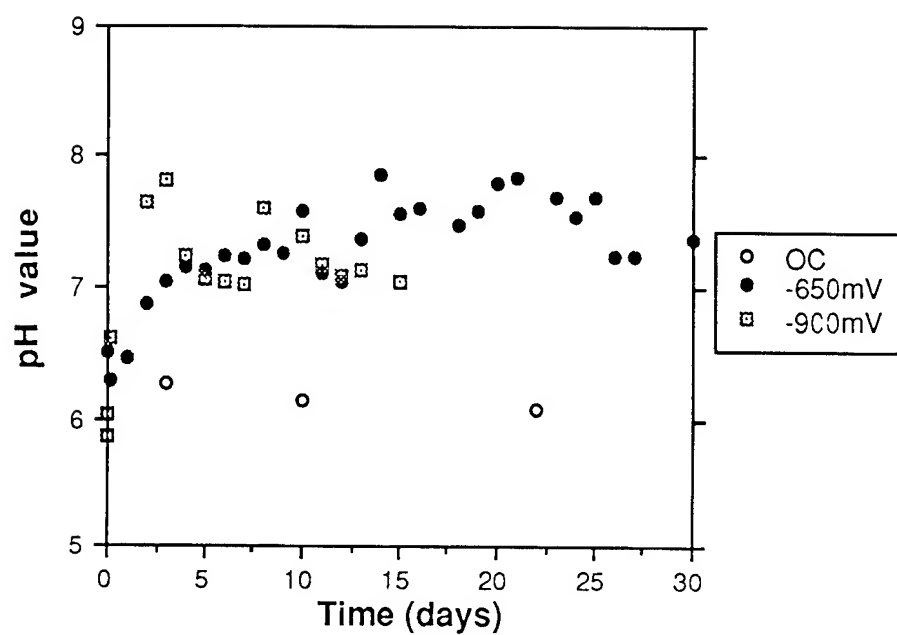


Figure 9. pH value vs. Time for AS4/3501-6 Composite

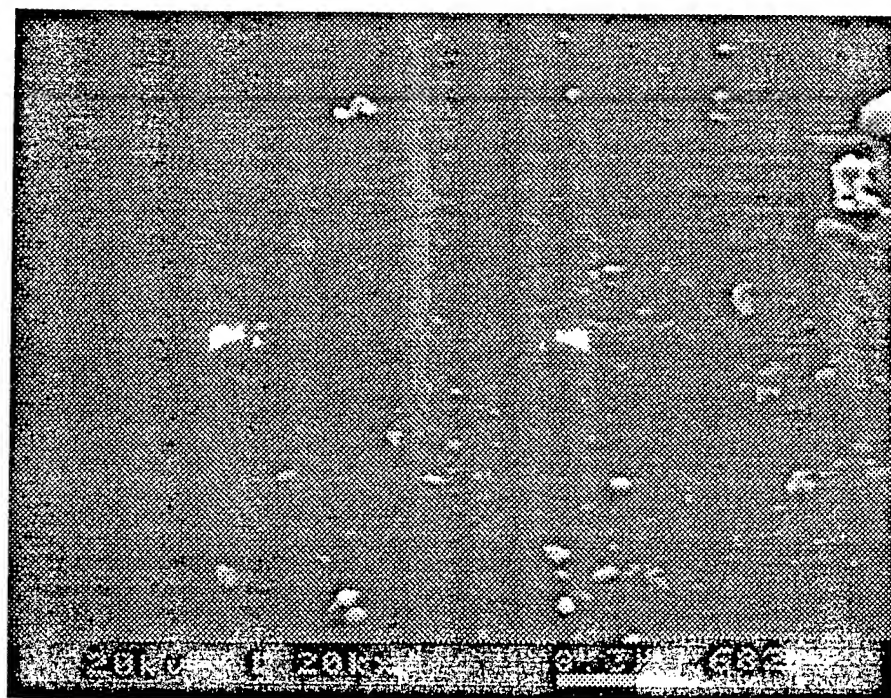


Figure 10. Unexposed Surface of IM6/3501-6 Composite Materials

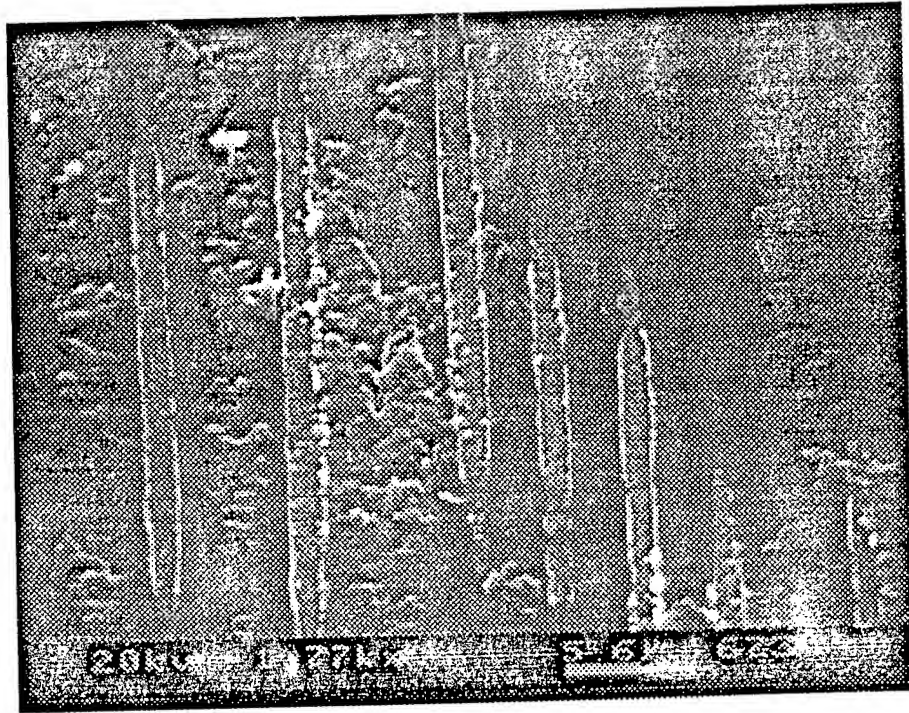


Figure 11. Exposed Surface of IM6 Composite at -650mV for 30 Days

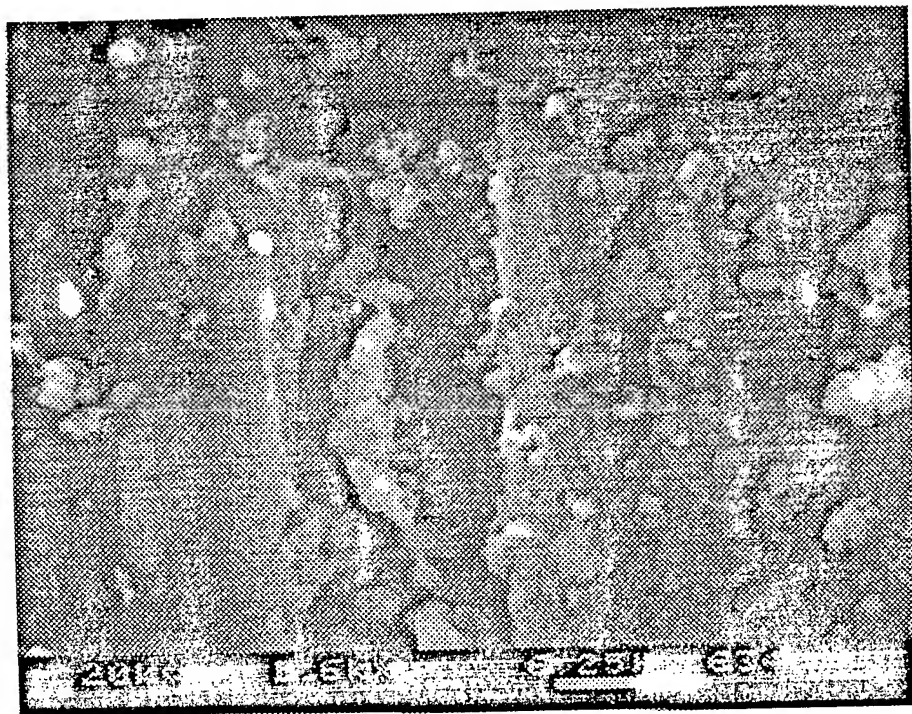
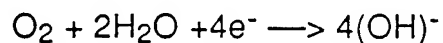


Figure 12. Exposed Surface of AS4 Composite at -650mV for 30 Days

The decrease in impedance upon initial application of potentials indicated that the cathodic reaction occurred at the carbon fiber/polymer interface immediately with no time delay. This implies that defects exist on the surface and permit the cathodic reaction to occur. The initial decrease in impedance is therefore a measure of the pre-existing defect content of the composites. Recent data indicated no difference in initial impedance response between open circuit and cathodic polarization conditions for a defect free specimen [11]. In the range of diffusion controlled potentials, the potential should not influence the initial impedance behavior.

The high pH of the solution indicated that the reduction of oxygen reaction occurred to produce hydroxyl ions (OH)⁻ under the applied potential conditions. The mechanism of this reaction can be represented by the following equation



This confirms the results from several previous studies that the increase of dissolved oxygen concentration in solution decreased the time of initiating blisters in a vinyl ester composites [3]. A typical diffusion limited curve for oxygen was reported for T-300 fiber reinforced composites tested in 3.0% NaCl solutions at cathodic potentials. Similar features were also found on other composite systems such as a carbon fiber vinyl ester composite at -650mV applied potential or coupled to steel after six months in sea water.

In addition, with increasingly cathodic potentials applied the impedance decreased. The impedance variation appeared to be dependent on a reaction occurring at the cathodic site and polymer thickness.

Surface Features and Impedance

Cracks and polymer separation were found on all exposed specimen surfaces. This damage permitted easier access of solution to the carbon fiber. The surface features confirmed the reasons for decreasing in impedance and polymer resistance in the EIS studies. There are several available mechanisms. One possible mechanism is that the osmotic pressure increased as the hydroxyl ions were formed at carbon fiber/polymer interface by cathodic reduction of oxygen. As a result of the osmotic pressure, the local osmotic stress at the carbon fiber interface increased. The rate of damage accumulation in this mechanism depends on the mechanical properties and the thickness of the polymer film. For a thick polymer layer (over 100μm), when the osmotic stress

overcomes the yield stress of polymer or the interfacial bonding stress, it resulted in localized plastic deformation or creeping of polymer and eventually caused blister burst or delamination, as schematically shown in fig. 13. The galvanic blistering processes were found in previous studies of vinyl ester polymer composites [2-4]. However, in this study, the polymer film separating fibers from the exposed surface is relatively thin. The thin film could not resist the higher stresses as the osmotic rate increased due to the decreased transport distance. The increased pressure overcomes the polymer rupture strength and the blisters burst, see fig. 14. These broken blisters opened up free path and allowed more electrolyte to cathodic site. The third possibility is that the cathodic reaction products react with components of composite to either dissolve the components or the polymer matrix [9]. This process will enlarge pores and permit more electrolyte down to the cathodic site.

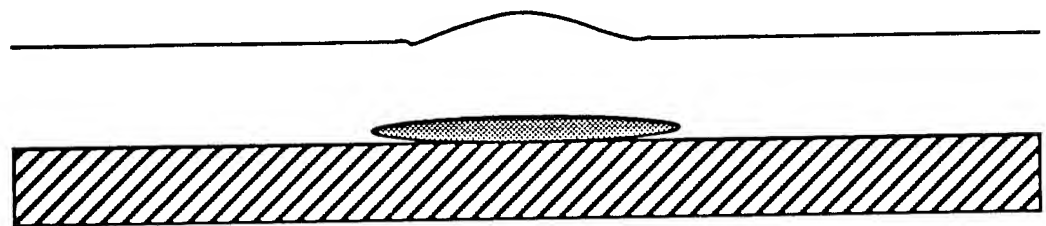


Figure 13. Schematic Diagram of Fluid Filled Blister From Osmotic Pressure

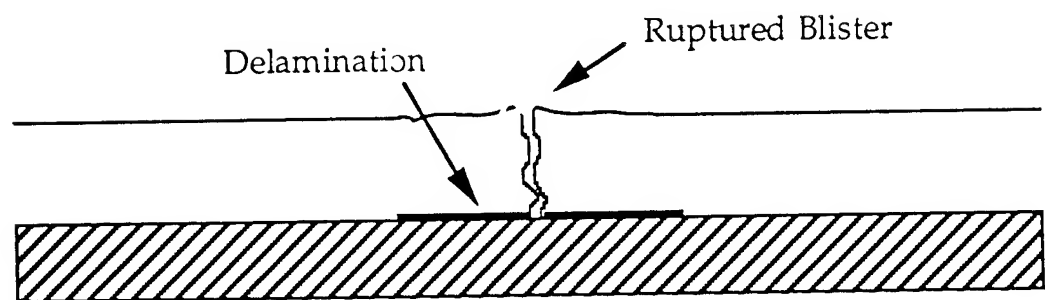


Figure 14. Rupture of Blister and Collapse Leaves Interfacial Delamination and Tortuous Path for Solution Down to Carbon Fibers

The difference in impedance behavior between the composites at -650mV applied potentials may imply that the sizing process used on IM6/3501-6 (fig. 5) but not on AS4/3501-6 (fig. 4) influenced the rate of damage. SEM examination showed different damage features for these two materials. It was found that a large portion of polymer was removed for IM6/3501-6 material, as shown in fig. 11 while narrow matrix cracking along the fibers was observed for AS4/3501-6 composite, see fig. 12. One explanation is that the sizing at the interface has a poor chemical bonding and mechanical properties in comparison with the bulk matrix material properties. The material of the sizing interface can rupture rapidly and in turn accelerate the damage process and open up a free path to the cathodic site in this case. On the other hand, the bulk matrix polymer for AS4/3501-6 may retard the blister rupture and cause the increase in impedance at low frequency because of a reaction product in the carbon/polymer matrix interface, as shown in fig. 4 for AS4/3501-6 composite. The polymer resistance R_p of IM6/3501-6 material at -650mV applied potential was slightly lower than that of AS4/3501-6 composite, fig. 7 and fig. 8. However, the damage rate at -900mV applied potential condition showed no difference between both materials, see figs. 4-5 and figs. 7-8.

Differences and Similarities in Composite Behavior

Some differences were found between the composites with same polymer matrix but different fibers in the present study. The parameters those control the damage processes are the polymer type, fiber type, fiber surface treatment, the manufacturing processes and the interfacial behavior between the fibers and polymer matrix. The polymer type, fiber surface treatment and manufacturing processes will control the permeation rate of oxygen and solution to the cathodic site and the content of initial defects. The fiber surface treatment and the interfacial behavior between the fibers and polymer significantly influences the rate of damage formation. Detailed study of the parameters which control the interface strength properties in carbon epoxy system was given in the reference [10]. As discussed in the previous section, the polymer thickness is another factor which affects the degree of damage. It is noted that the fiber type did not significantly influence the degradation mechanisms of the composites under cathodically polarized conditions. This suggests that the polymer condition and interface behavior between fibers and polymer matrix are the more important parameters. A good fiber surface treatment and interfacial strength between fibers and polymer matrix are necessary. Pre-existing defects can be avoided by good manufacturing processes.

CONCLUSIONS

1. The fiber type did not significantly influence the degradation mechanisms of the composites under galvanic exposure conditions. The polymer conditions, fiber surface treatment and interface behavior between fibers and polymer matrix are the more important control parameters.

2. The parameters from modeling provided an important degradation mechanisms of composites.

3. The decreasing in polymer resistance, R_p , with increasing time of exposure indicated that dynamic degradation processes were occurring due to the cathodic reaction at the fiber surface. The value of R_p also decreased with increasingly negative applied potentials.

4. The observed damage on exposed specimen provided an evidence of decreasing of impedance behavior of composites.

REFERENCES

1. Kaushik, D., M. N. Alias and R. Brown, Corrosion, Vol. 47, 1991, p.859.
2. M. N. Alias and R. Brown, Corrosion, Vol. 48, 1992, p.373.
3. S. Miriyala, W. C. Tucker, T. J. Rockett and R. Brown, "Proceedings of the Ninth International Conference on Composite Materials", Madrid, Spain, 1993, p. 586
5. F. Mansfeld, M. W. Kendig and S. Tsai, Corrosion, Vol. 38, No. 9, 1982, p.498.
6. W. M. Kendig, F. Mansfeld and S. Tsai, Corrosion Sciences, 23 (1983), p.317
7. R. Delasi and J. B. Whiteside, Advanced Composite Materials - Environmental Effects, ASTM STP 658, J. R. Vinson, Ed., ASTM, 1978, p.2.
8. G. Lubin, Handbook of Composites, SPE, p. 513.
9. W. H. E. Reynolds, R. Brown and M. N. Alias, "Comparison of the Performance of a Carbon Fiber Composite Materials in Distilled Water and Chloride Solutions", NACE, 1994, Baltimore, MD.
10. I. Verpoest, "Interfacial Phenomena in Composite Materials '91", Proceeding of the second international conference held 17-19 September 1991 in Leuven, Belgium.
11. J. Qin and R. Brown, unpublished data.

SESSION IV
DETECTION AND MONITORING OF
CORROSION NDI & E

Chairman: *W. Cox*

BLANK

The Use of Superconducting Magnetometry to Detect Corrosion In Aircraft Alloys

Delin Li^a, Yupei Ma^b, W. F. Flanagan^a, B. D. Lichter^a, and J.P. Wikswo, Jr.^{b*}

a. Department of Mechanical Engineering

b. Department of Physics and Astronomy

Vanderbilt University, Nashville, TN 37235

Abstract

The magnetic field distribution for three different types of in-situ corrosion has been measured using SQUID magnetometry. The variations of the magnetic field density with time differ for the three types of corrosion. The higher the corrosion rate, the more intense is the magnetic field. The SQUID magnetometer is also shown to be sensitive to corrosion activity occurring on the opposite side of a plate specimen.

1. Introduction

Over the last few decades, there have been many attempts to measure the corrosion current distribution during active corrosion, with little success. Since the net anodic current is equal to the net cathodic current in active corrosion, any non-local measuring methods would sense a net current approaching zero. By using a scanning reference electrode (SRE) technique¹⁻⁵, there has been some success in measuring the corrosion potential distribution on actively corroding samples. However, such results do not give directly the resulting corrosion current distribution, since many factors are involved in the interpretation of the data, not all of which are known.

It is recognized that magnetic fields are associated with current flow. Thus, the corrosion current should have an associated magnetic signature. The detectability of the magnetic fields depends on the magnitude and the spatial distribution of the corrosion current. The SQUID magnetometer enables sensitive

measurements of extremely small magnetic fields to be made non-invasively, that is, without any electrical or mechanical connections intruding on the sample. It offers the promise of monitoring both the magnitude and the spatial distribution of the corrosion current, which present corrosion methods do not allow. The ability of the SQUID magnetometer to measure magnetic signals due to electrochemical reactions has been proven recently⁶⁻¹⁰. The Vanderbilt Superconducting Quantum Interference Device (SQUID) magnetometer system, which incorporates a MicroSQUID magnetometer¹¹, a magnetic shield¹², a scanning stage¹³, and a computer control and data acquisition system¹⁴, has been developed and used for the detection of flaws in nonferromagnetic conductors^{14,15}, and for the detection of subsurface flaws¹⁶. In the present paper, we focus on the application of SQUID magnetometry to the detection and mapping of the magnetic field distribution on active in-situ corroding aluminum alloys used in the manufacture of aircraft. The analysis of these data in terms of the corrosion current distribution will be reported in a later paper.

2. Experimental

Three types of active corrosion were studied: pitting corrosion, pitting/intergranular corrosion, and "uniform" corrosion. Pitting corrosion was modeled using 1.5 mm thick 7075 aluminum alloy in solutions of 3.5% NaCl with differing Cu^{++} concentrations. Pitting/intergranular corrosion was modeled using 1.5 mm thick 2024 aluminum alloy in solutions of 3.5% NaCl with differing Cu^{++} concentrations. "Uniform" corrosion was modeled using 1.5 mm thick 2024 aluminum alloy in a solution of 2 ml 58% HF, 3 ml 71% HNO_3 , 5 ml 36.5% HCl, and 590 ml H_2O .

The physical details of the SQUID tests are shown in Figure 1a and 1b, respectively. For tests described by Figure 1a, the sample was placed in the corrosion cell with the solution extending to 2 mm above the sample surface. The corrosion cell was covered by a transparent film which served to protect the SQUID detector from the corrosive environment. The SQUID pick-up coils were located about 3 mm above the plastic film. Thus, the distance between the SQUID pick-up coils and the sample was about 5 mm. For tests described in Figure 1b, a large plate sample was placed on the corrosion cell, which had an 45 mm diameter area exposed to the solution, but on the bottom side of the plate, on the side opposite from the SQUID magnetometer. For this test, the SQUID pick-up coils were located 4 mm above the top sample surface. All aluminum alloy plates used in the tests were 1.5 mm thick. It should also be noted that the SQUID measures only the vertical component of the magnetic field, normal to the corroding surface.

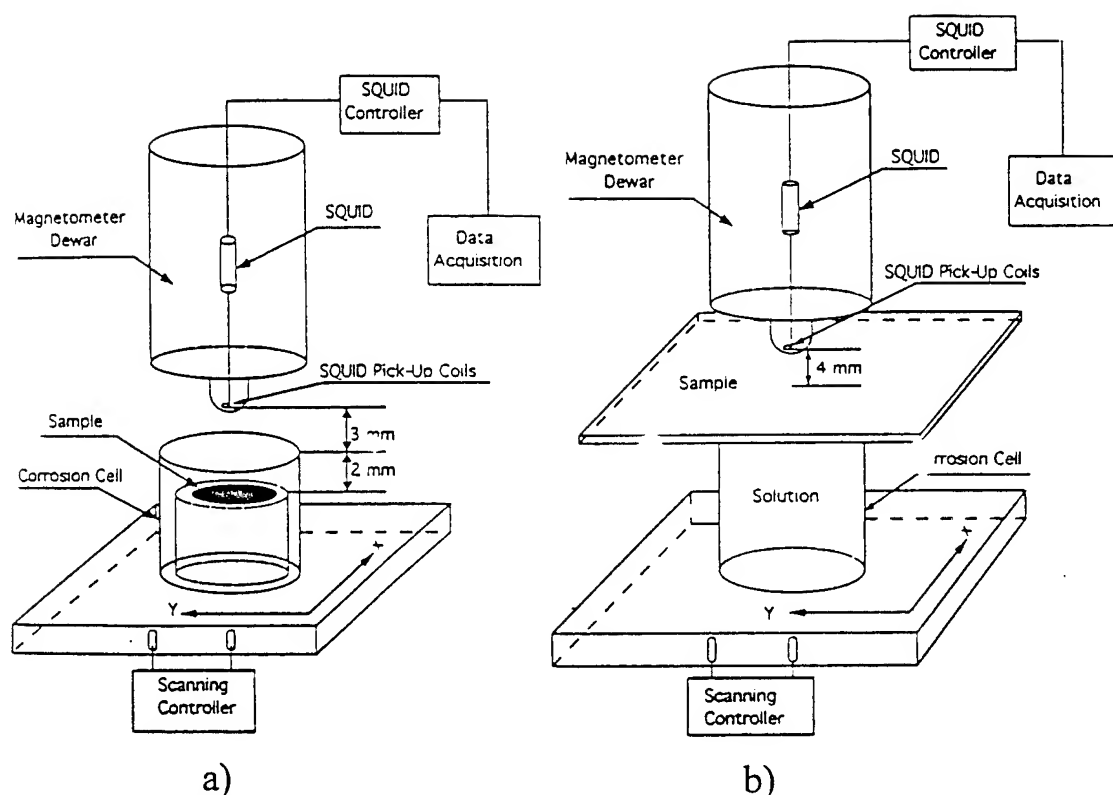


Figure 1. Schematic diagrams of the active in-situ corrosion test systems: a) The sample is placed in a corrosion cell so that the top surface is 2 mm below the solution surface; b) a large plate sample which has a 45 mm diameter area exposed to the solution at the bottom side of the plate, i.e., on the side away from the SQUID magnetometer.

The X-Y scanning of the corrosion cell was computer controlled. The scanning area was larger than the sample for all tests. The scanning rate in x-direction was 20 mm/s, and the orthogonal step in y-direction after each scan was 1 mm or 3 mm. The data acquisition rate was 4 points per mm in the x-direction. The magnetic field distribution for the sample was measured as a function of time by the SQUID magnetometer. For each test, the magnetic field distribution for the sample in air, without the corrosive environment, was also measured before and after the sample was exposed to the solution.

3. Experimental Results

3.1. Magnetic Field Measured by SQUID During Active Corrosion of Aluminum Alloys in the Test Described by Figure 1a

3.1.1. Magnetic Field Measured by SQUID on 7075 and 2024 Aluminum Alloys Undergoing Pitting and/or Intergranular Corrosion

Figure 2a-2c show typical magnetic field distributions detected by the SQUID near the surface of actively corroding 7075 aluminum alloy plate in a solution of 3.5% NaCl + 50 ppm Cu^{++} . The data shown in Figures 2a and 2b were obtained over periods of 25 to 43 minutes and 205 to 223 minutes after the sample was placed in the solution, respectively, which is considered to be representative of the interval involved in the initiation of pitting, and in Figure 2c over the period of 275 to 293 minutes, which are considered to be representative of the time involved in the growth of these pits. Figure 2d shows the magnetic field distribution over the

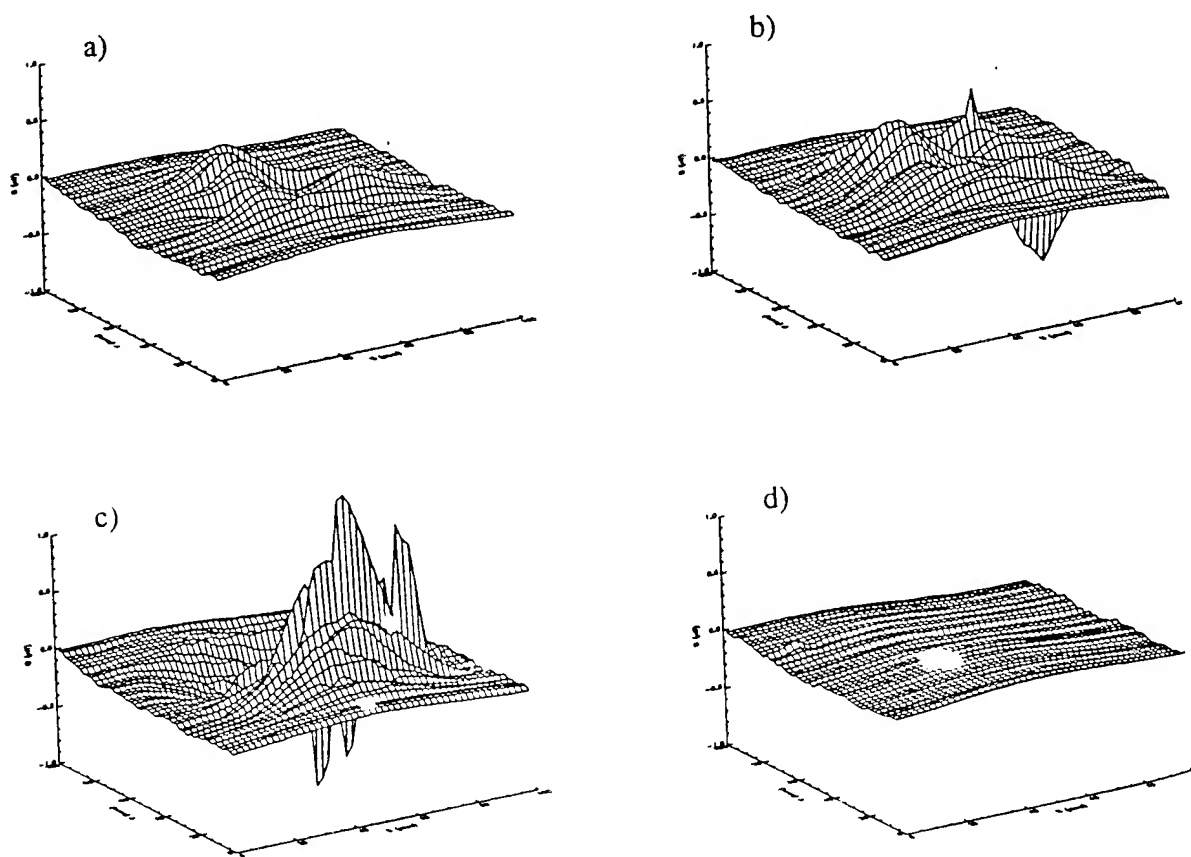


Figure 2. Typical magnetic field distributions for active pitting corrosion of a 32×32 mm 7075 aluminum alloy plate in a solution of 3.5% NaCl + 50ppm Cu^{++} . Data were obtained (a) in the time interval from 25 to 43 minutes after the sample was placed in the solution, (b) in the time interval from 205 to 223 minutes, (c) in the time interval from 275 to 293 minutes, and (d) in air after the corrosion attack.

sample in the absence of a corroding environment, after the corrosion attack. The above results give evidence that the magnetic fields measured by the SQUID magnetometer are due solely to corrosion current.

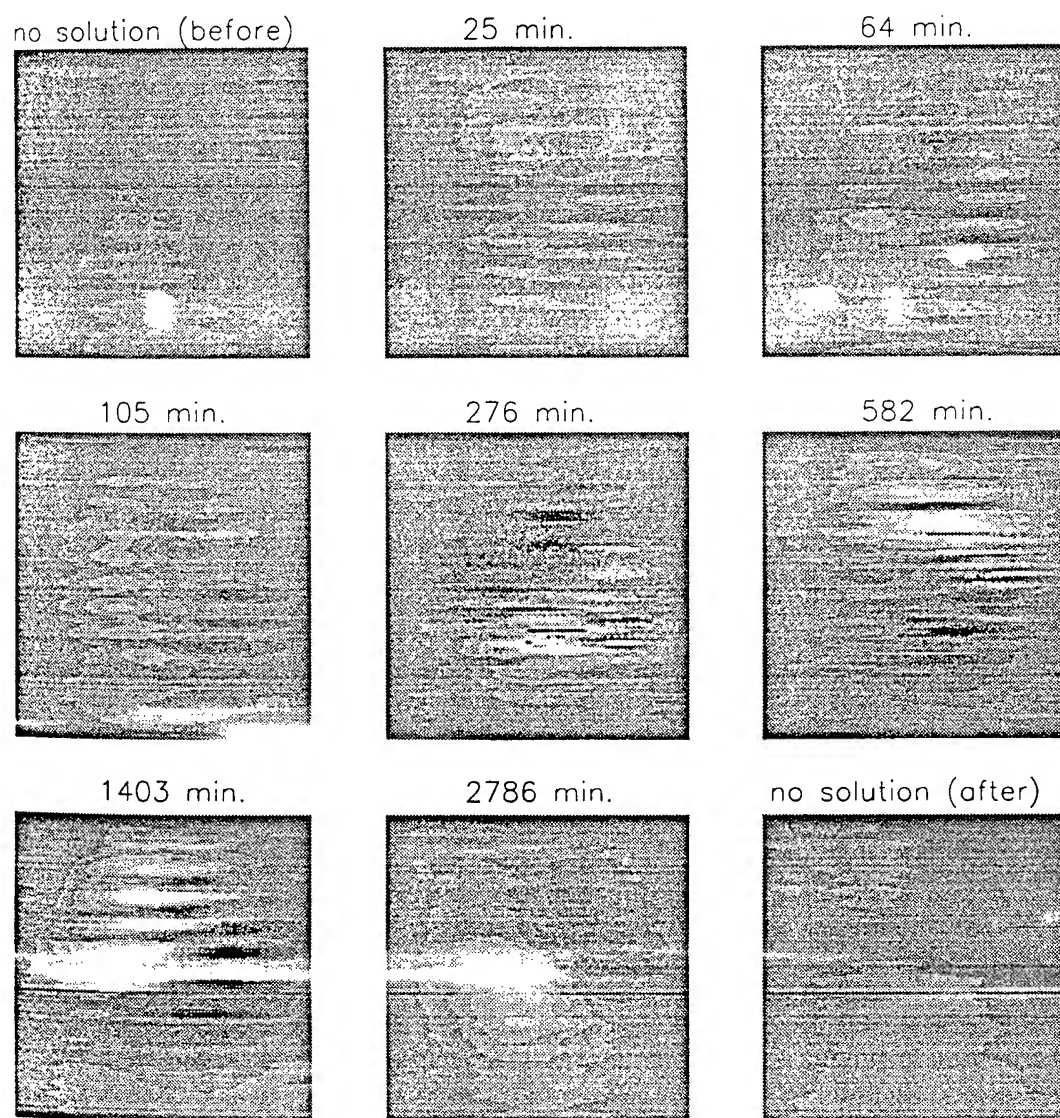


Figure 3. The magnetic field as a function of time during active pitting corrosion of a 32x32 mm 7075 aluminum alloy plate in a solution of 3.5% NaCl + 50 ppm Cu^{++} .

Figures 3 and 4 show typical magnetic field distributions on the sample as a function of time during active corrosion of 7075 and 2024 aluminum alloys, respectively, both in the same solution of 3.5% NaCl + 50 ppm Cu^{++} . Such

distributions are found to change from time to time, and are believed to be related to the variation of the local corrosion current in the sample.

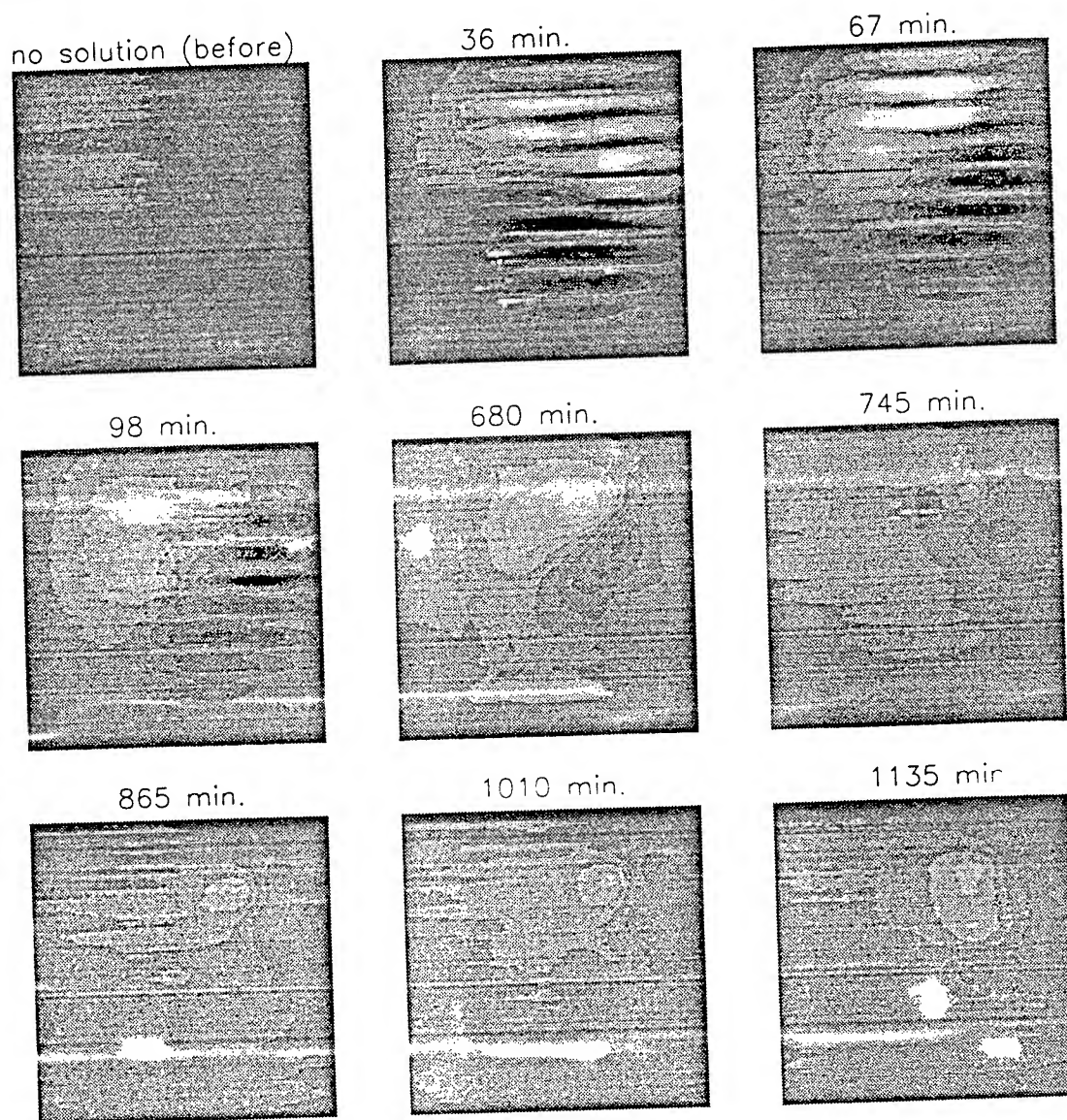


Figure 4. The magnetic field as a function of time during active corrosion of a 32x32 mm 2024 aluminum alloy plate in a solution of 3.5% NaCl + 50 ppm Cu^{++} .

Figure 5a and 5b show variation over time of the maximum positive and negative magnetic field density during active corrosion of 7075 and 2024 aluminum alloys in a solution of 3.5% + 50 ppm Cu^{++} , respectively. It is shown that this change is clearly different for the two alloys. Figures 6a and 6b show the variation of the maximum positive magnetic field density with Cu^{++} concentration for 7075

and 2024 aluminum alloy respectively during active corrosion at different times. It is seen that the difference of the maximum positive magnetic field density, as the Cu^{++} concentration varies from 10 ppm to 50 ppm, increases with time for 7075 aluminum alloy, but decreases with time for 2024 aluminum alloy. It is also shown that the maximum positive magnetic field density in the solution with 50 ppm Cu^{++} is larger than that in a solution with 10 ppm Cu^{++} , for both the 7075 and 2024 aluminum alloys.

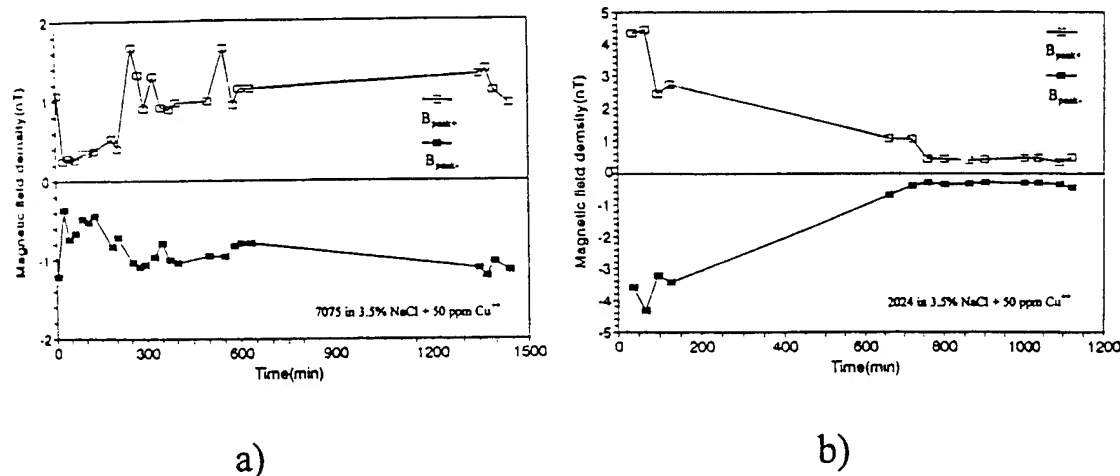


Figure 5. The maximum positive and negative magnetic field density as a function of time during active corrosion of (a) 7075 and (b) 2024 aluminum alloys in a solution of 3.5% NaCl + 50 ppm Cu^{++} .

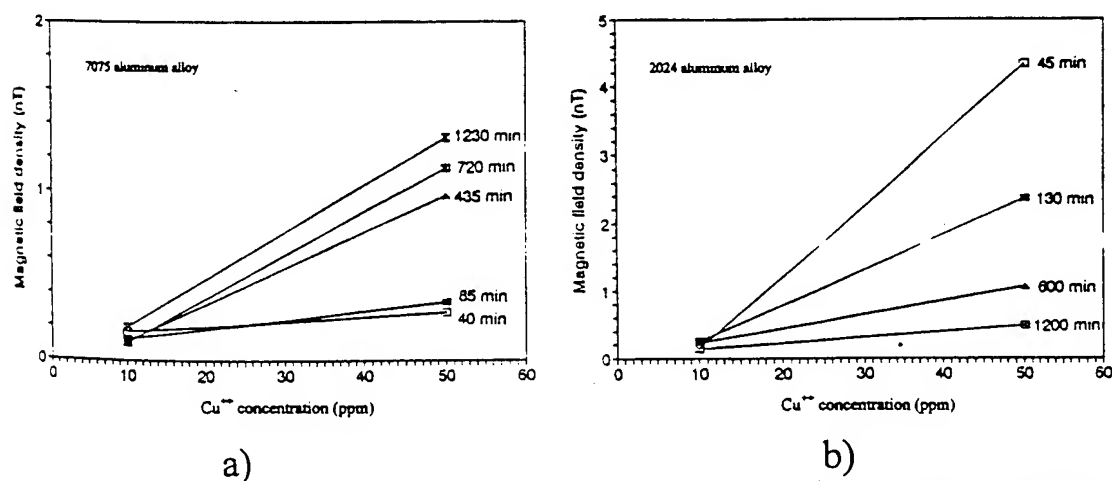


Figure 6. Variation of maximum positive magnetic field density with Cu^{++} concentration at different times for active corrosion of (a) 7075 aluminum alloy and (b) 2024 aluminum alloy.

A typical microstructure for 7075 aluminum alloy after corrosion is shown in Figure 7a; this involved a cumulative exposure time of about 1440 minutes in 3.5% NaCl + 50 ppm Cu^{++} . Figure 7b shows the corresponding microstructure for 2024

aluminum alloy after a cumulative exposure of 1220 minutes in an identical solution. The attack in the 7075 aluminum alloy was found to penetrate as pits deep into the sample, while the attack in the 2024 aluminum alloy was found to be mainly surface attack at grain boundaries and localized pits.

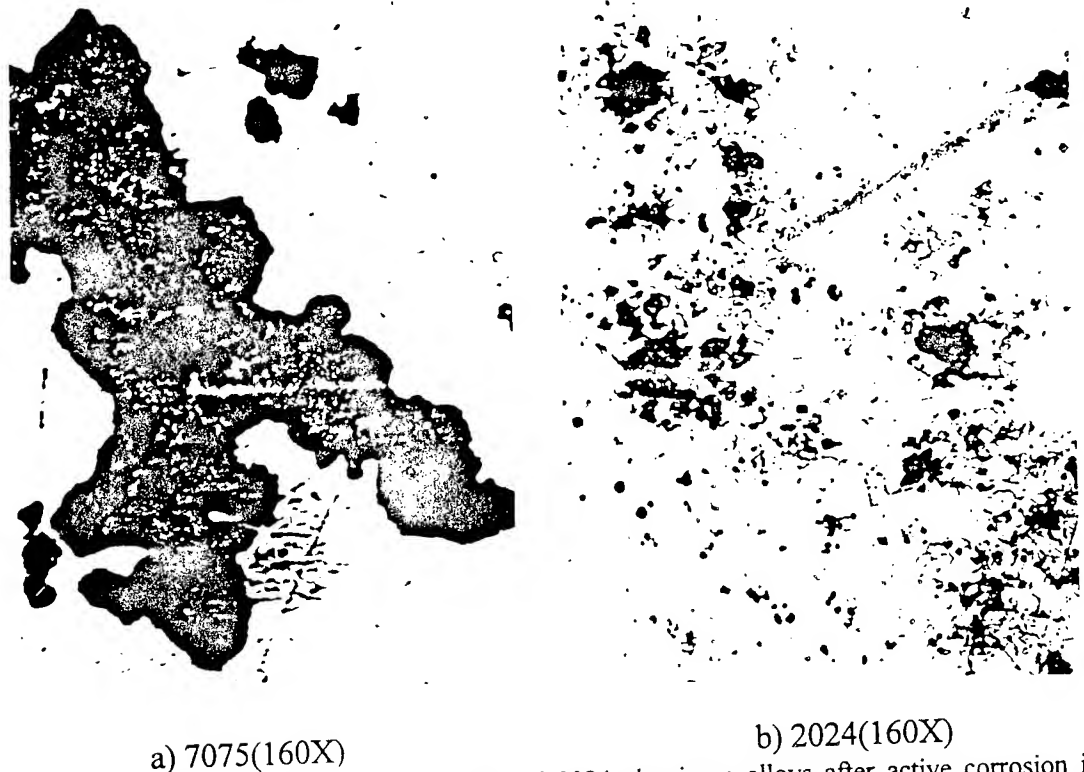


Figure 7. Typical microstructures of 7075 and 2024 aluminum alloys after active corrosion in a solution of 3.5% NaCl + 50 ppm Cu^{++} in the SQUID tests.

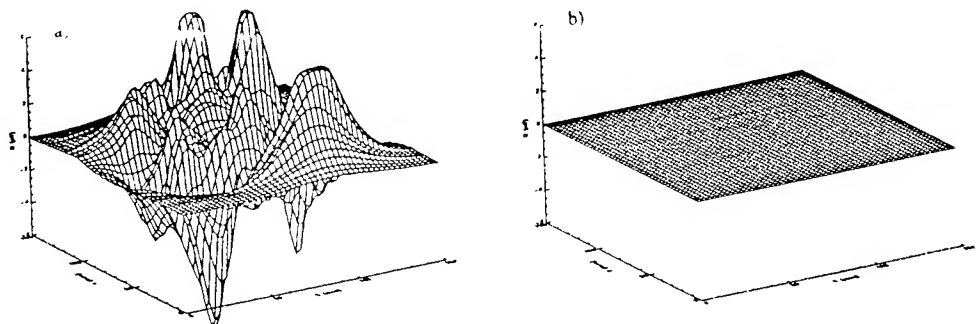


Figure 8. Typical magnetic field distributions for a 113 mm diameter circular plate of 2024 aluminum alloy undergoing active "uniform" corrosion in a solution of 2 ml 58% HF, 3 ml 71% HNO_3 , 5 ml 36.5% HCl, and 590 ml H_2O . Data was obtained (a) over the period from 183 to 198 minutes after the sample was placed in the solution, and (b) in air after the corrosion attack.

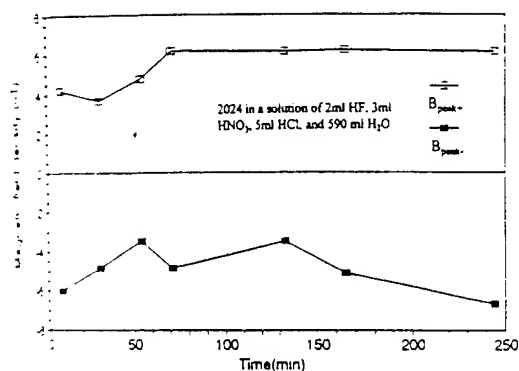


Figure 9. The maximum positive and negative magnetic field density as a function of time during active "uniform" corrosion of 2024 aluminum alloys in a solution of 2 ml 58% HF, 3 ml 71% HNO₃, 5 ml 36.5% HCl, and 590 ml H₂O.



160X

Figure 10. Typical microstructure of 2024 aluminum alloys after "uniform" corrosion in a solution of 2 ml 58% HF, 3 ml 71% HNO₃, 5 ml 36.5% HCl, and 590 ml H₂O.

2024 aluminum alloy plate, which has an 45 mm diameter area exposed to the solution at the bottom side of the plate, in solutions of 3.5% NaCl + 50 ppm Cu⁺⁺ and 2 ml 58% HF, 3 ml 71% HNO₃, 5 ml 36.5% HCl, and 590 ml H₂O,

3.1.2. Magnetic Field Measured by SQUID on 2024 Aluminum Alloy Undergoing "Uniform" Corrosion

Figure 8a shows a typical magnetic field distribution during "uniform" corrosion of 2024 aluminum alloy in a solution of 2 ml 58% HF, 3 ml 71% HNO₃, 5 ml 36.5% HCl, and 590 ml H₂O. Figure 8b shows the lack of any magnetic field distribution over the sample in the absence of the corroding environment after the corrosion attack. Figure 9 shows the variation of the maximum positive and negative magnetic field density with time during "uniform" corrosion. It is found that the change of the magnetic field density with time differs from that for pitting corrosion (Figures 5b and 9). The microstructure of 2024 aluminum alloy after "uniform" corrosion is shown in Figure 10, where it is seen that the attack is "uniform" over the sample surface.

3.2 Magnetic Field Measured by SQUID During Active Corrosion of Aluminum Alloys in the Test Described by Figure 1b

Figure 11a and 11b show typical magnetic field distribution detected by the SQUID for active corrosion of

respectively. The results give evidence that the SQUID magnetometer is sensitive to corrosion activity occurring on the opposite side of a plate specimen.

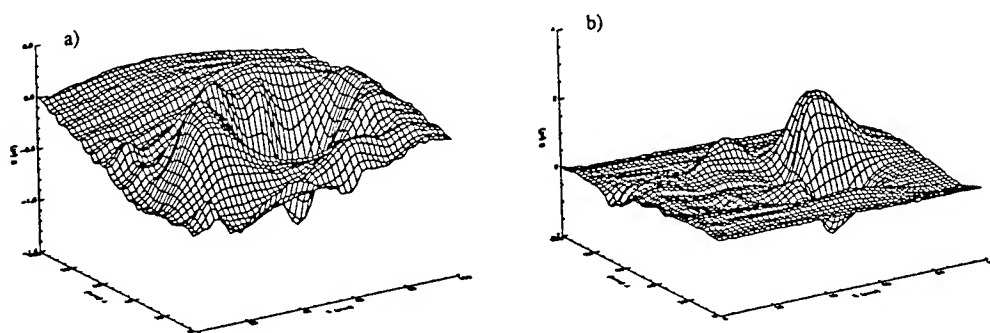


Figure 11. Typical magnetic field distribution measured by SQUID in the test described by Figure 1b for active corrosion of 2024 aluminum alloy (a) in a solution of 3.5% NaCl + 50 ppm Cu^{++} and (b) in a solution of 2 ml 58% HF, 3 ml 71% HNO_3 , 5 ml 36.5% HCl, and 590 ml H_2O .

4. Discussion

4.1. Magnetic Field Distribution as an Indicator of the Type of Corrosion

It is seen from Figure 7 that the microstructure of 7075 aluminum alloy undergoing pitting corrosion differs from that of 2024 aluminum alloy which shows pitting/intergranular corrosion. It is also seen that the variation of the maximum positive and negative magnetic field density with time for the 7075 aluminum alloy in a solution of 3.5% NaCl + 50 ppm Cu^{++} (Figure 5a) is very different from the results for 2024 aluminum alloy in the identical solution (Figure 5b), and also that the variation of magnetic field density with time for 2024 aluminum alloy in the "uniform" corrosion solution is clearly different from that in the pitting solution (Figure 5b and Figure 9). These results give evidence that the SQUID can be used to distinguish between the different types of corrosion in 7075 and 2024 aluminum alloys.

4.2. Magnetic Field Intensity as an Indicator of Corrosion Rate

As we can see in Figures 6a and 6b, the magnetic field density in the solution of 3.5% NaCl containing 50 ppm Cu^{++} is larger than that in the solution containing 10 ppm Cu^{++} . This can be explained by the fact that when copper ions are added to a solution containing chloride ions, the corrosion potential of the aluminum alloy immediately rises close to the pitting potential^{17,18}. The reason is that dissolved

Cu^{++} deposits on the aluminum alloy surface as metallic Cu, which acts as an efficient cathode, causing the corrosion potential of the aluminum alloy to shift up to near the pitting potential. The higher the Cu^{++} concentration in the solution, the more Cu^{++} is deposited on the aluminum alloy surface, and these cathodes in the aluminum alloy surface become more efficient. Figure 6a also shows that the increase of the extrema in the magnetic field density with time for 7075 aluminum alloy in the solution with 50 ppm Cu^{++} is much more rapid than that in the solution with 10 ppm Cu^{++} . This parallels the increase of corrosion current expected in each of these cases.

It is also seen that the maximum positive and negative magnetic field density for 2024 aluminum alloy in the "uniform" corrosion solution (Figure 9) is larger than that in the pitting solution (Figure 5b). This can be explained by the fact that the corrosion current of the sample in the former solution may be much larger than for that in the pitting case, i.e., the higher the corrosion current, the more intense is the magnetic field. The magnetic field density for 2024 aluminum alloy in the solution of 3.5% NaCl + 50 ppm Cu^{++} is larger than that for 7075 aluminum alloy in the identical solution for up to 700 minutes after the samples were placed in the solution (Figures 5a and 5b). This difference may be explained by the fact that different corrosion mechanisms are involved, so that different corrosion currents result. These facts also attest to the feasibility of using SQUID results to measure corrosion currents. The magnetic field distribution as affected by the geometry of the test sample and cell was also studied, and the results will be reported in a later paper.

5. Conclusions

1. Magnetic field distributions resulting from active in-situ corrosion in aluminum alloy samples can be measured by SQUID magnetometry.
2. The variation of maximum positive and negative magnetic field density with time is clearly different for the three types of active in-situ corrosion studied, allowing one to use SQUID magnetometry as an indicator of the type of corrosion that is actively involved.
3. The magnetic field density is an indicator of the magnitude of active in-situ corrosion occurring in the specimen.
4. The SQUID magnetometer is sensitive to corrosion activity occurring on the opposite side of a plate specimen.

Acknowledgments

This work is supported by Air Force of Scientific Research grant F49620-93-0268.

6. References

1. H.S. Isaacs, G. Kissel, J. Electrochem. Soc., 119, 1628(1972)
2. L.J. Gainer, G.R. Wallwork, Corrosion, 35,2,61(1979)
3. H.S. Isaacs, M.W. Kendig, Corrosion, 36, 6, 269(1980)
4. R.J. O'Halloran, L.G. Williams, and C.P. Lloyd, Corrosion, 40,7,344(1984)
5. H.S. Isaacs, Corrosion, 43,10,594(1987)
6. J.G. Bellingham, M.L.A. MacVicar, M. Nisenoff, P. Searson, J. Electrochem. Soc., 133, 8, 1753(1986)
7. J.G. Bellingham, M.L.A. MacVicar, M. Nisenoff, IEEE Trans. MAG., MAG-23, No.2, 477(1987)
8. Mira Misra, Scott Lordi, and M.L.A. MacVicar, IEEE Trans. MAG., 27, 2, 3245(1991)
9. J.C. Murphy, G. Hartong, R.F. Cohn, P.J. Moran, K. Bundy, and J.R. Scully, J. Electrochem. Soc., 135, 2, 310(1988)
10. J.C. Murphy, R. Srinivasan, and R.S. Lillard, Rev. of Progress in QNDE, D.O. Thompson and D.E. Chimenti, Eds., Plenum, NY, Vol. 8B, pp. 2149(1989).
11. D.S. Buchanan, D.B. Crum, D. Cox, and J.P. Wikswo, Jr., Adv. in Biomagnetism, S.J. Williamson, G. Hoke, G. Stroink, and M. Kotani, Eds., pp. 667-679, Plenum, NY (1990).
12. Y.P. Ma and J.P. Wikswo, Jr., Rev. Sci. Instrum., Vol. 62, pp. 2654(1991).
13. J.P. Wikswo, Jr., J.M. van Egeraat, Y.P. Ma, N.G. Sepulveda, D.J. Staton, S. Tan, and R.S. Wijesinghe, Digital Image Synthesis and Inverse Optics, A.F. Gmitro, P.S. Idell, and I.J. LaHaie, Eds., Vol. 1351, pp. 438-470, SPIE Proceedings(1990).
14. Y.P. Ma, D. J. Station, N.G. Sepulveda, and J.P. Wikswo, Jr., Rev. of Progress in Quantitative Nondestructive Evaluation, D.O. Thompson and D.E. Chimenti, Eds., Vol. 10A, pp. 979-986, Plenum, NY(1991).
15. J.P. Wikswo, Jr., D.B. Crum, W.P. Henry, Y.P. Ma, N.G. Sepulveda, and D.J. Station, J. of Nondestructive Evaluation, 12, 2, 109(1993).
16. Y.P. Ma and J.P. Wikswo, Jr., Rev. of Progress in Quantitative Evaluation, D.O. Thompson and D.F. Chimenti, Eds., Vol. 11A, pp. 1153-1159, Plenum, NY(1992).
17. H.H. Uhlig, J. Electrochem. Soc., 116, 906(1969).
18. S. Furuya and S. Soga, Corrosion, 46, 989(1990).

**OC-ALC Aging Aircraft Disassembly
and Hidden Corrosion Detection Program**

Mr. Donald E. Nieser, P.E.
OC-ALC/LACRA
3001 Staff Drive, Ste. 2AH190B
Tinker AFB, OK 73145-3040

2Lt Deric Kraxberger
OC-ALC/TIETR
3001 Staff Drive, Ste. 2AF66A
Tinker AFB, OK 73145-3040

Corrosion has been a part of the aviation industry since metal was first used to build aircraft. It was recognized right away that corrosion was an undesirable condition for structural integrity, and so we coated, primed, painted and created corrosion resistant alloys to "prevent" corrosion, or at least lessen its impact. Until recently, limited corrosion prevention measures; combined with a "find it and fix it" maintenance philosophy has been adequate to combat the ravages of age on our aircraft. Unfortunately, that was when an aircraft life was relatively short. Today, we are flying our aircraft well beyond their original expected services lives, nature is starting to take its tool on the fleets, and we are caught without answers.

The OC-ALC Aging Aircraft Disassembly and Hidden Corrosion Detection Program was initiated by Mr. Donald Nieser of the KC-135 engineering office, because this is the very problem being experienced on the KC-135. This aircraft was built between 1955 and 1963 and still constitutes the backbone of the USAF tanker fleet. It was never meant to handle its mission for this long, and therefore was not constructed with corrosion prevention as a primary concern. The original construction was without any sealants in the lap joints, and in fact, most fuselage skins have spot welded doublers attached to them (that means metal to metal contact, with no protective coatings at all). The upper wing skins are 7178 aluminum with steel fasteners (a perfect area for dissimilar metal corrosion).

If we were to make an estimate of the fatigue life left in the aircraft based on current flight profiles, the tankers would be able to fly easily to the year 2000. This assessment, however, is based on pristine aluminum and, unfortunately, the KC-135 no longer has the luxury of being able to claim an uncorroded structure. The areas of the aircraft described above are showing signs of massive corrosion problems, and nobody has the analytical tools necessary to incorporate the effects of corrosion into the damage tolerance and service life predictions of the airplane. This program was developed to find those tools, at least in their preliminary forms.

To reach our goal, we needed to implement several key program elements. These elements are: the disassembly of a retired -135; the development of non-destructive inspection (NDI) equipment capable of finding hidden corrosion; the creation of a corrosion information system; structural integrity testing of corroded material; the creation of a corrosion predictive model; corrosion quantification; corrosion growth rate studies; and a service life prediction and extension study.

The disassembly of a recently retired -135 was one of the first program elements to be started. We took this aircraft and cut it into 3'X3' sections. These sections had the paint stripped off, all the fasteners removed, and the corrosion byproducts and dirt stripped off in a light etching process. All of the corrosion (and cracks) are being documented and we will create a map of airframe corrosion. This map will be supplemented by maintenance history and surveys and then compared with what is being found on the Program Depot Maintenance (PDM) line to determine where we need to be looking for corrosion in the future. What we have found so far, is that there are several areas on the aircraft that are very difficult to inspect, and we are finding these areas to have some rather severe corrosion. What is more alarming though, is that we are finding light and moderate corrosion everywhere on the aircraft. Areas that were thought to be corrosion free are definitely not, and we simply don't have the technology available to find this hidden corrosion.

Therefore, the second element of the program is to find solutions to the NDI dilemma. We invited any vendor that thought they might have a piece of off-the-shelf equipment capable of finding hidden corrosion in lap joints and around wing skin fasteners, to come to Oklahoma City and prove it. We cut coupons from actual aircraft and had the vendors try to find the corrosion and tell us how bad the corrosion was. Those vendors that did reasonably well were invited back to try their equipment on actual aircraft in the PDM line. From those vendors trying to find corrosion in the laps, we purchased three systems that showed promise. These systems are currently being put through a validation phase and procedural development phase for eventual imple-

mentation on the PDM line. As for those vendors trying to find wing skin corrosion, none were successful, and no systems were purchased. It is clear to us that both problem sets will require the development of new technologies to give us reasonable inspection results.

Another valuable tool not yet available to us is an accurate and comprehensive corrosion history of the KC-135. Maintenance history for this 35 year old aircraft is sketchy and incomplete, and most every action is still performed by shuffling paper. It is imperative that we be able to build a better history of the aircraft's corrosion problems. To that end, we are creating an Integrated Corrosion Data Base (ICDB). The ICDB will be capable of accessing all current information resources and reading the narrative in those records to help us build a better history. It will eventually be able to access I.O.s and drawings to help us better recognize problem areas on the aircraft and give faster engineering disposition on required areas. Eventually, the information collected by the ICDB will be invaluable in creating a predictive model for corrosion on the -135.

The predictive model, is currently being evaluated to determine if it is possible to do. An actual predictive model would require much more information on the nature of corrosion than is currently available. What we hope to do in the short term, is at least be able to predict where we will find corrosion on the airplane given its station and flight profiles.

Along with knowing where the corrosion will be, we will need to know what it's doing to the strength of the material. To this end, we are engaging in structural integrity testing of material from an actual -135. We are supplementing the testing with pieces of similar structure for old 707 aircraft. To start off with, we will be doing stress vs. cycle testing on actual lap joints from a -135. We are hoping that we will be able to find enough samples that are not corroded and some that have light natural corrosion to make the test viable. As far as determining the effect of severe corrosion, one of our contractors is developing a quick laboratory method to grow severe, uniform corrosion on the faying surfaces of lap joints. We are hoping to find a very rough order of magnitude delta for the service life of those lap joints. Eventually, we will be conducting crack growth rate testing in corroded material to be incorporated into the damage tolerance assessments for the aircraft.

To incorporate the effects of corrosion into any engineering assessment, we must be able to describe the corrosion in a quantitative manner. Currently, the only descriptions of corrosion available are qualitative in nature (light, moderate and severe) and are extremely subjective. We are trying to develop a method to quantify corrosion that relates it to its effect on crack growth rates and crack nucleating potential. This number or series of numbers may

incorporate pit density, pit geometry, area covered by the corrosion and any other number of parameters that are found to be of importance.

We will also need to be able to measure corrosion when we try to assess its growth rates. Our plan for growth rate testing is to take old aluminum out of a -135, and create new lap joints with it. This is to be sure we know that there is no pre-existing corrosion. These samples will be set in various corrosive environments around the world and samples will be brought back annually to measure the growth of the corrosion at those places. Some of these samples will also be outfitted with some newly developed corrosion sensors to assess the effectiveness of the sensors and possible help in understanding the corrosion growth process.

All of the above program elements will be used in a service life engineering study to be conducted at a later date. Not only do we want to find the effective usable life of the aircraft, but we want to know what steps will be necessary to make that usable life longer. We want to know what the economic life of the aircraft is, and whether or not we should just buy new airplanes. We want to revise the Aircraft Structural Integrity Program (ASIP) to include the effects of corrosion for the -135 and other aircraft. In the short term, we want to use the disassembly to tell us where to look for corrosion, use the NDI equipment to look there, the quantification to tell how bad it is, the structural integrity testing and growth rate studies to determine if its bad enough that we need to fix a problem now or if we can let it wait. In short, we need to learn how to manage corrosion damage in the same manner we do fatigue cracks.

Unfortunately, our program is extremely small in scope. If we are ever truly going to manage this program like we hope to do, every element of this program must be expanded by orders of magnitude. We hope to be able to provide some better answers for the KC-135, but time presses on, and with it corrosion, and we have a lot of catching up to do.

Topographic Radioscopic Metrology for Corrosion Mapping

John C. Brausch
Wright Laboratory, Materials Directorate
Wright Patterson A.F.B.

INTRODUCTION

Corrosion of aging aircraft is a pivotal concern in today's Air Force as large transport and tanker aircraft are utilized well beyond their intended design life. The C/KC-135 aircraft, built in the late 1950's and early 1960's is currently projected for service through the year 2040. For such geriatric aircraft, corrosion is often the life limiting factor.

Inspection for lap-joint corrosion on the C/KC-135 during depot maintenance has historically been conducted in a quasi-destructive manner. Typically, maintenance personnel inspect fastener lines for visual indications of corrosion i.e. blistering paint, corrosion products, and skin pillowing. If a suspect region is located the fasteners are removed and a section of the skin lap-seam is peeled open for an invasive inspection. This method is both inefficient and costly.

The Aging Aircraft Disassembly and Hidden Corrosion Detection Program¹, conducted at the Oklahoma City Air Logistics Center (OC-ALC) is attempting to identify off-the-shelf nondestructive inspection (NDI) equipment and technologies that can accurately detect and quantify corrosion in fuselage lap-joint structures of the C/KC-135 and E-3 aircraft. OC-ALC requested that the Materials Directorate of Wright Laboratory develop a laboratory metrological tool by which the corrosion on disassembled aircraft fuselage skins can be accurately measured and mapped. This tool would be used to produce the solution set by which the vendor "round-robin" inspections would be graded.

The resulting technique, Topographic Radioscopic Metrology (TRM), exploits the calibrated gray scale of a digitized radiosopic image through image processing.

The resulting "corrosion maps" supply a topographical quantification of material loss due to corrosion.

This paper describes the technique development, the corrosion mapping process, and the technique validation through metallographic analysis.

BACKGROUND

Exfoliation and pitting are the two primary forms of corrosion found in the aluminum fuselage lap-joint skin structures of the KC-135. The corrosion process begins by the ingress of water at the seam. The trapped water sets up a corrosion cell between skin sheets. Material loss due to corrosion occurs at the skin interfaces. (Figure 1)

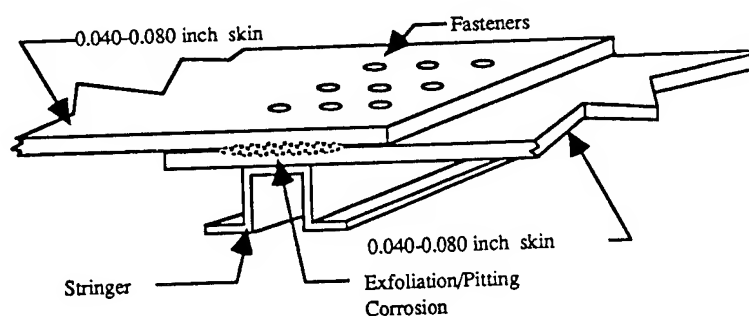


Figure 1. Lap-joint corrosion schematic.

Nondestructive methods² used for evaluation of material thickness loss due to corrosion include ultrasonic, eddy current and x-radiographic. Immersion ultrasonic and eddy current techniques were evaluated for lap-joint corrosion. However, neither could provide the spatial and thickness resolutions required. Using a focused transducer, in the pulse-echo time-of-flight mode, immersion ultrasonics can produce a two-dimensional representation of skin thickness. However, in the time-of-flight-mode the accuracy of the thickness measurements are limited by the irregular surface contours found in thin lap-joint skins. Immersion ultrasonic techniques are also limited by their slow scan rates. Eddy current techniques are also excellent tools for thickness measurements of flat surfaces. However, due to the nature of eddy currents, the abrupt and irregular thickness changes found in corrosion pits are averaged under the probe footprint resulting in poor thickness resolution.

X-ray imaging is less influenced by these geometric constraints. Therefore, an effort to develop a digitized x-ray imaging technique was conducted.

THEORY

If a parallel, monoenergetic beam of X-ray photons is directed against a thin sheet of material, the intensity of the beam will decrease through the thickness of the material according to the law:

$$I = I_0 e^{-ux} \quad (3)$$

Where I_0 is the incident intensity, I is the transmitted intensity, x is the thickness of the material, and u is a factor called the linear attenuation coefficient. The value of u depends on the energy of the incident photons and the elemental composition of the material. For aluminum at an incident energy of .05 MeV the value for u is 2.448 in^{-1} (0.964 cm^{-1})⁴. The transmitted intensity vs. material thickness for aluminum is plotted in Figure 2. As expected the transmitted intensity rises exponentially as the material thickness goes to zero. Over thickness ranges of less than 0.25 inches (0.635 cm) aluminum the curve can be assumed linear.

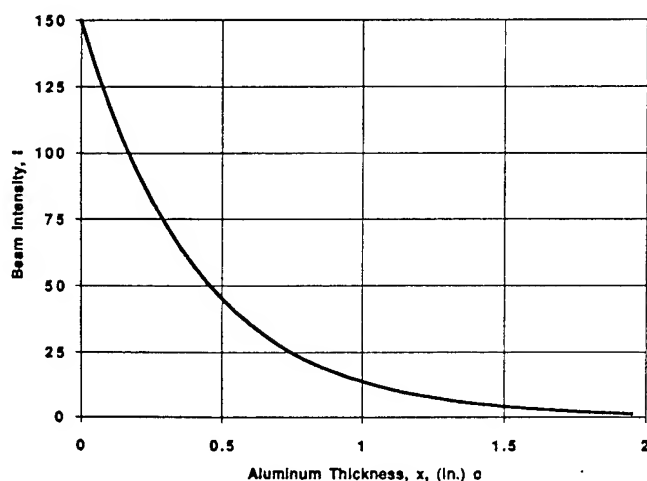


Figure 2. Plot of transmitted beam intensity versus material thickness for aluminum.

Variations in x-ray intensity due to differences in material thickness can be recorded via digital x-ray imaging. Measurement of these intensity changes are facilitated through the use of image manipulation software. For digital imaging this relationship can be expressed as the digital image intensity verses the thickness of the material. This "calibration curve" can be determined experimentally through the use of thickness standards milled from the desired material in the ranges of material thicknesses of interest. Each component of an x-ray imaging system (intensifier, camera, processor etc.) may affect this curve, therefore, this curve must be determined for the system as a whole.

EXPERIMENTAL PROCEDURE

The instrumentation used in this experiment incorporates a FeinFocus 160 kV microfocus x-ray source and a V.J. Technologies 600XDF x-ray intensifier to produce the visible image. A charge coupled device (ccd) camera generates the analog video signal for digitization by a NORAN TN-8502 image processing station (Figure 3).

Specimens can be remotely manipulated for inspection between the x-ray source and image intensifier. The limited detector size allows imaging of only 16 square inches per image. Processing of data for larger areas requires cutting and pasting.

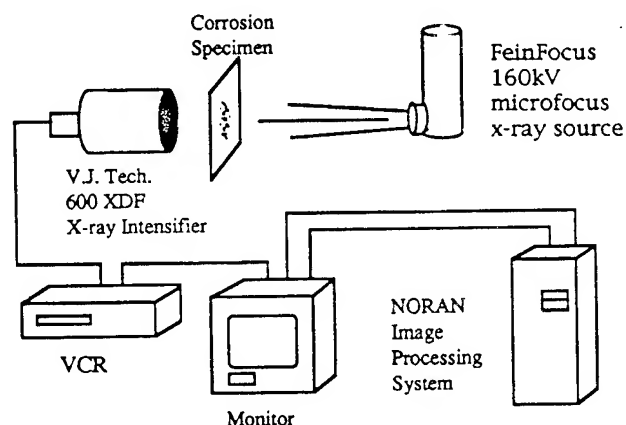


Figure 3. Equipment arrangement.

In order to define the calibration curve for relating image intensity to material thickness, thickness standards were manufactured. These standards were milled from 0.040 inch (1.016 mm) 7075-T6 aluminum fuselage skin material to represent material loss values of 2% - 27% (Figure 4). A radiosopic image of these standards was acquired with an exposure of 47 kV and 1.0 mA (Figure 5). The NORAN system captures the intensifier image through 500 frame continuous averaging.

Concentric image patterns caused by the intensity gradients of the x-ray beam are eliminated through digital image subtraction of a background image acquired from a standard of uniform base thickness.

Average pixel intensity measurements were obtained from the center of each step standard. Changes in the average pixel intensity changes were calculated from each step to the next and plotted versus percent material thickness loss as seen in Figure 6. The best fit line for the data set represents the calibration curve by which an image with corrosion may be scaled to derive experimental thickness loss values. Note the Correlation Coefficient ($R=0.98739$), shows a good fit to linearity. The slope of the calibration curve will be affected by the x-ray energy as well as material thickness. Therefore, this curve must be determined for each specimen inspection series. The experimental thickness losses, calculated via the equation for the best fit line, were compared to thickness losses measured via micrometer. The standard error was calculated to be (+/-) 1.2%; the level of accuracy that can be expected from this method.

(a)

#1	0.03915 in	0.03820 in	0.03710 in	0.03995 in
#2	0.03885 in	0.03800 in	0.03480 in	0.03995 in
#3	0.03255 in	0.03065 in	0.02885 in	0.03995 in

0.5 in

1.0 in 1.0 in 1.0 in

(b)



Figure 4. (a) Schematic of machined thickness standards and (b) photograph of standards.

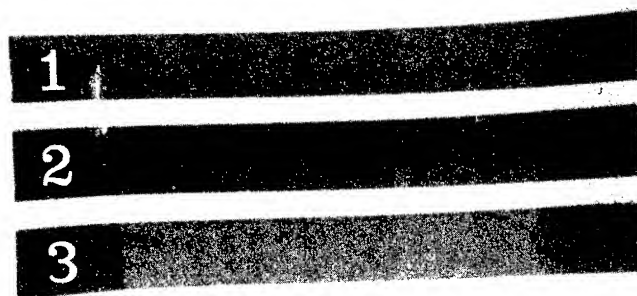


Figure 5. Digitized radioscopic image of thickness standards. Image used to determine the calibration curve relating image intensity and percentage material thickness loss.

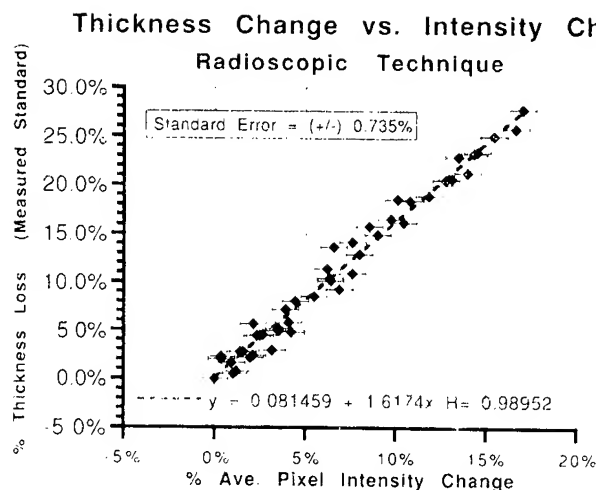


Figure 6. Plot of Percent Material Thickness Loss versus Percent Average Pixel Intensity Change.

A radioscopic image of a corroded region (Figure 7) on a 0.040 inch (1.016 mm) 7075-T6 aluminum fuselage lap-joint specimen and a 0.03009 inch (0.764 mm) thickness standard was acquired with an x-ray exposure of 47 kV at 1.0 mA. The image was digitally corrected for x-ray beam non-uniformity (Figure 8). Figure 9 represents the histogram of the image of the specimen.

Measuring average pixel intensities for the thickest and thinnest regions (uncorroded base material and thickness standard respectively), provides end points for histogram contrast expansion. The primary peak represents the corrosion specimen and the secondary peak represents the thickness standard. The peaks of these spikes are selected and the data between these peaks are chopped and stretched to fit the TN-8502's full dynamic range of 0 and 256. Colorization of the image is accomplished by dividing the dynamic range by 24 percent (thickness standard) resulting in a 10.4 point intensity change for a 1 percent change in material thickness. Assuming a linear relationship between material thickness and image intensity, the image's histogram is scaled and color banded accordingly. A colorized histogram will appear similar to Figure 10 with the resulting image as shown in Figure 11.

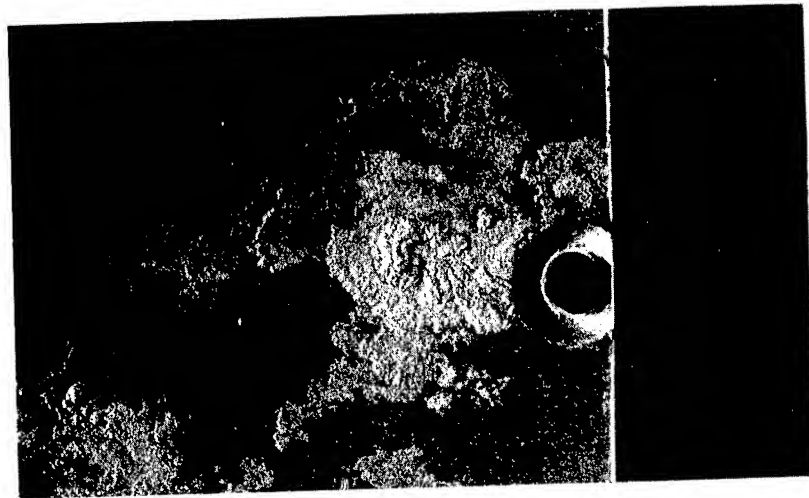


Figure 7. Photograph of corrosion site on 0.040 inch (1.016 mm) 7075-T6 aluminum fuselage skin from a C/KC-135.

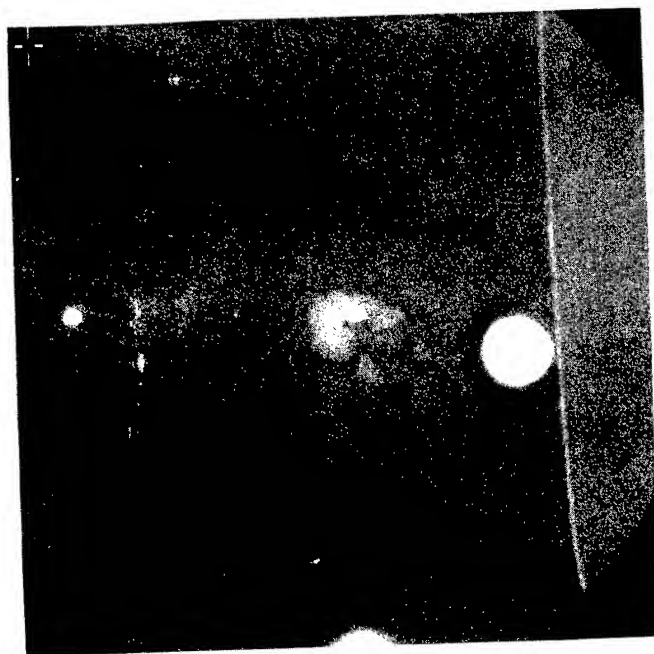


Figure 8. Digitized radioscopic image of corroded aluminum specimen. Image is unenhanced.

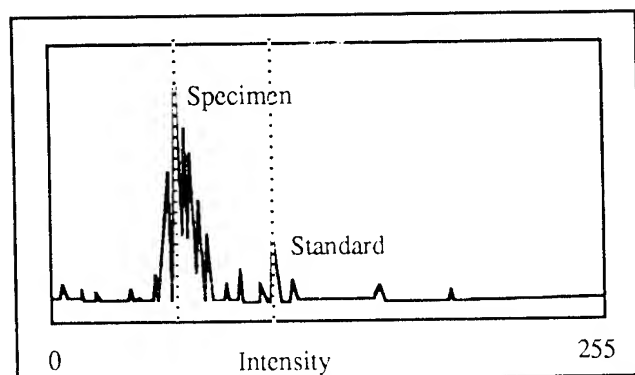


Figure 9: Representative histogram of radioscopic image.

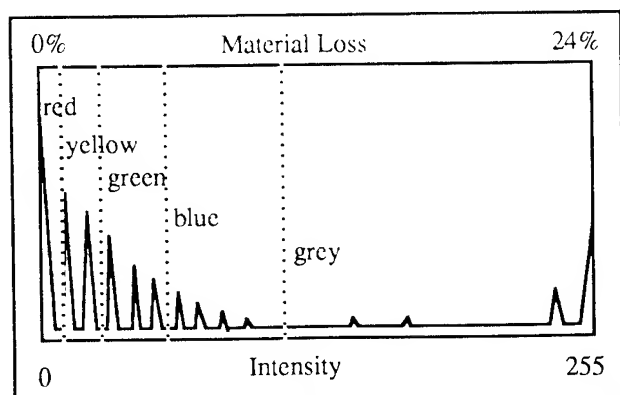


Figure 10. Resulting histogram after expansion and color scaling.

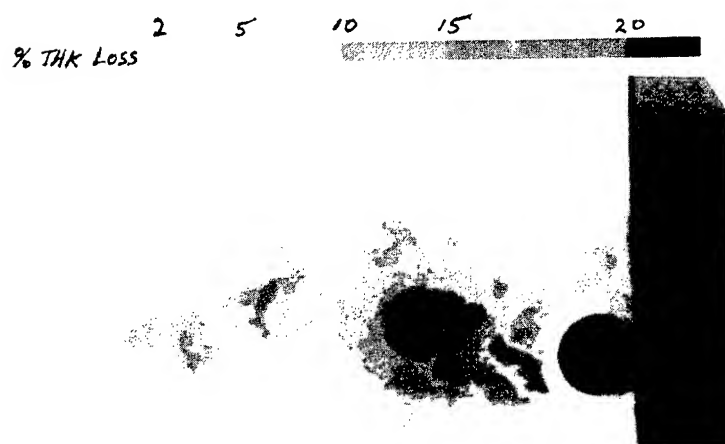


Figure 11. Digitized radioscopic image of corroded specimen after contrast expansion, calibration and colorization.

VALIDATION

Correlation to physical data was achieved through metallographic cross-sectional measurement of the corrosion sites and comparison to topographical data. Again, a colorized topographic map of material thinning of a 0.040 inch (1.016 mm) 7075-T6 aluminum skin was acquired using the method previously described (Figure 12). Two cross-section samples were cut from the corrosion area. These sections were mounted, polished, and percentage thickness losses were microscopically measured along the cross-sectional length. Comparative data are illustrated in Figures 13 and 14 for cross-sections A-A and B-B respectively. It can be seen that the physically measured data correlate very well with the experimental results.

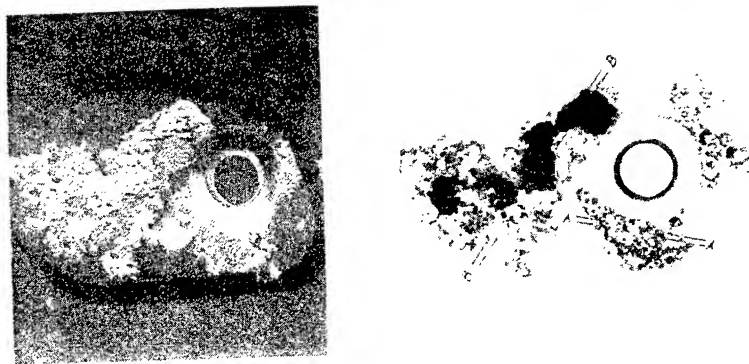


Figure 12. Photograph and scaled radiosopic image of a corrosion site on a 0.040 inch (1.016 mm) 7075-T6 aluminum skin. Bars A-A and B-B indicate segments of data for comparison to physical measurement.

Data Comparison: Section A-A Topography vs. Physical Measurement

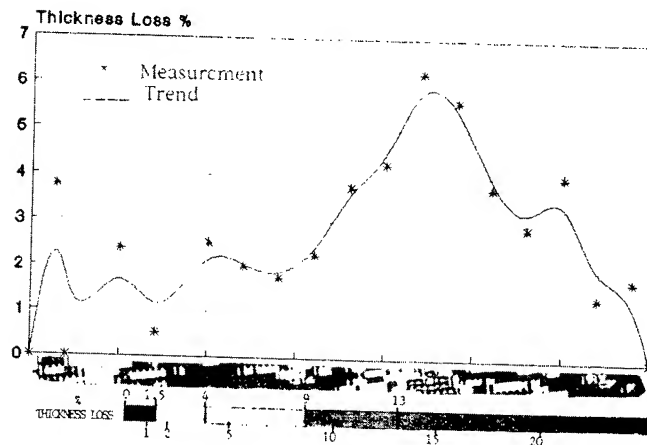


Figure 13. Plot of percentage thickness loss for cross-section A-A versus experimental topographical data obtained from Figure 12.

Data Comparison: Section B-B Topography vs. Physical Measurement

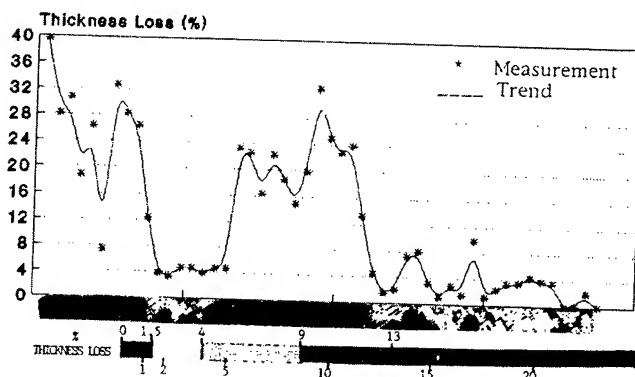


Figure 14. Plot of percentage thickness loss for cross-section B-B versus experimental topographical data obtained from Figure 12.

CONCLUSIONS

Topographic Radioscopic Metrology has demonstrated the ability to quantify and map material thickness losses on the order of 2.0% (+/-)1.2%.

TRM has been shown to be an effective tool for the quantification of thickness changes on thin aluminum sheets. The technique's high spatial resolution make it ideal for accurate quantification and mapping of the complex topography associated with corrosion.

SUMMARY

Oklahoma City Air Logistics Center identified a need for a nondestructive metrological tool for corrosion quantification of thin aluminum skins associated with fuselage lap-joints.

This paper discussed the development of an x-ray imaging technique, Topographic Radioscopic Metrology, which exploits the calibrated gray scale of a digitized radiosopic image for deriving material thickness values.

The process by which the calibration curve for x-ray image scaling was detailed. The histogram manipulation and colorization scheme was discussed with an example of corrosion maps given.

Verification of the technique was accomplished through metallographic examination.

REFERENCES

1. Alcott, J., "An Investigation of Nondestructive Inspection Equipment: Detecting Hidden Corrosion on USAF Aircraft," *Materials Evaluation*, Vol.52, No. 1, Jan., 1994, pp. 64-73.
2. ASTM: G46-92, *Standard Practice for Examination and Evaluation of Pitting Corrosion*, Philadelphia, PA: ASTM, 1993.
- 3.. Kaelble, E. F., editor, *Handbook of X-Rays for Diffraction, Emission, Absorption and Microscopy*, pp. 1.1-1.31, McGraw-Hill Book Co., New York, 1997.
4. American Society for Nondestructive Testing, *Nondestructive Testing Handbook*, Bryant, L.E., technical editor, McIntire, P, editor, Second Edition, Vol. 3, pg. 846.

A Determination of V_2O_5 Activity in Corrosive Molten Vanadate-Sulfate Phases

Dr. Robert L. Jones* and
Dr. Richard F. Reidy
(ONR-NRL Postdoctoral Fellow)

Naval Research Laboratory
Chemistry Division, Code 6170
4555 Overlook Ave., S.W.
Washington, DC 20375-5342

ABSTRACT

Although aggressive hot corrosion by molten vanadate-sulfate deposits in boilers and engines burning low-quality fuel has been known for 75 years or more, there is surprisingly little data in the literature on the thermochemistry of vanadate-sulfate melts, especially as to the activity of the corrosive V_2O_5 component. We have recently devised a thermogravimetric (TGA)/ SO_3 equilibrium technique that could potentially be used to "chart" the V_2O_5 activity in vanadate-sulfate melts over a wide range of Na/V ratios, SO_3 partial pressures and temperatures. The method is illustrated in a study of the reaction of CeO_2 with a $NaVO_3$ - Na_2SO_4 - V_2O_5 - SO_3 melt system ($Na/V = 1$) at $800^\circ C$. Results from the study define the conditions under which CeO_2 will be chemically nonreactive with the melt, and also show the V_2O_5 activity coefficient to be, for the given experimental conditions, of the order of 1×10^{-2} .

INTRODUCTION

Hot corrosion by molten vanadate-sulfate deposits resulting from vanadium and sulfur fuel impurities has been a recognized problem in boilers and engines for many years. One may wonder, however, why study vanadate-sulfate hot corrosion when the U.S. military, along with the civilian sector, is presently being pushed to burn only clean fuels because of environmental concerns. The primary answer, of course, is that in war there can be no guarantee of always

having clean fuel for our ship, tank and truck engines. It is important therefore that, even though "clean fuel" use is planned, we have engine materials and coatings that can tolerate low quality fuel if the wartime need arises.

A knowledge of the chemistry of vanadate-sulfate hot corrosion also has "dual usage" since many hot corrosion reactions are related to the reactions that can be used to clean up fuel. The removal of SO_3 from smoke stack gases by CaO or MgO additives, for example, involves the same type of chemical reactions as molten sulfate-induced hot corrosion. Similarly, the reaction between yttria (Y_2O_3) and V_2O_5 to form highly stable YVO_4 , which causes degradation of Y_2O_3 -stabilized zirconia thermal barrier coatings in engines burning vanadium-contaminated fuel, has been recently "turned around" and used as the basis for a yttrium-based fuel additive for the prevention of hot corrosion by vanadium-containing fuels (1).

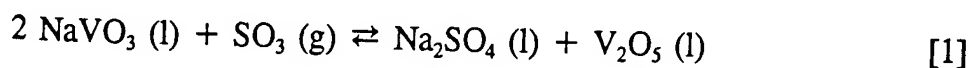
Attempts in the past to apply thermodynamics to predict and/or prevent hot corrosion have had limited success, perhaps partly because the difference in fuel impurity levels between "corrosive" and "noncorrosive" fuels is often small. Hot corrosion does not simply increase monotonically with fuel level, but frequently shows strongly accelerated attack for only small increases in fuel contaminants. For example, little hot corrosion is seen with aviation-quality ($< 0.05\% \text{ S}$) gas turbine fuel, whereas extensive hot corrosion has been encountered with marine-quality fuel ($< 1\% \text{ S}$), although the actual difference in sulfur content may be only 10-20X. In "low temperature" hot corrosion, even very small changes in the combustion gas SO_3 partial pressure can determine whether engine deposits of eutectic $\text{CoSO}_4\text{-Na}_2\text{SO}_4$ will be molten or not (2), which in turn can drastically effect the severity of hot corrosion (3,4). Vanadate hot corrosion has a similar short range of criticality, with vanadate-accelerated corrosion being generally negligible for V levels in fuel below 0.1 ppm, but often aggressive at V concentrations of only 1-10 ppm.

The importance of such small, but critical, changes in the fuel contaminant level is difficult to distinguish in the thermodynamic treatment of molten salt systems, since their energy effect is often hardly more than the probable error associated with much of our available thermodynamic data. For example, as shown below, a 10X change in the V_2O_5 concentration (or equivalently, the V_2O_5 activity coefficient) in a simulated vanadate-sulfate engine deposit typically corresponds to a difference of only about -10 kJ amidst calculations involving Gibbs energies of -1000 to -1500 kJ/mol, where each Gibbs energy may have a probable error of ± 2 kJ/mol or more. There is a strong need therefore for more accurate thermodynamic data, especially standard Gibbs energies of formation and activity

coefficients in melts, if thermodynamics are to be used with maximum effectiveness in predicting and/or preventing vanadate-sulfate hot corrosion.

The problem is compounded also by the uncertainty that still exists as to which "solution model" should be used for melts involving strong acid-base species such as Na_2O , K_2O , SO_3 , SiO_2 , V_2O_5 , etc. The solution model represents the framework by which the thermodynamicist seeks to describe how the activities of the various melt components change with concentration. In some cases, no solution model has been invoked, and the melts are simply assumed to be ideal (i.e., where the activity coefficient, γ , is unity, and the activity is equal to the mole fraction of the species). For example, Hwang and Rapp (5) assume that the Na-V-S-O systems at 900°C give ideal solution behavior, and that the activities of the component species can be equated to their molar concentrations. On the other hand, Bonnell and Hastie (6) believe that strong acid-base systems can be highly nonideal, with the activity of such species as Na_2O changing by many orders of magnitude over a narrow concentration range in some cases. Bonnell and Hastie have developed a solution model, the Ideal Mixing of Complex Components (IMCC) model, which they advocate as giving the best description of the solution behavior in strong acid-base melts. Numerous other possible solution models for melts have been proposed, however, as discussed, e.g., in the Proceedings of the Sixth International Conference on High Temperatures--Chemistry of Inorganic Materials (7).

In our own experience, we have found nonideal behavior for reaction [1],



which is, according to the thermodynamic calculations of Luthra and Spacil (8), the probable predominant reaction in blade deposits in gas turbine engines burning V- and S-containing fuels under normal marine operating conditions. Using a thermogravimetric analysis (TGA)/ SO_3 equilibrium technique (9), we equilibrated NaVO_3 at 700° and 800°C with fixed partial pressures of SO_3 ranging from 1×10^{-7} to 1×10^{-3} atm, and determined the equilibrium weight gain resulting from the uptake of SO_3 . From this data, we were able to calculate the mole fraction of V_2O_5 experimentally formed by reaction [1], which we then subsequently compared with the "ideal behavior" expected for reaction [1], as explained below.

The activity, a_i , of a given species is described by

$$a_i = \gamma_i \cdot X_i \quad [2]$$

where γ_i is the activity coefficient, and X_i is the mole fraction. If the species gives ideal solution behavior, then the activity coefficient is equal to 1, and the activity is simply the mole fraction of the species.

For reaction [1], we have

$$\Delta G_T^\circ = -RT \ln K \quad [3]$$

where R is 8.3144 joules/degree-mole and T is 1073° K (i.e., for 800° C conditions), while

$$K = (a_{V_2O_5})(a_{Na_2SO_4})/(a_{NaVO_3})^2(P_{SO_3}) \quad [4]$$

and ΔG_T° is determined by

$$\Delta G_T^\circ = \sum \Delta_f G_{T, \text{Products}}^\circ - \sum \Delta_f G_{T, \text{Reagents}}^\circ \quad [5]$$

If reaction [1] follows ideal solution behavior, then using the standard Gibbs energies of formation for $NaVO_3$ (l), SO_3 (g), Na_2SO_4 (l) and V_2O_5 (l) provided by Luthra and Spacil (8), we can reduce equation [3] to

$$K \cdot P_{SO_3} = (MF_{V_2O_5})(MF_{Na_2SO_4})/(MF_{NaVO_3})^2 \quad [6a]$$

or, as a quadratic equation,

$$91.61166 \cdot P_{SO_3} = x^2/(1-2x)^2 \quad [6b]$$

Solving equation [6b] by numerical approximation on the computer then yields the ideal mole fraction of V_2O_5 that should be formed at each given SO_3 partial pressure.

The experimental mole fraction of V_2O_5 was determined by converting the weight of SO_3 taken up in reaction [1] to reflect the millimoles of Na_2SO_4 and V_2O_5 formed, as well as the millimoles of $NaVO_3$ consumed, and calculating the resultant mole fraction of V_2O_5 . (Note that the amount of free SO_3 contained in the melt is so small that it can be ignored in this calculation.) The ideal vs. experimental mole fractions of V_2O_5 formed at the different SO_3 partial pressures are compared in Table 1, which also shows that division of the ideal V_2O_5 mole

TABLE 1

Experimental vs. Ideal Solution Mole Fractions of V_2O_5
Formed at 800° C at the SO_3 Partial Pressures Indicated

P_{SO_3} (atm)	Wgt. Gain (mg/50mg $NaVO_3$)	Ideal $M-F_{V_2O_5}$	Exptl. $M-F_{V_2O_5}$	"Activity Coeff.", γ
1×10^{-7}	2.0	0.003	0.06	0.05
1×10^{-6}	2.8	0.009	0.08	0.11
1×10^{-5}	4.0	0.028	0.12	0.23
1×10^{-4}	8.0	0.078	0.24	0.33
1×10^{-3}	11.0	0.18	0.34	0.53

fraction by the experimental V_2O_5 mole fraction yields an "activity coefficient" that indicates the nonideality of the V_2O_5 solution behavior. This "activity coefficient" is not quantitative, however, because the actual V_2O_5 activity in the melt is not (since $a_{V_2O_5} \neq a_{Na_2SO_4}$) the ideal V_2O_5 activity calculated here.

In the present paper, we describe a means, derived in a study of the reaction of CeO_2 with the $NaVO_3$ - SO_3 system at 800° C (10), by which it in fact appears possible to obtain quantitative values for the V_2O_5 activity coefficient in vanadate-sulfate melts.

EXPERIMENTAL

Our experiments were conducted using a Cahn 1000 thermobalance (Fig. 1) fitted with a system for controlling, and analyzing, the SO_2 concentration in the furnace input air stream. The SO_3 concentration was then established by equilibrating the SO_2 -air mixture over a Pt catalyst at

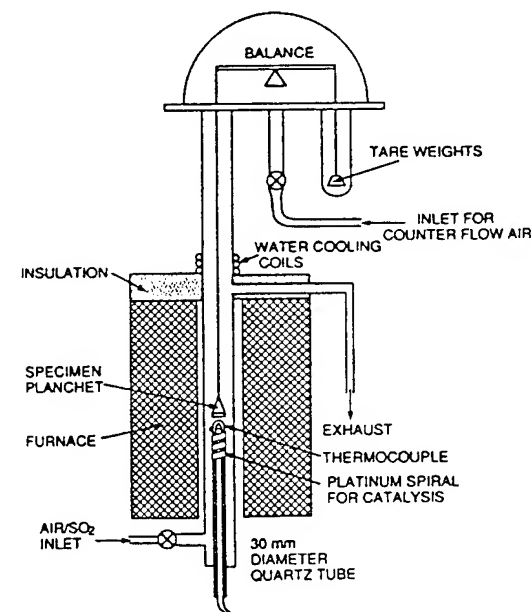


Fig. 1 Thermobalance/Furnace System

temperature in the furnace. Details of the experimental apparatus and procedure were published previously (9).

In the investigation, we first established a "baseline" curve of equilibrium weight gain vs. SO_3 partial pressure at 800°C for 50 mg (0.41 mmols) of pure NaVO_3 . We then ran duplicate experiments using just the same conditions except that 17 mg (0.1 mmols) of CeO_2 was now mixed with the 50 mg of NaVO_3 . The weight gain curve (Fig. 2) for $\text{CeO}_2\text{-NaVO}_3$ was just the same as for NaVO_3 alone (100% NaVO_3) up to the SO_3 partial pressure at which the V_2O_5 activity of the melt was increased sufficiently, by reaction [1], that reaction [7] could commence:



X-ray diffraction was used to confirm that only CeO_2 exists in the melts at SO_3 partial pressures below the critical P_{SO_3} for reaction [7], and that CeVO_4 is formed above this SO_3 partial pressure.

RESULTS AND DISCUSSION

Our experimental data are summarized in Fig. 2. The weight gain for $\text{CeO}_2\text{-NaVO}_3$ as a function of SO_3 partial pressure is the same as for NaVO_3 alone up to an SO_3 pressure of $2\text{-}3 \times 10^{-6}$ atm. The absence of any extra increment of weight gain at the lower SO_3 partial pressures shows that CeO_2 is chemically inert (just as the Pt weighing planchet is) to the $\text{NaVO}_3\text{-SO}_3$ system over this lower P_{SO_3} range.

However, an additional increment of weight gain begins to occur at $2\text{-}3 \times 10^{-6}$ atm of SO_3 , which marks the onset of reaction [7] where $\text{CeO}_2 \rightarrow \text{CeVO}_4$. The extra weight gain arises by the following mechanism. The Na_2O , V_2O_5 and SO_3 components of the melt are interrelated through two dissociation reactions,

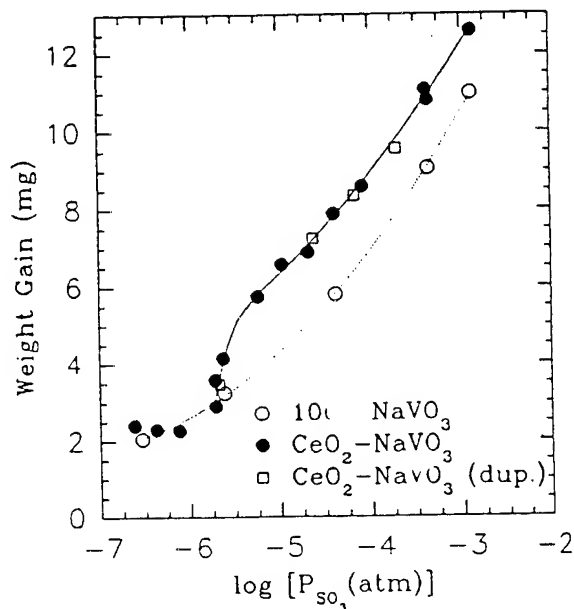
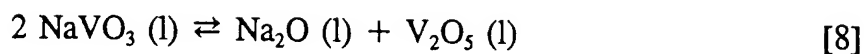
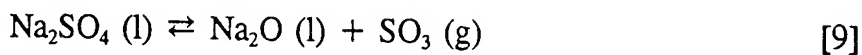


Fig. 2 Wgt. gain vs P_{SO_3} for NaVO_3 and $\text{CeO}_2\text{-NaVO}_3$ at 800°C .

one involving NaVO_3 ,



and the other, Na_2SO_4 ,



(Note that reversing reaction [9], and then adding reactions [8] and [9] to "cancel out" $\text{Na}_2\text{O} (\text{l})$ yields reaction [1].) When V_2O_5 begins to be consumed from the melt via reaction [7], this increases the Na_2O activity in the melt through reaction [8]. The increased Na_2O activity, in turn, allows more SO_3 to enter the melt to form additional Na_2SO_4 by reaction [9]. The combined reactions thus result in a "weight gain step" just at the P_{SO_3} at which reaction [7] commences.

The theoretical weight gain, by way of reactions [7]-[9], for the conversion of 0.1 mmols of CeO_2 totally to CeVO_4 is 3.2 mg. In an ideal, infinite system, one would thus expect a "vertical step" additional weight gain increment of 3.2 mg just at the critical P_{SO_3} at which reaction [7] becomes possible. In contrast, the maximum observed weight gain increment in Fig. 2 is only slightly more than 2 mg. However, subsequent work (10) since these initial experiments has confirmed that the experimental weight gain does in fact approach the theoretical value when higher dilutions (i.e., more NaVO_3 to CeO_2) are used. The failure to obtain full theoretical weight in Fig. 2 for $\text{CeO}_2 \rightarrow \text{CeVO}_4$ is therefore probably only the result of the experimental conditions.

In earlier work (11), we determined the solubility of CeO_2 in molten NaVO_3 at 800°C to be approximately 0.2 mole percent, and showed also that CeVO_4 crystals were precipitated at temperature from molten deposits produced by equilibrating NaVO_3 on ceria-stabilized zirconia at 700°C with SO_3 . In the latter case, the residual molten deposits were so depleted of vanadium (being strongly converted to sulfates) that no V could be detected by energy dispersive x-ray analysis. Only minimal solubility of the initial CeO_2 in 800°C NaVO_3 (less than 1/125 of the total CeO_2 present), or of the CeVO_4 product in the reaction melt, is expected therefore in the present experiments.

If ideal behavior is assumed, then the Gibbs energy for reaction [7], and an "ideal" Gibbs energy of formation for CeVO_4 , can be calculated as follows. As shown in Fig. 2, the amount of weight gain of the melt before reaction [7] begins is 3.0 ± 0.2 mg. This weight gain represents the uptake of 0.0375 mmols of SO_3 which, by reaction [1], corresponds to the formation of 0.0375 mmols

each of Na_2SO_4 and V_2O_5 , and the consumption of 0.075 mmols of the 0.41 mmols of NaVO_3 originally present. The resultant mole fraction of V_2O_5 is 0.091 which, for ideal behavior, equates to a V_2O_5 activity in the melt of 0.091. This is the V_2O_5 activity at which reaction [7] just begins, and for reaction [7] we therefore have the thermodynamic relationship,

$$\Delta G^\circ_{1073\text{K}} = -RT \ln \frac{(a_{\text{CeVO}_4})^2 (P_{\text{O}_2})^{0.5}}{(a_{\text{CeO}_2})^2 (a_{\text{V}_2\text{O}_5})} \quad [10]$$

where, as pure solids, CeVO_4 and CeO_2 have activities of 1, and the activities of O_2 in the air and V_2O_5 are 0.21 and 0.091, respectively. This yields a calculated $\Delta G^\circ_{1073\text{K}}$ for reaction [7] of -14.422 kJ, where the experimental uncertainty is ± 0.4 kJ assuming the melt weight gain to be 3.0 ± 0.2 mg, the weight of the initial NaVO_3 to be 50.0 ± 0.5 mg, and the temperature to be $1073 \pm 5^\circ \text{K}$. Taking the Gibbs energies of formation for CeO_2 (s) and V_2O_5 (l) at 800°C as -865.890 kJ/mol and -1098.211 kJ/mol (12), we can then derive, as indicated by equation [5], an "ideal" standard Gibbs energy of formation of CeVO_4 (s) at 800°C of -1422.207 kJ/mol.

There are no experimental $\Delta_f G^\circ$'s for CeVO_4 in the literature to compare with this "ideal" value, but Yokokawa *et al* (12) have estimated the Gibbs energy of formation of CeVO_4 (s) at 800°C as -1444.785 kJ/mol. This gives agreement to within about 20 kJ/mol. However, we know from our earlier study (9) that the NaVO_3 - V_2O_5 - Na_2SO_4 melt system is clearly nonideal, with the V_2O_5 activity coefficients being of the order of 0.1 to 0.01 at the lower V_2O_5 concentrations (Table 1). If V_2O_5 activity coefficients of 0.1, 0.01, etc. are introduced into equation [10], the resultant $\Delta_f G^\circ_{\text{CeVO}_4}$ becomes about 10 kJ/mol more negative for each 10X reduction in the activity coefficient, and equals -1442.749 kJ/mol for a V_2O_5 activity coefficient of 0.01. This last value agrees very well with the $\Delta_f G^\circ_{\text{CeVO}_4}$ of -1444.785 kJ/mol estimated by Yokokawa *et al*, and we take the agreement therefore as indicating that a $\Delta_f G^\circ$ for CeVO_4 at 800°C of about -1445 kJ/mol, and a V_2O_5 (l) activity coefficient in the melt of about 0.01, are both essentially correct.

Our TGA/ SO_3 equilibrium technique can be expanded to include different temperatures, vanadate-sulfate melt compositions (i.e., by using different Na/V ratios in the initial vanadate deposit), and "indicator" reaction pairs (i.e., $\text{CeO}_2 \rightarrow \text{CeVO}_4$). We have shown earlier (9), for example, that $\text{Sc}_2\text{O}_3 \rightarrow \text{ScVO}_4$ at $\sim 5 \times 10^{-6}$ atm of SO_3 , and $\text{In}_2\text{O}_3 \rightarrow \text{InVO}_4$ at $\sim 5 \times 10^{-4}$ atm of SO_3 , in the NaVO_3 - SO_3 system by reactions analogous to $\text{CeO}_2 \rightarrow \text{CeVO}_4$. The TGA/ SO_3 equilibrium

technique therefore has the potential to provide, by a series of studies of the various oxide \rightarrow vanadate reactions over an array of different sulfate-vanadate melt compositions and temperatures, the high accuracy thermodynamic data (including Gibbs energies of formation, activity coefficients, solution models, etc.) that are needed to understand and predict the reaction behavior of high temperature oxides with vanadate-sulfate melts.

CONCLUSIONS

A thermogravimetric analysis (TGA)/SO₃ equilibrium study of the reaction of CeO₂ with the NaVO₃-SO₃ system at 800° C shows CeO₂ to be inert to chemical reaction with the NaVO₃-SO₃ melt at SO₃ partial pressures up to $2-3 \times 10^{-6}$ atm, with CeVO₄ being formed above this SO₃ partial pressure.

Thermodynamic analysis of the reaction data indicates the $\Delta_f G^\circ$ for CeVO₄ (s) at 800° C as being -1445 kJ/mol, and the V₂O₅ activity coefficient of the melt at the point of CeVO₄ formation as being approximately 1×10^{-2} .

The TGA/SO₃ equilibrium technique has the potential to significantly increase our knowledge of the thermochemistry and melt solution chemistry involved in the reactions of high temperature oxides with molten vanadate-sulfate melts.

ACKNOWLEDGMENTS

This research was sponsored by the Office of Naval Research with Dr. A. J. Sedriks as Scientific Officer. The support is gratefully acknowledged.

REFERENCES

1. N. Bornstein, H. Roth and R. Pike, "Vanadium Corrosion Studies", Report R93-918120-2, Jun 30, 1993, Contract N00014-89-C-0053, United Technologies Research Center, E. Hartford, CT.
2. D.A. Shores and K.L. Luthra, J. Electrochem. Soc. **127**, 2202 (1980).
3. D.J. Wortman, R.E. Fryxell, K.L. Luthra and P.A. Bergman, "Mechanism of Low Temperature Hot Corrosion: Burner Rig Studies," in Proc. 4th Conf. on Gas Turbine Materials in a Marine Environment, pp. 317-337, Annapolis, MD (1979).

4. R.L. Jones, "Cobalt Oxide-SO₂/SO₃ Reactions in Cobalt-Sodium Mixed Sulfate Formation and Low Temperature Hot Corrosion," in High Temperature Corrosion, NACE-6, pp. 513-518, ed. R. A. Rapp, NACE, Houston (1983).
5. Y.-S. Hwang and R.A. Rapp, Corrosion **45**, 933 (1989).
6. D.W. Bonnell and J.W. Hastie, "A Predictive Thermodynamic Model for Complex High Temperature Solutions Phases XI," in Materials Chemistry at High Temperatures, Vol. 1, Characterization, ed. J.W. Hastie, pgs 313-334, Humana Press, Clifton, NJ (1990).
7. Proceedings of the Sixth International Conference on High Temperatures--Chemistry of Inorganic Materials, NIST, Gaithersburg, MD (1989), originally published in High Temperature Science Vols. **26-28** (1990).
8. K.L. Luthra and H.S. Spacil, J. Electrochem. Soc. **129**, 649 (1982).
9. R.L. Jones, J. Electrochem. Soc. **139**, 2794 (1992).
10. R.L. Jones and R.F. Reidy, "Thermogravimetric Analysis of the Reaction of CeO₂ with the NaVO₃-SO₃ System," submitted to J. Electrochem. Soc.
11. R.L. Jones and C.E. Williams, Surface and Coatings Technol. **32**, 349 (1987).
12. H. Yokokawa, N. Sakai, T. Kawada and M. Dokiya, J. Am. Ceram. Soc. **73**, 649 (1990).

SESSION V
ENVIRONMENTAL CRACKING

Chairman: *K. Jata*

BLANK

Yield Strength and Solution Composition Effects on Aqueous Environmental Cracking of Ti-8V-6Cr-4Zr-4Mo-3Al (Beta C)

Brian P. Somerday, Jennifer A. Grandle,
and Richard P. Gangloff

Department of Materials Science and Engineering
University of Virginia
Charlottesville, VA 22903-2442

ABSTRACT

A high-strength, α -precipitation hardened β titanium alloy (Ti-8V-6Cr-4Zr-4Mo-3Al, STA Beta C) is prone to intergranular environmentally assisted cracking (EAC) in neutral aqueous NaCl given an occluded crack, active crack tip strain rate and electrode potential near free corrosion. The threshold stress intensity for EAC is reduced to about one-third of the plane strain fracture toughness and subcritical crack growth rates are 30 to 100 $\mu\text{m}/\text{sec}$. STA Beta C is immune to EAC with static loading or sufficiently cathodic polarization. Lower strength solution treated Beta C resists EAC in both pure NaCl and acidic sulfur-species-bearing chloride solutions, where fracture is by transgranular microvoid formation. These results are consistent with findings for STA Beta 21S and are qualitatively understood based on hydrogen environment embrittlement. EAC propagation in STA Beta C exhibits slow-rapid oscillation under rising crack mouth opening displacement but not during constant rate loading. This result implies that stress intensity factor and crack tip strain rate interactively govern da/dt .

INTRODUCTION

High-performance applications of β titanium alloys in aggressive stress-chemical environments (e.g., geothermal brine and deep sour gas well tubulars, offshore production elements, marine fasteners, biomedical devices, and aerospace components⁽¹⁾) require definition of the windows of variables that promote the aqueous environment-assisted cracking (EAC)

susceptibility of these alloys. While such investigations are extensive for α and α/β titanium alloys,^[2-5] insufficient data exist to predict EAC for body-centered cubic β -based alloys. For titanium alloys, the challenge is complicated because EAC susceptibility is a function of test method; particularly, smooth versus cracked specimens.^[3]

The objective of this research is to characterize the ambient temperature, aqueous chloride EAC behavior of a modern β titanium alloy, Ti-3Al-8V-6Cr-4Zr-4Mo (Beta C), as a function of microstructure and/or yield strength, electrode potential, and solution composition for a single active loading rate. Precracked specimens and a fracture mechanics approach are employed. EAC susceptibility is characterized by the threshold for the onset of crack growth (K_{TH}), subcritical crack growth rate (da/dt), and the fracture mode in the aqueous environment versus the behavior in air. In addition to determining windows of variables for EAC susceptibility, these data are necessary input for damage-tolerant life prediction and fundamental studies of the crack tip damage mechanisms that govern EAC.

LITERATURE BACKGROUND

EAC of titanium alloys in aqueous halogen-bearing electrolytes is affected by several critical variables; including loading rate (crack tip strain rate), electrode potential, alloy composition, microstructure, and yield strength.

Titanium alloys, including α/β Ti-6Al-6V-2Sn, exhibit a minimum in K_{TH} for intermediate loading rates.^[6] Similar results were reported for the solution treated (ST) β alloy Ti-13V-11Cr-3Al (VCA 120),^[3] solution treated + aged (STA) β/α Ti-11.5Mo-6Zr-4.5Sn (Beta III),^[7] and modern STA β/α Ti-15Mo-3Nb-3Al (Beta 21S).^[8] STA β/α Beta 21S and a specific age-condition of β/α Beta III were immune to EAC under static load but susceptible under constant displacement rate deformation.^[7,8] This complex loading rate dependence of EAC is unique to titanium alloys; however, some titanium alloys, including an alternate age-condition of β/α Beta III, are susceptible to EAC under static load.^[7,9]

The threshold for EAC of titanium alloys in halogenated electrolytes is generally a minimum at electrode potentials near -500 mV_{SCE} . This behavior was reported for α/β Ti-8Al-1Mo-1V and for the β or β/α alloys Ti-8Mn, Beta III (STA) VCA 120 (ST), and Beta 21S (STA).^[2-5,8] Immunity to EAC was achieved at cathodic potentials greater than -1000 mV_{SCE} .

The chloride EAC susceptibility of titanium alloys depends on alloy composition, microstructure, and/or yield strength (σ_{YS}). ST β VCA 120 exhibits EAC under static loading,^[10] while the ST β alloys Beta III and Ti-

8Mo-8V-3Al-2Fe are immune. These latter two alloys become EAC-susceptible upon aging to precipitate the α phase.^[3] STA β/α Beta III is susceptible to EAC under static loading for the aging condition 480°C/100 hr ($\sigma_{ys} = 1000$ MPa), but not for 620°C/16 hr ($\sigma_{ys} = 800$ MPa).^[7] EAC was produced in STA β/α Beta 21S under rising displacement but not in STA β/α Ti-15V-3Cr-3Al-3Sn (Ti-15-3) for similar σ_{ys} (1300 MPa).^[8] The dependence of the EAC threshold on σ_{ys} for β and β/α titanium alloys is not clear; however, limited data suggest a trend similar to that for high-strength steels.^[3,5,11,12]

Sulfide additions to chloride solutions exacerbate EAC of ferritic and martensitic steels, particularly for lower strength levels.^[11] Sulfide-EAC of β and β/α titanium alloys has not been investigated broadly.^[13]

Considering Beta C, several studies show that this alloy is immune to chloride EAC, for the ST and STA conditions.^[13-18] While smooth, notched and precracked specimens were employed, it is possible that these experiments did not sufficiently probe the intersections of the variables that cause EAC in titanium alloys.

EXPERIMENTAL PROCEDURES

Material

Beta C, of composition Ti-3.4Al-8.3V-5.9Cr-4.4Zr-4.1Mo (wt.%; with trace amounts of Nb, Fe, C, N and O as reported by the manufacturer, RMI Titanium Company) was studied. This material was provided as hot-rolled 4.1-cm diameter round bar that was solution treated above the β transus at 815°C for 1 hour followed by air cooling. EAC specimens were tested in the ST and STA conditions. The aging treatment consisted of heating ST blanks at 500°C for 24 hours followed by air cooling. This treatment precipitated α as 1 to 5 μm long platelets within 120 μm grains and infrequently in a colony structure at β grain boundaries. Transmission electron microscopy was not conducted; particularly, the occurrence of a submicron α film on β grain boundaries was not determined. Rockwell C hardnesses were R_c 28 and R_c 41 for the ST and STA conditions, respectively, which correspond to yield strengths of 830 and 1280 MPa from a hardness- σ_{ys} correlation given for two β titanium alloys.^[8]

Environment

Experiments were conducted at 25°C in either moist air or neutral (pH 6) 0.6M (3.5 wt.%) aqueous NaCl at free corrosion or fixed electrode potentials of -150, -600, and -1000 mV_{SCE}. Experiments were also conducted in the acidified sulfur-species-bearing solutions indicated in Table I. A plexiglass cell was secured to the specimen in order to flow solution

at 25 ml/min from a two-liter reservoir through the machined notch tip and fatigue precrack. A schematic of the cell is shown in Fig. 1. Dissimilar metals did not contact the specimen and all tubing was PTFE. The grounded specimen (working electrode) was maintained at a constant potential by a Wenking potentiostat in conjunction with a chloridized silver wire reference electrode and a platinized niobium counter electrode. The reference electrode for polarization was located on one side of the specimen, near the notch (Fig. 1). A second reference electrode indicated that the potential of the opposite face was 0 to 200 mV more noble than the polarized side, depending on the magnitude of the current.

Table I. Sulfur-Species Additions to the Aqueous NaCl Environment

Solution	Salt	Acid / pH	Sulfur Compound	Sulfur Species
Sulfide + acetic	0.6 M NaCl	1.5M acetic, 0.1M acetate / pH 3.3	10 ppm S as Na ₂ S	CH ₃ COSH (?)
Sulfide + hydrochloric	0.6 M NaCl	0.1 M HCl pH 1.3	4 ppm S as Na ₂ S	H ₂ S
Thiosulfate + acetic	0.9 M NaCl	0.15 M acetic pH 2.6	60 ppm S as Na ₂ S ₂ O ₃	S ₂ O ₃ ²⁻ → S → H ₂ S(?)

EAC-Fracture Mechanics

Sidegrooved compact tension (CT) specimens were machined with the longitudinal axis of the round bar perpendicular to the crack plane and crack growth in the radial direction. CT specimen gross thickness was 6.3 mm, net thickness was 5.1 mm, and width was 30.5 mm. Specimens were fatigue precracked in room temperature moist air, terminating with a K_{MAX} of 25 MPa√m, R of 0.4 ($R = K_{MIN}/K_{MAX}$), and a crack length-to-width ratio (a/W) of approximately 0.52.

Precracked specimens were loaded under monotonically rising crack mouth opening displacement (CMOD) at a constant rate ($\dot{\delta}_m$) of 1.8 μm/min using a servohydraulic mechanical test system. CT specimens were instrumented to measure applied load, CMOD and crack extension. CMOD was measured and controlled using a clip gauge mounted across the mouth of the machined notch, as shown in Fig. 1. The direct current potential difference (DCPD) method was used to resolve crack tip process zone damage initiation and subsequent crack growth. The expression used to calculate a/W from measured voltage, and other details of the technique,

are given in References 8, 19 and 22. Applied load, DCPD, CMOD and time were recorded using a PC-based data acquisition system.

The fracture mechanics were characterized using the elastic-plastic J-integral, as detailed elsewhere.^[19]

For STA specimens J_{plastic} was small compared to the applied total J; thus small-scale yielding was maintained and elastic K analysis was sufficient. All experiments satisfied the criterion for plane strain defined in an ASTM Standard.^[20]

The plot of load and DCPD versus CMOD in Fig. 2 is typical of the experiments with high-strength STA specimens in NaCl. Two measures of the threshold K for the initiation of crack growth were determined. A lower-bound value is defined by the first deviation from the initial baseline DCPD versus CMOD trend when coincident with the onset of nonlinearity in the load versus CMOD plot.^[8,19] For loading in moist air, this value (K_{IC}) is a lower bound of the standardized plane strain fracture initiation toughness (K_{IC}),^[19] and in aggressive environments this value (K_{THI}) represents a lower bound of the threshold (K_{TH}) for subcritical crack growth initiation.^[21] K_{TH} is

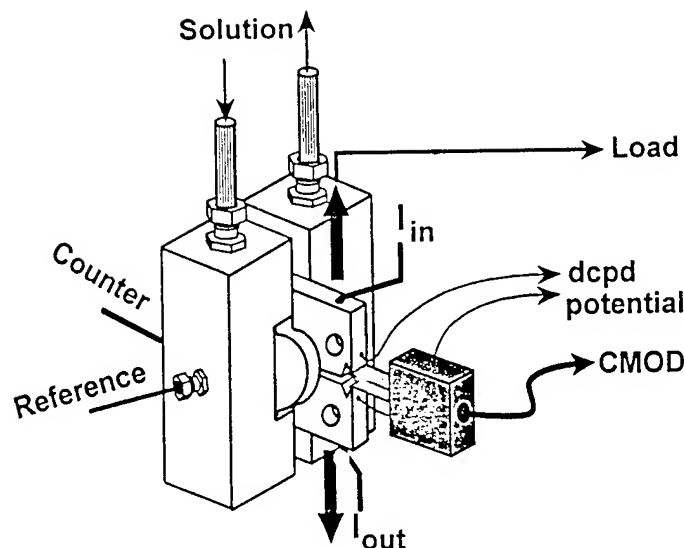


Figure 1. Cell and CT specimen for rising CMOD EAC experiments. ("dcpd" indicates the measurement probes for electrical potential difference due to a direct current, I , through the uncracked portion of the specimen.)

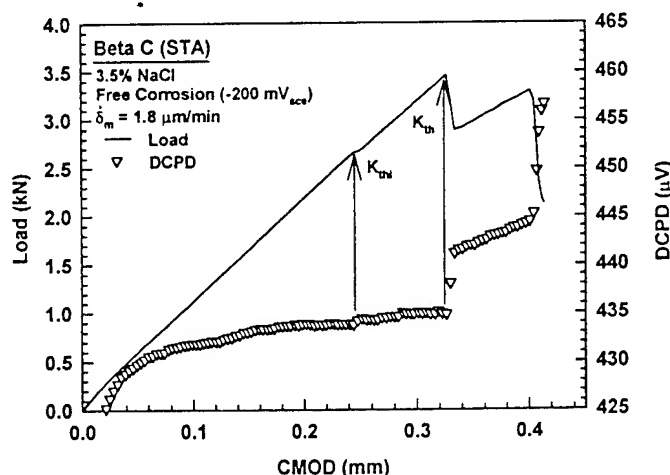


Figure 2. Load and DCPD versus CMOD data for STA Beta C in 3.5% NaCl. (Note the definition of threshold stress intensity (K_{TH}) and initiation threshold stress intensity (K_{THI}).)

defined at the first major load drop. At K_{TH} , the crack growth increment (Δa) is assumed to equal zero; subsequent crack lengths are calculated using DCPD values normalized with the potential at the known fatigue precrack length.^[19,22] Average subcritical crack growth rate (da/dt) was calculated using linear regression over a small time interval.

A single critical J for the initiation of crack growth was calculated for each ST experiment since DCPD versus CMOD data did not indicate crack initiation. The initiation point was determined from DCPD measurements with the measured final crack length as a reference, then selecting the P-CMOD data point corresponding to the measured fatigue precrack length.

RESULTS

ST Beta C in Air and Chloride

Static Crack / Threshold Behavior Results for ST Beta C tested in moist air and four different aqueous environments, each at the free corrosion potential, are shown in Fig. 3. These experiments establish that Beta C in the moderate strength, single phase condition is not embrittled by severe mechanical and environmental conditions. The CMOD rate used for these experiments produced maximum EAC susceptibility (minimum K_{TH}) for STA β/α Beta 21S in aqueous NaCl near free corrosion.^[8] The moist air fracture toughness (K_{IC}) of ST Beta C is 115 MPa \sqrt{m} , which compares favorably with a reported value of 96 MPa \sqrt{m} .^[23] The higher value may reflect the use of elastic-plastic fracture mechanics for small specimens of a moderate strength-high toughness alloy, compared to the less rigorous elastic analysis employed in Ref. 23. K_{TH} (114 MPa \sqrt{m}) in neutral NaCl ($E_{corr} = -200$ to -150 mV_{SCE}) was not reduced compared to K_{IC} .

The addition of sulfur species to NaCl solutions, particularly those that form hydrogen sulfide (H_2S), exacerbates EAC in steel.^[24-27] In contrast Fig. 3 shows that K_{TH} (113 to 120 MPa \sqrt{m}) for ST Beta C in three different sulfur-species-containing aqueous media ($E_{corr} \sim -250$ mV_{SCE}) is not reduced compared to either K_{IC}

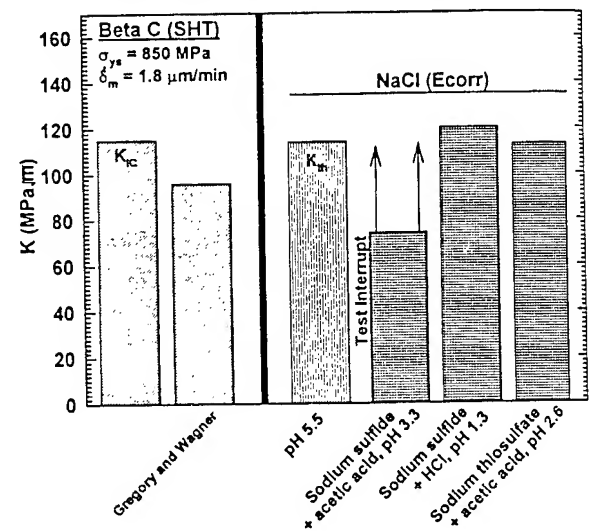


Figure 3. K_{IC} and K_{TH} data for ST Beta C. K_{IC} is for moist air, compared to the value from Ref. 23, while K_{TH} data are for the NaCl/sulfur-species solutions listed in Table I.

or K_{TH} for pure NaCl. In the Na_2S /acetic acid solution, Na_2S reacts to form thioacetic acid;^[24] H_2S gas was not detected by smell. (Crack growth was not detected at the point where this experiment was terminated due to cell leakage. K_{TH} therefore exceeded the K value calculated at the test-interrupt load.) H_2S formed in the Na_2S/HCl acid solution.^[25] The sodium thiosulfate/acetic acid solution forms elemental sulfur and H_2S in the presence of steel.^[26]

Figure 4 shows typical scanning electron microscope (SEM) fractographs of the K_{IC} or K_{TH} regions of CT specimens of ST Beta C, fractured in moist air or acidified NaCl/ Na_2S . The fracture mode is identical for moist air and all aqueous environments in Table I, and consists predominately of fine (of order $2\ \mu m$) transgranular microvoids.

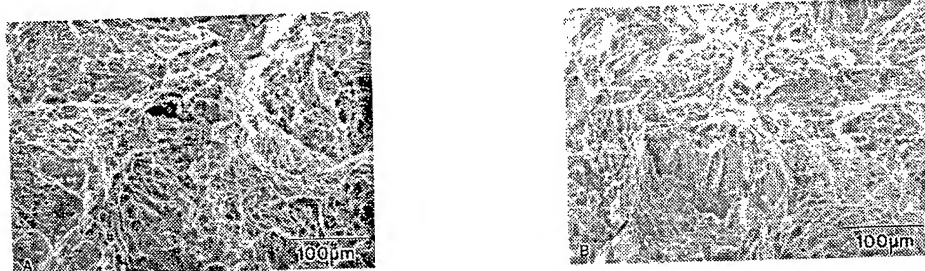


Figure 4. SEM fractographs for ST Beta C in (a) moist air and (b) acidic NaCl/ Na_2S . The crack grew from top to bottom, and the fractographs are located in the central crack initiation region.

Equal K_{IC} and K_{TH} , as well as identical fracture modes in moist air and the solutions, indicates that ST Beta C is immune to EAC, at least for the loading rate and electrode potential conditions that were examined.

STA Beta C in Air and Chloride

Static Crack/Threshold Behavior Results for high-strength STA Beta C, tested in moist air and neutral aqueous NaCl at $-600\ mV_{SCE}$ and fixed δ_M , are shown in Fig. 5. Filled circles represent the results of individual experiments, while averages are given by the bars. K_{IC} is 50% lower ($56\ MPa\sqrt{m}$) than for the ST condition, consistent with the substantially higher strength from aging. K_{TH} for chloride ($35\ MPa\sqrt{m}$) is reduced by about one-third compared to K_{IC} . Data for STA Beta 21S and STA Ti-15-3,^[8] obtained with single-edge-cracked specimens fractured in air and neutral aqueous NaCl at $-600\ mV_{SCE}$ by the same procedure as Beta C, are included in Fig. 5. The plane strain fracture toughness of STA Beta C is lower than that of the other two high-strength alloys. Similar to the behavior of Beta C, K_{TH} for

Beta 21S is reduced compared to K_{IC} . In contrast K_{TH} equals K_{IC} for Ti-15-3.

Figure 6 shows SEM fractographs from CT specimens of STA Beta C tested in moist air and aqueous NaCl. Fracture in air occurs predominately via transgranular microvoid coalescence. Both small (of order 2 to 5 μm) equiaxed and larger elongated microvoids are observed. Some facets are also present and may consist of fine (of order 1 μm) microvoids.

Fracture occurs by intergranular separation in the chloride environment. No transition region is evident between the fatigue crack front and EAC intergranular facets. Fine void-like features are present on grain facets. The moist air fracture modes for STA Beta 21S and STA Ti-15-3^[8,28] resemble that for Beta C in air. The air fracture mode was not altered for Ti-15-3 tested in aqueous NaCl, whereas Beta 21S failed by intergranular separation.^[8]

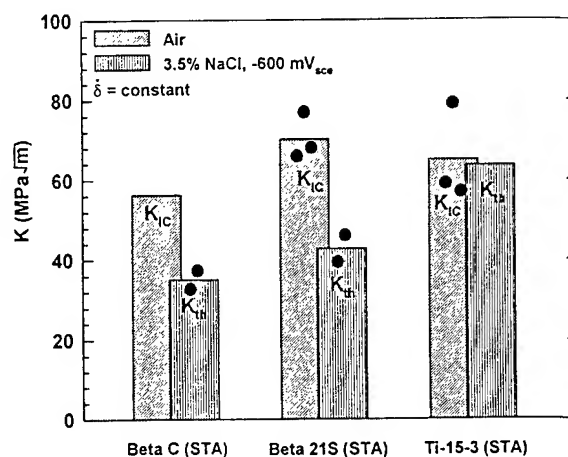


Figure 5. Rising CMOD K_{IC} and K_{TH} data for Beta C, Beta 21S^[8], and Ti-15-3^[8] (all STA) in air and aqueous NaCl. The bars are average values and filled circles represent individual results.

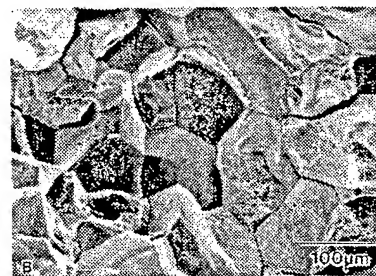
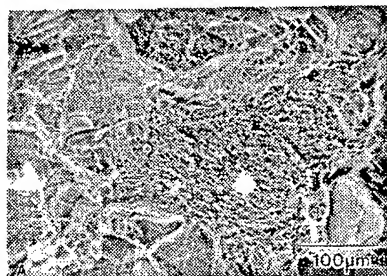


Figure 6. SEM fractographs for STA Beta C in (a) moist air and (b) 3.5% NaCl. The crack grew from top to bottom.

K_{TH} less than K_{IC} , as well as the change in fracture mode from transgranular microvoid rupture to grain boundary separation, indicates that STA Beta C is susceptible to EAC in neutral aqueous NaCl at electrode potentials near -600 mV_{sce} and under rising CMOD.

Figure 7 shows the effect of maintaining a CT specimen of Beta C at constant CMOD in aqueous NaCl after interrupting the rising CMOD at a

K level (47 MPa \sqrt{m}) greater than K_{TH} . (For this experiment, the rising CMOD was interrupted during decreasing load and rapid subcritical crack propagation.) Crack propagation continued for less than one minute after CMOD was fixed. At this point, DCPD data indicate no crack growth, or at most a limiting da/dt of 0.001 $\mu m/s$ over 90 hours. Crack growth-induced compliance changes were not detected (dP/dt was essentially zero over this time period), suggesting that da/dt was zero.

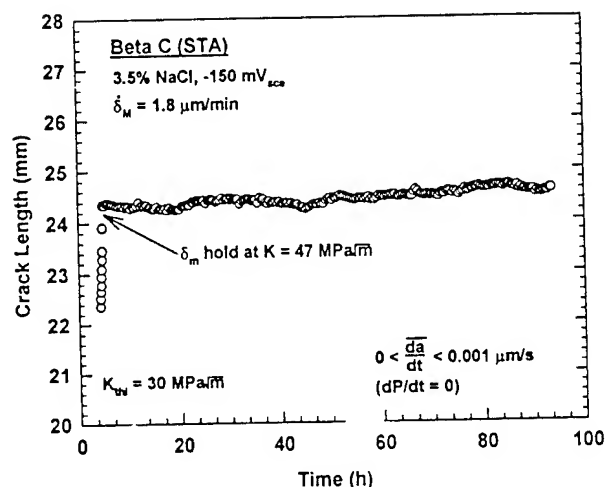


Figure 7. Crack length versus time for an experiment with STA Beta C in NaCl which was interrupted and maintained at constant CMOD (δ_M) for a K level above K_{TH} .

Potentiostatic Polarization The severity of EAC for STA Beta C in pure NaCl depends on applied electrode potential, as shown in Fig. 8. Both K_{THI} and K_{TH} are compared to K_{TH} data for Beta 21S.^[8,28] EAC is observed (K_{THI} and K_{TH} are less than K_{ICi} , coupled with intergranular cracking) for applied potentials between -150 and -600 mV_{SCE}, and threshold is a minimum for a potential of -600 mV_{SCE}. At a potential of -1000 mV_{SCE}, STA Beta C is immune to EAC (K_{THI} equals K_{ICi} and fracture is by microvoid rupture for chloride and moist air). The effect of potential is similar for STA Beta 21S.

Subcritical Crack Propagation Two distinct subcritical crack propagation rate responses were observed for STA Beta C in NaCl. Figure 9 shows results for an experiment at -150 mV_{SCE}. Subcritical crack propagation was slow (on the order of 0.1 $\mu m/s$) for rising K levels just above K_{THI} (30 MPa \sqrt{m}). At K equal to K_{TH} (41 MPa \sqrt{m}), the da/dt accelerated by two orders of magnitude under decreasing K from 41 to 35 MPa \sqrt{m} (applied K values are indicated at several points in Fig. 9). After a crack growth increment of 2 mm, da/dt decreased abruptly to near the initial rate. This slow-fast sequence was repeated several times as the

chloride crack propagated subcritically in several EAC experiments.¹

In contrast to the behavior in Fig. 9, alternating slow-fast da/dt was not observed for EAC experiments with STA Beta C/NaCl under rising load control. Figure 10 shows that rapid crack propagation is not arrested and continues until specimen fracture. The fast crack growth rates indicated in Figs. 9 and 10 are consistent with limited values reported for other β -titanium alloys.^[3,5,7,28] It is difficult to quantify the slower EAC rates in Fig. 10, at K just above K_{TH} . This behavior appears akin to the so-called Stage IIA behavior reported for α/β titanium alloys in aqueous chloride.^[29]

DISCUSSION

Comparison to Literature Results for EAC of Beta C

Literature results indicate that Beta C is immune to aqueous chloride EAC.^[13-18] Aylor studied ST Beta C ($\sigma_{YS} = 850$ MPa) with blunt-notched tensile specimens under rising displacement in aqueous NaCl at free corrosion and applied electrode potentials between

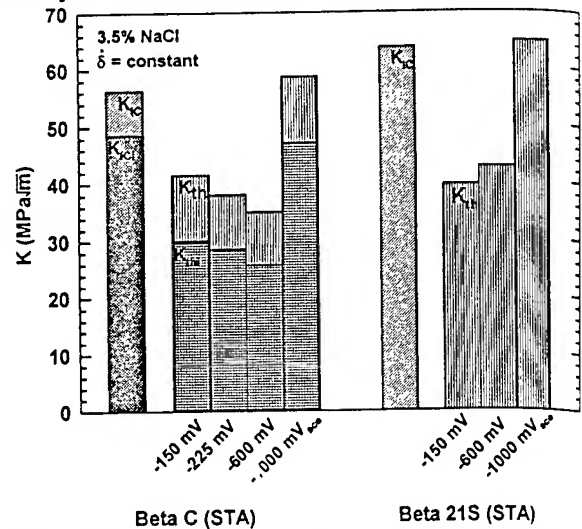


Figure 8. K_{TH} and K_{TII} as a function of applied electrode potential for STA Beta C and STA Beta 21S^[8] in aqueous chloride solution. Moist air K_{IC} is also shown.

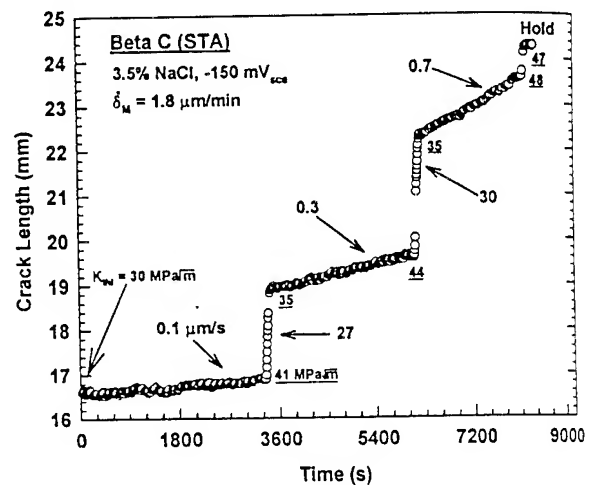


Figure 9. Crack length versus time for STA Beta C in 3.5% NaCl at -150 mV_{SCE} and constant d_a/d_t . Average crack growth rates at various K levels (underlined) are shown.

¹The point marked "Hold" in Fig. 9 shows the onset of the fixed CMOD experiment shown in Fig. 7, which did not produce EAC propagation in Beta C/NaCl. Here, CMOD was fixed during a rapid da/dt event under decreasing K . A similar result (viz., no subcritical EAC propagation for 50 hours at constant CMOD and applied K greater than K_{IC}) was observed for an experiment interrupted during slow da/dt and rising K .

-850 and -1250 mV_{SCE}.^[14] These conditions did not produce EAC in Beta C. This procedure indicated that α/β Ti-6Al-4V (Ti-6-4) at this same yield strength is chloride-cracking resistant,^[14] but such is not the case.^[9,30] Azkarate and Pelayo tested smooth tensile specimens of STA Beta C ($\sigma_{YS} = 1250$ MPa) under rising displacement in neutral NaCl at free corrosion, -1000 and -1500 mV_{SCE}.^[16] STA Beta C was immune to EAC for the conditions examined, but Ti-6-4 ($\sigma_{YS} = 1000$ MPa) exhibited EAC at -1500 mV_{SCE}. Wolfe *et al.* reported that smooth tensile specimens of STA Beta C ($\sigma_{YS} = 1100$ MPa) were immune to EAC in seawater with cathodic protection.^[15] Comparison of these results to the data in Figs. 5 and 6 attests to the importance of an occluded crack to promote EAC.

Limited studies with statically loaded precracked specimens showed that STA Beta C is immune to EAC. Thomas and Seagle did not produce brittle cracking in precracked C-rings in NaCl at several electrode potentials.^[13] (EAC was produced by this method when H₂S was added to the environment and specimens were polarized cathodically.) Early studies with statically loaded precracked cantilever beam specimens of Beta C in aqueous chloride demonstrated similar immunity to EAC, however, low plane strain fracture toughness clouded the results.^[17,18] Comparison of these findings to the data in Figs. 5, 6 and 7 attests to the importance of active loading to promote EAC of Beta C.

The experimental results for intergranular EAC of STA Beta C, showing the deleterious effects of the fatigue crack plus active loading and electrode potentials near free corrosion levels, are identical to data obtained for STA Beta 21S.^[8,28]

Comparison of EAC in β Titanium Alloys and Ferritic Steels

Figure 11 summarizes K_{TH} and K_{IC} versus σ_{YS} results for Beta C in chloride solutions, compared to data for STA Beta 21S and STA Ti-15-3,^[8] and superimposed with EAC K_{TH} for ferritic and martensitic steels in a variety

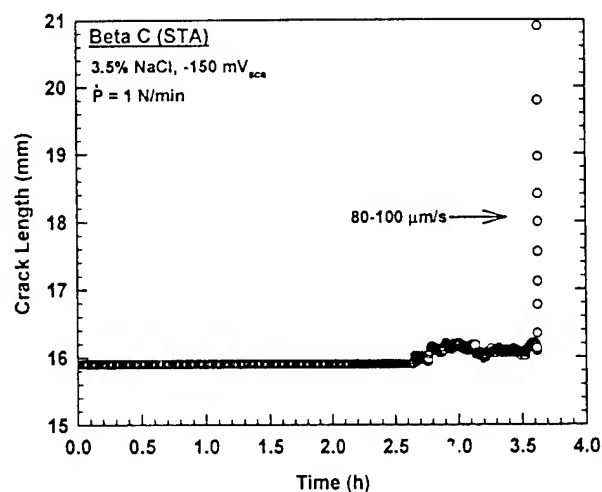


Figure 10. Crack length versus time for a constant loading rate of 1 N/min. (STA Beta C in 3.5% NaCl at -150 mV_{SCE}, $K_{TH} = 44$ MPa \sqrt{m} , $da/dt = 80$ to 100 $\mu\text{m/s}$.)

of hydrogen-producing gases and electrolytes.^{[11]2} The large shaded band shows the range of K_{TH} results, with upper (UB) and lower (LB) bounds on extensive threshold data for many steels in neutral chloride at free corrosion. (The open diamond shows a single K_{TH} result for moderate strength HY130 steel in NaCl, obtained with a single-edge-crack specimen and the fracture mechanics method used in the current study.)

For steels, it is well established that K_{TH} for hydrogen environment embrittlement decreases with increasing σ_{YS} .^[11,31] For the β -titanium alloys, plane strain fracture toughness decreases with increasing σ_{YS} (small filled circles), with a single trend observed for Beta C and Ti-15-3 and a higher strength-toughness trend seen for Beta 21S. K_{TH} values for STA Ti-15-3 (large open circles) and ST Beta C (large filled circles at σ_{YS} of 850 MPa) in NaCl essentially equal the K_{IC} - σ_{YS} trend line, indicating immunity to EAC. The results for ST Beta C (large filled circles) and STA Beta C (open squares) suggest a strength effect on K_{TH} that is similar to the trend for steels in neutral chloride. Alloy microstructure may play a critical role in determining the EAC resistance of β -titanium alloys. The relative contributions of microstructure and yield strength in governing the EAC resistance of ST Beta C and the susceptibility of STA Beta C are not defined.

Intergranular EAC and Microstructure of β -Titanium Alloys

An analysis of STA Beta 21S and Ti-15-3 correlated intergranular chloride EAC with microstructure, particularly α colonies precipitated at β grain boundaries and/or intense slip localization.^[8,28,32]

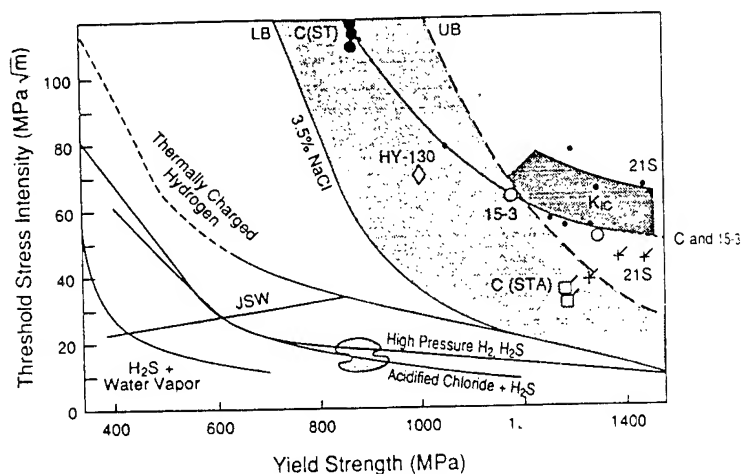


Figure 11. K_{TH} versus σ_{YS} for steels^[11] and selected β -Ti alloys in chloride and other hydrogen-producing environments including sulfur-species additions.

²Hydrogen-producing environments are capable of generating atomic hydrogen on strain-cleaned crack tip surfaces by cathodic proton or water reduction for aqueous electrolytes, by dissociative chemical adsorption for H_2 , or by chemical reaction for H_2S or H_2O gases. This hydrogen is available to embrittle metal within the crack tip process zone.^[31]

EAC-prone Beta 21S exhibited both microstructural features, but EAC-resistant Ti-15-3 did not. Both microstructural features, as well as EAC and internal hydrogen embrittlement, appear to be promoted by prolonged solution treatment (in excess of 1 hour) at high temperature (above 950°C).

Beta C, solution treated in the EAC-resistant regime of relatively shorter time and lower temperature, exhibited an α -precipitate distribution and slip morphology between that of Beta 21S and Ti-15-3. While STA microstructures are complex, heat treatment experiments indicated that grain boundary α -colonies are less frequent in STA Beta C,^[33] compared to both the microstructure of STA Beta 21S^[8] and the amount of intergranular EAC shown in Fig. 6. These preliminary microstructural results, and the low solution treatment time and temperature, are inconsistent with a correlation between large α -colonies at β grain boundaries and intergranular EAC in Beta C. Work is in progress to better address this issue.

Considering slip morphology, compression experiments showed that plastic deformation in ST Beta C is qualitatively homogeneous, with some grains deforming by locally intense slip bands.^[33] Upon aging to the STA condition, slip band spacing decreases, and bands appear more planar and likely to cross entire grains. Similar locally planar deformation modes are observed for STA Beta C and Beta 21S, compared to homogeneous deformation in STA Ti-15-3.^[8,32-35] This comparison suggests that slip localization plays a role in the intergranular chloride EAC of ST and STA β titanium alloys, however, additional research is required.

The present results for Beta C show that high solution treatment temperature and/or prolonged time are not the sole requisite for intergranular EAC in β titanium alloys. Interactions between yield strength and microstructure, or additional microstructural effects such as grain boundary impurity segregation,^[36] must be considered.

Sulfur-Species Additions

Figure 11 shows that acidified chloride/H₂S solution at 25°C severely decreases the threshold for EAC of ferritic steels from that of aqueous chloride alone. Also shown in Fig. 11 are the data for ST Beta C in neutral NaCl and the acidified chloride/sulfur compound solutions summarized in Table I (large filled circle symbols plotted from Fig. 3). Notably for Beta C, K_{TH} did not decrease for any of the sulfur-bearing solutions, even acidified (pH 1.3) NaCl with Na₂S which formed H₂S. This sulfide-EAC resistance of ST Beta C is striking. For steels at a similar yield strength, acidified chloride and H₂S decrease K_{TH} to values as low as 15 MPa√m. K_{TH} for ST Beta C in the various sulfur-species-bearing electrolytes is about 5-fold higher than this lower limit and equals K_{IC} .

The sulfide EAC resistance of ST Beta C may be reduced by long term exposure that allows bulk specimen hydrogen uptake from boldly exposed surfaces. The short term-rising displacement experiments employed to obtain the data in Fig. 3 involved 24 hour exposures to the solution and were designed to emphasize crack dissolution and hydrogen production. Given a typical hydrogen diffusivity (D_H) in single phase β titanium alloys of 4×10^{-7} cm²/sec or faster,^[32] about 12 hours are required for substantial hydrogen penetration from the root of the side-groove to the center line of the CT specimen, parallel to the crack front. If D_H is slower for ST Beta C or if reactions involving sulfide are relatively slow-building then longer exposure times could result in lower K_{TH} based on a hydrogen embrittlement scenario.^[11,13,28] This issue must be investigated for cases where ST β -titanium alloys encounter sulfide in an electrolyte, for example, as produced by sulfate-reducing bacteria in marine environments.^[37]

Potentiostatic Polarization and K_{TH} for EAC

The threshold for chloride EAC in STA Beta C depends on applied electrode potential. This alloy was immune to EAC under cathodic polarization to -1000 mV_{SCE}, showed a minimum resistance (K_{TH}) at -600 mV_{SCE}, and was somewhat less cracking-prone with increasing potential at -150 mV_{SCE} (Fig. 8). The beneficial effect of cathodic polarization was reported by others for α/β and β/α titanium alloys in halogenated electrolytes.^[2-5,38] In particular Young *et. al.*^[8] reported that the neutral chloride K_{TH} for STA Beta 21S increased to equal K_C when the specimen was polarized cathodically to -1000 mV_{SCE}, Fig. 8. Similar low K_{TH} values were observed at -600 and -150 mV_{SCE}, without evidence of a minimum EAC resistance. A speculative hydrogen environment embrittlement mechanism, focusing on atomic hydrogen production and uptake at the occluded and strain-hardened crack tip, was proposed to explain the electrode potential dependence shown in Fig. 8.^[8]

The chloride EAC resistance of STA Beta C, under cathodic polarization, may be reduced by long term exposures that allow bulk specimen hydrogen uptake from boldly exposed specimen surfaces. That is, hydrogen may be produced on such surfaces, even if crack tip production and uptake are minimized by cathodic polarization.^[39]

Implications of Slow-Rapid EAC Growth Rates

Alternating slow-rapid subcritical crack propagation could be explained mechanistically; hydrogen from cathodic reaction diffuses ahead of the crack tip, embrittles the process zone, and the crack rapidly propagates until arrest by surrounding non-embrittled material.^[28] For STA

Beta C in NaCl, rapid EAC propagation occurs over distances that are much larger than the crack tip process or plastic zone (Fig. 9), transitions in the fracture surface morphology are not observed by SEM, and oscillating crack growth kinetics are not evident under rising load control. Thus, the slow-rapid da/dt phenomenon is not ascribed to time-dependent hydrogen diffusion.

Meyn and Pao observed oscillating subcritical crack growth kinetics for α/β Ti-6-4 and perhaps β/α STA Ti-15-3 in neutral aqueous NaCl during slow constant extension rate experiments.^[40] At higher extension rates, continuous Stage II EAC occurred. It was proposed that a critical crack tip strain rate was necessary to maintain conditions conducive to Stage II crack growth. Webb and Meyn recently developed a crack driving force vs resistance model of oscillating EAC da/dt , based on assumed da/dt vs strain energy release rate (G) dependencies, and including test system compliance.^[41] While they do not provide a mechanistic explanation for the form of da/dt vs G necessary to produce slow-rapid da/dt during rising displacement loading, they suggest that titanium alloy/environment systems exhibiting Stage IIA-Stage II subcritical crack growth kinetics are unique candidates for oscillations. Oscillating crack growth kinetics are expected to yield a sawtooth $K-\Delta a$ curve, where the minimum and maximum K levels are constant. Measured minimum and maximum K levels for STA Beta C/NaCl in Fig. 9 are not constant.

Classically, subcritical EAC da/dt is measured and modeled based on either K -control or crack tip strain rate ($\dot{\epsilon}_{CT}$)-control.^[11,42] Rather, for titanium alloys in chloride, we propose that da/dt depends interactively on both K and $\dot{\epsilon}_{CT}$, with steep near-threshold regimes for both variables. This hypothesis is based on the notion that K governs the crack tip process zone, relevant to hydrogen embrittlement, while $\dot{\epsilon}_{CT}$ governs the extent of crack surface electrochemical reactions, pertinent to hydrogen production, or process zone dislocation transport. The slow-rapid crack growth behavior shown in Fig. 9 is then controlled by specimen compliance-based changes in K and $\dot{\epsilon}_{CT}$ for the experiments conducted in rising-CMOD control. Note that da/dt is not a unique function of K for STA Beta C. For example, both slow and rapid da/dt are observed at a K level of 40 MPa \sqrt{m} .

Determination of the three-dimensional relationship between da/dt , K and $\dot{\epsilon}_{CT}$ is complicated by uncertainties in the calculation of crack tip strain rate. For a propagating crack, this quantity depends on K , dK/dt and da/dt , however, the precise function is clouded by uncertain parameters in the continuum mechanics formulation,^[43,44] and by the role of localized dislocation processes. None-the-less, a continuum estimate of the crack tip opening displacement rate (δ_T),^[43,44] which may be proportional to $\dot{\epsilon}_{CT}$, shows

that δ_T at the onset of rapid crack propagation is at least an order of magnitude less than that at the point where rapid da/dt begins to arrest. This estimate indicates that da/dt must be controlled by the interaction of K and $\dot{\epsilon}_{CT}$. Experiments and additional analyses are required to test the relative contributions of stress intensity and crack tip strain rate, and to determine the extent to which slow-fast da/dt behavior is unique to titanium alloys in environments that form a passive film at the crack tip.

CONCLUSIONS

1. The high-strength β/α titanium alloy, STA Beta C, is embrittled by loading in neutral aqueous NaCl solution at 25°C, given an occluded crack, active strain rate and electrode potentials near free corrosion. This behavior is analogous to that of STA Beta 21S.
2. STA Beta C resists crack propagation in NaCl under static load/displacement or cathodic polarization, at least for short-term experiments. This behavior is analogous to that of STA Beta 21S.
3. Moderate strength, single phase (β) ST Beta C is immune to chloride EAC at the free corrosion potential and under short-term rising displacement. Sulfur-species and acid additions to NaCl that embrittle ferritic steels do not promote intergranular EAC in ST Beta C.
4. EAC in STA Beta C is intergranular; the contributions of grain boundary α precipitation, locally intense planar slip and impurity segregation are not defined. Moist air fracture of the STA and ST conditions, as well as ST fracture in chloride-sulfur-species solutions, are by transgranular microvoid rupture.
5. The rising CMOD method is effective, but requires instrumentation and analysis of da/dt as a function of K and crack tip strain rate.
6. Alternating slow-rapid EAC propagation rate is speculatively attributed to coupled K - and crack tip strain rate-control, and specimen compliance-induced changes in these driving force parameters.

ACKNOWLEDGEMENTS

This research was supported by the Office of Naval Research (Grant N00014-91-J-4164), with A. John Sedriks as Scientific Monitor and a National Science Foundation Graduate Research Fellowship (for JAG). Material was donated by RMI Titanium Company and R.W. Schutz. These contributions are gratefully acknowledged, as are informative discussions with J.R. Scully, R.G. Kelly, M.A. Gaudett, and D.G. Kolman.

REFERENCES

1. R.W. Schutz, JOM, vol. 46, no. 7, 1994, pp. 24-29.
2. R.W. Schutz and D.E. Thomas, in Metals Handbook: Corrosion, vol. 13, 9th ed., ASM Int'l, Materials Park, OH, 1987, pp. 669-706.
3. M.J. Blackburn, J.A. Feeney, and T.R. Beck, in Advances in Corrosion Science and Technology, M.G. Fontana and R.W. Staehle, eds., vol. 3, Plenum Publishing, NY, NY, 1972, pp. 67-292.
4. R.W. Schutz, in Stress Corrosion Cracking, R.H. Jones, ed., ASM Int'l, Materials Park, OH, 1992, pp. 265-297.
5. M.J. Blackburn, W.H. Smyrl, and J.A. Feeney, in Stress Corrosion Cracking in High Strength Steel and in Titanium and Aluminum Alloys, B.F. Brown, ed., Naval Research Laboratory, Washington, DC, 1972, pp. 245-363.
6. J.A. Moskovitz and R.M. Pelloux, Corrosion, vol. 35, 1979, pp. 509-514.
7. J.A. Feeney and M.J. Blackburn, Met. Trans., vol. 1, 1970, pp. 3309-3323.
8. L.M. Young, G.A. Young, Jr., J.R. Scully, and R.P. Gangloff, Metall. Mater. Trans. A, in review, 1994.
9. B.F. Brown, Mater. Res. Std., 1966, vol. 6, pp. 129-136.
10. D.N. Fager and W.F. Spurr, Trans. ASM, vol. 61, 1968, pp. 283-292.
11. R.P. Gangloff, in Corrosion Prevention and Control, M. Levy and S. Isserow, eds., US Army Laboratory Command, Watertown, MA, 1986, pp. 64-111.
12. Atlas of Stress-Corrosion and Corrosion Fatigue Curves, A.J. McEvily, Jr., ed., ASM Int'l, Materials Park, OH, 1990, pp. 457, 484.
13. D.E. Thomas and S.R. Seagle in Titanium Science and Technology, G. Lutjering, U. Zwicker and W. Bunk, eds., 1984, pp. 2533-2540.
14. D.M. Aylor, "An Environmental Cracking Evaluation of Fastener Materials for Seawater Applications" (paper No. 484 presented at NACE Corrosion '94, Houston, TX, 1994).
15. L.H. Wolfe, et al., Materials Performance, vol. 32, no.7, 1993, pp. 14-21.
16. I. Azkarate and A. Pelayo, "Hydrogen Assisted Stress Cracking of Titanium Alloys in Aqueous Chloride Environments" (paper presented at INASMET, San Sebastian, Spain, 1992).
17. W.F. Czyrkis and M. Levy, Corrosion, vol. 32, 1976, pp. 99-102.
18. J.W. Hagemeyer and D.E. Gordon, in Titanium Science and Technology, Plenum Press, New York, NY, 1973, pp. 1957-1968.
19. B.P. Somerday, Y. Leng, and R.P. Gangloff, Fatigue and Fracture of Engineering Materials and Structures, in review, 1994.

20. Annual Book of ASTM Standards, Designation E1152-87, vol. 3.01, ASTM, Philadelphia, PA, 1989, pp. 814-824.
21. R.A. Mayville, T.J. Warren, and P.D. Hilton, Trans. ASME, vol. 109, 1987, pp. 188-193.
22. J.K. Donald and J. Ruschau, in Fatigue Crack Measurement: Techniques and Applications, K.J. Marsh et al., eds., EMAS, West Midlands, UK, 1991, pp. 11-37.
23. J.K. Gregory and L. Wagner, "Heat Treatment and Mechanical Behavior in Beta C" (paper presented at GTT, Torino, Italy, 1991).
24. S. Mat and R.C. Newman, "Local Chemistry Aspects of Hydrogen Sulfide-Assisted Stress Corrosion Cracking of Stainless Steels" (paper No. 228 presented at NACE Corrosion '94, Houston, TX, 1994).
25. J.R. Scully and P.J. Moran, Corrosion, vol. 44, 1988, pp. 176-185.
26. S. Tsujikawa et al., Corrosion, vol. 49, 1993, pp. 409-419.
27. H.H. Uhlig, Materials Performance, vol. 16, no. 1, 1977, pp. 22-25.
28. L.M. Young, Environment-Assisted Cracking in Beta Titanium Alloys, MS Thesis, University of Virginia, Charlottesville, VA, 1993.
29. H.B. Bomberger, D.A. Meyn and A.C. Fraker, in Titanium Science and Technology, G. Lütjering, U. Zwicker and W. Bunk, eds., Deutsche Gesellschaft für Metallkunde e.V., Oberusel, West Germany, 1985, pp. 2435-2454.
30. H. Buhl, in Stress Corrosion Cracking-The Slow Strain Rate Technique, ASTM STP 665, G.M. Ugiansky and J.H. Payer, eds., ASTM, Philadelphia, PA, 1979, pp. 333-346.
31. R.P. Gangloff, Mats. Sci. Engr. A, vol. 103, 1988, pp. 157-166.
32. G.A. Young, Jr., Hydrogen Effects in Metastable β -Titanium Alloys, M.S. Thesis, University of Virginia, Charlottesville, VA, 1993.
33. M.A. Gaudett and J.R. Scully, unpublished research, University of Virginia, Charlottesville, VA, 1994.
34. G.A. Young, Jr. and J.R. Scully, Scripta Metall., vol. 28, 1993, pp. 507-512.
35. G.A. Young, Jr. and J.R. Scully, in Beta Titanium Alloys in the 1990s, D. Eylon, R.R. Boyer and D.A. Koss, eds., TMS-AIME, Warrendale, PA, 1993, pp. 147-158.
36. H.J. Rack, Metall. Trans. A, vol. 6A, 1975, pp. 947-949.
37. R.P. Gangloff and R.G. Kelly, Corrosion, vol. 50, 1994, pp. 345-354.
38. T.R. Burk, J. Electrochem. Soc., vol. 114, 1967, pp. 551-556.
39. A. Turnbull, Scripta Metall., vol. 20, 1986, pp. 365-369.
40. D.A. Meyn and P.S. Pao, in Slow Strain Rate Testing for the Evaluation of Environmentally Induced Cracking: Research and Engineering Applications, ASTM STP 1210, R.D. Kane, ed., ASTM, Philadelphia, PA, 1993, pp. 158-169.
41. T.W. Webb and D.A. Meyn, Fracture Mechanics 26th Volume, ASTM STP 1256, W.G. Reuter, J.H. Underwood and J.C. Newman, Jr., eds., ASTM, Philadelphia, PA, in review, 1994.
42. F.P. Ford, in Environment Induced Cracking of Metals, R.P. Gangloff and M.B. Ives, eds., NACE, Houston, TX, 1990, pp. 139-166.
43. J.R. Rice, W.J. Drugan and T-L. Sham, in Fracture Mechanics: 12th Conference, ASTM STP 700, ASTM, Philadelphia, PA, 1980, pp. 189-221.
44. J.R. Rice and E.P. Sorensen, J. Mech. Phys. Solids, vol. 26, 1978, pp. 163-186.

Fracture Toughness and Stress Corrosion Resistance of U-0.75 wt% Ti

**Dr. Chester V. Zabielski* and Mr. Milton Levy
U.S. Army Research Laboratory.
Watertown, Massachusetts 02172-001**

Introduction

Late in 1978, ARL-MD, Watertown was asked to participate in an investigation of several failures on launch of depleted-uranium cored XM774 rounds during low temperature firing. Failure occurred in the vicinity of the rear-most buttress groove of the core where the fillet stress approximates the yield strength of the U-0.75 wt% Ti core alloy. A simple fracture mechanics approach suggested that poor low temperature fracture toughness of the core alloy was contributory.

As a consequence, a systematic investigation of the fracture toughness of the currently produced U-0.75 wt% Ti core alloy was carried out. The U-0.75 wt% Ti alloy was provided by National Lead of Ohio (NLO) and Battelle Northwest (BNW). The failed cores were processed by NLO. The XM833 U-0.75 wt% Ti core material was also obtained from Rocky Flats (RF) for comparison. Representative cores from each source were fully characterized and processing parameters, mechanical properties, microstructure, and test temperature were correlated with fracture toughness.

Materials

The NLO XM774 penetrators were fabricated from a 1.4 in. diameter rod which was rolled from 8 in. diameter ingots. The bars were solution treated for 10 minutes at 899°C in NUSAL, plunge oil quenched, and aged at 350°C in a lead bath.

Six bars, 6 in. long and 1.4 in. in diameter, were received from BNW. These bars were the bottom portions of longer 16 in. bars and the first to enter the water on vertical quench. The 16 in. long extruded bars were vacuum solution treated at 800°C for two hours and 850°C for one-half hour, vertically water quenched at 18 in. per minute, and aged at 350°C in a lead bath for 16 hours.

The RF XM833 penetrators were fabricated from 1.4 in. diameter bars which were alpha extruded from 4 in. diameter ingots. The ingots were homogenized in vacuum at 1050°C for six hours prior to extrusion. The extruded bars were then solution treated for two hours at 800°C and one-half hour at 850°C, vertically water quenched at 18 in. per minute, and aged at 350°C in a lead bath for 16 hours.

Four additional 1.4 in. diameter bars which were received from NLO in the as-rolled condition were given STA treatments comparable to BNW and RF processing; i.e., they were vacuum solution treated at ARL-MD, Watertown for two hours at 800°C and one-half hour at 850°C, vertically quenched in water at 21 in. per minute, and aged in vacuum at 350°C, 370°C, and 390°C, respectively, for seven hours.

Fracture Toughness Test Procedures

Sampling

Two types of fracture toughness specimens were utilized: (1) a single edge-notched bend specimen conforming to plane strain requirements (K_{IC}) of ASTM E 399-74 (FT1); and (2) a slow-bend V-notched Charpy impact specimen (CV2) for approximate K_{IC} or K_Q . Both types of specimens were used for static fracture toughness measurements. Regardless of the type of specimen, the notches were always machined from the outer diameter of the bar or penetrator core so that the microstructure in the vicinity of the notch would be comparable to that of the penetrator buttress groove.

From each of four XM774 penetrators representative of NLO lots which failed on low temperature firing, two Charpy, K_Q specimens and two K_{IC} specimens were cut alternately starting at the nose of the penetrator; i.e., the end which entered the water first during the vertical quench. A total of four Charpy and four K_{IC} specimens were cut per penetrator. In a similar fashion, four K_{IC} specimens and four K_Q specimens were machined from three XM833 RF penetrators. Based on the similarity of K_{IC} and K_Q values obtained, it was decided to concentrate on the simplest and least costly specimen, the V-notch bend Charpy impact specimen only, and report K_Q values for the remaining materials evaluated. Therefore, only K_Q specimens were machined from four NLO as-rolled bars which had been vacuum solution treated, vertically water quenched, and aged at ARL-MD, Watertown and from six BNW bars which were similarly heat treated. In addition, tension and K_{ISCC} specimens were fabricated from the above materials to confirm the specified strength requirement and to determine susceptibility to stress corrosion cracking.

The stress corrosion specimens (see Figure 1) which were single edge notch specimens (3.0 x 0.20 x 0.20 in.) were cut with the long dimension parallel to the direction of maximum grain flow and notched so that crack growth and fracture would occur in the radial direction.

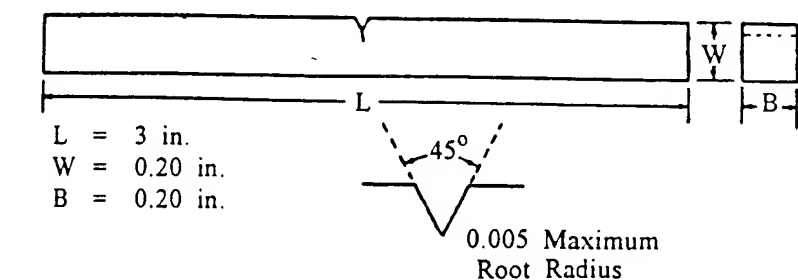


Figure 1. Specimen geometry and equation for K values.

$$K = \frac{4.12 (\alpha^{-3} - \alpha^{-5})^{1/2} M}{BW^{3/2}} \quad \text{where } \alpha = 1 - a/W$$

$M = \text{Moment}$
 $B = \text{Thickness}$
 $W = \text{Width}$

$a = \text{crack length + notch depth}$

Test Method

The procedure for KIC measurement involved three-point bend testing of notched specimens that had been precracked in fatigue. Load versus displacement across the notch was recorded autographically. The KIC value was calculated from the load corresponding to a 2% increment of crack extension by equations which have been established on the basis of elastic stress analysis of bend specimens. The detailed procedure is described in ASTM E 399-74. The method for KQ measurement employed a Charpy specimen provided with a sharp notch terminating in a fatigue crack tested in three-point bending. The maximum load in the test was recorded and the nominal crack strength was determined from this value as well as the original dimensions of the specimen using the single beam equation. A detailed description is contained in the proposed E24.03.03 draft dated February 7, 1979. Precracking of specimens for both test procedures involved initiation of the crack and subsequent growth in tension.

The method for stress corrosion measurements follows. The test uses a precracked bar stressed as a cantilever beam. A sharp notch is machined across the rectangular bar specimens at mid-length, and is sharpened by fatiguing. The specimen is held in a rack horizontally with the precracked central portion surrounded by a plastic bottle which contains the environment. One end of the specimen is clamped to the mast of the rack and the other end to

an arm from which weights are suspended. On evaluating the alloy, the specimen is first stressed in air at increasing loads until it fractures. The data are reduced to stress intensity using the Kies equation (see Figure 1). Having established stress intensity for dry conditions (K_{Ic}), a specimen is similarly tested in distilled H_2O and NaCl solutions at a somewhat lower stress intensity. If the specimen did not fail within an hour, the stress intensity was increased by approximately 3% each succeeding hour until failure occurred and the time required for rupture noted. Additional specimens were stressed at decreasingly lower stress intensities for 1000 hours or until failure occurred to give a more valid value for K_{Isc} , which was determined from a plot of stress intensity versus time to failure. K_{Isc} is the threshold stress intensity value for the onset of cracking.

Results

Comparison of Failed NLO XM774 Penetrators Versus the RF XM833 Processed Material

Chemistry, Microstructure, Mechanical Properties

Table 1 summarizes mechanical properties and chemistries for NLO XM774 and RF XM833 penetrators. Major differences were observed in hydrogen content, elongation, and RA values. The NLO material exhibited higher H and lower elongation and RA.

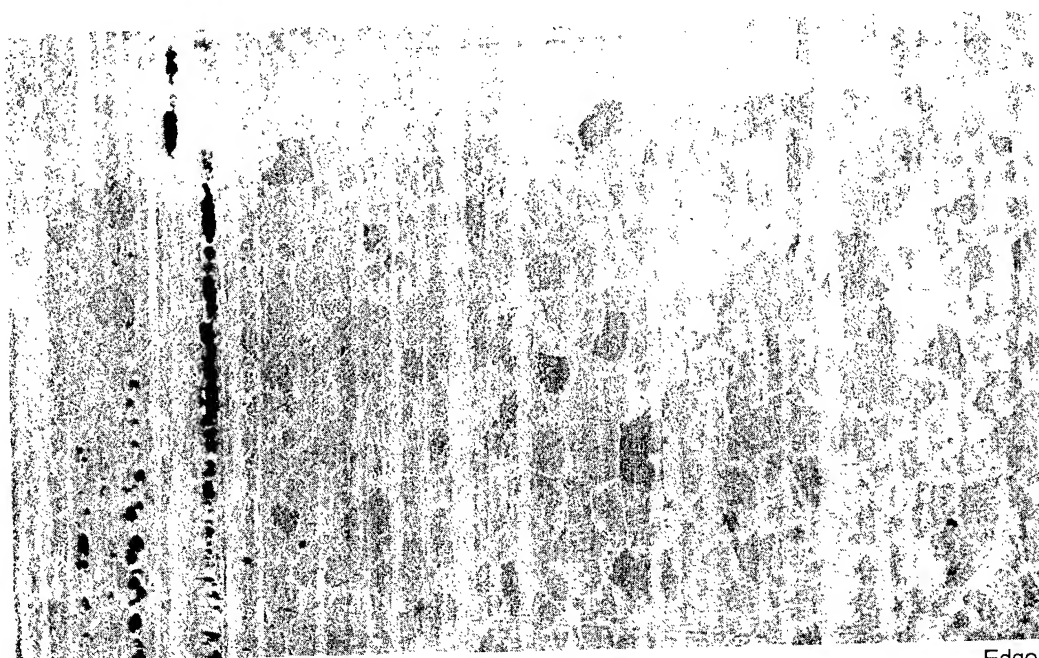
Table 1. XM774 Staballoy properties

	RF	NLO
Ultimate (ksi)	210	196
Yield (ksi)	115	114
Elongation (%)	12 - 16	5 - 9
RA (%)	12 - 16	4 - 8
Hardness (HR _C)	38 - 43	40 - 42
Ti (%)	0.69 - 0.73	0.69 - 0.71
C (ppm)	<100	<40
H (ppm)	<1	2 - 4

The structure of the NLO bars is shown in Figure 2. The view is perpendicular to the extrusion direction at the diameter and represents slightly more than one-half of the complete cross section. A coarse duplex grain size is observed along with banding and center-line porosity or voids.

The microstructure of an XM833 penetrator is shown at both the nose section from the bar entering the water first on vertical quenching

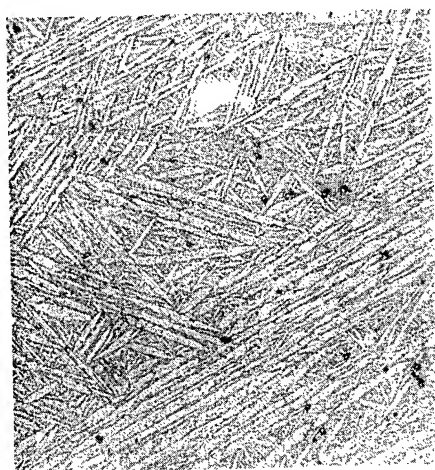
(see Figure 3) and at the tail, or rear, portion of the bar which entered the water last (see Figure 4). The microstructure in Figure 3 is essentially martensitic with evidence of incipient slack quench at the grain boundaries and small voids, particularly in the central area are observed. The tail or rear, views show a more pronounced slack quench and even larger voids, particularly in the central areas (see Figure 4).



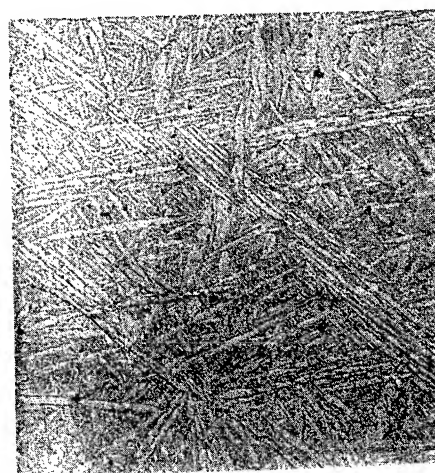
Center

Edge

Figure 2. U-0.75 wt% Ti (NLO) - solution treated (molten salt) 899°C for 10 minutes, oil quenched, and aged at 350°C for one hour. Mag. 9X.

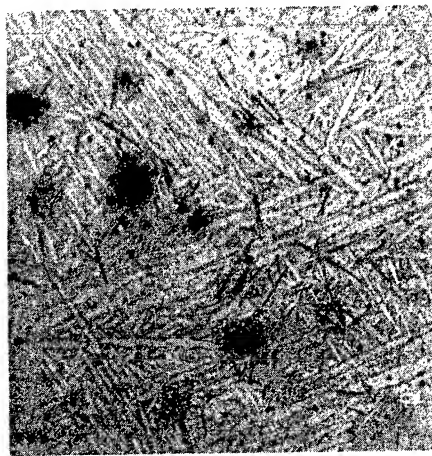


Center

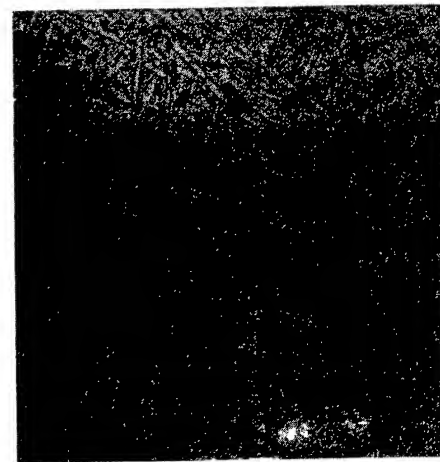


Edge

Figure 3. U-0.75 wt% Ti (RF) nose section - solution treated at 800°C for two hours, 850°C for one-half hour; vertically water quenched 18 inches per minute; aged (lead bath) for 16 hours at 350°C. Mag. 100X



Center



Edge

Figure 4. U-0.75 wt% Ti (RF) tail section - solution treated at 800°C for two hours, 850°C for one-half hour, vertically water quenched 18 inches per minute; aged (lead bath) for 16 hours at 350°C. Mag. 100X

Fracture Toughness Versus Temperature

Figure 5 compares fracture toughness data for the failed NLO penetrator material obtained from the two types of specimens employed. The data was designated K_{IC} if all the conditions of ASTM E 399-74 were met; otherwise, the values were designated K_Q .

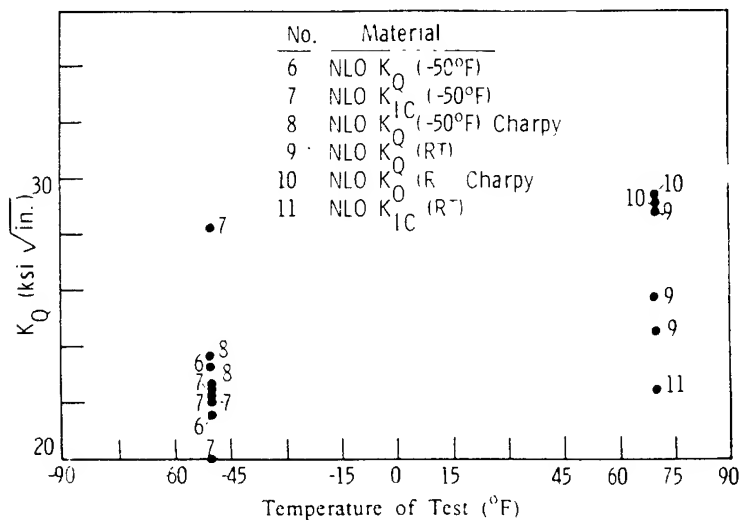


Figure 5. Fracture toughness of aged U-0.75 wt% Ti NLO penetrators versus temperature of test.

All K_{IC} and K_Q values were below 30 ksi $\sqrt{in.}$ regardless of test temperature. The K_{IC} and K_Q values were in fair agreement. The average value at -50°F was 22 ksi $\sqrt{in.}$, and at 75°F, 27 ksi $\sqrt{in.}$

Previous work at ARL-MD, Watertown has shown that fracture toughness values for titanium and steel alloys obtained with compact tension and bend specimens conforming to ASTM E 399-74, were in good agreement with those obtained with precracked Charpy specimens up to values of $40 \text{ ksi}\sqrt{\text{in.}}$ (2,3).

Fracture Toughness Versus Hardness

Figure 6 shows a plot of fracture toughness versus HRC hardness values for individual specimens taken from the NLO failed XM774 penetrator lots and the RF XM833 penetrators. The slightly softer vacuum solution treated, and vertically water quenched XM833 penetrators had significantly higher toughness values than the NLO XM774 penetrator lots which were molten salt solution treated, plunge quenched in oil, and had high hydrogen. At both room temperature and -50°F , fracture toughness values for specimens from RF XM833 penetrator lots were greater than $35 \text{ ksi}\sqrt{\text{in.}}$. All values were below $30 \text{ ksi}\sqrt{\text{in.}}$ for specimens from the NLO XM774 penetrator lots.

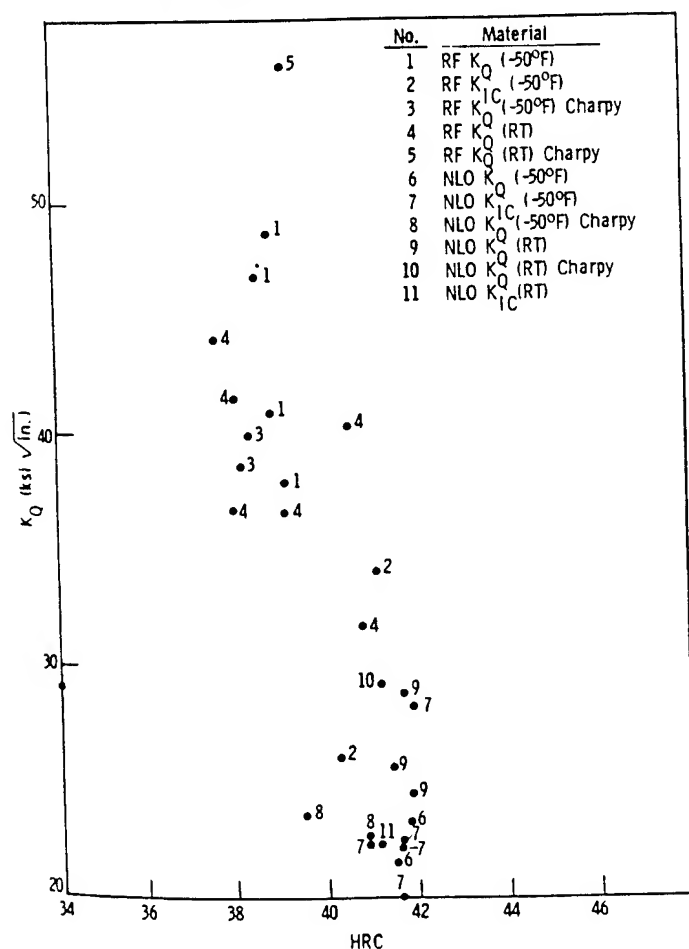


Figure 6. Fracture toughness of aged U-0.75 wt% Ti RF and NLO penetrators versus HRC.

As-Rolled NLO Bars Heat Treated at ARL-MD, Watertown

Chemistry, Mechanical Properties

The chemical composition of the as-rolled NLO bars is shown in Table 2. All chemical properties except hydrogen meet the requirements of the XM774 as-cast Staballoy core specification. The 1.8 ppm hydrogen exceeds the maximum requirement of 1 ppm. Table 3 summarizes mechanical properties for the alloy aged at three different temperatures: 350°C, 370°C, and 390°C. In all three cases, the mechanical properties meet or exceed the minimum requirements specified for the heat treated XM774 U-0.75 wt% Ti core alloy. Data from the unaged material is included for comparison.

Table 2. Chemical analysis data for as-received NLO bars

Ti 0.72% Top		C 14 ppm Top	
Ti 0.71% Bottom		C 23 ppm Bottom	
H 1.8 ppm Top			
Si	60 ppm	Mg	< 4 ppm
Fe	34 ppm	Ba	< 3 ppm
Al	14 ppm	Cr	2 ppm
Ni	10 ppm	Be	< 1 ppm
Pb	9 ppm	B	< 1 ppm
Mn	8 ppm	Sn	< 1 ppm
Cu	7 ppm	V	< 1 ppm
Zn	< 20 ppm		
Density = 18.64			

Table 3. Mechanical properties of aged U-0.75 wt% Ti NLO bars

	Hardness (HRC)	YS (0.2%)* (ksi)	TS (ksi)	Elong* (%)	RA* (%)
Unaged	36.2	93.8	187.4	17.9	16.5
Aged for 7 hours at					
350°C	37.5	108.0	192.0	17.2	17.4
370°C	39.0	109.1	196.0	13.9	18.7
390°C	41.5	115.6	206.2	12.5	14.9

All bars solution treated at 800°C for two hours, 850°C for one-half hour, and vertically water quenched at 21 in. per minute. *Average of 4 values

Fracture Toughness Versus Temperature

Fracture toughness (K_{Ic}) of the above mentioned materials were determined utilizing precracked Charpy specimens at test temperatures

ranging from -100°F to 70°F. The data are recorded in Table 4 and plotted in Figure 7. It should be noted that a limited number of specimens were available for test. Generally, fracture toughness increased with test temperature. The unaged alloy (solution treated and quenched) gave the highest fracture toughness values. As the aging temperature increased, fracture toughness decreased. The bars aged at 390°C gave the lowest fracture toughness values. Fracture toughness (K_Q) values were greater than 35 $\text{ksi}\sqrt{\text{in.}}$ for all aged bars at the -50°F and higher test temperatures. These data show that the fracture toughness of the NLO material can be substantially improved by changing the heat treatment procedure from solutionizing in NUSAL and fully plunge quenching in oil to solutionizing in vacuum and vertically quenching in water.

Table 4. Fracture toughness (K_Q) of aged U-0.75 wt% Ti NLO bars

	Test Temperature (°F)				
	-100	-50	-20	10*	R.T.*
	K_Q ($\text{ksi}\sqrt{\text{in.}}$)				
Unaged	33.8	38.35	46.4	54.0	61.55
Aged for 7 hours at					
350°C	34.6	36.30	41.3	48.2	54.95
370°C	29.5	35.20	43.9	43.1	58.45
390°C	28.8	35.60	39.2	42.7	43.2

All bars solution treated at 800°C for two hours and 850°C for one-half hour and vertically water quenched at 21 in. per minute

*Average of 2 values

Fracture Toughness Versus Hardness

Figure 8 plots fracture toughness (K_Q $\text{ksi}\sqrt{\text{in.}}$) versus HRC hardness for the unaged and aged bars. Room temperature fracture toughness values decreased significantly with increase in HRC hardness and aging temperature. At the -50°F and -100°F test temperatures the rate of decrease of fracture toughness values with increase in HRC hardness and aging temperature decreased markedly.

BNW Bars Vacuum Solution Treated, Vertically Water Quenched and Aged at 350°C for 16 Hours

Chemistry, Mechanical Properties

Table 5 shows that BNW processed alloy meets the chemical properties requirements of the XM774 specification. Note that the hydrogen content is 0.5 ppm.

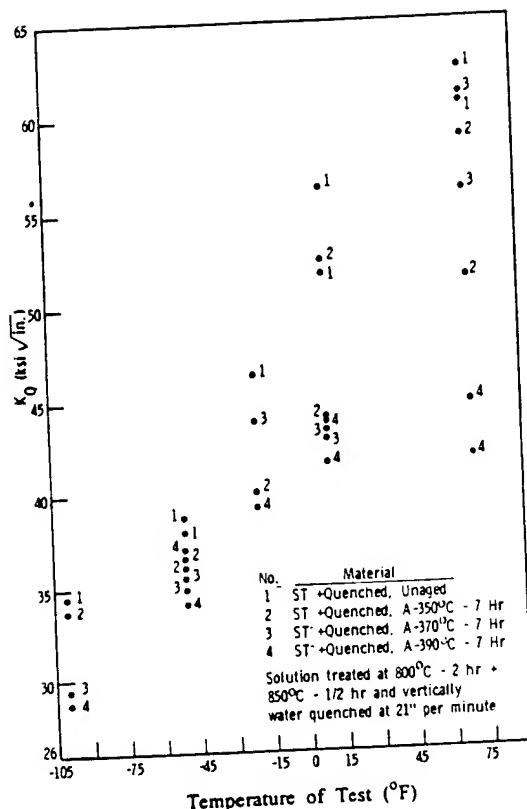


Figure 7. Fracture toughness of aged U-0.75 wt% Ti NLO bars versus temperature of test.

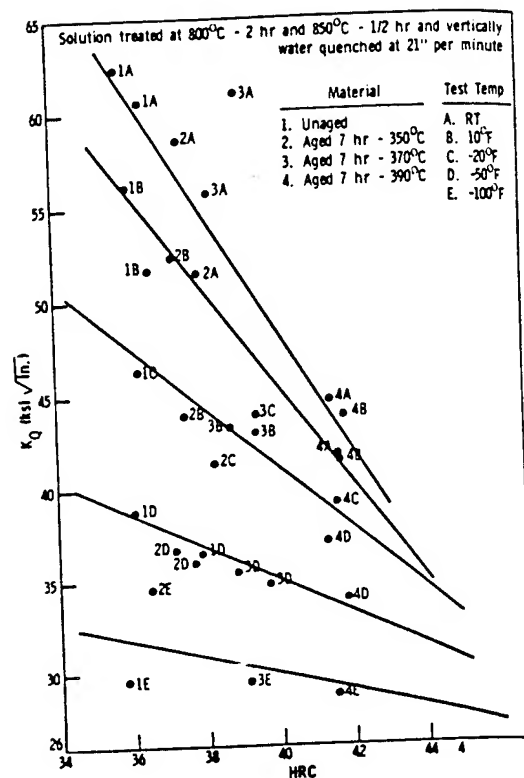


Figure 8. Fracture toughness of aged U-0.75 wt% Ti NLO bars (Charpy - K_Q) versus HRC.

Table 5. Chemical analysis of BNW bars (101, 103, 104, 105, 107, 108) from 4-1/2 in. diameter ingot

Ingot Analysis			
Ti Center	0.73%	Si	45 ppm
Ti Bottom	0.73%	Fe	30 ppm
H	0.5 ppm	Nb	<10 ppr
C	70-80 ppm	Ni	25 ppm
Al	5 ppm		

Figure 9 summarizes HRC traverse data taken across the diameter of transverse sections for six bars at 45° angles at the vertically water quenched end, marked A (first hits H₂O), and 6 in. from the end, marked B. The bars at position B were slightly harder than at position A. The central areas of the bars were quite uniform in hardness and slightly softer.

The tensile properties of the six aged U-0.75 wt% Ti bars versus temperature are shown in Table 6. The yield strength (YS) was found to increase slightly with decrease in test temperature. The strength of the material exceeds the minimum requirements of the XM774 specification.

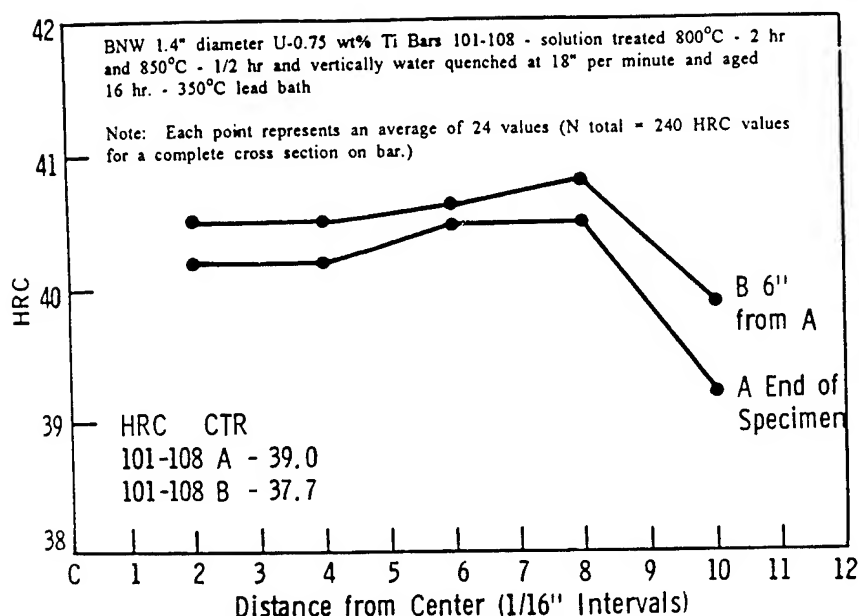


Figure 9. Transverse Rockwell C Hardness versus distance from center.

Table 6. Variation of tensile properties of aged U-0.75 wt% Ti BNW* bars with temperature

Temp (°F)	YS 0.1% (ksi)	YS 0.2% (ksi)	ULT (ksi)	E (psi x 10 ⁶)
70	101	114	199	20.5
40	104	116	196	19.3
10	102	115	206	18.5
-20	106	120	210	19.5
-50	110	124	206	19.5
-100	108	122	200	20.5

*Batelle Northwest 1.4 in. diameter U-0.75 wt% Ti bars #10 through 108 solution treated at 800°C for two hours, and 850°C for one-half hour; vertically water quenched at 18 inches per minute; aged for 16 hours at 350°C lead bath (4.5 in. diameter ingot α extruded).

NOTE: Average of 2 values

Fracture Toughness Versus Test Temperature

Figure 10 plots fracture toughness versus test temperature from -100°F to 100°F. Four test values were obtained at each temperature and lines were drawn through the outermost points to show the band of values. Fracture toughness increased with increasing test temperature. There was no evidence of change or decrease in slope at the +100°F test temperature, but below -50°F the slope decreased indicating a brittle region. The average K_{Ic} value for each test temperature is shown in Table 7. Note that the average K_{Ic} value at -50°F is 36.2 ksi $\sqrt{\text{in.}}$, which exceeds the recently established minimum XM774 requirement of 30 ksi $\sqrt{\text{in.}}$

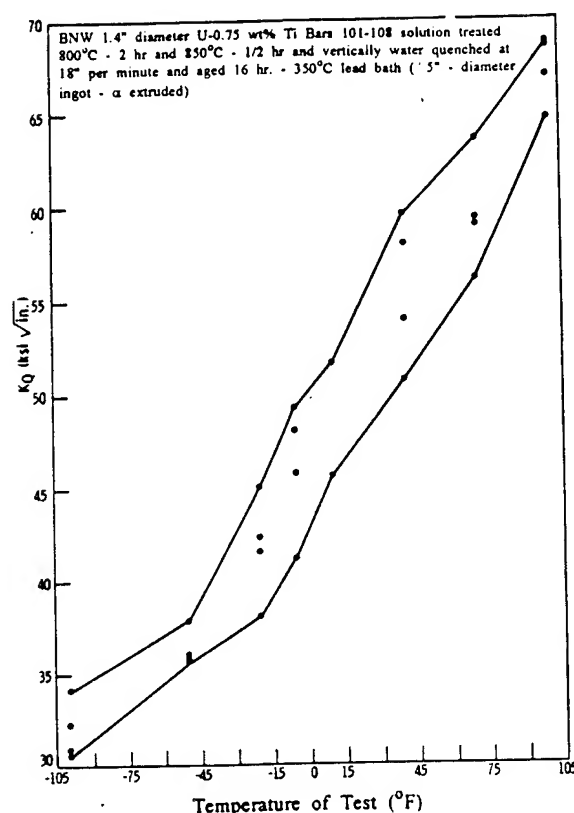


Figure 10. Fracture toughness of aged U-0.75 wt% Ti BNW bars versus temperature of test.

Table 7. Variation of fracture toughness of aged U-0.75 wt% Ti BNW bars with temperature

Temperature (°F)	Hardness* (HRC)	KQ† (ksi√in.)
100	39.4	67.2
70	39.5	59.4
10	39.7	55.6
10	39.7	47.6
-4	39.6	46.0
-20	39.4	41.8
-50	39.4	36.2
-100	39.7	31.9

*Average of 16 values †Average of 4 values
Battelle Northwest 1.4 inch diameter U-0.75% Ti bars #101 through 108 solution treated at 800°C for two hours and 850°C for one-half hour; vertically water quenched at 18 in. per minute and aged 16 hours at 350°C in lead bath (4.5 in. in diameter ingot α extruded).

Stress Corrosion Cracking

Table 8 compares the critical stress intensity for crack propagation in an aqueous solution containing 50 ppm C1-(K_{Isc}) for 1000 hours of the NLO processed XM774 U-0.75 wt% Ti alloy (solution treated in NUSAL and plunge quenched in oil and aged) with the RF processed

XM833 alloy (vacuum solution treated and vertically water quenched and aged). The RF XM833 U-0.75 wt% Ti alloy is less susceptible to stress corrosion than the NLO XM774 material due to the differences in processing. Crack extension in all of the alloys was transgranular and failure occurred by brittle quasicleavage fracture in NaCl solution (1,10).

Table 8. K_{Isc} data for 105 cal. penetrators in 50 ppm Cl-

NLO	XM774 (8 Specimens)	18 $\text{ksi}\sqrt{\text{in.}}$
RF	XM833 (6 Specimens)	23 $\text{ksi}\sqrt{\text{in.}}$

Ratio Analysis Diagrams (RAD)

$$K_{IC}/\sigma_{YS}$$

The best index of a material's fracture resistance is the K_{IC}/σ_{YS} ratio since it is this ratio of materials properties that determines flaw size and applied stress which are the parameters of interest to designers. The so-called ratio analysis diagram (RAD) (4,5) encompasses the range of strength and fracture resistance. Its framework is formed from the scales of YS versus K_Q . The technological limit line represents the highest values of fracture resistance measured to date.

Figure 11 contains the RAD constructed for the U-0.75 wt% Ti alloy (6-8). The envelope "B" encompasses fracture toughness data obtained for the NLO processed alloy which are representative of the failed (low temperature launch) penetrator lots. The material was molten salt solution treated, quenched in oil, and aged; it also contained high hydrogen (>1 ppm). Envelopes "A" and "D" contain data for penetrators which were vacuum solution treated, vertically water quenched, and aged with a low hydrogen content (<1 ppm).

The data shows that the fracture toughness of the alloy is highly sensitive to variations in heat treatment and concomitant interstitial content and microstructure. Under optimum conditions a fracture toughness of 80 $\text{ksi}\sqrt{\text{in.}}$ has been reported for the U-0.75 wt% Ti alloy at a YS of 115 ksi. Further processing improvements and alloy development may raise this current limit to 90 $\text{ksi}\sqrt{\text{in.}}$

$$K_{Isc}$$

The RAD shown in Figure 11 superimposes K_{Isc} data on the fracture toughness data displayed in Figure 12. The envelope shown contains earlier K_{Isc} data obtained in 50 ppm Cl- solution and

represents different sources of material, laboratories, and processing procedures. The data reported in Table 8 are shown above the envelope and the highest K_{ISCC} of $23 \text{ ksi}\sqrt{\text{in.}}$ which is in good agreement with other published data (9,11) represents a critical flaw size of 8 mils for crack propagation in the chloride solution. The other data represent tolerance to even smaller critical flaw sizes.

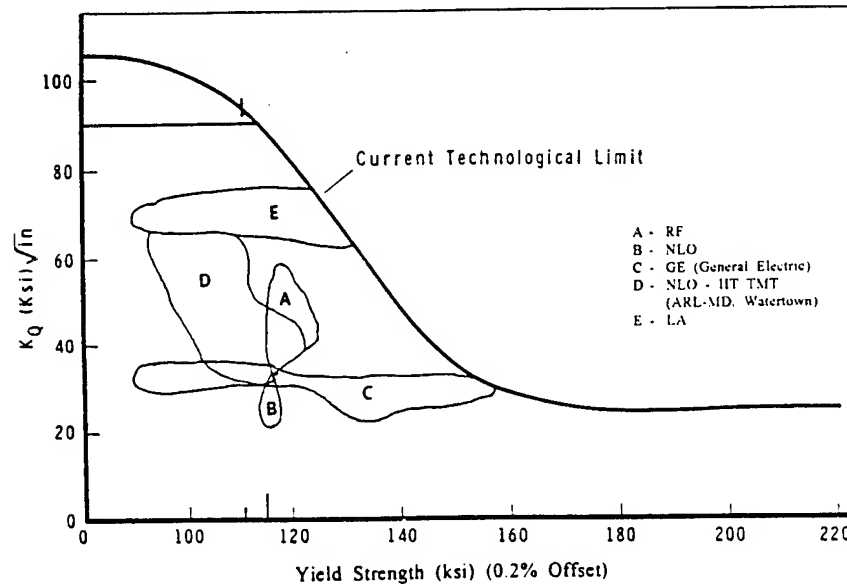


Figure 11. RAD for U-0.75 wt% Ti K_Q versus YS (0.2%).

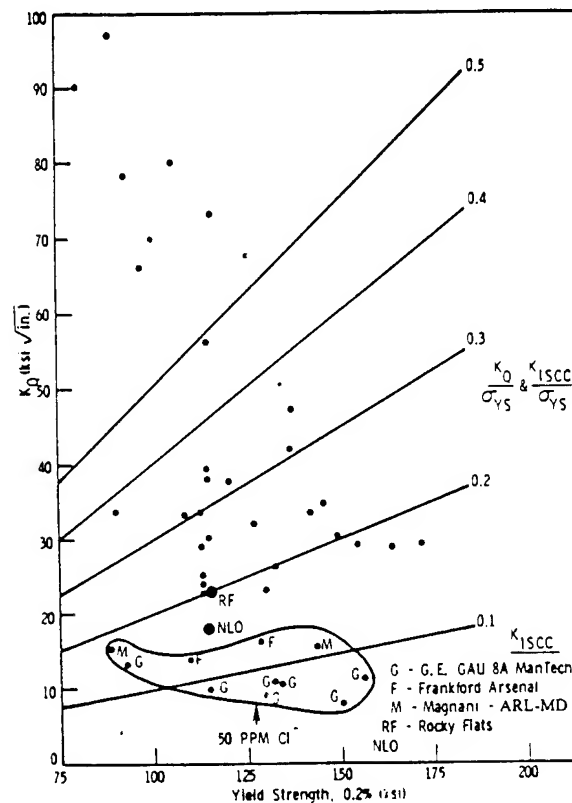


Figure 12. SCC and K_Q RAD for U-0.75 wt% Ti alloys.

Cooperative Test Program with ARDEC

ARDEC provided ARL-MD, Watertown with additional U-0.75 wt% Ti alloy which was similarly processed by three suppliers: Nuclear Metals, Inc. (NMI), NLO, and BNW (all vacuum solutionized, vertically water quenched, and aged).

Fracture toughness measurements were made and the data reported in Table 9. At -50°F , values in the range of 31 to 41 $\text{ksi}\sqrt{\text{in.}}$ were obtained. Based on these data, it was recommended that a minimum fracture toughness requirement of 30 $\text{ksi}\sqrt{\text{in.}}$ at -50°F be incorporated in the XM774 core specification.

Table 9. Fracture toughness of U-0.75% Ti similarly processed by three suppliers

Lot No.	Temp. (°F)	n	HRC	K _Q (ksi√in.)
		NMI		
48	69	2	42.4	46.4
	-50	4	41.5	31.4
72	69	2	39.2	59.4
	-50	4	38.9	37.3
		NLO		
732-734	74.8	4	41.9	52.8
	-50	8	41.4	34.9
		BNW		
*	73.8	12	40.4	66.3
	-50	23	40.2	40.9
307	-50	1	44.8	37.1
319	-50	2	43.3	36.3

*11, 83, 93, 152, 203, and 249 lot numbers

Conclusions

It was shown that the fracture toughness of the U-0.75 wt% Ti alloy is highly sensitive to variations in heat treatment and concomitant interstitial content and microstructure. The NLO processed U-0.75 wt% Ti alloy representative of the failed penetrators (low temperature launch) had appreciably lower fracture toughness ($\sim 20 \text{ ksi}\sqrt{\text{in.}}$ at -50°F) than the alloy processed either by BNW or RF ($\sim 35 \text{ ksi}\sqrt{\text{in.}}$ at -50°F).

The failed NLO material was characterized as high hydrogen content (2 to 4 ppm), low elongation (7%) material with microstructural features that included a coarse grain size, duplex structure, banding, and centerline porosity.

By comparison, the BNW and RF processed alloy contained less hydrogen (<1 ppm), exhibited higher elongation (14%), and essentially a martensitic structure with small voids in the central area. However, it was demonstrated that the NLO material could achieve comparability of fracture toughness to the BNW and RF processed alloy by solutionizing in vacuum, vertically water quenching, and aging instead of solutionizing in molten salt, fully plunge quenching in oil, and aging. Based on the extensive fracture toughness testing of XM774 core material similarly processed by several vendors for ARDEC, a minimum fracture toughness requirement of $30 \text{ ksi}\sqrt{\text{in.}}$ at -50°F should be incorporated into the XM774 specification to insure launch integrity.

The U-0.75 wt% Ti alloy is very susceptible to stress corrosion cracking in aqueous chloride solutions (K_{Isc} 18 to $23 \text{ ksi}\sqrt{\text{in.}}$). Residual stress measurements of the fabricated M774 penetrator should be made to determine the magnitude of the tensile stress introduced by the processing of the alloy.

References

1. CZYRKILIS, W. F., and LEVY, M. *Stress Corrosion Cracking Behavior of Uranium Alloys*. Corrosion, v. 30, no. 5, May 1974, p. 181-187.
2. CHAIT, R., and LUM, P. T. *Influence of Test Temperature on the Fracture Toughness and Tensile Properties of Ti-8Mo-8V-2Sn Alloys Heat Treated to High Strength Levels*. Toughness and Fracture Behavior of Titanium ASTM STP 651, American Society for Testing and Materials, 1978, p. 180-199.
3. DESISTO, T. Private Communication. U.S. Army Research Laboratory, Watertown, MA, 1978.
4. JUDY, R. W., and GOODE, R. J. *Ductile Fracture Equation for High-Strength Structural Metals*. NRL Report 7557, April 3, 1973.
5. JUDY, R. W., and GOODE, R. J. *Criteria for Fracture Prevention in Titanium Structures*. NRL Memorandum Report 3434, December 1976.
6. *Physical Metallurgy of Uranium Alloys*. Proceedings of the Third Army Materials Technology Conference. Brook Hill Publishing Company, Chestnut Hill, MA, 1976.
7. Proceedings of the High Density Alloy Penetrator Materials Conference. U.S. Army Research Laboratory, SP 77-3, April 1977.
8. ZABIELSKI, C. *Metallurgical Characterization of the General Electric ManTech GAU 8/A Penetrator*. U.S. Army Research Laboratory, SP 77-5, June 1977.
9. LEVY, M., ZABIELSKI, C., CHANG, F., and SCANLON, J. *Corrosion of High Density Penetrator Materials*. Final TTCP Report on Operating Assignment PTP, January 2, 1988.
10. BIRD, E. L. *Failure Analysis of Uranium - Titanium Alloys*. Proceedings of the International Symposium on Testing and Failure Analysis, Los Angeles, CA, ASM International, Metals Park, OH, 31 October - 4 November 1988.
11. MAGNANI, N. J. *The Effects of Environment, Orientation, and Strength Level on the Stress Corrosion Behavior of U-0.75 Wt% Titanium*. Journal of Nuclear Materials, North Holland Publishing Company, 1974, v. 54, p. 108-116.

The Resistance of High-Strength Alloys to Hydrogen Embrittlement

Dr. Bruce G. Pound
Materials Research Center
SRI International
333 Ravenswood Ave
Menlo Park, CA 94025-3493

Abstract

The resistance of an alloy to hydrogen embrittlement (HE) is strongly influenced by the presence of microstructural heterogeneities, which can provide sites to trap hydrogen. The entry and trapping of hydrogen in a range of high-strength alloys have been investigated with a technique referred to as hydrogen ingress analysis by potentiostatic pulsing (HIAPP). Data were analyzed by using a diffusion/trapping model to determine entry and trapping parameters for high-strength steels, precipitation-hardened and work-hardened nickel-base alloys, and titanium alloys. For most of the alloys studied, the observed resistance to HE appeared to be determined primarily by the alloy's intrinsic susceptibility as defined by the trapping characteristics; that is, the H entry flux generally has only a secondary effect on the resistance to HE. However, in one case, the HE resistance was attributable to a low entry flux. This type of case highlights the need for characterizing alloys in terms of both trapping capability and rate of H entry to account for differences observed in their HE resistance.

Introduction

Microstructural heterogeneities in alloys provide potential trapping sites for hydrogen and so can play a crucial role in determining an alloy's resistance to hydrogen embrittlement (HE). This role originates in the fact that the interaction of these heterogeneities with hydrogen can strongly influence the series of events leading to failure.¹ The accumulation of hydrogen at second-phase particles and precipitates, for example, is generally considered to promote microvoid initiation via the fracture of particles or the weakening of particle-matrix interfaces. Traps

with a large saturability and a high binding energy for hydrogen are highly conducive to HE,^{2,3} whereas alloys containing a high density of well-distributed irreversible (high binding energy) traps that have a low saturability should be less susceptible. Thus, the intrinsic susceptibility of an alloy to HE is highly dependent on the type of microstructural defect, with large irreversible traps typically imparting a high susceptibility.

The basic concept of trap theory is that the local concentration of hydrogen trapped at a defect must exceed some critical value (C_k) for cracks to be initiated.^{1,3} It should be recognized, however, that the mechanism by which such an accumulation triggers HE is not addressed. The value of C_k , and therefore the intrinsic susceptibility of an alloy, is determined by the type of trap, its size, concentration (density), and other parameters. A decrease in C_k will render the alloy more susceptible. However, whether embrittlement will actually occur is also affected by the amount of trapped H, which depends on factors such as the entry kinetics, exposure time, and transport mode. In some cases, an alloy may prove resistant during exposure because the amount of H that enters is small enough that the critical concentration at the traps is not exceeded. Likewise, when alloys have a similar intrinsic susceptibility in terms of their trapping characteristics, the difference in their actual resistance to HE is likely to be determined by the amount of H absorbed by each alloy.

Over the last few years, the entry and trapping of hydrogen in a wide range of high-strength alloys have been investigated at SRI.⁴⁻⁸ The rates of H entry and rate constants for irreversible trapping were determined using an electrochemical technique referred to as hydrogen ingress analysis by potentiostatic pulsing (HIAPP).^{4,9} The research was aimed in part at characterizing the intrinsic susceptibility of the alloys to HE in terms of their irreversible trapping constants. The relative intrinsic susceptibilities then could be compared with results for the actual resistance to HE observed in tests by other workers. In this paper, the irreversible trapping constants and, where necessary, H entry fluxes for the different alloys are compared, with the objective of providing a basis for explaining differences in the resistance of these alloys to HE.

Experimental

The alloy of interest is cathodically charged with hydrogen at a constant potential E_c for a time t_c , after which the potential is stepped in the positive direction. H diffuses back to the entry surface and is reoxidized, thereby generating an anodic current transient. Data are obtained over a range of charging times, typically from 5 to 60 s, at different overpotentials ($\eta = E_c - E_{oc}$) relative to the open-circuit potential

(E_{oc}), which is measured immediately before each charging time. E_{oc} is also used to monitor the stability of the alloy surface, since any oxides present should not be reduced during charging.

The pulse technique was applied to high-strength steels,^{4,5} precipitation-hardened and work-hardened nickel-base alloys,^{5,6} and titanium.⁷ The composition of each alloy is given in Table 1. Table 2 shows the yield strength of the alloys and the thermomechanical treatment used in each case.

Table 1
Alloy Composition (wt%)

	4340	18Ni	718	925	C-276	625	716	TiGr2
Al	0.031	0.13	0.60	0.30		0.18	0.22	
B		0.003	0.003					
C	0.42	0.009	0.03	0.02	0.002	0.03	0.011	0.021
Co		9.15	0.16		0.83		<0.01	
Cr	0.89	0.06	18.97	22.20	15.27	22.06	20.99	
Cu	0.19	0.11	0.04	1.93				
Fe	bal	bal	16.25	28.96	5.84	4.37	5.32	0.17
Mn	0.46	0.01	0.10	0.62	0.48	0.17	0.01	
Mo	0.21	4.82	3.04	2.74	16.04	8.70	8.10	
O	0.001							0.16
Nb+Ta			5.30			3.50	3.47	
Ni	1.74	18.42	54.41	40.95	57.5	60.33	60.5	
P	0.009	0.004	0.009		<0.005	0.012	0.004	
S	0.001	0.001	0.002	0.001	<0.002	0.001	0.001	
Si	0.28	0.04	0.11	0.17	<0.02	0.38	0.02	
Ti		0.65	0.98	2.11		0.27	1.35	bal
W		0.01			3.90			
Other	0.005N	0.05 Ca 0.02 Zr			0.12 V			<0.005H 0.007N

Test electrodes of each alloy were fabricated from a length (1.3-3.8 cm) of rod press-fitted into a Teflon sheath so that only the planar end surface was exposed to the electrolyte. The surface was polished before each experiment with SiC paper followed by 0.05- μ m alumina powder. Details of the electrochemical cell and instrumentation have been given elsewhere.⁴ The alloys were exposed in a deaerated solution containing 1 mol L⁻¹ acetic acid and 1 mol L⁻¹ sodium acetate with 15 ppm As₂O₃ added to promote H entry. The potentials were measured with respect to a saturated calomel electrode (SCE). All tests were performed at 22 \pm 2°C.

Table 2
Thermomechanical Treatment of Alloys

Alloy	Heat Treatment ^a	Test Condition	Yield Strength (MPa)
4340	Annealed	HRC 41	1206
		HRC 53	1792
18Ni K-500	Aged (482°C, 4 h) Cold drawn, unaged	As received	1954
		As received	758
		Aged (600°C, 8 h)	1096
35N 718	Cold drawn and aged Hot fin., solution treated	As received	1854
		As received	1238
925 C-276	Hot fin., annealed, aged Hot rolled	As received	758
		27% cold work	1237
625 716	Hot fin., annealed Annealed, aged	17% cold work	1195
		4% cold work	1186
Ti Gr2	Annealed (620°C, 1 h)	As received	380

^a Provided by producer.

Analysis

Although permeation methods have been used extensively, they suffer from several disadvantages, as discussed elsewhere.¹⁰ The main theoretical limitation is that most, if not all, diffusion/trapping models for these methods are based on an input boundary condition of constant concentration. Hence, these models are strictly applicable only for charging conditions without any entry limitation.

In the case of HIAPP, a model has been developed to allow for the effect of trapping on diffusion for cases involving either a constant concentration or a constant flux at the input surface.^{4,9} The constant flux model was found to apply to all alloys studied to date. In this model, the rate of hydrogen ingress is controlled by diffusion but the entry flux of hydrogen is restricted, which results in interface-limited diffusion control. Solution of the diffusion equation for a constant flux condition gives the following expression for the total anodic charge ($C\ m^{-2}$):

$$q'(\infty) = FJ t_c \{1 - e^{-R/(\pi R)}^{1/2} - [1 - 1/(2R)] \operatorname{erf}(R^{1/2})\} \quad (1)$$

where F is the Faraday constant, J is the ingress flux in $\text{mol}\ m^{-2}\ s^{-1}$, and $R = k_a t_c$. The charge $q'(\infty)$ is equated to the charge (q_a) associated with the experimental anodic transients. q_a can be associated entirely with absorbed H, since the adsorbed charge is almost invariably negligible.

k_a is an apparent trapping constant measured for irreversible traps in the presence of reversible traps. It is related to the irreversible trapping constant (k) by kD_a/D_L where D_a is the apparent diffusivity and D_L is the lattice diffusivity of H. The magnitude of k depends on the density of particles or defects (N_i) providing irreversible traps, the radius (d) of the trap defects, and the diameter (a) of the metal atom¹¹:

$$k = \frac{4\pi d^2 N_i D_L}{a} \quad (2)$$

The term, $d^2 N_i$, represents the trapping capability and underlies the use of k as an index of an alloy's intrinsic susceptibility to HE.

For the constant flux model to be applicable, it must be possible to determine a trapping constant for which J is independent of charging time. Data for q_a could in fact be fitted to Eq. (1) to obtain values of k_a and J that satisfied this requirement at each potential. Experimental and fitted values of q_a for various charging times are compared in Fig. 1, which illustrates the level of agreement obtained for the alloys in this work.

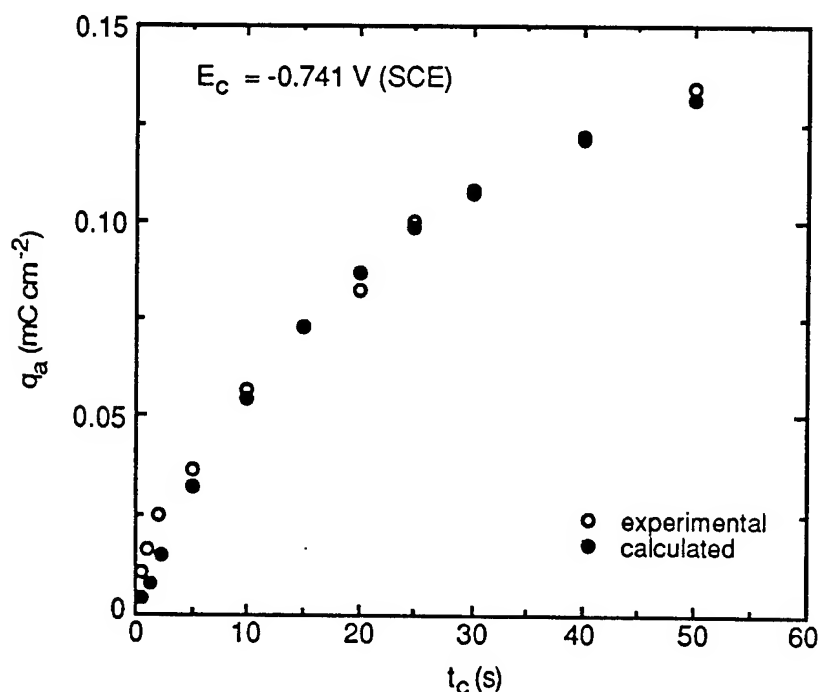


Figure 1. Dependence of anodic charge on charging time for Ti grade 2.

Results

The alloys were studied as a series of groups, which were then merged to provide an overall comparison of the irreversible trapping constants. The values of k_a and k for each group are summarized in Table 3. The first group consisted of a high-strength steel (AISI 4340), and two nickel-containing alloys (K-500 and 35N).⁴ The aim was to determine whether the irreversible trapping constants might assist in explaining differences observed in HE resistance between high-strength steels and nickel-base alloys. The values of both k and J for the steel were higher than those for alloys K-500 and 35N. Hence, both the irreversible trapping characteristics and the amount of H entering could account for the steel being less resistant to HE than the two nickel-containing alloys.

Table 3
Trapping Parameters

Alloy	k_a (s ⁻¹)	D_L/D_a	k (s ⁻¹)
4340 Steel	0.008 ± 0.001	500	4.0 ± 0.5
K-500 Unaged	0.017 ± 0.003	2.0	0.034 ± 0.006
Aged	0.021 ± 0.003	2.0	0.042 ± 0.006
35N	0.026 ± 0.002	1	0.026 ± 0.002
718	0.031 ± 0.002	4.0 ± 0.5	0.124 ± 0.024
925	0.006 ± 0.003	4.6 ± 0.6	0.034 ± 0.004
18Ni Steel	0.005 ± 0.002	300 ± 90	1.50 ± 1.05
	0.010 ± 0.005^a	300 ± 90	3.00 ± 2.40
C-276	0.025 ± 0.003	2.6 ± 0.8	0.090 ± 0.030
	0.019 ± 0.010^a	2.6 ± 0.8	0.068 ± 0.051
625	0.004 ± 0.002	2.6 ± 0.8	0.014 ± 0.010
716	0.054 ± 0.004	3.8 ± 0.8	0.20 ± 0.06
Ti grade 2	0.028 ± 0.002	1	0.028 ± 0.002
	0.012 ± 0.006^b	1	0.012 ± 0.006

^a Quasi-irreversible trapping; ^b Hydride formation.

Two further groups of alloys were then studied: precipitation-hardened alloys (718, 925, and 18Ni maraging steel)⁵ and work-hardened alloys (625 and C-276).⁶ Alloys 625, 718, and 925 were each characterized a single type of irreversible trap, whereas alloy C-276 and 18Ni maraging steel were characterized by both an irreversible trap and a quasi-irreversible trap. In irreversible trapping, the rate constant for release is assumed to be zero, whereas for the quasi-irreversible case,

the release constant is not zero but is too small to achieve local equilibrium between the lattice and trapped H.⁵ The maraging steel had the highest value of k , followed by alloys 718, C-276, 925, and 625. It is apparent from its value of k that the maraging steel is intrinsically somewhat less susceptible than 4340 steel. Test results have in fact shown that 18 Ni(250) maraging steel is more resistant to cracking than 4340 steel,¹² so the differing susceptibility of the two steels was matched by their actual resistances to HE.

A similar parallel was found to exist for the 18Ni steel and alloy 718. Stress-rupture tests during electrolytic charging have shown that 18Ni (1723 MPa) maraging steel undergoes severe HE, whereas alloy 718 exhibits negligible embrittlement.¹³ Likewise, gas-phase charging tests showed from the reduction in strength that the maraging steel was less resistant than alloy 718, although the embrittlement in both cases was characterized as extreme.¹³

No Ni-base alloys in the 900 series were included in the electrolytic embrittlement tests. However, gas-phase studies on alloy 903 have shown that short exposure to high-pressure hydrogen is not detrimental, though prolonged exposure, particularly at higher temperatures, can reduce ductility.¹⁴ In contrast, alloy 718 undergoes extreme embrittlement under gas-phase charging, as noted above. These results suggest that alloy 903 and, by implication, alloy 925 are less sensitive than alloy 718 to HE. Hence, the irreversible trapping constants of the three precipitation-hardened alloys are consistent with their relative resistances to HE observed in failure tests.

A similar comparison of the resistances of alloys C-276 and 625 is complicated by their sensitivity to cold work. However, the ranking of these alloys can be assessed indirectly from results for alloys C-276 and G.¹⁵ Time-to-failure and crack propagation data showed that alloy C-276 has a greater tendency to HE than alloy G cold-worked to an equivalent degree. Alloys G and 625 are comparable in their levels of Cr, Mo, and Nb+Ta, so they might be expected to be similar in their resistance to HE. For the degree of cold work involved, alloy C-276 should therefore be less resistant to HE than alloy 625,⁶ which coincides with the order of their trapping constants.

A lack of relevant data in the literature makes it difficult to determine whether the two cold-worked alloys fit in with the other alloys on the basis of their k values. The difficulty in evaluating the position of the cold-worked alloys is compounded by some uncertainty in these values. Nevertheless, the trapping constants for alloys 625 and 718 show a significant difference, and the sequence of values is consistent

with results from C-ring and U-bend exposure tests that indicated alloy 625 is more resistant to cracking than alloy 718.¹⁶

If allowance is made for the uncertainty in k , the position of alloy 625 is comparable to that of alloy 35N. Tests using C-ring specimens of these alloys showed that the time-to-failure of unaged alloy 625 with 59% cold reduction is intermediate between those for 35% and 51% cold reduced alloy 35N in the aged condition.¹⁷ Alloy 625 with 17% cold work, as was used in the present study, should withstand a longer exposure time than the same alloy with 59% cold work and therefore should be at least as resistant to HE as alloy 35N in the condition of interest (40-50% cold reduced and aged). In fact, the 625 specimen may be more resistant than the 35N alloy, as implied by their values of k . Thus, the order of the trapping constants parallels the relative resistance of these alloys to HE.

Ti grade 2 was also examined.⁶ It exhibited two values of k , depending on the overpotential (Fig. 2) and therefore on the level of H in the alloy. Hydride precipitates have been observed in Ti grade 2 at H levels above ~100 ppm, but gross embrittlement does not result until much higher levels.¹⁸ Thus, the similarity observed in the values of k for low-H Ti grade 2 and alloy 925 fits their relative resistance to HE in that both alloys must be exposed for long times to cause degradation of their mechanical properties.^{14,18} Furthermore, the higher value of k for Ti grade 2 coincides with its decreased resistance to embrittlement at high enough H concentrations.

An exception to these trends was observed with alloy 716, which is an age-hardenable alternative to alloy 625.¹⁶ Alloy 716 had a k of 0.2, which is the highest value among those for the nickel-base alloys and indicates that this alloy is intrinsically the most susceptible to HE. However, tests with C-ring and U-bend specimens have shown that it is comparable to alloy 625 of similar yield strength in being able to withstand exposure in aggressive environments.¹⁶ A likely explanation is that, although alloy 716 has a high intrinsic susceptibility, the H concentration at the dominant traps remains below the critical level required to initiate cracking. The entry flux was found to be low in the acetate buffer and could well have been low enough in the cracking test environments to delay failure in most cases (up to 1000 h). Thus, the resistance to cracking observed for alloy 716 was believed to be associated with the low entry flux of hydrogen.

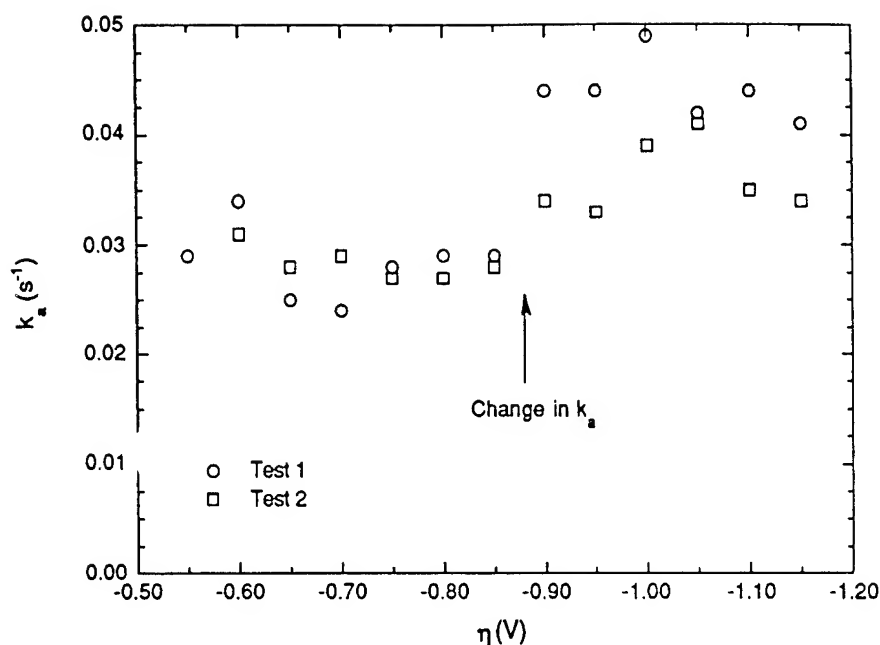


Figure 2. Variation in k_a with overpotential for Ti grade 2.

Discussion

The alloys studied were generally characterized by a single type of irreversible trap, but in some alloys the principal irreversible type of trap was supplemented by other traps of either a quasi-irreversible type or another irreversible type. Values of k associated with the principal irreversible traps are listed in Table 4 for all the alloys except 716. They are also presented graphically in Fig. 3 to highlight differences between them.

The steels, particularly 4340, exhibit high values of k that are indicative of a high intrinsic susceptibility to HE, whereas the nickel-base alloys are characterized by lower values of k and are therefore intrinsically less susceptible. Differences in the susceptibility of the nickel-base alloys are smaller than those for the steels but are clearly discernible. In particular, the trapping constants for alloys within groups defined by thermomechanical treatment (precipitation- and work-hardening) indicate that the susceptibilities can vary significantly.

For most alloys, there appears to be a correlation between the intrinsic susceptibility, as represented by k , and the actual resistance to HE observed in failure tests. This correlation suggests that the observed resistance to HE is determined primarily by the alloy's intrinsic

susceptibility — that is, by the irreversible trapping characteristics. Thus, the entry flux generally has only a secondary effect on the HE resistance.

Table 4
Irreversible Trapping Constants

Alloy	$k (s^{-1})$
4340 steel	4.0 ± 0.5
18Ni (300) steel	1.50 ± 1.05
718	0.128 ± 0.024
C-276 (27% cold work)	0.090 ± 0.030
K-500	0.040 ± 0.010
Ti grade 2 (high H)	0.040 ± 0.008
925	0.034 ± 0.004
Ti grade 2 (low H)	0.028 ± 0.002
35N	0.026 ± 0.002
625 (17% cold work)	0.014 ± 0.010

Exceptions to this correlation can be expected in cases where the ingress flux for an alloy is low enough that the alloy is relatively resistant to cracking even though it might have a high intrinsic susceptibility. Such an exception was observed with alloy 716. The intrinsic susceptibility of

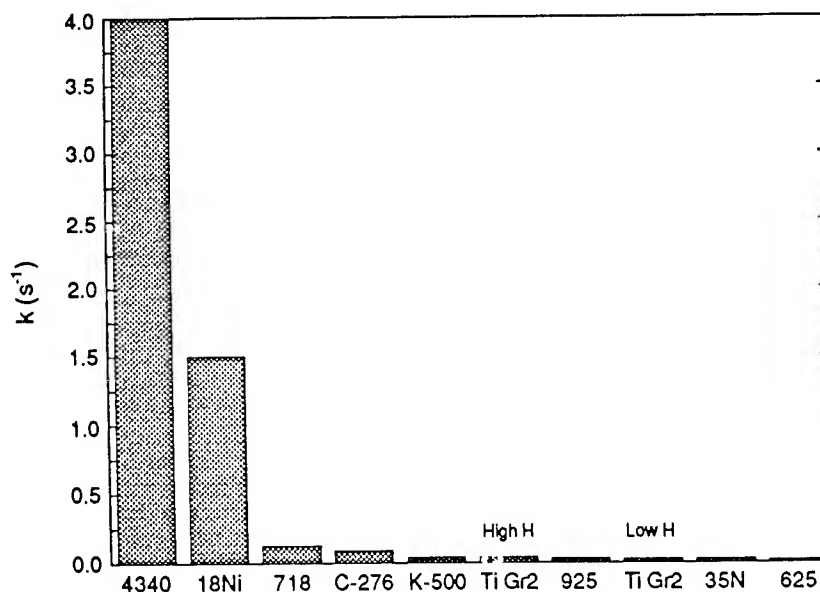


Figure 3. Variation in k for the different alloys.

this alloy was shown to be high ($k = 0.2$), yet the entry flux was apparently low enough that the alloy generally did not undergo cracking during exposure in aggressive environments for periods up to 1000 h.

The use of k to provide an index of HE susceptibility can be justified on the basis of Eq. (2), but there remains the question of why such a relatively simple parameter has the apparent ability in most cases to indicate the relative resistance actually observed to HE. Some insight may be gained by considering k , which encompasses the trapping capability (d^2N_i) as well as the alloy-specific characteristics of metal atom size and lattice diffusivity. The trapping capability has a strong influence on the critical concentration (C_k) required to initiate cracking at traps, while the diffusivity reflects the ease of H transport to different sites, including traps. Since the likelihood of crack initiation is highly dependent on both C_k and H accumulation, it is perhaps not surprising that k is effective as an index of susceptibility in being able to indicate the actual resistance of most alloys to HE. Underlying this rationale is the implication that, despite differences between alloys, the H entry flux is generally not low enough to become the controlling factor.

Finally, it should be noted that the density of particles or defects providing irreversible traps can be calculated from k , or k_a , by using Eq. (2). The trap radius (d) is estimated from the dimensions of heterogeneities that are potential irreversible traps, and trap densities are then calculated for the different values of d . In this way, the dominant irreversible trap can be identified by comparing the values of N_i with the actual concentrations of specific heterogeneities. Identification of the primary irreversible traps in the various alloys is described elsewhere.⁴⁻⁸

Summary

For a wide range of alloys, a correlation exists between the intrinsic susceptibility, as defined by the irreversible trapping constant, and the observed resistance to HE. Thus, the HE resistance appears to be determined primarily by the alloy's intrinsic susceptibility. This relationship implies that generally the H entry flux has only a secondary effect on the HE resistance, suggesting that it is not low enough to become the controlling factor for most alloys. However, in one case (alloy 716), the resistance to HE can be attributed to a low entry flux.

The irreversible trapping constant, by virtue of the observed correlation, appears to be an indicator of the relative resistance to HE for most alloys, and as such, it can be used to predict the relative resistance of alloys in a particular environment. However, the predicted relative resistance may not be reliable in cases where H entry is severely restricted. The ability of k to provide an indication of the relative

resistance to HE seems to be attributable to its dependence on both the trapping capability and the diffusivity. The combination of these two characteristics is crucial for crack initiation and therefore provides a rationale for the correlation observed between k and the actual resistance to HE.

Acknowledgment

Financial support of this work by the Office of Naval Research under Contract N00014-86-C-0233 is gratefully acknowledged.

References

1. I. M. Bernstein and G. M. Pressouyre, in *Hydrogen Degradation of Ferrous Alloys*, R. A. Oriani, J. P. Hirth, and M. Smialowski, Eds., (Noyes Publications, 1985), p. 641.
2. G. M. Pressouyre and I. M. Bernstein, *Metall. Trans.* **9A**, 1571 (1978).
3. G. M. Pressouyre and I. M. Bernstein, *Acta Metall.* **27**, 89 (1979).
4. B. G. Pound, *Corrosion* **45**, 18 (1989); **50**, 301 (1994).
5. B. G. Pound, *Acta Metall.* **38**, 2373 (1990).
6. B. G. Pound, *Acta Metall.* **39**, 2099 (1991).
7. B. G. Pound, *Corrosion* **47**, 99 (1991).
8. B. G. Pound, *Scripta Metall.* **29**, 1433 (1993).
9. R. McKibbin, D. A. Harrington, B. G. Pound, R. M. Sharp, and G. A. Wright, *Acta Metall.*, **35**, 253 (1987).
10. B. G. Pound, in *Modern Aspects of Electrochemistry*, J. O'M. Bockris, B. E. Conway, and R. E. White, eds. (Plenum, New York, 1993), No. 25, p. 63.
11. B. G. Pound, R. M. Sharp, G. A. Wright, *Acta Metall.*, **35**, 263 (1987).
12. T. P. Groeneveld, E. E. Fletcher, and A. R. Elsea, "A Study of Hydrogen Embrittlement of Various Alloys," Tech. Support Package to Tech. Brief No. 67-10141, (Washington D.C.: NASA, 1967), p. 135.
13. R. J. Walter, R. F. Jewett, and W. T. Chandler, *Mater. Sci. Eng.* **5**, 98 (1967/70).
14. C. G. Rhodes and A. W. Thompson, *Metall. Trans.*, **8A**, 949 (1977).
15. D. A. Mezzanotte, J. A. Kargol, and N. F. Fiore, *Metall. Trans.*, **13A**, 1181 (1982).
16. R. B. Frank and T. A. DeBold, *Properties of an Age-Hardenable, Corrosion-Resistant Nickel-Base Alloy*, *Corrosion* **88**, Paper No. 75, National Association of Corrosion Engineers, Houston, TX (1988).
17. R. D. Kane, M. Watkins, D. F. Jacobs, and G. L. Hancock, *Corrosion*, **33**, 309 (1977).
18. R. W. Schutz and D. E. Thomas, in *Metals Handbook*, 9th ed., Vol. 13 (American Society for Metals, Metals Park, OH, 1987), p. 669.

Hydrogen Effects on Some Titanium Aluminides at Ambient Temperature

Mr. James A. Smith
Naval Research Laboratory
Code 6314
Washington, DC 20375-5000

It is common to describe the corrosion damage of structural metals and alloys in terms of the eight basic types of metal/alloy corrosion: general corrosion, galvanic corrosion, crevice corrosion, pitting attack, erosion corrosion, selective leaching, intergranular corrosion, and environmental assisted fracture. The latter, environmental assisted fracture, may be further divided into subheadings of stress corrosion cracking, corrosion fatigue, and hydrogen embrittlement. Of particular interest is hydrogen embrittlement because of the serious problems and/or catastrophic failures that may result from the involvement of structural materials such as titanium and titanium alloys with hydrogen.

Previous investigators have shown that Ti-6Al-4V and indeed most conventional titanium alloys are susceptible to hydrogen embrittlement in hydrogen charging environments (22). Titanium aluminides, the materials studied in this report, are also believed to be subject to hydrogen embrittlement but preliminary studies show that the gamma based aluminides may be less prone to absorbing hydrogen at ambient and elevated temperatures than conventional Ti alloys (21). The major draw for use of these materials is the fact that they possess outstanding high-temperature strength, good creep behavior, and low density. Possession of these characteristics has warranted their consideration for a wide range of applications from automotive turbo charger motors, pistons, and valve material to advanced aerospace applications involving temperatures up to 1045°C. Therefore, it is important to ascertain their hydrogen embrittlement behavior if hydrogen-related property damage is to be understood and, hopefully, controlled in these materials.

Experimental Overview

A. Materials

The material used in this study was produced by Martin Marietta Laboratory. The material was arc melted, cast in a chilled copper mold, forged, and annealed at approximately 1200°C. The TiB₂ particulate dispersion was introduced in situ using XD™ processing (29). The chemical compositions of these cast materials are given in Table I.

B. Procedures

1. Polarization Test

Polarization curves were measured at a sweep rate of 0.2 mV/s in deaerated 0.6N NaCl solutions, using a saturated calomel (SCE) reference electrode. The working electrode (~13 mm disc) was polished through 600 grit SiC paper, then cleaned and rinsed with distilled water, and finally degreased with acetone prior to use.

2. Hydrogen Permeation Tests

Hydrogen permeation experiments were conducted on 1 mm thick discs using the electrochemical method. The experimental set-up, in Figure 1, shows an input chamber that contains the charging solution (0.6N NaCl) and an exit chamber that contains 0.2N NaOH. Both solutions were purged with high purity argon to remove dissolved oxygen. The permeation discs are surface ground on both sides thorough 600 grit paper and, subsequently, the exit surface is plated to provide several hundred angstroms of palladium. The purpose of the palladium plate is to provide a more uniform surface for the evolution of hydrogen and to provide the necessary surface conditions to ionize completely the hydrogen reaching the exit surface.

3. CERT (constant extension rate testing)

All CERT (constant extension rate testing) studies were performed at room temperature using a Cortest constant extension testing machine at a strain rate of 1.45×10^{-6} /sec. Data acquisition and analyses were performed using a computer.

Results and Discussion

A. Structure and Mechanical Properties:

Optical micrographs of cast Ti-48%Al with 5 Vol% and 10 Vol% TiB₂ are shown in Figs.2-3. The microstructures of these materials consist of a mixture of gamma (γ) grains and lamellar ($\gamma+\alpha_2$) grains. The TiB₂ particulate dispersion introduced in situ using XDTM processing tends to grow in clusters and exhibits a blocky morphology.

For the investigated alloys, Ti-48%Al+5Vol%TiB₂ and Ti-48%Al+10 Vol% TiB₂, the mechanical properties of ultimate yield strength and % elongation together with the physical properties of diffusivity and permeation current density are listed in Table 2. The data show that the diffusivities of the two alloys are about the same, and that the alloy possessing the highest volume percentage of TiB₂ possesses the greater ultimate yield strength. It is further noted that the yield strengths for Ti-48%Al+5 Vol% TiB₂ and Ti-48%Al+10 Vol% TiB₂ decrease respectively, 16 and 20 % when cathodically polarized at -1400mV in 0.6N NaCl. Reductions in the % elongation resulting from hydrogen charging show even larger decreases approximately 43% for Ti-48%Al+5 Vol% TiB₂ and approximately 50%

for Ti-48%Al+10 Vol% TiB₂. These figures, however, are somewhat tentative because of the small values involved in the measurements.

B. Polarization Study

Figure 4a. shows potentiodynamic polarization scans for the titanium aluminides reinforced with 5 Vol% TiB₂ and 10 Vol % of TiB₂. It is noted that an increase in the concentration of TiB₂ from 5 to 10 Vol% results in a significant diminution of the corrosion potential (E_{corr}), shifting it approximately 685mV in the cathodic direction and creating an irregular passive region that extends from the active E_{corr} value of alloy Ti-48%Al +10 Vol% TiB₂ to a value comparable to the more noble E_{corr} value of Ti-48%Al+5 Vol% TiB₂. The Ti-48%Al+5 Vol% TiB₂ alloy does not possess a passive region but goes immediately into transpassive behavior under anodic polarization.

In Figure 4a., the broken lines represent cathodic reactions that are thermodynamically possible on titanium surfaces during cathodic polarization in near neutral 0.6N NaCl solutions. It is noted that the discontinuities viewed in the curve for the low TiB₂ material, alloy #82, correspond to the commencement of cathodic reactions as reported by Pourbaix (34). At approximately -700 mV corresponds to the reaction $2H^+ + 2e^- \rightarrow H_2\uparrow$ and the discontinuity at approximately -1300 mV, corresponds to the reaction $H_2O + e^- \rightarrow OH^- + 1/2 H_2\uparrow$. Somewhat less distinct are the matchings of the cathodic reactions with discontinuities occurring in the cathodic polarization of alloy #83. It is suspected that increased chemical involvement of TiB₂ particulate at the higher TiB₂ particulate level causes the blurred matchings observed for this material.

In previous observations of cathodically charged titanium alloys in near neutral salt solutions it appeared that hydrogen was not readily absorbed by the titanium alloys even though the application of impressed current forced the potential well below the hydrogen evolution line (33). Hydrogen absorption, however, was found to occur naturally when the open circuit potential (E_{corr}) of the metal or alloy resides in the region below the hydrogen evolution line as seen in Fig.4b. This condition is encountered at very high and very low pH values. For the high TiB₂ content material, alloy #83, the fact that the E_{corr} value of -330 mV appears much closer to the $2H^+ + 2e^- \rightarrow H_2\uparrow$ evolution line than the E_{corr} value of alloy #82 suggests that under cathodic charging there is a greater possibility of significant hydrogen uptake in this material than in the low TiB₂ content alloy #82.

In these TiB₂ containing Ti-48%Al alloys the effect of hydrogen appears to involve a complex interplay between the amount and accumulation of hydrogen at an interface and the size and distribution of the microstructural features. This effect is viewed as being composed of two factors:

1. Chemical
2. Microstructural.

The first factor is denoted by the decrease in E_{corr} with increase in Vol% TiB₂ and the increase in cathodic Tafel slope with a decrease in Vol% TiB₂. Generally, the greater the magnitude of the cathodic Tafel slope the more difficult the reduction of

hydrogen. The second factor is denoted by the decrease in permeation current density (Table 2.) with increase in Vol% TiB₂. The latter observation suggests that hydrogen trapping may occur particularly in the alloy containing the higher TiB₂ content.

C. Hydride Formation

Microhardness values across a Ti-48%Al+10 Vol%TiB₂ specimen after 720 hrs of H-permeation at -1400mv in 0.6N NaCl solutions showed significant increases at the specimen center (Fig.5). Xray diffraction analysis of this high hardness region indicated the presence of titanium hydride (Fig.6). Similar increases were not detected in the Ti-48%Al+5 Vol%TiB₂ alloy (Fig.7). This observation indicates that hydride formation is possible in this material and suggests that the presence and amount of hydride may depend on the concentration of TiB₂.

Hydride formation in Ti-48%Al+10 Vol%TiB₂ in 0.6N NaCl at -1400mV is noteworthy because these and similar alloys are being considered for such diverse applications as aerospace and automobile systems. The formation of TiH_x by cathodic polarization would limit their use as structural materials. In view of the aforementioned observations, extreme care should be taken to guard against situations that subject these alloys to high cathodic currents for long periods of time.

The original purpose for the addition of TiB₂ to the TiAl base composition was to improve creep and "ductilize" the material. As the data show no significant benefits in ductility or fracture properties were obtained. The fracture mode remains transgranular cleavage for both the 5 and 10 Vol%TiB₂ material. Thus the addition of TiB₂ does not appear to preclude the occurrence of transgranular cleavage. The room temperature deformation behavior of the gamma titanium aluminides has been studied at this laboratory and others (25,35,36). These studies show that no well defined dislocation substructure is found in these materials, therefore, no persistent or recurrent slip band formation is expected. Thus, the classical model of crack initiation at recurrent/persistent slip bands and subsequent Stage I and Stage II crack growth does not hold true in these materials. It seems reasonable that microplastic deformation at stress levels close to the fracture stress and the absence of extensive activity of [011] and [101] easy-glide dislocations could easily lead to local stress concentrations. Such local stress concentrations could then initiate transgranular crack nucleation and propagation giving rise to the transgranular cleavage fracture seen in these materials. Additionally, in the case of the 10 Vol%TiB₂ material prolonged exposure to cathodic potentials could lead to the formation of hydrides which would further degrade material performance.

CONCLUSIONS

1. Increasing the Vol% of TiB₂ from 5 to 10 % does not preclude the low temperature cleavage-like failure experienced by titanium aluminide alloy Ti-48%Al in air and aqueous salt solution.

2. Cathodic polarization in 0.6N NaCl solutions produces detectable amounts of titanium hydrides in alloy Ti-48%Al+10 Vol%TiB₂ after 720 hrs.
3. No hydrides are detected in the alloy containing 5 Vol% TiB₂.
4. Permeation data indicate low level hydrogen trapping in titanium aluminide alloy Ti-48%Al+10 Vol%TiB₂ after 720 hrs.

ACKNOWLEDGMENTS

The author thanks D.A. Meyn and P. Pao for useful discussions during the preparation of this work. The author also thanks Advanced Funding Initiative Coordinator K. Sadananda for providing financial support for this work.

REFERENCES

1. Hideki Hagi, Trans. of the Japan Institute of Metals, Vol. 27, No. 4, 233-240 (1986).
2. T. Tanabe, K. Sawada, and S. Imoto, Trans. of the Japan Institute of Metals, Vol. 27, No. 5, 321-327 (1986).
3. R. M. Latanision and M. Kurkela, Corrosion, Vol. 39, No. 5, 174-181 (1983).
4. Acta Metallurgica Sinica Series A, 4.
5. D. Warren, Material Performance, Vol. 26, No. 1, 38-45 (1987).
6. B. B. Pound, SRI International Final Report, #N00014-86-C-0233, (Nov 1990).
7. B. G. Pound, Corrosion, Vol. 45, 18-25 (1989).
8. R. B. Hutchings, A. Turnbull, and A. T. May, Scripta Metall. Mater., Vol. 25, 2657-2662 (1991).
9. N. Kishimoto, T. Tanabe, T. Suzuki, and H. Yoshida, Journal of Nuclear Materials, Vol. 127, 1-9 (1985).
10. Y. Y. Li and Z. S. Xing, Journal of Nuclear Materials, Vol. 169, 151-157 (1989).
11. R. Dus and M. Smialowski, Acta Metallurgica, Vol. 15, 1611-1616 (1967).
12. Morihiko Nakamura, Kenki Hashimoto, and Tokuzo Tsujimoto, Journal of Material Research, Vol. 8, No. 1, 68-77 (1993).
13. H. A. Lipsitt, "Titanium Aluminides An Overview," High Temperature Ordered Intermetallic Alloys, ed. C.C. Koch et al. (Boston, MA):Materials Research Society, 351-364 (1985).
14. S.M.L. Sastry, T.C. Peng and L.P. Beckerman, Metall. Trans. A, Vol. 15A, 1465-1474 (1984).
15. H.A. Lipsitt, Mat. Res. Soc. Symp. Proc., Vol. 39, Materials Research Society (1985).
16. C. Nishimura and C.T. Liu, Acta Metall Mater., Vol. 40, No.4, 723-731 (1992).

17. G.M. Camus, N.S. Stoloff, and D.J. Duquette, *Acta Metall.*, Vol. 37, 1497 (1989).
18. C.T. Liu and M.T. Takayama, *Scripta Metall. Mater.*, Vol. 24, 1583 (1990).
19. B.J. Berkowitz and C. Miller, *Metall. Trans.* 11A, 1877 (1980).
20. Jia Gao, Yan-Bin Wang, Wu-Yang Chu, and Chi-Mei Hsiao, *Scripta Metall. Mater.*, Vol. 27, No. 9, 1219-1222 (1992).
21. C. T. Liu and Young-Won Kim, *Scripta Metall. Mater.*, Vol. 27, No. 5, 599-603 (1992).
22. Y-W. Kim, *Acta Metall. Mater.*, Vol. 40, 1121-1134, (1992)
23. W.Y. Chu and A.W. Thompson, *Scripta Metall. Mater.*, Vol. 25, 641-644 (1991).
24. L.M. Pike and C.T. Liu, *Scripta Metall. Mater.*, Vol. 27, 1313-1317 (1992).
25. Morihika Nakamura, Kennki Hashimoto, and Tokuzo Tsujimoto, submitted to *J. Mater. Res.*, Vol. 8, 68-77, (1991).
26. E. Manor and D. Eliezer, *Scripta Metall. Mater.*, Vol. 23, 1313-1318 (1989).
27. C.T. Liu, E.H. Lee, and C.G. Mckammey, *Scripta Metall. Mater.*, Vol. 23, 875, (1989).
28. C.T. Liu and W.C. Oliver, *Scripta Metall. Mater.*, Vol. 25, 1933 (1991).
29. L. Christodoulou, P.A. Parrish, and C.R. Crowe, *High Temperature/High Performance Composites*, F.D. Lemkey, S.G. Fishman, A.G. Evans, and J.R. Strife, eds., *MRS proc.*, MRS, Pittsburgh, PA, Vol. 120, pp. 29-34, (1988).
30. E. Smith and J.T. Barnby, *Met. Sci. J.*, Vol. 1, 56, (1967).
31. H.A. Lipsitt, D. Shechtman, and R.E. Schafrik, *Metall. Trans. A.*, Vol. 1A, 1369, (1980).
32. Fumio Hine, Masaki Yasuda, and Hitoshi Sato, *Corrosion*, Vol.33, No.5, 181-185, (1977).
33. R.E. Groover, J.A. Smith, and T.J. Lennox, Jr., *Corrosion*, Vol.28, No.3, pp.101-104, (1972).
34. M. Pourbaix, *Corrosion*, Vol.26, No.6, p267 (1969).
35. F. Appel, P. A. Beaven, and R. Wagner, *Acta Metall. Mater.*, Vol. 41, No.6, 1721-1732 (1993).
36. C.R. Feng, D.J. Michel, and C.R. Crowe, *Scripta Metall. Mater.*, Vol. 23, 241-246, (1989).

TABLE 1.

Alloy	Element (wt. %)		
	Ti	Al	TiB ₂ (Vol%)
#82	66	34	5
#83	66	34	10

TABLE 2.

Mat'l	Envir.	U.T Strength (MPa)	%El	Ecorr (mV)	Diffusivity (cm ² /sec)	H-Perm (nA/cm ²)	Fracture (Mode)
#82	Air	544.3	.14	-	-	-	clv
#82	-1400mV	457.2	.06	-	8.1x10 ⁻¹²	39	clv
#82	0.6N NaCl	-	-	+355	-	-	clv
#83	Air	554.5	.12	-	-	-	clv
#83	-1400mV	443.6	.06	-	8.0x10 ⁻¹²	35	clv
#83	0.6N NaCl	-	-	-330	-	-	clv

where:

#82 - Ti-48%Al+5 Vol% TiB₂

#83 - Ti-48%Al+10 Vol% TiB₂

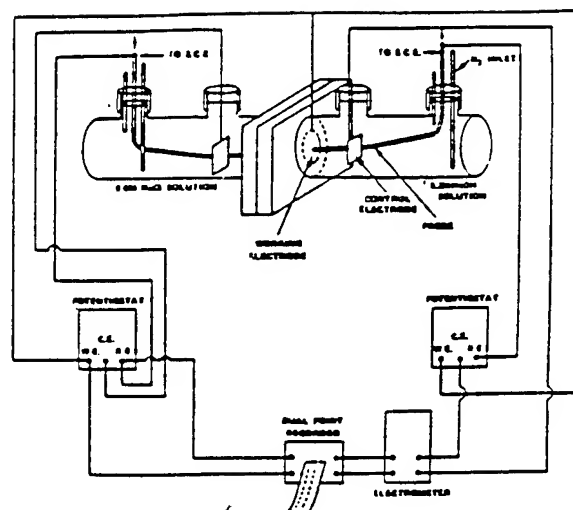


Fig. 1. Experimental set-up for the permeation test.

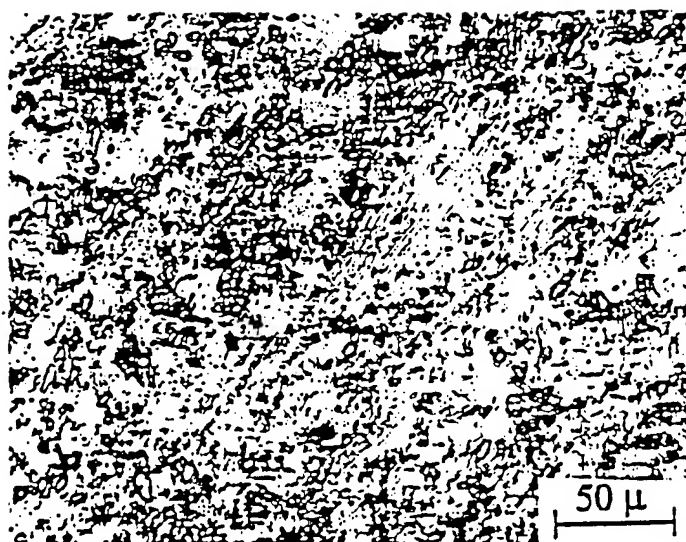
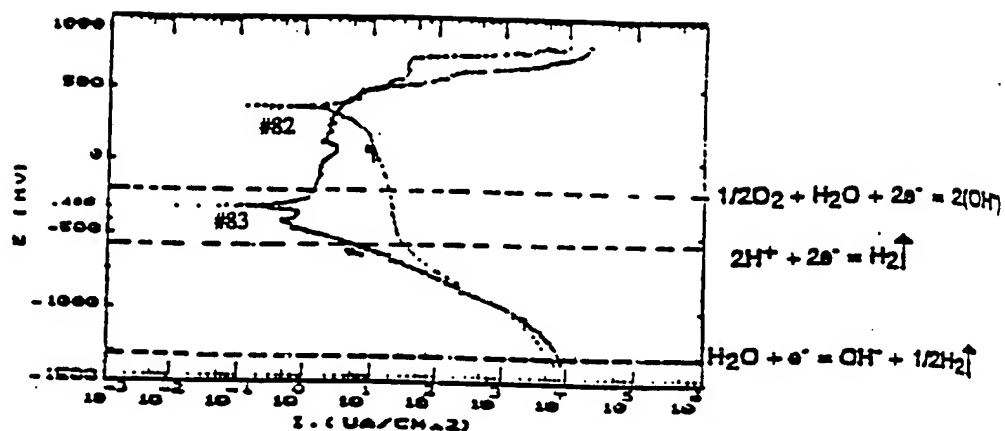


Fig. 2. The microstructure of as-cast Ti-48%Al+5vol%TiB₂.



Fig. 3. The microstructure of as-cast Ti-48%Al+10vol%TiB₂.



Potentiodynamic polarization curves for Ti-48%Al alloys
Fig. 4a. with 5vol% and 10vol%TiB₂ in 0.6N NaCl at ambient temperature.

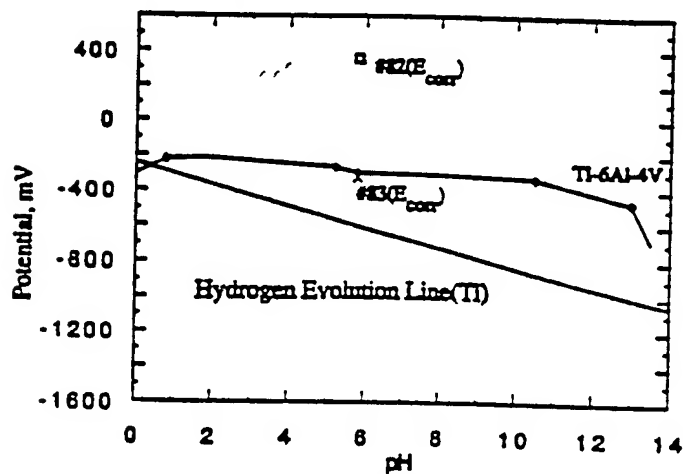


Fig. 4b. Titanium aluminide potentials in 0.6N NaCl after 48 hrs.

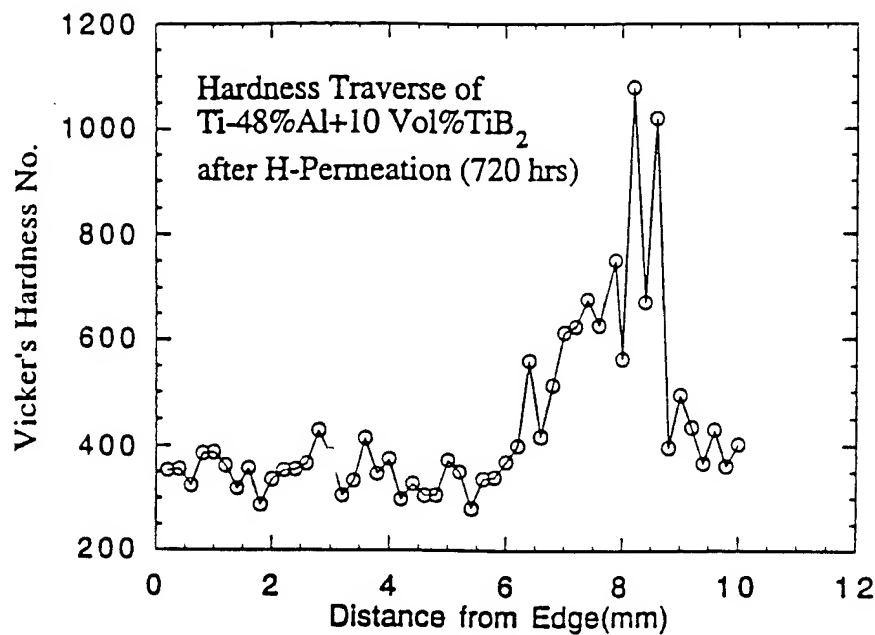


Fig. 5. Hardness traverse for Ti-48%Al+10 Vol%TiB₂

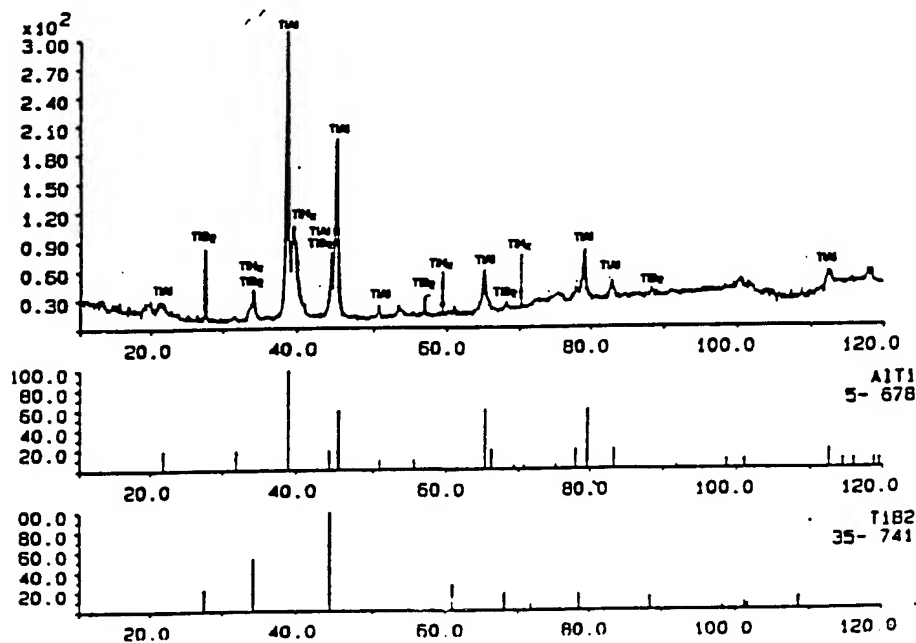


Fig. 6. X-ray diffraction pattern of Ti-48%Al+10 Vol% TiB₂ after H-permeation in 0.6N NaCl for 720 hrs.

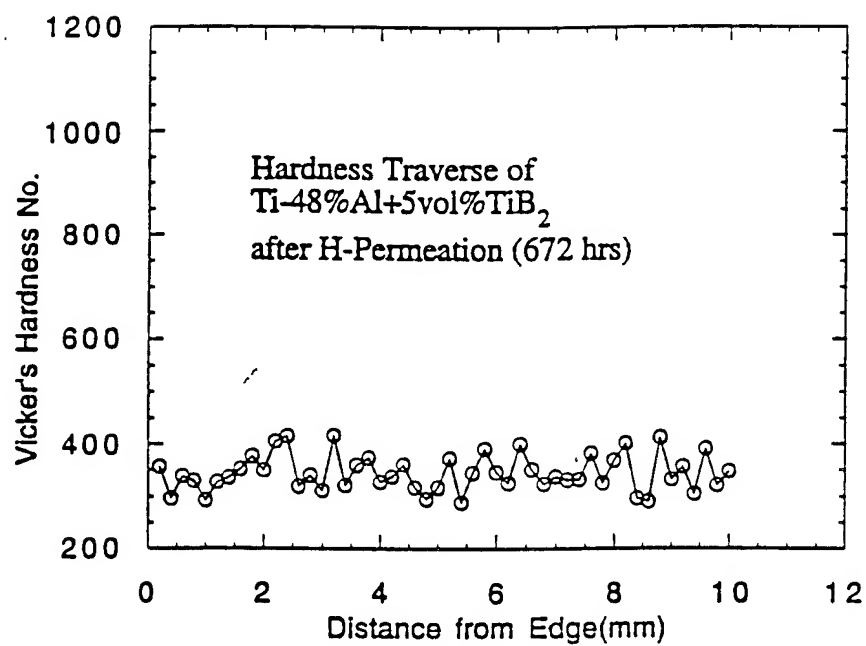


Fig. 7. Hardness traverse for Ti-48%Al+5 Vol% TiB₂

A Fracture Mechanics Based Approach for Quantifying Corrosion Damage

Mr. Mark T. Doerfler and Dr. Alten F. Grandt, Jr.*
School of Aeronautics and Astronautics
Purdue University, West Lafayette, IN 47907-1282
and

Dr. Robert J. Bucci and Mr. Michael Kulak
Aluminum Company of America
100 Technical Drive
Alcoa Center, PA 15069-0001

A fracture mechanics based approach to quantify the influence of initial corrosion damage on structural integrity is described. This approach assumes that corrosion can be approximated by a geometric structural change consisting of a general thickness reduction combined with a localized stress concentration. These two parameters enable quantification of the damage and the application of fracture mechanics principles to corrosion. Several numerical examples of this concept are discussed and a test program, combined with inspection capabilities, is introduced.

Introduction

The ever increasing age of the nation's transport fleet has caused escalated maintenance concerns due to the damage caused by fatigue and corrosion. Material degradation resulting from environmental attack poses a serious threat to the airworthiness of older aircraft, and as a larger number of aircraft operate beyond their original design lives, corrosion becomes more of an issue. Historically, corrosion damage assessment has been almost exclusively qualitative [1,2]. If the safety of so called "aging aircraft" is to be ensured, however, quantitative definitions of corrosion are required. One possible solution to this problem is to apply the principles of fracture mechanics to evaluate the effects of corrosion on

subsequent life. By modeling environmental degradation much like damage caused by fatigue cracking, a protocol for quantitative structural evaluation can be applied to corrosion in aging aircraft.

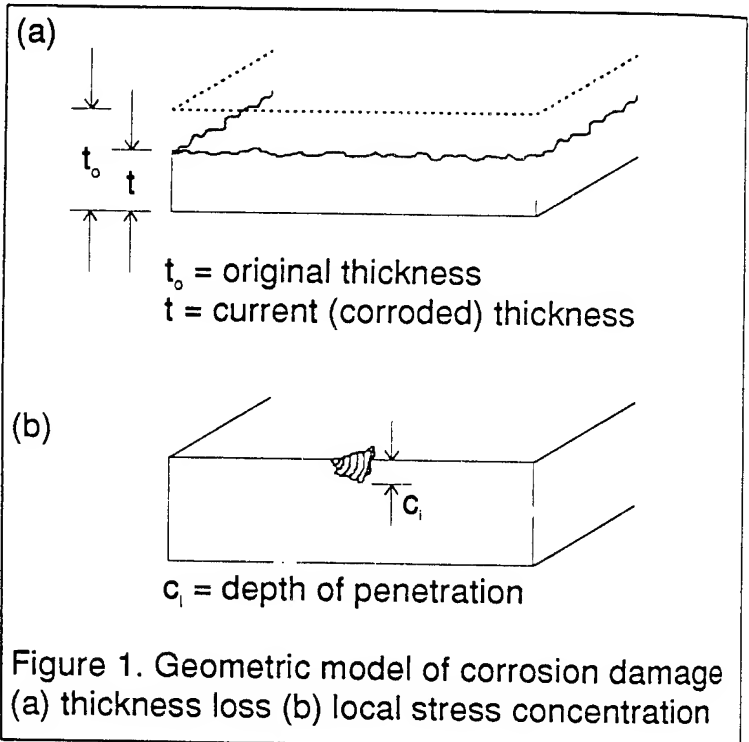
Model of Corrosion Damage

In order to apply fracture mechanics to evaluate corrosion, an initial damage assumption is required. As a first approximation, corrosion damage can be modeled as a combination of the following two geometric changes [3].

1. *Uniform damage*: a general thickness reduction that increases the stress experienced by the remaining structure.
2. *Local damage*: a stress concentration that can be considered to be an equivalent crack.

These two corrosion damage assumptions are presented schematically in Fig. 1. Corrosion in a structure can be modeled either by one of the parameters (exfoliation as a thickness reduction and pitting as local damage, for example) or by a combination of the two.

Once the corrosion parameters are obtained (by non-destructive measurement, for example), fracture mechanics can be applied by using the thickness loss and equivalent flaw size to compute the potential loss in residual strength due to subsequent loading (Fig. 2). More importantly, these geometric parameters can be used to quantify the existing corrosion state with respect to various remaining life criteria. This latter point could enable results to be placed in handbook-type form and therefore used as a structural evaluation tool. Parametric variations on damage, geometry, and loading could be incorporated into such a handbook for use by those responsible for airframe air-



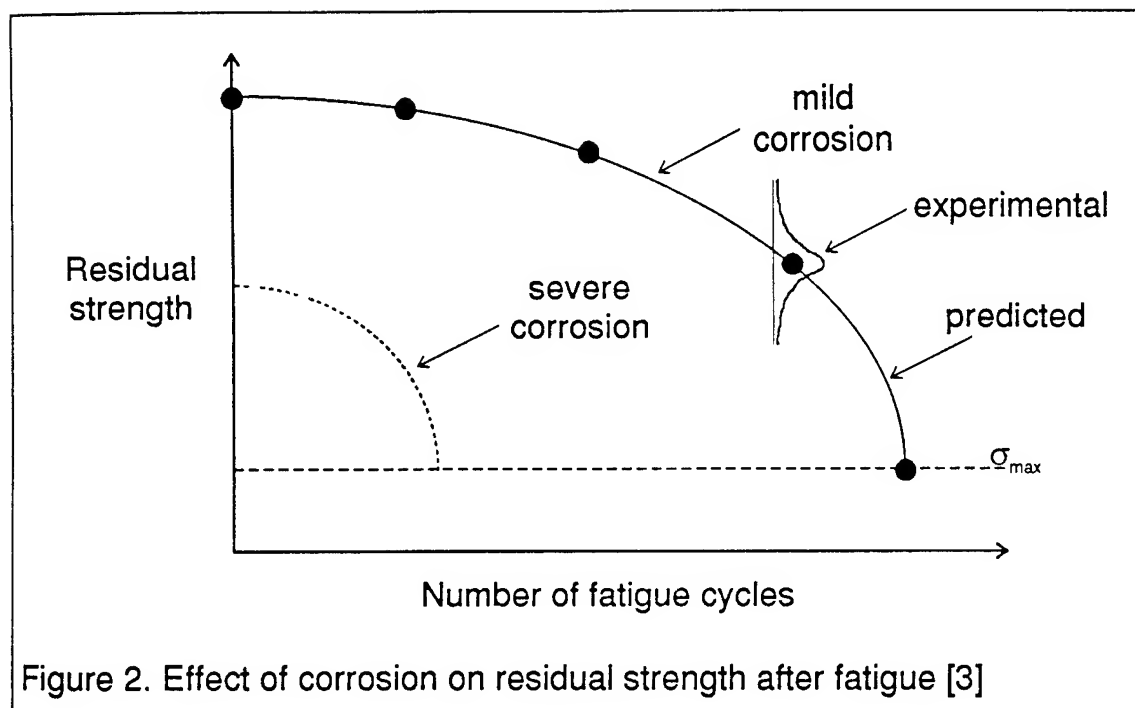


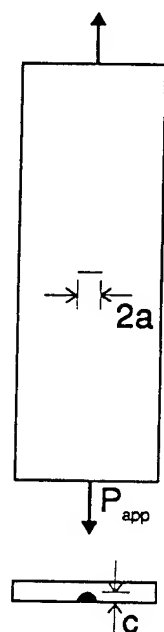
Figure 2. Effect of corrosion on residual strength after fatigue [3]

worthiness. One possible format for this evaluation tool could be a "constant-life diagram," where combinations of thickness reduction and effective flaw penetration are plotted for specific values of life-to-failure under given loading conditions. Several numerical examples are discussed to demonstrate this constant-life concept.

Examples of Corrosion Evaluation Protocol

Example 1. Simple plate specimen

For an initial example of the application of fracture mechanics to quantify corrosion damage, consider the small Al 2024-T3 plate in Fig. 3. Environmental attack on the plate would likely result in a thinning of the original 0.1 inch thickness, and this would correspond to an increase in the stress experienced by the remaining uncorroded thickness (assuming a constant applied cyclic load range). In addition, stress concentrations might result from pitting or some other local damage mechanism. The deepest one of these flaws (weakest link concept) is modeled as an "equivalent" initial crack. Cyclic loading upon this plate (after the environmental attack) would cause fatigue crack growth, and the initial flaw would propagate to failure. For this example, an iterative crack growth algorithm was employed to calculate combinations of thickness reduction and initial flaw depth that correspond to various life-to-failure values for the specimen loaded under a constant applied cyclic load. The results,



Aluminum 2024-T3 plate
height = 6.0 in
width = 2.0 in
original thickness (t_0) = 0.1 in
maximum load (P) = 4,000 lbs
stress ratio (R) = 0.1
initial semi-circular crack
Forman law [3]:

$$\frac{da}{dN} = \frac{C_f (\Delta K)^m}{(1-R)K_f - \Delta K}$$

$$C_f = 3.295 \times 10^{-7}$$

$$m = 2.70$$

$$K_f = 64.886$$

$$\left(\Delta K: \text{ksi}\sqrt{\text{in}}, \frac{da}{dN}: \frac{\text{in}}{\text{cycle}} \right)$$

Figure 3. Surface-cracked plate geometry for the first constant-life example

plotted in Fig. 4 as a constant-life diagram, reveal the relationship of the damage parameters to one another as well as to the expected life of the specimen. The y-axis of the graph corresponds to the initial depth of an assumed semi-circular initial flaw. The knee in the plot of 20,000 cycles-to-failure results from the ability of the plate to withstand a through-the-thickness crack with a thickness loss of 15% or less.

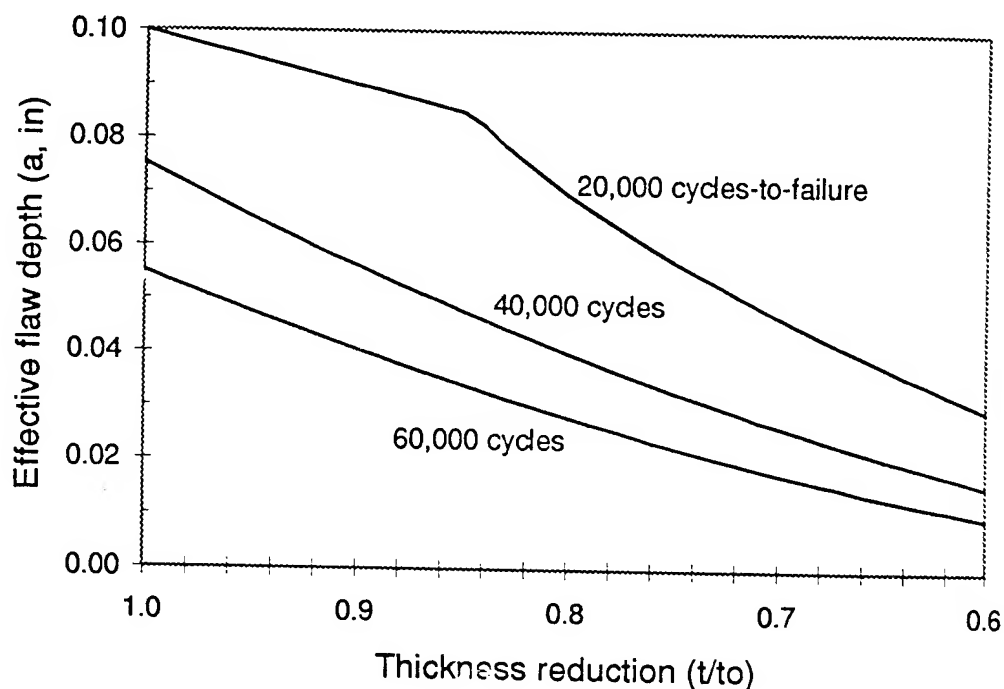


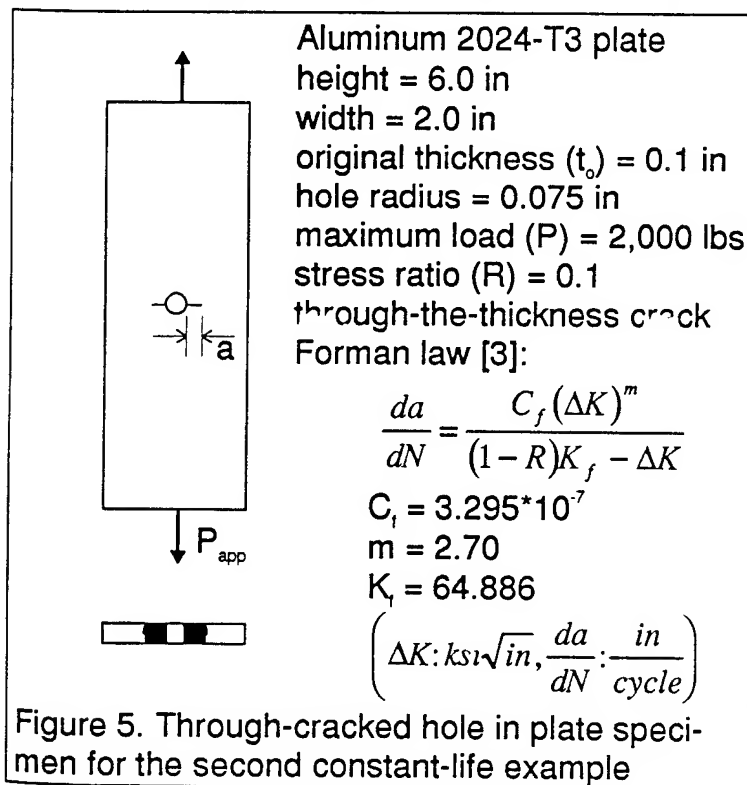
Figure 4. Constant-life diagram for the surface-cracked plate example

Results like those presented in Fig. 4 could be used as a structural evaluation tool by conducting parametric variations in loading conditions and component dimensions so as to include all combinations of interest. The results could be placed in handbook form and looked up according to the dimensions and loading experienced by a particular in-service structure. The corrosion damage to the structure would be measured as a combination of thickness loss and flaw penetration, allowing the corrosion to be quantified by the numerically generated constant-life plot. That is, one could predict the remaining life that a plate would be expected to survive under the specific loading conditions. The parametric variations would similarly allow assessment of damage under other loading conditions as well.

Example 2. Simple hole specimen

Analysis similar to example 1 can be conducted for other geometries as well, and this second example considers a single hole in a plate with symmetric through-cracks. Application of a crack growth algorithm to the Al 2024-T3 specimen presented in Fig. 5 allows one to generate constant-life diagrams similar to those for the simple plate geometry discussed above. Note that for this example, the equivalent flaw is defined by the

surface length rather than the depth of penetration as it was in the initial example. The results of the analysis (Fig. 6) could similarly be used as a structural evaluation tool that would be able to quantify corrosion damage in other like specimens. Parametric variations on the loading and specimen dimensions would additionally allow application of the corrosion definitions to any similar hole specimen with different loading.



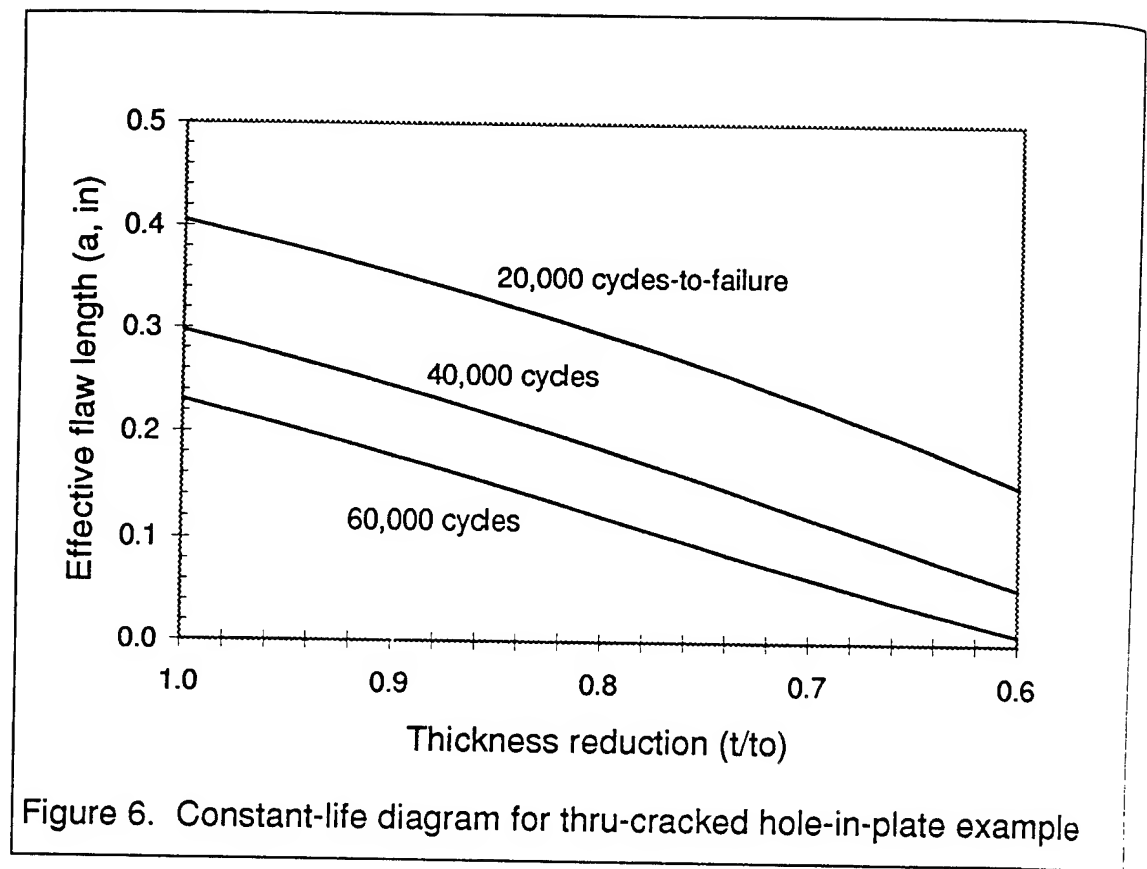
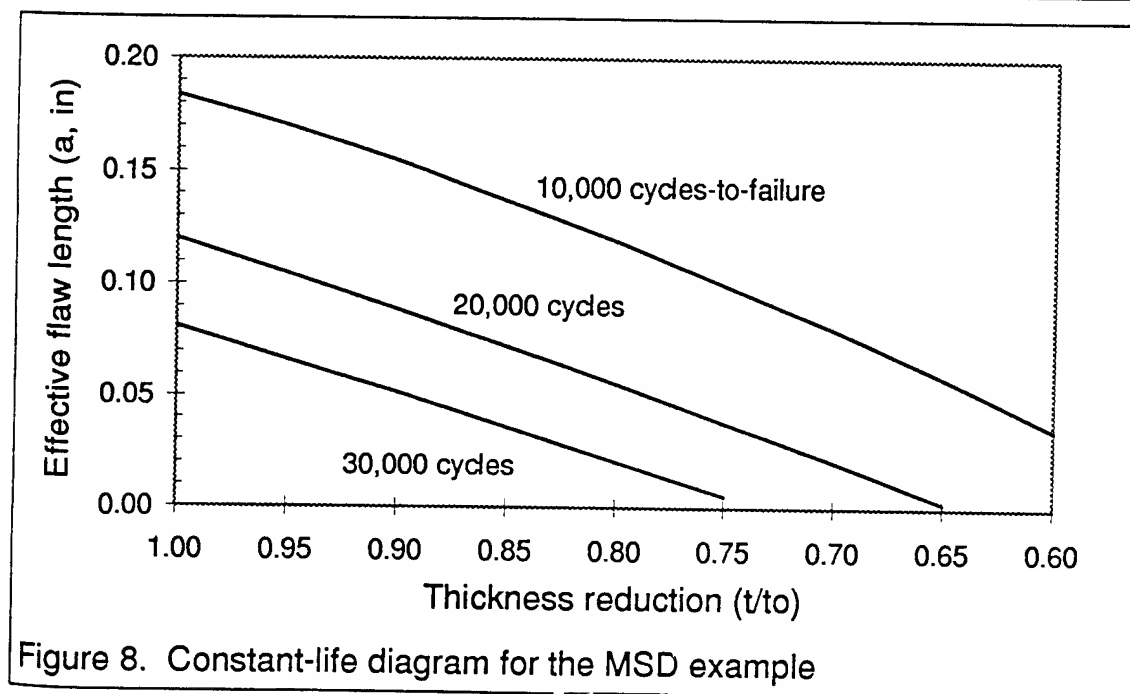
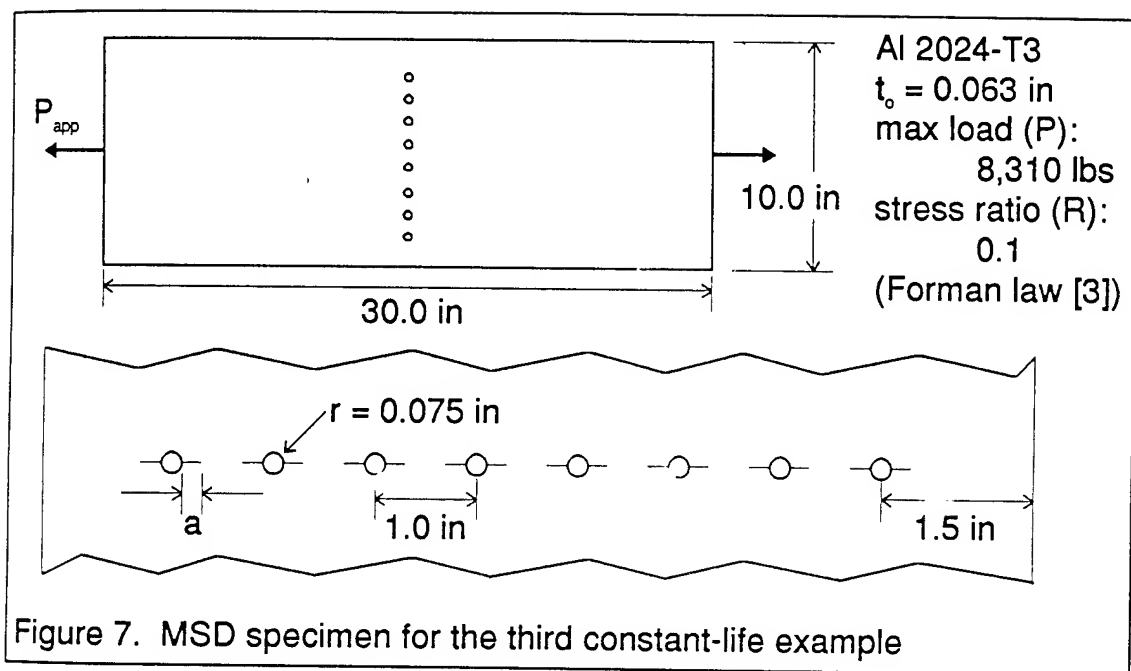


Figure 6. Constant-life diagram for thru-cracked hole-in-plate example

Example 3. Multiple site damage specimen

A more complex geometry is provided as a third example of the corrosion assessment technique. The multiple site damage (MSD) panel presented in Fig. 7 is a simple model of a row of fastener holes in an aircraft structure. A computer algorithm developed to accurately predict the growth of multiple cracks emanating from a row of holes [4] was modified here to compute a constant-life plot for an Al 2024-T3 MSD panel with 8 holes. The panel dimensions and loading conditions are presented in Fig. 7. For this simple example, it was assumed that each hole would have symmetric through-the-thickness cracks and that all cracks were of equal length. The results, presented in Fig. 8, provide insight to the relationship between the corrosion parameters of uniform thickness loss and local damage at all fastener holes. Once again, such plots could be used to evaluate damage in other similar MSD panels. This example shows that the corrosion evaluation protocol is not only applicable to simple geometries, but can be applied to complex geometries as well.



Example 4. Variation of applied loading for surface-cracked geometry

As discussed during the surface-cracked plate example, the corrosion evaluation protocol can be used as a structural evaluation tool by conducting analysis of similar geometries under various loading conditions. It is important to consider the effects of differing applied load because fracture mechanics concepts should be able to account for varying

stress levels in the assessment of corrosion damage. Here, in order to demonstrate the effect of load on the relationship between general thickness reduction and local initial flaw size, the surface-cracked plate geometry (Fig. 3) has been analyzed for three values of maximum applied cyclic load (3,000 lbs, 4,000 lbs, and 5,000 lbs). The results, presented in Fig. 9, compare the same geometry with a required life-to-failure of 40,000 cycles. As expected, the specimen is able to tolerate the smallest amount of damage at the largest applied load if it is to survive the desired number of cycles. The least severe load permits more environmental damage, and even allows for a through-the-thickness initial flaw with a thickness reduction of up to 23%.

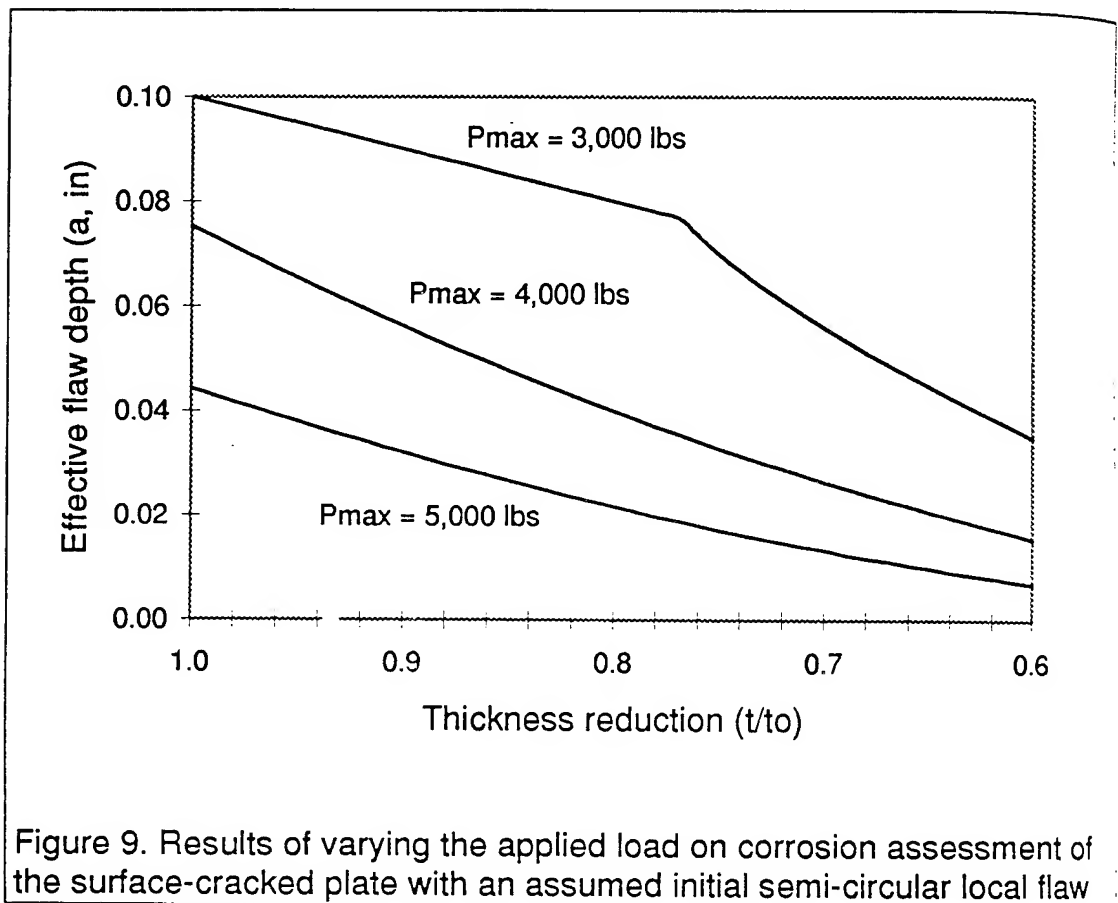


Figure 9. Results of varying the applied load on corrosion assessment of the surface-cracked plate with an assumed initial semi-circular local flaw

Example 5. Comparison of geometries

Not only can fracture mechanics principles be applied to the assessment of damage for the case of varying loading conditions on a single geometry, but to the case of different geometries under similar loading conditions. For this analysis, the effect of corrosion damage on three similar through-cracked geometries was considered. Figure 10 presents

a combined constant-life diagram for a center-cracked panel, a panel with symmetric cracks emanating from a single hole, and a multiple site damage panel with symmetric cracks at every hole. The overall dimensions of each Al 2024-T3 panel were equivalent (30.0 in x 10.0 in x 0.063 in, hole radii: 0.075 in), and the applied loading was such that the net-section stress for each undamaged panel (i.e. no thickness reduction or initial equivalent crack) was equal to 15.0 ksi. The applied stress ratio was the same as in previous examples ($R=0.1$), as was the crack growth rate curve [3]. The life-to-failure for each geometry was 20,000 cycles.

The results, as expected, reveal that the center-cracked panel can tolerate much larger initial equivalent cracks for a given value of thickness reduction, and that the presence of MSD significantly reduces the damage tolerance capabilities of the panel. It should be noted that the crack lengths plotted in Fig. 10 are the lengths that would need to be resolved in an inspection (by nondestructive testing, for example), and are not the tip-to-tip values for all crack types. The lengths presented for the MSD and single-hole geometries are those on one side of the hole, from the edge of the hole to the tip of the crack ("a" in Figures 5 and 7). The values given

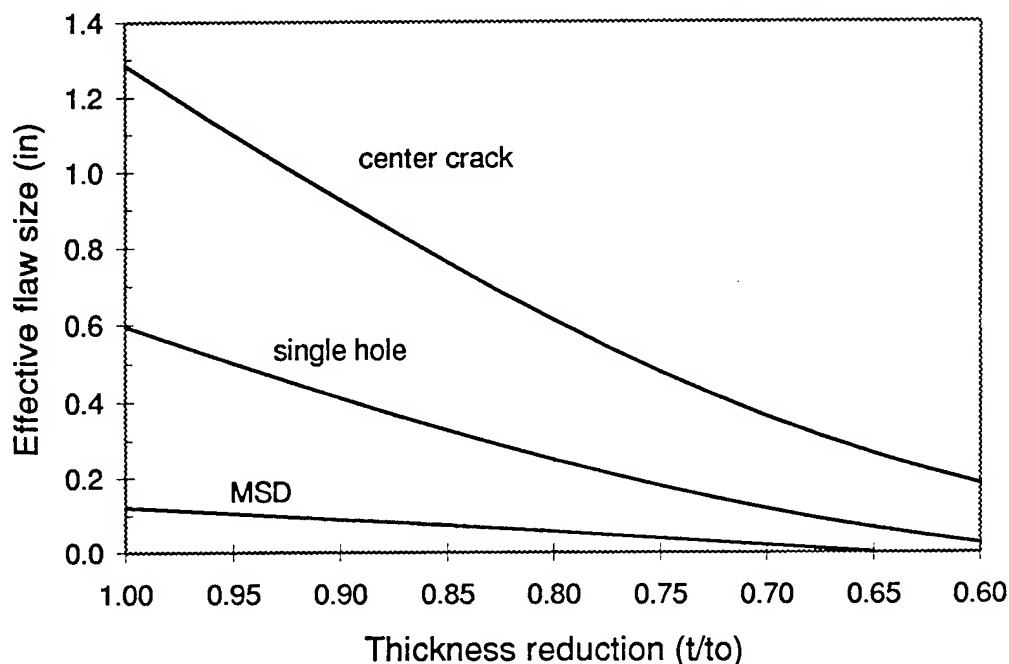


Figure 10. Comparison of constant-life curves for three similar geometries under equivalent loading conditions

for the center-cracked panel are the tip-to-tip values ("2a" in Fig. 3). The important result of this demonstration is that the application of fracture mechanics principles to corrosion assessment enables the comparison of the effect of environmental damage on different geometries.

Test Program

An experimental program is being developed to verify the concepts of the proposed corrosion quantification method. Simple specimens manufactured from an aircraft alloy will be artificially corroded [5-7], with the duration of exposure being varied in order to produce different degrees of corrosion damage. After the environmental attack, the specimens will be mechanically tested by two separate methods. One group of specimens will first be fatigue tested to a predetermined number of cycles. Following this, each specimen will undergo a residual strength test [8]. The second group will be fatigue tested to failure under constant amplitude loading.

The residual strength tests will be conducted in order to determine if fracture mechanics concepts can be used to predict the results of damage due to corrosion. Post-test measurements of specimen thickness and deepest flaw depth will provide a quantitative assessment of the degree of corrosion damage for one specimen geometry and duration of environmental exposure. These parameters will be used to predict the residual strengths of the original specimens as well as the residual strengths of the other specimen geometries (with equivalent durations of environmental exposure). This point is of great importance because in order to verify the validity of the concept, it must be proven that fracture mechanics can predict results for one geometry by using data obtained from a different geometry. Results would be in a form like that of Fig. 2. At least five specimens will be tested at each desired life interval in order to provide an estimate of the statistical nature of the results. It is planned to test several degrees of corrosion damage (i.e. exposure duration) and at least 5 intervals of applied fatigue cycles.

The group of specimens to undergo constant amplitude fatigue tests will have the damage characterized in a number of ways. One method will be to measure the final flaw size and specimen thickness after failure of the specimen. An equivalent initial flaw size will be calculated from these values using fracture mechanics concepts, and the results (to be compared with the residual strength results) will define the corrosion damage for the degree of exposure. This corrosion assessment will then be applied to the other specimen geometry. A second method will be to

predict the life-to-failure for the constant amplitude specimens using the corrosion assessment determined from the residual strength tests. And third, nondestructive inspection (NDI) methods will be applied as an attempt to measure the values of thickness loss and flaw size. These measured values will be used to predict the life-to-failure of each specimen. This latter method is understood to be of importance because in order for the concept of corrosion damage quantification to be of practical use, one must be able to assess environmental damage in an aircraft structure during a routine maintenance inspection. Although studies of present NDI techniques reveal that accurate and reliable measurement is often difficult [9,10], the knowledge of what specific parameters inspectors must measure could help to improve current NDI technologies.

Summary

A fracture mechanics based approach to the quantification of corrosion damage has been introduced and several examples of how this protocol might be applied were discussed. The concept relies on a geometric model of corrosion that assumes damage can be treated as a combination of a general thickness reduction and a local stress concentration. A test program that will make use of artificially corroded specimens and fracture mechanics principles has been suggested as a way to verify the concept of corrosion assessment for simple geometries. Once the applicability of the technique had been determined, corrosion in more complex geometries can be quantitatively defined, and constant-life diagrams can be used as structural evaluation tools for in-service use.

References

- [1] "Corrosion Prevention and Control," *Aerospace Engineering*, January/February 1994, pp. 49-52.
- [2] Murphy, E.E., "Aging Aircraft: Too Old to Fly?" *IEEE Spectrum*, June 1989, pp. 28-31.
- [3] Bucci, R.J., Konish, H.J., Kulak, M., and Macheret, Y., "Test/Evaluation Protocols for Corrosion Damage Assessment, C/KC-135 Corrosion Fatigue Round Robin Test Program," Report 57-93-24, Product Design and Mechanics Division, Alcoa Technical Center, Alcoa Center, PA, October 1993.

- [4] E.J. Moukawsher, "Fatigue Life and Residual Strength of Panels with Multiple Site Damage," M.S. Thesis, School of Aeronautics and Astronautics, Purdue University, May 1993.
- [5] "G44-88 Standard Practice for Evaluating Stress Corrosion Cracking Resistance of Metals and Alloys by Alternate Immersion in 3.5% Sodium Chloride Solution," *1993 Annual Book of ASTM Standards*, Section 3, Vol. 03.02, American Society for Testing and Materials, 1993, pp. 174-177.
- [6] "G34-90 Standard Test Method for Exfoliation Corrosion Susceptibility in 2XXX and 7XXX Series Aluminum Alloys (EXCO Test)," *1993 Annual Book of ASTM Standards*, Section 3, Vol. 3.02, American Society for Testing and Materials, 1986, pp. 132-137.
- [7] "G112-92 Standard Guide for Conducting Exfoliation Corrosion Tests in Aluminum Alloys," *1993 Annual Book of ASTM Standards*, Section 3, Vol. 3.02, American Society for Testing and Materials, 1993, pp. 479-485.
- [8] Bucci, R.J., Brazill, R.L., Sprowls, D.O., Ponchel, B.M., and Bretz, P.E., "The Breaking Load Method: A New Approach for Assessing Resistance to Growth of Early Stage Stress Corrosion Cracking," *Corrosion Cracking*, Proceedings of the International Conference and Exposition on Fatigue, Corrosion Cracking, Fracture Mechanics, and Failure Analysis, American Society for Metals, Metals Park, OH, 1986, pp. 267-277.
- [9] Alcott, J., "An Investigation of Nondestructive Inspection Equipment: Detecting Hidden Corrosion on USAF Aircraft," *Materials Evaluation*, Vol. 52, No. 1, January 1994, pp. 64-73.
- [10] Ansley, G., Bakanas, S., Castronuovo, M., Grant, T., and Vichi, F., "Current Nondestructive Inspection Methods," *Report No. DOT/FAA/CT-91/5*, FAA Technical Center, June 1992.

Shipboard Exposure Testing of Aircraft Materials

Edwin S. Tankins*, J. Kozol & E. Lee

Abstract

A study was performed comparing the corrosion resistance of various aluminum alloys in shipboard environments with an accelerated laboratory corrosion test environment. An Al-Li access panel for the F/A-18 was also tested. For comparison 7075 aluminum alloys were tested in the exfoliation susceptible T651 and the resistant T7351 temper.

Sulfur dioxide salt fog (ASTM G 85 A4-85) tests were conducted. The shipboard exposures were performed aboard aircraft carriers deployed to the Pacific Ocean, Persian Gulf and Indian Ocean during the monsoon season. The Al-Li alloys exhibited pitting corrosion similar to 7075 T7351.

- Aerospace Materials Division, Naval Air Warfare Center Aircraft
Division Warminster, PA. 18974-5000

Introduction

Considerable progress has been made recently in the development of new aluminum alloys and coatings for aerospace applications. The production of various aluminum-lithium alloys has made possible a density reduction and an increase in elastic modulus and strength. Over the last 20 years this Center has been testing many aerospace materials in marine environments as well as accelerated laboratory corrosion tests to compare the behavior of various alloys and coatings. The work presented here examines the corrosion behavior of a variety of aluminum alloys exposed to aircraft carrier environments. One of the in-house accelerated tests is also discussed for comparison to the carrier exposure. The high strength aluminum alloys are susceptible to various forms of corrosive attacks such as pitting, intergranular corrosion, stress corrosion, and exfoliation. Exfoliation is the most severe form of attack since it can destroy a structure. The objective of the entire program was to evaluate the behavior of various alloys on the decks of aircraft carriers as well as the effect of various locations in comparison to in-house accelerated tests. Although many different materials have been evaluated, the work presented concerns primarily aluminum alloys and various protective coatings.

Test Materials

A variety of materials has been evaluated including first and current generation Al-Li alloys. These include 2020 alloys from the 1950s used in the naval aircraft RA-5C, as well as present generation Al-Li alloys such as 2090 & 8090, and 1420 & 1421 produced in former Russia. The 2090 alloy was obtained through a Navy cooperative program and reported in Reference 1.

Commercially available 7075-T651 aluminum 1-in (2.54 cm) plate was used for comparison with the Al-Li alloys. After machining into step specimens, half of the specimens were overaged to the T7351 temper by heating for 24 hours at 120°C (350°F). There were a variety of the 7000 series aluminum alloys tested. The T6 and T7 conditions were similar to those shown in Table 1. In the 7000 series, the high conductivity is characteristic of the T-7 condition.

Step specimens of all alloys were utilized to determine exfoliation corrosion behavior. The specimen dimensions were approximately 3 x 6 in (75 x 150 mm). The plate materials were machined to expose the surface at one-tenth (T/10) and one-half (T/2) of the plate thickness. The bare aluminum alloys were chemically etched to present uniform, consistent clean surfaces. The specimens were degreased with solvent, etched in 5% sodium hydroxide at 80°C (176°F) for 1 to 3 minutes, rinsed in water,

Table I - Plate Test Characteristic

Material	Plane	Thickness		Hardness Rb	Conductivity % Iacs ^a
		in	mm		
7075-T651	T/0	1.0	25.4		
	T/10	0.90	22.9	91	32
	T/2	0.50	12.6	90	33.8
7075-T7351	T/0	1.0	25.4		
	T/10	0.90	22.9	81	39.9
	T/2	0.50	12.6	80	39.2
2020-T651	T/0	0.50	13.0		
	T/10	0.45	11.4	87	17.2
	T/2	0.15	6.5	89	17.2
8090-T851	T/0	1.80	45.7		
	T/10	1.64	41.6	77	19.8
	T/2	0.90	22.8	78	20.0

^a Electrical Conductivity was measured in Percentage of International Anneal Copper Standard %(Iacs) unit

desmuted in concentrated nitric acid for 30 seconds, rinsed in deionized water and dried with oil free compressed air.

SO₂ Salt Fog -- The sulfur dioxide salt fog tests attempt to closely mirror the service environments. The model used in developing the tests was a high humidity, salt-containing environment. However, the acidifying species used are those found in service from jet-engine exhausts, i.e., sulfurous acid. The addition of a dry air purge accelerated, but did not change the corrosion behavior. Sulfur dioxide salt fog testing has been successfully applied to structural materials, organic coatings, and avionics (2).

Sulfur dioxide fog testing was performed in accordance with ASTM practice for salt/SO₂ spray (fog) testing ASTM G85A.4. (2) Testing was performed with 5% sodium chloride salt constant fog, with sulfur dioxide injection into the dispersion tower for one hour at six hour intervals. The nominal chamber temperature was 35°C (95°F); the test specimens were bottom supported at a 45° angle by acrylic racks. The testing campaign was performed for four weeks and for much lesser periods if the corrosion was severe. The Cd

plated 4130 steel was examined daily. The visual observations were recorded. The A1 step specimens were examined every other day except for holidays and weekends.

Table 2 shows a comparison of laboratory and carrier environments. These results are averages over long time spans (1-5).

Table 2 - Characteristics of Laboratory and Carrier Environments

ASTM	Conditions	Acidifying Agent	pH	Temp, °C	Relative Humidity, %
G85.A4	Continuous salt spray	SO ₂	2.5-3.2	35	95
Shipboard	Cyclic salt spray	SO _x , NO _x , jet exhaust stack gases	2.4-4.0	23-29	71-87

Weather Reports

Weather reports were collected from hourly observations made by ship personnel (3). From these reports, data on temperature and relative humidity were taken four times daily at six hour intervals and analyzed. Conditions at the rack location may have differed from the meteorological data because of microclimate effects. For example, it is anecdotally reported that temperatures immediately above the black carrier deck can reach 140°F (60°C) during bright sunlight. Relative humidity was obtained by a procedure discussed elsewhere (4).

Aircraft Carrier Exposures

The study of various alloys included exposure aboard aircraft carriers as part of a series of exposures for the last ten years. Figure 1 summarizes the results of previous testing and shows that the carrier environment is more severe than seacoast or industrial environments (2). However, large differences exist between theaters of operations. Environmentally, the Indian Ocean deployment during the monsoon season is far more severe than the Atlantic or Mediterranean Sea deployment from which previous comparisons were made. Susceptible aluminum exposed aboard nuclear powered carriers (no stack gases) exhibited behavior similar to that aboard conventionally powered carriers (stack gases with jet engine

exhaust). It appears that the acidity of moist films measured on carriers is due primarily to exhausts from aircraft jet engines .

The exposure racks on which the specimens were mounted were on the flight decks. The racks were made of steel that had been cadmium plated, chromated, and painted. The specimens were insulated from the rack face by nylon washers and were fastened to the rack face with nylon bolts and nuts. Silicone sealant was applied in the bolt holes of the specimens and under the bolt heads to prevent crevice corrosion. The rack exposed the specimens at 45° to the horizontal. The steps of the specimens faced skyward. Single specimens of each material were exposed.

The racks were attached to radar towers from 1.8 to 2.1 m (6 to 12 ft) above the flight deck aft of the carrier island. Specimens in this study were exposed aboard two conventionally powered aircraft carriers. The *USS Constellation* was deployed to the Western Pacific and Indian Oceans for seven months (February through September), which included exposure during the monsoon season. The *USS John F. Kennedy* was deployed to the Mediterranean Sea for eight months. The *USS Nimitz* was deployed to the Western Pacific and Indian Ocean over a five year period. The *USS Ranger* was deployed to the Western Pacific and the Persian Gulf for 4 months. The various results have been published elsewhere (5-10).

Results and Discussions

There has been considerable testing performed in various locations. There are pronounced differences in locations and environments. For instance, the Indian Ocean during the monsoon appears to be more severe than the Atlantic or Pacific. The work of Ketchum, et al (2) showed a comparison of the various environments. Figure 1 was first shown in their work (2) and is an excellent comparison.

The macroscopic performance of the specimens after carrier exposure and laboratory testing was evaluated with the rating system of ASTM G34-87 (7). Thompson (7) discussed the procedure in detail. There are 8 by 10 in photographs that show the various rating systems. There are situations in which the corrosion cannot be compared to the ASTM standards. The results of recent tests are shown in Tables III and IV (8-10).

Aircraft Carrier Exposures

All shipboard exposed specimens were covered with a thin gray film. The analysis of similar films from previous exposures, indicated the film consisted largely of MIL-L-23699 engine oil deposits with some sulfur (2,5,7). The large

differences between similar specimens exposed aboard *USS Constellation* and *USS Kennedy* show a significant variation in corrosivity with deployment area (7).

The behavior of 2090-T8E41 and other Al-Li alloys exhibited pitting or very slight exfoliation. (7)

The shipboard exposures are from the *USS Nimitz* which was multiple deployment, the *USS Ranger*, which was a 4 month deployment, and a two year exposure in the Key West, Florida area (8-10).

Figure 2 shows a typical rack prior to deployment. The preparation of the rack as discussed elsewhere (8-10). Figure 3 compares a 7075-T6 step specimen with a T7 temper. This was a multiple deployment over a 5 year time period. The severe corrosion (ED) of the 7075 T6 can be seen. The T7 temper exhibits only general corrosion. The side view of the 7075 T6 is shown in Figure 4. The extensive exfoliation is readily available. Figure 5 compares a 7150-T651 alloy with a 2090 T8E41 alloy. The (E0) condition is readily apparent. The 2090 shows only general corrosion.

The results of the short time deployment of the *USS Ranger* is reported in table III. The results of the *USS Nimitz* multiple deployment is reported in table IV.

The results of the real time testing shows the T6 plate exhibits exfoliation on the T/2 plane. The T-76 temper demonstrated the improved exfoliation resistance of the overaged T76 condition. The remaining aluminum alloy control specimens in flat sheet configuration showed only some pitting and general corrosion. The Al-Li alloy step specimens showed only general corrosion and some pitting as reported in table IV.

After 2 years at Key West, Florida, a small amount of incipient exfoliation appeared on the T/2 plane of the 7075-T6. Figure 6a compares access panels of 7075T6 and 209078 Al-Li alloy for the F/A-18. Figure 6b shows what looks like a slight blistering at the scribe mark. By comparison Fig 6b looks clean at the scribe marks. The behavior is basically comparable.

The laboratory tests indicate at 96 hours the 0.3 mil and 0.5 mil Cd plated plate shows corrosion, and the 1 mil shows discoloration. These results are shown in Figure 7. This is similar to what is often seen on carrier exposure.

Laboratory tests of 7075 T7 sheet shows general corrosion or pitting within 1-2 days. The 7075 T6 sheet shows delineation of the grain boundaries but no exfoliation. 7075 T6 step specimens in previous tests showed exfoliation on the T/2 plane (7) after 700 hours of exposure. It appears that SO₂-salt fog testing is a relatively good simulation for the type of behavior of the aircraft material except the time involved is much shorter and the acceleration time varies with the material.

Conclusion

1. Shipboard exposure corrosion testing provides a real time test method for evaluating and ranking Naval aircraft materials and coatings.
2. The improved exfoliation resistance of 7075 T7 (overaged) aluminum alloy over fully aged 7075 T6 was demonstrated, even after a relatively mild exposure.
3. The general and pitting corrosion behavior of the aluminum lithium alloys (2090, 8090, and 1420, etc.), was comparable to that of the 7075-T7.

Acknowledgments

Funding for this program was provided by the 612 Aircraft Materials Block (NA2A). The authors wish to acknowledge Mr. Lee Biggs, Dr. Bart Boody, and Dr. John Deluccia for their assistance in evaluating the specimens after exposure testing.

References

- (1) Bucci, R.J., Malcolm, R.C., Colvin, E.L., Murtha, S.J., and James, R.S., "Cooperative Test Program for the Evaluation of Engineering Properties of Al-Li Alloy e2090-T8X Sheet, Plate, and Extrusion Products," Report No. NSWC TR 89-106, Naval Surface Warfare Center, Silver Spring, MD, 15 Sept. 1989.
- (2) Ketcham, S.J. and Jankowsky, E.J., "Developing an Accelerated Test: Problems and Pitfalls", *Laboratory Corrosion Tests and Standards, ASTM STP 866*, G.S. Haynes and R. Baboian, Eds., American Society for Testing and Materials Philadelphia, PA, 1985, pp. 14-23.
- (3) "Manual for Ship Reporting of Surface Observations from a Sea Station", NAVOCEANCOMINST 3144.1C, 22 March 1983.
- (4) Haynie, F.H., "Evaluation of the Effects of Microclimate Differences on Corrosion", *Atmospheric Corrosion of Metals, ASTM STP 767*, S.W. Dean, Jr., and E.C. Rhea, Eds., American Society for Testing and Materials, Philadelphia, PA, 1982, pp. 286-308.
- (5) Jankowsky, E.J., Ketcham, S.J., and Agarwala, V.S., "Aircraft Carrier Exposure of Aluminum Alloys," Report No. NADC-79251-60, Naval Air Development Center, Warminster, PA, 1 Nov 79.
- (6) Joseph Kozol and Edwin Tankins, "Aircraft Carrier Exposure Tests of Cast Magnesium Alloys", NAWCADWAR-93015-60, March, 1993.
- (7) J.J. Thompson, "Shipboard Exposure Testing of Aircraft Materiel, Aboard USS Constellation (Feb-Sept. 1985)", NADC-87125-60, Sept. 1987.
- (8) Joseph Kozol, E. Tankins & E. Lee, "Shipboard Exposure Testing of Aircraft Material Aboard USS Ranger", NAWCADWAR 94019-60, May, 1994.
- (9) J. Kozol, E. Tankins, & E. Lee, "Shipboard Exposure Testing of Aircraft Material Aboard the USS Nimitz", Unpublished Data.
- (10) J. Kozol, E. Tankins, & E. Lee, "Shipboard Exposure Testing Over A 2 Year Duration, Key West, Florida", Unpublished Data.

TABLE III. SPECIMEN DESCRIPTION AND OBSERVATIONS (Continued)

	Material Description	Designation	Configuration	Observation
17.	High Strength Aluminum Alloy	CW6TT7	Sheet	General discoloration, no exfoliation, general corrosion.
18.	Silane Coated Aluminum Alloy	2024 Coated	Plate	General corrosion, some pitting and surface discoloration.
19.	High Temperature Aluminum Alloy	CZ 42	Sheet	General corrosion, some pitting and surface discoloration.
20.	Melt spun Al-Li-Zr Alloy	644	Forged, extruded step specimen	General corrosion, some pitting and surface discoloration, exfoliation appears to be just starting at T/2.
21.	Aluminum Alloy	Control, 6061T6	Plate	General corrosion, and some pitting.
22.	Aluminum Alloy	Control, 2024T6	Plate	General corrosion, and some pitting.
23.	Aluminum Alloy	Control, 7075T6	Step specimen	Pitting and general corrosion.
24.	Aluminum Alloy	Control, 7075T6	Step specimen	Exfoliation starting on mid plane. No evidence on top plane.
25.	Chromate Corrosion Coating, Unicoat Variation	2024T3	Plate	Blister at scribe marks. Paint Surface looks good.
26.	Chromate Corrosion Coating, Unicoat Variation	2024T3	Plate	Blister at scribe marks. Paint Surface looks good.
27.	Non-Chromate Corrosion Coating, Unicoat Paint	2024T3	Plate	No corrosion, some surface darkening.
28.	Non-Chromate Corrosion Coating, Unicoat Paint	7075T6	Plate	No corrosion, some surface darkening.
29.	Non-Chromate Corrosion Coating, Unicoat Paint	6061T6	Plate	No corrosion, some surface darkening, blisters may be forming.
30.	Alodine, Unicoat Paint	2024T3	Plate	Blisters may be forming.

TABLE III. SPECIMEN DESCRIPTION AND OBSERVATIONS

	Material Description	Designation	Configuration	Observation
1.	High Temp. Al alloy (Al-Fe-V-Si)	FVS 0812	Sheet	General corrosion, slight pitting not deep, slight surface discoloration.
2.	High Temp. Al alloy (Al-Fe-V-Si)	FVS 1212	Sheet	General corrosion, slight pitting not deep, slight surface discoloration.
3.	Aluminum Alloy	Control, 7075-T6	Sheet	Slight pitting not deep, and some general corrosion.
4.	Sealed Magnesium Alloy	WE-43		* Pitting of Al fitting, no galvanic corrosion discernible.
5.	Sealed Magnesium Alloy	QE-22		* No pitting, looks good.
6.	Unsealed Magnesium Alloy	QE-22		* Pitting of Al fitting with obvious galvanic corrosion at base of fastener.
7.	Cadmium Plated Steel (1 mil)	Control	Plate	Surface darkening, very slight general corrosion.
8.	Cadmium Plated Steel (0.5 mil)	Control	Plate	Surface darkening with edge corrosion.
9.	Cadmium Plated Steel (0.3 mil)	Control	Plate	Severe surface rusting.
10.	Aluminum Metal Matrix Composite	2124 T6, 15 vol SiC	Plate	Small amount of pitting, general corrosion and some surface discoloration.
11.	Aluminum Alloy	Control, 7075 T7351	Plate	Small amount of pitting, general corrosion and some surface discoloration.
12.	Al-Li Alloy (Russian)	1421	Welded sheet	Pitting and general corrosion.
13.	High Strength Aluminum Alloy	CW67T7	Plate	Small amount of pitting, some surface discoloration, mostly general corrosion.
14.	Aluminum-Lithium Alloy	2090T8	Step specimen	General discoloration, no exfoliation, general corrosion.
15.	High Strength Aluminum Alloy	CW67 T6	Plate	General discoloration, no exfoliation, general corrosion.
16.	Molybdate, Silane Coated Aluminum Alloy	2024 Coated	Plate	General discoloration, no exfoliation, general corrosion.

TABLE III. SPECIMEN DESCRIPTION AND OBSERVATIONS (Continued)

	Material Description	Designation	Configuration	Observation
31.	Alodine, Unicoat Paint	7075T76	Plate	No corrosion, some surface darkening.
32.	Alodine, Unicoat Paint	6061T6	Plate	No corrosion, some surface darkening.
33.	Aramid Aluminum Laminate	Arall 5/4	Unsealed edges	General Corrosion - No discernible increase at laminated edges.
34.	Aramid Aluminum Laminate	Arall 5/4	Sealed edges	General Corrosion.
35.	Al-Li Alloy (Russian)	1420	Step specimen	Incipient exfoliation on both faces.
36.	Al-Li Mechanically Alloyed	Inco 905XL	Forging Step Specimen	No exfoliation, some pitting and general corrosion.
37.	High Strength Aluminum Alloy	CW67T7X1	Forging	Some pitting and general corrosion.
38.	Aluminum Metal Matrix Composite	2124 T6, 15 vol SiC	Sheet	Some pitting and general corrosion.
39.	High Temp. Aluminum Alloy	Al-12.6Mn, 4.8Si, 0.2 Fe	Extrusion	General corrosion, similar to #1 except darker discoloration.
40.	High Temp. Al Alloy (Al-Fe-V-Si)	FVS 1212	Extrusion	General corrosion, some pitting and surface discoloration.
41.	Unsealed Magnesium Alloy	QE-22		* Pitting of Al fitting, galvanic corrosion; coating at scribe in base material severely corroded.
42.	Sealed Magnesium Alloy	QE-22		* Severe corrosion at scribe, not as bad as #41.
43.	Sealed Magnesium Alloy	WE-43		* Tiny amount of corrosion at scribe, no galvanic effects noted.
44.	Al-Li-Mg Alloy (Russian)	1420w	Sheet	General corrosion, some surface discoloration.
45.	High Temp Al Alloy (Al-Fe-V-Si)	FVS 0812	Sheet	Incipient pits, slightly more general corrosion than #1.
46.	Al-Li-Mg Alloy (Russian)	1421w	Sheet	Some pits, general corrosion.

Table IV Exfoliation Rating of Aluminum Alloys
Exposed on the USS Nimitz 5 Year Span

Material	Thickness	Plane	Rating
7075-T651 Plate	1 in (2.5 cm)	T/10	EA
		T/2	ED
7075-T43 Plate	"	T/10	EA
		T/2	EA
7075 RRA Plate	"	T/10	EA
		T/2	EA
7150-T651 Plate	0.5 in (0.6 cm)	T/2	ED
7150 T7E95	"	T/2	Pitting(<EA)
7150 T7651	"	T/2	Pitting(<EA)
2020 T651	1 in (2.5 cm)	T/10	Pitting(<EA)
		T/2	Pitting(<EA)
2090 T8E41 Plate	0.5 in (1.2 cm)	T/10	Pitting(<EA)
		T/2	" "
8090 T8 Plate	2 in (5.08cm)	T/10	Pitting(<EA)
		T/2	" "
CW67 Plate	0.25 in (0.6 cm)	T/10	Pitting(<EA)
CW67 Plate	1 in (2.54 cm)	T/2	Pitting(<EA)
CW78 Plate	0.5 in (1.2 cm)	T/2	" "
7064 B1 Plate	0.5 in (1.2 cm)	T/10	" "
		T/2	" "
2519 (Plate)	0.5 in (1.2 cm)	T/2	Pitting(<EA)
2519 (Plate)	" "	T/10	" "

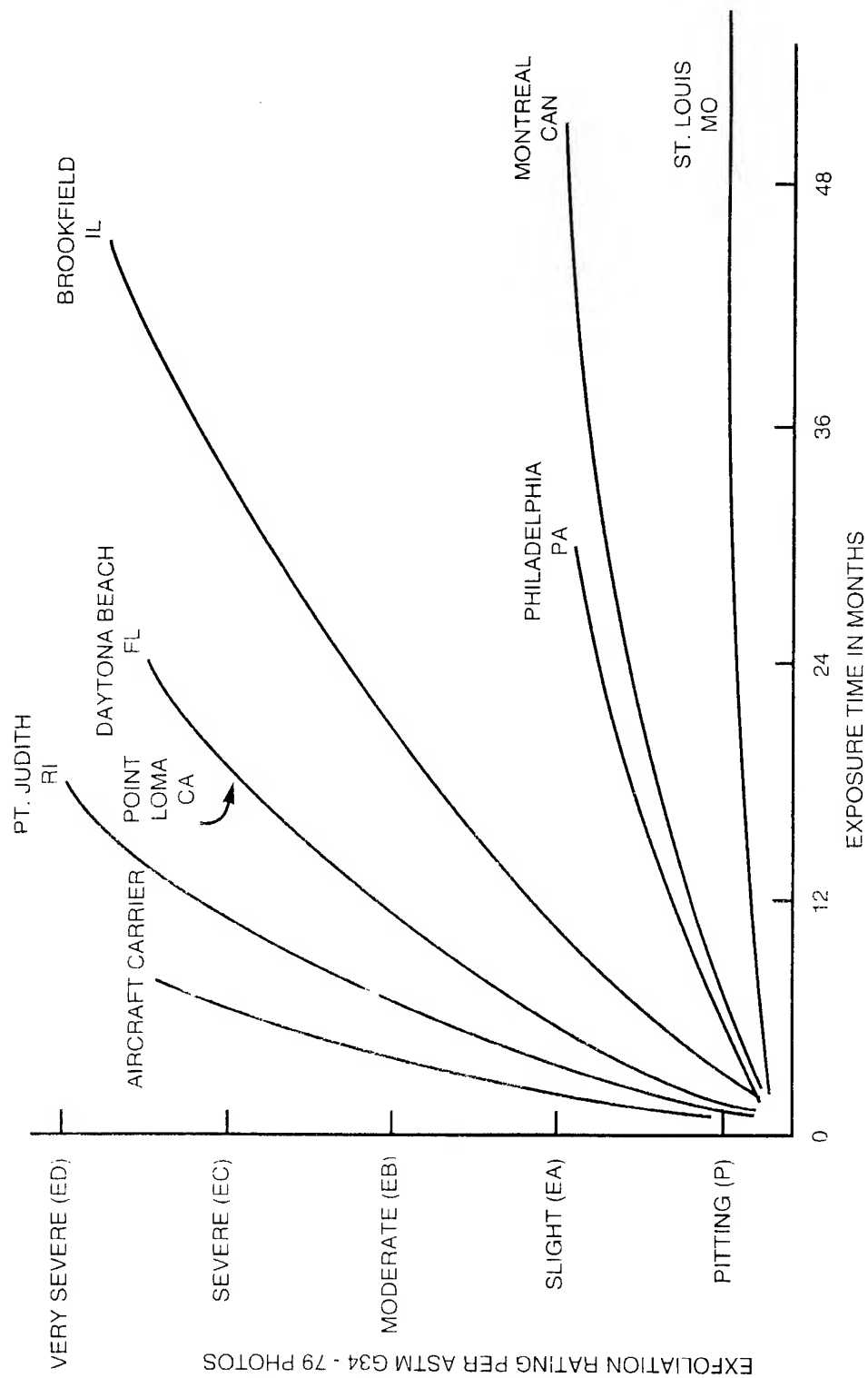


Fig. 1 - Comparative corrosivity of natural environments

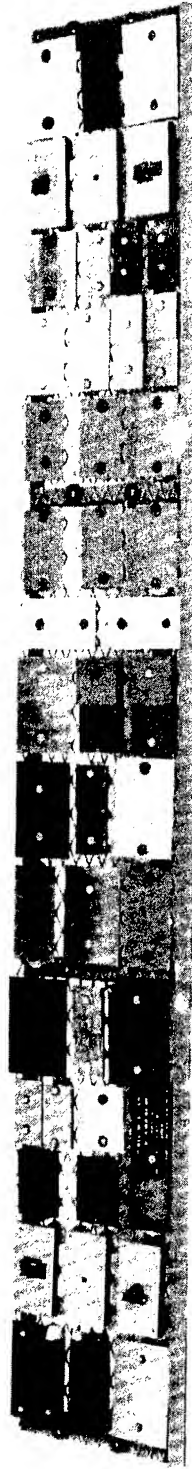
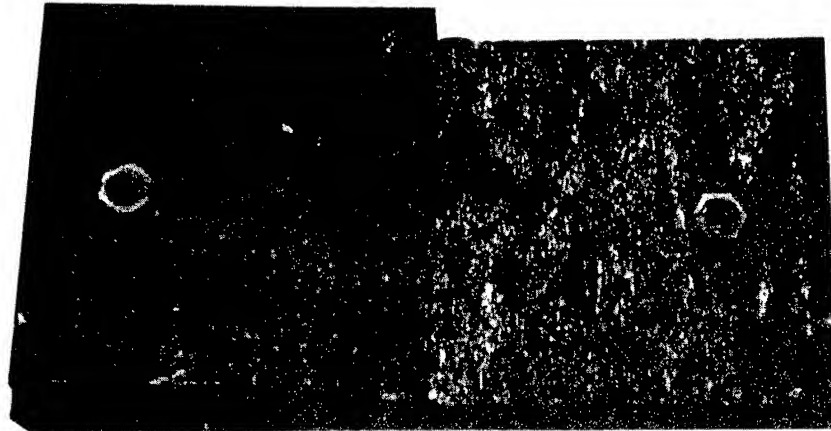


Fig. 2 - Photograph of a typical rack prior to deployment showing the Nylon Fasteners and their Protective Seal.

7075-T651



(a) *Exfoliation on T/2 Plane*

7075-T7651

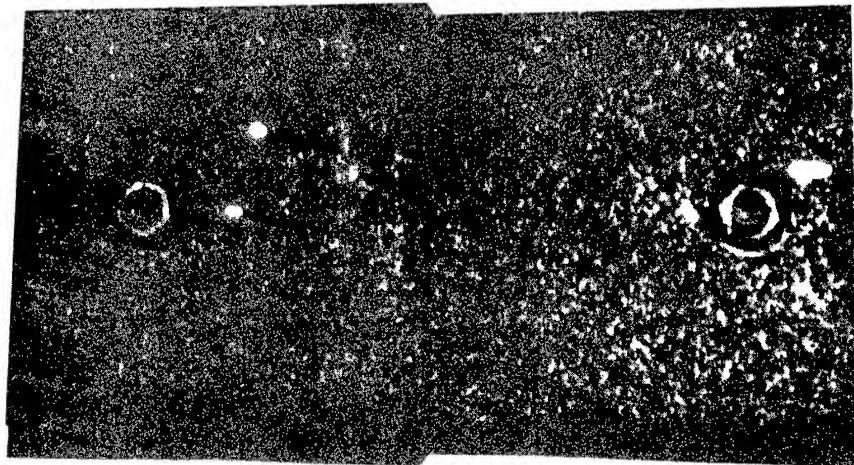
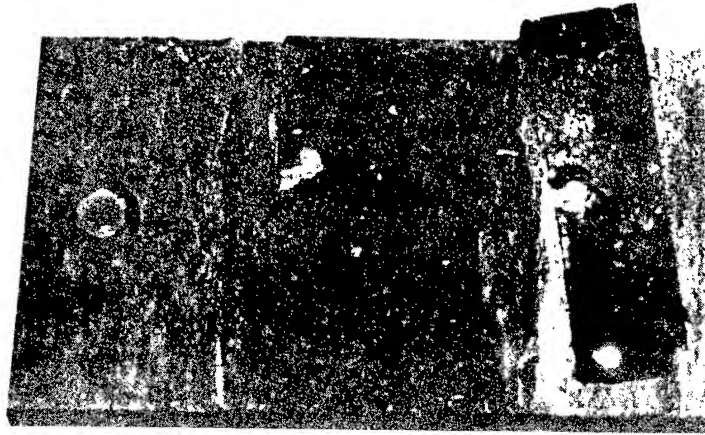


Fig. 3 - Photograph of a step specimen consisting of 7075 - T6 and T 7 after multiple deployments.

7 150-T65 1



(a) Exfoliation

2090-T8E4 1
0.5 IN

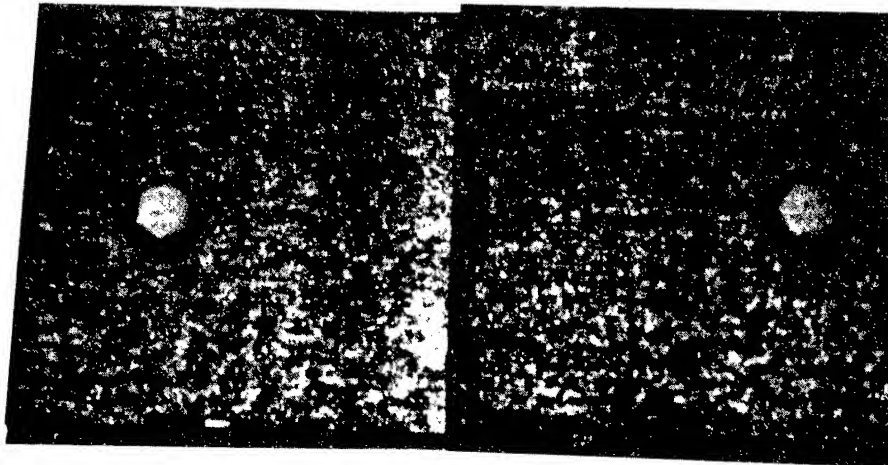


Fig. 4 - Photograph of step specimens 7150 - T6 and 2090 - T8 after multiple deployments.

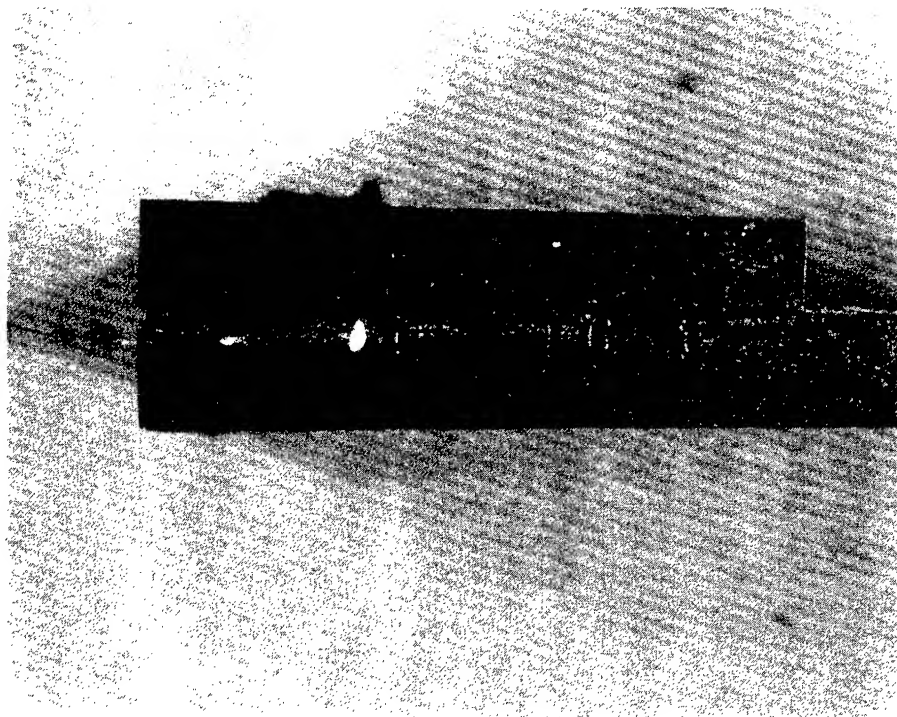
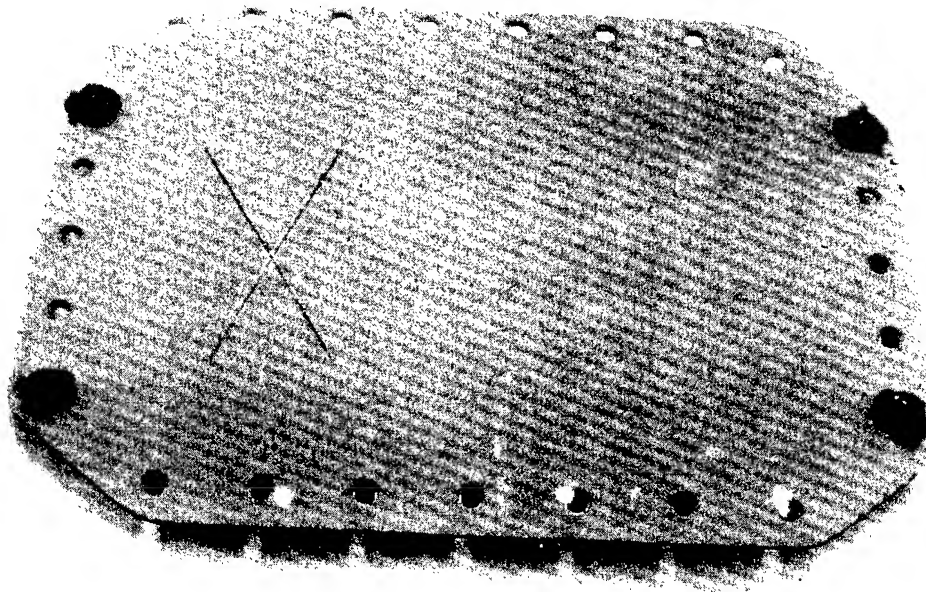
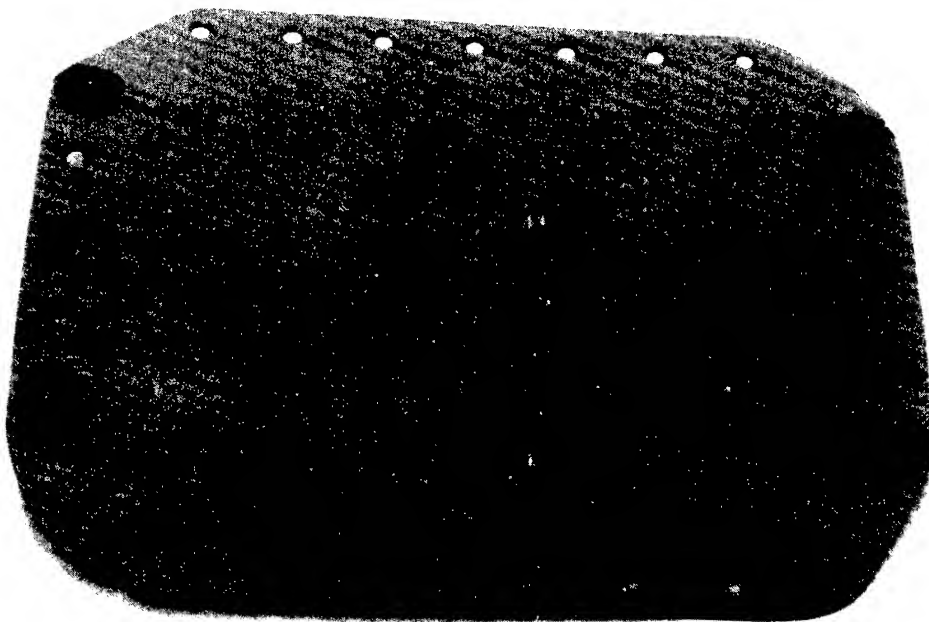


Fig. 5 - Side view of 7075 - 76 alloy showing extensive Exfoliation.

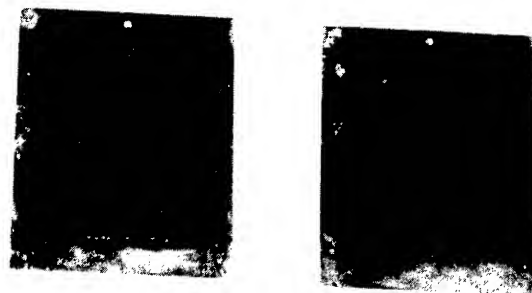


7075 T6
(a)



2090 T8
(b)

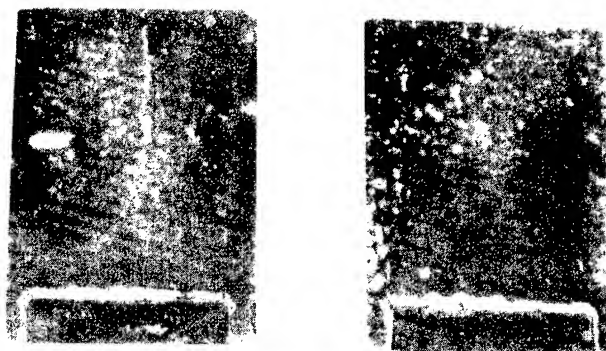
Fig. 6 - Access Panel from F/A - 18 with Scribe Marks.



0.3 mil Cd Plate



0.5 mil Cd Plate



1.0 mil Cd Plate

Fig. 7- Cadmium Plated Steel Panels after 120 hrs of laboratory SO₂ Salt Spray.

BLANK

SESSION VI
CORROSION MECHANISMS

Chairman: *J. Sedriks*

Evaluation of the Stress Corrosion Cracking Susceptibility of Fire
Suppressant Storage Container Alloys in Replacement
Candidates for Halon 1301.

M. R. Stoudt, J. L. Fink, and R. E. Ricker
Material Science and Engineering Laboratory
National Institute of Standards and Technology
Gaithersburg, MD 20899
(301) 975-6020

ABSTRACT

Halons 1301 and 1211 have been identified as chemicals with sufficient ozone depletion potential to warrant limitations on their production and use. Several candidates have been selected as replacements for Halon 1301 and because their behavior is not well understood, their compatibility with the alloys used in the storage and distribution systems is of great concern. The service conditions require long term exposure of these alloys to the replacement agent under high pressures and as a result, these alloys may be susceptible to environmentally assisted failures. Therefore, an evaluation was undertaken to determine the propensity for failure of any of the alloys selected for use as containment vessels by an environmentally assisted fracture mechanism as a result of exposure to the replacement candidates.

Data from *in-situ* slow strain rate tensile tests in the pure agent were used to formulate a ranking of each agent/alloy combination. The results of this ranking indicated that some alloy/agent combinations were less desirable than others, but overall, the potential for failure of the selected alloys by stress corrosion cracking (SCC) is relatively minor under the evaluated conditions. From this it was concluded that a suitable alloy can be selected for any of the replacement agents and that no agent should be eliminated from further evaluation because it promotes SCC in the containment vessel alloys. However, additional testing is required at lower temperatures, with and without the

presence of contaminants, before a final conclusion can be made regarding the susceptibility of these alloys to environmentally induced failure in the replacement candidates.

INTRODUCTION

The Montreal Protocol of 1987 identified a number of fully saturated, halogenated organic chemicals which possessed sufficient stratospheric ozone depletion potentials to warrant limitations on their production and use.⁽¹⁾ Two of the most common fire suppressants, Halon 1301(CF₃Br) and Halon 1211(CF₂Br₂) were included on that list. These agents have been the in-flight fire suppression agents of choice in engine nacelles and dry bay applications for many years because of their wide range of desirable properties. These include no residue after discharge, low toxicity, long term storage stability in addition to being non-corrosive and electrically non-conductive.⁽¹⁾

Due the projected unavailability of these agents, there is a great need for an environmentally favorable, alternative fire suppressant.⁽¹⁾ The results of intensive screening evaluations by the US Air Force produced a list of twelve potential candidates to replace Halon 1301 and Halon 1211 for use as in flight fire suppressants. The twelve agents selected for evaluation were: HCFC-22, HCFC-124 HFC-227, HFC-134a, HFC-236, HFC-125, HFC-125/HFC-32 (azeotrope), FC-31-10, FC-116, FC-218, FC-318, and NaHCO₃. The compatibility of these replacement candidates with the variety of materials used in the storage and distribution systems is of serious concern, and as a result, an extensive analysis was undertaken to evaluate the potential for corrosion-induced failure of these materials by the candidates. The specific mode of corrosion induced failure addressed in this paper is environmentally assisted fracture. Since the service conditions require both the storage bottles and the rupture disk materials to be exposed to the replacement agent under high pressures for long times, there is great potential for failure by environmentally assisted fracture.

The environmentally assisted fracture¹ mechanism can generally be described as: the formation and propagation of a crack in a material at a stress well below that required for cracking by purely mechanical means resulting from a simultaneous exposure to a chemically reactive environment and a mechanical stress.^{2,3} This form of attack occurs in

¹In the literature, environmentally induced failure is also referred to as, stress corrosion cracking (SCC), chloride stress cracking, hydrogen embrittlement, season cracking in brass, caustic embrittlement in steels, liquid metal embrittlement (LME) and sulfide stress cracking. (2,3)

specific material/environment combinations and while its effects may not be readily apparent, failures from environmentally induced cracking can be sudden and dramatic. Therefore, a series of experiments was conducted to determine whether a replacement candidate should be eliminated from further consideration because it promotes environmentally induced fracture of the alloys, either presently in service or under consideration for future use.

EXPERIMENTAL

Experiments were designed to evaluate the propensity for a failure of one or more of the selected alloys by an environmentally assisted means in the replacement candidate agents during storage. The technique chosen for this analysis was the slow strain rate (SSR) tensile test because it generates intrinsic mechanical properties data for a given alloy and it also reveals any interactions that may have occurred between that alloy and the testing environment; all within a relatively short time frame.⁽⁴⁾ In this technique, cylindrical specimens are loaded in tension by a slow increase in the strain until failure occurs by either normal mechanical or by an environmentally assisted means. The potential of each agent to promote environmentally induced failure is determined by comparing the load or strain necessary to cause failure in an inert environment to that required to cause failure in the agents at the same temperature.^(3,4)

The materials chosen for this study were representative of the range of metals presently in service or under consideration as either as storage bottles, distribution systems or as rupture disks. These alloys included: 304 austenitic stainless steel, PH13-8 Mo stainless steel, AM-355 stainless steel, stainless steel alloy 21-6-9 (Nitronic 50), 4130 alloy steel, Inconel alloy 625, copper/beryllium alloy CDA-172, and aluminum alloy 6061-T6. The compositions of these alloys and their nominal densities are given in Table 1.

All of the samples used for this analysis were machined with the tensile axis parallel to the rolling direction of the plate stock (Figure 1) and tested in the "as received" condition.⁽⁶⁾ The sample preparation for these experiments consisted of a measurement of the critical dimensions followed by a thorough degreasing—first in acetone and then in alcohol. The test vessels were commercially available autoclaves with a 250 ml total capacity. Modifications were made to the basic design so that a load could be applied directly to a tensile specimen *in-situ* under constantly maintained environmental conditions (5.86 ± 0.5 MPa at $150^\circ \pm 1^\circ$ C). These conditions were selected because they represent the

upper extreme of the range of normal storage conditions. A schematic diagram of the test vessel is shown in Figure 2.

The appropriate mass of each agent was determined by a computer program based on the available thermodynamic data and the ideal gas law. This approach was selected for two reasons: 1) the number of moles of agent was held constant for each test; regardless of the agent used, and 2) the actual final pressure was slightly lower than the predicted value which greatly reduced the possibility of damaging a vessel. The procedure used for charging the agent consisted of first evacuating the test vessels by attaching it to a mechanical vacuum pump for a minimum of thirty minutes. Next, the test vessels were chilled in a bath of either ice and water, or dry ice and alcohol, depending on the temperature required to maintain the liquid phase of the agent. After chilling the vessels were placed on a high capacity balance to monitor the mass of the liquid agent during filling. The vessels were then slowly heated to 150 ± 1 °C and held at that temperature for the duration of the test.

The mechanical tests were conducted with a computer controlled slow strain rate testing system which operated at a constant crosshead speed of $0.0254 \mu\text{m/sec}$. The computer was configured to sample and record the applied load, the crosshead displacement, and the elapsed time at ninety second intervals(4). After failure, the agent was released, the vessels were allowed to cool to ambient temperature, and the samples were removed from the vessel and stored in a desiccator until analyzed.

Reduction in area (RA) measurements were made on the fracture surfaces with an optical measuring microscope which had a resolution of $\pm 0.5 \times 10^{-6}$ m. The fracture surfaces were then cut from selected broken SSR samples and prepared for analysis. Scanning electron microscopy was performed on samples to verify the mode of cracking. The results of this analysis were then used to formulate a ranking of the potential for failure by stress corrosion cracking for each of the alloys in each replacement candidate.

RESULTS AND DISCUSSION

The susceptibility of a material to environmentally induced failure can be assessed by the three basic parameters generated by a slow strain rate tensile test. These are: the ultimate tensile strength (UTS), the strain to failure (STF) and the reduction in area (RA). The UTS is a measurement of the fracture strength of the alloy and it determined from the maximum load observed during the tensile test according to the

equation 1:

$$UTS = \frac{P_{\max}}{A_o} \quad (1)$$

where P_{\max} is the maximum load supported by the sample during the test and A_o is the initial cross-sectional area of the gauge section of the sample.⁽⁵⁾ If cracking, or some other environmental interaction that lowers the strength, occurred, it will produce a noticeable change in this parameter. Environmental interactions can also occur with deformational processes on the surfaces and at tips of cracks formed within the sample.⁽³⁾ These interactions will generally result in a reduction in the ductility. One of the two parameters used to measure the ductility is the engineering strain to failure (ϵ_f) which can be determined from equation 2:

$$\epsilon_f = \frac{l_f - l_o}{l_o} \quad (2)$$

where l_f is the total change in length of the sample during the experiment and l_o is the initial gauge length.⁽⁵⁾ This strain value includes both the elastic and plastic components necessary to induce failure. The other parameter used to measure of the ductility is the percent reduction in area. This is determined by a physical measurement of the fracture surface at the completion of the tensile test and equation 3:

$$RA = \left(\frac{A_f - A_o}{A_o} \right) 100 \quad (3)$$

where A_f is the cross sectional area of the fracture surface and A_o is the cross sectional area of the initial gauge section.⁽⁵⁾ Unlike the engineering strain to failure, this quantity is based solely on the plastic deformation required for failure and, as a result, it is a better measurement of the environmental interactions for most engineering alloys.

The results of the UTS, STF and RA analyses are shown in Tables 2, 3 and 4 respectively. The values presented in these tables are the numerical average of three tests performed in both the replacement candidate agents and in argon at 150 °C. The values from tests conducted in laboratory air at ambient temperature are also included in these tables for comparison. The results of these measurements were then quantified by forming a ratio between the values obtained from the

test environment and those obtained from argon, the inert reference environment. (3) Statistical analyses were also performed on these data sets to evaluate the significance of the observed variations. The results of the statistical analyses were combined with the ratio values and used to generate the final agent/alloy rankings presented in Table 5.

A significant decrease in the average UTS (Table 2) may be an indication of cracking but it could also be the result of corrosion reactions which reduced the effective cross-section or the result of a flaw in the sample. In general, an increase in the average UTS data is unusual and may reflect a sample/environment interaction that inhibited deformation and/or fracture. The increases present in Table 2 could also be the result of an interference between corrosion products generated on the sample and the seal of the autoclave through which the sample must slide. The most important point reflected in the UTS data is that no agent induced significant changes in all alloys. This indicates that a suitable material can be selected for use as containment vessels and distribution systems for any of these agents.

The majority of the environment/alloy combinations shown in the STF data (Table 3) exhibited increases in the measured strain to failure as compared to the argon values. This may be an indication that deformation was easier in those agents than in pure argon at that temperature. Since environmentally induced cracking usually results in a decrease in the measured strain to failure, the results of these measurements again indicate that a suitable material can be selected for use with these agents. It is important to note that these values were based on displacements of the load frame taken by a transducer outside of the autoclave during the experiment. Therefore, the reduction in area values which are calculated from physical measurements of the final fracture surfaces are a more reliable indication in the changes in ductility.

In Table 4 it can be seen that the reduction in area is significantly reduced (greater than 10%) in four of the 96 possible alloy/agent combinations: Al-6061 in HCFC-124, Al-6061 in NaHCO_3 , 304-SS in NaHCO_3 , and AISI-4130 in NaHCO_3 . Since three of these four were in the same agent, NaHCO_3 , it can be concluded that alloys exposed to NaHCO_3 may have trouble with environmentally assisted fracture.

Table 5 was constructed in order to summarize the results of the slow strain rate tensile tests. This was done by assigning a numerical value to the highest (worst) score received by each agent/alloy combination. The values used for this analysis were the absolute values of the differences between the mean for the alloy in the agent and Ar

divided by the standard deviation for the alloy and test parameter at 150 °C.⁽³⁾ Therefore, the ratings presented in Table 5 are measures of the significance of any postulated environmental influences on the deformation and fracture behaviors of any alloy/agent combination.⁽³⁾ If the maximum deviation was less than one standard deviation, that alloy/agent combination was assigned a value of one, if it was greater than one standard deviation, but less than two, it was assigned a two, etc.⁽³⁾ In this table, it can be seen that sixty-five of the 96 agent/alloy combinations received either a one or two rating. Every agent had at least one alloy with a one rating and only two agents had one alloy with a one rating. No alloy received only one's and two's in all agents and no agent received only one's and two's for all alloys. The 304 stainless steel samples demonstrated the best overall performance of the alloys by receiving a value of one in all but three of the 12 environments. HFC-236 was among the best performing agents.

These results indicate that none of the agents tested in this analysis induced stress corrosion cracking in each of the alloys examined and should not be eliminated from further consideration on that basis. Clearly, some agents were more aggressive than others and some agent/alloy combinations can be considered undesirable. However, a suitable material can be selected to contain these agents should one of them be selected to replace Halon 1301. It is important to note that this conclusion is valid only for the agent composition and temperature evaluated in this study and that the influence of contaminants (e.g., water) or residuals from synthesis should be evaluated before these materials are put into service.

SUMMARY AND CONCLUSIONS

The objectives of this analysis were: 1) to evaluate the propensity for failure of any of the alloys selected for use as containment vessels by an environmentally assisted fracture mechanism as a result of exposure to the candidate replacement agents and 2) to determine whether any of the replacement candidates should be eliminated from further consideration because they promote SCC in the containment vessel alloys. Slow strain rate tensile tests were conducted *in-situ* under extreme storage conditions in the pure agent in order to determine the susceptibility to stress corrosion cracking. The three parameters used to determine the susceptibility to SCC in this investigation (i.e., the ultimate tensile strength, the engineering strain to failure, and the reduction in area) all indicated that a suitable alloy could be identified for storage vessel and rupture disk applications for any of the twelve candidate

agents.

A statistical analysis was performed on each of the data set to determine the relative magnitude and significance of the variations observed in the data. The results of that analysis were then combined with values obtained from ratios between the environmental test results and the results obtained from tests in argon to formulate a best to worst ranking of each alloy/agent combination. The results of this ranking indicate that some alloy/agent combinations were less desirable than others, but again, a suitable alloy can be selected for any of the replacement agents.

The data used in this analysis were obtained from experiments conducted in the pure agent at relatively high temperatures. While the results of this analysis are encouraging, additional testing is required at lower temperatures with and without the presence of contaminants before a final conclusion regarding the susceptibility of these alloys to environmentally induced failure in the replacement candidates can be made.

REFERENCES

1. R. G. Gann, et al., "Agent/System Compatibility for Halon 1301 Aviation Replacement— Comprehensive Test Plan", NIST TN 1278, NIST, (1992).
2. M. G. Fontana and N. D. Greene, Corrosion Engineering, McGraw-Hill, Inc., (1987).
3. R. E. Ricker, et al., "Evaluation of Alternative In-Flight Fire Suppressants for Full Scale Testing in Simulated Aircraft Engine Nacelles and Dry Bays", NISTSP# 861, NIST, (1994).
4. M. R. Stoudt and R. E. Ricker, "Characterization of the Hydrogen Induced Cold Cracking Susceptibility at Simulated Weld Zones in HSLA-100 Steel", NISTIR 5408, NIST, (1994).
5. F. P. Beer and E. R. Johnston, Mechanics of Materials, McGraw-Hill Book Company, (1981).
6. ASTM, "Standard Test Methods of Tension Testing of Metallic Materials," Annual Book of ASTM Standards, Section 3, Metals Test Methods and Analytical Procedures, (1993).

Table 1

Composition of the alloys in weight percent.

<u>Element</u>	<u>Nit</u> <u>40</u>	<u>Al</u> <u>6061</u>	<u>In</u> <u>625</u>	<u>304</u> <u>SS</u>	<u>CDA</u> <u>172</u>	<u>13-8</u> <u>Steel</u>	<u>AM</u> <u>355</u>	<u>AISI</u> <u>4130</u>
Ni	7.1	--	61.39	8.26	0.06	8.4	4.23	0.08
Cr	19.75	0.04	21.71	18.11	0.01	12.65	15.28	0.98
Mn	9.4	0.15	0.08	1.41	--	0.02	0.8	0.51
Mg	--	1	--	--	--	--	--	--
Si	0.5	0.4	0.09	0.49	0.08	0.04	0.16	0.23
Mo	--	--	8.82	0.17	--	2.18	2.6	0.16
Nb	--	--	3.41	--	--	--	--	--
N	0.29	--	--	0.03	--	0	0.12	--
C	0.02	--	0.02	0.06	--	0.03	0.12	0.32
Be	--	--	--	--	1.9	--	--	--
Co	--	--	--	0.11	0.2	--	--	--
Zn	--	0.25	--	--	--	--	--	--
Cu	--	0.15	--	--	97.9	--	--	--
Fe	bal	0.7	3.97	bal	0.06	bal	bal	bal
Al	--	bal	0.23	--	0.04	1.11	--	0.04
g/cm ³ *	7.83	2.70	8.44	7.94	8.23	7.76	7.91	7.85

* Nominal Density

Table 2

Average Ultimate Tensile Strength (MPa) in Each Agent at 150 °C as Compared to Ar at 150°C and Air at 25°C.

<u>Environ-</u> <u>ment</u>	<u>Nit</u> <u>40</u>	<u>Al</u> <u>6061</u>	<u>In</u> <u>625</u>	<u>304</u> <u>SS</u>	<u>CDA</u> <u>172</u>	<u>13-8</u> <u>Steel</u>	<u>AM</u> <u>355</u>	<u>AISI</u> <u>4130</u>
Lab Air	727	341	957	773	763	1117	1005	610
Hot Ar	610	240	927	667	874	1136	969	647
HCFC-22	606	228	901	674	821	1161	932	612
HCFC-124	624	235	937	648	860	1027	945	665
FC-31-10	617	235	910	649	841	1176	935	673
HFC-227	610	235	911	667	865	1156	928	650
HFC-125	611	235	924	650	847	1154	917	669
FC-116	601	230	939	695	817	1128	942	653
HFC-134a	618	225	932	653	851	1144	929	688
HFC-236	612	245	930	633	861	1168	935	648
FC-C318	595	289	924	519	851	1182	950	445
FC-218	624	235	944	681	842	1170	928	663
HFC-32, i 25	639	227	913	693	844	1138	916	641
NaHCO ₃	623	252	947	643	852	1217	953	674
Alloy Avg.	615	239	926	650	846	1152	934	640
Std. Dev.	16	16	22	37	22	44	15	350

Table 3

Average Strain to Failure (%) in Each Agent at 150 °C as Compared to Ar at 150°C and Air at 25°C.

<u>Environ- ment</u>	<u>Nit 40</u>	<u>Al 6061</u>	<u>In 625</u>	<u>304 SS</u>	<u>CDA 172</u>	<u>13-8 Steel</u>	<u>AM 355</u>	<u>AISI 4130</u>
Lab Air 49.9	13.0	44.4	30.3	13.0	5.9	10.7	8.3	
Hot Ar	41.5	7.9	41.0	13.6	10.1	6.2	9.2	7.9
HCFC-22	30.3	6.6	31.6	12.5	12.0	7.6	9.5	8.1
HCFC-124	36.0	10.5	43.7	14.1	12.4	7.9	9.1	8.2
FC-31-10	34.3	10.1	37.2	12.4	12.9	6.5	7.8	8.0
HFC-227	37.8	10.7	42.6	13.6	11.7	6.9	9.6	7.7
HFC-125	40.4	9.8	43.4	15.1	11.6	6.7	9.8	8.1
FC-116	40.6	9.1	44.3	10.2	12.9	6.1	8.6	8.5
HFC-134a	37.7	9.4	46.5	12.7	10.1	7.7	9.2	7.8
HFC-236	36.3	9.7	41.5	16.9	9.7	7.0	9.7	8.2
FC-C318	42.2	8.5	43.1	9.5	12.8	8.1	9.1	9.6
FC-218	41.0	9.1	45.0	15.0	11.7	6.6	9.0	9.5
HFC-32/125	39.0	9.2	45.3	10.0	12.1	7.2	9.2	8.6
NaHCO ₃	42.5	7.5	46.0	17.4	11.5	10.5	9.5	7.5
Alloy Avg.	38.6	9.1	42.8	13.9	11.6	7.3	9.1	8.2
Std. Dev.	3.0	1.2	2.6	5.5	1.6	0.9	0.6	0.7

Table 4

Average Reduction in Area (%) in Each Agent at 150 °C as Compared to Ar at 150°C and Air at 25°C.

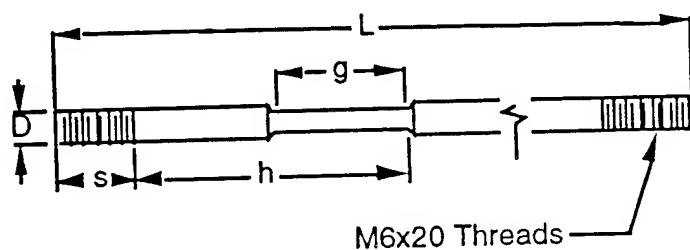
<u>Environ- ment</u>	<u>Nit 40</u>	<u>Al 6061</u>	<u>In 625</u>	<u>304 SS</u>	<u>CDA 172</u>	<u>13-8 Steel</u>	<u>AM 355</u>	<u>AISI 4130</u>
Lab Air	78.1	50.9	73.7	76.7	66.3	69.4	48.6	52.1
Hot Ar	79.2	42.3	69.5	67.8	27.5	60.0	48.6	50.8
HCFC-22	80.2	37.7	74.1	67.9	31.6	62.0	50.1	47.8
HCFC-124	79.8	35.8	65.7	71.7	36.6	56.2	48.3	48.7
FC-31-10	80.2	39.9	67.7	66.9	38.2	59.8	51.4	47.0
HFC-227	79.5	39.1	68.9	69.8	43.3	61.1	48.7	48.2
HFC-125	80.4	39.4	67.3	68.7	40.0	61.9	48.6	49.2
FC-116	79.3	45.4	72.1	67.0	36.4	63.9	49.3	49.2
HFC-134a	80.3	39.0	69.9	69.0	31.1	59.6	50.4	49.6
HFC-236	78.4	41.0	68.9	66.8	33.7	60.2	45.7	47.6
FC-C318	79.9	40.9	68.5	65.0	33.0	61.1	47.5	48.5
FC-218	86.2	42.2	69.3	70.8	31.4	59.5	47.2	47.5
HFC-32/125	82.2	41.9	70.9	65.9	42.1	62.6	46.2	47.1
NaHCO ₃	80.1	35.2	68.4	56.3	33.8	58.1	51.5	44.3
Alloy Avg.	80.4	39.9	69.3	67.7	35.3	60.6	47.9	51.4
Std. Dev.	2.3	2.3	3.2	5.3	3.2	6.4	2.2	5.10

Table 5

Slow Strain Rate Tensile Test Rankings for Each Alloy/Agent
Combination at 150 °C

<u>Environ- ment</u>	<u>Nit 40</u>	<u>Al 6061</u>	<u>In 625</u>	<u>304 SS</u>	<u>CDA 172</u>	<u>13-8 Steel</u>	<u>AM 355</u>	<u>AISI 4130</u>	<u>Agent Avg.</u>	<u>Std. Dev.</u>	<u>Agent Rank</u>
HCFC-22	4	3	4	1	3	2	3	2	2.75	1.04	10
HCFC-124	2	3	2	1	3	3	2	1	2.13	0.83	5
FC-31-10	3	2	2	1	4	1	3	1	2.13	1.13	5
HFC-227	2	3	1	1	5	1	3	1	2.13	1.46	5
HFC-125	1	2	1	1	4	1	4	1	1.88	1.36	3
FC-116	1	2	2	1	3	1	2	1	1.63	0.74	1
HFC-134a	2	2	3	1	2	2	3	2	2.13	0.64	5
HFC-236	2	2	1	1		1	3	1	1.63	0.74	1
FC-C318	1	4	1	5	2	3	2	6	3.00	1.85	12
FC-218	3	1	2	1	2	1	3	3	2.00	0.93	4
HFC-32/125	2	2	2	1	5	2	4	1	2.38	1.41	9
NaHCO3	1	4	2	3	2	6	2	2	2.75	1.58	10
Alloy Avg.	2.00	2.50	1.92	1.50	3.08	2.00	2.83	1.83			
Std. Dev.	0.95	0.90	0.90	1.24	1.16	1.48	0.72	1.47			
Alloy Rank	4	6	3	1	8	4	7	2			

<u>Rating</u>	<u>Freq</u>	<u>Interpretation</u>
1	32	No evidence of environment influence.
2	32	Slight indication of possible environmental influence.
3	19	Some evidence.
4	8	Strong evidence.
5	3	Nature of interaction should be evaluated.
6	2	Nature of interaction should be evaluated.
7	0	Nature of interaction should be evaluated.
8	0	Nature of interaction should be evaluated.
9	0	Nature of interaction should be evaluated.
10	0	Nature of interaction should be evaluated.



$D = 19 \text{ mm}$
 $L = 178 \text{ mm}$
 $g = 25.4 \text{ mm}$
 $h = 57 \text{ mm}$
 $s = 19 \text{ mm}$

Figure 1

6

Slow strain rate tensile sample design

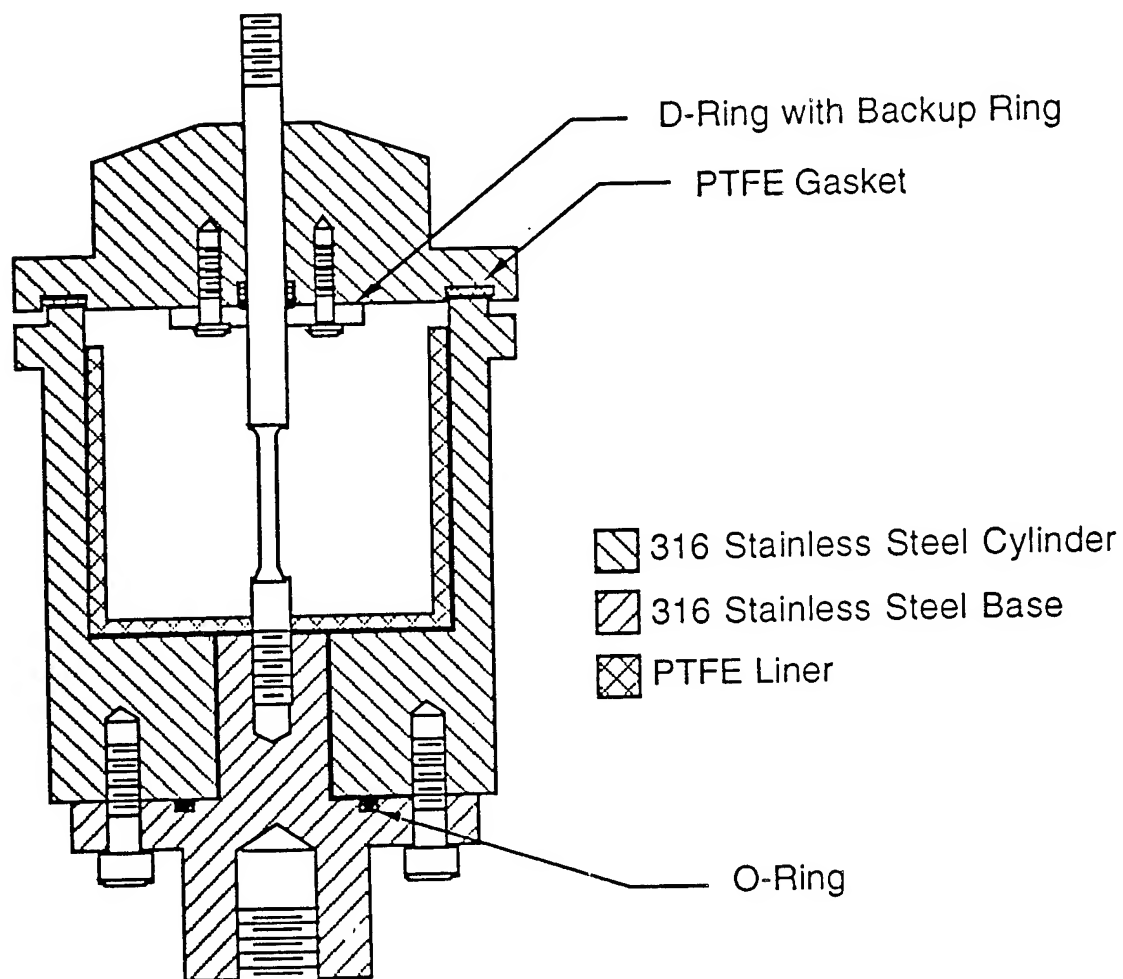


Figure 2

Slow strain rate tensile test chamber

Materials Degradation and Fatigue Under Extreme Conditions

Mr. Lance Ballard*,§, Department of Chemistry, University of Illinois, Urbana, Il. 61801

Dr. Jiri Jonas, Department of Chemistry, University of Illinois, Urbana, Il. 61801

Dr. Darrell Socie, Department of Mechanical and Industrial Engineering, University of Illinois, Urbana, Il. 61801

Dr. Steve Granick, Department of Materials Science and Engineering, University of Illinois, Urbana, Il. 61801

Dr. Andrew Gellman, Department of Chemical Engineering, Carnegie Mellon University, Pittsburgh, Pa., 15213-3890

Dr. K. Jimmy Hsia, Department of Theoretical and Applied Mechanics, University of Illinois, Urbana, Il. 61801

Dr. Jian Shang, Department of Materials Science and Engineering, University of Illinois, Urbana, Il., 61801

§Participant in the AASERT program.

RESEARCH OVERVIEW

This AFOSR University Research Initiative Program (F49620-93-1-0241) addresses complex research problems of materials degradation and fatigue in aerospace structures in severe or extreme environments. A better understanding of materials degradation and flaw initiation dynamics will be achieved through a multidisciplinary research program encompassing chemistry, surface physics, materials science and mechanics, both experimental and theoretical. The main scientific issues are as follows:

- Understanding of stress fields and sources of stress, leading to crack formation;
- Crack nucleation at surface defects;
- Understanding the kinetics and dynamics by which small cracks propagate through solids;

- Perfluoroalkylether surface chemistry, with emphasis on the decomposition reactions of specific functional groups, leading to understanding of fluid degradation and loss of lubricant properties;
- Macroscopic rheological measurements on extreme thin fluid films at extremely high shear rates, leading to understanding of the rheology of lubricant films so thin that continuum understanding does not apply; and,
- NMR and laser Raman scattering measurements of the dynamic structure of highly viscous fluids in contact with solid surfaces in confined geometries at high pressure and temperature.

RESEARCH ACCOMPLISHMENTS

SUB-PROJECT¹: SURFACE CRACK GROWTH UNDER COMBINED MECHANICAL AND HIGH PRESSURE FLUID LOADINGS

The focus of this sub-project has been investigations of the surface crack growth behaviors under combined high hydraulic pressure loading due to lubricants and mechanical loading due to rolling contact. The research work has been pursued with two parallel thrusts. One effort concentrates on the effects of the crack surface friction and the change of frictional stress due to the introduction of lubricants on surface crack growth. The second effort aims at providing a comprehensive solution to the problem involving the interaction between high pressure viscous fluid and a cracked body.

A micromechanics model has been developed to evaluate the effects of crack surface friction on fracture toughness of the materials. The model takes into account the microstructural parameters such as the grain size, grain shape, and frictional coefficient. A self-consistent approach was employed to derive the governing integral equation. The model is capable of predicting the toughening level due to surface friction for infinite and finite sized specimens under externally applied mode III loading. The results demonstrate that even under pure mode III loading, there will be mode I stress intensity at the crack tip induced by the crack surface roughness. The model predictions of mixed mode I/mode III fracture toughness agree very well with existing experimental measurements. Furthermore, the effect of lubricant is studied by changing the frictional coefficient. The result shows that, by introducing lubricant, the toughening is reduced, thus resulting in a higher crack tip stress intensity and a higher crack growth rate.

The effects of high pressure viscous fluid on surface crack growth have been studied by using fluid mechanics and fracture mechanics approaches. We considered a crack filled with a linear viscous fluid in a semi-infinite body and with a large fluid reservoir outside the crack mouth. The pressure history in the fluid reservoir was prescribed. It was found that the governing equations of this problem were two coupled non-linear integral equations of two unknown functions, the pressure distribution inside the crack $p(x,t)$ and the crack face opening displacement $h(x,t)$. To simplify the problem, a local pressure-displacement relation was assumed. Analytical solutions were obtained using separation of variables. The results indicate that there exists a characteristic time which is a function of viscosity of the fluid, Young's modulus of the solid, and the ratio of crack length to the average opening displacement of the crack. If the period of the external loading is much longer than the characteristic time, the pressure distribution in the crack is nearly uniform, resulting in a high crack tip stress intensity. On the other hand, when the period of external loading is much shorter than the characteristic time, pressure will not be transmitted deep into the crack, resulting in a low crack tip stress intensity. This result can be used to guide the experimental part of this project.

SUB-PROJECT²: FLUID-ASSISTED FATIGUE CRACK GROWTH IN CERAMICS

This sub-project is concerned with the role of the lubricant as a corrosive fluid assisting in fatigue crack growth. Under high pressure and high temperatures caused by the heat generated by friction at the contact location, the lubricant could decompose into corrosive fluid. At the crack tip, the interaction between the corrosive fluid and the crack tip is mutual: the chemical reaction (corrosion) will enhance the crack growth rate; on the other hand, the high crack tip stress will accelerate the chemical reaction rate. Thus when exposed to a corrosive environment, the crack growth rate will be faster.

As microcracks grow longer, transition from an initial Mode-II crack (also known as a stage-I crack) to a Mode-I (stage-II) may occur at some crack length. Crack growth is governed by different driving forces before and after the transition and will likely follow different growth laws. The growth laws will be established in terms of the growth rate as a function of stress or stress intensity as appropriate. The growth rate of microcracks will be measured by the surface replicating technique in combination with periodic inspection of crack shapes. The transition crack length will be determined in different microstructural and environmental conditions.

Our investigation thus far on fatigue crack growth in a fluorinated oil (Krytox, DuPont) and air has shown that lubricants can have a significant effect on the fatigue failure of silicon nitride (Si_3N_4). Fluorinated oil, despite its excellent chemical stability, accelerates fatigue crack growth in Yttrium (Y) - containing Si_3N_4 . In particular, the growth rate of surface microcracks in the fluorinated oil was found to be about twice the rate in air. Our preliminary work indicates that the oil assisted fatigue crack growth in Y-containing Si_3N_4 by dissolving Y-containing grain boundary phase, thereby reducing the effectiveness of acicular grains in crack bridging. The effect could be aggravated in real bearing applications where the chemical stability of the oil may be adversely affected by the high pressure and high temperature.

SUB-PROJECT³: SURFACE INDUCED DEGRADATION OF FLUOROCARBON LUBRICANTS

The focus of this sub-project has been a study of the surface chemistry of fluorocarbons, with a particular interest in the understanding of surface chemical reactions important in tribological applications. The relevance of fluorocarbons to tribological applications derives from the extremely high thermal stability of the perfluoroalkylethers (PFAEs) which makes them suitable for use as lubricants under high temperature conditions. Their deficiency arises from the fact that little is known about the types of materials that can be used as boundary layer additives. The materials classically used as boundary layer additives in hydrocarbon lubricant fluids are amphiphilic in nature and serve to coat metal surfaces with thin surfactant-like films. These prevent metal surfaces in sliding contact from actually reaching the point of direct metal-metal contact. These additives both lubricate the surfaces and prevent the wear that would result from direct metal-metal contact. Most of the hydrocarbons that would normally be considered for use as additives in hydrocarbon fluids are neither soluble in the fluorocarbons nor stable to the temperatures at which the fluorocarbons are used.

The fundamental goal of this program is an understanding of surface chemical problems in lubrication and in particular in lubrication by fluorocarbons. Over the past year we have studied a number of reactions of fluorocarbons on metal surfaces in order to deepen our understanding of the role that fluorine plays in influencing surface reaction kinetics. We have focused on the reactions of fluorinated olefins on copper (Cu) surfaces and on the coupling reactions of alkyl groups on silver (Ag) surfaces. While fluorination has little influence on the π -bonding of the olefins to metal surfaces, fluorination of alkyl groups dramatically lowers the rates of coupling. Other work has included

development of measurement techniques for our surface studies. In one case, our ultra-high vacuum (UHV) tribometer has been used to look at friction of Cu(111) surfaces lubricated by submonolayer films of fluorinated ethanol. Most recently we have set up a Fourier Transform Infrared (FTIR) spectrometer for measurements of vibrational spectra of adsorbed monolayers on metal surfaces in ultra-high vacuum. This has been used to obtain spectra of a series of fluorinated ethoxides on the Cu(111) surface. These are to be used to begin determining the orientations of adsorbed species used as lubricants.

SUB-PROJECT⁴: FLUIDS, INCLUDING LUBRICANTS, UNDER EXTREME CONDITIONS OF HIGH PRESSURE, HIGH TEMPERATURE, AND CONFINEMENT

This sub-project deals with nuclear magnetic resonance (NMR) and laser Raman scattering experiments on highly viscous liquids, including lubricants, both in bulk and in confined geometries, over a wide range of pressures and temperatures. In a general sense, we focus on the relationship between molecular level properties as obtained from our experiments and the macroscopic properties of the fluids studied, including fluids at the fluid-solid interface. This focus allows molecular correlations with rheological properties such as viscosity.

In continuation of our systematic efforts to improve the understanding of the dynamic behavior of confined fluids, we have carried out NMR relaxation experiments on a number of molecular fluids, including model lubricants. Our studies of confinement effects on relaxation of polar and nonpolar molecules have confirmed a two-dimensional theoretical explanation. Application of a two-state, fast exchange model allows separation of surface effects from bulk liquid effects, which in turn provides insight into the dynamic behavior and viscosity of the surface layer. Recent applications of the two-state, fast exchange model to additional model systems provide us with a stronger basis for actual lubricant studies in the near future.

A very important aspect of our research is the further development of unique NMR and other instrumentation to permit studies of various materials under extreme conditions of pressure and temperature. This includes our recent development of NMR probes and pressure generating systems which permit measurements up to pressures of 10kbars. Our long-term goal to improve our expertise in the experimental techniques for extreme conditions is not only of basic research importance, but it also has direct technological relevance to the Air Force mission.

This relevance is reflected in our work with the model lubricant ethylhexylbenzoate (EHB), including an earlier bulk liquid study to 5kbars and our recent confinement studies. The bulk liquid study has provided the framework for current work with the closely related lubricant, di-(2-ethylhexyl)phthalate (DEHP). These studies should help to separate the effects of structure on the motional dynamics of lubricants. Our confinement studies of EHB have shown the applicability of the two-state, fast exchange model to a model lubricant system, as well as the domination of geometric confinement effects over surface interaction effects at low frequency. We are currently in the process of extending these confinement studies to model fluorinated lubricants. These studies will be supplemented by studying pressure effects on confined liquids using our unique techniques.

SUB-PROJECT⁵: MOLECULAR TRIBOLOGY OF PERFLUOROETHER LUBRICANTS

This sub-project revolves around the tribology of perfluoroether fluids under extreme, but nonetheless well-defined, conditions of shear rate and confinement. The experimental design consists of an idealized single asperity: fluid films sandwiched between atomically smooth solid surfaces that are close together at a controlled separation (5-500 Angstroms) but not actually touching. The film thickness and shear displacements can be controlled to 1 Å, at shear rates from 10^{-2} to 10^5 sec^{-1} . A unique feature is the capacity to measure not only conventional dissipative friction, but also fluid elasticity.

The friction behavior of model lubricants, either fluorinated or hydrogenated, has been compared. In both cases, the liquids were confined between two atomically smooth parallel mica plates. The method of measurement was a surface forces apparatus, modified for oscillatory shear. Some observations were the same in both cases: (1) Predominantly elastic behavior in the linear response state was followed by a transition to a mostly dissipative state at larger deformations. The elastic energy stored at the transition was low, of the order of 0.1 kT per molecule. This transition was exactly repeatable in repetitive cycles of oscillation and reversible. (2) The dissipative stress in the sliding state was only little dependent on peak sliding velocity when this was changed over several decades. Significant (although smaller) elastic stress also persisted, which decreased with increasing deflection amplitude. (3) The transition back to the solid-like state appears to be more gradual than in the opposite direction, probably indicating different processes.

Two major differences between fluorinated and hydrogenated systems were observed: (1) For fluorinated molecules, the shear stress in the sliding regime was mostly higher than in the solid-like state, whereas for hydrogenated molecules this stress was significantly lower. (2) Fluorinated molecules needed long relaxation times (several minutes) to adjust to changes in the applied stress.

In the above experiments, the mica surfaces were not damaged, as was confirmed by the reproducibility of the results. However, at large amplitudes and high frequencies of oscillation, damage was observed giving rise to characteristic changes in the responding stresses, as well as the thickness of the lubricant film.

ACKNOWLEDGEMENT

This work was supported in part by the Air Force Office for Scientific Research (FOSR) under Grant F49620-93-1-0241 and by the Augmentation Awards for Science and Engineering Research Training (AASERT) Program under Grant F49620-93-1-0555.

REFERENCES

- 1.1 K.J. Hsia, T.L. Zhang, and D.F. Socie, "Effects of Crack Surface Friction on Mixed Mode Fracture in Ceramics," presented at American Ceramic Society Annual Meeting, Indianapolis, IN, April 24-28, 1994.
- 1.2 K.J. Hsia, Z.-Q. Xu, "Effects of Hydraulic Pressure on Rolling Contact Failure of Ceramic Components," presented at American Ceramic Society Annual Meeting, Indianapolis, IN, April 24-28, 1994.
- 1.3 K.J. Hsia, Z.-Q. Xu, R.E. Johnson, "Effect of Hydraulic Pressure on Surface Crack Propagation," an invited presentation at International Symposium on Fracture and Strength of Solids, Xi'an, China, July 4-7, 1994.
- 2.1 D. Yao and J.K. Shang, "Fluid-Assisted Fatigue Crack Growth in Si_3N_4 ," *Ceramic Eng. & Sci. Proc.*, 1994, in press.
- 2.2 D. Yao and J.K. Shang, "Lubricant-Assisted Fatigue Crack Growth in Si_3N_4 ," *Trans. ASLE*, 1994, submitted.

- 3.1 A.J. Gellman, Q. Dai, "The Mechanism of β -Hydride Elimination in Adsorbed Alkoxides," *J. Am. Chem. Soc.* **115**, (1993), 714-722.
- 3.2 Q. Dai, A.J. Gellman, "Fluorine Substituent Effects in Alkoxide Chemistry on the Cu(100) Surface," *J. Phys. Chem.*, **97**, (1993), 10783-10789.
- 3.3 J. Forbes, A.J. Gellman, "The β -Hydride Elimination Mechanism in Adsorbed Alkyl Groups," *J. Am. Chem. Soc.*, **115**, (1993), 6277-6283.
- 3.4 B. Parker, A.J. Gellman, "Interactions of Hydrocarbon and Fluorocarbon Acids with the Ag(110) Surface," submitted to *J. Amer. Chem. Soc.*
- 4.1 J. Zhang and J. Jonas, "NMR Study of the Geometric Confinement Effects on the Anisotropic Rotational Diffusion of Acetonitrile-d₃," *J. Phys. Chem.*, **97**, (1993), 8812.
- 4.2 S. Xu, Y.J. Kim, and J. Jonas, "Pressure Effects on the Anisotropic Rotational Diffusion of Acetonitrile-d₃ in Confined Geometry," *Chem. Phys. Lett.*, **218**, (1994), 329-332.
- 4.3 J. Zhang and J. Jonas, "High Resolution ¹³CNMR Study of Liquid 2-Ethylhexyl Benzoate Confined to Porous Silica Glasses," *J. Phys. Chem.*, in press.
- 4.4 J.P. Korb, A. Delville, S. Xu, Y.J. Kim, G. Demeulenaere, P. Costa, and J. Jonas, "Relative Role of Surface Interactions and Topological Effects in NMR of Confined Liquids," *J. Chem. Phys.*, submitted.
- 4.5 "Pressure as an Experimental Variable in NMR Studies of Molecular Dynamics," in *Nuclear Magnetic Resonance Probes of Molecular Motions*, Ed. R. Tycko, Kluwer Publ., New York, 1994, in press.
- 5.1 G. Reiter, A.L. Demirel, and S. Granick, "From Static to Kinetic Friction in Confined Liquid Films," *Science*, **263**, (1994), 1741-1744.
- 5.2 G. Reiter, A.L. Demirel, J. Peanasky, L. Cai, and S. Granick, "Stick to Slip Transition and Adhesion of Lubricated Surfaces in Moving Contact," *J. Chem. Phys.*, in press.

Growth and Breakdown of Surface Films and Localized Corrosion of Aluminum in Concentrated Chloride Media

Jiajing Lee* and Ajit K. Mal
Mechanical, Aerospace and Nuclear Engineering Department
University of California
Los Angeles, CA 90024-1597

and

Ken Nobe**
Chemical Engineering Department
University of California
Los Angeles, CA 90024-1592

INTRODUCTION

Oxide films and salt films form on metal surfaces during anodic dissolution. In high chloride concentration environments the oxide films break down and salt films form. A number of investigations by Beck [1-9] and Isaacs and his co-workers [10-12] and others [13-18] have been directed to the elucidation of the role that salt films play in localized corrosion of metals and in mass transport of the active species that contribute to the formation and breakdown of these surface films.

Current/potential fluctuations or oscillations have been observed and related to localized corrosion [19-30]. These fluctuations have often been associated with depassivation and repassivation events involved in pitting. This erratic temporal behavior had been considered by many to occur randomly. As a result, current fluctuations have been analyzed by stochastic methods (see reviews, refs. 30, 31).

Oscillating behavior during anodic dissolution of metals have been reported for over a century (see references in ref. 32). Oscillations in potential or current have been associated with the instability of the anodic oxide and salt films formed during anodic dissolution of metals.

Oscillatory behavior was first observed in our UCLA Electrochemical Laboratory during H. C. Kuo's studies of high rate iron electrodisolution in concentrated chloride solutions in 1972 [33]. Temporal formation and disappearance of black surface films were visually observed to occur in concert with potential oscillations. The black salt film was identified as FeCl_2 [13].

*author to whom correspondence should be addressed

Hudson and co-workers at the University of Virginia [34,35] and investigators in the UCLA Electrochemical Laboratory [36,37] and others [38,39] have recently begun to apply nonlinear dynamic analysis to the potential/current oscillations observed during anodic dissolution of metals. With more extensive studies the results of these analyses may provide new insights into the role of salt films on localized corrosion processes such as pitting and stress corrosion cracking.

Our overall goal is to ascertain the relationships between pitting and crack initiation, the formation and breakdown of salt films (including oxides) and mechanical stress for aluminum and titanium alloys in aggressive corrosion environments. This report presents results of some very preliminary experiments on aluminum alloys and titanium during anodic dissolution in chloride media. With more extensive studies, we seek to determine if nonlinear dynamic techniques can provide further information regarding the relationship between the fluctuations and oscillations observed during anodic metal dissolution and localized corrosion phenomena.

EXPERIMENTAL

The electrochemical studies have been performed with a rotating disk electrode system. The schematic diagram of the electrochemical cell (2 liter beaker), its components, the associated instrumentation and electrode assembly has been given elsewhere [40]. The disk electrodes were prepared from alloy rods of 0.635 cm (0.25 in) diameter. The surface of each disk electrode to be exposed to the electrolyte was polished after being embedded in a Teflon cylinder with waterproof alumina paper of various grit sizes (200, 400 and 600), polished on a polishing wheel using one micron alumina powder, washed thoroughly with distilled water, degreased with acetone and finally rinsed in distilled water before being immersed in the solution.

The aluminum alloys selected for study were 6061T5 (97.9% Al, 1% Mg, 0.6% Si, 0.3% Cu, 0.2% Cr) and 2024T4 (93.5% Al, 4.4% Cu, 1.5% Mg, 0.6% Mn). The reference electrode was a saturated calomel electrode. The solutions (0.1, 1.0 and 5.0 M) were prepared from distilled water and reagent grade sodium chloride. All experiments were conducted at room temperature.

The polarization experiments were carried out with a PAR potentiostat/galvanostat (model 273). Data acquisition was performed with a PC using GPIB interface card.

RESULTS AND DISCUSSION

A series of experiments were performed with the 6061 alloy in 5 M NaCl. Figure 1 shows a current sweep at 50 mA/s when the alloy disk was rotated at 500 rpm. Potential fluctuations were observed and examination of the surfaces by an optical microscope shows considerable pit formation. Time series of the potential oscillations, power spectra and phase portraits for stationary 6061 alloy disks in 5 M NaCl at constant applied currents of 1, 5 and 50 mA are compared in Fig. 2. The amplitudes of the potential oscillations increased somewhat when the current increased from 1 to 5 mA. However, when the applied current is increased to 50 mA, the amplitudes increased by over an order of magnitude. At 1 and 5 mA, tangled trajectories in the phase portraits are seen with a higher density of the trajectories obtained at the higher current. These results indicate the

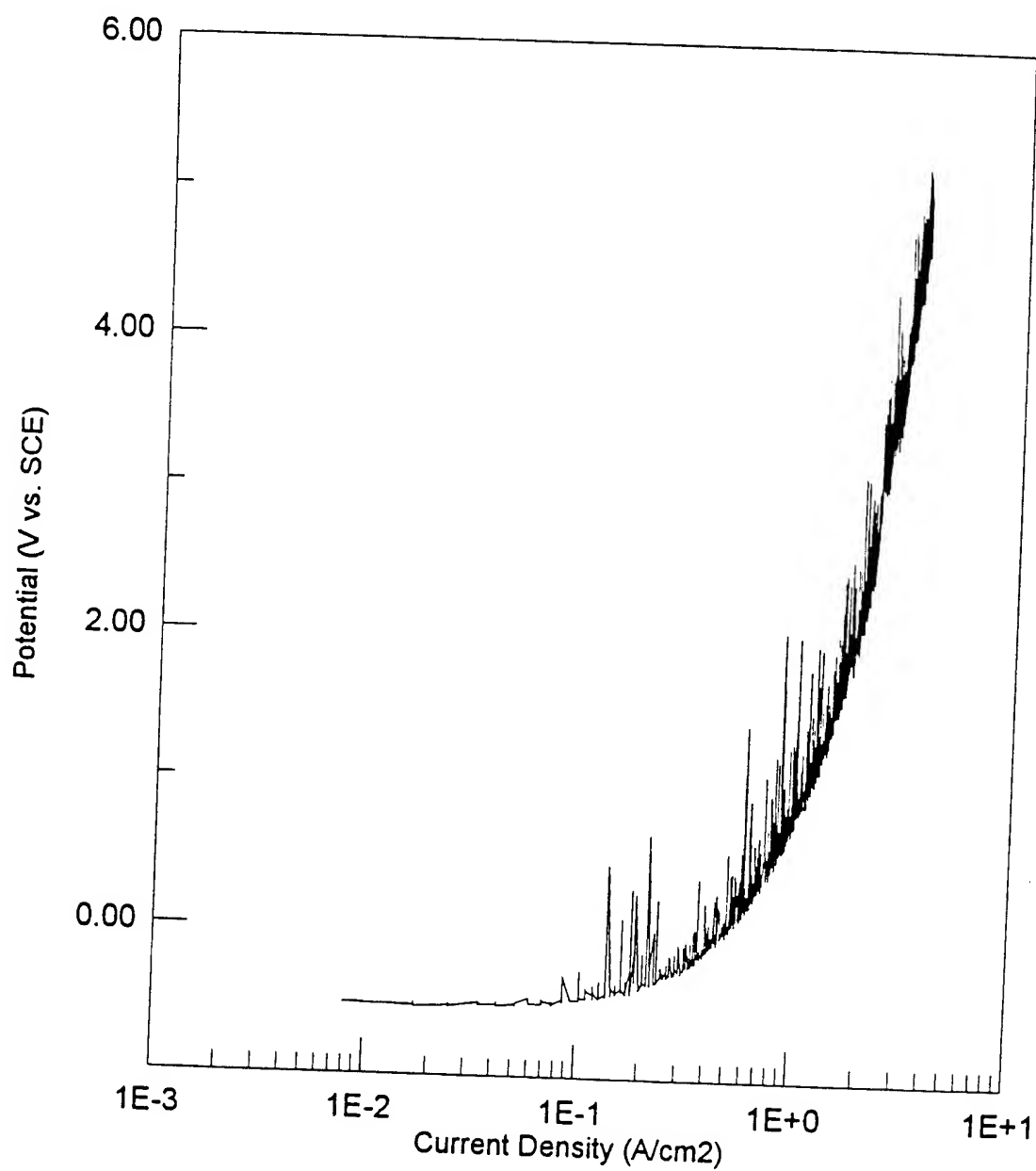


Fig 1. 6061 aluminum in 5M NaCl and 500 rpm with current sweep rate of 50 mA/sec.

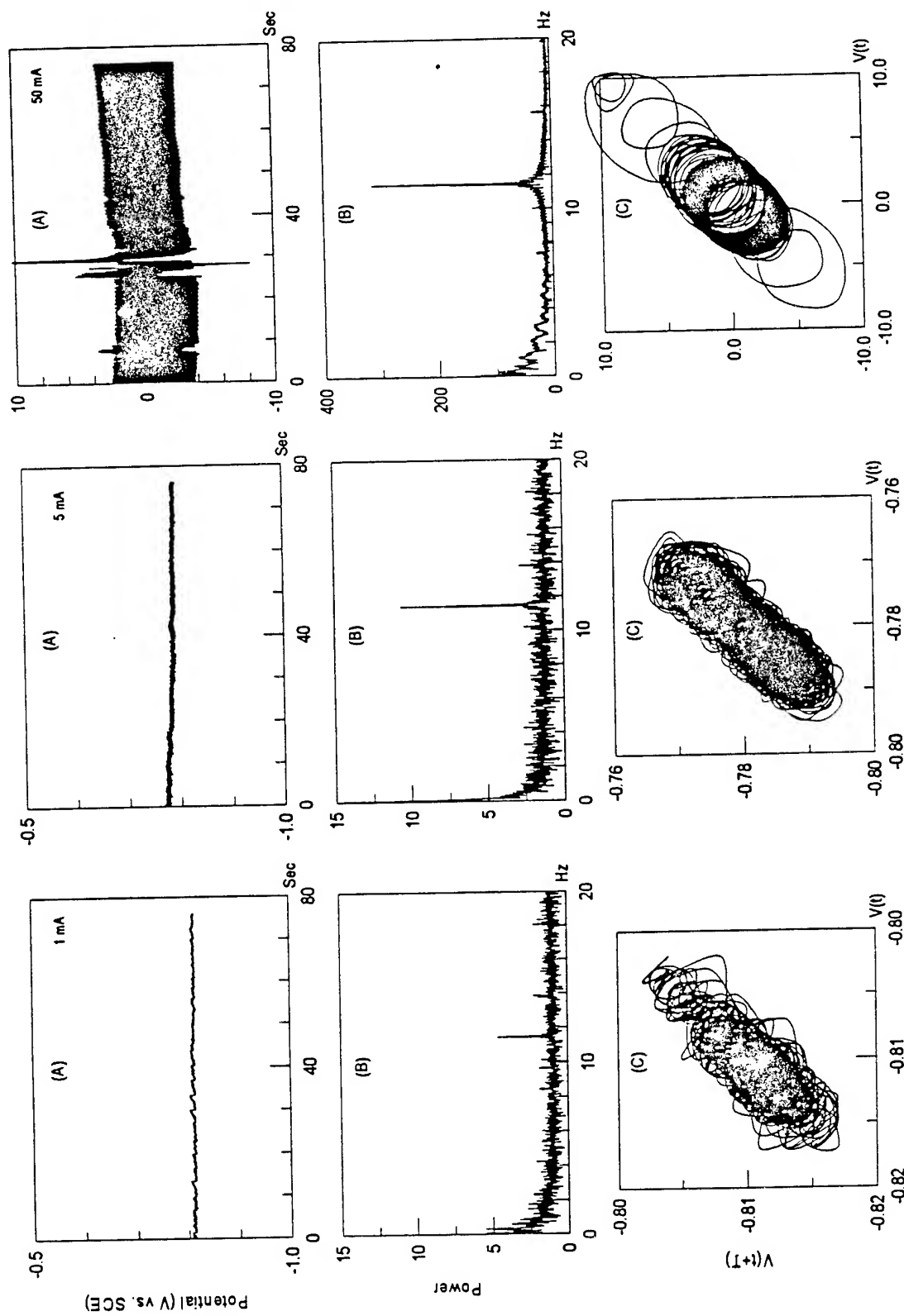


Fig 2. 6061 aluminum in 5M NaCl with applied constant current, (A) time serie, (B) power spectra, (C) phase portrait.

deterministic nature of the aperiodic potential oscillations. On the other hand, at 50 mA, a more regular appearing attractor suggests quasi-periodicity in the oscillatory behavior.

Figure 3 shows the potential sweep behavior of the 2024 alloy in 0.1, 1.0 and 5 M NaCl at rotation rates of 0, 500 and 1000 rpm. At 5 M NaCl and 100 rpm, the current fluctuations were larger at potentials near the corrosion potential. As the potential increased and approached 0.0 V vs. SCE, the current oscillations decreased. At 1 M NaCl and 1000 rpm the current fluctuations were less than observed for 5 M. It is also seen that during the potential sweep the currents decreased substantially as the rotation rates increased to 5 M. In comparison, in 0.1 M NaCl there was a small increase in currents when the rotation rates increased. By comparing the potential sweeps of the 2024 alloy in 1 M and 5 M NaCl at 1000 rpm the currents were significantly less in the higher concentration. This observation is similar to that reported during iron electrodisolution in concentrated chloride solutions and had been attributed to the change in solubility of FeCl_2 in NaCl [41]. The potential-current density behavior has been magnified between 0.7 to 0.9 V vs. SCE to enable a more detailed examination of the current fluctuations and their dependence on the chloride concentration and hydrodynamic conditions (Fig. 4).

Potential oscillations of the 2024 alloy in 0.1 M NaCl during constant current experiments of 0.0001, 1.0 and 100 mA at 500 and 1000 rpm for the first two seconds are shown in Fig. 5. An increase in rotation rate decreased the mean potential of the oscillation amplitudes. The potential oscillations at 1 mA during the first 120 seconds are shown in Fig. 5. The power spectra and the phase portraits corresponding to the time series at both 500 and 1000 rpm are also shown. Major differences in the power spectra and portraits were not evident at the two rotation rates.

Figure 6 compares the time series (first five seconds) of the potential oscillations of the 2024 alloy in 1 M NaCl during constant current experiments of 1 and 100 mA for stationary disks. In addition, a comparison of the time series (first 120 seconds) of the potential oscillations, the power spectra and phase portraits at 1 and 100 mA are shown in Fig. 6. Significant differences in all three sequences at the two currents are clearly evident.

The surfaces of the 2024 alloy after the constant current experiments were examined by optical microscopy. The density of the pits increased substantially as the chloride concentration increased from 0.1, 1.0 and 5 M NaCl. The size of the pits appeared larger for the alloy exposed to 0.1 M NaCl than either 1.0 and 5 M NaCl. Additional experiments are required to more conclusively determine the dependence of the surface morphology on the magnitude of the applied current and hydrodynamic conditions.

Some preliminary results of the oscillatory behavior of titanium (65 A) in 1 M HCl are shown in Fig. 7. The aperiodic potential oscillations, power spectra and phase portraits during constant current (1.047 A/cm^2) anodic dissolution of titanium in 1 M HCl suggest that the observed oscillations correspond to deterministic chaos rather than to random noise. Additional experiments and further analyses are needed to establish the validity of this preliminary assessment.

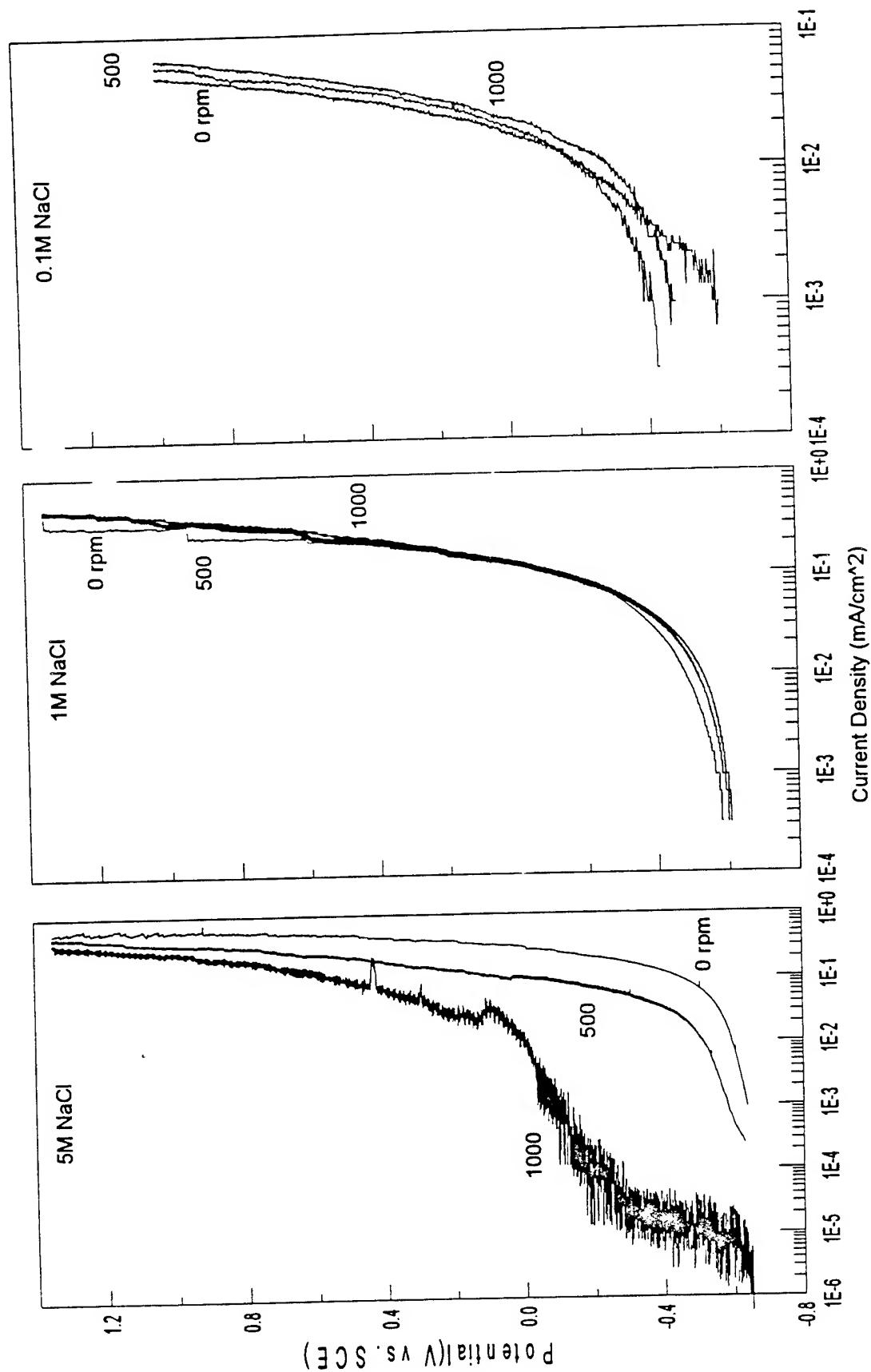


Fig 3. Potential sweep performed on 2024T4 aluminum. (sweep rate=10mV/sec)

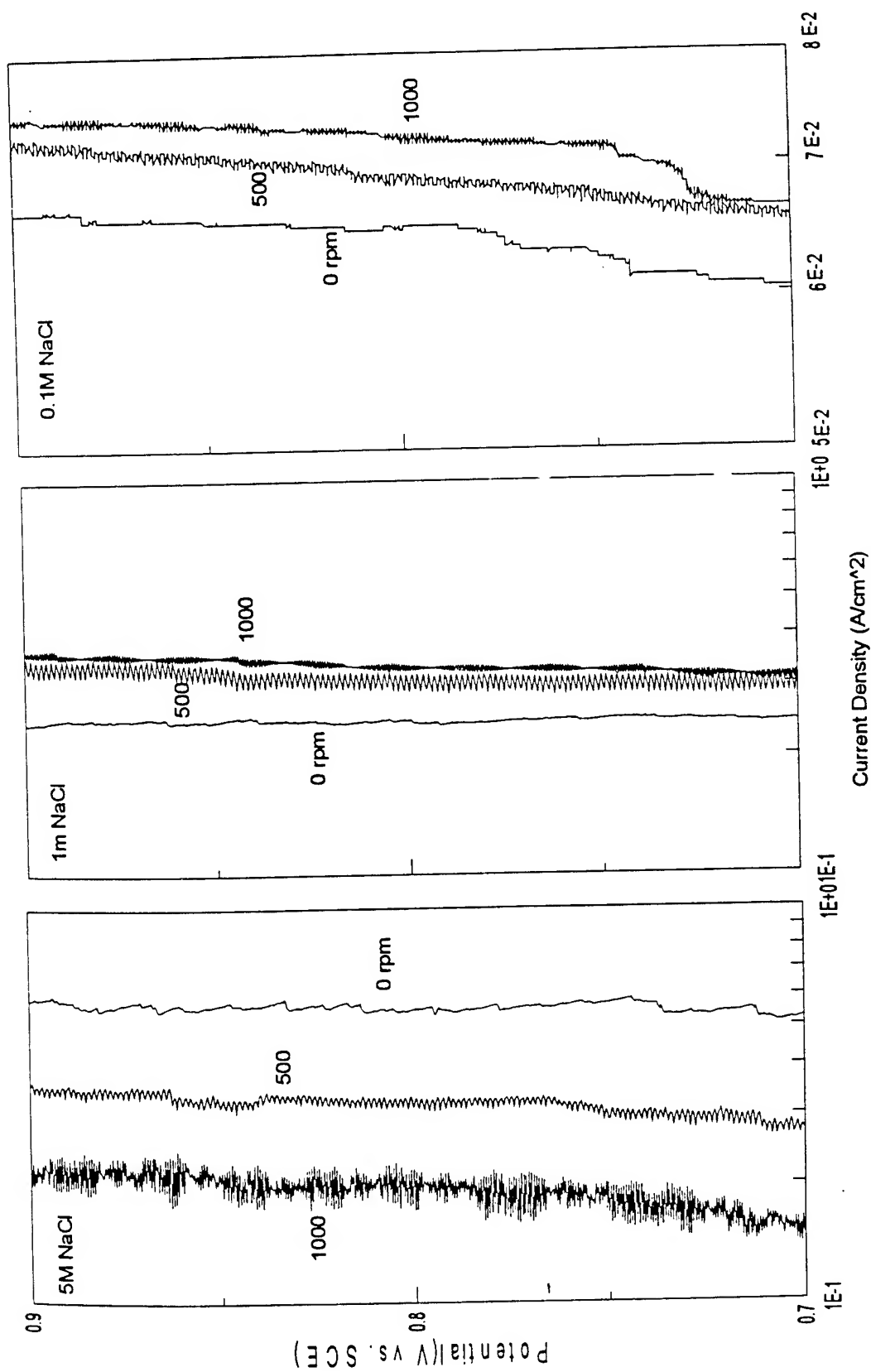
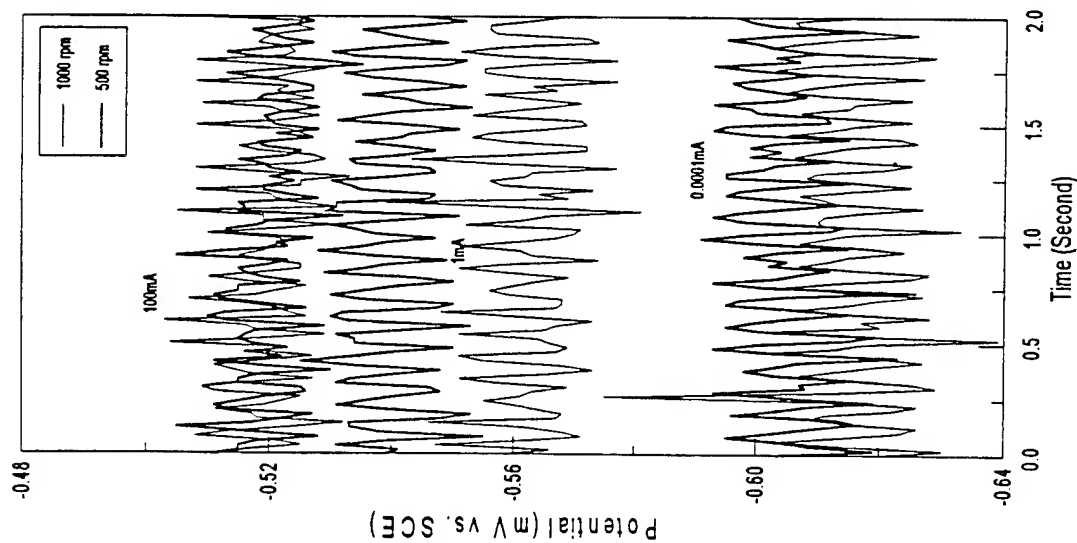


Fig 4. Potential sweep performed on 2024T4 aluminum. (sweep rate=10mV/sec)



2024 aluminum in 0.1M NaCl, Time series.
(sampling rate = 0.02 sec/pt.)

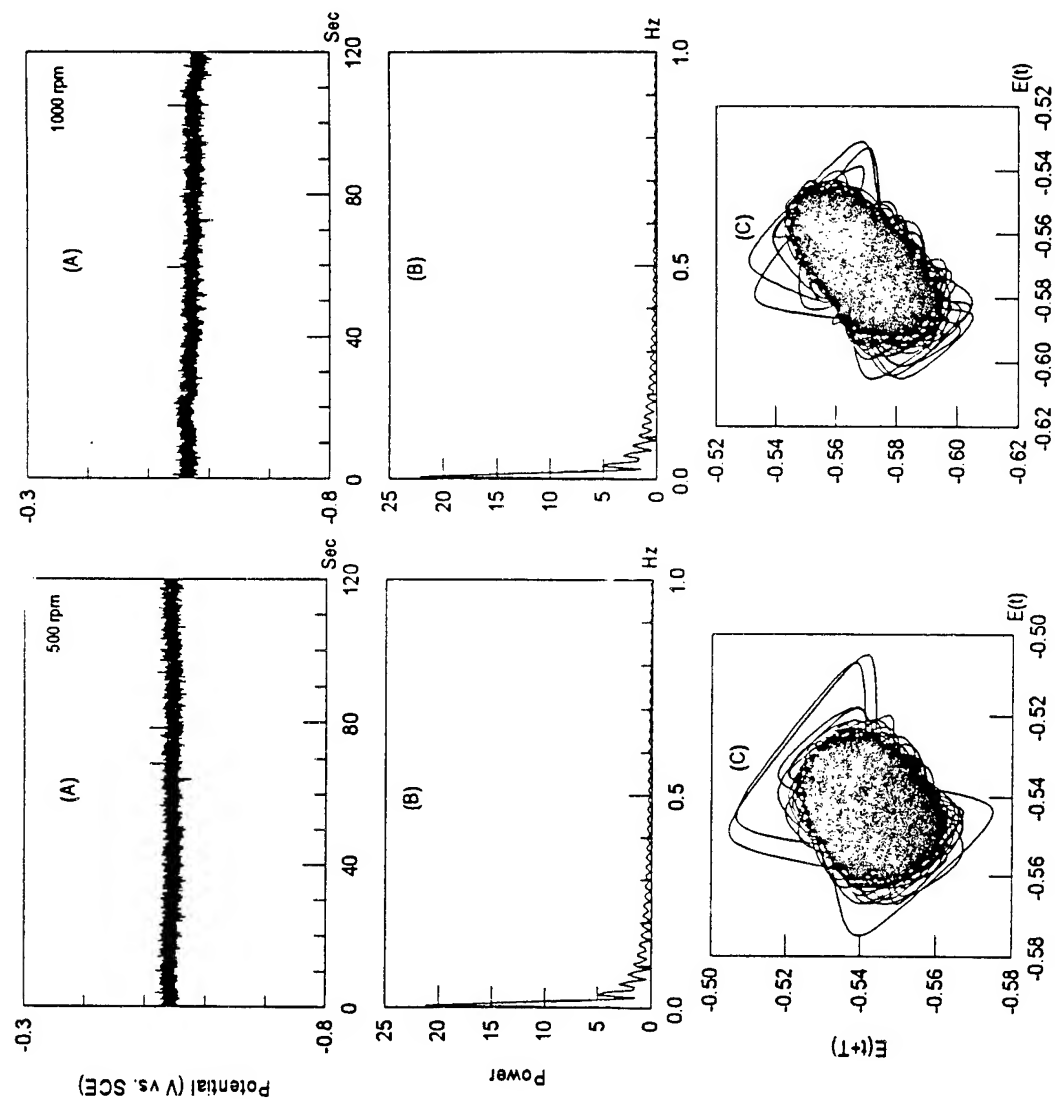


Fig 5. 2024 aluminum in 0.1M NaCl with applied constant current 1 mA
(A) time serie, (B) power spectra, (C) phase portrait.

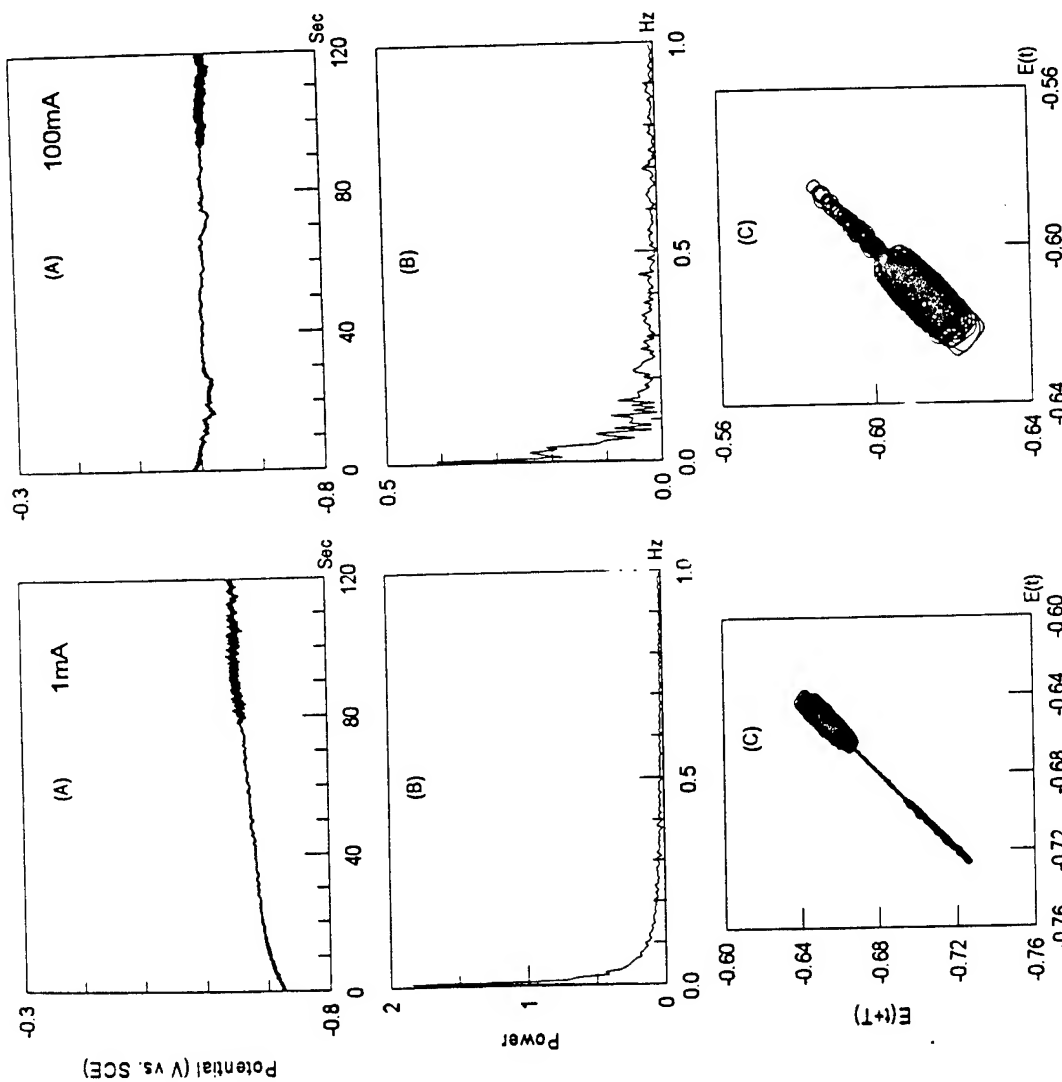
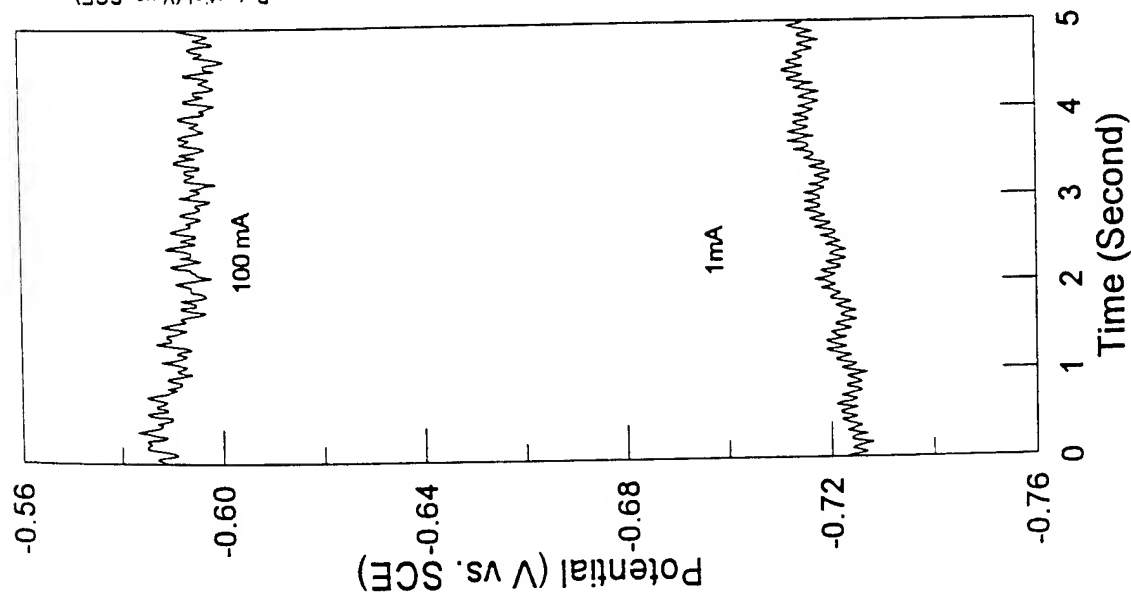


Fig 6. 2024 aluminum in 1 M NaCl with applied constant current, (A) time series, (B) power spectra, (C) phase portrait

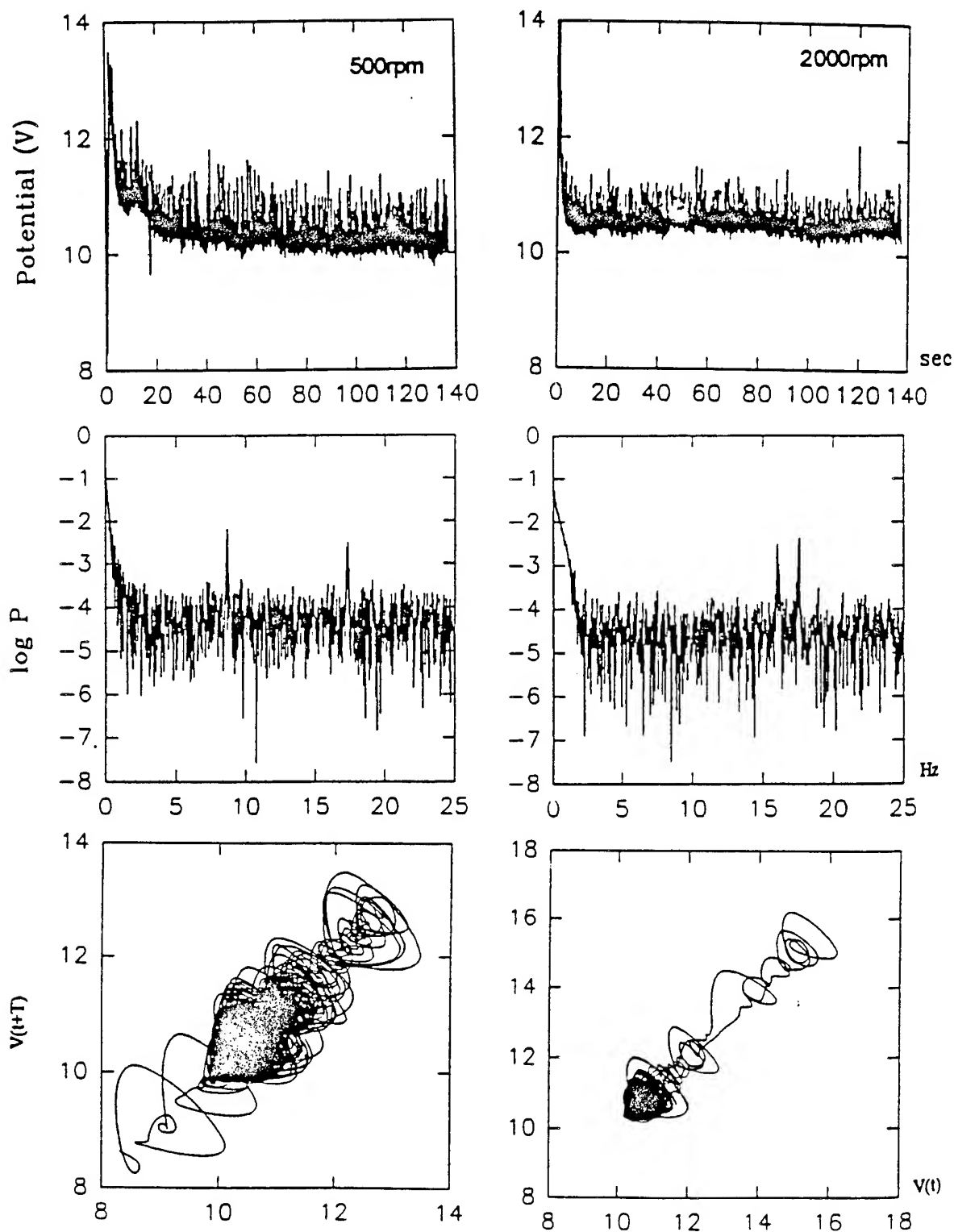


Fig 7. Titanium rotating disk electrode in 1 M HCl, 1.047A/cm²

SUMMARY OF PRELIMINARY RESULTS

Fluctuations or oscillations of potential/current were observed during preliminary anodic dissolution experiments of 6061 and 2024 aluminum alloys, and pure titanium in chloride media.

Characterization of the time series in the potential oscillations by power spectra and phase portraits suggests that the erratic temporal behavior is associated with a deterministic strange attractor and is not driven by external noise. However, further analysis is required to establish this preliminary assessment.

Examination of the surface after anodic dissolution of 2024 alloy disks by optical microscopy indicate that the density of pits increased substantially as the chloride ion concentration increased from 0.1, 1.0 to 5.0 M. Pits were larger when the alloy was exposed to 0.1 than to either 1.0 or 5.0 M NaCl.

ACKNOWLEDGMENTS

This work was supported by the U.S. Air Force/Office of Scientific Research (F49620-93-1-0320P00001). Jarrod Williamson performed the titanium experiments and analysis.

REFERENCES

1. T.R. Beck, *Localized Corrosion*, R. W. Staehle, Ed., NACE, Houston, TX, p. 644 (1974).
2. T.R. Beck, *J. Electrochem. Soc.*, **120**, 1310 (1973).
3. T.R. Beck, *Ibid*, **120**, 1317 (1973).
4. T.R. Beck, *Corros. J.*, **30**, 408 (1974).
5. T.R. Beck, *Ibid*, **33**, 9 (1977).
6. T.R. Beck and S.G. Chan, *Ibid*, **37**, 665 (1981).
7. T.R. Beck, *J. Electrochem. Soc.*, **129**, 2412 (1982).
8. T.R. Beck, *Electrochim. Acta*, **29**, 485 (1984).
9. T.R. Beck, *Ibid*, **30**, 724 (1985).
10. H.S. Isaacs, *J. Electrochem. Soc.*, **120**, 1456 (1973).
11. U. Steinsmo and H.S. Isaacs, *Ibid*, **140**, 643 (1993).
12. U. Steinsmo and H.S. Isaacs, *Corros. Sci.*, **35**, 83 (1993).
13. H.C. Kuo and D. Landolt, *Electrochim. Acta*, **20**, 393 (1975).
14. K.H. Strehblow and J. Wenner, *Electrochim. Acta*, **22**, 421 (1977).
15. R. Alkire, D. Ernsberger and T.R. Beck, *J. Electrochem. Soc.*, **125**, 1382 (1978).
16. P. Russell and J. Newman, *Ibid*, **133**, 59 (1986).
17. C. Moina and D. Posadas, *Electrochim. Acta*, **32**, 1203 (1987).
18. M.J. Danielson, *J. Electrochem. Soc.*, **135**, 1326 (1988).
19. I.L. Rosenfeld and I.S. Danilov, *Corros. Sci.*, **7**, 129 (1967).
20. Z. Szklarska-Smialowska and M. Janik-Czachor, *Br. Corros. J.*, **4**, 138 (1969).
21. J.R. Galvele, S.M. de DeMicheli, I.L. Muller, S.B. deWexler and I.L. Alanis, *Localized Corrosion*, K.W. Staehle, Ed., NACE, Houston, TX, p. 580 (1974).

22. G.C. Wood, W.H. Sutton, J.A. Richardson, T.N.K. Riley and A.G. Malherbe, *Ibid*, p. 526 (1974).
23. U. Bertocci, *J. Electrochem. Soc.*, 127, 1931 (1980).
24. U. Bertocci and Y. Yang-Xiang, *Ibid*, 131, 1011 (1984).
25. U. Bertocci, J.L. Muller and Y. Yang-Xiang, *Passivity of Metals and Semiconductors*, M. Froment, Ed., p. 229, Elsevier, Amsterdam (1983).
26. C. Gabrielli, F. Huet, M. Keddam, R. Oltra and C. Pallota, *Ibid*, p. 193 (1983).
27. U. Bertocci, M. Koike, S. Leigh, F. Qiu and G. Yang, *J. Electrochem. Soc.*, 133, 1782 (1986).
28. C. Gabrielli, M. Keddam, M. Krarti and C. Pallota, *Computer Aided Acquisition and Analysis of Corrosion Data*, M.W. Kendig, U. Bertocci and J.E. Strutt, Eds., p. 210, The Electrochem. Soc. Softbound Proc. Ser., PV 85-3, Pennington, NJ (1985).
29. R.A. Cottis and C.A. Lots, *Corros*, 46, 12 (1990).
30. C. Gabrielli, F. Huet, M. Keddam and R. Oltra, *Ibid*, 46, 266 (1990).
31. S.M. Sharland, *Corros. Sci.*, 27, 289 (1987).
32. H.-P. Lee, Ken Nobe and Arne J. Pearlstein, *J. Electrochem. Soc.*, 132, 1031 (1985).
33. H.C. Kuo, M.S. thesis, UCLA (1973).
34. C.B. Diem and J.L. Hudson, *A.I.Ch.E. J.*, 33, 218 (1987).
35. M.R. Bassett and J.L. Hudson, *J. Electrochem. Soc.*, 137, 922 (1990).
36. W. Li, K. Nobe and A.J. Pearlstein, *Corros. Sci.*, 31, 615 (1990).
37. W. Li, K. Nobe and A.J. Pearlstein, *J. Electrochem. Soc.*, 140, 721 (1993).
38. O. Lev, A. Wolffberg, M. Sheintuch and I.M. Pismen, *Chem. Eng. Sci.*, 43, 1339 (1988).
39. J. F. Albahadily and M. Schell, *J. Chem. Phys.*, 88, 4312 (1988).
40. H.P. Lee, Dissertation, UCLA (1983).
41. W. Li, X. Wang and K. Nobe, *J. Electrochem. Soc.*, 137, 1184 (1990).

Mechanism of Ennoblement by Biofilms on Active/Passive Alloys Immersed in Seawater

Dr. Stephen C. Dexter
College of Marine Studies, University of Delaware,
Lewes, DE 19958-1298, USA.

Introduction

The purpose of this paper is to present a brief review of how microbial fouling films affect the corrosion behavior of passive metals in natural waters. It has often been reported that microbial films shift the open circuit corrosion potential (OCP) of passive metals in the positive (or noble) direction and enhance the kinetics of the cathodic oxygen reduction reaction¹⁻¹⁰. The significance of this effect lies in its influence on localized corrosion initiation and propagation. In chloride bearing waters, initiation of pitting and crevice corrosion is statistical, with the probability of initiation increasing directly with chloride ion activity and OCP. Thus, at a given chloride level, the probability of localized corrosion initiation is increased by anything (such as a biofilm and its metabolic products) that causes the OCP to become ennobled.

The investigators cited above¹⁻¹⁰ found that the OCP of an alloy resistant to chloride initiation of localized corrosion, such as N08367 (6XN), usually became shifted to a steady noble value between +350 and +500 mV vs. the saturated calomel electrode (SCE) as a microbial biofilm formed at the metal/water interface⁹. In contrast, the OCP of the same metal in the same water ranged from -100 to +150 mV SCE if the microbial biofilm was inactivated or prevented from forming⁹. On alloys with less resistance to localized corrosion (e.g., S30400), the OCP was first shifted noble, but as soon as pitting or crevice corrosion initiated, the current supplied by the active corrosion polarized the potential back to a

more active value⁹. Thus, potential ennoblement is only sustained for long periods of time in the absence of corrosion initiation.

It has been established by many authors, as reviewed by Scotto⁷ and Dexter¹⁰ that ennoblement of the OCP in the presence of a microbial film is a direct result of the metabolic activity of microorganisms in the film. Other citations in the literature report no ennoblement effect. Mansfeld et al.¹¹ showed that ennoblement did not occur under conditions in which the film consisted of a scatter of individual cells (insufficient surface coverage), while Little, et al.¹² showed no ennoblement when a very thick film formed rapidly. Thus, the question arises as to what factors promote or suppress the effect. Biofilms formed from natural aqueous environments are noted for providing spotty, rather than continuous coverage of solid surfaces. Dexter, et al.¹³ showed that 30 to 40 percent coverage was required for the OCP to rise above the +150 mV SCE level, while substantially complete coverage was required for the maximum amount of ennoblement.

Dexter and Zhang^{8,9} have shown that biofilms grown at all salinities from 0.02 to 28 ppt were able to ennoble the OCP. The most noble potentials (about +500 mV SCE) and the largest amount of ennoblement (over 500 mV) were found in fresh water, and both decreased with increasing salinity^{8,9}. Temperature in the range of 2 to 30°C and dissolved oxygen content in the bulk water from 0.5 to 10 ppm have small effects in the direction predicted by electrochemical thermodynamics¹⁴.

ENNOBLEMENT MECHANISMS

Biofilms can affect electrochemical parameters at a metal surface through both their physical presence and their metabolic activity. Physically, the film acts as a diffusion barrier, tending to concentrate chemical species produced at the metal-film interface and to retard diffusion of species from the bulk water toward the metal surface. One effect of reduced diffusivities¹⁵ perpendicular to the metal surface is to concentrate acidic by products from the metabolism of microorganisms in the biofilm. It is well known that the reversible oxygen potential shifts about 60 mV in the noble direction for each unit decrease in pH. This more than balances the decrease in potential as dissolved oxygen is decreased by biological processes¹³. Based on thermodynamics, the maximum calculated ennoblement¹³ for a reversible oxygen electrode

would be 280 mV for changes in pH and O_2 from 8 (and 0.2 atm) to 3 (and 0.02). Since the oxygen electrode is not strictly reversible, even on platinum, one would expect the actual noble shift to be smaller than the calculated value. Actual measurements have shown that the OCP for a pH change from 8 to 3 in both aerated and deaerated seawaters varied from 170 mV on platinum to nearly 250 mV on S31600 stainless steel^{13,16}. These data show that the often observed ennoblements of 250 mV or less on common stainless steels in natural seawater can be explained by the pH mechanism alone for a pH of about 3 at the metal surface. The larger amounts of ennoblement often observed on superalloys and platinum in seawater and on all alloys in lower salinity waters, however, require another mechanism in addition to that of pH.

One question is whether a pH of 3 is possible at the metal surface under a biofilm. We have two types of evidence that it is. In one set of experiments, organisms scraped from marine biofilms on platinum were grown on Difco Marine Agar containing various pH indicating dyes. The pH of many of the colonies that grew was observed¹⁷ to be below 3. In other experiments currently under way we are measuring the pH directly using microelectrodes of the iridium oxide type (Montana St. University). These data show variations from point to point along the metal surface with pH values ranging from 0.4 to 3.7.

Scotto proposed that oxygen reduction at the cathode surface might be enhanced by bacterially produced enzymes¹⁷. One possibility for this mechanism¹³ involves the suite of enzymes that bacteria produce to control toxic oxygen derivatives. Superoxide, hydrogen peroxide, and hydroxyl radical are all toxic by-products of oxygen reduction (or respiration). The concentration of these by-products must be controlled by the organisms for survival. The enzyme, superoxide dismutase, catalyses the destruction of superoxide free radical (O_2^-) by Equn (1) below. Superoxide dismutase, however, is inactivated by the build up of H_2O_2 . Therefore, it is associated with two other enzymes, catalase and peroxidase, which break down H_2O_2 according to Equn (2):



We have proposed^{13,17} that the mechanism for ennoblement may involve both low pH and peroxide within the biofilm. Peroxide would contribute to the mechanism by virtue of its noble redox potential (1.76 V NHE vs. 1.23 V for oxygen). The toleration limit of most microorganisms for H₂O₂ is about 15 mM¹⁸. The above reactions assure that some peroxide will always be present within the biofilm, but limit the concentration. Peroxide in the high micromolar to low millimolar range has been identified¹⁷ in the film by peroxide indicating enzyme strips (from E. Merck Co.). Chemical simulation experiments on bare platinum electrodes have verified that additions of peroxide in this range shift the OCP of platinum in the noble direction. The only set of chemical conditions we found¹³ that was able to reproduce the OCP of +400 to 450 mV SCE observed for biofilmed platinum was deaerated seawater with less than 0.5 ppm O₂ and 250 μ M peroxide at pH 2.9. Cyclic voltammetry also reproduced the peroxide peak from the biofilmed platinum electrode only under this same set of conditions¹³. It is significant to note that, although the oxygen concentration at the metal surface must be low, the entire effect disappears if the bulk environment is made anaerobic¹⁹. This means that some oxygen must reach the metal surface, but considerable variability from point to point along the surface is also possible.

Another suggested mechanism for ennoblement involves the catalytic action of bacterially produced organo-metallics on the oxygen reaction^{2,5}. Such compounds are used to catalyze reduction of oxygen to water in fuel cells²⁰. A transition metal ion (such as Fe, Mn, Co or Ni) is chelated in a square planar complex by a macrocyclic organic molecule of the phthalocyanin, porphyrin or tetraazaannulene types, having four nitrogen atoms as ligands^{20,21}. The enzymes mentioned above are also porphyrin based organo-metallic complexes. Thus, we now believe that this mechanism is essentially the same as the enzyme mechanism, and that both of them involve hydrogen peroxide and heavy metals. Most of the passive alloys ennobled by biofilms contain one or more of the necessary heavy metals as alloying elements. Another source of heavy metals is the seawater itself. Microorganisms in the biofilm require most of these heavy metals as micronutrients. Hence, in a mature biofilm the needed heavy metals, as well as the porphyrins, may be provided by decaying organisms at the base of the film. EDAX data on biofilms grown on platinum at our location showed Fe and Mn peaks¹⁹.

Based on the literature and research results outlined above, the following general model for the ennoblement mechanism is proposed and illustrated schematically in Figure 1. A shift in the OCP to values in the +300 to +500 mV SCE range by biofilms less than about 100 μm thick requires sharp gradients in both pH and dissolved oxygen within the film. The outer layers of the film should be aerobic and at near neutral pH, while immediately adjacent to the metal surface the film will be acidified, with a generally low oxygen concentration, possibly becoming anaerobic over some portions of the metal surface. Under these conditions the primary contribution to ennoblement would come from the thermodynamic effect of pH on the OCP. An important secondary contribution would come from the cathodic reaction: the acidic form of O_2 reduction (when O_2 is present, Equn. 3) and the reduction of H_2O_2 to water (Equn. 4).



Both of these reactions have more noble redox potentials than the oxygen reaction at neutral pH. The metabolic action of the biofilm itself would be both the primary source and regulator of peroxide through the enzyme system of the aerobic organisms as described above. We also think that peroxide, being a powerful oxidizer may help in maintaining the low pH within the film through the oxidation of reduced heavy metals, which could then hydrolyze to form more acid within the film. This suite of conditions would require a consortia of various types of microorganisms as typically found in biofilms grown from natural waters. The outer portions of the film would contain mostly aerobic and acid producing organisms consuming oxygen. Beneath these would be the Fe and Mn reducers and the fermenters. Finally, at the base of the film, the anaerobic sulfate reducing bacteria (SRB) may play a role.

This general biofilm model is supported by a vast literature on biogeochemical cycling of heavy metals in marine sediments and aquatic environments²²⁻²⁵. The material in citations 22 through 25 give a picture of the cycling of Fe and Mn in environments with limited oxygen availability, such as we find in mature biofilms. The main difference is in the physical dimension over which the cycling takes place. As illustrated schematically in Figure 2, this cycling in stratified lakes takes place over

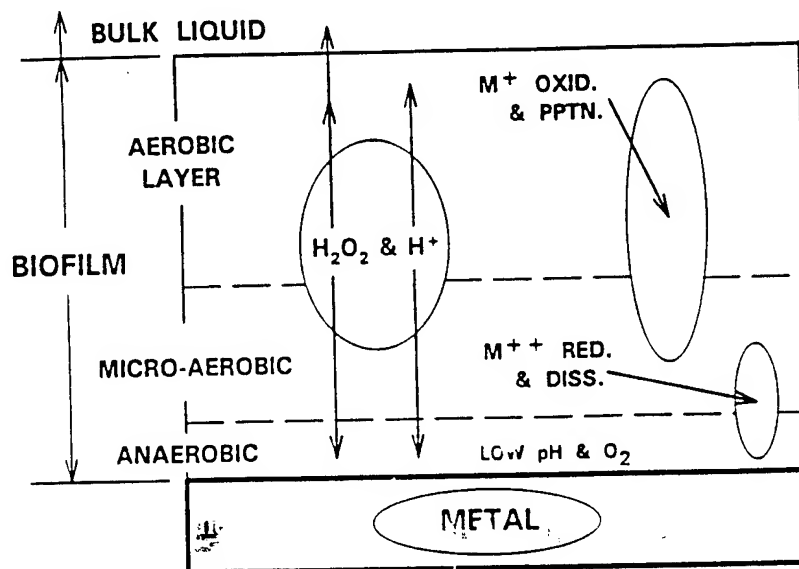


Figure 1. Schematic diagram of the biofilm model showing production and diffusion of H_2O_2 and acidity. Heavy metal cycling takes place by both chemical and biological processes.

Trace Element Cycling in A Lake (After Stumm, 1992)

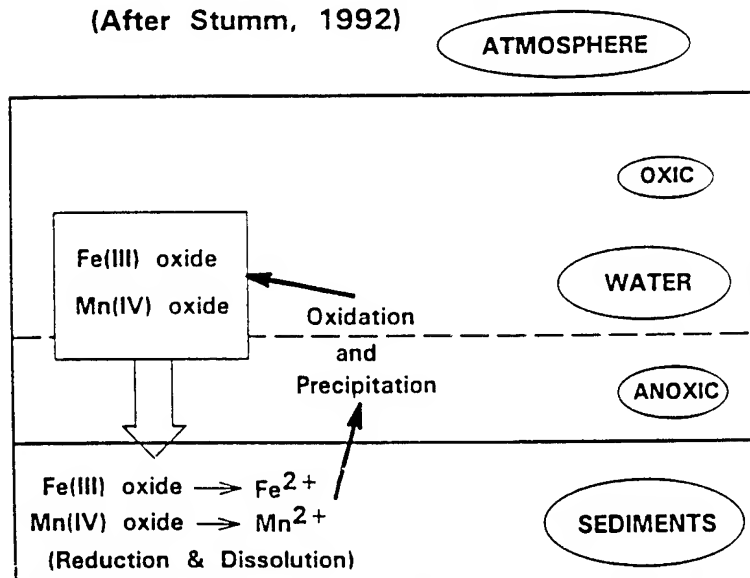


Figure 2. Heavy metal cycling by chemical and biological processes in a stratified lake. (Redrawn from Stumm²²). Note the similarity to the biofilm processes in Figure 1.

dimensions of meters²². In marine sediments, the same thing takes place within centimeters, while within a biofilm it occurs within about 100 μm .

One or more species of SRB are known to be dominant in many forms of MIC. Do they play a substantial role in the ennoblement process? They are certainly present in the coastal and estuarine waters that produce ennoblement at the Lower Delaware Bay site. So far, we think that they are not important in maintaining ennoblement under a mature biofilm. This judgment is based on four types of data. First, the pH is generally too low in the anaerobic portions of the film near the metal surface, although the model would accommodate neutral pH micro-niches in which they might flourish. Second, they cannot be dominant because ennoblement is lost if one makes the entire environment anaerobic¹⁹. The third and fourth types of data have been obtained in our lab just recently, and they will be published in detail elsewhere. Radioisotopic studies have been done to determine if appreciable sulfate reduction is taking place in the biofilm. Ennobled platinum coupons were incubated in seawater containing the radioactive tracer $^{35}\text{SO}_4^{2-}$ as the sodium salt. When SRB are active, they convert this to H_2^{35}S , which is trapped and then detected by a scintillation counter. Large signals were obtained when this technique was used on samples of anaerobic sediment containing SRB. In contrast, no detectable signal was produced by the organisms in the ennobling biofilm. Finally, ennoblement on platinum was neither reduced nor eliminated by exposing the coupons to seawater containing the SRB inhibitor, molybdate.

This model accommodates two major points that have been brought up in discussions of the mechanism. Some argue that oxygen cannot be involved because microelectrode measurements have shown zero oxygen tension at the metal surface under a mature biofilm²⁶. The model allows for large portions of the metal surface to be anaerobic as long as it is not totally so. Others contend that bacterial enzymes are active only at neutral pH values²⁷, so ennoblement by that mechanism cannot occur at acid pH. The model as proposed requires only the inner portions of the film to be acidified.

EFFECT ON CORROSION

The question now is, what effect does the observed ennoblement of the OCP have on corrosion of passive metals and alloys in marine

environments? Initiation of pits on passive alloy surfaces in chloride containing media depends on chloride ion concentration and electrode potential. The more electropositive (or noble) the potential, the easier it will be for chloride ions to penetrate the passive film and create small anodic areas. Thus, anything that causes the OCP to change in the positive direction (such as ennoblement by biofilms) increases the probability of pit initiation at a given chloride ion concentration. If one could measure the critical pitting potential at the metal-biofilm interface, it would be possible to predict when a biofilm would cause pit initiation just by measuring the OCP. Dexter and Zhang^{8,9} tried comparing maximum ennobled potentials to the critical pitting potential for stainless alloys S30400 and S31600 as a function of water salinity. From this data they concluded that the maximum salinities at which these alloys should be resistant to pit initiation in the absence of crevices should be reduced by the ennobling action of a biofilm. The general conclusion is correct, but the results cannot be used for predicting localized corrosion behavior in practical applications for at least two reasons. First is the uncertainty in chemistry at the metal surface under a biofilm¹³, and second is that crevice corrosion occurs at lower potentials than pitting.

Under service conditions, crevices are always present. Johnsen and Bardal said that OCP ennoblement should decrease crevice initiation times and increase propagation^{2,3}. Dexter et al. showed that bacteria in the crevice solution could contribute to depletion of oxygen, potentially decreasing crevice initiation times²⁸. Other tests of crevice initiation times in our laboratory have sometimes shown a decrease in crevice initiation times by factors of 2 to 5, but the results are not consistent²⁹. The data are much more convincing for the effect of biofilms on crevice propagation. Recently, Zhang and Dexter have used remote crevice assembly tests to show that propagation of crevice corrosion is accelerated by biofilms on alloys with low resistance (S30400 and S31603) and intermediate resistance (N08904 and S31725) to crevice corrosion in coastal seawater²⁹. Crevice corrosion current densities (see Figure 3) were one to three orders of magnitude higher in natural seawater than in a control water made by filtering to remove most of the film forming microorganisms. On these same alloys they also measured increases in: percentage of crevice area attacked under the washer, maximum and average depths of attack, and weight loss for the biofilmed samples versus controls²⁹. Gallagher, et al.⁶ found similar results. Zhang and Dexter concluded that acceleration of crevice corrosion by the action

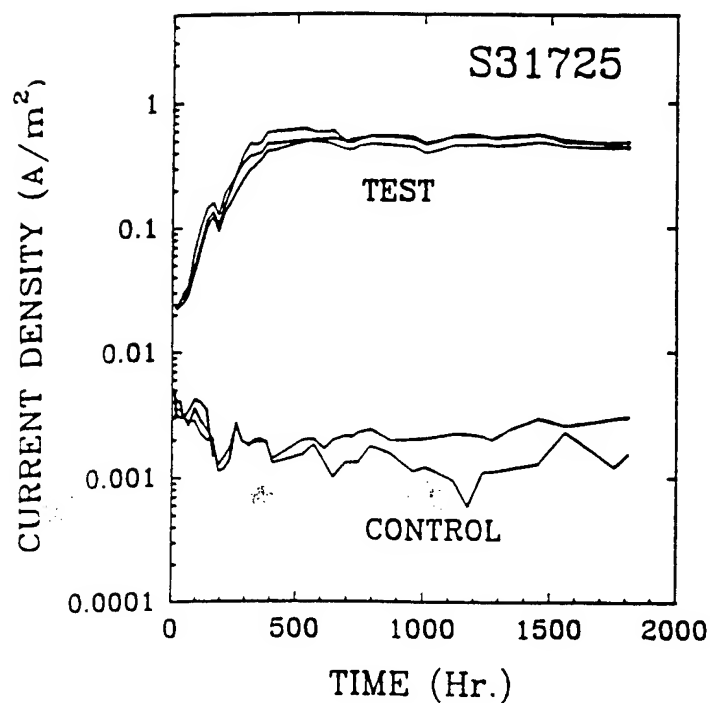


Figure 3. Crevice corrosion current density vs. time from remote crevice assembly tests on biofilmed (test) and bare (control) samples of alloy S31725 as read on a zero resistance ammeter (after Zhang and Dexter²⁹).

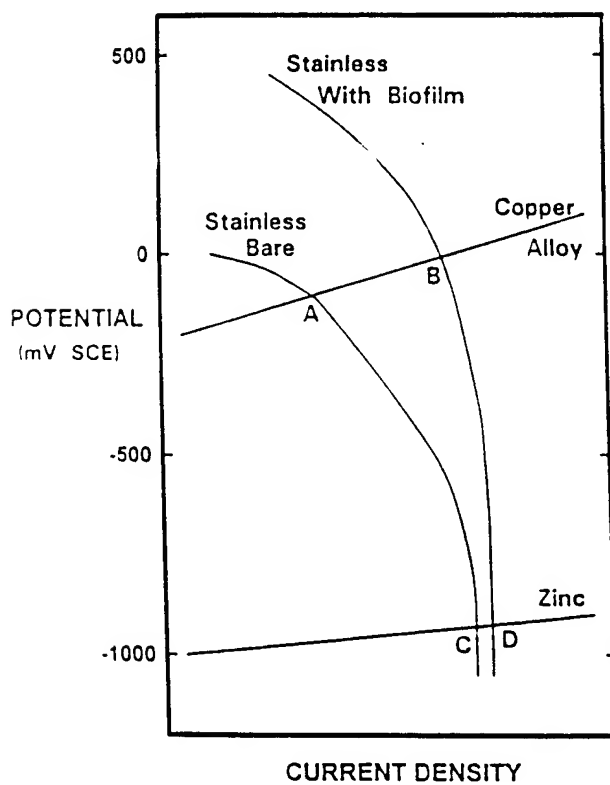


Figure 4. Schematic polarization diagram showing the influence of a biofilm on the stainless steel cathode of galvanic couples with copper and zinc. A greater effect of the biofilm on galvanic corrosion is predicted for copper than for zinc.

of biofilms in their coastal waters was more significant on the intermediate resistance alloys, N08904 and S31703, than it was on S30400 and S31603, which corrode readily with or without biofilms. The biofilm had no effect in their two-month tests on alloy N08367.

The rate of galvanic corrosion is often controlled by the reduction reaction on the cathodic member of the couple. Therefore, any increase in kinetics of the cathodic reaction on passive metals has the potential to increase the severity of these metals as cathodes in galvanic couples¹³. Work summarized by Scotto⁷ showed that the upper portion of the cathodic polarization curve was shifted toward higher current densities, while the lower portion, dominated by the limiting current for oxygen diffusion, was affected to a lesser extent. These data suggested that the rate of galvanic corrosion on the anodic member of the couple should be affected by the action of a biofilm more (as shown in Figure 4) if the mixed potential of the couple is within the upper portion of the cathodic polarization curve than if the mixed potential is more negative. For example, if copper and steel were both connected to similar biofilmed stainless steel cathodes, the data predict that corrosion of copper will be accelerated more by the action of the biofilm than corrosion of steel. An important related question is whether consumption of Al, Mg and Zn sacrificial anodes is increased by the action of biofilms on the protected structure. The cathodic polarization data predict the effect on these active materials will be small because the couple potential is very negative.

Galvanic corrosion experiments in coastal seawater have been run for 24 Hr on couples of copper, 90-10 Cu-Ni, 1020 steel, 3003 Al and Zn, each connected to bare (control) and ennobled passive alloy cathodes, and the galvanic corrosion currents were read on a zero resistance ammeter. The results for steel and aluminum showed that the galvanic current for the couple with the filmed cathode was nearly an order of magnitude larger than that with the bare cathode¹³. The data for Zn showed the reverse effect¹³, the current for the couple with the filmed cathode being less than control by a factor of 2. These data are consistent with the idea that biofilms on the cathode increase the rate of galvanic corrosion. Coupling to an active anode such as Zn, however, produces enough alkali at the metal surface to interfere with the metabolism of microorganisms in the biofilm³⁰. Instead of stimulating the cathode reaction in this case, the biofilm acts as a diffusion barrier. Experiments are currently underway to obtain longer term data.

SUMMARY

The mechanism of ennoblement is not yet completely understood. A model has been proposed in which the effect is explained by a decrease in pH and an increase in hydrogen peroxide concentration at the metal surface under the biofilm. The model calls for a layered biofilm structure with sharp gradients in both oxygen and pH. The outer layers of the film are at ambient pH and oxygen concentration, while the inner layers are acidic with low oxygen. Within the film, acids are produced by the consortia of organisms, and peroxide is both produced and regulated below toxic levels by bacterial enzymes. Acidity and peroxide produced in the film diffuse both toward the metal and the bulk liquid, building up in the low oxygen environment near the metal surface, but being neutralized in the outer portions of the film. Accumulation and hydrolysis of heavy metals help establish the low pH. The model is consistent with biogeochemical data showing heavy metal cycling in stratified lakes and marine sediments.

Ennoblement of the OCP increases the propagation rate of crevice corrosion on susceptible passive alloys, and it may also decrease the initiation time. Short term (24 hour) tests showed that biofilms can increase the severity of stainless steels as the cathodes of galvanic couples when the anode member of the couple is more positive than Al. For very active anodes, such as Zn, the biofilm acted as a diffusion barrier, reducing the galvanic corrosion rate. Predictive capability for the effect of biofilms on localized corrosion awaits a greater understanding of the chemistry at the metal surface and its variability under the biofilm.

ACKNOWLEDGMENTS

The work on which this paper is based was sponsored by the Office of Naval Research under Contract No. 01490J1947 and NOAA Office of Sea Grant, U.S. Dept. of Commerce, under Grant No. NA86AA-D-SG040

REFERENCES

1. A. Mollica, A. Trevis, Proc. 4th Intl. Cong. Marine Corrosion and Fouling, Juan-Les Pins, Antibes, France, 1976, p. 351.
2. R. Johnsen, E. Bardal, Corrosion, 41, 1985, p. 296.
3. R. Johnsen, E. Bardal, CORROSION/86, paper No. 227, NACE, Houston, TX, 1986.
4. V. Scotto, R. DiCintio, G. Marcenaro, Corrosion Science, 25, 1985, p. 185.
5. S.C. Dexter, G.Y. Gao, Corrosion, 44, 1988, p. 717.
6. P. Gallagher, R. Malpus, E. Shone, Br. Corrosion J., 23, No. 4, 1988, p. 229.

7. V. Scotto, "Electrochemical studies of biocorrosion of stainless steel in seawater." Proc. EPRI Workshop on Microbial Corrosion, Electric Power Research Institute, Palo Alto, CA, 1988, p. B-1.
8. S.C. Dexter, H-J. Zhang, Proc. 11th Intl. Corrosion Cong., Florence, Italy, Vol. 4, 1990, p. 333.
9. S.C. Dexter, H-J. Zhang, "Effect of biofilms, sunlight and salinity on corrosion potential and corrosion initiation of stainless alloys," EPRI NP-7275, Final Rep., Proj. 2939-4, Electric Power Research Inst., Palo Alto, CA, 1991.
10. S.C. Dexter, Biofouling, 7, 1993, p. 97.
11. F. Mansfeld, R. Tsai, H. Shih, B. Little, R. Ray, P. Wagner, Corrosion Science, 33, No. 3, 1992, p. 445.
12. B. Little, R. Ray, P. Wagner, Z. Lewandowski, W. Lee, W. Characklis, F. Mansfeld, CORROSION/90 paper No. 150, NACE, Houston, TX, 1990.
13. S. Dexter, P. Chandrasekaran, H. Zhang and S. Wood, "Microbial Corrosion in Marine Environments: Effect of Microfouling Organisms on Corrosion of Passive Metals, Proc. 1992 Biocorrosion and Biofouling Workshop, Videla, Lewandowski and Lutey, Eds., Buckman Laboratories, Memphis TN, 1993, p. 171.
14. N. Dowling, J. Guezennec, J. Bullen, B. Little, D. White, Biofouling, 5, 1992, p. 315.
15. R.C. Aller, J. Marine Res., 41, 1983, p. 299.
16. B. Little, R. Ray, P. Wagner, Z. Lewandowski, W. Lee, W. Characklis, and F. Mansfeld, Biofouling, 3, 1991, p. 45.
17. P. Chandrasekaran and S. Dexter, CORROSION/93 paper No. 493, NACE, Houston, TX, 1993.
18. B. Christensen, H. Tronnes, K. Vollan, O. Smidsrod and R. Bakke, Biofouling, 2, 1990, p. 165.
19. P. Chandrasekaran and S. Dexter, CORROSION/94 paper No. 276, NACE, Houston, TX, 1994.
20. F. Van den Brink, E. Barendrecht, W. Visscher, W., Recueil. J. Royal Netherlands Chemical Soc., 99, No. 9, 1980, p. 253.
21. R.D. Hancock, A.E. Martell, Chem. Rev., 89, 1989, p. 1875.
22. W. Stumm, Chapter 9, in: Chemistry of the Solid-Water Interface, John Wiley, New York, 1992, p. 309.
23. K. H. Nealson, "The Microbial Manganese Cycle," in: Microbial Geochemistry, W. Krumbein, Ed., Blackwell Scientific, Boston. 1983, p. 191.
24. F. Morel and J. Hering, Chapter 6, in: Principles and Applications of Aquatic Chemistry, John Wiley, New York, 1993, p. 319.
25. F. Morel and B. Palenik, The Aquatic Chemistry of Trace Metals in Biofilms, in: Structure and Function of Biofilms, W. Characklis and P. Wilderer, Eds., John Wiley, New York, 1989, p. 239.
26. Z. Lewandowski, W. Lee, W. Characklis. CORROSION/88 paper No. 93, NACE, Houston, TX, 1988.
27. S. Maruthamuthu, M. Eashwar, S. Sebastin Raja and K. Balakrishnan, Proc. Corrosion Asia, 1992.
28. S.C. Dexter, K.E. Lucas, G.Y. Gao, "The role of marine bacteria in crevice corrosion initiation," In: Biologically Induced Corrosion, S. C. Dexter, Ed., National Assoc. of Corrosion Engineers, Houston, TX, 1986, p. 144.
29. H-J Zhang, S.C. Dexter, CORROSION/92 paper No. 400, NACE, Houston, TX, 1992.
30. A. Gaudy, E. Gaudy, Microbiology for Environmental Scientists and Engineers McGraw-Hill Book Co., New York, 1980, p.183.

SESSION VII
COATINGS

Chairman: *C. Handsy*

BLANK

NONCHROMATE, LOW DENSITY, WATERBORNE EPOXY PRIMER

Dr. Robert Chiang*, Technical Director
Mr. Chris Athanasopoulos, Product Manager

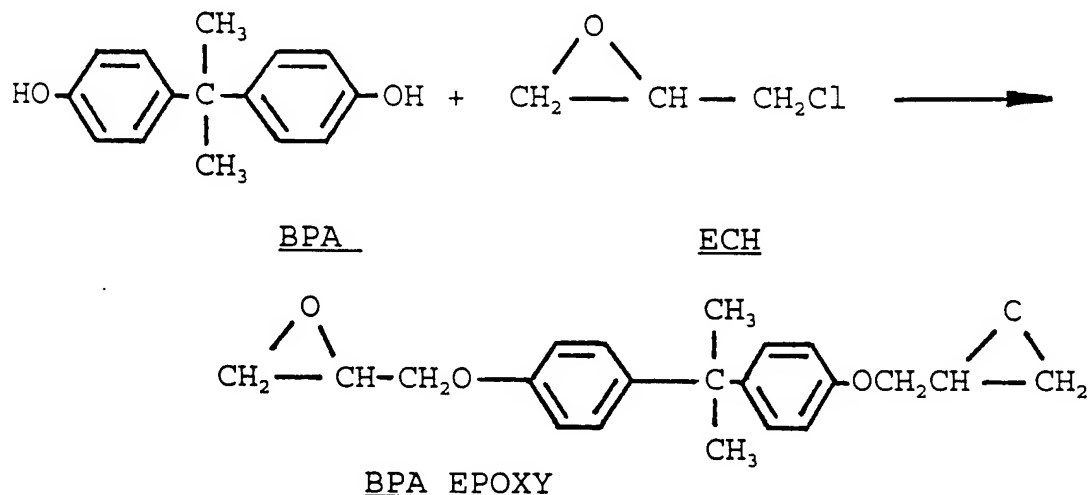
Aerospace Coatings Division
Spraylat Corporation, Chicago, IL 60633-2362

ABSTRACT:

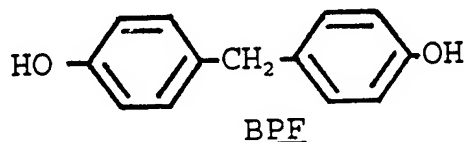
A chrome-free, low density, waterborne epoxy primer was developed to meet MIL-P-85582B Specification. This primer does not contain toxic pigments and provides comparable corrosion protection as strontium chromate counterparts. Its dry film density was calculated at 0.0073 lbs/mil/square ft. It can be top coated with MIL-C-83286 and MIL-C-85285 urethane coatings within an hour at 77° F and 50% RH.

INTRODUCTION:

Epoxies were developed over fifty years ago. They are made by reacting Bisphenol A (BPA) and epichlorohydrin (ECH). Depending on the ratio of BPA and ECH and reaction conditions, epoxies with different molecular weight can be obtained.

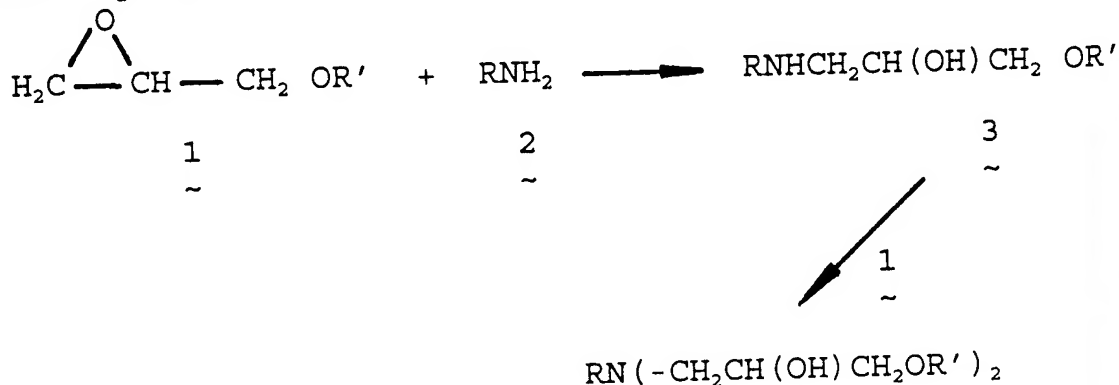


Other epoxy resins have also been synthesized. For example, Bishphenol F (BPF) epoxies are made by reacting BPF with ECH. BPF epoxies give lower viscosities as compared with BPA epoxies.



Exterior durable epoxies, cycloaliphatic epoxies, are also commercially available. These are derived from alkenes by epoxidation.

The most widely used epoxy curing agents in coatings are modified amines and polyamides. The curing mechanism is as follows. Epoxy (1) reacts with primary amine (2) to form secondary amine (3). The secondary amine (3) further reacts with epoxy (1) to give a tertiary amine (4).



Epoxies are widely used in surface coatings. They provide excellent corrosion protection, adhesion, and chemical resistance.

Because of the stringent environment requirements, waterborne epoxy coatings have been extensively studied and used as viable alternatives to traditional solvent-based coatings.¹⁻³ Water-borne epoxy systems provide additional advantages such as lower VOC (volatile

organic compounds), fast tack-free time and easy cleaning among others. The recent advances in water-borne epoxy dispersion technology have resulted in water borne epoxy primers with equal or better corrosion protection properties than those of the solvent-based epoxy counterparts.⁴

In addition to lowering VOC, the need to eliminate carcinogenic compounds such as hexavalent chromium in coating systems has also been emphasized.⁵ Revisions of current military coatings specifications have been proposed^{6,7} to address this need.

In response to these challenges and the demand to reduce the VOC and eliminate hazardous chromate pigments, Spraylat Corporation launched a new development program in 1993. The goal was to formulate a nonchromate waterborne epoxy primer maintaining the corrosion protection of its chromate counter parts. It was intended for MIL-P-85582B specification.

RESULTS AND DISCUSSIONS:

In late 1993, an experimental nonchromate waterborne epoxy primer was developed at Spraylat Corporation based on proprietary technology. The physical characteristics of the primer, EWDY048A/B, are listed below:

Table 1. Physical Characteristics of EWDY048A/B

Solids	44 +/- 1% by weight 36 +/- 1% by volume
LBS/GAL	9.5 +/- 0.2
Mixing Ratio	3:1 by volume
#4 Ford Cup Viscosity	30-40 seconds
Sprayable Pot Life	4 hours
Coverage	572 sq.ft/mil/gal
Dry Film Density	0.00732 lbs/sq.ft/mil

The VOC for this coating is 2.64 lbs/gal (317gm/liter).

The viscosity of the admixed primer remains very stable during its 8 hour pot life. No induction time is required. The theoretical dry film density is 25% less than that of the chromate counterpart. The performance of EWDY048A/B primer was measured on the dry film of 1 mil thickness on 2024-T3 and T0 aluminum panels. The coated panels were allowed to dry at ambient temperature for 7 days before testing. Table 2 shows the performance properties of this coating.

Table 2. Performance Properties of EWDY048A/B

Tack-Free Time, Hrs	0.5
60° Gloss	< 5
Cross-Hatch Tape Adhesion	Excellent
G.E. Impact, Elongation, %	60
MEK Resistance	Excellent
Pencil Hardness	H
Compatibility w/ Urethane Topcoats	Compatible

The corrosion resistance properties (Salt Fog Test, ASTM B117) of EWDY048A/B were compared with its chromate counterpart, EWDE072A/B, and several commercially available chromate containing water-borne epoxy primers. EWDE072A/B is a newly approved coating on QPL (Qualified Products List) from Spraylat Corporation for MIL-P-85582A, Type I, Class 2 Specification. Both EWDY048A/B and EWDE072A/B did not show defects after 2000 hours of salt fog test. Competitor B system passed 1500 hours exposure. Both competitors A and C coatings had some field blistering after 1000 hours. They also had some undercut rusting after 1500 hours of testing. Table 3 and Figure 1 summarize the results. All EWDY072A/B and competitor's materials are intended for MIL-P-85582A specification which require 1000 hours salt fog test. An upgrade of increase to 2000 hours corrosion test is proposed in the revised MIL-P-85582 Specification.⁶ The new Specifications also call for chromate-free systems. Based on its performance, EWDY048A/B system would meet these revised requirements.

Table 3. Salt Fog Test of EWDY048A/B And Other Systems

<u>Salt Fog HRS</u>	<u>EWDY048A/B¹</u>	<u>EWDE072A/B^{1,2}</u>	<u>BRAND A²</u>	<u>BRAND B^{2,3}</u>	<u>BRAND C^{2,3}</u>
1000	No Defects	No Defects	9 #8 FB ⁴	No Defects	10 #8 FB
1500	No Defects	No Defects	11 #8 FB undercut rust	No Defects	12 #8 FB undercut rust
2000	No Defects	No Defects	----	undercut rust	----

1. MIL-P-85582A, Type I, Class 2; QPL, Spraylat Corp.
2. chromate containing
3. low density
4. FB: field blisters

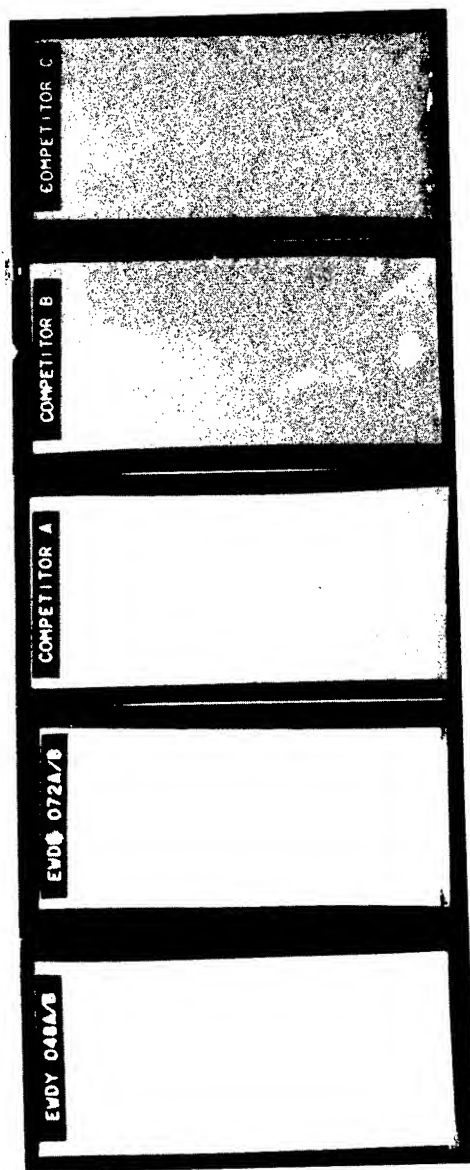


FIGURE 1 | SALT FOG CORROSION TEST RESULTS OF EVDY 048A/B AND OTHER SYSTEMS

Waterborne epoxy primers generally give somewhat longer pot life than their high solids solvent-based counterparts. The effect of pot life of EWDY048A/B on its properties was studied. The flexibility and corrosion resistance of this coating at various pot life intervals were compared. It was found that the coating's impact elongation determined by a G.E. impact tester decreased over its pot life. A 60% elongation was obtained when the coatings was applied 6 hours after the coating and hardener were mixed. The elongation reduced to 10% when the coating was applied 30 hours after mixing. The salt fog corrosion resistance also decreased with pot life. Table 4 and Figure 2 illustrates that the coating showed minor field blistering after 1080 hours of salt fog test when it was applied 6 hours after mixing or longer.

Table 4. Pot Life vs. Performance of EWDY048A/B

A. Corrosion Resistance

<u>SALT FOG HOURS</u>	<u>HOURS BEFORE ADMIXED COATING WAS APPLIED</u>		
	<u>0.5</u>	<u>6</u>	<u>30</u>
1080	No Defects	1 #4	1 #4
2600	Undercut Rust	1 #4 & Undercut	1 #2, 2, #4 Undercut Rust

B. Impact Elongation %

60	60	<10
----	----	-----

CONCLUSION:

A low VOC (317 grams/liter), low density, chromate free waterborne epoxy primer intended for revised MIL-P-85582 Specification has been developed by Spraylat Corporation. This coating, EWDY048A/B, has excellent salt fog corrosion resistance (2000 hours). Its corrosion resistance is superior to that of the

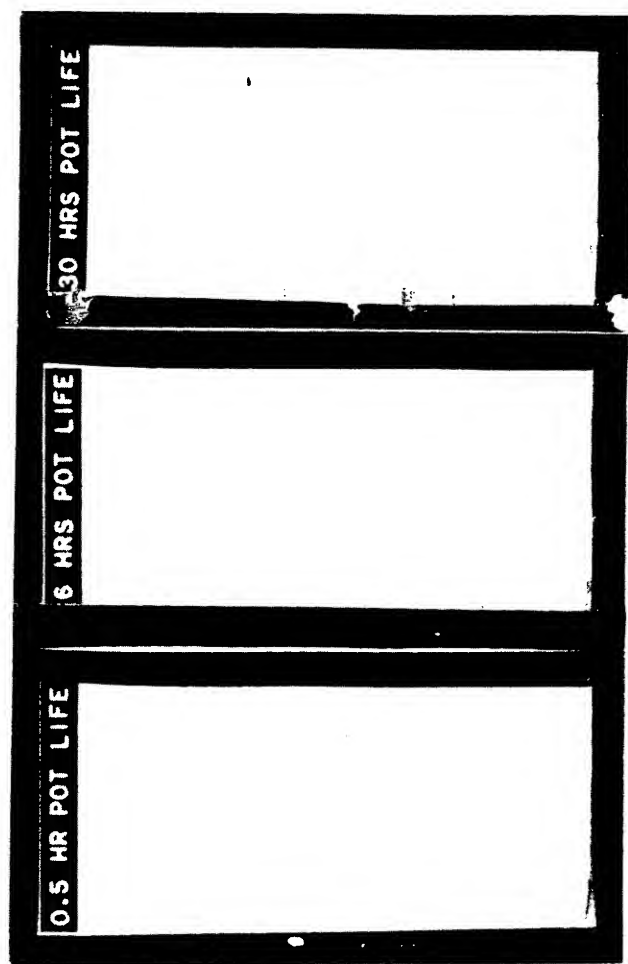


FIGURE 2 | CORROSION VS. POT LIFE OF ENDY 048A/B

In addition to its high performance, lower VOC, ease of handling, and toxic-free pigments, it also provides the advantage of lower density.

ACKNOWLEDGEMENT:

The authors wish to appreciate the management of Spraylat Corporation for their encouragement and support. Special thanks are due to Kelly Myers for preparing the manuscript.

REFERENCES:

1. M.A. Jackson, An Evaluation of Anti-Corrosion Pigments, J. Protective Coatings & Linings, Vol 7, No. 4, 54, 1990.
2. (a) E.C. Galgoci and P.C. Komar, Waterborne Epoxy Resins for Ambient Temperature Cure: Property Comparison of Pigmented Coatings, Proceedings of the 21st Water-Borne, Higher Solids, and Powder Coatings Symposium, New Orleans, LA, 54, 1994.
(b) A.B. Pangelian and P.R. Rhodes, Barrier Property Comparison of Traditional Solvent Borne and New Low VOC Waterborne Coatings. Publication 1926-93, 1993. Shell Chemical Co., Houston, TX.
3. MIL-P-85582A, Primer Coatings: Epoxy, Waterborne, Aircraft Div., Naval Air Warfare Center, The Department of The Navy, 1988.
4. G. Reinhard, Formulation of Waterborne Dispersions for Corrosion-Protective Primers, Progr. Org. Coatings, 18, 123, 1990.
5. Revision of Navy Paint Specifications To Meet EPA Standards. David Pulley, Naval Air Warfare Center, The Department of The Navy, Wright Laboratory Aircraft Paint/Coatings Workshop, May 12-13 1994.
6. Proposed MIL-P-85582B, Primer Coatings: Epoxy, Waterborne, Naval Air Warfare Center, The Department of The Navy, 1993.
7. Proposed MIL-P-23377G, Primer Coatings: Epoxy, Chemical And Solvent Resistance, Naval Air Warfare Center, The Department of the Navy, 1994.

INTERFACES OF HIGH-PROTECTION PERFORMANCE POLYARYLS-COATED ZINC PHOSPHATED STEELS

Dr. Toshifumi Sugama
Energy Efficiency and Conservation Division
Department of Applied Science
Brookhaven National Laboratory
Upton, N.Y. 11973

P P E E K

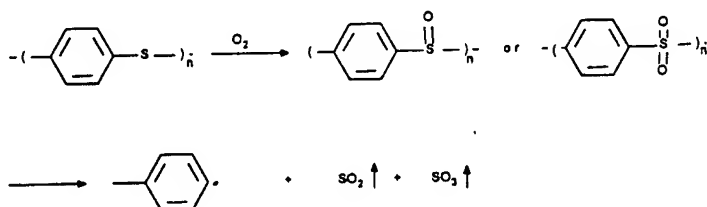
Abstract

To evaluate the ability of polyaryl thermoplastic coatings such as polyphenylenesulfide (PPS) and polyphenyletheretherketone (PEEK), to protect zinc phosphate (Zn·Ph)-treated steels from corrosion in a wet, harsh environment (1.0 wt% H₂SO₄, 3.0 wt% NaCl and 96.0 wt% water at temperature from 25° to 200°C), we exposed them in autoclave to measure their performance in heating-cooling cyclic fatigue tests (1 cycle = 12 hr at 200°C + 12 hr at 25°C) for up to 90 cycles. Although no changes in appearance were seen in the PEEK specimens after 60 cycles, extension to 90 cycles caused delamination of the coating film from the Zn·Ph; the major reason was the degradation of the PEEK polymer caused by its hydrothermal-catalyzed esterification. In urea hydrogen peroxide (UHP) modified PPS-coating systems, chemical reactions at the interfaces between the PPS and Zn in the Zn·Ph layer led to the formation of a ZnS reaction product, which enhanced the Zn·Ph-to-PPS adhesive bond; correspondingly, there were no signs of peeling nor separation of the coating after 90 cycles. In addition, because these intermediate reaction products are insoluble at high pH, they minimized the rate of delamination of the PPS coating caused by the cathodic reaction, $H_2O + 1/2O_2 + 2e^- \rightarrow 2OH^-$, at the corrosion side of a defect in the film. In contrast, PEEK coatings containing non-reactive Zn·Ph underwent cathodic delamination because of the susceptibility of Zn·Ph to alkali dissolution.

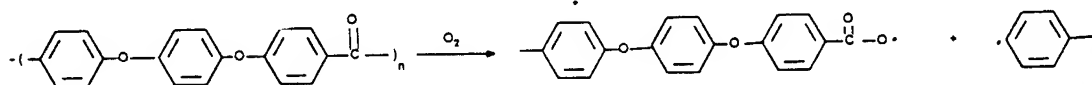
Introduction

Semi-crystalline polyphenyletheretherketone (PEEK) and polyphenylenesulfide (PPS) thermoplastics are very attractive for application as corrosion-protective coatings of cold-rolled steels in harsh environments at hydrothermal temperatures up to 200°C. The major characteristic of these linear polyaryls is the molecular orientation caused by the chain extension at their melting point, -

290°C for PPS^{1,2}, and ~ 340°C for PEEK^{3,4}. This orientation leads to the crystallization of these polymers during cooling. Such melt-crystallization behavior of these polyaryls give them specific, desirable characteristics as coatings; they show high-temperature stability, chemical and hydrothermal resistance, and have good mechanical properties. In addition, there are no limitations on their shelf- or pot-life, nor problems of waste disposal because any excess crystallized polyaryl phase reverts to the molten phase in a hot oven. Also, the surfaces of powdered form of these polyaryls have a good wettability in water, suggesting that the water-based polymer slurries can be formulated to use in simple dip-withdrawing and cold spray coating methods. In a previous study^{5,6}, we investigated the interface of polyaryls-to-steel joints prepared in oxygen or nitrogen environments at ~ 350°C. With PPS, its oxidation reaction in hot O₂ caused the emission of corrosive reactants, such as SO₂ and SO₃ gases, in accordance with following O₂ associated degradation routes;



The interfacial interaction of these gases with Fe₂O₃ at the outermost surface side of steel introduced sulfur-related reaction products, such as Fe₂(SO₄)₃, FeSO₄, and FeS, into the critical interfacial boundary zones. However, although these reaction compounds are known as the corrosion products of steel, they significantly improved the bond strength between the PPS and steel. In contrast, the adherence of PPS prepared in hot N₂ to steel was very poor. In the PEEK/steel joint systems, the O₂-catalyzed degradation of PEEK promoted the incorporation of carboxylate groups into the chain-scissored linear structure;



Such degradation not only corresponded to a low degree of crystallinity of PEEK, but also caused its separation from the steel. A good adhesion performance of PEEK to steel was noted in the joint specimens prepared in a N₂.

We also searched the rate of cathodic delamination of polyaryl films from steel, brought about by the cathodic reaction, H₂O + 1/2O₂ + 2e⁻ → 2OH⁻, which occurs under the coating adjacent to the

defect^{7,8}. A considerable attention in this corrosion reaction processes was given to the creation of a high pH environment at the cathodic sites; namely, the created alkali circumstance beneath the coating not only causes the formation of corrosion products, but also promoted the alkali-catalyzed decomposition of the interfacial reaction products, especially for $\text{Fe}_2(\text{SO}_4)_3$ and FeSO_4 , at the PPS/steel interfaces, and the saponification of the PEEK polymer in contact with the steel. Subsequently, these phenomena led to a high rate of cathodic delamination of the polyaryl films from the steels. Thus, the necessity of the interface tailoring and modification to inhibit the onset of the cathodic reaction and to avoid the direct contact of polyaryl with steel becomes a more important subject. Regarding the interfacial tailoring material systems, the introduction of zinc or zinc alloy and zinc phosphate ($\text{Zn}\cdot\text{Ph}$) conversion coatings into the intermediate layers is widely employed as a post-treatment of steel surfaces in the autobody industry.

On the basis of this information, an emphasis in this present work was directed toward exploring the changes in chemistry and morphology occurring at the interfaces between peroxide modified PPS or unmodified PEEK coatings and phosphated steels after heating-cooling cycle fatigue tests of the defect-free polyaryl topcoat/ $\text{Zn}\cdot\text{Ph}$ /steel systems in an accelerated corrosion environment at 25° to 200°C.

Materials

PPS and PEEK powders for the slurry coatings were supplied by the Phillips 66 Company and the Imperial Chemical Industry (ICI), respectively. The urea hydrogen peroxide (UHP) received from Aldrich was used as the peroxidic reagent which promote the rate of oxidation of sulfur in the PPS. These polyaryl films were deposited on the surfaces of the $\text{Zn}\cdot\text{Ph}$ -treated steel substrate in the following way. First, the substrates were dipped into the polyaryl slurries (see Table 1) at 25°C. The PPS slurry-coated substrates were heated in air for 2 hrs at 350°C; and the PEEK slurry-coated substrates were heated in N_2 for 2 hrs at 400°C, and then cooled to room temperature at the rate of - 10°C/min. The thickness of the polyaryl coating films of all specimens ranged from 0.075 to 0.1 mm.

Table 1
Formulation of UHP-Modified and Unmodified PPS and PEEK Slurries

<u>Polyaryl</u>	<u>Slurry formulation</u>
PEEK	40 wt% PEEK-52 wt% water-8 wt% propyleneglycol
PPS	40 wt% PPS-52 wt% water-8 wt% propyleneglycol
PPS	39 wt% PPS-50 wt% water-8 wt% propyleneglycol-3 Wt%UHP
PPS	37 wt% PPS-48 wt% water-8 wt% propyleneglycol-7 wt%UHP

Measurements

The cyclic fatigue tests for the PPS and PEEK-coated Zn·Ph steel panels (7.5 cm x 7.5 cm) were accomplished as follows; the coated specimens were directly soaked in a corrosive solution consisting of 1.0 wt% H₂SO₄, 3.0 wt% NaCl, and 96.0 wt% water at temperatures from 25 to 200°C, and then the heating-cooling cycles (one cycle = 12 hrs at 200°C + 12 hrs at 25°C) were repeated up to 90 times. The overall appearance and the interfaces of the specimens after 1, 5, 10, 20, 30, 60, and 90 cycles were examined to gain the information on their hydrothermal durability or the decomposition of coatings, and the changes in chemical nature occurring at the polymer-substrate interfaces. These information were gained using the combined technologies of scanning electron microscopy (SEM), energy-dispersion x-ray spectrometry (EDX), and x-ray photoelectron spectroscopy (XPS). The integrated data from all these approaches were correlated directly with the corrosion-related data, such as the impedance, $|Z|$, obtained from AC electrochemical impedance spectroscopy (EIS) in an aerated 0.5 N NaCl electrolyte at 25°C, and also cathodic delamination tests. The latter were conducted in an air-covered 1.0 M NaCl solution using an applied potential of - 1.5 V vs. SCE for 8 days. The total area of film in contact with the NaCl solution was $6.0 \times 10^3 \text{ mm}^2$. A defect was made using a 1-mm diameter drill bit. After exposure, specimens were removed from the cell and allowed to dry. The polyaryl coating was removed by cutting, revealing a delaminated region that appeared as a light gray area adjacent to the defect.

Results and Discussion

Table 2 shows the changes in appearance of coatings for the PEEK/Zn·Ph/steel, and the UHP-modified and unmodified PPS/steel and /Zn·Ph/steel joint systems as a function of cycle number. Using PEEK

Table 2
Visual Observation of PPS and PEEK Coating Films as a Function of Heating-Cooling Cycles

Polymer	Substrate	UHP %	Cycles					
			1	5	10	30	60	90
PEEK	Zn·Ph/steel	0	good	good	good	good	good	peels
PPS	steel	0	peels	-	-	-	-	-
PPS	steel	3	good	peels	-	-	-	-
PPS	steel	7	good	blister	peels	-	-	-
PPS	Zn·Ph/steel	0	good	good	good	good	good	good
PPS	Zn·Ph/steel	3	good	good	good	good	good	good
PPS	Zn·Ph/steel	7	good	good	good	good	good	good

coating, no blistering and lifting in appearance were observed in the specimens after 60 cycles; however, an increase to 90 cycles caused the peeling of the film from the Zn·Ph. Rust stains were clearly seen on the separated substrate surfaces. When the PPS coating was deposited directly to the steel surfaces in the absence of Zn·Ph, the durability of the bond between the coating and the steel depended on the concentration of UHP. The incorporation of 3 wt% UHP into the PPS gave a better performance; peeling of the film occurred after 5 cycles, compared with only one cycle for film without UHP. A further increase in concentration of UHP to 7 wt% extended the service life to 10 cycles. An encouraging result was obtained from cyclic tests of all the PPS-coated zinc phosphated steel specimens; there are no visual signs of delamination and damage after 90 cycles in either the modified and unmodified coating films. This result proved that the bond durability at the interfaces between PPS and Zn·Ph is outstanding, even in such a harsh environment.

To establish the interfacial bond structure and chemical states that govern such poor and good bond durability of polyaryl coatings, we investigated the interfacial polyaryl coating and Zn·Ph sides of the PEEK/ and PPS/Zn·Ph/steel joints before and after 90 cycles by XPS. The XPS C_{1s} core-level spectra of the PEEK side separated from the phosphated steel before and after 90 cycles were illustrated in Figure 1. The C_{1s} region of uncycled PEEK side can be deconvoluted by four resolvable Gaussian components at BEs of 285.0 eV, 286.5 eV, 288.0 eV, and 291.5 eV. All these components correspond to the structure of PEEK itself. A striking difference in spectral features was observed from the PEEK interface after 90 cycles; the width of the overall peak from 282 to 290 eV was more extensive, suggesting that an additional chemical component was introduced into the interfacial PEEK side during the fatigue tests. The new component, which is reflected in peak No. 5 at 289.4 eV, can be ascribed to the formation of $-COO-$ (carboxylic acid or ester) groups. Such an additional component clearly verified that the PEEK coating itself undergoes hydrothermal-catalyzed esterification. Thus, a high susceptibility of PEEK to hydrothermal-catalyzed esterification causes the degradation of the polymer film, thereby resulting in its delamination.

In the 0, 3, and 7 wt% UHP-modified PPS/Zn·Ph/steel joint systems, the $Zn_{2p_{3/2}}$ spectra for the interfacial Zn·Ph side of uncycled specimens are depicted in Figure 2. The spectrum of the control (0 wt% UHP) reveals only a single symmetric peak at 1024.6 eV, caused by Zn originating from the Zn·Ph. A noticeable change in the shape of the $Zn_{2p_{3/2}}$ signal from the 3 wt% UHP specimen was the emergence of a new signal at 1022.7 eV, corresponding to the Zn in the ZnS reaction product derived from the interaction between PPS and Zn·Ph; the intensity of this peak grew with the increasing concentration of UHP. At 7 wt% UHP, the peak at 1022.7 eV becomes the dominant component, while the Zn·Ph-related peak at 1024.6 eV

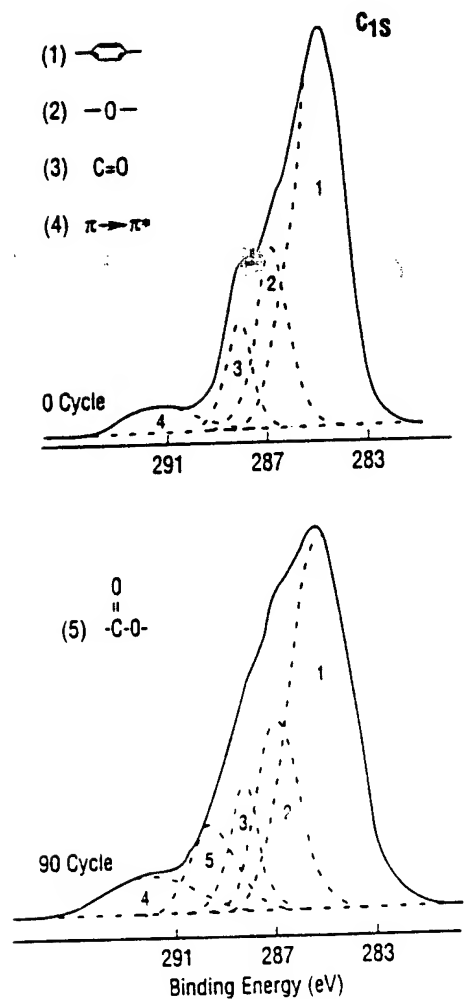


Figure 1. XPS C_{1s} core-level spectra for interfacial PEEK sides before (0 cycle) and after 90 cyclic tests.

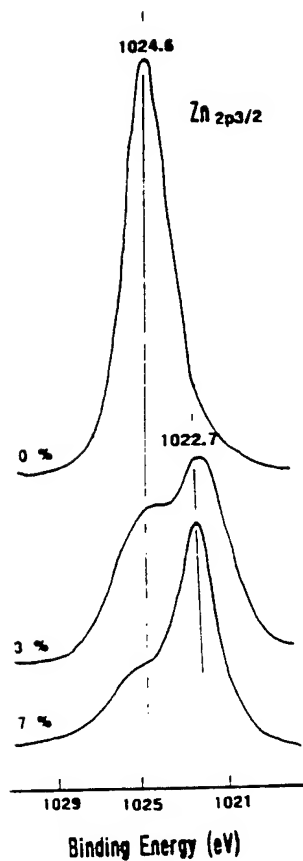


Figure 2. $Zn_{2p3/2}$ region of interfacial Zn:Ph sides removed from the 0, 3, and 7 wt% UHP-modified PPS before cyclic tests.

considerably decays. We note that there were no signals reflecting zinc sulfite (ZnSO_3) or sulfate (ZnSO_4) compounds. Hence, it is possible to assume that the peroxidic reaction of PPS with UHP emits SO_2 or SO_3 gases adjacent to the $\text{Zn} \cdot \text{Ph}$ layers, and then the emitted gases favorably react with the Zn in $\text{Zn} \cdot \text{Ph}$ to form ZnS . If this interpretation is correct, a high rate of peroxidic reaction increasingly promotes the transformation of anhydrous α - and γ - $\text{Zn}_3(\text{PO}_4)_2$ as the major phases of $\text{Zn} \cdot \text{Ph}$, into ZnS . For more interesting, we found that although UHP-unmodified PPS was used, ZnS also forms at interfaces between the PPS and the $\text{Zn} \cdot \text{Ph}$ during the cyclic tests. Figure 3 displays the changes in spectral features in

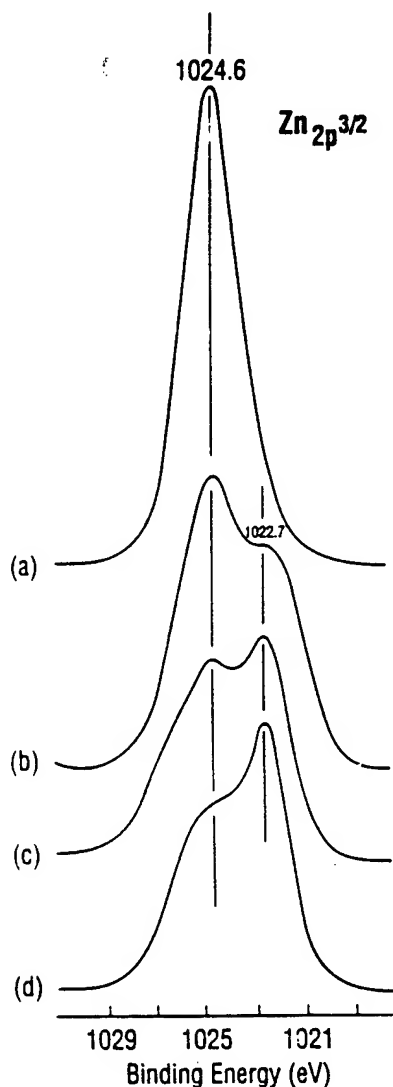


Figure 3. $\text{Zn}_{2p_{3/2}}$ region of the $\text{Zn} \cdot \text{Ph}$ interface of 0(a)-, 30(b)-, 60(c)-, and 90(d)-cycled specimens.

the $\text{Zn}_{2\text{p}_{3/2}}$ region of the $\text{Zn}\cdot\text{Ph}$ side removed from the unmodified PPS as a function of cycle number. The data clearly verified that the line intensity of the signal at 1022.7 eV, corresponding to ZnS , grew with the increase in the number of cycles, while the peak line of $\text{Zn}\cdot\text{Ph}$ at 1024.6 eV conspicuously attenuated. It is apparent that the ZnS reaction product formed at the PPS- $\text{Zn}\cdot\text{Ph}$ contact zones plays a major role in forming an intermediate cross-linking structure, which improves the $\text{Zn}\cdot\text{Ph}$ -to-PPS adhesive forces.

All this information was correlated directly with the results from electrochemical impedance spectroscopy (EIS) and cathodic delamination tests of the uncycled and cycled polaryl-coated $\text{Zn}\cdot\text{Ph}$ specimens. Figure 4 shows the changes in impedance, $|Z|$, at 0.01 Hz for these coatings as a function of cycle number. For the uncycled

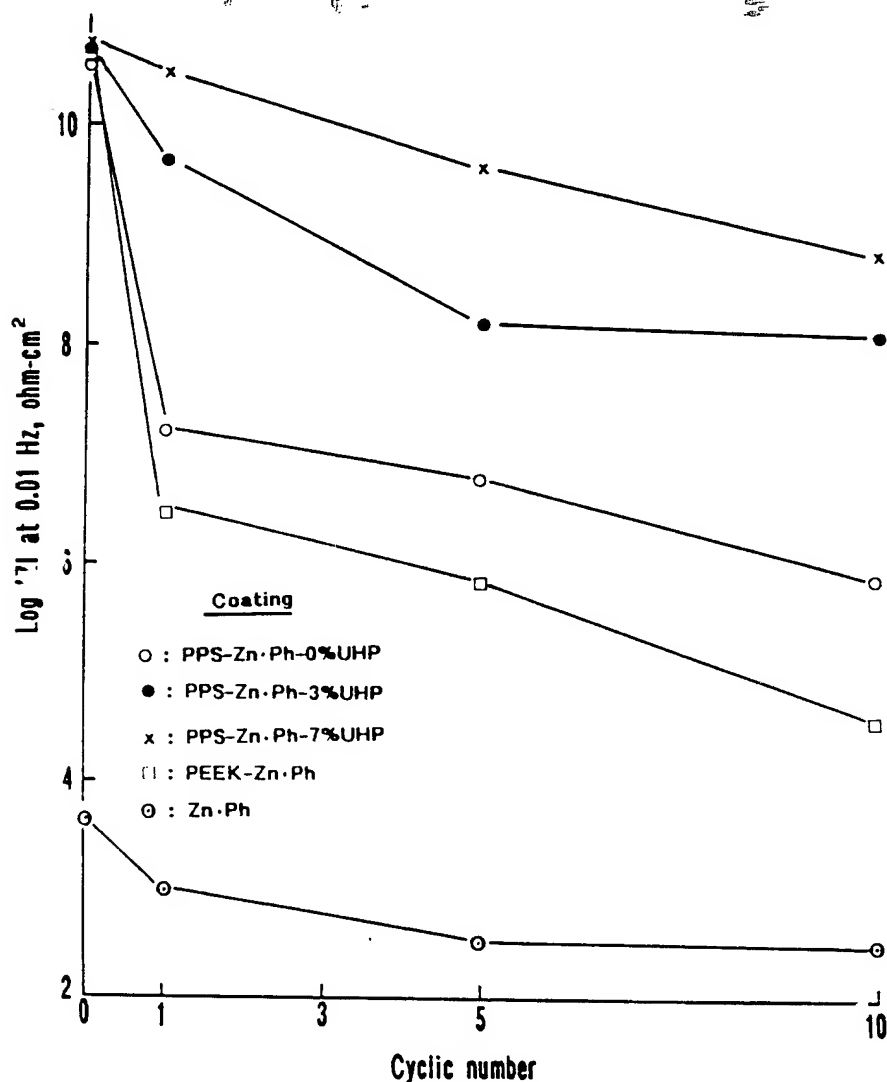


Figure 4. Changes in impedance, $|Z|$, for UHP-modified and unmodified PPS/ $\text{Zn}\cdot\text{Ph}$, and unmodified PEEK/ $\text{Zn}\cdot\text{Ph}$ and single $\text{Zn}\cdot\text{Ph}$ systems as a function of cycle number.

specimens, the impedance of Zn·Ph-coated steel in the absence of the polyaryls was $\sim 7.0 \times 10^3$ ohm-cm². Once the Zn·Ph surfaces were coated with the polyaryls, the IZl value increased by seven orders of magnitude. The IZl value for all the specimens tends to decrease with an increased cyclic number. Thus, a prolonged test must have led to the uptake of more electrolytes by the coatings. However, the rate of its uptake depended mainly on the coating systems and the concentration of UHP; the lowest rate, reflecting the gradual reduction of IZl value, was determined from the 7 wt% UHP-modified PPS/Zn·Ph coating. In contrast, the PEEK/Zn·Ph coating had the highest rate of electrolyte uptake, corresponding to a shift in IZl value from $\sim 6 \times 10^{10}$ ohm-cm² at 0 cycle to $\sim 4 \times 10^4$ ohm-cm² after 10 cycles. The data also demonstrated that the drop in IZl to low value for the UHP-free PPS/Zn·Ph coating was much faster than those for UHP-modified coatings. For the single Zn·Ph coating, after 5 cycles the IZl value remained at 5×10^2 ohm-cm², implying that there was anodic corrosion of the underlying steel. Comparing the IZl values, we ranked these coatings on a low degree of penetration of electrolyte in the following order; 7 wt% UHP- > 3 wt% UHP- > 0 wt% UHP-modified PPS/Zn·Ph > PEEK/Zn·Ph > Zn·Ph.

An important question that still remains concerned the ability of the ZnS reaction products to reduce the rate of cathodic delamination of the coating film from the Zn·Ph. Because ZnS is substantially insoluble in water and alkaline solutions, we would expect that this reaction product would suppress the delamination of polymer film caused by alkali-catalyzed dissolution of the Zn·Ph layers occurring at the cathodic reaction side, $\text{H}_2\text{O} + 1/2\text{O}_2 + 2\text{e}^- \rightarrow 2\text{OH}^-$. Figure 5 shows the delaminated area of PEEK, and UHP-modified and unmodified PPS films from the Zn·Ph layers for 0-, 20-, 30-, 60-, and 90-cycled specimens after 8 days of cathodic tests. For PEEK/Zn·Ph/steel joint systems, the curve indicates that there is a low rate of delamination of PEEK in the first 30 cycles. However, an increase to 60 cycles resulted in the increase in the rate of delamination. As mentioned earlier, further extension to 90 cycles led to the delamination of film caused by esterification-induced decomposition of the PEEK structure at the interfaces. In contrast, the rate of delamination for the unmodified PPS joint systems was progressively reduced as a function of cyclic number; the delaminated value of ~ 1.8 mm² after 90 cycles was ~ 20 times lower than that for the control specimens. Such a dramatic reduction was due mainly to the rapid rate of in-situ conversion of the Zn·Ph layers into ZnS reaction products in the PPS-Zn·Ph interfacial regions; that is, a high conversion rate of Zn·Ph as the cycles increased caused the formation of large amounts of the ZnS reaction compound which have no effect on the cathodic reaction-caused decomposition of the interfacial intermediate layers. Thus, it is reasonable to assume that the intermediate ZnS formation, which is insoluble in alkali solution at pH ~ 13 , has a high resistivity to

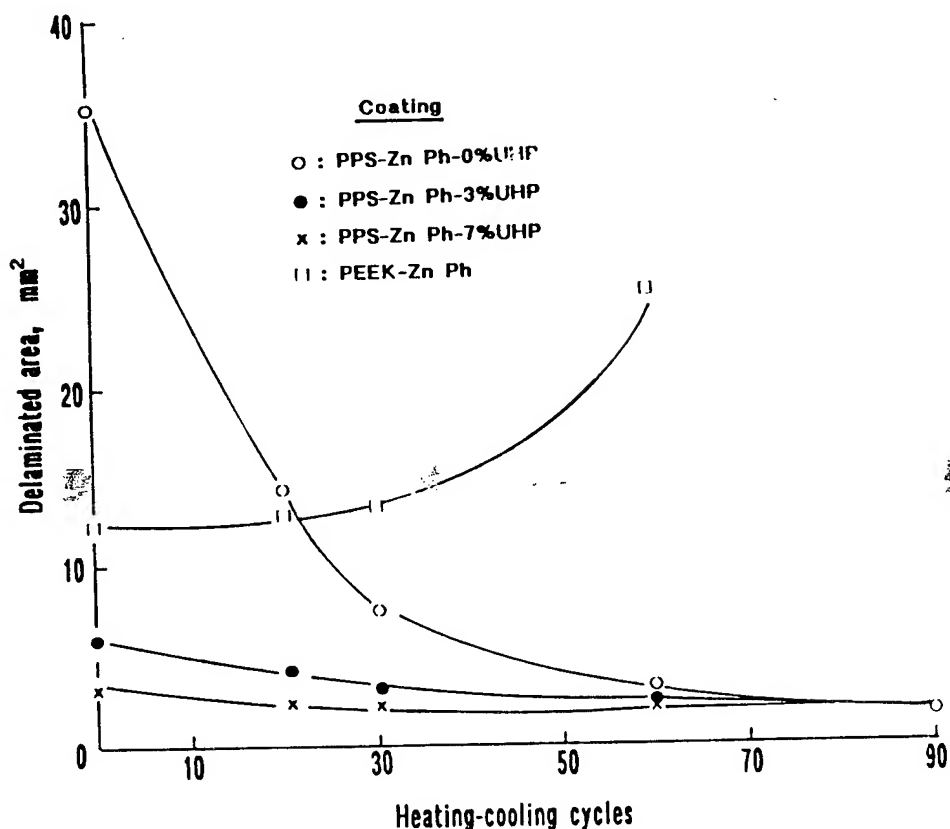


Figure 5. Rate of delamination of PEEK, and UHP-modified and unmodified PPS coating films from the substrate after cathodic tests for 8 days for polyaryl/Zn·Ph/steel joint systems as a function of heating-cooling cycles

cathodic reaction-created alkaline environments, thereby minimizing the rate of delamination. This concept directly explains why the rate of delamination for the UHP-modified PPS systems before cycling is lower than that of unmodified specimens at 0 cycle, because of the presence of large amounts of the ZnS compound which is not susceptible to alkali-catalyzed dissolution.

Conclusion

When urea hydrogen peroxide (UHP)-modified polyphenylene sulphide (PPS) was used as the topcoat for zinc phosphate (Zn·Ph)-deposited steel substrates, the interaction between the SO₂ or SO₃ emitted from the peroxidized PPS and the Zn in Zn·Ph layers led to the formation of ZnS compounds in the interfacial boundary regions. This reaction product, in conjunction with excellent hydrothermal stability of PPS itself, played an important role in improving the PPS-to-Zn·Ph bond durability and in providing a great protection of the steel from corrosion during its exposure to a wet, harsh environment. Although the UHP-unmodified PPS was coated over the

Zn·Ph, the exposure of this coating system in autoclave at 200°C introduced the same sulfide compound into the intermediate layers; its amount progressively increased with an increased number of heating-cooling cycles. Furthermore, a specific characteristic of this reaction product was to inhibit the alkali-induced delamination of the PPS film from the substrate that was caused by the cathodic reaction, $\text{H}_2\text{O} + 1/2\text{O}_2 + 2\text{e}^- \rightarrow 2\text{OH}^-$, occurring at corrosion sites in the steel, because this reaction product was insoluble at pH ~ 13. In contrast, a shortcoming of the polyphenyletheretherketone (PEEK) coating was its susceptibility of hydrothermal-catalyzed esterification. Thus, despite achieving a good bond at the PEEK-to-Zn·Ph interfaces due to the mechanical anchoring of the PEEK polymer, the esterification-induced degradation of the structure after 90 cycles caused the buckling delamination of film. As expected, PEEK coating systems which do not have any alkali-insoluble reaction products underwent the cathodic delamination because they were undermined by the alkali dissolution of Zn·Ph layers. Nevertheless, it is believed that the combined layers of PPS and Zn·Ph afford great protection to steels in a harsh environment with temperatures up to 200°C.

References

1. Lenz, R.W., Handlovity, C.E. and Smith, H.A. J. Polym. Sci., 58, 351 (1962).
2. Port, A.B. and Still, R.H., J. Appl. Polym. Sci., 24, 1145 (1979).
3. Waddon, A.J., Hill, M.J., Keller, A. and Blundell, D.J., J. Mater. Sci., 22, 1773 (1987).
4. Horner, P.J. and Whiteley, R.H., J. Mater. Chem., 1, 271 (1991).
5. Sugama, T., and Carciello, N.R., Int. J. Adhesion and Adhesives, 11, 97 (1991).
6. Sugama, T., Carciello, N.R. and Miura, M., Int. J. Adhesion and Adhesives, 12, 27 (1992).
7. Leidheiser, H. Jr. and Wang, W., "Corrosion control by organic coatings" Leidheiser, H. Jr (Ed.), National Association of Corrosion Engineers (NACE), pp. 70-77, Huston, (1981).
8. Dickie, A.R. "Adhesion aspects of polymeric coatings" Mittal, K.L. (Ed.), Plenum Press, pp. 319-327, New York (1983).

AN INNOVATIVE DC POLARIZATION METHOD FOR EVALUATING COATINGS

Mr. Alan S. Fabiszewski⁺
NAVMAR Applied Sciences Corporation
65 West Street Road, Suite C-200
Warminster, PA 18974
and
Dr. Vinod S. Agarwala
Naval Air Warfare Center, Aircraft Division
Code 6062
Warminster, PA 18974-0591

ABSTRACT

A new coating evaluation technique based on electrochemical polarization of specimens with scribed defects was developed and evaluated as a method for assessing corrosion protection by coatings on metals. A unique scribe method was developed to create reproducible defects on the specimens in a manner such that the coating/metal interface was consistently exposed. Various organic and inorganic coating systems were examined on aluminum substrates in 3.5% NaCl solution. Electrochemical results were compared to standard coating evaluation techniques. Preliminary results indicate that this technique is useful for comparative evaluation of coating systems, and offers a number of advantages such as fast and quantitative measurements, good reproducibility and sensitivity.

INTRODUCTION

Coating systems, composed of an inorganic surface pretreatment along with an organic primer and topcoat, have been the prevalent

⁺ On-site Contractor at Naval Air Warfare Center, Aircraft Division Warminster

method for protecting metallic structures against corrosion. These coating systems however are ever changing especially with the advent of stringent hazardous materials regulations. Along with the development of these new coating systems there is a need for a technique to rapidly evaluate their performance. Currently several electrochemical techniques have been used to evaluate coating system performances⁽¹⁻⁹⁾. Each of them however have their slight draw backs most of which being long time duration's for testing.

Factors influencing a coating system's performance are the metal substrate, the coating, the metal/coating interface, and the operating environment. In this study an evaluation technique which could effectively study these factors was developed and evaluated. The technique is based on electrochemical dc polarization of an metal/coating interface scribed as defect. Thus, several coating systems will be tested to establish electrochemical parameters which can be used to describe coating performance. The results will be also compared with standard non-electrochemical coating evaluation methods.

EXPERIMENTAL PROCEDURE

Instrumentation

The electrochemical scribe testing (EST) technique is carried out by running a potentiodynamic scan from the cathodic to anodic domain on the exposed metal/coating interface in a corrosive medium (electrolyte). The metal/coating interface is exposed by creating a circular scribed defect in the test specimen. A cross section of this scribed defect is as shown in Figure 1. This defect is produced mechanically using a unique device developed in-house and is shown in Figure 2. The purpose of making a circular scribe on the coated panel is to expose the metal/coating interface in omnidirection to the test medium for occurrence of interfacial corrosion. The circular geometry also eliminates problems of end-effects which are quite common to cross scribe, and probably represents a most severe defect geometry for accelerated testing.

The scribing device as shown in Figure 2 applies a constant force between the scribing tip and the test specimen. The constant force is controlled by the load applied to the spring by a weight (mass) as shown. Once the scriber tip comes in contact with the specimen, the tip is rotated to produce the circular scribe. The scriber cuts through the coating down into the metal substrate. The depth profile and notch radius of the scribe

are dependent upon the coating thickness and the nature of metal substrate. However, for a given metallic substrate the notch (scribe) geometry is fairly consistent and reproducible (Figure 1).

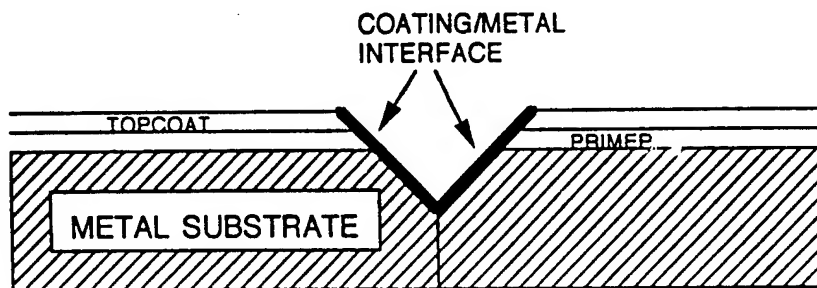


Figure 1: Cross section illustration of scribed defect.

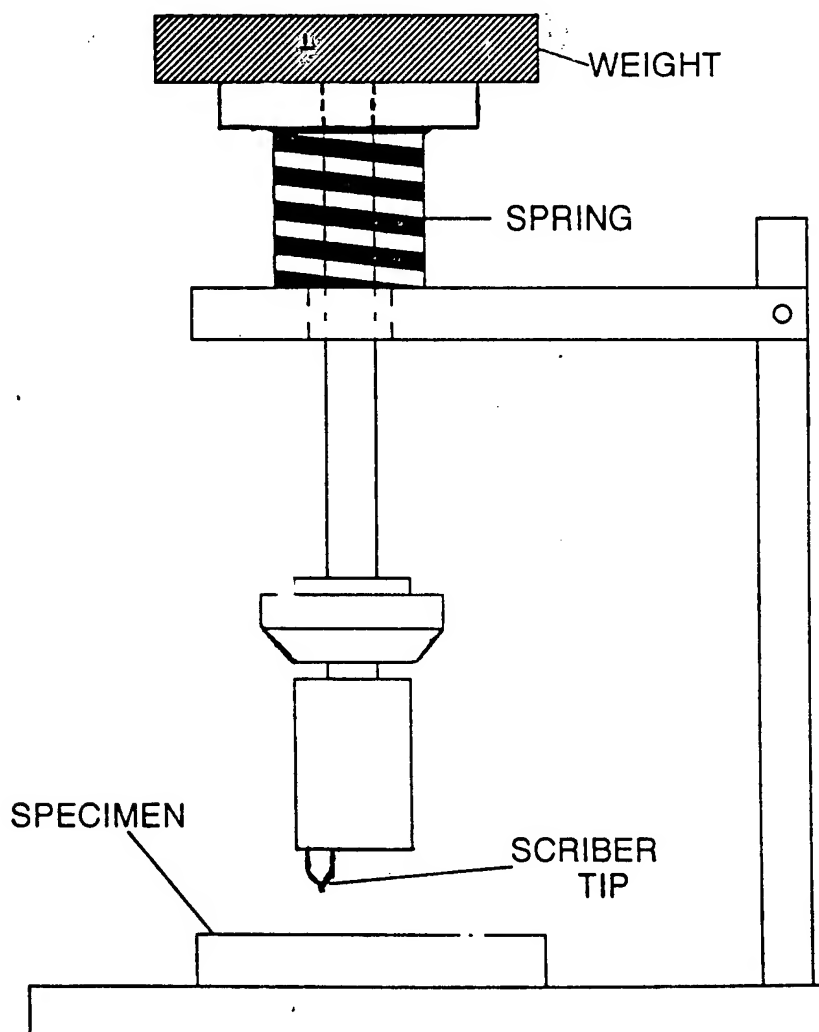


Figure 2: Schematic of scribing device.

Substrate and Coating Systems

Aluminum 7075-T6 alloy panels were used for evaluation of various pretreatments, primers and paints. Thus, panels were prepared using the following four coating schemes:

(1) Chromate Conversion Coated Aluminum Panels [Mil Spec No.]

- Top Coat Only [85285]
- Primer [23377] + Top Coat [85285]
- Self-Priming Topcoat (one-coat, unicoat)

(2) Tri-Chrome Conversion Coated Aluminum Panels

- Top Coat Only [85285]
- Primer [23377] + Top Coat [85285]
- Self-Priming Topcoat (one-coat, unicoat)

(3) Cleaned & Deoxidized Aluminum Panels

- Top Coat Only [85285]
- Primer [23377] + Top Coat [85285]
- Self-Priming Topcoat (one-coat, unicoat)

(4) Heavy Chromate Conversion Coated Aluminum Panels

- Primer [23377] + Top Coat [85285]

The protocol for specimen preparation includes the substrate preparation (conversion coating), primer (optional), and topcoat layers. A defect via the fore mentioned scribing technique was produced on the panels prior to exposure and testing. The interfacial area exposed consisted of the product of the length of scribed defect along coating thickness and the bare metal notch-width of the substrate.

Electrochemical Measurements

The electrochemical test cell consisted of a glass cylinder with an O-ring seal at one end mounted and clamped over the desired area of the test panel. The total exposed surface area created by this cell was $\sim 7.5 \text{ cm}^2$. The cell was then filled with approximately 50 ml of electrolyte. The counter electrode was a platinum disk with a hole in the middle to allow the capillary of the saturated calomel reference electrode tip to extend within 2mm of the specimen surface. The test cell configuration is illustrated in Figure 3.

The dc electrochemical polarization measurements were made using a Gamry CMS100 instrumentation system. The electrolyte used was a 3.5% NaCl solution (starting pH 6.25) and at room temperature (24°C).

Potentiodynamic electrochemical scans were run on the exposed area which included the scribed defect, from the cathodic to the anodic region. The scan was started at a preset -2.50 volts scanned to -0.50 volt versus the saturated calomel electrode (S.C.E.). A scan rate of 1.0 mV/sec was used to run the scans. The specimens were pre-exposed to the electrolyte solution for either 1, 3, or 7 days prior to testing. Three to five redundant tests were run at each condition for statistical verification of reproducibility of the test.

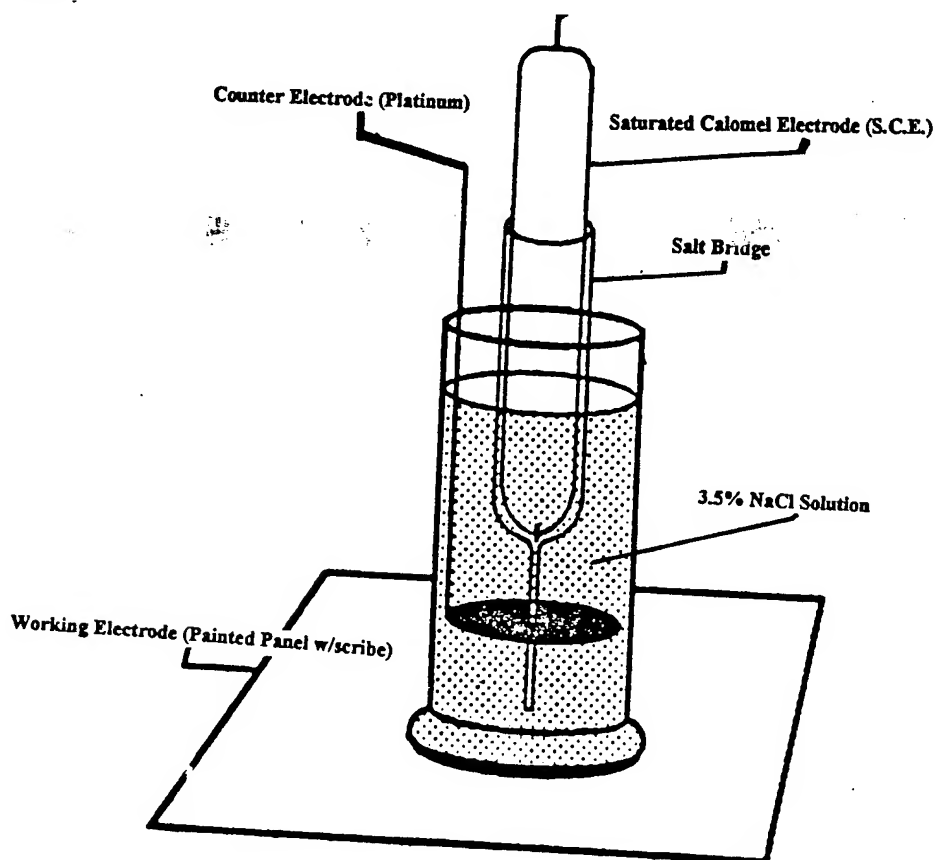


Figure 3: Electrochemical test cell

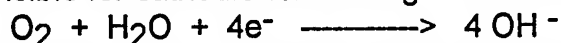
Salt Spray Exposure

Two sets of panels were scribed with a figure "X" through the coating into the metal substrate according to ASTM Standard Method D1654. The test panels were then exposed according to an ASTM Standard Method B-117 in salt spray environment and the test was run for 1000 hours. After testing, the panels were examined for debonding/lifting of the coatings and for corrosion product in the scribed area.

RESULTS AND DISCUSSION

The first set of experiments were conducted to determine whether the EST technique could distinguish between good and poor coating adhesion. Thus, prior to painting the aluminum panels were pretreated with (a) standard mil Spec (Mil-C-5541) chromate conversion coating (CCC) and (b) a heavy chromate conversion coating (HCCC). It is fairly well known that HCCC causes poor adhesion of the primer. The coating used on these test panels was a standard two coat system, a primer [23377] & topcoat [85285].

An examination of the cathodic regions of the potentiodynamic polarization diagrams, shown in Figure 4, show a large difference in the limiting current densities for the two pretreatments, i.e. current densities at potentials below -2.0V. When cathodic currents reach a limiting value, become independent of potential change, the reduction of oxygen becomes diffusion controlled. For the purpose of this study, a lower limiting current density value indicates lower availability of oxygen to the coating/metal interface, thus, lesser production of hydroxyl ions responsible for cathodic disbonding. This reaction can be written as



It is this production of hydroxyl ions that attacks the resin (paint system) and results in disbonding.

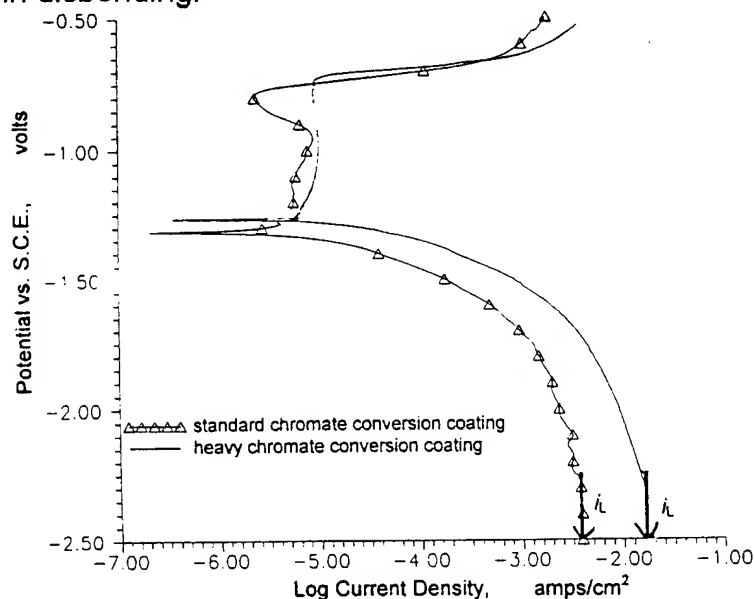


Figure 4: Polarization curves comparing surface pretreatments of a standard chromate conversion coating vs. a heavy chromate conversion coating under a Primer[23377] & topcoat[85285] paint system.

The results of salt spray exposure testing of these specimens are in agreement with those of EST. As shown in Figure 5, the CCC panels show no signs of adhesion loss or corrosion in the scribe area, where as, the HCCC specimens exhibit severe paint lifting and corrosion product all along the scribe. Most probably, the corrosion product in the scribe correspond to higher anodic currents observed in the passive domain the polarization curve.

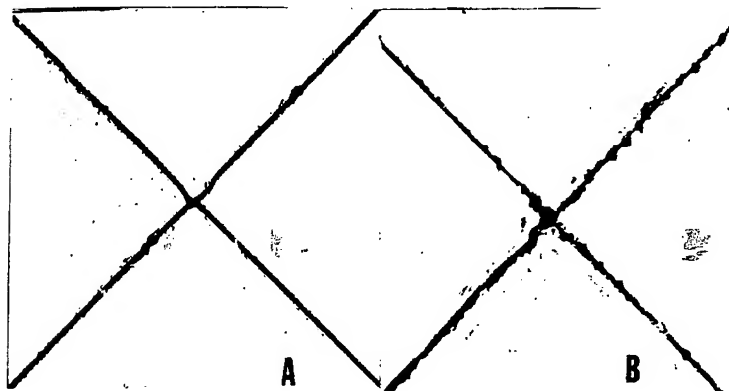


Figure 5: Photographs of primer[23377] & topcoat[85285] paint system with A) standard chromate conversion coating; B) heavy chromate conversion coating pretreatment after being scribed and exposed in 5% salt fog for 1000 hours.

The reliability of EST technique to evaluate and characterize the adhesion and corrosion resistant properties of the pretreatments (substrate preparation), both the standard two coat and a new one coat systems was selected. The two coat system again consisted of a standard primer [23377] and topcoat [85285] while the one coat system was a formulation that meets a particular mil specification for a single coat paint system. In this study, the substrate preparation was either a simple cleaning and deoxidizing of the surface (CD) or a conventional chromate conversion coating (CCC). The third substrate preparation was a new trivalent chromium conversion coating (TCC).⁽¹¹⁾ The number 2 or 1 will be used after the acronyms for the surface pretreatment to identify two coat or one coat system, respectively.

The polarization curves on the two coat system (CCC2) specimens showed an interesting cathodic polarization behavior (cf. Figure 6). The limiting current density, i_L , for the CCC2 was higher than that for either TCC or CD2. As known conventionally, the CCC2 painted panels should

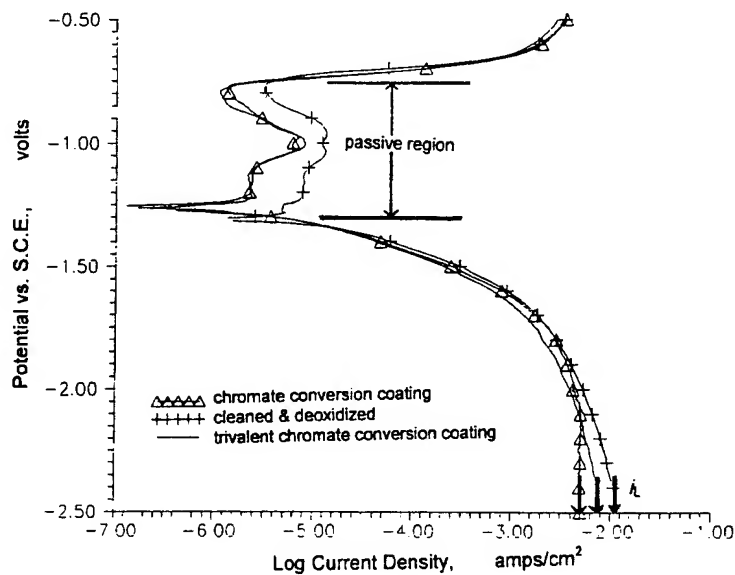


Figure 6: Polarization curves comparing surface pretreatments of a standard chromate conversion coating, trivalent chromium conversion coating and just cleaned and deoxidized under a Primer[23377] & topcoat[85285] paint system.

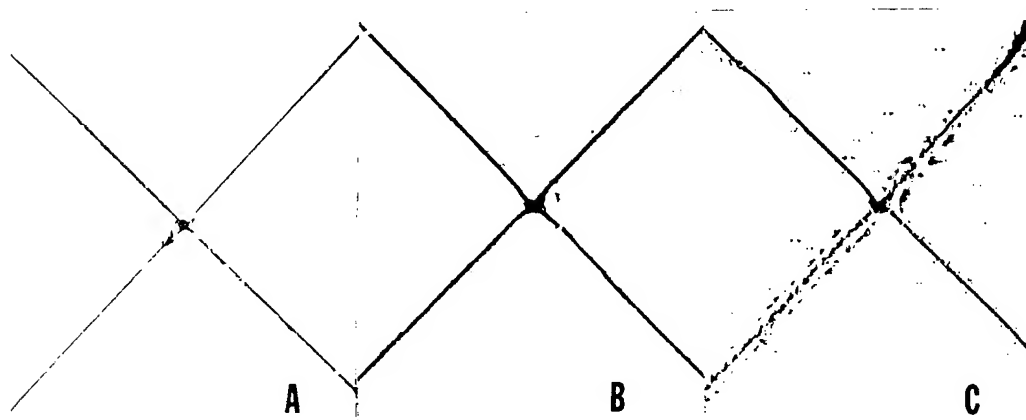


Figure 7: Photographs of primer[23377] & topcoat[85285] paint system with A) cleaned and deoxidized; B) trivalent chromium conversion coating; C) chromate conversion coating; pretreatment after being scribed and exposed in 5% salt fog for 1000 hours.

have lower i_L and perform the best. The CD2 and TCC2 had lower and identical current density in this region. As was also observed in Figure 4, an i_L value above 10^{-2} A/cm^2 could be an indication of a coating with an adhesion problem. The i_L for the CCC2 was approximately 10^{-2} A/cm^2 while the CD2 and TCC2 were at least a half decade lower. This difference of half a decade (5 m A/cm^2) could be an indication of a better adhesion of paint coating. This deduction was confirmed with the examination of the salt spray exposure specimens as shown in Figure 7, where plates A and B represent the pretreatments CD and TCC, respectively, and the plate C represents the CCC. A loss of paint the TCC2 and CD2 panels show no significant signs of disbonding (cf. plates A and B with plate C in Figure 7).

In the case of one coat system, the i_L values of the cathodic polarization curves for the above mentioned three surface pretreatments separate themselves in following order, $\text{CD1} > \text{TCC1} > \text{CCC1}$ (cf Figure 8), i.e., the CCC1 treated panel showed the lowest and CD1 the highest i_L value. The worst being the CD1 panels followed by the TCC1 and CCC1 panels. However, none of them were much better than the other. Relatively speaking, the coating system which gives a lowest possible i_L values is better for adhesion and corrosion resistance. The polarization curve in the anodic domain, region of passivity, show a significant increase in the current density in the case of panel CD1 which did not have any inhibitor, i.e., cleaned and deoxidized surface. This difference could only be observed on one coat system (cf Figure 6 with Figure 8). The separation of curves in the anodic domain for the two coat system was indistinguishable. Since CD process does not contain any corrosion inhibitor in the bath, the corrosion of the substrate metal was quite obvious in the scribe area. The other two processes, CCC and TCC, contain Cr^{+6} and Cr^{+3} which serve as good corrosion inhibitors, thus, showed lower current densities. As before when these results are compared with the salt exposure tests, as shown in Figure 9, the results correspond well. Severe lifting and blistering was observed on the CD1 specimen, plate A. The TCC1 (plate B) and CCC1 (plate C) panels also showed some signs of poor adhesion with the TCC1 being slightly inferior, however no where to the extent of the CD1. Significant amount of corrosion product also appeared in the scribed area for CD1, while for the TCC1 and CCC1 specimens only slight corrosion product was evident.

If the polarization curves in Figures 6 and 8 are compared, it becomes quite evident that the two-coat system out performs the one-coat

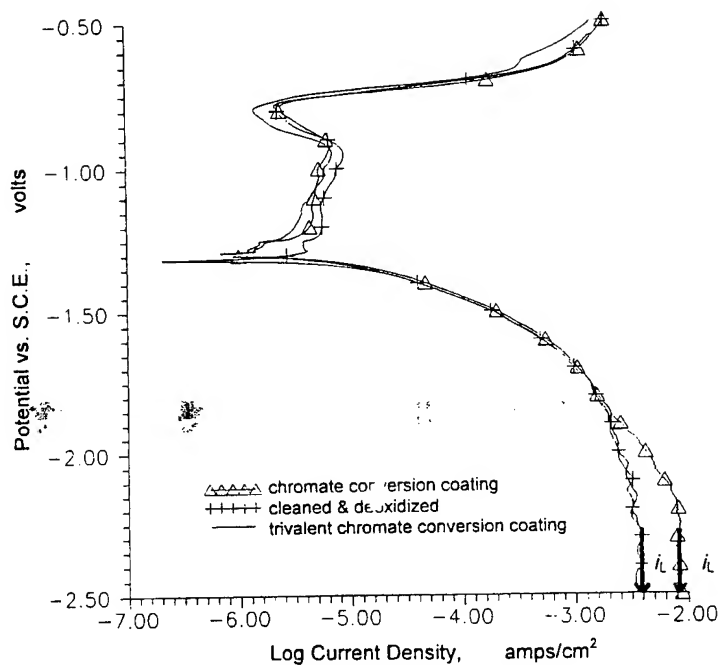


Figure 8: Polarization curves comparing surface pretreatments of a standard chromate conversion coating, trivalent chromium conversion coating and just cleaned and deoxidized under a Self-priming topcoat system (one-coat system).

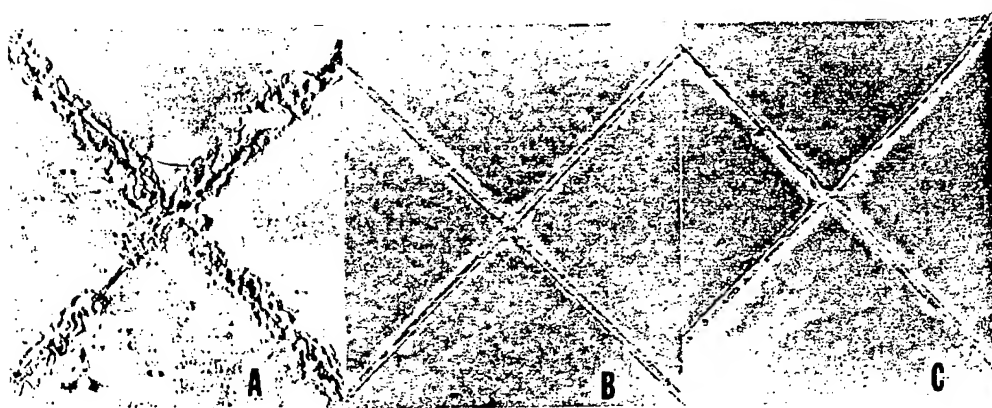


Figure 9: Photographs of Self-priming topcoat (one-coat) paint system with A) cleaned and deoxidized; B) trivalent chromium conversion coating; C) chromate conversion coating; pretreatment after being scribed and exposed in 5% salt fog for 1000 hours.

system. The anodic (passive region) currents from both sets of scans provide information which indicates that the two-coat system, including the cleaned and deoxidized surface, produces a decade lower current density than the one-coat system. Examination of the cathodic regions of both sets also predict greater adhesion problems with the one-coat system. These findings are well supported up by the results of salt exposure tests (cf. Figures 7 and 9).

Thus far it has been established that EST technique was able to show that different surface pretreatments had a great effect on the performance characteristics of the organic coatings. However, the corrosion inhibiting effects of the surface pretreatment were not fully confirmed as the coating system, both the primer and top coat, used always contained an inhibitor as an additive. Thus, new sets of panels pretreated as CD, TCC and CCC were prepared and coated with just a polyurethane topcoat containing no inhibitors. The reason for applying the topcoat for this testing was to prevent the pretreatment from leaching out into the electrolyte solution rather than migrating toward the scribed defect. The panels were electrochemically tested after one day pre-exposure in the test medium. The polarization diagrams obtained were as shown in Figure 10. They very clearly demonstrated that in the case of

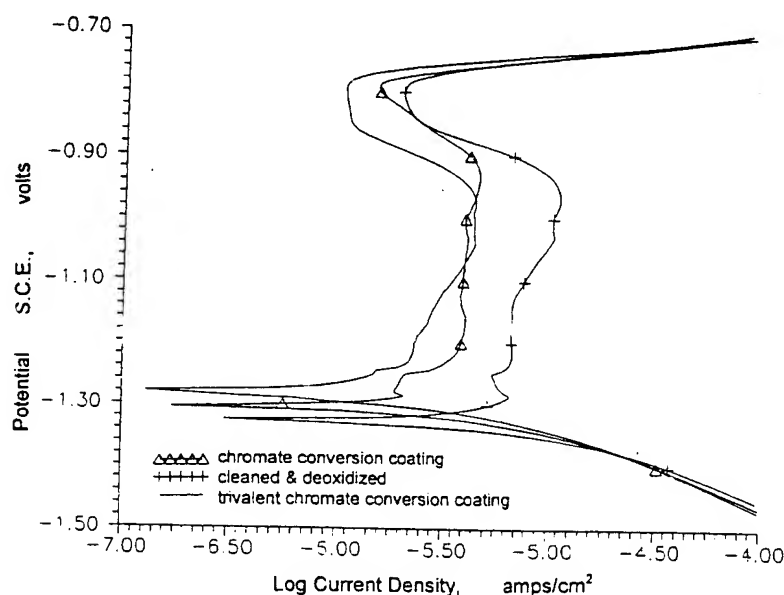


Figure 10: Polarization curves comparing the self-healing effects of chromate conversion coating and trivalent chromium conversion coating under an inhibitor free polyurethane topcoat[85285].

current density values, while they were highest for the cleaned and deoxidized specimen. The differences between passive regions of TCC and CCC were probably insignificant, although the currents appeared slightly lower for TCCC. In the cathodic domain the results were similar to those reported earlier; showed poor adhesion properties due to the fact they had only topcoat with no inhibitors. In actual salt exposure tests TCC and CCC specimens showed almost identical and least corrosion in the scribed area. Low corrosion current densities at anodic polarization potentials show that pretreatments have a self-healing effect on bare metal or the defect sites.

CONCLUSIONS

A novel scribing technique was developed to create reproducible defects on coated metal panels to characterize their corrosion and electrochemical behavior. The metal coating interface was studied through a potentiodynamic polarization method in which the interface was polarized from a very cathodic potential to a potential above open circuit in the anodic direction. The coating decohesion property was studied from the cathodic polarization effects and the corrosion resistance property of the substrate metal pretreatment was examined with respect to anodic polarization effects. The analyses of polarization curves was compared with the salt spray tests of the scribed panels. It was found that the values of limiting current densities, i_L , were directly related to metal-coating bond strength or adhesion, lower the i_L better the adhesion. This explanation was based on the understanding that interfacial cathodic reactions lead to oxygen reduction reactions and produce hydroxyl ions which attack the resin system to cause coating debonding. The corrosion resistance or passivating property of the pretreatments, conversion coatings, was related to values of the anodic currents in the passive region of the polarization curves, lower the current greater the resistance to corrosion.

Thus, the EST testing technique as described in this paper was found to be a valuable screening method for the assessment of corrosion protection properties of both the organic coatings and inorganic pretreatments (conversion coatings). It offers many advantages in the comparative evaluation of coating systems, such as quantitative measurements in relatively short test periods (compared to 1000 hour salt spray exposure testing), high reproducibility and sensitivity. The efforts are continued to further fine tune this method for routine testing.

REFERENCES

- [1] H. Leidheiser, Jr., *Prog. Organic Coatings* 7, 79 (1979).
- [2] J. Wolstenholme, *Corrosion Science* 13, 521 (1973).
- [3] T. Szaurer, *Progr. Organic Coatings* 10, 157 (1982).
- [4] B.S. Skerry and D.A. Eden, *Progr. Organic Coatings* 15, 269 (1987).
- [5] G.W. Walter, *Corrosion Science* 26, 39 (1986).
- [6] G.W. Walter, *Corrosion Science* 26, 681 (1986).
- [7] J.D. Scantlebury, K. N. Ho and D.A. Eden, *Electrochemical Corrosion Testing*, ASTM STP 727, F. Mansfield and U. Bertocci, Eds., ASTM, Philadelphia, 1981, p 187.
- [8] C. Lin and T. Nguyen, *National Institute of Standards and Technology Technical Note* 1253, 1988.
- [9] D.C. Mills and J.E. O. Mayne, in "Corrosion Control by Organic Coatings," H. Leidheiser, Jr., Ed., NACE, Houston, 1981, p.12.
- [10] H.P. Hack and J.R. Scully, *J. Electrochem. Soc* 138, 33 (1991).
- [11] F. Pearlstein and V.S. Agarwala, *Plating and Surface Finish* 7, 50 (1994).

BLANK

548

**Assessment of Some Advanced Protective Schemes,
Including Chromate and Non-Chromate Conversion
Coatings for Mg Alloy ZE41A-T5 Using
Electrochemical Impedance Spectroscopy**

Dr. Frank Chang*, Mr. Robert Huie, and Mr. Brian Placzankis
U.S. Army Research Laboratory, Materials Directorate
Watertown, MA 02172-0001

ABSTRACT

A study has been conducted to evaluate the suitability of a non-chromate conversion coating (Tagnite 8200) for replacing the currently used chromate conversion coating (Dow 17) on Mg alloy ZE41A-T5. This replacement must be accomplished without compromising the corrosion resistance and protection efficacy of other advanced coating schemes. Electrochemical Impedance Spectroscopy (EIS) and salt spray tests have been employed to compare the corrosion behavior in chloride containing solutions of Mg alloy ZE41A-T5 which has been coated with various combinations of a conversion coating (Tagnite 8200 or Dow 17), primer (Sermetel 1083 or epoxy) and topcoat (Sermetel 1089, polyurethane, or epoxy electrodeposited E-coat). Results indicate that there are several coating schemes which perform better than the currently used system and that the EIS and the salt spray tests show a direct correlation.

INTRODUCTION

Magnesium alloys are known for their low specific weight and excellent mechanical properties, thus they are considered to be one of the best structural materials for aircraft applications. However, U.S. Army experience with magnesium helicopter components has shown that significant corrosion problems exist which require increased maintenance, impacting both cost and readiness. During the Vietnam era magnesium alloys were used widely to reduce weight and increase performance. But in a recent modernization program, a number of magnesium parts were replaced with aluminum alloys

to reduce corrosion problems, resulting in a concomitant weight penalty. It is clear that improved protective schemes are needed to provide corrosion resistant magnesium components before its inherent weight advantage can be fully utilized.

The current practice for protecting magnesium employs an anodizing chromate conversion pretreatment, an epoxy primer and a polyurethane topcoat. Previously, we described¹ the beneficial results achieved by interposing a baked epoxy resin sealer between the conversion coating and primer application. In a recent paper², we reported some of our results on the corrosion resistance of magnesium alloys ZE41A-T5 and WE43A-T6 which were subjected to various coating schemes. These results were compared to the corrosion resistance of the current standard coating used at Sikorsky. In this paper, we present additional results obtained from ZE41A-T5 alloy panels with similar protective schemes, but replacing the Dow 17 surface pretreatment (with chromates) with Tagnite 8200 (non-chromate). Since the Tagnite is chromate free, it is considered to be more environmentally acceptable. However, the protection efficacy of various coating schemes in combination with the Tagnite pretreatment must be investigated prior to its qualification as a replacement for Dow 17.

MATERIALS

Magnesium alloy ZE41A-T5 (UNSM16410) was selected because it is being used in newer aircraft. Table 1 contains the mechanical properties and the nominal composition in wt% of elements. Each coating has been given a letter designation which is described in Table 2. Table 3 lists each of the evaluated protective schemes and thicknesses.

The Scrimetel 1083 primer (SP) is a high temperature polymer coating formulated with metallic pigmentation and corrosion inhibitors. This primer is applicable over conversion (anodized or immersion) pretreated surfaces such

Table 1
Mechanical Properties of ZE41A with Nominal Compositions in Wt% Solute

Alloy	Mechanical Properties						Composition				
	UTS	1% YS	2% YS	Modulus	%RA	%EL	Zn	RE	Zr	Y	Mg
ZE41A T-5(Ksi)	31.40	20.80	22.30	6520	4.30	4.80	4.3	1.5	0.73	-	93.47
ZE41A T-5(MPa)	216.50	143.42	153.76	44960							

Table 2
Letter Designations for Protective Schemes

Coating Designation	Pretreatment	Primer	Topcoat	Notes
dSP	Dow 17	Sermetel 1083		Sermetel Primer
dSPT	Dow 17	Sermetel 1083	Sermetel 1089	Sermetel Primer + Topcoat
dSk	Dow 17	MIL-P-85582	MIL-C-46168	Sikorsky (Standard)
tSP	Tagnite 8200	Sermetel 1083		Sermetel Primer
tSPT	Tagnite 8200	Sermetel 1083	Sermetel 1089	Sermetel Primer + Topcoat
tSPn	Tagnite 8200	Sermetel 1321		Sermetel Non-Cr Primer
tE	Tagnite	Epoxy E-Coat		E-Coat

Table 3
Protective Schemes Evaluated by US Army Research Laboratory

Substrate	Anodic Pre-Treatment (Thickness)		Coating System (Thickness)
	Dow 17	Tagnite	
ZE41A-T5			
✓	✓	✓	SP- (1mil, 2mil)
✓	✓	✓	SPT- (1mil, 2mil)
✓	✓		SP- (1mil) +Sk
✓	✓		SP- (2mil) +Sk
✓	✓		Sk
✓	✓		SPn (1 mil)
✓		✓ (0.35mil)	
✓		✓ (0.80mil)	
✓		✓ (0.90mil)	(phosphate sealed)
✓		✓ (1.0mil)	(phosphate sealed) +E
✓		✓ (0.30mil)	E-(0.80mil)
✓		✓	SPn (1 mil)

as Dow 17 (Dow Chemical Co. anodized, MIL-M-45202B, type II, class D, $\text{Na}_2\text{Cr}_2\text{O}_7 \cdot 2\text{H}_2\text{O}$ sodium dichromate) and Tagnite 8200 (non-chromate, Technology Application Group, Inc.). This primer is also compatible with a variety of topcoats, including Sermetel 1089 (T) a high temperature polymer and the currently used system by Sikorsky (Sk) which incorporates both an epoxy VOC compliant primer (MIL-P-85582) and a polyurethane topcoat (MIL-C-46168, chemical agent resistant topcoat, CARC). Tagnite 8200 is a two step (non-chromate anodizing and immersion) surface pretreatment. It contains silicon oxide and can be topcoated with an epoxy sealer/primer/topcoat combination such as SP, SPT, or electrodeposited epoxy E-coat (E).

EXPERIMENTAL

The testing program included both exposure to salt spray (ASTM

B117) and immersion in 0.5N NaCl solution, open to the air, for electrochemical impedance spectroscopy (EIS) measurements. EIS has been used extensively for assessing coating protection efficacy at the Army Research Laboratory (ARL) ¹⁻³. In salt spray testing, the specimens were visually examined periodically for corrosion. Testing was terminated if a panel was found to have corroded through its coating thickness. In most cases, only one panel for each test with each coating scheme was tested due to a limited number of coated panels available.

The cell used for EIS testing has been described elsewhere¹. EIS tests were performed with a PAR 378 system consisting of a model 5208 two-phase lock-in analyzer, a model 273 potentiostat/galvanostat, and a IBM PC XT computer. Periodic measurements were taken for the samples exposed to 0.5N NaCl solution at the corrosion potential (stabilized within 1 hour) over the frequency range of 100 KHz-0.005 Hz for a period of up to 100 days at room temperature. In the initial two or three weeks of immersion, EIS measurements were conducted more frequently since large variations were expected to occur; at longer times readings were taken less frequently since the impedance had stabilized. The single sine technique with an input sinusoidal potential of 5mV was applied in the frequency range 100KHz-5 Hz. At the lower frequency of 10-0.005 Hz, the multi-sine technique was employed with an input sinusoidal voltage of 10 mV. The dimensions of the magnesium alloy test panels were 6"x4"x1/4" (15.2cm x 10.2cm x 0.64cm). They were coated by various vendors on both front and back surfaces as described in Table 2. EIS tests were conducted only on the coated machined surface of the panels. EIS tests were performed in duplicate with results expressed as an average of the two panels or two different areas on the same panel due to panel availability. Before testing, the coated surfaces were cleaned with compressed filtered air and only areas without visually detectable defects were selected for exposure to chloride solutions.

The collected data was plotted and evaluated in the Bode as well as the Nyquist formats. It was found that the Bode formats were easier to analyze, and thus more useful in terms of determining coating efficacy. The Bode formats display the magnitude ($\log|Z|$) and phase angle (Θ) of the impedance as a function of applied frequency ($\log f$). The total impedance of the specimen, defined as the $\log|Z|$ value extrapolated to 1 mHz in the Bode magnitude plot, was also plotted as a function of exposure time for comparison of the efficacy of each coating system.

RESULTS AND DISCUSSION

Salt Spray

Table 4 contains ZE41A-T5 salt spray data for the various protective schemes. These schemes are comprised of either the Dow 17 (d) or the Tagnite (t) pretreatment, then coated with either the primer only (SP), primer and topcoat (SPT), or with the Sikorsky (Sk) system. Included also is a Tagnite/sealer/electrodeposited epoxy E coat system (tE) and a proprietary non-Cr primer, Sermetel 1321 (tSPn).

Table 4
Salt Fog Performance Summary of Coated ZE41A-T5
Dow 17

Hours	Coating dSPT (1 mil)	Coating dSP (1 mil) + Coating Sk	Coating dSPT (2 mil)	Coating dSP (2 mil) + Coating Sk
% Area Failed				
6	0	0	0	0
24	0	0	0	0
5424	10	50	0	0
6024	Failed	Failed	0	0
6696			0	0
14976			0	0
↓			↓	↓
19440			0	0

Tagnite 8200

Hours	Coating tSPT (1 mil)	Coating tSP (1 mil)	Coating tSPT (2 mil)	Coating tSP (2 mil)	Coating tSPn (1 mil) + 1321
% Area Failed					
6	0	0	0	0	0
720	0	0	0	0	0
1200	0	4	0	0	0
1632	0	7	0	0	0
1944	0	7	0	0	0
2532	0	10	0	0	0
3384	0	10	0	0	0
3624	0	12	0	0	0
4224	0	15	0	0	0
4368	0	18	0	0	0
4560	0	20	0	0	0
4872	0	22	0	0	0
4968	0	25 - Failed	0	0	0
5376	0		0	0	0
5664	0		0	0	0
6168	0		0	0	0
6480	5		0	0	0
6840	10 - Failed		5	7	0

Note: Failures of ZE41A panels were defined by non-edge nucleating pits which corroded through the entire thickness of the test panel.

All panels pretreated with Dow 17 and coated with various schemes

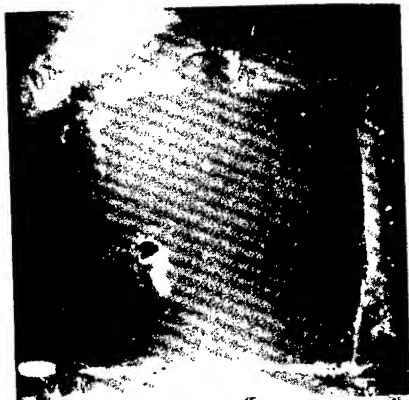
completed at least 5000 hours of salt spray exposure without failure. However, for coatings with only 1 mil (.0254mm) of either the primer (dSP) or the primer/topcoat combination (dSPT), corrosion occurred through the thickness shortly thereafter at 6024 hours. When the total thickness of these coatings was increased to 2 mils (.0508 mm), they performed significantly better. No failure occurred up to 15,000 hours of exposure, yielding a 3X improvement.

For those panels pretreated with Tagnite and coated with various coating schemes, failure was defined as corrosion of a panel through its entire thickness at a non-edge nucleation site. Edge related corrosion attacks were ignored since they resulted from improper sealing along the edges. The panel coated with 1 mil total of tSP was first to fail at 4968 hours followed by the panel coated with 1 mil total of tSPT at 6840 hours. The panels coated with 2 mil total coatings contained some small corroded pits or blisters, but no failures occurred at 6840 hours. These results indicate that the corrosion resistance of the coated panels are more affected by coating thickness regardless of the type of pretreatment employed. It is also shown that the corrosion resistance of the coated samples appear to be comparable if the coating schemes and their total thickness are the same. The same may be said based on their EIS results as presented later. Additional ARL salt spray data for the Tagnite pretreated samples is unavailable due to the limited number of panels provided. However, Sikorsky⁴ did conduct 96 hours of salt spray testing (ASTM B117) on magnesium alloy panels pretreated with Dow 17, HAE (non-Cr type), or Tagnite only. Their results showed that Tagnite provided greater protection with only minor corrosion occurring as compared to the extensive corrosion observed on the other samples.

It was noted that the panel coated with a 1 mil non-Cr primer, Sermetel 1321 (tSPn), showed no corrosion occurring at 6840 hours. This non-Cr primer appears to be a potential candidate for the replacement of the Cr containing Sermetel 1083 (SP). Additional results will be reported at a later date since the testing is still in progress.

Figure 1(a-c) shows the front and back of tested panels coated with 1 mil dSPT, 1 mil tSPT, and 2 mils tSPT respectively. In the 1 mil specimens, the non-edge nucleated corrosion has proceeded through the thickness of the substrate after having been subjected to at least 5,000 hours of salt spray testing. The corroded area appearing on the front surface is small but spreads quickly, exhibiting much broader corrosion on the rear surface. The non-edge nucleated corrosion has not occurred on the panel coated with 2 mil tSPT.

as shown in Figure 1c.



(a)

Front



Back

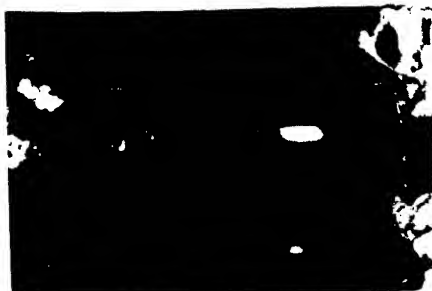


(b)

Front



Back



(c)

Front



Back

Figure 1. Front and Back of Failed Salt Spray Tested Specimens; a) 1 mil dSPT Failed at 5,000 hours, b) 1 mil tSPT Failed at 6840 hours, c) 2 mil tSPT Unfailed at 6840 hours,

Electrochemical Impedance Spectroscopy

The EIS data obtained from each test was plotted in both Bode and Nyquist formats. Certain parameters were examined to ascertain whether they might be used to characterize protection efficacy of the coatings. Representative plots are shown in Figure 2. Impedance values at low frequency ($|Z|$ @ 1 mHz) can distinguish between good and poor coatings⁵. For example⁶, for aluminum alloys, any coating with total impedance values $<10^5 \Omega \cdot \text{cm}^2$ indicates repainting is necessary; values between 10^6 and $10^8 \Omega \cdot \text{cm}^2$ indicate reexamination is required in 6 months to a year; when values $>10^9 \Omega \cdot \text{cm}^2$ are measured, the coating is functioning properly. Murray and Hack⁷ accumulated EIS data over a frequency range of 5×10^{-3} to 10^5 Hz for relatively thick MIL-P-24441 epoxy coated steel specimens which were exposed to artificial ocean water for up to 3 years. They found that the most useful parameter is Z_{max} , defined as the maximum impedance at low frequency. Samples with Z_{max} values greater than $10^9 \Omega \cdot \text{cm}^2$ were characterized as superior coatings. (Note that a factor of 5.06 cm^2 should be multiplied to the impedance magnitude shown in the figures to obtain comparable $\Omega \cdot \text{cm}^2$ values.)

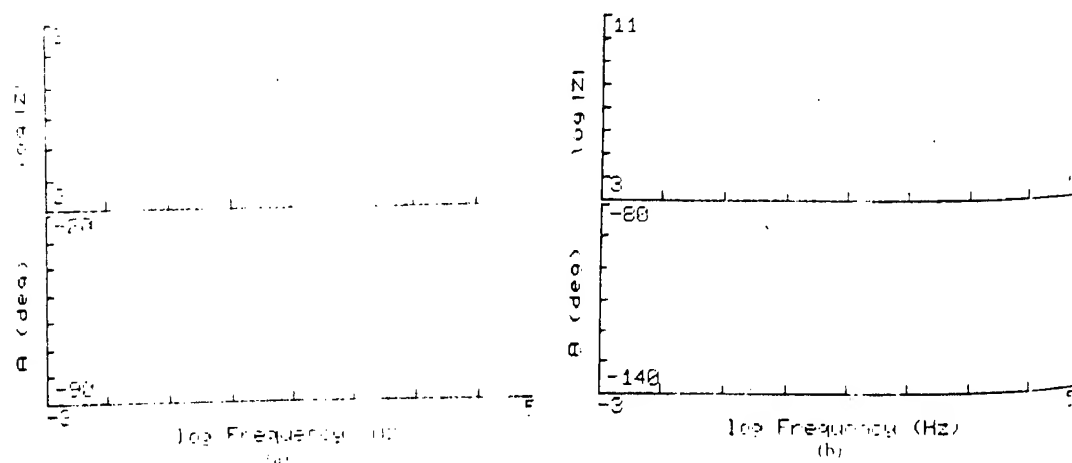


Figure 2. EIS Data Plotted in Bode Format a) 1 mil dSP , b) 1 mil tSP with 0.8 mil Coating E after 87 days of immersion in 0.5 N NaCl.

Figures 3 to 10 contain plots of impedance values extrapolated to 1 mHz as function of exposure time for the ZE41A-T5 coated samples described in Table 2.

Figure 3 compares the impedance of 1 mil thickness of coatings dSP, tSP, dSPT and tSPT. The beneficial effect of the Sermetel 1093 (T) barrier topcoat is shown on the Dow 17 (d) pretreated samples. The impedance of dSPT increased from $10^{9.5} \Omega$ to $> 10^{10} \Omega$ over the first 40 days. Although this value was higher than the impedance of the dSP at that time, the impedance of both samples was very much the same at the end of the test at 95 days, as seen in Figure 3(a). However, with the Tagnite (t) pretreated samples, Figure 3(b), the impedance data does not show the beneficial effect of the barrier topcoat. In the first 15 days, the impedance of the 1 mil tSP is higher than that of the 1 mil tSPT, $10^{9.5}$ vs. $10^{6.5} \Omega$. Afterwards, the impedance of both tSP and tSPT fluctuate between $10^{5.5}$ and $10^7 \Omega$ until the end of the test. Examination of samples after testing revealed that localized corrosion near the O-ring seal occurred in one of the 1 mil tSPT samples, resulting in lower impedance values, $\approx 10^5 \Omega$. The corrosion which occurred early in the test may have resulted from local O_2 content variation or pre-existing, macroscopic defects. Nevertheless, the application of a barrier topcoat layer does not appear to be beneficial at 1 mil total thickness since they both approach the same lower impedance values.

The comparison of the impedance of panels coated with 1 mil of Cr vs. non-Cr primer (Sermetel 1093 vs. Sermetel 1321) on Dow 17 (d) or Tagnite (t) is shown in Figure 4. It is clearly seen that the Tagnite/Sermetel 1321 shows a stable and higher impedance from the beginning to the end of the test period. This has been found to be in very good agreement with the results obtained from the salt spray test described previously. It also demonstrates that a good correlation exists between the EIS and salt spray test results qualitatively. Future tests have been planned to investigate further the compatibility of this non-Cr primer with other advanced coating schemes since it has exhibited excellent corrosion resistance in this initial study.

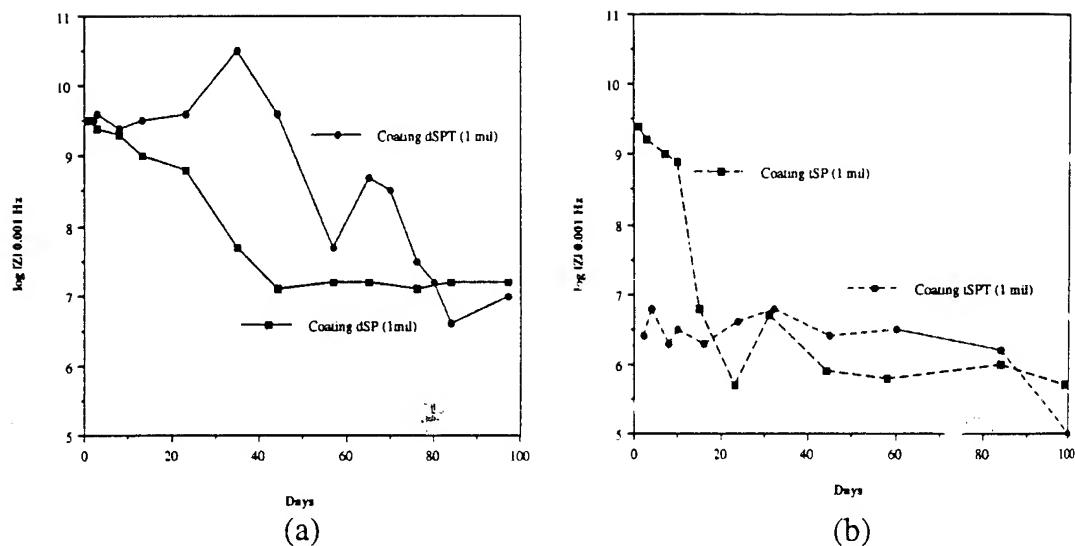


Figure 3. EIS data on 1 mil SP vs 1 mil SPT on ZE41A with
a) Dow 17 and b) Tagnite 8200

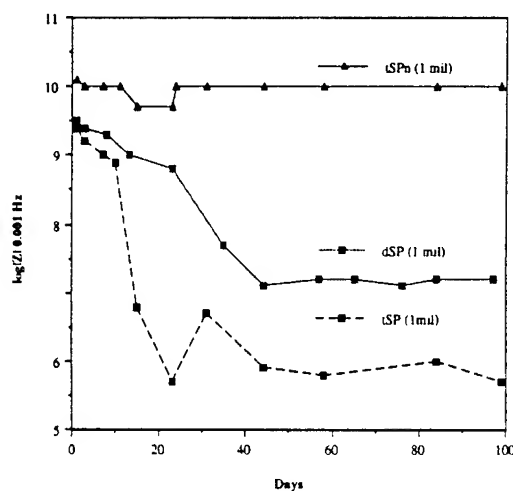


Figure 4. EIS data on 1 mil tSP, tSPn, and dSP.

Figure 5 shows the effect of coating thickness, 1 mil (25.4 mm) vs. 2 mil (50.8 mm) of SP on the performance of samples pretreated either by Dow 17(d) or by Tagnite (t). The impedances of the 2 mil (50.8mm) dSP or tSP coatings remained relatively constant, $>10^9 \Omega \cdot \text{cm}^2$, over a period up to 100 days, regardless of the type of pretreatment employed. This indicates that both are excellent coatings. The tSP coating also showed a similar magnitude

of impedance to the dSP coating over the test period. Generally, impedance is proportional to the thickness of the coating, since increased coating thickness restricts the corrosion inducing agents penetration to the substrate/coating interface by reducing the probability of a continuous defect pathway traversing through the thickness of the coating. Higher impedance values from EIS testing show the beneficial effect of increasing the thickness from 1

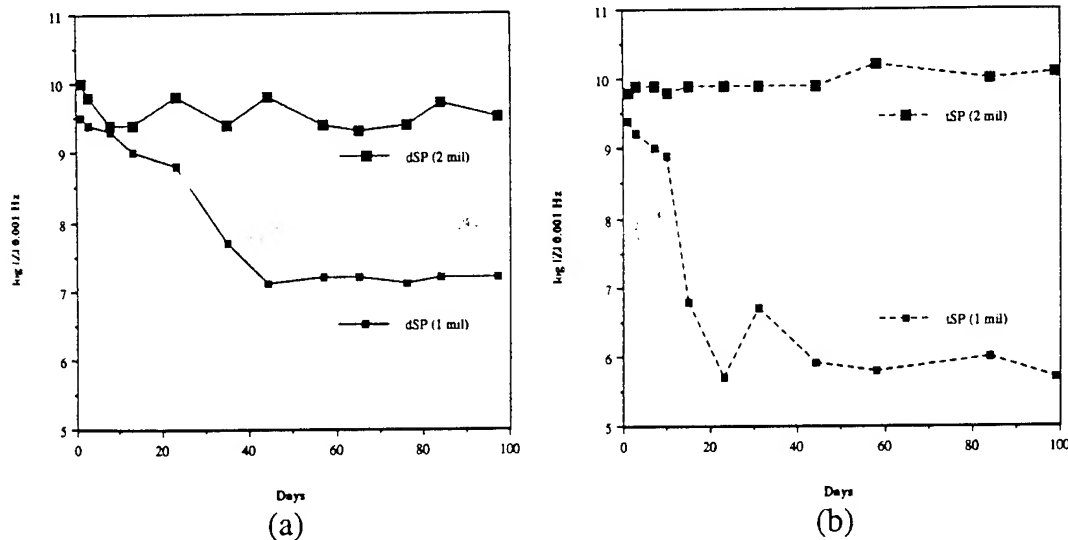


Figure 5. EIS data on 1 vs 2 mil SP on ZE41A with a) Dow 17 and b) Tagnite 8200.

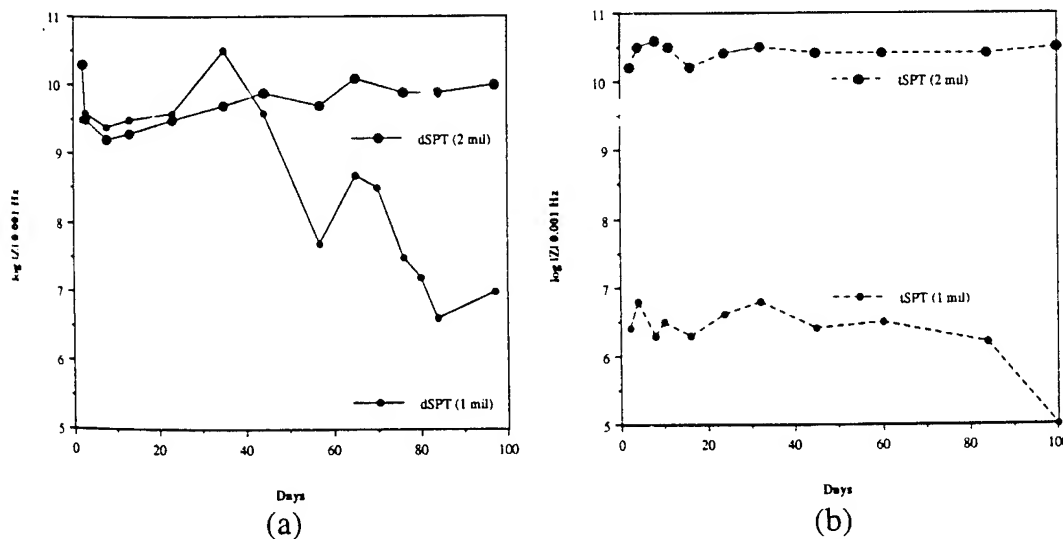


Figure 6. Effect of thickness, 1 vs 2 mil SPT on ZE41A with a) Dow 17 and b) Tagnite 8200.

to 2 mils of dSPT and tSPT. This is clearly shown in Figure 6, from 10^7 (dSPT) or from 10^5 (tSPT) to at least $10^{10} \Omega \cdot \text{cm}^2$ after 100 days of exposure to chloride solution.

When the total thickness is increased to 2 mil, the impedance of both coating systems, SP and SPT is comparable over the entire 100 day exposure period, with impedance values exceeding $10^9 \Omega \cdot \text{cm}^2$, as shown in Figure 7. The application of the barrier topcoat is beneficial to both the dSP and tSP coatings. For the dSP and dSPT coatings, Figure 7(a), impedance values begin to increase after 10 days following the initial drop. In the tSP and tSPT coatings, Figure 8(b), the impedance values show only slight temporal variation, with the 2 mil tSPT having somewhat higher values than the tSP. It should be noted that these impedance values are of the same order of magnitude, indicating that the incremental effect of a barrier topcoat is much less significant than an increase in thickness.

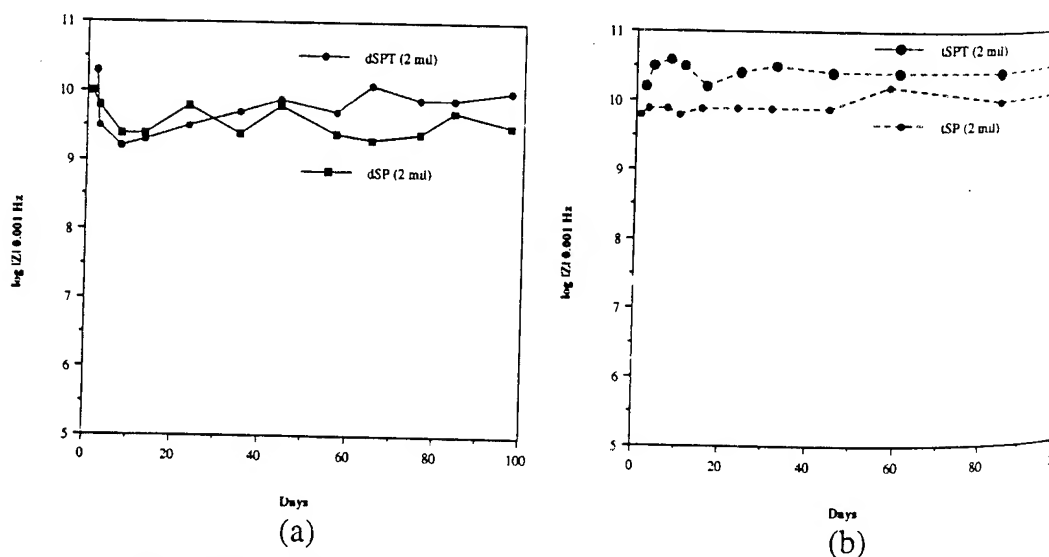


Figure 7. EIS data on 2 mil SP vs SPT on ZE41A with
a) Dow 17 and b) Tagnite 8200.

Figure 8 (a) compares the performance of coating dSP, at both 1 mil and 2 mils, with or without the currently used Sk coating system on top of it. The impedance of the currently used system, dSk (≈ 3 mil) is higher than that of the 1 mil dSP coating scheme, 10^8 vs. $10^7 \Omega \cdot \text{cm}^2$. It also remained relatively constant throughout the entire test while the latter scheme dropped dramatically over the first 41 days and remained constant thereafter. There is no further beneficial effect of applying the currently used Sk system on the top of the thicker 2 mil dSP coating system. In both cases impedance values were high and approximately the same, $10^{9.5} \Omega \cdot \text{cm}^2$. Figure 8(b) also

compares the impedance values of the currently used dSk coating with other schemes on top of Tagnite pretreated panels, including the 1 mil tSPn (non-Cr). It shows that the impedance of the 2 mil tSP and tSPT, as well as the 1 mil tSPn is consistently higher than the dSk over the test period of 100 days. However, similar to the data shown in Figure 8(a), the impedance of the 1 mil tSP and tSPT coatings are lower than that of the dSk system due to its thinness. For an impedance value of $10^9 \Omega \cdot \text{cm}^2$ over a 100 day testing period, a coating scheme minimum thickness of 2 mils is required to ensure its protection efficacy equal or greater than the currently used dSk scheme. There appears to be at least 6 coating systems; 2 mil dSP, 2 mil dSP/Sk, 2 mil dSPT, 2 mil tSP, 2 mil tSPT, 1 mil tSPn, which would meet this requirement, as shown in Figure 7 and 8.

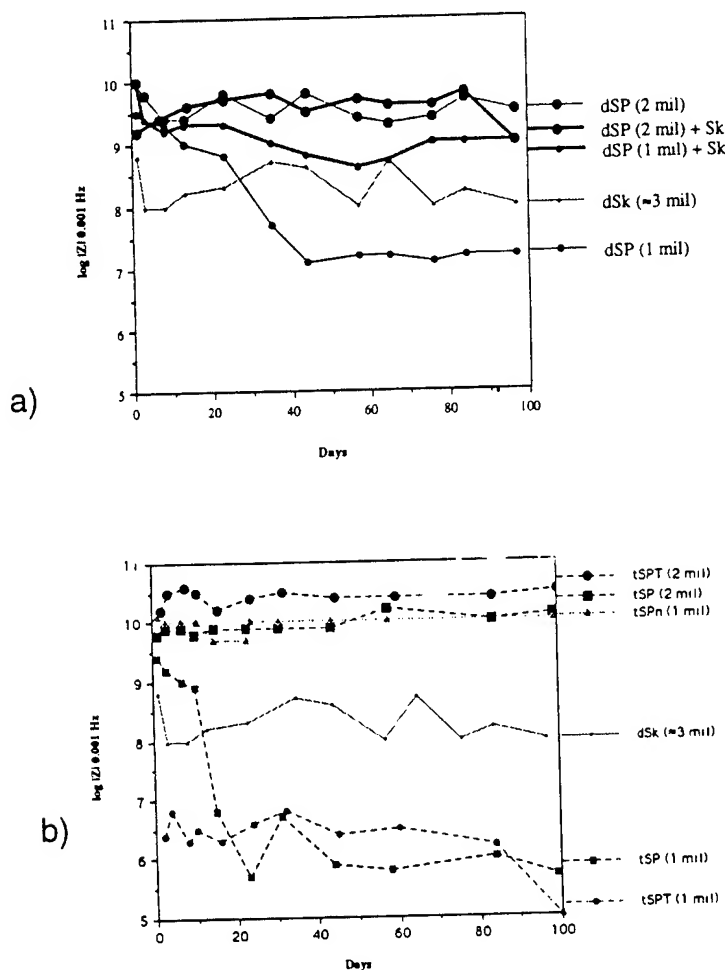


Figure 8. Efficacy of protective schemes on ZE41A with
a) Dow 17 and b) Tagnite 8200.

Figure 9 compares the impedance of the Tagnite pretreated ZE41AT5 panels with various combinations of phosphate sealant, and electrodeposited epoxy E-coat. The impedance of the E-coated samples exhibited consistently high impedance, with values above $10^{10} \Omega \cdot \text{cm}^2$, indicating excellent corrosion resistance. This Tagnite/E-coat combination clearly presents itself as an alternative scheme which may perform better than the currently used dSk system. It also shows that the impedances of the Tagnite samples, with or without a phosphate sealant, are roughly equal, indicating the apparent irrelevance of the sealant for these test conditions.

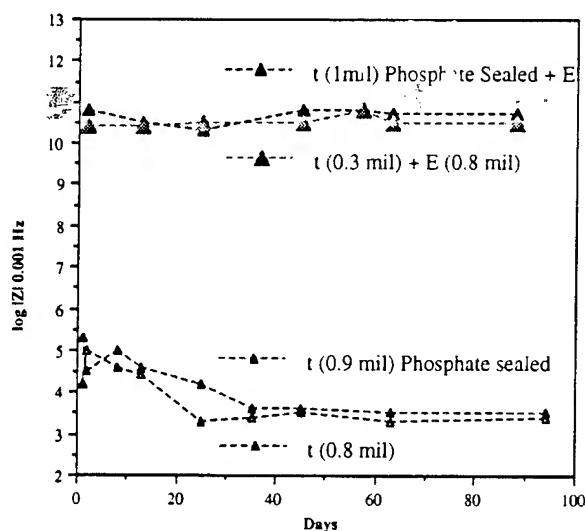


Figure 9. Effect of Tagnite 8200 on ZE41A.

It is a known fact that most of the conversion coatings such as Dow 17 which are produced by chemical immersion or anodizing are porous in nature. However, the Tagnite conversion coating layer is produced by a dual immersion and electrodeposition processes. It was reported that the pores are not continuous through the thickness of the coating layer, thus a sealant may not be required. Figure 9 shows the low impedance of Tagnite pretreated samples, $\approx 10^4 \Omega \cdot \text{cm}^2$ with or without a phosphate sealing. This fact along with the observation of gas bubbles (H_2) generated in the initial stages of the immersion test, suggest that the Tagnite conversion coating does have continuous defect pathways through to the substrate. In addition, since the sealed Tagnite performed similarly to the unsealed sample, the phosphate sealant seemed ineffective for this application. Thus a compatible sealant will definitely be required for application in a mild environment or else a sealant primer/topcoat combination such as coating-E will be required for more

severe applications.

CONCLUSIONS

For coated ZE41A-T5 samples, there was good qualitative correlation between salt spray and EIS data. The protective schemes providing the best salt spray resistance exhibited the highest impedance values with slower rates of degradation. Impedance increases from 10^8 to $10^{10} \Omega \cdot \text{cm}^2$ indicate an upgrade in corrosion resistance from good to excellent. Several advanced protective schemes, based on either Dow 17 or Tagnite 8200 pretreatment, have shown higher impedance than the currently used coating, *provided the total thickness of the coatings is equal to or greater than 2 mils*. However, both salt spray and EIS results suggest that a 1 mil Tagnite/non-Cr primer (tSPn) coating may also provide an alternative scheme with good protection efficacy. Also, the impedance data obtained from the 1 mil Tagnite/E-Coat combination indicate that it may be another viable system. These advanced schemes should provide excellent corrosion resistance. Furthermore, the EIS testing method could also lead to a non-destructive approach to monitoring coating integrity and extrapolating the useful life of coatings. However, it should be noted that before any advanced protective schemes can be transitioned to components of operating Army aircraft, outdoor exposure testing in Army environments must be completed. In the next phase of the Army study, the degradation of these coatings during outdoor exposure studies will be monitored with a portable EIS system for correlation with laboratory test data. This information will be provided to Sikorsky Aircraft in a cooperative effort to complement their fatigue, oil exposure, strippability and touch up test program.

ACKNOWLEDGEMENTS

The authors wish to thank Sikorsky Aircraft, Stratford, CT, Sermetech International, Limerick, PA and Technology Applications Group, Inc. Grand Forks, ND for their assistance.

REFERENCES

1. M. Levy, R.T. Bombard, and R.M. Huie, MTL TR 89-9, February 1989, also Magnesium Developments, World Materials Congress, pp.172. September 1988, Chicago, IL.
2. M. Levy, F. Chang, B. Placzankis, and R. Huie, "Improved Protective

Schemes on Magnesium Aircraft Alloys", Paper No. 617, Corrosion 1994 (Baltimore, Maryland, March 1994).

3. F.Chang, M.Levy, and R. Huie, "Assessment of Chromate and Non-Chromate Conversion Coatings for Aluminum Alloys Using Electrochemical Impedance Spectroscopy", Proceedings of the 1992 Tri-Service Conference on Corrosion, pp 181, (Plymouth, MA, May 1992).
4. R. Guillemette, United Technologies, Sikorsky Aircraft(unpublished work), Briefing Document, April 27, 1993.
5. F. Mansfield and M.W. Kendig, Impedance Spectroscopy as Quality Control and Corrosion Test for Anodized Aluminum Alloys, Corrosion 41(1985),p.490.
6. S. Spadafora, et al., Environmental Materials Program, Report No.NAWCAD WAR 9207560,1992, Naval Air Warfare Center, Warminster, PA, presented at 1989 Tri-service Conference on Corrosion, Atlantic City, NJ.
7. J.N. Murray and H.P.Hack, "Long-Term Electrochemical Characterization of MIL-P-24441 Epoxy Coated Steel Using Electrochemical Impedance Spectroscopy", Proceedings of the 12th International Corrosion Congress, pp.151-155(Houston, TX, 1993).

Effectiveness of Thin Film Fluoropolymers as Protective Coatings in Marine Environments

Dr. J.F. McIntyre
Department of Ocean Engineering
Florida Atlantic University
Boca Raton, FL 33431

Mr. R.K. Conrad
Naval Surface Warfare Center
Dahlgren Division
Code R33
Silver Spring, MD 20903-5000

Mr. A. Sheetz
Department of Ocean Engineering
Florida Atlantic University
Boca Raton, FL 33431

ABSTRACT

Topside weapon systems and their associated hardware are exposed to a harsh marine environment that often includes high temperatures, periodic seawater wetdown and exposure to exhaust gases. Hence, it is necessary to employ corrosion resistant materials and protective coating systems to ensure availability and reliability of the weapon system. A recognized topside maintenance problem involves fretting corrosion associated with sliding parts. Wear surfaces are typically protected from corrosion by the application of lubricants. Although lubricants can be effective in controlling corrosion, they require frequent replacement to provide maximum protection. Candidate replacements for lubricants are a family of fluorocarbon impregnated thin film resins. The corrosion performance of several of these coatings as applied to aluminum, low alloy steel and stainless steel substrates is

described herein. Test panels were exposed to a marine atmospheric environment and a marine atmospheric environment with periodic seawater wetdown. Companion specimen panels were also exposed to constant immersion in aerated seawater and characterized using electrochemical impedance spectroscopy. The findings of this research indicated that fluoropolymer coatings provided better long-term protection than solid-film lubricants.

INTRODUCTION

Topside weapons systems are exposed to many different environments. For example, these might include some combination of marine atmospheric, seawater splash and spray, stack gases, fresh water, high temperature, oils, lubricants and various solvents. Therefore, concerted efforts are made to employ the best available corrosion protection schemes with the principal objectives of ensuring that weapon systems are available, reliable and maintainable. A recognized topside corrosion problem involves fretting corrosion associated with sliding parts on weapon systems. In many cases wear surfaces are coated with solid-film lubricants, which provide only modest corrosion protection. This class of lubricants are often high maintenance items and when neglected corrosion between sliding parts takes place.

The objective of this study was to compare the corrosion properties of several conventional solid-film lubricants, e.g., dry-film lubricants embedded in an organic matrix, with the behavior of thin-film fluoropolymer coatings. Test coupons were exposed to several marine environments and evaluated in the laboratory using electrochemical impedance spectroscopy (EIS). The EIS technique has been used successfully by others¹⁻⁷ to characterize and follow the degradation of protective coatings. Because impedance data are collected over a broad frequency range, typically 1 mHz to 65 kHz, the procedure is capable of identifying and quantifying individual factors contributing to coating failure, such as moisture uptake, coating conductance and interfacial corrosion.

EXPERIMENTAL

Test panels were prepared and supplied by the coating manufacturer. The fluoropolymer coatings were applied to a HY-80 steel, AISI 304 stainless steel and AA6061-T6. A list of test specimens is provided in Table 1. Two types of coatings were studied: (1) solid-film lubricants that conformed to weapon specification 20290 and are designated as 6255 and 6256; and (2) thin-film fluoropolymer coatings which are designated as 6108 and STF.

Panels were exposed for two years or more to 1) a marine atmosphere and 2) a marine atmosphere with periodic seawater wetdown. The atmospheric test racks face east and are located approximately twenty meters from the Atlantic Ocean in Ft. Lauderdale, FL. Specimens were secured to a fiberglass support using nonmetallic fasteners and positioned 30° to the horizontal. Specimens exposed to periodic seawater wetdown were positioned and secured to fiberglass supports in an identical manner; however, these racks are located about fifty meters from the ocean, but within ten meters of the Port Everglades shipping channel. Specimens placed on these racks were periodically sprayed with fresh seawater every hour for ten minutes. All outdoor specimens were examined visually and photographed periodically.

Companion panels were also exposed to aerated seawater and periodically evaluated using EIS. EIS measurements were made using a Solartron 1260 Gain Phase Analyzer coupled to an EG&G PARC 273A potentiostat and interfaced to a personal computer for scanning and data manipulation. A three electrode cell configuration was employed that utilized a glass clamp-on cell and included a commercial Ag/AgCl reference electrode and a graphite auxiliary electrode. The exposed surface area was approximately 24 cm². Impedance scans were generally run between 65 kHz and 10mHz at an applied amplitude of 20-40 mV. Specimens were removed from constant immersion in aerated seawater for periodic EIS testing and were immediately returned to this environment at the conclusion of the EIS scan. Data analysis was performed using Scribner and Associates ZFit® which incorporates a complex nonlinear least squares (CNLS) fitting routine.

[REDACTED]

A static friction test was also performed on virgin coated panels and coated panels after 310 days of constant immersion in aerated seawater. This test was conducted according to ASTM D 1894⁸.

RESULTS AND DISCUSSION

Marine Atmospheric Exposure

All coated HY-80 steel panels experienced slight to extensive rust through and complete loss of coating adhesion on a few panels. The fluoropolymer coating (6108) provided protection that was equal to 6255 (solid-film) and was superior to the 6256 (solid-film) coating. A comparison between 6255 and 6256, each containing an intentional defect, is shown in Fig. 1. The 6256 coating had completely failed with uniform rust through and sizeable amounts of coating loss. Conversely, the 6255 and 6108 (not shown) panels exhibited moderate rusting in the "x" scribe and a few isolated rust through spots in areas away from the defect. A large number of small blisters were located adjacent to the "x" scribe on the 6255 panel but were not observed for 6108. 6256 panels without an initial defect experienced uniform failure and rust through, whereas only a few pin-head size rust spots were found on the 6108 and 6255 coated panels without intentional defects.

Coatings applied to the AA6061-T6 substrate performed well in marine atmospheric exposure. The STF coated panel showed no signs of underfilm attack or loss of adhesion near the "x" scribe on those panels containing intentional defects. 6255 coated panels also showed no evidence of coating adhesion loss or underfilm corrosion, however the 6155 coating contained a uniform distribution of discolored spots.

All coated AISI 304 panels experienced severe discoloration of the coating (Fig. 2). The nature of this deterioration remains unclear; however, no underfilm corrosion or coating adhesion loss was observed. Because of the nearly identical appearance of all coated stainless steel panels, it was impossible to rank the individual coatings in terms of performance.

Marine Atmospheric Exposure with Seawater Wetdown

Exposure to periodic seawater wetdown proved to be a more aggressive environment. All 6256 panels, those with and without intentional defects, exhibited complete loss of coating adhesion and the build-up of voluminous corrosion products. In comparison, 6255 exhibited the best performance with moderate pin-hole rusting on panels without an intentional defect and sizable corrosion product build-up along the "x" scribe on the panel containing the intentional defect. Two of five 6108 panels experienced severe uniform rusting, while the other panels showed moderate localized rusting.

Both 6255 and STF coatings on AA6061-T6 panels held up well to the more aggressive seawater wetdown environment. The discolored spots on the 6255 coating were in greater number and larger in size compared to those observed on panels exposed to the marine atmosphere only environment; however, the coating remained intact with no apparent loss of adhesion. Attack of the bare metal in the "x" scribe was more extensive for these panels compared to those exposed only to the marine atmosphere (Fig. 3). The STF coated panels also performed well however localized, white corrosion spots about the size of a pin-head were present on all panels. As with the 6255 coating no loss of adhesion was observed (Fig. 3).

The coated stainless panels exposed to the periodic seawater environment behaved identically to those specimens exposed only to the marine atmospheric environment (Fig. 2). This behavior was not exhibited by these same coatings on the HY-80 substrate, which suggests that the stainless steel substrate influenced the deterioration of the coatings. The nature of this interaction remains unclear at this time.

Electrochemical Impedance Spectroscopy

The impedance data was analyzed using a CNLS program. The electrical analogs are shown in Fig. 4. The impedance behavior of coated HY-80 specimens was best represented by Model A; whereas, Model B typically applied to both AA6061-T6 and AISI 304 coated specimens. The two models are similar except Model B contains a constant phase element in series with the coating pore resistance (R_{po}) which is associated with diffusion within coating pores. This diffusional impedance manifests itself as a broadening of the phase angle minimum in the Bode-angle plot at intermediate frequencies (ca. 100 Hz). Examples of the CNLS fit for each substrate type are shown in Figs. 5-7.

A summary of impedance data as a function of time for each coating system is provided in Tables 2-4.

From the impedance data (Table 2) and visual observations, the 6108 coating on HY-80 performed better than the 6255 and 6256 coatings. Although the R_{po} values are lower than those obtained for the 6255 coating, the change in coating capacitance (C_c) is less for the 6108 coating and the charge transfer resistance (R_{ct}) remains higher than values obtained for both 6255 and 6256. A sizeable number of coating blisters occurred on the 6255 coating while localized rust through of the 6256 coating was observed. Conversely, no signs of deterioration of the 6108 coating was evident. Results from EIS correlated well with the two years of field testing. The 6108 coated panels performed better in the marine atmospheric environment compared to the 6255 and 6256 coatings; however, performed slightly worse than the 6255 in the marine atmosphere with periodic seawater wetdown, but performed better than the 6256 in the latter environment.

As observed for coated HY-80 panels, the 6108 coating on the AISI 304 substrate performed better than the 6255 and 6256 coatings. Higher R_{po} values were obtained for the 6108 coated panel compared to both 6255 and 6256 coated specimens. In addition, the R_{ct} was higher for the 6108 coating compared to the 6256 coating but was about two times lower compared to the 6255 coating. Visual observations showed 1) no signs of deterioration of the 6108 coating, 2) the presence of several areas of localized attack on the 6256 coated specimen (as indicated by the local build-up of rust colored corrosion products) and 3) blistering of the 6255 coating. Based on the impedance responses of these specimens, it would be predicted that the 6108 coating should perform better than the 6255 and 6256 coatings; however, evidence from field testing was inconclusive.

R_{po} and R_{ct} values for the 6255 coating were higher than those obtained for the STF coating. However, both the STF and 6255 coating performed similarly in the aerated seawater environment as indicated by the lack of coating deterioration. This slight difference in impedance behavior may reflect the observed performance when these coated panels were exposed to the seawater wetdown environment. As noted previously, some apparent localized attack of the aluminum substrate occurred through the STF coating whereas no deterioration of the 6255 coating was evident.

Static Friction

Static friction tests were performed in order to determine whether exposure to a corrosive environment would degrade the coating's lubricity. It is apparent from the results summarized in Table 5 that deterioration of the coatings on HY-80 steel substrates leads to an increase in the static friction. On the other hand, the values for static friction decrease for most of the coatings on AISI 304 and AA6061, with the exception of the STF coating on AA6061-T6.

SUMMARY

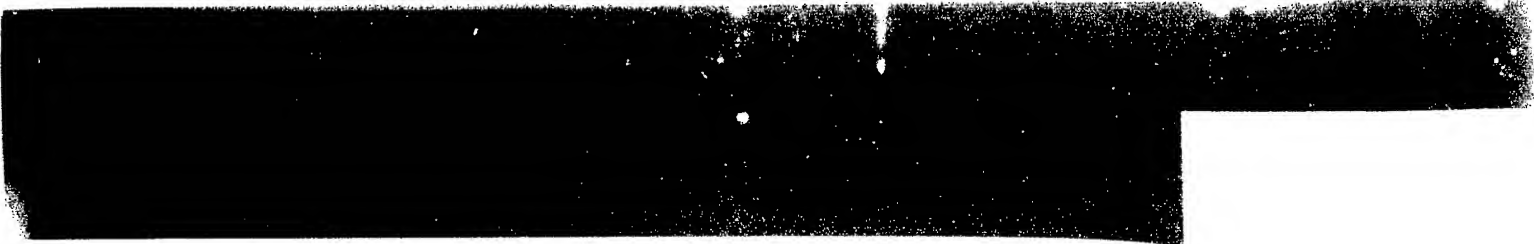
- In general, the EIS data correlated well with the results from field testing and demonstrated that relatively short-term laboratory testing using EIS is capable of predicting the performance of these coatings when exposed for extended times in field environments.

- Results from both laboratory testing and field exposures indicated that the fluoropolymer coatings (6108 and STF) are better than the 6256 solid-film lubricant and equal to and sometimes better than the 6255 solid-film lubricant.

- Limited static friction tests revealed that the lubricity of coatings on AA6061-T6 and AISI 304 substrates did not deteriorate, while static friction values were higher for two of the three coatings on the HY-80 substrates.

REFERENCES

- 1) F. Mansfeld and M. Kendig, "Electrochem. Impd. Tests for Protective Coatings," Ed: Haynes and Baboian, ASTM STP 866 (Philadelphia, PA: ASTM, 1985), p. 122.
- 2) M. Kendig, A.T. Allen, S. L. Jeanjaquet and F. Mansfeld, "The Appl. of Impedance Spec. to the Evaluation of Corr. Protection by Inhibitors and Polymer Coatings," CORROSION/85, Paper # 74 (Houston, TX: NACE International, 1985).



3) M. Kendig and J.R. Scully, "Basic Aspects of the Appl. of Electrochem. Impd. Spec. for the Life Pred. of Org. Coatings on Metals," CORROSION/89, Paper # 32 (Houston, TX: NACE International, 1989).

4) J.F. McIntyre and H. Leidheiser, JECS 133(1), 43 (1986).

5) M. Kendig and H. Leidheiser, JECS 123, 123 (1976).

6) L. Beaunier, I. Epelboin, J.C. Lestrade and H. Takenouti, Surf. Tech. 4, 237 (1976).

7) J.R. Scully, JECS 136(4), 979 (1989).

8) ASTM D 4518-85, "Measurement of Static Friction of Coating Surfaces," American Society of Testing Materials, Philadelphia, PA.

Table 1. Test Specimens.

Specimen ID #	Substrate	Coating System	Coating Thickness (μm)
T1	Steel	6108	12
T2	Steel	6256	<1
T3	Aluminum	STF	34
T4	Steel	6255	10
T5	Stainless	6255	13
T6	Aluminum	6255	45
T7	Stainless	6108	3
T8	Stainless	6256	<1

Table 2. Summary of EIS Data for Coated HY-80 Steel.

Specimen #	Time, d	$R_{po} \Omega \cdot \text{cm}^2$	$C_c \text{ nF/cm}^2$	$R_{ct} \Omega \cdot \text{cm}^2$
T1	0	6.6×10^5	1.1	3.1×10^7
	54	5.3×10^5	3.0	2.9×10^7
	245	7.5×10^4	2.0	2.0×10^7
T4	0	1.0×10^7	0.4	1.9×10^8
	20	3.8×10^5	4.4	7.4×10^5
	41	3.9×10^5	4.6	1.6×10^6
	250	2.5×10^5	5.0	3.5×10^6
T2	0	2.5×10^4	132	5.9×10^5
	35	1.8×10^4	450	1.3×10^5
	116	1.4×10^4	350	6.9×10^4
	245	5.7×10^3	200	1.4×10^5

Table 3. Summary of EIS Data for Coated AISI 304 Stainless Steel.

Specimen #	Time, d	$R_{po} \Omega \cdot \text{cm}^2$	$C_c \text{ nF/cm}^2$	$R_{ct} \Omega \cdot \text{cm}^2$
T7	0	9.9×10^6	2.4	3.1×10^9
	53	7.9×10^6	7.1	6.9×10^7
	245	3.5×10^6	22.0	6.7×10^7
T8	0	3.2×10^5	137	-
	11	2.7×10^5	296	2.5×10^7
	50	6.2×10^5	887	8.8×10^6
T5	0	1.2×10^6	0.95	7.4×10^9
	55	1.9×10^6	2.0	1.3×10^9
	246	1.2×10^5	1.1	1.5×10^8

Table 4. Summary of EIS Data for Coated AA6061-T6.

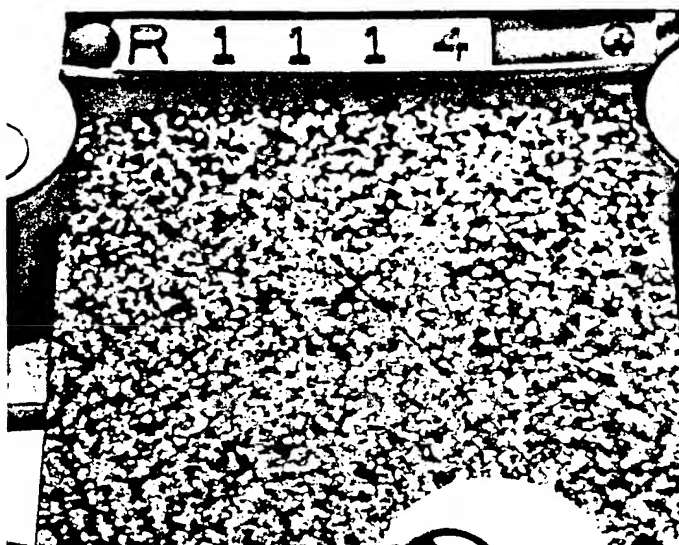
Specimen #	Time, d	$R_{po} \Omega \cdot \text{cm}^2$	$C_c \text{ nF/cm}^2$	$R_{ct} \Omega \cdot \text{cm}^2$
T3	0	1.2×10^7	0.7	1.2×10^8
	14	4.5×10^5	16.0	6.7×10^7
	36	3.1×10^5	5.6	1.5×10^8
	57	1.8×10^5	2.2	9.7×10^7
	116	1.1×10^5	1.2	9.3×10^7
	245	1.2×10^5	2.3	1.7×10^7
T6	0	8.4×10^{10}	0.2	-
	12	3.6×10^5	1.7	1.5×10^7
	55	1.6×10^8	0.7	6.9×10^8
	246	7.2×10^7	0.5	3.3×10^8

Table 5. Summary of Static Friction Test.

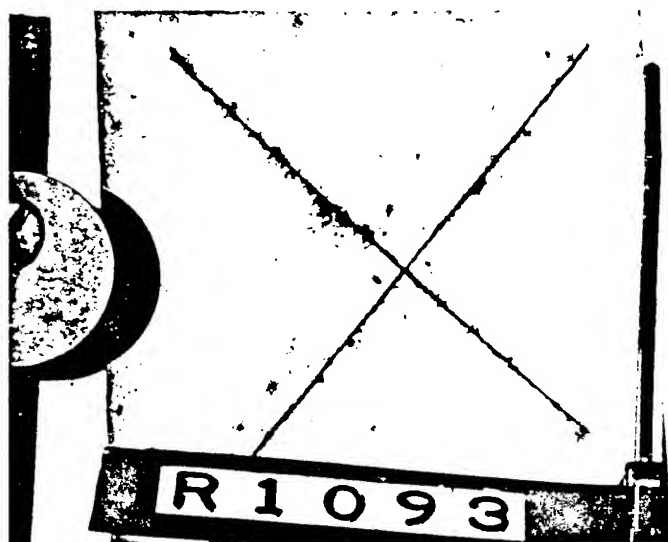
Specimen #	Static Friction	
	$\tan \theta$ (0 d)	$\tan \theta$ (310 d)
T1	.194	.271
T2	.435	.344 ⁽¹⁾
T4	.299	.445 ⁽²⁾
T5	.315	.277
T7	.325	.225
T8	.325	.217
T3	.197	.249
T6	.344	.296

⁽¹⁾ Localized rust spots present.

⁽²⁾ Large number of small diameter blisters present.

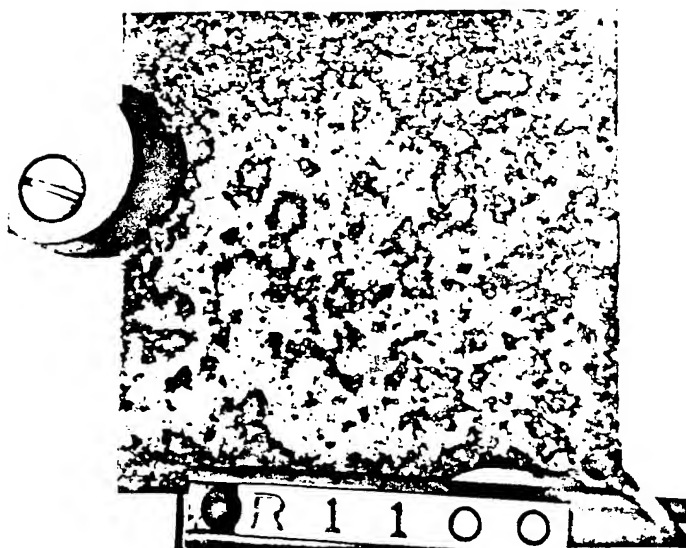


(a)



(b)

Fig. 1. Photographs of HY-80 Panels Coated with (a) 6255 and (b) 6256 after Two Years Exposure to a Marine Atmosphere.

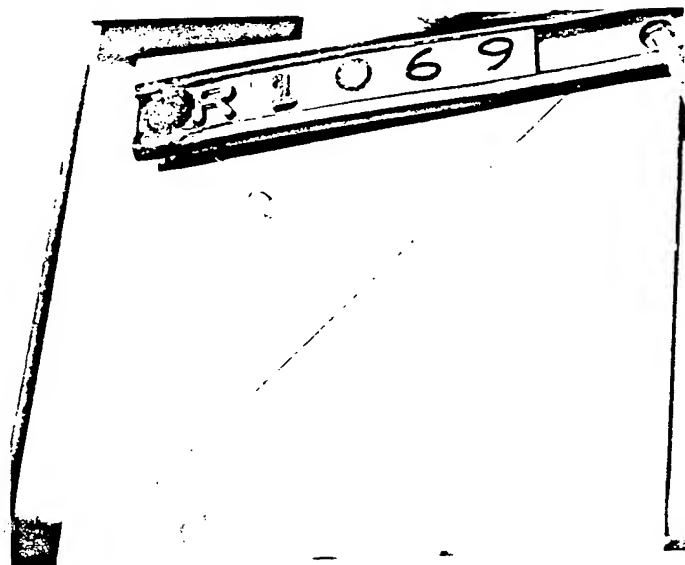


(a)



(b)

Fig. 2. Photographs of AISI 304 Panels Coated with (a) 6255 after Two Years Exposure to a Marine Atmosphere and (b) 6108 after Two Years in Marine Atmosphere with Periodic Seawater Wetdown.



(a)



(b)

Fig. 3. Photographs of AA6061-T6 Panels Coated with (a) 6255 and (b) STF after Two Years in a Marine Atmosphere with Periodic Seawater Wetdown.

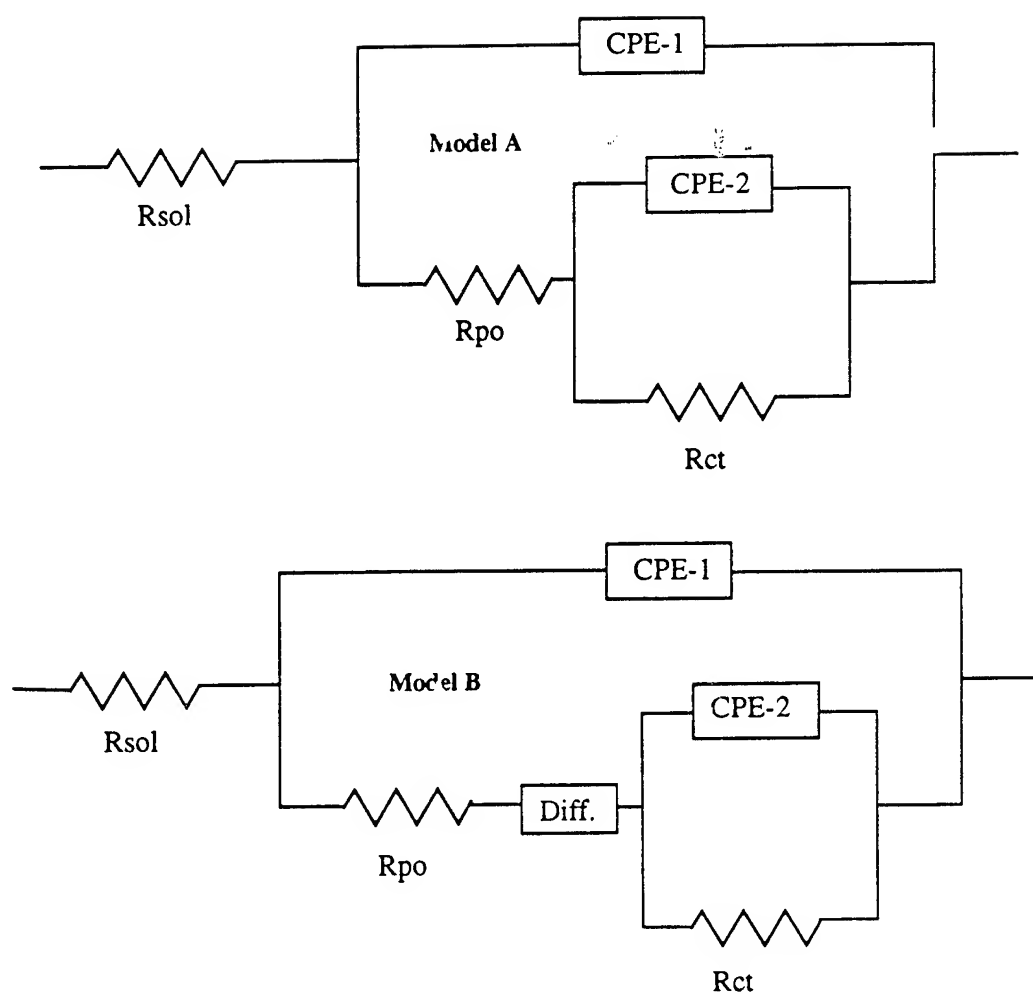


Fig. 4. Equivalent Circuit Models for (a) Coated HY-80 Steel and (b) Coated AA606-T6 and AISI 304. R_{sol} is the Solution Resistance, R_{po} the Coating Pore Resistance, $CPE-1$ a Constant Phase Element that Represents the Coating Capacitance, R_{ct} the Charge Transfer Resistance at the Coating/Metal Interface $CPE-2$ a Constant Phase Element that Represents the Capacitance at the Coating/Metal Interface and $Diff.$ is a Diffusion Element ($CPE-3$).

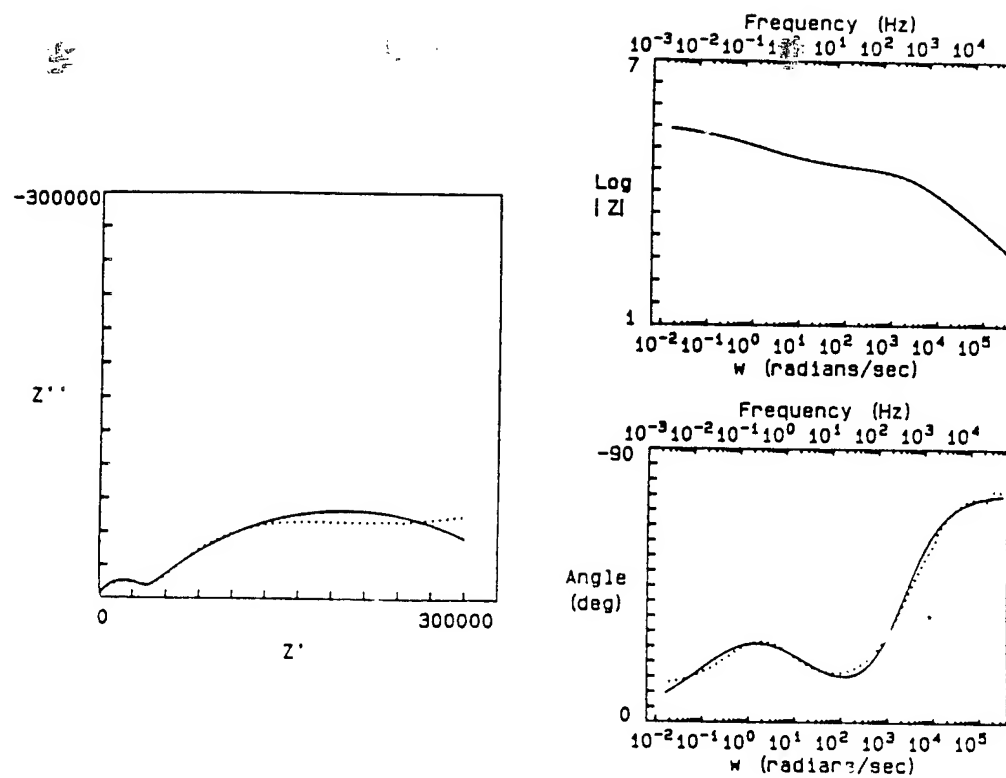


Fig. 5. Impedance plots for 6108 coated HY-80 steel immersed in aerated seawater for 120 days. Dotted lines represent experimental data and solid lines the CNLS fit (Model A).

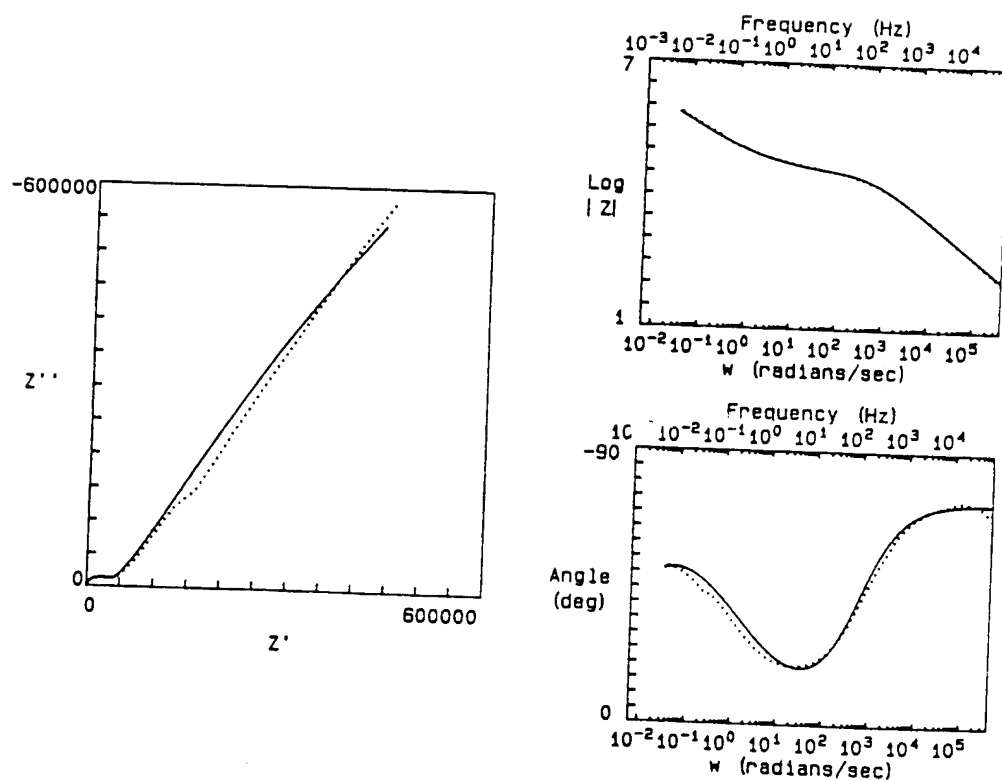


Fig. 6. Impedance plots for 6108 coated AISI 304 stainless steel immersed in aerated seawater for 53 days. Dotted lines represent experimental data and solid lines the CNLS fit (Model B).

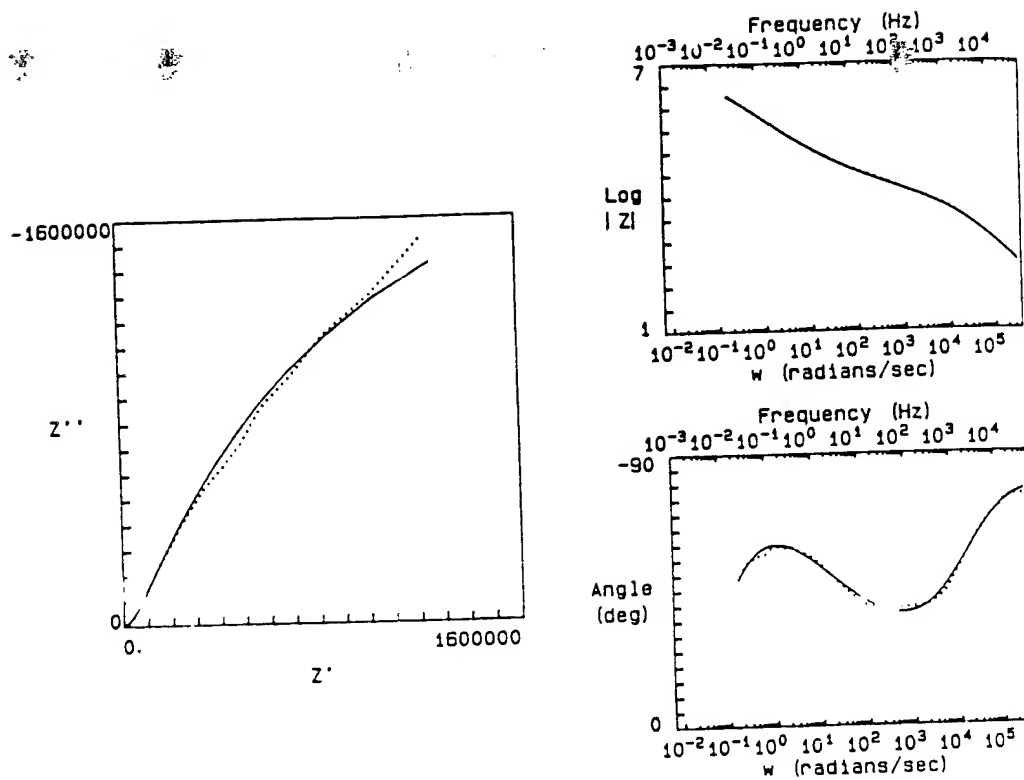


Fig. 7. Impedance plots for STF coated AA6061-T6 immersed in aerated seawater for 116 days. Dotted lines represent experimental data and solid lines the CNLS fit (Model B).

WARM WEATHER SURFACE TOLERANT COATINGS

STEPHEN C. HOBAICA

NSWC, CODE 41, ANNAPOLIS, MD. 21402

FEBRUARY 1993

OBJECTIVE

TO INVESTIGATE COATINGS FOR NAVY USE IN SEAWATER BALLAST TANKS THAT ARE:

SURFACE TOLERANT

CAN BE APPLIED IN WARM WEATHER (50°F OR GREATER)

SAFE TO USE

MEET CURRENT AND PREDICTED FUTURE ENVIRONMENTAL REGULATIONS

BACKGROUND

THESE TOUCHUP COATINGS ARE NEEDED SINCE COMPLETE GRITBLASTING AND REPAINTING OF BALLAST TANKS WILL OCCUR WITH LESS FREQUENCY IN THE FUTURE DUE TO THE EXPENSE AND ENVIRONMENTAL PROBLEMS.

FINAL PRODUCT

FINAL PRODUCT WILL BE A MODIFICATION TO MIL-SPEC-23236B FOR TOUCHUP PAINTS DETAILING PRODUCT QUALIFICATION TEST PROCEDURE AND RECOMMENDED PAINTS FOR SURFACE TOLERANT APPLICATIONS.

APPROACH

SURVEY THE COMMERCIAL INDUSTRY FOR SURFACE TOLERANT COATINGS THAT PERFORM WELL AND DEVELOP SHORT TERM TESTING PROTOCOL FOR PREDICTING FIELD PERFORMANCE.

TEST PAINT CRITERIA

1. SURFACE TOLERANT OVER TIGHT CLEAN RUST
2. VOC LESS THAN 340 GR./LITER
3. CLOSE CUP FLASH POINT GREATER THAN OR EQUAL TO 100°F
4. EASY TO APPLY
5. AVOID CARCINOGENS, TOXIC MATERIALS, AND MINIMIZE SOLVENTS AND OTHER HAZARDOUS MATERIALS

LABORATORY AND MARINE SITE TESTING

32 PAINTS ARE CURRENTLY TESTED OVER HALF RUSTED AND HALF PAINTED PANELS AND TOTALLY RUSTED PANELS.

- A. SOLVENT BASED EPOXY
- B. 100% SOLIDS EPOXY
- C. WATER BASED EPOXY
- D. LATEX
- E. ACRYLIC EMULSION
- F. PRETREATMENTS

APPLICATION OF TEST PAINTS TO PANELS

- A. EACH TEST PAINT APPLIED TO 14 PANELS.
- B. PANELS GRIT BLASTED TO A NEAR WHITE METAL FINISH (2-3 MILS PROFILE).
- C. 6 PANELS ARE HALF PAINTED WITH MIL-P-24441 PAINT (NAVY FORMULA 150, 152 AND 151, TYPE 1).
- D. PAINT GIVEN 10 DAYS TO CURE.
- E. ALL PANELS ARE HUNG ON A FENCE BY THE CHESAPEAKE BAY TO CORRODE.
- F. AFTER CORRODING ABOUT 1 YEAR, THE PANELS ARE WIRE BRUSHED TO GIVE A TIGHT RUST. THE PAINT IS ALSO WIRE BRUSHED TO ROUGHEN THE SURFACE.
- G. TEST PAINT APPLIED TO ALL PANELS AT ONCE ACCORDING TO MANUFACTURES INSTRUCTIONS.
- H. THE CONTROL FOR EACH SET OF PAINTS BEING TESTED IS MIL-P-24441, TYPE 1 (NAVY FORMULA 150, 152 AND 151).

TEST PROCEDURES

- A. SAL^T SPRAY (ASTM B 117) FOR 3240 HOURS
- B. DEIONIZED 180^OF HOT WATER IMMERSION BLISTER RESISTANCE TEST FOR 10 DAYS
- C. MARINE TEST SITE LONG TERM IMMERSION TEST
- D. FIELD TEST BEST PERFORMING TOUCHUP PAINTS ON NAVY SHIPS

MARINE TEST SITE

1. FOUR CONDITIONS ARE TESTED.
 - A. GALVANICALLY ISOLATED; UNSCRIBED (2 ALL RUSTED PANELS)
 - B. CONNECTED TO A ZINC ANODE; UNSCRIBED (2 ALL RUSTED PANELS)
 - C. CONNECTED TO A ZINC ANODE; SCRIBED (2 HALF PAINTED AND HALF RUSTED PANELS)
 - D. CONNECTED TO A ZINC ANODE; UNSCRIBED (2 HALF PAINTED AND HALF RUSTED PANELS)
2. PANELS IMMERSSED IN SEAWATER FOR 3 MONTHS IN A DARK TANK. SEAWATER FILTERED TO PREVENT HARD FOULING, ONLY SLIME IS PERMITTED.
3. PANELS ARE AIR DRIED FOR 2 WEEKS IN A HUMID TANK.
4. CYCLE REPEATED UNTIL PANEL FAILS OR SIX CYCLES.
5. TO ENSURE BETTER REPEATABILITY IN FUTURE TESTING THREE PANELS INSTEAD OF TWO SHOULD BE TESTED.

RESULTS

RESULTS FOR BEST PERFORMING PAINTS ARE GIVEN AND COMPARED TO THE CONTROL (TYPE 1; F-150, 152 AND 151 POLYAMIDE EPOXY). THE FOLLOWING RESULTS WERE OBTAINED FOR 23 PAINTS TESTED. THESE PAINTS CONSISTED OF:

- A. HIGH SOLIDS SOLVENT BASED EPOXY
- B. WATER BASED EPOXY
- C. PRETREATMENTS
- D. 100% SOLIDS EPOXY PAINT

BEST OVERALL PERFORMING PAINT AT THE MARINE TEST SITE WAS A HIGH SOLIDS SOLVENT BASED EPOXY.

RATING PANELS

1. PANELS ARE RATED FOR THE FOLLOWING:

- A. % CORROSION USING EXTENT DIAGRAM.
- B. BLISTERING USING ASTM D 714.
- C. UNDERCUTTING OF THE SCRIBE.
- D. DETERMINATION USING EXTENT DIAGRAMS.

2. PANELS WITH EXCESS CORROSION (5% OR GREATER) OR EXCESS BLISTERING (MEDIUM DENSE OR GREATER) FAIL AND ARE REMOVED FROM THE TEST.

ACCELERATED BLISTER RESISTANCE TEST

TEST PROCEDURE: 180°F, DEIONIZED WATER, 10 DAYS DURATION; OVER RUSTED PANEL

RESULTS

- A. CONTROL: 3.5 *
TYPE 1 F-150, 152, 151 POLYAMIDE EPOXY
- B. BEST PERFORMING PAINT IN THIS TEST: 5.5
ONE COMPONENT ALUMINUM PIGMENTED SOLVENT PAINT
- C. HOW DID A GOOD HIGH SOLIDS SOLVENT BASED EPOXY PAINT PERFORM IN THIS TEST? 4.7

- * RATINGS FROM BLISTER POPULATION AND SIZE
 - 10 BEST WITH NO BLISTERS
 - 0 WORST WITH TOTAL AREA BLISTERED

SALT SPRAY RESULTS

TWO ALL RUSTED AND TWO HALF PAINTED HALF RUSTED PANELS WERE TESTED FOR EACH PAINT SYSTEM. PANEL SIZE WAS 4" X 6".

- A. BEST PERFORMING PAINTS IN THIS TEST WERE: 100% SOLIDS EPOXY, HIGH SOLIDS EPOXY, MIL-P-24441, TYPE 1 (CONTROL)

HALF PAINTED - HALF RUSTED PANELS

TOP HALF: 0% CORROSION AND 0% BLISTERS
BOTTOM HALF: 0% CORROSION AND 0% BLISTER
SCRIBE: NO UNDERCUTTING

ALL RUSTED PANELS:

0% CORROSION AND 0% BLISTERING.
SCRIBE: NO UNDERCUTTING.

- B. HOW DID A GOOD HIGH SOLIDS SOLVENT BASED EPOXY PERFORM IN THIS TEST?

HALF PAINTED - HALF RUSTED PANELS

TOP HALF: 0% CORROSION AND 0 BLISTERS
BOTTOM HALF: 0% CORROSION AND 4 MD BLISTER
SCRIBE: NO UNDERCUTTING

ALL RUSTED PANELS:

0.01% CORROSION AND 6 M BLISTERING.
SCRIBE: NO UNDERCUTTING.

MARINE TEST SITE

AFTER 21 MONTHS EXPOSURE AT THE MARINE TEST SITE, THE FOLLOWING RESULTS WERE OBTAINED AND ARE BEING PROPOSED FOR THE MODIFICATION TO MIL-SPEC-23236B. 21 MONTHS WAS FOUND TO BE SUFFICIENT TO SCREEN COATINGS AND ACHIEVE A CORRELATION WITH SHIPBOARD RESULTS.

MINIMUM PERFORMANCE SPECIFICATION FOR WARM WEATHER TOUCHUP PAINTS
AFTER SIX CYCLES

Immersion Resistance Results. +

	%Corrosion		Blistering		Undercutting	
1. Attached to Zinc Anode, All Rusted, Unscribed	0.1%		2-8 MD		None	
2. Electrically Isolated All rusted, Unscribed	0.3%		2-8 M**		None	
	Top	Bottom	Top	Bottom	Top	Bottom
3. Attached to Zinc Anode, Unscribed Half Rusted	0.1%	0.1%	2-8 MD	2-8 M**	None	None
4. Attached to Zinc Anode, Scribed Half Rusted"	0.1%	0.1%	2-8 MD	2-8 MD	1.5"	1.5"

+ For at least 2 of 3 panels, ignore effects within one inch of any edge

** 8 MD Blisters allowed

OVERALL RESULTS

1. THE NAVY HAS INVESTIGATED SURFACE TOLERANT COATINGS USING THREE SHORT TERM TESTS AND FIELD TESTS ON NAVY SHIPS.
2. FOR THE MARINE TEST THE BEST PERFORMING COATINGS BECOME APPARENT IN 21 MONTHS.
3. A TESTING PROTOCOL FOR SURFACE TOLERANT PAINTS HAS BEEN DEVELOPED. THE RESULTS FROM THE FIELD TEST CORRELATE WELL WITH THE MARINE TEST.

BLANK

590

Non Chromated Epoxy Primer for Aerospace Applications

*Mr. Dennis Vorse, Chemist
Mr. Joseph Gausman, Chemist
Lord Corporation
2000 West Grandview Blvd.
Erie, Pennsylvania 16514-0038

Abstract

Aeroglaze® 9740 is a low volatile organic content, chromate free, two-component, solvent based epoxy primer. Its primary use is for aluminum surfaces with a proper surface treatment.

Aeroglaze 9740 contains no photochemically reactive solvents nor any known or suspected carcinogens. Aeroglaze 9740 Part A is made up of a difunctional bisphenol A resin, calcium metasilicate pigment, monoazo pigment, dispersant, suspension additive and solvent. Aeroglaze 9740 Part B consists of a polyamidoamine, amine and solvent.

Aeroglaze 9740 Non-Chromated Epoxy Primer can be applied by brush and roller. It can also be applied by Electrostatic, High Volume Low Pressure (H.V.L.P.) and conventional spray equipment. Aeroglaze 9740 adheres to a broad range of substrates and treatments which will be addressed in the body of the paper.

Introduction

Aeroglaze 9740 can be applied via siphon, high volume low pressure and electrostatic spray. It also can be successfully topcoated with a Mil-C-83286, Mil-C-85285, or any of the various Aeroglaze urethane topcoats.

When Aeroglaze 9740 Part A and Part B are mixed 3 to 1 by volume or 100.00 to 22.35 by weight and allowed to induct for 30 minutes, it will produce a coating that exhibits the characteristics found on Data Table 1.

[REDACTED]

Aeroglaze 9740 was tested over ¹Parker Amchem Alodine® 1200, ²San Chem® full process, ³Allied-Kelite Chemidize® 727A and Lord Sol-Gel process. The Parker Amchem Alodine® 1200 treatment is a chromate containing system. The San Chem® full process, Allied-Kelite Chemidize® 727A and Lord Sol-Gel process are all chromate-free treatments. These treatments were done on 2024T3 Alclad aluminum. A .9 mil dry film thickness of Aeroglaze 9740 was sprayed on panels over each treatment. Three panels for each treatment were primed and topcoated with 2 dry mils of Mil-C-85285 Gloss White and 3 primed panels for each treatment remained untopcoated.

The previously mentioned panels and treatments were then scribed using a pointed punch at approximately a 1/32" wide scribe line making sure that the Alclad layer was penetrated. After being scribed, the panel edges were waxed and placed in the salt fog running the test as outlined in ASTM B117.

Failure in the salt fog was characterized by any blistering or corrosion 1/8" beyond the scribe line or panel edge.

In addition to the salt fog test, several others were performed:

- 7-day distilled water immersion at ambient conditions, after immersion adhesion test to ASTM D3359
- Dry adhesion to ASTM D3359
- Gloss of Mil-C-85285 over Aeroglaze 9740 on each individual surface treatment.

The results can be found on Data Table 2.

As shown by the results, Aeroglaze 9740 performs without failure after water immersion adhesion testing and dry adhesion. The coatings have excellent gloss over each surface individual treatment. Salt fog resistance over each individual treatment varies but clearly Aeroglaze 9740 performs well over the San Chem® full process, Parker Amchem Alodine® 1200, Lord Sol-Gel process and Allied-Kelite Chemidize® 727A, in that order.

In addition to the screening tests over a variety of different surface treatments, Aeroglaze 9740 was evaluated against Mil-P-23377F Type I Class II specification. A summary of these results can be found in Data

Table 3, which shows that Aeroglaze 9740 meets or exceeds all physical test requirements of Mil-P-23377F Type 1 Class II specifications.

Other substrates that Aeroglaze 9740 adheres to are chromic and sulfuric acid anodized aluminum, sanded fiberglass laminates, sanded epoxy graphite composite, galvanized steel and sand blasted steel.

Some additional evaluations have been performed over sand blasted steel. The steel panels were blasted to a 2 mil profile and MEK solvent rinsed. Aeroglaze 9740 was spray applied at a dry film thickness of 1 mil and 2 mils. Three panels were Mil-C-85285 topcoated at 2 dry mils and three panels remained primed only for each individual primer thickness. Using a pointed punch approximately a 1/32" wide line scribe was made. After being scribed, the panel edges were sealed with wax and subjected to salt fog as outlined in ASTM B117. Results of the testing are summarized in Data Table 4.

This shows that Aeroglaze 9740 performs best at higher primer film thicknesses on blasted steel surfaces topcoated or untopcoated.

Conclusion

Aeroglaze 9740 has a broad range of compatibility with different substrates, treatments and topcoats.

<u>Substrates</u>	<u>Treatments</u>	<u>Topcoats</u>
<ul style="list-style-type: none">• Aluminum• Steel• Composite• Fiberglass	<ul style="list-style-type: none">• Chromate conversion• Non-chromate conversion• Anodized• Zinc phosphate• Galvanized	<ul style="list-style-type: none">• Mil-C-83286• Mil-C-85285• Aeroglaze moisture cure urethanes• Aeroglaze two-component urethanes

In addition, Aeroglaze 9740 can be easily applied by brush, roll electrostatic, conventional and H.V.L.P. spray.

This can benefit the manufacturers and repair facilities of aircraft, space structures, satellites, ground vehicles and ground support equipment.

Data Table 1
Aeroglaze 9740
Typical Mixed Properties

Volatile organic content mixed		312 g/liter 2.6 lbs./gal.
Color mixed ready to apply		Bright yellow
Solids content ASTM D2569-87		
	% by weight	75
	% by volume	64
Initial viscosity ASTM D1200, #4 Ford cup at 77°F (25°C)		
	Seconds	30
4 hour viscosity ASTM D1200, #4 Ford cup at 77°F (25°C)		
	Seconds	60
8 hour appearance		Highly viscous liquid
24 hour appearance		Gelled solid
Theoretical coverage ft ² /gallon/mil		1,030
Dry to recoat at 77°F and 50% R.H.		5 hours minimum 18 hours maximum
Coating film dry weight theoretical		
	Lbs./ ft ² /mil	.0077
	Gm/ ft ² /mil	3.49
Paint Resistance, ⁴ Ransburg® meter		.2 megohms

Data Table 2

Aeroglaze 9740
Salt Fog Results

	<u>Primed</u>	<u>Primed/Topcoated</u>
Parker Amchem, Alodine® 1200	2,000 hours	1,500 hours
Sanchem, Full Process	Ongoing	3,000 hours
Allied-Kelite, Chemidize® 727A	500 hours	500 hours
Lord, Sol-Gel Process	1,000 hours	1,250 hours

Distilled Water Immersion

	<u>Primed</u>	<u>Primed/Topcoated</u>
Parker Amchem, Alodine® 1200	*Pass	*Pass
Sanchem, Full Process	*Pass	*Pass
Allied-Kelite, Chemidize® 727A	*Pass	*Pass
Lord, Sol-Gel Process	*Pass	*Pass

Dry Adhesion

	<u>Primed</u>	<u>Primed/Topcoated</u>
Parker Amchem, Alodine® 1200	*Pass	*Pass
Sanchem, Full Process	*Pass	*Pass
Allied-Kelite, Chemidize® 727A	*Pass	*Pass
Lord, Sol-Gel Process	*Pass	*Pass

Gloss

	<u>Primed/Topcoated</u>
Parker Amchem, Alodine® 1200	60°/94
Sanchem, Full Process	60°/93
Allied-Kelite, Chemidize® 727A	60°/93
Lord, Sol-Gel Process	60°/92

*Pass constitutes no adhesion loss when tested to ASTM D3359 or in the case of water immersion, no blistering or discoloration besides no adhesion loss.

Data Table 3

Aeroglaze 9740 Non-Chromated Epoxy Primer

Tested to Mil-P-23377F Specification Type I Class II

Primer Aeroglaze 9740 .9 dry mils

Topcoat Mil-C-85285 Gloss White 2.0 dry mils

	<u>Test</u>	<u>Result</u>
3.6.1.	Color	Bright Yellow
3.6.2.	Odor	Pass
3.6.3.	Viscosity, mixed	Pass 31 seconds
3.6.4.	Pot life, 4 hours	Pass 61 seconds
3.6.6.	Storage stability, one year	In progress
3.6.7.	Accelerated stability	Pass
3.7.1.	Surface appearance	Pass
3.7.2.	Dry time	Pass
3.7.3.	Lifting	Pass
3.7.5.	Adhesion	Pass
3.7.6.	Flexibility	Pass 10%
3.7.7.	Strippability	Pass
3.7.8.	Infrared reflectance	N/A
3.8.1.	Water resistance	Pass
3.8.2.1.	Salt spray	Pass
3.8.2.2.	Filiform	Pass
3.8.3.	Solvent resistance	Pass
3.8.4.	Fluid resistance	Pass
3.9.1.	Mixing	Pass
3.9.3.	Application	Pass

Data Table 4

Hours of Successful Completion

• 1 dry mil of Aeroglaze 9740	500
• 1 dry mil of Aeroglaze 9740 2 dry mils of Mil-C-85285 topcoat	500
• 2 dry mils of Aeroglaze 9740	1,000
• 2 dry mils of Aeroglaze 9740 2 dry mils of Mil-C-85285 topcoat	1,000

References:

1. Parker Amchem, a division of Henkel Corporation, 32100 Stephenson Highway, Madison Heights, Michigan 48071.
Phone: 313-583-9300
2. Sanchem, Inc., 1800 South Canal Street, Chicago, Illinois 60616
Phone: 312-733-6100
3. Allied-Kelite, a Witco Company, 2701 Lake Street, Melrose Park, Illinois 60160
Phone: 800-323-9784
4. DeVilbiss-Ransburg, P.O. Box 913T, Toledo, Ohio 43697-0913
Phone: 419-470-2000

BLANK

598

SESSION VII
CORROSION CONTROL AND
PREVENTION

Chairman: *V. Agarawala*

BLANK

600

Effects of Alloy Chemistry Changes
on Sacrificial Aluminum Anode Performance

Dr. John N. Murray*, Mr. Richard A. Hays
and Mr. Douglas W. Smith
Carderock Division, Naval Surface Warfare Center, (CDNSWC)
Marine Corrosion Branch, Code 613
3A Leggett Circle
Annapolis, MD 21402

ABSTRACT

The set of aluminum alloy sacrificial anodes taken from the upper starboard stern array from a Navy submarine was evaluated at CDNSWC to determine the cause of non-uniform utilization during the approximately 30 month anode service period. Physical data from the used anodes as well as electrochemical characterizations were determined. The evidence indicated that the three distinct levels of anode weight change (and estimated discharge current) could be attributed to distinct levels of mercury contamination in the three heats of alloy from which these particular anodes were taken. The experience shows that reasonable vendor care in alloy preparation and anode casting must be taken for uniform anode performance to be achieved in multi-anode array applications.

INTRODUCTION

A US Navy submarine was outfitted with a ship set of Galvalum III, indium activated, aluminum alloy sacrificial anodes during the February 1990 post shakedown availability. The anodes had been procured by the Electric Boat (EB) Division of General Dynamics using an EB purchase specification. The EB purchase specification was modeled on a CDNSWC draft version of a military specification (Draft MIL-SPEC), "Anodes, sacrificial, aluminum alloy". Anodes from essentially all heats of the procurement were selected by the EB inspectors, shipped to CDNSWC and subjected to the QA/QC procedures by CDNSWC as outlined in the EB purchase specification. In general, the electrochemical performance of the anode heats was found to be acceptable. However, Heat 3069 was

The anode installations and various outfitted tanks and spaces were reinspected in early October 1992. In general, the anode consumption rates were found to be as expected for the approximately 30 months of service exposure. The tanks and voids were also found to be protected with little paint deterioration or metal corrosion which might be attributed to improper anode installation or inadequate anode performance. However, there was a rather marked non-uniform anode consumption which was observed on each of the four stern array anode strings. A typical view of the first 11 of the 21 AHC-10 anodes from the upper starboard array is shown as Figure 1. Counting from forward to aft, anodes 2, 3, 7 and 11 appeared to be essentially unused. On-site visual estimates of 40-60% alloy consumption of the majority of the anodes were made. Simple on-site checks of the mounting-bolt-to-alloy-body electrical continuity showed all anodes of the upper string were electrically connected to the hull. Although there were only 17 of 84 anodes on the stern which had this "unused" appearance, the behavior was of sufficient concern to warrant a low level investigation as to cause. It should be noted that the 67 "good" anodes would be sufficient for cathodic protection of the stern. One possible assumption of cause of anode non-use was that these 17 anodes were "dead", that is, the surface oxide coating which had formed during the 6 months following fabrication and before wetting in the estuary waters was sufficiently tenacious that the pieces were completely passivated, i.e., inactive.

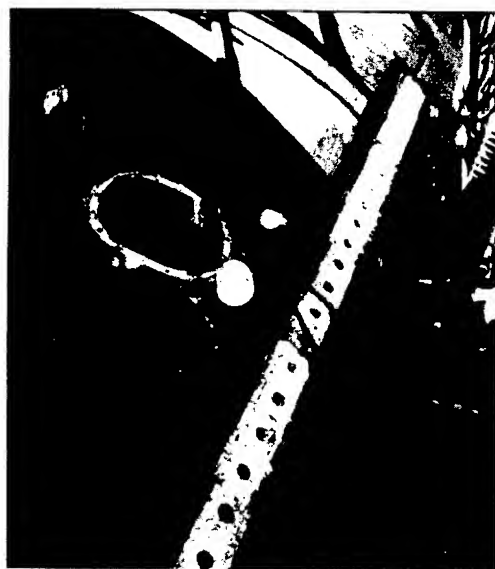


Figure 1. Upper stern aluminum alloy array, 688 Class, 30 months service.

If one makes that assumption, then removing and evaluating the anodes from the array after they became exposed in the dry dock environment carries the risk of different reactivations in the subsequent laboratory test environment. This might suggest the laboratory test results would not relate to the anode status just prior to drydocking. In addition, the submarine sat pierside for an undisclosed period prior to drydocking, during which time metal ion impurities (such as copper from the anti-fouling coating system) could have electrodeposited on the sacrificial anode surfaces affecting the general electrochemical performance characteristics. With at least these two caveats, as the stern arrays were to be replaced with new aluminum anodes, a decision was made to mark and return the upper stern array to CDNSWC for further analysis. The initial effort was to be limited to weighing the anodes and simple electrochemical testing.

Therefore, the overall objective of this effort was to attempt to determine if the cause of non-uniform anode consumption could be identified. This paper summarizes the effort and findings of the study.

EXPERIMENTAL

The anodes were purchased by EB in accordance with the EB material specification. Material chemistry and electrochemical performance data of samples taken from unused anodes from all of the heats were determined previously and selected values are included later in the Results and Discussion section.

The tagged, 6 x 12 x 1.25", AHC-10 anodes from the upper starboard stern array were received at CDNSWC, weighed in the as-received condition, nylon brush cleaned under flowing water, dried overnight at ambient conditions and reweighed. The heat numbers of many of the anodes were still legible on the "backside" of the anodes and these were noted. Physical dimensions of each anode were also recorded.

Two types of electrochemical tests were performed. The full sized, cleaned anodes were positioned vertically in a 12" x 12" x 12" polyethylene tank. A carbon steel plate counterelectrode was positioned approximately 7 inches from and parallel with the test anode. The electrochemical reactivating characteristics were determined by monitoring the anode potential for roughly a one day period while discharging the test anode at a constant current of 288 mA. This current was selected as approximating the discharge current density of 4 mA/in² used in the previous smaller sample QA/QC test effort. The 288 mA current assumes only the alloy surface facing the counterelectrode contributed appreciably to the discharge process.

All testing was performed at laboratory ambient temperature (20-23°C, 68-75°F) using aerated ASTM-D-1141, substitute ocean water. The electrolyte bath was not changed until after testing three anodes, as the small amount of accumulated anode reaction products was judged not to be affecting the electrochemical performance.

Three anodes, selected as typical for each observed type of repassivation behavior, were tested further. Two preselected pairs from these three anodes were subjected to an overnight galvanic couple experiment, followed by full potentiodynamic scans in the range of - 1200 to - 700 mV. vs. saturated calomel reference electrode (SCE). Several additional runs were made with new zinc and new Galvalum III anodes as well as used zinc and estuary-exposed Galvalum III pieces. After the test electrolyte was contaminated with zinc anode reaction products, another zinc anode was tested or the test cell was replenished with fresh test solution.

RESULTS AND DISCUSSION

The weights of the cleaned anodes are summarized in Table 1 by tag number which should correspond to the linear position coming aft in the upper starboard stern array. The anode tag numbers of the four anodes which showed little consumption do not quite agree with the photographic data and notes from the inspection but the tag numbers will be utilized throughout the rest of this report. Subtracting the used anode weight from the 3951 gram alloy average initial weight as well as the 272 gram steel strap weight determined previously for the AHC-10 anodes (and correcting for the machined leading and lagging taper of the two end anodes), results in the approximate weight change values shown in Table 1 for the anodes during the approximately 30 month exposure. The weight change values were converted to averaged anode currents utilizing 90% averaged Faradaic efficiencies determined previously. The calculated current data are then summarized as Figure 2. A column of percentage used (or percentage consumed) is included in Table 1. As the actual values of the "active" anodes ranged from 15 to 35%, the availability of a set of comparative visual standards would probably have resulted in better estimates than the 40-60% range made during the drydock inspection.

Table 1
Anode Weights Calculated Weight Changes and Anode Currents

Anode Number	Cleaned Weight (g)	Calculated Weight loss (g)	Percent Used	Calculated (mA) Anode Current	Heat Number
1	3061.1	1095	28	134	*3160
2	2924.9	1298	32	159	3070
3	4042.0	181	5	22	3069
4	4122.0	101	3	12	- -69
5	2811.5	1418	36	174	3130
6	3145.9	1077	27	132	-130
7	2955.2	1267	32	155	3130
8	4225.4	0	0	0	3069
9	3290.8	932	24	114	3070
10	3126.9	1096	28	134	3130
11	4215.7	7	0	1	3069
12	3108.2	1093	28	134	3130
13	3251.9	971	25	118	3130
14	3469.6	753	19	92	3070
15	3414.6	808	20	99	-070
16	3212.1	1011	26	124	3130
17	3623.8	599	15	73	3070
18	3066.1	1157	29	142	3130
19	3519.6	703	18	86	3070
20	3019.5	1204	30	147	3130
21	2437.7	1719	44	211	3130

* = incorrect heat number

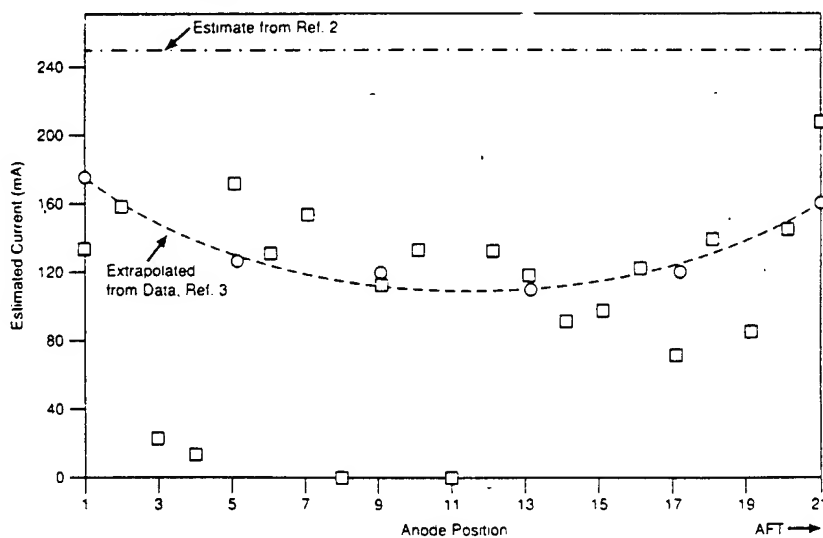


Figure 2. Calculated anode currents by anode position in stem array.

Two reference lines are included in Figure 2. The upper horizontal line represents the average anode current expected using the formula published by Waldon and Peterson². The lower curved line is an estimated current distribution derived from experimental data from a six anode array which showed the end anodes to contribute more current than the inner anodes in a linear array³. Although there is considerable scatter and associated risk in drawing conclusions with these estimated weight loss data, the calculated currents tend to indicate the first ten anodes in the array contributed somewhat more protection current than the anodes further aft excluding the last two anodes. The electrical and mechanical linkage of the propeller through the shaft to the hull does occur forward of the array and the potential drop through the hull may account for the apparent maldistribution. An equivalent argument could be made regarding the distribution of ionic currents which would allow the greater consumption at the aft end of the string. Unfortunately, the computer program BEASY cannot be used to model this problem as electrical current through the metallic elements is assumed to be uniform⁴.

The four under-utilized anodes at positions 3, 4, 8 and 11 obviously would not be explained by the current distribution considerations. However, as one

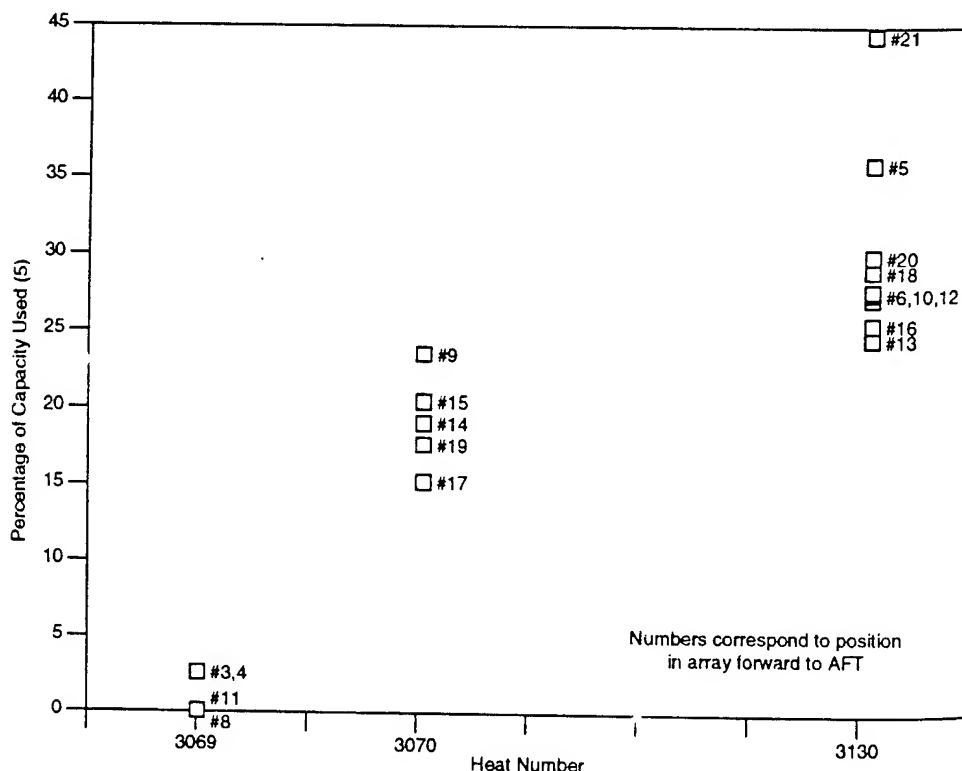


Figure 3. Percentage of alloy contained in 30 months vs. heat number.

might have observed in the Table 1 data, the four anodes in question were the only anodes associated with fabrication Heat 3069. Anode consumption is plotted against the heat number as Figure 3. Interestingly, the amounts of alloy consumed fell into three groups which then were associated with three particular heats.

The reactivation (constant current, voltage-time) data also tended to group within the same heat number pattern. Nearly all the 21 anodes allowed an initial on-current potential of -0.9 V vs SCE, inferior to the maximum required potential level of < -0.98 V vs. SCE. The Heat 3130 anode potentials started to decrease (become more negative) somewhat rapidly after about 3 hours exposure, still decreasing at a slower rate from the 20+ hour end-of-test exposure of approximately -1.01 V vs SCE. Heat 3069 anodes tended to stabilize at a potential of approximately -0.95 V vs SCE at 10 hours exposure whereas Heat 3070 anodes tended to stabilize at a higher potential of -0.92 V vs SCE. The general anode voltage behavior patterns are summarized in Figure 4. An examination of the short-term QA/QC electrochemical test data from these three heats also shows the same general trends but somewhat lower potentials which might be expected with fresh chemically cleaned metallic surfaces exposed only to laboratory air prior to electrochemical testing. The relevant electrochemical test data are presented in Table 2.

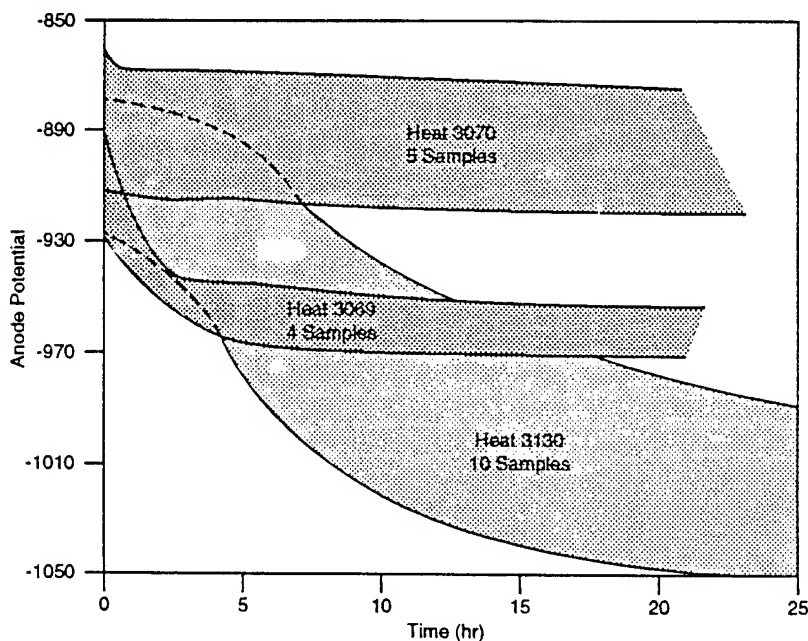


Figure 4. Summary of reactivation time characteristics, 288mA constant current, full size, used anodes.

Table 2
Anode Potential Data from QA/QC and Reactivation Tests

Heat Number	QA/QC Potentials			Reactivation Potentials		
	1 Hour	3 Hours	24 Hours	1 Hour	3 Hours	20 Hours
3069	-1.016	-1.017	-0.993	-0.930	-0.950	-0.955
3070	-0.971	-1.023	-1.070	-0.900	-0.905	-0.910
(av. 3)						
3130	-1.094	-1.101	-1.110	-0.910	-0.920	-1.005

In addition, the QA/QC test, Faradaic efficiency (η) of Heat 3069 was observed to be particularly high at 95 % (weight loss efficiency, wt η) and 97% (efficiency from evolved H_2 gas rate, $H_2 \eta$).

The QA/QC electrochemical test results were attributed to the presence of a high degree of mercury contamination which was introduced into the process in Heat 3069. The mercury contamination was diluted in Heat 3070 and subsequently found to be at very low levels by Heat 3104. The specific chemistry results for the relevant heats, the specification ranges and the averaged values for the purchase lot are represented as Table 3. As can be seen, the mercury contamination appears to be one factor of importance at these contamination levels. The mercury activated aluminum alloy composition, Galvalum I¹ corresponds to the chemistry found with this heat and previous testing had shown the mercury activated aluminum alloys were technically acceptable as sacrificial anodes.⁵ The Navy rejection of utilization of mercury activated aluminum alloy anodes was based on potential environmental (sea water) contamination considerations.

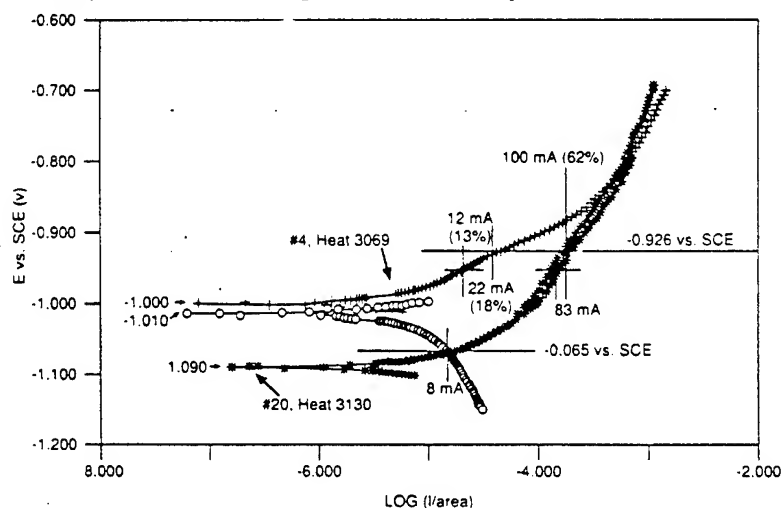


Figure 5. Polarization curves from Anode 20 (Heat 3130) and Anode 4 (Heat 3069) after overnight galvanic coupling.

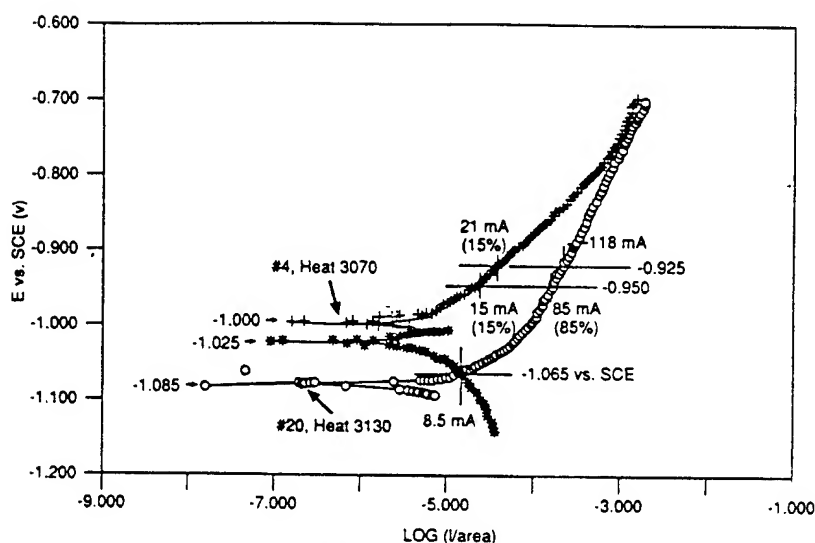


Figure 6. Polarization curves from Anode 20 (Heat 3130) and Anode 14 (Heat 3070) after overnight galvanic coupling.

Table 3
Chemistry Values for Relevant Heats

Element	Specification		Heat	Heat	Heat	Lot
	Min.	Max.	3069	3070	3130	Avg.
Zinc	2.5	6.0	4.5	4.0	4.0	4.2
Silicon	-	0.210	0.10	0.113	0.11	0.098
Indium	0.012	0.020	0.003	0.013	0.0125	0.0127
Iron	-	0.090	0.046	0.049	0.020	0.046
Copper	-	0.004	0.006	0.005	0.003	0.004
Mercury	-	0.020	0.027	0.0006	0.0001	<0.0001
Tin	-	0.020	<0.004	<0.004	<0.004	<0.004
Bismuth	-	0.020	0.0046	0.0032	0.0035	<0.0020
Cadmium	-	0.020	<0.001	<0.001	<0.001	<0.001
Titanium	-	0.020	<0.002	<0.002	0.004	<0.002
Magnesium	-	0.020	<0.001	<0.001	<0.001	<0.001
Lead	-	0.020	<0.002	<0.002	<0.002	<0.002
Boron	-	0.020	<0.001	<0.001	<0.001	<0.001

	<u>Zn</u>	<u>Si</u>	<u>In</u>	<u>Fe</u>	<u>Cu</u>
MIL-A-24779	4.0-6.5	0.08-0.2	0.014-0.020	≤0.19	≤0.004
Remainder	≤0.020 each, ≤0.10 Total.				
(Added in 1992)	Hg and Sn .0010 each.				

As might be expected, the galvanic coupling of a Heat 3130 anode with an anode from Heat 3069 or 3070 showed the Heat 3130 material to protect the inferior material cathodically at a low level of between 5 and 10 mA. Polarization curves obtained following the overnight galvanic couple runs are presented as Figure 5 (Heat 3130 sacrificial anode, Heat 3069 protected "cathode") and Figure 6 (Heat 3130 anode, Heat 3070 cathode).

Evans-type diagram is included in the figure and the anodic/cathodic intercept currents agree with the measured galvanic couple currents. Although these data show the different levels of mercury contamination can result in an anode which could be cathodically protected, in the real application, coupled with a moderate current source, the anodes would probably all be involved in the discharge process but at significantly different rates.

The anodic curves from each heat can be used to quantify the nonuniform consumption rates. Each anode maintains the same potential as determined by the overall protection system current demand. In Figure 5 as an example, if the overall requirements are such that Heat 3130 anode is at -0.925 V (vs SCE) consuming 100 mA current, the Heat 3069 anode also held to or polarized at -0.925 V would consume 22 mA current or 18% of the total. If the demand were slightly lower so that the potentials were -0.95 V, then the anode from Heat 3130 would consume 83 mA whereas the Heat 3069 anode would decrease to 12 mA (12% of total). As can be seen in the figures, if the current consumption were sufficiently high so as to polarize the anodes to approximately -0.82 V, the anodes would consume equal currents.

Previously, a question was raised as to the resulting performance from a mixed aluminum alloy anodes and zinc anodes in a given installation. Several experimental runs were made using either a previously used or a new zinc anode in combination with several of the used Galvalum III aluminum alloy anodes. The effort was intended to demonstrate the mixed potentials and the probable cathodic protection of the zinc by the aluminum alloy. One, frustrating and perhaps interesting, result reoccurred when the two anodes were kept in the same 28 tank for longer than 3 hours during the non-coupled, pre-run electrolyte soak period; the zinc anode potential would decrease to that of the aluminum alloy anode. The polarization curves taken at that point would indicate approximately the same anodic activity. Possibly indium ion (introduced from the native corrosion of the aluminum alloy) into the electrolyte may have electrodeposited onto the zinc anode resulting in a surface alloy with lower (more negative) potentials than is usually observed and reported. This would suggest that for a mixed anode system in a closed tank application, the potential of the zinc would change and the current would essentially match that of the Galvalum III alloy.

However, on open sea stern arrays, where the ionic reaction products should be more completely removed, no indium addition to the zinc surfaces would be expected and the aluminum alloy should consume the majority of the cathodic protection current. Successful polarization runs were made by pre-soaking the two anodes in separate tanks for the 24 hour pre-run period and then limiting the co-exposure to approximately two hours. A comparison of the polarization curves for a new aluminum alloy anode (Heat 3253) and a used zinc anode tested using the modified test protocol is presented as Figure 7. As can be seen, the aluminum alloy anode with the more negative discharge curve would consume the majority of the current. The zinc discharge curve tends to show one smooth transition from the corrosion potential to the current limit. The discharge potential range is also in the same general range as the potential inflection in the aluminum alloy discharge curve. Natishan et al,⁶ studying surface implanted binary aluminum alloys had considered the inflection to be the pitting potential of aluminum, shifted to these low potentials by the presence of zinc in the alloy. However, the inflection as seen in Figure 7 would also appear to be associated with the onset of the anodic oxidation of zinc itself and not necessarily a pitting process in aluminum. Additional work would be required to determine the relative role of each process.

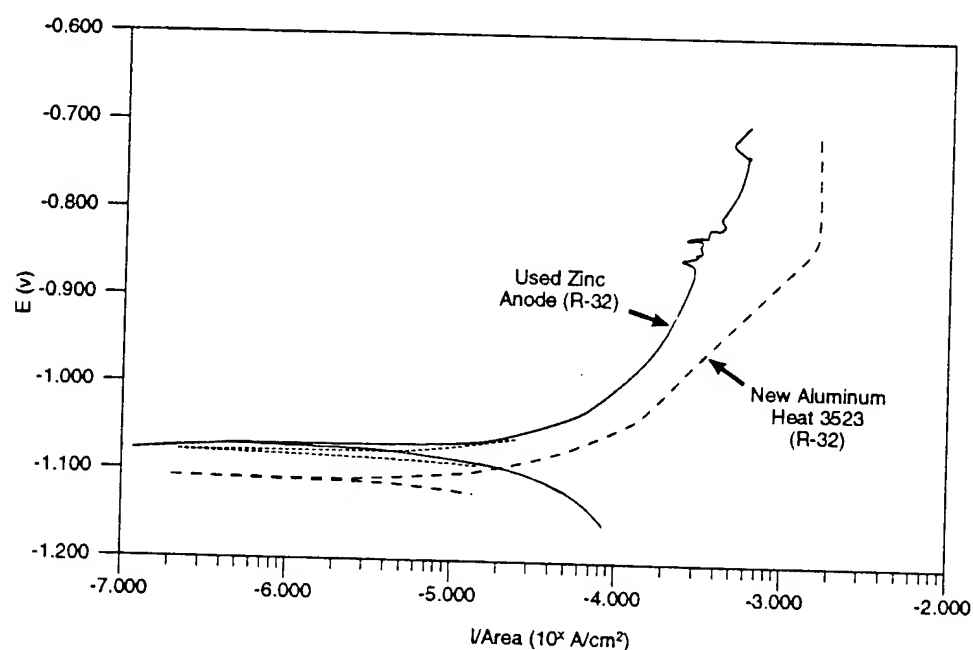


Figure 7. Polarization curves from new aluminum alloy anode (Heat 3253) and used zinc anode after overnight soaking.

SUMMARY

The objective for this study was to attempt to determine if the cause of non-uniform anode consumption on the stern hull array could be identified.

- A test protocol was constructed demonstrating that the electrochemical characteristics of used, air dried aluminum alloy anodes can be evaluated after removal from an installation.

- The evidence clearly points to the cause of non-uniform anode consumption as being the initial material composition used in fabricating the anodes.

- Anodes shown to be associated with a heavily mercury contaminated aluminum alloy (Heat 3069) were shown to have more positive (less negative) anodic potentials than properly fabricated material. Anodes with what might be considered as a minor mercury contamination (Heat 3070) were also shown to be affected. The anodes with the more negative potentials would subsequently consume more of the cathodic protection current and exhibit greater weight and dimension losses.

- Properly fabricated aluminum alloy anodes could be substituted into existing zinc anode arrays and would tend to be selectively consumed.

CONCLUSIONS

- The significant non-uniform consumption of Galvalum III, AHC-10 aluminum alloy anodes in a linear array on the stern of the submarine was the result of differences in anode alloy composition and not the result of passivated anode surfaces.

- Reasonable care must be maintained by vendors to adhere to the required chemical composition for the aluminum alloy in fabricating anodes. The presence of even low levels of mercury contamination in the Galvalum III composition is sufficient as to affect anode discharge rates.

- For the case of ballast or CHT tanks, installed but unused zinc anodes (eg., located high in tanks) could be left in place, replacing only the lower anodes with the aluminum alloy pieces as consumption allowances dictate.

ACKNOWLEDGMENTS

This project was funded by Mare Island Naval Shipyard, Code 211 in support of Work Request N00070POS2058. The work was performed under Work Unit 1-2813-052 at CDNSWC in the Marine Corrosion Branch, Code 613, under the supervision of Mr. Robert J. Ferrara. The experimental effort at CDNSWC was performed by Mr. Douglas W. Smith (Code 613). E.B. Bieberich (Code 613) provided a detailed review of the text.

REFERENCES

1. Reding, J.T. J.J. Newport III and J.R. Minderhout; US Patent 3,321,306, "Galvanic Anode Alloy and Products Produced Therefrom", 23 May 1967.
2. Walden, L.J. and M.H. Peterson; Corrosion, 14, No. 6, pp 289t-294t, June 1958.
3. Knuckey, P.J. and B.S. Smith; Mat. Perf., 16, No. 5, pp 44-51, May 1977.
4. Hack, H.P., Private Communication, March 1992, November 1992 and again in February 1993: Code 613 CDNSWC, Annapolis, MD 21402.
5. Lucas, K.E., M.H. Peterson and R.J. Guanti; P/N 277, Corrosion'89, 17-21 April 1989, NACE, Houston, TX.
6. Natishan, P.M., E. McCafferty and G.K. Hubler, J. ECS, 135, No. 2, pp 321-327, Feb. 1988.

BLANK

614

USMC Corrosion Reduction Program: Vehicle Corrosion Surveys at Camp Lejeune, Camp Pendleton, and Twentynine Palms Marine Corps Bases.

Mssrs. E. B. Bieberich*, T. J. Jackovic, and R. M. Janeczko
Naval Surface Warfare Center, Marine Corrosion Branch
34 Leggett Circle, Annapolis Maryland, 21402-5067

INTRODUCTION

The United States Marine Corps (USMC) has recently identified corrosion of vehicles as a major problem area. Higher life cycle costs of equipment, reduced operational availability, and excessive manpower requirements to maintain operability are some of the problems associated with corrosion. Current corrosion control methods have been identified as deficient, either in effectiveness or ability to be implemented. The Amphibious Warfare Technology Directorate (AWT) of the Marine Corps Systems Command (MARCORSYSCOM) tasked the Naval Surface Warfare Center (NSWC) Marine Corrosion Branch to conduct research and development of new materials, procedures and design improvements which will reduce corrosion of USMC vehicles.

BACKGROUND

As an amphibious force, the United States Marine Corps is required to transport most of its equipment by ship and deliver it over-the-beach to shore. To permit rapid response in fulfillment of its mission, Marine Corps bases and equipment stockpiles are situated close to ocean ports. Forward-deployed equipment is primarily stowed in prepositioned ships. Not surprisingly, the primary operating environment of Marine Corps equipment is a marine environment, including seawater immersion during amphibious operations, splash and salt-spray during ocean transport and on the beach, as well as salt-laden air. This is a most aggressive corrosion environment, and requires higher initial investment in equipment specifically designed to resist salt water corrosion and higher maintenance to achieve required vehicle lifetimes, ref 1-4.

Other than amphibious assault vehicles, most Marine Corps equipment is purchased by the US Army, whose inland mission removes

most of their equipment from exposure to the ocean environment. Neither Army bases nor training areas are normally located near saltwater areas, and as a result, no driving impetus exists in the Army procurement system to absorb initial higher costs associated with corrosion resistance to the marine environment. Marine Corps vehicles can be expected to have higher corrosion failures and associated maintenance burdens than Army (or Air Force) equipment.

For the most part, high initial procurement costs for more corrosion resistant equipment and vehicles eliminates the option of buying new materielle for all armed services that are sufficiently corrosion resistant to provide adequate maintenance-free service for the Marine Corps. However in some cases, upgrading to improved standards will provide cost savings for all. For instance, it may be possible to upgrade some non-structural parts to non-metallic materials that are inherently corrosion-free and cheap. Some design aspects (such as drain holes in frames) are prudent for any service vehicle.

For those vehicles and equipment procured specifically by and for the Marine Corps only, it makes very good sense to include corrosion resistant design in the specifications. Improved availability for service and reduction in maintenance man-hours should provide ample cost-justification for some moderately expensive improvements during procurement, while some design aspects which impart improved corrosion performance are essentially free when included in the initial design.

Although corrosion control maintenance actions are currently required at each of the different maintenance echelons for USMC vehicles, little data has been summarized on the extent of use and resulting effectiveness of the various corrosion control measures specified for USMC application. These corrosion control measures consist primarily of the application and maintenance of various coatings and compounds which are intended to exclude the corrosive environment from a corrosion-susceptible base metal. Manuals are available for vehicle types and maintenance echelons, but the use of these manuals is erratic and service performance data on the recommended methods is limited. In order to identify research and development approaches which will provide cost-effective payback upon implementation, the effectiveness must be determined of presently specified corrosion control methods in reducing corrosion problems in service.

APPROACH

Four interconnected subtasks have been identified by NSWC to improve corrosion performance of Marine Corps vehicles:

The first effort is to conduct inspections of Marine Corps vehicles by corrosion engineers to identify those components, materials and design aspects common to most vehicles which result in high corrosion susceptibility and resulting maintenance costs, which can not be substantially improved by present corrosion control efforts. A high payback R&D effort should result when the most expensive problems are then addressed for solution.

An evaluation of improved maintenance practices based on state-of-the-art corrosion control in both private industry and all military services will lead to immediate improvements through technology transfer, while identifying promising technologies requiring R&D evaluation for USMC applications. A literature review is in progress.

Design analyses will be conducted of present and proposed vehicle and equipment designs to identify life-enhancing backfits for existing assets and to permit inclusion of corrosion control criteria in purchase specifications which will lead to extended service life.

Research and Development Test and Evaluation (RDT&E) will be conducted for improved materials, designs, repairs and backfits to identify comparatively outstanding candidates for fleet evaluation and ultimate integration.

In order to develop cost-effective corrosion countermeasures for USMC vehicles, the current corrosion problems require definition. The first part of this task is to identify the corrosion problem areas of operating vehicles and review current corrosion control procedures and their overall effectiveness. In order to accomplish this, corrosion inspections of vehicles and equipment are being performed at major USMC bases and maintenance facilities. At these sites, inspections and discussions are conducted with personnel responsible for corrosion control and maintenance of vehicles.

During early FY94, personnel from NSWC visited Camp Lejeune, Camp Pendelton, and Twenty-nine Palms Marine Corps Bases. These sites were selected due to the variety and amount of vehicles, and the differing environments. Most of the inspected vehicles were in operational condition and had been in typical environments around their respective bases since their last major refurbishment or overhaul. Future inspections are planned for vehicles at Depot Level Maintenance Activities (5th echelon) and vehicles returning from deployment aboard ship. Vehicle types inspected included Amphibious Assault Vehicles (AAV), High Mobility Multipurpose Wheeled Vehicles (HMMWV), Light Armored Vehicles (LAV), Logistic Vehicle Systems (LVS), M1A1 Main Battle Tanks, 5-ton trucks, and various heavy landing support equipment. This report

summarizes the inspections, reviews current maintenance practices, and provides initial identification of general corrosion problems affecting USMC vehicles. These initial inspections will provide a baseline for corrosion control recommendations for present vehicles and will direct the research and development of future vehicles.

CORROSIVITY OF LOCAL ENVIRONMENTS

In general, the severity of marine environments is directly related to salt water exposure time. For equal time periods, severity of exposure is generally highest for direct immersion, followed by splash/spray, and then salt air exposure as a function of distance from the ocean ref 5. However, any exposure that results in collection of salt (chlorides) in metal crevices will continue to cause corrosion in any humid environment until the salt is flushed out.

In the atmosphere, corrosivity increases as the moisture level and the chloride concentration increases. The two primary sources of chlorides in the atmosphere are sea salt near coastal locations and road salt which is used primarily for deicing roads. For Marine Corps vehicles, the effect of road salt is expected to be insignificant when compared to the effect of sea salt in the marine atmosphere.

Transportation and Operation

Marine Corps vehicles are subject to salt water immersion during coastal and amphibious operations, and to salt spray during transportation aboard LCAC's and assault ships. These factors contribute to a severe service environment in which corrosion is a major maintenance consideration. Particular consideration should be given to proper application of corrosion control materials and procedures before and during ship transport.

Base Location

The corrosion surveys revealed the operating location of the vehicles to be a major factor in determining the amount of corrosion observed. In general, the vehicles inspected at 29 Palms had the least corrosion. Those inspected at Camp Lejeune had the most corrosion. Those inspected at Camp Pendleton had slightly less corrosion than those seen at Lejeune but markedly more than those seen at 29 Palms.

The primary influences at both Camp Lejeune and Camp Pendleton would be exposure to the marine atmosphere and the use of vehicles for amphibious operations. The vehicles at 29 Palms are not subject to either of these influences and have very little corrosion. The

factors differentiating between Pendleton and Lejeune are less obvious. They consist of total precipitation and the number of days with rainfall as well as the concentration of industrial pollutants.

No surveys were conducted of III MEF vehicles on Okinawa. As Okinawa is an island, the chloride concentration in the atmosphere is likely to be higher than at any of the other locations. Therefore, the corrosion of vehicles based on Okinawa is expected to be greater than at the other sites.

GENERAL VEHICLE CORROSION PROBLEM AREAS

Coatings

In general, the use of Chemical Agent Resistant Coating (CARC) was considered a problem by most of the maintenance activities. Although CARC appeared to have adequate performance if applied properly, the environmentally strict application allowances severely limited its overall effectiveness. Only one quart per day per area is permitted according to volatile organic compound (VOC) regulations. This greatly restricts reapplication of a poor coating and allows very little touch-up.

Because of the problems associated with CARC, Zn-Silicate IC-531 coating has been proposed as an alternate coating for USMC vehicles. IC-531 has a zero VOC rating so it can be applied without the restrictions found with CARC. It has already been applied on a few vehicles at Camp Pendleton for in-service testing. However, poor controls were exercised during application, coatings experts were not involved, and the resulting applications poorly documented. In addition to a better controlled evaluation of the IC-531 system, more comprehensive research is needed on possible CARC alternatives.

Certain areas on the vehicles suffer severe environments where coatings often failed and a more effective coating was needed. These included high temperature areas on the engine and exhaust systems. 1st Recon. at Camp Pendleton was field testing a high heat aluminum paint overcoated with Amguard on certain high temperature connectors on the LAV engine. A coating was also needed on the underside of motor transport vehicles. Heavy amounts of corrosion were found in areas where coatings had failed or where coatings had not been applied.

Electrical Connectors

Electrical connectors were found to be consistently corroded on the various inspected vehicles. The design and geometry of these aluminum connectors leave these components susceptible to corrosion. Crevice areas were found to be the primary problem, especially under locking

collars and rubber seals. These crevices allow moisture and salt deposits to build-up which then caused accelerated attack.

Certain corrosion control methods were being attempted, but the effectiveness of these methods was unclear. Primarily, Amlguard or similar coatings were used in an attempt to exclude the connectors from the environment. Sometimes the connectors were wrapped with electrical tape. It is not known whether the observed failures were from improper application of these methods or whether the methods themselves were inadequate to prevent corrosion. More failures were observed at Camp Lejeune. It could be that the Amlguard-type coatings may work well for Camp Pendleton's drier environment but can not adequately withstand the harsher environment of Camp Lejeune. However, it is also possible that the application procedures are more easily followed at Camp Pendleton (drier surfaces during application), and better training is required at Lejeune. Field testing is needed where application of the coatings are documented and known to be correct, and performance of the coatings subsequently tracked.

If the current corrosion control methods prove to be ineffective, then other methods may require research. While the backfit of aluminum electrical connectors with non-metallic bodies may provide adequate performance, water exclusion methods from the present aluminum connectors involving coatings and/or plastic tapes or wraps could be comparatively evaluated.

One method approved for use with topside electrical connectors on Navy ships is cold-shrink tubing. Cold-shrink tubing is similar to heat-shrink tubing, but requires no heat guns or other application appliances. Application of cold-shrink tubing should work better than properly applied electrical tape and is easier to apply. The Navy has conducted an extensive evaluation of various methods (tapes, heat and cold shrink tubing) to reduce corrosion of electrical connectors. The comprehensive Navy report of those evaluations recommended cold/heat shrink tubing as interim corrosion control methods, until more corrosion resistant connectors could be fielded.

Seawater Leakage Through Turrets

On the amphibious and light armor vehicles, leakage of seawater through turret areas (particularly during LCAC transport) was found to be a major problem. The turrets were found to be ineffectively sealed and allowed seawater to leak through during any waterborne operation or transport on ship where seawater splashed on the vehicles. This typically caused corrosion of components below the turret area including

connectors, fittings, fasteners, etc. These components are usually inadequately protected since they are inside the vehicles and not designed for direct exposure to seawater.

Although some maintenance activities were concentrating on applying protective coatings to the susceptible components beneath the turrets, an effective sealing method for the turrets would be a simpler and less labor intensive fix. Development of a nonmetallic skirt or boot for installation around the turrets is one possibility.

Vision Blocks

The steel frame around the vision blocks in the turrets of amphibious and light armor vehicles were often corroded. This becomes a problem when the steel corrosion products leak onto the glass surface and subsequently impair vision. The current sealant appears to be ineffective in keeping moisture from coming into contact with the steel frame. 1st Recon. Bn. at Camp Pendleton reported this to be a poor sealant application at the depot level so they remove and reseal vision blocks on newly acquired vehicles. The performance of properly applied sealant should be tracked to assess its effectiveness and whether a new sealant or method is needed.

Water Collection Areas and Crevices

Water collection areas are areas that allow build-up of pockets of water, or moisture and deposits which increases the rate of corrosion due to the prolonged exposure to a corroding environment. These areas were found in many instances on the inspected vehicles including the frame of the HMMWV, hatch areas on the LAV, spot welds on trucks and trailer beds, and battery boxes for trucks. Proper corrosion control design of a vehicle should minimize any areas where moisture could be trapped.

Certain actions could be taken to limit the problems associated with water build-up. Drain holes can be drilled which allow water to leak out of trapped areas. This is especially needed for the frame of the HMMWV where holes in the side of the frame allow water in, but the bottom of the frame does not contain any holes to allow the water to drain out. Some newly acquired frames had drain holes but this was not always the case. The various maintenance activities could drill drain holes on any HMMWV frame without them. Battery boxes could also use better drain holes. Another option for battery boxes would be to also include a plastic insert which houses the batteries and allows the acid/water mixture to drain without coming into contact with the steel box. A new development, which should be tracked for general performance, is the introduction of plastic

battery boxes on m800 series trucks. The effort could easily be expanded to include their evaluation on other vehicles, and perhaps to include tool boxes as well.

To eliminate crevices from spot-welding, a continuous weld should be considered on future manufactured vehicles. On existing vehicles, an evaluation could be made of thin water displacing compounds which may fill crevices by capillary action, and provide some measure of corrosion resistance.

Fasteners

Failure of the cadmium electroplating was often observed on the Cd-plated fasteners and many of the fasteners had heavy rusting of the steel substrate. A change to a corrosion resistant coating for low strength bolts might provide better performance. An example is Sermetel, an aluminum-rich ceramic coating used with success on fasteners on Navy ships. Marine atmosphere and immersion exposure tests (environments similar to those experienced by USMC vehicles) showed improved performance over cadmium electroplate, ref 6.

Hydraulic Pistons

On heavy landing support equipment, hydraulic piston rods often had pitting of the chrome plating. This reportedly causes wear and eventual failure of the piston seals. Alternative coating materials should be examined. While other electroplating materials, such as nickel, can be evaluated, two promising methods include superpolished high-velocity oxy-fueled plasma sprayed titanium (or other metals) and plasma sprayed materials which contain ceramics, such as Ceramax 1000tm. The Ceramax 1000 is used on underwater hydraulic cylinders which open and close canal locks (gates).

Headlight Frames

Corrosion of steel headlight frames on HMMWVs is a problem which should be easily corrected by using an alternative material. An aluminum alloy should be available which has the mechanical properties required for the steel frames but has improved corrosion performance.

MAINTENANCE PRACTICES AND GUIDANCE

The maintenance and corrosion control practices varied considerably between the maintenance activities. Although standardized technical manuals and guidances are available, activities follow their own guidelines for corrosion control. These guidelines typically incorporate

some of the methods in the standard guidances but often include familiar or available materials and practices. Both 2nd and 3rd Bn. AAV maintenance have developed their own manuals for corrosion control.

The non-standard use of maintenance practices makes assessing the performance of the recommended methods of corrosion control in the technical manuals very difficult. Without standard practices uniformly implemented, no assumptions can be made with respect to the proper use or application of a corrosion control method. When a corrosion problem area on a vehicle was observed, it was often not determinable whether the recommended method had been used or applied properly, or applied properly but still provided ineffective performance. Before further research and development is conducted to solve vehicle corrosion problems, the service performance of the presently recommended corrosion control methods should be quantified. If the presently recommended methods are effective but are not being followed, research and development of new methods will not provide any improved performance. The Marine Corps Systems Command is in the process of developing a new corrosion control order which should assure the proper use of the technical manuals and implementation of the recommended corrosion control methods. Tracking of these methods in service is needed to evaluate their effectiveness and direct R&D efforts. At this point, the fastest determination of effectiveness may be to do a side-by-side demonstration of the recommended corrosion control methods on several vehicles, comparing their performance to two untreated controls.

It is occasionally evident that no corrosion control is practiced at all for certain maintenance evolutions. During corrosion surveys at Twentynine Palms, a rebuilt engine for an AAV was observed to be in poor condition. Corrosion of previously identified susceptible components had neither been repaired nor treated with corrosion preventive compounds.

The lack of authoritative guidance for corrosion control has permitted maintenance activities to implement new corrosion control methods where existing methods were presumed ineffective. In particular, 1st Recon. at Camp Pendleton has attempted to develop an effective corrosion control program for the LAV. Unofficial field tests are being conducted on alternate methods for problem areas including a high temperature Al paint for fittings on the engine. To provide benefit to the entire corps, the tests should be repeated under controlled and documented conditions.

A recommendation was proposed by 1st Recon. to incorporate any corrosion control procedures into the vehicle assembly guidance. This

would require only the use of one manual during assembly and simplify the application of corrosion control. 1st Recon. had already handwritten their corrosion control methods in the margins of their assembly manual.

RESEARCH AND DEVELOPMENT, TEST AND EVALUATION

Coatings

While new low-VOC CARC coatings are presently under evaluation, corrosion tests will be required to determine which primer coatings as well as CARC coatings provide the best corrosion resistance to both steel and aluminum substrates. Included in the evaluation should be the zinc silicate coatings which have already been applied to several Marine Corps vehicles at Camp Pendleton. While fluidized bed epoxies should be considered for evaluation on vision ports, alternate vision port body materials, like aluminum or stainless steel should be considered.

Compounds

Most of the presently approved thin coatings for field use, except for the AMLGARD spray coatings, provide poor protection. Substitutes which provide high capillarity, water displacement and film "toughness" will be sought for comparative evaluation.

Materials

Both new materials for future marine corps vehicles and materials substitutions for existing components on present vehicles will be evaluated for life cycle improvements in performance. Aluminum alloys 2519 and 5083 presently being considered as hull materials for the new amphibious assault vehicle, and austenitic stainless steel fasteners (as well as coated steel fasteners) which are being considered for AAV applications can be comparatively tested in the marine environment. Based on the poor fleet performance of aluminum electrical connectors, a significant effort is justified in the development of alternate materials (stainless steel or composite material) for electrical connectors.

An aluminum headlamp retention bracket should be fabricated and placed in comparative marine exposure tests with the standard steel ones presently used on HUMVEEs and trucks.

Exhaust system components are repaired and replaced often, and would significantly benefit from an aggressive evaluation effort of advanced materials for backfit exhaust systems, as well as high temperature coatings. Both ceramic and metallic based plasma sprayed materials may provide improved service life for hydraulic cylinder rods, but require some development for specific Marine Corps applications and

eventual marine corrosion testing.

Plastics and composites may provide significant relief from corrosion attack on some non-structural components, such as battery and tool boxes. An effort to utilize non metallic materials (skirts, boots, tarps) to exclude the environment from vehicles and components may also be fruitful.

Environment Control

One means to reduce atmospheric corrosion is to isolate materials from the aggressive environment. Several approaches are available to exclude the environment from vehicles.

Since LCAC-transport is considered to be among the harshest operating environments to which Marine Corps vehicles are exposed, a means to reduce the amount of salt spray to which vehicles are exposed while in transit may serve to alleviate corrosion damage. The use of covers for LCAC's would shield vehicles from the salt spray and may reduce corrosion by isolating materials from an aggressive environment.

Corrosion of the internal components of some amphibious vehicles is worsened by seawater ingress during waterborne operations. The turrets generally provide the easiest path for seawater intrusion into the vehicle, and may benefit from the use of a skirt designed to make the turret more watertight.

Another technique for environmental control under investigation by the Marine Corps is the use of active dehumidification. It has been found that maintaining a relative humidity of 30% - 40% greatly diminishes the effects of atmospheric corrosion.

Active dehumidification has been used by Israeli Defense Forces, the Swedish and Danish Air Forces, and Swedish and German Armies. It has been applied to aircraft by the U.S. Army, Navy and Air Force.

Dehumidification is currently being pursued by the Marine Corps (II MEF), both for the preservation of materials in long term storage, and for active-status materials. Active dehumidification is currently used by the U.S. Navy for the preservation of some inactive ships. It may be feasible for Marine Corps vehicles intended for long-term storage to be loaded aboard inactive assault ships already equipped for the dehumidification of internal spaces. The feasibility and cost-effectiveness of storing Marine Corps vehicles aboard inactive assault ships should be investigated.

Design Analysis

The feasibility of integrating corrosion engineering into new vehicle and component design will be demonstrated. Particular attention will be

paid to when during the design process that corrosion engineering should be applied, as well as the initial development of standard phraseology for integration into design standards and specifications.

Using the AAV, and other new Marine Corps vehicle designs (perhaps the 8 ton truck), performance and materials compatibility issues resulting from the new designs which may require corrosion tests to resolve will be identified.

Field Tests

While comparative corrosion testing of standard coupons is often necessary to resolve a range of candidates for service evaluation, there is also the opportunity to immediately evaluate some materials in service to demonstrate improved performance or the need to develop alternate materials and methods. As the Marine Corps has not implemented many of their own standard corrosion control practices fleetwide, it would be prudent to field test some of their specified materials for corrosion control alongside a few alternate or optional replacement materials and methods. A demonstration could be conducted on two vehicle types (eg, AAVs and HUMVEES) of say, five vehicles each, while holding another five each as controls with no special corrosion countermeasures. Properly set up and controlled, the field tests would provide numerical justification for fleetwide implementation of corrosion control and an excellent training opportunity in corrosion control application. Field tests should probably be conducted simultaneously at Camps Lejeune and Pendleton, and at Okinawa.

SUMMARY AND RECOMMENDATIONS

Inspections of United States Marine Corps amphibious vehicles, tanks, transport vehicles, heavy landing support equipment and artillery are in progress to identify common corrosion problems which may require research and development to improve. Issues related to establishment of a consistent and coherent corrosion control program for USMC vehicles have been discussed in order to emphasize existing methods which may reduce corrosion without further development effort. The role of the severity of environmental exposure conditions has been identified to assist in the separation of materials issues from design or maintenance requirements. Backfit of new materials, coatings and compounds into existing equipment for improved corrosion performance as well as into new design may require comparative corrosion tests to validate life cycle cost payback.

REFERENCES

1. Metals Handbook on Corrosion, Ninth Ed., Vol. 13, ASM International, 1987.
2. Designing for Automotive Corrosion Prevention, Society of Automotive Engineers, P-78, 1978.
3. Atmospheric Corrosion of Metals, ASTM, STP 767, 1980.
4. Degradation of Metals in the Atmosphere, ASTM, STP 965, 1986.
5. Materials for Marine Systems and Structures, Treatise on Materials Science and Technology, Vol. 28, Academic Press, 1988.
6. Aylor, D.M. and P.A. Klein, "Corrosion Resistant Fasteners " Proceedings, 1985 Tri-Service Conference on Corrosion

BLANK

HIGH STRENGTH ALLOYS FOR SEAWATER FASTENER APPLICATIONS

Denise M. Aylor
Naval Surface Warfare Center
Code 613
Annapolis, MD 21402-5067

ABSTRACT

Slow strain rate tests were conducted on Rene 41, Alloy 925, and Alloy A286. Specimens were evaluated in 3.5% NaCl solution in both freely corroding and cathodically polarized conditions and compared to similar specimens run in air. 5000 hour statically-loaded proving ring tests were also conducted in natural seawater under both freely corroding and cathodically polarized environments to assess the validity of the slow strain rate method in predicting long-term environmental cracking resistance. The proving ring tests were performed on Alloy K-500, Alloy 625 Plus, Alloy 625PH, Ti-6Al-4V ELI, and Beta C titanium. Slow strain rate results indicated good environmental cracking resistance for Alloy A286 in all environments evaluated. Rene 41 exhibited a hydrogen embrittlement susceptibility when polarized to -1000 and -1250 mV vs. SCE. Alloy 925 was susceptible to hydrogen embrittlement at -1250 mV and showed a reduced load bearing capacity in freely corroding, -850, and -1000 mV vs. SCE environments. The proving ring results showed that the slow strain rate method is valid for assessing long-term environmental cracking resistance of fastener alloys.

INTRODUCTION

High strength materials that are utilized in Navy fastener applications require good hydrogen embrittlement/stress corrosion cracking (HE/SCC) resistance as well as galvanic compatibility with the components that they are fastening. Alloy K-500 is currently an approved fastener material per MIL-S-1222 and is typically used in high

strength applications. Alloy K-500 is, however, known to be susceptible to hydrogen embrittlement when cathodically protected (1-3). Due to this environmental cracking susceptibility and to its poor galvanic compatibility with noble metal components, alternate fastener materials are being considered. A research program assessing the HE/SCC resistance of a variety of nickel-base, titanium-base, and iron-base alloys has been ongoing for the past three years. Slow strain rate test (SSRT) results of particular alloys have been previously published (4,5). In this paper, the slow strain rate results of three additional fastener alloys will be presented. Specifically, these alloys are Rene 41, Alloy 925, and Alloy A286. Proving ring test data on nickel- and titanium-base fastener alloys will also be presented to assess the validity of the slow strain rate method in predicting long-term environmental cracking resistance.

MATERIALS

SLOW STRAIN RATE TESTING

The materials evaluated by the slow strain rate test method included Rene 41, Alloy 925, and Alloy A286. The chemical composition and mechanical property data for these alloys is included in Table 1.

PROVING RING TESTING

The fastener alloys utilized in the proving ring tests consisted of Alloy K-500, Alloy 625 Plus, Alloy 625PH, Ti-6Al-4V ELI, and Beta C titanium. The chemical composition and mechanical property certifications by the manufacturer for these alloys was reported previously (5).

EXPERIMENTAL PROCEDURE

SLOW STRAIN RATE TESTING

Slow strain rate tests were performed using notched tensile specimens (5). Specimens were pulled to failure using a displacement rate of 9×10^{-7} in/sec. Each of the fastener alloys were evaluated in conditions of air, freely corroding, and cathodically polarized to -850 mV, -1000 mV, and -1250 mV levels versus a saturated calomel reference electrode (SCE). The freely corroding and cathodic polarization tests were done in 3.5% NaCl solution. Duplicate tests were performed per

condition on each alloy. After testing, each specimen was removed from the test assembly and the fracture surfaces were preserved with plastic spray until SEM examination could be performed.

PROVING RING TESTING

The proving ring tests utilized the same notched tensile specimens as in the slow strain rate tests. Specimens were uniaxially loaded to the 90% yield load level based on slow strain rate air tests performed on each alloy. Static load testing was conducted in ambient temperature, natural seawater with specimens either a) freely corroding or b) polarized to -1000 mV vs. a Ag/AgCl reference electrode. Specimens were tested to failure or were removed from test if no failure had occurred after 5000 hours' exposure. The unfailed specimens were then pulled to failure in air using a 9×10^{-7} in/sec displacement rate, and their fracture surfaces were examined in the SEM.

RESULTS AND DISCUSSION

SLOW STRAIN RATE TESTING

Tables 2-4 document the slow strain rate results for Rene 41, Alloy 925, and Alloy A286. These tables include the time to failure, maximum load attained, and the air/seawater environment ratio for each specimen as well as a summary of the fracture surface appearance after the slow strain rate testing.

The Rene 41 SSRT specimens exhibited predominantly ductile transgranular fracture behavior in air, freely corroding, and -850 mV vs. SCE conditions. For these specimens, approximately 5% of the fracture surfaces contained low ductility areas but no indication of intergranular failure was evident. The SSRT specimens tested at -1000 mV vs. SCE showed a moderate amount of intergranular failure with secondary cracking. The SSRT specimens polarized to -1250 mV vs. SCE displayed fracture surfaces similar to the -1000 mV specimens, but a larger amount of secondary, intergranular cracking was present on the -1250 mV specimens. Although intergranular cracking was found on specimens polarized at both the -1000 and -1250 mV levels, a reduction in the maximum load data versus air was only evident for the -1250 mV specimens. The degree of secondary, intergranular cracking present on the -1000 mV specimens was presumably not enough to show a significant reduction in the maximum load attained as compared to air.

The Alloy 925 material behaved similarly in air, freely corroding,

-850 mV, and -1000 mV environments. The maximum loads attained in all four conditions fell within the same range of values. The appearance of the fracture surfaces after slow strain rate testing showed ductile fracture combined with secondary, intergranular cracking which predominantly occurred at the notch root. This ductile intergranular failure mode indicates a reduced load bearing capacity for this alloy as compared to a material that fractures in a ductile transgranular mode.

The Alloy 925 SSRT specimens that were cathodically polarized to -1250 mV exhibited evidence of hydrogen embrittlement. Both specimens contained a moderate amount of secondary intergranular cracking that was concentrated at the notch root. The maximum load values were also reduced in comparison to the air values.

The Alloy A286 SSRT specimens exhibited good environmental cracking resistance in all of the environments evaluated. The SSRT data for this alloy indicated a slight reduction in maximum load for the cathodically polarized specimens as compared to air; however, examination of the fracture surfaces did not suggest a hydrogen-assisted cracking mechanism. The fracture surface appearance of all of the Alloy A286 specimens showed ductile transgranular behavior over 95% of the surfaces. The remaining 5% of the fracture surfaces contained low ductility areas with porosity present around precipitates. Energy dispersive x-ray analysis of these areas showed the precipitates to be titanium-rich.

PROVING RING TESTING

A comparison of the proving ring and slow strain rate test results for nickel- and titanium-base fastener alloys is found in Tables 5-6. The SSRT data in these tables was reported previously (5). With the exception of the Alloy 625PH proving ring specimens that were cathodically polarized to -1000 mV, all of the proving ring specimens were in test for 5000 hours without failure and then were pulled to failure in air at a displacement rate of 9×10^{-7} in/sec. The cathodically polarized Alloy 625PH proving ring specimens failed after <48 and <120 hours, respectively.

The nickel- and titanium-base alloys exhibited a ductile fracture mode for both the proving ring and slow strain rate specimens tested in freely corroding conditions. Although some cracking was present on the titanium alloy specimens, the cracking was not intergranular and did not indicate an environmental cracking susceptibility. The three nickel-base alloys tested at -1000 mV all displayed a hydrogen embrittlement susceptibility in both the proving ring and slow strain rate tests.

Moderate to extensive secondary intergranular cracking was found on all cathodically polarized nickel-base alloy specimens except Alloy 625 Plus SSRT specimens. The Alloy 625 Plus specimens exhibited isolated areas of intergranular fracture concentrated at the notch root. The two titanium-base alloys exhibited a ductile failure mechanism under -1000 mV conditions in both the proving ring and slow strain rate tests. The slight to moderate degree of cracking evident on the titanium specimens was not intergranular and showed no indication of environmental cracking.

The maximum loads attained on the nickel-and titanium-base alloys did show some variability between the slow strain rate and proving ring tests. In the freely corroding environment, the maximum loads for the nickel-base proving ring specimens were either similar or lower than the slow strain rate specimens. In the cathodically polarized condition, the Alloy K-500 and Alloy 625 Plus proving ring specimens were consistently lower than the slow strain rate specimens. These reduced loads were presumably due to more extensive intergranular cracking present on the proving ring specimens, which resulted in a reduction in the maximum load attained. The Alloy 625PH material exhibited similar maximum loads for both the slow strain rate and proving ring tests, corresponding to a similar degree of intergranular cracking present on these specimens. For the Ti-6Al-4V ELI and Beta C alloys, the maximum loads attained in both freely corroding and cathodically polarized conditions were either similar or lower in the proving ring tests as compared to the slow strain rate tests.

In summary, there was good correlation between the proving ring and SSRT results. SSRT results for these high strength fastener alloys have typically shown variability in the maximum loads reported and thus, the primary criteria for predicting environmental cracking resistance has been the fracture surface appearance (5). Based on the fracture surface evaluation of the nickel- and titanium-base alloys, the resistance or susceptibility to environmental cracking in the freely corroding and cathodically polarized environments was consistent between the slow strain rate and proving ring tests. Thus, the accelerated slow strain rate test appears to be valid for predicting long-term environmental cracking resistance of high strength fastener alloys.

CONCLUSIONS

o Rene 41 has good environmental cracking resistance in freely

corroding and -850 mV vs. SCE conditions. This nickel-base alloy is susceptible to hydrogen embrittlement when polarized to -1000 and -1250 mV vs. SCE.

o Alloy 925 exhibited a ductile intergranular fracture mode in air, freely corroding, -850, and -1000 mV vs. SCE conditions; this intergranular fracture behavior indicates a reduced load bearing capacity for this alloy as compared to an alloy that fractures in a ductile transgranular mode. Alloy 925 is susceptible to hydrogen embrittlement when cathodically polarized to -1250 mV vs. SCE.

o Alloy A286 displayed good environmental cracking resistance in air, freely corroding, and cathodically polarized environments.

o A comparison of short-term slow strain rate and long-term proving ring tests indicated that the slow strain rate method is valid for assessing the long-term environmental cracking resistance of high strength fastener alloys.

REFERENCES

1. Efird, K.D., "Failure of Monel Ni-Cu-Al Alloy K-500 Bolts in Seawater," Materials Performance, Vol. 24, No. 4, 1985.
2. Faller, K. and W.A. Edmonds, "The Incentives for Titanium Alloy Fasteners in the Navy/Marine Environment," 1991 Ship Maintenance in the 21st Century Symposium, American Society of Naval Engineers, Virginia Beach, VA, 1991.
3. Joosten, M.W., and L.H. Wolfe, "Failures of Nickel-Copper Bolts in Subsea Applications," 19th Annual Offshore Technology Conference, Paper No. 5553, Houston, TX, 1987.
4. Aylor, D.M., "A Hydrogen Embrittlement Evaluation of High Strength, Non-Ferrous Materials for Fastener Application," Proceedings of the Tri-Service Conference on Corrosion, Plymouth, MA, 1992.
5. Aylor, D.M., "An Environmental Cracking Evaluation of Fastener Materials for Seawater Applications," Corrosion '94, National Association of Corrosion Engineers, Paper No. 484, Baltimore, MD, 1994.

TABLE 1 - Chemical composition and mechanical property data for fastener alloys

Manufacturers' Certification

Material	Composition	Condition	UTS (ksi)	0.2% YS (ksi)	% Reduction in Area	% Elongation
Rene 41 (GX)	Ni-19Cr-10Mo-11Co- 3Ti-3Fe-1.5Al	1975F 1 Hr/WQ, 1400F 16 Hrs/Air Cool	203.6	141.5	37.0	28.8
Alloy 925 (GYP)	Ni-27Fe-21Cr-3Mo- 2Ti-2Cu	1850F/WQ, 1365F 8 Hrs, Fu nace Cool at 50 deg/hr to 1150F 8 Hrs/Air Cool	168.3	110.5	45.0	27.0
Alloy A286 (GYO)	Fe-25Ni-14Cr- 2Ti-1Mo	1800F 1 Hr/Oil Quench, 1325F 16 Hrs/Air Cool	152.6	143.0 *	48.9	11.2

Specification Requirements

Material	Specification	UTS ksi, min.	0.2% YS ksi, min.	% Reduction in Area, min	% Elongation, min.
Rene 41	AMS 5712	170	130	10	8
Alloy A286	ASTM A453	130	85	18	15

TABLE 2—Rene 41 slow strain rate test results

Test Environment	Time to Failure (hrs)	Maximum Load (lbs)	%Air Average	Fracture Surface Appearance After Slow Strain Rate Testing
Air	15.3	2305	—	95% Ductile transgranular; 5% low ductility areas but no IG cracking.
Air	16.3	2364	—	95% Ductile transgranular; 5% low ductility areas but no IG cracking.
Freely Corroding	17.1	2281	97.7	Unable to assess fracture surface due to tenacious lacquer coating sprayed on surface after slow strain rate testing.
Freely Corroding	14.0	2297	98.4	Ductile transgranular with low ductility areas but no IG cracking.
-850 mV	19.1	2212	94.8	95% Ductile transgranular; 5% low ductility areas but no IG cracking.
-850 mV	13.6	2302	98.6	95% Ductile transgranular; 5% low ductility areas but no IG cracking.
-1000 mV	13.9	2271	97.3	IG Cracking - Moderate
-1000 mV	15.8	2363	101.2	IG Cracking - Moderate
-1250 mV	14.5	2052	87.9	IG Cracking - Extensive
-1250 mV	18.1	2156	92.4	IG Cracking - Extensive

TABLE 3 - Alloy 925 slow strain rate test results

Test Environment	Time to Failure (hrs)	Maximum Load (lbs)	% Air Average	Fracture Surface Appearance After Slow Strain Rate Testing
Air	15.7	2510	—	Ductile Intergranular
Air	14.7	2545	—	Ductile Intergranular
Freely Corroding	17.5	2554	101.0	Ductile Intergranular
Freely Corroding	15.2	2572	101.8	Ductile Intergranular
-850 mV	15.4	2508	99.2	Ductile Intergranular
-850 mV	15.8	2516	99.5	Ductile Intergranular
-1000 mV	15.7	2447	96.8	Ductile Intergranular
-1000 mV	15.8	2524	99.9	Ductile Intergranular
-1250 mV	15.4	2349	92.9	IG Cracking - Moderate
-1250 mV	14.8	2312	91.5	IG Cracking - Moderate

TABLE 4 — Alloy A286 slow strain rate test results

Test Environment	Time to Failure (hrs)	Maximum Load (lbs)	% Air Average	Fracture Surface Appearance After Slow Strain Rate Testing
Air	13.5	2460	—	95% Ductile Transgranular; 5% Low ductility areas but no IG cracking
Air	14.7	2435	—	95% Ductile Transgranular; 5% Low ductility areas but no IG cracking
Freely Corroding	15.9	2490	101.7	95% Ductile Transgranular; 5% Low ductility areas but no IG cracking
Freely Corroding	15.1	2484	101.5	95% Ductile Transgranular; 5% Low ductility areas but no IG cracking
-850 mV	14.7	2345	95.8	95% Ductile Transgranular; 5% Low ductility areas but no IG cracking
-850 mV	15.6	2324	95.0	95% Ductile Transgranular; 5% Low ductility areas but no IG cracking
-1000 mV	15.3	2300	94.0	95% Ductile Transgranular; 5% Low ductility areas but no IG cracking
-1000 mV	15.3	2333	95.3	95% Ductile Transgranular; 5% Low ductility areas but no IG cracking
-1250 mV	15.5	2358	96.3	95% Ductile Transgranular; 5% Low ductility areas but no IG cracking
-1250 mV	15.8	2374	97.0	95% Ductile Transgranular; 5% Low ductility areas but no IG cracking

TABLE 5-Proving ring and slow strain rate test results for nickel-base alloys

Material	Test Method	Environment	Maximum Load (lbs)	Maximum Stress (psi)	Fracture Surface Appearance After Slow Strain Rate Testing
Alloy K-500	Proving Ring	Freely Corroding	2005	163906	Ductile Transgranular
		Freely Corroding	2718	222193	Ductile Transgranular
		-1000 mV	1615	132236	IG Cracking - Extensive
		-1000 mV	1623	130577	IG Cracking - Extensive
	Slow Strain Rate	Freely Corroding	2572	209585	IG Cracking - Trace
		Freely Corroding	2528	205671	Ductile Transgranular
Alloy 625 Plus	Proving Ring	-1000 mV	2320	191803	IG Cracking - Moderate
		-1000 mV	2152	175080	IG Cracking - Moderate
		Freely Corroding	3570	290445	Ductile Transgranular
		Freely Corroding	3344	272058	Ductile Transgranular
	Slow Strain Rate	-1000 mV	2386	192576	IG Cracking - Moderate
		-1000 mV	2304	188048	IG Cracking - Moderate
		Freely Corroding	3448	285518	Ductile Transgranular
		Freely Corroding	3438	281503	Ductile Transgranular
		-1000 mV	2912	234656	IG Fracture - Slight
		-1000 mV	2888	231983	IG Fracture - Slight
Alloy 625PH	Proving Ring	Freely Corroding	2635	214034	Ductile Transgranular
		-1000 mV	3092*	251155	IG Cracking - Moderate
	Slow Strain Rate	-1000 mV	3092*	251155	IG Cracking - Moderate
		Freely Corroding	3724	281429	Ductile Transgranular
		Freely Corroding	3274	266789	Ductile Transgranular
		-1000 mV	3086	249234	IG Cracking - Moderate
		-1000 mV	3035	245347	IG Cracking - Moderate

*Specimens failed in proving rings <48 and <120 hours, respectively after exposure in natural seawater and cathodically polarized to -1000 mV vs. Ag/AgCl. All other proving ring specimens were unfailed after 5000 hours exposure and were pulled to failure in air.

TABLE 6-Proving ring and slow strain rate test results for titanium-base alloys

Material	Test Method	Environment	Maximum Load (lbs)	Maximum Stress (psi)	Fracture Surface Appearance After Slow Strain Rate Testing
Ti-6Al-4V ELI	Proving Ring	Freely Corroding	2686	218525	Ductile Transgranular-Slight Cracking
		Freely Corroding	2112	171826	Ductile Transgranular-Slight Cracking
		-1000 mV	2106	171338	Ductile Transgranular-Slight Cracking
		-1000 mV	2088	170418	Ductile Transgranular-Slight Cracking
	Slow Strain Rate	Freely Corroding	2542	207473	Ductile Transgranular
		Freely Corroding	2774	225324	Ductile Transgranular
		-1000 mV	2840	234038	Ductile Transgranular
		-1000 mV	2780	229093	Ductile Transgranular
Beta C	Proving Ring	Freely Corroding	1996	162649	Ductile, Faceted Areas-Moderate Cracking
		Freely Corroding	2610	212682	Ductile, Faceted Areas-Moderate Cracking
		-1000 mV	1955	159308	Ductile, Faceted Areas-Moderate Cracking
		-1000 mV	2479	202655	Ductile, Faceted Areas-Moderate Cracking
	Slow Strain Rate	Freely Corroding	2697	216297	Ductile, Faceted Areas-Slight cracking
		Freely Corroding	2516	203392	Ductile, Faceted Areas-Slight cracking
		-1000 mV	2580	206913	Ductile, Faceted Areas-Slight cracking
		-1000 mV	2700	216537	Ductile, Faceted Areas-Slight cracking

Cost-effective and Environmentally Safe Corrosion Prevention for 2nd Marine Air Wing Support Equipment Using Desiccant Wheel Dehumidification (DEW)

Mr. David J. McCarthy*
Munters Cargocaire
79 Monroe St.
Amesbury, MA 01912

MMSGT. Albert Sandoval, USMC (Ret)
307 Tall Pine Road
Havelock, NC 28582

MSGT. Harry Miller USMC (Ret)
2040 Wells Rd. Apt. #5A
Orange Park, FL 32073

Introduction

To reduce corrosion, equipment users and designers have essentially three choices: change the material, coat its surface or keep the item dry.

In an effort to reduce the cost and environmental impact of maintaining contingency support equipment, the 2nd Marine Air Wing (2nd MAW) has successfully utilized desiccant wheel dehumidification equipment to prevent corrosion by surrounding the material with dry air. 2nd MAW has found this greatly reduces the need for petroleum-based coatings, lubricants and corrosion-inhibitors, which improves compliance with environmental program goals while reducing costs. The DEW program also allows the 2nd MAW to redirect scarce man-hours to in-service equipment, maintaining high optempo capability in spite of reduced manpower. In implementing this program, the organization has reduced the need for appropriations of either capital or operating and maintenance funds by using existing manpower, equipment and supplies.

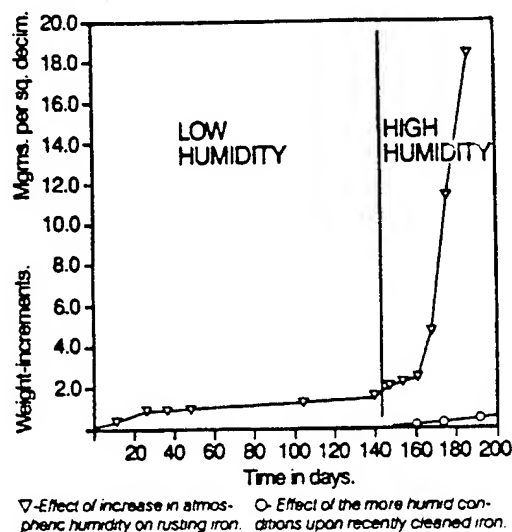


Figure 1. Corrosion rates depend on relative humidity (1)

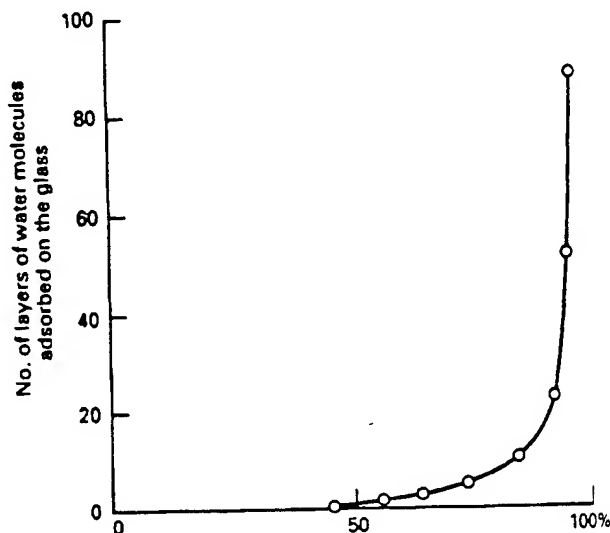


Figure 2. Corrosion increases because more water molecules settle on the surface at higher rh (2)

Keeping Equipment Dry

The idea of preserving material by keeping it dry is not new. In the most obvious example, valuable artifacts from Egyptian tombs have been preserved by dry air for more than 3,000 years.

As early as 1927, the English electrochemist W.H.J. Vernon observed the close relationship between the relative humidity in the environment and the rate of corrosion of ferrous metals (1). In more recent times, it has become clear that the number of water molecules adsorbed onto a surface held at room temperature is a function of the relative humidity of the air surrounding the surface(2). Figures 1 and 2 show the close correlation between the number of monolayers of water adsorbed on a surface and the rate of corrosion of ferrous metal as defined by Vernon in 1927.

The intuitive theory of keeping military equipment dry to reduce corrosion was reduced to practice following the Second World War. The U.S. Reserve fleet was protected by dry air generated by desiccant dehumidifiers, with results that were favorable enough to encourage the use of the method for long-term preservation of shore-side ships' parts in Mechanicsburg, PA. and in Army warehouses as well. The history of this technique was reviewed in 1986 by the Army Materiel Command(3).

In the early 1970's, European military organizations, notably the Swedish and Danish Armed Forces, began a series of trials to assess the use of desiccant dehumidifiers to reduce corrosion of active-duty military hardware. Unlike the U.S. Military during the 80's, the smaller, less-well-supported military establishments of Europe have always been highly conscious of the cost of corrosion in terms of required replacement equipment, and the environmental impact of preservation liquids and solvents.

These tests were highly successful in terms of reducing costs and improving the mean time between failures (MTBF) of sensitive electronic equipment in aircraft and combat vehicles. (4,5,6) Consequently, dry air protection has become a common feature of corrosion control programs in Europe for everything from active-duty aircraft to main battle tanks in long-term storage. The practice is in widespread use throughout Scandinavia, Germany, France and the Netherlands, and U.S. Materiel stored in NATO depots has been protected in controlled humidity warehouses (CHW) since 1983.

As a result of these successes with desiccant technology, the Department of Defense initiated a DOD-wide pilot program to evaluate the economic potential of more widespread use of desiccant wheel (DEW) technology in CONUS installations. This investigation has been underway since 1978 as part of the ongoing program to evaluate foreign weapons (FWE) to fulfill US requirements. For the FWE program within the Marines, the 2nd Marine Air Wing, with headquarters at Cherry Point, North Carolina, has been the lead organization evaluating DEW technology.

2nd Marine Air Wing Evaluation of Desiccant Wheel Technology

The 2nd MAW operates both rotary and fixed-wing aircraft from four locations: Cherry Point, NC, New River, NC, Cecil Field, FL and Beaufort, SC. Rotary wing aircraft include the UH-1N and AH-1N Cobra attack helicopters, the CH-46 Sea Knight and the CH-53 Sea Stallion transport helicopters. The primary fixed-wing aircraft within 2nd MAW is the AV-8B Harrier. Other fixed wing craft include the FA-18 Hornet jet, the EA-6B Prowler and the KC-130 Hercules tanker. Until recently, the 2nd MAW also maintained a large number of A-6E close air support jets as well.

Maintenance for these aircraft includes both organizational level tasks and the more specialized intermediate level tasks carried out by the Marine Aviation Logistics Squadrons (MALS) which are part of the air wing. These squadrons include MALS-14 at Cherry Point, MALS 26 and 29 at New River and MALS-31 at Beaufort. Because the 2nd MAW includes a wide variety of aircraft and a broad mix of maintenance activity from simple tasks to more complex intermediate maintenance, the organization was ideally suited to assess the real-world performance of desiccant technology in an operational environment.

While the final audit of the FWE program within the Navy is not yet complete, results to date are very encouraging. In May, 1994, a preliminary progress report on audit project #94-0016, prepared by the Naval Audit Service/Pensacola, estimates that dehumidification of in-service AV-8B Harrier aircraft within 2nd MAW has reduced humidity-related maintenance man-hours by 51%, increased mission-capable rates by 4% and lengthened the average avionics component MTBF by 33%. For the A-6E aircraft, the report estimates a 29% reduction in maintenance man-hours, and a 33% improvement in MTBF. The final report is expected in December 1994.

Since the FWE program has completed its preliminary investigation phase, the prototype desiccant equipment became available for other activity within 2nd MAW. That equipment has now been put to use throughout the organization in an effort to reduce the cost and environmental impact of maintaining contingency support equipment. As of June, 1994, more than 4,000 pieces of support equipment including generators, power supplies, recharger carts and portable inert gas bottles have been placed under dry air protection using 20 pieces of DEW equipment, much of which was originally acquired for the FWE program.

DEW Operating Principles

Desiccant wheel dehumidifiers produce dry, warm air continuously. The desiccant, which adsorbs moisture from air, is formed in-place in a wheel. The wheel looks like corrugated fiberboard rolled into the shape of a drum, so that air can pass easily through the desiccant-lined corrugations. As the air passes through the wheel, its moisture is adsorbed by the desiccant so the air emerges from the wheel warm and dry. For example, if air entered the wheel from a foggy spring morning in South Carolina at a temperature of 55°F and 100% relative humidity, it would leave the wheel at about 95°F and 11 grains per pound moisture content—which is about 4% relative humidity.

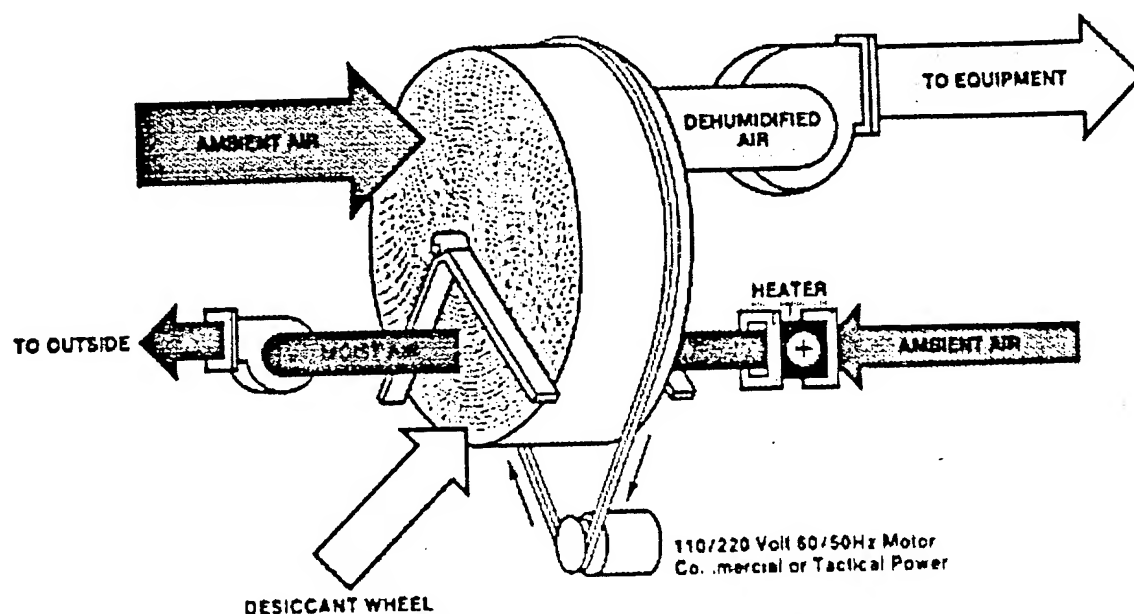
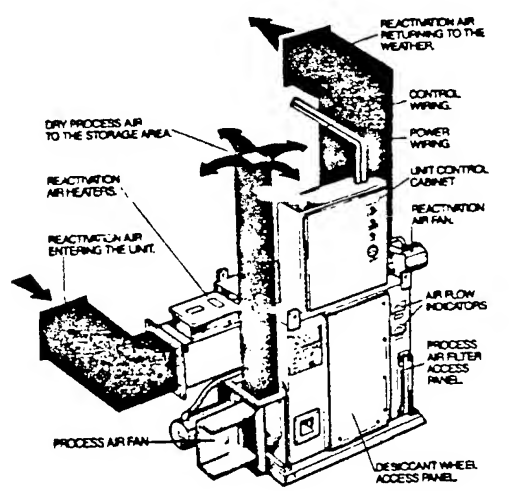


Figure 3. Desiccant Wheel (DEW) Operating Principles

The desiccant wheel rotates slowly (8 rph) between two counter-current air streams. The larger air stream, called the process air, is dried by the desiccant as explained above. As the wheel rotates through the process air and adsorbs moisture, the desiccant becomes saturated. But the wheel continues to rotate, passing through the smaller air stream, called the reactivation air. That air is heated, so it can remove the moisture from the desiccant. Since the wheel rotates continuously, it produces a constant stream of dry air. The desiccant wheel has a typical life of 350,000 cycles, which translates to five to ten years of normal operation before replacement is required.



The fact that the dehumidifier wheel rotates continuously gives it an important capacity advantage over the traditional passive desiccant storage technique of placing bags of desiccant around stored equipment. When bags of desiccant come to equilibrium with a high-humidity environment, they cannot absorb more moisture unless they are heated to drive off the moisture they have already adsorbed. A dehumidifier which operates continuously can remove hundreds or thousands of times more moisture than passive bags given the same amount of time.

Most will be familiar with the cooling-based dehumidifiers often sold for residential and commercial humidity control. Such equipment is quite inexpensive, but it suffers from two limitations which preclude its use in military applications. First, cooling-based dehumidifiers freeze when the weather is cool. When they freeze, such dehumidifiers lose all moisture removal capacity. Second, cooling-based units cannot dry air deeply enough to maintain the 30 to 40% rh that military organizations have found is necessary to eliminate the "sweating" (condensation) that causes corrosion when the weather moisture level rises rapidly around cold equipment.

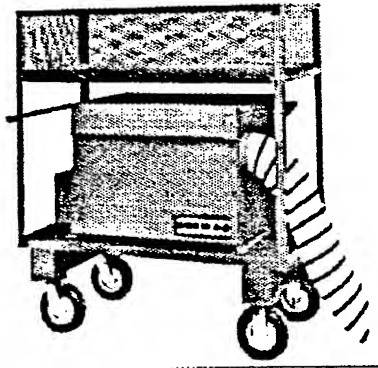


Figure 4. 300 cfm DEW unit

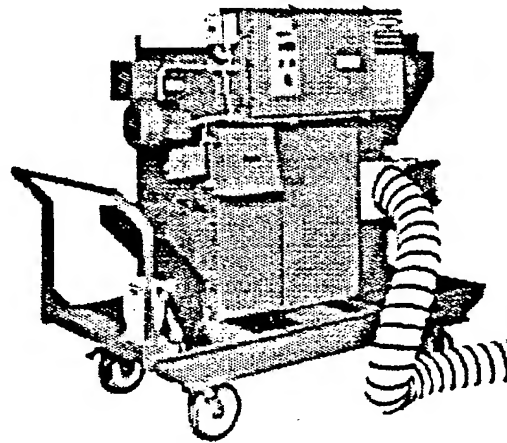


Figure 5. 600 cfm DEW unit

Figures 4 and 5 show typical DEW equipment used for military applications. The dehumidifier is mounted on a cart, which also holds the power cord and connecting hoses. Desiccant dehumidifiers need power for the process and reactivation air fans, desiccant wheel drive motor and the reactivation air heaters. The smaller unit shown here provides 300 cubic feet per minute of dry air, and uses 6.75 kw of either 208-230 single-phase or 3-phase power, or 440-480 volt, 3-phase power. Equipment shown here meets the appropriate military requirements, including:

- Paint to MIL-C-46168 or MIL-C-53039
- Technical manuals to MIL-M-7298
- Rated for outdoor operation in temperatures from -40°F to 120°F

Methods of Using DEW Equipment For Dry Air Protection

DEW technology assumes that items protected from corrosion will be isolated and surrounded by dry air. In traditional controlled humidity warehouses, this is a simple condition to arrange. A tight building is equipped with a desiccant dehumidifier and dry air is circulated throughout the building whenever a humidistat indicates the humidity is above the set point. Such warehouses have been built by the hundreds all over the world in the last 45 years. Figure 6 shows a typical example. The structure is a small version of the several dozen erected in Europe to contain US military equipment assigned to NATO.

While these warehouses are certainly effective and very economical compared to alternative means of preventing corrosion, they are expensive when compared to the typical operating and maintenance budget of a Marine Air Wing. Large, dedicated controlled humidity warehouses require years of planning, and extensive military construction appropriations. Fortunately, there are less elaborate means of applying DEW equipment.

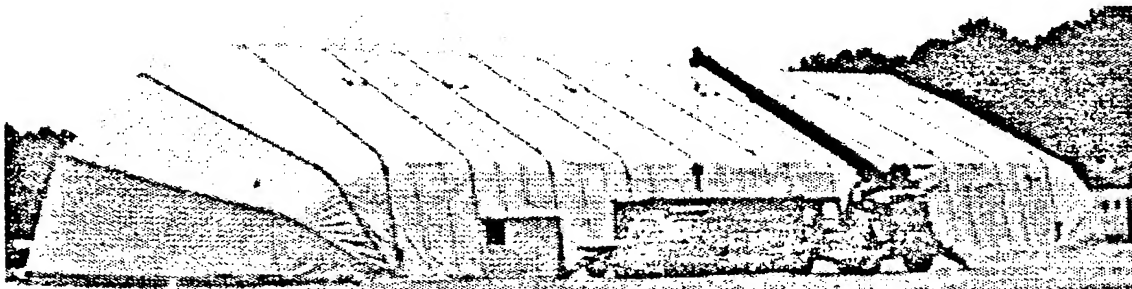


Figure 6. Larger versions of this type of shelter have been erected in Europe to protect NATO equipment

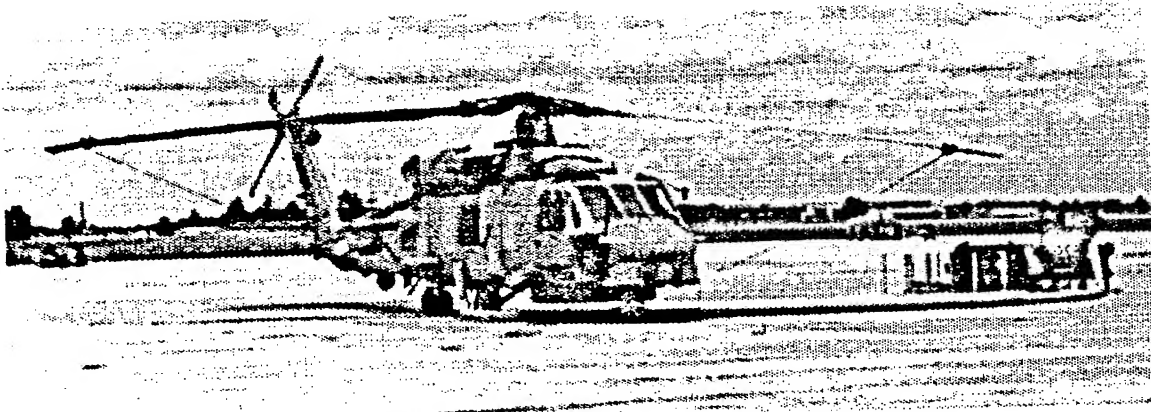


Figure 7. DEW units can be connected directly to larger pieces of weather-tight equipment.

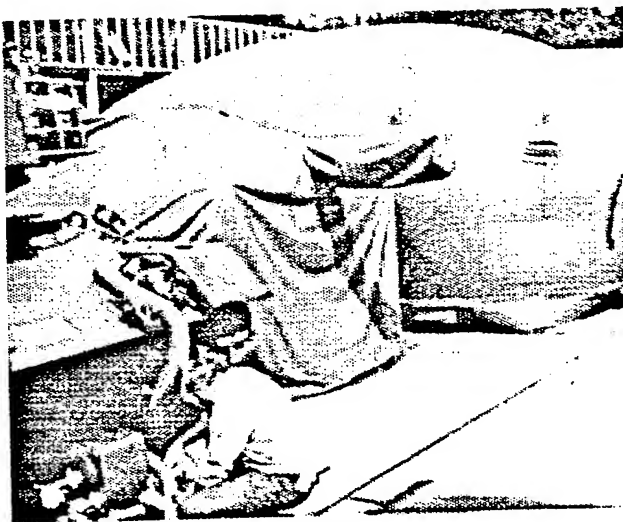


Figure 8. If equipment must have weather protection when warehouses are not available, smaller shelters can be made economically and connected to DEW units.

Figure 7 shows how DEW units can be connected directly to larger equipment. This configuration is commonly used for active-duty equipment which is basically weather-tight, and which must be available for action within minutes. Dry air from the DEW unit is blown into the helicopter through an 8" reinforced flexible air duct. The DEW unit operates continuously, purging the aircraft with dry air to prevent humid air from leaking into the aircraft.

Figure 8 shows another alternative. Heavy-duty reinforced vinyl fabric is made into fitted shelters which enclose the equipment under protection. Then a DEW unit is connected to the shelter and it circulates dry air throughout the enclosure. When the cover is loose, the DEW unit purges the shelter with fresh, dry air from the weather, putting the shelter under a slight positive air pressure to prevent humid air infiltration into the joints of the fabric. If the cover is tightly sealed, as is the cases with semi-permanent shelters, the DEW unit recirculates dry air within the enclosure, which reduces the operating time required to maintain the enclosure below the humidity set point.

Figure 9 shows a fourth option, in which equipment is shrink-wrapped for long-term storage or for ocean transport. Again, the DEW unit is connected to the shrink-wrapped enclosure to purge the equipment and prevent humid air infiltration. Experience with shrink-wrapped equipment is mixed. The method is easy to apply and can be made water-tight. But if the equipment contains water inside at the time of wrapping, a thin film

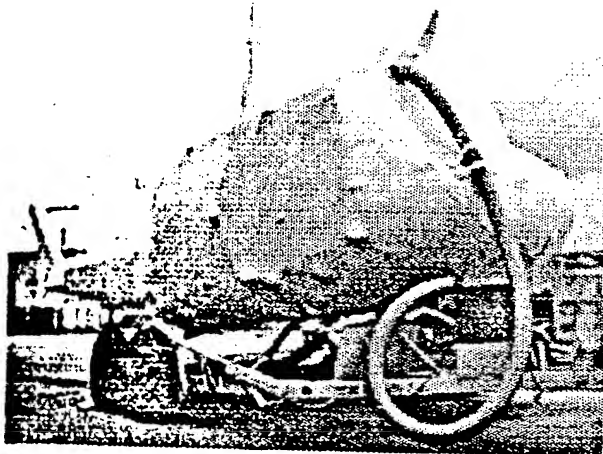


Figure 9. For long-term storage or for ocean transport, equipment can be shrink-wrapped and connected to DEW units to eliminate internal sweating when temperatures change.

of liquid can be trapped between the skin of the equipment and the wrapping material. Such films are nearly impossible to dry out because air does not circulate easily between the equipment and its tight wrapping. For shrink-wrapped equipment, dry air protection works best when the object is dried completely before the wrapping material is applied.

2nd MAW Support Equipment Dry Air Protection Program

While all of the four classic, proven means of installing DEW units are cost-effective, they were still beyond the resources available to 2nd MAW. But the organization, like others, faces the prospect of reduced manpower and further budget reductions in the future. In short—the resources for corrosion protection are minimal, and are likely to decline further.

The problem is especially acute for contingency support equipment. While the contingency material awaits its next operational use, it must be maintained in accordance with the NA 17-1-125 support equipment corrosion control and preservation manual to ensure it will function properly when brought into active service. The procedures outlined in the manual call for a six-month maximum length of inactive storage. Twice every year, the equipment must be de-preserved, scheduled maintenance must be performed and then the equipment must be re-preserved with the appropriate fluids and coatings.

Experienced maintenance technicians know that these tedious, "by-the-book" requirements are not always followed faithfully and meticulously. However, even allowing for "creative documentation" and deferring these tasks when personnel are overworked, the fact is that 2nd MAW requires over 4,000 pieces of contingency equipment. The manpower required to ensure proper maintenance of that much preserved equipment becomes a substantial drain on skilled personnel resources.

Additionally, the environmental impact of such extensive use of petroleum-based solvents, oils, greases and hydraulic fluids is considerable. For example, MALS-29, located at New River, is responsible for 392 pieces of contingency support equipment. In order to properly preserve, de-preserve and maintain that equipment, compliance with preservation procedures requires the use of 6,173 gallons of fluids over three years. Much of that liquid is considered hazardous waste, which creates an additional burden for personnel in applying the liquid, and a cost burden on the organization when it must be properly disposed of.

Given the conditions of reduced manpower, no budget available for capital equipment or construction, and the need to minimize hazardous waste generation, 2nd MAW faced a

considerable challenge in maintaining contingency equipment. But such situations are familiar in the Marine Corps, since the service is often called on to accomplish large tasks with minimal resources.

The four MALS of 2nd MAW responded by using ingenuity and existing equipment to create dry enclosures within existing structures, and then connecting the existing DEW equipment from the FWE program to provide the humidity control within these enclosures. The program was entirely self-help within each MALS, requiring only minimal reprogramming of maintenance material for air barrier sheeting and in some cases support cables for the barriers.

Example 1 - Building 4183 - MALS-14 - Cherry Point, NC

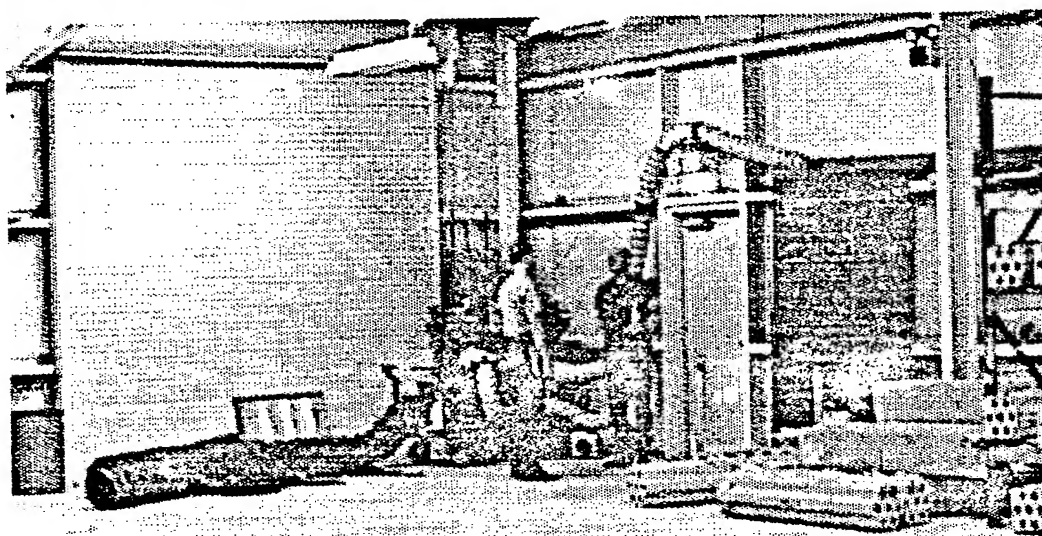
Building 4183 was originally built as an ordnance warehouse. In some respects, it was ideal for conversion to a controlled humidity facility, because it was insulated and has fairly tight, steel-panel walls. While there is no need for insulation in a humidity control situation, the insulation layer helps block air, which might otherwise infiltrate through joints in steel wall sections. The building measures approximately 70' x 100' with a 25' ceiling. The side-wall ventilation grills were cranked shut, and covered with polyethylene sheeting. The sheeting was taped to the building walls with ordnance tape. This cloth-reinforced tape is durable, and has an extremely aggressive tack. It is used for a wide variety of fast repairs and temporary fastening jobs. Apart from vent sealing, the only other air-tightening consisted of caulking obvious air leaks with standard construction-grade silicone sealant.

Initially, MALS-14 installed a DEW-300 desiccant wheel dehumidifier in the building. However, strip-chart humidity recorders located in the space showed that 300 cfm dehumidification capacity was not sufficient to keep the area between 30 and 40% rh.



Left: The exterior of building 4183

Below: The inside of the building showing the DEW unit and simple air ducting



That control level is recommended by NAVAIR 15-01-500, the Navy's aircraft preservation manual, which outlines the use of DEW equipment for corrosion-prevention.

The 300 cfm unit was replaced with a 600 cfm DEW unit, but the humidity recorder still showed a failure to control humidity to 40% rh maximum. The recorder indicated that the building was maintained at 40% consistently between the middle of the morning up until about 7:00 P.M. in the evening. Then the humidity would rise above set point, sometimes reaching 65 to 70% rh by 2:00 am in the morning. So the inside condition tracked the weather. Note that this pattern is typical in all climates—during the day, the dry bulb temperature rises, but the dew point lags behind, so the relative humidity is low. But as the ambient temperature falls at night, it approaches the dew point closely—so the relative humidity registers close to saturation (100%rh). The initial assumption was that personnel were entering the building and leaving the doors ajar, but this was monitored and found not to be the case.

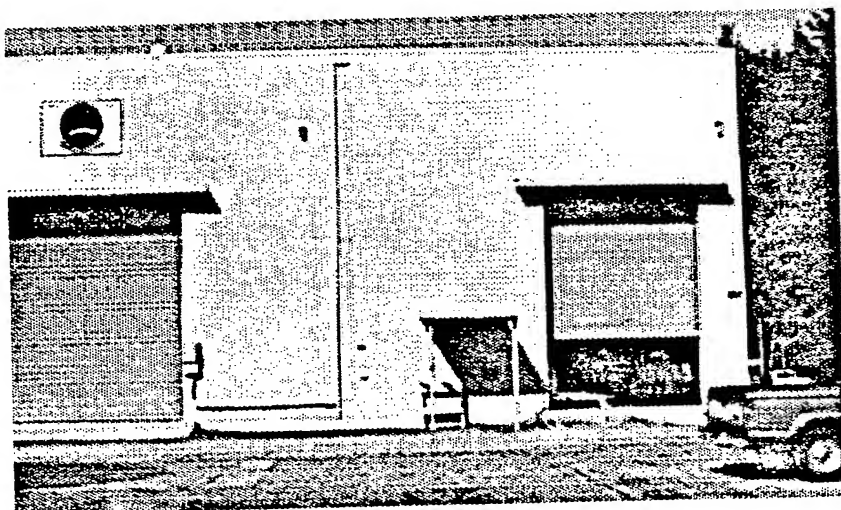
Careful investigation then uncovered the fact that a 4 in. x 12 ft. air gap existed out of sight at the top of each garage door opening between the rolling door and the building wall. The gap was needed to allow the rolling door sections to move smoothly into a roll as the door opens. To reduce air infiltration, MALS-14 obtained advice from the facilities management group on base. They cut strips of 1/8 in. rubber sheeting about 8" wide, and fastened the sheeting to the building with a 4" strip of galvanized flashing material through-bolted to the building wall. This arrangement forms a flexible wiper seal which allows the door to retract and extend smoothly, but greatly reduces the humid air infiltration—especially when the weather is windy. Now the 600 cfm dehumidifier has no difficulty keeping the humidity below 40% rh no matter what the weather is like.

The installation of the DEW unit is very simple. It sits inside the building near the personnel entry way. A flexible duct laid loose on the floor pulls humid air from the middle of the building into the process air inlet of the DEW unit. The dry air leaves the dehumidifier and is sent through 8"-round, galvanized steel duct work fastened to the wall. The air is carried up the wall, over the ceiling and discharged from a Y-connection near the roof. One leg of the Y blows air towards the center of the building, and the other sends air down one side wall. A humidistat is located in the middle of the space, such that dry air does not blow on the sensing element directly.

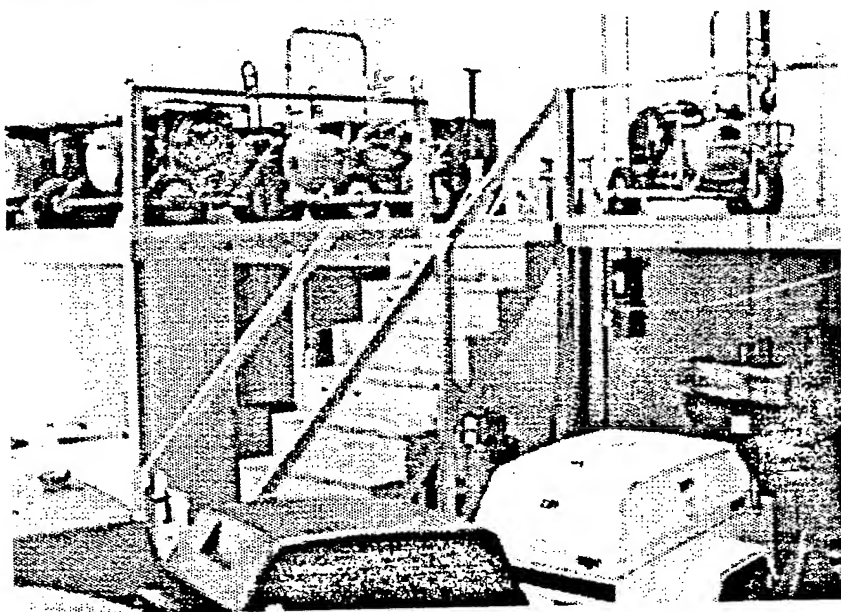
The cost of this installation was very low. The DEW unit and humidistat were obtained from the Army, which had completed its tests for the FWE program for the Blackhawk helicopter. The flexible process air inlet duct on the floor is recycled pre-heater hose, formerly used for air ducting for the pre-heaters used to warm tents and temporary shelters in field maneuvers. The galvanized process air distribution duct work was recycled from an old vehicle exhaust air system originally mounted in another building. And the material cost for polyethylene sheeting, ordnance tape, rolling door gaskets and construction caulk came to less than \$100. The building was converted to dry air storage in April of 1993, and has protected approximately 250 pieces of ordnance support equipment in excellent condition since that date.

Example 2 - F-4 Training Facility - MALS-31 - Beaufort, SC

This single-story building was originally built as a naval maintenance training facility for the F-4 jet. It measure 100' x 200' with 15' ceilings. The building consists of offices and classrooms, and several of these rooms have not been in use for several years. MALS-31 converted one of these rooms to a dry air storage area. The room measures 20' x 20' with a 15' ceiling. As the room was inside the building, and had been built for



Left: The exterior of the former F-4 Naval Maintenance Training Building. The room at the right formerly housed the hydraulic test stand training room and is now used for dry storage



Left: A second level was built from plywood and framing lumber to accommodate more equipment under dry air protection.

normal classroom use, the walls, ceiling and floor were fairly airtight in comparison to hangers and warehouses. Also, the room had been used for training on hydraulic test stands, so it was equipped with a useful garage door so large equipment could move in and out of the building easily.

Any obvious cracks between walls and floor and ceiling were caulked with construction sealant, but little preparation was required. To make maximum use of the space, MALS-31 built a lumber-frame-and-plywood mezzanine above the floor level for smaller pieces of support equipment, while the floor level accommodates the larger items, so that up to 150 pieces can be protected in this small space.

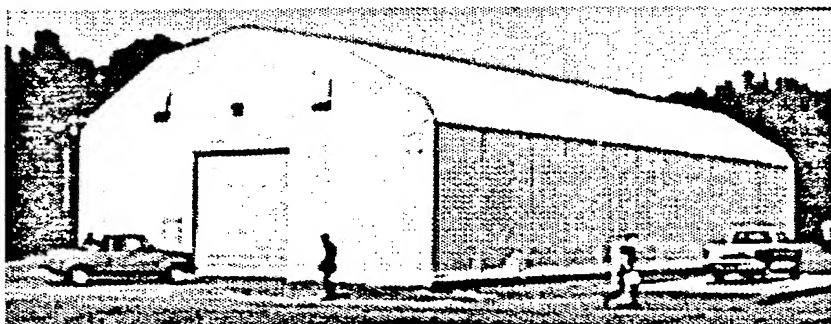
Initially, a DEW-150 dehumidifier was used for humidity control. One useful feature of this small unit is its low energy consumption. It can operate on 110 volt, single phase power—ideal for smaller installations which generally have such current in all parts of the building. However, the unit ran continuously, indicating it was operating at or near its capacity in order to maintain the space at 40% rh. Additionally, a check of the unit showed that the reactivation air temperature leaving the unit was under 120°F. This low

temperature indicated that the desiccant wheel was not being completely dried on each rotation, confirming that the unit was working at or above its maximum capacity. The 150 unit was replaced with a DEW 300, and the expected favorable results were achieved. The 300 cfm unit operates intermittently, indicating that it has the needed capacity to meet peak loads when they occur.

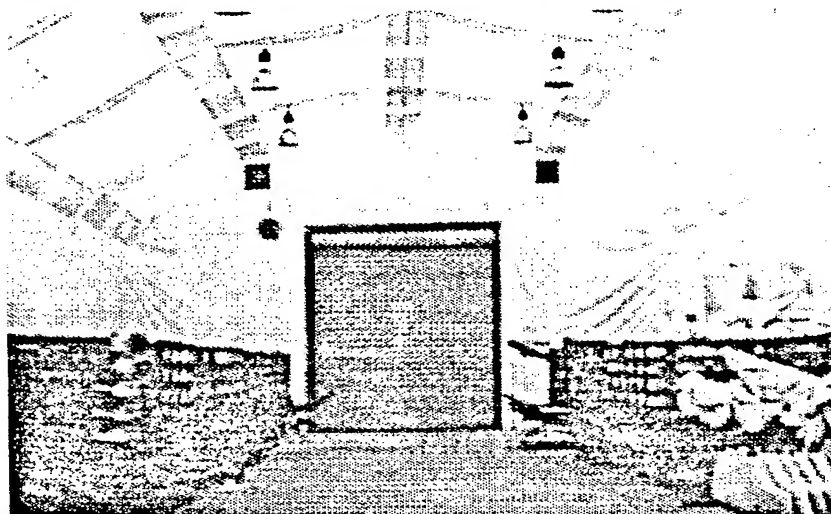
In past experience with controlled humidity warehouses and tightly-sealed spaces such as the reserve fleet ships, dehumidifiers operate between 20 and 40% of the total hours in a month. Once the material stored in the facility loses its excess moisture and comes to equilibrium with the low humidity, the total moisture load on the dehumidifier reduces, and consists mainly of humid air infiltration. When air infiltration is minimized, the unit operates most frequently during evening hours when reductions in air temperature cause the relative humidity to rise above the control set point of 40% rh.

Example 3 - Fabric-on-frame Structure - MALS-31 - Beaufort, SC

This building shows the type of buildings planned for dry storage within 2nd MAW. The program has achieved some impressive success at virtually zero capital cost, but nearly all the 58 units acquired through the termination of test programs have been redeployed. It will probably be necessary to invest in additional equipment in the future to continue gaining benefits from this technology. When that time comes, the organization currently plans to erect low-cost, but large-capacity shelters similar to this building at Beaufort. It measures 40' x 90' with a 30' ceiling. It now protects approximately 1,054 pieces of AWSE (Airborne Weapons Support Equipment).



This fabric-on-frame structure, originally procured for another mission, was easily converted to a dry storage facility by the addition of a DEW unit and minimal work to seal the walls to the concrete slab.



Inside the structure, MALS-31 has placed approximately 1,054 pieces of contingency support equipment under dry air protection.

Once again, this particular structure was originally used for a different purpose, but is nearly ideal for dry storage. The structural frame is lightweight steel tubing with cast steel joints. Over the frame, a durable reinforced vinyl fabric is stretched and secured with webbing and lanyard cord. The structure is relatively portable, and it can be erected without special equipment, by Marines with minimal experience in constructing buildings.

This particular shelter was erected over a poured concrete slab, which provides a durable floor for the storage of heavier equipment. But where such a slab is not available, the shelter could be provided with a plywood floor laid over low-cost 6 or 8-mil polyethylene sheeting. Some barrier is necessary to avoid water vapor infiltration from the moist ground under the shelter.

In this case, the fabric wall does not provide a watertight seal where the walls meet the concrete slab. This was improved considerably by simply running a bead of silicone construction caulk along the joint. Some leaks remain, but these are not apparently large enough to disturb the 40% rh control level.

The shelter is equipped with two DEW-600 units, one at each end of the structure. The units blow the process air (dry air) into the center of the space. Each unit is controlled by a separate humidistat. These are mounted in the middle of the structure, in a location that avoids direct contact with the process air stream.

This shelter, like all the dry storage areas within 2nd MAW, is equipped with a low-tech "moisture load reduction device". In other words, a sign on the personnel access door which clearly states: "This is a humidity-controlled room. Please keep the door shut." Just as a refrigerator cannot control temperature if its door is open, so will a dry storage room be difficult to maintain within specifications if moist air flows freely through the space.

Summary - Progress Report For The Dry Air Storage Program

Within 2nd MAW, the dry air storage program is considered a success. Each MALS has plans to expand the program as resources allow. Interestingly, one of the unexpected aspects of the program is its popularity with the working-level personnel. The active-duty equipment FWE DEW program suffered initially from personnel resistance to "another new technology to learn". In contrast, the support equipment (SE) program has considerably reduced the unpleasant, boring and time-consuming chore of preserving and de-preserved equipment with fluids and oils. So the squadrons report that the program has enjoyed support at all levels. Those in charge of maintenance are favorably impressed with the increased availability of manpower for more critical mission requirements, and those who have to apply and clean the grease are glad to reduce the time they spend scrubbing equipment. Each MALS has made a preliminary assessment of the benefits of the program. These estimates are not official, nor have they been audited, but some of the points they have made in their reports include:

- **MALS-14 Cherry Point, NC**

148 pieces of equipment are currently under consideration for an expansion of dry air protection facilities. Based on their experience to date, the organization estimates that the projected five-year cost of past practices would be \$113,486. The same equipment under dry air protection would cost \$3,785 over the five-year period, for an estimated savings of \$109,701. In terms of manpower, past practices would consume 14,707 man-hours over five years, while the dry air program would require only 486 man-hours over the same period, allowing 14,221 hours to be redirected to more mission-critical tasks.

- MALS-31 - Beaufort, SC

A total of 372 pieces of equipment were eligible for the dry air program, but the organization only had space to accommodate 114 pieces. Maintenance required by NA-17-1-125 for all 372 items was reviewed and compared with the hours required under dry air protection. The total requirement would have been 7,768 hours, but that was reduced by 1,176 hours because of the 114 dry-protected items. At the standard manpower cost of \$16.00/hr, dry air protection allowed redirection of \$18,816 in manpower resources over the last year. MALS-31 is seeking funding to place an additional 10,000 sq.ft. under dry air protection, which they estimate will allow redirection of \$39,600 in manpower resources annually to more critical tasks in the future.

Mals-31 has not yet completed their benefit analysis for the 1,050 pieces of weapons support equipment under protection as described in example 3, but responsible personnel estimate that savings will be similar in proportion to the savings gained on the 114 pieces of other equipment under protection.

- MALS-29 - New River, NC

392 pieces of equipment were surveyed for preventive maintenance requirements. The total man-hours required for traditional preservation would be 535 per year, against a total of 7.3 man-hours for dry air protection.

Going beyond the other squadron's analyses of labor hours, MALS-29 has estimated the annual fluid requirement for each piece of equipment. The total comes to 6,173 gallons of hazardous liquid over three years with traditional preservation, against only 8.3 gallons for the same equipment under dry air protection.

The purchase cost of these liquids ranges between \$2.93 per gallon for MIL-L-2104DS engine oil to \$46.18/gal for P/N 75448 ferrous chemical conversion compound. Disposal costs vary between \$4.00 and \$8.00 per gallon. Using a typical disposal cost of \$6.00 per gallon, and a typical purchase cost of \$8.14 per gallon for hydraulic fluid, the liquid waste savings can be estimated at \$50,180 to purchase and \$36,988 for disposal over three years. In other words, in addition to freeing manpower resources, dry air protection provides an estimated \$29,056 that can be redirected to better uses each year by reducing the need for hazardous liquids.

Differences between these reports reflect the fact that different equipment is under protection in each MALS. Also, because this program was relatively informal and "self-help", there was no established test plan to bring the results to a single, consolidated conclusion. Now, since program results have been so positive, the Naval Aviation Preservation Program Managers at the Naval Aviation Depot at North Island, CA, have drafted a uniform test plan. This will be used in the coming year to simplify evaluation of future dry storage installations. But looking at the results of the last two years, one cannot help but be impressed that the working level managers certainly believe that the dimension of the savings is substantial, and that dry storage represents an excellent use of government resources compared to the expensive and wasteful practices of the past.

References

1. Vernon, W.H.J., Second experimental report to the atmospheric corrosion research committee. Transactions of the Faraday Society, No. 23, 1927, pp.113-204
2. McHaffie, J.R. and Lehner, S., The adsorption of water from the gas phase on plane surfaces. J Chem. Soc, 127, 1559-1568, 1925.
3. Controlled humidity criteria evaluation, Project Report AMC-32-85, May 1986., U.S. Army Materiel Command, Packaging, Storage and Containerization Center, Tobyhanna, PA POC: Stuart Dougherty, Distribution Facilities Specialist
4. Niepoort, J. Protection of jet engines from corrosion by removal of moisture. Lecture at Vaerløse Air Base, Denmark, 1977
5. Dehumidification of aircraft, Report 389/86, Task 292/85, October 1986, Royal Air Force, Swanton Morley
6. Long-term storage of tanks, Review of EDAM Test Results (11 years of dry air storage), Bundeswehr Materialamt des Heeres (MatAH) TID-543, 15 October, 1987 , 5483 Bad Neuenahr-Arweiler

Ion Beam Enhanced Deposition as Alternative Pretreatment for Adhesive Bonding of Aircraft Alloys

Dr. Gerhardus H. Koch*
CC Technologies
2704 Sawbury Blvd.
Columbus, OH 43204-1821

and

Dr. Arnold H. Deutchman
BeamAlloy Corporation
6360 Dublin Industrial Lane
Dublin, OH 43017-3241

ABSTRACT

Surface treatment of aluminum alloys based on wet chemical processes is subject to increasing regulations. The objective of the work described in this paper was to demonstrate the feasibility of applying a non-chemical technique to generate an aluminum oxide surface with adhesive bonding properties comparable to that generated with the traditional technique. This paper describes the use of ion beam enhanced deposition which meets the objective of this work.

INTRODUCTION

Adhesively bonded structures are being used extensively as structural components for both military and civilian aircraft. Proper surface treatment is essential in order to achieve a good bonding surface that can be the basis for high strength adhesive bonds with good durability in corrosive environments. Surface treatments based on wet chemical processes have been shown to create excellent surfaces for adhesive bonding and coating application. The most common surface treatments

used in the United States are: (1) the Forest Product Laboratory (FPL) process for pickling, and (2) the Phosphoric Acid Anodizing (PAA) process.

The state-of-the-art surface pretreatments for adhesive bonding and organic coatings contribute to high strength and durable adhesive bonds. However, Environmental Protection Agency (EPA) regulations impose increasingly strict limitations on the wet chemical surface preparation processes. Particularly, surface treatment processes such as pickling and anodizing which rely on wet chemistry techniques and are large water users, are subject to regulations.

In order to find replacements for the wet chemical surface treatment techniques, a research program was initiated to develop alternative non-chemical techniques that do not produce waste detrimental to health and environment, and are compliant with present and future EPA regulations. An important requirement for such a technique is that it produces surfaces that result in mechanical strength and durability equal to or better than those produced by the wet chemical methods. In order to achieve the objective of this research program, a physical coating technique based on ion implantation was applied.

BACKGROUND

Research into the area of surface treatment of aluminum alloy components for purposes of adhesive bonding appears to have started in the 1950's, where surface preparation methods were developed primarily through an empirical approach¹. The main increase in research activity and development occurred in Europe and the United States during the 1970's and early 1980's, where researchers suggested that the macroscopic surface morphology, and surface oxide structure and composition are important for the bondability of aluminum alloys²⁻⁶. In the early 1970's, research was concentrated on mechanical strength and durability testing of adhesive bonds, and the relationship between adhesive bond strength and surface treatment. By the early 1980's, the technology of adhesive bonding was fairly well established, but research into the mechanism of adhesion and adhesive bond failure continued.

Aluminum Oxide Structure And Morphology

Some of the significant features of aluminum oxides were recognized as early as 1953. Keller and coworkers¹ described the basic structure of anodic aluminum oxide films as consisting of close-packed cells of oxide, predominately hexagonal in shape, each of which contains a single pore. Much later in the 1970's and early 1980's, transmission electron microscopy (TEM)² and scanning transmission electron microscopy (STEM)^{7,8} analyses were used to gain a better understanding of the surface oxide morphology and how the various morphological differences could affect bondability and durability of adhesive bonds of aluminum alloys.

The most common anodizing pretreatments for adhesive bonding of aluminum alloys used in the United States is phosphoric acid anodizing (PAA)⁹. Venables and coworkers⁸ characterized the surface morphology of the PAA treated surface treatments using the STEM^{7,8}. Figure 1 shows an isometric projection drawing depicting the PAA oxide morphology. The figure shows that the oxide consists of a dense barrier layer with a network of hollow well developed hexagonal pores, and whisker like protrusions. The porous layer is approximately 4000Å thick. The microscopic roughness of the oxide film, i.e. whiskers, created by pickling is an essential feature in establishing the bondability of the surface to an adhesive or to a coating. Chemically, the PAA oxide is amorphous Al_2O_3 , with the equivalent of a monolayer of phosphate (AlPO_4) incorporated into the surface film.⁸ When exposed to a humid environment, water will adsorb onto the oxide film, changing both the chemical composition and morphology of the oxide.

The morphology of the aluminum surface has been shown to be a strong determining factor in the adhesive bond strength. High surface roughness can provide a high density of locations where the primer or adhesive can form mechanical interlocks with the surface, thereby enhancing adhesion beyond that provided by chemical adhesion. Surface texture on a very fine scale (tens to hundreds of Ångstrom) is provided by the current generation of wet chemical techniques. Similar microscopic scale fine structure can also be generated by ion beam sputtering and deposition techniques¹⁰.

Ion Beam Enhanced Deposition Process

The IBED process is implemented as shown schematically in Figure 2. The process is carried out in a working chamber held at a vacuum in the 1×10^{-6} Torr range. The flux of atoms of the material to be deposited is produced by vacuum evaporation in an electron gun evaporator which is contained within the working chamber. The substrate to be coated is positioned such that it intercepts the flux of filming materials produced by the electron gun evaporator. A broad beam ion source generates a flux of inert atoms, usually Argon, which is directly aimed at the surface to be coated. Thus, the flux of filming atoms plus the secondary flux of Argon atoms strike the substrate surface simultaneously. The two fluxes of atoms can be controlled independently allowing a wide latitude in the ratios of atom arrival rates and energies. This allows complete control of the film deposition and growth environment, and therefore a high degree of control over the morphology of the deposited film.

During the initial phases of film growth, the film atoms can be mechanically mixed into the substrate surface, thereby significantly improving the film adhesion to the substrate. After the substrate surface is sufficiently doped with the film atoms to effect excellent adhesion, a contiguous film can then be grown from the substrate surface. The morphology of this film can be determined by controlling the energies of the respective film and augmenting ion fluxes.

Based on the present knowledge of required surface structure and morphology for good adhesion, namely a large surface area for mechanical anchoring and physical/chemical adhesion, the aluminum alloy surfaces were cleaned and coated using the IBED process. Test specimens were prepared similar to those prepared with pickling and anodizing, and subjected to mechanical testing. Durability tests were conducted after iterative testing to determine the resistance of the oxide surface film to corrosive environments.

EXPERIMENTAL PROCEDURES

In the first section, the non chemical technique (IBED) to pretreat aluminum alloy 2024-T3 for adhesive bonding is described. In the following sections the test procedures comparing IBED with the standard chemical pickling and anodizing (PAA) process are presented.

Ion Beam Enhanced Deposition

The oxide films formed on the surfaces of aluminum alloys must satisfy three criteria in order to promote strong adhesive bonding. These criteria are as follows:

- 1) The oxide films must adhere well to the aluminum alloy substrate,
- 2) The oxide films must be water and corrosion resistant, and
- 3) The outermost layers of the surface films must have a morphology that promotes adhesive bonding.

Two different types of IBED oxide film structures were deposited on aluminum alloy 2024-T3 substrates and examined. In both structures, the oxide films were initially ion beam mixed into the alloy substrate to promote strong oxide-substrate adhesion. In both structures, the bulk of the aluminum oxide (α Al_2O_3) film deposited was grown under the influence of a high energy inert (Argon) augmenting ion flux. This produced a dense microcrystalline (amorphous) oxide film, with good corrosion resistance. In the first type of structure the outer surface was designed to retain the morphology of the bulk oxide itself. This outer surface, which is microcrystalline or amorphous, may be smooth and may not have the micro roughness necessary for good adhesive bonding.

A second type of IBED oxide film structure was designed and deposited such that the outer surface presented a larger grained crystalline surface. In this case, the 1st few layers grew as larger grained alumina (α Al_2O_3), and presented a surface for adhesive bonding that has a crystalline, as opposed to a mostly amorphous structure.

Adhesive Bonding and Testing

Immediately following the various surface treatments, the surfaces were primed with the epoxy polyamide primer Cyanamid BR 127, and were adhesively bonded with the epoxy polyamide adhesive Cyanamid FM 73. Per manufacturer's instructions, the adhesive bonding was accomplished at a pressure of 40 psi and a temperature of 120°C. Adhesive bonding was accomplished over a period of 75 minutes.

Mechanical Testing

In order to assess the initial mechanical strength of the adhesive bonds, standard peel tests were conducted.

Peel Testing

The floating roller peel test (ASTM D 3167)¹¹ is intended to determine the relative peel resistance of adhesive bonds between one rigid adherend and one flexible adherend. Due to the nature of the specimen configuration and loading procedure the highest stresses are exerted on the interface between the flexible adherend and the adhesive which makes this test well suited to evaluate the quality of surface treatments. In this program, the flexible adherend was 0.025 inch thick 2024-T3 sheet with the various surface treatments, whereas the rigid adherend was the same for all tests, namely, 0.063 inch thick 2024-T3 sheet with HNO₃-HF pickling treatment.

Durability Testing

In order to evaluate the effect of aggressive environments on the durability of the surface oxides, various coated and uncoated test coupons were exposed to a 100% relative humidity (RH) water fog and a 5% NaCl salt fog environment (ASTM B-117)¹². These environments were selected because of their different effects on the oxide film. Specifically, water is known to have a potential detrimental effect on aluminum oxide by hydration resulting in disbonding and subsequent adhesive failure, with no or very little contribution of corrosion to the failure. Salt condensate, on the other hand, is extremely corrosive, and the failure mode of bonded or coated structures exposed to such an environment will be corrosion of the adherend or substrate.

Bare coupons were exposed to the water fog and NaCl salt fog environments in order to determine the resistance of HNO₃-HF pickled, PAA treated and IBED treated test coupons to water and chloride salts. The coupons were inspected and photographed at 24 hour intervals. The bare treated coupons were exposed to the salt fog for 48 hours and to the water fog for 288 hours.

In addition to exposure of the treated bare coupons, primer coated and scribed coupons were exposed to the two environments. The PAA and

IBED treated panels were coated with BR 127 primer, which was applied with a soft brush. After curing of the primer, the coupons were scribed diagonally with a scalpel according to ASTM D 1654¹³. The scribed coupons were inspected and photographed at 24 or 48 hour intervals up to a total exposure time of 336 hours.

RESULTS

The results of this investigation are divided into two separate sections: (1) the effect of surface treatments on the initial mechanical strength, and (2) the durability of some selected surface treatments.

Mechanical Strength

Aluminum alloy panels were pickled, using the HNO_3 - HF and the FPL processes, and phosphoric acid anodized. The results of mechanical strength tests of the chemically treated panels served as reference for the mechanical strength of ion beam cleaned, and IBED treated panels. The results of the mechanical strength testing of aluminum 2024-T3 panel with these treatments are presented in the following sections.

Pickling And Phosphoric Acid Anodizing

The peel strength of the pickled surfaces show relatively low peel values for the HNO_3 - HF treated surfaces with an average peel strength of around 25 lbs/inch, with FPL etched specimens yielding higher peel strengths, ranging from about 25 to 45 lbs/inch. High peel strengths were obtained on PAA treated specimens. Figure 3 which shows a typical peel diagram, indicates peel strengths of phosphoric acid anodized specimens in the range of 70-90 lbs/inch. These values are well above the minimum peel strength specified by the manufacturer for the FM 73 adhesive.

Ion Beam Enhanced Deposition

The IBED film with a dense microcrystalline (amorphous) morphology had a very smooth outer surface and provided little mechanical anchoring for adhesive bonding. Thus, the peel tests resulted in relatively low peel strength value. The IBED film with the larger grained crystalline outer

surface was much rougher allowing more mechanical anchoring. This treatment resulted in high peel strengths as shown in Figure 4.

Durability

The durability of an adhesive bond or organic coating interface is an essential characteristic of an adhesively bonded or painted structure. In order to assess the corrosion resistance of the different oxide films and the durability of adhesive/organic primer - aluminum oxide interface, testing in a water fog and a 5% NaCl salt fog environment was performed.

PAA and IBED treated, uncoated coupons and PAA and IBED treated coupons, coated with BR 127 primer and scribed, were exposed to the water and salt fog environments.

Uncoated Coupons

The treated, uncoated specimens exposed to the water fog were inspected and photographed at frequent intervals. As indicated in Figure 5, the PAA treated surface is not resistant to the wet environment. Pitting attack was observed after as little as 48 hours of exposure. On the other hand, IBED treated surfaces (both with the 2000 Ångstrom and 5000 Ångstrom thick oxide film) resisted the wet environment much longer, and only after 120 hours of exposure some signs of pitting was observed.

Similar specimens were exposed to the 5% NaCl salt fog. The photographs in Figure 6 clearly indicate pitting of the pickled and anodized surfaces after only 5 hours. After 48 hours corrosion was widespread on these surfaces. The IBED treated surfaces showed much higher resistance to the salt fog with some minor attack occurring after 24 hours. Even after an exposure time of 48 hours, pitting corrosion on the IBED surfaces was relatively light.

Coated Coupons

Treated test coupons were coated with the epoxy polyamide primer BR 127. After curing, they were scribed with a sharp instrument such that the substrate metal was exposed. This test provides a good indication of

the quality of adhesion between the aluminum oxide and the primer. Figure 7, which show photographs of IBED treated and anodized coupons exposed to water and salt fog, demonstrate that the IBED treated coupons resist the wet environment much longer than the anodized coupon. Corrosion of the anodized panel started only after 24 hours and spread rapidly under the coating. Corrosion was also found in the grooves of the IBED treated panel, but underfilm corrosion was observed only after an exposure time of 216 hours.

DISCUSSION

The results of this work have clearly demonstrated the feasibility of Ion Beam Enhanced Deposition (IBED) as a non chemical alternative to Phosphoric Acid Anodizing (PAA) as pretreatment for adhesive bonding. The program has succeeded in developing a surface that has high mechanical strength, i.e. peel strength, which is equivalent to that obtained by PAA. Moreover, the corrosion resistance of the IBED treated surface exceeded that of the PAA treated surface.

The parameters that are essential for good adhesion and bond line durability were defined. The IBED process allowed the formation of a highly dense amorphous aluminum oxide with no distinct interface between the aluminum alloy substrate and the aluminum oxide which results in very strong bonding between the alloy and the oxide. In order to achieve a surface that would provide mechanical anchoring along with durability, the IBED aluminum oxide film was deposited with a large grained crystalline outer surface thus providing good mechanical anchoring features. The oxide deposition and growth parameters used to achieve good adhesive and durability properties, were as follows:

- 1) Clean the surface with a degreasing medium as good as or better than acetone-methanol.
- 2) Apply a 5000 Ångstrom thick aluminum oxide film directly onto the cleaned surface, having a large grained crystalline outer surface.
- 3) Following the IBED treatment, the vacuum chamber is backfilled with dry nitrogen gas, followed immediately with priming of the surface.

It was suspected that the above described surface was susceptible to water uptake and subsequent hydration, which could destroy the anchoring features of the surface. To minimize exposure of the oxide surface to humid air, the processing chamber was back filled with dry nitrogen, after which the part surface was immediately primed with the epoxy polyamide primer. Once the surface was primed, no effect of humidity or water on the bondability of the surface was found.

Although the IBED process was proven feasible, the process parameters need to be refined, and a mechanistic understanding of the growth of both the amorphous barrier layer and the crystalline top layer is required to implement this procedure with a high level of confidence. Also, the parameters for scaling up the process such that full scale aircraft components can be treated, need to be defined such that implementation of the process can proceed at as low a risk as possible.

ACKNOWLEDGEMENT

This work was performed under U.S. Air Force Contract No. F33615-93-C-5323 which was administered under the technical direction of Mr. Theodore J. Reinhart, WL/MLSE.

REFERENCES

1. F. Keller, M. S. Hunter, and D. L. Robinson, "Structural Features of Oxide Coatings on Aluminum," J. of Electrochemical Society, September, 1953, pp. 411-419.
2. P.F.A. Bijlmer, "Influence of Chemical Pretreatments on Surface Morphology and Bondability of Aluminum," J. Adhesion, 1973, Vol. 5, pp 391-331.
3. T. P. Remmel, "Characterization of Surfaces Prior to Adhesive Bonding," Report No. NOR-76-58, July 1976, 92pp, Northrop Corp, Hawthorne, CA.
4. R. E. Herfert, "Fundamental Investigation of Anodic Films on as a Surface Preparation for Adhesive Bonding," Report No NOR-76-101, August, 1976, 111 pp, Northrop Corp, Hawthorne CA.
5. W. L. Russell and C.A.L. Westerdahl, "Characterization of Chromic-Acid Anodized 2024-T3 Aluminum Adherents," Report No. ARLCD-TR-77040, September 1977, 35 pp, Army Armament Research and Development Command, Dover, NJ.
6. T. Smith, "Surface Treatment for Aluminum Bonding," Report No. SC 5180. 17FTR, October 1979, 204 pp, Rockwell International, Thousand Oaks CA.
7. J. D. Venables, D. K. McNamara, J. M. Chen, and T. S. Sun, "Oxide Morphologies On Aluminum Prepared for Adhesive Bonding Applications of Surface Science," Vol 3:1, 1979, p 88.
8. T. S. Sun, G. D. Davis, J. D. Venables, and J. M. Chen, "Effects of Surface Morphology and Chemical Composition on the Durability of Adhesively Bonded Aluminum Structures," Final Report MMLTR81-45C, October 1981, Martin Marietta Corp. Baltimore MA, pp 34.
9. D. B. Arnold, and C. S. Carter, "Service History of Phosphoric Acid Anodized Aluminum Structure," 27th National SAMPE Symposium, 1982, Asuza, CA p. 769.

10. Radiation Effects On Solid Surfaces, Manfred Kaminsky, Ed., American Chemical Society (Advances In Chemistry Series #158), Washington D.C., 1976, pp. 1-63.
11. "Standard Test Method for Floating Roller Peel Resistance of Adhesives," ASTM D3167-76 (1986).
12. Standard Method of Salt Spray (Fog) Testing, ASTM, B117-85.
13. "Evaluation of Painted or Coated Specimens Subject to Corrosive Environments," ASTM D1654 (1984).

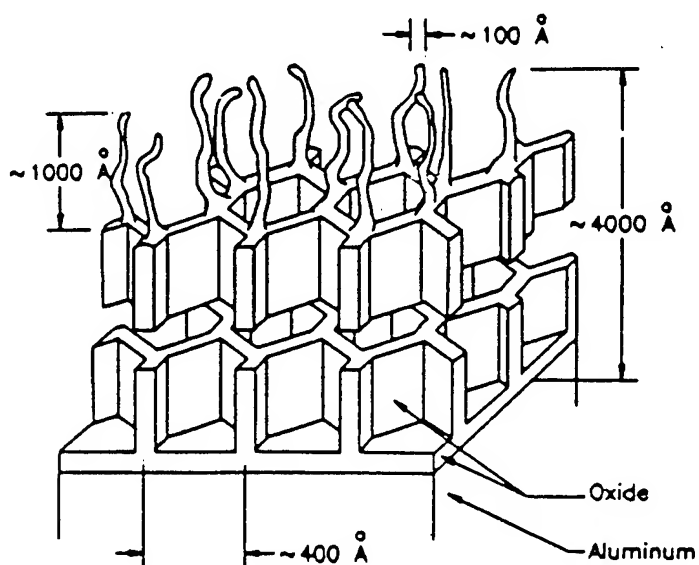


Figure 1. Schematic Representation of Oxide Morphology on a Al Surface After Phosphoric Acid Anodizing

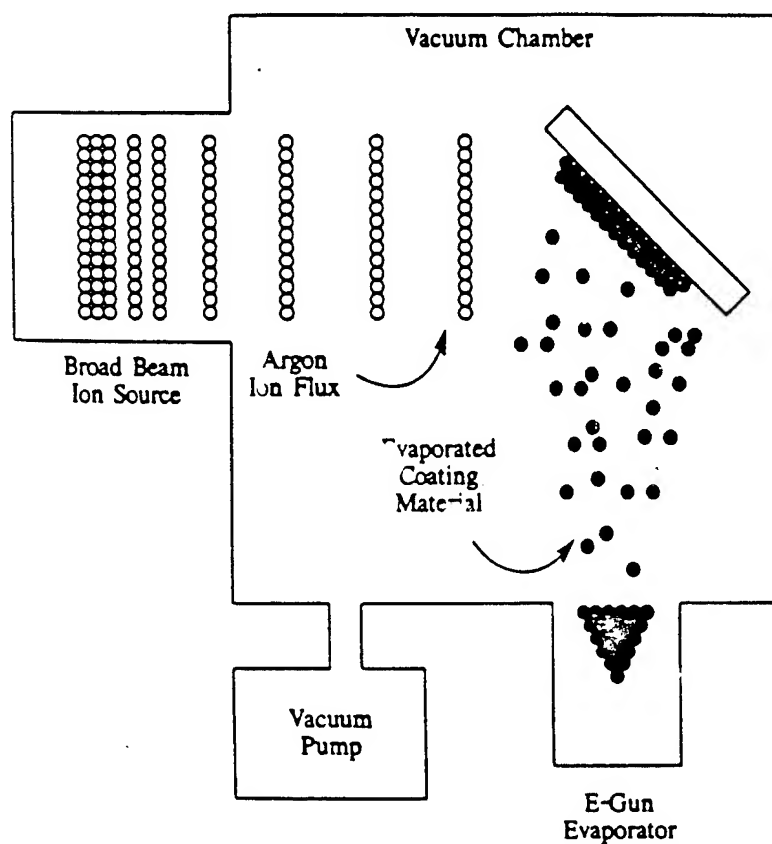


Figure 2. Schematic Drawing of Ion Beam Enhanced Deposition (IBED Process)

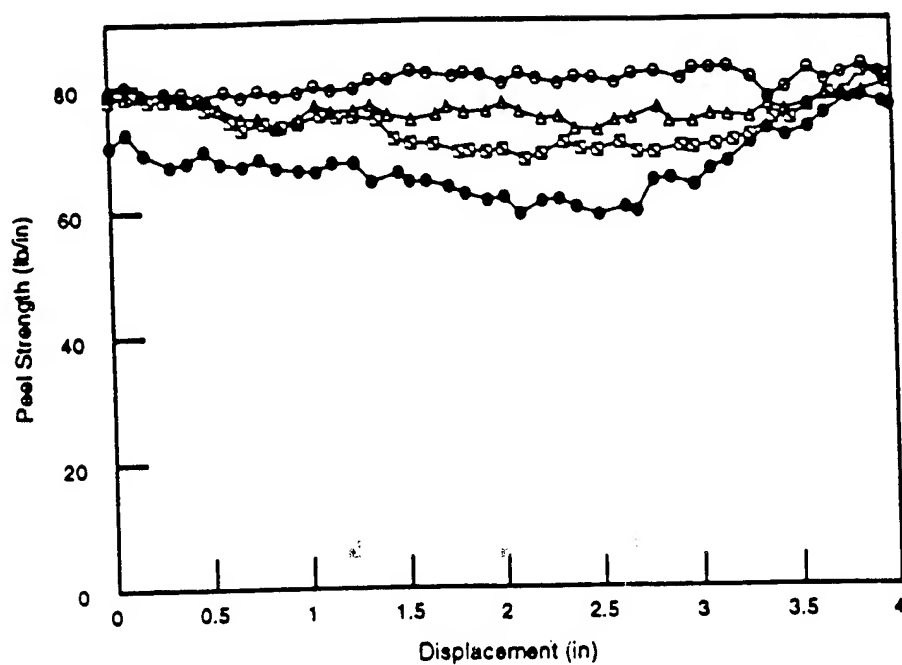


Figure 3. Peel Strength Diagram of Aluminum Alloy 2024-T3 with PAA Treated Surface

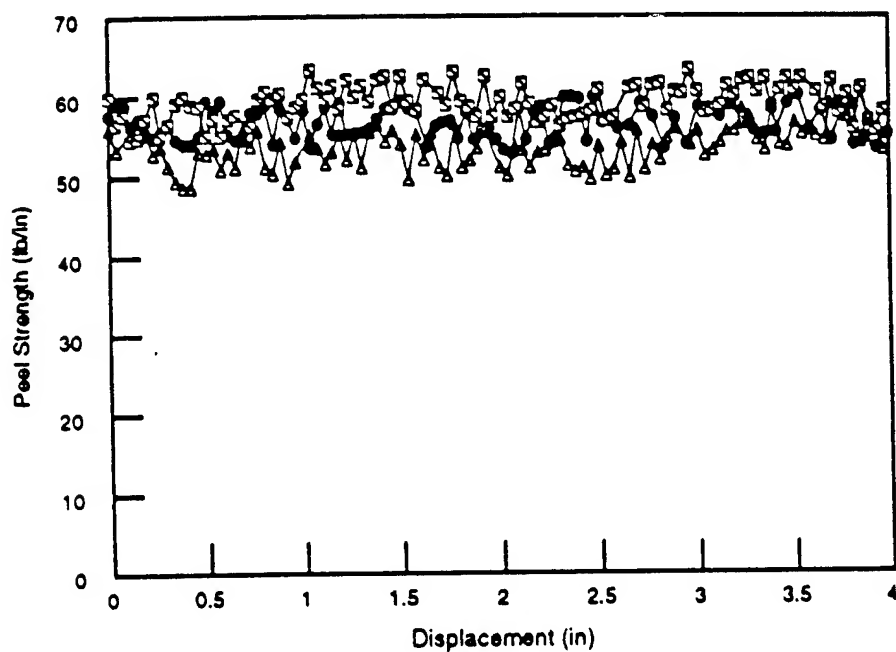


Figure 4. Peel Strength Diagram of Aluminum Alloy 2024-T3 with a 4000Å IBED Barrier Film and a 1000Å Crystalline Top Film (After the Treatment the Vacuum Chamber was Backfilled with Dry N₂ Gas and the Surface was Primed Immediately)



**PAA Bare - 48 Hours
100% RH**



**PAA Bare - 120 Hours
100% RH**



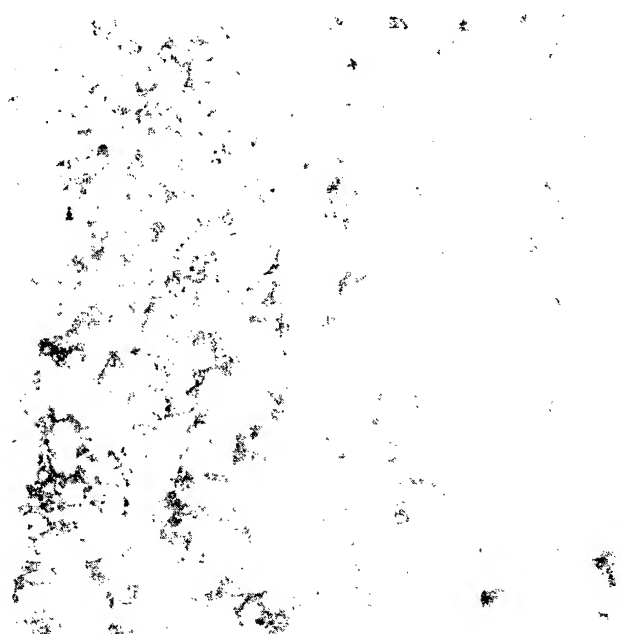
**5000 IBED Bare - 48 Hours
100% RH**



**5000 IBED Bare - 120 Hours
100% RH**

Figure 5. Photographs Of PAA And IBED Treated Aluminum Alloy 2024-T3 Exposed To Water Fog For 48 Hours And 120 Hours, Respectively

PAA



IBED

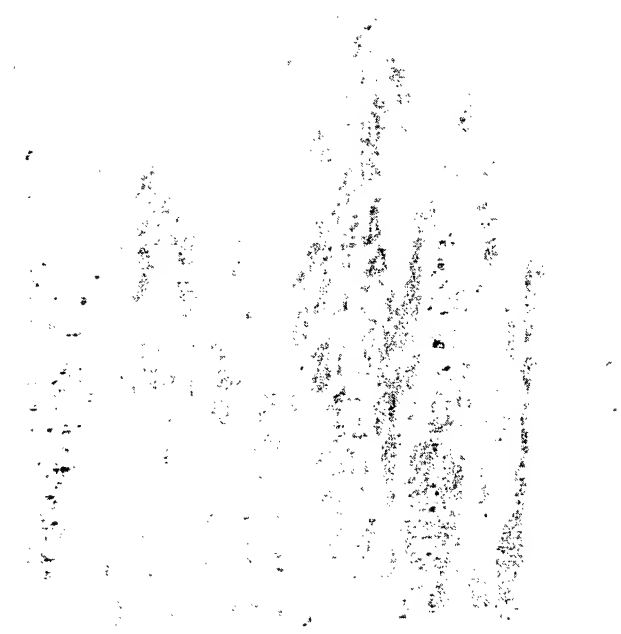


Figure 6. Photographs Of PAA And IBED Treated Aluminum Alloy 2024-T3 Exposed To A 5% NaCl Fog For 48 Hours

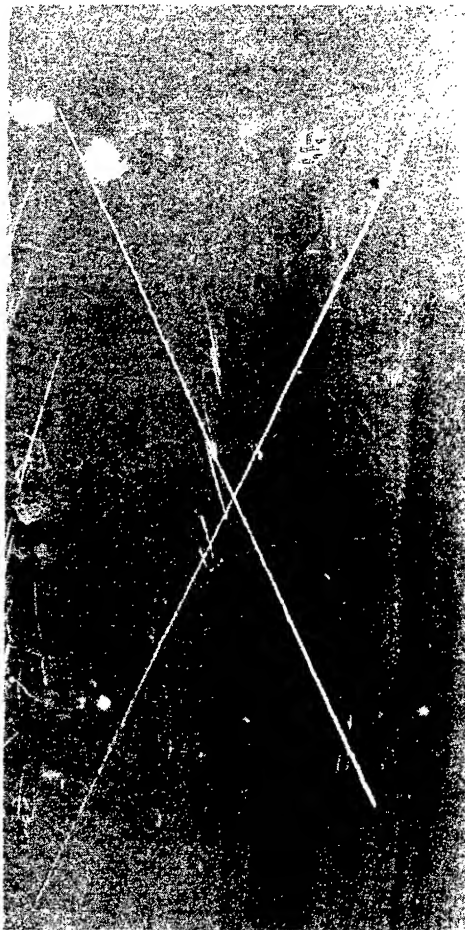


PAA Water

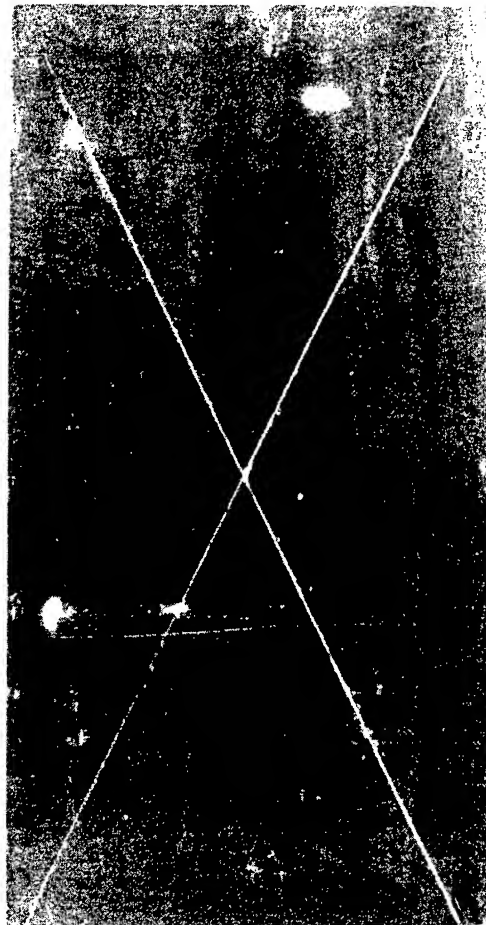


PAA - 5% NaCl

Figure 7. Photographs Of PAA Treated Aluminum Alloy 2024-T4 Coated With BR127 Primer And Scribed After 216 Hour Exposure To Water And Salt Fog, Respectively



IBED Water



IBED - 5% NaCl

Figure 7, Continued.

Photographs Of IBED Treated Aluminum Alloy 2024-T4
Coated With BR127 Primer And Scribed After 216 Hour
Exposure To Water And Salt Fog, Respectively

Verification of the Boundary Element Modeling Technique for Cathodic Protection of Large Ship Structures

by Harvey P. Hack^{*} and Robert M. Janeczko
Carderock Division, N. S. W. C., Annapolis, MD 21402-5067

ABSTRACT

Boundary Element computer modeling is gaining acceptance as a tool for predicting the distribution of cathodic protection potentials on a variety of large immersed structures. This technique should be valuable for placement of cathodic protection anodes and reference cells on ship hulls. Much has been published on this technique, including experimental verification on a laboratory scale. However, there has been little published information on experimental verification of the model predictions on large structures, especially for ships.

A 42-foot (14-m) barge was outfitted with a steel "rudder", copper-based alloy "propeller", zinc sacrificial anodes, and an array of reference cells to measure the distribution of potential over the surface of the hull and appendages. The barge was exposed in natural seawater for four months. A computer model was developed to predict the distribution of protection, using a boundary element analysis program (BEASY) and long-term, potentiostatic polarization curves as boundary conditions. The model predictions are compared to the measured potential distributions.

Polarization curves are presented which give good agreement between model predictions and the actual measurements on the uncoated steel barge hull under low flow conditions. More information on polarization behavior for surfaces under flowing conditions is needed for accurate predictions to be made over a full range of ship operating conditions.

ADMINISTRATIVE INFORMATION

This project was supported by the Carderock Division, Naval Surface Warfare Center Ship and Submarine Materials Block Program under the administration of Code 0115. The program manager is Mr.

Ivan Caplan. The work was conducted in the Marine Corrosion Branch, Code 2813, under the direction of Mr. Robert Ferrara. Outfitting and testing of the barge were conducted by the staff of the LaQue Center for Corrosion Technology under the direction of Mr. Dennis Melton. Help with computer programming difficulties was given by Jon Trevelyan of Computational Mechanics, Inc.

INTRODUCTION

Submerged steel structures, such as platforms and ships, usually require cathodic protection to minimize corrosion damage in seawater. This protection is provided by impressed current or sacrificial anodes located at discrete points on the structure. The level of protection is greatest near the anodes and falls off at large distances[1]. The non-uniformity of protection can lead to overdesign of the protection system. This is because the overall level of protection must be increased until the point with the least protection on the structure is receiving adequate protection. This overdesign can lead to wasted current or anode material, and can also lead to paint blistering or hydrogen embrittlement in areas near the anodes. Cathodic protection system designers therefore strive for uniformity of protection on the structure.

Uniformity of protection was, until recently, arrived at in a cathodic protection system design primarily by the use of rules-of-thumb and empirical experience. More recently, construction of physical scale models has been used with some success to optimize placement of anodes[2]. In many cases the use of physical scale modeling will produce results of sufficient accuracy for optimizing anode placement. There is some theoretical basis for a belief that there are inherent inaccuracies in this type of modeling for large structures in seawater, however[3]. In addition, effects of flow on moving structures are difficult to reproduce in scale model tests. For these reasons, as well as for reasons of cost of model construction, the use of computers to predict uniformity of protection is emerging as a viable alternative. Although computer modeling accuracy has been verified in small scale laboratory situations[4-5], there is to date little published evidence of verification of this technique on large structures.

Boundary element computer analysis is similar to finite element analysis in that the LaPlace Equation is solved within the structure of interest after first defining conditions at the edge (boundary).[6] The structure of concern is divided into small elements, or discretized, and a series of simultaneous equations is obtained from the LaPlace

Equation, one for each element.[7] The boundary element method requires that only the edges of the structure be modeled.[5]

In corrosion, the boundary conditions are the relationships between current and potential (called polarization behavior) for the materials and environment. Polarization behavior may not be single-valued or monotonic, requiring special consideration in programming.[8] This area of work is so new that only two companies have boundary element programs that can handle corrosion boundary conditions, and one of these programs has other limitations.[9] The other program, called Boundary Element Analysis System (BEASY) was used for this study.

The intent of this paper is to illustrate that computer modeling can accurately predict the distribution of cathodic protection on large structures resembling ship hulls in seawater. The polarization curves used to obtain the best agreement between the computer model and measurements on a large structure are also presented.

EXPERIMENTAL PROCEDURE

BARGE TESTS

Accuracy of computer modeling for ship hulls was investigated by using an 18 by 42-foot (6 by 14-m) steel barge to compare with the computer model. The barge was exposed without coatings for 4 months.

The barge was first hauled and sand blasted. It was then fitted with sacrificial anodes as follows: a group of six anodes at the stern midline, a group of eight anodes at the center midline with a group of four additional anodes on each end of the central grouping, and two groups of six anodes each at the outer edges on both sides. The anode groups were electrically isolated from the barge and externally connected to allow measurement of the protection current each group provided. A copper-nickel plate, roughly 32 by 36-inches (0.8 by 0.9-m) was suspended 0.9-feet (0.3-m) below the keel at the aft portion of the barge and oriented athwartships. This plate was designed to simulate a copper-alloy propeller and the plate-to-hull area was set to be representative of a real ship. A second plate, 37 by 38.5-inches (1.0 by 1.0-m) square made of steel, was suspended with its leading edge even with the stern, 3-feet (1-m) behind the first, and with its top edge parallel to the stern and at a height even with the keel. The area and orientation of this plate were set to simulate the rudder of a real ship. Both plates were wired back to the hull so that protection current could be measured. Finally, the barge was outfitted with an array of 34

silver/silver-chloride reference cells to measure the uniformity of protection. The locations of the anodes and reference cells are shown in figure 1.

After outfitting, the barge was placed in the water on the Cape Fear River in Wilmington, NC, with the port and starboard anode groups disconnected. This is brackish water with a conductivity of 145- μ mho/cm (0.81 ppt chloride). The barge was then towed to the test site in Banks Channel near Wrightsville Beach, NC. This location has full strength seawater with a conductivity of 50-mmho/cm (34.99 ppt chloride). The barge was moored at a location where the mean depth was roughly 11-feet (3.5-m). A series of current and potential measurements were then taken daily except for weekends until the total exposure period elapsed. Initially the anode groups at the edges of the barge were not connected, but it was determined that the barge required the additional anodes to get adequate protection, and so these anode groups were connected after eight days. A total exposure period of 4 months was chosen because earlier tests at this location had shown that stability of protection current was reached in that time[10]. At the conclusion of the test, all but the aft set of zincs were disconnected to get a greater potential gradient along the barge length. Measurements were taken after the protection system had been allowed to stabilize for 7 days. The barge was then towed back to the shipyard where measurements were taken in the lower conductivity water for an additional two days.

Besides monitoring currents from each bank of zincs, currents to the rudder and prop plates and potentials of the reference cells, weight loss data was taken for each zinc to compare to integrated currents. This gave a check on the current measurement procedure and allowed for determination of zinc efficiencies.

COMPUTER MODEL

The exact barge geometry was modeled using the Boundary Element Analysis System (BEASY). This program is designed for corrosion problems and can handle time-dependent analysis[11], although that feature was not used in this study. The element structure used for the barge is shown in figure 2. The model was symmetric about the centerline and waterline, and non-conducting surfaces were placed at the mud line and at a distance of 330-feet (100-m) around the barge. 330-feet was chosen as it was expected that the potential gradients would be minimal at that distance. These surfaces were

necessary since the program required that the model be totally enclosed.

The zinc surfaces were initially assigned the polarization conditions shown in figure 3, the steel surfaces were initially assigned the conditions shown in figure 4, and the copper-nickel surfaces assigned the conditions in figure 5. These polarization curves were obtained from long-term potentiostatic polarization tests conducted in a previous project[10].

RESULTS AND DISCUSSION

BARGE TEST

Figure 6 shows the current, in Amperes, for each of the cathode surfaces. As expected, the current mostly went to the hull. Currents to all cathode surfaces initially began to fall, but jumped upwards after eight days when the two edge anode groups were connected. Current continued to fall throughout the exposure, probably due to the buildup of calcareous deposits and fouling. Another drop in current was experienced near the end of the exposure when all of the anode groups except one were disconnected. Total current at the conclusion of the exposure was roughly one third of the maximum current experienced after all anode groups were first connected. Figure 7 shows the output of each of the anode groups during the same time period. Current output was zero from the two edge groups until they were connected at day eight, and was the highest thereafter, probably because each group was so far from any other group. Near the end of the exposure when all other anode groups were disconnected, current from the aft group increased to try to make up for the difference.

Weight losses of each of the anodes are given in table 1. These values are summed for each group and compared to the integrated current for that group to calculate an electrochemical efficiency for each anode group and for all anodes on each barge. Efficiencies for each group ranged from 65 to 114 percent, indicating that the current measurement or integration technique was not sufficiently accurate. This is probably due to sampling times for current data of 1-3 days being too high. The average efficiencies for the anodes were 86%, which is low for zinc anodes. Initial high currents occurred for several hours before the first readings were taken, and currents could not be read during the two towing operations for each exposure. Both of these would lead to lower measured efficiencies than were actually experienced by the anode material.

COMPUTER MODEL

It was desired to determine the sensitivity of the computer solutions to changes in the input polarization curve shape in order to see how accurately polarization behavior must be determined in order to get an accurate solution. To this end, a number of variations in polarization curve shape were tried during the modeling effort for the uncoated barge. These included changing current magnitudes for the anodic and cathodic materials individually by multiplying the currents for all points for a given material by the same factor, and changing currents for individual points on the steel cathode in order to change the magnitude and slope of the curve in the 900-1000 mV range.

The shape and magnitude of the polarization curves used in the analysis had little effect on which area of the structure was predicted to receive the most or the least cathodic protection. Curve shape and magnitude outside of the range where the predicted potentials will lie also had no effect on the results of the analysis. Cathodic curves affected the predicted currents more than predicted potentials. The opposite was true for the anodic curves, where the predicted potentials were affected more than the predicted currents. Finally, it was easier to predict potentials accurately than to predict currents accurately.

COMPUTER PREDICTIONS VERSUS ACTUAL MEASUREMENTS

Protection Potentials

Use of the original polarization curves for uncoated, unfouled steel did not result in good agreement between the computer prediction and the measured potentials for the uncoated barge. The best agreement was obtained if the computer model was run under the assumption that 50% of the cathode surfaces were electrochemically blocked by fouling. This is consistent with the amount of hard fouling observed visually, and was accomplished by reducing the current densities of the cathode surfaces by 50% in the polarization curves used as boundary conditions. The result of this assumption was an agreement between measured and predicted potentials at the various reference cell locations which was within 20 mV except for three locations which were within 60mV. These three locations, at cells 6, 11, and 23, were all predicted to have more protection than actually measured. Since these cells were all at the waterline, this effect could be due to wave action wetting more hull surface than was modeled. This is excellent agreement considering the number of reference cells and complexity of the barge structure. The measured and predicted

potentials are plotted together in figure 8. The reference cells in this figure are in no particular order.

Currents

Table 2 lists the measured and the predicted currents for the barge hull, rudder plate, propeller plate, and currents from individual zinc groupings. The predicted currents were always a factor of 1.4 to 1.5 higher than those measured, and the relative amount of current from or to each area is the same for the predictions and the measurements. This shows that current distributions are easier to predict than absolute values of current. The factor of 1.4-1.5 is reasonable, and is in the right direction for a conservative design for a cathodic protection system.

CONCLUSIONS

Based on the BEASY computer model predictions and actual measurements on a 42-foot (14-m) barge simulating a steel ship, the following conclusions can be drawn:

1. Computer modeling accurately predicts potential distributions and currents for uncoated barges when the polarization curves are adjusted for fouling under low flow conditions.
2. It is easier for a computer model to accurately predict potentials than currents.
3. If inaccurate polarization data is used in the computer model, resulting in disagreement between predicted and actual magnitudes of potentials and currents, the areas of the most and the least protection are still predicted accurately.

REFERENCES

1. L. L. Shreir, Ed., Corrosion - Volume 2 - Corrosion Control, Chapter 11, Newnes-Butterworths, Boston, MA, ©1976.
2. D. J. Tighe-Ford, J. N. McGrath, and L. Hodgkiss, "Design Improvements for a Ship's Impressed Current Cathodic Protection System Using Dimension and Conductivity Scaling (DACs)," Corrosion Prevention and Control, October 1985.
3. H. P. Hack, "Scale Modeling for Corrosion Studies," Corrosion, Vol. 45, No. 7, July 1989.
4. P. Doig and P. E. J. Flewitt, "A Finite Difference Numerical Analysis of Galvanic Corrosion for Semi-Infinite Linear Coplanar Electrodes," Journal of the Electrochemical Society, December 1979, pp. 2057-2063.
5. J. W. Fu and J. S. K. Chow, "Cathodic Protection Designs Using an Integral Equation Numerical Method," Materials Performance, Vol. 21, No. 10, October 1982.
6. C. A. Brebbia, Ed, The Boundary Element Method for Engineers Computational Mechanics, Woburn, MA, 1980.
7. M. A. Warne, "Applications of Numerical Analysis Techniques," Proceedings of the Conference on Cathodic Protection Theory and Practice - The Present Status, Coventry, U. K., April 1982.
8. R. G. Kasper, "Theoretical and Experimental Comparisons of Nearfield Electrogalvanic Fields Due to Nonlinear Polarization Layers," NUSC Technical Report 7299, February 1985.
9. J. R. Scully and H. P. Hack, "Prediction of Tube-Tubesheet Galvanic Corrosion Using Long Term Electrochemical Polarization Data," in Galvanic Corrosion, H. Hack, Ed., STP 978, ASTM, 1988.
10. H. P. Hack and J. R. Scully, "Galvanic Corrosion Prediction Using Long and Short Term Polarization Curves," Corrosion, Vol. 42, No. 2, February 1986.
11. R. A. Adey and S. M. Niku, "Boundary Element Simulation of Galvanic Corrosion - the Story of a Major Success for Boundary Elements," Boundary Elements X, Vol. 2: Heat Transfer, Fluid Flow and Electrical Applications, C. A. Brebbia, Ed., Computational Mechanics Publications, Ashurst, UK, 1988.

Table 1 - Anode Weight Losses for the Barge

ANODE NO	ORIG WEIGHT, g	FINAL WEIGHT, g	WEIGHT LOSS, g	GROUP WEIGHT LOSS, g	THEORETICAL WEIGHT LOSS FROM CURRENTS, g (efficiency)
1	4996.8	3794.6	1202.2	6042.8	STERN 5180.6 (86%)
2	4768.0	3874.1	893.9		
3	4823.1	3862.0	961.1		
4	4813.0	3921.1	891.9		
5	4870.3	3946.4	923.9		
6	4801.2	3631.4	1169.8		
7	4862.2	3592.4	1269.8	added to anode.s 19-22	ENDS added to anodes 19-22
8	4932.1	3981.1	951.0		
9	4724.4	3830.6	893.8		
10	4780.5	3859.8	920.7		
11	4857.2	3991.9	865.3	7894.6	MIDDLE 5098.1 (65%)
12	4954.3	3962.0	992.3		
13	4863.7	3650.3	1213.4		
14	4929.8	4019.7	910.1		
15	4791.1	3659.9	931.2		
16	4905.3	3965.4	939.9		
17	4773.9	3889.2	884.7		
18	4809.3	3651.6	1157.7		
19	4850.2	4022.7	827.5	7407.4	ENDS 6089.0 (82%)
20	4844.2	4144.4	699.8		
21	4758.4	3939.8	818.6		
22	4983.6	3957.4	1026.2		
23	4462.2	3710.3	751.9	4572.2	STARBOARD 5228.2 (114%)
24	4640.9	3977.3	663.6		
25	5000.8	4236.7	764.1		
26	5047.0	4242.7	804.3		
27	4978.9	4153.4	825.5		
28	4786.0	4023.2	762.8		
29	4842.0	4135.3	706.7	5222.4	PORT 5223.9 (100%)
30	4655.2	3926.3	728.9		
31	4875.2	3692.2	1183.0		
32	4666.1	3791.3	874.8		
33	4766.1	3885.1	881.0		
34	4914.2	4066.2	848.0		
TOTAL	164327.2	133187.8	31139.4	31139.4	26819.8 (86%)

Table 2 - Currents for Barge, Amperes

COMPONENT	MEASURED	PREDICTED	DIFFERENCE FACTOR
Hull	4.20	5.79	1.38
Propeller Plate	0.08	0.11	1.38
Rudder Plate	0.07	0.10	1.43
Outboard Zincs	-0.92	-1.26	1.37
Aft Zincs	-0.74	-1.12	1.51
End Midships Zincs	-0.96	-1.43	1.49
Center Midships Zincs	-0.81	-1.24	1.53

Figure 1 - Anode and Reference Cell Locations on Test Barge

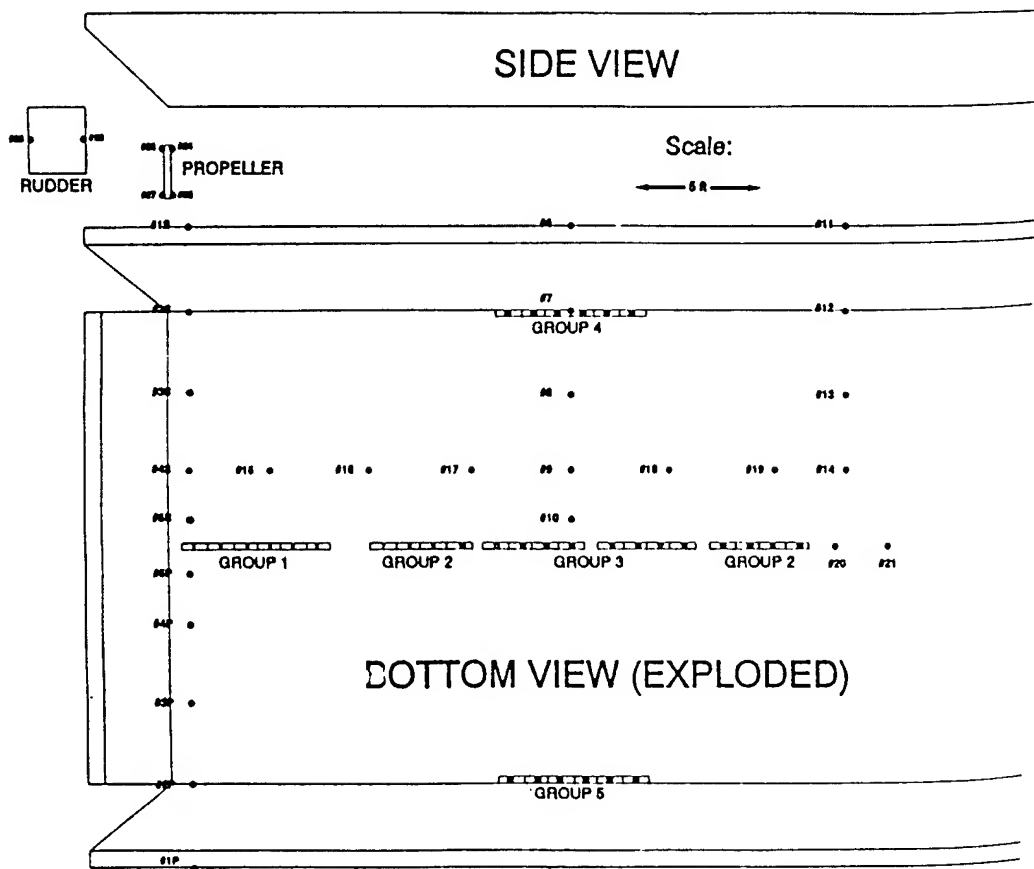


Figure 2 - Boundary Element Grid

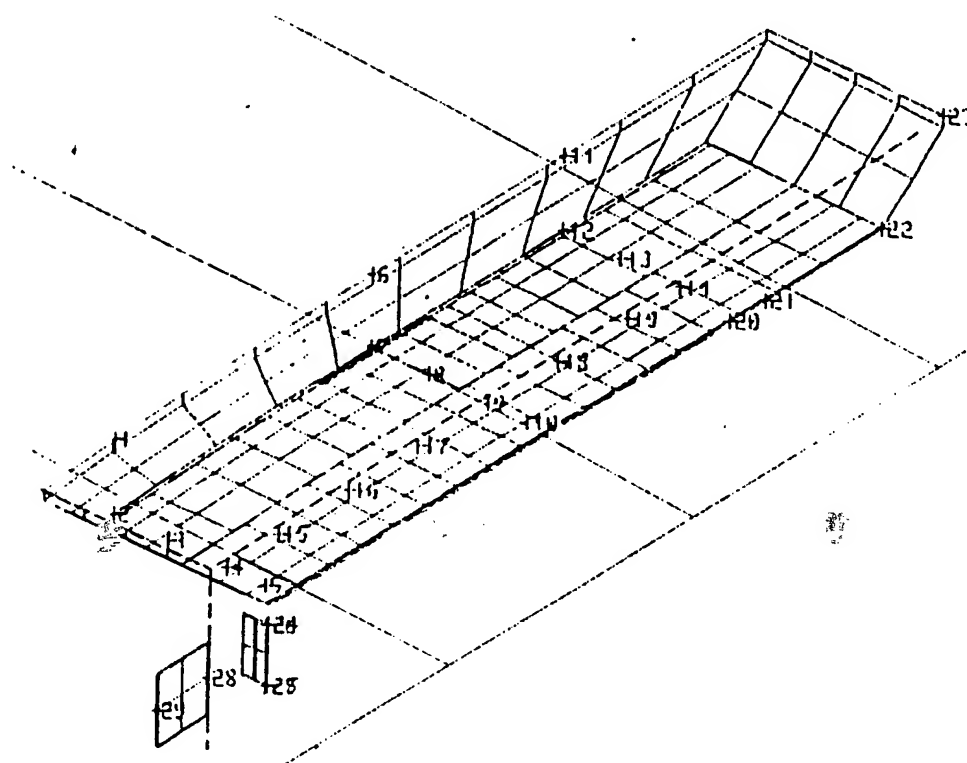


Figure 3 - Zinc Polarization Data

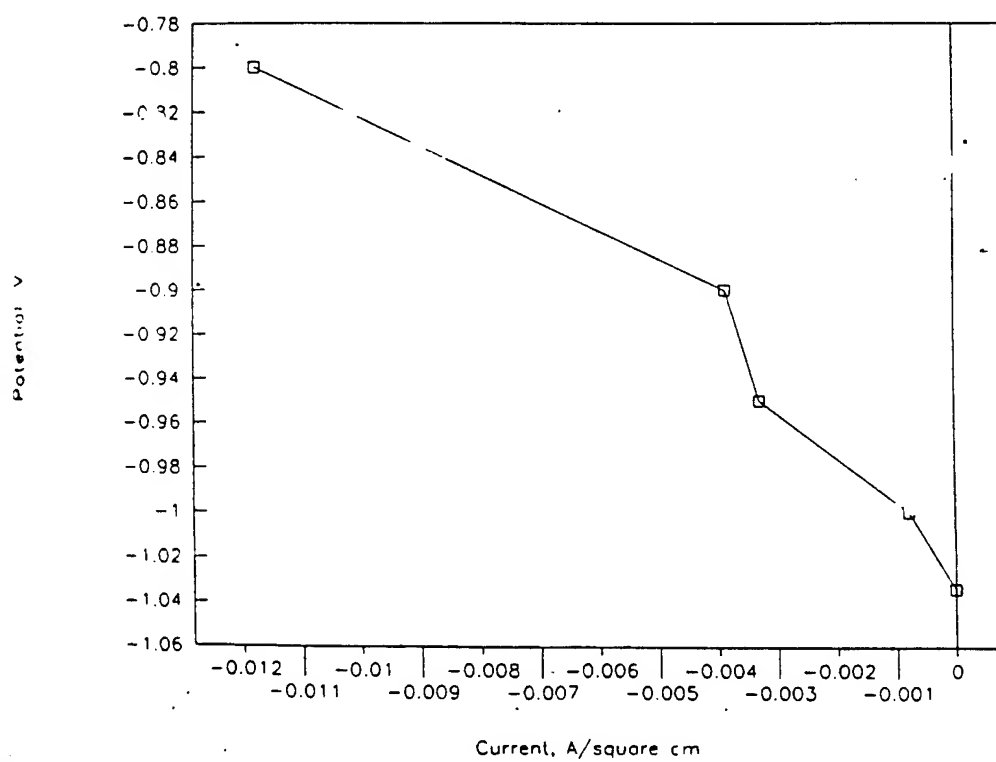


Figure 4 - Steel Polarization Data

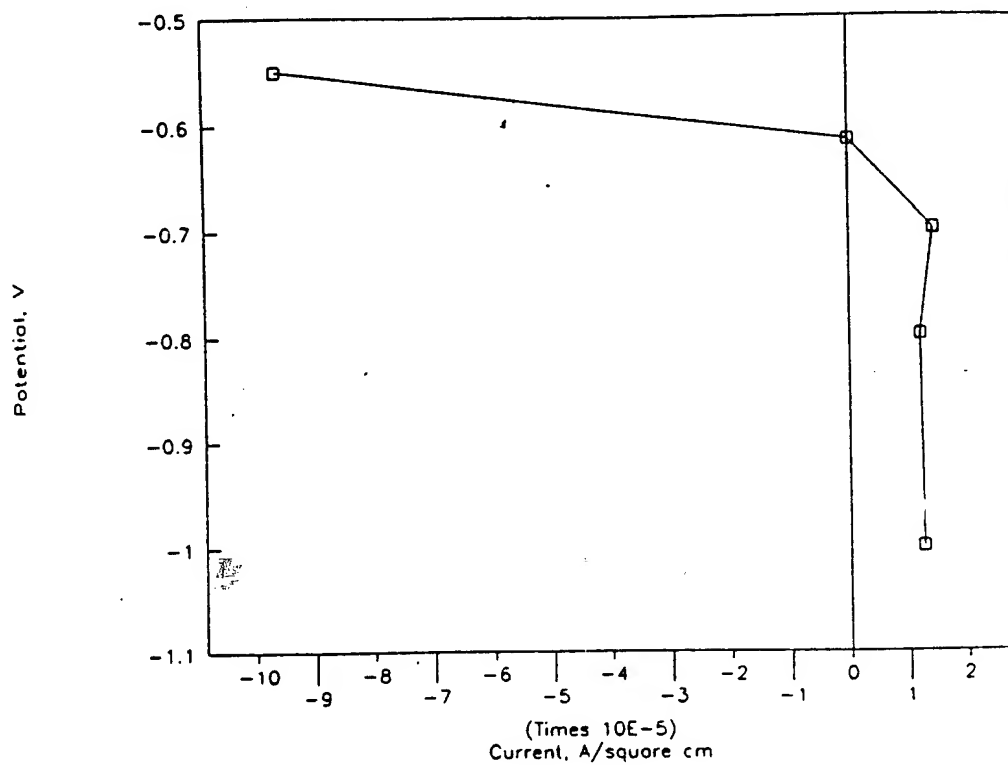
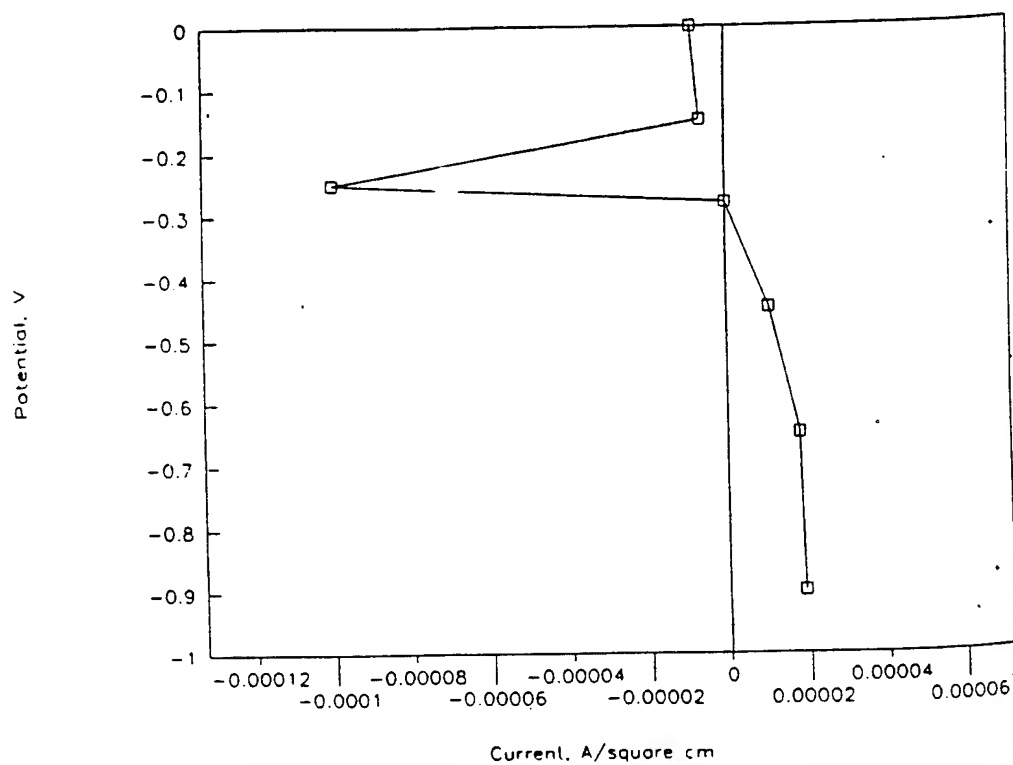


Figure 5 - Copper-Nickel Polarization Data



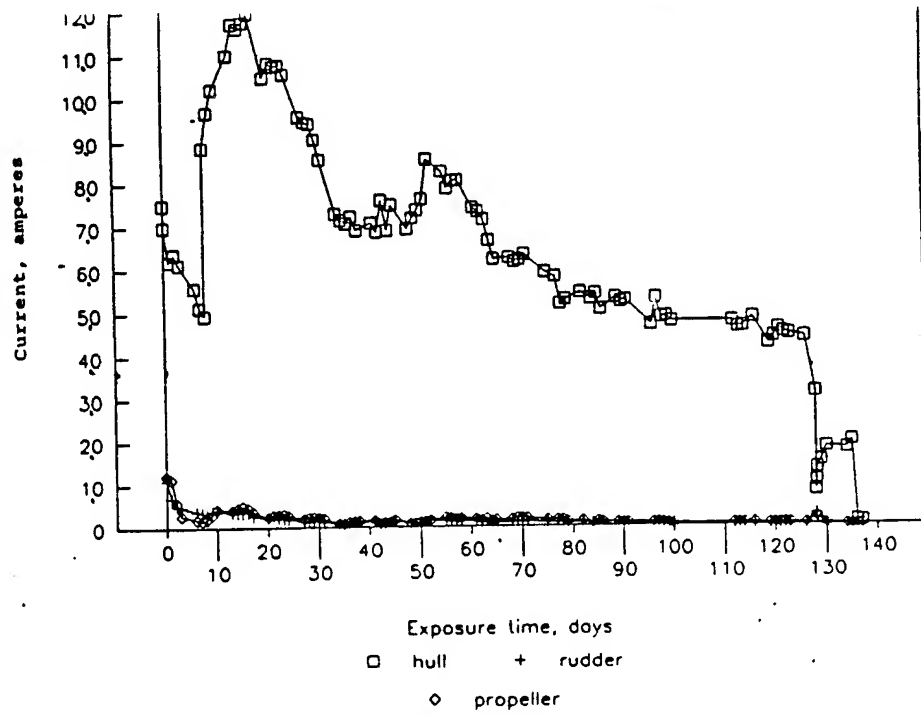


Figure 7 - Anode Currents

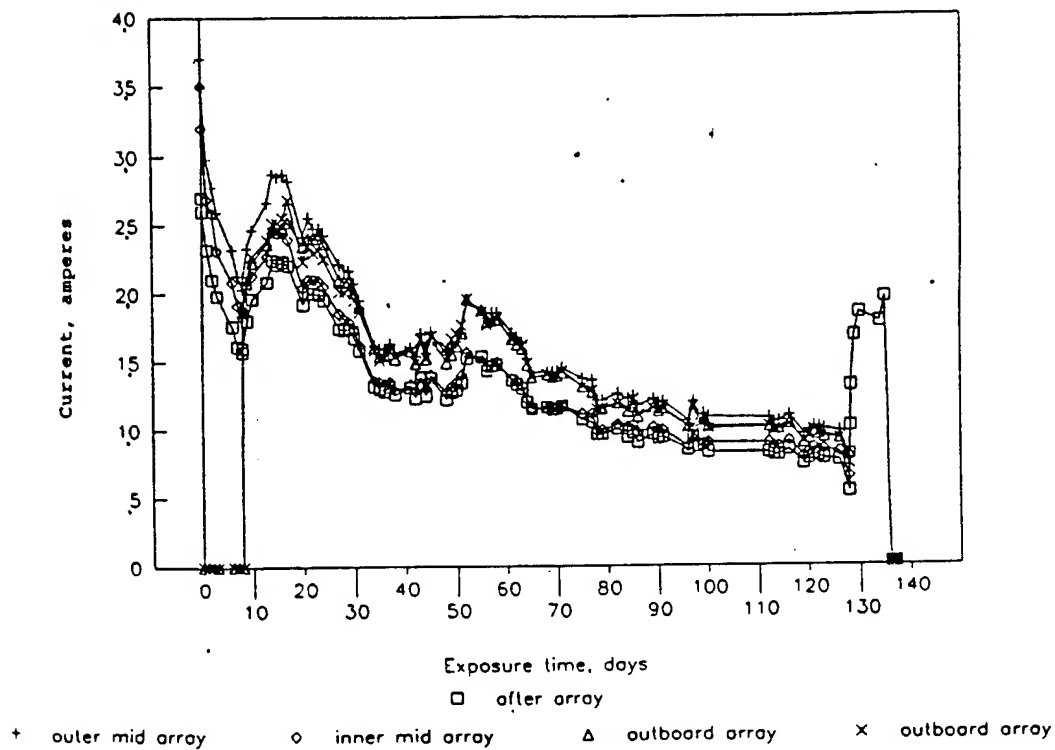
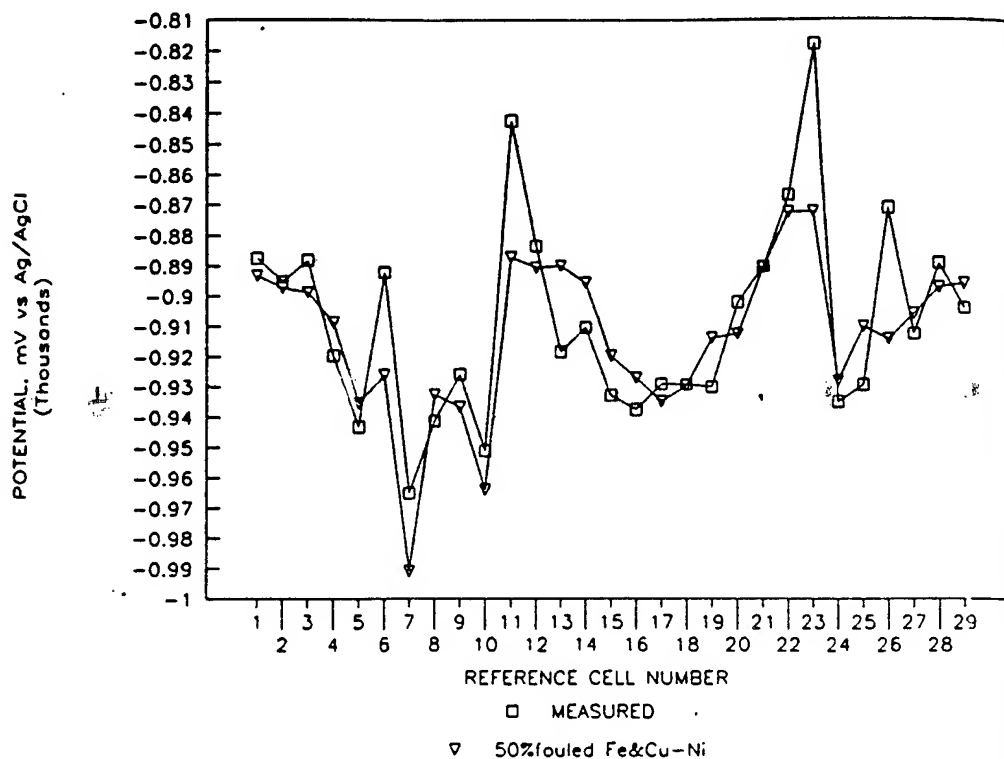


Figure 8 - Comparison of Model and Measured Potentials



A Comparison of Alternatives to Chromic Acid Anodizing

Mr. Stephen J. Spadafora*
Naval Air Warfare Center
Aircraft Division Warminster
P.O. Box 5152 (Code 6062)
Warminster, PA 18974-0591

Mr. Frank R. Pepe
NAVMAR Applied Sciences
65 W. Street Road, Suite B104
Warminster, PA 18974

ABSTRACT

Chromic acid anodizing (CAA) is an aluminum surface pretreatment currently used on military aircraft and equipment. Chromium VI, present in this process, is a carcinogen and federal, state and local environmental agencies have implemented legislation which restricts the use of this material. The Naval Air Warfare Center Aircraft Division Warminster investigated several alternatives to CAA including: Sulfuric-Boric Acid Anodize, Sulfuric Acid Anodizing, and Phosphoric Acid Anodizing. Physical performance properties of these processes were characterized and as a result of this program, the MIL-A-8625 anodize specification was modified to include some of these alternatives.

INTRODUCTION

Chromic acid anodizing (CAA) is a common surface pretreatment for aluminum currently used on Navy aircraft, weapon systems and ground support equipment. This anodize process forms a thick oxide film which provides protection against chemical degradation from the operational environment. MIL-A-8625F "Anodic Coatings, for Aluminum and Al Alloys" Type I covers the performance requirements of CAA. While this anodize process offers satisfactory performance, it contains Chromium VI which is a carcinogen. Recently, California's South Coast Air Quality Management District's (AQMD) Rule #1169 governing the hazardous emissions limits for electrolytic chromium processes went into effect. A national regulation on emissions

from chromium electroplating operations was also issued by the Environmental Protection Agency under the Clean Air Act Amendment of 1990 with limits similar to the SCAQMD Rule #1169. Finally, the Department of Defense (DoD) has determined that Chromium is one of the major components in the waste generated by its maintenance depots and operations (Ref 1). Therefore, Chromium must be eliminated or minimized from the emissions of this process.

Two approaches are available to attain this goal. One approach is through the incorporation of process emission controls. The other approach is to eliminate the source of the hazardous material (i.e. CAA) through the use of alternative technologies. While both of these methods reduce the amount of hazardous material released, the latter also solves Chromium disposal and handling concerns and eliminates the need for expensive control equipment required by 1994 under current AQMD laws. Control equipment for each Navy Depot has been initially estimated at \$500K-1,000K for capital costs and \$250K-600K for annual operating and disposal costs. An adequate replacement to provide protection against environmental degradation is particularly important to the Navy, considering the severe environment in which it operates, as well as the cost of the aircraft, weapon systems and ground support equipment. The Naval Air Warfare Center Aircraft Division at Warminster (NAWCADWAR) has an extensive environmental materials program aimed at the elimination of hazardous materials from Navy aerospace processes (Ref 2 & 3). An effort under these programs was established to evaluate alternative technologies to CAA. The following is a description of this program.

DESCRIPTION OF PREPARATION AND ANODIZE PROCESSES

Surface preparation is an essential step in the process of forming protective pretreatments for aluminum. Surface preparation consists of several steps: cleaning, etching (optional) and deoxidizing. Alkaline cleaners, etchants and deoxidizers were used to remove organic contaminants and any remaining surface oxides prior to chemical treating. The materials used in the preparation of the test specimens were non-silicated, non-chromated alternatives which are described in reference 4. The CAA control process used in this investigation is covered by MIL-A-8625F Type I. Specific details on CAA of aluminum are provided in references 5-6.

Several potential alternatives have been identified for replacement of chromic acid anodizing. These alternatives are: Sulfuric Acid Anodize (SAA), Sulfuric Boric Acid Anodize (SBAA), and Phosphoric Acid Anodize (PAA). Descriptions of these processes are provided in References 6 - 10. Thin Film Sulfuric Acid Anodizing is another alternative currently being investigated and will be reported on at a later date. To evaluate these alternatives, laboratory scale process lines were set up at NAWCADWAR. These operations were used to analyze the performance properties of the different anodizing processes in comparison to CAA, both sealed and unsealed on various substrates. These films were examined as pretreatments for standard Navy coatings using the procedures described below. The results from this evaluation were used to determine the effectiveness of these non-chrome alternatives to provide equivalent corrosion resistance and paint adhesion to that provided by CAA. The fatigue characteristics of these processes were not evaluated as part of this study and would have to be evaluated prior to use of any of these alternatives. A previous study examined the fatigue properties of SBAA and found them to be comparable to CAA (Ref 12).

EXPERIMENTAL

The performance properties of the anodize processes were evaluated on common aluminum alloys and with standard Navy coating systems. Physical performance tests (i.e. bare and painted corrosion resistance, coating adhesion, coating weights, etc.) were used to evaluate the anodize films. The following is a description of the substrates, coatings, and experimental procedures used in this investigation.

Materials - The substrates used in this study were bare 2024 T-3 and 7075 T-6 aluminum alloys. Table 1 lists the coatings applied to these substrates in this investigation. Sets of test specimens were prepared at NAWCADWAR following the manufacturers' recommended procedures. A non-silicated, non-chromated alkaline cleaner and non-chromated deoxidizer were used in the preparation of all specimens (Turco's 4215-NC-LT and Smut-Go-NCB products, respectively).

Anodize Seals - The chromic and sulfuric acid anodized specimens were sealed using the standard 5% dichromate seal at 93°C for 15 minutes as specified in MIL-A-8625E. The sulfuric/boric and thin film sulfuric acid anodize specimens were sealed with a dilute

chromic acid seal which is described in reference 7. The Phosphoric Acid Anodize specimens were not sealed.

Coating Weight Determination - Anodize film coating weights were obtained using the test procedure outlined in MIL-A-8625E. Weights for sealed and unsealed films were determined on the test alloys. The weights were recorded in mg/ft².

Adhesion and Water Resistance - Adhesion of organic coating systems to the anodize films was evaluated using two methods: wet tape adhesion and scrape adhesion. The wet tape test is a modified version of the American Society for Testing and Materials ASTM D 3359, method A. This test was performed by immersing a specimen in distilled water for a period of time at a specific temperature. Three immersion conditions were used for this test: 24 hours at 23°C, 96 hours at 49°C, and 168 hours at 65°C. Upon removal, two parallel scribes, 3/4 inch apart, were cut through the coating and into the substrate. An "X" was subsequently scribed through the coating between the two initial scribes. A strip of 3M 250 masking tape was applied firmly to the coating surface perpendicular to the scribe lines and immediately removed with one quick motion. The specimens were examined for removal and uplifting of the coating from the substrate and the adhesion rating was recorded. Table 2 gives the performance description for these adhesion ratings. In addition, the water resistance of the pretreatment and coating systems was characterized by examining the test panels for softening, uplifting, blistering, and other coating defects and substrate corrosion which may have resulted from the exposure.

The scrape test was performed in accordance with ASTM D 2197, method A on specimens with a section of the substrate surface exposed. The instrument used to perform this test was a SG-1605 Scrape Adhesion Test Apparatus manufactured by Gardner Laboratory. The test was performed by guiding a weighted stylus at a 45° angle to the specimen along the exposed substrate into the coating system. The scrape adhesion was recorded as the heaviest weight used without shearing the coating from the substrate.

Corrosion Resistance - Five aluminum specimens 3"x10" of each anodize process were exposed in 5% salt spray (ASTM B 117) for 336 hours. Upon removal, the panels were inspected for evidence of corrosion. In addition, four aluminum specimens of each unsealed anodize film/coating system were scribed with a figure

"X" through the coating into the substrate. Two specimens were exposed in 5% salt spray (ASTM B 117) for 2000 hours and two were exposed in SO₂/salt spray (ASTM G 85) for 500 hours. The panels were then inspected for corrosion in the scribe area and blistering of the coating. Subsequently, one panel from each exposure was chemically treated to remove the organic coating without disturbing the substrate and the specimen was examined for corrosion.

RESULTS AND DISCUSSION

Test panels were processed with non-chromate cleaners and deoxidizers, and then anodized with the subject processes. Coating adhesion, water resistance, & corrosion tests were performed using MIL-P-23377 epoxy primer, MIL-P-85582 epoxy/waterborne primer, and TT-P-2760 polyurethane/elastomeric primer. Also, specimens primed with MIL-P-23377 and topcoated with MIL-C-85285 high solids polyurethane were tested. These coatings are described in references 13-16. The following is a summary and discussion of the results.

Table 3 shows coating weights for the anodize processes on the two different aluminum alloys. Coating weight gives an indication of oxide film thickness and is determined by processing variables such as amps/ft², time, etc. Both sealed and unsealed weights were obtained for each process except for PAA. Sealed PAA specimens were not evaluated since the morphology of PAA is not the same as the other anodize films and sealing is not applicable to this process. The relative coating weights for unsealed specimens ranged from 40 mg/ft² for PAA, to 300-600 mg/ft² for CAA & SBAA, to greater than 1000 mg/ft² for SAA.

Enhanced coating adhesion is one of the primary function of a surface pretreatment. These coating adhesion tests were performed on unsealed anodize films immediately after the 7 day cure time for the coatings. With further aging of the finishing system, adhesion normally improves, so these results are considered the minimum values. The results of the adhesion/water resistance tests are provided in Tables 4 to 6.

The results from the 24 hour tape tests performed on these processes showed adhesion values of 5A (one 4A result) for all coating systems tested (Table 4). These results indicate virtually no susceptibility to coating-substrate disbondment upon exposure to water. Most aerospace coatings use this adhesion requirement. In the expanded adhesion tests (4 & 7 day), all of the

anodize processes, with various coating systems, continued to exhibit good to excellent adhesion & water resistance (Tables 5 & 6). The SBAA and CAA processes were consistently the best performing. This is evidenced by the tape test 5A results after extended immersion in water.

A standard aerospace requirement for scrape adhesion is 3 kg. The overall scrape adhesion results for all processes tested ranged from 0.5 kg to 10.5 kg. (Table 7). This indicated that other factors (such as the coating edge effects, pretreatment thickness, pre-paint surface cleanliness, etc.) affected the outcome of the tests. The results from the sulfuric/boric acid anodized process ranged from 2.0 kg to 7.0 kg. and was the process most comparable to chromic acid anodizing.

Sealed, unpainted specimens from all of the processes were exposed to 5% salt spray (ASTM B117) on 6° racks and examined at 24 hour intervals for evidence of corrosion. Total exposure time was 336 hours. These results are summarized in Table 8. The PAA panels failed in less than 72 hours indicating poor bare corrosion resistance. This is not unexpected considering the stalagmite structure of this oxide. All of the remaining anodic processes passed 336 hours of exposure on all alloy specimens without any evidence of surface corrosion, indicating excellent anodic coating performance.

Corrosion resistance is an important property for Navy aircraft coatings due to the severe operational environment in which the aircraft are deployed. Therefore, most aircraft primer specifications have a minimum of 1000 hours exposure to salt spray as the corrosion resistance requirement. The anodic coating plays an integral role in meeting this requirement by maintaining the integrity of the coating/substrate interface. To evaluate this property, painted specimens for all anodize processes were exposed to 5% salt spray (ASTM B117) and examined for corrosion in the scribe area and blistering of the coating. These results are summarized in Tables 9 & 10. All of the anodize processes, with all coating systems, passed 1000 hours of exposure. There was little to no corrosion products in the scribe and no blistering of any of the coatings.

Since all processes performed well for over 1000 hours on both substrates, the test was continued for another 2500 hours. At 3500 hours, there was still virtually no corrosion products in the scribe or

blistering of the coating on any of the specimens. Subsequently, the coatings were carefully removed from the surface with a chemical stripper, without disturbing the underlying substrate. Upon further examination, there was no evidence of underlying corrosion on these panels. At 3500 hours, while all of the primed and primed/topcoated specimens performed well, the SBAA and CAA specimens showed the least amount of corrosion products in the scribe area.

Painted specimens exposed to SO₂/salt spray (ASTM G85) were also examined for damage to the coating and corrosion in and away from the scribe, and these results are summarized in Tables 11 & 12. The SO₂/salt spray environment simulates industrial exhaust gases, such as those found on aircraft carriers from engine exhausts, and it is an extremely aggressive environment. Most aircraft coating specifications do not have exposure to SO₂/salt spray as a corrosion resistance requirement. Therefore, the exposure periods selected were based on differences in finishing system performance.

Primed panels, after being exposed for 168 hours, were examined for signs of corrosion. As seen in Table 11, the results for this test were mixed between the alloys, primers and anodize films. In these tests, the SBAA appeared to show the weakest performance. However, the diversity of these results (from passing to complete failure) made drawing specific conclusions difficult and is partially the reason why coating specifications do not call out this test. The primed and topcoated 7075 specimens all failed between 168 hours and 336 hours. The primed and topcoated 2024 specimens were borderline failures at 500 hours, except for the CAA which failed at 336 hours. On both alloys, the CAA process performed the worst of all those tested.

In general, the corrosion resistance of several of the anodize processes, in combination with the standard epoxy primer or the epoxy primer/polyurethane topcoat coating systems, was equivalent to the performance of the chromic acid anodize controls. This equivalent performance for these non-chromated anodic coatings as compared to the chromated anodic coating is due to a high degree of interfacial integrity between the coating and substrate.

SUMMARY

The goal of this effort was to evaluate non-chromated alternatives for chromic acid anodizing used on current aerospace structures. The results from this evaluation show that some of the alternative anodize processes have comparable performance properties to CAA. The SBAA and SAA test results show that they provide acceptable performance for corrosion resistance and coating adhesion. The coated PAA specimens performed fairly well, however, the unpainted specimens failed rapidly in the corrosion tests. As stated earlier in the report, the fatigue characteristics of these processes were not evaluated and may be an issue for the use of these materials. For example, Sulfuric Acid Anodize has traditionally been considered to be a fatigue sensitive process and should not be used in fatigue critical areas. The MIL-A-8625 military specification, which covers CAA and SAA, has been revised to include the SBAA alternative. In 1993, the SBAA was authorized by the Naval Air Systems Command as an alternative to CAA. The use of a non-chromated process will allow the Navy to meet stringent environmental standards while maintaining operational readiness and efficiency of system performance. In addition, significant cost savings (\$M) will be recognized by avoiding the need to implement emission control equipment.

ACKNOWLEDGMENT

The authors would like to express their thanks to Mr. William Green, Mr. John Deitzel, and Mr. Donald Hirst for their contributions to this effort. Without their dedication and inspiration this work would not have been possible.

REFERENCES

1. Cornelius, Col.K., "DoD Hazardous Waste Minimization Efforts," Presentation at the Fifth Aerospace Hazardous Waste Minimization Conference, Costa Mesa, CA, May 1990
2. Spadafora, S.J. et al., "Naval Air Warfare Center Aircraft Division at Warminster Environmental Materials Program Phase I," Naval Air Warfare Center Aircraft Division Warminster, Report #NAWCADWAR-92075-60, Warminster, PA. 24 June 1992
3. Spadafora, S.J. et al., "Naval Air Warfare Center Aircraft Division at Warminster Environmental Materials Program Phase II," Naval Air Warfare Center Aircraft

- sion Warminster, Report #NAWCADWAR-93057-60,
 Warminster, PA. 22 August 1993
- Spadafora, S.J., "Non-Chromated Surface
 Treatments for Aluminum," Naval Air Warfare Center
 Aircraft Division Warminster, Report #NAWCADWAR-92077-
 Warminster, PA. 18 August 1992
- Wernick, S., et al., *THE SURFACE TREATMENT AND
 FINISHING OF ALUMINUM AND ITS ALLOYS*, Finishing Pub.
 Co., 5th Ed., Vol. 1, pp. 289-365 & 430-441, 1987
- Cochran, P.G.C., "Sulfuric and Chromic Acid
 Anodizing of Aluminum," *ELECTROPLATING ENGINEERING
 HANDBOOK*, Durney, L.J., Van Nostrand Reinhold Co., 1984
- Moji, Y., "Boric Acid - Sulfuric Acid Anodizing
 Process Development (PAC 5632)," Boeing Report No. D6-
 313TN, Feb 6, 1990
- Howard, M., "Corrosion Resistance and Paint Adhesion
 Evaluation of Sealed Sulfuric/Boric Acid Anodize
 Treatments," Rohr Ind. Report No. RHR-90-194, Dec 1990.
- American Society for Testing and Materials ASTM
 Method D-3933, "Preparation of Aluminum Surfaces for
 Structural Adhesive Bonding (Phosphoric Acid
 Anodizing)," 1980.
10. "Phosphoric Acid Anodize," *ADHESIVE BONDING OF
 ALUMINUM ALLOYS*, Thrall, E.W. and Shannon, R.W., Marcel
 Dekker Inc., 1985
11. Chang, T.C., "Effect of Anodic Film Type (Thin Film
 Sulfuric vs Chromic Acid) on Fatigue Life of Aluminum
 Alloys," McDonnell Douglas Report No. MDC-K5784,
 January 28, 1991
12. Spadafora, S.J. and Pepe, F.R., "A Comparison of
 Sulfuric/Boric Acid Anodize and Chromic Acid Anodize
 Processes," Naval Air Warfare Center Aircraft Division
 Warminster, Report #NADC-93042-60, Warminster, PA. 22
 June 1993
13. Ketcham, S.J., "A Handbook of Protective Coatings
 For Military and Aerospace Equipment," TPC Publication
 10, National Assoc. of Corrosion Engineers (NACE), 1983
14. Spadafora, S.J., et al., "Corrosion Preventive
 Primers For Military Equipment," National Association
 of Corrosion Engineer's Corrosion 85 Conference, Paper
 No. 194, Boston Massachusetts, March 1985
15. Hegedus, C.R. et al., "A Review of Organic Coating
 Technology For U.S. Navy Aircraft," *Journal of Coatings
 Technology*, Nov 1989
16. DeLuccia, J.J., et al., "AGARD Corrosion Handbook,
 Volume 2, Aircraft Corrosion Control Documents: A
 Descriptive Catalogue," AGARDograph No. 278, North
 Atlantic Treaty Organization (NATO), March 1987

TABLE 1: ORGANIC COATING SYSTEMS EVALUATED*

MIL-SPEC	TYPE	FUNCTION	THICKNESS
MIL-P-23377D	1	Epoxy Primer	0.6-0.9 mils
MIL-P-85582A	1	Epoxy Primer	0.6-0.9 mils
TT-P-2760	1	Polyurethane Primer	0.8-1.2 mils
MIL-P-23377D	1	Epoxy Primer	0.6-0.9 mils
MIL-C-85285	1	Polyurethane Topcoat	1.8-2.2 mils

* All coatings were applied by conventional air spray & allowed to cure for seven days prior to testing.

TABLE 2. ASTM D3359 ADHESION RATINGS

Rating	Description
5A -	No peeling or removal
4A -	Trace peeling or removal along incisions
3A -	Jagged removal along incisions up to 1/16 in. (1.6 mm) on either side
2A -	Jagged removal along most of incisions up to 1/8 in. (3.2 mm) on either side
1A -	Removal from most of the area of the X under the tape
0A -	Removal beyond the area of the X

TABLE 3. COATING WEIGHT TEST RESULTS - (mg/ft²)
ANODIZE PROCESSES

ALLOY	PAA	SBAA	CAA	SAA
2024-T3 Sealed	---	150.9	576.4	1115.2
7075-T6 Sealed	---	429.9	567.2	1731.2
2024-T3 Unsealed	40.3	372.8	416.0	904.3
7075-T6 Unsealed	43.2	576.0	315.5	1397.9

TABLE 4. 24 HOUR ADHESION/WATER RESISTANCE TEST RESULTS
ANODIZE PROCESSES

ALLOY (Unsealed)	PAA	SBAA	CAA	SAA
2024 - MIL-P-23377	5A	5A	5A	5A
- MIL-P-85582	5A	5A	5A	5A
- TT-P-2760	5A	5A	5A	5A
- MIL-P-23377/ MIL-C-85285	5A	5A	5A	4A
7075 - MIL-P-23377	5A	5A	5A	5A
- MIL-P-85582	5A	5A	5A	5A
- TT-P-2760	5A	5A	5A	5A
- MIL-P-23377/ MIL-C-85285	5A	5A	5A	5A

TABLE 5. 4 DAY ADHESION/WATER RESISTANCE TEST RESULTS
ANODIZE PROCESSES

ALLOY (Unsealed)	PAA	SBAA	CAA	SAA
2024 - MIL-P-23377	5A	5A	5A	5A
- MIL-P-85582	3A	5A	5A	5A
- TT-P-2760	5A	5A	5A	5A
- MIL-P-23377/ MIL-C-85285	5A	5A	5A	5A
7075 - MIL-P-23377	5A	5A	5A	5A
- MIL-P-85582	3A	5A	5A	5A
- TT-P-2760	5A	5A	5A	5A
- MIL-P-23377/ MIL-C-85285	5A	5A	5A	4A

TABLE 6. 7 DAY ADHESION/WATER RESISTANCE TEST RESULTS
ANODIZE PROCESSES

ALLOY (Unsealed)	PAA	SBAA	CAA	SAA
2024 - MIL-P-23377	5A	5A	5A	5A
- MIL-P-85582	4A	5A	5A	5A
- TT-P-2760	5A	5A	5A	5A
- MIL-P-23377/ MIL-C-85285	5A	5A	5A	4A
7075 - MIL-P-23377	5A	5A	5A	5A
- MIL-P-85582	5A	5A	5A	5A
- TT-P-2760	5A	5A	5A	5A
- MIL-P-23377/ MIL-C-85285	5A	5A	5A	5A

TABLE 7. SCRAPE ADHESION TEST RESULTS - (kg)
ANODIZE PROCESSES

ALLOY (Unsealed)	PAA	SBAA	CAA	SAA
2024 - MIL-P-23377	0.5	3.0	6.5	1.5
- MIL-P-85582	7.0	3.5	9.0	3.0
- TT-P-2760	1.5	3.0	3.5	4.0
- MIL-P-23377/ MIL-C-85285	6.0	4.0	6.0	10.5
7075 - MIL-P-23377	2.0	7.0	5.0	4.5
- MIL-P-85582	6.0	4.5	7.0	5.5
- TT-P-2760	1.5	2.0	3.0	1.5
- MIL-P-23377/ MIL-C-85285	4.0	3.5	6.0	3.0

TABLE 8. 5% SALT SPRAY RESULTS - 336 HRS (BARE PANELS)
ANODIZE PROCESSES

ALLOY	PAA	SBAA	CAA	SAA
2024-T3 Sealed	FAIL*	PASS	PASS	PASS
7075-T6 Sealed	FAIL*	PASS	PASS	PASS

(* Failure occurred at less than 72 hours of exposure)

TABLE 9. 5% SALT SPRAY TEST RESULTS (1000 HRS)

		ANODIZE PROCESSES			
ALLOY (Unsealed)		PAA	SBAA	CAA	SAA
2024 - MIL-P-23377		PASS	PASS	PASS	PASS
- MIL-P-85582		PASS	PASS	PASS	PASS
- TT-P-2760		PASS	PASS	PASS	PASS
- MIL-P-23377/ MIL-C-85285		PASS	PASS	PASS	PASS
7075 - MIL-P-23377		PASS	PASS	PASS	PASS
- MIL-P-85582		PASS	PASS	PASS	PASS
- TT-P-2760		PASS	PASS	PASS	PASS
- MIL-P-23377/ MIL-C-85285		PASS	PASS	PASS	PASS

TABLE 10. 5% SALT SPRAY TEST RESULTS (3500 HRS)

		ANODIZE PROCESSES			
ALLOY (Unsealed)		PAA	SBAA	CAA	SAA
2024 - MIL-P-23377		PASS	PASS	PASS	PASS
- MIL-P-85582		PASS	PASS	PASS	PASS
- TT-P-2760		PASS	PASS	PASS	PASS
- MIL-P-23377/ MIL-C-85285		PASS	PASS	PASS	PASS
7075 - MIL-P-23377		PASS	PASS	PASS	PASS
- MIL-P-85582		PASS	PASS	PASS	PASS
- TT-P-2760		PASS	PASS	PASS	PASS
- MIL-P-23377/ MIL-C-85285		PASS	PASS	PASS	PASS

TABLE 11. SO₂/SALT SPRAY TEST RESULTS (168 HRS)

		ANODIZE PROCESSES			
ALLOY (Unsealed)		PAA	SBAA	CAA	SAA
2024 - MIL-P-23377		P	F @108	P	P
- MIL-P-85582		P	F @168	F @168	P
- TT-P-2760	F @108		F @48	F @168	F @108
7075 - MIL-P-23377	P		F @108	-	P
- MIL-P-85582	F @168		F @168	+	F @108
- TT-P-2760	F @108		F @48	P	F @48

(P = Pass, + = Borderline Pass, - = Borderline Failure
and F @### = Failure at # Hours)

TABLE 12. SO₂/SALT SPRAY TEST RESULTS (336 HRS)

		ANODIZE PROCESSES			
ALLOY (Unsealed)		PAA	SBAA	CAA	SAA
2024 - MIL-P-23377/ MIL-C-85285		-	-	F @336	-
7075 - MIL-P-23377/ MIL-C-85285		F @336	F @250	F @168	F @168

Suitability of Prepainted (Coil Coated) Metal
and Adhesive Assembly for Military Application

Mr. I. Carl Handsy
U.S. Army Tank-Automotive Command
Warren, MI 48397-5000

* Mr. Merle T. Wolff
U.S. Army Tank-Automotive Command
Warren, MI 48397-5000

Corrosion of vehicles is a major cost to the Army.

Independent Cost Analysis which agrees with our available records indicate a cost per vehicle per year of \$500 to \$1,100.

Much of the fleet has 30 to 40 year old design. In many cases current technology for material selection, component design and manufacturing processes is not incorporated into procurement specifications.

The Automotive and Steel Industries in recent years has done much research in this field of corrosion. We have attended conferences by the Society for Automotive Engineering Automotive Corrosion and Prevention Committee, The American Iron and Steel Institute Task Force on Automotive Corrosion and the Society of Manufacturing Engineers Association for Finishing Process. Our office is also in regular contact with individual automotive company engineers.

The information obtained from all these sources indicates that probably the best cost effective results in corrosion control are achieved by a system consisting of:

- 1.) Galvanized Steel
- 2.) Zinc Phosphate Pre-Treatment
- 3.) Electro-Deposited Cathodic Primer

The Army requirements are different from the automobile market for many reasons, chief of which are:

- More variations and extremes in environment
- Off road use
- Low mileage with high percent non-operating time
- Chemical agent resistance requirements

To evaluate the finding of the automotive industry and determine modifications beneficial to the Army, a study was made of corrosion of Jeep vehicle bodies with different coating systems. These bodies were exposed to a sea coast environment at Cape Canaveral. This site was selected for these characteristics.

- Severe corrosion environment
- High humidity
- Salt laden air
- Frequent rain showers
- Frequent strong ocean winds
- Abundance of solar radiation

After 12 months the following was reported:

"An evaluation of the results of 12 months exposure testing indicate that of the body configurations tested, optimum corrosion protection is achieved by utilization of the following body coating configuration in descending order.

- Galvanized, Two-Sided
- E-Coat Primer (Cathodic Electrodeposition)
- High Solids Enamel Topcoat (PPG-DHT 45323)
- Rust Proofing - Per MIL-R-46164

- Galvanized, Two-Sided
- E-Coat - Primer (Cathodic Electrodeposition)
- High Solids Enamel Topcoat (PPG-DHT 45323)

- Non-Coated Steel
- E-Coat - Primer (Cathodic Electrodeposition)
- High Solids Enamel Topcoat (PPG-DHT 45789)
- Rust Proofing

- Non-Coated Steel
- Alkyd - Primer
- Alkyd - Topcoat
- Rust Proofing

Non-Coated Steel
Alkyd - Primer
Alkyd - Topcoat

"In the writer's opinion, a single component change to offer the most improvement to the standard M151A2 body's corrosion protection system of Alkyd primer, Alkyd topcoat and rust proofing would be two sided galvanized coating on the body in place of non-coated steel. The next most effective single component would be to use E-Coat in lieu of alkyd type primer.

"Only one body had spray CARC primer and topcoat and it rated at the bottom of the eight tests. CARC (Chemical Agent Resistant Coating) is the specified topcoat for new procurements and this one test may be misleading as to CARC's capabilities as the body was non-coated steel, was the only one with epoxy primer and was not rustproofed."

Of particular significance was the fact that on the galvanized bodies the only corrosion showing was at welded areas.

While this project was continuing it was decided to evaluate the potential of coil coated metal for military vehicles with these expectations.

Lower cost/Better paint
Improved environment/No VOC's
No metallurgical changes of steel with
resulting corrosion sites
No damage to zinc coating

The following different constructions were planned for this evaluation:

Group:	Steel:	Construction:	Prime:
Control	C. R. Steel	Welded	Spray CARC
1	C. R. Steel	Welded	E-Coat
2	C. R. Steel	Adhesive	CARC Coil Coat
3	C. R. Steel	Adhesive	Flex Coil Coat
4	Galvanized	Adhesive	Flex Coil Coat
5	Galvanized	Adhesive	E-Coat

The first production of coil coated steel was disappointing in that it was learned that CARC epoxy primer would not take 1T bend as required for the door hem assembly.

The paint manufacturers tried many formulations to develop a more flexible prime paint that would also be resistant to DS2, the solvent used to clean vehicles after a nuclear, chemical or biological attack.

The most suitable was a combination of thin epoxy and polyester.

This more flexible paint was still subject to microfracturing when subjected to a 1T bend.

The doors with the different systems were subjected to the following tests:

- Accelerated corrosion: General Motors 9540P
- Mechanical strength: General Motors Truck Door
- Slam Durability Test
- Field Test: Trucks at Camp Lejeune Marine Drivers Training School
- Coastal exposure: Cape Canaveral, Florida

Thirty-six sample test doors were subjected to extensive testing to determine the suitability of prepainted metal and adhesively bonded assemblies for military application.

The thirty-six doors consisted of thirteen standard doors and twenty-three adhesively bonded test doors. The thirteen standard doors were of current production methods and techniques. Seven of the doors were cold rolled steel with standard primer and rust proofing. The remaining six were cold rolled steel with E-Coat primer and rust proofing.

The twenty-three adhesively bonded test doors were manufactured using four different material/process systems. Five were cold rolled steel with CARC coil coated primer and no internal paint. Five were cold rolled steel with flex coil coated primer and internal E-Coating.

Ten were galvanized steel with flex coil coated primer and internal E-Coating. The final three doors were adhesively bonded galvanized steel with E-Coat primer.

Four tests were performed. Nine were subjected to an accelerated corrosion test and six were subjected to a durability test. A marine exposure test was performed on twelve doors and nine were installed on vehicles for a military user test. The results of the tests were conclusive in that galvanized cold rolled steel with an E-Coat primer is the best combination of material and processes.

It was concluded that coil coating is not practical for this application. Manufacturing operations such as bending, tool markings, handling, blanking and stamping are detrimental to the prepainted surface. The epoxy CARC precoat could not withstand the 1T bend of the hemming operation. E-Coating was found to be highly superior to coil coating because it is not subjected to these manufacturing processes. The E-Coat application process also assures that all internal parts, cavities, seams and joints received a specific thickness of coating.

Adhesive was determined to be considerably better than spotwelds from a corrosive standpoint. Adhesive is mechanically equal to or better than spotwelding.

Galvanized steel was substantiated as being the door skin. The galvanized covering is very compatible with an E-Coat primer and a zinc phosphate pretreat.

Durability Test (SLAM) - All six sample test doors met GM 0075-A-01-LP1C test specification requirements. No cracking or separation occurred in the bonded areas (both adhesive and spotweld) between the door structure and the sheet metal outer skin. No adhesive failure occurred in any of the six doors even though the test far exceeded the normal life of the doors. Damage, other than adhesive bonded areas, clearly indicates that other parts of the door failed long before the adhesive bonding.

Accelerated Corrosion (SCAB) - Nine sample doors received forty complete cycles of testing in accordance with GM9540-P. The GM test was selected because it best correlates the test with the field life (actual service life) of the door. Three of the nine doors were subjected to an additional forty cycles in order to more nearly approach the normal service life of the door. Galvanize gave the best performance. Evaluation of E-Coating and coil coating did not detect any difference on a flat surface. The coil coat evidenced degradation on surfaces subjected to manufacturing operations. E-Coat performed very well with galvanize but experienced a shorter life when used by itself.

Marine Exposure Test - Twelve doors were tested for 21 months. Results indicate galvanized steel is better than cold rolled steel. E-Coating is the best primer.

Military User Test - Nine test doors were subjected to this 21 month test. Both the military user and the marine exposure tests, have corroborated the results of the accelerated corrosion tests.

Results clearly indicate the two galvanized doors to be better than the cold rolled steel doors.

Our basic conclusions from these studies are:

Cleaning and pretreatment are critical

Zinc phosphate best pretreatment for corrosion resistance

G90 Galvanizing (.75 mil) min. 10-12 year life

E-Coat superior corrosion resistance in both tests
About halfway from spray prime to galvanizing

"Rustproofing" can add up to 20% life to spray paint; but only where applied and if replaced as needed

Most cost effective coating system:

- 1.) Galvanizing
- 2.) Zinc phosphate pretreatment
- 3.) E-Coat prime

This combination provides at least 90% of total corrosion protection.

From the observations this far in our research these correlations have been indicated:

1 Year static coastal exposure = 3-4 years
real life average exposure

10 cycles G.M. 9540P = approximately 1 year
real life average exposure

Support SAE/AISI finding that the GM9540P
accelerated test has .96 correlation to real life

The things we foresee for future work in this area are:

Adhesive assembly of other parts

Further evaluation of potential of a flexible coil
coated prime paint

Non-CARC application of coil coating

More extensive use of galvanizing

More extensive use of E-Coating

BLANK

706

Electroplating and Epoxy Repair Methods for Corroded 70/30 CuNi and Alloy 400 Seawater System Components.

Mr. Timothy J. Jackovic*
Mr. Edward B. Bieberich

Carderock Division
Naval Surface Warfare Center
Code 613
3A Leggett Circle
Annapolis, MD 21402-5067

ABSTRACT

70/30 CuNi and alloy 400 components used for Navy seawater immersion applications suffer a variety of corrosion problems including pitting, crevice corrosion, and galvanic corrosion. An effective method for repair of corroded components would result in significant cost savings by allowing refurbishment rather than replacement of damaged components. Electroplating and epoxy repair methods were tested to determine their effectiveness for repair of these alloys. Materials and techniques were selected based on availability and current usage at Navy shipyards. Corrosion tests were developed which represented typical corrosion environments for 70/30 CuNi and alloy 400 components. Pipe specimens that contained both control and repair areas were tested for approximately 1 year in static seawater. Based on the test results, recommendations were made for repair of corroded 70/30 CuNi and alloy 400 components using electroplating and epoxy repair techniques.

INTRODUCTION

70/30 CuNi and alloy 400 components used for Navy seawater immersion applications are susceptible to a variety of corrosion mechanisms including pitting, crevice corrosion, and galvanic corrosion. Problems resulting from corrosion can adversely affect overall performance of a system constructed with these alloys and can result in

high repair or replacement costs. Effective, long-lasting repair methods would result in significant cost-savings by eliminating the need for replacement parts and reducing the need for reapplication of an inadequate repair method.

Navy shipyards presently use electroplating or epoxy coatings to repair corroded surfaces on 70/30 CuNi and alloy 400 ship seawater system components. These systems include submarine shaft seals, seawater pumps, seawater piping and valves, and logistics escape trunks to name a few. Copper or a combination of copper and nickel are used for electroplate repair. Repairs are normally accomplished in accordance with MIL-STD-219 (SH) (Brush Electroplating on Marine Machinery) [1]. Repairs of corroded components are also made with a variety of epoxy filler materials. However, the corrosion performance of electroplated or epoxy repaired surfaces has not been tracked in the fleet in a systematic manner. As a result, the service performance lifetime of the various types of repair (and on different depths of attack) is unknown. There is no data base to permit selection of one repair method as the most suitable one for a particular repair application. Since no performance data exists, there is no standard repair method and each shipyard or intermediate maintenance activity (IMA) uses whatever method that has appeared to be "successful" during previous repairs. The identification of superior materials and methods to repair corrosion and minor surface defects would have widespread application in the submarine and surface fleet.

Corrosion tests were developed to evaluate electroplate and epoxy repair methods for corroded 70/30 CuNi and alloy 400 components. Test conditions were selected to simulate a typical corrosion environment for these alloys. Specimens were tested with control areas without repair and areas which had been repaired with electroplate and epoxy techniques. At the completion of testing, effectiveness of the repairs versus the control areas was evaluated. The objective of this report is to present the results of the electroplating and epoxy repair tests and provide recommendations to develop standard repair procedures.

MATERIALS AND SPECIMEN PREPARATION

To simulate repair of O-ring sealing surfaces, a test matrix was designed to comparatively evaluate seawater corrosion performance of epoxy compounds and electroplating on 70/30 CuNi and alloy 400 pipe specimens, Table 1.

Table 1. Test matrix for electroplating and epoxy repair specimens.

Substrate Material	Repair Method	Repair Material	Depth of Repair, inches			Specimens/ Substrate*
70/30 CuNi Mil-T-16240K 70/30 CuNi or Alloy 400 ASTM B 127-85 UNS N04400	Epoxy	Phillybond Blue 6A		0.015"	0.025"	8
		Belzona Molecular Ceramic Metal		0.015"	0.025"	8
		Belzona Molecular Super Metal		0.015"	0.025"	8
		Devcon Ceramic Compound Type I		0.015"	0.025"	8
		Devcon Underwater (UW)		0.015"	0.025"	8
	Electroplating	Copper 2050	0.008"	0.015"		8
		Copper 2050 with Nickel 2080 cap	0.006" Cu 0.002" Ni	0.013" Cu 0.002" Ni		8
		Copper 2050 with Aeronikl 250 cap	0.006" Cu 0.002" Ni	0.013" Cu 0.002" Ni		8
Alloy 400	Electroplating	Aeronikl 250	0.008"			4
Total Specimens =						68

* 4 specimens per depth of repair

Two types (type I and II) of test specimens were used to represent repaired surfaces, Figures 1 and 2, respectively. Type I (one wide groove) had the repair treatment applied to all of the area adjacent to and under the O-ring sealing surface (Figure 1), while the type II (two narrow grooves) had the repair treatment applied only adjacent to each side of the O-ring sealing surface (Figure 2). Crevice corrosion of 70/30 CuNi and alloy 400 typically occurs adjacent to O-ring sealing surfaces. Each pipe specimen had five O-ring repair sites and one O-ring control site. The pipe/O-ring test created severe crevice situation which permitted a relative ranking of repair techniques.

The electroplating materials tested included Sifco Solutions Copper 2050* (Cu2050), Copper 2050 with a Nickel 2080* (Ni2080) cap, Copper 2050 with an AeroNikl 250* (Ni7280) cap, and AeroNikl 250; while the epoxies tested included Phillybond Blue 6A* (Phillybond), Belzona Molecular Ceramic Metal R* (Belzona Ceramic), Belzona Molecular Super Metal* (Belzona Super Metal), Devcon Ceramic Compound type I* (Devcon Ceramic), and Devcon Underwater*.

* Trademark of Sifco Industries, Inc.

+ Trademark of ITW Philadelphia Resins, Inc.

Trademark of Belzona Molecular Metalife, Inc.

& Trademark of ITW Devcon, Inc.

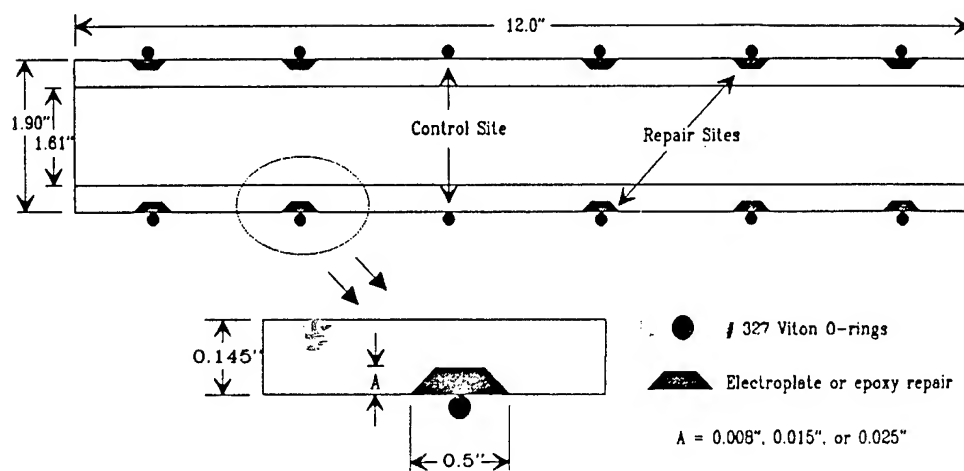


Figure 1. Electroplate/epoxy type I specimen (all dimensions in inches (")).

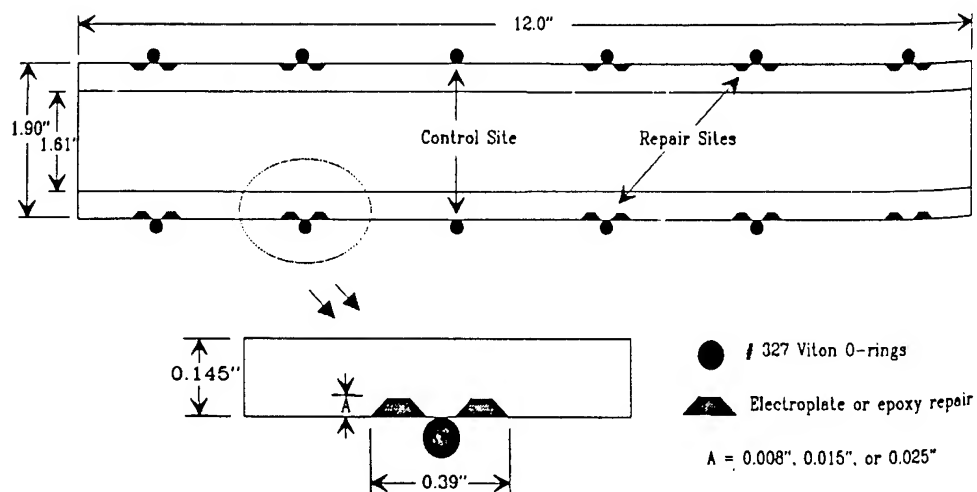


Figure 2. Electroplate/epoxy type II specimen (all dimensions in inches (")).

For a given repair treatment, there were four test conditions per substrate material: type I (two depths of repair) and type II (two depths of repair). The electroplating solutions were applied to repair depths of 0.008 and 0.015 in. while the epoxies were applied to depths of 0.015 and 0.025 in.

CDNSWC tasked both Puget Sound Naval Shipyard (PSNS) and Pearl Harbor Naval Shipyard (PHNS) to apply the epoxy compounds and electroplating solutions. Each shipyard was requested to apply the same repair treatments and to document their application procedures.

AS-RECEIVED CONDITION OF REPAIRS


Before the tests were initiated, the condition of the repaired areas on the pipe specimens and the repair application procedures were examined. Significantly different procedures were followed by each shipyard which varied the initial condition of the repairs. In the remainder of this report, the specimens from Puget Sound will be designated as PS while the specimens from Pearl Harbor will be PH.

The final surface condition was found to vary between the two shipyards. All of the PH specimens were machined to a smooth surface finish after the repairs were made; whereas the PS specimens were delivered in the as-applied condition. Final machining provided a smoother surface finish than the as-applied condition but also reduced the nickel cap thickness of the electroplate repairs.

A major difference was found between the initial surface preparation of the epoxy repair specimens. Repair areas of the PS specimens were sandblasted before applying the epoxies, whereas PH specimens were not. Sandblasting significantly improves the adhesion of epoxies compared to epoxies applied to a smooth, machined surface [2].

TEST CONDITIONS

A total of 132 electroplate and epoxy repair specimens, or 792 O-ring sites, were immersed in natural seawater for 11 months (Dec 18, 1990 to Nov 18, 1991) at the Naval Research Laboratory (Key West, FL). The pipe specimens were placed in PVC racks and immersed in a seawater trough parallel to the seawater flow. Each specimen rested on its outer two O-rings to avoid creating additional crevices. Seawater was continually refreshed at a trickle flow rate. The average seawater temperature during the test exposure was 27.7°C while the average salinity was 37.1 ppt and average pH 8.1.



After 11 months in seawater, the specimens were removed and examined for corrosion of the substrate and coating performance. Depth of attack measurements were taken under and adjacent to the O-ring at the control site, adjacent to the epoxy coatings, and under and adjacent to the O-ring on the electroplate coatings. Photographs were taken to document the inspection.

RESULTS AND DISCUSSION

After removal and cleaning of the test specimens, relative performance of both electroplate and epoxy repairs were evaluated. Each specimen had 5 repair sites; the performance of the repair method on each specimen was rated based on how many sites were completely intact (0-5 with 5 being the best rating since all sites would have passed).

The electroplate repairs were considered to have failed when any corrosion damage occurred to the electroplate. Results of this evaluation are provided in Figure 3.

The epoxy coatings were rated as having passed or failed based on the following conditions for failure: blistering, chipping, spalling, swelling, or movement of the coating. The coatings were also considered failures if they could be twisted off by hand. The results of this inspection are provided in Figure 4.

A significant difference in performance of the repairs was seen as a result of variations in procedure between the two shipyards. The nickel-capped electroplate specimens which were left in the as-electroplated condition remained intact more often than the specimens which had been final machined. Also, the epoxy coatings which had been sandblasted consistently provided better adhesion and showed less instances of failure than the specimens which had no sandblasting. A discussion of the results for each repair type follows.

Percentage of Sites

Electroplating Repair

Percentage of Sites without Damage

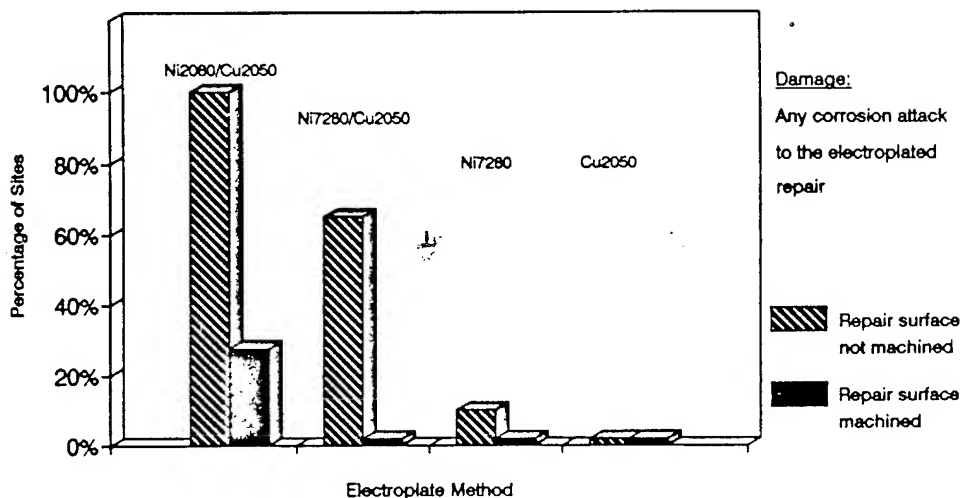


Figure 3: Results of electroplate repair corrosion tests.

Epoxy Repair

Percentage of Sites that Passed

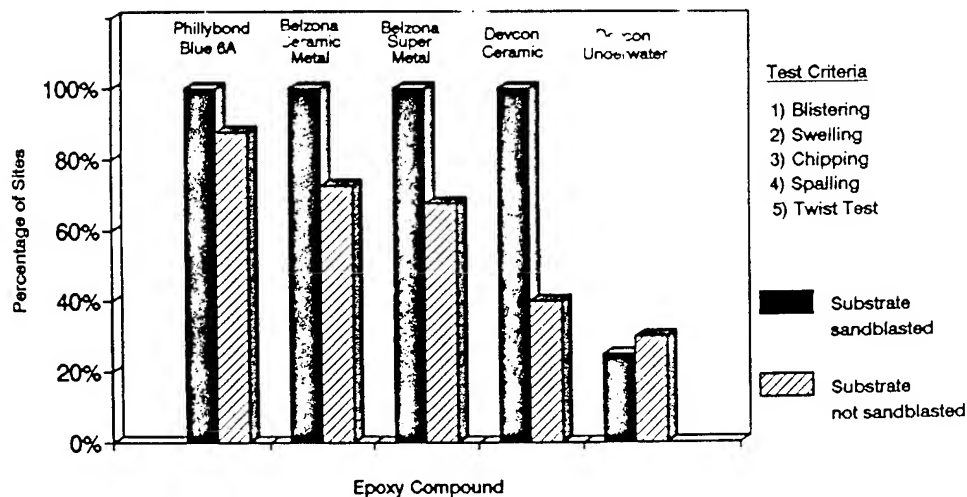


Figure 4: Results of epoxy repair corrosion tests.

ELECTROPLATE REPAIR

Cu2050 performed poorly as an O-ring sealing surface repair on both 70/30 CuNi and alloy 400. Cu2050 was found to be less noble than either substrate material and subsequently the O-ring seal area was damaged by galvanic corrosion, Figure 5. The corrosion was most severe adjacent to the O-ring which suggests that crevice corrosion was also a factor. Cu2050 was able to suppress some corrosion of the substrate, including reduced attack at the control sites. However, once the copper was sufficiently depleted, crevice corrosion of the substrate initiated. Electroplating with copper over a large surface area may suppress corrosion for a limited time, but the electroplate will galvanically corrode away leaving the original damaged area. It is recommended that Cu2050 not be used as a repair method on 70/30 CuNi or alloy 400.

Ni7280 without a copper preplate also performed poorly on the three alloy 400 specimens tested. The electroplate was subject to crevice attack directly under the O-ring and also showed some evidence of galvanic corrosion. Electroplate repair with Ni7280 was also shown to perform poorly on metal-to-metal crevices of alloy 400 in previous CDNSWC testing. Based on the limited data collected in this test and the data from previous tests, Ni7280 without a preplate is not recommended for repair of alloy 400 surfaces.

Ni2080 with a Cu2050 preplate performed best of the electroplated repair specimens, Figure 6. The only damage on the electroplating repairs was seen on the finished PH specimens. Machining of these specimens reduced the thickness of the nickel cap to a level insufficient to blanket the entire copper preplate. By adjusting the procedure to specify a minimum cap thickness, this problem should be avoidable. In addition, Ni2080 without a preplate applied to alloy 400 has previously been recommended for repair of corrosion in alloy 400 and 70/30 CuNi metal-to-metal crevices. Omitting the copper preplate guarantees that the electroplate will not fail from exposure of copper. However, a Cu2050 preplate is sometimes used since it is easier to deposit and thicker layers can be applied before additional surface preparation (reactivation) is required. The maximum one layer buildup before reactivation is 0.007 in. for Ni2080 and 0.015 in. for Cu2050 [3]. If feasible, the Ni2080 should be used without a preplate. However, if a preplate is necessary, a minimum Ni2080 cap thickness of 0.004 in. should be maintained over the entire preplate after finishing the surface is completed. This is to ensure that no copper is exposed at the surface of the repair. It is recommended that a fleet evaluation be performed of Ni2080 electroplate repair of either alloy 400 or 70/30 CuNi components.

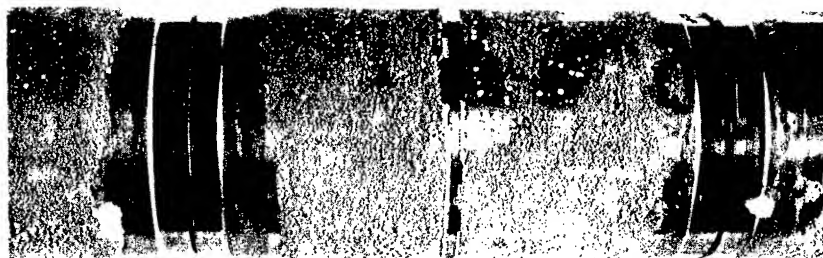


Figure 5. Control site (middle) and corroded electroplated sites on alloy 400 specimen electroplated with Cu2050.

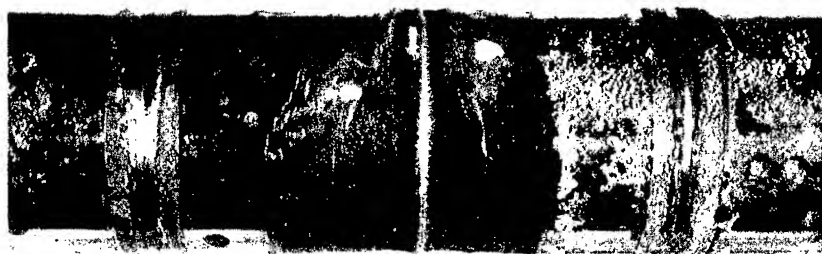


Figure 6. Control site (middle) and electroplated sites on alloy 400 specimen electroplated with Ni2080 (Cu2050 preplate).

Ni7280 capped over Cu2050 was less successful than the Ni2080 capped specimens. The Ni7280 was susceptible to crevice corrosion directly under the O-ring and also showed signs of galvanic attack. Once exposed, the Cu2050 galvanically corroded under corroded areas of the Ni7280 causing failure of the entire repair. The machined PH specimens showed higher rates of failure for reasons similar to the Ni2080 caps (reductions in cap thickness, attack of the copper preplate). Based on the results of this test, Ni7280 should not be used as a repair for O-ring seal O-ring sealing surfaces.

For some of the nickel capped specimens, corrosion of the median on the type II specimens also caused exposure of the copper preplates. This occurs because corrosion directly adjacent to O-rings on 70/30 CuNi and alloy 400 can undercut the nickel cap. To prevent exposure of copper, the nickel cap should be applied to a wider area than the preplate.

EPOXY REPAIR

The PS specimens which had the grooves sandblasted prior to application of the epoxy showed superior resistance to failure. When sandblasted, 4 of the 5 epoxies had no failures on type I specimens. A representative specimen showing the good performance of epoxy is shown in Figure 7. Surface preparation is extremely important when applying mechanically bonded materials [2]. The roughened surface produced from sandblasting significantly increases the bond strength and therefore provides a longer lasting coating. Wherever feasible, it is recommended that sandblasting be done on all surfaces which are to be repaired by epoxy. Methods to sandblast limited access areas (eg., narrow width O-ring grooves) and to sandblast small areas on components aboard ship (without grit dust in the air) should be developed.

Most failures of epoxy coatings were seen on unsandblasted and type II specimens. These failures were caused by poor adhesion of the coatings allowing seawater to leak under the coatings. The Devcon Underwater had the worst performance of any of the epoxy repairs, Figure 8. Seawater leakage under this coating caused blistering and spalling of the coating. Of the 80 sites that were repaired with Devcon Underwater, 58 failed. Sandblasting of the grooved surface did not improve this coating's resistance to failure.

The other four epoxies evaluated: Phillybond, Belzona Ceramic, Belzona Super Metal, and Devcon Ceramic, all showed similar modes of failure. First, adhesion problems would permit water penetration, to



Figure 7. Control site (middle) and epoxy repaired sites on alloy 400 specimen repaired with Phillybond Blue 6A.



Figure 8. Control site (middle) and blistered epoxy repair sites on alloy 400 specimen repaired with Devcon Underwater.

some extent, under the coating. This has been confirmed by the presence of stains on the substrate underneath coatings which have been manually removed. A crevice situation would then develop under the coating causing corrosion at the edge of the repair. For type II repairs, water leakage under the coatings was also a result of crevice attack of the median undercutting the epoxy edges. Corrosion products apparent at the edges of epoxy confirm the median corrosion. Both the water under the coating and the undercutting of the substrate from corrosion of the type II median reduced the adhesion strength of the epoxy. This poor adhesion eventually resulted in failure. Excluding Devcon Underwater, about one third of the unsandblasted PH repairs failed. Phillybond Blue 6A had the least amount of failures (5) suggesting this epoxy had the best adhesive bond strength. Phillybond was followed in order by Belzona Molecular Ceramic Metal (11), Belzona Molecular Super Metal (13), and Devcon Ceramic Compound (24).

The surface condition of the epoxy repairs can be qualitatively evaluated based on observations of the finished PH specimens. These specimens were compared based on surface smoothness and voids. The Phillybond appeared to provide the smoothest finish of the epoxies evaluated. Belzona Ceramic and Belzona Super Metal both showed slightly rougher surfaces than Phillybond. The surface condition of Devcon Ceramic could not be accurately determined because PH specimens did not have the epoxy topcoat applied. The Devcon Ceramic undercoat was fairly smooth, but contained numerous voids. The topcoat may help to reduce the number of voids on the epoxy surface. The Phillybond and the Belzona Ceramic both had few voids of very small dimensions. The Belzona Super Metal contained only a few voids, but they tended to be larger on average than for the other epoxies.

REPAIR METHOD SELECTION

Factors influencing which method is most suitable for a specific repair include the resistance to failure, the effect of a failure on subsequent system performance, the cost of the repair, and the time required for the repair. Epoxy repairs and electroplated repairs both offer good resistance to failure if proper application procedure is followed.

Areas with less than 0.007 in. of attack should be electroplated with Ni2080 whenever feasible. Although immediate repair of damage of this extent may not be required, it is recommended whenever time permits. Early repair of damage will reduce or even eliminate the need to make repairs in the future. For areas with deeper attack than 0.007 in.,

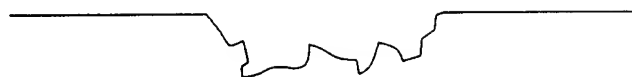
Cu2050 may be applied as a preplate under a Ni2080 cap as long as the cap has a minimum thickness of 0.004 in. Care must be taken to ensure that this minimum thickness is maintained after the surface is machined. The Ni2080 cap must also be applied to an area wider than the area plated with Cu2050 to ensure that the edges of the repair are properly covered. It is essential that no copper be exposed at the surface or edge of the repair.

A proposed procedure when using a copper preplate, shown in Figure 9, would be to first fill the damaged area with Cu2050 to within 0.004 in. of the substrate. Grind down an area a minimum of 0.063 in. wider than the Cu2050 to a minimum depth of 0.004 in. Finally, overfill this area with Ni2080 and finish to a smooth surface even with the substrate.

If electroplating repair is not feasible, epoxy repair can be considered. Epoxy repairs may be more appropriate for areas with depth of attack greater than 0.020 in. since electroplate deposit thicknesses may be difficult to achieve due to cost and/or time limitations. Epoxy repairs should have the corroded area carefully cleaned and sandblasted prior to coating application. It is recommended that Phillybond Blue 6A be used over a sandblasted surface although Belzona Molecular Ceramic Metal R, Belzona Molecular Super Metal, and Devcon Ceramic Compound (type I) may also provide good performance with this surface preparation. Since epoxies were seen to be susceptible to seawater penetration at the edges, they should be applied over as wide an area as possible to achieve the best adhesion. Epoxies must be used with caution since crevice corrosion may occur at the coating edges.

The effect of expected service environment on repair performance, and the effect of possible repair failure on subsequent component performance may dictate a particular repair selection. For instance, if an epoxy coating applied to a boldly exposed surface fails, it may completely disbond from the substrate. This failure may be catastrophic and fragments of the coating may become dislodged. On the other hand, electroplated repairs tend to fail more gradually as corrosion attacks the surface or the underlying preplate. On boldly exposed surfaces or sliding seal surfaces, and for shallow repairs, electroplate repairs would be suggested. However, epoxy coatings may be ideal for deep attack in between captured surfaces, on flange faces or pump casing halves, for instance.

The cost of a certain repair consists of the material costs and labor. The cost of the epoxy materials and the electroplating solutions is



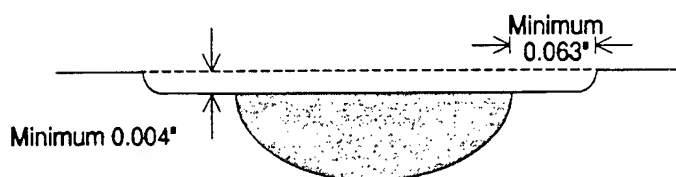
Sample cross-section of a corroded area



Step 1: Grind out pitted area




Step 2: Fill area with Cu2050  to within 0.004" of the surface



Step 3: Grind out at least 0.063" wider area to a depth of 0.004"



Step 4: Overfill this area with Ni2080 



Step 5: Machine surface until even with substrate

Figure 9. Recommended procedure for electroplating Ni2080 with Cu2050 preplate.

fairly insignificant compared to the labor costs involved. Electroplating generally requires more labor time than epoxy applications, especially when multiple layers of electroplate are required. Therefore, electroplating may be more feasible for shallower grooves where two or less layers of electroplate is required. However, the effect of possible failure on service performance will probably be the determinant factor in repair method selection.

In addition to service environment and labor costs, restricted availability for repair also contributes to selection of repair method. For example, during time-restricted component availabilities, epoxy may be easier to apply than electroplating, especially for deeper repairs.

When electroplating, it is recommended that MIL STD 2197 (SH), "Brush Electroplating on Marine Machinery" [1] be followed supplemented by the instruction manual for the electroplate solutions. The Sifco Selective Plating Dalic Process Instruction Manual [3] was utilized by both shipyards. It is also recommended that when a copper preplate is being used, a minimum cap thickness of 0.004 in. be maintained over a minimum 0.063 in. wider area than the preplate as previously detailed (Figure 9).

Proper surface preparation was found to be the most important criteria when applying epoxies. Therefore, it is recommended that sandblasting be performed on all surfaces repaired with epoxy. The details on applying each epoxy type; e.g. temperature, mixing, curing time, etc., were unique to the instructions supplied by the manufacturer of each epoxy and it is recommended that these specific instructions be followed for each compound.

SUMMARY AND RECOMMENDATIONS

Corrosion tests were conducted to evaluate the relative performance of electroplate and epoxy repair methods presently used by Navy Shipyards to refurbish areas of corrosion on 70/30 CuNi and alloy 400 components. In approximately one year seawater immersion tests, both electroplating and epoxy repairs were found to offer protection from corrosion in the repaired area. The performance of the several repair methods was similar on both 70/30 CuNi and alloy 400. Test results indicate electroplating can provide excellent service when used as a repair in the shaft seals area. Epoxy repairs should probably be limited to captured surfaces, or large areas of deep repair to obviate problems with disbondment and subsequent dislodgement of chunks of epoxy into operating systems.

Of the electroplating materials evaluated, Ni2080 had the best

performance and is recommended over Ni7280 or Cu2050. Cu2050 may be used to fill under the Ni2080, provided a minimum cap thickness of 0.004 in. should be maintained over a minimum 0.063 in. wider area than the preplate.

Of the epoxies, Phillybond Blue 6A had the best performance on unsandblasted specimens and the smoothest surface finish. If the substrate surface was sandblasted before applying epoxy, four epoxies had good performance: Phillybond Blue 6A, Belzona Molecular Super Metal, Belzona Molecular Ceramic Metal R, and Devcon Ceramic Compound (type I). Devcon Underwater performed poorly in this test and is not recommended. Epoxy repairs should be applied on a sandblasted or equivalently prepared substrate surface.

REFERENCES

1. MIL-STD-2197 (SH), "Military Standard: Brush Electroplating on Marine Machinery," 28 March 1989, Superseding NAVSEA 0900-LP-038-6010, September 1972.
2. Surface Preparation: The State of the Art, Proceedings of the SSPC Annual Symposium, May 1985.
3. SIFCO Selective Plating, Dalic Process Instruction Manual, 4th Edition SIFCO Industries, Inc., 1985.

SESSION IX
ENVIRONMENTAL TECHNOLOGY

Chairman: *J. Beatty*

BLANK

724

Revision of Navy Paint Specifications

Mr. David Pulley
Naval Air Warfare Center
Aircraft Division
Box 5152
Warminster, PA 18974-0591

Introduction

The Navy maintains a number of specifications for the organic coatings applied to aircraft and ground support equipment. These documents are periodically revised and amended to include lessons learned from qualification testing, improvements in the state-of-the-art, and new regulatory requirements. To accomplish these objectives, we will revise ten different specifications by the end of this year. They include:

- MIL-C-8514 wash primer
- TT-P-1757 alkyd primer
- MIL-P-23377 and MIL-P-85582 epoxy primers
- TT-P-2760 polyurethane primer
- MIL-L-81352 acrylic lacquer
- MIL-P-52905 temporary, acrylic lacquer
- MIL-C-22750 epoxy topcoat
- MIL-C-85285 polyurethane topcoat
- MIL-C-85322 polyurethane, rain-erosion coating

All of these specifications (including every type and class) will comply with air-pollution regulations that limit the volatile organic compounds (VOC) content. This will be accomplished using water-borne or high-solids coatings technology. The maximum VOC content will generally be set at 340 grams/liter for primers and 340-420 grams/liter for other coatings. The use of 1,1,1-trichloroethane (exempt from VOC regulations) will no longer be permitted due to its classification as an ozone-depleting substance. This solvent will be banned, along with other chlorinated

and fluorinated compounds, in the near future. In addition, the use of hexavalent chromium is being restricted since it is a suspected carcinogen. Strontium and other chromates are the accepted standard for the protection of aluminum structures. We will continue to use them as long as possible, but will also include provisions for non-chromate inhibitors. Finally, we are revising several specifications to introduce three new materials. This includes a water-reducible, wash primer; a one-component, touch-up paint; and a temporary, camouflage paint.

1,1,1-trichloroethane

1,1,1-trichloroethane is widely used as a cleaning solvent, particularly for vapor degreasing of metal parts. It is also used as a solvent in formulating and thinning various paints. This includes the following aircraft coatings:

MIL-P-23377F, Class 3 epoxy primer
TT-P-2760, Class 3 polyurethane primer
MIL-C-22750E, Type II epoxy topcoat

A number of contractors have used these products to meet VOC regulations, because they involve a simple paint reformulation with little additional cost and similar application properties. The viscosity is lower and the pot life is longer than typical high-solids coatings. There are also disadvantages. Chlorinated solvents, such as 1,1,1-trichloroethane, can react with certain metals (particularly at high temperatures or pressures). Spray equipment must have all wetted parts made of stainless steel or other resistant materials. Many high-strength aluminum, steel, and titanium alloys are susceptible to stress-corrosion cracking. Paints applied to these metals must be formulated with an inhibited grade of 1,1,1-trichloroethane (such as Dow CHLOROTHENE SM) and cannot be used on hot, engine parts or in areas where the solvent could be trapped. This includes faying surfaces and the wet installation of fasteners.

1,1,1-trichloroethane is one of several chlorinated solvents that are exempt from current air pollution regulations, because they are not

photochemically reactive and do not contribute to smog (ozone) formation in the lower atmosphere. However, they are members of a class of chlorinated and fluorinated compounds that contribute to the destruction of the ozone layer in the upper atmosphere. All of them will be banned or severely restricted from use by the end of 1995. We will comply by eliminating the affected types and classes in all Navy specifications.

Chromate Pigments

The use of hexavalent chromium is greatly restricted, since it is a suspected carcinogen. Corrosion inhibitors such as strontium, barium, and zinc chromates are the accepted standard for the protection of aluminum structures. They are used in the following primers:

MIL-C-8514 wash primer
TT-P-1757 alkyd primer
MIL-P-23377 and MIL-P-85582 epoxy primers
TT-P-2760 polyurethane primer

We will continue to use chromates as long as possible, but will also include provisions for non-chromate inhibitors. Blends of phosphates, molybdates, borates, and other novel compounds are being formulated into corrosion-resistant primers and self-priming topcoats. These coatings, due to their low toxicity, are becoming an acceptable alternative for many applications. Unfortunately, we know little about their performance in long-term use. Many of our aircraft will be in service for 40 years or more. Exterior surfaces are generally stripped and repainted every 4-8 years. However, the interior surfaces may never be touched unless there is a known corrosion problem. These areas are subject to the intrusion of water and other corrosive media. The use of non-chromate primers in such areas could involve some risk. Paint manufacturers consider the formulations to be a proprietary trade-secret. We must rely totally on the corrosion resistance requirements in the specifications to assure performance. We will, therefore, upgrade the requirement for salt-spray exposure from 1,000 to 2,000 hours to improve our level of confidence.

In addition, we will forbid the use of lead and cadmium compounds in all of the revised specifications. Chromate compounds will also be forbidden in coatings other than primers. The primer specifications will be divided into Class 1 (chromate inhibitors) and Class 2 (non-chromate inhibitors) materials. Steps will be taken to prevent the procurement of non-chromate primers by unauthorized users. Existing stock numbers will be transferred to the appropriate class in the new specifications. Warnings will be added to the documents, stating that Class 2 primers should only be used with the approval of the engineering authority and buyers should obtain Class 1 primers unless Class 2 is specifically requested.

Water-reducible, Wash Primer

Specification MIL-C-8514 describes a wash primer, composed of a polyvinyl butyral resin reacted with a phosphoric acid catalyst. Because of their ability to bond directly to bare metals, wash primers are also referred to as pretreatment coatings. Zinc chromate is the specified corrosion inhibitor. Unfortunately, the VOC content of a typical primer is about 780 grams/liter. Variations in the chemistry have helped to reduce the VOC content. Sherwin-Williams has developed a water-reducible "prep primer", with the same corrosion inhibitor but a different acid catalyst, that performs well in all applications. At 420 grams/liter, it still exceeds the 340 grams/liter limit for aircraft primers. A water-reducible epoxy primer from Deft, with a non-chromate inhibitor, bonds to bare metal by virtue of an amine catalyst and adhesion promoters. With the exception of galvanized steel, it adheres well to all substrates. The VOC content is 250 grams/liter, well below the limit.

We intend to revise specification MIL-C-8514, without requiring a specific formulation, to achieve VOC compliance with both chromate and non-chromate corrosion inhibitors. The performance requirements will be based on the Sherwin-Williams and Deft primers.

One-component, Touch-up Paint

Courtaulds Aerospace has developed a one-component, water-borne, polyurethane topcoat that is ideal for touch-up applications. Since it is supplied in a single package, the paint is easy to mix and apply and has a minimum pot life of eight hours. Unused material can be poured back into the original container (reducing hazardous wastes). Although it is a polyurethane, the resins are prereacted to remove all free isocyanates. This greatly reduces the toxicity and may allow the coating to be used aboard ship. Its performance is almost equal to that of standard, two-component, polyurethane topcoats. The use of this material for touch-up will eliminate the "spotted" appearance obtained when epoxy topcoats are applied over the existing polyurethane coating system. The VOC content is 340 grams/liter.

Service tests have been scheduled on aircraft and ground support equipment at air stations in Oceana, Patuxent River, Miramar, and Whidbey Island. The touch-up paint will be included as a separate type in specification MIL-L-81352 (currently an acrylic lacquer). This would be a good fit, since both materials are one-component topcoats.

Temporary, Camouflage Paint

The camouflage scheme for tactical aircraft is a combination of various shades of gray. This color scheme is a compromise, based on cloudy conditions over a variety of terrain. During rapid-deployment missions or war-game exercises, it may be necessary to change aircraft colors on short notice to match the terrain in a specific area (desert, forest, etc.). This can be done with a temporary paint containing water-borne, acrylic resins similar to that used in floor polish. The paint is applied over the existing polyurethane coating system with a brush, roller, or spray equipment. It dries to a smooth, flat finish that resists common aircraft fluids with the exception of alkaline cleaners. After completion of the mission, the paint is removed using a mild stripper with no effect on the underlying coatings.

Service tests on both in-house and proprietary formulations (Seagrave Coatings) were conducted at air stations in Oceana, Beaufort, Tustin, and North

Island. The only problem involved some difficulty in removing the paint when left on for several months in a hot, sunny location. The next revision of specification MIL-P-52905 will include provisions for various colors of the temporary paint. This is an Army document for a similar material used in arctic camouflage.

Optimization and Prototyping of Medium Pressure Water (MPW) Depaint Process

Mr. John Stropki*
Battelle, Columbus
505 King Avenue
Columbus, OH 43201-2693

Mrs. Robin Lee Stearns
OC-ALC/EMV
Tinker Air Force Base
OK 73145-9100

Introduction

This research program was designed to evaluate the potential of a paint stripping process that utilizes a medium pressure water jet as a viable alternative to the current practice of paint stripping and cleaning of aircraft with hazardous chemicals. The means of determining the viability of this environmentally safer blast process was predicated on establishing a set of process parameters at which paint stripping was accomplished at an economically sound rate, while minimizing any possible substrate damage.

A complete evaluation of the Aqua Miser® medium pressure water (MPW) blasting process and four candidate nozzles was conducted through three discrete tasks. Task 1 concentrated on (1) establishing depaint efficiency and (2) characterizing any potential substrate damage as a result of stripping with the MPW process. Tasks 2 and 3 included a field-level demonstration and evaluation of the Aqua Miser system on aircraft component parts and partial aircraft airframes, respectively.

A description of the technical activities and results obtained from each of the three tasks is provided in the following text.

Technical Approach

A summary of several OC-ALC requirements which are scheduled to be satisfied throughout the next 18 months includes:

(1) MINI-LARPS (Large Aircraft Robotic Paint Stripping Facility)

- Installed and operational in Fall, 1994
- Use confined to depainting aircraft and component parts

(2) LARPS Facility

- Installed and operational in Spring, 1995
- "Full-scale" depainting of KC-135 and B-1 aircraft

(3) MPW Process

- Use confined to either touch-up or backup to LARPS on KC-135 and B-1 aircraft
- Use on B-52 and E-3 aircraft which cannot be depainted by LARPS because of facility limitations
- Full or partial depainting/cleaning of aircraft components.

Detailed descriptions of the various tasks conducted as a part of this study are provided in the following text.

Task No. 1. Optimization Testing of MPW Process

Task activities were divided into the following four subtasks: (1) Production Rate Assessment, (2) Qualitative Damage Assessment, (3) Spot Weld Integrity Assessment, and (4) Structural Vibration Stress Test. All four subtasks concentrated on determining the process parameters that produce the most efficient paint stripping rate with minimal blast imparted damage to common aluminum aircraft alloys. Production rates obtained during all optimization testing were determined by calculating the rate at which paint is removed from test panels with only water. Potential blast damage was determined by (1)

measuring any deformation which developed on the surfaces of small test coupons (arc height samples) after the paint removal operation, (2) characterizing the integrity of spot welds, and (3) measuring the stresses imposed on aluminum test panels that are configured to be representative of actual aircraft structures.

Production Rate Assessment

The type and dimensions of materials that were used to perform all optimization testing of the Aqua Miser water-only process with four (dual orifice, rotating head, fan, and LARPS) nozzles that were evaluated include:

- AL2024-T3 alclad - 0.032 inch by 24 inches by 24 inches.

Individual panels were coated with several "in-service" coating systems which included: polysulfide primer/polyurethane topcoat, Koroflex primer/polyurethane topcoat, self priming topcoat (SPT), solvent-based epoxy/polyurethane topcoat, and water-borne epoxy/polyurethane topcoat. The dry film thicknesses of most coatings ranged between 0.002 and 0.003 inches. Panels were cured for 7 days in a controlled laboratory environment that was maintained at 72 F and 50 percent relative humidity. All panels were then artificially aged in an oven at 210 F for 50 hours.

The process used for all optimization testing included a Government-furnished Model E25 Aqua Miser BOSS Blasting System that was manufactured by Carolina Equipment and Supply Company. By design, this electric unit is rated at 3.2 GPM @ 15,000 psi and capable of being adapted for use with the four different types of nozzles that were evaluated.

Control of the paint removal process on all test panels used for process optimization was achieved with a computer-controlled table assembly that was available at Tinker AFB. The horizontal axis of the table was capable of achieving speeds up to 4.0 inches per second and traveling approximately 24.0 inches in both directions. Individual test panels were mounted to the table and were positioned

[REDACTED]

at a minimum distance of 2 inches and at a 60-degree angle from the blast nozzle.

Qualitative Damage Assessment

The type and dimensions of the Almen specimens used to determine the potential blast-induced damage to thin aluminum airframe materials included:

- A12024-T3 bare-- 0.032 inch by 0.75 inch by 3 inches.

The 3-inch dimension of all specimens was oriented in the sheet rolling direction. In addition, all Almen specimens were sheared from painted panels. Blasting of individual specimens was on the common face of the original panel.

Panels from the individual Almen specimens were painted with each of the "in-service" coating systems and aged in accordance with the previously described procedures.

The protocol used to develop arc height data (blast-induced specimen deformation) included a quasisaturation blasting of the Almen specimens. Individual specimens were not repainted between the initial depainting cycle and after the subsequent four blast cycles. This form of testing represents a "worst-case" situation that may occur from either excessive dwell time during paint removal operations or the equivalent of an expected depainting cycle of Air Force aircraft.

The Almen specimen test fixture was mounted on the x-y table in a direction that ensured that the blast stream traversed the specimens perpendicular to the rolling direction of the Type 2024-T3 aluminum alloy. This alignment permitted full coverage of the test specimen with one pass of the blast stream. Final Δh measurements were made from Almen specimens that are blasted with the traversing direction perpendicular to the roll direction of the specimens. This was done to ensure that the Δh measurements were consistent with the procedures established by Battelle during previous Air Force paint removal programs.

Spot Weld Eddy Current Inspection Testing

Test panels for the spot weld integrity tests were prepared using two panel configurations: flat and 2-inch radius bend. Bends applied to the appropriate panels were applied prior to spot welding. Panels were constructed from the following materials and thicknesses:

- A12024-T3 alclad, 0.032 inch
- A12024-T3 alclad, 0.080 inch
- A17075-T6 alclad, 0.032 inch
- A17075-T6 alclad, 0.080 inch.

Fabrication and testing protocol for the various sets of metal test panels was in accordance with the OC-ALC LARPS Qualification Plan (paragraph 4.2.19).

The procedures used to conduct all spot weld eddy current inspections are as follows:

- Preparation of two (flat and 2-inch radius bend) panels for each of the four materials per LARPS Qualification Plan (paragraph 4.2.19).
- Establish baseline measurements by nondestructively eddy current inspecting every spot weld per T.O. IC-135-36.
- Blast panels with each of the four nozzles and optimized blast parameters that were obtained from testing performed in Subtasks 1 and 2. Two stripping cycles per panel.
- Nondestructively inspect every spot weld on stripped panels per T.O. IC-135-36.
- Compare all baseline measurements with post-stripping measurements to determine the location and frequency of broken spot welds.

[REDACTED]

The spot welding of all test panels was performed at OC-ALC. Additionally, all pre- and poststripping eddy current inspection testing was conducted by OC-ALC.

Structural Vibration Testing

A simulated aircraft fuselage section or test box was constructed to perform several stress tests during this subtask. The approximate dimensions of the box are 9 inches by 21 inches. As was discussed with OC-ALC/TIESM and OC-ALC/LAPEP personnel, the frame of the box was constructed from aluminum angles that are spaced to simulate the dimensions between ribs and stringers on an aircraft. Two different 8 inch by 8 inch test panels are scheduled to be evaluated on the frame. One panel is fabricated from 0.032-inch Type 7075-T6 bare aluminum sheet, and the second panel from 0.032-inch Type 2024-T3 bare aluminum sheet. Panels are to be secured to the angles with 0.0125-inch threaded fasteners, which are evenly spaced around the perimeter of the panel being evaluated. The strategic placement of several strain gages and an accelerometer onto the underside surfaces of the test panels permitted a recording of all stress and vibration measurements.

The intent of this test was to measure the induced strains and frequencies generated by the MPW process on a simulated aircraft fuselage section and assess the potential for fatigue damage.

Construction of the test box included the mechanical fastening of a single test panel to the aluminum frame. No sealant was used between the test panels and frame. Six strain gages were instrumented along the internal surfaces of each test panel. All components were secured and sealed to ensure maximum protection from potential water damage.

Stresses introduced onto the test panel as a result of the MPW process were measured by the strain gages at several intervals throughout the blasting process. Various combinations in nozzle stand-off distance, traverse rate, and blast jet rotational rate were investigated. The pressure of the water blast stream was maintained at approximately 15,000 psi. Testing did not include bicarbonate-of-soda media.

Task No. 2. Prototyping of MPW Process With BOSS Media on Aircraft Component Parts

Activities performed during this task concentrated on depainting aircraft component parts at Tinker AFB. Process parameters established for MPW and MPW plus bicarbonate-of-soda media blasting of the standard polyurethane coating system during testing conducted at WR-ALC and OC-ALC were used. All blasting operations were performed by OC-ALC personnel in Building 2122. This facility represented a production environment, therefore, was equipped with the power, air, water, and drainage requirements to complete this task. A summary of the activities performed, as well as the protocol for conducting this task, is provided in the following text.

The MPW plus media process was used to clean and/or repaint four (4) engine cowling parts that were selected and removed from B-52 aircraft. All components were painted and heavily soiled with carbon residues and oil contaminants. Components had a metallurgical composition of either A12024 and A17075 and were classified MISTR (Maintenance Items Subject to Repair) parts that are authorized by OC-ALC to repaint with plastic media beads (PMB).

The Model E25 Aqua Miser unit used during the water-only optimization phase of Task I was used for blasting all painted component parts. However, a controlled rate of bicarbonate-of-soda media was introduced into the blast stream to increase repaint efficiency. Process efficiency was maximized by using the results of controlled testing that was performed on standard epoxy/polyurethane test panels that were repainted during Task I and at WR-ALC. The standard two-handed fan nozzle was the only nozzle that was to be used with the bicarbonate-of-soda media. Additional prototype testing with the LARPS mini-nozzle and water-only is also scheduled for repainting "select" airframe components.

Additional activities performed as part of this task included: (1) on-site technical assistance and/or training of OC-ALC production personnel responsible for operating and maintaining the MPW system, (2) measuring and documenting operational parameters which included safety and health-related hazards, and (3) an identification of all costs (shop floor time, man-hours, consumables, and equipment

[REDACTED]

amortization) associated with the efficient operation of the Aqua Miser process. Process efficiency was determined by the production-level strip rates that were obtained at the initiation of this task.

Task No. 3. Prototyping of MPW Process on Partial Airframe Sections

Activities performed during this task focused on depainting Air Force designated airframe sections on large aircraft (KC/C-135 and B-52) that are maintained at Tinker AFB. Integration and testing of the optimized MPW process was conducted in conjunction with OC-ALC production personnel. Optimal blasting parameters established for a single nozzle that was selected during Task 1 was used in the testing conducted during this task.

On-site assistance was provided during the actual blasting operations that were performed by OC-ALC production personnel in a designated section of Building 2122 at Tinker AFB. Numerous aircraft depainting operations are performed in this facility; therefore, the basic (air, water, and electrical) requirements of the MPW system are available.

A summary of the activities that were performed, as well as the protocol for conducting this task, is provided in the following text.

Testing performed during this task is limited to the various aluminum (A12024, A17075 and A17079) airframe structures that are able to be depainted with the MPW process. OC-ALC/LAPEP stated that all depainting was to be performed on select areas (approximately 100 square feet) of structures on E-3 or B-52 aircraft. Possible areas included:

- top/bottom sides of wing
- fuselage (2 areas)
- vertical stabilizer
- engine nacelle.

OC-ALC personnel plan to provide Battelle with a mapping of the various coating systems applied to the structures that are to be

depainted. The majority of airframe structures are painted with the standard epoxy/polyurethane coating system. However, prototyping is to include a complete removal of the Koroflex primer/polyurethane coating system. No observable process-induced substrate damage is anticipated for these structures. Areas adjacent to the depainted structures are to be masked by OC-ALC personnel prior to testing.

Selective stripping of any non-standard coating systems that are on airframe structures are also scheduled to be investigated during this task. This stripping process involves the removal of only the outermost (topcoat) protective coating from the airframe structure. If proper techniques are used the primer on the structure will remain intact after being blasted with the medium pressure water.

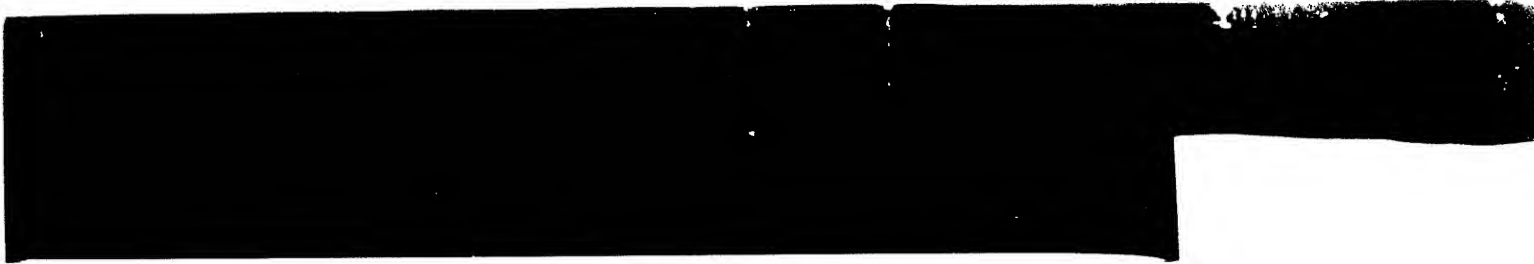
The efficiency of the MPW process on aircraft structures is to be assessed by (1) determining the production strip rates for the various structures, and (2) visually characterizing the condition of the depainted structures.

All stripping parameters selected as a result of the testing performed during Task I are to be used to depaint approximately 1,000 square feet of select airframe structures. Carolina Equipment and Supply personnel were responsible for providing all services related to equipment set-up and the training of production personnel. On-site technical direction to OC-ALC production personnel was also provided to ensure that the optimized stripping parameters are maintained from structure to structure. This process summarized any problems that may develop in the production environment as a result of hardware limitations.

An additional aspect of this task will be to work closely with production personnel at Tinker to measure and document a final set of depainting parameters that maximizes the efficiency and safety of the MPW process.

Results

The results obtained from a limited amount of optimization and prototype testing that has been performed on each of the three tasks confirms that the water-only blasting process is capable of meeting



the depaint production requirements of OC-ALC. Process capabilities that have been successfully demonstrated during Task I testing include (1) selective (topcoat only) and, (2) full depaint of "in-service" coating systems that are on OC-ALC aircraft. To date, all testing has been conducted on painted test panels with water-only blasting parameters. No bicarbonate-of-soda media was used on partial airframe test panels or sections of aircraft.

Optimization Testing

A total of four MPW blast nozzles were evaluated on 0.032-inch A12024-T3 alclad/bare panels. Included in the test matrix were panels coated with five different paint systems. A set of optimized blast parameters were obtained for each nozzle/coating system combination.

Results indicate that the highest production depaint rates and least damage on coated panels were obtained for the one-jet "hammerhead" or rotating nozzle and modified LARPS nozzles. Acceptance criteria for both nozzles were based on the quality of the surface finish for full and selective depainting with the MPW process.

The production rates and damage (Almen arc heights) measured for the various nozzles (selective and full depaint) are provided in Figures 1 and 2. As shown, no one nozzle will efficiently depaint all "in-service" coating systems. The highest selective depaint rates (1.1 to 2.3 ft²/min) were obtained for nozzles on the polysulfide/polyurethane coating system. Conversely, the LARPS, fan, and one-jet nozzles were the only nozzles capable of completely depainting all coating systems at an efficient (0.5 ft²/min) or acceptable rate. Disadvantages associated with the LARPS and fan nozzles, and related depaint parameters are the small standoff distances, narrow "footprints" and residues that remain on the surfaces of the aluminum panels coated with the Koroflex and polysulfide primers. These residues require a chemical (thinned version of SR-125A) clean-up prior to repaint processing. This clean-up is also required for the epoxy/polyurethane and Koroflex/polyurethane coatings that are removed with the one-jet or "hammerhead" rotating nozzle.

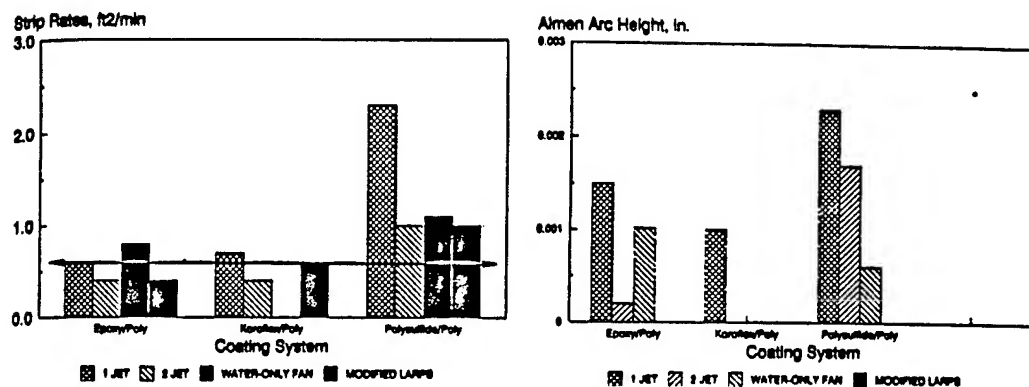


Figure 1. "Best" Selective Strip Processes

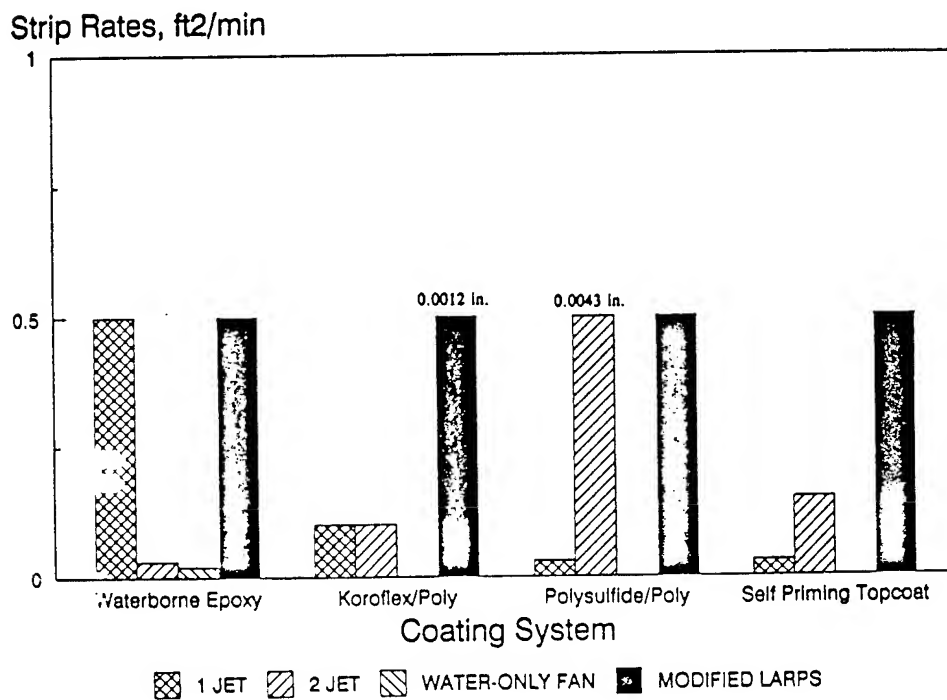


Figure 2. "Best" Full Strip Processes

All depaint parameters obtained for the LARPS and one-jet nozzles are to be used for component parts and partial airframe prototyping activities. Production rates on the "aged" Koroflex/polyurethane coating system of E-3 or B-52 aircrafts are scheduled to be obtained and compared to rates measured during laboratory testing. An assessment of the quality of the surface finish of the depainted airframe sections also will be performed and used to verify the production efficiency of the MPW-process. Final acceptance of the process will be based on the results obtained from the stress and spot-weld tests.

Stress and Spot-Weld Testing

To date, no results are available for these two tests as all testing has not yet been completed. Limited depainting of spot-weld panels has been performed and no damage or cracking has been measured for the examined spot welds. Testing included 2-pass processing with the dual-orifice nozzle on both flat and curved panels. Additional testing with each of the remaining three nozzles is required before a final set of results are provided to OA-ALC/LAP personnel.

Component Parts and Partial Airframe Prototyping

All prototyping activities are scheduled for completion during July, 1994. This particular task was intentionally delayed until the results of the stress and spot-weld tests are available. If the results of these tests indicate that the MPW process is a viable production tool, then the aircraft prototyping activities will be completed.

Preliminary cleaning and depainting of coating systems applied to the internal surfaces of B-52 engine cowlings have been completed. The results of these exercises have confirmed that the MPW process is capable of efficiently cleaning "baked on" carbon residues from the components. A post-blast examination of the depainted surfaces indicates that the process is acceptable and capable of providing a quick clean-up of these components. Additional cleaning and depainting of component parts is scheduled at OC-ALC. The results of these depaint exercises will be reviewed for input into the final report that is scheduled for issuance during September, 1994.

Evaluation of Environmentally Acceptable Protection Schemes for High Strength Steel Fasteners

B. Placzankis, M. Levy, J. Beatty, S. Isserow, M. Kane
US Army Research Laboratory
Materials Directorate
Metals Research Branch
Corrosion Science Team
Watertown, MA 02172-0001

Accelerated corrosion tests were carried out to assess the performance of selected coated fastener assemblies representative of those used in the M1 Abrams tank and Bradley fighting vehicle. The samples consisted of various coatings on grade 8 steel bolts inserted through/into armor steel or Al 5083 blocks. The coatings tested included currently used electroplated Cadmium as well as IVD (Ion Vapor Deposited) Aluminum, and a proposed binary, Zn-Ni electroplate. The effects of co-mingling electroplated Cadmium with the other coatings utilized in the test assemblies were determined. Salt spray testing was performed in accordance with ASTM B117. In addition, salt water immersion tests were performed with continuous monitoring of the electrochemical potential. Breakaway torque values obtained after completion of either immersion or salt spray tests were compared against coefficient of friction measurements taken from the scratch tests.

Cadmium electroplate exhibited excellent corrosion protection for grade 8 steel bolts in salt spray or immersion tests. The IVD Aluminum (chromated) and Zn-Ni coatings were the best overall alternatives to Cadmium plate. Co-mingling of Cadmium with the other coatings did not create significant galvanic corrosion problems. Loosening of the Zn-Ni alloy plated fasteners will not likely occur if torque values specified for Cd plate are used. Breakaway torque values were proportional to the respective coefficient of friction measurements from scratch tests for all but the IVD Aluminum coated specimens.

Background

Initial corrosion testing was done by ARL Materials Directorate in 1991 in a TACOM (Tank/Automotive Command) sponsored study to determine the effects of substituting Zinc or various other coating systems

in the place of electroplated Cadmium. In addition to test assemblies utilizing a single coating, mixed assemblies comprised of various coated bolts and Cadmium coated washers/nuts were evaluated. The results were published in a technical report (MTL TR 92-40),¹ which contains complete corrosion data and photographic documentation of the corrosion observed throughout the test program for Cd, Zn-Ni, Zn OD (Olive Drab finish), Zn-Co, Sn-Zn, and modified phosphate coatings. This paper will summarize these results, and add data for IVD Al. Three types of IVD Al are compared against the Cadmium and Zn-Ni plating.

Program Outline

The test program and fasteners assemblies were developed by G. MacAllister, TACOM (retired), and M. Levy, ARL-MD (retired). The test assemblies consist of sections of actual armor plate and the coatings tested are described in more detail in the following section. The two methods of testing used on the assemblies were saltspray, and 3.5% saltwater immersion in which E-corr values were measured vs. time.

Materials

All bolts were fabricated of SAE Grade 8, J429 steel, HRC 33-39 (Figure 1) and meet the requirements of MS-90728.



Figure 1 - Grade 8 Test Bolt

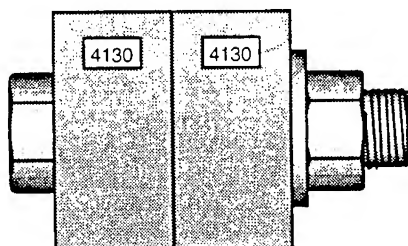


Figure 2 - Joint A Assembly

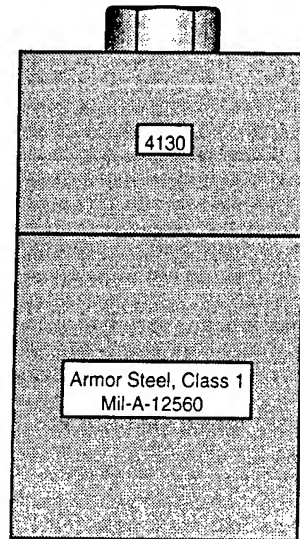


Figure 3 - Joint B Assembly

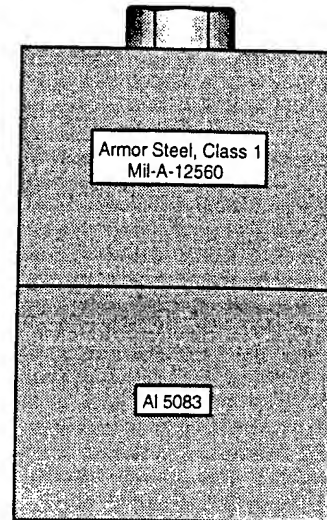


Figure 4 - Joint C Assembly

In material and dimensions the nuts and washers were compatible with the grade 8 bolts. The two blocks in (assembly) Joint A (Figure 2) are fabricated of SAE Grade 4130 steel, HRC 30. The Joint B blocks (Figure 3) use armor steel described in MIL-A-12560, class 1 (HRC 28-33) in conjunction with 4130 steel. The Joint C assemblies use Aluminum alloy Al 5083 with 12560 armor steel. Chemical analysis of the armor alloys utilized is shown in Table 1.

Table 1 - Chemical Analysis of Test Blocks

Alloy	C	Mn	P	S	Si	Cr	Ni	Mo	V
4130	0.32	0.49	0.013	0.002	0.23	0.97	0.09	0.23	<0.01
Mil-A-12560	0.28	1.36	0.016	0.001	0.23	0.12	0.09	0.47	<0.01
Al 5083	*	0.55	*	*	<0.15	0.10	<0.05	*	*

Alloy	B	Fe	Cu	Mg	Ti	Sn	Zn	!
4130	<0.0005	base	*	*	*	*	*	*
Mil-A-12560	0.002	base	*	*	*	*	*	*
Al 5083*	*	0.35	<0.05	4.2	<0.15	<0.05	<0.09	base

* Denotes alloying elements not measured

Coating Parameters

Cadmium plating was performed by Cadillac Plating Corp and processed in accordance with QQ-P416 Type II Class 3 and baked with a minimum thickness of 0.0002 in. FMC processed the Zn-Ni plating in accordance with their proposed specification covering the requirements for electrodeposited zinc-nickel alloy plating Class 3, Type II, minimum thickness 0.00030 in. The Zn-Ni alloy plate is 6-20% Ni. The IVD Al

coating was processed at Anniston Army Depot, Anniston, AL. Pressure, wire feed rate, and current density were all held constant. The rack speeds and number of passes varied. The first run of specimens post treated with the sodium chromate treatment had a deposition period of 25 min and a measured thickness of 24.7 mils. The following two runs, IVD Al only, and IVD with Ni acetate treatment, both were deposited for about 12 min and measured 2.8 and 3.0 mils respectively.

Experimental Procedure

Accelerated corrosion tests were carried out to assess the performance of the coated fasteners described above. Salt fog testing was performed in accordance with ASTM B117. Observations were made and recorded every 24 hours of exposure up to 312 hours. The salt spray specifications for currently used electrodeposited coatings of Zinc and Cadmium require that these treatments shall show neither their white corrosion products nor basic metal corrosion products at the end of 96 hours of salt spray exposure. Identical specifications were applied for Ion Vapor Deposited Al. Due to a shortage of test blocks, the IVD Al, and IVD w/Ni acetate were not tested in saltspray (when sufficient test blocks are prepared, saltspray tests will be conducted). In addition, salt water immersion tests (3.5% NaCl solution) were performed in a circulating bath at 25°C with continuous electrochemical potential measurements (see Figure 5) and visual examinations made every 24 hours up to 312 hours of exposure.

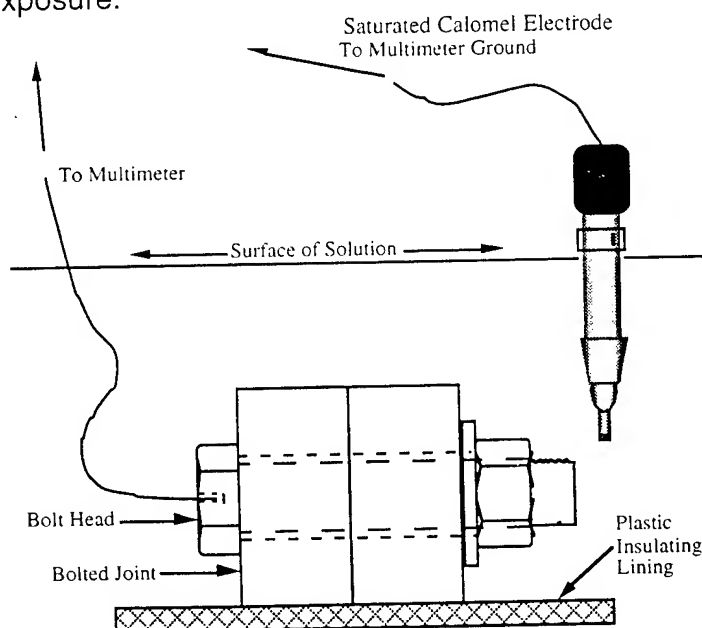


Figure 5 - Immersion Bath Setup

The electrical contact was made at the bolt head by drilling a small hole in its center and then soldering in an insulated wire. Silicone sealant was used to prevent erroneous readings caused by electrochemical interactions with the solder or wire (Figure 6). Photographs of the fastener assemblies were taken before and after testing to show the degree of corrosion developed. The coefficient of friction of the various platings were determined by the CSEM Revetest Scratch Tester, where a moving diamond stylus "scratches" the plated surface under either constant or linearly increasing load. This instrument is equipped with an integrated optical microscope, an acoustic emission detection system and a device to measure the tangential frictional force (in the scratching direction), from which the coefficient value is determined. Breakaway torque values for Joints A, B, C were obtained after either immersion or salt spray tests were completed.

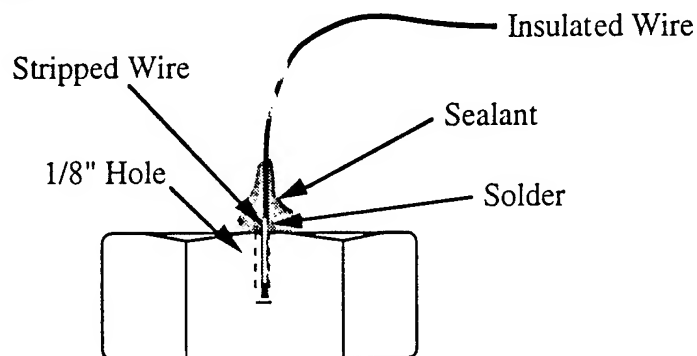


Figure 6 - Close up of immersion test bolt head

Results

For a high strength fastener used in a corrosive environment, a series of certain traits is desired. The protective coating, must be inexpensive, thin, uniform, and anodic with respect to the substrate material while not being so anodic that hydrogen assisted cracking may result. Electroplated Cadmium easily meets these criteria. However, because of the potential health risks posed by Cadmium, alternative coatings must be identified. Further, the "environmental acceptability" of any potential protective coating must also be considered an important selection criteria. All of the other coating materials tested are considered environmentally acceptable alternatives to Cd plating.

Salt Spray, Controls

The control assembly was used to observe the corrosion behavior of the bolt, nut, and washer without the influence of the joint assemblies. Table

2 contains observations made for the various coated control assemblies as a function of exposure time. Supporting photographs are contained in Appendix A, Figures I-III. The Cadmium coated components and chromate treated IVD Al showed no evidence of corrosion products (white or red rust) even after 312 hours (13 days) of exposure (Table 2, Figures I & II). The performance of the Zn-Ni coating, the first of a series of newer coatings being evaluated for military applications, is described in Table 2 and shown at 312 hours in Figure III. This coating protected the bolt, nut and washer assembly for 192 hours (8 days) although some staining was observed after 96 hours of exposure. White corrosion products appeared between 216-312 hours. Though not as good as the Cd or the thick chromated IVD Al, the Zn-Ni is superior to all previously studied Zn and Zn alloy coatings. In summary, the coatings may be ranked in the following order of decreasing protection: Cd and IVD Al (chromated), Zn-Ni. Clearly Cadmium and chromated IVD Al were the best performers.

Salt Spray, Joint A

The Joint A assembly has been described in Figure 2. Note that both blocks of the assembly were fabricated of 4130 steel. For each assembly the bolt, washer and nut were coated with the same material. Table 2 summarizes observations made as a function of time exposure for a total of 312 hours. Figures IV-VI, Appendix A, contain supporting photographic evidence. Cadmium plate and IVD Al (chromated) again were the best performers (no corrosion products 312 hours) followed by Zn-Ni. The Zn-Ni plate (shown at 312 hours) showed no evidence of white corrosion products for 120 hours of exposure.

A Zn-Ni coated bolt was tested with a Cadmium plated nut and washer in joint A in order to create a potential galvanic corrosion problem. Visual observations showing the results of exposing such assemblies to salt spray are contained in Table 2 and Figure VII. A comparison of the results contained in Table 2 show the Cadmium plated nut and washer on the mixed assembly with Zn-Ni were largely unaffected by the galvanic coupling. There appeared to be little effect of the Cd on the Zn-Ni plated bolt since it remained free of corrosion products for 96 hours.

Time (hours)	Controls			
	A	B	C	D
6	N	N	N	N
24	N	N	N	N
48	N	N	N	N
72	N	N	N	N
96	N	N (Stains)	N	N
120	N	N (Stains)	N	N
144	N	N (Stains)	N	N
168	N	N (Stains)		N
192	N	N	N	N
216	N	20% WP	N	N
240	N	20% WP	N	N
312	N	20% WP	N	N

Joint A			
A	B	E	C
N	N	N	N
N	N	N	N
N	N	N	N
N	N	N	N
N	N	N	N
N	N	2% WP on Bolt Head	N
N	5% WP	5% WP, Cd Unaffected	N
N	5% WP with YGS in Crevice	5% WP, YGS Cd unaffected	N
N	5% WP with YGS in Crevice	5% WP, YGS Cd unaffected	N
N	30% WP with YGS in Crevice	20% WP, YGS Cd unaffected	N
N	30% WP with YGS in Crevice	25% WP, YGS Cd unaffected	N
N	35% WP with YGS in Crevice	40% WP, YGS Cd unaffected	N

Abbreviation Legend:

A - Cd Plated
B - Zn-Ni Plated
C - Chromated IVD Aluminum

D - Chromated IVD Al Bolt with Cd Nut
E - Zn-Ni Plated Bolt with Cd Nut
YGS - Yellow-Green Stains

WP - White Products
N - No Corrosion

Table 2 - Salt spray Observations, Control and Joint A Assemblies

Salt Spray, Joint B

The Joint B assembly has been described in Figure 3. The two blocks employed in this assembly were fabricated of 4130 steel and Armor Steel, Class 1 (MIL-A-12560). For each assembly the bolt, washer and nut were coated with the same material. Table 4 summarizes the observations made as a function of exposure time. Accompanying photographs, taken at 312 hours are contained in Figures VIII-X. The coatings may be ranked in the following order of decreasing merit: Cd - IVD Al (chromated), Zn-Ni. The Cadmium and IVD Al (chromated) provided protection for 312 hours of exposure. The Zn-Ni showed white zinc oxide corrosion products but no visible rust at 312 hours.

Salt Spray, Joint C

This Joint C assembly has been described in Figure 4. Note the different compositions of the two blocks in the assembly; Armor steel and Al 5083. For each assembly tested, the bolt, nut and washer were coated with the same material. Table 4 summarizes observations made for each coating as a function of exposure time. Figures XI-XIII, Appendix A, (312 hours) contain corresponding photographs. There was no evidence of white

corrosion products or rust for either the Cd or IVD Al (chromated) coated assemblies throughout the 312 hours. Zinc-Nickel coatings were free of white corrosion products for 96 hours. White corrosion products appeared thereafter increasing with increasing time of exposure. These coatings may be ranked in the following order of decreasing merit, based on a total exposure time of 312 hours: Cd, tied with IVD Al (chromated), followed by Zn-Ni.

Time (hours)	Joint B		
	A	B	C
6	N	N	N
24	N	N	N
48	N	N	N
72	N	N	N
96	N	YGS in the Crevice	N
120	N	30% WP with YGS in the Crevice	N
144	N	30% WP with YGS in the Crevice	N
168	N	25-35% WP with YGS in the Crevice	N
192	N	40% WP with YGS in the Crevice	N
216	N	40% WP with YGS in the Crevice	N
240	N	40% WP with YGS Covering 40% of Bolt	N
312	N	65% WP with YGS and YGS	N

Joint C		
A	B	C
N	N	N
N	N	N
N	N	N
N	YGS in the Crevice	N
N	YGS in the Crevice	N
N	1% WP with YGS in the Crevice	N
N	3% WP with YGS in the Crevice	N
N	3-5% WP with YGS in the Crevice	N
N	5% WP with YGS in the Crevice	N
10% Chromate Breakdown, no rust	5% WP with YGS in the Crevice	N
40% Chromate Breakdown, no rust	10-15% WP with YGS Covering 40% of Bolt	N
50% Chromate Breakdown, no rust	50% WP with pink stains in crevice due to misfit of Blocks.	N

Abbreviation Legend:

A - Cd Plated
B - Zn-Ni Plated
C - Chromated IVD Aluminum

WP - White Products
N - No Corrosion
YGS - Yellow-Green Stains

Table 2 - Saltspray Observations, Joint B and Joint C Assemblies

3.5% NaCl Immersion - Controls

Figure 7 contains plots of potential measurements made for the coated control assemblies during the course of their immersion in 3.5% NaCl solution. Though not rate sensitive, this technique will show "breakdown" or "loss of protection" when the corrosion potential changes from the base value of the coating towards that of uncoated steel. Photographs of the coated control assemblies after immersion for 312 hours complement the potential time data (Figures XIV-XIX).

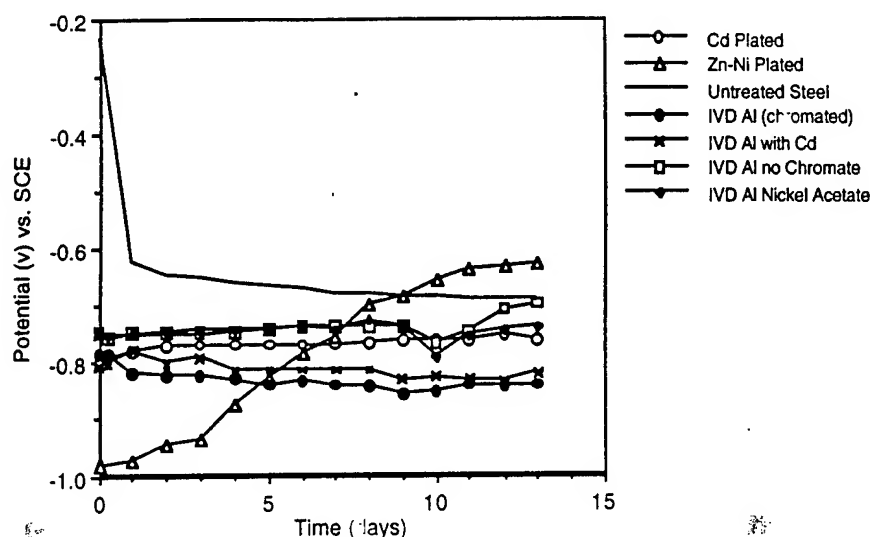


**Figure 7 - Potential vs. Time
3.5% NaCl Immersion - Controls**

Referring to Fig. 7, the potential of the uncoated steel drops markedly in the more active direction (from -0.231 to -0.624) within a 24 hour period indicative of the onset of corrosion which is confirmed by the first appearance of rust. The changes in potential thereafter are minimal and a fairly constant potential (-0.675) is achieved after 7 days of exposure when 50% of the steel surfaces are covered with rust. If the potentials of the coated parts approach or attain this potential then the coating has "broken down" and is no longer cathodically protecting the steel. The Zn-Ni coating shows a moderate rate of change of potential approaching the potential of corroding steel after 9 days of immersion time. In contrast, the potential of the Cadmium plated parts remains relatively constant (-0.76) throughout the 312 hours of immersion and provides the best protection for the steel substrate. The potentials and coating performances of the IVD Al assemblies correlated with the thicknesses of the IVD coatings. In the case of the chromated IVD Al, the extremely thick (24.7 mil) coating most greatly contributed to the favorable stable behavior similar to the behavior of the Cadmium plate. When mixed with a Cadmium nut, the thick IVD assembly behaved similar to the unmixed specimen although it shifted to slightly more noble behavior. In contrast to the thick, chromated IVD Al, the thin IVD (3 mils) coatings, (with and without the Ni acetate), the zone of stable E-corr values decayed after about 168 hours (7 days). This fluctuation corresponded with the loss of coating and the appearance of rust. While both thin IVD coatings showed heavy rust, the nickel acetate treated control assembly retained a few patches of coating after 312 hours. The coated control assemblies

may be ranked in the following order of decreasing merit: Cd, chromated IVD Al, Zn-Ni, IVD Al with Ni acetate, and untreated IVD Al.

Immersion - Joint A

All possible Joint A coupling schemes were not tested due to the limited number of test blocks available. Potential measurements and observations were made during the course of immersion testing of the coated Joint A assemblies. Their potentials are plotted as a function of time in Figure 8.

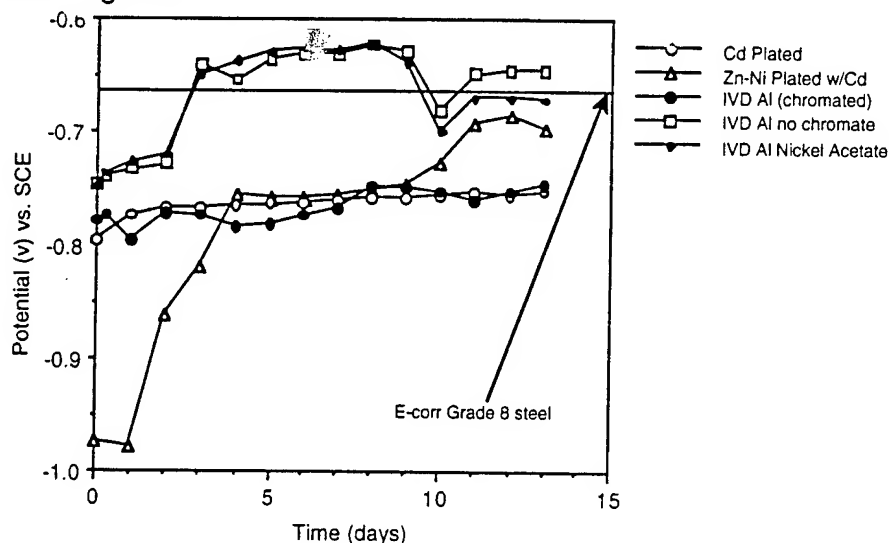


**Figure 8 - Potential vs. Time
3.5% NaCl Immersion - Joint A**

Complementary photographs at 312 hours of immersion are shown in Figures XX-XXV: Appendix B. The potential of the Cadmium coated assembly remained relatively stable throughout the entire test, indicative of its excellent corrosion resistance. The Zn-Ni plated bolt with Cd washer and nut exhibited very little rust on the bolt and washer after 12 days of immersion. This coincided with the potential stabilizing to that of Cadmium after an initial rapid increase over the first two days to the Cadmium potential. A gradual rise in potential beginning between 9 and 10 days culminating with the appearance of rust indicated that the Cd coating on the nut and washer had broken down. The IVD Al specimens again displayed performance that was dependent upon coating thickness. In the case of the thick chromated IVD Al, E-corr measurements, while somewhat less stable, slowly increased from (-0.775) to (-0.750) similar to the values recorded for Cd. The two thin IVD coatings began negative with respect to steel at around (-0.75) and

rapidly climbed to the potential of steel within 96 hours. Aluminum sacrificial products were not visible as in the Zinc plated fasteners as they either dissolved or were carried away in the circulation of the bath. At the 96 hour mark all that was visible was red rust with a few small patches of IVD Al which disappeared and were replaced by rust after 120 hours. The coated Joint A assemblies may be ranked in the following order of decreasing merit: Cd, chromated IVD Al, Zn-Ni with Cd washer and nut; IVD Al (no treatment), IVD Al with nickel acetate.

Immersion - Joint B

For these joint assemblies, potential-time curves are plotted in Figure 9, and corresponding photographs are contained in Figures XXVI-XXX.

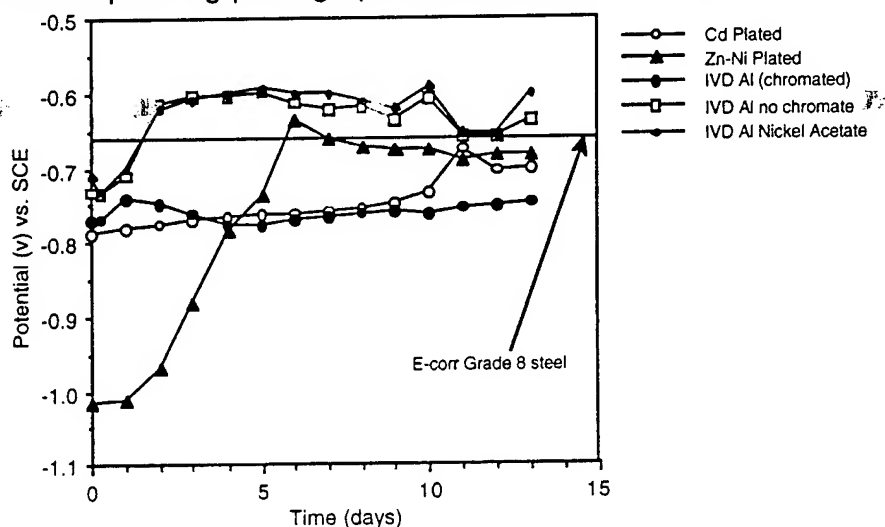


Figure 9 - Potential vs. Time
3.5% NaCl Immersion - Joint B

It should be noted that Cd washers were not incorporated in the assemblies due to the unavailability of additional steel blocks. The potential for the Cd plated joint was relatively stable for 10 days and then increased to the steel potential as rusting of the edges of the Cd plated washers was observed. The Cd plated bolt was free of corrosion products. The Zn-Ni plated joint reached the steel potential after 5 days immersion time when rust was observed on the washers. The IVD Al specimens displayed behavior similar to data observed in joint A, with a strong dependence on coating thickness. In the case of the thick chromated IVD Al, E-corr measurements remained relatively stable, settling in at (-0.76) after an initial peak at (-0.73) at the 24 hour mark. With zero visible rust after 312 hours, the thick chromated IVD Al was able to provide equal to better performance than Cd. The two thin IVD

coatings which began negative with respect to steel at around (-0.73), rapidly climbed to the potential of steel within 96 hours. Again Al sacrificial products were not visible. With no trace of the thin IVD coatings visible at 96 hours, corrosion of the steel bolt substrate was characterized as even more severe than the rusting observed on joint A. Due to the gross rusting present, an assessment as to which thin IVD coating performed better was not possible. The ranking of these coatings for Joint B in decreasing order of protection is: Chromated IVD Al, Cd, Zn-Ni, IVD Al (no treatment) tied with IVD Al, nickel acetate.

Immersion - Joint C

Armor steel and Al 5083 blocks were used in this assembly. Again because of the limited number of blocks available Cd washers were not incorporated in assemblies containing the other coatings. Plots of potential as a function of immersion time are shown in Figure 10.

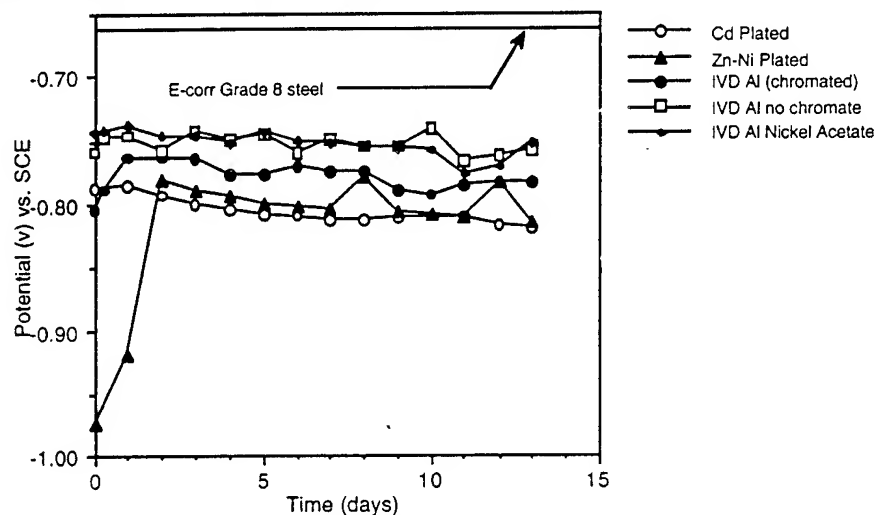


Figure 10 - Potential vs. Time
3.5% NaCl Immersion - Joint C

A photograph representative of each coating after 312 hours is Figure XXXI. The Cadmium potential was relatively stable throughout the test and showed no evidence of corrosion. The potential of the Zn-Ni coating approached the potential of Aluminum within a three day period when white corrosion products formed. There was little or no evidence of rust on any of the assemblies at the conclusion of the test with the exception of the thin IVD Al coatings which displayed moderate rusting of about 10% of the total surface area. The observed moderation in corrosion severity was due to the presence of the Al 5083 block found in Joint C. The Al 5083 is anodic to steel, and provides additional cathodic

protection. Cadmium again is the best performer followed by chromated IVD Al @ 24.7 mils, Zn-Ni, Sn-Zn, IVD Al and IVD Al with Ni acetate @ ≈ 3.0 mils.

Breakaway Torques

Tables 4 and 5 contain breaking torque values for the various joints which were exposed to either Saltspray or immersion in chloride solution. It should be noted that the threaded portion of the bolt was lubricated with oil prior to assembly and torquing of each joint. Each joint was torqued to 180 ft. lbs. except for those joints involving the Zn-Ni coating where the initial torque was 90 ft-lbs. due to the smaller diameter of the bolt. For comparison, data from the previous report containing the other Zn and Zn alloy coatings is included.¹

Table 4 - Saltspray Breakaway Torques

Joint A's	Breakaway Torque, As fraction of initial torque
Fastener Coating	0.648
Modified Phosphate	0.741
Modified Phosphate w/Cd Nut & Washer	0.694
Cd (BWN)	0.879
Zn OD (BWN)	0.741
Zn OD w/Cd Nut & Washer	0.926
Zn-Co (BWN)	0.741
Zn-Co w/Cd Nut & Washer	0.833
Zn-Sn (BWN)	0.833
Zn-Sn w/Cd Nut & Washer	0.833
Zn-Ni (BWN)*	0.833
Zn-Ni w/Cd Nut & Washer	0.833
IVD Aluminum, (Chromated)	0.833
Joint B's	Breakaway Torque, As fraction of initial torque
Fastener Coating	0.648
Modified Phosphate	0.787
Cd	0.741
Zn OD	0.926
Zn-Co	0.787
Zn-Sn	0.833
Zn-Ni*	0.718
IVD Aluminum, (Chromated)	
Joint C's	Breakaway Torque, As fraction of initial torque
Fastener Coating	0.833
Modified Phosphate	0.833
Cd	0.972
Zn OD	0.926
Zn-Co	0.926
Zn-Sn	1.019
Zn-Ni*	0.648
IVD Aluminum, (Chromated)	
*Zn-Ni used smaller bolts with initial torquing at 90.0 ft-lbs	

Generally the superphosphate coated joints exhibited significantly reduced breaking torques indicating the fastener could loosen during service. In most cases, the Zn and Zn alloy coatings exhibited breaking torques which were either comparable to or higher than Cadmium. Breaking torques measured for IVD Al were sometimes higher and sometimes lower than readings for Cd and are inconclusive. Generally little evidence of corrosion was observed in the threaded portion of these coated bolts in the various joints and loosening in service is therefore not anticipated.

Table 5 - Immersion Breakaway Torques

Joint A's	
<u>Fastener Coating</u>	<u>Breakaway Torque, As fraction of initial torque</u>
Cd (BWN)	0.787
Zn OD (BWN)	0.741
Zn OD w/Cd Nut & Washer	0.879
Zn-Ni w/Cd Nut & Washer*	0.741
IVD Aluminum, Anniston (Chromated) (BWN)	0.741
IVD Aluminum, Anniston (No Seal)(BWN)	0.694
IVD Aluminum, Anniston (Ni Acetate)(BWN)	0.787
Joint B's	
<u>Fastener Coating</u>	<u>Breakaway Torque, As fraction of initial torque</u>
Modified Phosphate	0.602
Cd	0.741
Zn OD	0.972
Zn-Co	0.879
Zn-Sn	0.879
Zn-Ni*	0.741
IVD Aluminum, (Chromated)	0.833
IVD Aluminum (No Seal)	0.787
IVD Aluminum (Ni Acetate)	0.833
Joint C's	
<u>Fastener Coating</u>	<u>Breakaway Torque, As fraction of initial torque</u>
Modified Phosphate	0.787
Cd	0.741
Zn OD	0.926
Zn-Co	0.926
Zn-Sn	0.833
Zn-Ni*	0.741
IVD Aluminum, (Chromated)	0.787
IVD Aluminum, (No Seal)	0.833
IVD Aluminum, (Ni Acetate)	0.972

*Zn-Ni used smaller bolts with initial torquing at 90.0 ft-lbs

Coefficient of Friction

The frictional force per unit contact area (frictional stress), F_t , between the nut and the washer, or that between the washer and the armor plate, whichever is lower, will guarantee that the assembly will remain fastened at the set level. This force F_t is given by $F_t = \mu \cdot \sigma'$, where $\mu = \tan \phi$ is the

friction coefficient between the two surfaces in contact and σ' is the normal, compressive stress within the nut and the part of the washer in contact with the nut. This stress is proportional to the tensile stress σ within the threaded rod (bolt).

The friction coefficient $\mu^* = \mu_a + \mu_p$, where μ_a and μ_p are the adhesive and ploughing components, respectively. The adhesive component depends on the intrinsic nature of the coating, namely on atomic bonding, chemistry and mutual solubility between coating and substrate materials and the ploughing component depends on surface roughness and the stress required to shear surface asperities. The friction coefficient was determined by automatic scratch testing, using a 200 μm radius diamond stylus, a loading rate $dL/dt = 100 \text{ N min}^{-1}$, a scratching speed $dx/dt = 1 \text{ mm min}^{-1}$, hence a load gradient $dL/dx = 10 \text{ N mm}^{-1}$, where L (N) is applied normal load within the 0-60 N range, x (mm) is the distance and t (min) is time. Average coefficient of friction values μ^* are listed in table 7 for the included coatings as well as coatings from the prior study. If F_t is the friction stress required to maintain an appropriate fastening, and two coatings, for example Zn and Cd, are compared, then:

$$F_t = \mu^*_{\text{Zn}} \sigma'_{\text{Zn}} = \mu^*_{\text{Cd}} \sigma'_{\text{Cd}} = \mu^*_i \sigma'_i \quad (1)$$

where μ^*_{Zn} and μ^*_{Cd} and μ^*_i are the coefficients between two Zn, two Cd or two "i" metal coatings, respectively, and σ'_{Zn} , σ'_{Cd} , σ'_i are the respective compressive stresses within the Zn-coated, Cd-coated and "i" metal-nuts. The proportionality between compressive stresses within the nuts and the respective tensile stresses within the bolts, σ_{Zn} and σ_{Cd} , may be expressed by:

$$\sigma'_{\text{Zn}} / \sigma'_{\text{Cd}} = \sigma_{\text{Zn}} / \sigma_{\text{Cd}} \quad (2)$$

hence,

$$\mu^*_{\text{Zn}} \sigma_{\text{Zn}} = \mu^*_{\text{Cd}} \sigma_{\text{Cd}} \quad (3)$$

These friction coefficients are not readily measurable, whereas those between the diamond stylus and the two coatings are. The ratios of the two groups of coefficients may be assumed to be approximately equal. Hence:

$$\mu^*_{\text{Zn-Zn}} / \mu^*_{\text{Cd-Cd}} = \mu^*_{\text{Zn-dia}} / \mu^*_{\text{Cd-dia}} \quad (4)$$

In the present case, see Table 7 for virgin, as-coated specimens $\mu^*_{\text{Zn}} = 0.488$ and $\mu^*_{\text{Cd}} = 0.377$, hence $\sigma_{\text{Zn}} = 0.772 \sigma_{\text{Cd}}$. Thus the tension inside the Zn-coated bolt that maintains good fastening may be 22.8% lower than that inside the Cd-coated bolt and so may the required torque to achieve the same level of fastening. These conclusions remain valid, if we consider the various friction coefficients following salt-spray or

immersion tests in chloride solution. Thus, for salt-sprayed specimens, (see Table 7) $\mu^*_{Zn} = 0.551$ and $\mu^*_{Cd} = 0.447$, and $\sigma_{Zn} = 0.811\sigma_{Cd}$, and for chloride solution immersed specimens, $\mu^*_{Zn} = 0.424$ and $\mu^*_{Cd} = 0.330$, and $\sigma_{Zn} = 0.778\sigma_{Cd}$, hence the respective tensions inside the Zn-coated bolts that maintain good fastening may be 18.9% and 22.2% lower than those inside the Cd-coated bolts and so may the required torques to achieve the same level of fastening. Similar calculations show comparable reductions attributable to the following virgin coatings: Thick IVD Al (chromated) 39.4 %, Zn-Ni 22.8%, Zn-Co 15.3%, and Sn-Zn 11.7%. The thin IVD Al coatings, plain and with Ni acetate will require 12.2 and 20.8% higher torques respectively, to maintain the same level of fastening as the Cd plated parts. Superphosphate also required a higher torque of 11.2%. With the exception if the IVD Al fasteners these data complement and support the breakaway torque results; loosening of the Zn and Zn alloy coated fasteners will not occur when Cd torque values are used, whereas loosening of the superphosphate coated fastener will most likely occur. No consistent trend was apparent in the IVD Al data. The breakaway torque readings were inconsistent with the friction coefficients, and data measured for just the friction coefficients was inconsistent. Continued studies of IVD Al coatings should reveal more frictional data. Microscopic investigation by Kattamis revealed that in most cases, the platings exceeded the thickness requirements and were relatively uniform, contiguous and adherent.²

Table 7 - Average Friction Coefficients, μ^* , of Coated Specimens

<u>Coating</u>	<u>Virgin</u>	<u>Salt Spray</u>	<u>NaCl Immersion</u>
Zn-Ni	0.532	0.472	0.422
Zn-Co	0.415	0.467	0.496
Zn-Sn	0.427	0.287	0.406
Cd	0.377	0.417	0.330
Modified Phosphate	0.355	0.286	0.237
Zn (OD)	0.488	0.551	0.424
IVD Al (chromated)	0.697 0.622*	no data	0.390
IVD Al	0.336	no data	0.290
IVD Al (w/Ni acetate)	0.312	no data	0.300
Steel Substrate	0.277	no data	no data

* After thinning from 24.7 mils to 3.1 mils

Discussion

In all test situations, the thick chromated IVD Al met or exceeded the corrosion resistance found in Cadmium plate and always outperformed Zn-Ni. While this performance level is impressive, it is not always practical from a coating thickness standpoint. All of the grade 8 fasteners tested used a coarse thread which allowed the use of the 24.7 mil IVD Al coating. An examination of the disassembled assemblies also showed that gauling had occurred in the threaded regions. For high strength aerospace applications where a fine thread is used, thick coatings are impractical if not impossible. While Zn-Ni performance was not stellar, it met the 96 hour requirement in all cases with a much more reasonable 3 mil coating. For non-threaded applications and situations not requiring tight tolerances, IVD Al is a good replacement for electroplated Cd protective coatings.

Conclusions

- (1) Cadmium exhibited the best corrosion per unit coating thickness protection for grade 8 steel bolts in salt spray and immersion tests.
- (2) In situations where coating thickness is not an issue, IVD Al performs comparably to Cd in protection of steel.
- (3) On a per unit coating thickness, Zinc-Nickel coating was the best overall alternative to Cadmium plate and met the corrosion resistance requirements for Zinc plating.
- (4) Co-mingling of Cadmium with the other coatings in the Controls or Joint A showed little or no effect on Zn-Ni and thick chromated IVD Al coatings.
- (5) The substitution of Al 5083 for one of the steel blocks in Joint C did not diminish the performance of Cd, chromated IVD Al, and Zn-Ni coatings when compared to both joints A + B and improved the performance of the thin IVD Al coatings.
- (6) Loosening of the Zn-Ni or thick IVD Al coated fasteners will not likely occur when Cd torque values are used (under wet conditions).

Recommendations

- (1) Use Zinc-Nickel plating as an alternative to Zinc plating.
- (2) Continue to implement the TARDEC policy of using the torque values for fasteners which are currently provided in technical manuals regardless of co-mingling of Cd and Zn plated bolts.

- (3) Continue investigating Cd plate alternatives including IVD Al in varying thicknesses with chromate and non-chromate treatments.
- (4) Evaluate Cd plating alternatives for aerospace fasteners of high strength steels such as 4340 and Aermet® 100.

References

- 1.) M. Levy, B. Placzankis, R. Brown, R. Huie, and M. Kane, The Effects of Co-mingling Dissimilar Fastener Coatings on the Corrosion Behavior of Steel Bolt Assemblies, MTL TR 92-40, (July 1992)
- 2.) T.Z. Kattamis, R. Huie, J. Kelley, C. Fountzoulas, and M. Levy, Microstructure, Adhesion and Tribological Properties of Conventional Plasma-Sprayed Coatings on Steel Substrates. (Submitted for Publication in: Journal of Adhesion Science and Technology)

Appendix A
Salt spray Test Assemblies After 312 Hours

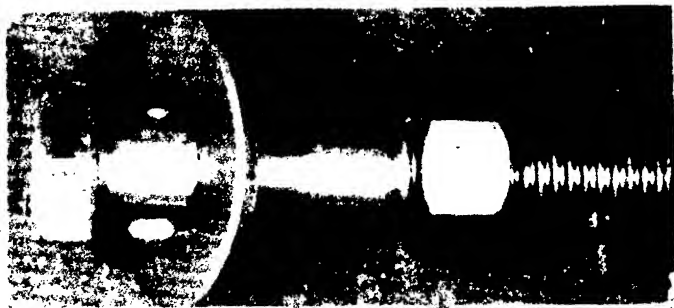


Figure I - Cd Plated Control

Figure II - Chromated IVD Al Control.

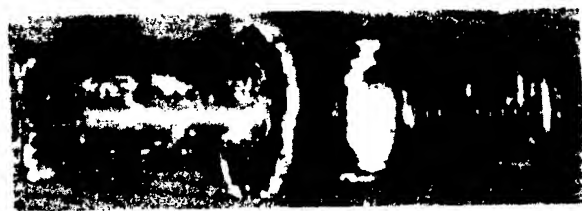


Figure III - Zn-Ni Plated Control



Figure IV - Cd Plated
Joint A Assembly



Figure V - Chromated
IVD Aluminum Joint A
Assembly

Appendix A (continued)
Saltspray Test Assemblies After 312 Hours



Figure VI - Zn-Ni Plated Joint A Assembly



Figure VII - Zn-Ni Plated Joint A Assembly Mixed with Cd

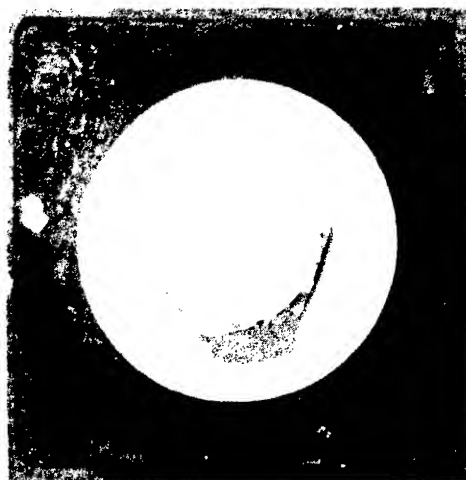
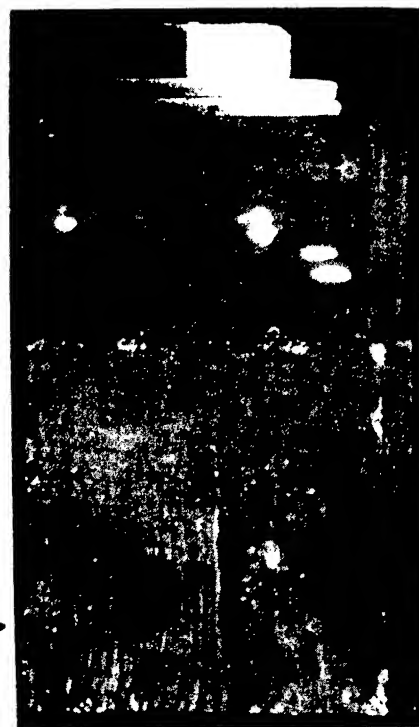


Figure VIII - Cd Plated Joint B Assembly

Figure IX - Chromated IVD Al Joint B Assembly



Appendix A (continued)
Saltspray Test Assemblies After 312 Hours

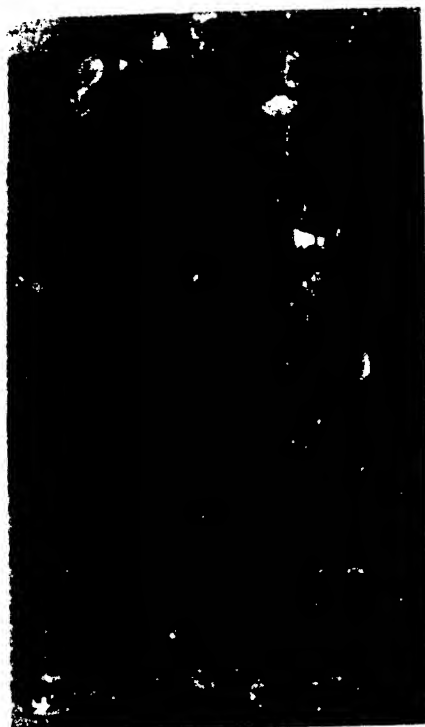


Figure X - Zn-Ni Plated Joint B Assembly

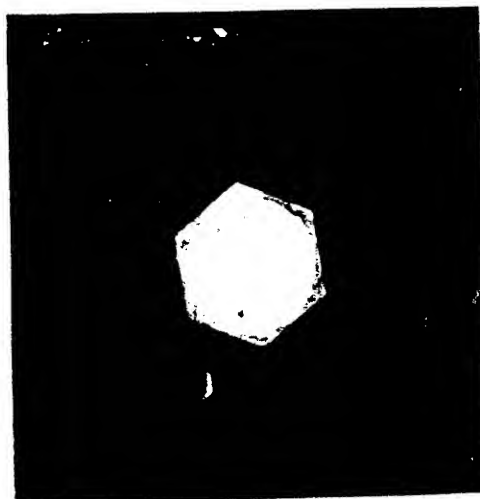


Figure XI - Cd Plated Joint C Assembly

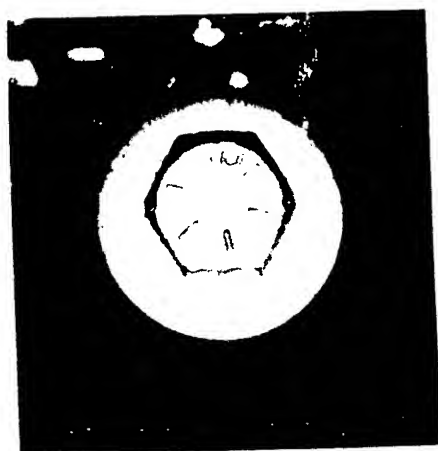


Figure XIII - Chromated IVD Al Plated Joint C Assembly



Figure XII - Zn-Ni Plated Joint C Assembly

Appendix B
Immersion Test Assemblies After 312 Hours



Figure XIV - Cd Plated Control



Figure XV - Zn-Ni Plated Control

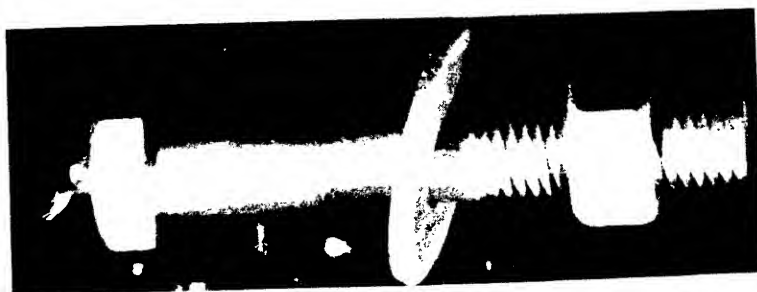


Figure XVI - Chromated IVD Al Control

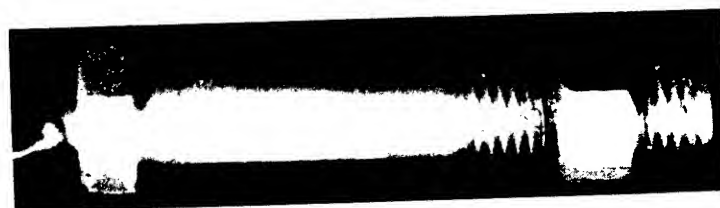


Figure XVII - Chromated IVD Al Control
with Cd Nut

Appendix B (continued)
Immersion Test Assemblies After 312 Hours



Figure XVIII - IVD Al (3 mil, No Treatment)



Figure XIX - IVD Al (3 mil, Ni Acetate Treated)

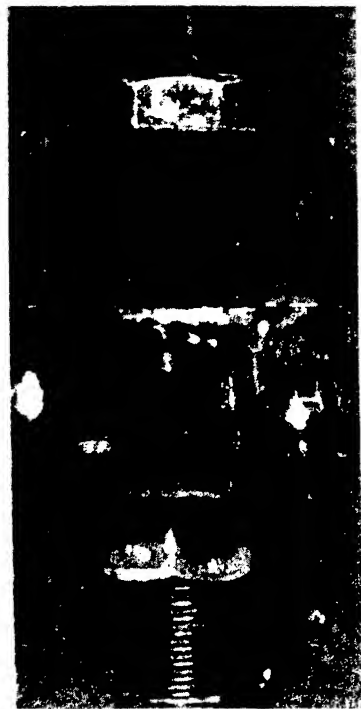


Figure XX - Cd Plated
Joint A Assembly



Figure XXI - Chromated IVD
Al Joint A Assembly

Appendix B (continued)
Immersion Test Assemblies After 312 Hours



Figure XXII - Zn-Ni Plated
Joint A Assembly

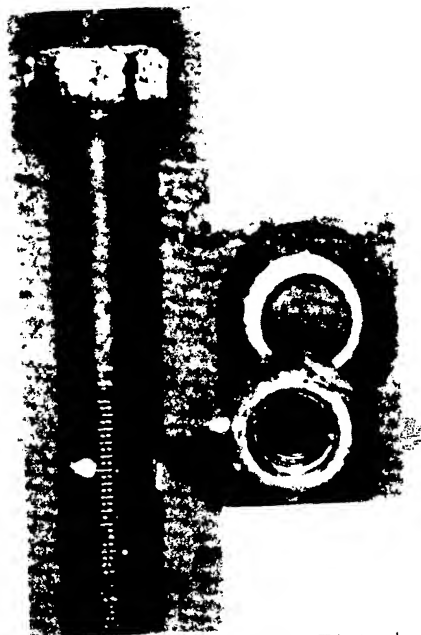


Figure XXIII - Zn-Ni Plated
Joint A Assembly. Mixed with
Cd. Disassembled to Show
Amounts of Corrosion

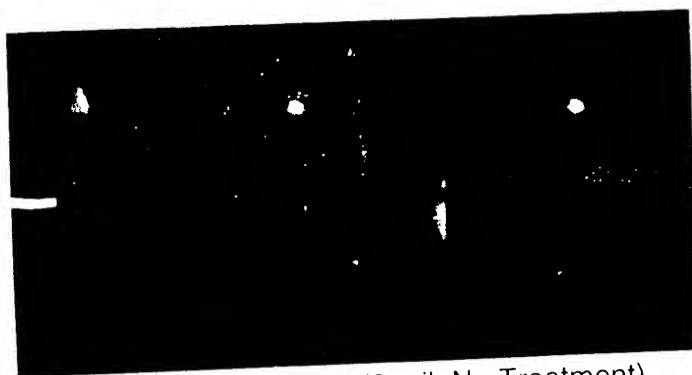


Figure XXIV - IVD Al (3 mil. No Treatment)
Joint A Assembly

Appendix B (continued)
Immersion Test Assemblies After 312 Hours

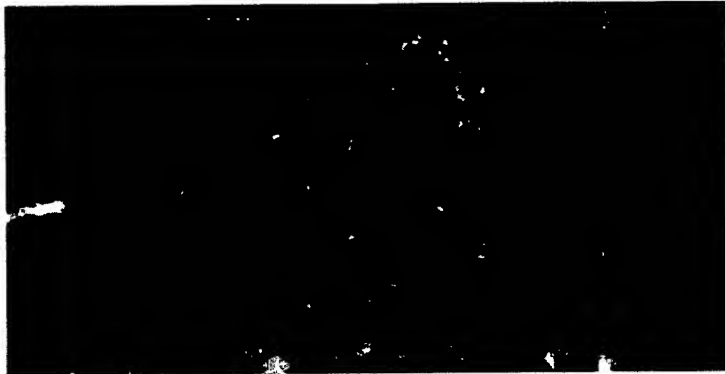


Figure XXV - IVD Al (3 mil. Ni Acetate Treated) Joint B Assembly



Figure XXVI - Cd Plated
Joint B Assembly

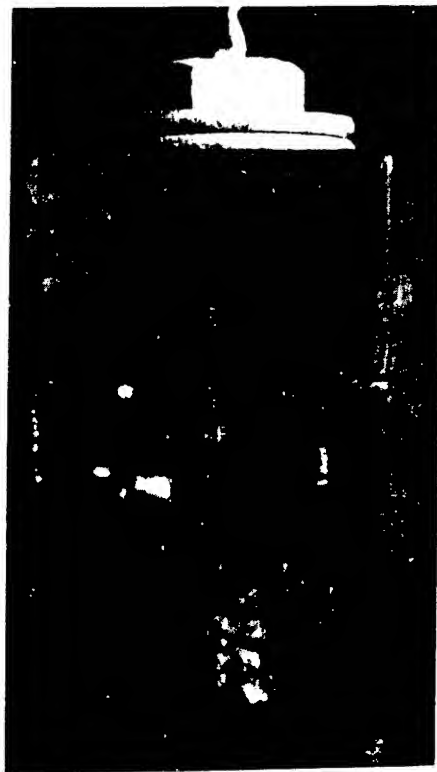


Figure XXVII - Chromated
IVD Al Joint B Assembly

Appendix B (continued)
Immersion Test Assemblies After 312 Hours



Figure XXVIII - Zn-Ni Plated Joint B Assembly

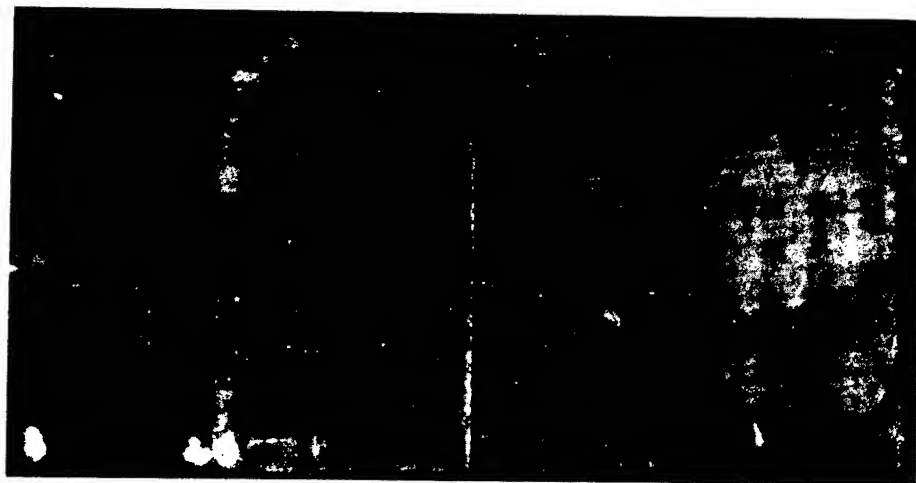


Figure XXIX - IVD Al (3 mil, No Treatment), Joint B Assembly

Appendix B (continued)
Immersion Test Assemblies After 312 Hours

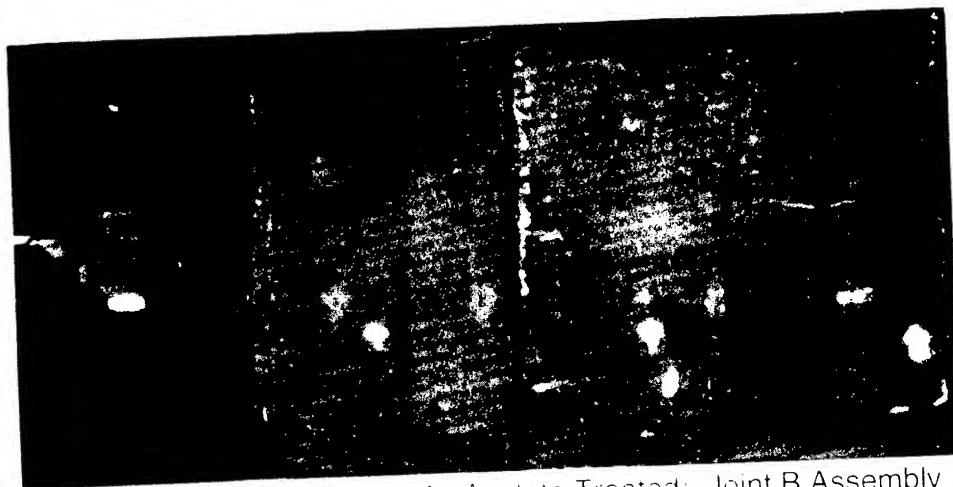


Figure XXX - IVD A (3 mil. Al Anelate Treated), Joint B Assembly



Figure XXXI - IVD Al (3 mil. No Treatment), Joint C Assembly
Showing Much Original Coating Intact, Cathodically Protected by the
Large Al 5083 Block, as Observed in All Other Joint C Assemblies.

BLANK

770

ELIMINATION OF CHROMATE CONVERSION COATINGS FROM ARMY TACTICAL VEHICLE MANUFACTURING PROCESSES

Mark Ingle
Ocean City Research Corporation

ABSTRACT

Many United States Army light tactical vehicles are fabricated from armor-grade aluminum. Aluminum-hulled tactical vehicles are coated with the Army's standard Chemical Agent Resistant Coating (CARC) system. The CARC system includes chemical pretreatments, epoxy primers, and polyurethane topcoats. The MIL-C-5541 chromate conversion coating pretreatment process included in the CARC specification contains hazardous chromic acid. Chromic acid is a SARA Title III extremely hazardous substance and air emissions of the material will be regulated by the 1990 Clean Air Act Amendments. In 1989, Red River Army Depot (RRAD) staff investigated replacing the hazardous chromate conversion coating with a more environmentally acceptable production process. The Army Acquisition Pollution Prevention Support Office reviewed the RRAD results and tasked Ocean City Research Corporation (OCRC) to conduct a comprehensive coating performance assessment and develop appropriate non-chromate production process control documents. The evaluation program demonstrated that chromate conversion coatings may be eliminated from aluminum-hulled tactical vehicle painting operations without degrading overall coating system performance.

KEY WORDS: Military, corrosion, coatings, painting, chromates, conversion coatings, abrasive blasting.

1. INTRODUCTION

The United States Army currently manufactures light tactical vehicles (i.e. armored personnel carriers, rocket launchers, and self-propelled artillery) from armor-grade aluminum. The 5000 series (Al, Mg, Mn, Cr) aluminum alloys used to manufacture these vehicles are inherently corrosion resistant.(1) Thick aluminum (i.e greater than 1.0 inch [25.4 mm]) sections are typically welded together to form the tactical vehicle's hull.

The vehicle hull manufacturing process includes the application of Army's Chemical Agent Resistant Coating (CARC) system. The CARC system is a family of chemical pretreatments, epoxy primers, and polyurethane topcoats. CARC coatings are produced in specific camouflage colors and are designed not to absorb toxic chemical warfare agents. The CARC system materials and associated production

processes are described in MIL-C-53072, "Chemical Agent Resistant Coating (CARC) System Application Procedures and Quality Control Inspection."

All CARC system coatings are lead-free and many do not contain soluble chromates. However, the CARC approved chemical pretreatments for aluminum alloys do contain hexavalent chromium. Hexavalent chromium is a known human carcinogen, a SARA Title III extremely hazardous substance, and is included in the 1990 Clean Air Act Amendment's Hazardous Air Pollutants (HAPs) list.(2) Because many Army production/maintenance facilities have already adopted the lead and soluble chromate-free CARC coatings, these aluminum pretreatments are frequently the only hazardous chromate source in the paint shop.

Red River Army Depot (RRAD) re-manufactures aluminum-hulled tactical vehicles and applies the CARC coating system. The RRAD painting production process utilizes the following CARC materials:

- MIL-C-5541, "Chemical Conversion Coating for Aluminum and Aluminum Alloys."
- MIL-P-53 2B, Type I, "Primer Epoxy, Corrosion Inhibiting, Lead and Chromate-Free."
- MIL-C-22/50, "Coating, Epoxy-Polyamide."
- MIL-C-46168D, "Coating Aliphatic Polyurethane, Chemical Agent Resistant."

In 1989, RRAD personnel initiated an evaluation of alternative environmentally acceptable production processes that might be considered alternatives to the hazardous chromate conversion coating process. RRAD staff identified a two-stage abrasive blasting process as a viable alternative. Using this environmentally acceptable alternative production process as a replacement for chromate conversion coatings would reduce RRAD's yearly raw material costs by approximately \$200,000 and could save approximately \$3,000,000 in potential air emission control equipment upgrade costs. Even though adopting the environmentally acceptable alternative production process was economical, RRAD staff were required to generate additional coating system corrosion control performance data to obtain alternative production process approval.

In 1990, the Army Acquisition Pollution Prevention Support Office (AAPPPO) initiated a cooperative program with RRAD to generate the data required to obtain approval for replacing chromate conversion coatings with an environmentally acceptable alternative production process. The AAPPPO tasked Ocean City Research Corporation (OCRC) to conduct a comprehensive coating system corrosion control performance assessment and to use the performance assessment results to generate production process control documents for RRAD. The AAPPPO sponsored research program included a natural marine atmosphere exposure test of realistically complex, armor-grade aluminum specimens, numerous Army specific adhesion assessments, and a production process demonstration program.

2. TECHNICAL APPROACH

2.1 Realistic, Long-Term Performance Assessment Table I presents the coating system corrosion control performance evaluation program test matrix. The matrix presents both the chemical pretreatments and the alternative production processes used to produce test panels. The alternative production processes listed in Table I include the current RRAD production process, abrasive blasting with aluminum oxide media, and no pretreatment other than a solvent wipe. The current RRAD production process includes removal of old paint using AISI 303 stainless steel shot, hull rework, final abrasive blasting with garnet media, and primer application. Although RRAD currently uses only the MIL-P-53022 solvent-based epoxy primer, the test matrix also includes the MIL-P-53030 water-reducible epoxy primer. The water-reducible primer was included in the program to ensure results would be applicable to facilities that have already adopted this lower Volatile Organic Compound (VOC) content primer. All systems were topcoated with the two component MIL-C-46168 material.

Two test panel types were used during the program. Complex test panels were used to evaluate coating system corrosion control performance in the natural marine atmosphere. Flat laboratory test panels were used in various adhesion and electrochemical evaluations.

Figure 1 shows a schematic of the complex marine atmosphere exposure test specimen. These complex specimens were fabricated by sectioning 1/4 inch (6.3 mm) thick armor-grade aluminum panels into two parts. These two parts were then single penetration fillet welded to produce an L-shaped panel. By creating the L-shape with a single penetration weld, a crevice was established that would present a "worst case" for localized corrosion. The panels also included a hole that would be inherently difficult to coat. The flat test specimens were fabricated from the same stock as the complex panels. Flat panel dimensions were nominally 4 x 9 inches (102 x 229 mm).

Both test panel types were pretreated and coated using the systems described in Table I. An Elcometer 300 dry film thickness measurement gauge was used to measure coating thicknesses. After inspection, the complex test panels had a 1/4 inch (6.3 mm) diameter hole cut through the coating and into the substrate aluminum. This intentional defect was added to create favorable conditions for substrate corrosion and coating undercutting.

The complex atmospheric exposure test panels were placed at OCRC's Sea Isle, NJ marine test site for two years. The panels were placed on racks facing south at an angle of 45 degrees and subject to daily seawater spray. During the two-year exposure period, substrate corrosion was evaluated in accordance with ASTM D 610 (modified to account for the aluminum substrate) and panel blistering was evaluated in accordance with ASTM D 714.3(4). Underfilm corrosion around the coating defect was also measured and recorded.

The laboratory test panels were evaluated for adhesion in the wet and dry conditions. The dry adhesion test (ASTM D 2197) used a weighted stylus to scrape the coating away from the aluminum substrate (greater stylus loads are associated with more adherent coatings). Wet adhesion was evaluated in accordance with Federal Standard 141C, Method 6301. The wet adhesion test used flat panels with two parallel scribes. After soaking the scribed panels in room temperature water for 24-hours, adhesive tape is applied over the scribed region. The tape was removed and the area of paint pulled away from the panel evaluated. Large areas of paint stuck to the adhesive tape indicated poor wet adhesion performance.

Additional laboratory tests were conducted to determine coating system resistance to the Army's powerful DS-2 chemical warfare cleaning agent. DS-2 is a strong alkali used in actual chemical warfare and during training. Because alkalies can strip paints, test panels with intentional defects were evaluated. Panels were soaked in a 140 F (60 C) DS-2 solution for 24-hours and then inspected for coating delamination or undercutting. Coating blistering was evaluated in accordance with ASTM D 714 guidelines.

2.2 Trial Production Process Implementation A production process control document was created for the modified, non-chromate based coating process. The document was generated in the current RRAD Depot Process Control Pamphlet (DPCP) format to ensure acceptance by shop personnel. This new DPCP, given the code number 0026 by RRAD staff, described the non-chromate aluminum hulled armored vehicle coating system production process and the required engineering controls. In addition, DPCP 0026 included a training material package to allow each worker, in a Total Quality Management (TQM) mode, to understand the overall process and contribute to successful coating application.

The modified, non-chromate production process was implemented on the test M577 over a four-week period. The M577 was tracked through each production phase and evaluated in accordance with MIL-C-53072 and DPCP 0026 guidelines. Parameters measured during the production process trial included; surface cleanliness, surface profile, coating wet film thickness, coating dry film thickness, and coating adhesion.

3. RESULTS & DISCUSSION

3.1 Realistic, Long-Term Performance Assessment Table II summarizes marine atmosphere test panel coating system corrosion control performance after two-years of testing. The coating systems listed in Table II correlate with those described in Table I. The ASTM B 610 and D 714 data show all panels maintained a 10 rating. The 10 rating signifies no substrate corrosion or coating blistering was apparent. The scribe undercutting data show that no panels exhibited undercutting. The qualitative weld crevice corrosion and coating failure (i.e. near the hole) data also show no degradation over the two-year period. These "real-world" test results prove that CARC coated, armor-grade aluminum test panels prepared with and without the

chromate conversion exhibit equivalent, excellent marine atmosphere corrosion control performance.

Figure 2 shows laboratory ASTM D 2197 scratch adhesion test results. Given that lower scratch failure loads are associated with less adherent coatings, the Figure 2 data show that specimens with the chromate conversion pretreatment were less adherent than panels prepared with the phosphoric acid rinse or those prepared with two primer coats. The specimens prepared with the RRAD standard abrasive blasting technique performed less effectively than those with the chromate. However, panels prepared using the phosphoric acid rinse process outperformed the chromated specimens. The only systems that performed poorly in the scratch adhesion test were those with no surface preparation other than a solvent wipe. These systems scratched at loads that were significantly lower than those for better performing systems. Figure 2 data show that chromate conversion coatings are one of many alternative, acceptable surface pretreatments that provide superior adhesion to unprepared (solvent wiped) surfaces.

The wet adhesion test results indicated that only the specimens with no surface treatment (i.e. solvent wipe) produced failures. All solvent wipe test panels exhibited significant wet adhesion failures. These findings tend to confirm the trends observed in the Figure 2 data.

Figure 3 shows the laboratory DS-2 test data. The Figure 3 ASTM D 714 blistering data include both a numerical rating and a qualitative description of blister density. Given that higher numerical ratings are associated with smaller blisters, Figure 3 data show that chromate conversion coated test specimens had larger and more frequent blisters than all but the panels prepared with just a solvent wipe. These Figure 3 data show that panels prepared with the chromate conversion coating were more susceptible to DS-2 induced blistering than virtually any other pretreatment.

Overall, these realistic coating system corrosion control and laboratory performance tests demonstrate that chromate conversion coatings are only one of many alternative surface pretreatments that offer adequate overall performance. These results demonstrated that chromate conversion coatings could be replaced by mechanical surface preparation. Based on these findings, AAPPISO staff tasked OCRC to develop a non-chromate production process control technical data package and conduct an implementation trial.

3.2 Trial Production Process Implementation The production process technical data package was developed by modifying existing RRAD production processes to address research findings. Whenever possible, current RRAD equipment and processes were used to simplify transition from the chromate to the non-chromate surface pretreatment production process. The key issues identified during the technical data package development program were that an adequate surface profile was essential to overall performance and that a high degree of surface cleanliness would help ensure effective coating adhesion.

Generating a consistent and adequate surface profile was complicated by the current RRAD abrasive blasting processes. RRAD currently removes coatings using an 303 stainless steel centrifugal shot blast cabinet. This device produces a heavy surface profile of between 2.8 and 3.5 mils (0.071 to 0.089 mm). After this coating removal operation, vehicles are reworked, welded, and refitted. To remove the oxides and contaminants deposited on the hulls during these various manufacturing operations, the vehicles are blasted with 20 mil (0.5 mm) garnet media just before final painting. The fine garnet media actually reduces the surface profile.

Table III presents final profile data from four standard production aluminum hulls. As shown, average profiles varied considerably between 1.60 mils (0.04 mm) and 3.72 mils (0.09 mm). In addition, the profiles varied on the individual vehicles. Because test data indicated that heavier surface profiles would improve adhesion, the production process control package was developed to ensure workers obtained a minimum profile of 2.0 mils (0.05 mm).

The surface cleanliness analysis proved vital to overall program success. Many RRAD production processes contaminated the hull surfaces with lubricants and waxes that were extremely difficult to remove. If these contaminants remained on the hull in the paint shop, the final coatings would exhibit virtually no adhesion. To address surface cleanliness, the process control data package includes both training and quality assurance provisions. Workers in the final garnet blasting area were trained to identify the oil/wax contaminated regions and effectively remove the materials. Workers in the prepaint preparation shop were provided with a simple "water break" test to verify surface cleanliness before painting. Thus, the production process controls maintain an internal verification of surface cleanliness.

Figure 4 shows the final mechanical surface preparation production process flow chart. As shown, the process includes both surface profile and cleanliness verification.

Figure 5 shows a similar flow chart for the primer application process. In the past, an initial stage of this flow chart would have been chromate conversion coating application. As shown, the proposed production process does not use hazardous chromate materials.

The Figure 4 and 5 production processes were used as a basis for trial coating application to an M577 vehicle in March 1993. The vehicle was successfully coated and inspected by RRAD quality assurance personnel. All inspections indicated the M577 without the chromate conversion coating was indistinguishable from a standard production vehicle.

Based on the successful implementation trial, RRAD staff are awaiting final Army approval for chromate conversion coating elimination. Upon obtaining final Army approval, a comprehensive training program will be initiated to ensure workers

understand the chromate elimination process and the importance of effective process control.

4. CONCLUSIONS

The following are the program conclusions:

1. Natural marine atmosphere exposure test performance data, collected over two-years, indicate that complex armor-grade aluminum panels prepared both with and without the chromate conversion pretreatment did not experience any coating failures or substrate corrosion.
2. Scratch adhesion test data indicate that the chromate conversion coating is one of many acceptable pretreatment processes. Panels pretreated with abrasive blasting followed and a phosphoric acid solution offered the most effective scratch adhesion resistance. Wet adhesion test results indicate that only panels without any form of pretreatment experienced failures.
3. DS-2 blister test data suggest chromate conversion coatings were one of the least effective surface pretreatments. Panels prepared by abrasive blasting with aluminum oxide offered significantly more resistance to blistering than those prepared with the chromate conversion coatings.
4. Production process controls that emphasize surface profile and cleanliness are essential to effectively applying CARC coatings to non-chromate conversion coated aluminum armored vehicle hulls. When implemented, effective production process controls allow aluminum-hulled armored vehicles to be coated without the use of any hazardous chromate bearing materials.

5. REFERENCES

1. Metals Handbook, Ninth Edition, Volume 13, Corrosion, ASM International, 1987, page 586.
2. 1990 Clean Air Act Amendments, Title III (Section 112 in Title I), Hazardous Air Pollutants.
3. ASTM D 610, "Method for Evaluating Degree of Rust on Painted Steel Surfaces"
4. ASTM D 714, "Method for Evaluating Degree of Blistering of Paints"
5. ASTM D 2197, "Test Method for Adhesion of Organic Coatings by Scrape Adhesion Tester"

TABLE I
CHROMATE ELIMINATION PROGRAM TEST MATRIX

SYSTEM #	NUMBER OF PANELS	ABRASIVE BLAST	PRETREATMENT TYPE	PRIMER TYPE	TOPCOAT
1	14	RRAD	CHROMATE	MIL-P-53030	MIL-C-46168
2	14			MIL-P-53022	
3	14		PHOSPHORIC	MIL-P-53030	
4	14			MIL-P-53022	
5	14		NONE	MIL-P-53030	
6	14			MIL-P-53022	
7	14			MIL-P-53030 (2 COATS)	
8	14			MIL-C-53022 (2 COATS)	
9	14	ALUMINUM OXIDE		MIL-P-53030	
10	14		MIL-P-53022		
11	14		MIL-P-53030 (2 COATS)		
12	14		MIL-P-53022 (2 COATS)		
13	14		NONE	SOLVENT WIPE	

Aluminum=Aluminir m Oxide f ist, 2 - 3 mils profile.
RRAD=Stainless Steel Shot a .J River Sand (garnet) as per SOP-71.
Chromate-Chromate Conversion Coating, MIL-C-5541.
Phosphoric-Phosphoric Acid Wash, MIL-C-5541.
MIL-P-53022=Solvent-based Epoxy.
MIL-P-53030=Water Reducible Epoxy.

Table II
Two-Year Marine Atmosphere Exposure Test Results

System Number	ASTM D 610 Rating (avg.)	ASTM D714	Scribe Cut-back (avg.)	Weld Area Corrosion	Hole Corrosion
1	10	0	0	None	None
2	10	10	0	None	None
3	10	10	0	None	None
4	10	10	0	None	None
5	10	10	0	none	None
6	10	10	0	None	None
7	10	10	0	None	None
8	10	10	0	None	None
9	10	10	0	None	None
10	10	10	0	None	None
11	10	10	0	None	None
12	10	10	0	None	None
13	10	10	0	None	None

Table III
RRAD Surface Profile Data

Vehicle	Average Profile (mils/mm)	Maximum Profile (mils/mm)	Minimum Profile (mils/mm)
M113AT34	1.60/0.04	2.20/0.06	1.20/0.03
M112AT24	2.56/0.06	3.00/0.08	2.00/0.05
M577LH24	2.76/0.07	3.00/0.08	2.50/0.06
M577LH17	3.72/0.09	4.00/0.10	3.00/0.08

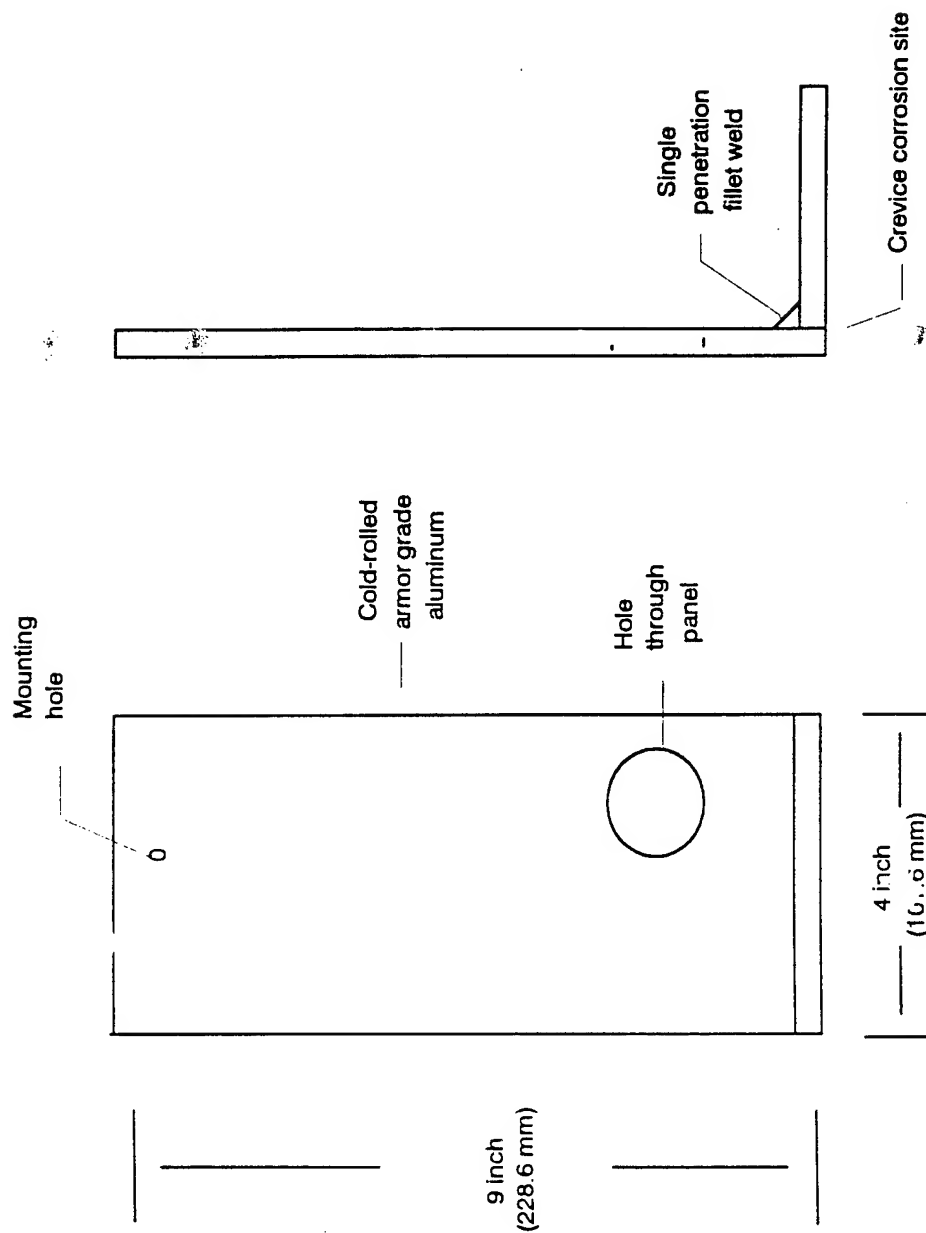


Figure 1 Marine Atmosphere Exposure Test Panel.

Figure 2 Scratch Adhesion
Data

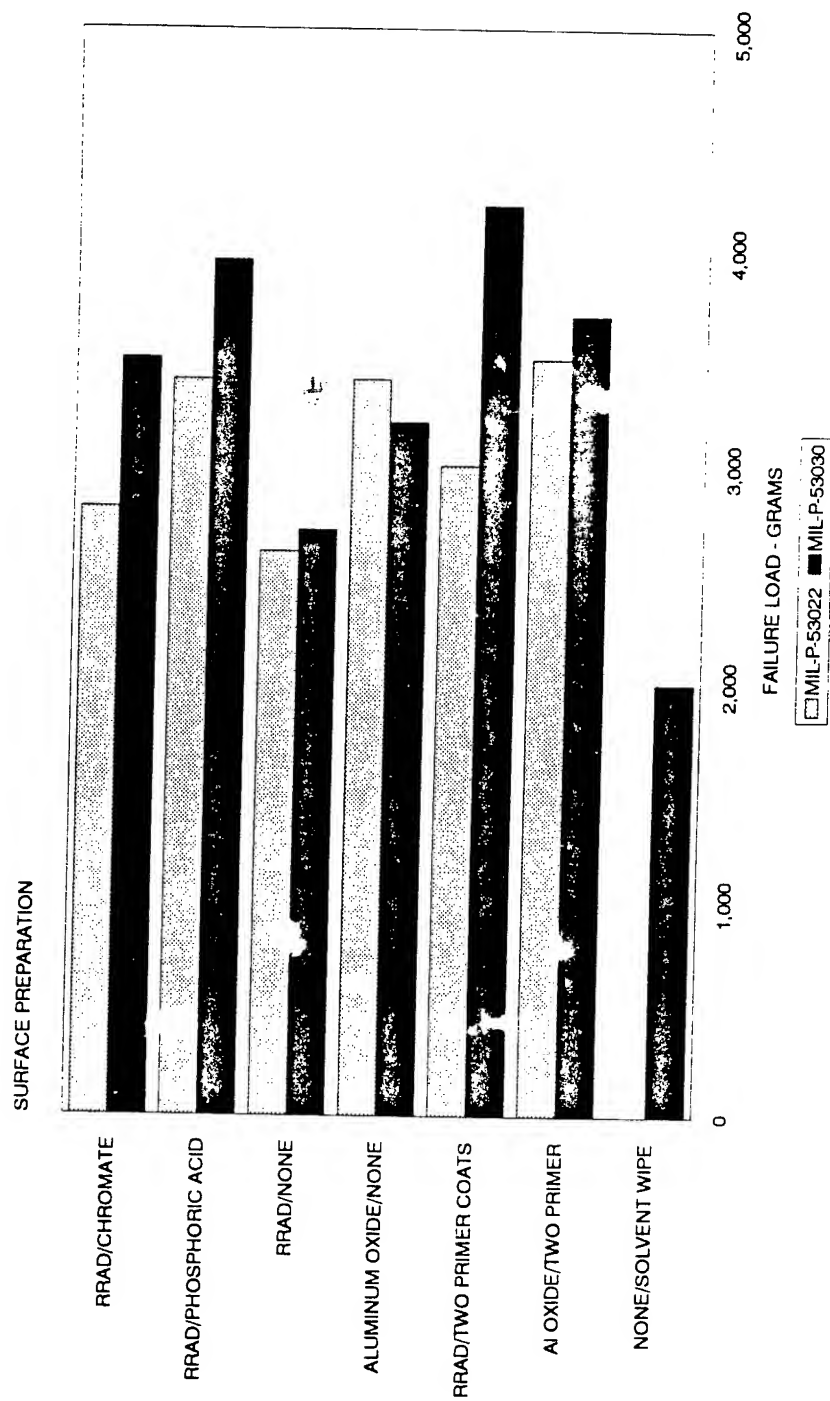
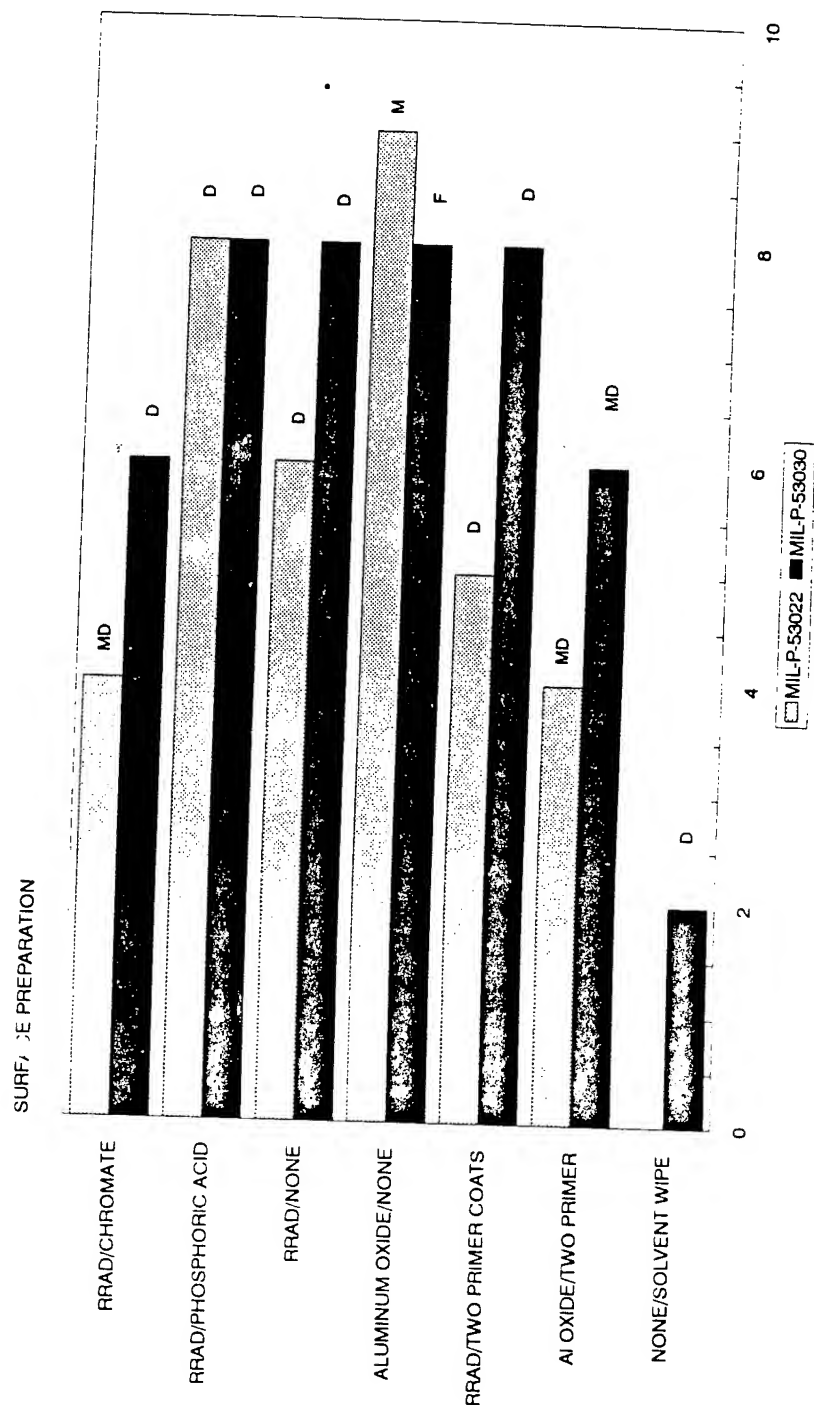


Figure 3 DS-2 Blister Test Data



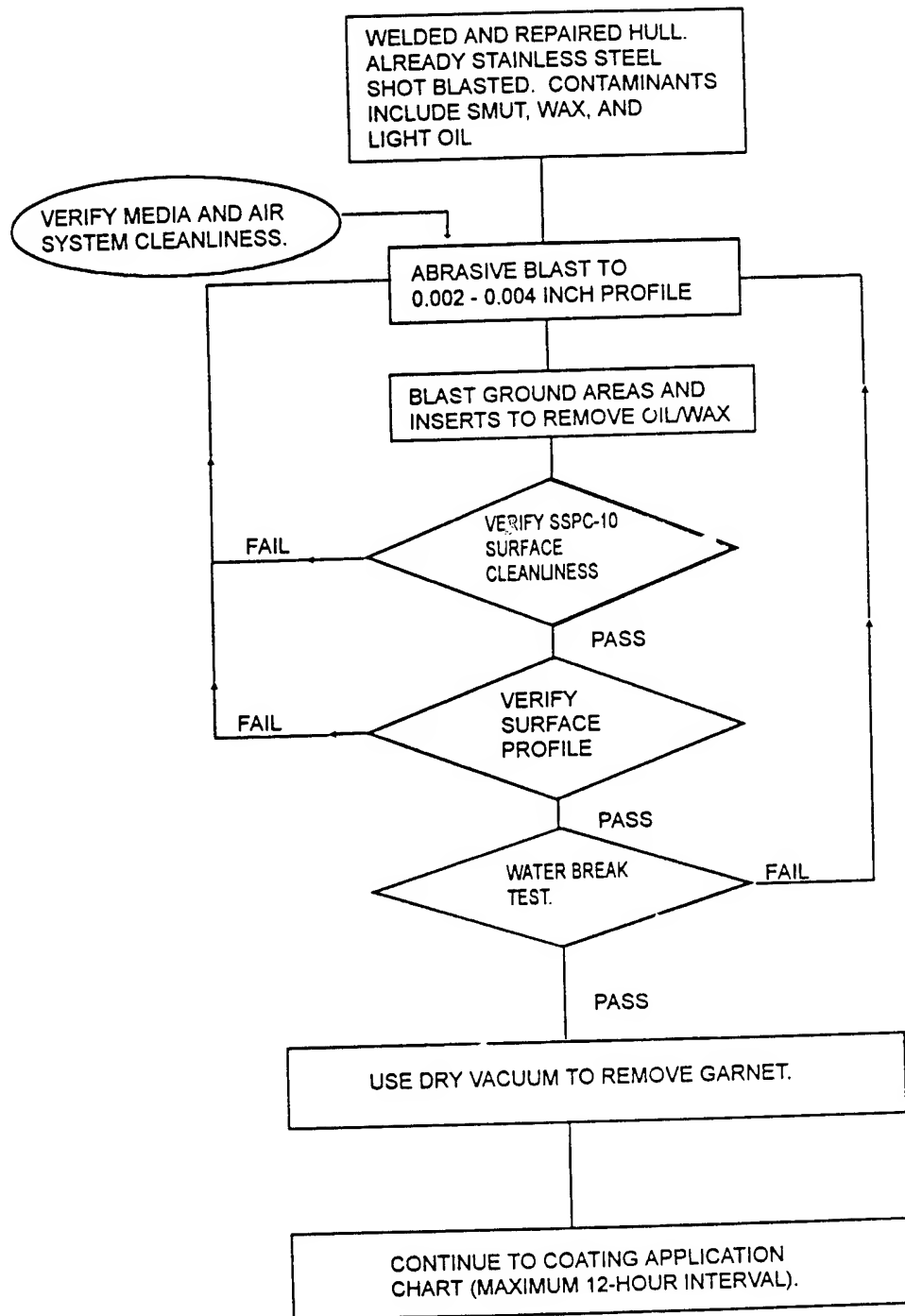


Figure 4 Dry Aluminum Hull Blasting Process

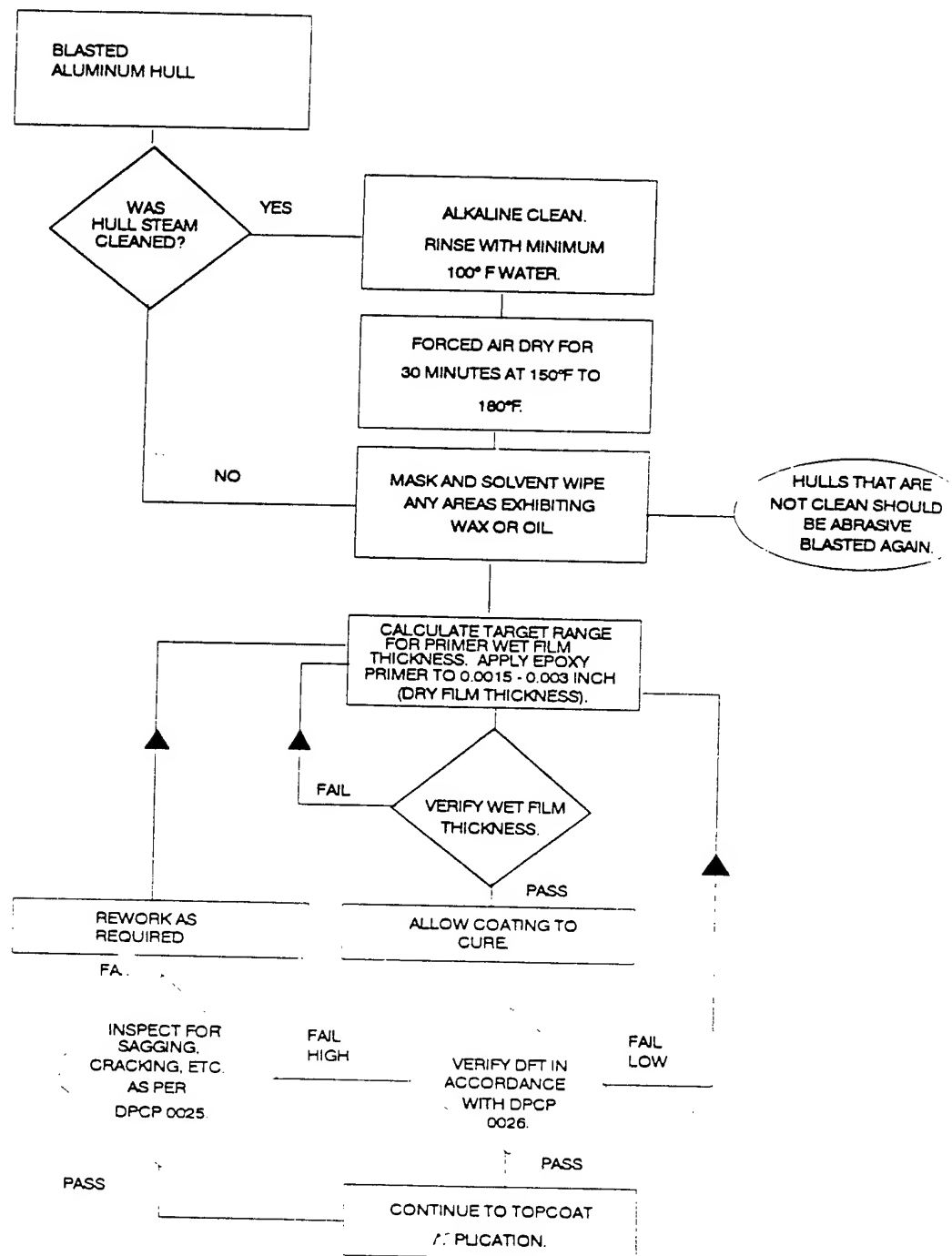


Figure 5 Primer Application Process

EVALUATION OF ENVIRONMENTALLY ACCEPTABLE MULTI-LAYER COATING SYSTEMS AS DIRECT SUBSTITUTES FOR CADMIUM PLATING ON THREADED FASTENERS

Mark W. Ingle
Ocean City Research Corporation
Alexandria, VA 22304

I. Carl Handsy
U.S. Army Tank and Automotive Command
Warren, MI 48397

B. S. Schorr

ABSTRACT

Cadmium has been identified by the United States Army's Tank and Automotive Command as a threat to worker health and the environment. Based on already completed cadmium substitute testing, an evaluation program was conducted to quantify the performance of environmentally acceptable, multi-layer coatings that could be directly substituted for cadmium on threaded fasteners. The performance issues investigated included coating system lubricity and corrosion control performance. Data were generated from both natural marine atmosphere exposure tests and laboratory evaluations. Test specimens were prepared by applying sacrificial plating layers and lubricous topcoat materials to commercially available 1/2-20 UNC Fine, Grade 5 fasteners. Experimental analyses included realistic torque-tension curve development, marine atmosphere exposure testing, and ASTM B 117 salt fog evaluations. Program findings indicate that ASTM B 633 zinc coatings (without the Type II or III chromate passivation treatment) exhibited torque tension behavior that was directly comparable to that of the cadmium experimental controls. Corrosion control performance test results indicated that regardless of underlying plating chemistry, systems topcoated with Everlube 6108 performed as well as the cadmium experimental controls.

INTRODUCTION

The Army Materiel Command's, Acquisition Pollution Prevention Support Office (AAPPSO) identified cadmium plating as an environmentally unacceptable process in 1989. Cadmium is considered unacceptable because it adversely impacts the environment and poses a threat to worker health. Cadmium is considered such a threat to workers that the Occupational Safety and Health Administration (OSHA) recently revised their cadmium regulations. OSHA, in its September 14, 1992 "Occupational Exposure to Cadmium; Final Rules," reduced the allowable airborne concentration of cadmium in the work-place by 95% (from the previously accepted Permissible Exposure Limit or PEL). Compliance with the OSHA Cadmium Standard is expected to cost domestic industries \$159 million/year.(1)

The environmental unacceptability of cadmium has prompted many other countries to develop regulations or "bans" on the material. For example, Sweden enacted a comprehensive cadmium ban in 1985.(2) Finland also restricted cadmium usage in 1992 and Germany has prohibitions against the use of some cadmium compounds.(3)

Given the environmental and worker health problems associated with continued cadmium use, many Army activities are trying to eliminate their applications for the metal. The AAPPSO has been researching cadmium alternatives since 1989 and completed a major environmentally acceptable alternative screening program in 1991.(4) Based on the AAPPSO sponsored cadmium alternative screening program results, and private sector data, representatives of the Army's Tank and Automotive Command (TACOM) decided to research "direct" cadmium substitutes.(5)

The "direct" cadmium substitute concept evolved when TACOM staff reviewed the available technical literature and concluded that no universal, "one-for-one" cadmium substitute was likely to be developed in the near future. However, TACOM staff felt that by combining sacrificial plating layers and lubricious topcoats, a coating system that would mimic the performance of cadmium plating (both to queue-tension and corrosion control) closely enough to allow direct substitution on Army tactical vehicles could be developed. The development of this "direct" substitute coating would allow TACOM to avoid the high costs associated with rewriting all the Army vehicle maintenance manual fastener torque requirements that were originally developed using cadmium coated fasteners.

TACOM staff commissioned Ocean City Research Corporation to conduct a realistic test program with the overall objective of identifying a "direct" cadmium

substitute that would mimic the torque-tension relationship exhibited by QQ-P-416E, Class 3, Type II cadmium coatings on Grade 5 carbon steel fasteners and still exhibit comparable (or better) substrate corrosion control performance.

TECHNICAL APPROACH

TEST MATRIX - Table I presents the multi-layer cadmium substitute program test matrix and target coating thickness summary. The matrix lists the sacrificial plating layers and the six alternative lubricous topcoat materials. The test matrix shows the coating systems roughly divided into three base plating layer groups. For clarity, these three data set groupings will be used throughout this discussion.

The plating layers described in the Table I test matrix were applied in accordance with the following Federal or consensus specifications.

Cadmium	-	Federal Specification QQ-P-416E, Class 3, Type II
Zinc	-	ASTM B 633, Type I
Zinc/Nickel	-	Draft ASTM specification
Zinc/Cobalt	-	Commercial specification

Because chromic acid based passivation treatments are considered environmentally unacceptable, none of the test cadmium alternatives were passivated with these solutions. However, because many Army tactical vehicle maintenance manuals were developed using chromated cadmium fastener performance data, the cadmium coated experimental controls did receive a Type II chromate treatment. Excluding these experimental controls, the alternative plating layers are considered environmentally acceptable because they do not contain lead, chromium, or cadmium, and are not plated from a cyanide bath.

The lubricous topcoats shown in Table I were applied by commercial vendors using their "best practices." The Xylan 5420, Everlube 6108 and Everlube 9000 coatings were applied from low VOC solutions and contain PTFE (Teflon). The SACI 445A coating was applied from an aqueous bath and contains calcium carbonates and sulfonates. The Alumzite 132 coating consists of aluminum particles in an organic binder. Finally, the Molykote M3400A (a MIL-L-46010A molybdenum disulfide dry film lubricant) was included in the program even though the as applied material contains more than 5 lbs/gallon VOCs. Because these MIL-L-46010A lubricants are widely used by the Army, this material was included in the test matrix as an experimental control. None of the lubricous topcoats contained lead or soluble chromates.

TEST SPECIMENS - Figure 1 shows a representative cadmium coated test fastener set. Each test fastener set included a 3-inch long, 1/2-20-UNC Fine, Grade 5 threaded bolt, a mating nut, and two 1/2-inch washers. The fasteners were procured from commercial suppliers and were not undersized to accommodate subsequent coatings. Plating vendors were required to coat entire specimen lots using the same military or commercial specifications. Topcoat vendors were also instructed to coat the plated fastener lots using the same "best practices" on each item.

COATING THICKNESS QUALIFICATION - An Elcometer 300 film thickness gauge was used to measure non-magnetic coating thicknesses. Because the Zn/Ni and Zn/Co coatings might have exhibited magnetic properties, their thicknesses were initially measured using representative metallography. Metallographic thicknesses were found to correlate well with Elcometer 300 readings and this device was used for all subsequent measurements. After the plating and topcoating processes, layer thicknesses were measured at replicate sites on individual nuts, washers, bolt heads, and bolt shanks. After coating, ten representative fastener sets were selected from each plating/topcoat system group. The thickness data from these representative fasteners were then collected and analyzed.

TORQUE-TENSION TESTING - Figure 2 shows the program torque-tension measurement apparatus. The apparatus is an evolutionary design based on devices described in published literature and in the SAE Recommended Practice J174, "Torque-Tension Test Procedure." (6,7) The apparatus shown in Figure 2 consists largely of conventional automotive mechanic's tools. These conventional tools were combined with extremely accurate compression and torque sensors to allow both realistic and accurate data collection. The Omega DP-41-S strain gauge and DP-80 digital strain indicators were calibrated by the vendors (+ or - 0.25%) and programmed to directly convert the torque and strain sensor inputs into foot*lbs and kips units for direct, real-time scaling on an X-Y recorder. The use of actual mechanics tools, similar to those available in Army tactical vehicle maintenance shops, allowed fastener head slippage, galling, and misfits to realistically contribute to the data collection process.

The bolt head shown in Figure 2, Detail A was placed in a fixed socket and the instrumented torque wrench was mounted on the nut. To minimize program variables and address specific Army needs, only unlubricated (no oil or grease) fasteners were tested. As shown in Detail A, a series of machined stainless steel spacing washers and a leveling device were mounted on either side of instrumented compression load cell (calibrated to measure compression loads up to 100 kips or 444,820 Newtons [N]). The leveling device consisted of a nested hardened steel convex disk and concave

plate. The nesting components have large holes in their centers through which the test fastener passed. Any eccentricity in the applied load across the leveling device was absorbed by motion between the two (convex/concave) mating surfaces. As torque was manually applied to this assembly, the instrumented wrench sensor and compression cell directly generated a data plot on an X-Y recorder.

EXPOSURE TESTING - Test fasteners were exposed at the Ocean City Research Corporation, Sea Isle, NJ marine exposure test site. The fasteners were exposed using two different test specimen support assemblies to facilitate subsequent analyses. Both marine site fastener test assemblies were subject to daily seawater spray.

Figure 3 shows two of the marine atmosphere exposure test rigs. The fasteners shown in the upper portion of the picture were threaded onto non-conductive phenolic/glass composite plate/tube assemblies with the nut/bolt interface exposed to the marine environment at an angle of 45 degrees facing south. The orientation of these specimens maximized the corrosive conditions at the nut/bolt interface. These specimens were torqued uniformly to create an estimated 10 kips [44,482 N] tensile load on each fastener. The breaking torques required to disassemble groups of selected test fasteners were measured after 2500, 5000, and 7000 hours of marine atmosphere exposure testing. During testing, all specimens were inspected for visible corrosion in accordance with a modified ASTM D 610 rating scale. The ASTM D 610 standard was modified to compensate for the difficulties associated with accurately measuring corroded areas on complex fastener surfaces.

The horizontally mounted fasteners with the exposed shanks shown in Figure 3 were intended to create conditions favorable for shank/thread corrosion and stress corrosion cracking. These loaded fasteners were initially torqued to create a fastener tensile load of 10 kips [44,482 N]. During testing, these fasteners will be further tensioned at regular intervals to absorb any system compliance or support frame deformation. These specimen sets were also inspected for visible corrosion in accordance with the modified ASTM D 610 rating scale.

SALT FOG TESTS - Salt fog tests were performed in accordance with ASTM B 117. Three replicate test specimens, from each test coating system group, were assembled and mounted on insulated racks. The assembled fastener specimens were exposed to the salt fog atmosphere for 1000 hours. During testing, all specimens were inspected for visible corrosion in accordance with the modified ASTM D 610 rating scale. These salt fog tests are intended to generate results that may be compared with the Army's historical salt fog test data-base. TACOM staff

acknowledge that salt fog tests have limited usefulness in evaluating corrosion. However, they feel such results could be compared with existing historical data.

RESULTS AND DISCUSSION

COATING APPLICATION ACCURACY - Table II summarizes the average coating thicknesses on the test fastener sets. As shown, the average actual test coating thicknesses varied both above and below the specified target thicknesses. Of the twenty-one test systems (including the cadmium experimental controls), four had average thicknesses lower than those specified. The remaining seventeen systems were thicker than specified and in four cases thicknesses were more than three times (300%) greater than those specified.

The standard deviation data shows that in addition to the overall average thicknesses being inaccurate, many systems varied around those averages by almost as much as the original target system thickness. For example, the actual cadmium thickness standard deviation is 0.19 mils which is almost as large as the specified target thickness of 0.2 mils. Nine of the test systems actually had standard deviations that were greater than the specified coating thickness. These data, when combined with previously reported findings, suggest that specified plating thicknesses on commodity grade fasteners are poorly controlled.(4) Thus, provided cadmium alternative system performance is acceptable, thickness variations assembly should not disqualify environmentally acceptable alternative coatings.

TORQUE TENSION RELATIONSHIPS - Torque-tension curves were generated using replicate as-received fasteners. Initially, fifteen to twenty fasteners from representative coating lots were evaluated using the Figure 2 apparatus. The resulting raw data from these tests were a series of X-Y recorder plots. To facilitate analysis torque intervals of 20 ft*lbs [27 N*m] were arbitrarily selected and corresponding data points on the X-Y plots were identified. Tension values corresponding to these torques were then interpreted from each of the individual raw data plots and loaded onto a computer spreadsheet. These interpreted data are presented in the following figures.

An initial analysis was conducted to determine if coating system torque-tension data distribution were "normal" or "Gaussian." Figure 4 shows the tension data distribution for twenty replicate cadmium coated fasteners at an applied torque of 80 ft*lbs [108 N*m]. As shown, the distribution is nearly normal and as such descriptive statistical analyses would be applicable. Figure 4 and all figures in this paper were initially generated using english measurement units. For clarity, these units are

retained in the figures. SI unit conversions are provided in square brackets below the plot labels and on the actual plot axes.

Figure 5 shows a tension data distribution histogram generated using fifteen replicate zinc-Molykote M3400A coated fasteners. An applied torque of 100 ft*lbs [135 N*m] was selected as the basis for comparison. Again, the distribution appears nearly normal and justifies the application of descriptive statistics. All tested fastener groups exhibited similar "normal" data distributions.

Figure 6 shows the complete torque-tension data from the twenty replicate cadmium coated fasteners used to generate Figure 4. Figure 6 includes the average, minimum, maximum, and standard deviation data. The most important feature of this plot is the significant data scatter. The tension data range at an applied torque of 80 ft*lbs [108 N*m] varies between 7,510 kips [33,406 N] and 10,580 kips [47,062 N]. This range is approximately 36% of the average target tension. The standard deviation at this torque value is also quite large at 720 kips [972 N]. Understanding that these data were generated from the cadmium experimental control, this wide scatter suggests that alternative coatings may also exhibit considerable torque-tension data scatter and still be considered acceptable cadmium substitutes. For the purposes of this discussion, a substitute will be considered acceptable if its torque-tension curve lies within + or - one standard deviation of the cadmium results.

Figure 6 also shows that cadmium coatings exhibit relatively consistent behavior over the entire measured torque-tension range. Cadmium coated fastener tension increased at a slightly decreasing rate as a function of increasing applied torque. To be considered acceptable, any potential cadmium alternative coating would have to exhibit similar, consistent behavior.

The Figure 4, 5, and 6 results were generated by evaluating many replicate fasteners. To improve program efficiency, average and standard deviations from smaller sample sizes were compared to those generated from fifteen or twenty replicates. The objective of this analysis was to identify the minimum number of specimens required to produce representative data. Figure 7 shows representative torque-tension curves generated using five, ten, and fifteen replicate fasteners coated with the Zn-M3400A system. Using the previously stated + or - one standard deviation criteria, Figure 7 shows that results generated from five replicate test fasteners would be as representative of the overall population as those generated from ten or fifteen specimens.

Figure 8 shows the torque-tension data generated from five replicate test specimens with the zinc plating layer substrate and the six alternative topcoats. The cadmium experimental control data has been included on the plot as a reference. With the exception of the Zn-Xylan system, all of the alternative's torque-tension curves have slopes greater than that exhibited by the cadmium experimental control. These greater slopes signify that the alternative coating systems are appreciably more lubricious than cadmium. Because many Army tactical vehicle maintenance manuals specify application torque values, the use of an appreciably more lubricious coating as a "direct" cadmium substitute would result in higher than anticipated clamping forces and possibly cause fastener tensile overload failures. Thus, none of the lubricious topcoat based systems exhibiting slopes greater than cadmium would be considered acceptable substitutes.

However, Figure 8 also shows that the non-topcoated zinc and the Zn-Xylan systems were quite similar to cadmium in overall torque-tension performance. The zinc curve falls almost exactly over the cadmium plot and easily satisfies the one standard deviation criteria as an acceptable cadmium substitute. These data suggest, from a torque-tension standpoint, that zinc plating would be an effective cadmium substitute.

The performance similarities between the Zn-Xylan system and cadmium are surprising. Xylan is a PTFE based coating that is supposedly lubricious. However, the Figure 8 data show the material was actually less lubricious than the uncoated plating layer. Although the Zn-Xylan data falls slightly outside the one standard deviation range, it is interesting that the Zn-Xylan system actually produced torque-tension relationships quite similar to those exhibited by the cadmium controls.

Figure 9 shows the torque-tension data generated from five replicate test specimens with the Zn/Ni plating layer substrate and the six alternative topcoats. The trends discussed during the Figure 8 analysis apply to the Figure 9 data although to a lesser degree. The Figure 9 results show both the un-topcoated Zn/Ni and the Zn/Ni-Xylan systems were slightly less lubricious than cadmium. However unlike Figure 8, the Zn/Ni-Everlube 6108 system was only slightly more lubricious than cadmium and falls just outside the cadmium data one standard deviation range. Thus, although the performance of the Zn/Ni-Everlube system is similar to that of cadmium it would not be considered a direct cadmium substitute.

Figure 10 shows the torque-tension data generated from five replicate test specimens with the Zn/Co plating layer substrate and the six alternative topcoats. The trends discussed during the Figure 9 analysis apply to the Figure 10 results. Again,

both the un-topcoated Zn/Co and the Zn/Co-Xylan systems were slightly less lubricious than cadmium. However unlike Figure 9, the Zn/Co-SACI 445A system, not the Everlube 6108, was only slightly more lubricious than cadmium and is just outside the range to be considered a potential cadmium substitute.

The torque-tension data presented in Figures 8-10 show zinc coatings would be considered a direct cadmium substitute. The Zn-Xylan, Zn/Ni-Everlube 6108, and Zn/Co-SACI 445A would be considered possible cadmium substitutes even though their torque tension curves fell just outside of the cadmium data one standard deviation range.

BREAKING TORQUE ANALYSIS - Figure 11 shows average (five data sets) torque data for the "best performing" cadmium substitutes identified during the Figure 8-10 discussion. The torque data presented includes the applied clamping torque required to create an estimated 10,000 kips [44,482 N] of fastener tension and the average breaking torque required to loosen fastener assemblies that had been subject to 2500-hours of marine atmosphere exposure. By comparing the average clamping and breaking torques, Figure 11 allows the relative interfacial corrosion control performance of the fastener systems to be assessed (i.e. systems with severely corroded nut/bolt interfaces will typically exhibit significantly increased breaking torque values).

Comparing the Figure 11 average applied clamping and breaking torque data does not conclusively demonstrate that any of the Figure 8-10 "best performing" systems experienced nut/bolt interfacial corrosion. With the exception of the un-topcoated zinc specimens, all of the "best performing" cadmium alternatives exhibited breaking torques that were lower than the clamping torques - an anticipated result considering that no interfacial corrosion was visually detected. The slight increase in the breaking torque relative to the clamping torque for the un-topcoated zinc specimen is not statistically significant, but does suggest that longer term interfacial corrosion tests (to be presented in October 1993) must be carefully reviewed. If the un-topcoated zinc fastener breaking torque values increase with extended marine atmosphere exposure, the acceptability of this system as a cadmium substitute would be questionable.

MARINE ATMOSPHERE/SALT FOG CORROSION CONTROL PERFORMANCE - Figure 12 presents the average, modified ASTM D 610 substrate corrosion control ratings generated by averaging data from three representative, replicate test fasteners. Marine site corrosion control performance data was collected after 2500 hours of atmospheric exposure. Salt fog data was

collected after 1000 hours of ASTM B 117 exposure. An initial review of the Figure 12 data shows that the salt fog test results do not correlate well with the marine atmosphere exposure test results. For example, the marine atmosphere data shows the following four systems exhibited no substrate corrosion after the 2500 hour exposure period; cadmium, Zn-Everlube 6108, Zn/Ni-Everlube 6108, and Zn/Co-Everlube 6108. The salt fog data exhibited a completely different trend. Based on the salt fog data, the systems offering the most effective corrosion control performance were: Zn-Everlube 6108, Zn/Co-Xylan, cadmium, Zn/Ni-Xylan and Zn/Ni-Alumzite. Because the salt fog results do not accurately reflect the corrosion control performance trends apparent at the marine atmosphere exposure site, the remainder of this discussion will focus on the marine atmosphere results.

A comparison of the "best performing" cadmium substitutes identified during the Figure 8-10 discussion with the Figure 12 results shows the un-topcoated zinc systems that mimicked cadmium's torque tension performance so closely, performed relatively poorly in the marine atmosphere corrosion control tests. However, the Zn-Xylan and Zn/Ni-Everlube 6108 systems that appeared to offer roughly comparable torque-tension performance to the cadmium controls also appear roughly comparable in the corrosion control tests. Because the Zn-Xylan and the Zn/Ni-Everlube 66108 systems offered comparable corrosion control performance and exhibited torque-tension performance comparable to cadmium, these two systems might be considered as possible cadmium substitutes.

CONCLUSIONS

The following are the program conclusions to-date:

1. The actual, average applied thicknesses on seventeen systems were thicker than specified and in four cases thicknesses were more than three times (300%) greater than specified. In addition, variations within groups were frequently as large as the original target thickness. These data suggest that only the most significant fastener thickness variations should impact the cadmium alternative selection.
2. Torque-tension analyses indicate that cadmium coatings are not appreciably more lubricous than ASTM B 633, Type I zinc plating layers and that the addition of a lubricous topcoat may actually allow excessive fastener tension for given torque levels. On the basis of torque-tension tests, a simple zinc coating appears to be the most effective cadmium substitute coating.

3. Corrosion control performance data show ASTM B 117 salt fog test results do not accurately reflect marine atmosphere corrosion control performance.
4. Corrosion control performance data show that any plating substrate, when topcoated with Everlube 6108 provided corrosion control performance comparable to that of the cadmium experimental controls.

REFERENCES

1. Department of Labor, Occupational Safety and Health Administration, Occupational Exposure to Cadmium; Final Rules; Code of Federal Regulations, Title 29, Part 1910 1027, September 14, 1992.
2. The Swedish Ban on Cadmium, National Swedish Environmental Protection Board Information Unit, ISBN 91-620-3446-4, 1988.
3. Finland: Products Containing Cadmium and its Compounds, Commerce Business Daily Announcement, November 25, 1992.
4. Ingle M., Marchesani T., Proceedings of the 5th Automotive Corrosion and Prevention Conference, SAE P-250, 1991.
5. Groshart E. C., Boeing Defense and Space Systems Corp. Presentation to the Army Environmentally Acceptable Materials Treatments and Processes Program Quarterly Program Review Meeting, August 1, 1991.
6. Monaghan J. M., Journal of Strain Analysis, Volume 26, Number 2, 1991.
7. Parmley R. O., Standard Handbook of Fastening and Joining, McGraw-Hill Inc., 1989

TABLE I

Coating System Test Matrix and Specified Thickness

SYSTEM NUMBER	PLATING LAYER	TARGET THICKNESS (μ m)(mils)	LUBRICOUS TOPCOAT	TARGET THICKNESS (μ m)(mils)	TOTAL SYSTEM TARGET THICKNESS (μ m)(mils)
Control	Cadmium	5.1/0.2	None	0.0/0.0	5.1/0.2
1 Control	Zinc	12.7/0.5	None	0.0/0.0	12.7/0.5
2	Zinc	12.7/0.5	Xylan	12.7/0.5	25.4/1.0
3	Zinc	12.7/0.5	E6108	25.4/1.0	38.1/1.5
4	Zinc	12.7/0.5	E9000	12.7/0.5	25.4/1.0
5	Zinc	12.7/0.5	M3400A	12.7/0.5	25.4/1.0
6	Zinc	12.7/0.5	Saci 445A	12.7/0.5	25.4/1.0
7	Zinc	12.7/0.5	Alumzite	12.7/0.5	25.4/1.0
8 Control	Zn/Ni	5.1/0.2	none	0.0/0.0	5.1/0.2
9	Zn/Ni	5.1/0.2	Xylan	12.7/0.5	17.8/0.7
10	Zn/Ni	5.1/0.2	E6108	25.4/1.0	30.5/1.2
11	Zn/Ni	5.1/0.2	E9000	12.7/0.5	17.8/0.7
12	Zn/Ni	5.1/0.2	M3400A	12.7/0.5	17.8/0.7
13	Zn/Ni	5.1/0.2	Saci 445A	12.7/0.5	17.8/0.7
14	Zn/Ni	5.1/0.2	Alumzite	12.7/0.5	17.8/0.7
15 Control	Zn/Co	5.1/0.2	none	0.0/0.0	5.1/0.2
16	Zn/Co	5.1/0.2	Xylan	12.7/0.5	17.8/0.7
17	Zn/Co	5.1/0.2	E6108	25.4/1.0	30.5/1.2
18	Zn/Co	5.1/0.2	E9000	12.7/0.5	17.8/0.7
19	Zn/Co	5.1/0.2	M3400A	12.7/0.5	17.8/0.7
20	Zn/Co	5.1/0.2	Saci 445A	12.7/0.5	17.8/0.7
21	Zn/Co	5.1/0.2	Alumzite	12.7/0.5	17.8/0.7

TABLE II

Coating System Applied Thickness

SYSTEM NUMBER	PLATING LAYER	LUBRICOUS TOPCOAT	TOTAL SYSTEM TARGET THICKNESS (μm)(mils)	AVERAGE ACTUAL SYSTEM THICKNESS (μm)(mils)	ACTUAL SYSTEM STANDARD DEVIATION (μm)(mils)
Control	Cadmium	None	5.1/0.2	8.44/0.33	4.79/0.19
1 Control	Zinc	None	12.7/0.5	9.89/0.39	5.98/0.24
2	Zinc	Xylan	25.4/1.0	36.86/1.45	13.80/0.54
3	Zinc	E6108	38.1/1.5	30.92/1.22	13.78/0.54
4	Zinc	E9000	25.4/1.0	83.66/3.29	45.59/1.79
5	Zinc	M3400A	25.4/1.0	27.77/1.09	15.17/0.60
6	Zinc	Saci 445A	25.4/1.0	60.70/2.39	28.06/1.10
7	Zinc	Alumzite	25.4/1.0	24.88/0.98	11.96/0.47
8 Control	Zn/Ni	none	5.1/0.2	11.57/0.46	5.65/0.22
9	Zn/Ni	Xylan	17.8/0.7	36.87/1.45	11.02/0.43
10	Zn/Ni	E6108	30.5/1.2	18.75/0.74	6.62/0.26
11	Zn/Ni	E9000	17.8/0.7	65.67/2.59	24.50/0.96
12	Zn/Ni	M3400A	17.8/0.7	28.36/1.12	20.49/0.81
13	Zn/Ni	Saci 445A	17.8/0.7	61.60/2.43	29.72/1.17
14	Zn/Ni	Alumzite	17.8/0.7	29.22/1.15	12.08/0.48
15 Control	Zn/Co	none	5.1/0.2	15.69/0.62	8.45/0.33
16	Zn/Co	Xylan	17.8/0.7	39.94/1.57	12.93/0.51
17	Zn/Co	E6108	30.5/1.2	22.20/0.87	8.48/0.33
18	Zn/Co	E9000	17.8/0.7	69.55/2.74	23.21/0.91
19	Zn/Co	M3400A	17.8/0.7	30.76/1.21	14.43/0.57
20	Zn/Co	Saci 445A	17.8/0.7	61.07/2.40	35.98/1.42
21	Zn/Co	Alumzite	17.8/0.7	29.75/1.17	7.84/0.31

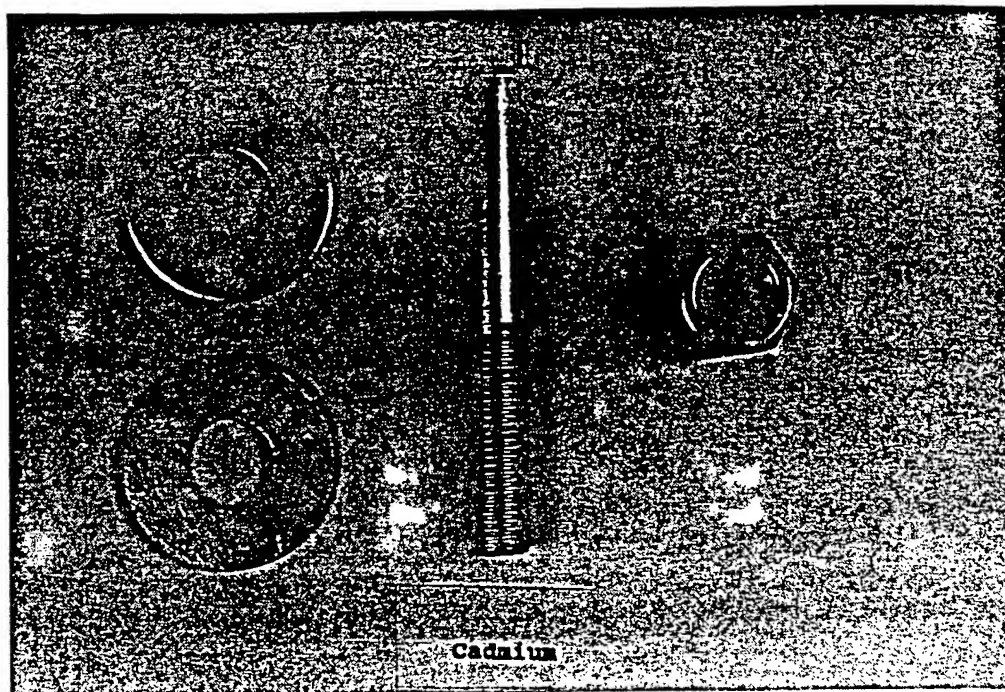
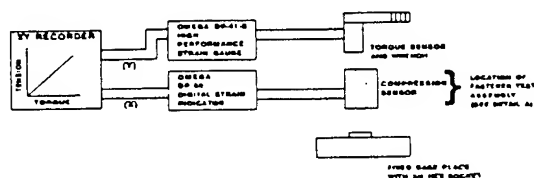


Figure 1 Representative Test Fastener Set (1/2-20 UNC Fine, Grade 5) Coated with QQ-P-416E, Class 3, Type II Cadmium Plating.

APPARATUS



DETAIL A

FASTENER TEST ASSEMBLY

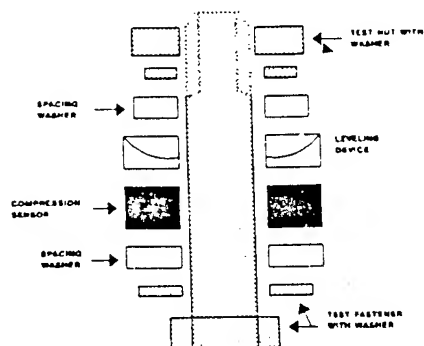


Figure 2 Torque-Tension Measurement Apparatus.

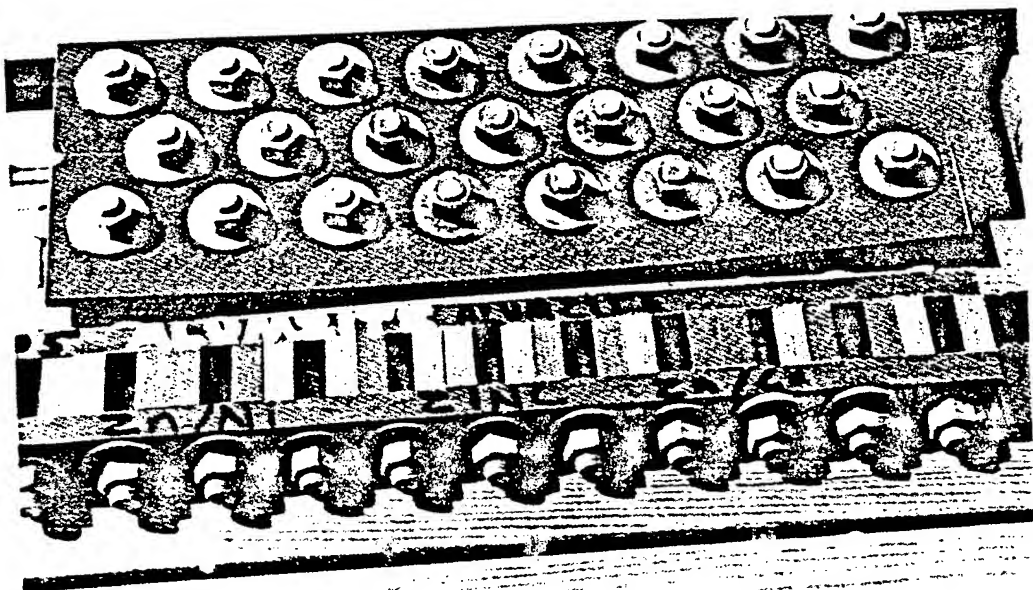


Figure 3

Marine Atmosphere Exposure Test Racks Showing Alternative Specimen Orientations.

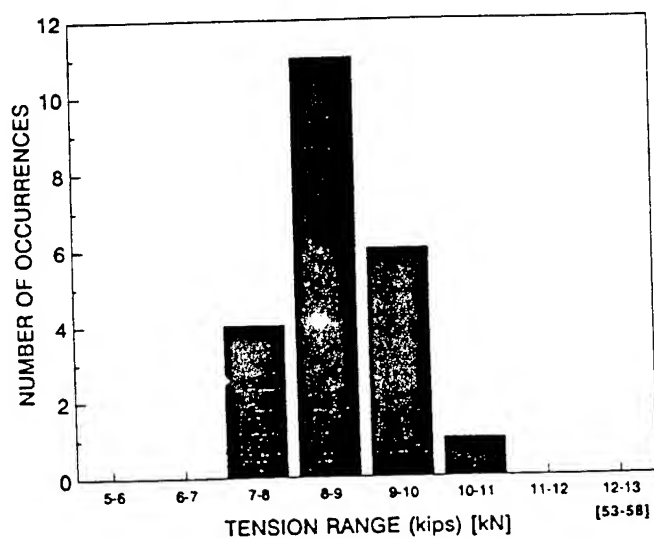


Figure 4

Tension Distribution Histogram Based on Twenty Replicate Cadmium Coated Fasteners at an Applied Torque of 80 ft • lbs [108 N • m].

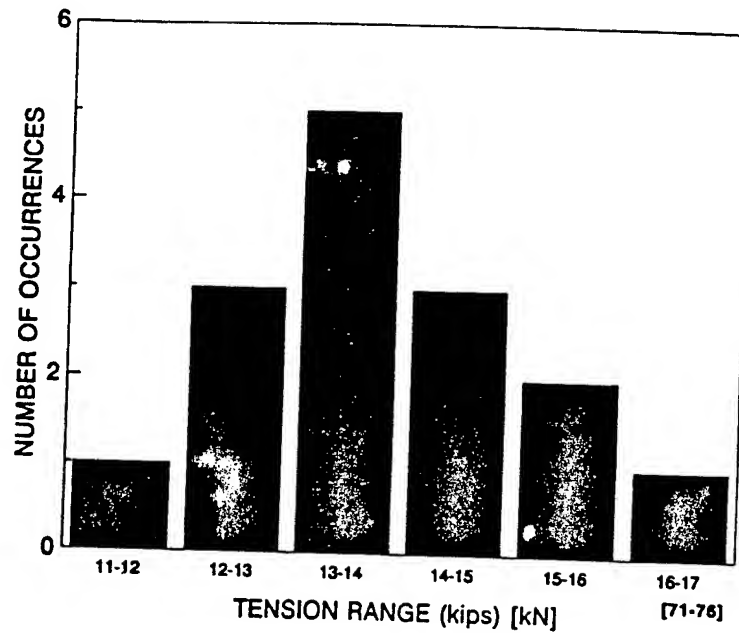


Figure 5 Tension Distribution Histogram Based on Fifteen Replicate Zinc-Molykote 3400A Coated Fasteners at an Applied Torque of 100 ft * lbs [135 N * m].

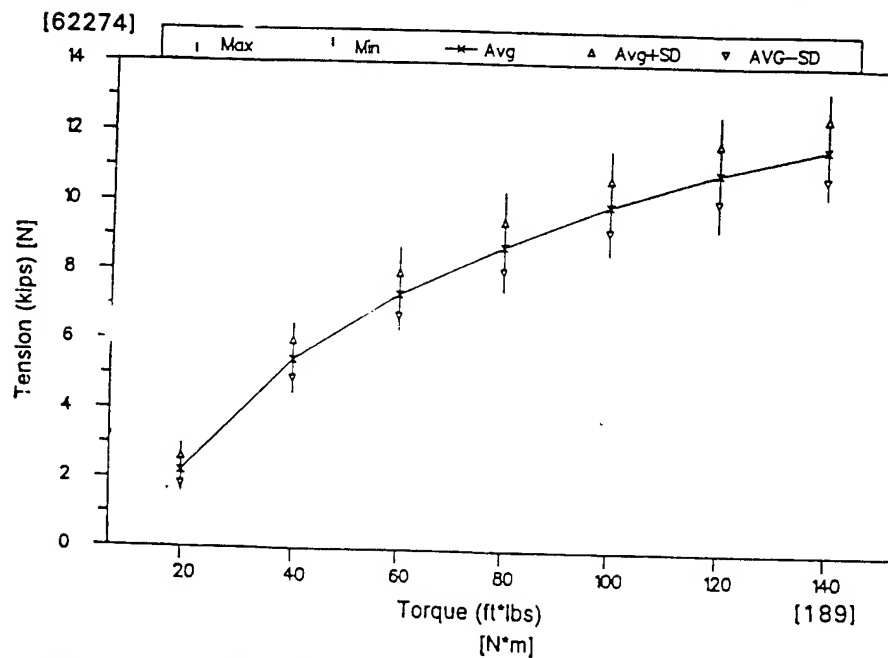


Figure 6 Torque-Tension Data From Twenty Replicate Cadmium Coated 1/2-20 UNC Fine, Grade 5 Fasteners.

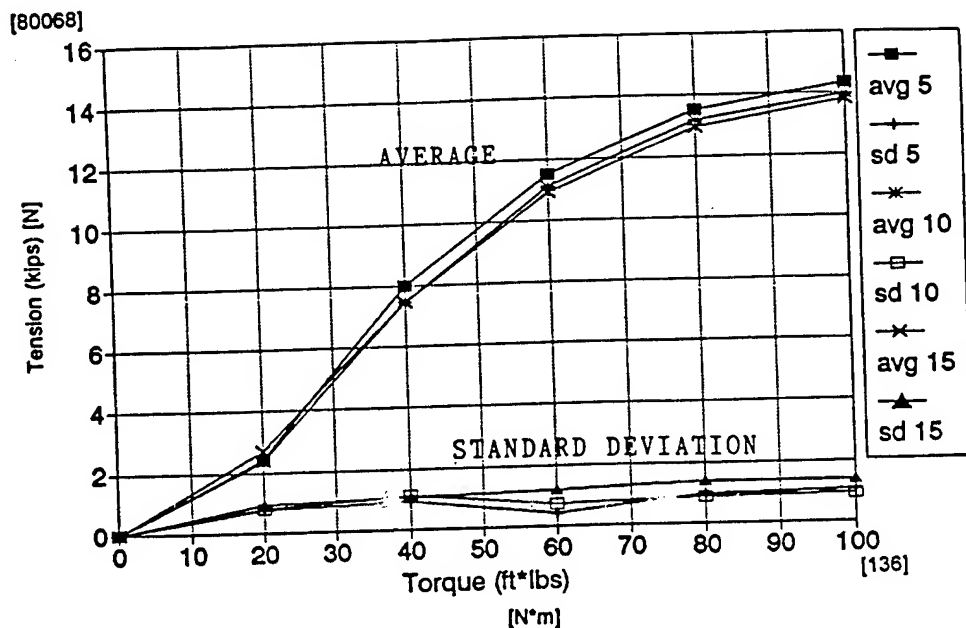


Figure 7 Torque-Tension Plots for Five, Ten, and Fifteen Duplicate Zinc-Molykote 3400A Coated Fasteners.

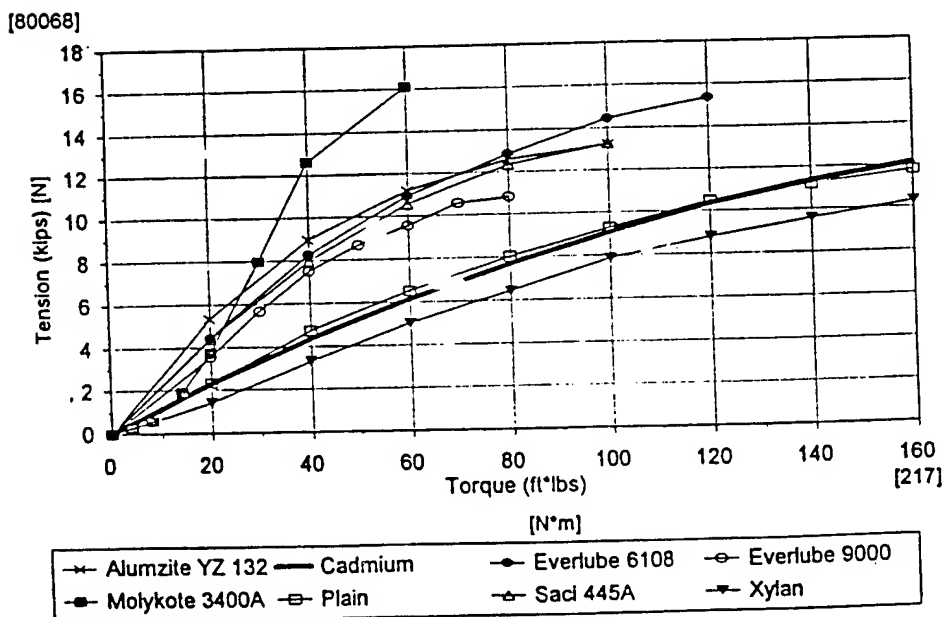


Figure 8 Torque-Tension Data From Five Replicate Fasteners Coated with Zinc and the Alternative Lubricious Topcoats.

[80068]

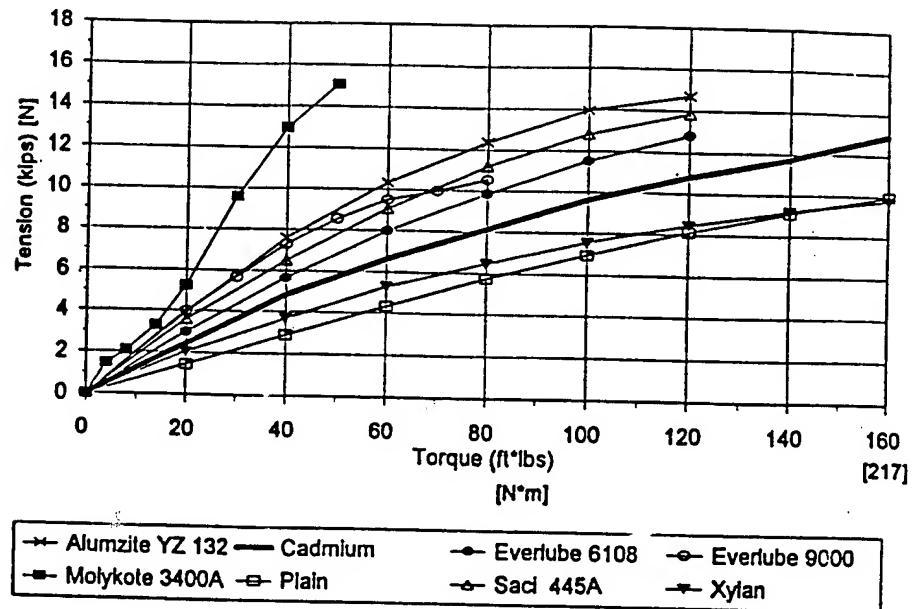


Figure 9 Torque-Tension Data From Five Replicate Fasteners Coated with Zn/Ni and the Alternative Lubricious Topcoats.

[71171]

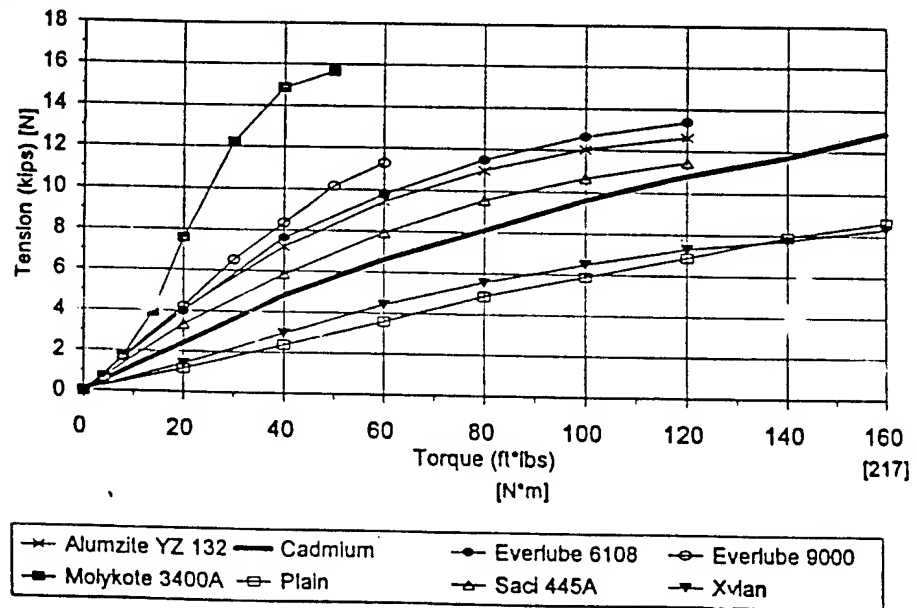


Figure 10 Torque-Tension Data From Five Replicate Fasteners Coated with Zn/Co and the Alternative Lubricious Topcoats.

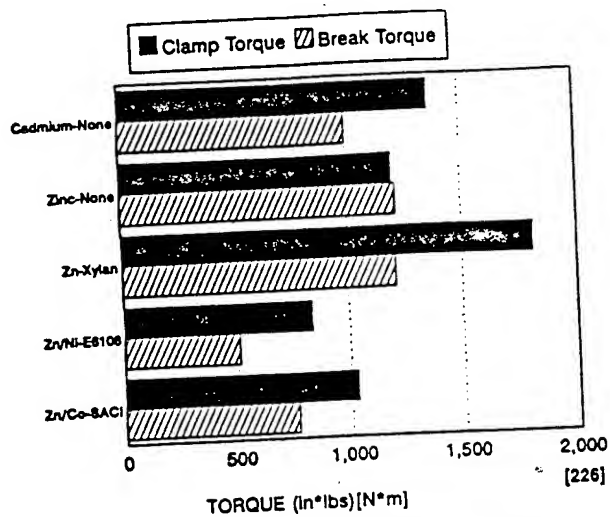


Figure 11

Average Applied Torque Required to Tension Fasteners to 10,000 kips [44,482] and to Break Tensioned Fasteners Loose After 2500-hours of Marine Atmosphere Exposure.

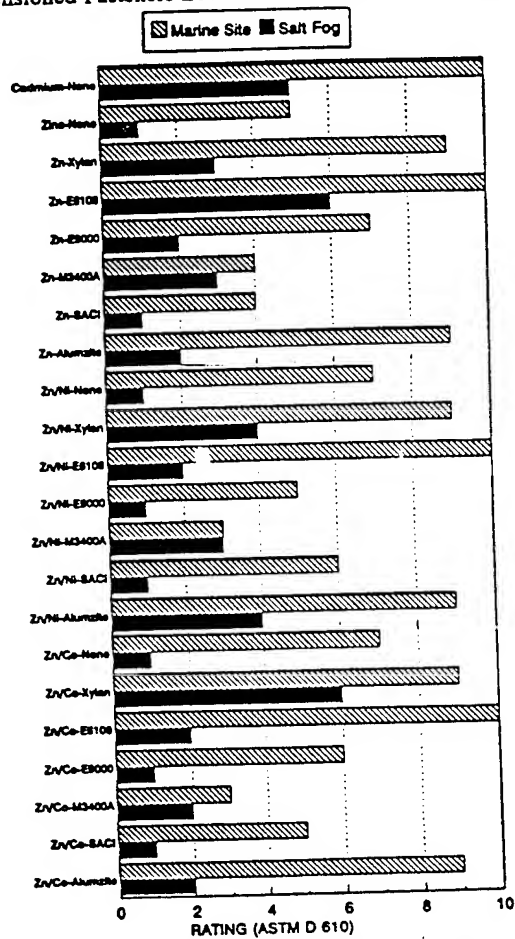


Figure 12

Average Coating System Corrosion Control Performance as Measured by 2500-hour Marine Atmosphere Exposure Testing and 1000-hour of ASTM B 117 Salt Fog Testing.

BLANK

804

Adhesion Promotion and Corrosion Prevention from Coatings Based on Sol-Gel Technology

Dr. Lynn C. Yanyo
Staff Scientist
Lord Corporation
405 Gregson Drive
Cary, NC 27511

Using a unique form of sol-gel technology, thin organic/ceramic (ceramer) coatings have been applied to metal surfaces to enhance such surface properties as adhesion promotion and corrosion prevention. Isotropic coatings derived from tetraethoxysilane, for example, have been found to effectively inhibit corrosion while being only 100-1000 Å thick. The formation of anisotropic (functionally gradient) coatings permits greater flexibility over the resulting properties. Using combinations of monomers with appropriate reactivities permits the single-step synthesis of anisotropic coatings that can both promote adhesion and prevent corrosion.

Introduction

Sol-gel processing is a method whereby small molecules can be converted into polymeric or ceramic materials [1-7]. Typically, one starts with molecules of the form MR_4 , where the R groups are either organic radicals, such as CH_3CH_2- and CH_3CH_2O- or halogens. The metal (M) is typically silicon but can be many other species such as titanium, zirconium, aluminum, etc. [1]. Representative compounds include tetraethoxysilane, dimethyldichlorosilane, and titanium isopropoxide. These small molecules are mixed in an appropriate solvent with water and a catalyst. After a period of time the monomers condense into a matrix that can later be dried and perhaps fired to form solid three-dimensional objects. Depending on the nature of the metal and the R groups, one can form anything from organic polymers such as polydimethylsiloxane to inorganic ceramics such as silicon dioxide.

Sol-gel coatings can be applied to substrates using two different methods. The first, and most widely used, involves making a coating

material from the acid-catalyzed hydrolysis and partial condensation of metal alkoxides. This material is spread, dipped or spun onto the substrate and subsequently cured or hardened. An alternative, patented [8-10] approach reported in this paper is the base-catalyzed growth of coatings directly on the substrate.

In this method, metal alkoxides are mixed with solvent, water, and a basic catalyst in the presence of a substrate (such as aluminum). As the monomers condense, some of them react with the surface of the substrate. As the condensation continues a coating is deposited onto, or more correctly reacted with, the substrate.

If the initial coating solution is formulated such that it contains several metal alkoxides of differing reactivity then the nature of the coating being formed will be a function of time. The lowest layers of the coating will be derived from the most reactive monomers while the upper layers will be made from the least reactive monomers.

The properties of the coating can be optimized so that each part of the coating provides optimum properties. One might choose, for example, for the first layer to interact strongly with the substrate, an intermediate layer to provide some sort of barrier, and a final layer to provide compatibility with a subsequently applied top coat (e.g. paint, primer or adhesive). Properties that can be altered as a function of depth into the coating include elastic modulus, free volume, density, index of refraction, chemical reactivity, barrier properties, electrical and thermal conductivity and extent of crosslinking.

Experimental

The substrates used for corrosion testing were thin films (1000-2000 Å) of aluminum (99.99%) or iron (99+%) that had been evaporated onto glass microscope slides or coupons of 2024-T3 aluminum. Corrosion testing was performed in either 0.1N NaOH or 0.1 N HCl (for aluminum) or pH 3 buffer (for iron, potassium acid phthalate/HCl) by monitoring the presence of the reflective metal surface visually until it disappeared. Corrosion testing of metal coupons was performed by monitoring the rate of weight loss of samples exposed to either 0.1 N NaOH or 0.1 N HCl. The coupons were bonded as lap shears with a 2.5 x 2.5 cm overlap using Tyrite 7520 (Lord Corporation) two part urethane adhesive. The samples were cured for 4 days at room temperature before testing. Selected samples were exposed to boiling water for 24 hours in an all glass apparatus.

The sol gel coating solutions, unless otherwise specified, contained 70 ml of ethanol, 27 ml of water, 3 ml of concentrated ammonium hydroxide and the silane monomers of choice (typically 6 ml). Samples were treated by immersion at room temperature for 10 minutes to 24

hours as indicated, rinsed in ethanol and/or water and allowed to air dry. Some samples for corrosion testing were heated to 100°C for 1 hour prior to testing.

ESCA sputtering was performed with 4keV argon ions. Atomic concentrations were determined from integrated peak areas. Binding energies were corrected for charging by arbitrarily assigning the adventitious carbon peak a binding energy of 284.6 eV. Ellipsometry was performed on a Rudolph Instruments Model 432A42B41 null point ellipsometer using 632.8 nm laser radiation. Thickness values were obtained by computer analysis with the assumption that the index of refraction of the coating was 1.4 [11].

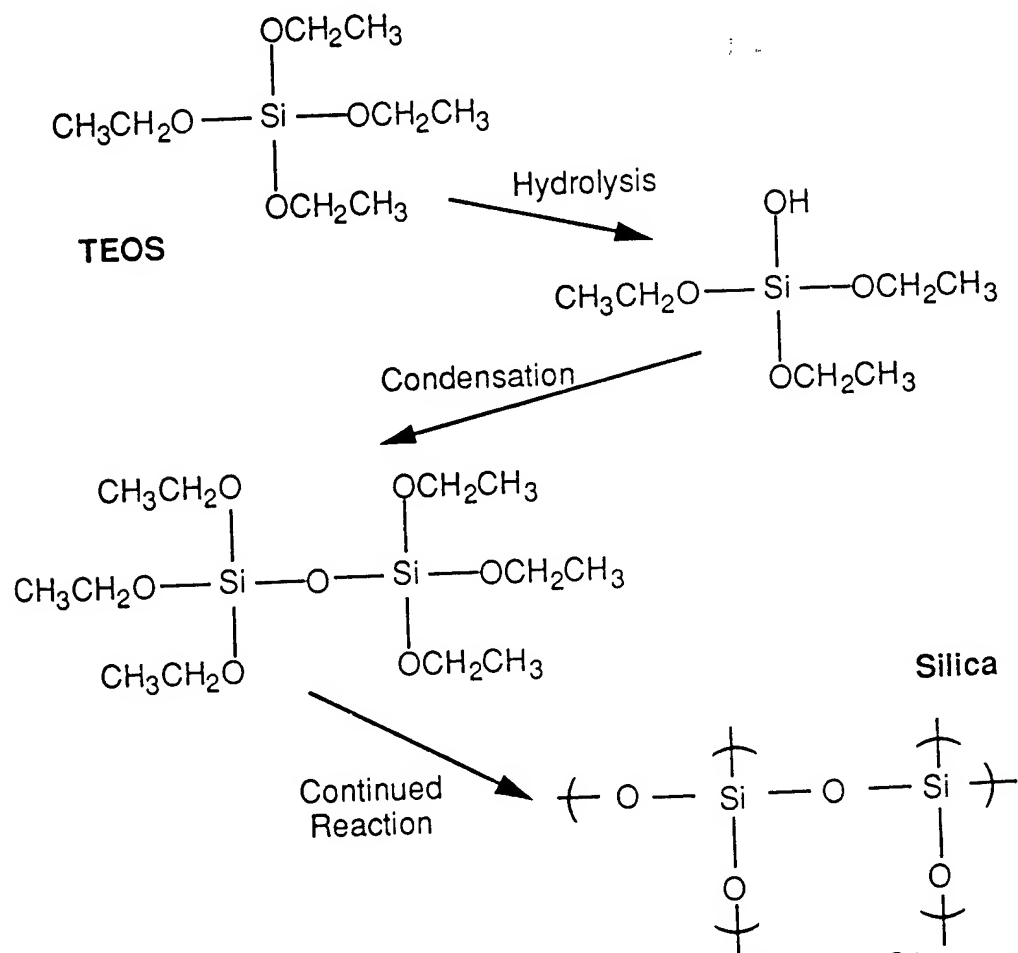


Figure 1. Reactions involved in the hydrolysis and condensation of TEOS to amorphous silica.

Results and Discussion

Isotropic coatings can be made by reacting a single monomer (or multiple monomers with similar reactivity) with an appropriate substrate. The substrates used in this work were films of aluminum or iron that had been evaporated onto glass or aluminum coupons. Isotropic films were made on these substrates by allowing TEOS (tetraethylorthosilicate or tetraethoxysilane) to react with water in a solution containing ethanol and ammonium hydroxide. As the hydrolysis and condensation reactions proceed (Fig. 1) colloids are formed in solution, causing the solution to become blue then milky white. At the same time, the silane species are reacting with active sites on the substrate surface, forming a thin coating consisting of SiO_2 (and aluminosilicates in the case of the aluminum substrate).

Under typical reaction conditions, it takes approximately 20 minutes for the coating to reach its maximum thickness of about 400-700 Å (Fig. 2). This thickness was determined by ellipsometry and was confirmed by several other techniques, including ESCA sputter depth profiling, profilometry, gravimetric analysis, and other techniques. The coating that results from this treatment is invisible to the unaided eye. In scanning electron microscopy at 10,000-100,000X, the coating has few discernible features other than those of the substrate.

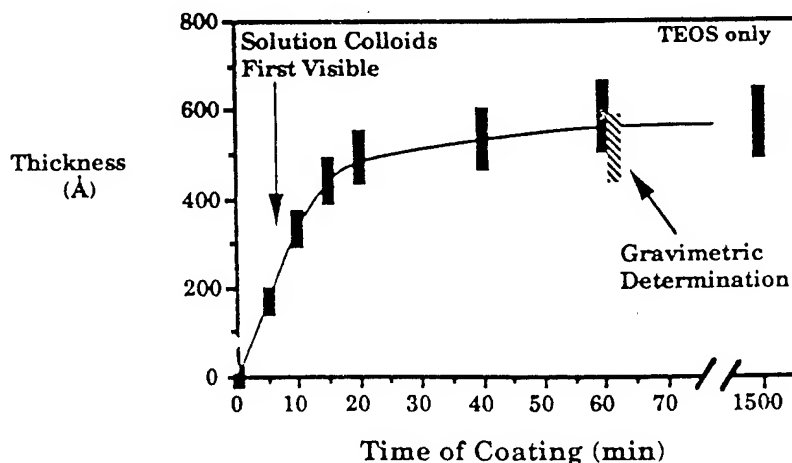


Figure 2. Coating thickness by ellipsometry as a function of the time that aluminum samples (2000Å thick on glass) were immersed in the reacting solution of ethanol, water, concentrated ammonium hydroxide and TEOS.

The corrosion protection afforded by the isotropic coating was quantified in several ways. The simplest method involved analysis of the mirror-like evaporated metal samples described above. The time

necessary for 1000Å of aluminum to corrode and become transparent is recorded (Table 1). It is evident from the data that these coatings do provide significant protection to the surfaces of aluminum and iron. In each case, the rate of corrosion has been reduced by a factor of 150-2000. Similar protection can be obtained on steel and aluminum alloy coupons.

Table 1. Corrosion protection from sol-gel coatings

Sample	Time (min) to corrode in <u>0.1 N NaOH</u>	Time (min) to corrode in <u>0.5 N HCl</u>
Untreated Aluminum (1000 Å)	3	420
Aluminum with 1 coat	1500	74,880
Aluminum with 2 coats	1500-2000	
Aluminum with 20 coats	2200	

Sample	Time (min) to corrode in buffered <u>water, pH 3</u>
Untreated iron (200Å)	2
Iron with 1 coat	1000-4000

The properties of the coating can be changed by varying the amounts and types of ingredients used and the reaction conditions. Figure 3 shows a plot of the thickness of the resulting coating as a function of the amount of TEOS present. As the amount of TEOS increases, the thickness of the coating increases in a straightforward manner. This result is consistent with the theory that the coating is limited in thickness by the availability of silane monomers in the solutions. These monomers are used up by the reaction with the substrate and by reaction to form colloids in solution. If the number of nucleation sites in solution is relatively unaffected by the TEOS concentration, the thickness of the surface coating and the diameter of the solution colloids should increase as the amount of TEOS increases.

This hypothesis is also consistent with the effect observed when the colloids are allowed to form partially before immersing the sample in the solution. In this case most of the monomers are no longer available for reaction with the surface; only pre-colloids, and these would be less likely to attach to the surface in a well-packed manner to form an integral coating. As the length of time between formulation of the solution and the

immersion of the substrate increases, the thickness of the coating decreases (Fig. 4).

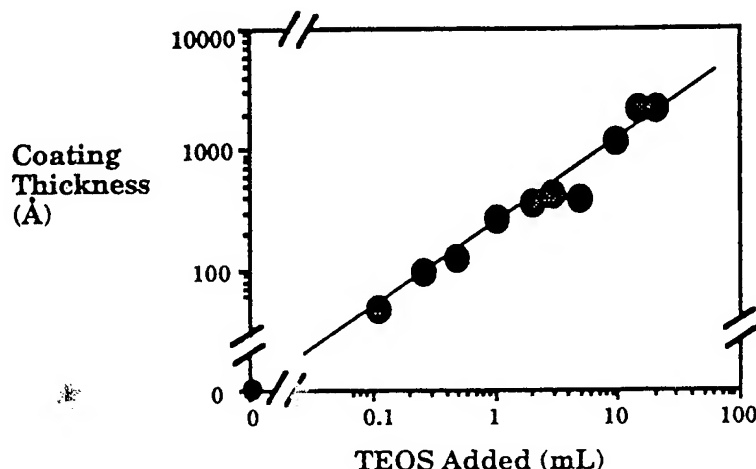


Figure 3. Coating thickness by ellipsometry as a function of the amount of TEOS added to the reacting solution. Aluminum samples (2000Å) were coated for 24 hours and baked dry at 100 °C for 60 minutes prior to testing.

Remarkably, the ability of the coatings to prevent corrosion of the underlying substrate does not seem to be directly related to the thickness of the coating. Figure 5 shows a plot of the time necessary to corrode 2000Å of aluminum in aqueous base after being treated with coating solutions containing various levels of TEOS. Protection increases slightly as the level of TEOS is increased from 0 to 0.003 ml. Between 0.003 and 0.01 ml of TEOS, the corrosion protection increases by a factor of nearly 100. Additional TEOS seems to do little to further increase the corrosion protection. In fact the maximum corrosion protection is reached while the coating is significantly less than 100Å thick.

It is thought that the corrosion protection of aluminum is actually being provided by a layer of aluminosilicate formed by reaction of TEOS with the native oxide on the aluminum. Further coating material (SiO_2) that builds up above the aluminosilicate layer provides little additional protection. This hypothesis is supported by data obtained by corrosion testing of samples with multiple coatings and ESCA.

The application of multiple coats does not significantly increase the corrosion protection over that offered by one coat. (Table 1) Even a sample with 20 coats that is thick enough (1 mm) to offer significant scratch and wear resistance has a corrosion resistance similar to that of a sample with one coat. If the entire coating had been acting as a barrier, one would expect that 20 coats would be significantly more effective than

one coat. If it is a layer of aluminosilicate at the metal surface that is actually providing the protection, it is not surprising that additional silicon dioxide above it does not improve the protection.

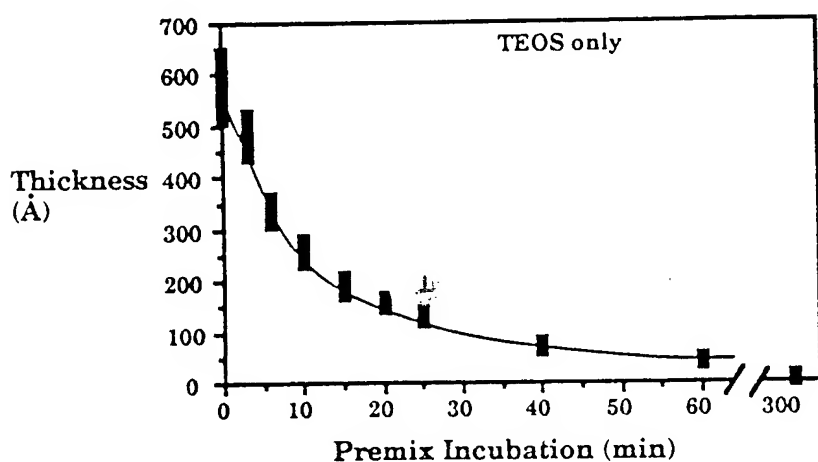


Figure 4. Coating thickness (by ellipsometry) as a function of the time between mixing the solution and the immersion of the substrate. Aluminum samples (2000Å on glass) were coated for 24 hours and baked dry at 100°C for 1 hour prior to testing.

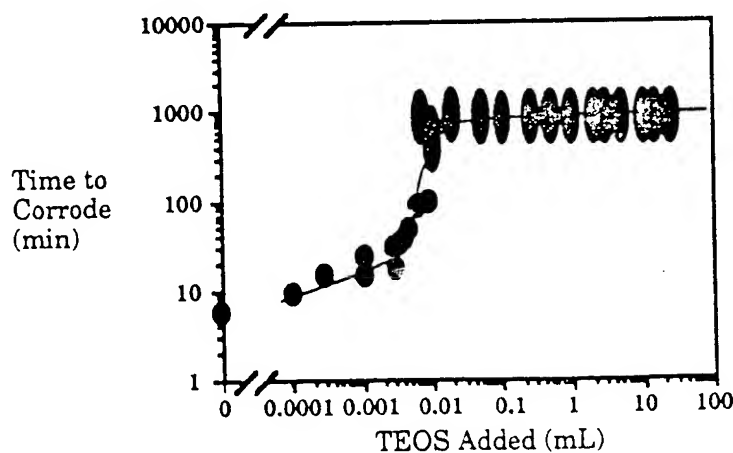


Figure 5. Corrosion protection as a function of the amount of TEOS added to the reaction solution. Aluminum samples (2000Å on glass) were coated for 24 hours and baked at 100°C for 1 hour prior to corrosion testing in 0.1 N NaOH.

ESCA analysis also supports the contention that corrosion protection is provided by the aluminosilicate layer. Figure 6 shows the ESCA analysis of the coated surfaces used in the corrosion testing of Figure 5. When very thin SiO₂ coatings are applied, the binding energies of the silicone atoms on the surface are similar to those obtained for the

aluminosilicate materials but not to those for silica gel [12]. As the amount of TEOS is increased, the average binding energy gradually shifts toward that of silica gel. The corrosion protection is essentially at its maximum when the surface begins to look like silica gel.

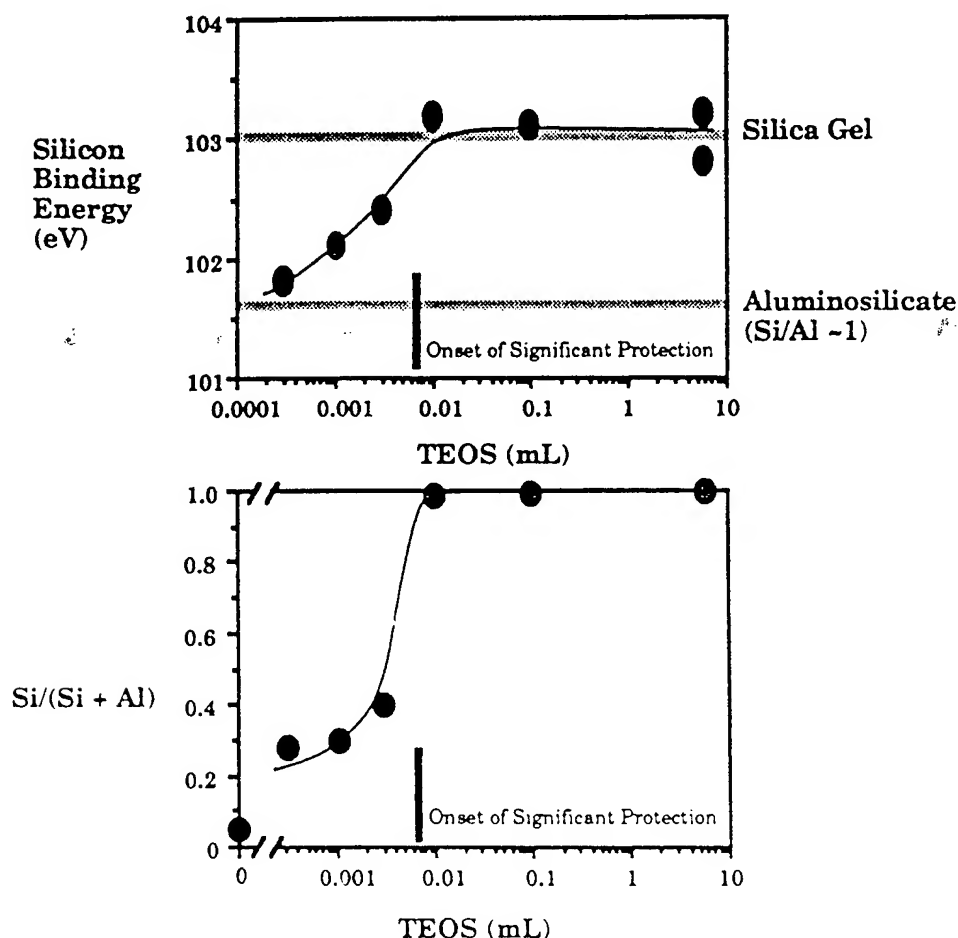


Figure 6. ESCA analysis of aluminum surfaces coated with various amounts of TEOS as in Figure 5. Top: Silicon binding energy corrected for charging by assigning the adventitious carbon peak a value of 284.6 eV. The binding energies obtained for a typical aluminosilicate and for silica gel are shown for reference. Bottom: The atomic proportion of silicon to the total of aluminum and silicon.

Likewise, Figure 6 shows the relative abundance of silicon on the aluminum surface as the coating is applied. In this case, the maximum corrosion protection has been reached in samples where the aluminum is just covered by the silica. Again, significant quantities of silica on top of the aluminosilicate do not contribute to corrosion protection. The mechanism by which this aluminosilicate layer provides protection may

be similar to that afforded by traditional silicate coatings that have been used in anodic protection of aluminum surfaces [13].

The addition of certain organic moieties to the ceramer coating might be expected to lead to better adhesion between organic adhesives and the coating, just as traditional adhesion promoters function. One drawback, however, is that the addition of many organic species leads to a decrease in the corrosion protection of the coating. If one could design coatings where little or no organics were incorporated until an effective barrier had fully formed, one might avoid the problem of the presence of organics within the coating, reducing the corrosion protection. Obviously such layered structures can be formed in multiple steps, but from an engineering or processing perspective, this would be much less desirable than producing a layered effect in one step.

The key to formation of functionally gradient coatings in a single step is controlling the reactivity of the various components in the reaction. The silanes that react more quickly coat the substrate first and as time proceeds the coating forms from less and less reactive materials. One then only needs to control the reactivity to such an extent that the desired materials end up in the desired places in the coating.

There are three methods of controlling the reactivity of metal alkoxides in solution. The first is to change the metal. Titanium alkoxides are, for example, much more reactive than silicon alkoxides. A second method is to influence the reactivity of the metal alkoxide through the nature of the non-alkoxy groups attached to the metal. Methyltriethoxysilane is less reactive than tetraethoxysilane by a factor of more than 100. This method of reducing reactivity is limited because of the usual reason for the incorporation of organic groups is to effect the physical properties of the coating not just the process.

The final way of controlling the reactivity of these materials is through the alkoxy group itself. Larger alkoxy groups are less reactive, both for steric and electronic reasons. One can order the reactivity of alkoxy groups as follows:

methoxy > ethoxy > isopropoxy > s-butoxy

In practice one can gain a measure of the reactivity of various silanes by mixing them into a reaction solution and observing how long it takes for colloids to form. Using this information, one could, for example, control the relative reactivity of a vinyl silane to a methyl silane by having different alkoxy groups on them. To form a coatings with methyl silane in the lower regions of the coating and vinyl silanes near the surface, one could use methyltrimethoxysilane and vinyltriethoxysilane.

In addition to the ability to use various simple alkoxy structures, one can obtain further control by using other ligands attached to the metal atom such as acetoxy, phenoxy, halides, hydrides and hydroxyls.

Applications

There are, of course, a wide range of potential applications for such anisotropic coatings. Combination of corrosion protection and adhesion promotion is a case where a single isotropic coating cannot provide the same benefits as anisotropic or layered coating. Adhesion promotion by aminosilanes is a widely practiced technology, and 3-aminopropyltriethoxysilane is an effective adhesion promoter for bonding aluminum substrates with a urethane adhesive (while TEOS alone is not).

Conversely, coatings derived from TEOS provide significant corrosion protection while those derived from aminosilane do not. In fact, in mixed coatings of TEOS and aminosilane, it is most important for the N/Si atomic ratio to be low (<0.05) for optimum corrosion protection and high (>0.1) for optimum adhesion promotion. If one makes coatings where the lower regions are primarily derived from TEOS (forming a corrosion resistant barrier) and the upper regions are primarily aminosilane (promoting adhesion) then one can get both properties optimized at once, a feat not possible with a single isotropic coating.

Table 2 illustrates the dramatic effect of silane reactivity and its distribution within the coating on adhesion and corrosion. TEOS is more reactive than 3-aminopropyltriethoxysilane which is more reactive than TBOS (tetrabutoxysilane). In formulations where the aminosilane is not at the surface of the coating, adhesion is poor. In formulations where the aminosilane forms the base of the coating, corrosion protection is poor. In the formulation of TEOS and 3-aminopropyltriethoxysilane, corrosion protection is conferred by the TEOS and the aminosilane is at the surface to provide adhesion promotion.

Conclusions

Anisotropic, multilayered coatings can be formed by taking advantage of the relative reactivity of monomers present in sol-gel reactions. These anisotropic coatings permit the properties of different regions of a coating to be independently optimized for different functions. Anisotropic coatings can, for example, provide corrosion protection as effectively as silicate only coatings and provide adhesion promotion as effectively as organically modified coatings. There are instances where underbond corrosion must be prevented in order to attain maximum environmental resistance in bonding to metal. In these cases, both

adhesion promotion and corrosion prevention must be simultaneously optimized, as is obtained from anisotropic coatings.

Table 2. Bond strengths of joints made from aluminum alloy coupons with various coatings using a two part commercial urethane adhesive, Tyrite 7520. The joints were exposed to boiling water for 2 hours prior to testing. The table also shows corrosion rates for evaporated aluminum samples with similar coatings in aqueous base. Highlighted formulation shows both properties optimized.

<u>Coating Ingredients</u>	<u>Bond Strength (kg/in²)</u>	<u>Corrosion Rate</u>
None	15	1 (by definition)
TEOS only	0	0.002
Aminosilane only	475	0.6
TEOS + Aminosilane	620	0.002
TBOS + Aminosilane	75	0.01
TEOS + Aminosilane + TBOS	30	0.003
<u>Two step coatings</u>		
TEOS, then Aminosilane	580	0.002
Aminosilane, then TEOS	0	0.3

References

- 1 R. Roy, *Science*, **238**, 1664 (1987)
- 2 H. Schmidt, H. Scholze and A. Kaiser, *J. Non-Cryst. Solids*, **63**, 1, (1984)
- 3 H. Schmidt and H. Scholze, in *Glass - Current Issues*, A. F. Wright and J. Dupuy (eds.) p. 263, Martinus Nijhoff, Boston (1985).
- 4 H. -H. Huang and G. L. Wilkes, *Polym. Bull.*, **18**, 455 (1987); H. -H. Huang, B. Orler and G. L. Wilkes, *ibid.*, **14**, 557 (1985); H. -H. Huang, B. Orler and G. L. Wilkes, *Macromolecules*, **20**, 1322 (1987).
- 5 B. Seiferling and H. Schmidt, *Mater. res. Soc. Symp. Proc.*, **73**, 739 (1986).
- 6 D. Ravaine, A. Seminel, Y. Charbouillot and M. Vincens, *J. Non-Cryst. Solids*, **82**, 210 (1986).
- 7 D. R. Ulrich, *Chemtech*, 242 (1988).
- 8 S. R. Holmes-Farley and L. C. Yanyo, *Ultra-Thin, Uniform Sol-Gel Coatings*, U.S. Patent 5,175,027, Dec. 29, 1992.
- 9 S. R. Holmes-Farley, L. C. Yanyo and Anna M. Thuer, *Method for Metal Bonding*, U.S. Patent 5,139,601, Aug. 18, 1992.
- 10 S. R. Holmes-Farley and L. C. Yanyo, *Layered Sol-Gel Coatings*, U.S. Patent 5,182,143, Jan. 26, 1993.
- 11 F. L. McCrackin, E. Passaglia, R. R. Stromberg and H. L. Steinberg, *J. Res. (NBS)*, **67A**, 363 (1963).
- 12 C. D. Wagner, W. W. Riggs, L. E. Davis, J. R. Moulder and G. E. Muilenberg, *Handbook of X-ray Photoelectron Spectroscopy*, Perkin Elmer, Eden Prairie, MN (1979).
- 13 G. Wranglen, *An Introducton to Corrosion and Protection of Metals*, p. 169, Chapman and Hall, New York, (1985).

**TRI-SERVICE CONFERENCE
ON CORROSION**

21 - 23 JUNE 1994

ATTENDANCE LIST

BLANK

PROF JAN D ACHENBACH
NORTHWESTERN UNIV
R R MCCORMICK SCHL OF
ENGRG & APPLIED SCI
2137 N SHERIDAN RD
EVANSTON IL 60208-3020
(708)-491-5527
FAX: (708)-491-5227

MR DAN AGOSTINI
MKI SYSTEMS
STE 1000
6564 LOUISDALE CT
SPRINGFIELD VA 22150-0001
(703)-719-7200
FAX: (703)-719-9302

DR PETER ANGELL
CTR FOR ENVIRON BIOTECH
STE 300
10515 RESEARCH DR
KNOXVILLE TN 37932-2575
(615)-974-8014
FAX: (615)-974-3086

MS DENISE M AYLOR
MATLS ENGR
NAVAL SURFACE WARFARE CTR
CODE 613
CORROSION BRANCH
ANNAPOLIS MD 21402-5067
(410)-267-3151
FAX: (410)-267-4885

DR JOHN H BEATTY
CORR SCI TECH LDR
US ARMY RES LAB
AMSRL-MA-MA
WATERTOWN MA 02172-0001
(617)-923-5212
FAX: (617)-923-5219

MR MALCOLM J BENFER
ROYAL AUSTRALIAN AIR FORCE
350 ST KILDA RD T-6
SQD LDR
MELBOURNE VICTORIA AUSTRALIA-3004

MR BRADLEY BIEBERICH
NAVAL SURFACE WARFARE CTR
CODE 613
3 A LEGETT CIRCLE
ANNAPOLIS MD 21402-5067
(410)-267-2191
FAX: (410)-293-4885

DR VINOD S AGARWALA
RES METALLURGIST
NAVAL AIR WARFARE CTR
CODE 6062
JACKSONVILLE RD
WARMINSTER PA 18974-0591
(215)-441-1122
FAX: (215)-441-1925

MR M H ALLEN
DEXTER AERO MATL DIV
4001 RIVERDALE CT
ATLANTA GA 30337-6018
(404)-994-7575
FAX: (404)-994-7466

MR CHRIS G ATHANASOPOULOS
SPRAYLAT CORP
1701 E 122ND ST
CHICAGO IL 60633-0001
(708)-698-7535
FAX: (708)-698-7536

MR LANCE E L BALLARD
UNIV OF ILLINOIS
BOX 12-1
505 S MATTHEWS
URBANA IL 61801-0001
(217)-333-3897
FAX: (217)-244-8068

DR HAROLD D BEESON
NASA-WSTF
PO DRAWER MM
M/S RF
LAS CRUCES NM 88004-0001
(505)-524-5542
FAX: (505)-524-5260

DR RAMESH C BHARDWAJ
PRIN SCIENTIST
ROCKWELL INTL
PO DRAWER MM
LAS CRUCES NM 88004-0001
(505)-524-5686
FAX: (505)-524-5260

MR JOHN C BRAUSCH
US AIR FORCE
WL/MLSA BLDG 652 STE 1
2179 TWELFTH ST
WRIGHT-PATTERSON AFB OH 45433-7718
(513)-255-5117
FAX: (513)-476-4600

MS ANGELA BROWN
BOEING DEF SPACE GRP
M/S 82-32
PO BOX 3999
SEATTLE WA 98124-2499
(206)-773-2647
FAX: (206)-773-4946

MR RICHARD BROWN
UNIV OF RHODE ISLAND
KINGSTON MI 02881-0805
(401)-792-2655
FAX: (401)-782-1180

MR WILLIAM CABE
ROCKWELL INTL CORP
M/S ZK-36
PO BOX 21105
KENNEDY SPACE CTR FL 32899-0001
(407)-861-4577
FAX: (407)-861-0908

MR STEVEN F CARR
USAMICOM
AMSMI-RD-ST-GM
REDSTONE ARSENAL AL 35898-5247
(205)-876-7472
FAX: (704)-842-1359

DR FRANK CHANG
US ARMY RES LAB
AMSRL-EMM
ARSENAL ST
WATERTOWN MA 02172-0001
(617)-923-5168

COL RONALD CHANNELL
DEPUTY DIR
US AIR FORCE
WL/ML BLDG 653
2977 P ST STE 1
WRIGHT-PATTERSON AFB OH 45433-7734
(513)-255-2738
FAX: (513)-476-7734

DR ROBERT N CHIANG
SPRAYLAT CORP
AEROSPACE COATINGS DIV
1701 E 122ND ST
CHICAGO IL 60633-2362
(312)-646-5900
FAX: (312)-646-3743

MS CAROLE COLCLOUGH
US AIR FORCE
WL/MLSA
2179 12TH ST
WRIGHT-PATTERSON AFB OH 45433-0001
(513)-255-5117

MR THOMAS D COOPER
CHF SYS SUPPORT DIV
US AIR FORCE
WL/MLS BLDG 652
2179 TWELFTH ST STE 1
WRIGHT-PATTERSON AFB OH 45433-7718
(513)-255-2282
FAX: (513)-476-4419

DR WALTER G COX
NAVAL SURFACE WARFARE CTR
10901 NEW HAMPSHIRE
CODE 433
SILVER SPRING MD 20903-5000
(301)-394-1519
FAX: (301)-394-4062

MR ROBERT CUMMINGS
US AIR FORCE
255 2ND ST STE 122
ROBINS AFB GA 31098-1637
(912)-926-4489

MR JIM DANTE
NATL INST OF STDS & TECH
BLDG 223 RM B254
QUINCE ORCHARD RD
GAITHERSBURG MD 20899-0001
(301)-975-2057
FAX: (301)-926-7975

DR STEPHEN C DEXTER
UNIV OF DELAWARE
COLL OF MARINE STUDIES
700 PILOTTOWN RD
LEWES DE 19958-1298
(302)-645-4261
FAX: (302)-645-4007

MR LUC DOAN
US NAVY
NADEP N ISLAND
BLDG 469 CODE 344
SAN DIEGO CA 92135-0001
(619)-545-9753
FAX: (619)-545-7810

MR MARK T DOERFLER
PURDUE UNIV
M/S AAE
1282 GRISSOM HALL
W LAFAYETTE IN 47907-1282
(317)-494-9101
FAX: (317)-494-0307

MR PATRICK G DOYLE
NAVAL AIR WARFARE CTR
SYS REQ DEPT
CODE SR32
LAKEHURST NJ 08733-5100
(908)-323-1281
FAX: (908)-323-7228

MR DENNIS L DULL
BOEING DEF & SPACE GRP
M/S 82-32
PO BOX 3999
SEATTLE WA 98124-2499
(206)-773-8438
FAX: (206)-773-4946

MS LAURA S ELLIOTT
PURDUE UNIV
CTR FOR NUM DATA ANALYSIS
AND SYNTHESIS
1293 POTTER ENGRG CTR
W LAFAYETTE IN 47907-1293
(317)-494-1873
FAX: (317)-494-2351

MR WILLIAM L ELMQUIST
TECH APPL GROUP INC
4957 10TH AVE SOUTH
GRAND FORKS ND 58201-0001
(701)-746-1818
FAX: (701)-746-1910

MR ALAN FABISZEWSKI
NAVAL AIR WARFARE CTR
AIRCRAFT DIV
CODE 6062
65 W S REET RD
WARMINSTER PA 18974-000
(215)-441-2811
FAX: (215)-441-1925

MR VICTOR E FERRELL
LORD CORP
2000 W GRANDVIEW BLVD
PO BOX 10038
ERIE PA 16514-0038
(814)-868-3611
FAX: (814)-864-8066

MR STEVEN D FLAHERTY
USE CORP
2550 HUNTINGTON AVE
ALEXANDRIA VA 22303-0001
(703)-329-4443
FAX: (703)-960-3748

MR DAVID R FREDERICK
US AIR FORCE
OO-ALC/TIELM
7278 4TH ST
HILL AFB UT 84056-5205
(801)-775-2992
FAX: (801)-775-2628

DR HOWARD GABEL
INNOVATIVE TECH INC
21065 FREEDOM DR
CUPERTINO CA 95014-0001
(408)-973-0433
FAX: (408)-973-8972

DR RICHARD P GANGLOFF
UNIV OF VIRGINIA
DEPT MATERIALS SCIENCE/ENGR
THORNTON HALL
CHARLOTTESVILLE VA 22903-2442
(804)-982-5782
FAX: (804)-982-5799

TRACY GARRETT JR
DEFT COATINGS
17451 VON KARMAN AVE
IRVINE CA 92714-0001
(800)-544-3338
FAX: (714)-474-7269

MR DAVID GLADD
US ARMY PEO
AMSTA-CMB-C
WARREN MI 48397-5000
(313)-574-8951
FAX: (313)-574-7859

DR L M GOLD
DEXTER SPECIALTY COAT DIV
PO BOX 5695
GREENVILLE SC 29606-0001
(803)-277-1870
FAX: (803)-277-3244

MR SCOTT D GORDON
LORD CORP
2000 W GRANDVIEW BLVD
PO BOX 10038
ERIE PA 16514-0038
(814)-868-3611
FAX: (814)-864-8066

MR ROBERT G GOULDING
USAF RESERVES
5864 PRICE AVE
MCCLELLAN AFB CA 95652-1270
(916)-643-1575
FAX: (916)-643-1604

DR ALTEN F GRANDT JR
PURDUE UNIV
AERO & ASTO
1282 GRISSOM HALL
W LAFAYETTE IN 47907-1282
(317)-494-5141
FAX: (317)-494-0307

MR JI-DONG GU
HARVARD UNIV
DIV OF APPL SCI
40 OXFORD ST
CAMBRIDGE MA 02138-0001
(617)-496-4742
FAX: (617)-495-5672

MS KIM GUDMUNDSON
NAVAL AVIATION DEPOT
CODE 34400 BLDG 469
N S N ISLAND
SAN DIEGO CA 92135-7058
(619)-545-9759
FAX: (619)-545-7810

MR HARVEY HACK
NAVAL SURFACE WARFARE CTR
CARDEROCK DIV ANNAPOLIS DET
3A LEGGETT CIRCLE
ANNAPOLIS MD 21402-5067
(410)-267-3502

MR C HANDSY
US ARMY TACOM
WARREN MI 48397-5000

MR AL HARTLINE
BRUSH WELLMAN
17876 ST CLAIR AVE
CLEVELAND OH 44110-0001
(216)-383-4003
FAX: (216)-383-4005

DR FRED HEDBERG
US AIR FORCE
AFOSR/NC
110 DUNCAL AVE STE B115
BOLLING AFB DC 20332-6448
(202)-767-4963
FAX: (202)-767-4961

MR DON HILEMAN
NAVAL SURFACE WARFARE CTR
ORDSTA
CODE 209A
5403 SOUTHSIDE DR
LOUISVILLE KY 40214-5000
(502)-364-5231
FAX: (502)-364-5354

MR STEVE HOBAICA
NAVAL SURFACE WARFARE CTR
CODE 641
3A LEGGETT CIRCLE
ANNAPOLIS MD 21402-0001
(410)-293-2751
FAX: (410)-293-2839

MR MARK INGLE
OCEAN CITY RES CORP
M/S 204 E
4805-B EISENHOWER AVE
ALEXANDRIA VA 22304-0001
(703)-212-9006
FAX: (703)-212-9017

MR HAROLD S ISSEN
LOCKHEED SPACE OPS CO
M/S L50-232
1100 LOCKHEED
TITUSVILLE FL
(407)-861-7101
FAX: (407)-861-7241

MR TIM JACKOVIC
NAVAL SURFACE WARFARE CTR
CODE 613
3A LEGGETT CIRCLE
ANNAPOLIS MD 21402-5067
(410)-293-3754
FAX: (410)-297-4885

MS JULIE A JACKS
MARCORSYSCOM
COMMANDER
PSE-P STE 315
2033 BARNETT AVE
QUANTICO VA 22134-5010
(703)-640-4551
FAX: (703)-640-3432

KUMAR V JATA
US AIR FORCE
WL/MLSA
WRIGHT-PATTERSON AFB OH 45433-7718
(513)-255-3623
FAX: (513)-476-4600

DR CHRIS J JOHNSON
BOEING DEF & SPACE GRP
M/S 8R-15
PO BOX 3999
SEATTLE WA 98124-0001
(206)-773-9299
FAX: (206)-773-2282

DR ROBERT L JONES
NAVAL RESEARCH LAB
CODE 6170
4555 OVERLOOK AVE SW
WASHINGTON DC 20375-5342
(202)-767-2632
FAX: (202)-767-3321

DR WALTER F JONES
PROG MGR
US AIR FORCE
AFOSR/NA STE B-115
110 DUNCAN AVE
BOLLING AFB DC 20332-0001
(202)-767-0470
FAX: (202)-767-4988

DR JOANNE JONES-MEEHAN
NAVAL SURFACE WARFARE CTR
CODE R301
10901 NEW HAMPSHIRE AVE
SILVER SPRING MD 20903-5640
(301)-394-4839
FAX: (301)-394-4841

MR JOHN JUSKO
US AIR FORCE
OO-ALC-TIELM
7278 4TH ST
HILL AFB UT 84056-5205
(801)-777-9409
FAX: (801)-775-2628

MR MICHAEL KANE
US ARMY RES LAB
AMSRL-MA-MA
ARSENAL ST
WATERTOWN MA 02172-0001
(617)-923-5212

MR TOM KEARNEY
COURTAULDS AEROSPACE
26 W 119 TOMAHAWK DR
WHEATON IL 60187-0001
(708)-668-1912
FAX: (708)-668-1964

MR RICHARD C KINZIE
US AIR FORCE
STE 122 WR-ALC/CNC
255 2ND ST
ROBINS AFB GA 31098-1637
(912)-926-3284
FAX: (912)-926-6619

DR GERHARDUS M KOCH
CC TECHNOLOGIES
2704 SAWBURY BLVD
COLUMBUS OH 43235-0001
(614)-761-1214
FAX: (614)-761-1633

LT DERIC V KRAXBERGER
US AIR FORCE
OC-ALC/TIETR
STE SAF66A
3001 STAFF DR
TINKER AFB OK 73145-3040
(405)-736-5015
FAX: (405)-736-5431

JIA-JING LEE
UCLA
MANE DEPT 48-121 ENGRG IV
405 HILGARD AVE
LOS ANGELES CA 90024-1597
(310)-825-2447
FAX: (310)-206-4107

DELIN LI
VANDERBILT UNIV
24TH AVW S AND GARLAND
RM 101
NASHVILLE TN 37235-0001
(615)-343-3052
FAX: (615)-343-6687

MR GEORGE J LICINA
STRUCTURAL INTEGRITY ASSOC
STE 145
3150 ALMADEN EXPRESSWAY
SAN JOSE CA 95118-0001
(408)-978-8200
FAX: (408)-978-8964

N LINDSEY
NAVAL SURFACE WARFARE CTR
WHITE OAK DETACHMENT
ELECTROCHEMISTRY BRCH
CODE R33
SILVER SPRING MD 20903-5000

DR BRENDA J LITTLE
NAVAL RESEARCH LAB
BLDG 1105 RM D415
STENNIS SPACE CENTER MS 39529-5004
(601)-688-5494
FAX: (601)-688-5379

MR JEFFREY A LOY
ESSI
2600 MCCORMICK DR
CLEARWATER FL 34619-0001
(813)-726-0966
FAX: (813)-725-1728

SHAHRAM MALEKPOUR
MATLS ENGR
CORPUS CHRISTI ARMY DEPOT
MAT POL BR (FXA00)
308 CREACY ST
CORPUS CHRISTI TX 78419-5260
(512)-939-3688
FAX: (512)-937-1152

PROF FLORIAN MANSFELD
UNIV OF S CALIFOR A
M/S 0241
3651 WATT WAY
LOS ANGELES CA 90089-0241
(213)-740-4428
FAX: (213)-740-7797

DR AZZAM MANSOUR
NAVAL SURFACE WARFARE CTR
CODE R34 BLDG 30-213
10901 NEW HAMPSHIRE AVE
SILVER SPRINGS MD 20903-5000
(301)-394-3480
FAX: (301)-394-4472

MR JOSEPH MARTINEZ JR
NAVAL AVIATION MAINT OFC
BLDG 446B CMDG OFFICER
NAVAL AVIATION MAIN OFC
PATUXENT RIVER MD 20670-5446
(301)-826-7934

MS DONNA MAYTON
ARINC
M/S 1-203
2551 RIVA RD
ANNAPOLIS MD 21401-0001
(410)-266-4955

MR DAVID MCCARTHY
MUNTERS CARGOCAIRE
79 MONROE ST
PO BOX 640
AMESBURY MA 01913-0001
(800)-843-5360
FAX: (508)-388-4556

MR DAVID C MCCLURG
MILES INC
BLDG 8
MOBAY RD
PITTSBURGH PA 15205-9741
(412)-777-4963
FAX: (412)-777-2940

MR STEPHEN M MEIER
SR METALLURGIST
NAVAL SURFACE WARFARE CTR
CODE 3120A3 BLDG 1576
INDIAN HEAD MD 20640-5035
(301)-743-4528
FAX: (301)-743-4153

MR HAROLD T MICHELS
LAQUE CTR FOR CORROS TECH INC
HWY 76 & AUDITORIUM CIRCLE
WRIGHTSVILLE BEACH NC 28480-0001
(910)-256-2271
FAX: (910)-256-9816

PROF RALPH MITCHELL
HARVARD UNIV
DIV OF APPL SCI
PIERCE HALL
CAMBRIDGE MA 02138-0001
(617)-495-2846
FAX: (617)-496-1471

DR JOHN N MURRAY
NAVAL SURFACE WARFARE CTR
CARDEROCK DIV
CODE 613
3A LEGGETT CIRCLE
ANNAPOLIS MD 21402-5067
(410)-267-3151
FAX: (410)-293-4885

MR THOMAS NAGUY
MATLS ENGR
US AIR FORCE
WL/MLSA BLDG 652 RM 55
2179 TWELFTH ST STE 1
WRIGHT-PATTERSON AFB OH 45433-7718
(513)-255-5117
FAX: (513)-476-4600

LCDR MICHAEL A NEUSSL
US COAST GUARD
USCG ARSC
ELIZABETH CITY NC 27909-5001
(919)-335-6556
FAX: (919)-335-6463

MR CHET OGRABISZ
MKI SYSTEMS
STE 1000
6564 LOISDALE CT
SPRINGFIELD VA 22150-2205
(703)-719-7200
FAX: (703)-719-9302

MR WILLIAM PALDINO
EM CORP
ONE JOHN DOWNEY DR
NEW BRITAIN CT 06051-0001
(203)-224-9148
FAX: (203)-224-9172

MR BRIAN F PLACZANKIS
US ARMY RES LAB
AMSRL-MA-CC
ARSENAL ST
WATERTOWN MA 02172-0001
(617)-923-5198
FAX: (617)-923-5219

MS KAREN M POOLE
NAVAL SURFACE WARFARE CTR
CODE 641
3A LEGGETT CIRCLE
ANNAPOLIS MD 21402-5067
(410)-293-2275
FAX: (410)-293-3052

DR BRUCE G POUND
SRI INTL
MATERIALS RES LAB
333 RAVENSWOOD AVE
M/S PS323
MENLO PARK CA 94025-3493
(415)-859-5527
FAX: (415)-859-3678

MR DAVID F PULLEY
NAVAL AIR WARFARE CENTER
PO BOX 5152
CODE 6062
WARMINSTER PA 18974-0591
(215)-441-1904
FAX: (215)-441-1925

DR DASARA V RATHNAMMA
RES CHEMIST
NAVAL SURFACE WARFARE CTR
CODE 642
3A LEGGETT CIRCLE
ANNAPOLIS MD 21402-5067
(410)-293-2677
FAX: (410)-293-2839

MR CHRIS B RAWLINS
ROCKWELL INTL CORP
M/S ZK-36
PO BOX 21105
KENNEDY SPACE CTR FL 32815-0001
(407)-861-4596
FAX: (407)-861-0908

MR RONALD W REDFERN
HQ MARINE CORPS
3033 WILSON BLVD
ARLINGTON VA
(703)-696-1059
FAX: (703)-696-1079

DR ROBERT R REEBER
US ARMY
PO BOX 12211
RES TRIANGLE PARK NC 27709-0001
(919)-549-4318

MR ROBERT R RENNELL
ARINC
STE 500A
5600 LIBERTY PKWY
MIDWEST CITY OK 73110-2833
(405)-739-0939
FAX: (405)-739-0003

MR WILLIAM RHINESMITH
ROCKWELL INTL CORP
M/S ZK36
PO BOX 21105
KENNEDY SPACE CTR FL 32815-0001
(407)-861-4594
FAX: (407)-861-0908

MR RICHARD W RUSSELL
NASA
TV-PEO-12
KENNEDY SPACE CTR FL 32899-0001
(407)-861-4168
FAX: (407)-867-3139

CHANDRA P SANKHLA
DOD INSPECTOR GENERAL
M/S ROOM 801
400 ARMY NAVY DR
ARLINGTON VA 22202-2884
(703)-614-6298
FAX: (703)-614-8542

MR KENNETH SEBEK
US AIR FORCE
OC-ALC/LACRA STE 2AC489D
3001 STAFF DR
TINKER AFB OK 73145-3019
(405)-736-3832

DR JOHN A SEDRIKS
PROG MGR
OFC OF NAVAL RES
M/S 332
800 N QUINCY ST
ARLINGTON VA 22217-5660
(703)-696-4402

DR BARBARA A SHAW
THE PENN STATE UNIV
DEPT OF ENGR SCIENCES
207 HOLLOWELL BLDG
UNIVERSITY PARK PA 16802-6804
(814)-865-7828
FAX: (814)-863-0490

MR GEORGE SHAW
US ARMY TACOM
AMSTA-QHS
WARREN MI 48397-5000
(313)-574-8738
FAX: (313)-574-8725

MS JOY M SIEJA
TRW
STE 115
1650 RESEARCH DR
TROY MI 48083-0001
(810)-689-6354
FAX: (810)-689-0488

MR JAMES A SMITH
US NAVY RES LAB
M/S 6314
4555 OVERLOC AVE SW
WASHINGTON DC 20375-5000
(202)-767-2784
FAX: (202)-404-7297

MR STEPHEN J SPADAFORA
NAVAL AIR WARFARE CTR
M/S 6062
PO BOX 152
WARMINSTER PA 18974-0591
(215)-441-2704
FAX: (215)-956-4141

MR EUGENE A STOHRE
NAVMAR APPLIED SCI CORP
STE B-104
65 W ST RD
WARMINSTER PA 18974-0001
(215)-675-4900
FAX: (215)-972-0597

MR MARK R STOUT
NATL INST OF STDS & TECH
BLDG 223 RM B254
GAITHERSBURG MD 20899-0001
(301)-975-6025
FAX: (301)-926-7975

MR JOHN T STROPKI
BATTELLE
OC-ALC/EMV
505 KING AVE
COLUMBUS OH 43201-2693
(614)-424-5414
FAX: (614)-424-3457

DR TOSHIFUMI SUGAMA
BROOKHAVEN NATL LAB
DEPT OF APPLIED SCI
BLDG 526 SIXTH ST
PO BOX 5000
UPTON NY 11973-5000
(516)-282-4029
FAX: (516)-282-2359

MR EDWIN S TANKINS
NAVAL AIR WARFARE CTR
M/S 6063
STREET & JACKSONVILLE
WARMINSTER PA 18974-0001
(215)-441-2075
FAX: (215)-441-1773

MS KATIE THORP
UNIV OF DAYTON RES INST
300 COLLEGE PARK
DAYTON OH 45469-0168
(513)-255-1138
FAX: (513)-258-8075

MR ISHMAEL L VILLALVA
NAVAL AVIATION ENGRG SERVICE
NAS CECIL FIELD
BOX 152 NAS
JACKSONVILLE FL 32215-0152
(904)-778-6161
FAX: (904)-778-6480

MR DENNIS VORSE
LORD CORP
2000 W GRANDVIEW BLVD
PO BOX 10038
ERIE PA 16514-0038
(814)-868-3611
FAX: (814)-864-8066

DR MARIANNE WALCH
NAVAL SURFACE WARFARE CTR
CODE R301
15526 PLAID DR
SILVER SPRING MD 20903-5640
(301)-394-4839
FAX: (301)-394-4841

MR JAMES A WHITFIELD
NAVAL AVIATION DEPOT
CODE 35420 STOP 9
CHERRY POINT NC 28533-0001
(919)-466-7342

DR DOW WHITNEY
UNIV OF FLORIDA
DEPT OF SCI & ENGRG
123 RHINES HALL
GAINESVILLE FL 32611-2066
(904)-392-6687
FAX: (904)-392-6359

DR JOHN WIKSWO JR
VANDERBILT UNIV
STATION B
PO BOX 1807
NASHVILLE TN 37235-0001
(615)-322-2977
FAX: (615)-322-4977

MR SAM R WINTERS
ALLISON GAS TURBINE
M/S S-52
PO BOX 420
INDIANAPOLIS IN 46206-0420
(317)-230-5117
FAX: (317)-230-3356

MR RICHARD A WOLF SR
BOEING DEF & SPACE GRP
M/S K86-83
3801 S OLIVER
WICHITA KS 67277-7730
(316)-526-8820
FAX: (316)-523-2972

MR MERLE T WOLFF
US ARMY
WARREN MI 48347-5000
(810)-574-8834
FAX: (810)-574-6501

DR LYNN C YANYO
LORL CO P
THOMAS LORD RES CTR
405 GREGSON DR
CARY NC 27511-7900
(919)-469-2500
FAX: (919)-460-9648

MR THOMAS H YENTZER
US AIR FORCE
WR-ALC/TIEDM
ROBINS AFB GA 31098-0001
(912)-926-4489
FAX: (912)-926-6619

DR CHESTER ZABIELSKI
US ARMY RES LAB
AMSRL
WATERTOWN MA 02172-0001
(617)-923-5332
FAX: (617)-923-5219